

Springer Series in Optical Sciences 171

Kai-Erik Peiponen

J. Axel Zeitler

Makoto Kuwata-Gonokami *Editors*

Terahertz Spectroscopy and Imaging



Springer

Springer Series in Optical Sciences

Volume 171

Founded by

H. K. V. Lotsch

Editor-in-Chief:

W. T. Rhodes

Editorial Board:

Ali Adibi, Atlanta

Toshimitsu Asakura, Sapporo

Theodor Hänsch, Garching

Takeshi Kamiya, Tokyo

Ferenc Krausz, Garching

Bo A.J. Monemar, Linköping

Herbert Venghaus, Berlin

Horst Weber, Berlin

Harald Weinfurter, München

For further volumes:

<http://www.springer.com/series/624>

Springer Series in Optical Sciences

The Springer Series in Optical Sciences, under the leadership of Editor-in-Chief William T. Rhodes, Georgia Institute of Technology, USA, provides an expanding selection of research monographs in all major areas of optics: lasers and quantum optics, ultrafast phenomena, optical spectroscopy techniques, optoelectronics, quantum information, information optics, applied laser technology, industrial applications, and other topics of contemporary interest.

With this broad coverage of topics, the series is of use to all research scientists and engineers who need up-to-date reference books.

The editors encourage prospective authors to correspond with them in advance of submitting a manuscript. Submission of manuscripts should be made to the Editor-in-Chief or one of the Editors. See also www.springer.com/series/624

Editor-in-Chief

William T. Rhodes
School of Electrical and Computer Engineering
Georgia Institute of Technology
Atlanta, GA 30332-0250
USA
e-mail: bill.rhodes@ece.gatech.edu

Editorial Board

Ali Adibi
Georgia Institute of Technology
School of Electrical and Computer Engineering
Atlanta, GA 30332-0250
USA
e-mail: adibi@ee.gatech.edu

Toshimitsu Asakura
Hokkai-Gakuen University
Faculty of Engineering
1-1, Minami-26, Nishi 11, Chuo-ku
Sapporo, Hokkaido 064-0926, Japan
e-mail: asakura@eli.hokkai-s-u.ac.jp

Theodor W. Hänsch
Max-Planck-Institut für Quantenoptik
Hans-Kopfermann-Straße 1
85748 Garching, Germany
e-mail: t.w.haensch@physik.uni-muenchen.de

Takeshi Kamiya
Ministry of Education, Culture, Sports, Science
and Technology
National Institution for Academic Degrees
3-29-1 Otsuka Bunkyo-ku
Tokyo 112-0012, Japan
e-mail: kamiyatk@niad.ac.jp

Ferenc Krausz
Ludwig-Maximilians-Universität München
Lehrstuhl für Experimentelle Physik
Am Coulombwall 1
85748 Garching, Germany *and*
Max-Planck-Institut für Quantenoptik
Hans-Kopfermann-Straße 1
85748 Garching Germany
e-mail: ferenc.krausz@mpq.mpg.de

Bo A. J. Monemar
Department of Physics and Measurement Technology
Materials Science Division
Linköping University
58183 Linköping, Sweden
e-mail: bom@ifm.liu.se

Herbert Venghaus
Fraunhofer Institut für Nachrichtentechnik
Heinrich-Hertz-Institut
Einsteinufer 37
10587 Berlin, Germany
e-mail: venghaus@hhi.de

Horst Weber
Optisches Institut
Technische Universität Berlin
Straße des 17. Juni 135
10623 Berlin, Germany
e-mail: weber@physik.tu-berlin.de

Harald Weinfurter
Sektion Physik
Ludwig-Maximilians-Universität München
Schellingstraße 4/III
80799 München, Germany
e-mail: harald.weinfurter@physik.uni-muenchen.de

Kai-Erik Peiponen · J. Axel Zeitler
Makoto Kuwata-Gonokami
Editors

Terahertz Spectroscopy and Imaging

 Springer

Editors

Kai-Erik Peiponen
Department of Physics and Mathematics
University of Eastern Finland
Joensuu
Finland

Makoto Kuwata-Gonokami
Department of Physics
Graduate School of Science
The University of Tokyo
Bunkyo-ku, Tokyo
Japan

J. Axel Zeitler
Department of Chemical Engineering
and Biotechnology
University of Cambridge
Cambridge
UK

ISSN 0342-4111

ISSN 1556-1534 (electronic)

ISBN 978-3-642-29563-8

ISBN 978-3-642-29564-5 (eBook)

DOI 10.1007/978-3-642-29564-5

Springer Heidelberg New York Dordrecht London

Library of Congress Control Number: 2012942720

© Springer-Verlag Berlin Heidelberg 2013

This work is subject to copyright. All rights are reserved by the Publisher, whether the whole or part of the material is concerned, specifically the rights of translation, reprinting, reuse of illustrations, recitation, broadcasting, reproduction on microfilms or in any other physical way, and transmission or information storage and retrieval, electronic adaptation, computer software, or by similar or dissimilar methodology now known or hereafter developed. Exempted from this legal reservation are brief excerpts in connection with reviews or scholarly analysis or material supplied specifically for the purpose of being entered and executed on a computer system, for exclusive use by the purchaser of the work. Duplication of this publication or parts thereof is permitted only under the provisions of the Copyright Law of the Publisher's location, in its current version, and permission for use must always be obtained from Springer. Permissions for use may be obtained through RightsLink at the Copyright Clearance Center. Violations are liable to prosecution under the respective Copyright Law.

The use of general descriptive names, registered names, trademarks, service marks, etc. in this publication does not imply, even in the absence of a specific statement, that such names are exempt from the relevant protective laws and regulations and therefore free for general use.

While the advice and information in this book are believed to be true and accurate at the date of publication, neither the authors nor the editors nor the publisher can accept any legal responsibility for any errors or omissions that may be made. The publisher makes no warranty, express or implied, with respect to the material contained herein.

Printed on acid-free paper

Springer is part of Springer Science+Business Media (www.springer.com)

Preface

There is no commonly agreed definition of the upper and lower frequency limits of terahertz (THz) radiation. Its spectral range overlaps with the far-infrared at the higher frequency end and the microwave region at lower frequencies. Some authors refer to the range of 0.1–1.0 mm in wavelength as terahertz radiation while others extend this range to wavelengths as short as 30 μm .¹ The term thus refers to a relatively narrow part of the electromagnetic spectrum. Despite this narrowness, which it shares, for example, with visible light, terahertz radiation is of great importance in terms of fundamental research as well as in technology and the life sciences. And yet, while nobody would question the importance of research involving radiation such as visible light, until recently research into terahertz radiation has been relatively obscure.

There can be no doubt that the main reasons for the surge in interest in performing spectroscopy at terahertz frequencies were the development of ultrafast lasers and the discovery of the Auston switch in the 1970s. These led to a new generation of spectrometers in the early 1990s that were able to generate and detect pulses of coherent terahertz radiation with previously unprecedented ease and sensitivity. Today, most of the research in terahertz spectroscopy and imaging is carried out using such time-domain spectrometers. Terahertz time-domain spectroscopy (THz-TDS), therefore, is the main focus in this book; though of course other technologies, such as far infrared spectroscopy, remain of great importance and are discussed or referred to where appropriate. The book is structured into roughly three areas. In the first seven chapters, the technology and fundamental physics of terahertz spectroscopy are introduced. The following 13 chapters give a detailed overview of how terahertz radiation can be used to study a wide range of materials. The final three chapters provide a fascinating glimpse into

¹ Brüdermann, Hübers, and Kimmitt recently presented an introduction to the history of terahertz research as part of their monograph on terahertz techniques. Their book is an excellent general introduction with a lot of background information regarding the underlying technology. E. Brüdermann, H.-W. Hübers, and M. F. Kimmitt, *Terahertz Techniques* (Springer, Heidelberg, 2011), pp. 394.

future developments in the field, including physics at terahertz frequencies. Due to space constraints, it has been decided to omit from the present volume in-depth discussions of gas spectroscopy or applications in astronomy and astrophysics.

We are very fortunate in that we have been able to secure some of the leading experts in the field as contributors of chapters to this book. Our aim is to provide a representative, though by no means exhaustive, overview of the current state of research in terahertz spectroscopy and imaging. Terahertz spectroscopy has developed into a very active research community and we hope that this book will provide a go-to source of assistance for its new researchers as well as a reference for its more experienced members.

Joensuu, Cambridge and Tokyo

Kai-Erik Peiponen
J. Axel Zeitler
Makoto Kuwata-Gonokami

Contents

1	Generation and Detection of Terahertz Radiation	1
1.1	Broadband THz Pulse Generation and Detection	2
1.1.1	Femtosecond Laser Systems	2
1.1.2	A General Scheme for Generation/Detection of Broadband Pulses	3
1.1.3	Photo-Conductive Antennae	4
1.1.4	Detection with Photo-Conductive Antennae	7
1.1.5	Optical Rectification and Electro-Optic Sampling	7
1.1.6	Other Broadband Emitters	13
1.1.7	Future Prospects for Development of THz Radiation	15
1.2	CW THz Generation	15
1.2.1	Photomixing	15
1.2.2	Difference Frequency Generation	17
1.2.3	Parametric Amplification	17
1.2.4	Gas Lasers	18
1.2.5	Microwave Frequency Multipliers	18
1.2.6	Back Wave Oscillators	19
1.2.7	Free Electron Lasers	20
1.2.8	P-Type Germanium Lasers	21
1.2.9	Quantum Cascade Lasers	22
1.3	Detectors	23
1.3.1	Thermal Detectors	23
1.3.2	Heterodyne Detection	24
1.3.3	Intersubband Detectors	25
1.4	Conclusions	25
	References	25
2	Terahertz Optics	29
2.1	Introduction—Optics at THz Frequencies	29

2.2	Gaussian Beam Propagation in Ideal Optical Systems	30
2.2.1	Propagation Properties of a Simple Gaussian Beam Mode	30
2.2.2	Focussing Gaussian Beams: Simple Optical Systems	32
2.2.3	ABCD Matrices and Propagation in General Optical Systems	34
2.3	Optical Components and Subsystems	35
2.3.1	Coupling Beams and Focussing Elements	35
2.3.2	Off-Axis Focussing Mirrors	36
2.3.3	Thick Lenses	38
2.3.4	Beam Splitters, Polarising Grids, Roof Mirrors, Interferometers and Filters	39
2.3.5	Diffractive Elements and Phase Gratings	40
2.4	Beam Coupling Issues	41
2.4.1	Coupling to Radiating Elements	41
2.4.2	Mismatched Gaussian Beams and Defocussing Effects	42
2.5	Detailed Modelling	45
2.5.1	Higher Order Gaussian Beam Modes	45
2.5.2	Aberrations, Truncation, Beam Distortion	46
2.5.3	Other Modelling Techniques	48
2.5.4	Partial Coherence and Multi-Moded Systems	50
2.6	Design of Optical Systems	50
2.6.1	Choice of Mirror/Lens Parameters	50
2.6.2	Layout of Systems	51
2.6.3	Issues for Imaging in THz Spectroscopy Systems	52
2.7	Summary and Conclusions	53
	References	55
3	Complex Refractive Index of Media in the THz Spectral Range	57
3.1	Introduction	57
3.2	Complex Permittivity and Refractive Index	58
3.3	Complex Transmission and Reflection Coefficient	62
3.4	Effective Medium Models	65
3.5	Modified Kramers–Kronig Dispersion Relations in THz Spectra Analysis	67
3.6	Maximum Entropy Method in the Time-Domain THz Reflection Spectroscopy	74
3.7	Conclusions and Outlook	78
	References	78

- 4 Complex Refractive Index Determination Using Planar and Converging Beam Transfer Functions.** 81
 - 4.1 Material Parameter Extraction Using a Transfer Function 81
 - 4.2 Planar Transfer Function Algorithm 82
 - 4.2.1 Experimental and Theoretical Transfer Function. 82
 - 4.2.2 Phase Unwrapping 85
 - 4.3 Modeling a Converging Beam 86
 - 4.3.1 Angular Weighting Function 87
 - 4.3.2 Transmission of the Converging Beam Through a Slab. 88
 - 4.3.3 Phase Unwrapping in a Converging Algorithm. 90
 - 4.3.4 Simulated Data. 90
 - 4.4 Experimental Data 90
 - 4.5 Conclusions 93
 - References 93

- 5 Terahertz Scattering.** 95
 - 5.1 Introduction 95
 - 5.2 Terahertz Reflection and Transmission from Samples with Smooth Planar Interfaces 96
 - 5.2.1 Reflection and Transmission at a Single Interface. 96
 - 5.2.2 Reflection and Transmission from a Layer. 99
 - 5.3 Random Media. 100
 - 5.3.1 Terahertz Reflection from Random Rough Surfaces 101
 - 5.4 Volume Scattering and Absorption 106
 - 5.4.1 Scattering from Individual Particles 106
 - 5.4.2 Scattering from Randomly Distributed Collections of Particles. 108
 - 5.4.3 Numerical Calculations and Monte Carlo Simulations 113
 - 5.5 Conclusions 115
 - References 115

- 6 Phase-Space Processing of Terahertz Radiation.** 117
 - 6.1 Introduction 117
 - 6.2 Parameters Used for Characterization of THz Fields. 118
 - 6.3 Phase-Space Techniques for Characterization and Processing of Terahertz Radiation 121
 - 6.3.1 The Wigner Distribution Function and Its Applications in Signal Processing. 125
 - 6.3.2 The Ambiguity Function and Its Applications in Signal Processing 131

6.3.3	The Spectrogram and Its Applications in Signal Processing	133
6.3.4	The Wavelet Transform and Its Applications in Signal Processing	138
6.3.5	The Fractional Fourier Transform and Its Applications in Signal Processing	143
6.4	Conclusions	147
	References	147
7	Computational Methods for the Assignment of Vibrational Modes in Crystalline Materials	151
7.1	Introduction	151
7.1.1	Single Molecule Versus Periodic Crystal Structure Calculations	152
7.2	Theory of Crystal Phonons	155
7.2.1	Phonon in a 1-Dimensional Crystal	155
7.2.2	Normal Modes in Vacuum and in Condensed State	158
7.2.3	Phonons in a 3D Crystal	159
7.2.4	The Atom–Atom Potential (Force Field) Method	163
7.2.5	Quantum Mechanical Electronic Structure Calculations	166
7.2.6	Example Calculations	169
7.3	Molecular Dynamics	178
7.4	Conclusions, Summary and Limitations of the Methods	181
7.4.1	Force Fields Versus Electronic Structure (DFT) Calculations	181
7.4.2	Lattice Dynamics Versus Molecular Dynamics	182
7.4.3	General Problems to Address	182
	References	187
8	Terahertz Spectroscopy of Crystalline and Non-Crystalline Solids	191
8.1	Introduction	192
8.2	Measurement Considerations	193
8.2.1	Scattering	193
8.2.2	Sample Preparation	198
8.2.3	Calculation of Optical Constants	200
8.2.4	Dynamic Range	205
8.3	Spectroscopy of Crystalline Solids	206
8.3.1	Biomolecules	207
8.3.2	Small Organic Molecules	208
8.3.3	Explosives	215
8.3.4	Other Crystalline Materials	216

8.4	Spectroscopy of Non-Crystalline Solids.	217
8.4.1	Glasses	217
8.4.2	Ordered Carbonaceous Materials.	219
8.5	Summary	224
	References	224
9	Terahertz Spectroscopy of Liquids and Biomolecules.	229
9.1	Liquids	230
9.1.1	Terahertz Response for Liquids	230
9.1.2	Liquid Transmission	232
9.1.3	Major Findings and Current Directions	238
9.2	Biomolecules	238
9.2.1	Terahertz Response from Biomolecule	238
9.2.2	Major Findings and Current Directions	246
	References	248
10	Pump-Probe Spectroscopy at Terahertz Frequencies	251
10.1	Introduction	251
10.2	Technique	252
10.2.1	Experimental Details	252
10.2.2	Parameter Extraction	254
10.2.3	Conductivity Models	255
10.3	Inorganic Semiconductors	259
10.3.1	Bulk	259
10.3.2	Excitonic Systems.	260
10.3.3	Nanostructures	261
10.4	Organic Semiconductors	263
10.4.1	Graphite and Graphene	263
10.4.2	Carbon Nanotubes.	264
10.4.3	Semiconducting Polymers	265
10.5	Inorganic–Organic Hybrids	266
10.6	Outlook	268
	References	269
11	Terahertz Spectroscopy: Ellipsometry and Active Polarization Control of Terahertz Waves	273
11.1	Introduction	273
11.2	Transmission-Mode Time Domain Ellipsometry.	274
11.2.1	Method of Polarization State Measurement with Wire-Grid Polarizers	274
11.2.2	Calculation of Dielectric Tensor	275
11.2.3	Example of Polarization Measurements	277
11.3	Reflection Mode Time Domain Magneto-Optical Ellipsometry	280

11.3.1	MOKE Signal at Oblique Incidence	281
11.3.2	Analysis Based on Intensity Measurements	285
11.3.3	Analysis Based on the Time Domain THz Ellipsometry	285
11.3.4	Analysis Example	287
11.4	Active Polarization Control of Terahertz Wave	293
11.5	Conclusion.	298
	References	298
12	Liquid Crystals and their Applications in the THz Frequency Range	301
12.1	Liquid Crystals at THz Frequencies	301
12.1.1	Introduction	301
12.1.2	State of the Art.	302
12.1.3	Liquid Crystals Phases.	303
12.1.4	Key Properties	303
12.1.5	Positive versus Negative Dielectric Anisotropy.	303
12.1.6	Pure Liquid Crystals versus Mixtures	304
12.1.7	Macroscopic Properties – from kHz to UV	304
12.1.8	THz Spectroscopy on Liquid Crystals	305
12.1.9	Macroscopic THz Properties of Liquid Crystals	306
12.1.10	Molecular THz Properties of Cyanobiphenyls.	314
12.1.11	Summary and Outlook.	320
	References	321
13	Terahertz Spectroscopy of Polymers	327
13.1	Introduction	327
13.2	Dielectric Properties of Polymers in the Terahertz Regime	328
13.2.1	Grouping Polymers in the THz Frequency Range	329
13.2.2	Origin of the Spectral Features.	330
13.2.3	Monitoring the Glass Transition	334
13.2.4	Polymeric Compounds.	337
13.3	Applications for THz Systems in the Polymer Processing Industry.	339
13.3.1	Controlling Compounding Processes with THz Sensors	340
13.3.2	Moisture Monitoring in Plastic Components.	342
13.3.3	Inspection of Plastic Weld Joints	343
13.3.4	THz Spectroscopy on Adhesive Bonds	344
13.3.5	Determining the Fiber Orientation in Reinforced Plastics	347
	References	349

- 14 Nonlinear Terahertz Spectroscopy** 355
 - 14.1 Introduction 355
 - 14.2 Generation of High Intensity THz Pulses. 357
 - 14.2.1 THz Pulse Generation by Photoconductive
Switches 357
 - 14.2.2 Terahertz Generation in Gas Plasmas 359
 - 14.2.3 THz Pulse Generation by Optical Rectification. 362
 - 14.2.4 Intense THz Multicycle Pulses by Difference
Frequency Generation in GaSe
and ZnTe Crystals. 366
 - 14.3 THz Nonlinear Spectroscopy Methods 367
 - 14.3.1 Intensity Dependent Transmission. 367
 - 14.3.2 THz-Pump/THz Probe Experiments. 370
 - 14.3.3 THz-Pump/Optical-Probe Measurements 370
 - 14.3.4 Two-Dimensional THz Spectroscopy. 371
 - 14.4 THz Nonlinear Optics 373
 - 14.5 Nonlinear THz Spectroscopy of Semiconductors 375
 - 14.5.1 The Ponderomotive Force of THz Fields 376
 - 14.5.2 THz-Driven Ballistic Transport. 377
 - 14.5.3 Manipulation of Excitons by THz Fields 379
 - 14.6 Nonlinear Vibrational Spectroscopy 380
 - 14.7 Magnetic Field Effects of THz Pulses. 382
 - 14.8 THz Excitation of Strongly Correlated Materials 383
 - 14.9 Conclusion and Outlook 385
 - References 385

- 15 Terahertz Near-Field Imaging**. 389
 - 15.1 Introduction: The Near-Field, the Far-Field,
and the Diffraction Limit. 390
 - 15.1.1 The Diffraction Limit and the Far Field. 390
 - 15.1.2 The Near Field 390
 - 15.2 Apertureless Near-Field Microscopy 391
 - 15.2.1 Variations on the ANSOM Theme 396
 - 15.3 Aperture Techniques 397
 - 15.3.1 Waveguides, Dynamic Apertures
and Quasi Apertures 399
 - 15.4 Near-Field Imaging. 401
 - 15.4.1 Imaging the THz Electric Near-Field. 402
 - 15.5 Conclusions and Outlook. 410
 - References 410

- 16 Biomedical Imaging** 415
 - 16.1 Why Is Terahertz Radiation Suitable for Investigating
Biomedical Systems? 415

16.1.1	Safety	415
16.1.2	Sensitivity toward Intermolecular Interactions	416
16.2	Sample Preparation	416
16.2.1	Tissue (de)hydration	416
16.2.2	Repeatability	417
16.2.3	Example Checklist	417
16.3	Systems for Samples	417
16.3.1	Thin Versus Thick	418
16.3.2	Homogenous Versus Inhomogenous	418
16.3.3	Bandwidth and Axial Resolution	419
16.3.4	Signal to Noise Ratio and Penetration Depth	420
16.3.5	Structural Versus Spectroscopic Information	421
16.3.6	Imaging Versus Spectroscopy	422
16.4	Sample Holders and Effects on Calculations	422
16.4.1	Transmission Geometry	423
16.4.2	Reflection Geometry	424
16.5	Interpreting Data in the Time Domain	425
16.5.1	Deconvolution	425
16.5.2	Worked Example	425
16.6	Medical Applications Investigated	426
16.6.1	Breast Cancer	427
16.6.2	Skin Cancer	427
16.6.3	Colon Cancer	427
16.6.4	Dental Caries	428
16.6.5	Skin	428
16.6.6	Protein Spectroscopy	430
16.7	Summary	430
	References	430
17	THz Tomography	433
17.1	Computed Tomography Using THz and Millimeter Waves	433
17.1.1	Principle of CT	434
17.1.2	Examples of the Application of THz-CT	437
17.2	Time-of-Flight Terahertz Tomography	441
17.2.1	Principle of TOF Tomography	441
17.2.2	Examples of TOF-THz Tomography	443
	References	448
18	Industrial Applications of Terahertz Imaging	451
18.1	Introduction	451
18.2	Industrial Imaging	452
18.2.1	General Principles	452
18.2.2	Contrast Mechanisms	453
18.2.3	Nondestructive Testing	456

18.2.4	Real-Time Imaging	459
18.3	Pharmaceutical Industry	460
18.3.1	Specific Imaging Requirements	460
18.3.2	Instrumentation	461
18.3.3	Signal Processing	463
18.3.4	Imaging of Pharmaceutical Tablets	468
18.3.5	Applications	473
18.4	Outlook	484
	References	485
19	Millimeter-Wave and Terahertz Imaging in Security	
	Applications	491
19.1	Introduction	491
19.2	Phenomenology of Security Screening	492
19.2.1	System Performance Metrics in Passive MMW Imaging	492
19.2.2	Contrast in Passive MMW Imagers	493
19.2.3	Passive MMW Imaging Phenomenology	494
19.2.4	Active (Coherent) Millimeter Wave Imaging	497
19.2.5	Active Millimeter Wave Imaging Phenomenology	498
19.2.6	Atmospheric Transmission	499
19.2.7	Material Properties	499
19.3	Imaging System Design Overview	501
19.4	Detector Technologies	502
19.4.1	Coherent up or Downconversion	503
19.4.2	Preamplified Direct Detection	504
19.4.3	Incoherent (Unamplified) Direct Detection	505
19.5	Millimeter-Wave Portals	506
19.5.1	L-3 ProVision	506
19.5.2	Millivision	506
19.6	Stand-off Imaging	508
19.6.1	Passive Stand-Off Imaging Systems	508
19.6.2	Active Stand-Off Imaging Systems	512
19.7	Multispectral and Spectroscopic Imaging	513
19.7.1	Multispectral Imaging	513
19.7.2	THz Spectroscopic Imaging	514
19.8	Future Directions	515
	References	516
20	Characterisation of Works of Art	521
20.1	Introduction	521
20.2	State of the Art of Imaging Techniques Applied to the Characterisation of Artworks	524

20.3	THz Imaging and Art Conservation: Chronicle	525
20.4	Conclusions	535
	References	537
21	Terahertz Plasmonic Structures	539
21.1	Introduction	539
21.2	The Physics of THz Plasmonic Phenomena	542
21.2.1	Introductory Theory and Classification of Plasmonic Phenomena	542
21.2.2	THz Frequency Plasmons at the Planar Metal/Dielectric Interface	546
21.2.3	Corrugated Structures with Characteristic Dimensions Commensurate with the THz Wavelength	549
21.2.4	The Spoof SPP	551
21.2.5	Gratings and Arrays of Apertures	553
21.3	Applications	559
21.3.1	Guiding THz Waves with Plasmons	559
21.3.2	Manipulation: Modulators and Switches	560
21.3.3	Engineering the THz Wavefront with Plasmonic Devices	561
21.3.4	Sensing	562
21.3.5	Imaging	563
21.4	Conclusion	564
	References	565
22	Metamaterials	569
22.1	Introduction and a Few Historical Remarks	569
22.2	Length Scales: Averaging of Electric and Magnetic Quantities	570
22.2.1	Atomic Scale	570
22.2.2	Composites	572
22.2.3	Metamaterials	577
22.2.4	Comparison with Photonic Crystals	579
22.3	Numerical Calculations and Software	581
22.4	Experimental Characterization	581
22.4.1	Electric and Magnetic Resonances	582
22.4.2	Retrieval of Effective Properties	583
22.4.3	Retrieval of N and Z from Time-Windowed Signal	586
22.4.4	Near-Field Methods	589
22.5	Fabrication of THz Metamaterials	590
22.5.1	Lithography	590
22.5.2	Laser Writing	591
22.5.3	Other Techniques	592

22.6	Applications	593
22.6.1	Negative Permeability	594
22.6.2	Tunable Metamaterials	596
22.6.3	Other Applications	601
22.7	Concluding Remarks	603
	References	604
23	THz Control in Correlated Electron Solids: Sources and Applications	611
23.1	Introduction	612
23.2	Quantum Phase Control with High-Field THz Pulses	613
23.2.1	High-Field Single-Cycle Terahertz Pulses: Generation	613
23.2.2	Nonlinear Interlayer Coupling in High Tc Superconductors	614
23.3	Quantum Phase Control Through Vibrational Excitation	617
23.3.1	Control of the Semicovalent Bond	617
23.3.2	Mid-Infrared Pulses with Stable Absolute Phase	621
23.3.3	Vibrational Control as Nonlinear Phononics	623
23.4	Undulator-Based Sources for Nonlinear THz Physics	626
23.5	Conclusion	628
	References	629
	Index	633

Contributors

Aurèle J. L. Adam Faculty of Applied Sciences, University of Technology Delft, Lorentzweg 1, 2628 CJ Delft, The Netherlands, e-mail: a.j.l.adam@tudelft.nl

Vasilis Apostolopoulos School of Physics and Astronomy, University of Southampton, Southampton, SO17 1BJ, UK, e-mail: v.apostolopoulos@soton.ac.uk

Roger Appleby MilliLab co VTT Technical Research Centre of Finland, Finland, Europe, e-mail: applebyroger@yahoo.co.uk

Adam J. Baragwanath Department of Physics, Durham University, South Road, Durham DH1 3LE, UK, e-mail: a.j.baragwanath@durham.ac.uk

Harvey E. Beere Cavendish Laboratory, University of Cambridge, Cambridge CB3 0HE, UK

A. Cavalleri Max Planck Department for Structural Dynamics, University of Hamburg—CFEL, Hamburg, Germany; Department of Physics, Clarendon Laboratory, University of Oxford, Oxford, UK, e-mail: andrea.cavalleri@mpsd.cfel.de

J. Martyn Chamberlain Department of Physics, Durham University, South Road, Durham DH1 3LE, UK, e-mail: martyn.chamberlain@durham.ac.uk

Geoff Daniell Department of Physics and Astronomy, University of Southampton, SO17 1BJ, Southampton, UK

Graeme M. Day Department of Chemistry, University of Cambridge, Lensfield Road, Cambridge CB2 1EW, UK, e-mail: gmd27@cam.ac.uk

A. Dienst Department of Physics, Clarendon Laboratory, University of Oxford, Oxford, UK

Daniela Dragoman Physics Department, University of Bucharest, Bucharest, Romania, e-mail: daniela.dragoman@yahoo.com

Bernd M. Fischer Institut franco-allemand de recherches de Saint-Louis, Saint-Louis Cedex 68301, France, e-mail: bernd.fischer@isl.eu

Joshua R. Freeman Laboratoire Pierre Aigrain, École Normale Supérieure, 24 rue d'Ulm, Paris 75231 Cedex 05, France, e-mail: freeman@lpa.ens.fr

M. Först Max Planck Department for Structural Dynamics, University of Hamburg—CFEL, Hamburg, Germany

Kaori Fukunaga National Institute of Information and Communications Technology (NICT), Koganei, Tokyo 184-8795, Japan, e-mail: kaori@nict.go.jp

Andrew J. Gallant School of Engineering and Computing Sciences, Durham University, South Road, Durham DH1 3LE, UK, e-mail: a.j.gallant@durham.ac.uk

M. Gensch Helmholtz-Zentrum Dresden-Rossendorf, Dresden, Germany

Deepu K. George Physics Department, University at Buffalo, The State University of New York, New York, NY 14260, USA

Lynn F. Gladden Department of Chemical Engineering and Biotechnology, University of Cambridge, Cambridge CB2 3RA, UK, e-mail: lfg1@cam.ac.uk

Evgeny Gornov Department of Physics and Mathematics, University of Eastern Finland, PL 111, 80101 Joensuu, Finland, e-mail: evgeny.gornov@gmail.com

Matthias C. Hoffmann LCLS LST Division, SLAC National Accelerator Laboratory, 2575 Sand Hill Road, M/S 20, Menlo Park, CA 94025, USA, e-mail: hoffmann@slac.stanford.edu

Christian Jansen Department of Physics, Philipps-Universität Marburg, 35032 Marburg, Germany, e-mail: christian.jansen@ihf.tu-bs.de

Peter U. Jepsen Department of Photonics Engineering, Technical University of Denmark, 2800 Kongens Lyngby, Denmark, e-mail: puje@fotonik.dtu.dk

Michael B. Johnston Clarendon Laboratory, University of Oxford, Oxford, UK, e-mail: m.Johnston1@physics.ox.ac.uk

S. Kaiser Max Planck Department for Structural Dynamics, University of Hamburg—CFEL, Hamburg, Germany

Kodo Kawase Department of Electrical and Electronic Engineering and Information Engineering, Graduate School of Engineering, Nagoya University, Nagoya 464-8603, Japan, e-mail: kawase@nuee.nagoya-u.ac.jp

Mike Kemp Iconal Ltd, Cambridge, UK, e-mail: mike.kemp@iconal.com

DaiSik S. Kim Department of Physics and Astronomy, Center for Subwavelength Optics, Seoul National University, Seoul, Korea, e-mail: dsk@phya.snu.ac.kr

Martin Koch Department of Physics, Philipps-Universität Marburg, 35032 Marburg, Germany, e-mail: martin.koch@physik.uni-marburg.de

Petr Kužel Institute of Physics, Academy of Sciences of the Czech Republic, Prague, Czech Republic, e-mail: kuzelp@fzu.cz

Makoto Kuwata-Gonokami Department of Physics, University of Tokyo, Tokyo, Japan, e-mail: gonokami@phys.s.u-tokyo.ac.jp

James Lloyd-Hughes Clarendon Laboratory, University of Oxford, Oxford, UK, e-mail: james.lloyd-hughes@physics.ox.ac.uk

Arttu Luukanen MilliLab co VTT Technical Research Centre of Finland, Finland, Europe, e-mail: arttu.luukanen@vtt.fi

Emma MacPherson Department of Electronic and Computer Engineering, The Hong Kong University of Science and Technology, Hong Kong, China, e-mail: eeemma@ust.hk

C. Manzoni Dipartimento di Fisica, Politecnico di Milano, Milan, Italy

Andrea G. Markelz Physics Department, University at Buffalo, The State University of New York, New York, NY 14260, USA, e-mail: amarkelz@buffalo.edu

J. Anthony Murphy Department of Experimental Physics, NUI Maynooth, Kildare, Co. Kildare, Ireland, e-mail: anthony.murphy@nuim.ie

Hynek Němec Institute of Physics, Academy of Sciences of the Czech Republic, Prague, Czech Republic, e-mail: nemec@fzu.cz

Créidhe O’Sullivan Department of Experimental Physics, NUI Maynooth, Kildare, Co. Kildare, Ireland, e-mail: creidhe.osullivan@nuim.ie

Edward P. J. Parrott Department of Electronic Engineering, The Chinese University of Hong Kong, Hong Kong, China, e-mail: parrott@ee.cuhk.edu.hk

Kai-Erik Peiponen Department of Physics and Mathematics, University of Eastern Finland, PL 111, 80101 Joensuu, Finland, e-mail: kai.peiponen@uef.fi

Marcello Picollo “Nello Carrara” Institute for Applied Physics of the Italian National Research Council (IFAC-CNR), Via Madonna del Piano 10, 50019 Sesto Fiorentino, Italy, e-mail: m.picollo@ifac.cnr.it

Paul C. M. Planken Faculty of Applied Sciences, University of Technology Delft, Lorentzweg 1, 2628 CJ Delft, The Netherlands, e-mail: p.c.m.planken@tudelft.nl

M. Rini Joint Research Centre, European Commission, Karlsruhe, Germany

David A. Ritchie Cavendish Laboratory, University of Cambridge, Cambridge CB3 0HE, UK

Neil Salmon MMW Sensors Ltd, Manchester, UK, e-mail: Neil.Salmon@MMW-Sensors.com

Scott Schecklman Electrical and Computer Engineering Department, Portland State University, Portland, OR, USA

Yao-chun Shen Department of Electrical Engineering and Electronics, University of Liverpool, Brownlow Hill, Liverpool L69 3GJ, UK, e-mail: y.c.shen@liverpool.ac.uk

Takayuki Shibuya Tokyo Metropolitan Industrial Technology Research Institute, Kitaku, Tokyo, Japan, e-mail: shibuya.takayuki@iri-tokyo.jp

R. I. Tobey Physics Division, Brookhaven National Laboratory, Upton, NY 11973-5000, USA

Daniele Tomerini Department of Chemistry, University of Cambridge, Lensfield Road, Cambridge CB2 1EW, UK, e-mail: dt334@cam.ac.uk

Nico Vieweg Department of Physics, Philipps-Universität Marburg, 35032 Marburg, Germany

Steffen Wietzke Department of Physics, Philipps-Universität Marburg, 35032 Marburg, Germany, e-mail: steffen.wietzke@ihf.tu-bs.de

J. Axel Zeitler Department of Chemical Engineering and Biotechnology, University of Cambridge, Cambridge CB2 3RA, UK, e-mail: jaz22@cam.ac.uk

L. M. Zurk Electrical and Computer Engineering Department, Portland State University, Portland, OR, USA, e-mail: zurkl@cecs.pdx.edu

Symbols

A	Absorbance, amplitude ambiguity function, autocorrelation function
A_i	Mode coefficient
a	Radius, acceleration
a_m	Mie coefficient
B	Magnetic induction
\mathbf{b}	Local magnetic induction
b_m	Mie coefficient
C	Autocorrelation function, constant
c	Light velocity in vacuum
D	Electric induction, aperture, dynamical matrix
\mathbf{D}	Electric induction
d	Thickness, penetration depth
d_{il}	d -Matrix
E	Electric field, energy
e	Elementary electric charge, emissivity
\mathbf{e}	Local electric field
F	Force
f	Frequency, focal length, polynomial, volume fraction
f_c	Center frequency
\mathbf{f}	Lorentz force
G	Gain, reciprocal lattice vector
$G_{m,n}$	Gabor coefficients
g	Absorbance
H	Magnetic field, transfer function
h	Root-mean-square height, transfer function, impulse response
$H_{meas}(\omega)$	Measured transfer function
$H_{theory}(\omega)$	Theoretical transfer function
I	Intensity, irradiance, current, input signal
II	Interface index
Im	Imaginary part
I_{PC}	Photo-current
i	Imaginary unit

j	Imaginary unit, local current
J	Current density
K	Wave number
\mathbf{K}	Wave vector
K_{eff}	Effective complex wave number
k	Extinction coefficient, wave number, Coverage factor
L	Cavity length, inductance
L_c	Coherence length
l	Length
M	Optical transfer matrix
\mathbf{M}	Magnetization, transfer matrix
m	Mass, magnetic quantum number
m^*	Effective mass
N_0	Avogadro constant
n	Real refractive index
\tilde{n}	Complex refractive index
n_e	Extraordinary refractive index
n_g	Group index
n_o	Ordinary refractive index
P	Power, polarization, Fresnel polarization coefficient, Coverage probability
\mathbf{P}	Polarization
P_m	Materials interaction term
P_{NL}	Nonlinear polarization
p	Dipole moment
q	Complex radius
Q_{ext}	Mie extinction coefficient
Q_N	Phonon mode
R	Reflectance, Fresnel reflection coefficient, interatomic separation
\Re	Real part
R_{eff}	Effective reflection coefficient
$R(z)$	Phase radius of curvature
Re	Real part
r	Complex reflection coefficient, radius
S	Area, ray transfer matrix, spectrograph, scalogram, order parameter, surface, optical thickness
T	Transmittance, temperature, Fresnel transmission coefficient, wavelet transform
T_c	High temperature superconductor
T_{eff}	Effective transmission coefficient
t	Time, thickness
T_g	Glass transition temperature
u	Reduced size parameter, atomic displacement
U_p	Ponderomotive potential

V	Volume, voltage, potential
v	Velocity
v_g	Group velocity
W	Water absorption
W	Beam width, Wiener filter
W_0	Beam radius
$W(k_1, k_2)$	Weighting function
$W(u, v)$	Wigner distribution function
$X(\omega)$	Input electric field
x, y, z	Cartesian coordinates
Y	Main polarizability
$Y(\omega)$	Spectrum
Z	Impedance
Z_n	Effective charge
\angle	Phase

Greek Symbols

α	Absorption coefficient, angle, degree of fractionality, Cole-Cole parameter, effective polarizability
β	Propagation constant, Cole-Davidson parameter
γ	Scattering coefficient, polarizability, tilt angle, transmittance
ν	Wave number
Γ	Damping factor, reflectance
ε	Permittivity
ζ	Principal polarizability
η	Efficiency, shape factor
ε_{eff}	Effective permittivity
Δ	Optical path length, thickness
Δf	Bandwidth
Δl	Spatial resolution
$\Delta \nu$	Spectral band width
Δt	Time delay
$\Delta \tau$	Pulse duration
ΔT	Time resolution
Δx	Displacement
ΔR	Range resolution
θ	Angle, phase, polarization azimuth rotation, ellipticity angle
$\tilde{\theta}$	Complex refraction angle
θ_c	Critical angle
θ_s	Scattering angle
κ	Extinction coefficient
λ	Wavelength
μ	Permeability
μ_{gr}	Group position/delay
Π	Hertzian vector or the electric polarization potential
ν_{loc}	Local frequency
ξ	Dilatation
ρ	Radial coordinate, charge density
σ	Conductivity, surface charge density, cross-section
σ_a	Absorption cross section
σ_d	Scattered power
σ_s	Scattering cross section
τ	Complex transmission coefficient, mean scattering time, pulse duration
φ	Fill fraction, angle, potential energy, polarization rotation
ϕ	Phase, error phase
Φ	Father function
χ	Susceptibility
$\chi^{(n)}$	Nonlinear susceptibility

Ψ	Wavelet
ω	Circular frequency
ω_p	Plasma frequency
ζ	Volume fraction, principle polarizability
Ω	Frequency

Acronyms

AFM	Atomic force microscopy
ANSOM	Apertureless near-field scanning optical microscopy
ATR	Attenuated total reflection, automated target recognition
AWGN	Additive white Gaussian noise
BL	Beer-Lambert
BWO	Back wave oscillator
CaCO ₃	Calcium carbonate
COC	Cyclic olefin copolymers
CEP	Carrier envelope phase
CNF	Carbon nanofibre
CNT	Carbon nanotube
CSG	Customised skewed Gaussian
CT	Computed tomography
CW	Continuous wave
DAST	4- <i>N,N</i> -dimethylamino-4'- <i>N'</i> -methyl stilbazolium tosylate
DFG	Difference frequency generation
DFT	Density functional theory
DG	Double Gaussian
DL	Drude-Lorentz model
DMA	Dynamic mechanical analysis
DSC	Differential scanning calorimetry
EMA	Effective medium approximation
EO	Electro-optic
EOT	Extraordinary optical transmission
EOTPR	Electro optical terahertz pulse reflectometry
FBP	Filter back projection
FDTD	Finite difference time domain
FEA	Finite element analysis
FEL	Free electron laser
FFT	Fast Fourier transform
FIR	Far infrared spectroscopy
FOV	Field of view

FTS	Fourier transform spectroscopy
FROG	Frequency-resolved optical gating
FRFT	Fractional Fourier transform
FTIR	Fourier transform infra-red
GTD	Geometrical theory of diffraction
HEP	Hot electron polometer
HDPE	High-density polyethylene
HPMC	Hydroxylpropyl cellulose
HRS	Hyper Raman scattering
HRTEM	High resolution transmission electron microscope
IF	Intermediate frequency
IR	Infrared
IRS	Ionic Raman scattering
LC	Liquid crystal
LCP	Liquid crystal polymer
LDA	Local density approximation
LDPE	Low-density polyethylene
LLDPE	Linear low-density polyethylene
LM	Lattice mode
LNA	Low-noise amplification
LO	Local oscillator
LO-phonon	Longitudinal optical phonon
LT-GaAs	Low temperature grown gallium arsenide
MAF	Mobile amorphous fraction
MD	Molecular dynamics
MDT	Mean dissolution time
MIR	Mid-infrared
MM	Molecular mechanics
MMW	Millimeter wave
MoM	Method of Moments
MOKE	Magneto-optical Kerr effect
NDA	Negative dielectric anisotropy
NDT	Non-destructive testing
NEP	Noise equivalent power
NIR	Near infrared
NM	Normal mode analysis
OCT	Optical coherence tomography
OP	Orientation polarization
OPA	Optical parametric amplifier
OPTP	Optical-pump-THz probe
OR	Optical rectification
PA	Polyamide 12
PA6	Polyamide 6
PC	Polycarbonate
PCA	Photo-conductive antenna

PE	Polyethylene
PEC	Perfectly electrically conducting
PMMA	Polymethylmethacrylate
PMP	Polymethylpentene
PO	Physical Optics
POM	Polyoxymethylene
PP	Polypropylene
PS	Polystyrene
PTFE	Polytetrafluorethylene
PVC	Polyvinyl chloride
PVDF	Polyvinylidene fluoride
PW	Pulse width
RAF	Rigid amorphous fraction
QCL	Quantum cascade laser
SEM	Scanning electron microscope
SHG	Second harmonic generation
SMRA	Small magneto-optical response approximation
SMMW	Submillimeter-wave
SNR	Signal to noise ratio
SPM	Small Perturbation Method
SPP	Surface plasmon polariton
SRR	Split-ring resonator
SV	Skeletal vibration
SWNT	Single walled carbon nanotube
QCL	Quantum cascade laser
SRR	Split-ring resonator
TDS	Time-domain spectroscopy
TDTS	Time-domain terahertz spectroscopy
THz	Terahertz
TiO ₂	Titania
TO	Transverse optical
TOF	Time of flight
UV	Ultraviolet
VDOS	Vibrational density of states
WDF	Wigner distribution function
WGP	Wire-grid polarizer
WPC	Wood plastic composite
XRR	X-ray radiography

Chapter 1

Generation and Detection of Terahertz Radiation

Joshua R. Freeman, Harvey E. Beere and David A. Ritchie

Abstract Methods for generating and detecting terahertz (THz) radiation are reviewed with emphasis on the physical mechanisms involved as well as the typical characteristics of the generated radiation. We first discuss methods for generating and detecting broadband pulses of THz radiation, which are based on optical femtosecond laser systems. The second section describes techniques used to generate continuous-wave THz radiation and finally we review THz detectors.

There are many methods of generating and detecting terahertz (THz) radiation that have been developed in recent years, and in many cases are still being developed. Here we will survey these methods, giving particular attention to those which are used most frequently for spectroscopy. Sources of THz radiation can roughly be divided into two categories; broadband sources which are typically based on the conversion of ultra-short optical pulses into few cycle THz pulses and continuous wave (CW) sources which tend to be more spectrally narrow. Commonly used detection methods can also be divided along these lines: for sources based on short optical pulses coherent detection methods based on optical gating are available. Most other types of detector rely on detecting the temperature rise induced by the absorption of THz radiation, or in some cases detecting the THz photon directly.

J. R. Freeman (✉)
Laboratoire Pierre Aigrain, École Normale Supérieure,
24 rue d'Ulm, Paris 75231 Cedex 05, France
e-mail: freeman@lpa.ens.fr; joshua.r.freeman@gmail.com

H. E. Beere · D. A. Ritchie
Cavendish Laboratory, University of Cambridge,
Cambridge CB3 0E, UK

1.1 Broadband THz Pulse Generation and Detection

Much of the early work on the generation and detection of THz radiation was performed using Auston switches, developed by Auston et al. at Bell Laboratories [1]. An Auston switch consists of a material that has a conductivity which strongly depends on the optical illumination of the photoconductive material. When a short pulse of optical radiation is used to turn on the switch, a corresponding short electrical pulse is produced which has frequencies in the THz region. This work was extended and developed by Grischkowsky et al. at IBM research center [2, 3] to a system that used femtosecond laser pulses to generate and detect free-space THz radiation.

1.1.1 Femtosecond Laser Systems

The most widely used systems for THz spectroscopy are based on femtosecond pulses from mode-locked lasers. Mode-locking is a technique for producing short, high-power, and periodic laser pulses. A laser cavity which includes a broad gain medium will support lasing on many cavity modes, however, in a free-running laser these cavity modes will have no particular phase relationship and the resulting output of the laser over time will randomly fluctuate on short time scales about an average level. In mode-locked lasers all cavity modes are forced to have a fixed phase relationship, when these modes are summed the result is a single pulse with a period of the cavity round-trip time, depicted in Fig. 1.1. Several methods exist which can induce mode-locking. In active mode-locking the cavity losses are modulated at the cavity round-trip time. In passive mode-locking an element is introduced into the cavity that reduces the losses of more intense pulses; most commonly used techniques are ‘Kerr-lensing’ or a saturable absorber. More information on mode-locked lasers can be found in Ref. [4].

A key result from the theory of mode-locked lasers is that for any pulse the time-bandwidth product must conform to the relation, $\Delta\nu\Delta\tau \geq \frac{2\ln 2}{\pi} \simeq 0.44$, where $\Delta\nu$ is the spectral bandwidth of the laser and $\Delta\tau$ is the duration of the mode-locked pulse. Thus, to achieve the shortest pulses a large spectral bandwidth is required. The most commonly used material is titanium-doped aluminum oxide (Ti:Sapphire), this material has a particularly large spectral bandwidth, from 650 to 1,100 nm. In addition to this Ti:Sapphire also has a high thermal conductivity, which allows for high optical pumping. Other laser gain mediums that are regularly used in femtosecond laser systems, include Nd:glass (1,040–1,070 nm), Nd-doped fiber (1,040–1,070 nm), Yb-doped fiber (1,030–1,080 nm), and Er-doped fiber (1,520–1,580 nm). There has been particular interest recently in moving to fiber-based femtosecond systems, because of the reduced size and cost of these systems [5].

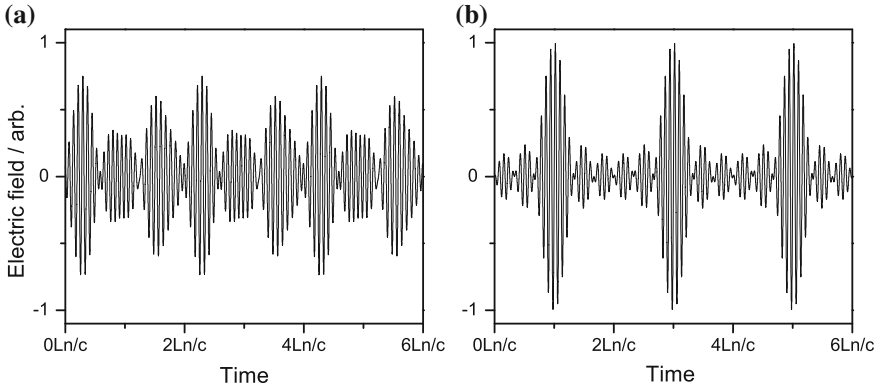


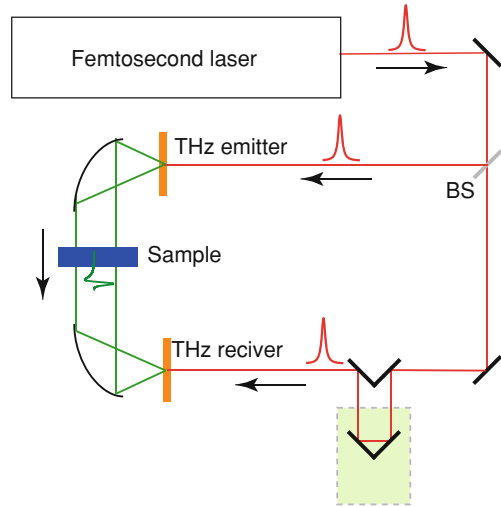
Fig. 1.1 **a** Pulses produced by a laser cavity where the modes have random phases. The cavity round-trip time is $2Ln/c$, where L is the cavity length, n is the refractive index in the cavity, and c is the speed of light. **b** Pulse produced by a cavity which has a fixed phase relationship between the modes. In this calculation only five modes have been used for clarity, in real systems, the number of modes will be much higher and the width of the pulses correspondingly shorter

1.1.2 A General Scheme for Generation/Detection of Broadband Pulses

All the methods for the generation and detection of THz radiation described in this section follow the same basic experimental set-up, depicted in Fig. 1.2. A pulse from the femtosecond laser is split at a beam splitter, one portion, we shall refer to as the ‘pump’ is directed to the THz emitter and generates a single-cycle of THz radiation. This THz pulse is collected and directed to the sample from where it is focused on the THz receiver. Meanwhile, the other portion of the femtosecond pulse (‘probe’) is directed through a variable time delay, before being focused on the THz receiver.

There are several important points to note with this scheme. The detector will only register a signal when both the probe pulse and the THz field are present, and for the detectors under discussion in this section the signal is proportional to the *electric field* of the THz pulse. As the probe pulse is short compared to the THz field this arrangement will effectively sample the value of the THz electric field, with a resolution dictated by the width of the femtosecond pulse. By varying the time delay of the probe pulse, the point at which the THz field has sampled changes, thus by recording the detector value as a function of time delay one may map out the electric field (amplitude and phase) of the THz pulse as a function of time. Once the electric field of the THz pulse has been recorded it can be Fourier-transformed to obtain the amplitude and phase of the pulse. Because of the Fourier transform, the obtainable frequency resolution is $\propto \frac{1}{\Delta T}$, where ΔT is the time resolution of the electric field, dictated by the step size of the delay stage. Finally, by comparing THz pulses with and without the sample present one may obtain the THz absorption spectrum and dispersion present in the sample.

Fig. 1.2 A generic arrangement for a THz time-domain-spectroscopy (TDS) system. Pulses from the femtosecond laser are split at the beam splitter (BS). There is an optical delay which can be changed to alter the time of arrival at the THz receiver between the THz pulse and the femtosecond pulse.



An important aspect of the system is the gated nature of the detection; a THz pulse is only detected when the femtosecond pulse is present. This gives the system the time resolution, but also, ensures the detector is insensitive to background radiation. As the repetition rate of the femtosecond laser is usually high ($\sim 10^8$ MHz) each point in time for the electric field will be averaged over many femtosecond pulses. Because the detector is sensitive to the electric field, a source of radiation not *in phase* with the femtosecond source must be average to zero. This ensures that the detector is insensitive to background radiation and these types THz systems can exhibit a very high signal-to-noise ratio.

Two crucial elements of the above scheme are the THz emitter and detector. In the following sections, we will examine the materials and methods that are used for these emitters and receivers and how they generate THz radiation.

1.1.3 Photo-Conductive Antennae

A photo-conductive antenna (PCA) comprises a fast optically activated switch which is embedded in an antenna structure. In practice, this usually takes the form of metal electrodes on a semiconductor substrate, with a geometry similar to that shown in Fig. 1.3. The femtosecond optical pulse is focused into the gap between two electrodes. Provided that this optical pulse has a wavelength corresponding approximately to the bandgap of the semiconductor, electron-hole pairs will be produced. These charges are then accelerated by an electric field generated in the gap by a

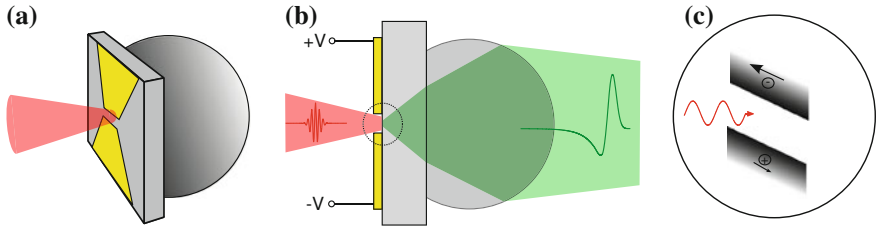


Fig. 1.3 **a** The photo-conductive antenna (PCA) with a bow-tie antenna. **b** The PCA shown in profile. The femtosecond pulse arrives from the *left* and the THz field is radiated to the *right*. A silicon lens collects radiation from the substrate. **c** Illustrates the generation of electron-hole pairs in the semiconductor band-structure

voltage applied between the metal electrodes.¹ These accelerated charges will then be recaptured into the semiconductor bandstructure on a picosecond time-scale and the system returns to its equilibrium state. Therefore, the effect of the femtosecond pulse is to generate a transient electrical current in the gap between the electrodes, which we may describe as a Hertzian dipole. It is a standard result from electromagnetic theory (see for example Ref. [6]) that the far field produced by this type of dipole is described as:

$$E_{\text{THz}} \propto \frac{dI_{\text{PC}}(t)}{dt}, \quad (1.1)$$

where E_{THz} is the THz electric field far from the emitter structure and I_{PC} is the photocurrent generated in the gap. It is also possible to estimate the transient photocurrent, I_{PC} , produced by the femtosecond pulse from the Drude-Lorentz model [7, 8]. Figure 1.4 shows calculated values of the photocurrent, I_{PC} , and the THz far-field, E_{THz} , for a 100 fs optical pulse.

Figure 1.4 captures some of the important aspects of PCA design to achieve single-cycle THz pulses. The first half-cycle of the electric field is mostly governed by the duration of the optical pulse, whereas the second half-cycle is governed by the recapture time in the semiconductor material, thus for intense large bandwidth THz pulses, a short recapture time is required in addition to a short femtosecond pulse. There has been much research into the materials for PCA, but the most commonly used material is low-temperature grown gallium arsenide (LT-GaAs). Other possible materials are radiation-damaged silicon-on-sapphire (RD-SOS), semi-insulating GaAs (SI GaAs), indium phosphide (InP), and amorphous silicon. For each material the optical pulse wavelength is chosen to match the bandgap in that material. For example, the bandgap of GaAs, around 850 nm, is well matched to the Ti:sapphire laser system. With all these materials, one seeks to minimize the carrier recapture time, in the case of LT-GaAs this is done by inducing defects during the growth process by incorporating an excess of arsenic [9].

¹ In all materials of interest the mobility of electrons is much larger than that of the holes so that electrical dynamics of the system can be described solely by the motion of electrons.

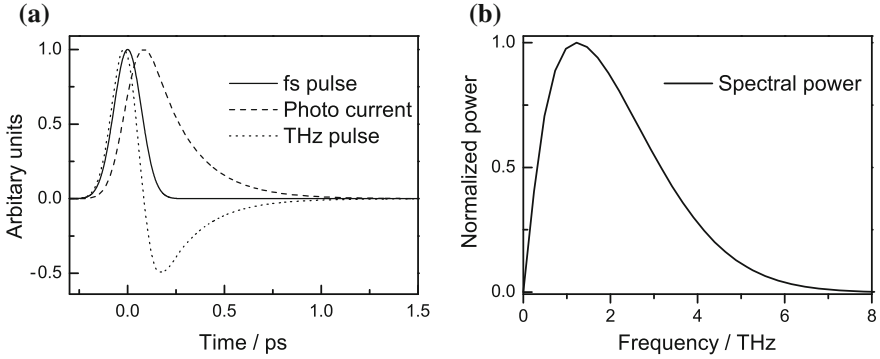


Fig. 1.4 Calculations based on the simple current model outlined in the text, with a optical pulse length of 100 fs and a recapture time of 200 fs. **a** Shows the femtosecond optical pulse (*solid*), induced transient photo-current (*dashed*) and the radiated THz far field (*dotted*). **b** The Fourier transform of the THz far field. Model data provided by R. Faulks

Design of the metal electrodes is another important parameter, the shape of which chiefly determines the coupling of THz radiation produced in the gap to the far field. Several designs, such as the strip-line, Hertzian dipole, offset dipole, and bow-tie have been tested [10–12]. One common technique is to design the electrodes to be resonant with frequencies above 2 THz where generation is less efficient. This ensures that the relatively weak radiation generated at higher frequencies reaches the far-field efficiently. The gap between the two electrodes is also an important factor, larger gaps require a larger bias to produce the same electric field, however large-gap antennae have also been used to produce high power THz pulses [13].

Other factors which can affect the power of a PCA are the femtosecond pulse power and the electric field applied across the gap. The pump power shows a saturation behavior, however, the level at which this saturation occurs is dependent on the electrode design and photoconductive material. The electric field that can be applied across the gap is largely determined by the breakdown voltage in the semiconductor material. The operating value of the biasing field is usually chosen to be as large as can be maintained without damaging the device through electrical discharge because the THz power scales with applied field as $E_{\text{THz}} \propto V^2$.

Device resistance is also a consideration. In an ideal device the resistance is infinite in the absence of illumination and very low when illuminated. However, there will usually be some dark current due to the finite resistance of the device and the electric field applied. This will reduce the modulation of the conductivity that is available and hence the THz generation efficiency. Dark currents can be a problem in some materials, such as InGaAs which has seen more interest recently due to the fact that it can be pumped with a femtosecond laser operating around 1.5 μm . This wavelength has the advantage that relatively cheap fiber lasers are available. One solution to the problem of dark currents is to use multilayer structures, as Ref. [5].

1.1.4 Detection with Photo-Conductive Antennae

Up to now we have only discussed the use of PCAs for generation of THz radiation, however, the same devices can be used for detection of THz radiation in the scheme set out in Sect. 1.1.2. When used for detection a femtosecond ‘probe’ pulse is focused onto the device, generating electron–hole pairs, as above. The incident electric field of THz pulse, \mathbf{E}_{THz} , then accelerates these charges before they are again recaptured. The net effect is to generate a current in the gap, proportional to a convolution,

$$J(t) = \int_{-\infty}^t \mathbf{E}_{\text{THz}}(t') \sigma(t - t') dt', \quad (1.2)$$

where $\sigma(t)$ is the conductivity induced by the femtosecond pulse, implying that the induced current will persist for the carrier lifetime. From this we can also see that,

$$\tilde{J}(\nu) = \tilde{\sigma}(\nu) \tilde{E}_{\text{THz}}(\nu), \quad (1.3)$$

where $\tilde{J}(\nu)$, $\tilde{\sigma}(\nu)$ and $\tilde{E}_{\text{THz}}(\nu)$ are the Fourier transforms of $J(t)$, $\sigma(t)$ and $E(t)_{\text{THz}}$, respectively. From this relationship we see that the recapture time is the key parameter, a slow recapture time will limit the detectable bandwidth. The current produced is amplified and converted to a voltage, and then usually detected using sensitive lock-in techniques. The lock-in technique requires the incident signal to be modulated at a known frequency, which can be achieved by either chopping the femtosecond beam, or modulating the electric field applied to the PCA emitter. In this way, the signal measured at different delay times of the probe pulse will map the electric field of the generated THz field. A typical THz pulse and the corresponding spectrum is shown in Fig. 1.5.

1.1.5 Optical Rectification and Electro-Optic Sampling

Nonlinear Optics

Broadband THz radiation can also be generated and detected using crystals with nonlinear optical properties. In linear optics the polarization of a medium has a linear relation to the electric field present through the relation

$$\mathbf{P} = \epsilon_0 \chi \mathcal{E}, \quad (1.4)$$

where \mathbf{P} is the induced polarization, χ is the electrical susceptibility, and \mathcal{E} is the electric field. In a nonlinear medium, however, the polarization is described by a series of terms of increasing order:

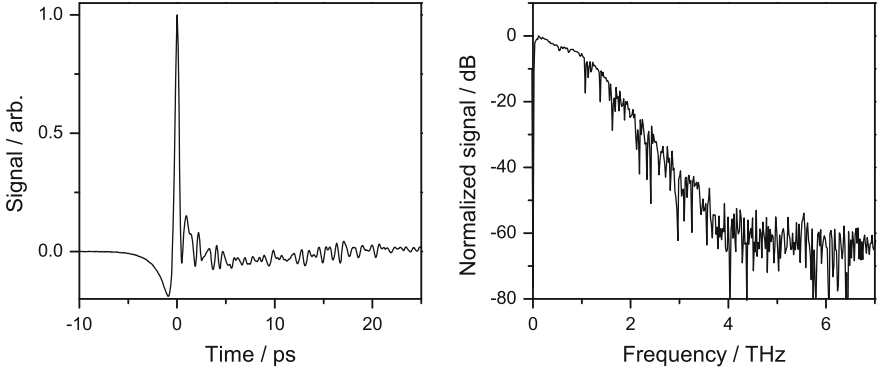


Fig. 1.5 A THz pulse measured using an LT-GaAs emitter with a resonant dipole antenna and a $2\ \mu\text{m}$ gap, there was 50 V applied between the electrodes. The receiver was also based on LT-GaAs and had a bow-tie antenna with $2\ \mu\text{m}$ gap. The bias of the emitter was modulated at 33 kHz and a lock-in amplifier used for recovery of the receiver signal. The 100 fs optical pulses were supplied by a Ti:sapphire laser with a 76 MHz repetition rate and around 10 mW was focused onto each emitter and detector. Water absorption lines are visible in the spectrum. Data provided by R. W. Faulks

$$\mathbf{P} = \mathbf{P}^{(1)} + \mathbf{P}^{(2)} + \mathbf{P}^{(3)} + \dots, \quad (1.5)$$

where $\mathbf{P}^{(1)}$ is the first-order term corresponding to Eq. 1.4 and $\mathbf{P}^{(n)}$ represents the n th order term. For the cases of optical rectification and electrooptic (EO) sampling we consider the second-order term, which is written [14]

$$P_i^{(2)} = \epsilon_0 \sum_{j,k=x,y,z} \chi_{ijk}^{(2)} \mathcal{E}_j \mathcal{E}_k, \quad (1.6)$$

where i , j , and k correspond to the Cartesian coordinate axis x , y , and z . The electric field components, \mathcal{E}_j and \mathcal{E}_j may come from different light beams; however, for our purposes the two components will just be the components of the electric field vector of the light resolved along the appropriate axes. The second-order nonlinear susceptibility tensor, $\chi_{ijk}^{(2)}$, requires 27 elements, however, due to crystal symmetry this reduces to 18 and in many classes of crystal this reduces further because many elements are zero. The 18 element tensor is commonly written as a d -matrix

$$d_{il} = \frac{1}{2} \chi_{ijk}^{(2)}, \quad (1.7)$$

such that Eq. 1.6 can be rewritten:

$$\begin{pmatrix} P_x \\ P_y \\ P_z \end{pmatrix} = 2\epsilon_0 \begin{pmatrix} d_{11} & d_{12} & d_{13} & d_{14} & d_{15} & d_{16} \\ d_{21} & d_{22} & d_{23} & d_{24} & d_{25} & d_{26} \\ d_{31} & d_{32} & d_{33} & d_{34} & d_{35} & d_{36} \end{pmatrix} \begin{pmatrix} E_x^2 \\ E_y^2 \\ E_z^2 \\ 2E_y E_z \\ 2E_x E_z \\ 2E_x E_y \end{pmatrix}. \quad (1.8)$$

This expression describes the polarization induced in an EO crystal by general electric fields. In the following section, we will see how this effect is used to generate and detect THz radiation.

Generation of THz in Nonlinear Crystals

Several nonlinear crystals have been used for the generation and detection of THz radiation [15], such as GaAs, GaP, InP, GaSe, LiNbO₃, and LiTaO₃, however, the most commonly used crystal is ZnTe [16], for which the d -matrix has a conveniently simple form:

$$\mathbf{d} = \begin{pmatrix} 0 & 0 & 0 & d_{14} & 0 & 0 \\ 0 & 0 & 0 & 0 & d_{14} & 0 \\ 0 & 0 & 0 & 0 & 0 & d_{14} \end{pmatrix}. \quad (1.9)$$

All zinc-blende crystals have d -matrices of this form and for ZnTe the value of d_{14} is 4 pm/V. Due to the d -matrix, the induced nonlinear polarization in the crystal is dependent on the direction of the radiation, to see this we will calculate the second-order component of the polarization, $\mathbf{P}^{(2)}$, induced by an arbitrary electric field:

$$\mathbf{E}_0 = E_0 \begin{pmatrix} \sin \theta \cos \phi \\ \sin \theta \sin \phi \\ \cos \theta \end{pmatrix}. \quad (1.10)$$

Substituting this into Eq. 1.8, after a little algebra yields

$$\begin{pmatrix} P_x \\ P_y \\ P_z \end{pmatrix} = 4\epsilon_0 d_{14} E_0^2 \sin \theta \begin{pmatrix} \cos \theta \sin \phi \\ \cos \theta \cos \phi \\ \sin \theta \sin \phi \cos \phi \end{pmatrix}. \quad (1.11)$$

Thus we can see that the induced polarization will vary depending on the angle the incident light makes with the crystal axes. In the case of zinc blende structures the maximum polarization occurs when the optical field is parallel to the $[\bar{1}\bar{1}1]$ or $[1\bar{1}\bar{1}]$ crystal axes.

Up to this point we have been considering a constant optical field, $E(t) = E_0 e^{i\omega t}$, which, according to Eq. 1.11 will produce a static polarization, $|\mathbf{P}| \propto |E_0|^2$. This is known as optical rectification, the effect where a field at optical frequencies gives rise to a static electric field. In the case of THz generation the optical field is a femtosecond

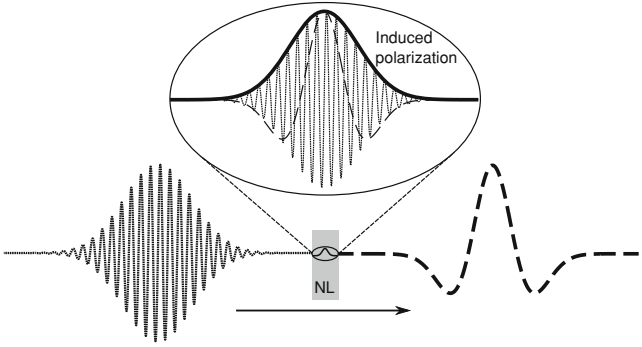


Fig. 1.6 The basic scheme for optical rectification. The femtosecond pulse (*dotted line*) enters from the left and propagates through the nonlinear medium (NL). In the nonlinear medium the induced polarization (*solid line*) gives rise to a THz electric field (*dashed line*)

pulse, hence the optical field does have a time dependence, $E(t) \sim E_0 e^{-at^2} e^{i\omega t}$, which also leads to a time dependence in the polarization:

$$|\mathbf{P}| \propto E_0^2 e^{-2at^2}. \quad (1.12)$$

Thus the induced polarization is proportional to the *envelope* of the femtosecond pulse. It is this time varying polarization that is the source of the THz radiation, which can be calculated by using Maxwell's equations to form the wave equation with a driving polarization term:

$$\nabla^2 \mathbf{E}_T - \frac{n_T^2}{c^2} \frac{\partial^2 \mathbf{E}_T}{\partial t^2} = \frac{1}{\epsilon_0 c^2} \frac{\partial^2 \mathbf{P}^{(2)}}{\partial t^2}. \quad (1.13)$$

The subscript '*T*' in the above equation denotes the THz field, \mathbf{E}_T , and refractive index, n_T^2 . The solution, together with the generation scheme, are sketched in Fig. 1.6. A full derivation of this equation and solutions can be found in, for example, Ref. [14]

In a non-dispersive nonlinear medium, where the optical refractive index, n_O , is the same as the THz refractive index, n_T , the optical pulse, and the generated THz radiation will travel at the same speed. This means that the amplitude of the THz pulse will grow linearly with distance as the polarization induced by the optical pulse will be in phase with the THz pulse. However, in practice, all media are dispersive to some extent, so that the optical and THz radiation will propagate at different velocities. This means that after some distance the induced polarization will contribute destructively to the generated THz pulse and over a large distance the generated THz radiation will be average to zero. This leads to the definition of 'walk-off length',

$$l_w = \frac{c\tau_p}{(n_T - n_O)}, \quad (1.14)$$

where τ_p is the duration of the femtosecond pulse. For efficient THz generation the nonlinear material should have a long walk-off length and be thinner than the walk-off length. In practice, the condition for phase matching is more critical; the group velocity at optical frequencies (the velocity of the optical pulse) should match the phase velocity at THz frequencies. With careful choice of nonlinear crystal and optical wavelength this condition can be reached for a limited spectral range. Around 800 nm, where ultra-short pulses from Ti:Sapphire laser are available, the nonlinear medium which best achieves this criteria is ZnTe. However, while the coherence length for certain frequencies can be long (~ 2 mm), if phase matching is required over a broad range of frequencies, to produce a wide THz bandwidth then thin nonlinear crystals are still required [17].

Phase Matching by Tilt

As mentioned above, for efficient nonlinear generation of THz, phase matching between the optical and THz pulses is required. One novel method for achieving this is by tilting the EO crystal, in particular this has been done successfully with Lithium Niobate (LiNbO_3) [18]. Lithium niobate is a widely used EO crystal because it is highly transparent and has a large EO coefficient (the largest is $d_{33} = 27$ pm/V), however, because of the refractive index mismatch it is not efficient for generating THz in the colinear geometry described above. This mismatch can be overcome by tilting the optical pulses, shown in Fig. 1.7, so that the pulse front of the optical pulse travels at the THz phase velocity. This generates THz radiation at an angle given by

$$\theta_c = \cos^{-1} \left(\frac{n_O}{n_T} \right) \quad (1.15)$$

which for LiNbO_3 is around 64° . This has analogies with Cherenkov radiation and the sonic boom of a supersonic object. This technique has been shown to produce high powers (10 μ W average power), however, the bandwidth available is often not as wide as other techniques [19].

Detection of THz Radiation by Nonlinear Crystals

Besides generating THz radiation, EO crystals can also be used to detect THz pulses. This can be achieved in a conceptually similar way to the scheme above by making use of the Pockels effect; when a (quasi-)static electric field is applied to an EO crystal it induces a change in the polarization of radiation passing through it. This is the inverse of optical rectification, described above, where the presence of an optical field induces a (quasi-)static electric field in the crystal. With reference to Eq. 1.6, we take \mathcal{E}_j to be the optical femtosecond pulse, as before, and \mathcal{E}_k to be the quasi-static field of the THz pulse. Thus the induced change in polarization, $P_i^{(2)}$, is proportional

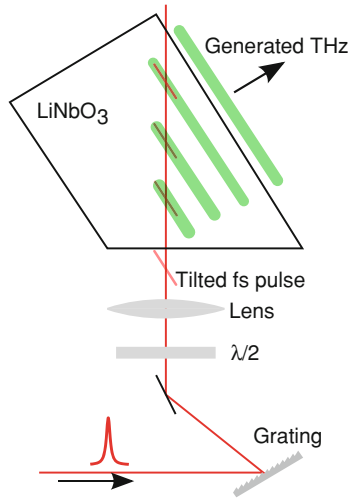


Fig. 1.7 Generation of THz pulses in LiNbO_3 . The femtosecond pulse is tilted by a grating, as it propagates through the nonlinear medium it remains in phase with the generated THz pulses. Several consecutive pulses are shown in the figure

to the product of the optical field from the femtosecond pulse and the THz electric field.

As above, the magnitude of the induced effect is dependent on the alignment of the optical and THz fields to the crystal axes. For example, when using a $\langle 110 \rangle$ orientated ZnTe crystal, the maximum change in polarization is seen when the optical and THz fields are parallel to the $[1\bar{1}0]$ direction, however, the induced polarization is orthogonal to this, so there is a field induced birefringence. Thus, the linearly polarized optical pulse will become slightly elliptically polarized as it travels through the EO crystal in the presence of a THz field. Because the femtosecond pulse is short compared to the THz pulse the induced change in polarization is effectively proportional to the instantaneous value of the THz field which overlaps in time with the femtosecond pulse. Then in a very similar way as described above for PCA detection, by varying the delay between the femtosecond pulse and the THz field and measuring the induced change polarization one may map out the amplitude and phase of the THz pulse. Now all that remains is to measure the change in polarization of the crystal, this is done by analyzing the change in polarization of the femtosecond pulse, outlined in Fig. 1.8.

There are three factors which limit the detection bandwidth achievable with EO sampling. (i) The finite duration of the femtosecond pulse, (ii) the mismatch between the optical group and THz phase velocities, and (iii) the dispersion of the nonlinear susceptibility. In practice this means that ZnTe can achieve very high bandwidths if the optical pulse is short and EO crystal is thin (well below the walk-off length).

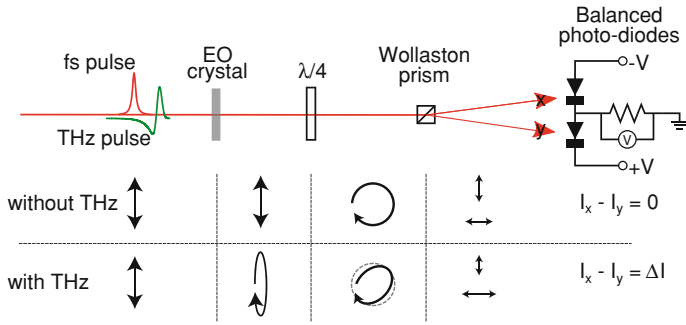


Fig. 1.8 The detection of THz pulses with an EO crystal. The manipulation of the polarization is shown below for the cases with and without THz. The balanced photo diodes measure the difference between the polarization in the x and y direction

1.1.6 Other Broadband Emitters

While PCAs and EO crystals are the most widely used methods for generation and detection of broadband THz radiation, there are several other methods that have been used, we include a short description of these below for completeness.

Air/Laser-Induced Plasmas

Intense laser pulses have the ability to ionize the air or gas they are passing through. This plasma can be used to generate pulses of THz radiation. The advantage of this scheme is that very high laser powers can be used without fear of damaging the nonlinear medium. In the first demonstrations of THz generation from air-plasmas single frequency beams were used [20, 21]. The THz radiation was generated by ponderomotive acceleration of electrons in the plasma. More recently, however, there have been promising results from a technique known as two-color mixing [22], where the generation efficiency is much higher. In this scheme the laser pulse is mixed with its second harmonic. It is thought that the bound electrons of the gas are rapidly ionized by tunnel ionization due to coulomb barrier suppression induced by the instantaneous laser field. The ionized electrons are accelerated by the asymmetric superposition of the laser field (fundamental and second harmonic) to give rise to a directional transient photo current [23]. In a similar way to PCAs, this directional transient photocurrent produces a THz far field because of the femtosecond time scales on which the current is generated.

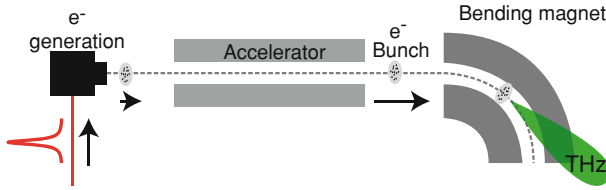


Fig. 1.9 The generation of THz pulses from an electron accelerator by synchrotron radiation. Generation by Bremsstrahlung is not shown

Electron Accelerator Methods

Electron accelerators can produce extremely intense pulses of THz radiation, orders of magnitude brighter than the table-top sources that have so far been discussed. When relativistic electrons are accelerated they produce electromagnetic radiation; by accelerating relativistic bunches of electrons, which have similar spatial extent to THz wavelengths, THz radiation is produced. The scheme is shown in Fig. 1.9, short bunches of electrons are produced by a femtosecond pulse incident on a GaAs surface. This ultra-short electron bunch is accelerated by the accelerator to relativistic speeds. There are then two methods available to produce THz, either the bunch is steered by a magnetic field to produce synchrotron radiation or the electrons are fired at a metal target to produce Bremsstrahlung (braking radiation) (not shown). THz radiation has been produced by, amongst others, Brookhaven National Laboratory [24], Jefferson Laboratory [25] and BESSY [26]. More details and applications of this technique are given in Chap. 23.

Photo-Dember Emitters

Electrons and holes in a semiconductor in general have different diffusivities, thus if the spatial environment is asymmetric (the surface of a semiconductor for example) photogenerated electrons and holes will diffuse to form an antisymmetric charge distribution, known as the photo-Dember effect. This transient current will be in the direction of the asymmetry, so in the case of a semiconductor surface the transient current will be perpendicular to the surface and the resulting far-field THz will propagate in the plane of the surface, making efficient collection of the THz field very challenging. It has recently been shown, however, that by simply masking the semiconductor surface it is possible to generate the transient current in the plane of the surface, causing the far-field radiation to be emitted perpendicular to the semiconductor surface [27].

1.1.7 Future Prospects for Development of THz Radiation

While THz time-domain spectroscopy is a mature technique, it is still being actively developed around the world. Two parameters in which there is particular interest in improving are the THz pulse power and bandwidth. The characteristics of the femtosecond laser affect both the bandwidth and power of the THz pulse. Femtosecond lasers with ultrashort pulses, down to around 5 fs have become more widely available over time and output powers are improving. Femtosecond fiber lasers have also generated much interest in the THz community recently, owing to the reduced size and cost of these systems over conventional bulk lasers; pulses of less than 100 fs are now available from these systems and repetition rates as high as 10's GHz are possible allowing faster data acquisition. Looking further to the future, semiconductor-based vertical external-cavity surface-emitting lasers (VECSELs) are an exciting possibility for reducing both size and cost of femtosecond laser systems [28, 29].

The other important parameter for improving the performance of THz systems is the materials for generation and detection of THz pulses. If the material is used as a PCA then the important parameter is the electron recapture time, which can be engineered by introducing defects into the material, this can be done during crystal growth, or postgrowth by radiation damage or temperature treatment. Work on developing materials and treatments to provide the fastest trapping times is still an active area of research. Another potential system for improved electron recapture times are intersubband transition which show very fast scattering rates [30]. There is also active research into new nonlinear materials for THz generation; organic materials, such as Diethylaminosulfur trifluoride (DAST) have recently received much attention [31]. There are a wide range of other materials in this category, such as amorphous electrooptic polymers, semiconducting polymers, and molecular salt EO crystals which are also the focus of current research and offer exciting possibilities for custom-designed THz nonlinear mediums.

1.2 CW THz Generation

Up to this point, we have been concerned with producing and detecting broadband THz pulses, however there are also several technologies for producing CW, narrow band THz radiation, which we will discuss in this section.

1.2.1 Photomixing

Photomixing is conceptually similar to the PCAs discussed in Sect. 1.1, the difference being that rather than a broadband femtosecond pulse to excite the electrons in the semiconductor two CW lasers are used, Fig. 1.10. The PCA is replaced with a

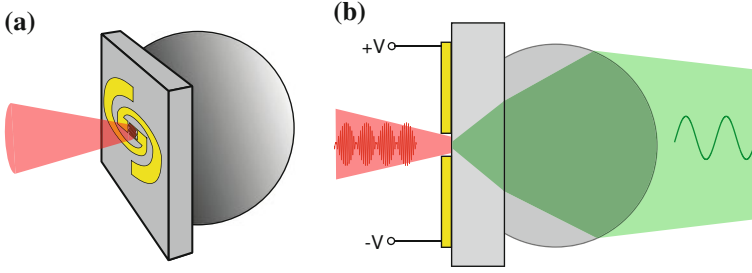


Fig. 1.10 **a** A photomixer device with a log-spiral antenna. **b** The THz radiation that is generated has a frequency at the difference between two incoming optical beams. A silicon lens attached to the device enhances the collection of generated radiation, as in a PCA

photomixer, which is usually LT-GaAs grown on an SI-GaAs substrate [32]. On this layer a planar antennae structure is defined [33]. With an LT-GaAs photomixer the CW lasers are chosen to have a wavelength around 800–850 nm to match the bandgap of the material. When the radiation from the CW lasers arrives at the photomixer the signals interfere to cause a beat signal:

$$I(t) \propto |E_1 e^{-i\omega_1 t} + E_2 e^{-i\omega_2 t}|^2 = |E_1|^2 + |E_2|^2 + 2E_1 E_2 \cos(\omega t), \quad (1.16)$$

where the last term represents the beat modulation, at frequency $\omega = |\omega_1 - \omega_2|$. Thus, the photogenerated current in the LT-material is modulated at the beat frequency. The resultant is an oscillating dipole that emits radiation at a frequency, ω , which is the difference of the CW lasers. By tuning the frequency of one of the lasers the frequency of the radiation emitted by the photomixer can be tuned over a wide range.

The tuning range at the high-frequency end is primarily limited by the response time of the material. Generating a high-frequency THz field corresponds to more rapid oscillation of the induced photocurrent; a typical working limit is around 3 THz.

As for PCAs, the design of the antenna structure is an important topic. Several antenna designs have been tested, including log-spiral designs, dipole antenna, and more complex designs. Log-spiral designs aim to operate effectively over a wide range of frequencies, allowing maximum tuning, whereas a dipole antenna design will generally be optimized for higher frequency ranges (1–2 THz), where the efficiency of the photomixer is lower.

The advantages of photomixer devices are the broad tunability, which typically ranges from 0.1–3 THz, and the integration that is possible with diode and fiber technologies [34, 35]. The frequency resolution available with photomixers (<1 GHz) is also generally higher than pulsed methods of Sect. 1.1.2 (~10 GHz) which means that photomixers are often favored for gas spectroscopy. These advantages are offset by the low powers available, which are typically in the microwatt range. More details of the operation and performance of photomixers can be found in Refs. [36, 37].

1.2.2 Difference Frequency Generation

Difference frequency generation (DFG) [14] makes use of the same type of second-order nonlinearities present in EO crystals that are used for optical rectification, described in Sect. 1.1.5. With reference to Eq. 1.6, if the two electric fields, \mathcal{E}_j and \mathcal{E}_k , are from two different monochromatic light beams, which have different frequencies then the polarization of the medium will oscillate at both the sum and difference frequencies:

$$\begin{aligned}
 P_i^{(2)} &\propto \sum_{j,k=x,y,z} \chi_{ijk}^{(2)} \mathcal{E}_{0,j} \cos(\omega_1 t) \mathcal{E}_{0,k} \cos(\omega_2 t) \\
 &\propto \frac{1}{2} \sum_{j,k=x,y,z} \chi_{ijk}^{(2)} \mathcal{E}_{0,j} \mathcal{E}_{0,k} [\cos((\omega_1 + \omega_2)t) + \cos((\omega_1 - \omega_2)t)]
 \end{aligned}
 \tag{1.17}$$

The polarization oscillating at the difference frequency is the source of THz radiation. Thus, with careful phase matching THz radiation can be produced with a frequency equal to the difference between the two input beams.

In practice, the most crucial aspect of DFG is the phase matching; ensuring that the oscillating polarization is in phase with the generated THz wave throughout the crystal. Typically the angle of the nonlinear medium is tuned to ensure phase matching. The most commonly used material for DFG is GaSe [38]. There are several reasons for the popularity of GaSe: it has a large EO coefficient, $d_{22} = 54 \text{ pm/V}$, it is highly transparent to both THz and optical radiation and phase matching is possible with pump beams in the infrared region, where powerful lasers such as Nd:YAG are available. Another possible geometry for DFG is to place the nonlinear medium inside a cavity, such as the example of reference [39], where the DFG is integrated into an optical parametric oscillator (OPO). The typical average powers available for DFG around a few μW s for wide tuning.

1.2.3 Parametric Amplification

Parametric amplification is also based on optical nonlinearities present in EO crystals, in particular LiNbO_3 is widely used for this purpose. It is similar to DFG, however, for parametric amplification a single input beam is used rather than two input beams used for DFG. The single input beam is known as the ‘pump’, which, in the nonlinear medium generates two beams, $\omega_p = \omega_s + \omega_i$, where ω_s is the signal beam and ω_i is the idler frequency. The frequency of the signal beam is then controlled by the phase matching condition, $\mathbf{k}_p = \mathbf{k}_s + \mathbf{k}_i$, where \mathbf{k} is the wave vector. The phase matching condition is controlled by changing the angle that the idler beams makes with the pump beam in the nonlinear medium. A separate laser beam can be used to seed the idler, or more usually an idler cavity is used, this arrangement is shown in Fig. 1.11.

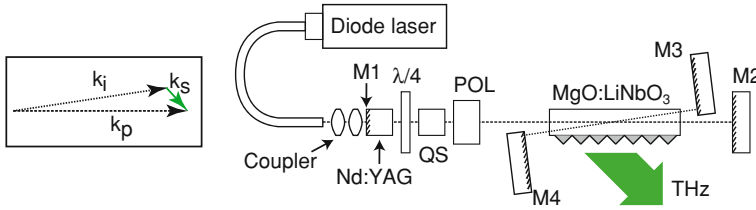


Fig. 1.11 The phase matching condition and optical arrangement for parametric amplification. A diode laser is used to pump the Nd:YAG laser, which in turn pumps the nonlinear medium, placed in the laser cavity. The quarter-wave plate ($\lambda/4$), Q-switch (QS), and polarizer (POL) are used to Q-switch the cavity. A silicon grating assists in coupling out the THz radiation. Reproduced from Ref. [41]

The idler cavity ensures that there is always a strong idler seed present, this increases the output efficiency, further details can be found in Ref. [40]. The tuning range of these type of arrangements is generally in the 1–3 THz range, and peak powers can exceed 3 W peak power and $10\ \mu\text{W}$ average power [41].

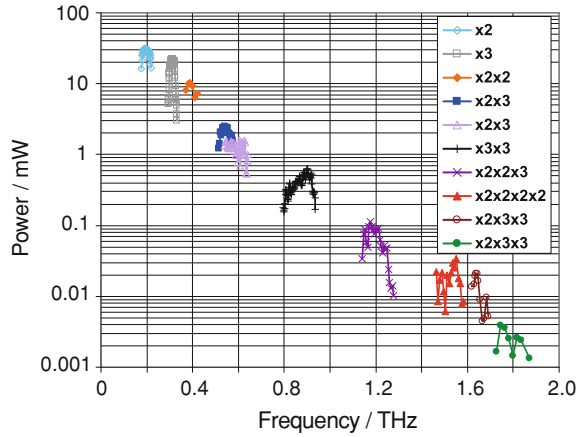
1.2.4 Gas Lasers

Gas lasers operating in the THz frequency range are a relatively old technology, and are conceptually very similar to gas lasers operating in the visible region of the spectrum. The chemical species that are used are molecular gases, commonly CH_3OH , NH_3 , CH_2F_2 , CH_3Cl and CH_3I . These molecules have permanent dipole moments so transitions between rotational modes couple to electromagnetic radiation directly, through electric dipole transitions. These transitions form the active laser transition. The gas is typically pumped with a CO_2 laser at around $\lambda = 10\ \mu\text{m}$. The power levels from these lasers can be very high, exceeding 100 mW. However, because the transition is due to a molecular species there is no tuning available, other than by changing to different discrete lines or changing the gas species to operate on another fixed frequency. Another draw-back of these systems is the bulk and power required for their operation. Further details can be found in Ref. [42].

1.2.5 Microwave Frequency Multipliers

Microwave sources up to around 100 GHz are a relatively mature technology, that has received significant interest due to applications in communications and military hardware. Microwave sources at higher frequencies are usually based on Gunn diodes and impact ionization avalanche transit-time (IMPATT) diodes. These sources are

Fig. 1.12 The relation between power and frequency for a range of frequency multipliers at room temperature. Modified from Ref. [46]



compact, solid state, and operate at room temperature, more information on these can be found in Ref. [43].

In recent years the range of these sources have been extended by the use of frequency multipliers [44, 45]. Frequency multipliers are usually based on Schottky diodes, which have a nonlinear response to the electromagnetic waves, in an analogous way to optical nonlinear media. The Schottky diode will generate harmonic components of the incoming wave (generated by, e.g. Gunn diode) and with a suitable waveguide for output coupling these harmonics are collected. It is also possible to use several frequency multipliers in series to produce even higher frequencies. The power available from these devices remains lower, however, and drops with frequency like $\frac{1}{\omega^3}$. This power reduction is illustrated in Fig. 1.12.

1.2.6 Back Wave Oscillators

Back wave oscillators (BWOs) [47] are based on the motion of electrons in vacuum tubes, the name comes from the fact that the electron beam and electromagnetic wave move in opposite directions. A schematic of a BWO device is shown in Fig. 1.13. At one end of the vacuum tube is a heated cathode which emits electrons, that are accelerated by a DC electric field toward an anode at the other end. A magnetic field is also applied along this length to collimate the electron beam. Along the length of the vacuum tube is a metal grating known as a comb slow-wave structure. This periodic structure induces a spatial modulation of the electron beam and the electrons are driven into bunches. These bunched electrons then excite surface waves on the grating. If the velocity of the electrons is equal to the phase velocity of the electromagnetic wave then the energy of the electrons is transferred to the electromagnetic wave. The frequency generated is therefore proportional to the velocity of

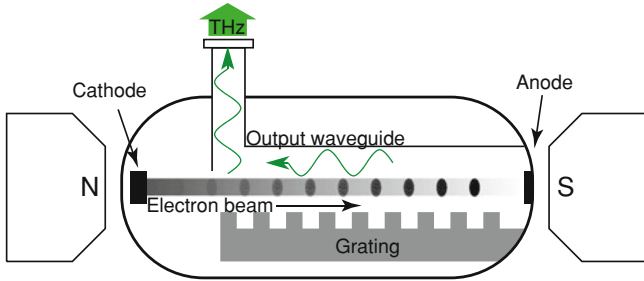


Fig. 1.13 Schematic diagram of a back wave oscillator. Reproduced from Ref. [48]

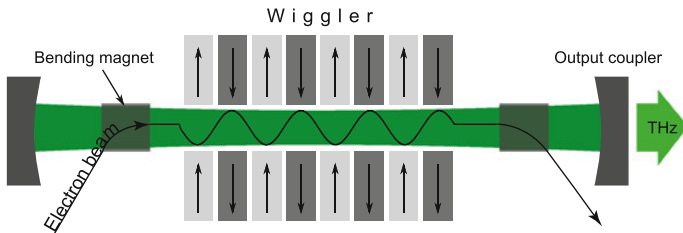


Fig. 1.14 The electron beam is directed into the laser cavity where it performs a sinusoidal motion, producing THz radiation

the electrons and hence the DC bias. The THz electromagnetic wave is coupled out through a waveguide.

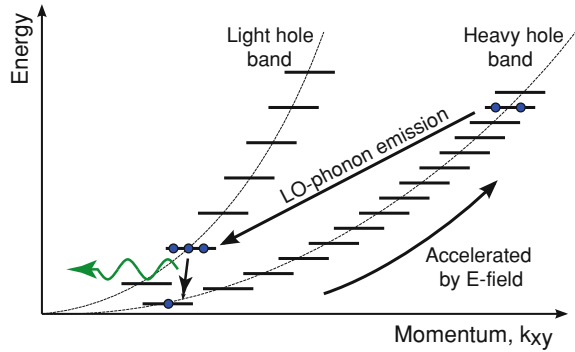
The power available from BWOs below 300GHz is in the 100s of mW range, however, the power available above this frequency drops of quickly and above 1 THz BWOs are rarely used. They have been used for imaging in the 500–700 GHz range though, where powers around 15 mW are obtained [49].

1.2.7 Free Electron Lasers

In many ways free electron lasers (FELs) are the ultimate THz source; high power, broadly and continuously tunable, and coherent. The one and severe drawback is the size and cost of these systems which limit their use to large facilities.

Despite their complexity, the operational principals of FELs are relatively simple, depicted in Fig. 1.14. A beam of electrons are injected into a region where there is a magnetic field that varies periodically with distance. This periodic array of magnets is known as a ‘wiggler’. The wiggler generates coherent monochromatic electromagnetic radiation because of the sinusoidal motion of the electrons. The generated radiation resonates in an optical cavity which is collinear with the electron beam. Thus the FEL is very similar to a conventional laser, with the electrons in sinusoidal motion taking the place of the gain region. A full analysis of the beam

Fig. 1.15 Diagram of the dispersion curves for holes in a p-Ge laser. The active transition is from a meta-stable light-hole state to a heavy-hole state



generation requires the inclusion of relativistic effects because the electrons are traveling close to the speed of light [50].

As mentioned, the use of FELs is limited to large facilities. Some that are open to outside researchers include iFEL (Japan), FELIX at FOM (Netherlands), CLIO at LURE-orsay (France), FELBE at FZ Rossendorf (Germany), FIREFLY at Stanford CA (USA), and FIR-FEL at UCSB CA (USA) [51].

1.2.8 P-Type Germanium Lasers

P-type germanium lasers are a solid state electrically pumped source of THz radiation which typically emit between 1 and 4.5 THz [52, 53], the power produced can be large, upto around 5 W peak power for pulsed operation [54]. There are a few drawbacks to these sources, however, such as spectral purity, the requirement for high magnetic fields and operating temperature. The maximum operating temperature is around 40 K and cooling capacity of several watts is required because of the large input powers. This need for low temperatures is due to the mechanism by which these devices produce population inversion, which requires emission of LO-phonons. Because of the sensitivity to temperature these devices can only be operated at low duty cycles.

A diagram indicating the lasing mechanism is shown in Fig. 1.15. The germanium, usually beryllium doped, is placed in a magnetic field, this splits the hole states into discrete (Landau) levels. An electric field is applied perpendicular to the magnetic field, this electric field accelerates the holes in the heavy hole bands and they move up the dispersion curves. When the heavy hole achieves an energy that is greater than the LO-phonon energy it may spontaneously emit an LO-phonon. Some of these holes will end up in the quantized light hole states which have a relatively long lifetime. As indicated in Fig. 1.15, a population inversion can build up between the long-lived light hole state and heavy hole states away from the Brillouin zone center. By changing the electric and magnetic fields across the sample the frequency of the laser emission can be tuned.

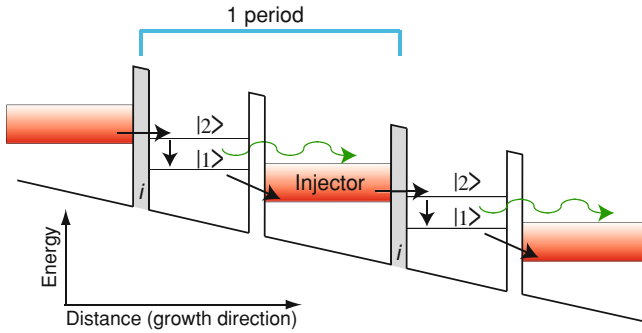


Fig. 1.16 A generic QCL design. The *lower* and *upper* laser levels are labeled $|1\rangle$ and $|2\rangle$ respectively. The shaded red region labeled ‘injector’ indicates a number of electronic states. *Black arrows* indicate electron transport, the *green arrow* represents the emission of a photon

1.2.9 Quantum Cascade Lasers

Quantum cascade lasers (QCLs) rely on transport of electrons² in the conduction band of semiconductor heterostructures. The band structure of QCLs can vary widely, however, the essential characteristics of any QCL can be represented by the simplified diagram in Fig. 1.16.

The diagram depicts the conduction band of the device with an external bias applied. There are two materials present in the structure; the conduction band offset between these two materials provides the ‘wells’ and ‘barriers’ that can be seen in the diagram. The structure is made up from a number of periods which each contain the same sequence of wells and barriers. Each period has a pair of states, in this case labeled $|1\rangle$ and $|2\rangle$, between which the laser transition occurs. This scheme means that an electron may make an optical transition every period, giving the quantum cascade laser its name. Also marked on the diagram is the ‘injector’, this is a collection of electronic states that collect electrons from the lower laser level, $|1\rangle$, and inject electrons into the upper laser level, $|2\rangle$. Figure 1.16 shows the injector existing in a large well, however, in practice this region will contain several wells and barriers to allow many electron states to exist.

One of the most attractive features of the QCL scheme is that the emission wavelength is set only by the design of the active region, rather than the bandgap of the material, as for interband diode lasers. Since the first THz QCL was demonstrated at 4.4 THz there have been reports of devices working over a large range of frequencies, down to 1.3 THz [55]. With magnetic field assistance the lowest frequency is 830 GHz [56]. The temperature performance has also showed marked improvement from the maximum operating temperature of 50 K achieved in pulsed mode in the original paper; CW operation was soon achieved [57] and currently the maximum operating temperatures of THz QCLs is 186 K [58], and 225 K when a strong

² p-type QCLs, relying on hole transport are thought to be possible but have not been demonstrated.

magnetic field is used [59]. Peak powers for THz QCLs are typically around 10s of mW and can reach up to above 100mW.

1.3 Detectors

We have already discussed a few detection schemes in Sect. 1.1. These detectors relied on a femtosecond optical pulse to trigger the detection; the same pulse that triggered the THz pulse generation. In this section we turn our attention to detectors which do not use this type of trigger. With the exception of heterodyne detection, the detectors in this section do not provide any spectral information about the incoming radiation. Typically these detectors are used in conjunction with a Fourier transform infrared (FTIR) spectrometer. An FTIR is a Michelson interferometer, comprising a beam splitter, a fixed mirror, and a scanning mirror. The interferogram is recorded by the detector as a function of mirror displacement, the Fourier transform of the interferogram reveals the spectrum [60].

1.3.1 Thermal Detectors

Many of the most widely used detectors for THz radiation are based on thermal detection, these comprise of an absorbing element which absorbs the THz radiation, resulting in a small rise in temperature. It is this rise in temperature which is detected. One advantage of this thermal detection scheme is that the detector is sensitive to a wide range of frequencies; however; the most sensitive detectors require cooling and are intrinsically slow compared to the coherent nonlinear detectors and photon detectors. A good recent review of all types of THz detector can be found in Ref. [61].

A bolometer operates by sensing the change in the electrical resistance of the absorber [62]. Typically the active element is a highly doped semiconductor, such as Si or Ge, because the resistance of these materials is highly sensitive to temperature. These detectors are also cooled with LHe to further increase their sensitivity. The detection circuit is an important part of bolometric detection, bolometers often use a Wheatstone bridge or similar circuit to detect the change in resistance.

A pyroelectric detector exploits the pyroelectric effect. Many crystals are pyroelectric, also known as polar crystals, since they have a permanent dipole in the unit cell such that the whole crystal is polarized. A pyroelectric detector works by measuring the change in this polarization with temperature [63]. Crystals that are used commonly used for the detection of THz radiation are deuterated triglycine sulfate (DTGS), lithium tantalate (LiTaO_3), and triglycine sulfate (TGS). The detection is performed by effectively forming a capacitor with the pyroelectric crystal as the region between the plates. Because of the permanent dipole of the crystal there will be charge on the capacitor plates. When the THz radiation is absorbed by either

the crystal or the electrodes the temperature of the crystal will increase, changing the polarization. This change in polarization will cause charge to flow between the plates, which is measured.

Golay detectors were first developed over 60 years ago and the principal of operation is quite simple [64, 65]. A Golay detector comprises a gas cell, usually Xenon, and a flexible window. As the gas is heated, by the absorbed THz radiation it expands and deforms the diaphragm. The displacement of the diaphragm is measured by a photodiode.

Of these thermal detectors LHe cooled bolometers are by far the most sensitive, with typical noise equivalent power (NEP) in the range of $2\text{p WHz}^{-1/2}$, however, they are also the largest, most expensive, and require cryogenics to operate. Of the room temperature detectors, Golay cells have a slightly lower NEP, typically around $0.1\text{--}1\text{n WHz}^{-1/2}$, whereas the NEP for pyroelectric detectors is typically $3\text{--}5\text{n WHz}^{-1/2}$. Another consideration for detectors is their speed. For cooled bolometers this is generally in the 100s of Hz, whereas for Golay cells the figure is around $10\text{--}50\text{Hz}$ and pyroelectric detectors tend to be $<10\text{Hz}$. This parameter is important as a lock-in measurement is usually made; the THz source is modulated either by an optical chopper or some other means and a lock-in amplifier is used to recover the signal. The detector speed dictates the optimum rate at which one may modulate the source.

1.3.2 Heterodyne Detection

The principals of heterodyne detection are similar to the nonlinear mechanisms already discussed in Sects. 1.1.5 and 1.2.2. The scheme relies on having a powerful THz source available, this is known as the local oscillator. The local oscillator radiation and the signal beam both impinge on the nonlinear detector and generates harmonics, including a signal at the difference frequency; all other frequencies being filtered out. The difference signal will be weak, but it will be in the GHz range thus it can be easily amplified and analyzed readily with RF electronics. In this way not only the amplitude of the signal can be measured, but also the frequency separation from the local oscillator (the frequency of the local oscillator is well known).

The nonlinear detectors used are Schottky diodes and hot electron bolometers (HEBs) [66]. Below 1 THz Schottky diodes work well but require large local oscillator powers, the local oscillator in this case is usually a solid state source (Sect. 1.2.5). Above 1 THz HEBs are the most sensitive, the most common local oscillators were once gas lasers but increasingly QCLs are being used [67, 68] due to their compact size, high power output and intrinsically narrow line widths.

1.3.3 Intersubband Detectors

Intersubband detectors in the THz frequency range are a relatively recent development [69, 70]. They are based on the same type of intersubband transitions on which QCLs operate; the incoming THz photon is absorbed by an electron in a quantum well and is excited to a continuum of states, from where it can flow to the contact and be detected. The major advantage of intersubband detectors is the speed at which they can operate; expected to be in the picosecond range, the development is still in the early stages however.

1.4 Conclusions

In this introductory chapter we have surveyed many of the methods used for generation and detection of THz radiation and outlined the physical origin of the processes involved. Although we have discussed a range of methods here, the method which is most applicable to spectroscopy is THz TDS, described in Sect. 1.1, and the following chapters of this book reflect that. Most of the following chapters make use of table-top THz spectrometer systems which are very similar to the scheme set out in Sect. 1.1.2 using PCAs (Sect. 1.1.3) for the generation of THz pulses and either PCAs or EO sampling for detection. The reader will note that many of the experiments discussed use fiber-fed systems to increase robustness and useability. The exception to use of PCAs is when very high power pulses of THz radiation are required such as in Chaps. 9 and 18. In these cases one must turn either to nonlinear methods (titled LiNbO₃, plasma generation) or accelerator methods such as FELs.

References

1. D.H. Auston, K.P. Cheung, P.R. Smith, *Appl. Phys. Lett.* **45**(3), 284 (1984). doi:[10.1063/1.95174](https://doi.org/10.1063/1.95174)
2. C. Fattinger, D. Grischkowsky, *Appl. Phys. Lett.* **53**(16), 1480 (1988). doi:[10.1063/1.99971](https://doi.org/10.1063/1.99971)
3. C. Fattinger, D. Grischkowsky, *Appl. Phys. Lett.* **54**(6), 490 (1989). doi:[10.1063/1.100958](https://doi.org/10.1063/1.100958)
4. O. Svelto, *Principles of Lasers* (Plenum Press, New York, 1998), pp. 330–359
5. B. Sartorius, H. Roehle, H. Künzel, J. Böttcher, M. Schlak, D. Stanze, H. Venghaus, M. Schell, *Opt. Express* **16**(13), 9565 (2008). <http://www.opticsexpress.org/abstract.cfm?URI=oe-16-13-9565>
6. J. Jackson, *Classical Electrodynamics*, 3rd edn. (Wiley, New York, 1998), pp. 410–413
7. L. Duvillaret, F. Garet, J.F. Roux, J.L. Coutaz, *IEEE J. Sel. Top. Quantum Electron.* **7**(4), 615 (2001). doi:[10.1109/2944.974233](https://doi.org/10.1109/2944.974233)
8. D.C. Look, D.C. Walters, G.D. Robinson, J.R. Sizelove, M.G. Mier, C.E. Stutz, *J. Appl. Phys.* **74**(1), 306 (1993). doi:[10.1063/1.354108](https://doi.org/10.1063/1.354108)
9. K.A. McIntosh, K.B. Nichols, S. Verghese, E.R. Brown, *Appl. Phys. Lett.* **70**(3), 354 (1997). doi:[10.1063/1.118412](https://doi.org/10.1063/1.118412)
10. M. Tani, S. Matsuura, K. Sakai, S.I. Nakashima, *Appl. Opt.* **36**(30), 7853 (1997). <http://ao.osa.org/abstract.cfm?URI=ao-36-30-7853>

11. M. Tani, Y. Hirota, C. Que, S. Tanaka, R. Hattori, M. Yamaguchi, S. Nishizawa, M. Hangyo, *Int. J. Infrared Millim. Waves* **27**(4), 531 (2006). doi:[10.1007/s10762-006-9105-8](https://doi.org/10.1007/s10762-006-9105-8)
12. F. Miyamaru, Y. Saito, K. Yamamoto, T. Furuya, S. Nishizawa, M. Tani, *Appl. Phys. Lett.* **96**(21), 211104 (2010). doi:[10.1063/1.3436724](https://doi.org/10.1063/1.3436724)
13. P.K. Benicewicz, J.P. Roberts, A.J. Taylor, *J. Opt. Soc. Am. B* **11**(12), 2533 (1994). <http://josab.osa.org/abstract.cfm?URI=josab-11-12-2533>
14. A. Yariv, P. Yeh, *Optical Waves in Crystals*, (Wiley, New York, 2003), Chap. Nonlinear Optics
15. Y.J. Ding, I.B. Zotova, *Opt. Quantum Electron.* **32**(4), 531 (2000). doi:[10.1023/A:1007099701272](https://doi.org/10.1023/A:1007099701272)
16. G. Gallot, J. Zhang, R.W. McGowan, T.I. Jeon, D. Grischkowsky, *Appl. Phys. Lett.* **74**(23), 3450 (1999). doi:[10.1063/1.124124](https://doi.org/10.1063/1.124124)
17. A. Leitenstorfer, S. Hunsche, J. Shah, M.C. Nuss, W.H. Knox, *Appl. Phys. Lett.* **74**(11), 1516 (1999). doi:[10.1063/1.123601](https://doi.org/10.1063/1.123601)
18. A.G. Stepanov, J. Hebling, J. Kuhl, *Appl. Phys. Lett.* **83**(15), 3000 (2003). doi:[10.1063/1.1617371](https://doi.org/10.1063/1.1617371)
19. K.L. Yeh, M.C. Hoffmann, J. Hebling, K.A. Nelson, *Appl. Phys. Lett.* **90**(17), 171121 (2007). doi:[10.1063/1.2734374](https://doi.org/10.1063/1.2734374)
20. H. Hamster, A. Sullivan, S. Gordon, W. White, R.W. Falcone, *Phys. Rev. Lett.* **71**(17), 2725 (1993). doi:[10.1103/PhysRevLett.71.2725](https://doi.org/10.1103/PhysRevLett.71.2725)
21. T. Löffler, F. Jacob, H.G. Roskos, *Appl. Phys. Lett.* **77**(3), 453 (2000). doi:[10.1063/1.127007](https://doi.org/10.1063/1.127007)
22. K.Y. Kim, A.J. Taylor, J.H. Glowina., G. Rodriguez, *Nat. Photon* **2**(10), 605 (2008). doi:[10.1038/nphoton.2008.153](https://doi.org/10.1038/nphoton.2008.153)
23. K.Y. Kim, *Phys. Plasmas* **16**(5), 056706 (2009). doi:[10.1063/1.3134422](https://doi.org/10.1063/1.3134422)
24. Y. Shen, T. Watanabe, D.A. Arena, C.C. Kao, J.B. Murphy, T.Y. Tsang, X.J. Wang, G.L. Carr, *Phys. Rev. Lett.* **99**(4), 043901 (2007). doi:[10.1103/PhysRevLett.99.043901](https://doi.org/10.1103/PhysRevLett.99.043901)
25. G.L. Carr, M.C. Martin, W.R. McKinney, K. Jordan, G.R. Neil, G.P. Williams, *Nature* **420**(6912), 153 (2002). doi:[10.1038/nature01175](https://doi.org/10.1038/nature01175)
26. M. Abo-Bakr, J. Feikes, K. Holldack, G. Wüstefeld, H.W. Hübers, *Phys. Rev. Lett.* **88**(25), 254801 (2002). doi:[10.1103/PhysRevLett.88.254801](https://doi.org/10.1103/PhysRevLett.88.254801)
27. G. Klatt, F. Hilser, W. Qiao, M. Beck, R. Gebis, A. Bartels, K. Huska, U. Lemmer, G. Bastian, M. Johnston, M. Fischer, J. Faist, T. Dekorsy, *Opt. Express* **18**, 4939 (2010)
28. Z. Mihoubi, K.G. Wilcox, S. Elsmere, A. Quarterman, R. Rungsawang, I. Farrer, H.E. Beere, D.A. Ritchie, A. Tropper, V. Apostolopoulos, *Opt. Lett.* **33**(18), 2125 (2008). <http://ol.osa.org/abstract.cfm?URI=ol-33-18-2125>
29. A.H. Quarterman, K.G. Wilcox, V. Apostolopoulos, Z. Mihoubi, S.P. Elsmere, I. Farrer, D.A. Ritchie, A. Tropper, *Nat. Photonics* **3**(12), 729 (2009). doi:[10.1038/nphoton.2009.216](https://doi.org/10.1038/nphoton.2009.216)
30. E. Baumann, F.R. Giorgetta, D. Hofstetter, H. Lu, X. Chen, W.J. Schaff, L.F. Eastman, S. Golka, W. Schrenk, G. Strasser, *Appl. Phys. Lett.* **87**(19), 191102 (2005). doi:[10.1063/1.2126130](https://doi.org/10.1063/1.2126130)
31. X. Zheng, C.V. McLaughlin, P. Cunningham, M.L. Hayden, *J. Nanoelectron. Optoelectron.* **2**, 58 (2007)
32. E.R. Brown, F.W. Smith, K.A. McIntosh, *J. Appl. Phys.* **73**(3), 1480 (1993). doi:[10.1063/1.353222](https://doi.org/10.1063/1.353222)
33. S. Matsuura, M. Tani, K. Sakai, *Appl. Phys. Lett.* **70**(5), 559 (1997). doi:[10.1063/1.118337](https://doi.org/10.1063/1.118337)
34. K.A. McIntosh, E.R. Brown, K.B. Nichols, O.B. McMahan, W.F. DiNatale, T.M. Lyszczarz, *Appl. Phys. Lett.* **67**(26), 3844 (1995). doi:[10.1063/1.115292](https://doi.org/10.1063/1.115292)
35. S. Verghese, K. McIntosh, E. Brown, *IEEE Trans. Microwave Theory Tech.* **45**(8), 1301 (1997)
36. D. Saeedkia, S. Safavi-Naeini, *J. Lightwave Technol.* **26**(15), 2409 (2008). <http://jlt.osa.org/abstract.cfm?URI=JLT-26-15-2409>
37. E. Brown, in *Proceedings of the Society of Photo-Optical Instrumentation Engineers (SPIE)*, 2011
38. W. Shi, Y.J. Ding, N. Fernelius, K. Vodopyanov, *Opt. Lett.* **27**(16), 1454 (2002). doi:[10.1364/OL.27.001454](https://doi.org/10.1364/OL.27.001454)
39. J.E. Schaar, K.L. Vodopyanov, M.M. Fejer, *Opt. Lett.* **32**(10), 1284 (2007). doi:[10.1364/OL.32.001284](https://doi.org/10.1364/OL.32.001284)

40. K. Kawase, J. ichi Shikata, H. Ito, J. Phys. D Appl. Phys. **35**(3), R1 (2002). <http://stacks.iop.org/0022-3727/35/i=3/a=201>
41. D.J.M. Stothard, T.J. Edwards, D. Walsh, C.L. Thomson, C.F. Rae, M.H. Dunn, P.G. Browne, Appl. Phys. Lett. **92**(14), 141105 (2008). doi:10.1063/1.2907489
42. G.W. Chantry, *Long-Wave Optics* (Academic Press, London, 1984)
43. R.G. Carter, *Electromagnetic Waves: Microwave Components and Devices* (Chapman and Hall, London, 1990)
44. V.G. Bozhkov, Radiophys. Quantum Electron. **46**, 631 (2003). doi:10.1023/B:RAQE.0000024993.40125.2b
45. I.R.M. Weikle, T.W. Crowe, E.L. Kollberg, Multiplier and Harmonic Generator Technologies for Terahertz Applications, in *Terahertz Sensing Technology* (World Scientific Publishing, Singapore, 2003)
46. J. Ward, G. Chattopadhyay, J. Gill, H. Javadi, C. Lee, R. Lin, A. Maestrini, F. Maiwald, I. Mehdi, E. Schlecht, P. Siegel, in *33rd International Conference on Infrared, Millimeter and Terahertz Waves, IRMMW-THz 2008*. 15–19 Sept 2008, pp. 1–3. doi:10.1109/ICIMW.2008.4665437
47. G. Kozlov, A. Volkov, in *Millimeter and Submillimeter Wave Spectroscopy of Solids*, ed. by G. Grüner. Topics in Applied Physics, vol. 74, (Springer, Berlin, 1998), Chap. 3, pp. 51–109. doi:10.1007/BFb0103420.10.1007/BFb0103420
48. Y.S. Lee, *Principles of Terahertz Science and Technology* (Springer, New York, 2009), p. 141
49. A. Dobroiu, M. Yamashita, Y.N. Ohshima, Y. Morita, C. Otani, K. Kawase, Appl. Opt. **43**(30), 5637 (2004). doi:10.1364/AO.43.005637
50. K.J. Kim, A. Sessler, Science **250**(4977), 88 (1990). doi:10.1126/science.250.4977.88
51. Ucsb, FEL database. http://sfbfel1.ucsb.edu/www/fel_table.html. Accessed 21 Feb 2011
52. L.A. Reichertz, O.D. Dubon, G. Sirmain, E. Bründermann, W.L. Hansen, D.R. Chamberlin, A.M. Linhart, H.P. Röser, E.E. Haller, Phys. Rev. B **56**(19), 12069 (1997). doi:10.1103/PhysRevB.56.12069
53. E. Brundermann, D.R. Chamberlin, E.E. Haller, Appl. Phys. Lett. **76**(21), 2991 (2000). doi:10.1063/1.126555
54. F. Keilmann, V.N. Shastin, R. Till, Appl. Phys. Lett. **58**(20), 2205 (1991). doi:10.1063/1.105235
55. G. Scalari, C. Walther, M. Fischer, R. Terazzi, H. Beere, D. Ritchie, J. Faist, Laser Photonics Rev. **3**(1–2), 45 (2009). doi:10.1002/lpor.200810030.0214
56. G. Scalari, C. Walther, L. Sirigu, M.L. Sadowski, H. Beere, D. Ritchie, N. Hoyler, M. Giovannini, J. Faist, Phys. Rev. B **76**(11), 115305 (2007). doi:10.1103/PhysRevB.76.115305.0215
57. S. Barbieri, J. Alton, S. Dhillon, H. Beere, M. Evans, E. Linfield, A. Davies, D. Ritchie, R. Kohler, A. Tredicucci, F. Beltram, IEEE J. Quantum Electron. **39**(4), 586 (2003). B017
58. S. Kumar, Q. Hu, J.L. Reno, Appl. Phys. Lett. **94**(13), 131105 (2009). doi:10.1063/1.3114418.0235
59. A. Wade, G. Fedorov, D. Smirnov, S. Kumar, B. Williams, Q. Hu, J. Reno, Nat. Photonics **3**(1), 41 (2009). doi:10.1038/nphoton.2008.251.0217
60. P. Griffiths, J.A.D. Haseth, *Fourier Transform Infrared Spectrometry*, (Wiley, New Jersey, 2007)
61. F. Sizov, OptoElectron. Rev. **18**(1), 10 (2010). doi:10.2478/s11772-009-0029-4
62. P.L. Richards, J. Appl. Phys. **76**(1), 1 (1994). doi:10.1063/1.357128
63. E. Putley, in *Infrared Detectors*, vol. 5, ed. by R. Willardson, A.C. Beer (Academic Press, New York, 1970), pp. 259–285. <http://www.sciencedirect.com/science/article/B7W5P-4SD21XD-B/2/fe15f961c5f5e0cacab06ae91d22e45a>
64. M.J.E. Golay, Rev. Sci. Instrum. **20**(11), 816 (1949). doi:10.1063/1.1741396
65. T.W. Kenny, J.K. Reynolds, J.A. Podosek, E.C. Vote, L.M. Miller, H.K. Rockstad, W.J. Kaiser, Rev. Sci. Instrum. **67**(1), 112 (1996). doi:10.1063/1.1146559
66. P. Yagoubov, M. Kroug, H. Merkel, E. Kollberg, G. Gol'tsman, S. Svechnikov, E. Gershenzon, Appl. Phys. Lett. **73**(19), 2814 (1998). doi:10.1063/1.122599
67. H.W. Hübers, H. Richter, S. Pavlov, A. Semenov, A. Tredicucci, L. Mahler, H. Beere, D. Ritchie, Frequenz **62**(5), 0202 (2008)

68. H. Richter, A.D. Semenov, S.G. Pavlov, L. Mahler, A. Tredicucci, H.E. Beere, D.A. Ritchie, K.S. Il'in, M. Siegel, H.W. Hubers, *Appl. Phys. Lett.* **93**(14), 141108 (2008). doi:[10.1063/1.2988896.0205](https://doi.org/10.1063/1.2988896.0205)
69. H. Liu, H. Luo, C. Song, Z. Wasilewski, A.S. Thorpe, J. Cao, *Infrared Phys. Technol.* **50** (2–3), 191 (2007). doi:[10.1016/j.infrared.2006.10.026](https://doi.org/10.1016/j.infrared.2006.10.026)
70. C.H. Yu, B. Zhang, W. Lu, S.C. Shen, H.C. Liu, Y.Y. Fang, J.N. Dai, C.Q. Chen, *Appl. Phys. Lett.* **97**(2), 022102 (2010). doi:[10.1063/1.3462300](https://doi.org/10.1063/1.3462300)

Chapter 2

Terahertz Optics

J Anthony Murphy and Cr idhe O’Sullivan

Abstract This chapter covers the basic principles of terahertz (THz) optics, beginning with a review of Gaussian beam propagation and including a section on the design of quasi-optical systems. We review the range of optical components and subsystems typically encountered, and discuss the limitations of practical systems. A section on higher precision modelling is also included that summarises techniques for the analysis of aberration, truncation and cross-polarisation effects.

2.1 Introduction—Optics at THz Frequencies

In this chapter we will look in particular at THz optics, design and modelling. Sandwiched between the optical and microwave regimes, the THz portion of the electromagnetic spectrum with frequencies in the range 300 GHz–3 THz (wavelength 1 mm–100 μm , sometimes up to 10 THz) is a challenging one in which to work and so technologies and analysis techniques are often borrowed from other bands. The lack of readily available THz sources and detectors has led to this relatively unexplored region of the electromagnetic spectrum being termed the “THz gap” [1]. Most of the radiation emitted in the universe since the Big Bang is in this range but at these frequencies the Earth’s atmosphere is a strong absorber, mainly due to the presence of water vapour.

Although radiation is typically propagated and analysed as free-space beams, unlike traditional optics, beams may be only a few wavelengths in diameter and diffraction effects can become important [2, 3]. Modelling such beams requires a different approach to geometrical optics, commonly used in the visible where wave-

J. A. Murphy (✉) · C. O’Sullivan
Department of Experimental Physics,
NUI Maynooth, Kildare, Co Kildare, Ireland
e-mail: anthony.murphy@nuim.ie

C. O’Sullivan
e-mail: creidhe.osullivan@nuim.ie

lengths are assumed to be negligible when compared with component and beam sizes. On the other hand, the physical optics techniques used for radio and microwave systems [4], although very accurate, can be computationally slow and inefficient in the design and analysis process of multi-element systems. A Gaussian beam mode analysis, the basis for most of the discussion on optical design and analysis in this chapter, is a useful compromise between the two. The technique, originally developed for dealing with laser beam propagation, is based on a modal description of electromagnetic field propagation [5] and is appropriate for the description of compact optical systems in which diffraction effects are inevitably important (so called “quasi-optical systems”) [3, 6–8].

2.2 Gaussian Beam Propagation in Ideal Optical Systems

2.2.1 Propagation Properties of a Simple Gaussian Beam Mode

In general, Gaussian beam modes are solutions to the paraxial wave equation such that the form of the mode (i.e. intensity distribution) does not change with propagation. They constitute a very convenient basis set of fields with which to simulate the behaviour of propagating beams in quasi-optical systems. The theory of Gaussian beam mode propagation for long-wavelength systems has been elaborated on by a number of authors [1, 3, 6–10] and is the basis for the discussion here.

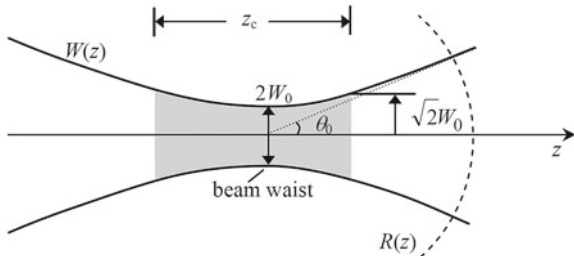
We begin by assuming quasi-collimated propagation of a monochromatic and spatially coherent beam. Such a paraxial beam travels in a well-defined direction and is by definition of finite transverse extent (and not an infinite plane wave, for example). Thus, for a component E of the complex electric field that satisfies the time-independent wave equation (i.e. the Helmholtz Equation: $\nabla^2 E + k^2 E = 0$ where $k = \omega/c = 2\pi/\lambda$), we search only for paraxial solutions travelling in the z -direction, where the amplitude of the electric field varies gradually over a number of wavelengths in the x - and y -directions and the z -direction variation is still dominated by a term of the form $\exp(-jkz)$. Then re-writing the electric field as $E(x, y, z) \equiv u(x, y, z)\exp(-jkz)$ we can re-express the Helmholtz equation as $\nabla^2 u - 2jk\partial u/\partial z = 0$. For paraxial behaviour $u(x, y, z)$ can only change slowly with z over many wavelengths implying: $|\partial^2 u/\partial z^2| \ll |k\partial u/\partial z|$, thus yielding the so-called paraxial wave equation: $\partial^2 u/\partial x^2 + \partial^2 u/\partial y^2 - 2jk\partial u/\partial z = 0$, which relates how u varies with z in the longitudinal direction to how it varies with x and y in the transverse directions.

It is easy to show that a simple solution for u can be written down in the form

$$u(x, y, z) = \frac{u_0}{(q_0 + z)} \exp\left(-j \frac{k(x^2 + y^2)}{2(q_0 + z)}\right), \quad (2.1)$$

where u_0 and q_0 are constants. Clearly at $z = 0$ we obtain a Gaussian-shaped beam if we choose $q_0 = jkW_0^2/2$ (i.e. q_0 is pure imaginary so that $u(x, y, z) \propto$

Fig. 2.1 Characteristic parameters of a Gaussian beam



$\exp(-(x^2 + y^2)/W_0^2)$, a Gaussian-shaped intensity pattern with a $1/e$ in amplitude beam radius of W_0 and a planar phase front. On propagating away from $z = 0$ the exponent in the expression for $u(x, y, z)$ has both real and imaginary terms in $(x^2 + y^2)$, the off-axis transverse distance squared. The imaginary part corresponds to a parabolic phase front on the axis. This has the usual quadratic variation in x and y that one gets in paraxial approximations to a spherical wave front. Re-expressed in the more familiar form

$$E_G(x, y, z) = \sqrt{\frac{2}{\pi W^2(z)}} \exp \left[-\frac{(x^2 + y^2)}{W^2(z)} - jk \left(z + \frac{(x^2 + y^2)}{2R(z)} \right) + j\phi_0(z) \right], \quad (2.2)$$

where the field has been normalised so that $\int_0^\infty \int_0^\infty |E(x, y)|^2 dx dy = 1$.

Setting $z_c = kW_0^2/2$, the $1/e$ beam width parameter $W(z)$ obeys the relationship $W^2(z) = W_0^2 (1 + (z/z_c)^2)$ while for the phase radius of curvature $R(z) = z + z_c^2/z$. The phase-slippage term $\phi_0(z)$ can be re-expressed as $\phi_0(z) = \tan^{-1}(z/z_c)$, (so called as it represents the phase slippage with respect to a plane wave $E = E_0 \exp(-jkz)$ travelling in the z -direction). This may be important in interferometers, for example, in which split beams are recombined after travelling different path lengths so that the phase slippage term is not the same for the two paths.

The beam has a beam waist radius, W_0 , at $z = 0$, where by definition it is of minimum extent and also has an infinite radius of curvature (i.e. has a plane wave front). The wave remains quasi-collimated (i.e. $W(z)$ only increases by a factor of less than $\sqrt{2}$) for values of $-z_c < z < z_c$, known as the confocal distance (or Rayleigh range, see Fig. 2.1). This also represents the “depth of focus” of the beam in some sense although the term focus here does not imply an image. The phase slippage varies only gradually with z between the beam waist and the far field (at which point it settles down to $\pi/2$). The paraxial wave equation thus forces the simplest Gaussian beam solution to have certain characteristic parameters: $W(z)$, $R(z)$, $\phi(z)$, which vary with z in a particular way and thus determine its propagation properties.

If we regard E (complex) as representing the electric field, then the power flux $I = \langle \mathbf{E} \times \mathbf{H}^* \rangle = |E|^2/2\mu_0 c$ (i.e. power per unit area). For convenience we drop the $2\mu_0 c$ and normalise the mode so that the so-called “generalised” power given by: $P = \int_S (|E|^2/2\mu_0 c) dS$ is unity, where S is a transverse plane surface.

Because of the scalar nature of the treatment here, E cannot in reality represent the electric field fully. Instead one can think of it as representing the dominant (for example, the co-polar) component. In fact each component of \mathbf{E} satisfies the wave equation separately and we can use Maxwell's equations to derive all the components of \mathbf{E} and \mathbf{H} if we know two of the components (as the case with waveguide modes [11]). Thus, for cases where detailed information about the polarisation properties of a beam is of interest a vector approach is necessary. It is also possible to carry out a Gaussian beam mode analysis for both transverse components E_x and E_y independently and thus include polarisation at the level of approximation of paraxial optics, although in this case Maxwell's equations are not strictly satisfied [7, 12].

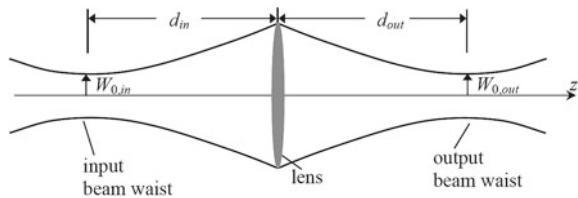
It is worth noting that the same approximations are valid for Gaussian beam mode propagation as for the Fresnel diffraction approximation [7, 9]. In fact we can model both the Fresnel and Fraunhofer regions conveniently with a Gaussian beam mode analysis [13]. Often a simple Gaussian mode is a good approximation both to the radiated beam produced by a typical THz source and to the reception pattern of a typical detector feed, as discussed later. This allows one to readily design optical systems to guide and re-collimate the propagating beam as required for a compact and efficient design [6].

2.2.2 Focussing Gaussian Beams: Simple Optical Systems

A Gaussian beam can be re-collimated using a re-focussing element such as a simple thin lens or curved mirror acting as a phase transformer operating on the spherical incident wavefront of the beam [3, 10]. The correct approach is to regard the effect of an ideal thin lens placed in the path of a Gaussian beam as transforming the radius of curvature R_{in} of the incident wavefront to R_{out} for the transmitted wavefront according to the relationship $1/R_{out} = 1/R_{in} - 1/f$, where f is the focal length of the focussing component. In this formalism, we regard R_{out} as negative if the centre of curvature lies at a more positive value of z than the plane of interest [6]. Clearly, once the power of the thin lens is high enough, we can re-collimate or re-focus a beam. Thus, by appropriate combination of phase curvature transformations we can maintain a quasi-collimated beam over a long distance using a series of re-focussing thin lenses to form a so-called beam guide.

For Gaussian beams, however, the phase radius of curvature R is generally not equal to the distance back to the beam waist or "focus", which complicates optical system design when dealing with Gaussian beams. Clearly, therefore, the usual formulas for imaging in geometrical optics cannot be used in long-wavelength systems to predict the position of the beam waists. At short wavelengths a focussing thin lens of sufficient power will form an image of a point source (a distance u from the thin lens) at a distance $v = uf/(u - f)$ from the thin lens, whereas at long wavelengths $R_{in} \neq d_{in}$ and $R_{out} \neq d_{out}$, where d_{in} and d_{out} are the respective distances back to the respective beam waists. In fact it is important to make a distinction between forming a beam waist (beam at its narrowest extent) and re-imaging the amplitude pattern of a

Fig. 2.2 The focussing of a Gaussian beam



single beam with a complex structure, or indeed even re-imaging an array of beams. A complex field pattern at some plane, even if at a beam waist, will not generally be re-imaged at another beam waist, except for very specialised optical systems such as Gaussian beam telescopes to be discussed below in this section. In general for single-beam systems in which a simple Gaussian beam propagates, imaging issues do not have to be considered.

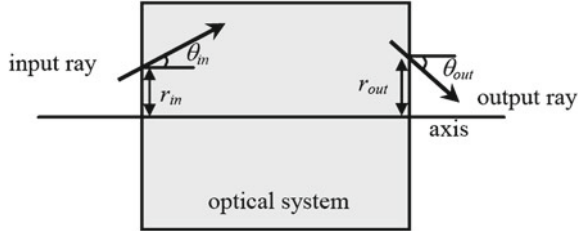
Given that the width of the transmitted beam at an ideal thin lens (i.e. a planar phase transformation) must match that of the incident beam allows us to derive some useful relationships for the position and width of the beam waist on the output side $W_{0,out}$ (see Fig. 2.2), where in terms of the incident beam width parameter $W_{0,in}$ and the focal length of the thin lens (as given in [3, 6] for example)

$$W_{0,out}^2 = \frac{W_{0,in}^2}{\left(1 - \frac{d_{in}}{f}\right)^2 + \left(\frac{k W_{0,in}^2}{2f}\right)^2} \quad \text{and} \quad d_{out} = f + \frac{d_{in} - f}{\left(1 - \frac{d_{in}}{f}\right)^2 + \left(\frac{k W_{0,in}^2}{2f}\right)^2}. \quad (2.3)$$

On considering these, an interesting solution arises if $d_{in} = f$, as then also $d_{out} = f$ (independent of input beam parameters or wavelength!) and both beam waists are on the focal planes of the focussing thin lens and satisfy $W_{0,out}W_{0,in} = (2f/k) = (\lambda f)/\pi$. This behaviour is in marked contrast to geometrical optics and illustrates typical pitfalls in long-wave optics if a geometrical optics design is assumed adequate.

A very convenient optical system is obtained if we arrange a pair of thin lenses separated by the sum of their focal lengths $f_1 + f_2$ with the input beam waist at the focal plane of the first thin lens (of focal length f_1). In this case the output beam waist at thin lens 2 (of focal length f_2), the output focal plane of the system, becomes *independent of frequency*. The system has the optical configuration of a perfect classical optical telescope where $d_{out} = f_2$ and $W_{0,out} = (f_2/f_1)W_{0,in}$! In fact this arrangement is known as a Gaussian beam telescope. These have very important applications in long-wave optical systems particularly where wide-bandwidth behaviour is required. In a multi-element thin lens system we can build up a beam guide by cascading Gaussian beam telescopes thus producing a broadband arrangement that is independent of frequency and has constant magnification if all focal lengths are equal.

Fig. 2.3 Input and output ray trajectories defined by (r_{in}, θ_{in}) and (r_{out}, θ_{out})



2.2.3 ABCD Matrices and Propagation in General Optical Systems

For multi-element optical systems we can use the convenient *ABCD* ray transfer matrix formalism commonly used in geometrical optics [3, 5, 10]. In this case the *ABCD* transfer matrix \mathbf{M} operates on a vector made up of r , the distance from the optical axis to a point on the ray trajectory and the angle θ it makes with the axis (see Fig. 2.3), transforming (r_{in}, θ_{in}) at the input reference plane into (r_{out}, θ_{out}) at the output reference plane according to the matrix equation

$$\begin{bmatrix} r_{out} \\ \theta_{out} \end{bmatrix} = \mathbf{M} \cdot \begin{bmatrix} r_{in} \\ \theta_{in} \end{bmatrix} = \begin{bmatrix} A & B \\ C & D \end{bmatrix} \cdot \begin{bmatrix} r_{in} \\ \theta_{in} \end{bmatrix} = \begin{bmatrix} Ar_{in} + B\theta_{in} \\ Cr_{in} + D\theta_{in} \end{bmatrix}. \quad (2.4)$$

For a multi-element system made up of a series of thin lenses and other optical components, the full *ABCD* matrix is given by a simple matrix product of the corresponding *ABCD* matrix for the individual components but taking care to include any distance propagated in free space or in a medium between components.

The connection with a Gaussian beam is made through the effect of an optical system on the phase curvature of the beam [5]. At short wavelengths a spherical wave emanating from a point source on the optical axis of the system can be modelled as a fan of rays impinging on the input plane where for each ray $r_{in}/\theta_{in} = R_{in}$ is a constant which corresponds to the radius of curvature of the phase front and is equal to the distance back to the point source. Thus, the relationship between the input plane and output plane phase curvatures can readily be derived, $R_{out} = r_{out}/\theta_{out} = (AR_{in} + B)/(CR_{in} + D)$. The *ABCD* matrix formalism for tracing rays thus allows one calculate how the radius of curvature for this beam varies with propagation through the optical system.

Analogously a Gaussian beam can be treated as a complex point source with complex radius of curvature $q(z) = q_0 + z$ on re-expressing the equation for a simple Gaussian as $u(x, y, z) \propto \exp(-jk(x^2 + y^2)/2q(z))$, consistent with Eq. 2.1. The same relationship can be applied in this case to the *complex* phase radius of curvature term q_{in} on propagation of a Gaussian beam from the input to the output plane of some component, $q_{out} = (Aq_{in} + B)/(Cq_{in} + D)$, where q_{out} is the complex radius of curvature at the output plane. We can then recover $(W_{out}, R_{out}, \phi_{out})$ at the output plane for a given $(W_{in}, R_{in}, \phi_{in})$ at the input plane, where $1/q_{in} = 1/R_{in} - j\lambda/\pi W_{in}^2$. The recovered beam parameters at the output plane are

Table 2.1 Examples of $ABCD$ matrices

	$ABCD$ Matrix \mathbf{M}
Propagation a distance L in free space (or a medium of constant refractive index)	$\begin{bmatrix} 1 & L \\ 0 & 1 \end{bmatrix}$
Transformation at a thin lens of focal length f	$\begin{bmatrix} 1 & 0 \\ -1/f & 1 \end{bmatrix}$
Transformation for a Gaussian beam telescope with thin lenses of focal lengths f_1 and f_2	$\begin{bmatrix} -f_2/f_1 & 0 \\ 0 & -f_1/f_2 \end{bmatrix}$
Refraction at a curved interface of radius of curvature R (where n_1 is the initial refractive index, n_2 is the final refractive index, $R < 0$ for convex (centre of curvature after interface))	$\begin{bmatrix} 1 & 0 \\ -(n_1 - n_2)/Rn_2 & n_1/n_2 \end{bmatrix}$

$$R_{\text{out}} = \left(\text{Re} \left[\frac{C + D/q_{\text{in}}}{A + B/q_{\text{in}}} \right] \right)^{-1} \quad W_{\text{out}} = \sqrt{\frac{-\lambda}{\pi}} \left(\text{Im} \left[\frac{C + D/q_{\text{in}}}{A + B/q_{\text{in}}} \right] \right)^{-1}$$

$$\phi_{0,\text{out}} = \phi_{0,\text{in}} - \text{Arg} [A + B(1/q_{\text{in}})]. \quad (2.5)$$

The $ABCD$ matrices for a number of important examples are given in Table 2.1. If a beam propagates through several optical elements (and we include diffraction effects over the path lengths between the components) a single $ABCD$ matrix may be computed for the system, which is the matrix product of all the individual matrices. The first optical element must be on the right-hand side of that product.

$$\mathbf{M}_{\text{total}} = \mathbf{M}_N \cdot \mathbf{M}_{N-1} \cdot \dots \cdot \mathbf{M}_2 \cdot \mathbf{M}_1 = \begin{bmatrix} A & B \\ C & D \end{bmatrix}_{\text{total}}. \quad (2.6)$$

This turns out to be a very powerful technique in designing quasi-optical systems. In the next section we consider the practical issues that arise with re-imaging beams using both focussing mirrors and thick lenses, as well as other optical devices which can be used for developing sophisticated quasi-optical “circuits”.

2.3 Optical Components and Subsystems

2.3.1 Coupling Beams and Focussing Elements

In general when coupling a source to a detector we have to ensure that the source beam is well matched to the reception beam of the detector feed antenna. Any mismatches will give rise to power losses and partial reflections with a reduction in performance. To a reasonable level of accuracy we can design a system with acceptable optical

performance if we can assume that a simple Gaussian beam approximation is valid and that the focussing elements to re-collimate and re-focus the beam are ideal.

In practical applications both re-focussing mirrors as well as lenses tend to be used as phase curvature transformers. Lenses can be easily manufactured from various plastic materials with convenient indices of refraction for the purpose, along with other dielectric and semiconductor materials such as quartz, fused silica, sapphire and silicon [1]. However, some potentially useful materials have non-ideal properties such as non-negligible loss tangents. Also, unless anti-reflection coated, the air–dielectric interface can give rise to partial reflections, especially for materials with high refractive indices such as silicon. Furthermore, any nonuniformities in such materials will introduce extra aberrations and possible cross-polarisation effects which are difficult to model. Useful discussions and reviews are to be found in [3]. Also the recent development of artificial materials including metamaterials at THz frequencies holds out the promise of high resolution imaging [1].

Off-axis focussing mirrors are often preferred for re-collimating the beams because the optical behaviour of the lenses are so affected by the material properties. Although such mirrors do introduce some distortion and cross-polarisation effects, such effects can be precisely modelled and the resulting non-ideal effects predicted [14, 15]. Off-axis mirrors are also easy to manufacture from inexpensive materials, and because the mirror deflects a beam, they lend themselves to compact folded optical systems. For high-sensitivity applications it is possible to cryogenically cool mirrors.

As well as guiding waves using beam guides based on focussing optical components, waveguides and optical fibres (including bare metal wires as effective waveguides) may also be employed depending on the application [16].

Other imaging modalities based on holographic techniques are reported for example in [17, 18]. Such an approach can be used to recover THz images of an actively illuminated object, including phase information. The technique relies on the interference of the object beam with a reference beam, both derived from the same coherent source.

2.3.2 *Off-Axis Focussing Mirrors*

Off-axis ellipsoidal and parabolic mirrors are often used for re-focussing beams. An ellipsoid of revolution provides the ideal phase transformer for matching an input and output spherical wavefront. Projection effects may give rise to some slight asymmetric distortion of the amplitude which can usually be neglected [14, 15]. The centres of curvature of these spherical phase surfaces should coincide with the corresponding foci of the ellipsoid (see Fig. 2.4) [3]. If we wish to re-focus and deflect the beam, and the phase radii of curvature at the point where the deflected beam axis intersects the mirror surface are given by $R_{\text{in}} = R_1$ and $R_{\text{out}} = -R_2$, then the semi-major axis of the appropriate ellipsoid is given by $a = (R_1 + R_2)/2$, while the semi-minor axis is $b = \sqrt{R_1 R_2} \cos \theta_i$, where θ_i is the angle of incidence

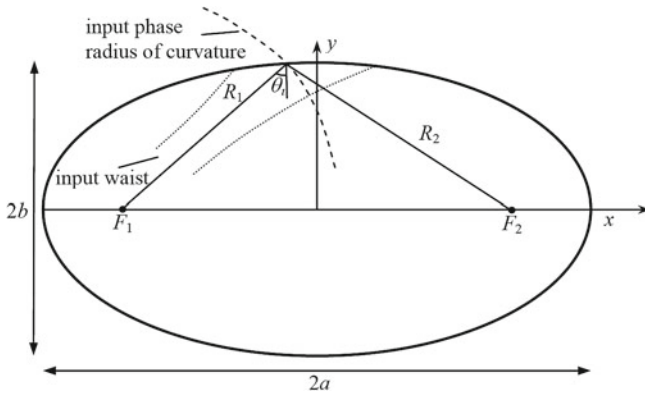


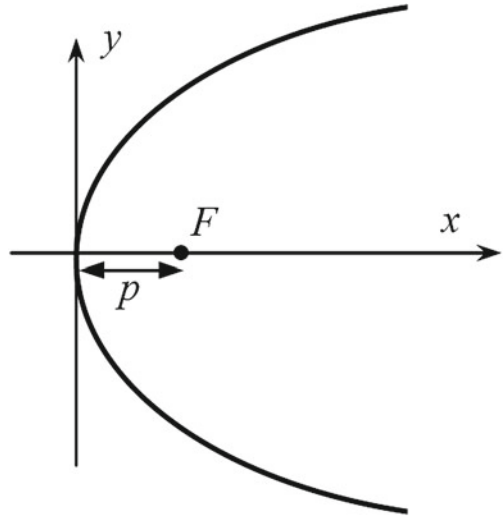
Fig. 2.4 Ellipsoid with foci at F_1 and F_2

(half the deflection angle) and the usual equation for an ellipse applies: $x^2/a^2 + y^2/b^2 = 1$, with the actual mirror surface part of a surface of revolution around the x -axis as shown in the figure. The focal length of an ellipsoidal mirror is given by $1/f = 1/R_1 + 1/R_2$ so that the mirror effectively behaves as a thin lens. Note of course that the beam waists do not coincide with the geometrical foci of the ellipse F_1 or F_2 (see Fig. 2.4). Instead, the distance back to the input beam waist is given by: $d_{in} = R_{in}/[1 + (\lambda R_{in}/\pi W_m^2)^2] < R_1$, where W_m is the beam width parameter at the mirror.

If the input or output beam waist is at the mirror itself then the appropriate mirror reduces to an off-axis parabolic mirror (i.e. the limit for an ellipsoid when R_1 or R_2 is very large). The mirror produces a perfect phase transformation between a spherical and a plane wave front, although projection effects again give rise to some asymmetric distortion on reflection [15]. A parabolic (or more strictly paraboloidal) mirror is the correct conic reflecting surface for a large beam waist at the mirror (plane wavefront) imaged to narrower beam waist near the geometrical focus of parabola (typical in astronomical telescopes etc.). Given R_1 and the angle of incidence θ_i we can determine the correct paraboloidal surface (paraboloid of revolution around x -axis where $y^2 = 4px$, see Fig. 2.5) with $p = R_1 \cos^2 \theta_i$. Parabolic mirrors are often used as good substitutes for ellipsoidal mirrors if $R_2 \gg R_1$, or vice versa (e.g. if the mirror is in far field of a source or detector, for example).

When dealing with multi-beam systems, off-axis mirrors do introduce significant aberrations and distortion effects across the field of view (region over which beams are spread), especially away from the optical axis of the system. In that case very careful optical design is necessary to reduce the phase aberrations across the field of beams while at the same time properly accounting for the dominant diffraction effects. This is solved using an approach which couples design-technique principles from both optical engineering (and normally applied at short wavelengths) along with long-wave optics leading to compensated systems, e.g. the Planck satellite focal plane [19]. Also, for example, in specialised systems cross-polar effects can

Fig. 2.5 Paraboloid with focus at F



be minimised using so-called Dragone-Mitzsugushi configurations [20]. However, these effects are not generally a significant issue for single beam systems where a small amount of beam squint can be tolerated [15]. There is further discussion on these points in the section on the design of optical systems, particularly for broadband THz spectroscopy systems, where the use of parabolic mirrors is popular.

2.3.3 Thick Lenses

There will be some diffraction effects associated with the transmission of a beam through a thick lens. We can derive the $ABCD$ transformation matrix $\mathbf{M}_{\text{thick lens}}$ for a thick lens with spherical surfaces in a general form. If R_1 and R_2 are the radii of curvatures of the surfaces on the input and output sides, respectively, then this can be written (where d is the lens thickness, n_2 is the refractive index of the lens material and n_1 and n_3 are the refractive indices of the media on the input and output sides, respectively) as:

$$\mathbf{M}_{\text{thick-lens}} = \begin{bmatrix} \frac{n_2 R_1 - (n_1 - n_2)d}{n_2 R_1} & \frac{n_1 d}{n_2} \\ \frac{n_3 - n_2}{n_3 R_2} - \frac{n_1 - n_2}{n_3 R_1} + \frac{(n_3 - n_2)(n_2 - n_1)n_1 d}{n_2 n_3 R_1 R_2} & \frac{n_1(n_2 R_2 - (n_2 - n_3)d)}{n_2 n_3 R_2} \end{bmatrix}. \quad (2.7)$$

For the case where $n_1 = n_3 = 1$ and $n_2 = n$, the refractive index of the lens material, this yields:

$$\mathbf{M}_{\text{thick-lens}} = \begin{bmatrix} 1 + \frac{(n-1)d}{nR_1} & \frac{d}{n} \\ (n-1) \left(\frac{1}{R_1} - \frac{1}{R_2} - \frac{(n-1)d}{nR_1R_2} \right) & 1 - \frac{(n-1)d}{nR_2} \end{bmatrix}. \quad (2.8)$$

Short focal length lenses may require the surface to be shaped to deal with non-paraxial rays in order to reduce aberrations (this is discussed in [3], for example). This would be appropriate when a lens is used at the aperture of a horn antenna. Goldsmith [3] also discusses other refracting focussing elements such as zoned (Fresnel) lenses. Antireflection coatings have been developed particularly for lenses made of high refractive index materials, e.g. [1, 21, 22].

2.3.4 Beam Splitters, Polarising Grids, Roof Mirrors, Interferometers and Filters

Useful components have also been developed which function as optical devices in so-called quasi-optical circuits, mimicking waveguide devices and circuitry. Both frequency-selective devices (e.g. filter plates) and frequency-independent devices (e.g. roof-mirrors) are widely utilised in both frequency-dependent and frequency-independent applications. There is an extensive review of the operation and application of such components in [1, 3], for example. Clearly, as well as their basic function, various aspects of Gaussian beam propagation through such devices need to be considered, such as beam spreading, truncation levels and phase slippage. For example, as a rule of thumb the component should not truncate the beam at a radius of less than 2 beam width parameters, W , otherwise undesired diffraction of the beam as well as loss in transmitted power will occur.

One example of a very useful but simple optical device is the roof mirror, which rotates the direction of polarisation of an incident wave by an angle of 2α , if the angle between the incident polarisation and the axis of the roof mirror is α (see Fig. 2.6). The roof mirror produces the rotation as the field component parallel to the flat surfaces is not affected while the component normal to surface has its direction reversed in the double reflection. When combined with a polarising grid, roof mirrors can be configured as path-length modulators for a single beam [3] or as the polarisation rotation mirrors in a Michelson polarising interferometer (see Fig. 2.6) [23]. In both these applications a polarising grid is present which reflects polarisation parallel to the polarising grid wires and transmits, without significant loss, polarisation perpendicular to the grid wires. Path-length modulators are useful for introducing propagation delays, while polarising Michelson interferometers can be utilised as low-loss beam combiners for two beams closely spaced in frequency (local oscillator injection in heterodyne systems) or as single-sideband filters, e.g. [24] as well as in Fourier transform spectroscopy. Alternatively, a wire-grid attenuator or power divider that is free of reflections back into the incident beam can be designed by using wire grids as beam splitters.

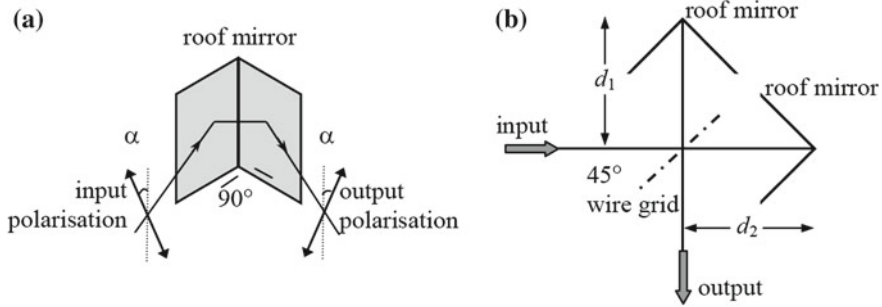


Fig. 2.6 **a** Roof mirror rotating the input polarisation direction and **b** polarisation-rotating interferometer (90° polarisation rotation when $d_1 - d_2 = \lambda/2$)

Polarisation transducers are useful quasi-optical devices that produce an arbitrary differential phase shift between two orthogonal electric-field polarisation directions. For example, a half-wave plate provides a differential phase shift of π between two orthogonal electric field polarisation directions while a quarter-wave plate transforms linear to circular polarisation. Wave plates have artificially generated (through mechanical milling) fast and slow axes (the names refer to the speed of a wave along the axis) [25]. A quasi-optical polariser based on self-complementary subwavelength hole arrays are reported in [26].

It is also possible to make anisotropic materials from one that is naturally isotropic by altering its geometry, thus simulating a birefringent dielectric, for example [27]. Dielectric strips of alternating permittivities can be combined to form composite dielectrics with the required dielectric constant, provided the wavelength is much longer than the strip thickness. Such strips can also be used as filters, mirrors, etc. [28].

Extremely useful high- and low-pass filters can also be made with inductive and capacitive grids, respectively, [29] while resonant grids can be used for band-pass filtering and a perforated plate filter as a high-pass filter with a sharp cutoff, even with profile shaping for lensing [25]. A transmission line matrix method can be used as a convenient way of calculating the frequency response of systems composed of cascaded elements [27].

2.3.5 Diffractive Elements and Phase Gratings

Diffractive optic elements are optical components that redirect segments of a wavefront through the use of interference and/or phase control [30]. They can be used to transform the intensity distribution of a coherent beam of light at one plane into another intensity pattern at a second plane (the far field, for example) by imposing a phase distribution on the field. Examples include the Fresnel phase plate, Dammann

Gratings and Fourier Gratings [31–33] that can be used to generate multiple images of a single input beam. Such devices are useful for quasi-optically multiplexing a local oscillator source with an array of detectors in a heterodyne system. There are a number of dielectric materials whose mechanical and optical properties in the far infrared make them ideal candidates for use in transmission phase gratings [1, 3].

In designing phase gratings, no analytical solution exists for finding the phase profile required to transform a given arbitrary input field to a given arbitrary output field, and in fact an exact transform may not even be possible [34]. Optimisation techniques, such as simulated annealing or genetic algorithms, and phase-retrieval techniques such as the Gerchberg-Saxton algorithm have all been applied to find optimal phase solutions [35, 36].

Another useful example of beam-shaping is in the production of “diffraction-free beams”, in which the amplitude does not change in form or scale while propagating [37]. These beams have an amplitude cross-section of a Bessel function and, ideally, are infinite in extent. Pseudo-Bessel beams (having finite extent and power) have been generated using dielectric conical-shaped lenses called axicons [38, 39].

2.4 Beam Coupling Issues

2.4.1 Coupling to Radiating Elements

Many different kinds of radiating elements are used as feed systems for launching and detecting THz waves. These systems ideally produce quasi-Gaussian beams so that the sidelobe content is not very significant and a simple Gaussian beam can be used as a good approximation in designing optical systems and beam guides. For higher levels of accuracy a multi-moded description of the beam can be applied as discussed below (Sect. 2.5.1).

One of the most predictable feed types, in terms of producing a well-controlled and understood beam, is the horn antenna. The field at a horn aperture can be predicted from wave-guide theory, and this is an ideal plane at which to determine the decomposition into higher order modes for a multi-mode analysis. To a good approximation the field at the aperture has a well-defined phase radius of curvature R with the centre of curvature located at the apex of the horn flare. This is true for both the typical conical and pyramidal shapes encountered (i.e. $R = L_{\text{axial}}$, the axial slant length of the horn). Note that in terms of fitting a Gaussian beam to the field, the spherical phase variation off-axis can be expressed using the usual quadratic approximation for paraxial beams, and we choose a value for beam width parameter, W , that optimises coupling to the fundamental, $E(x, y) \approx A_0 E_G(x, y)$, where A_0 is the fundamental mode coefficient and $E_G(x, y)$ is a simple Gaussian (fundamental mode).

For a corrugated horn antenna the beam width at the aperture (radius a) can be set to $W_{\text{ap}} = 0.6435a$, and the phase curvature is given by the horn axial length as

Table 2.2 Gaussian approximation to horn beams

Horn type	Beam width W
Corrugated conical	$0.643a$ (radius) [40]
Smooth walled conical	$0.765a$ (radius) [12]
Rectangular	$0.35a \times 0.51b$ (width \times height) [42]
Diagonal	$0.42a$ (sidelength) [43]

above [40, 41]. This approximate Gaussian fit can be used to represent the actual corrugated horn antenna beam in designing any optical beam guides required. It is worth noting that although the Gaussian is a good fit (with 98% fractional power coupling) to the beam from a corrugated horn, it cannot represent the side-lobe structure (typically below the -20 dB level). In fact it only poorly predicts the intensity on axis, and only if one calculates the integrated power (inside radius r) is much better agreement obtained between the Gaussian and horn fields. Of course this is what is essentially optimised in finding the “best-fit” Gaussian. In Table 2.2 we list the best-fit Gaussian parameters for typical horn antennas.

The fractional coupling of the lowest order one-dimensional Gaussian mode to a truncated uniform field (of width a) has its maximum value when $W = 0.51a$ and to a simple cosine tapered field when $W = 0.35a$. The fractional coupling of a square TE_{10} waveguide field to the lowest order two-dimensional fundamental Gaussian mode $E_G(x, y)$, with the beam waists in the x and y coordinates equal, has its maximum value when $W = 0.43a$, where a is the sidelength of the square waveguide (the same as for a diagonal horn). In the latter case, 84% of the power is contained in the fundamental mode, which compares with 98% for the HE_{11} mode of a corrugated horn antenna.

Clearly one needs to include higher order Gaussian beam modes for a more accurate description of real fields (non-Gaussian effects) in order to simulate how the beam pattern of a horn antenna evolves and develops sidelobe structure for example. These so-called sidelobes are equivalent to subsidiary maxima in classical wave optics, of course, as normally simulated using Fresnel and Fraunhofer diffraction integrals.

Horn antennas become difficult to manufacture at frequencies around 1 THz and above, and other structures including planar lens antenna schemes are often employed [3]. Generally the beams produced by these other structures are not as well behaved, nor indeed as well understood, as the horn antenna feeds and the power coupling to a fundamental Gaussian (the Gaussicity of the beam) will be somewhat lower with higher sidelobe levels. These issues are discussed further in Sect. 2.6.3.

2.4.2 Mismatched Gaussian Beams and Defocussing Effects

In designing quasi-optical systems and analysing potential losses in non-ideal systems, the coupling of beams together becomes an issue (such as how a source beam is matched to a detector, for example). Generally two situations arise: (i) the

coupling of an incident beam from a source to a beam that characterises a component such as a detector or the recombination of a pair of beams in an interferometer such as a Michelson for example, or (ii) the imperfect coupling that occurs because of mechanical misalignment, defocusing or other tolerancing effects in a quasi-optical beam guide.

A beam coupling efficiency analysis requires the calculation of the fraction of power coupled from an incident beam to the beam of the component of interest, as a function of some mismatch between the parameters (W_a, R_a) and (W_b, R_b) of the two beams a and b , respectively. The power coupling coefficient between two fields E_a and E_b over a transverse plane S is defined by the overlap integral $C_{ab} = \left| \int \int_S E_a^*(x, y; W_a, R_a) \cdot E_b(x, y; W_b, R_b) dx dy \right|^2$. Since a scalar field has been assumed, one must be careful with polarisation effects and normalisation (as the true field coupling is a vector equation). Here therefore it is assumed that both fields are polarised in the same sense (since we are using a scalar approximation). A number of interesting common cases arise for different kinds of mismatched beams. We will assume that for these cases Gaussian beam approximations are adequate descriptions of the beams, particularly as it is often the order of magnitude of the fractional power coupling loss due to mismatch that is required.

We first consider a defocussed system which occurs when the two beams are axially aligned (optical axes aligned) but the beam waists do not coincide as they should for maximum power coupling (for example the detector feed phase centre is not quite on the focal plane in a telescope system). Thus, there will be a mismatch in the beam width W and phase curvature R at some arbitrary plane. It may also be that the beams have mismatched beam waist sizes (such as a detector feed antenna with the wrong parameters to match the incident source field). For the general case, therefore, neither beam waists coincide nor are the beam waist radii $W_{0,a}$ and $W_{0,b}$ equal. The on-axis phase slippages will be different in general as well, $\phi_{0,a} \neq \phi_{0,b}$, which could be an issue for an interferometer or delay line, for example. For such a mismatched and defocussed system the fractional power coupling can be shown to be expressible in terms of the beam waist parameters and the distance between the beam waist positions as

$$C_{ab}^{\text{axial}} = \frac{4}{\left(\frac{W_{0,b}}{W_{0,a}} + \frac{W_{0,a}}{W_{0,b}}\right)^2 + \left(\frac{\lambda \Delta z}{\pi W_{0,a} W_{0,b}}\right)^2}, \quad (2.9)$$

where Δz is the shift of the beam waist [3]. Even if the beams are otherwise well matched in terms of their optical parameters, mechanical mismatches may still occur (due to realistic tolerancing errors, for example) which cause the optical axes of the two beams to be misaligned [44]. We can analyse these tolerancing errors in terms of lateral shifts and tilts. Figure 2.7 illustrates defocusing as well as tilt and offset mismatched beams.

In the case of tilts, a mismatch gives rise to a phase slope in one of the fields relative to the other across the plane where their optical axes intersect. For Gaussian beams which have the same beam parameters (no other mismatches other than tilt)

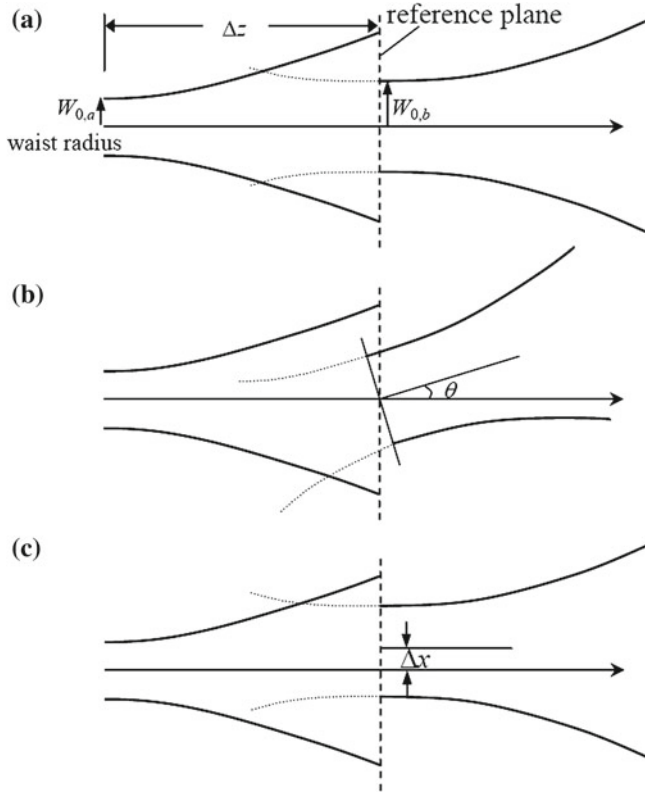


Fig. 2.7 Gaussian beam misalignment: **a** defocus, **b** defocus and tilt, and **c** defocus and off-offset

it can be shown [3] that the fractional power coupling between the beams is given by

$$C_{ab}^{\text{tilt}} = \exp \left[- \left(\frac{\theta}{\theta_W} \right)^2 \right], \quad (2.10)$$

where $\theta_W = \frac{\lambda}{\pi W}$ and where the tilt occurs at the beam waist. For lateral offsets if we assume a beam displacement of Δx in the x direction, (but otherwise beam widths and waist locations are the same), the fractional power coupling including the loss due to offset can be shown to be given by

$$C_{ab}^{\text{offset}} = \exp \left[- \left(\frac{\Delta x}{W_0} \right)^2 \right], \quad (2.11)$$

a similar dependency to that for tilt misalignments. In general more than one type of mismatch may be present particularly when tolerancing errors are large and thus may affect system performance (see Fig. 2.7).

Often for system design or a basic analysis of tolerancing, a simple Gaussian beam mode approach is an excellent compromise in terms of speed of computation particularly for optimisation. When a more precise analysis of loss in a system is required however a full modal description of a beam also including the higher order modes in the analysis may be necessary, as will be discussed in the next section.

2.5 Detailed Modelling

2.5.1 Higher Order Gaussian Beam Modes

A Gaussian beam is the simplest solution to the paraxial wave equation and suffices in many cases to describe beam propagation in an optical system. There are situations, however, when we need to model more complex field distributions and in these cases we can use higher order beam mode solutions (see e.g. [3]). These higher order Gaussian modes are characterised by the same beam radius $W(z)$ and phase radius of curvature $R(z)$ as the fundamental mode, only the phase slippage, (with respect to a plane wave) differs. The most appropriate mode-set to use depends on the symmetry of the system being modelled. In cylindrical coordinates (r, φ, z) we can use Gaussian–Laguerre modes

$$\begin{aligned}
 E_{\text{pm}}(r, \varphi, z) = & \left[\frac{2p!}{\pi(p+m)!} \right]^{0.5} \frac{1}{W(z)} \left[\frac{\sqrt{2}r}{W(z)} \right]^m L_p^m \left(\frac{2r^2}{W^2(z)} \right) \\
 & \times \exp \left[\frac{-r^2}{W^2(z)} - jkz - \frac{j\pi r^2}{\lambda R(z)} + j(2p+m+1)\phi_0(z) \right] \\
 & \times \exp(jm\varphi),
 \end{aligned} \tag{2.12}$$

where $L_p^m(s)$ are generalised Laguerre polynomials, and in Cartesian coordinates (x, y, z) Gaussian–Hermite modes

$$\begin{aligned}
 E_{\text{mn}}(x, y, z) = & \left(\frac{1}{\pi W^2(z) 2^{m+n-1} m! n!} \right)^{0.5} H_m \left(\frac{\sqrt{2}x}{W(z)} \right) H_n \left(\frac{\sqrt{2}y}{W(z)} \right) \\
 & \times \exp \left[-\frac{x^2 + y^2}{W^2(z)} - jkz - \frac{j\pi(x^2 + y^2)}{\lambda R(z)} + j(n+m+1)\phi_0(z) \right],
 \end{aligned} \tag{2.13}$$

where $H_m(t)$ are Hermite polynomials and the modes are normalised so that the generalised power is unity (orthonormal mode sets). ϕ_0 is the usual phase slippage of

the fundamental mode. These higher order solutions consist of polynomials superimposed on the fundamental Gaussian mode and constitute complete orthonormal sets of modes that are each solutions to the paraxial wave equation. Any paraxial beam $E(x, y, z)$ can therefore be expressed as a superposition of Gaussian modes (for example in the case of Cartesian coordinates),

$$E(x, y, z) = \sum_i A_i E_i(x, y, z), \quad (2.14)$$

where A_i are the mode coefficients and i represents the pair of indices (m, n) for the mode. If the field is known over the surface S then the mode coefficients are determined by calculating the overlap integrals

$$A_i = \int \int_S E_i(x, y, z)^* E(x, y, z) ds \quad (2.15)$$

(see [13] for examples). This higher order mode decomposition of a field is the computationally intensive step but it only has to be carried out once if there is no scattering of power between modes (if mirrors and lenses are treated as perfect phase transformers with no truncation). Optical elements can, however, introduce a significant amount of power scattering between modes as described in the next section.

The choice of the optimum beam mode set (in terms of the parameters W and R) is crucial to the efficiency of the Gaussian beam mode approach and several approaches can be taken. Very often a source field can be represented to a high accuracy by the sum of only a few modes and the mode set that maximises the power in the fundamental is chosen. In some cases, however, this can cause the power in the higher order modes, although small, to be spread essentially over a large number of modes with the result that they are all required to accurately model the field. The choice of W might more usefully take into account the ability of the highest order mode to model the edge of the field. If we consider Gaussian–Hermite modes, for example, the final zero crossing of the n th mode is approximately given by $\sqrt{0.75n}/W$. Matching this to the extent of the field to be decomposed gives a value for W [45, 46]. R can be chosen to match the phase curvature of the field. Once the mode coefficients are known, it is straightforward to model the propagation of a beam by simply keeping track of the evolution of the beam width, the phase radius of curvature and the phase slippage between modes (using, for example, $ABCD$ matrices).

2.5.2 Aberrations, Truncation, Beam Distortion

If the beam guide or optical coupling system is not perfect then there may be truncation and aberration effects which distort the field [46–50]. It is also possible to have

a mismatched or defocussed beam as discussed above (Sect. 2.4.2). A propagating beam in an non-ideal quasi-optical system can be analysed in terms of what happens to its component modes and the non-ideal propagation can be viewed as resulting in the mode coefficients for the beam varying with propagation, a process we call scattering. There may also be some partial reflections present resulting in power travelling both in the forward and reverse directions through the optical system. For the case where we are concerned with the coupling of beams not well described by a Gaussian we can readily include higher order modes, which of course complicates the description but provides a higher level of accuracy in the analysis.

$$\begin{aligned}
 C_{ab} &= \left| \int \int \sum_i A_i^* E_i^*(x, y; W_a, R_a) \sum_{i'} B_i E_{i'}(x, y; W_b, R_b) dx dy \right|^2 \\
 &= \left| \sum_{ii'} A_i^* B_{i'} I_{ii'} \right|^2
 \end{aligned} \tag{2.16}$$

where $I_{ii'} = \int \int E_i^*(x, y; W_a, R_a) E_{i'}(x, y; W_b, R_b) dx dy$, [51, 52].

When designing a millimetre or THz quasi-optical system it is important, particularly in terms of truncation and vignetting, to know at what radius the propagating beam can be truncated without losing power (by a stop, edge of a mirror, lens, etc.). If the stop is in the far field of a source (such as a horn antenna feed) this can be straightforward as we can integrate the far-field beam pattern over the region defined by the stop. However, if the beam has been re-focussed and re-collimated a number of times, the beam pattern is no longer immediately obvious particularly in terms of its sidelobe structure at that plane. This can be very conveniently analysed using higher order Gaussian beam modes [53, 54]. The azimuthally symmetric Gaussian-Laguerre modes above (Sect. 2.5.1) are useful, for example, if the stop has circular symmetry and the propagating beam can be expressed efficiently in terms of the same modes.

Such effects can also be described by a scattering matrix \mathbf{S} for the optical system which expresses how the component modes E_i are scattered by the optical system so that on a transverse output plane: $E_j^{\text{sc}} = \sum_i S_{ij} E_i$. Any incident beam can be expressed as a coherent sum of such modes $E_{\text{in}} = \sum_j A_j E_j$, so that the scattering matrix then acts on the mode coefficients, with the transmitted field mode coefficients given by: $B_i = S_{ij} A_j$. Thus, the transmitted field is expressed in terms of a different set of mode coefficients for non-ideal propagation $E_{\text{out}} = E_{\text{in}}^{\text{sc}} = \sum_m B_i E_i$. We can express the evolution of the modes coefficients from A_i to B_i in matrix notation as $\mathbf{B} = \mathbf{S} \cdot \mathbf{A}$. In certain cases a quasi-analytical approach can be taken. Thus, for example, if the beam is symmetrically truncated for a cylindrically symmetric system useful recursion relationships can be derived [54]. In the case of aberrating systems plotting mode amplitudes allows the Gaussicity (the pure simple Gaussian mode content in power) and higher order structure to be investigated.

A Gaussian beam mode analysis can be applied to any quasi-optical system in which there are partial reflections by also including the backward travelling modes (z and $R(z)$, change sign in Eq. (2.2)). Such reflections have the potential to set up standing waves in the system [55]. A full scattering matrix formulation can incorporate backward-going waves by considering a quasi-optical component as a two-port device with incident fields on port 1 and 2 described by sets of mode coefficients \mathbf{A} and \mathbf{C} , respectively, then the corresponding reflected fields are given by sets of coefficients \mathbf{B} and \mathbf{D}

$$\begin{bmatrix} \mathbf{B} \\ \mathbf{D} \end{bmatrix} = \begin{bmatrix} \mathbf{S}_{11} & \mathbf{S}_{12} \\ \mathbf{S}_{21} & \mathbf{S}_{22} \end{bmatrix} \begin{bmatrix} \mathbf{A} \\ \mathbf{C} \end{bmatrix}. \quad (2.17)$$

and the individual scattering matrices are calculated from the overlap integrals of the appropriate transmitted and reflected fields.

We calculate the scattering matrix for the overall system by cascading the scattering components appropriately. Thus, we get the total transmission to the output port and reflection back at the input port for the system as a whole. Furthermore, in horn antenna fed systems it is straightforward to combine a scattering matrix description of a horn antenna using waveguide modes with that for a quasi-optical system based on Gaussian beam modes, and we can model the standing waves between two horn antennas as discussed in [56].

Alternatively, the scattering matrix can be re-cast in terms of transmitted fields as

$$\begin{bmatrix} \mathbf{D} \\ \mathbf{C} \end{bmatrix} = \begin{bmatrix} \mathbf{T}_{11} & \mathbf{T}_{12} \\ \mathbf{T}_{21} & \mathbf{T}_{22} \end{bmatrix} \begin{bmatrix} \mathbf{A} \\ \mathbf{B} \end{bmatrix} = \begin{bmatrix} \mathbf{S}_{21} - \mathbf{S}_{22} [\mathbf{S}_{12}]^{-1} \mathbf{S}_{11} & \mathbf{S}_{22} [\mathbf{S}_{12}]^{-1} \\ -[\mathbf{S}_{12}]^{-1} \mathbf{S}_{11} & [\mathbf{S}_{12}]^{-1} \end{bmatrix} \begin{bmatrix} \mathbf{A} \\ \mathbf{B} \end{bmatrix}, \quad (2.18)$$

and sequential matrices can again be multiplied directly to model a system with multiple components. (Singular value decomposition can be used, if necessary, to invert the \mathbf{S}_{12} scattering matrix, using the singular values to keep only the modes that are not truncated [45, 46]).

One of the limitations of Gaussian beam mode analysis is that polarisation effects in particular are not strictly speaking included in the theory which is a paraxial scalar theory. It is possible to include polarisation effects approximately, however, by defining two sets of orthogonally polarised modes (as discussed in [7, 12] for example and utilised in several papers on the Gaussian Beam Mode Analysis of horn antennas, e.g. [43]). It should be noted however that the scattering between co-polar and cross-polar fields cannot be rigorously included in the theory. In the case where more accurate polarisation behaviour is required therefore, other modelling techniques have to be applied as discussed in the next section.

2.5.3 Other Modelling Techniques

Optical modelling is concerned with the problem of calculating an electromagnetic field over a surface in an optical system when the field, or currents, over some other

surface is known. Techniques such as the Method of Moments [57] attempt to calculate the current distribution over a surface precisely but the full solution to Maxwell's equations is usually extremely difficult to find and in practice approximations have to be made. In the physical optics (PO) approximation made by the software package GRASP [58], for example, when a field is incident upon an aperture it is assumed that the field over the opaque region is zero and the field over the transparent region is the same as if no aperture were there. This is a reasonable approximation to make when the radius of curvature of the reflector is many wavelengths, but is not valid at an edge. The geometrical theory of diffraction (GTD), therefore, is often used in addition to geometrical optics (GO) to estimate the effect of aperture edges on the sidelobes. The PO technique is extremely powerful and is standard for analysing antennas and reflectors in radio and submillimetre systems.

The electromagnetic field over an input surface is a vector field but in some cases considering only one component of the field leads to relatively simple scalar solutions. For THz systems the question of whether a vector or a scalar solution is required is intrinsically related to whether the field is of a paraxial or wide-angle nature. In practice, when considering narrow-angle paraxial beams, it is sufficient to consider the components of the vector field separately. Propagation of the field onto the next optical component (solving the wave equation) requires diffraction integrals to be calculated for each field point. Kirchhoff's approximation is the arithmetic average of the rigorous solutions when there is ambiguity over which vector quantity (\mathbf{E} or \mathbf{H}) is being analysed. The averaging process appears in the form of the well-known $(1 + \cos \theta)/2$ obliquity term. Rather than evaluating diffraction integrals directly, it is possible to decompose an assumed source field into modes, each a solution of the wave equation. Propagation to the next optical surface is usually straightforward and simply involves recombining scaled modes with an appropriate mode-dependent phase slippage term included. Commonly used mode sets include Gaussian beam modes as discussed here, Gabor modes [59] (used by the commercial software package ASAP [60], for example) and plane waves (used by the software packages Zemax [61], GLAD [62]). A plane wave analysis has the significant advantage that it does not have to be limited to paraxial fields.

At optical wavelengths, away from boundary shadows and abrupt changes in intensity distribution, energy can be considered to be transported along curves, or light rays, obeying certain geometrical laws. For system design at visible wavelengths this technique is widely used and ray-tracing packages, such as CODE V [63] and Zemax have proved to be very successful. Ray-tracing can also be accurate for systems that are highly over moded. In the submillimetre and THz regimes, however, the wavelength is typically an appreciable fraction of component sizes and so cannot be neglected. Systems tend to be at most few-moded and often have a compact optical layout. In this regime diffraction effects are important and the approach of geometrical optics is inadequate.

2.5.4 Partial Coherence and Multi-Moded Systems

In a multi-moded quasi-optical system the radiation field will be partially spatially coherent. Each true component mode of propagation, although having no fixed phase relationship with other modes, will of course propagate according to the laws of diffraction and the total field intensity at any point will be given by the sum of the intensities of these component modes (fields add in quadrature). Geometrical optics can be employed in highly over-moded systems as an efficient accurate approach. However, in the long-wavelength limit systems tend to be at most few moded and an approach incorporating diffraction techniques is necessary. When this is applied to a modal approach, for example, propagation can be very elegantly described in terms of coherence matrices. These track the evolution of the mutual coherence function [64, 65]. Over moded horn antennas can be used to couple to such beams [66–68].

2.6 Design of Optical Systems

2.6.1 Choice of Mirror/Lens Parameters

In many cases we wish to design a quasi-optical system that couples one beam (such as that produced by a feed horn antenna) to another (determined by a receiver system, for example). If the desired input and output beam waists are $W_{0,\text{out}}$ and $W_{0,\text{in}}$, respectively, then the magnification of the system is given by $\mathcal{M} = W_{0,\text{out}}/W_{0,\text{in}}$. If the separation of the beam waists is a free parameter then the distances d_{in} and d_{out} of the input and output waists, respectively, are given by

$$d_{\text{in}} = f \pm \mathcal{M}^{-1} \left[f^2 - f_0^2 \right]^{0.5} \quad \text{and} \quad d_{\text{out}} = f \pm \mathcal{M} \left[f^2 - f_0^2 \right]^{0.5}, \quad (2.19)$$

where

$$f_0 = \frac{\phi W_{0,\text{in}} W_{0,\text{out}}}{\lambda}. \quad (2.20)$$

We are free to choose the focal length of the system but it must have a minimum value of $f = f_0$. The choice of f determines the input and output distances and in the case where $f = f_0$, $d_{\text{in}} = d_{\text{out}} = f$ (independent of wavelength). Often, however, the distances between the beam waists, $d = d_{\text{in}} + d_{\text{out}}$, is fixed and therefore is the focal length. For $\mathcal{M} \neq 1$

$$f = \frac{\pm \left[(\mathcal{M} - \mathcal{M}^{-1})^2 f_0^2 + d^2 \right]^{0.5} (\mathcal{M} + \mathcal{M}^{-1}) - 2d}{(\mathcal{M} - \mathcal{M}^{-1})^2}, \quad (2.21)$$

while for $\mathcal{M} = 1$

$$f = \frac{d}{4} + \frac{f_0^2}{d}. \quad (2.22)$$

These and other examples of Gaussian beam transformations are discussed in Goldsmith [3]. Once the component focal lengths and separations have been fixed a simple $ABCD$ matrix analysis of an equivalent on-axis system (approximating the focussing elements by thin lenses of focal length f) can be performed in order to determine the beam waist, W , and radii of curvature, R_{in} and R_{out} at each optical component. The component sizes required depend on the level of beam truncation that can be tolerated but component diameters of $4W$ (giving -35 dB edge taper) are typical. If an off-axis geometry is required then the angle-of-throw needed at each component and the radii of curvature can be used together with the equations in Sect. 2.3.2 to define the reflecting surface. Although a geometrical optics design and analysis software packages can help with the initial layout of systems, a diffraction analysis (such as Gaussian beam modes) must be used to check minimum component sizes. If the optical system is to be used over a wide bandwidth then the beam-mode analysis should be carried out at a few wavelengths across the band as only in certain cases are beamwidths, etc., independent of wavelength.

Gaussian beam modes can be used to assess an optical design in terms of its beam Gaussianity (fractional power coupling to a given beam radius and phase curvature). Once designed, a more rigorous PO analysis should be used to verify the system performance in terms of other parameters such as loss and polarisation behaviour.

2.6.2 Layout of Systems

Once a Gaussian beam-mode analysis of an equivalent on-axis system has been used to determine component parameters and sizes, the layout of the system can be chosen depending on more specific performance requirements. For on-axis systems truncation (Sect. 2.5), standing waves and blockage may be issues while for off-axis systems stray light, beam distortion (Sect. 2.5), cross-polarisation and shadowing may be of more concern.

An important consideration is the introduction by optical components of polarisation effects (again, Gaussian beam modes are typically assumed to describe one linear polarisation). The cross-coupling of orthogonal polarisations is known as cross-polarisation and it can be introduced into a beam after reflection from a curved focussing element. In certain circumstances (an axially symmetric reflector viewed on-axis) the cross-polar component can cancel but this is generally not the case when using off-axis mirrors, for example. Such cross-polarisation has been investigated by Gans [69] and Murphy [15] and for quadratic reflector surfaces the fraction of the power in an incident beam that is reflected into the cross-polar component is

$$P_{xp} = \frac{W_m^2}{4f^2} \tan^2 \theta_i, \quad (2.23)$$

where W_m is the incident beam radius at the mirror, θ_i is its angle of incidence and f is the focal length of the mirror (twice that lost due to beam distortion). Instrumental polarisation effects arise even in lens-based on-axis systems. At each vacuum/dielectric interface (or in fact any surface with finite conductivity) there is a difference in transmission for radiation polarised perpendicular or parallel to the plane of incidence (given by the Fresnel coefficients) and this difference increases with increasing angle of incidence. The result is that an unpolarised source may be detected as being polarised after transmission through the optical system. This may be true even for anti-reflection coated lenses if the optics are used at high angles of incidence or for signals of large bandwidth.

Partial reflections and standing waves are also issues for quasi-optical systems, in particular those with on-axis components (lenses, dielectric cryostat windows, central blockages, etc.). Partial reflections from interfaces can give rise to return loss and standing waves [55, 56]. These standing waves are particularly troublesome in spectrometers where they can appear as a baseline ripple in spectra. In addition, truncation and aberration effects in real optical components can be expected to scatter power between modes and modal resonances can occur when even a small amount of power is scattered into a higher order mode and that mode becomes trapped [70].

2.6.3 Issues for Imaging in THz Spectroscopy Systems

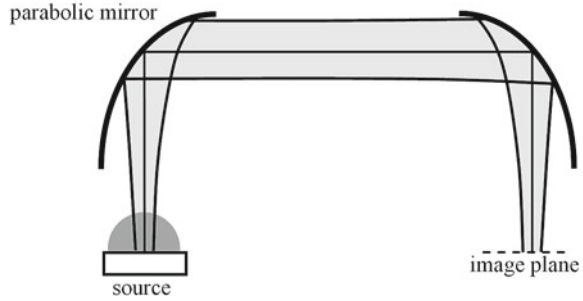
Most standard time-domain spectroscopy systems used in the laboratory operate in transmission and collimate or re-focus the THz beam using off-axis parabolic mirrors [71]. Reflection of the diverging beam from a source by a single parabolic mirror gives rise to distortion of the beam amplitude pattern, with beam squint because of projection effects [15]. For a pure Gaussian source the reduced Gaussicity of the distorted beam (fractional power coupling to a pure Gaussian) is given by

$$P_G = 1 - \frac{W_m^2}{8f^2} \tan^2 \theta_i, \quad (2.24)$$

where W_m is again the beam width parameter at the mirror, f is the focal length of the mirror and θ_i is the angle of incidence.

However, if a focussed beam is required, then by an appropriate compensating Gaussian beam telescope arrangement of two identical parabolic mirrors it is possible to eliminate this distortion [48]. The focal length of the mirrors should be long enough that a collimated beam (with width parameter W_m) is formed between the parabolic mirrors (with $W_m \gg W_0$, the waist size at the source). At THz frequencies this is not difficult to achieve for typical source beams. The two parabolic surfaces provide the required phase transformations, while the correct relative orientations, as shown in Fig. 2.8, result in cancellation of the amplitude distortions. Then if the phase centre of the source antenna is located at the input focal plane of the first mirror, an essentially undistorted image of this field with a planar wave front (i.e. a waist) is produced at the

Fig. 2.8 Compensated arrangement of parabolic mirrors



output focal plane of the second mirror to illuminate the sample to be investigated, for example. A second similar compensated arrangement of a pair of parabolic mirrors can be used to produce an image of the sample at the detector plane by raster scanning (e.g. [71, 72]). However, the alignment of off-axis parabolic mirrors in these set ups is highly sensitive to the generation of unexpected aberrations. A similar set up can be arranged for reflection measurement systems [73].

For a broadband pulse the width of the illuminating spot (waist) at the sample will be frequency dependent, this clearly being determined by the frequency dependence of the source antenna scheme. Generally for the source and detector, photoconductive planar lens antennas are employed. The beams produced by these structures are not as well behaved nor indeed as well understood as the horn antenna feeds referred to above in Sect. 2.4.1. Useful discussions are given in Jepsen [74] and Rudd [75]. However, it is clear from these studies that there is a strong wavelength dependence of the beam source waist size [1, 74]. Thus, the illuminating beam at the sample in a Gaussian beam telescope arrangement will also be strongly frequency dependent.

If the sample is thick then diffraction in the sample may be significant and the optical path length through the sample needs to be taken into account in any optical design. The distance to the next focussing element can be adjusted accordingly to ensure that the phase centre of the beam scattered by the sample is positioned at the input focal plane of the second pair of parabolic mirrors so that an image of the sample is still formed at the detector plane. The $ABCD$ matrix for propagation through the sample including the effects of refraction at the air-medium interfaces is given by $((1, t/n), (0, 1))$, where n is the refractive index and t is the thickness of the sample. Thus, the distance to the first parabolic mirror should be adjusted by $t(1 - 1/n)$.

2.7 Summary and Conclusions

The THz portion of the electromagnetic spectrum is a challenging one in which to work, as although radiation is typically propagated and analysed as free-space beams, unlike traditional optics, beams may be only a few wavelengths in diameter and diffraction effects are important. The Gaussian beam mode analysis described

here is a useful compromise between the vector physical optics analyses that are feasible at radio wavelengths and the ray-tracing techniques that have proven so successful at visible wavelengths.

Often a simple Gaussian amplitude distribution is a good approximation both to the radiated beam produced by a typical THz source and to the reception pattern of a typical detector feed. A Gaussian mode, since it is a solution to the paraxial wave equation, retains its amplitude distribution as it propagates and simply scales in beam width and phase-front radius of curvature. For multi-element optical systems we can use the convenient *ABCD* ray-transfer matrix formalism from geometrical optics to keep track of the beam parameters and to design compact and efficient optical systems. There are situations when we need to model more complex field distributions and in these cases we can use higher order beam-mode solutions, again for a paraxial regime. These higher order Gaussian modes are characterised by the same beam radius and phase radius of curvature as the fundamental mode, but slip in phase with respect to it as they propagate. This phase slippage can also be calculated from the *ABCD* matrix of an optical component. Indeed since Gaussian beam modes are the natural modes with which to describe propagation of quasi-collimated long-wavelength beams, only a small number of modes are required for many practical applications.

Gaussian beams can be re-collimated in a beam guide using re-focussing elements such as simple thin lenses or mirrors. Care must be taken, however, as the usual formulas for imaging in geometrical optics cannot be used in long-wavelength systems to predict the position of beam waists. Again *ABCD* matrices can be very useful in this regard. We have described focussing elements and some other optical components commonly used in long-wave optics such as polarising grids, roof mirrors and phase gratings. If a beam guide or optical coupling system is not perfect then there may be truncation and aberration effects which distort the field. Off-axis ellipsoidal and paraboloidal mirrors in particular are often used and these can introduce significant aberrations and extra diffraction effects across the beam; thus, very careful optical design is crucial for good performance.

A propagating beam in a non-ideal quasi-optical system can be analysed in terms of what happens to its constituent modes. Then non-ideal propagation can be viewed as resulting from power being scattered between these modes. There may also be some partial reflections present in a system resulting in power travelling both in the forward and reverse directions. We have discussed how both partial reflections and the scattering of power between modes can be described using Gaussian mode scattering matrices. Furthermore, Gaussian beam mode techniques can also be extended to model incoherent and partially coherent fields.

One of the limitations of Gaussian beam mode analysis is that polarisation effects such as the scattering between co-polar and cross-polar fields cannot be rigorously included in what is a paraxial scalar theory. In the case where the accurate polarisation behaviour is required other modelling techniques, such as physical optics, should be used.

In conclusion, in this chapter we have discussed the design and analysis of THz beam guides and optical coupling systems, including an overview of the large range

of typical quasi-optical components. A powerful and efficient approach to modelling propagation based on Gaussian beam mode analysis has been developed which has proved invaluable for the reliable design and optimisation of the performance of the unique optical systems encountered in the THz band.

References

1. Y-S. Lee, *Principles of Terahertz Science and Technology* (Springer, New York, 2009)
2. P.F. Goldsmith, Proc. IEEE **80**, 1729 (1992)
3. P.F. Goldsmith, *Quasioptical Systems* (IEEE Press, New York, 1998)
4. L. Diaz, T. Milligan, *Antenna Engineering Using Physical Optics: Practical CAD Techniques and Software* (Artech House, Boston, 1996)
5. A.E. Siegman, in *Lasers* (University Science Books, Mill Valley, 1986)
6. P.F. Goldsmith, in *Infrared and Millimeter Waves*, vol. 6, ed. by K.J. Button (Academic Press, New York, 1982)
7. D.H. Martin, J.W. Bowen, IEEE Trans. Microw. Theory Tech. **41**, 1676 (1993)
8. J.C.G. Lesurf, *Millimetre-Wave Optics, Devices and Systems* (Adam Holger, Bristol, 1990)
9. G. Goubau, in *Millimetre and Submillimetre Waves*, ed. by F.A. Benson (Iliffe Press, London, 1969)
10. H. Kogelnik, T. Li, Proc. IEEE **54**, 1312 (1966)
11. S. Ramo, J.R. Whinnery, T. Van Duzer, *Fields and Waves in Communication Electronics*, 3rd edn. (Wiley, New York, 1994)
12. J.A. Murphy, IEEE Trans. Antennas Propag. **36**, 570–574 (1988)
13. J.A. Murphy, A. Egan, Eur. J. Phys. **14**, 121–127 (1993)
14. S. Withington, J.A. Murphy, K.G. Isaak, Infrared Phys. Technol. **36**, 723 (1995)
15. J.A. Murphy, Int. J. IR Millim. Waves **8**, 1165 (1987)
16. K. Wang, D.M. Mittelman, Nature **432**, 376 (2004)
17. R.J. Mahon, J.A. Murphy, W. Lanigan, Opt. Commun. **260**, 469 (2006)
18. A. Tamminen, J. Ala-Laurinaho, A.V. Räisänen, Indirect holographic imaging at 310 GHz, Proceeding of the 5th European Radar Conference, 2008, pp. 168–171
19. B. Maffei, F. Noviello, J.A. Murphy et al., Astron. Astrophys. (Pre-launch status of the Planck mission: Special feature), **520**, A11 (2010)
20. C. Dragone, Bell Syst. Tech. J. **57**, 2663 (1978)
21. J. Lau et al., Appl. Opt. **45**, 3746–3751 (2006)
22. J.W. Fowler, Appl. Opt. **46**, 3444 (2007)
23. D.H. Martin, E. Pulett, Infrared Phys. **10**, 105 (1969)
24. R. Padman, Int. J. Infrared Millim. Waves **13**, 1487 (1992)
25. P.F. Goldsmith, IEEE Trans. Antennas Propag. **39**, 834 (1991)
26. M. Beruete et al., IEEE Microw. Wirel. Compon. Lett. **17**, 834 (2007)
27. B. Rulf, Am. J. Phys. **56**, 76 (1988)
28. T. Finn, N. Trappe, J.A. Murphy, J. Opt. Soc. Am. A **25**, 80 (2008)
29. P.A.R. Ade, G. Pisano, C. Tucker, Proc. SPIE **6275**, 62750U (2006)
30. D.C. O'Shea, Th.J Suleski, A.D. Kathman, D.W. Prather, *Diffraction Optics Design, Fabrication, and Test*, (Tutorial Texts in Optical Engineering), vol. TT62 (SPIE Press, Washington, 2004)
31. H. Dammann, E. Klotz, Opt. Acta **24**, 505 (1977)
32. J.A. Murphy, C. O'Sullivan, N. Trappe, W. Lanigan, R. Colgan, S. Withington, Int. J. IR Millim. Waves **20**, 1469 (1999)
33. R. May, Proc. SPIE **6893**, G8930 (2008)
34. H. Kim, B. Yang, B. Lee, J. Opt. Soc. Am. A **21**, 2353 (2004)

35. E. Johnson, M. Abushagur, *J. Opt. Soc. Am. A* **12**, 1152 (1995)
36. J. Lavelle, C. O'Sullivan, *J. Opt. Soc. Am. A* **27**, 350 (2010)
37. J. Durmin, *J. Opt. Soc. Am. A* **4**, 651 (1987)
38. S. Monk, J. Arlt, D. Robertson, J. Courtial, M. Padgett, *Opt. Commun.* **170**, 213 (1999)
39. N. Trappe, R. Mahon, W. Lanigan, J.A. Murphy, S. Withington, *Infrared Phys. Technol.* **46**, 233 (2005)
40. R.J. Wylde, *Proc. IEE Part H* **131**, 258 (1984)
41. R.J. Wylde, D.H. Martin, *IEEE Trans. Microw. Theory Tech.* **41**, 1691 (1993)
42. J.A. Murphy, R. Padman, R.E. Hills, *Int. J. IR Millim. Waves* **9**, 325 (1988)
43. S. Withington, J.A. Murphy, *IEEE Trans. Antennas Propag.* **40**, 198 (1992)
44. W.B. Joyce, B.C. DeLoach, *Appl. Opt.* **23**, 4187 (1984)
45. D. White, Dissertation, National University of Ireland Maynooth, 2006
46. M.L. Gradziel, C. O'Sullivan, J.A. Murphy et al., *Proc. SPIE* **6472**, D4720 (2007)
47. A. Yoshida, T. Asakura, *Opt. Commun.* **25**, 133 (1978)
48. J.A. Murphy, S. Withington, *Infrared Phys. Technol.* **37**, 205 (1996)
49. N. Trappe, J.A. Murphy, S. Withington, *Eur. J. Phys.* **24**, 403 (2003)
50. T. Finn, N. Trappe, J.A. Murphy, S. Withington, *Infrared Phys. Technol.* **51**, 351 (2008)
51. J.A. Murphy, M. McCabe, S. Withington, *Int. J. IR Millim. Waves* **18**, 501 (1997)
52. H. Jiang, D. Zhao, *Optik* **117**, 215 (2006)
53. J.A. Murphy, A. Egan, S. Withington, *IEEE Trans. Antennas Propag.* **41**, 1408 (1993)
54. J.A. Murphy, S. Withington, A. Egan, *IEEE Trans. Microw. Theory Tech.* **41**, 1700 (1993)
55. J.A. Murphy, N. Trappe, S. Withington, *Infrared Phys. Technol.* **44**, 289 (2003)
56. N. Trappe, J.A. Murphy, S. Withington et al., *IEEE Trans. Antennas Propag.* **53**, 1755 (2005)
57. R.F. Harrington, *Field Computation by Moments Methods* (Mac Millan, New York, 1968)
58. TICRA Engineering Consultants, GRASP9, <http://www.ticra.dk/>
59. P.D. Einziger, S. Raz, M. Shapira, *J. Opt. Soc. Am. A* **3**, 508 (1986)
60. Breault Research Organization (BRO), <http://www.breault.com/software/asap.php>
61. ZEMAX Development Corporation, Zemax-EE, <http://www.zemax.com/>
62. G. Lawrence, SPIE no. 766-18, O-E/Lase, 1987
63. Code, V, Optical Research Associates, http://www.opticalres.com/cv/cvprodds_f.html
64. S. Withington, J.A. Murphy, *IEEE Trans. Antennas Propag.* **46**, 1650 (1998)
65. S. Withington, G. Yassin, J.A. Murphy, *IEEE Trans. Antennas Propag.* **49**, 1226 (2001)
66. R. Padman, J.A. Murphy, *Infrared Phys.* **31**, 441 (1991)
67. E. Gleeson, J.A. Murphy, B. Maffei et al., *Infrared Phys. Technol.* **46**, 493 (2005)
68. J.A. Murphy, T. Peacocke, B. Maffei et al., *JINST* **5**(Art. No. T04001), (2010)
69. M.J. Gans, *Bell Syst. Tech. J.* **55**, 289 (1976)
70. P.A.S. Cruickshank, D.R. Bolton, D.A. Robertson, R.J. Wylde, G.N. Smith, in *Proceeding of The Joint 32nd International Conference on Infrared and Millimeter Waves and 15th International Conference on Terahertz Electronics*, Cardiff, 3-7 September, 2007, vol. 2, pp. 941-942
71. W.L. Chan, J.A. Deibel, D.M. Mittleman, *Rep. Prog. Phys.* **70**, 1325 (2007)
72. P.C.M. Planken, H.J. Bakker, *Appl. Phys. A Mater. Process.* **78**, 465 (2004)
73. S. Huang, P.C. Ashworth, K.W. Kan, Y. Chen, V.P. Wallace, Y-t Zhang, E. Pickwell-MacPherson, *Opt. Express* **17**, 3848 (2009)
74. P. Uhd Jepsen, R.H. Jacobsen, S.R. Keiding, *JOSA B* **13**, 2424 (1996)
75. J. Van Rudd, D.M. Mittleman, *JOSA B* **19**, 319 (2002)

Chapter 3

Complex Refractive Index of Media in the THz Spectral Range

Kai-Erik Peiponen and Evgeny Gornov

Abstract This chapter considers complex permittivity and refractive index of a medium, and basic laws for the terahertz (THz) plane wave interaction with media. We present simple effective medium models for the permittivity of two-phase media, and deal with the Kramers–Kronig relations and maximum entropy model that are used for the THz spectra testing and correction.

3.1 Introduction

The interaction of electromagnetic field with a medium in the microscopic world is described in terms of the interaction of the field with the electric charges. The wavelength of the radiation has a great role regarding the strength of the interaction and the type and size of the electric charges that contribute to the interaction. The same rules hold for the terahertz radiation (THz). However, due to the relatively long wavelength of THz radiation relatively large units such as crystals can interact with the THz field.

In the macroscopic world the interaction, for instance, of light waves can be observed via different mechanisms which are refraction, reflection, and diffraction. Refraction and reflection of the light waves can be observed when the wave is incident on a homogeneous and isotropic or anisotropic medium. Refraction is described by the real refractive index, and reflection with reflection coefficient of the medium. In the case when the medium absorbs light these two physical quantities are replaced by more general concepts namely complex refractive index and complex reflection

K.-E. Peiponen (✉) · E. Gornov
Department of Physics and Mathematics, University of Eastern Finland,
PL 111, 80101 Joensuu, Finland
e-mail: kai.peiponen@uef.fi

E. Gornov
e-mail: evgeny.gornov@gmail.com

coefficient, respectively. Diffraction of light can be observed both in the near- and far-field regions. If the medium has regular features such as grooves or regular spatial refractive index variation diffraction can be detected in transmission and/or reflection modes of the incident light beam. If the grooves or the spatial refractive index variation become irregular or random, then one observes scattering of the light, i.e., a combination of refraction, reflection, and diffraction which however cannot be separated from each other. Scattering of the light is difficult to describe theoretically except for regular scattering units such as spheres which obey the law of Mie scattering [1].

THz waves obey the classical laws of refraction and reflection but in the case of relatively large scattering units, e.g., pores in the structure weak or relatively strong scattering may occur. In the frame of weak scattering the models of the effective medium such as those of Maxwell Garnett and Bruggeman can be used for approximate description of the optical constants of the medium in the THz gap.

The advantage of the time-domain THz spectroscopy is that one gets information both on the amplitude and phase of the interacting field. This has opened an important door, namely from the measured data it is possible to extract complex refractive index or reflection coefficient. Since the complex refractive index is purely a material parameter it is possible to identify different species of a medium from spectral features displayed in THz transmission or reflection spectra. In an ideal case one should get, e.g., the complex refractive index of a known or unknown medium easily. However, this is not always the case because the spectra obtained from the THz measurements may be distorted due to problems in experimental setup or due to the fact that the sample is scattering THz radiation. In the case of homogeneous or effective medium the classical Fresnel's laws for transmission and reflection of the THz radiation can be used, whereas once the scattering is strong enough these laws are only approximate.

In this chapter the complex permittivity, refractive index, and reflection coefficient are defined, and the laws for transmission and reflection of THz radiation using Fresnel's formulas are expressed. Furthermore, formulas that are useful to express the complex permittivity in the frame of effective medium model are spelled out along with Wiener bounds [2]. Modified Kramers–Kronig (KK) dispersion relations are introduced for spectra analysis and testing the consistency of the spectra obtained in THz measurements. The maximum entropy method (MEM) is explained and its usefulness in time-domain THz reflection spectra correction due to the sample misplacement.

3.2 Complex Permittivity and Refractive Index

When an electromagnetic wave propagates in vacuum its velocity is the speed of light, $c = 299792.458$ km/s, which is the maximum speed that can be reached when transferring information from one point to another. If the electromagnetic wave propagates in a medium its speed is reduced to $v < c$. The ratio $n = v/c$ is called the refractive index of a transparent medium. A traditional method to investigate

refractive index in the spectral range of visible light is to investigate dispersion of light using a prism. The light will be dispersed because the refractive index of the medium (prism) is subject to change as a function of the wavelength of the incident light. This is true not only in the visible spectral range but for different wavelengths covering the whole semi-infinite spectral range. The dispersion can be rather weak at some spectral ranges but also rather strong at some other ranges. Relatively strong spectral variation of refractive index can be observed for some materials that are probed by THz radiation.

If we reject the assumption of a transparent medium then absorption process has an important role. In the visible range a medium that absorbs light has usually some specific color. If a medium looks red then, e.g., in light transmission wavelengths that present red light are transmitted without or with weak attenuation, whereas other wavelengths are attenuated more along the propagation direction. Absorption and dispersion of light are closely connected with each other. This connection is expressed by the concept of the complex refractive index. The complex refractive index is an observable quantity. However, we first introduce the complex permittivity, which is a primary quantity with respect to the complex refractive index since the permittivity describes properties of a medium and its interaction with an electromagnetic wave.

From the theory of classical electromagnetism we know that the polarization, P , of electric charges of a medium is proportional to the incident electric field, E , by the relation [3]

$$P = \varepsilon_0 \chi E, \quad (3.1)$$

where ε_0 is the permittivity of vacuum and χ is so-called electrical susceptibility of the medium. Equation (3.1) is written in a scalar form, but it holds also for vectors under assumption of isotropic media. The electric induction D is defined by the following formula:

$$D = \varepsilon E = \varepsilon_0 E + P, \quad (3.2)$$

where ε is the permittivity of the medium. From Eqs. (3.1) and (3.2) we get a relation:

$$\varepsilon_r = \frac{\varepsilon}{\varepsilon_0} = 1 + \chi \quad (3.3)$$

and ε_r is called the relative permittivity which is a bare number and important in description of the interaction of an electromagnetic field with a medium. Note that we have not yet said anything about the interaction of the magnetic field with a medium. Since the scope of this book is in THz range the interaction of magnetic field with the medium is assumed to be weak. The role of the interaction of the magnetic field with conventional media such as conductors becomes important typically for long wavelengths such as radio waves.

The complex nature of the permittivity becomes evident by considering the equation of motion of microscopic electric charges that are driven by an external electric field, and deriving the induced dipole moment and macroscopic polarization of the electric charges. Such derivations for electrons are presented in [4] for the case of

linear oscillator model of electrons. Hence, for the qualitative (and sometimes also quantitative) description of the permittivity of an insulator one gets a model that is known as the Lorentz model and for conductor so-called Drude model. The permittivity of semiconductor is qualitatively the sum of the Lorentz and Drude permittivity. The basic principle of causality plays an important role in absorption–dispersion processes (see [4]). The response function, $\chi(t)$, (where t is the time) of the medium that is disturbed by an external field can be given by the Fourier transform

$$\chi(\omega) = \chi_1(\omega) + i\chi_2(\omega) = \int_0^{\infty} \chi(t) e^{i\omega t} dt, \quad (3.4)$$

where ω is the circular frequency of the electric field and i is the imaginary unit. The lower bound of the integration is zero because the response of the system is always later than the disturbance that causes the response. This is how causality affects the response of the system. Since $\chi(t)$ is a real function we got a complex function via the Fourier transform. The physical interpretation is that the real part in Eq. (3.4) describes dispersion, whereas the imaginary part is related to absorption of the electric field. Due to the complex value of the susceptibility, Eq. (3.3) leads to the complexity of the relative permittivity of the medium.

For the sake of simplicity (in the frame of scalar theory) the wave equation for an electric field propagating in the x -direction can be given by the following expression:

$$\frac{\partial^2 E}{\partial x^2} = \frac{1}{v^2} \frac{\partial^2 E}{\partial t^2}, \quad (3.5)$$

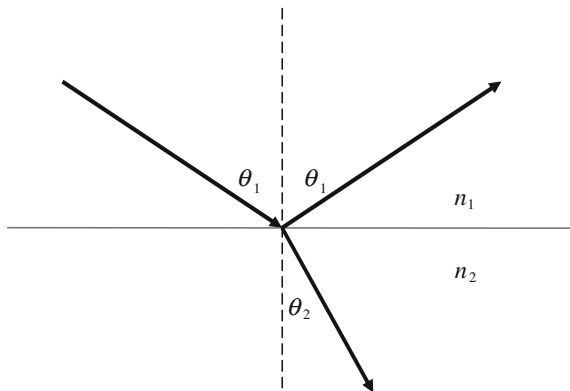
which can be derived using the Maxwell's equations [3]. As already noted the velocity v of an electric field in medium depends on the real refractive index. The factor $1/v^2$ can be replaced by a factor $\varepsilon\mu$, where μ is the permeability of the medium. In the absence of absorption Eq. (3.5) has a simple solution which is a plane wave. In the case of absorption the concept of refractive index has to be revised, and it has to be replaced by the complex refractive index, $N = n + ik$, where k is the so-called extinction coefficient. The extinction coefficient describes the strength of the attenuation of the amplitude of the electric field. The definition of the complex refractive index is as follows:

$$N^2 = \varepsilon_r \mu_r = \frac{\varepsilon}{\varepsilon_0} \frac{\mu}{\mu_0}, \quad (3.6)$$

where μ_r is the relative permeability of the medium and μ_0 is the permeability of the vacuum. It is evident from the definition (3.6), by taking into account that $1/v^2 = \varepsilon\mu$, introducing complex permittivity, and using for THz radiation the assumption $\mu = \mu_0$ that the complex refractive index is obtained from the relation

$$N = \sqrt{\varepsilon_r}. \quad (3.7)$$

Fig. 3.1 Refraction of electromagnetic field at an interface of two media having different refractive indices n_1 and n_2



In the case that the internal magnetic field is different from the incident field, and loss of the magnetic field is present, one has to introduce a complex permeability using the definition (3.6) in order to get the complex refractive index. But as stated previously this situation is supposed to be relevant for low circular frequencies with conventional materials. In the case of metamaterials a subject that will be considered later in this book, the negative real refractive index is obtained by adjusting both the permittivity and the permeability of the metamaterial [5, 6, 8].

The refraction of an electromagnetic field can be illustrated using the Snell's law as shown in Fig. 3.1. A ray that is incident at an angle θ_1 is reflected at the same angle and refracted at an angle θ_2 in the interface between two media having different refractive indices. The Snell's law reads as:

$$n_1 \sin \theta_1 = n_2 \sin \theta_2. \quad (3.8)$$

In the case of the complex refractive index Snell's law becomes an equation involving complex numbers, and physical interpretation of this law is no more a simple task.

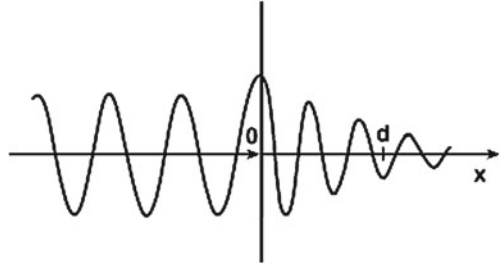
In Fig. 3.2 is illustrated the case of the absorption of the electric field. The field is incident from the left and the medium is on the right-hand side of the vertical axis. The amplitude of the field is attenuated in the vertical direction. If the medium is homogeneous then one can apply the Beer–Lambert law that is valid for transmission and can be written as follows:

$$I = I_0 e^{-\alpha(\omega)d}, \quad (3.9)$$

where I_0 is the incident intensity, I intensity measured at distance d and α is the absorption coefficient of the medium. Equation (3.9) is the basic equation utilized in transmission spectroscopy of homogeneous media. The extinction and absorption coefficient are coupled by the formula:

$$k = \frac{c\alpha}{2\omega}. \quad (3.10)$$

Fig. 3.2 Absorption of electromagnetic field. The *vertical line* denotes interface of two media



In transmission data analysis one has to take care about the internal and external reflections of the radiation incident on the sample.

3.3 Complex Transmission and Reflection Coefficient

In the case of homogeneous and isotropic or anisotropic media transmission and reflection of electromagnetic radiation from a bulk medium that involves a planar interface can be described with the aid of Fresnel's formulas in the frame of plane wave approximation. The mathematical expressions for absorbing media depend on the angle of incidence, polarization state of the incident electric field, and isotropy or anisotropy of the medium. In Fig. 3.3 is depicted both reflection and refraction by assumption of a monochromatic plane wave that is incident at the boundary of two isotropic media. Typically, two cases of linear polarization of light are considered, namely one with electric field perpendicular to the plane of incidence, i.e., *s*-polarization and one with electric field oscillating in the plane of incidence, i.e., *p*-polarization. Making use of the continuity of the electric field at the interface it is possible to derive the following Fresnel's formulas for the complex transmission, τ :

$$\begin{aligned} \tau_s &= \frac{2 \cos \theta}{\cos \theta + \sqrt{N^2 - \sin^2 \theta}}, \\ \tau_p &= \frac{2N \cos \theta}{N^2 \cos \theta + \sqrt{N^2 - \sin^2 \theta}} \end{aligned} \quad (3.11)$$

and reflection coefficient r :

$$\begin{aligned} r_s &= \frac{\cos \theta - \sqrt{N^2 - \sin^2 \theta}}{\cos \theta + \sqrt{N^2 - \sin^2 \theta}}, \\ r_p &= \frac{N^2 \cos \theta - \sqrt{N^2 - \sin^2 \theta}}{N^2 \cos \theta + \sqrt{N^2 - \sin^2 \theta}}, \end{aligned} \quad (3.12)$$

where $N = N_2/N_1$ is the relative complex refractive index. In the case of homogeneous anisotropic media the formulas are to some extent different because the relevant expressions involve the complex ordinary and extraordinary refractive indices of a

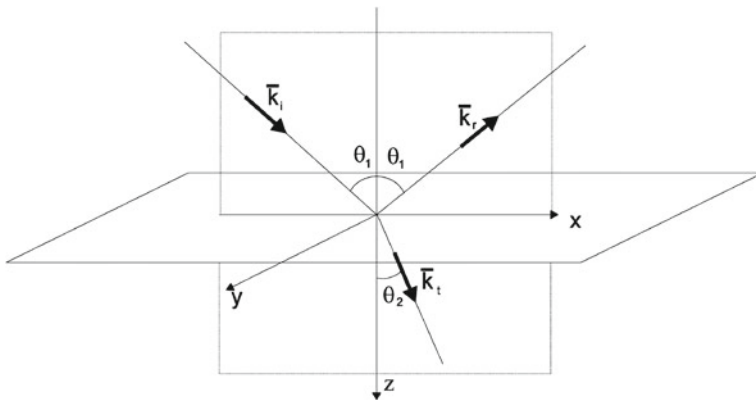


Fig. 3.3 Reflection and refraction of an incident electromagnetic field at an interface of two media. The *bold arrows* denote the wave vectors

uniaxial anisotropic system [8]. The case of a bi-axial system is even more complicated. The Fresnel's formulas (3.11 and 3.12) are simplified for the case of normal incidence, as can be observed by setting $\theta = 0$, and then the polarization state of the light is not an issue.

Finite thickness of a sample has to be taken into account regarding the transmission and reflection of an electromagnetic field in the case of a slab or a thin film. As a result the complex transmission and reflection coefficients will take expressions different from (3.11, 3.12). These systems are treated in standard books of optics [8]. Especially in the case of a thin sample the role of multiple reflections from the boundaries is important to take into account regarding the exit electric field. Explicit expressions for the complex transmission and reflection coefficients of a slab are given in [1] for the case of normal incidence. For a finite thickness sample the transmission coefficient has the following approximation for $\theta = 0$:

$$\tau = \tau_{12}\tau_{21} \exp\left(i \frac{N_2 - N_1}{c} \omega d\right), \quad (3.13)$$

where τ_{12} and τ_{21} are the complex transmission coefficients that are obtained from Eq. (3.11) which equations take the same form for normal incidence of electromagnetic radiation. Equation (3.13) can be used for extracting the complex refractive index of a medium. In the case of relatively thin slab the etalon effect is usually present. As a result the transmittance shows oscillation and has to be taken into account in the extraction of the complex refractive index by numerical algorithm [9].

Measurement of the complex refractive index in the time-domain THz spectroscopy by utilizing ellipsometric measurement technique is possible [10] by making use of basic theory of ellipsometry [11]. Simplification on measurement geometry and data analysis has been proposed in the context of the ellipsometric THz spectroscopy [12].

The electric field of a THz pulse in time-domain terahertz spectroscopy is dependent on the time. Both in recording a transmission or a reflection spectrum one changes the time delay of the THz pulse and measures waveforms for a reference and a sample. In the case of a transmission measurement the reference is typically a setup without the sample, whereas in the case of reflection measurement the reference is a highly reflecting metal mirror. The time-dependent electric field $E(t)$ is transformed to the circular frequency space using a Fourier transform such as

$$E(\omega) = \int_{-\infty}^{\infty} E(t) e^{i\omega t} dt. \quad (3.14)$$

This expression will yield real and imaginary parts so it is possible to extract both the amplitude and the phase of the electric field as a function of the circular or linear frequency. Since the electric field is measured for the sample and the reference the complex transmission coefficient in the case of transmission spectrum is usually expressed as the ratio

$$\frac{E_{\text{Sample}}}{E_{\text{Ref}}} = |\tau| e^{i\varphi(\omega)}, \quad (3.15)$$

where φ is the phase. The complex transmission coefficient on the right-hand side of Eq. (3.15) is compared with appropriate theoretical expression in order to resolve the complex refractive index. Typically, the first analysis involves calculation of the refractive index with the aid of the delay of the pulse. Once the thickness of the sample is known the real refractive index is obtained from the optical path length $\Delta = nd$, where n is the real refractive index of the medium and d is its thickness. The delay time δt which is measured by the THz spectrometer obeys for homogeneous and isotropic medium the law

$$\delta t = \frac{d(n_{\text{Sample}} - n_{\text{Ref}})}{c}. \quad (3.16)$$

In the case of air or buffer gas such as nitrogen the refractive index of the reference is set $n_{\text{Ref}} = 1$. The absorption coefficient of the homogeneous sample can be estimated with the aid of the Beer–Lambert law. However, if we wish to know the wavelength-dependent complex refractive index we have to use Fresnel's expressions or their modifications depending on the thickness of the sample because multiple reflections may occur at the boundaries of the sample. Experimental problems such as uncertainty in the geometry and time sampling may cause misinterpretation of the complex refractive index obtained in THz spectroscopy [13].

Time-domain THz reflection spectrum is obtained from a ratio

$$\frac{E_{\text{Sample}}(\omega)}{E_{\text{ref}}(\omega)} = |r(\omega)| e^{i\varphi(\omega)}. \quad (3.17)$$

The complex refractive index is extracted for a homogeneous isotropic or anisotropic media using the Fresnel's formulas for reflection either given for bulk, slab or a thin film. Unfortunately, in the case of time-domain reflections spectroscopy the extracted complex refractive index may be erroneous due to the sample misplacement with respect to the reference mirror. This case will be dealt with in Sects. 3.5 and 3.6.

3.4 Effective Medium Models

The extraction of the complex permittivity and refractive index using the Fresnel's formulas is possible from a two- or multi-phase composite if the inclusions in the host material are so small that scattering of the electromagnetic radiation is negligible from the system. The research of colloids, e.g., nanoparticles (NP) in gas, liquid, or solid phase has a long history both in chemistry and physics. Optical properties of NPs embedded in a host medium such as gold NPs in water have gained much attention due to the surface-plasmon-resonance (SPR) [14] that an incident light experiences while interacting with the gold inclusions, and as a result the gold colloid typically has a reddish color. To explain the color of glasses and solutions containing minute metal particles Maxwell Garnett (MG) formulated the model of an effective medium, which consists of a host medium, and embedded inclusions. The model assumes the absence of light scattering and spherical shape of the non-interacting inclusions which are distributed uniformly in the host medium [15]. The MG model as well as the Bruggeman (B) effective medium model [16] are the standard models for effective media. There are other effective medium models too but here we concentrate on the two simple standard models. The basic physics and properties of the MG and B models are nicely described by Aspnes [17]. The main difference between the MG and B models is that in the B model the fill fraction of inclusions is not restricted to low values as is the case of the MG model, and the inclusions are embedded in the effective medium itself in the B model. It is typical to deal with the complex permittivity as concerns the effective medium models. In the case of the MG model the effective permittivity of a two-phase composite is as follows:

$$\frac{\varepsilon_{\text{eff}}(\omega) - \varepsilon_h(\omega)}{\varepsilon_{\text{eff}}(\omega) + 2\varepsilon_h(\omega)} = f_i \frac{\varepsilon_i(\omega) - \varepsilon_h(\omega)}{\varepsilon_i(\omega) + 2\varepsilon_h(\omega)}, \quad (3.18)$$

where ε_{eff} is the effective permittivity, ε_h permittivity of the host, and ε_i that of inclusion. The fill fraction of inclusions is denoted by f_i . The problem arises usually when the fill fraction of host material and inclusion are equal. Then it is difficult to say which material actually is the host. Bruggeman solved this problem by introducing his model for spherical inclusions as follows:

$$f_a \frac{\varepsilon_a(\omega) - \varepsilon_{\text{eff}}(\omega)}{\varepsilon_a(\omega) + 2\varepsilon_{\text{eff}}(\omega)} + f_b \frac{\varepsilon_b(\omega) - \varepsilon_{\text{eff}}(\omega)}{\varepsilon_b(\omega) + 2\varepsilon_{\text{eff}}(\omega)} = 0, \quad (3.19)$$

where a and b denote two components having different complex permittivity and fill fractions. Both models (3.18) and (3.19) can be generalized to take into account multi-phase structures of spherical inclusions. These models have been generalized to other regular structures such as ellipsoids, but one has to take some care in their utilization for irregular shape inclusions. From the colloid physics it is known that the size, shape, fill fraction, and complex permittivity of the inclusions as well as the complex permittivity of the host medium rule the optical properties of the effective medium. Typically, one observes shift in the spectral feature as a function of the fill fraction. The shortcoming of the MG and B models is that they omit the size of the scattering unit. Using the Mie scattering theory it is possible to modify, e.g., MG model so that the diameter of the spherical inclusion is taken into account in the calculation of the effective permittivity [18].

As it is quite obvious in reality there are inclusions that have an irregular shape, and these inclusions are in many cases randomly dispersed. Then the effective permittivity of the MG and B models provide usually only a rough approximation. Usually an easier procedure is then to utilize Wiener bounds [2], which treat two extreme cases namely maximum screening and no screening of a microstructure. These bounds for two-phase composite can be expressed as

$$\begin{aligned} f_a \varepsilon_{\text{eff}} &= f_a \varepsilon_a + f_b \varepsilon_b \\ \varepsilon_{\text{eff}} &= \left(\frac{f_a}{\varepsilon_a} + \frac{f_b}{\varepsilon_b} \right)^{-1}. \end{aligned} \quad (3.20)$$

These bounds do not assume anything about the shape of the inclusion. Wiener bounds hold for multi-phase systems, and graphical presentation of the bounds for a system involving complex permittivity, as well as more stringent bounds have been presented in the literature [19–21].

The effective medium model and Wiener bounds can be used in THz spectroscopy for qualitative and sometimes for quantitative description of the effective complex permittivity or the refractive index of a system because in many cases inclusions or pores have a dimension much smaller than the wavelength of the THz radiation. In other words the situation is that the scattering of the THz wave is negligible. First steps have been taken in making use of the MG model and Wiener bounds in the THz spectral range to describe the material properties of pharmaceutical compacts [22, 23]. Parrott et al. deal with the MG and B models in Chap. 8, Jansen et al. deal with the MG model in Chap. 13, and Kuzel and Nemeč deal with MG and B model in the context of metamaterials in Chap. 22.

3.5 Modified Kramers–Kronig Dispersion Relations in THz Spectra Analysis

When recording THz spectra there is a nice feature because it is possible to get information both on the amplitude and the phase of the electric field that has interacted with a sample. As a result it is possible to extract the complex refractive index of the sample unless scattering is too strong. However, due to the scattering of THz waves in transmission experiments, or mismatch between the sample and reference in reflection experiments the extracted spectra may be erroneous. Therefore, it is important to test the obtained spectra, and whenever possible to try to correct the spectra. In this section we present some dispersion relations that have been found useful for resolving the real refractive index and also for testing the validity of THz spectra.

If we consider, e.g., optical spectroscopy such as normal transmission and reflection spectroscopy the phase information is lost unless an ellipsometer is used for the measurement of the complex refractive index. The problem with an ellipsometer is that usually one has to choose an appropriate model to be applied for complex samples, which model in reality may be approximate, and that the spectral range which can be gained by an ellipsometer may be relatively narrow. Therefore, most of the data covering wide spectral range for optical constants in table books such as [24] rely on the conventional spectral measurements and Kramers–Kronig (KK) analysis [25–27]. Quite often the data analysis by KK is based on the phase retrieval from reflection spectra. Fresnel theory and numerical algorithm can be exploited in resolving the complex refractive index of the medium in the THz gap in the plane wave approximation. However, in the case of the validity of the Beer-Lambert law it is possible to calculate easily the imaginary part of the complex refractive index, and furthermore, the real part with appropriate KK analysis. This was shown for a narrow band data related to pharmaceutical compact which was microcrystalline cellulose [28].

Next, we write the traditional KK dispersion relations for the complex refractive index. The real refractive index and the extinction coefficient are coupled by a pair of dispersion relations that can be expressed as:

$$\Delta n(\omega') = n(\omega') - 1 = \frac{2}{\pi} P \int_0^{\infty} \frac{\omega k(\omega)}{\omega^2 - \omega'^2} d\omega \quad (3.21)$$

and

$$k(\omega') = -\frac{2\omega'}{\pi} P \int_0^{\infty} \frac{n(\omega) - 1}{\omega^2 - \omega'^2} d\omega, \quad (3.22)$$

where P stands for the so-called Cauchy principal value. The singular point ω' is reached in a symmetric manner from the left and the right-hand sides in the numerical

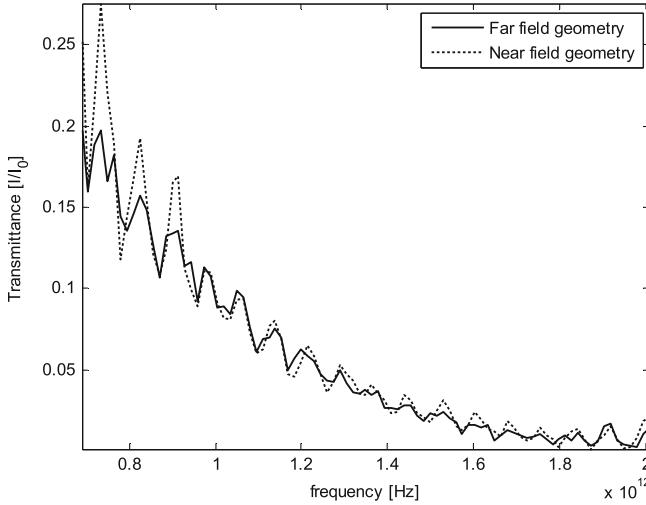


Fig. 3.4 Transmittance for a tablet with porosity 23.3 %

integration and the integration is stopped once the value of the integral is hardly changing. Thus, in the numerical procedure the value for circular frequency that would match the singular point is not allowed. A MATLAB computer code for the data inversion is given in [26]. Typically, the data inversion using transmittance data and Eq. (3.21) is most common. However, for spectra testing both dispersion relations (3.21) and (3.22) are valuable. A singly subtractive KK (SSKK) relation [26, 29] that can be used, e.g., for calculation of the absolute value of the refractive index of the porous tablet is as follows:

$$n(\omega') - n(\omega'') = \frac{2(\omega'^2 - \omega''^2)}{\pi} P \int_0^{\infty} \frac{\omega k(\omega)}{(\omega^2 - \omega'^2)(\omega^2 - \omega''^2)} d\omega, \quad (3.23)$$

where $n(\omega'')$ is a priori known refractive index at an anchor point ω'' .

In Fig. 3.4 is shown transmittance detected from a tablet compacted from microcrystalline cellulose. Cellulose was studied by Taday [30] and he considered it as a “good” THz matrix material. A recent review on THz pulsed spectroscopy and imaging pharmaceutical applications was written by Shen [31]. In Fig. 3.4 the transmittance was detected with a detector positions in the near- and far-field geometries. This is to check possible scattering of the THz wave. The oscillation of the transmittance is not fulfilling the usual etalon mode equation. Probably the oscillation is due to higher refractive index distribution of the two faces of the tablet in comparison to the inner part.

In Fig. 3.5 (upper panel) is shown the extinction coefficient of the tablet and this curve is fluctuating. In Fig. 3.5 (lower panel) are shown both the absolute refractive

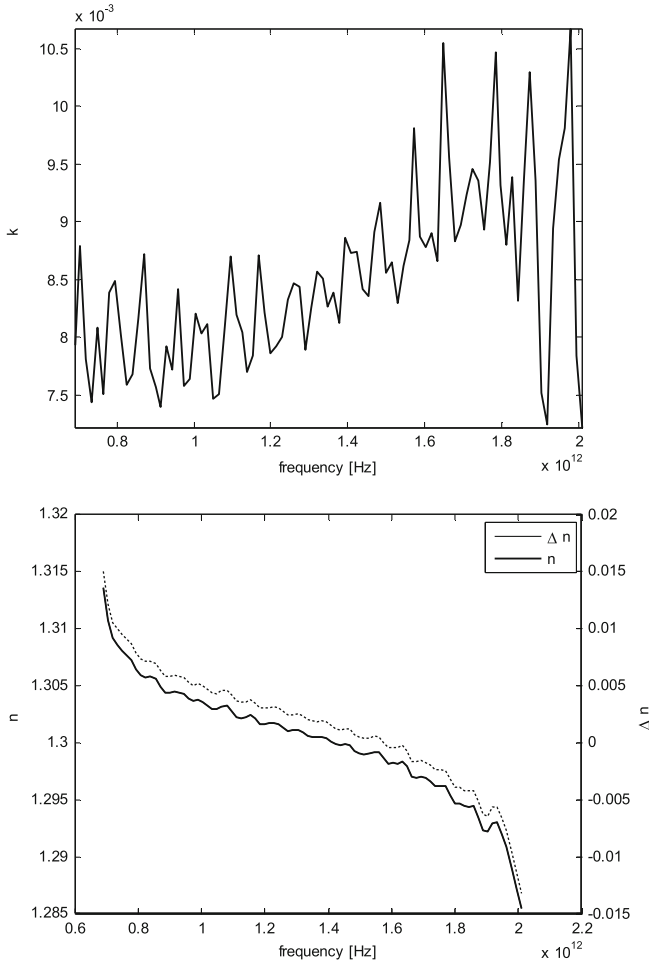


Fig. 3.5 Extinction coefficient (*upper panel*) and absolute refractive index and its change (*lower panel*) for a tablet compressed from microcrystalline cellulose. Reproduced with permission from Ref. [28]. Copyright [2011], Optical Society of America

index and its change that were calculated using Eqs. (3.21) and (3.23). The refractive index $n(\omega'') = 1.3036$ was obtained at the maximum value of the THz pulse. The corresponding anchor point was at the frequency 1.0045×10^{12} Hz. In Eq. (3.23) the denominator is proportional to ω^{-4} which is the reason for expected stronger convergence of the integral of Eq. (3.23) for high frequencies in comparison to the integral of Eq. (3.21). The well-known problem of convergence of the dispersion integral at the initial and final points of the refractive index spectra is present both for Eqs. (3.21) and (3.23). The shape of the curves in Fig. 3.5 (lower panel) is quite similar. The curves in Fig. 3.5 were calculated without data extrapolations beyond

the measured range. Extrapolation of the extinction spectra beyond the measurement range usually improves the success of the KK analysis. The advantage of the refractive index change Δn data is that it is due to units only that contribute to the dispersion.

Yasuda and Hosako [32] exploited KK analysis in their study of the refractive index of metal in THz gap. It is a recommended procedure to check the consistency of the complex refractive index obtained from experimental data with the data inverted by KK relations, i.e., with the principle of causality.

As concerns KK relations for reflection spectra we utilize the following dispersion relations

$$\varphi(\omega') = -\frac{2\omega'}{\pi} P \int_0^{\infty} \frac{\ln |r(\omega)|}{\omega^2 - \omega'^2} d\omega \quad (3.24)$$

and

$$\ln |r(\omega')| - \ln |r(\omega'')| = \frac{2\omega'}{\pi} P \int_0^{\infty} \omega \varphi(\omega) \left(\frac{1}{\omega^2 - \omega'^2} - \frac{1}{\omega^2 - \omega''^2} \right) d\omega \quad (3.25)$$

In Eq. (3.24) one has to know the reflectance *a priori* at one circular frequency ω'' . The problem with conventional KK relations is that one should know the spectra ranging the whole semi-infinite circular frequency interval. Usually what one gets also in the THz region are spectra on a finite interval. Data extrapolation beyond the measured range is one solution such as using constants wings for reflection spectrum also in the case of THz spectral range [27]. However, more effective modified KK relations have been suggested that can be applied to finite range spectra and without data extrapolations. Different types of modified KK dispersion relations have been reported in [33–36], and also reviewed in [37] in the case of testing THz spectra. Here, we present modified KK dispersion relations that were useful in testing transmission spectra from pharmaceutical tablets [36], and reflection spectra from a semiconductor [35].

It is possible to test the validity of THz transmission data obtained from homogeneous or porous media. The idea is that the complex refractive index that is extracted from the transmission data using Fresnel's theory is tested by the following dispersion relations [36]:

$$\Re \{f(\omega')\} = \frac{2}{\pi} P \int_{\omega_a}^{\omega_b} \frac{\omega \Im \{f(\omega)\}}{\omega^2 - \omega'^2} d\omega \quad (3.26)$$

and

$$\Im \{f(\omega')\} = -\frac{2\omega'}{\pi} P \int_{\omega_a}^{\omega_b} \frac{\Re \{f(\omega)\}}{\omega^2 - \omega'^2} d\omega \quad (3.27)$$

where $[\omega_a, \omega_b]$ is a range where the complex refractive index has been obtained and the polynomial f is defined as follows:

$$f(\omega) = [N(\omega) - N(\omega_a)] [N(\omega) - N^*(\omega_a)] [N(\omega) - N(\omega_b)] [N(\omega) - N^*(\omega_b)] \quad (3.28)$$

where $*$ denotes the complex conjugate. The polynomial (3.28) fulfills the criteria needed for the validity of the KK relations. The advantage of using of a polynomial in the spectra testing relies on the fact that it provides convergence of the dispersion integral at the initial and final points of the measured spectrum, whereas conventional KK relations (3.21) and (3.23) typically diverge at such points.

In Figs. 3.6 and 3.7 are shown the results for the testing of the complex refractive index of pellets obtained by mixing lactose α -monohydrate and polycrystalline powder of Carbamazepine form I with polyethylene. The solid curves were obtained from experimental data, which was measured by TPS spectra 1,000 V spectrometer (TeraView, Cambridge, UK), and using Fresnel's theory, whereas the dashed curves were obtained by application of (3.26–3.28) to the complex refractive index data. Both the solid and dashed curves show similar features but the magnitude is slightly different. The slight discrepancy is supposed to result from modest scattering of THz wave from the pellet.

For the purpose of testing THz reflection spectra a method that couples the SSKK dispersion relations and Eq. (3.28) was shown to be useful [35]. In this method the SSKK relations are truncated to a finite circular frequency interval by changing the bounds of the integrals as follows:

$$\Re \{f(\omega')\} \approx \Re \{f(\omega_1)\} + \frac{2}{\pi} (\omega'^2 - \omega_1^2) P \int_{\omega_a}^{\omega_b} \frac{\omega \Im \{f(\omega)\}}{(\omega^2 - \omega'^2)(\omega^2 - \omega_1^2)} d\omega \quad (3.29)$$

and

$$\frac{\Im \{f(\omega')\}}{\omega'} \approx \frac{\Im \{f(\omega_1)\}}{\omega_1} + \frac{2}{\pi} (\omega'^2 - \omega_1^2) P \int_{\omega_a}^{\omega_b} \frac{\Re \{f(\omega)\}}{(\omega^2 - \omega'^2)(\omega^2 - \omega_1^2)} d\omega \quad (3.30)$$

and the polynomial f is obtained from (3.28) but replacing the complex refractive index N by the natural logarithm of the complex reflection coefficient namely $\ln r$. This method is useful in the case when the reference and the sample are not at the same positions. This means that there will be in measured spectra a misplacement error due to the phase shift of the electric field. The misplacement can be observed but what is more important is that the erroneous complex refractive index that is obtained from the experimental data can be corrected. To see how the correction works we deal with a complex experimental reflection coefficient $r_{\text{exp}} = r e^{i\beta}$, where r is the true reflection coefficient and the constant β presents a phase shift due to the sample misplacement. Next, a norm that is defined by the equation [33, 35],

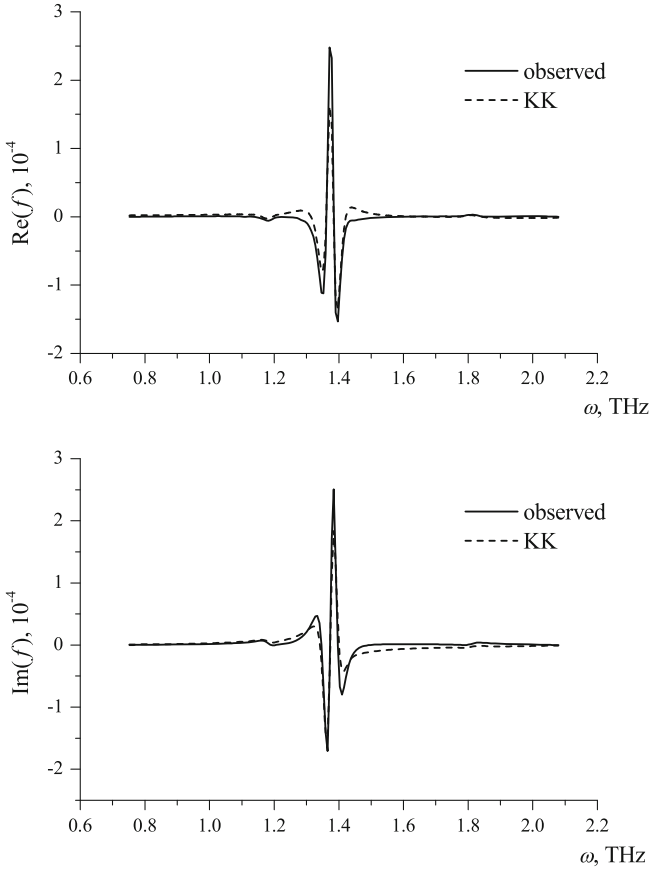


Fig. 3.6 Real (*upper panel*) and imaginary part (*lower panel*) of dispersion data functions of Carbamazepine form I pellet. Experimental data (*solid curve*) and KK analysis (*dashed curve*). Reproduced with permission from Ref. [36]. Copyright [2010], Optical Society of America

$$A(\gamma) = \int_{\omega_a}^{\omega_b} \left| f_\gamma(\omega) - f_\gamma^{\text{SSKK}}(\omega) \right| d\omega \quad (3.31)$$

is minimized. The function f_γ is given by (3.28) where N is replaced by $\ln[r_{\text{exp}} e^{i\gamma}]$ and the real and imaginary parts of f_γ^{SSKK} are obtained by substituting f_γ into the right-hand sides of (3.29) and (3.30). The minimum is reached at $\gamma_{\text{min}} = -\beta$, which compensates the sample misplacement error.

As an example we show data for reflection coefficient of n-type undoped (100) InAs wafer measured in the spectral range from 0.5 to 2.5 THz. In Fig. 3.8 are shown the real and imaginary parts of $f(\ln r)$ for raw experimental data and corresponding data obtained by SSKK dispersion relations. Apparently the curves shown in Fig. 3.8

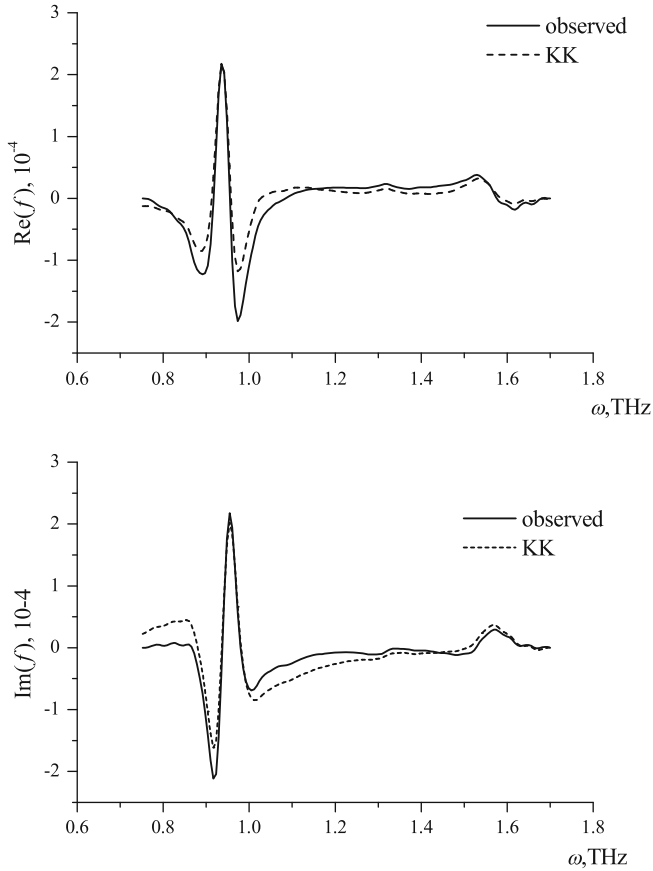


Fig. 3.7 Dispersion curves of lactose α -monohydrate pellet. Real (*upper panel*) and imaginary part (*lower panel*). Reproduced with permission from Ref. [36]. Copyright [2010], Optical Society of America

depart from each other. In Fig. 3.9 are shown the curves that were obtained after correction based on (3.31), and finally in Fig. 3.10 the corrected complex refractive index of the semiconductor.

The correction of spectra may be important also in cases of reflection of THz pulse from rough surface. The reflectance is modified by the roughness. The simplest case is a surface with Gaussian surface height distribution. Such a surface has been investigated by analyzing terahertz reflection spectra of metals [38]. The modified KK relations presented above can be applied for testing data obtained from rough surfaces, and also in the case of media that can be described with the MG and B effective medium model.

In the following section we introduce another method that is useful for phase retrieval and data correction in the case of THz reflection spectra.

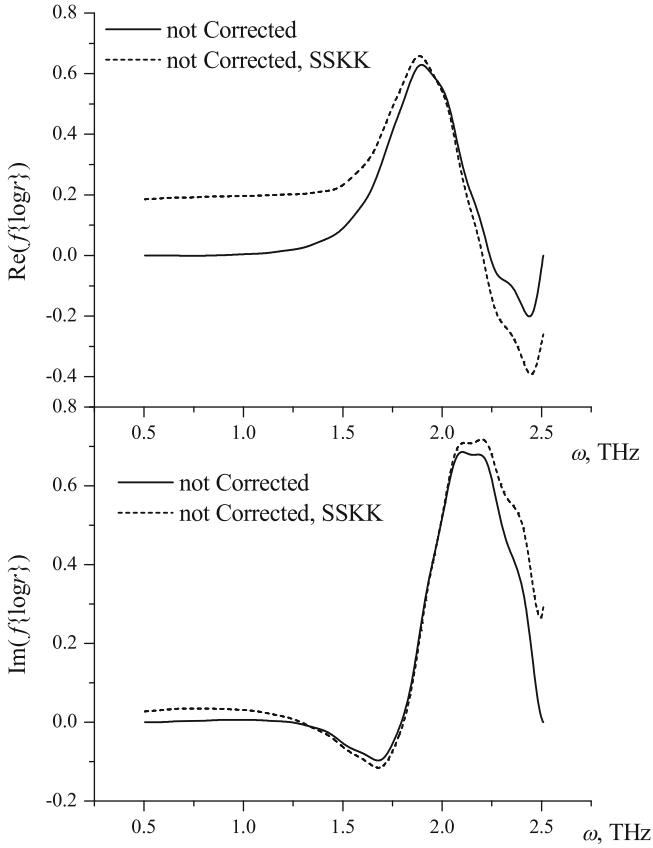


Fig. 3.8 Real (*upper panel*) and imaginary part (*lower panel*) of a test function used to test the validity of THz spectra of InAs wafer. Reproduced with permission from [35]. Copyright [2006], American Institute of Physics

3.6 Maximum Entropy Method in the Time-Domain THz Reflection Spectroscopy

The usage and applicability of the maximum entropy method (MEM) as a phase retrieval procedure in linear and nonlinear optical spectroscopy has been verified, e.g., in the books [25, 26]. The maximum entropy model is based on a more general concept of entropy than that of the thermodynamics. Shannon [39] laid the foundations of a general concept of entropy in the information technology. Vartiainen et al. [40] introduced this method for phase retrieval problems in optical reflection spectroscopy. One significant merit of MEM is that it does not require reflectance determination over the entire electromagnetic spectrum, but only within the region of interest. However, in addition to the reflectance data information about the

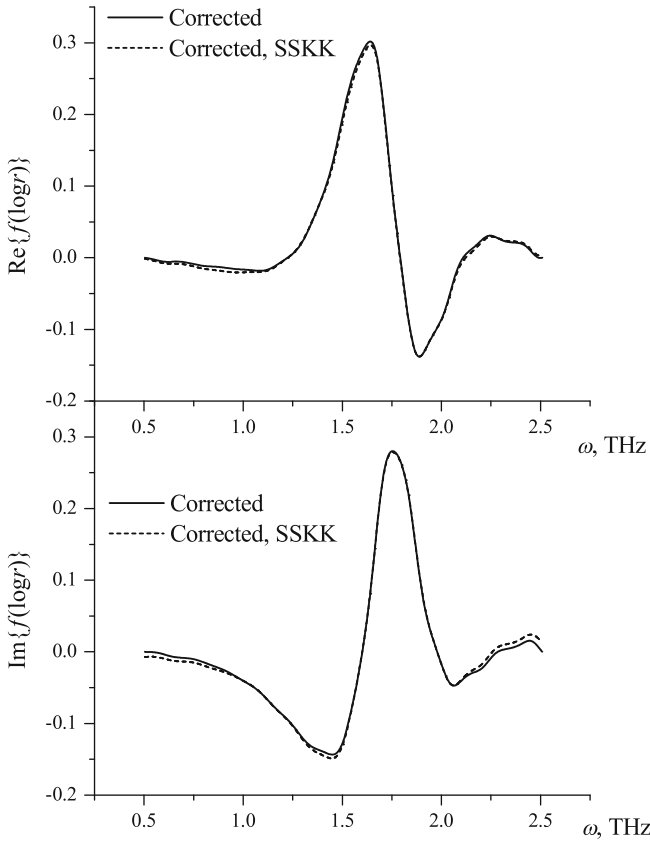


Fig. 3.9 Real (*upper panel*) and imaginary part (*lower panel*) after finding the sample misplacement correction term. Reproduced with permission from [35]. Copyright [2006], American Institute of Physics

optical properties of the sample at discrete frequencies is usually required in order to determine its complex refractive index in the frame of the MEM. Such information at anchor points commonly comprises the real and/or imaginary parts of the complex refractive index of the sample determined at least for one frequency within the finite spectral range. In practice, the MEM phase retrieval procedure includes the experimental reflectance R given by the following formula (a somewhat lengthy mathematical derivation can be found in the book [25]):

$$R(\nu) = \frac{|\zeta|^2}{\left|1 + \sum_{m=1}^M a_m \exp(-i2\pi m\nu)\right|^2}, \tag{3.32}$$

where the normalized angular frequency ν is defined by

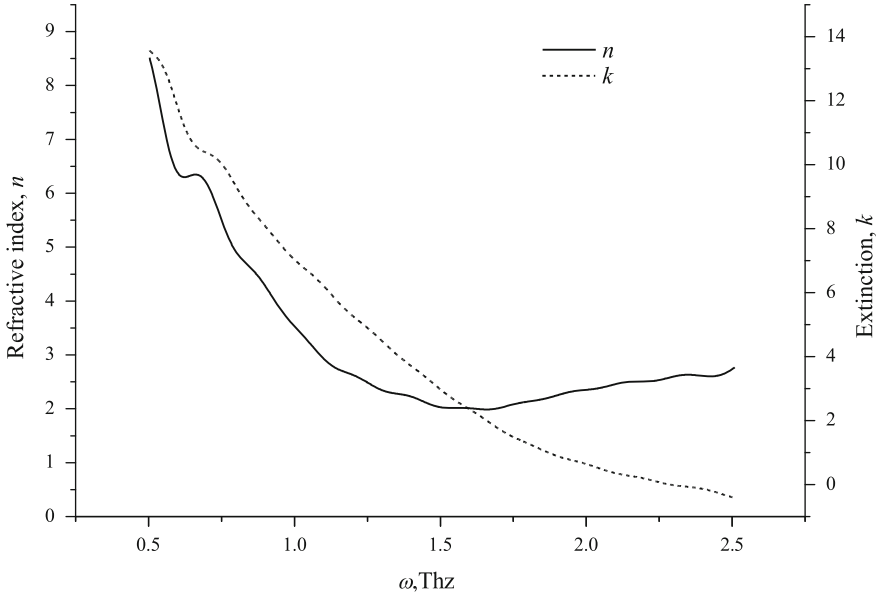


Fig. 3.10 Refractive index and extinction coefficient of InAs sample after spectra correction

$$v = \frac{\omega - \omega_a}{\omega_b - \omega_a}. \quad (3.33)$$

The unknown MEM coefficients a_m and $|\zeta|$ can be obtained from a set of linear Yule-Walker equations

$$\sum_{m=0}^M a_m (M - m) = \begin{cases} |\zeta|^2 & \text{if } n = 0 \\ 0 & \text{if } n = 1, \dots, M, \end{cases} \quad (3.34)$$

where the auto-correlation $C(t)$ is computed by a Fourier transform of reflectance R as

$$C(t) = \int_0^1 R(v) \exp(i2\pi tv) dv. \quad (3.35)$$

Phase retrieval is performed using the complex reflectivity

$$r(v) = \frac{|\zeta| \exp[-i\phi(v)]}{1 + \sum_{m=1}^M a_m \exp(-i2\pi mv)}. \quad (3.36)$$

In (3.36), the error phase ϕ is the only quantity that cannot be obtained by a measurement of $R(v)$. The idea in MEM phase retrieval is that the problem of finding the true phase φ is reduced to a problem of finding the error phase ϕ which is

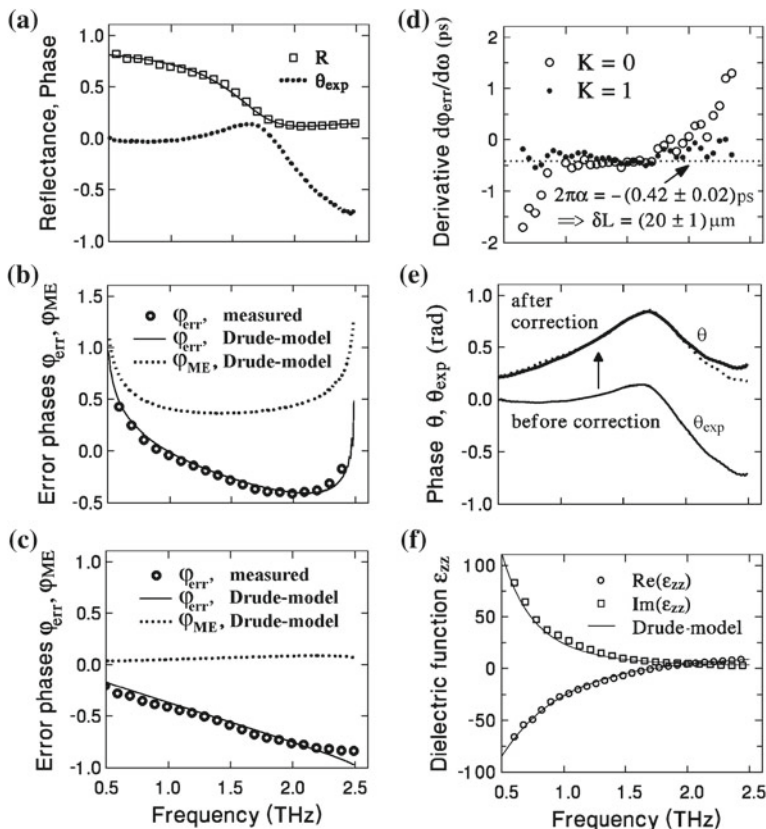


Fig. 3.11 **a** Measured reflectance (*squares*), reflectance obtained from Drude model for permittivity of InAs and the phase (*dotted line*). **b** and **c** Measured and calculated error phase for $K = 0$ and $K = 1$. **d** Derivative of error phase which was used to get the phase error due to misplacement of sample. **e** Corrected and uncorrected phase. **f** Permittivity of InAs obtained after phase correction. Reproduced with permission from [41]. Copyright [2004], American Institute of Physics

typically a much simpler function than the true phase. Additional information about $r(\nu)$, determined at $L + 1$ discrete normalized frequencies ν_l , is used to find an estimate for the error phase with a polynomial

$$\phi = \sum_{l=0}^L B_l \nu^l \quad (3.37)$$

where B_l is obtainable from a Vandermonde system. The error phase is usually a slowly varying function, and in favorable cases only one or two anchor points are necessary; in other words, the optimum degree of the polynomial is low.

The MEM was applied to the THz reflection data from the semiconductor InAs, and the misplacement was obtained from a derivative of the experimental phase. The

calculated permittivity of the semiconductor was compared with the Drude model for the permittivity of InAs. The results obtained by MEM and Drude model agree well as can be observed from Fig. 3.11. In this case the procedure of so-called spectrum squeezing was applied. The MEM is good for spiky spectra, therefore the squeezing process was applied. The squeezing is explained in more detail in [41]. MEM can be also utilized in the simultaneous inspection of complex refractive index and surface topography of an object [42] by THz radiation.

Recently, a new application of MEM was in the context of determination of the time origin in time-domain THz emission spectroscopy [43].

The KK analysis and the MEM are alternative methods for phase retrieval. However, the applicability of the MEM is more general because it can be exploited in a case when the KK analysis is invalid namely in the presence of complex zeros of the complex reflection coefficient in the upper half of complex frequency plane [44], a case that can appear also in the THz reflection spectroscopy.

3.7 Conclusions and Outlook

In the case of homogeneous, effective, and porous media it is possible to exploit traditional dispersion relation such as Kramers–Kronig relations to check the consistency of the measured spectra with the causality-based dispersion relations. In addition, this consistency check can be done in reflection spectroscopy with the aid of the maximum entropy method. Although the complex refractive index or the permittivity can be extracted directly from THz time-domain measurements there are sources such as sample misplacement in conventional reflection spectroscopy or volume and surface scattering in the case of measurement of transmission. Causality, one of the fundamental physical laws results to the existence of the Kramers–Kronig relations. Invalidity of the Fresnel’s laws due to, e.g., scattering, surface curvature, or other pathological situations can cause an error in the estimate of the complex refractive index, and this can be revealed by appropriate dispersion relations.

In the future it is expected that Kramers–Kronig relations and modified dispersion relations are implemented in the software of THz spectrometers since they provide efficient tools to estimate the reliability of the measured complex refractive index. The calculation is typically fast both in the case of Kramers–Kronig and maximum entropy analysis, which is an advantage when considering real-time and online measurement of the complex refractive index or permittivity depending on the application.

References

1. C.F. Bohren, D.R. Huffman, *Absorption of Light by Small Particles* (Wiley, New York, 1983)
2. O. Wiener, *Abh. Math. Phys. K1 Königl. Ges.* **32**, 509 (1912)

3. J.D. Jackson, *Classical Electrodynamics* (Wiley, New York, 1962)
4. H.M. Nussenzveig, *Causality and Dispersion Relations* (Academic Press, New York, 1972)
5. D.R. Smith, N. Kroll, *Phys. Rev. Lett.* **85**, 2933 (2000)
6. J. Yao, Z. Liu, Y. Liu, Y. Wang, C. Sun, G. Bartal, A.M. Stacy, X. Zhang, *Science* **321**, 930 (2008)
7. V.G. Veselago, *Sov. Phys. Usp.* **10**, 509 (1968)
8. M. Born, E. Wolf, *Principles of Optics*, 6th edn. (Pergamon, New York, 1980)
9. T.D. Dorney, R.G. Baraniuk, D.M. Mittleman, *J. Opt. Soc. Am. A.* **18**, 1562 (2001)
10. T. Nagashima, M. Hangyo, *Appl. Phys. Lett.* **79**, 3917 (2001)
11. R.M.A. Azzam, H.M. Bashara, *Ellipsometry and Polarized Light* (North-Holland, New York, 1977)
12. E. Gornov, K.-E. Peiponen, *Phys. Stat. Sol. (b)* **244**, 2619 (2007)
13. X. Xu, X. Wang, L. Wang, *Appl. Opt.* **45**, 648 (2006)
14. H. R  ther, *Surface Plasmons and Smooth and Rough Surfaces and Gratings* (Springer, Berlin, 1988)
15. J.C. Maxwell Garnett, *Trans. R. Soc.* **203**, 385 (1904)
16. D.A.G. Bruggeman, *Ann. Phys.* **24**, 636 (1935)
17. D. Aspnes, *Am. J. Phys.* **50**, 704 (1982)
18. R. Ruppini, *Opt. Commun.* **182**, 273 (2000)
19. G.W. Milton, *Appl. Phys. Lett.* **37**, 300 (1980)
20. D.E. Aspnes, *Phys. Rev. Lett.* **48**, 1629 (1980)
21. K.-E. Peiponen, E. Gornov, *Opt. Lett.* **31**, 2202 (2006)
22. E.P.J. Parrott, J.A. Zeitler, L.F. Gladden, *Opt. Lett.* **34**, 3722 (2009)
23. H. Tuononen, K. Fukunaga, M. Kuosmanen, J. Ketolainen, K.-E. Peiponen, *Appl. Spectrosc.* **64**, 127 (2010)
24. E.D. Palik, *Handbook of Optical Constants of Solids I–III* (Academic, Orlando, 1993)
25. K.-E. Peiponen, E.M. Vartiainen, T. Asakura, *Dispersion, Complex Analysis and Optical Spectroscopy* (Springer, Heidelberg, 1999)
26. V. Lucarini, J.J. Saarinen, K.-E. Peiponen, E.M. Vartiainen, *Kramers–Kronig Relations in Optical Materials Research* (Springer, Berlin, 2005)
27. E. Gornov, E.M. Vartiainen, K.-E. Peiponen, *Appl. Opt.* **45**, 6519 (2006)
28. P. Silfsten, V. Kontturi, T. Ervasti, J. Ketolainen, K.-E. Peiponen, *Opt. Lett.* **36**, 778 (2011)
29. R.K. Ahrenkiel, *J. Opt. Soc. Am.* **61**, 1651 (1971)
30. P.F. Taday, *Phil. Trans. R. Soc. Lond. A.* **362**, 351 (2004)
31. Y.-C. Shen, *Int. J. Pharm.* **417**, 48 (2011)
32. H. Yasuda, I. Hosako, *Jpn. J. Appl. Phys.* **47**, 1632 (2008)
33. V. Lucarini, Y. Ino, K.-E. Peiponen, M. Kuwata-Gonokami, *Phys. Rev. B* **72**, 125107 (2005)
34. K.-E. Peiponen, E. Gornov, Y. Svirko, Y. Ino, M. Kuwata-Gonokami, *Phys. Rev. B* **72**, 2451091 (2005)
35. E. Gornov, K.-E. Peiponen, Y. Svirko, Y. Ino, M. Kuwata-Gonokami, *Appl. Phys. Lett.* **89**, 1429031 (2006)
36. H. Tuononen, E. Gornov, J.A. Zeitler, J. Aaltonen, K.-E. Peiponen, *Opt. Lett.* **35**, 631 (2010)
37. K.-E. Peiponen, J.J. Saarinen, *Rep. Prog. Phys.* **72**, 056401 (2009)
38. A. Jagannathan, A.J. Gatesman, R.H. Giles, *Opt. Lett.* **34**, 1927 (2009)
39. C.E. Shannon, *Bell Syst. Tech. J.* **28**, 656 (1949)
40. E.M. Vartiainen, K.-E. Peiponen, T. Asakura, *Opt. Commun.* **89**, 37 (1992)
41. E.M. Vartiainen, Y. Ino, R. Shimano, M. Kuwata-Gonokami, Y.P. Svirko, K.-E. Peiponen, *J. Appl. Phys.* **96**, 4171 (2004)
42. Y. Ino, J.B. Heroux, T. Mukaiyama, M. Kuwata-Gonokami, *Appl. Phys. Lett.* **88**, 41114 (2006)
43. T. Unuma, Y. Ino, M. Kuwata-Gonokami, E.M. Vartiainen, K.-E. Peiponen, K. Hirakawa, *Opt. Exp.* **18**, 15853 (2010)
44. K.-E. Peiponen, E.M. Vartiainen, *J. Opt. Soc. Am. B* **23**, 114 (2006)

Chapter 4

Complex Refractive Index Determination Using Planar and Converging Beam Transfer Functions

Vasilis Apostolopoulos, Geoff Daniell and Aaron Chung

Abstract Terahertz time domain spectroscopy can help us to determine the complex refractive index of materials. To achieve this a theoretical model of the spectrometer has to be implemented; a usual method for refractive index determination is to fit a theoretically calculated transfer function to the experimental data. Material parameter extraction models based on transfer functions can be of varying complexity based on the requirements for accuracy and also the difficulty of factoring all experimental parameters. Here, we are going to show how algorithms based on transfer functions with different complexity can be setup. It will be described how a transfer function can be used to extract the refractive index of material and the key stages of the analysis, the fitting algorithm, and the need for phase unwrapping. Transfer functions of an increasing complexity will be shown, with and without the etalon term, using planar or converging beam.

4.1 Material Parameter Extraction Using a Transfer Function

Terahertz time domain spectroscopy can help us to determine the complex refractive index of materials. To achieve this a theoretical model of the spectrometer has to be implemented; a usual method for refractive index determination is to fit a theoretically calculated transfer function to the experimental data. Material parameter extraction models based on transfer functions can be of varying complexity based on the requirements for accuracy and also the difficulty of factoring all experimental parameters. There is a lot of research that treats a planar THz wave case, one of the first publications in the subject were from Duvillaret et al. [1, 2], where a transfer function is used with and without etalon effects. The same group in [2] extends their

V. Apostolopoulos (✉) · G. Daniell · A. Chung
Physics and Astronomy, University of Southampton,
SO17 1BJ, Southampton, UK
e-mail: v.apostolopoulos@soton.ac.uk

work in a treatment that also calculates the thickness of the sample. There is an ongoing research that treats the problem of material parameter determination in time domain experiments usually focussing in specific material systems [3–7].

At present, the most commonly used refractive index extraction methods are based on theoretical transfer functions that assume a plane wave and neglect the etalon effect. The etalon effect can be ignored if the data are truncated, so multiple reflections are not present. This is acceptable in thick samples or scattering samples but limits the accuracy of parameter extraction on thin samples with a strong etalon effect. Furthermore, the effect of the converging beam until now has not been investigated; using a planar THz beam treatment is correct when parallel beams are used and is likely to incur an acceptably small accuracy penalty when only slow focusing beams are used. However, this may restrict the accuracy of the calculated refractive index especially when strongly converging THz beams are used, e.g., in THz imaging. There is published research calculating or characterizing the beam of a THz system [8–12] and limited experimental investigation showing the difference on the material parameter extraction when a converging beam or plane beam was used [13]. Recently, we have presented our work, which compares a traditional planar algorithm to a converging beam algorithm [14]. Furthermore, there is recent work on Gaussian beam propagation used for THz material parameter extraction without taking into account multiple reflections [15].

Here, we are going to show how algorithms based on transfer functions with different complexity can be setup. It will be described how a transfer function can be used to extract the refractive index of material and the key stages of the analysis, the fitting algorithm, and the need for phase unwrapping. Transfer functions of an increasing complexity will be shown, with and without the etalon term, using planar or converging beam. Results shown will be analyzed using the algorithms as examples to show what is the expected behavior of transfer function extraction algorithms and also to show where a complex THz extraction algorithm can be useful.

4.2 Planar Transfer Function Algorithm

4.2.1 *Experimental and Theoretical Transfer Function*

A transfer function fully characterizes the effect of the material on an arbitrary input electric field, it describes mathematically the relation of input and output signals on a system, which is linear and time-invariant. It can be written as,

$$Y(\omega) = H(\omega)X(\omega) \tag{4.1}$$

where $X(\omega)$ is the input electric field in the frequency domain, $Y(\omega)$ is the spectrum of the output electric field, and $H(\omega)$ is the transfer function of the material. Time invariance and linearity can be assumed true in a THz spectrometer. In the case of

a THz spectrometer the input should be the THz electromagnetic wave generated by the emitter and the output should be the wave after it is transmitted through the investigated material system. In practice the experimental transfer function is easily calculated when performing a THz-TDS experiment using the relation:

$$H_{\text{experiment}}(\omega, \tilde{n}) = \frac{S_{\text{sample}}(\omega)}{S_{\text{reference}}(\omega)} \quad (4.2)$$

The transfer function is the ratio of one measurement with the sample and one measurement without the sample, usually called, reference scan. As everything in the system, up to the material, and after it, is the same for both measurements, all these elements cancel out and the ratio of the reference and sample scan reveals only the transfer function of the sample.

The complex refractive index can be determined by comparing the experimental transfer function to a theoretical transfer function of the material. Both of the transfer functions are dependent on the complex refractive index. To construct the theoretical transfer function the electric field propagation through the material is modeled using the Fresnel coefficients and propagation in their usual terminology.

$$R_{ab} = \frac{\tilde{n}_a - \tilde{n}_b}{\tilde{n}_a + \tilde{n}_b} \quad (4.3)$$

$$P_a = \exp\left(-\frac{i\tilde{n}_a\omega l}{c}\right) \quad (4.4)$$

$$E(\omega) = n(\omega) \cdot P_1(\omega, l_1) \cdot T_{12} \cdot P_2(\omega, l_2) \cdot T_{21} \cdot P_1(\omega, l_1) \cdot \sum_{k=0}^{\infty} [R_{21} \cdot P_2(\omega, l_2) \cdot R_{21} \cdot P_2(\omega, l_2)]^k \quad (4.5)$$

This is the electric field of the THz wave passing through the air, which is material 1, and a bulk sample, material 2, then air again, and finally it reaches the detector antenna. Here the length of propagation in air is chosen to be l_1 from the emitter to the sample and equal from the sample to the detector. The length of propagation in the sample has been chosen to be l_2 . The sum series represents the internal reflections in the sample that can be omitted for simplified analysis. In order to extract a transfer function for the system we will have to divide this with a reference electric field, which is only propagation in air; the transfer function including the etalon effect of the sample will be

$$H_{\text{model}}(\omega, \tilde{n}) = \frac{E(\omega)_{\text{sample}}}{E(\omega)_{\text{reference}}} = \frac{T_{12} \cdot P_2(\omega, l_2) \cdot T_{21} \cdot \sum_{k=0}^{\infty} [R_{21} \cdot P_2(\omega, l_2) \cdot R_{21} \cdot P_2(\omega, l_2)]^k}{P_1(\omega, l_2)} \quad (4.6)$$

This expression is a function of the complex refractive index; therefore, we have to vary the refractive index in this expression in order to equalize it to the experimental transfer function. When the fit is correct, of course the refractive index of the material versus frequency is revealed. The Newton–Raphson method maybe the simplest method that can be used to fit, which is an iterative method for finding the roots of functions.

$$\tilde{n}_{x+1} = \tilde{n}_x - \frac{f(\tilde{n}_x)}{f'(\tilde{n}_x)} \quad (4.7)$$

The variable parameter \tilde{n} is the complex refractive index, which is estimated for each frequency component. The function used contains the difference of the natural logarithm of each transfer function, the function is calculated and the root is found for each frequency component.

$$f(\omega, \tilde{n}) = \ln(H_{\text{model}}(\omega, \tilde{n})) - \ln(H_{\text{experiment}}(\omega, \tilde{n})) \quad (4.8)$$

The method would also work with a function that would be the difference of the transfer functions. The reason why natural logarithm is considered more convenient is because it naturally derestricts the phase of the theoretical transfer function; therefore, there is no need to unwrap its phase. Except Newton–Raphson it is possible to also use minimization algorithms to extract the refractive index, the target is to find an algorithm that will scale favorably with number of points in order to give acceptable computation times. However, in general, a parameter extraction algorithm will usually complete within a minute; therefore, algorithm efficiency is rarely a problem.

In Fig. 4.1, it can be seen how a planar algorithm with internal reflections can be used to extract the refractive index of quartz and how mismatching the thickness will create ripples in the refractive index, which show that the modeled etalon is not matching the real thickness of the sample. It has to be noted that experimental errors especially related with the delay line, such as starting points or stepping errors can give similar effects as they affect the delays between the reference pulse and the delayed pulse and pulse echoes observed with transmission through the sample. In essence, these are violations of the time-invariance condition that usually stem from instabilities of temperature or laser noise. Therefore, although an extraction algorithm can be used to determine thickness it is better if thickness is measured with an alternative method to reduce uncertainty and reveal potential errors.

When deciding on an appropriate transfer function for the experiment the number of reflections should be considered. The simpler case is to completely ignore reflection terms in the theoretical transfer function; then the data should also be truncated before the first reflection, which also limits frequency resolution. The importance of etalon effects depends on the nature of the sample: transparent, thin, high index samples with polished faces will exhibit strong etalon effects. Thick, porous samples with scattering surfaces have negligible etalon effects but may show other types of complex behavior that may require use of the Kramers–Kronig relation to be analyzed.

Fig. 4.1 Real part of the refractive index for a 0.5 mm quartz sample, the extraction was made by a planar algorithm that used the transfer function of Eq.4.6 and by varying the thickness of the sample by 10 μm steps

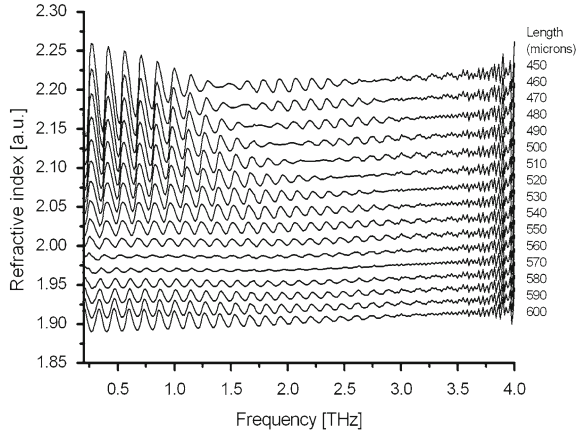
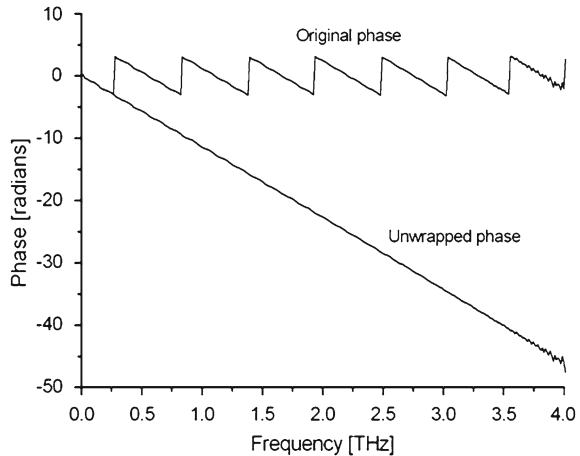


Fig. 4.2 Phase unwrapping of a transfer function



4.2.2 Phase Unwrapping

Phase unwrapping is a process, which is applied to the experimental transfer function to recover the correct phase. The reason for phase unwrapping is that the output of sinusoidal functions is ambiguous, that is, to say for a given output of a sinusoidal function there are multiple solutions. Therefore, when using the output of sinusoidal functions to calculate the phase of a transmitted EM wave, this is restricted between the range of plus and minus π . However, the real solution is a multiple number of 2π 's of the calculated phase. As an example let us assume propagation through a thickness d of material of refractive index n , so that is given by $\exp(-in\omega d/c)$; there are multiple values of n such that $n\omega d/c$ differs by 2π . In the case of the experimental transfer function the phase has a saw tooth appearance however it should vary sequentially as the frequency varies because the wavelength is becoming

smaller with respect to the sample thickness. Because we know from physics that discontinuities in phase are not due to discontinuities of the refractive index we can attribute them to phase changes of 2π . Thus, the phase unwrapping algorithm works by detecting erroneous jumps in phase, which are then corrected by a multiple of 2π 's; the results can be seen in Fig. 4.2. The phase unwrapping should begin at the peak of high SNR and extrapolate to zero frequency as this produces the most accurate results. Starting the phase unwrapping at low or high frequencies where the SNR is low usually puts an artificial bias to the calculated refractive index.

In conclusion, the Newton–Raphson method applied to the raw transfer function converges on a complex number, which is a root of a function for which there are multiple solutions; phase unwrapping allows the Newton–Raphson method to converge to the correct solution. Taking the natural logarithm of the transfer functions can separate the amplitude and phase of the theoretical transfer function into the real and imaginary terms, this improves the fitting process because it produces a linear imaginary term and ensures that the phase of at least the theoretical transfer function is no longer ambiguous.

4.3 Modeling a Converging Beam

At the focus of a THz spectrometer the wavefront is planar, but it still contains a spectrum of wavevectors; consequently, it is not a plane wave and the propagation through the sample cannot be represented by a single-phase retardation. Therefore, even if the sample is placed in the focus of the spectrometer a converging beam has to be theoretically used. Here we will build a converging focusing beam of a THz setup using a summation of plane waves propagated at different angles. This analysis of converging beam through the sample does not depend on the position of the sample.

In order to define our problem, axes are taken with the z-axis normal to the plane of the sample and y-axis parallel to the dipole transmitter axis. It is convenient to let \mathbf{x} , \mathbf{y} and \mathbf{z} to be unit vectors along the axes. The field of a transmitting dipole is expressed as an angular spectrum of plane waves and then the angles, which are used to form an image of the dipole antenna on the sample, are limited. The electric field of a transmitting dipole can be derived [16] from a Hertz vector along \mathbf{y} using

$$\mathbf{E} = \nabla \nabla \cdot \boldsymbol{\Pi} + \mathbf{k}^2 \boldsymbol{\Pi} \quad (4.9)$$

and $\boldsymbol{\Pi}$ has only a y component

$$\boldsymbol{\Pi}_y = \frac{e^{ikr}}{r} \quad (4.10)$$

Specifically,

$$E_x = \frac{\partial^2 \Pi}{\partial x \partial y}, \quad E_y = \left(k^2 \Pi + \frac{\partial^2 \Pi}{\partial y^2} \right), \quad E_z = \frac{\partial^2 \Pi}{\partial y \partial z} \quad (4.11)$$

The spherically symmetric quantity Π_y can be written

$$\Pi = \frac{e^{ikr}}{r} = \frac{i}{2\pi} \int_{-\infty}^{\infty} \int_{-\infty}^{\infty} \frac{e^{i\mathbf{k}\cdot\mathbf{r}}}{\sqrt{k^2 - k_1^2 - k_2^2}} dk_1 dk_2 \quad (4.12)$$

where $k_1^2 + k_2^2 + k_3^2 = k^2 = \omega^2/c^2$, where \mathbf{k}_1 , \mathbf{k}_2 and \mathbf{k}_3 are the orthogonal components of the wavevector \mathbf{k} , and \mathbf{k}_3 is the propagation direction.

4.3.1 Angular Weighting Function

We will introduce a weighting function $W(k_1, k_2)$ to account for the fact that waves with only a limited range of directions contribute to the image. This will take into account the effect of the parabolic lenses used in a typical Terahertz experiment. The simplest model would be a sharp cutoff at some angle; however, this would create large oscillations in the field along the z -axis, which may complicate the results. These oscillations can be thought of as Fresnel diffraction; as one moves along the axis different numbers of Fresnel zones are included in the angular spectrum. It is clear that the easiest case to analyze would be a gentle cut-off and an obvious model is a Gaussian. The beam out of a silicon lens can be approximated with a Gaussian as shown in [17]. In neither case can the necessary integral be done analytically but we know that if we use a smooth (Gaussian-like) cutoff in the angular spectrum this should produce a smooth focus without diffraction oscillations. Of course, in most experiments the parabolic lens is going to most likely impose a cutoff value for the angles of the experiment. This cutoff is going to be more important for low frequencies where the diffraction can make the spread of angles emitted by the antenna greater than the acceptance angle of the parabolic. Therefore, it is also important that we match the dependence of the angular spread as a function of frequency. Although it is possible to characterize or simulate the beam profile of a THz system [8–11] it is quite impractical as it is quite likely that small changes such as a new antenna or different lenses would make a significant and difficult to predict change. Therefore, the easiest way to find the appropriate weighting function for a measurement is to try different functions and different frequency dependencies and choose the one that better fits our data. Of course the type of parabolics, the gap of the antennas, the existence, or not of a silicon lens, can give significant insight on the parameters that should be chosen.

4.3.2 Transmission of the Converging Beam Through a Slab

The electric field components are obtained by doing the differentiations set out above in Eq. 4.11, this introduces factors of

$$\mathbf{E}(k_1, k_2) = \left(\frac{k_1 k_2}{k^2}, -\frac{(k^2 - k_2^2)}{k^2}, \frac{k_2 k_3}{k^2} \right) \quad (4.13)$$

This shows that $\mathbf{k} \cdot \mathbf{E} = 0$ so \mathbf{E} is perpendicular to \mathbf{k} as is required for a transverse wave. \mathbf{E} lies in the plane of \mathbf{k} and \mathbf{y} , also,

$$|E|^2 = 1 - k_2^2/k^2 = 1 - \cos^2 \alpha \quad (4.14)$$

where α is the angle between \mathbf{k} and y -axis, so the magnitude of E is $\sin \alpha$ as required for dipole radiation. To work out the reflection and transmission coefficients this electric field must be resolved into components \mathbf{E}_{\parallel} in the plane of incidence and \mathbf{E}_{\perp} normal to the plane of incidence. The plane of incidence is that containing k and z so the vector $\mathbf{k} \times \mathbf{z} = (k_2, -k_1, 0)$ is perpendicular to it and a unit vector in this direction is $\mathbf{p} = (k_2/\bar{k}, -k_1/\bar{k}, 0)$ where $\bar{k}^2 = k_1^2 + k_2^2$. The perpendicular component of \mathbf{E} normalized is therefore

$$\mathbf{E}_{\perp} = (\mathbf{E} \cdot \mathbf{p})\mathbf{p} = \frac{k_1}{\bar{k}}\mathbf{p} = \left(\frac{k_1 k_2}{\bar{k}^2}, -\frac{k_1^2}{\bar{k}^2}, 0 \right) \quad (4.15)$$

and the parallel component can be computed as

$$\mathbf{E}_{\parallel} = \mathbf{E} - \mathbf{E}_{\perp} = \left(-\frac{k_1 k_2 k_3^2}{k^2 \bar{k}^2}, -\frac{k_2^2 k_3^2}{k^2 \bar{k}^2}, \frac{k_2 k_3}{k^2} \right) \quad (4.16)$$

At the first surface of the sample the angle of incidence is given by $\cos \theta_1 = k_3/k$ or $\sin \theta_1 = \bar{k}/k$ and the angle of the transmitted wave θ_2 by $n_1 \sin \theta_1 = n_2 \sin \theta_2$. The path length in the sample is $D/\cos \theta_2$ where D is the sample thickness and this introduces a phase shift represented by multiplying the electric fields by $P_2 = \exp(-ikD(n_2 \cos \theta_2 - n_1 \cos \theta_1))$.

The reflection and transmission coefficients are:

$$\begin{aligned} r_{\perp} &= \frac{n_i \cos \theta_i - n_t \cos \theta_t}{n_i \cos \theta_i + n_t \cos \theta_t} & r_{\parallel} &= \frac{n_t \cos \theta_i - n_i \cos \theta_t}{n_i \cos \theta_t + n_t \cos \theta_i} \\ t_{\perp} &= \frac{2n_i \cos \theta_i}{n_i \cos \theta_i + n_t \cos \theta_t} & t_{\parallel} &= \frac{2n_i \cos \theta_i}{n_i \cos \theta_t + n_t \cos \theta_i} \end{aligned} \quad (4.17)$$

where n_i and n_t are the refractive indices and θ_i and θ_t are the angles of incidence and transmission appropriate for the interface involved.

The direct transmission through the sample then involves, transmission through the first interface, propagation to the second interface and transmission through the second interface, which multiplies the field by $T_2 P_2 T_1$ where, $T_1 = t(\theta_1, \theta_2)$ and $T_2 = t(\theta_2, \theta_1)$.

Transmission with one pair of internal produces a factor of $T_2 (P_2^2 R^2) P_2 T_1$. For a thin sample the above series can be summed to yield an overall factor $F = T_2 [1 - P_2^2 R^2]^{-1} (P_2 / P_1) T_1$.

The electric field of the emerging wave is then:

$$\mathbf{E} = F_{\parallel} \mathbf{E}_{\parallel} + F_{\perp} \mathbf{E}_{\perp} \quad (4.18)$$

The emerging waves are focused on the detector. The focusing lens or mirror is a device that introduces phase delays so that all the waves arrive at the detector simultaneously. The signal at the detector is therefore obtained by summing over all k_1 and k_2 . As mentioned above we will introduce a weighting function $W(k_1, k_2)$ at least to cutoff the waves traveling at large angles to the axis. The final result is that the detected signal is

$$\int \int \frac{W(k_1, k_2)}{k_3} (F_{\parallel}(k_3) \mathbf{E}_{\parallel} + F_{\perp}(k_3) \mathbf{E}_{\perp}) dk_1 dk_2 \quad (4.19)$$

The x and z components are antisymmetric in either k_1 or k_2 and so the integrals vanish and, as expected, there is only a y component at the focus. If we convert to polar coordinates $\bar{k} = k \sin \theta$ and $k_3 = k \cos \theta$ the final result is

$$- \pi \int_0^{\theta_{\max}} W(\theta) [\cos^2 \theta F_{\parallel}(\theta) + F_{\perp}(\theta)] \sin \theta d\theta \quad (4.20)$$

The upper limit of ∞ is irrelevant because the weight $W(\bar{k})$ is intended to reduce the integrand to zero at some finite \bar{k} . The reference signal can be obtained by writing $n_1 = n_2 = 1$ when F_{\parallel} and F_{\perp} are both equal to unity. The transfer function is therefore obtained by dividing Eq. 4.20 with,

$$\int_0^{\theta_{\max}} W(\theta) (1 + \cos^2 \theta) \sin \theta d\theta \quad (4.21)$$

These values must be compared with the transfer function for a plane wave, which in this notation is just $F_{\perp}(0)$. The calculation of the transmission of the converging beam through the sample requires the numerical evaluation of these integrals during the fitting process; however, the integrands are smooth and this is not a significant computational burden.

4.3.3 Phase Unwrapping in a Converging Algorithm

In the converging beam case, it is difficult to perform phase unwrapping because each wave for a single frequency undergoes a different phase shift. Whereas in the case of the planar beam we could derive the logarithm of the theoretical transfer function and thus extract the phase; we cannot do the same in the converging beam. Therefore, the converging beam transfer function is fitted to the experimental amplitude and raw phase. To improve the extraction process we use a plane wave algorithm first to find the approximate value for the refractive index, which is then set as the initial refractive index value for the converging beam extraction. The fitting process used again is the Newton–Raphson method.

4.3.4 Simulated Data

Simulated data were produced in order to show how the converging beam algorithm works. To produce simulated converging beam data a reference scan from a converging beam setup was used. The converging beam code was applied to this reference scan with a known angular distribution, refractive index and thickness. The simulated data used in Fig. 4.3 had an angular distribution of $\pm 30^\circ$ for all frequencies, refractive index of $2.0 - 0.005i$, and thickness of 2 mm. Figure 4.3 shows the converging beam algorithm extracting the correct complex refractive index. Figure 4.4 shows the plane wave extraction on the same data, there are oscillations present on the complex refractive index, which are consistent with the sample thickness. The plane wave algorithm fails to remove these etalon oscillations, which originate from the amplitude of the transfer function.

Figure 4.5 shows the converging beam extraction on the same data; however, the extraction parameters use an angular distribution of $\pm 25^\circ$ where as the data were produced with an angular spectrum of $\pm 30^\circ$. The complex refractive index has oscillations similar to the plane wave extraction. The oscillations are due to the incorrect calculation of the phase and amplitude, which is caused by the difference between the actual length of propagation in the data and the assumed length of propagation for the extraction. The amplitude of the oscillations in the complex refractive index decreases with increasing frequency because the number of wavelengths present in the sample increases; therefore, the total effect of these wavelengths has a smaller effect on the error. The simulated data show that the plane wave approximation is theoretically inadequate for simulated converging beams and that in order to correctly extract the converging beam data the correct angular distribution must be used.

4.4 Experimental Data

Figure 4.6 shows the converging beam algorithm processed on data from a THz-TDS setup for a 2 mm crystalline quartz window. The setup had a converging geometry (f:2) and the sample was placed in the beam focus. The setup used photoconductive

Fig. 4.3 The resultant complex refractive index extracted using converging algorithm for simulated converging beam data. The simulated data had an angular distribution of $\pm 30^\circ$, refractive index $2.0 - 0.005i$ and thickness of 2 mm

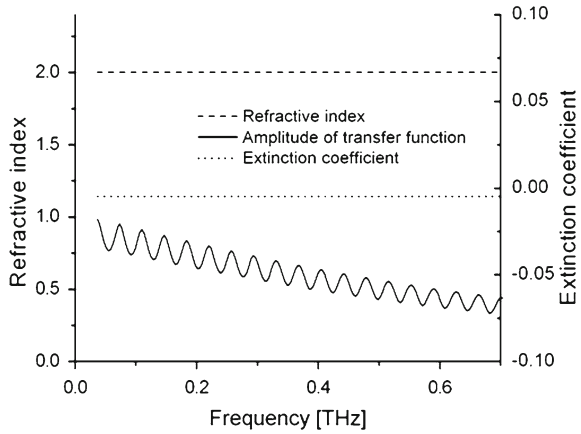
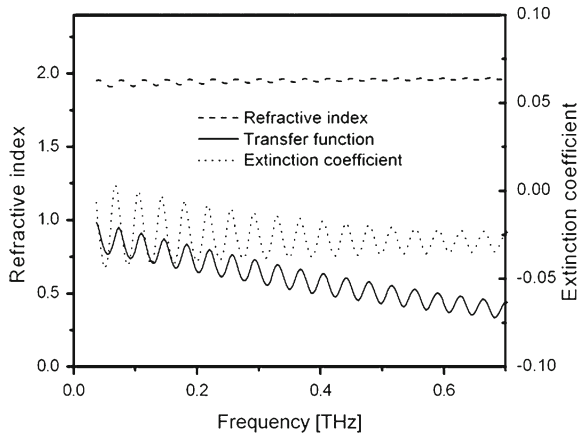


Fig. 4.4 The resultant complex refractive index extracted using plane wave algorithm for simulated converging beam data. The simulated data had an angular distribution of $\pm 30^\circ$, refractive index $2.0 - 0.005i$ and thickness of 2 mm



emitter and receiver with Si lenses. For these results we have used a square weighting function with smooth edges that vary its width to match our sample better. The angular spread used starts from the planar option and increased in small steps. The angular spread also varies with frequency using an $1/f$ dependence. There is also a hard cutoff, which restricts the angle to 0.35 radians and is significant at low frequencies (<500 GHz). Figure 4.6 shows how the converging beam algorithm extracts the complex refractive index of quartz and that when using different angular spectra, there is difference in the amplitude of the etalon oscillations, which can be used to judge how good is the match with the experimental conditions. In a converging beam geometry such as the one used here, the THz beam is undergoing in average higher phase retardation than the nominal thickness of the sample. This difference is depending on the spread of angles in the experiment. This results in that using the planar algorithm the thickness is slightly underestimated and therefore the refractive index will be slightly overestimated. This can also be seen in Fig. 4.6.

Fig. 4.5 Extraction using converging beam algorithm with a mismatch of angle $\pm 25^\circ$. The simulated data had an angular distribution of $\pm 30^\circ$, refractive index $2.0 - 0.005i$, and thickness of 2 mm

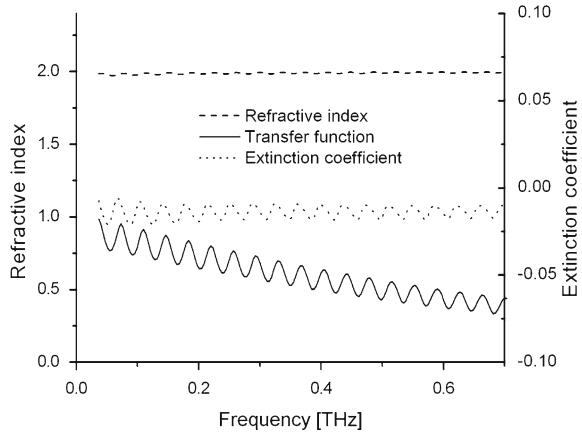
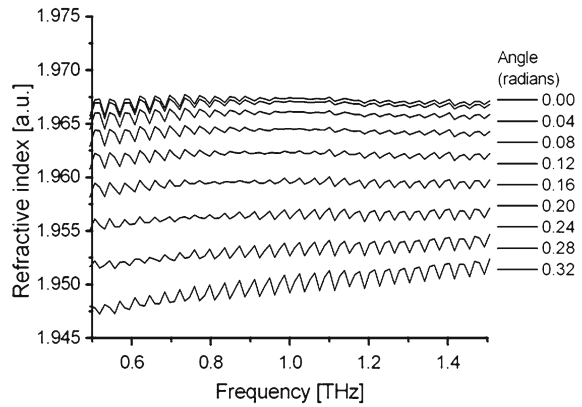


Fig. 4.6 The resultant complex refractive index extracted for a 2 mm quartz sample placed at the focus of the beam in THz-TDS setup



The results shown in Fig. 4.6 were taken in a setup with a slow focusing lens system. Still, there are improvements over the plane wave algorithm (0 radians line) if we use as a criterion the refractive index oscillations, which we know is an artifact of the data extraction process. However, comparison between the algorithms can be quite difficult to quantify objectively; the refractive index oscillations in the planar case are approximately $2 \cdot 10^{-3}$, which for a lot of purposes may not present a problem. What all this analysis shows is that the extraction algorithm should be chosen according to the required accuracy and taking into account the complexity of the algorithm. There are a lot of options in building an extraction algorithm based on a transfer function and a lot of decisions in which the scenario fits best with each case.

4.5 Conclusions

We have described in this chapter how a transfer function can be used to extract the refractive index of materials investigated in a THz-TDS and the key stages of the analysis such as the fitting algorithm and the need for phase unwrapping. Transfer functions of an increasing complexity have been shown; with and without the etalon term, using planar or converging beam. The etalon effect can be ignored if the data are truncated so multiple reflections are not present. This is generally acceptable in thick samples or scattering samples but limits the accuracy of parameter extraction on thin samples with a strong etalon effect. Also, using a planar THz beam treatment is correct when parallel beams are used and is likely to incur an acceptably small accuracy penalty when only slow focusing beams are used. However, this may restrict the accuracy of the calculated refractive index especially when strongly converging THz beams are used, e.g., in THz imaging.

We have shown that refractive index oscillations present in analyzed THz data are an artifact of the data extraction process and show a mismatch between the experimental data and the theoretical transfer function. The extracted refractive indices in Fig. 4.1 show how minimization of the refractive index oscillations can help to identify the thickness of a sample. Similarly, in Fig. 4.6 we have analyzed with a converging beam algorithm, data that were taken in a setup with a slow focusing lens system, and we have used the minimization of refractive index oscillations to identify the correct angular profile for extraction. However, concluding, we should stretch that almost any mismatch between the experiment and the theoretical transfer function will result to oscillations in the refractive index, e.g., delay line errors such as time offset between reference and sample scan or changing sampling interval; tilted sample orientation; wrong phase interpolation, etc. Therefore, someone has to be very careful to draw conclusions only based on the refractive index oscillations as thickness or angular profile may mask other experimental errors. The thickness of the sample or the angular profile of the THz-TDS should be measured experimentally in order for the results of an extraction algorithm to be verified.

Therefore, there are a lot of options in building a transfer function extraction algorithm and a lot of decisions in which scenario fits best with each case. Comparison between algorithms can be quite difficult to quantify objectively; the refractive index oscillations in the planar case are approximately $2 \cdot 10^{-3}$, which for a lot of purposes may not present a problem. This shows that the extraction algorithm should be chosen according to the required accuracy and taking into account the complexity of the algorithm.

References

1. L. Duvillaret, F. Garet, J. Coutaz, *IEEE J. Sel. Top. Quant.* **2**, 739–746 (1996)
2. L. Duvillaret, F. Garet, J. Coutaz, *Appl. Opt.* **38**, (1999)
3. T. Dorney, R. Baraniuk, D. Mittleman, *J. Opt. Soc. Am. A* **18**, 1562–1571 (2001)

4. L. Duvillearet, F. Garet, J. Roux, J. Coutaz, *IEEE J. Sel. Top. Quant.* **7**, 615–623 (2001)
5. E.P.J. Parrott, J.A. Zeitler, L.F. Gladden, *Opt. Lett.* **34**(23), 3722–3724 (2009)
6. E.P.J. Parrott, J.A. Zeitler, L.F. Gladden, S.N. Taraskin, S.R. Elliott, *J. Non-Cryst. Solids* **355**(37–42), 1824–1827 (2009)
7. W. Withayachumnankul, B. Ferguson, T. Rainsford, S. Mickan, D. Abbott, *Electron. Lett.* **41**, 14 (2005)
8. A. Bitzer, H. Heim, M. Walther, *IEEE J. Sel. Top. Quant.* **14**(2), 476–481 (2008)
9. A. Bitzer, M. Walther, A. Kern, S. Gorenflo, H. Helm, *Appl. Phys. Lett.* **90**(7) (2007)
10. M.T. Reiten, S.A. Harmon, R.A. Cheville, *J. Opt. Soc. Am. B-Opt. Phys.* **20**(10), 2215–2225 (2003)
11. Z.P. Jiang, X.C. Zhang, *Opt. Express* **5**(11), 243–248 (1999)
12. J.W. Bowen, G.C. Walker, S. Hadjiloucas, E. Berry, *Conference Digest of the 2004 Joint 29th International Conference on Infrared and Millimeter Waves and 12th International Conference on Terahertz Electronics*, vol. 842, pp. 551–552 (2004)
13. M.R. Stringer, M. Naftaly, N. Maragkos, R.E. Miles, E. Linfield, A.G. Davies, *IRMMW-THz2005: The Joint 30th International Conference on Infrared and Millimeter Waves and 13th International Conference on Terahertz Electronics*, vols. 1 and 2, 421–422, 660 (2005)
14. A.L. Chung, Z. Mihoubi, G.J. Daniell, A.H. Quarterman, K.G. Wilcox, H.E. Beere, D.A. Ritchie, A.C. Tropper, V. Apostolopoulos, *Presented at the 2010 35th International Conference on Infrared, Millimeter, and Terahertz Waves (IRMMW-THz 2010)*
15. P. Kuzel, H. Nemeč, F. Kadlec, C. Kadlec, *Opt. Express* **18**(15), 15338–15348 (2010)
16. J.A. Stratton, *Electromagnetic Theory* (McGraw-Hill, New York, 1941)
17. P.U. Jepsen, S.R. Keiding, *Opt. Lett.* **20**(8), 807–809 (1995)

Chapter 5

Terahertz Scattering

L. M. Zurk and S. Schecklman

5.1 Introduction

Terahertz (THz) Time Domain Spectroscopy (TDS) measurements have the unique ability to detect both the amplitude and phase of the electric field, simultaneously. This eliminates complications introduced by Kramers–Kronig relations typically used in near-infrared spectroscopy. Many materials of interest contain resonant features in their refractive indices in the far-infrared (THz) spectrum, while their packaging materials are generally transparent. Thus, an important application for THz TDS is the ability to see inside packaging materials and detect the material features of their contents. Such applications are promising for security screening (concealed drugs, explosives, etc.) in post offices and airports as well as for non-destructive evaluation (NDE) of products on an assembly line or tissue damage due to burns or cancer [1–6].

The advancement of these technologies is complicated, however, because the wavelength of THz waves are on the same order as geometric features of the samples [7–10]. For example, spectral material features may be obscured by things like a transparent covering layer on the order of 100 microns (for example, the thickness of a piece of paper), a rough surface on the order of 10's of microns (sandpaper or fingerprint impressions), or scattering from grains or air bubbles on the order of 10's of microns. In addition, many materials of interest have relatively high absorption at THz frequencies. In particular, THz waves have skin depths of only a few millimeters in objects that contain high water content, such as the human body.

While carefully prepared samples may be studied in a controlled laboratory environment, it is expected that most practical applications of THz technology will be restricted to a reflection geometry. Measurements will probably also require some

L. M. Zurk (✉) · S. Schecklman
Electrical and Computer Engineering Department,
Portland State University,
Portland, OR, USA
e-mail: zurkl@cecs.pdx.edu

signal processing to correct for the frequency-dependent geometric scattering from layers, rough surfaces, and particles. The effects of these scattering phenomena are briefly introduced in this chapter.

5.2 Terahertz Reflection and Transmission from Samples with Smooth Planar Interfaces

This section addresses scattering phenomena that may occur at an interface between two media. Transmission and reflection coefficients are introduced to define the field above and below the interface. The etalon effect is briefly considered for a thin layer of material. Finally, scattering from random media is introduced and methods to detect material features from rough surface scattering are discussed.

5.2.1 Reflection and Transmission at a Single Interface

This section will consider the simplest transmission and reflection configurations, such as might be encountered while using prepared samples in a laboratory setting. Figure 5.1a shows a horizontally polarized plane wave incident on a smooth interface between two infinite half-spaces. The incident field is given by,

$$\bar{E}_i(f, \bar{k}_i) = \hat{y}E_0 e^{ixk_{xi} - izk_{zi}} e^{-i2\pi ft}, \quad (5.1)$$

where f is the frequency (in Hz) and t is time. In the remainder of this chapter, time-dependence will be suppressed. In (5.1), $k_{xi} = k \sin \theta_i$ and $k_{zi} = k \cos \theta_i$ are the horizontal and vertical components of the incident wave vector, $\bar{k}_i = k_{xi}\hat{x} + k_{zi}\hat{z}$ and θ_i is the incident angle. Throughout this chapter, $k = 2\pi/\lambda$ will be used to represent the wavenumber, where $\lambda = c/f$ is the wavelength and $c = 3 \times 10^8$ m/s is the speed of light in free space. This standard convention in electromagnetics is different from the terminology sometimes used in spectroscopy where “wavenumber” is often defined as $1/\lambda$. We note that the notation in this chapter is different from other chapters in this text where wavenumber is represented as K , and k is used for the extinction coefficient.

For infinite planar surfaces the reflected and transmitted fields, \bar{E}_r and \bar{E}_t , are given by the horizontal Fresnel reflection and transmission coefficients,

$$R_{01}^h = \frac{N_0 \cos \theta_i - N_1 \cos \theta_t}{N_0 \cos \theta_i + N_1 \cos \theta_t}, \quad (5.2)$$

$$T_{01}^h = 1 + R_{01}^h. \quad (5.3)$$

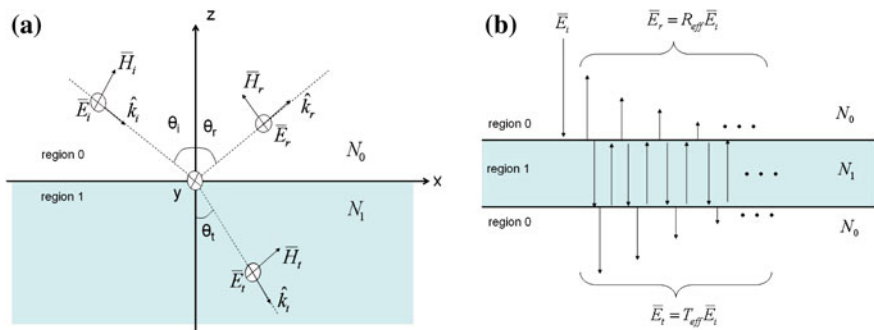


Fig. 5.1 Panel A Plane of incidence for reflection and transmission at a smooth interface between media 0 (free space) and 1. The horizontally polarized incident field, \vec{E}_i is reflected at the specular angle, $\theta_r = \theta_i$. The refractive index, N_1 , may be dependent on the THz frequency. Note, the incident, transmitted and reflected electric fields and the y-axis are illustrated as vectors pointing into the page. Panel B Reflected and transmitted pulses from a single layer of material for normal incidence, $\theta_r = \theta_i = 0$

In (5.2) and (5.3), R_{01} is the reflection coefficient for a field reflected from medium 1 into medium 0, T_{01} is the transmission coefficient for a field transmitted from medium 0 into medium 1, and θ_t is the refracted angle inside medium 1. The complex index of refraction, N_1 , is generally frequency-dependent in the THz portion of the spectrum so that

$$N(f) = \sqrt{\epsilon(f)\mu}, \quad (5.4)$$

where

$$\epsilon(f) = \epsilon'(f) + i\epsilon''(f). \quad (5.5)$$

The real part, $\epsilon'(f)$, and imaginary part, $\epsilon''(f)$, of the complex relative permittivity in (5.5) often contain unique spectral information which can be used for material detection and identification. The relative permeability, μ , of non-magnetic materials is 1. Figure 5.2 shows the complex permittivity for α -lactose monohydrate, calculated from the Lorentz parameters. It has been shown that the 1st derivative of the reflection coefficient magnitude or the 2nd derivative of the reflection coefficient phase may yield a similar signature to the imaginary part of the permittivity when $\epsilon' \gg \epsilon''$ [11–13].

The primary objective of THz spectroscopy is to gain information about a material from either the transmitted or reflected fields. For smooth surfaces, the reflected angle is called the “specular” angle and is given by the law of reflection, $\theta_r = \theta_i$. In general, the extraction of N_1 from (5.2) is complicated by the dependence of θ_t on N_1 due to Snell’s Law of Refraction [14]. The process of extracting N_1 is greatly simplified if the angle of incidence is chosen to be normal. The transmitted field is preferred over the reflected field for THz spectroscopy, because it is more heavily influenced

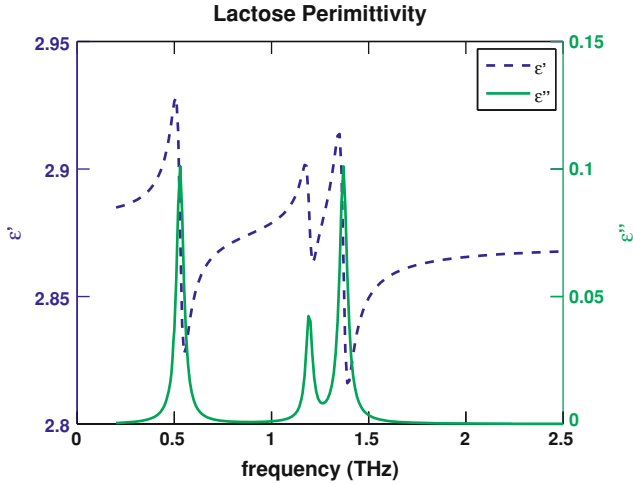


Fig. 5.2 Relative permittivity for alpha-lactose-monohydrate calculated from the Lorentz parameters. The imaginary part shows peaks near 0.54, 1.2, and 1.4 THz which may be used for material identification

by the absorption features and because most materials of interest have relatively low reflectivity.

It is difficult to accurately account for the transfer functions of all of the individual components in a THz TDS system. This problem is by-passed by making an additional *reference* measurement without the sample material in place. Thus, normalizing the sample measurement by the reference measurement removes the unknowns and isolates the material parameters in a process called deconvolution [14]. Thus, for a given geometry with fixed incident and transmitted or reflected angles, the electric field of the sample and reference THz pulses are measured as time-domain waveforms and the corresponding complex frequency spectra, $\overline{E}_{\text{sample}}(f)$ and $\overline{E}_{\text{ref}}(f)$, are then computed using numerical Fast Fourier Transforms (FFT's). Finally, the ratio gives the deconvolved sample spectrum,

$$E_{\text{deconv}}(f) = \frac{E_{\text{sample}}(f)}{E_{\text{ref}}(f)}. \quad (5.6)$$

For transmission measurements the reference is the electric field with the source and receiver in the same position, but without a sample in the propagation path. The reference for reflection measurements is the specular reflection from a mirror. Although it is more practical, the reflection configuration presents a number of challenges. First, it is difficult to align the emitter, sample, and detector precisely at the specular angle to capture the reflected signal. Similarly, the deconvolution operation requires the mirror to be placed at exactly the same location as the sample. For example, if the mirror is misplaced by only a few hundred microns there may be several wavelengths difference in the propagation path between the sample and reference

measurements. This subtle difference can result in a large error in the phase and ultimately the extracted material properties. In addition, it is more difficult to extract the material properties from reflection measurements because the calculation of θ_t requires a-priori knowledge of the material's index of refraction. Finally, an even more important challenge for reflection spectroscopy is that most materials of interest have a relatively small reflection coefficient (on the order of 10 percent) making it difficult to achieve the signal to noise ratio (SNR) needed to identify spectral features [15]. For these reasons it is expected that the detection and identification procedures used in security or medical screening applications will rely on comparison of reflection spectra of the in situ samples with absorption spectra from a library of known materials, derived from laboratory measurements made in transmission mode.

5.2.2 Reflection and Transmission from a Layer

Transmission through thin pellet samples in a laboratory environment will generally be used to extract material properties, which can be recorded in a database or library of known material signatures. Samples are prepared by pressing powder in a hydraulic press to create a pellet with smooth level surfaces on each side. However, interference between the internal reflections within the pellet (etalon effect) may still obscure spectral features of the sample material. This section will briefly describe the complexities associated with transmission at normal incidence through a single pellet with just two interfaces as illustrated in Fig. 5.1b.

For an electric field at normal incidence, the effective reflection, and transmission coefficients for a layer of thickness, d , can be written as [16],

$$R_{\text{eff}} = \frac{R_{01} + R_{10} \exp(i2k_1d)}{1 + R_{01}R_{10} \exp(i2k_1d)}, \quad (5.7)$$

and

$$T_{\text{eff}} = \frac{T_{01}T_{10} \exp(ik_1d)}{1 + R_{01}R_{10} \exp(i2k_1d)}, \quad (5.8)$$

where $k_1 = 2\pi f/N_1c$ is the wavenumber inside region 1. Extraction of the refractive index from a thin sample as illustrated in Fig. 5.1b will generally require (5.7) or (5.8) to be solved using numerical methods. If the sample is thick enough so that only the first transmitted pulse can be detected, then R_{10} in the denominator of T_{eff} goes to zero, and N_1 can be extracted more easily using the methods in the literature [14]. This is the most desirable scenario, but is difficult to achieve in practice because thin samples can become brittle and fall apart. Therefore, the sample material is often mixed with a transparent binding material (such as polyethylene or Teflon). The grain sizes of the sample and binding material must be small enough to avoid scattering within the sample. The samples must also be pressed with sufficient pressure to

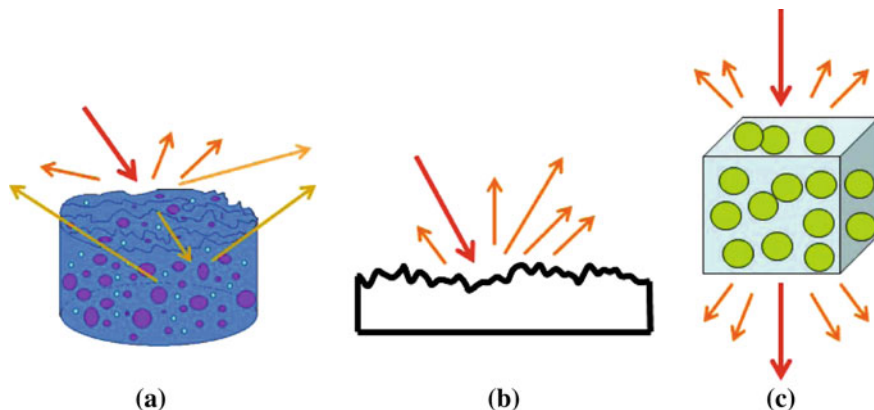


Fig. 5.3 Most materials of interest for THz TDS must be modeled as random media (*panel A*). The scattered field above random rough surfaces (*panel B*) will be discussed in Sect. 5.3.1. Scattering from inhomogeneities randomly located inside a medium (*panel C*) will be discussed in the second half of this chapter

reduce the size of air voids within the sample. Volume scattering will be considered in the second part of this chapter.

In more practical applications of THz technology, accounting for the etalon effect in the layers above a material of interest (clothing, packaging material, etc.) is imperative. This has been done using optimization routines within an inverse model for a single layer [17].

5.3 Random Media

As discussed above, THz TDS may be used to extract spectroscopic information from homogeneous materials with smooth surfaces. However, most naturally occurring materials will contain randomly distributed particles and/or surface protrusions or indentations which are on the same order as THz wavelengths. This is illustrated in panel A of Fig. 5.3. Scattering from random rough surfaces may dominate over volume scattering within materials that are opaque (small skin depths) as shown in (Fig. 5.3b), and discussed in the following section. Scattering from inhomogeneities randomly distributed throughout materials with smooth surfaces (Fig. 5.3c) will be discussed in the second half of this chapter.

For either case the scattered field will be the sum of the mean field and a fluctuating field,

$$\bar{E}_s(f, \bar{k}_i, \bar{k}_s) = \bar{E}_m(f, \bar{k}_i, \bar{k}_s) + \bar{E}_f(f, \bar{k}_i, \bar{k}_s), \quad (5.9)$$

where \bar{k}_s is the scattered wave vector in the θ_s direction, and the expected value of the fluctuating field is equal to zero, $\langle \bar{E}_f(f, \bar{k}_i, \bar{k}_s) \rangle = 0$. It is important to note that since the fluctuating part of the field is (by definition) phase incoherent the phase structure corresponding to the material spectrum is contained solely within the mean (or coherent) field component. Although the incoherent field averages to zero, the incoherent power does not, and may therefore be used to obtain spectral information.

5.3.1 Terahertz Reflection from Random Rough Surfaces

Since most materials are opaque at THz frequencies, it is expected that more practical detection systems will need to operate in a reflection configuration. Furthermore, many common surfaces will have roughness on the order of THz wavelengths (hundreds of microns), and cause the spectroscopic signatures to be altered by scattering. Since the surface of most materials will have some random roughness, it will be necessary to average a number of measurements in order to characterize a typical sample material. In fact, dozens or possibly hundreds of sample measurements may be required. The complexity of the rough surface scattering physics motivates the development of mathematical models and computer simulations that can accurately and efficiently provide these answers.

A rough surface can be considered as an ergodic random process where the height at any given location is a random variable, ζ . It is reasonable to assume that for most random rough surfaces all of the heights will have the same probability distribution and the same mean value. For a zero-mean surface the root-mean-square (rms) height is given by

$$h = \sqrt{\langle \zeta^2(x, y) \rangle}. \quad (5.10)$$

Along a single line in the y-dimension, the covariance between two points $\zeta(x_1)$ and $\zeta(x_2)$, on a random rough surface is

$$\langle \zeta(x_1)\zeta(x_2) \rangle = h^2 C(x_1 - x_2), \quad (5.11)$$

where $C(x_1 - x_2)$ is the autocorrelation function. The correlation length is defined as the horizontal distance, l_c , that causes the autocorrelation function to decrease by $1/e$, where $e = 2.7183$.

The strength of a wave reflected from a rough surface will depend on three factors: material properties, viewing geometry (incident and detection angles), and rough surface statistics. The impact of the surface on the scattering depends on the surface height relative to a wavelength. As wavelength decreases (with increasing frequency) a surface will appear more rough to the incident plane wave, resulting in more diffuse scattering. According to the Fraunhofer Criterion a surface can be considered rough

if it causes a $\frac{\pi}{8}$ phase shift as compared to a smooth surface [18, 19]. Thus, a surface is “rough” if the rms height, h , satisfies the inequality

$$h \geq \frac{\lambda}{32 \cos \theta_i}. \quad (5.12)$$

The scattered field, \bar{E}_s , from a horizontally polarized wave incident on a rough surface will have both horizontal and vertical components. The horizontal component is given by [20],

$$\bar{E}_s^h(\bar{r}) = \hat{y} \left[\frac{ike^{ikr}}{4\pi r} \right] \int_{S'} dS' \left[\hat{y} \cdot \left(\hat{k}_s \times [\hat{n} \times \bar{E}(\bar{r}')] + \eta [\hat{n} \times \bar{H}(\bar{r}')] \right) e^{-i\bar{k}_s \cdot \bar{r}'} \right], \quad (5.13)$$

where it has been assumed that the detector is in the plane of incidence. In (5.13), r is the distance from the origin to the observation point, and \bar{r}' is a vector from the origin to a patch of area, dS' , on the surface, S' . \bar{E} and \bar{H} are the electric and magnetic fields, respectively, on the surface. The surface normal, \hat{n} , points outward from the surface, and the impedance of the (non-magnetic) surface material is $\eta \approx 377/\sqrt{\epsilon_1}$ ohms, where ϵ_1 is the relative permittivity of the surface material.

Although (5.13) is exact, the integral is difficult to solve for random rough surfaces. The integration may be solved using numerical techniques, such as Method of Moments (MoM) [21] or Finite Difference Time Domain (FDTD) [22, 23].

At a distance, r , from a scatterer, the differential cross-section, σ_d , gives the relative amount of scattered power

$$\sigma_d(f, \bar{k}_i, \bar{k}_s) = 4\pi r^2 \frac{|\bar{E}_s(f, \bar{k}_i, \bar{k}_s)|^2}{|\bar{E}_i(f, \bar{k}_i, \bar{k}_s)|^2} d\Omega_s, \quad (5.14)$$

with units of area. In (5.14), $d\Omega_s = \sin \theta_s d\theta_s d\phi_s$ is the differential solid angle in the scattered direction, \hat{k}_s . Note, this is similar to THz TDS deconvolution as defined in (5.6), where the normalized intensity is

$$I_{\text{deconv}}(f, \bar{k}_i, \bar{k}_s) = \frac{|\bar{E}_s(f, \bar{k}_i, \bar{k}_s)|^2}{|\bar{E}_{\text{ref}}(f, \bar{k}_i, \bar{k}_s = \text{specular})|^2}. \quad (5.15)$$

Thus, THz TDS intensity measurements will be proportional to differential cross-section calculations.

The dimensions of rough surfaces are generally larger than the incident beam. Therefore, the differential cross-section is often normalized by the incident beam cross-section to give the (dimensionless) scattering coefficient,

$$\gamma(f, \bar{k}_i, \bar{k}_s) = \frac{\sigma_d(f, \bar{k}_i, \bar{k}_s)}{A_0 \cos \theta_i}, \quad (5.16)$$

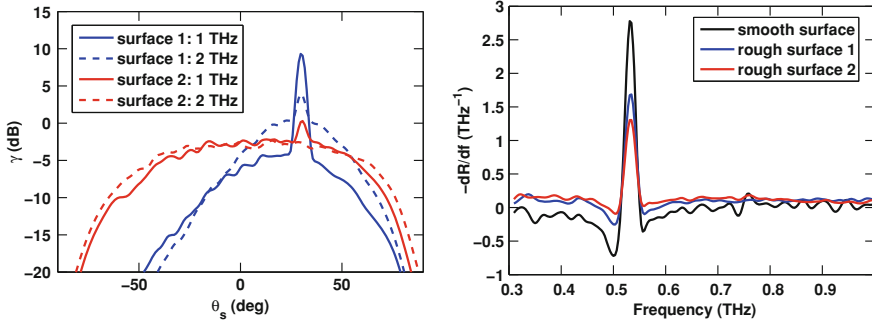


Fig. 5.4 *Panel A* Angular distribution of the scattering coefficient above two random rough conductive surfaces at two frequencies, simulated with the MoM. At each frequency the rougher surface (surface 2) diverts more energy away from the specular angle. For both surfaces, more scattering occurs at the higher frequency. *Panel B* Spectral derivatives for specular reflection measured [24] by a THz TDS system from a smooth lactose surface compared with lactose with rough surface 1 and 2, as in *panel A*. The peak near 0.54 THz corresponds to the peak in the extinction coefficient in Fig. 5.2

where A_0 is the area of the rough surface projected onto the x-y plane. Figure 5.4a shows the scattering coefficients for two rough conductive surfaces at two frequencies. The scattering coefficients were calculated using MoM [21] for 1D surfaces of length $2L$, where $L = 25\lambda$. The heights of surfaces 1 and 2 are both Gaussian random variables with rms heights of $21 \mu\text{m}$ and $55 \mu\text{m}$, respectively, and their correlation lengths are $161 \mu\text{m}$ and $151 \mu\text{m}$, respectively. Each case shows the average scattering coefficient from 200 independent surface realizations.

For both surfaces in Fig. 5.4a the peak (main lobe) is centered at the specular angle. The width of the specular peak is proportional to $1/(2L)$, and the height of the main lobe decreases exponentially with increasing rms height, frequency, and incident angle. At each frequency the rougher surface (surface 2) diverts more energy away from the specular angle. For both surfaces, more scattering occurs at the higher frequency. The scattering at the specular angle decreases with increasing frequency as the diffuse scattering increases. For very rough surfaces, the coherent peak disappears completely, as illustrated by surface 2 in Fig. 5.4a at 2.0 THz.

Terahertz TDS measurements were made in reflection mode to demonstrate the ability to detect material features from rough surface scattering at the specular angle [24]. The sample materials were prepared at the Indian Head Division, Naval Surface Warfare Center (IHD NSWC) [25], and THz TDS measurements were conducted at the Northwest Electromagnetics and Acoustics Research Laboratory (NEAR-Lab) at Portland State University. Lactose powder was mixed with a (transparent) polytetrafluoroethylene (PTFE) binding material in a 20% / 80% PTFE/lactose weight ratio and pressed into circular pellets 2 inches in diameter. The sample thickness, approximately 9 mm, was large enough so that all etalon reflections could be time-gated out without significant loss of frequency resolution. A smooth surface sample was compared with two rough surface samples. The rough surface samples were

impressed with the same roughness statistics as surface 1 and surface 2 by inserting a piece of 80 grit and 40 grit sandpaper in the bottom of the die, respectively. The samples and THz TDS transmitter and receiver were placed inside an acrylic enclosure purged with Nitrogen to remove narrow-band water vapor attenuation. The incident (collimated) beam was centered half-way between the center and the edge of the 2 in lactose pellet, which was rotated (in 12 degree increments) about its center to create 30 surface realizations. Reflection spectra were obtained by deconvolution using a gold mirror as the reference. Figure 5.4b shows the negative derivatives of the reflected power with respect to frequency for each surface. As discussed earlier, the 1st derivative of the reflection coefficient magnitude (and thus also power) can reveal a spectral signature similar to the imaginary part of the permittivity when $\epsilon' \gg \epsilon''$ [11–13], a condition satisfied by lactose (Fig. 5.2). Thus, the spectral feature of lactose near 0.54 THz is clearly apparent in Fig. 5.4b for the smooth surface, but becomes smaller as the surface roughness increases because more energy is diverted away from the specular angle.

Since the scattered power decreases exponentially with increasing frequency and disappears altogether for very rough surfaces, it can be more helpful to work with the diffuse scattering (incoherent power) from rough surfaces. Diffuse scattering will be produced at all angles and thus no particular alignment is necessary. Improvement in the SNR of the diffuse signatures may be realized by averaging over many scatter angles. In addition, signal processing techniques such as correlation detection [26] and Cepstrum filtering [27] have been applied to improve detections algorithms for diffuse scattering.

5.3.1.1 Rough Surface Scattering Approximations

Insight into scattering behavior can be gained by considering approximate solutions for (5.13). The two most common analytic approximations, the Kirchhoff Approximation and Small Perturbation Method, will be introduced in this section.

Kirchhoff Approximation

The Kirchhoff Approximation assumes the facets of a rough surface can be approximated locally as tangent planes. For surfaces with large radius of curvature the Kirchhoff Approximation simplifies (5.13) to give [18, 20],

$$\bar{E}_s^h(\bar{r}) = \hat{y} \left[\frac{ike^{ikr}}{4\pi r} \right] E_0 \int_{A_0} \left[a \frac{\delta}{\delta x} \zeta(x, y) - b \right] e^{i(\bar{k}_i - \bar{k}_s) \cdot \bar{r}'} dx' dy', \quad (5.17)$$

where A_0 is the total surface area, with dimensions $2L_x \times 2L_y$, and the coefficients are given by $a = (1 - R_{01}^h) \sin \theta_i + (1 + R_{01}^h) \sin \theta_s$, and $b = (1 + R_{01}^h) \cos \theta_s - (1 - R_{01}^h) \cos \theta_i$. It is important to note that in (5.17) the emitter and detector are assumed to be in the xz plane. In this case, only tangent planes of the surface which

are perpendicular to the xz plane are relevant in the integration. Although these tangent planes have no slope in the y -direction, a two-dimensional integration is still necessary to account for the width of the planes. Since the local normal of each of these planes will be parallel to the xz plane, the local polarization of the incident wave is still in the y -direction and the horizontal reflection coefficient can be used to compute the a and b coefficients. More general scattering scenarios are presented in the literature [18, 20].

The scattered field from the Kirchhoff Approximation may be solved numerically for a random surface realization, $\zeta(x, y)$, in (5.17). However, if the surface has small slopes, then (5.17) can be simplified further [20],

$$\bar{E}_s(\bar{r}) = \hat{y} \left[\frac{ik e^{ikr}}{4\pi r} \right] E_0 [-b] \int_{A_o} e^{i(\bar{k}_i - \bar{k}_s) \cdot \bar{r}'} dx' dy'. \quad (5.18)$$

The Kirchhoff Approximation is valid for all frequencies for which the radius of curvature is much larger than a wavelength. However, at large angles of incidence, shadowing and multiple reflections in-between facets of the surface may occur. The basic form of the Kirchhoff Approximation, presented here, does not account for these effects.

If the surface has a Gaussian probability density function, then the scattering coefficient can be solved analytically [20],

$$\gamma = \frac{k^2}{4\pi A_0 \cos \theta_i} (| -b |^2 (\langle I \rangle + D_I)), \quad (5.19)$$

where the first and second terms within the parenthesis represent the coherent and incoherent scattered intensity, respectively. If the transmitter and receiver are both in the xz plane, and the surface area includes many correlation lengths, then the coherent scattering is given by [20],

$$\langle I \rangle = A_0 \exp \left[-\frac{1}{2} k_{dz}^2 h^2 \right] \text{sinc}(k_{dx} L_x), \quad (5.20)$$

where $\text{sinc}(x) = \sin(x)/x$, $k_{dx} = k(\sin \theta_i - \sin \theta_s)$ and $k_{dz} = k(\cos \theta_i - \cos \theta_s)$. It is important to note that this is similar to the scattered field from a flat plate of width $2L_x$, but here the rough surface attenuates the field by an exponential factor which is dependent on the rms height, angle of incidence, and wavelength.

Small Perturbation Method

For surfaces that have small rms height, $kh \ll 1$, the Small Perturbation Method (SPM) can be used to estimate the scattering coefficient for a Gaussian surface [20],

$$\gamma^{(1)} = \left[4k^4 h^2 l_c^2 \cos^2 \theta_s \cos \theta_i \right] \left| \frac{(k_1^2 - k^2)}{(k_z + k_{1z})(k_{zi} + k_{1zi})} \right|^2 \exp \left[-\frac{1}{4} k_{d\rho}^2 l_c^2 \right]. \quad (5.21)$$

where the superscript on the scattering coefficient indicates a first-order approximation. In the medium above the rough surface, the vertical component of the scattered wave vector is given by $k_z = k \cos \theta_s$, and $k_{d\rho}$ is the difference between the horizontal components of the incident and scattered wave vectors where $k_{d\rho}^2 = k^2(\sin^2 \theta_s + \sin^2 \theta_i - 2 \sin \theta_s \sin \theta_i)$. Similarly, the vertical components of the incident and scattered wave vectors are given by $k_{z1i} = k_1 \cos \theta_i$ and $k_{1z} = k_1 \cos \theta_s$, respectively.

The SPM model is useful for frequencies at which the small height approximation is valid. Therefore, SPM is only applicable for a band of frequencies bracketed by the Fraunhofer Criterion (5.12) and the small height requirement, $kh \ll 1$.

5.4 Volume Scattering and Absorption

This section considers an electromagnetic wave propagating in a material that has volume inhomogeneities (i.e., grains or bubbles), as shown in the right-hand part of Fig. 5.3. The energy in an electromagnetic wave propagating through such a material will be scattered and absorbed by the particles. This is commonly observed (experimentally) as a loss of energy from the incident or coherent wave, but the scattering will also in general re-distribute energy into a scattered electric field that propagates in other directions (much as rough surface scattering produces energy in non-specular directions). The strength of the scattering depends on the size of the scatterers relative to the THz wavelength; the dielectric contrast between the scatterer and the background; and the shape, concentration, and orientation of the scatterers.

In random media, the exact positions and characteristics of the particles are not precisely known, but often their properties can be described in terms of the particle statistics. Given these statistics, it is possible to predict the mean field properties, either with analytical approximations or numerical calculations (using Monte Carlo techniques). In this section, several of the more commonly used approaches and approximations for calculating the volume scattering and absorption are provided.

5.4.1 Scattering from Individual Particles

Consider the case of a single particle of permittivity ϵ_p (which differs from the background permittivity ϵ) illuminated by the incident electric field as defined in (5.1). In the far field, the field scattered from the particle will be a spherical wave with dependence e^{ikr}/r , where r is the distance from the particle to the observation point. The electric field scattering in the direction \hat{k}_s is

$$\bar{E}_s = \hat{e}_s f_s(\hat{k}_s, \hat{k}_i) E_o \frac{e^{ikr}}{r} \quad (5.22)$$

and $f_s(\hat{k}_s, \hat{k}_i)$ is the scattering amplitude from direction \hat{k}_i into direction \hat{k}_s . The scattered power can be determined by integrating over all scattered angles to give the scattering cross-section

$$\sigma_s = \int d\Omega |f_s(\hat{k}_s, \hat{k}_i)|^2 \quad (5.23)$$

where $d\Omega$ is a differential solid angle. In addition to scattering, the particles may also introduce absorptive loss, which is quantified by the absorption cross-section σ_a . The extinction cross-section, $\sigma_e = \sigma_s + \sigma_a$ accounts for both effects.

The analytic solution for the scattering amplitude (and hence the far-field scattered field) can be found by expressing the incident, scattered, and internal fields in terms of a complete orthonormal basis, such as spherical vector wave functions. Electromagnetic boundary conditions are then imposed at the particle boundaries, resulting in expressions for the unknown expansion coefficients [28]. Typically, this process only yields closed form solutions for canonical objects (e.g., spheroids, cylinders, etc.); more complicated objects require numerical approaches.

The scattered field can be computed using the T-matrix [29, 30] method (see [31] for a recent review on the approach), which represents the scattered field in terms of the regular vector spherical wave functions $\overline{M}_{mn}^{(1)}$ and $\overline{N}_{mn}^{(1)}$ as

$$\overline{E}_s(\vec{r}) = \sum_{m,n} [a_{mn}^{s(M)} \overline{M}_{mn}(kr, \theta, \phi) + a_{mn}^{s(N)} \overline{N}_{mn}(kr, \theta, \phi)] \quad (5.24)$$

where θ and ϕ are the elevation and azimuthal angles in spherical coordinates and $a_{mn}^{s(M)}$ and $a_{mn}^{s(N)}$ are the (unknown) coefficients of the spherical wave functions which can be expressed in terms of the T-matrix as

$$\begin{bmatrix} \overline{a}^{s(M)} \\ \overline{a}^{s(N)} \end{bmatrix} = \begin{bmatrix} \overline{\overline{T}}^{(11)} & \overline{\overline{T}}^{(12)} \\ \overline{\overline{T}}^{(21)} & \overline{\overline{T}}^{(22)} \end{bmatrix} \begin{bmatrix} \overline{a}^{e(M)} \\ \overline{a}^{e(N)} \end{bmatrix}. \quad (5.25)$$

and each of the sub-matrices have dimensions $L_{\max} \times L_{\max}$, where L_{\max} is determined by the number of spherical harmonics necessary in the expansion in (5.24).

The scattering from spherical particles of radius a is referred to as Mie scattering [33, 32], and for spherical scatterers the T-matrix is diagonal with

$$T_{mnm'n'}^{(11)} = \delta_{mm'}\delta_{nn'}T_n^{(M)}; \quad T_{mnm'n'}^{(22)} = \delta_{mm'}\delta_{nn'}T_n^{(N)}; \quad T_{mnm'n'}^{(12)} = T_{mnm'n'}^{(21)} = 0 \quad (5.26)$$

where

$$\begin{aligned}
T_n^{(M)} &= \frac{j_n(k_s a) [ka j_n(ka)]' - j_n(ka) [k_s a j_n(k_s a)]'}{j_n(k_s a) [kah_n(ka)]' - h_n(ka) [k_s a j_n(k_s a)]'} \\
T_n^{(M)} &= \frac{[k_s^2 a^2 j_n(k_s a) [ka j_n(ka)]'] - [k^2 a^2 j_n(ka) [k_s a j_n(k_s a)]']}{[k_s^2 a^2 j_n(k_s a) [kah_n(ka)]'] - [k^2 a^2 h_n(ka) [k_s a j_n(k_s a)]']} \quad (5.27)
\end{aligned}$$

where j_n and h_n are the spherical Bessel and Hankel functions, respectively, and the prime indicates differentiation. The scattering and extinction cross-section for spheres can then be written in terms of the T-matrix elements as

$$\sigma_s = \frac{2\pi}{k^2} \sum_{n=1}^{\infty} (2n+1) (|T_n^{(M)}|^2 + |T_n^{(N)}|^2), \quad (5.28)$$

$$\sigma_e = -\frac{2\pi}{k^2} \sum_{n=1}^{\infty} (2n+1) \{Re(T_n^{(M)} + T_n^{(N)})\}. \quad (5.29)$$

The above expressions account rigorously for the scattering and absorption from spherical particles. However, the computation requires a summation over spherical harmonics, and the larger the particle the more terms are required in the summation. For small dielectric spheres ($ka \ll 1$) the only term that needs to be retained is the electric dipole term. Thus, the scattering and absorption cross-sections for small particles (called Rayleigh scattering) can be simplified to

$$\sigma_s = \frac{8\pi}{3} k^4 a^6 \left| \frac{\epsilon_p - \epsilon}{\epsilon_p + 2\epsilon} \right|^2 = \frac{8\pi}{3} k^4 a^6 |y|^2, \quad (5.30)$$

$$\sigma_a = k \frac{Im\{\epsilon_p\}}{\epsilon} \frac{4\pi a^3}{3} \left| \frac{3\epsilon}{\epsilon_p + 2\epsilon} \right|^2, \quad (5.31)$$

and $y = (\epsilon_s - \epsilon)/(\epsilon_s + 2\epsilon)$.

5.4.2 Scattering from Randomly Distributed Collections of Particles

Many inhomogeneous materials can be modeled as a collection of finite scatterers randomly distributed in a background media as shown in Fig. 5.3. The presence of these scatterers will introduce scattering and absorption to an electromagnetic wave propagating through the media. To compute the loss associated with this scattering and absorption, consider the scattering and absorption of a wave passing through a small volume dV which contains a large number of particles (with a density of n_0 particles per unit volume) but is also larger than λ^3 .

The first case to consider is when the randomness of the particle separation is not much smaller than a wavelength, so that that their positions will not introduce coherent, correlated scattering. Under this condition, the independent scattering assumption

tion can be utilized, and the scattering from the collection of particles is computed as the product of the particle number density and the scattering from an individual particle. The scattering, absorption, and extinction coefficients (κ_s , κ_a , κ_e respectively) are defined as the cross-sections per unit volume, and under an independent scattering approximation these can be written as

$$\kappa_s = n_0 \sigma_s, \quad \kappa_a = n_0 \sigma_a \quad (5.32)$$

$$\kappa_e = \kappa_s + \kappa_a = n_0 (\sigma_s + \sigma_a). \quad (5.33)$$

The physical interpretation of the above can be seen in the context of a THz wave of intensity I traveling through a volume of scatterers over a distance Δz and with a cross-sectional area S . The power extinguished due to scattering and absorption is then

$$\Delta P = -I \kappa_e S \Delta z \quad (5.34)$$

giving the solution for the intensity as a function of distance z as

$$I = I_0 e^{-\kappa_e z}. \quad (5.35)$$

Thus κ_e is the attenuation per unit distance due to scattering and absorption.

For many materials, the particles are not a single size, but can be described with a size distribution $p(a)$. Using the independent scattering assumption, the coefficients for the multi-size particle mixture can be written,

$$\kappa_s = \int_0^{\infty} da \, p(a) \sigma(a) \quad (5.36)$$

$$n_0 = \int_0^{\infty} da \, p(a) \quad (5.37)$$

where the integration is over the particle radius, a . For Rayleigh scattering under the independent scattering assumption, particles with size distribution $p(a)$ give

$$\kappa_s = \frac{8\pi}{3} k^4 \left| \frac{\epsilon_p - \epsilon}{\epsilon_p + 2\epsilon} \right|^2 \int_0^{\infty} da \, p(a) a^6 \quad (5.38)$$

$$\kappa_a = k \frac{\text{Im}\{\epsilon_p\}}{\epsilon} \frac{4\pi}{3} \left| \frac{3\epsilon}{\epsilon_p + 2\epsilon} \right|^2 \int_0^{\infty} da \, p(a) a^3, \quad (5.39)$$

and $\kappa_e = \kappa_s + \kappa_a$.

As an example, consider a material composed of a randomly distributed collection of lactose (dielectric properties given in Fig. 5.2) spheres of radius a in a background of air, with the lactose particles having a fractional volume of f_v . Let us assume that the particle concentration is sufficiently small that the independent scattering assumption is valid, and thus the total loss due to scattering and absorption through a distance l of the material is given by $\kappa_e l$ with κ_e given in (5.33). (Note: the independent scattering assumption for this example is examined in the next section, and it is shown that it can over-predict the amount of scattering—indicating an effective media calculation is needed.) The scattering and absorption cross-sections can be calculated with (5.30) and (5.31) if the particles are small (Rayleigh), but the general solution requires the Mie expression in (5.28) and (5.29).

The total wave extinction is due to both scattering and absorption, and the portion of the loss caused by absorption versus scattering is dependent on the particle radius. Consider the results shown in the left-hand plot of Fig. 5.5, which shows the predicted loss for single size particles with a fractional volume of 5%, computed for three different particles radii: $a = 8 \mu\text{m}$ (dotted line), $a = 50 \mu\text{m}$ (dashed line), and $a = 200 \mu\text{m}$ (solid line). The smallest particles ($a = 8 \mu\text{m}$) are Rayleigh scatterers at all frequencies in the 0.0–3.0 THz band, and the wave extinction through the particles is dominated by absorption. Thus, the spectral features of the extinction prominently show the peaks present in material absorption spectra (see Fig. 5.2). The largest particles ($a = 200 \mu\text{m}$) are in the Mie regime. These particles have strong classical scattering resonances, and thus the features visible in the THz spectra are due to scattering, not the material absorption. The mid-size particles transition from Rayleigh into the Mie regime as a function of frequency, hence the lowest lactose peak (0.54 THz) is evident in the extinction curve, while the higher peaks are obscured by scattering losses.

Note the example above considered dielectric spheres in a background of air. A more common mixture in THz transmission measurements is pellets formed from pressing a sample material of interest under strong pressure to attempt to remove residual air and form a homogeneous sample. However, small residual air gaps are present in the mixture, and these can lead to scattering losses. The scattering losses can be estimated by modeling the air gaps as scatterers in a background of the dielectric material [34].

5.4.2.1 Dense Media Calculations

In dense media, particles are close together giving rise to correlated scattering and the independent scattering approximation is not valid. In this situation, the scattering calculation needs to take into account the interaction between particles based on the statistics of their positions. There are two general approaches to achieving this. The first is to analytically compute the expectation operator to obtain an expression for the mean field properties. The second approach is to numerically calculate the field for a given ensemble of particles (taking into account correlated scattering) and

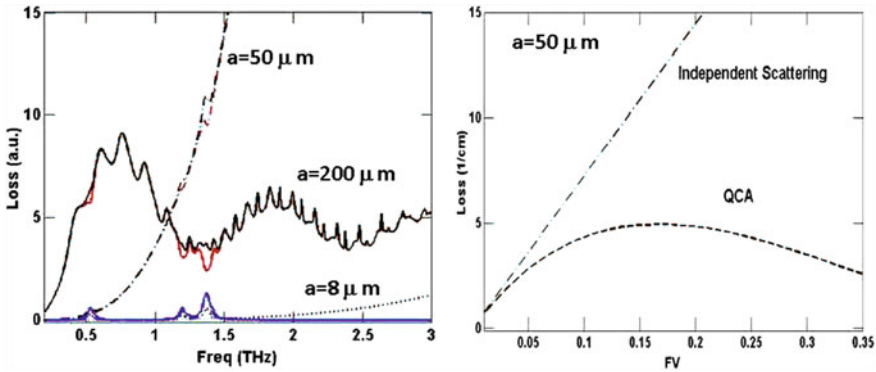


Fig. 5.5 *Left-hand plot* THz wave extinction (loss) for a randomly distributed collection of spherical lactose particles. The particles are a single size, and the loss is computed for three different radii: $a = 8 \mu\text{m}$ (dotted line), $a = 50 \mu\text{m}$ (dashed-dot, and dashed lines) and $a = 200 \mu\text{m}$ (solid line). Plot shows frequency dependence of the loss computed under the independent scattering assumption for a fractional volume of 5%. The total extinction loss is shown in black, and is the sum of the scattering loss (red) and absorption loss (blue). *Right-hand plot* extinction loss as a function of fractional volume shown as predicted by the independent scattering assumption and QCA, calculated at 1.0 THz for particles with $a = 50 \mu\text{m}$. Note the overprediction in scattering loss under the independent scattering assumption, indicating the losses in the left-hand plot are higher than expected. See text for discussion

then use Monte Carlo averaging to obtain the mean field statistics. The numerical approach is discussed in the next section.

One method of obtaining an analytic solution is to use the Quasi-Crystalline Approximation (QCA) [28]. In this formulation, the multi-particle conditional probability can be written using Bayes’ rule to generate a hierarchy of equations, and under the QCA, the resulting equation is truncated at the bivariate level. Thus, for QCA, the particle distribution statistics are represented with a pair distribution function, $g(r)$, which is a bivariate statistic whose value is proportional to the probability of finding any two particle separated by a distance of r . For statistically isotropic media in which non-penetrable particles are randomly positioned, the pair distribution function is given by the Percus Yevick (PY) pair distribution function. Several other types of particle distributions can be considered, including densely packed particles with a known size distribution or particles that exhibit some attraction or clustering behavior [35].

An approximate solution under QCA is obtained by representing the scattered wave in terms of an effective (complex) wavenumber

$$K_{\text{eff}} = \sqrt{\epsilon_{\text{eff}}}\omega/c. \tag{5.40}$$

where the real part of K_{eff} represents the coherent phase progression of the wave in the random media, and the imaginary part represents the attenuation due to scattering and absorption. This effective media model can be used in the equation for the exciting

field coefficient, and terms with the effective wavenumber K_{eff} balanced to satisfy a generalized Lorentz-Lorenz law. Then the Ewald-Oseen extinction theorem is used to balance the integral equation for waves traveling with the background wavenumber k . Physically, this ensures that the medium generates a wave that extinguishes the incident wave. This process yields a single scalar equation in the form of the Ewald-Oseen extinction theorem,

$$K_{\text{eff}} - k = -\frac{\pi i n_0}{k^2} \sum_n (T_n^{(M)} X_n^M + T_n^{(N)} X_n^{(N)}) (2n + 1). \quad (5.41)$$

In (5.41), X_n^M and X_n^N are unknown amplitudes that satisfy a system of simultaneous equations resulting from the Lorentz-Lorenz law (see [28] for full detail). In general, a closed form solution can only be obtained in the low-frequency limit (i.e., small ka), which yields

$$K_{\text{eff}}^2 = k^2 + \frac{3f_v k^2 y}{1 - f_v y} \left\{ 1 + i \frac{2}{3} \frac{(ka)^3 y}{1 - f_v y} \times \left[1 + 4\pi n_0 \int_0^\infty dr r^2 [g(r) - 1] \right] \right\} \quad (5.42)$$

where f_v is the fractional volume, and y is defined in (5.30). For Rayleigh particles described by the PY pair distribution (single size non-penetrable particles, statistically isotropic random placement) this reduces to

$$K_{\text{eff}}^2 = k^2 + \frac{3f_v k^2 y}{1 - f_v y} \left\{ 1 + i \frac{2}{3} k^3 a^3 y \frac{(1 - f_v)^4}{(1 - f_v y)(1 + 2f_v)^2} \right\}. \quad (5.43)$$

For larger values of ka , the solution to (5.41) can be determined numerically.

The QCA solution accounts for multiple scattering between the particles and hence can predict correlated scattering phenomenon. However, the derivation assumes that the wave moves between the particles in the background media (dielectric with permittivity ϵ). For high concentrations of particles, a more accurate approach would be to use the wavenumber of the effective media for the propagating wave - or replace the wavenumber k with the effective wavenumber K_{eff} . This approach is called the QCA with coherent potential (QCA-CP) [28].

For dense media, the effective wavenumber, K_{eff} , characterizes the coherent wave propagation, and thus the imaginary part of $2K_{\text{eff}}$ represents the amount of power (per unit length) extinguished in the media due to scattering and absorption. This is analogous to the extinction coefficient in (5.33), which was derived for sparse media using the independent scattering assumption. The choice of which expressions to use to estimate (κ_e or $2\text{Im}\{K_{\text{eff}}\}$) depends on particle density.

An example of dense media scattering is presented in the plot in the right-hand of Fig. 5.2. The extinction loss is plotted as a function of fractional volume, f_v , for lactose spheres of radius $a = 50 \mu\text{m}$ in a background of air. The extinction coefficient κ_e computed with (5.29) is shown as a dash-dot line, and the quantity $2\text{Im}\{K_{\text{eff}}\}$ obtained from the QCA approximation using (5.41) is shown as a dashed line. Under

both approximations, the scattering increases as the particle density increases. However, since κ_e is proportional to the particle density, it increases linearly with an increase in the fractional volume of the particles ($n_0 = f_v/v_0$) with v_0 denoting the volume of a single particle. Clearly this is non-physical, since in the limit of $f_v = 1.0$ the material is homogenous, and the absence of particles means there should be no scattering. In contrast, the imaginary part of the QCA effective wavenumber (which accounts for absorption and scattering losses) is seen to initially increase as a function of f_v , agreeing at low densities with the independent scattering approximation, but then peaks and begins to decrease as the f_v increases further. Thus, for appreciable particle densities, the independent scattering assumption overpredicts the amount of scattering. Comparing the curves in the right-hand plot of Fig. 5.2 at 5% fractional volume, it can be seen the losses in the left-hand plot (under the independent scattering assumption) are about 25% higher than predicted with a dense media (QCA) calculation (and thus the scattering is over-predicted).

5.4.3 Numerical Calculations and Monte Carlo Simulations

In 5.4.1, the T-matrix expressions were presented for a single particle, and explicit expressions were provided for Mie scattering for spherical particles. The T-matrix method can also be used for systems of particles with random positions. However, for collections of particles, each particle is excited not only by the incident electromagnetic field, but by the field scattered by all the other particles in the collection. This can be represented mathematically by writing the exciting field for the l th particle as

$$\bar{a}^{(e,l)} = \sum_{j=1, j \neq l}^J \bar{\sigma}(k\bar{r}_{lj}) \bar{T} \bar{a}^{(e,j)} + e^{i\bar{k}_i \cdot \bar{r}_l} \bar{a}_{\text{inc}} \quad (5.44)$$

where \bar{a}_{inc} is a vector of the incident field coefficients, $\bar{\sigma}(k\bar{r})$ is a $2L_{\text{max}} \times 2L_{\text{max}}$ matrix of terms accounting for a coordinate transformation, $\bar{r}_{lj} = \bar{r}_j - \bar{r}_l$ is the vector pointing from center of the l th particle to the center of the j th particle, and \bar{T} is the T-matrix for the particles, as given in (5.27) for spherical particle. The physical interpretation of (5.44) is that the excitation for the l th particle in the system is a combination of the incident wave and the waves scattered from all the other ($j = 1..J, j \neq l$) particles in the system. Once $\bar{a}^{(e,l)}$ is determined, the scattered field coefficients can be computed using (5.24) to compute the scattered field coefficients and hence the scattered field.

The expression in (5.44) is a rigorously derived expression for the scattered field that includes all orders of multiple scattering. However, the solution for the coefficients depend on the exact position and nature (shape, orientation, etc.) of the particles; they are thus difficult to solve exactly for most practical problems. For some problems, an iterative numerical approach can be employed [36].

Another option is to calculate the solution using a numerical approach based on the discretization of Maxwell's equations. For time-domain THz systems, a particularly appropriate method is the Finite Difference Time Domain (FDTD) approach, because the broadband data is generated in a single simulation pass. The FDTD method originally reported by Yee is based on a discrete approximation of the point form of Maxwell's equations [37]. This basic algorithm breaks the simulation space into discrete points where the electric and magnetic fields are sampled in space and time. Furthermore, FDTD allows computation of dielectric media which can contain both volume scatterers and rough interfaces; the complexity of the material is limited only on the ability to capture the material characteristics in a discretely sampled representation. FDTD has been used extensively for electromagnetic scattering calculations, and has more recently been applied to THz sensing [23]; see [22] for a complete background.

The electromagnetic field calculated for a single ensemble of particles represents the response for a single realization, but does not provide the mean field properties. In the previous section, the mean (or coherent) field was obtained by computing an analytical expectation operator. For numerical computations, a Monte Carlo approach can be used to generate a number of realizations drawn from the same statistical characterization, and then computing the mean field by coherently averaging over a sufficiently large number of realizations. To separate the coherent and incoherent components, the scattered field is averaged to give the coherent scattered field. The coherent scattered field is calculated by

$$\langle \bar{E}_s \rangle = \frac{1}{N_r} \sum_{q=1}^{N_r} \bar{E}_s^q \quad (5.45)$$

where q is the realization index with $q = 1, 2, \dots, N_r$ realizations, and \bar{E}_s^q is the scattered field from the elemental volume of many scatterers (includes their coherent near and intermediate range interactions). The incoherent field is the difference between the total field and the coherent field $\bar{\mathcal{E}}_s^q = \bar{E}_s^q - \langle \bar{E}_s \rangle$. Calculation of the scattering coefficient κ_s from the incoherent scattered field $\bar{\mathcal{E}}_s$ can be expressed as

$$\kappa_s = \frac{1}{V} \int_0^\pi d\theta_s \sin(\theta_s) \int_0^{2\pi} d\phi_s \frac{R^2}{N_r} \sum_{q=1}^{N_r} |\bar{\mathcal{E}}_s^q|^2. \quad (5.46)$$

Note that the Monte Carlo approach is a valid approach for computing the field propagating through a random distribution of particles, as well as for computing the field scattered from a rough surface interface.

5.5 Conclusions

This chapter provided short introduction into electromagnetic phenomenon observed in THz applications. In particular, it described the reflection and scattering of THz waves from flat or rough interfaces, and the scattering and absorption of THz waves through materials with volume inhomogeneities (such as grains). Since the length scale of many naturally occurring media are comparable to the THz wavelength, some of the scattering effects can be quite pronounced, and can be visible in the material spectra

References

1. K. Kawase, Y. Ogawa, Y. Watanabe, H. Inoue, Non-destructive terahertz imaging of illicit drugs using spectral fingerprints. *Opt. Express* **11**(20), 2549–2554 (2003)
2. M.C. Kemp, P.F. Taday, B.E. Cole, J.A. Cluff, A.J. Fitzgerald, W.R. Tribe, in Security applications of terahertz technology, *Proceedings of SPIE The International Society for Optical Engineering*, (2003), vol. 5070, pp. 44–52
3. W.R. Tribe, D.A. Newnham, P.F. Taday, M.C. Kemp, in Hidden object detection: security applications of terahertz technology. *Proceedings of SPIE The International Society for Optical Engineering*, (2004), vol. 5354, pp. 168–176
4. D.L. Woolard, E.R. Brown, M. Pepper, M. Kemp, Terahertz frequency sensing and imaging: a time of reckoning future applications? *Proc. IEEE*. **93**(10), 1722–1743 (2005)
5. K. Yamamoto, M. Yamaguchi, F. Miyamaru, M. Tani, M. Hangyo, T. Ikeda, A. Matsushita, K. Koide, M. Tatsuno, Y. Minami, Noninvasive inspection of C-4 explosive in mails by terahertz time-domain spectroscopy. *Jpn. J. Appl. Phys. Part 2 Lett.* **43**3B, 414–417, (2004)
6. X.-C. Zhang, Terahertz wave imaging: horizons and hurdles. *Phys. Med. Biol.* **47**(21), 3667–3677 (2002)
7. Y. Dikmelik, J.B. Spicer, M.J. Fitch, R. Oslander, Effects of surface roughness on reflection spectra obtained by terahertz time-domain spectroscopy. *Opt. Lett.* **31**(24), 3653–3655 (2006)
8. M. Ortolani, J.S. Lee, U. Schade, H.W. Hubers, Surface roughness effects on the terahertz reflectance of pure explosive materials. *Appl. Phys. Lett.* **93**(8), 081906 (2008)
9. L.M. Zurk, B. Orłowski, G. Sundberg, Z. Zhou, A. Chen, in Terahertz scattering from a Rough Granular Surface, *IEEE Antennas and Propagation Society, APS International Symposium (Digest)*, (2007), pp. 4929–4932
10. L.M. Zurk, G. Sundberg, S. Schecklman, Z. Zhou, A. Chen, E.I. Thorsos, in Scattering effects in terahertz reflection spectroscopy. *Proceedings of SPIE The International Society for Optical Engineering*, (2008), vol. 6949, 694907
11. H. Zhong, A. Redo-Sanchez, X.-C. Zhang, Identification and classification of chemicals using terahertz reflective spectroscopic focalplane imaging system. *Opt. Express* **14**(20), 9130–9141 (2006)
12. H. Zhong, Terahertz Wave Reflective Sensing and Imaging. PhD Thesis, Rensselaer Polytechnic Institute, 2006
13. H. Zhong, A. Redo-Sanchez, X.-C. Zhang, Standoff sensing and imaging of explosive related chemical and bio-chemical materials using thz-tds. *Int. J. High Speed Electron. Syst.* **17**(2), 239–249 (2007)
14. S. Mickan, X.-C. Zhang, T-ray sensing and imaging. *Int. J. High Speed Electron. Syst.* **13**(2), 601–676 (2003)
15. M.R. Leahy-Hoppa, M.J. Fitch, and R. Oslander, in Terahertz reflection spectroscopy for the detection of explosives, *Proceedings of SPIE The International Society for Optical Engineering*, (2008), vol. 6893, pp. 689305

16. M. Born, E. Wolf, *Principles of Optics* (Pergamon Press, Oxford, 1980)
17. G.P. Kniffin, S. Schecklman, J. Chen, S.C. Henry, L.M. Zurk, B. Pejcinovic, A.I. Timchenko, in Measurement and modeling of terahertz spectral signatures from layered material, *Proceedings of SPIE The International Society for Optical Engineering, Terahertz Technology and Applications III*, (2010), vol. 7601
18. P. Beckmann, A. Spizzichino, *The Scattering of Electromagnetic Waves from Rough Surfaces* (Artech House Inc, Norwood, 1987)
19. F.T. Ulaby, R.K. Moore, A.K. Fung, *Microwave remote sensing: active and passive*, vol. 2 (Addison-Wesley, Advanced Book Program/World Science Division, Reading MA, 1986)
20. L. Tsang, J.A. Kong, R.T. Shin, *Theory of Microwave Remote Sensing* (Wiley, New York, 1985)
21. L. Tsang, J.A. Kong, K.H. Ding, *Scattering of Electromagnetic Waves Numerical Simulations* (Wiley, New York, 2001)
22. A. Taflov, S. Hagness, *Computational Electrodynamics The Finite-Difference Time-Domain Method* (Artech House Inc, Norwood, 2005)
23. G. Sundberg, L.M. Zurk, S. Schecklman, S. Henry, Modeling rough surface and granular scattering at terahertz frequencies using the finite-difference time-domain method. *IEEE Trans. Geosci. Remote Sens.* **48**, 3709–3719 (2010)
24. S. Henry, G. Kniffin, S. Schecklman, L. Zurk, A. Chen, in Measurement and modeling of rough surface effects on terahertz spectroscopy and imaging, *Proceedings of SPIE—The International Society for Optical Engineering*, (2010), p. 7601
25. C. Konek, J. Wilkinson, O. Esenturk, E. Heilweil, M. Kemp, in Terahertz spectroscopy of explosives and simulants—rdx, petn, sugar and l-tartaric acid, *Proceedings of SPIE—The International Society for Optical Engineering*, (2009), vol. 7311
26. L.M. Zurk, S.C. Henry, S. Schecklman, D.D. Duncan, Physics-based processing for terahertz reflection spectroscopy and imaging, *Proceedings of SPIE The International Society for Optical Engineering Infrared, Millimeter Wave, and Terahertz Technologies*, (2010), vol. 7854
27. S. Schecklman, L.M. Zurk, S.C. Henry, G. P. Kniffin, Terahertz material detection from diffuse surface scattering, *J. Appl. Phys.* **109**(9) (2011)
28. L. Tsang, J.A. Kong, K.H. Ding, *Scattering of Electromagnetic Waves, Theories and Applications* (Wiley, New York, 2000)
29. P.C. Waterman, Matrix formulation of electromagnetic scattering. *Proc. IEEE* **53**, 80512 (1965)
30. P.C. Waterman, Symmetry, unitarity, and geometry in electromagnetic scattering. *Phys Rev D* **3**, 82539 (1971)
31. M.I. Mishchenko, L.D. Travis, D.W. Mackowski, T-matrix method and its applications to electromagnetic scattering by particles: A current perspective. *J. Quan. Spec. & Rad. Trans.* **111**, 1700–1703 (2010)
32. C.F. Bohren, D.F. Huffman, *Absorption and Scattering of Light by Small Particles* (Wiley, New York, 1998)
33. H.C. van de Hulst, *Light Scattering by Small Particles* (Dover Publications, New York, 1981)
34. L.M. Zurk, B. Orłowski, D.P. Winebrenner, E.I. Thorsos, M. Leahy-Hoppa, M.R. Hayden, Terahertz scattering from granular material. *J. Opt. Soc. Am. B: Opt. Phys.* **24**(9), 2238–2243 (2007)
35. K.H. Ding, L.M. Zurk, L. Tsang, Pair distribution functions and attenuation rates for sticky particles in dense media. *J. Electromagnet. Waves Appl.* v **8**(12), 1585–1604 (1994)
36. L.M. Zurk, L. Tsang, K.H. Ding, D.P. Winebrenner, Monte Carlo simulations of the extinction rate of densely packed spheres with clustered and non-clustered geometries. *J. Opt. Soc. Am.* **12**, 1772–1781 (1995)
37. K.S. Yee, Numerical solutions of initial boundary value problems involving maxwells equations in isotropic media, *IEEE Trans. Antennas Propag.* **14**(3), 302–307 (1966)

Chapter 6

Phase-Space Processing of Terahertz Radiation

Daniela Dragoman

Abstract A short overview of phase-space distribution functions and of their applications in characterizing and processing terahertz radiation is presented. The most commonly used phase-space distributions functions: the Wigner distribution function, the ambiguity function, the spectrogram, the wavelet transform, and the fractional Fourier transform, are discussed in some details.

6.1 Introduction

The spectral range of terahertz (THz) radiation, situated between millimeter-wave and infrared wavelengths (see [1] for a recent review), encompasses frequencies between 100 GHz and 10 THz, or wavelengths between $30\ \mu\text{m}$ and 3 mm. THz fields can be generated either by continuous-wave sources, such as free-electron lasers, IR-pumped gas lasers, electronic tubes and quantum-cascade lasers [2], or by pulsed sources, which produce a single pulse or a train of ultrashort pulses. In the first case, the electric field of the THz wave is characterized by an analytic function $E(\mathbf{r})$, which depends on the spatial coordinate $\mathbf{r} = (x, y, z)$ and is invariant in time (up to a phase factor), while in the second case the THz pulse measured at a certain location, $E(t)$, is a function of time only. In order to present in a unified manner the characterization methods of THz radiation, we denote the argument of the analytic function as u , where u stands for \mathbf{r} for THz waves and t for THz pulses. In some cases, especially for ultrashort pulses, $E(u)$ is not easily measured, since this would require detectors with a shorter response time than the optical cycle of the pulse, so that experiments are focused on recovering the information in the spectral domain. The analytical function in this domain, $\tilde{E}(v)$, is related by a Fourier transform to $E(u)$:

D. Dragoman (✉)
University of Bucharest, Bucharest, Romania
e-mail: daniela.dragoman@yahoo.com

$$\begin{aligned}
E(u) &= (2\pi)^{-d/2} \int_{-\infty}^{\infty} \tilde{E}(v) \exp(-iuv) dv, \\
\tilde{E}(v) &= (2\pi)^{-d/2} \int_{-\infty}^{\infty} E(u) \exp(iuv) du,
\end{aligned} \tag{6.1}$$

where v denotes the spectral coordinate of the wavevector (or angular/spatial frequency) \mathbf{k} for THz waves and the (spectral) frequency ω for THz pulses. In the following, we refer to v simply as frequency. In the equations above d indicates the dimensionality of the problem: $d = 1$ or 2 for THz waves propagating along a certain direction with fields that depend on one or two transverse coordinates, respectively, and $d = 1$ for THz pulses.

There are situations, however, when the spatial (or angular) and temporal (or spectral) factors in the expression of the electric field do not separate, case in which we have spatio-temporal coupling, and $u = (\mathbf{r}, t)$, $v = (\mathbf{k}, \omega)$, and $d = 2, 3$, or 4 for pulses depending, respectively, on one, two, or three spatial coordinates. Spatio-temporal couplings are especially significant in pulses with broad bandwidths, in nonlinear interactions, such as filamentation and nonlinear refraction, and in set-ups containing singlet lenses or dispersion elements (gratings or prisms) for pulse compression or shaping [3], when a frequency-dependent refraction index causes different frequency components to follow different paths [4]. In fact, there are eight first-order spatio-temporal couplings, coupling in one domain being generally accompanied by couplings in at least two Fourier domains [4].

A complete characterization of THz radiation implies knowledge of both the amplitude and the phase of $E(u) = A(u) \exp[i\theta(u)]$ or $\tilde{E}(v) = \tilde{A}(v) \exp[i\tilde{\theta}(v)]$. The detailed knowledge of THz signals is essential for optimizing THz sources and systems, for investigating and controlling phenomena taking place on femtosecond or picosecond timescales, such as plasma dynamics, chemical reactions or magnetization, and for understanding light-matter interactions for high-intensity THz pulses. The aim of this chapter is to offer a bird-eye view on joint u - v representations, or phase-space representations, of THz signals, and to exemplify some of their applications for THz signal processing. Although complete field characterization can be achieved from measurements in either u or v domains, a more efficient and sometimes easier to implement way of characterizing and processing THz signals is offered by phase-space characterization techniques.

6.2 Parameters Used for Characterization of THz Fields

Besides the amplitude and phase of the electric fields in the u or v domains, other functions of interest for the characterization of THz radiation are the intensity of the signal, $I(u) = |E(u)|^2 = A^2(u)$, and its spectrum $\tilde{I}(v) = |\tilde{E}(v)|^2 = \tilde{A}^2(v)$.

The local frequency can be defined as $v_{\text{loc}} = -\partial\theta/\partial u$ and the group position/delay as $u_{\text{gr}} = \partial\tilde{\theta}/\partial v$. Mean expressions for these parameters are obtained from

$$\bar{v} = \int v_{\text{loc}}(u)I(u)du / \int I(u)du = \int v\tilde{I}(v)dv / \int \tilde{I}(v)dv, \quad (6.2a)$$

$$\bar{u} = \int u_{\text{gr}}(v)\tilde{I}(v)dv / \int \tilde{I}(v)dv = \int uI(u)du / \int I(u)du, \quad (6.2b)$$

whereas the standard deviations in the u and v domains can be defined, respectively, by

$$(\Delta u)^2 = \int (u - \bar{u})^2 I(u)du / \int I(u)du, \quad (\Delta v)^2 = \int (v - \bar{v})^2 \tilde{I}(v)dv / \int \tilde{I}(v)dv. \quad (6.3)$$

They satisfy the uncertainty relation $\Delta u \Delta v \geq 1/2$, the equality taking place only for Gaussian signals.

It is important to emphasize that, especially when measurements are performed with averaging detectors over an ensemble of signals, the correlation function of the THz radiation is also of interest. The second-order correlation function describes the fluctuations in the electric field at u_1 relative to those at u_2 ; these are sufficient to fully describe the ensemble of signals for normal fluctuations, which obey the Gaussian statistics, but higher-order correlations are needed otherwise. The second-order correlation function in the u domain can be defined as

$$C(u_1, u_2) = \langle E(u_1)E^*(u_2) \rangle = C(u, u'), \quad (6.4)$$

where $u = (u_1 + u_2)/2$ and $u' = u_1 - u_2$ are the center and difference coordinates, respectively, and the angle brackets indicate an averaging procedure over the ensemble of signals. The corresponding correlation function in the v domain is obtained by a 2D Fourier transform:

$$\tilde{C}(v, v') = (2\pi)^{-d/2} \int \int du du' C(u, u') \exp[i(uv' + u'v)], \quad (6.5)$$

where the parameters $v = (v_1 + v_2)/2$ and $v' = v_1 - v_2$ denote the center and difference coordinates, respectively, in the spectral v domain.

From an experimental point of view, information about the intensity/amplitude of the THz radiation, $A(u)$ or $\tilde{A}(v)$, is readily offered by photodetectors for both THz waves and pulses. For example, CCD cameras record the intensity of a wave $I(\mathbf{r}) = A^2(\mathbf{r})$, while for ultrashort pulses spectrometers record $\tilde{I}(\omega) = \tilde{A}^2(\omega)$. The intensity of the signal in the Fourier transform domain can be easily recorded by the same devices if Fourier-transform setups are implemented. These involve the use of lenses for THz waves and dispersion elements for THz pulses [3]. However, the phase $\theta(u)$ or $\tilde{\theta}(v)$ is more difficult to retrieve from experimental data and it involves a generally laborious algorithm. The phase determines the shape

and the width (duration for pulses or spatial extent for waves) of THz radiation if the amplitude is given; the shortest width, referred to also as the Fourier-limited width, corresponds to a flat phase. For a Fourier limited THz radiation, the full width at half maximum of the amplitude, Δu , is inversely proportional to the corresponding quantity in the spectral domain, Δv . The product of these parameters determines the bandwidth of THz radiation; the larger the bandwidth the more dissimilar the signal is from an ideal Fourier-limited one. The width of a Fourier-limited pulse can be determined from autocorrelation measurements [5], i.e. from measurements of $R(u) = \int E(u')E^*(u' - u)du'$, if some information about the pulse shape exists, while the width of arbitrary, complex-shaped pulses are obtained from cross-correlation experiments [6] that use an ancillary short pulse $G(u)$, i.e. from measurements of $X(u) = \int E(u')G^*(u' - u)du'$.

A complete characterization of THz radiation can be achieved by either referenced or self-referenced methods [5, 7], using spectrographic, tomographic, or interferometric techniques. Referenced methods require a reference signal E_{ref} with well-known intensity and phase. For example, if the intensity of the unknown signal is determined as discussed above, the phase $\tilde{\theta}(v)$ or, more precisely, the difference between the phase of the THz radiation and that of the reference signal, can be retrieved in the Fourier transform spectroscopy technique if the unknown and the reference signals are launched with a difference u' in the u coordinate (are delayed, for pulses, or displaced, for waves), and the Fourier transform term of

$$I_2(u') = \int |E(u) + E_{\text{ref}}(u - u')|^2 du \quad (6.6)$$

is determined at the center spectral coordinate v_0 of the reference pulse. This term equals $\tilde{E}(v)\tilde{E}_{\text{ref}}^*(v) = \tilde{A}(v)\tilde{A}_{\text{ref}}(v) \exp[i(\tilde{\theta}(v) - \tilde{\theta}_{\text{ref}}(v))]$. Alternatively, the phase is obtained in the spectral interferometry technique from spectrometer readings, by Fourier transforming the signal

$$\tilde{I}_2(v) = |\tilde{E}(v) + \tilde{E}_{\text{ref}}(v) \exp(ivu')|^2, \quad (6.7)$$

filtering out the term at u' , and Fourier transforming back this term. The result is the complex function $\tilde{E}(v)\tilde{E}_{\text{ref}}^*(v) \exp(-ivu') = \tilde{A}(v)\tilde{A}_{\text{ref}}(v) \exp[i(\tilde{\theta}(v) - \tilde{\theta}_{\text{ref}}(v) - vu')]$, from which it is possible to extract the phase of the unknown THz signal [5].

Interference patterns between the unknown and reference signals are obtained if they are coherent and if u' and the spectral resolution of the spectrometer/reconstructed signal are appropriately chosen. According to the Whittaker–Shannon theorem, if the THz signal has compact support in the u domain over an interval Δu , it can be reconstructed only if the sampling of $\tilde{E}(v)$ takes place at the Nyquist rate $2\pi/\Delta u$. Thus, there is a trade-off between the resolutions in u - and v -domains. Moreover, a successful reconstruction of the signal with referenced methods occurs only when the reference signal is similar to the unknown signal (see discussions in [5] for details).

Self-referenced methods for reconstructing THz radiation do not require a well-characterized reference signal. For example, for coherent or partially coherent THz waves, the phase can be recovered in self-referencing interferometry techniques [8] or in tomographic techniques, by measuring the intensity distribution along the direction of field propagation, at least when the intensity distribution has no zeros [9]. Slices of the correlation function in (6.4), from which one can recover the amplitude and phase of the THz signal as $A(u) = \sqrt{C(u, 0)}$ and $\theta(u) = \tan^{-1}[\text{Im}C((u+u_2)/2, u-u_2)/\text{Re}C((u+u_2)/2, u-u_2)]$ for fixed u_2 , are obtained in interferometric techniques, in which the phase information is transformed in amplitude information (see [10] for an insightful treatment of the subject). Tomography, as well as techniques of reconstructing electric fields starting from interferometry data are simple to use and robust since the inversion procedure is direct (non-iterative). On the other hand, for THz pulses self-referenced phase recovery usually employs nonlinear or non-stationary optics. When the reference pulse in spectral interferometry is a delayed (in time with t' and in frequency with ω') replica of the unknown pulse, the characterization method is called SPIDER, which is an acronym for spectral phase interferometry for direct electric-field reconstruction [5]. In this case, the obtained phase $\tilde{\theta}(\omega) - \tilde{\theta}_{\text{ref}}(\omega) - \omega t' = \tilde{\theta}(\omega) - \tilde{\theta}(\omega - \omega') - \omega t'$ contains information about the phase gradient of the unknown pulse, $\partial\tilde{\theta}(\omega)/\partial\omega \cong [\tilde{\theta}(\omega) - \tilde{\theta}(\omega - \omega')]/\omega'$, from which the unknown phase is determined by concatenation, i.e. by a series of linear transformations, with no need of iterative algorithms [11]. Therefore, SPIDER can be used for real-time pulse characterization or for single-shot characterization of few-cycle pulses [12]. An accurate phase determination implies that ω' is small enough so that no information is lost, but large enough so that the effect of noise is minimized. The spectral shift ω' is generated by non-stationary or nonlinear processes. Complete field reconstruction of spatio-temporal signals, more precisely of $E(\mathbf{r}, \omega)$, can be performed with the SEA TADPOLE technique which is an acronym for spatial encoded arrangement for temporal analysis by dispersing a pair of light E -fields [13]. It consists of crossing and spectrally resolving the unknown pulse and a reference pulse, the Fourier filtering being done along the spatial axis of a camera.

6.3 Phase-Space Techniques for Characterization and Processing of Terahertz Radiation

We have seen that a complete characterization of THz radiation can be performed in either u or v domains. However, sometimes THz radiation reconstruction is simpler to perform or more accurate starting from a set of u - v data than from samples of u - or v -dependent functions. Such joint u - v representations, referred to also as phase-space distribution functions, are preferred when the u and v properties are coupled. This is the case, for example, when the frequency content of the signal in the v domain is different for different u values, or when transient components of the signal must be analyzed. These transient components are often hidden in the averaging Fourier

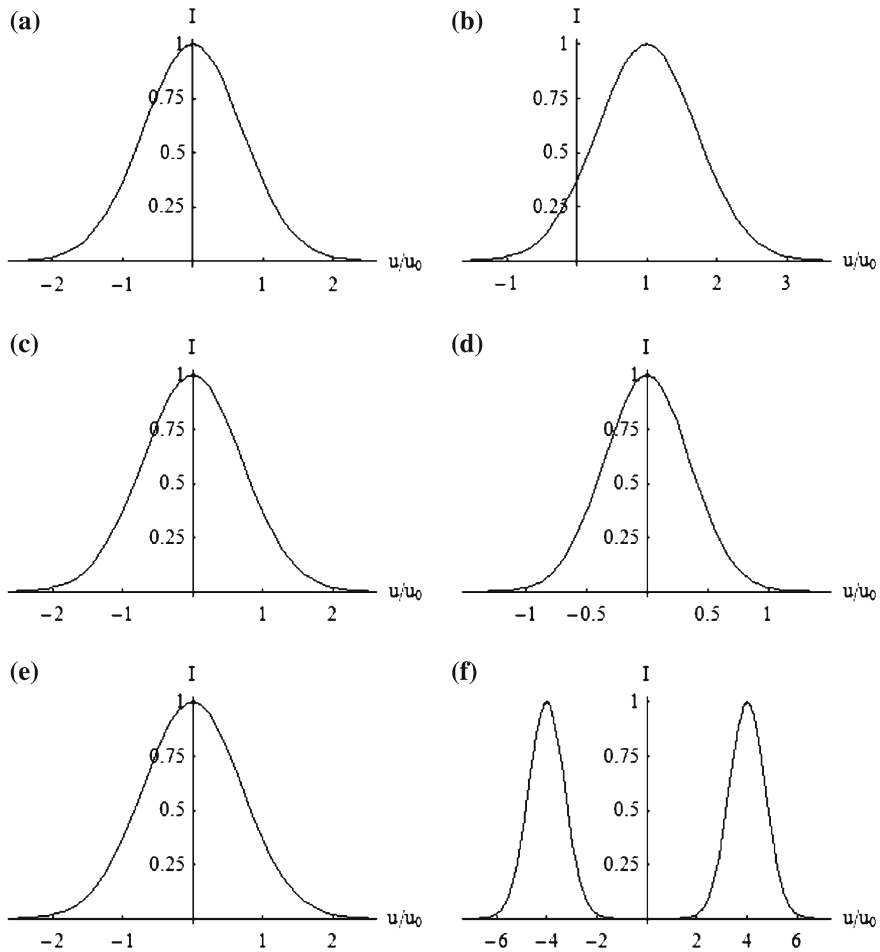


Fig. 6.1 Normalized intensity of **a** a Gaussian signal, **b** its shifted version, **c** its phase modulated counterpart, **d** the scaled signal, **e** the chirped signal, and **f** a superposition of two Gaussians

analysis and require sufficient resolution in both u and v domains for their detection, i.e. high resolution decomposition in the u - v plane (see [14]). This requirement can be met by joint u - v distribution functions since the inherent trade-off between the resolutions in u and v domains that appear when measuring THz signals in only one domain does not necessarily apply for measurements in phase space. The joint time–frequency representation is also called chronocycle representation of a pulse.

A phase-space distribution function provides simultaneous information about the extent and characteristics of the signal in u and v domains, so that there is no need to Fourier transform the information in one domain in order to obtain information in the other. For a better understanding of the advantages of using phase-space distribution

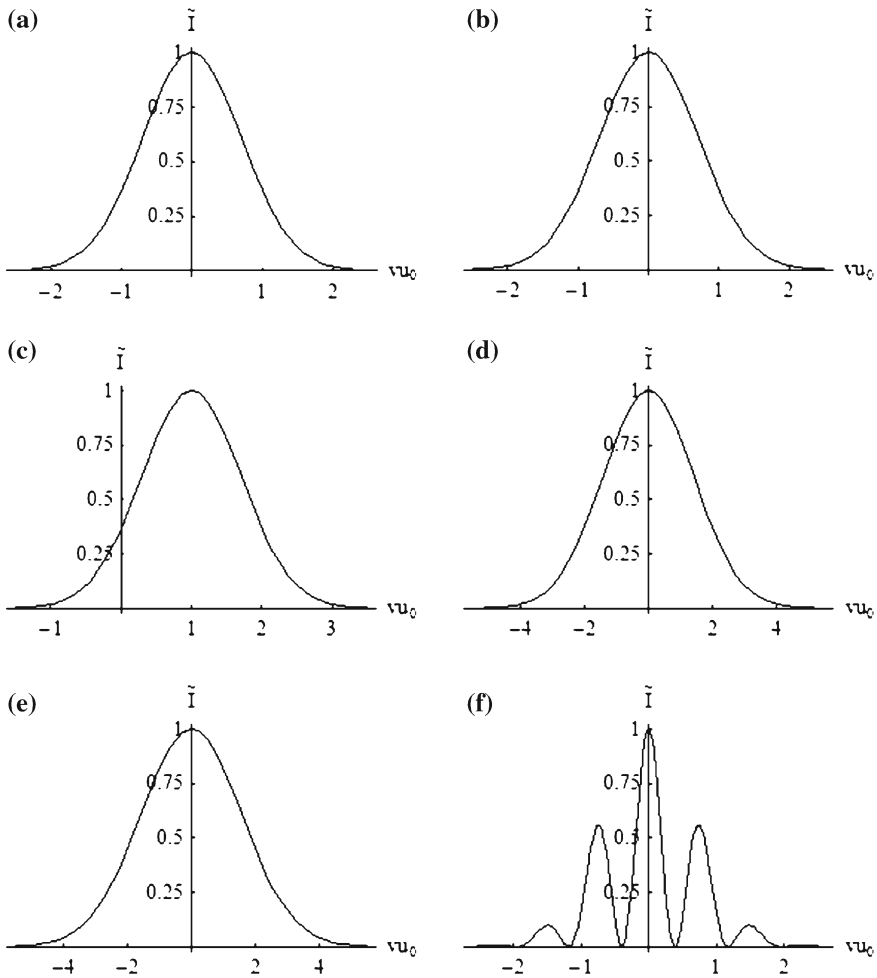


Fig. 6.2 Normalized spectrum of the same input signals as in Fig. 6.1

functions for signal characterization, we have represented in Figs. 6.1a–f and 6.2a–f the (normalized to unity) intensity $I(u)$ and spectrum $\tilde{I}(v)$, respectively, of:

- (a) A Gaussian signal $E(u) = \exp(-u^2/2u_0^2)$,
- (b) Its shifted in u version $E(u - u_0)$,
- (c) Its phase modulated counterpart, $E(u) \exp(-iu/u_0)$,
- (d) The scaled signal $E(2u)$,
- (e) The chirped signal $E(u) \exp(iu^2/u_0^2)$,
- (f) A superposition of two Gaussians, $E(u - 4u_0) + E(u + 4u_0)$.

The transforms (b)–(f) of an input signal are usual transformation encountered in many set-ups.

As obvious from its definition, the intensity of the signal does not offer information about chirping and phase modulation, and the spectrum does not sense the u shift. Moreover, at least in the example chosen, the spectrum cannot discriminate between the scaled and chirped signal. Note that at scaling a narrowing in the u distribution/intensity is associated to a widening in the v distribution/spectrum, according to the uncertainty relation. It is also instructive to observe that interference manifests as oscillations of the spectrum in the v domain. From Figs. 6.1 and 6.2 it follows that neither one of the u - or v - domain functions (intensity or spectrum) offers complete information on the input signal. An additional measurement of the phase of the signal in either u or v domains is required, or one can use both intensity and spectrum to recover information on the field distribution. This is already joint u - v information, but still embodied in two different functions. A phase-space distribution function offers joint u - v information simultaneously, so that a single measurement of such a distribution function is sufficient for complete field recovery.

Despite being better suited for a complete representation of pulses, there are, however, some disadvantages when working with phase-space distribution functions, especially regarding their implementation. The reason is that for THz radiation with dimension d , a phase-space distribution function has dimension $2d$, which makes it impossible to implement phase-space distribution functions for $d \geq 2$; only sections of these distribution functions can be generated in this case. From the experimental point of view, the phase-space distribution functions can be obtained directly, from simultaneous measurements of the complementary variables u and v , or indirectly, by inferring the distribution functions from measurements of their marginals. In the last case we deal with tomographic techniques. In particular, to reconstruct the complex field in N points, $2N$ independent data points are needed, that can be obtained by measuring N^2 points in phase space (only $2N$ measurements are needed if the correlation function, for example, is recorded). The recovering procedure simplifies considerably for coherent signals.

Very often, setups use to implement joint u - v distribution functions in the spatial-angular phase space are derived from the corresponding setups in the time–frequency phase space and vice versa, using the space–time duality [15]. This is possible since in the spatial domain most setups include free spaces of length d and lenses with focal lengths f , which have as analogs in the temporal domain dispersive elements and phase modulators, respectively. The space–time analogy holds because the equation that governs paraxial diffraction of a (say, one-dimensional) wave propagating along the z axis with transverse wavevector component k_x and wavenumber k_0 , $\partial E/\partial z = (i/2k_x)\partial^2 E/\partial x^2$, is similar to the narrow-band dispersion of a light pulse with propagation constant $\beta(\omega)$ and central frequency ω_0 . The last phenomenon is described by $\partial E/\partial z = (i\beta_2/2)\partial^2 E/\partial \tau^2$, where $\beta_2 = \partial^2 \beta/\partial \omega^2|_{\omega=\omega_0}$ is the dispersion coefficient and $\tau = t - z/v_g$, with $v_g = \partial \beta/\partial \omega|_{\omega=\omega_0}$ the group velocity. As a result, the transmission function of free-space propagation through a distance d in the Fresnel approximation, $\exp[-ik_x^2/(2k_0)]$, is analogous to the transmission function of a pulse propagating through a dispersive element of length L , $\exp[i(\omega - \omega_0)^2 \beta_2 L/2]$, the temporal distance covered by the pulse being $d_T = -\beta_2 L$. On the other hand, a time lens can be implemented with an

electro-optic modulator with half-wave switching voltage V_π driven by a voltage $V(t) = V_0 \cos(\omega_m t)$, which is quadratic in time around $t = 0$. In this case, the phase modulation $\phi(t) = (\pi V_0/V_\pi)(1 - \omega_m^2 t^2/2)$ is equivalent to that induced by a thin lens, with a transmission function $\exp(-ik_0 x^2/2f)$. Therefore, the electro-optic modulator acts as a temporal lens with focal length $f_T = \omega_0/[(\pi V_0/V_\pi)\omega_m^2]$, which can be positive or negative depending on the sign of V_0 .

There are extensive review papers on phase-space distribution functions [7, 16–18]. There are several distribution functions that differ in their definition, properties and ease of implementation, which make them suitable in specific applications. However, all distribution functions contain the same amount of information and can be obtained one from the other. The most commonly used phase-space distribution functions, namely the Wigner distribution function (WDF), the ambiguity function, the spectrogram, the wavelet and the fractional Fourier transform (FRFT), will be described in the following.

6.3.1 The Wigner Distribution Function and Its Applications in Signal Processing

For coherent THz fields the WDF is defined as

$$\begin{aligned} W(u, v) &= (2\pi)^{-d/2} \int E\left(u + \frac{u'}{2}\right) E^*\left(u - \frac{u'}{2}\right) \exp(iu'v) du' \\ &= (2\pi)^{-d/2} \int \tilde{E}\left(v + \frac{v'}{2}\right) \tilde{E}^*\left(v - \frac{v'}{2}\right) \exp(-iu'v') dv' \end{aligned} \quad (6.8)$$

while for partially coherent radiation the corresponding definition is

$$\begin{aligned} W(u, v) &= (2\pi)^{-d/2} \int C(u, u') \exp(ivu') du' \\ &= (2\pi)^{-d/2} \int \tilde{C}(v, v') \exp(-iu'v') dv'. \end{aligned} \quad (6.9)$$

The WDF satisfy some of the most desirable properties of a phase-space distribution function, i.e. it satisfies the marginals

$$\begin{aligned} (2\pi)^{-d/2} \int W(u, v) dv &= I(u) = C(u, 0), \quad (2\pi)^{-d/2} \int W(u, v) du \\ &= \hat{I}(v) = \tilde{C}(v, 0), \end{aligned} \quad (6.10)$$

case in which the total energy of the signal is obtained as $\text{Energy} = (2\pi)^{-d/2} \int W(u, v) du dv$.

The WDF has also the same finite support as its variables, i.e. it is limited to the u and v intervals that limit the electric field and its Fourier transform, respectively, and it allows a simple definition of global or local characteristics of a signal. For example, if $f(u, v)$ is an arbitrary function of u and v , its global average can be defined as

$$\overline{f(u, v)} = \int f(u, v)W(u, v)du dv / \int W(u, v)du dv, \quad (6.11)$$

whereas its local averages in the u and v domains can be expressed as

$$\begin{aligned} \overline{f(u, v)}_u &= \int f(u, v)W(u, v)dv / \int W(u, v)dv, \\ \overline{f(u, v)}_v &= \int f(u, v)W(u, v)du / \int W(u, v)du. \end{aligned} \quad (6.12)$$

In particular, the instantaneous frequency of a pulse is $\bar{\omega}_t$. Moreover, the global and local spreads of the signal in the u and v domains can be defined in terms of WDF-based averages, respectively, as

$$\Delta u = \sqrt{u^2 - (\bar{u})^2}, \quad \Delta u_v = \sqrt{u^2_v - (\bar{u}_v)^2} \quad (6.13a)$$

$$\Delta v = \sqrt{v^2 - (\bar{v})^2}, \quad \Delta v_u = \sqrt{v^2_u - (\bar{v}_u)^2}. \quad (6.13b)$$

In addition, the WDF is real but not positive defined, except for Gaussian signals, so that its interpretation as a phase-space density function is not straightforward.

The electric field and its Fourier transform can be retrieved (up to constant phase factors) from the WDF as follows:

$$E(u)E^*(0) = (2\pi)^{-d/2} \int W(u/2, v) \exp(-iuv)dv \quad (6.14a)$$

$$\tilde{E}(v)\tilde{E}^*(0) = (2\pi)^{-d/2} \int W(u, v/2) \exp(iuv)du \quad (6.14b)$$

In particular, the first real-time and accurate characterization of a pure phase object using the WDF dates from 1993 [19].

Although the WDF is helpful in characterizing single/isolated signals, it contains cross-terms when superposition of signals occur, which makes its usefulness limited in these cases. On the other hand, the cross-terms disappear for sets of mutually incoherent signals, revealing the correlation properties of the ensemble. More precisely, for coherent fields $E(u) = \sum_m a_m E_m(u)$, we have

$$W(u, v) = \sum_m |a_m|^2 W_m(u, v) + \sum_{m, n \neq m} a_m a_n^* W_{mn}(u, v), \quad (6.15)$$

where $W_m(u, v)$ are the WDFs of the signals $E_m(u)$ and the cross-terms are defined as

$$W_{mn}(u, v) = (2\pi)^{-d/2} \int E_m\left(u + \frac{u'}{2}\right) E_n^*\left(u - \frac{u'}{2}\right) \exp(iu'v) du'. \quad (6.16)$$

To avoid cross-terms, other phase-space distribution functions, such as the Choi-Williams distribution, or the spectrogram, can be used. More detailed reviews on the properties of WDF of continuous and pulsed signals and of their applications can be found in [20–23]. Discrete forms of WDF are introduced in [24, 25].

The contour plots of WDF for the (a)–(f) functions considered above are represented in Figs. 6.3a–f respectively. As can be seen from these figures, all transformations of the Gaussian signal considered have different WDFs, so that a single measurement of this phase-space distribution is enough to discriminate between various signals.

One of the appealing features of the WDF is its transformation through linear optical systems, which resembles that of geometrical optics. In particular, u and v shifts in the signal induce u and v shifts in the WDF: for $E(u - u_0)$ the WDF is $W(u - u_0, v)$, while for $\tilde{E}(v - v_0)$ we have $W(u, v - v_0)$, as illustrated in Figs. 6.3b and c, respectively. In general, in a linear optical system characterized by a symplectic ray transfer matrix S that relates the output to the input ray vectors as

$$\begin{pmatrix} u \\ v \end{pmatrix}_{\text{out}} = S \begin{pmatrix} u \\ v \end{pmatrix}_{\text{in}} = \begin{pmatrix} A & B \\ C & D \end{pmatrix} \begin{pmatrix} u \\ v \end{pmatrix}_{\text{in}} \quad (6.17)$$

we have

$$W_{\text{out}}(u, v) = W_{\text{in}}(uD - vB, -uC + vA), \quad (6.18)$$

i.e. the WDF is constant along ray paths. In particular, in agreement to the uncertainty relation, scaling corresponds to $A = D = 0$ and $C = 1/B$, as can be seen from Fig. 6.3d, while a chirp is characterized by $A = D = 1$ and $C \neq 0$, as illustrated in Fig. 6.3e. In agreement with (6.15), the WDF of a superposition of two coherent signals, represented in Fig. 6.3d, shows both superposing signals, as the outer Gaussians, as well as the oscillating cross-term, which indicates interference. Note the relationship between the WDF and the intensity and spectrum of a signal, as revealed by Figs. 6.1, 6.2, and 6.3, and described by equations (6.10).

Ray transfer matrices can be defined not only for waves, but also for pulses and even for spatio-temporal coupled signals [26]. Such ray transfer matrices can be used, for example, for a WDF analysis of a pulse shaper [27]. The simple transformation law in (6.17) can be generalized to the moments of the WDF.

While in gated/referenced transforms, such as the spectrogram, the resolution in the u or v domains is determined by the extent of the window and the uncertainty principle imposes a trade-off between the u and v resolutions, in self-referenced u - v distributions, such as the WDF or the ambiguity function, there is no restriction on temporal and spectral resolutions. In fact, the WDF is known to have the best u - v

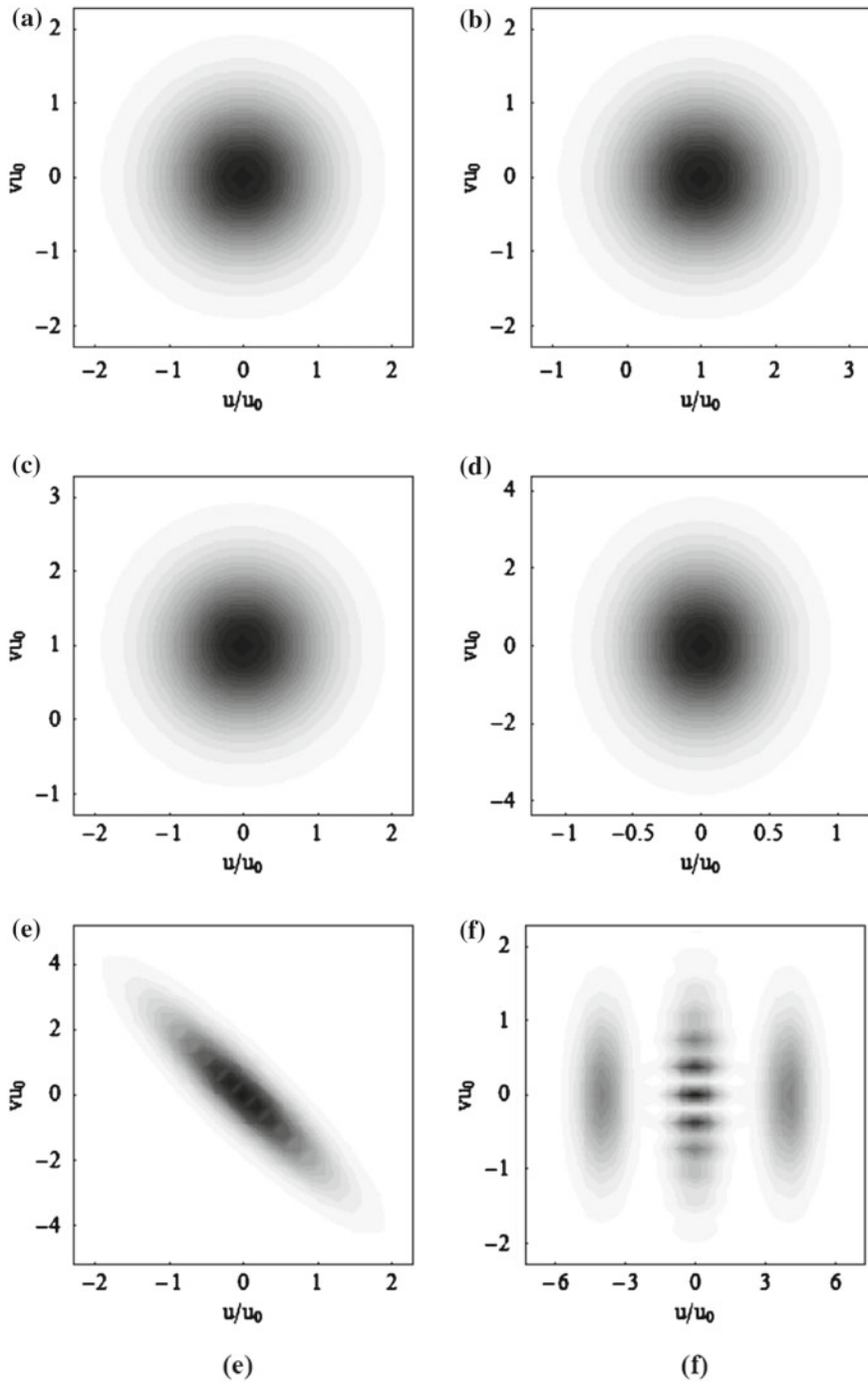


Fig. 6.3 Contour plots of the WDF of the same input signals as in Fig. 6.1

resolution [16]. However, the implementation of WDF is very sensitive to noise [16]; the noise extends practically over the whole WDF even if present only along certain intervals of u and/or v variables. This is an example of the nonlocality property of WDF, which partially explains its success in quantum mechanics.

Although it is not possible, in general to measure simultaneously the u and v variables, a direct measurement of the WDF (in fact, of its modulus) is possible by transforming the v variable into a scaled u coordinate. For obvious reasons the direct generation of the WDF is possible only for $d = 1$, which means the time–frequency phase space or the phase space of 1D waves; otherwise, only slices of the WDF are obtained. The main problem in implementing the WDF is to generate $E(u + u'/2)E^*(u - u'/2)$ or $C(u, u')$, because the following Fourier transform poses no problem. There are several setups for the implementation of these functions, which can be used in particular cases (real or complex, 1D or 2D fields) or for particular phase-space types (spatial-angular or time–frequency). They are mentioned in the review article [21].

Although setups that implement spatial-angular distribution functions involving free spaces and lenses can be simply transformed into setups that implement time–frequency distribution using the space–time duality, in the case of the WDF the space–time duality must be extended to include devices such as rotated optical quadrupoles, rotated or moving windows, or roof top prisms. In particular, the action of a rotated optical quadrupole placed between free space propagation regions with defined distances can be mimicked in the temporal domain by a birefringent and dispersive fiber [28]. An optical quadrupole in the spatial domain consists of a cylindrical convergent and a cylindrical divergent lens with the same focal distance but perpendicular axes. This device generates the WDF of 1D signals [29].

Tomographic techniques allow measurements of marginals of the WDF. More precisely, measurements of light intensity at different planes along the propagation axis correspond to rotated phase-space slices, the relevant rotation angles α spanning the interval from $-\pi/2$ to $\pi/2$. The slices are the fractional power spectra $\int W(u \cos \alpha + v \sin \alpha, v \cos \alpha - u \sin \alpha) du$, from which the distribution function can be recovered via the inverse Radon transform, irrespective of the degree of coherence of the signal. Rotation in phase space requires either a shear transformation (parabolic phase modulation of $E(u)$) or a quadratic modulation in both u and v [10]. For THz pulses a shear transformation is achieved by a phase modulator driven by a sinusoidal voltage, while for THz waves free-space propagation is sufficient to implement such a transformation. The complete field reconstruction from a tomographic measurement of the chronocyclic WDF [30] is described in [31].

The second-order moments of the WDF describe the quality of a signal, i.e. the relative bandwidth of a signal relative to an ideal Fourier-limited one, while higher-order moments indicate the symmetry and sharpness of optical waves. The spatial-angular WDF can be used to characterize optical systems, such as magnifiers, lenses and their different types of possible aberrations, optical waveguides and the coupling efficiency of coherent or partially coherent light waves into waveguides, and nonlinear optical systems and soliton waves [21]. All these applications are based on the fact that the WDF of a signal is highly sensitive to the shape of that signal

and to the altering of this shape at propagation through optical systems. Optical systems can then be characterized by monitoring the input and output WDF. The spatial-angular WDF has also been used to characterize the high-frequency radiation emitted from a prebunched electron beam in an undulator synchrotron [32]; such prebunched electron beams are encountered in free electron lasers. The brightness of the radiation source can be inferred from the WDF.

In another application, a masked time–frequency WDF was used to reconstruct fiber Bragg gratings profiles from the reflected signal. Masks, which are in fact spectrograms, are used to eliminate the cross-terms in the high-resolution WDF, such that the characteristics of concatenated uniform fiber gratings, superimposed linearly chirped fiber gratings, and strongly nonlinearly chirped fiber gratings can be obtained [33].

The spatial-angular WDF can be used also to determine the exact three-dimensional location of small particles, as those in smoke, fog, or airborne aerosols, from 1D in-line holograms. This task can be achieved without digital or optical field reconstruction (focusing), but directly from the WDF analysis of the constant-level-adjusted holograms, at least if the particle concentration is not too high such that the cross-terms in the WDF become a real problem [34]. This technique can be extended to 2D in-line holograms by analyzing fixed-frequency WDF slices, the cross-term problems being solved by using fixed-frequency slices of other bilinear phase-space distribution functions in the Cohen class. In particular, this can be achieved by suitably choosing the representation parameters in the ambiguity-function domain [35].

Optical systems can be analyzed with the spatial-angular WDF, even for illumination with polychromatic light distributions. For example, a temporally restricted superresolving system consisting of a time multiplexer with moving gratings that sends signals through a finite-width aperture by dividing them in parts with different but not too dissimilar wavelengths and then reconstructing the signal, was analyzed with a generalized WDF [36].

The application of WDF for THz pulses in THz spectroscopy is discussed in [37]. The chronocycle WDF has been used to represent heralded single-photon wave packets generated by detecting one photon from a photon pair produced in spontaneous parametric down conversion processes [38]. These heralded photons are not Fourier transform limited if spectral entanglement in the photon pair exists, which induces spectral mixedness, but factorable photon pair states can also be generated under specific conditions.

The WDF was used also for estimating the space-bandwidth product of a signal that propagates through an optical system, which implements an amplitude encoded double random phase encryption/decryption procedure using spatial light modulators [39]. Optical encryption is useful in digital holographic techniques applied to complex signals. WDF-based synthesis techniques that can filter pulses and can separate multi-component signals are described in [40].

6.3.2 The Ambiguity Function and Its Applications in Signal Processing

Another distribution function closely related to the WDF is the ambiguity function [41]. While the WDF was defined as a Fourier transform of the correlation function with respect to the difference coordinates, the ambiguity function is defined as a Fourier transform of the second-order correlation function with respect to the center variables:

$$\begin{aligned} A(u', v') &= (2\pi)^{-d/2} \int C(u, u') \exp(iuv') du \\ &= (2\pi)^{-d/2} \int \tilde{C}(v, v') \exp(-ivu') dv. \end{aligned} \quad (6.19)$$

A similar expression holds for coherent fields if $C(u, u')$ is replaced by $E(u + u'/2)E^*(u - u'/2)$. As for the WDF, the complex field is recovered (up to a constant factor) through an inverse Fourier transform. The WDF and the ambiguity function are related through a double Fourier transform. In particular, the ambiguity function satisfies the same simple transformation law through first-order optical systems as the WDF: $A_{\text{out}}(u', v') = A_{\text{in}}(Du' - Bv', -Cu' + Av')$.

Contour plots of the absolute value of the ambiguity function for the (a)–(f) signals considered in the examples above are represented in Figs. 6.4a–f, respectively. From the definition (6.19) and from a comparison of Figs. 6.3 and 6.4, it follows that, even if apparently quite similar, the ambiguity and the WDF have completely different properties. For example, although for even or odd electric fields, $E(u) = \pm E(-u)$, in particular for the chirp $E(u) = \exp(iau^2/2)$, the ambiguity and the WDF are scaled versions of one another: $W(u, v) = \pm 2A(2u', 2v')$, the ambiguity function is in general complex even for real signals, while the WDF is real for any signal [42]. In particular, shifts in u and v domains with u_0 and v_0 , respectively, which lead to corresponding shifts in the WDF, affect the ambiguity function only through the phase factors $\exp(iu_0v')$ and $\exp(-iv_0u')$, respectively. These phase factors do not influence the absolute value of the ambiguity, as shown in Figs. 6.4b and 6.4c, but scaling, chirp, and superposition affect it (see Figs. 6.4d–e). More importantly, the ambiguity function does not satisfy the marginal properties, i.e. the requirement that the integral over the phase-space distribution with respect to one variable gives the intensity with respect to the other variable. Indeed, the intensity of the THz radiation and of its spectrum can be obtained not as marginals of $A(u', v')$, but as Fourier transforms:

$$\begin{aligned} I(u) = C(u, 0) &= \int A(0, v') \exp(-iu v') dv', \quad \tilde{I}(v) = \tilde{C}(0, v) \\ &= \int A(u', 0) \exp(-iv u') du'. \end{aligned} \quad (6.20)$$

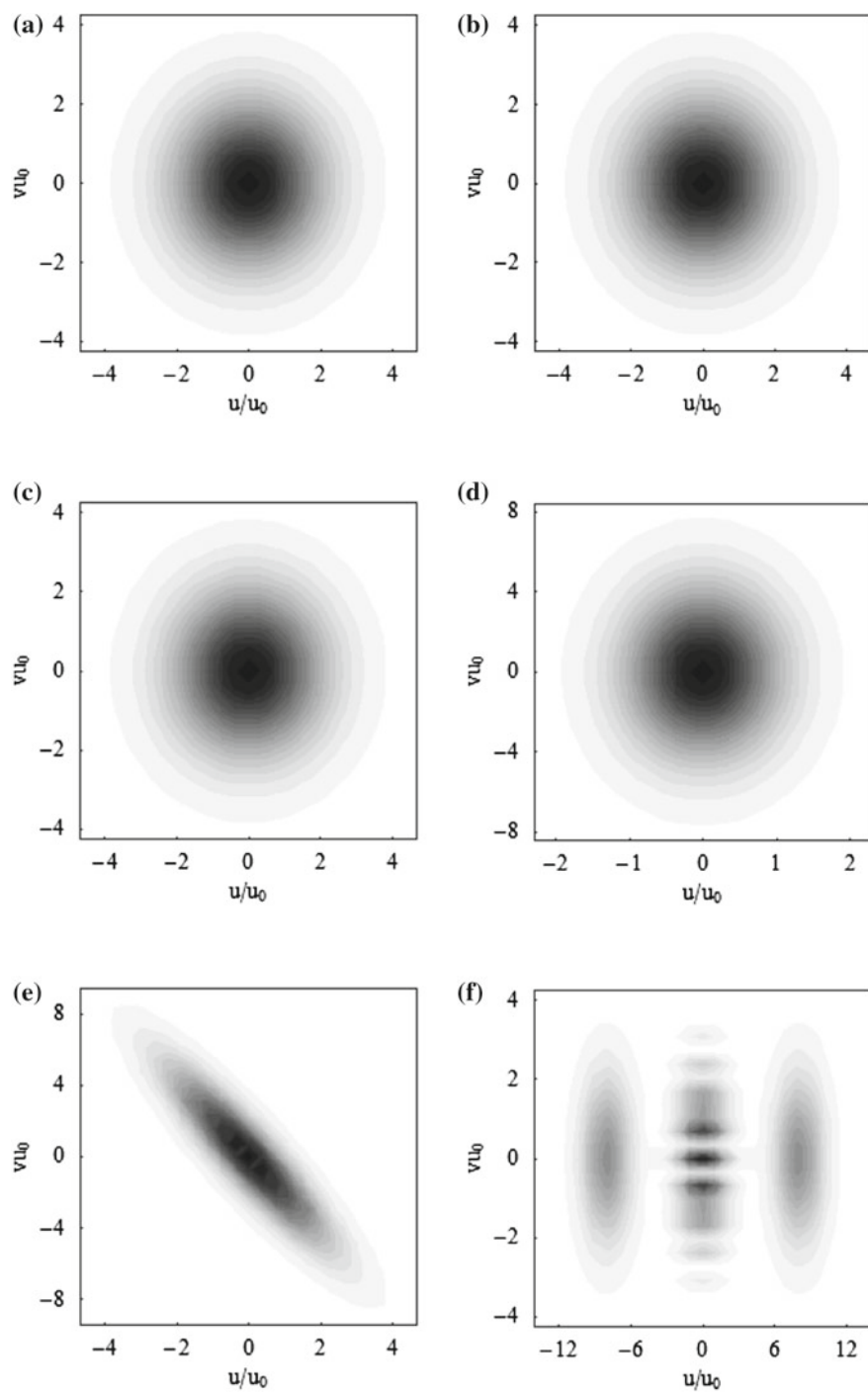


Fig. 6.4 Contour plots of the ambiguity function of the same signals as in Fig. 6.1

Although containing the same information about the signal as the WDF, the ambiguity function is more suited for complete signal recovery from tomographic measurements, i.e. for intensity distributions recorded along the propagation axis of a wave, since it can be estimated from a Fourier transform of the data, and thus can be computed fast using a digital algorithm, whereas the reconstruction based on the WDF requires a filtered back-projection algorithm for the inverse Radon transform. This is the reason why reconstruction based on the tomographic method of complex fields emitted by vertical-cavity surface-emitting lasers, for example, is performed simpler using the ambiguity function [43].

Because the ambiguity function is so closely related to the WDF, setups that generate one of these distribution functions can readily be transformed to measure the other. More precisely, once $E(u + u'/2)E^*(u - u'/2)$ or $C(u, u')$ is generated, the ambiguity function is obtained performing a Fourier transform with respect to the u variable while the implementation of the WDF requires a Fourier transform with respect to the u' variable. An alternative to implementing sections of the ambiguity function (or WDF) for 2D signals is to generate the function $E(u + u'/2)E^*(u - u'/2)$, for example, and then to perform numerically the Fourier transform. For instance, the $E(u + u'/2)E^*(u - u'/2)$ function for a 2D coherent light wave can be generated using two rotated beam splitters to generate replicas of the light source, which can then be superimposed [44].

The ambiguity function in both time–frequency and spatial-angular phase spaces [45] has been used in radar and sonar applications. Its success relies on the fact that the signal parameters to be determined (delay time and carrier frequency, or displacement of antenna aperture and displacement of spatial frequency of the signal) are related by a pair of Fourier transformations.

6.3.3 The Spectrogram and Its Applications in Signal Processing

The WDF and the ambiguity function are self-referenced phase-space methods, which do not require a gated signal. There are also phase-space distribution functions based on gated/window signals, such as the spectrogram. The spectrogram is defined as

$$S(u', v) = \left| \int E(u)G(u - u') \exp(ivu) du \right|^2, \quad (6.21)$$

and is determined from measurements of the spectrum of the gated signal $E(u)G(u - u')$ for different delays/displacements u' between the unknown signal E and the gate G . The amplitude and phase of E are then recovered with a sophisticated iterative algorithm for data inversion. A good u resolution in the spectrogram requires short- u windows, while good- v resolutions need long- u windows.

The spectrogram, as defined above, can be seen as the intensity of the short- u (short-time for pulses) Fourier transform

$$S_F(u', v) = \int E(u)G(u - u') \exp(i\nu u) du, \quad (6.22)$$

i.e. as $S(u', v) = |S_F(u', v)|^2$. Unlike the Fourier transform, which only incorporates global averaged information about the signal, the short- u Fourier transform incorporates a u -domain resolution through the window function $G(u)$, and so describes changes in the ν domain at different u' values.

The spectrogram is positive defined and therefore can be regarded as the phase-space energy density of the signal. Contour plots of the spectrogram of the (a)–(f) functions above are represented in Figs. 6.5a–f, respectively, for a gate $G(u) = \exp[-(4u)^2/2u_0^2]$. As evident also from Figs. 6.5b and 6.5c, the spectrogram, similar to the WDF, is shifted with the corresponding amounts on u and ν axes when the electric field and its Fourier transform are shifted. The scaling transformation modifies the extent of the spectrogram along the u and ν axes, as shown in Fig. 6.5d, and the chirp is easily observable in Fig. 6.5e. However, the spectrogram integrals over one variable are not proportional to the intensity with respect to the other, i.e. it does not satisfy the marginals. More precisely,

$$\begin{aligned} \int S(u', v) dv &= \int |E(u)|^2 |G(u - u')|^2 du, & \int S(u, v') du \\ &= \int |\tilde{E}(v)|^2 |\tilde{G}(v' - v)|^2 dv. \end{aligned} \quad (6.23)$$

The spectrogram is related to the WDF. In particular, since for any functions E and G their respective WDFs satisfy the relation

$$\int W_E(u, v) W_G(u, v) du dv = \left| \int E(u) G^*(u) du \right|^2 = \left| \int \tilde{E}(v) \tilde{G}^*(v) dv \right|^2 \quad (6.24)$$

or

$$\int W_E(u, v) W_G(u, v) du dv = \int C_E(u, u') C_G(u, u') du du', \quad (6.25)$$

for partially coherent fields, the spectrogram is a convolution of the WDF of the unknown signal, W_E , with that of the gate, W_G :

$$S(u, v) = \int W_E(u', v') W_G(u' - u, v - v') du' dv'. \quad (6.26)$$

The spectrogram represents thus only a smoothed, “blurred” version of the WDF, in which phase information is lost. Partial smoothing can be an advantage though, since it reduces the cross-terms that appear in the WDF of superpositions of several signals, while still retaining information on phase. In particular, Fig. 6.5d illustrates the complete loss of cross-terms (interference terms) at the superposition of two Gaussians.

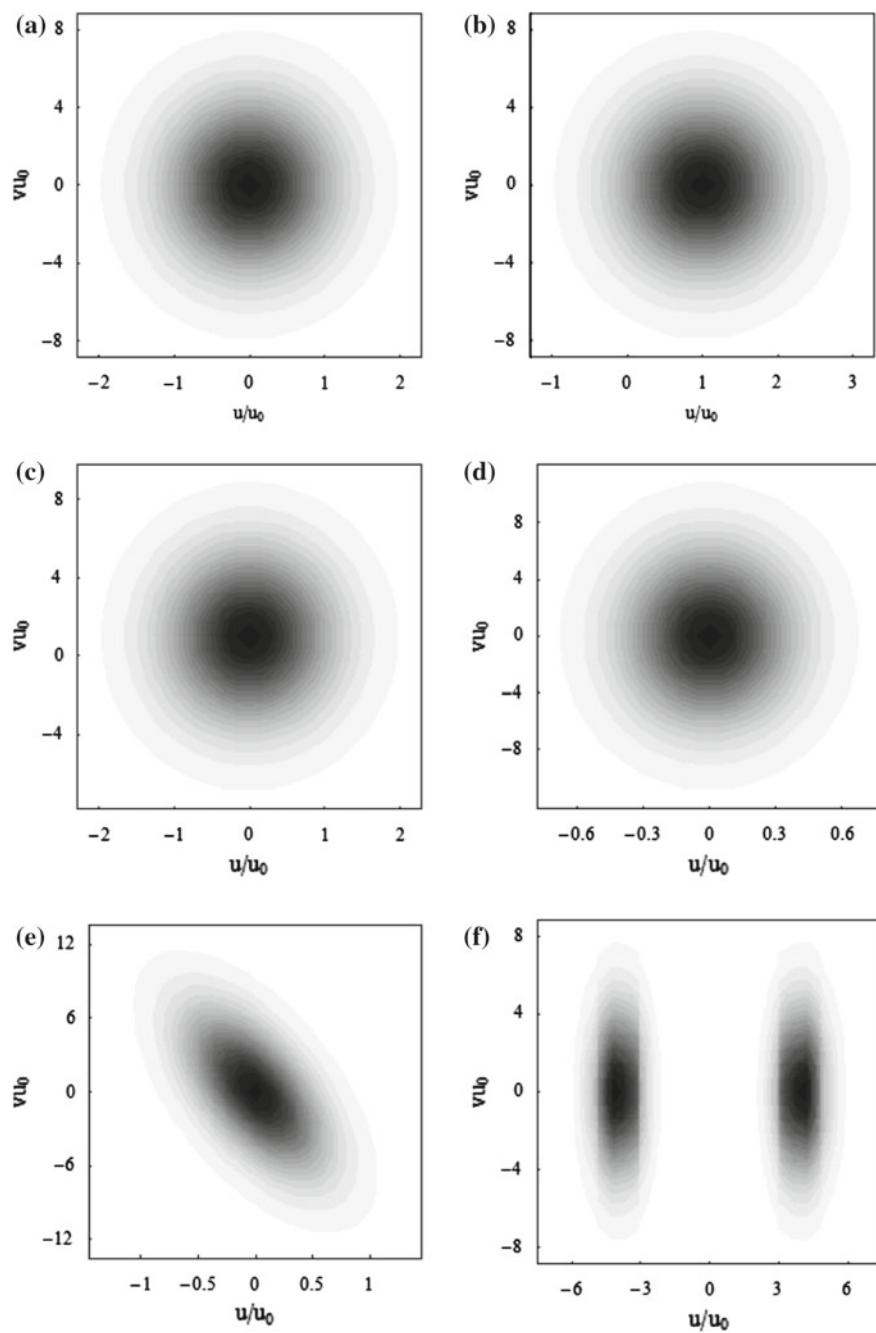


Fig. 6.5 Contour plots of the spectrogram of the same input signals as in Fig. 6.1

To measure a spectrogram one needs a spectral filter in v , a filter in u (for the gate), and a square-law detector. Note that the spectrogram, which is a measure of the spectrum of different slices in u , is equivalent to the u distribution of different slices in v (the order of the filters are inverted), i.e. is equivalent to

$$S(u, v') = \left| \int \tilde{E}(v) \tilde{G}(v' - v) \exp(-iuv') dv \right|^2, \quad (6.27)$$

the corresponding distribution function for pulses being called sonogram [10]. The first form of the spectrogram, given in (6.21), is used when a high spectral resolution can be achieved, whereas the second form is of interest when a high resolution in the u domain can be attained with the available detectors. Relying on gates that filter the signal in u or v domains, the resolutions in u and v cannot both be small enough for the same gate; different gates should be used when studying the u and v properties of the signal. Sonograms have been used for complete characterization of ultrashort 80 fs pulses [46], and provide the same information on the pulse as self-referenced spectrograms but, since it does not require nonlinear elements for signal mixing, it can achieve large bandwidths.

The spectrogram was first used for speech recognition. Spectrograms in the spatial-angular phase space that use a transparency as a window function, have been used to measure optical systems such as cylindrical and spherical lenses with sub-millimeter dimensions [47]. The focal length of the lens is obtained from the slope of spectrogram, and the aberrations can be identified as deviations of the spectrogram from a straight tilted line. Moreover, different aberrations types can be identified through their phase-space image [21]. Such spatial-angular spectrograms can also be used in speckle metrology, more precisely for determining the local displacement, or deformation of an object, which are digitally coded in specklegrams [48]. The technique is particularly suitable for detecting nonuniform deformations such as compression or stretching.

Self-referenced spectrograms use gated signals related to the unknown signal. In particular, self-referenced spectrograms used for characterization of pulses are called frequency-resolved optical gating or FROG techniques. Reviews on FROG techniques that include a detailed discussion on their implementation can be found in [5, 49]. Different FROG versions use different gates, generated by nonlinear interactions. Therefore, FROG needs angular tuning or very thin nonlinear crystals to access a wide frequency interval. Moreover, FROG are not suitable for low-power THz sources, in which nonlinear effects are quite difficult to achieve. Generally, the FROG technique needs a recording camera with high linearity and high dynamic range, and becomes awkward to use for complex pulses, for which the time needed for the iterative algorithm to converge increases significantly. In contrast to SPIDER, FROG implementation is simpler and the results of field recovery can be checked by complementary experiments.

An example of FROG is the polarization gating or PG-FROG, for which $G(u) = |E(u)|^2$ is generated by a Kerr-optical gate. This FROG technique can indicate

directly the sign of the signal and the presence of a chirp. A real-time device that implements a PG-FROG in a single-shot geometry, as well as the iterative algorithm for phase retrieval are presented in [50].

One of the most widespread FROG, which is also easier to implement than PG-FROG, is the second-order harmonic SHG-FROG, which is a spectrally resolved second-harmonic pulse obtained by nonlinear mixing the unknown pulse with a delayed replica. In this case, $G(u) = E(u)$ but in field recovery applications it is not possible to distinguish between $E(u)$ and $E(-u)$ because the signal is symmetric in time. The time ambiguity can be solved by an additional measurement of the unknown pulse after propagation through a material with known dispersion [51]. The amplitude and spectral phase are retrieved through an iterative algorithm [51, 52]. An implementation of the SHG-FROG in a noncollinear geometry in the single-cycle regime is described in [53]. SHG-FROG can determine the amplitude and phase of nonamplified pulses generated by femtosecond oscillators [51]. The use of SHG-FROG of 0.6 THz pulses for studying the complex spectral modulation pattern in polarization domain walls is reported in [54], while single-cycle measurements of pulses as short as 4.9 fs is demonstrated in [55].

An example of SHG-FROG study of dynamical processes related to self-compression by filamentation of ultrashort pulses can be found in [56]. This study evidenced the role of spatio-temporal reshaping in pulse propagation, caused by the competition between group velocity dispersion and self-phase modulation. SHG-FROG was also recently used to characterize the performance of fiber links at 1550 nm designed to deliver ultrashort low-energy (of 1 nJ) pulses [57]. Such studies allow the observation of the transition between the low-power propagation regime, dominated by dispersive effects, and the high-power regime, where nonlinear phenomena become significant. The fiber link is composed of a dispersion-compensated fiber section, which has high dispersion and nonlinear coefficients, pigtailed with single-mode fiber sections which stretch and compress the pulse.

A particular realization of the SHG-FROG for THz pulses is the single-shot spectrally resolved autocorrelation, referred to also as GRENOUILLE [5]; in this case the output of the autocorrelator is focused on the input slit of the spectrometer and the SHG-FROG is recorded by a CCD camera situated at the output of the spectrometer. Another SHG-FROG-related technique, especially suitable for characterizing weak and broadband pulses, is the rotaryFROG [58]. In this technique, the SHG crystal is rotated about an axis that is almost collinear with the direction of the incident pulse. In this way, the requirement of pulse bandwidth being less than the phase-matching bandwidth of the SHG crystal (determined by its thickness) is alleviated, since the narrow bandwidth of the thick SHG crystal is mechanically scanned over the much wider bandwidth of the signal.

Another FROG version is the THG FROG, for which $G(u) = E^2(u)$. It has the advantage of no ambiguity in the direction of time with the exception of (improbable) pure Gaussian intensity pulses and pure linear chirps. However, this technique can recover the relative phase of two well-separated pulses modulo $2\pi/3$. (For comparison, SHG FROG can recover the relative phase modulo π .) Unlike usual third-order processes, which are suitable for measuring high-energy pulses, of about $1 \mu\text{J}$ in

single-shot measurements, surface third-harmonic generation processes can be used for recovering pulses with powers of few nW [59]. The setup and the retrieval algorithm are similar to those for SHG FROG.

An exception of FROG family techniques is the referenced XFROG, which records the spectrally resolved cross-correlation between two different pulses, so that G is not related to E . Its disadvantage is that it cannot determine the relative phase of non-overlapping pulses. XFROG traces have been used to characterize pulses as short as 63 fs, produced by a BiB₃O₆-based femtosecond optical parametric generator [60]. XFROG has been recently used to completely characterize the field of attosecond pulses [61] generated from below-threshold harmonics generated from the nonperturbative interaction of a laser with an atomic gas. In this case XFROG is obtained from two adjacent harmonic orders and helps to elucidate the generation mechanism of below-threshold harmonics.

6.3.4 The Wavelet Transform and Its Applications in Signal Processing

The wavelet is a referenced phase-space transform that is mostly used for analyzing and coding complex nonstationary or transient signals, such as seismic signals, speech, or electrocardiogram signals. Transient signals can be encountered also in biology. For example, Minke whales and bottlenose dolphins emit sounds that have FM components. Although similar to the short- u Fourier transform in that it contains information about the signal in the joint u - v domain due to a window function, the wavelet is more flexible because the window has a variable width and shape, the analyzing functions being no longer limited to sinusoids. In this sense, the wavelet decomposes the signal in components in a much more effective way than the short- u Fourier transform, both short- u and high- v components and long- u and low- v components being distinguished with a reasonable degree of accuracy. Another advantage of the wavelet transform, shared with the short- u Fourier transform and the spectrogram, is the absence of cross-terms that appear in the WDF when a superposition of signals is considered. The flexibility of the wavelet transform is guaranteed by v -dependent windows, which allow high resolution in both u and v domains, and by the choice of many mother wavelet functions. The wavelet transform of the electric field is defined as

$$T(\xi, u') = \frac{1}{\sqrt{\xi}} \int E(u) \Psi^* \left(\frac{u - u'}{\xi} \right) du = \frac{1}{\sqrt{\xi}} \int \tilde{E}(\xi v) \tilde{\Psi}^*(v) \exp(i v u') dv, \quad (6.28)$$

where $\Psi(u)$ is the mother wavelet, u' is the location parameter and ξ is the dilation/scaling parameter. The wavelet transform expands the signal in terms of daughter wavelets $\Psi((u - u')/\xi)$, which are translated and dilated versions of the mother wavelet. Unlike sinusoids, the wavelets are localized in u and v domains, which implies that reconstruction and manipulation of signals can be performed

with greater numerical stability. The dilation parameter is related to the ν -domain information on the signal since the spectral components are inversely proportional to the dilation: $\nu = \nu_c/\xi$, where ν_c is the characteristic frequency of the mother wavelet [14]. So, the dilation parameter determines the scale in the frequency domain: high-frequency wavelets have $\xi < 1$, whereas low-frequency wavelets correspond to $\xi > 1$.

A function is a wavelet if:

- (a) It has finite energy: $\int |\Psi(u)|^2 du < \infty$,
- (b) Its Fourier transform has no zero- ν components, i.e. $\tilde{\Psi}(0) = 0$ or $C_T = \int_0^\infty (|\tilde{\Psi}(v)|^2/\nu) dv < \infty$, where $\tilde{\Psi}(v) = (2\pi)^{-d/2} \int \Psi(u) \exp(iuv) du$, and
- (c) For analytic signals the Fourier transform of the mother wavelet must be real and must vanish for negative ν values.

Among the best known mother wavelets we mention the (original) Haar wavelet

$$\Psi_H(u) = \begin{cases} 1, & 0 < u \leq 1/2 \\ -1, & 1/2 < u \leq 1 \\ 0, & \text{otherwise} \end{cases} \quad (6.29)$$

which is not continuous and decays only as $1/|v|$, the Meyer wavelet, the Mexican hat wavelet, $\Psi_h(u) = (1 - u^2) \exp(-u^2/2)$, the Morlet wavelet $\Psi_M(u) = \pi^{-1/4} [\exp(iau) - \exp(-a^2/2)] \exp(-u^2/2)$ [14], in which the second term in the brackets can be neglected for $a > 5$, and the compactly supported Daubechies wavelet [62].

Analogous to the Fourier transform, the signal can be recovered from the wavelet through an inverse transform

$$E(u) = C_T^{-1} \xi^{-1/2} \int_{-\infty}^{\infty} \int_0^{\infty} T(\xi, u') \Psi\left(\frac{u - u'}{\xi}\right) \frac{d\xi du'}{\xi^2} \quad (6.30)$$

In analogy to the spectrogram, the square modulus of the wavelet, $S_T(\xi, u') = |T(\xi, u')|^2$ is called scalogram. Because the relative energy of the signal at a specific ξ scale is defined as $\text{En}(\xi) = C_T^{-1} \int |T(\xi, u')|^2 du'$, the peaks in $\text{En}(\xi)$ represent the dominant energy scales in the signal. Moreover, the wavelet ridges, determined from $d(S_T(\xi, u')/\xi)/d\xi = 0$ are related to the local (instantaneous, for pulses) frequencies and amplitudes of the signal, whereas the modulus maxima, defined as $dS_T(\xi, u')/du' = 0$ are related to the singularities in the signal [14].

The wavelet transform offers quite an intuitive representation of the signal: the wavelet has an upward slope for a signal with a linearly increasing frequency, for example, peaks in the wavelets indicate discontinuities in the input signal, and superpositions of signals that start at different times are represented by superpositions of wavelets starting at different times [62].

Apart from the continuous wavelet transform described above, the discrete wavelet transform is extensively used [14]. In this case, the wavelet transform is computed at

u' values discretized at the chosen sampling interval, i.e. $u' = nu'_0$, and at ξ values discretized logarithmically, i.e. $\xi = \xi_0^m$. The discrete wavelet transform is defined as

$$\Psi_{m,n}(u) = \frac{1}{\sqrt{\xi_0^m}} \Psi\left(\frac{u - nu'_0 \xi_0^m}{\xi_0^m}\right) = \xi_0^{-m/2} \Psi(\xi_0^{-m} u - nu'_0), \quad (6.31)$$

or $\Psi_{m,n}(u) = 2^{-m/2} \Psi(2^{-m} u - n)$ for the dyadic grid for which $\xi_0 = 2$, $u'_0 = 1$. If $m \ll 0$, the window narrows since ξ_0^m is compressed, and thus the frequency of the wavelet is high and the u -step, $u'_0 \xi_0^m$, is small. On the contrary, for $m \gg 0$ the window dilates, the wavelet frequency is low, and the u -step is high. If $\xi_0 = 2^{1/\nu}$ with ν an integer, the set of ν discrete wavelet transforms can be processed as one group, which is referred to as voice in acoustics. Then, ν is the number of voices per octave [62].

One can introduce orthonormal wavelet bases functions $\int \Psi_{m,n}(u) \Psi_{m',n'}(u) du = \delta_{m,m'} \delta_{n,n'}$, which have the advantage that the information in the discrete wavelet transform $T_{m,n} = \int E(u) \Psi_{m,n}(u) du$ is not redundant and can be used to completely recover the original signal [14]. $T_{m,n}$ are the detail coefficients or wavelet coefficients of the signal. Orthonormal discrete wavelets are associated with a set of displaced and dilated scaling functions which, for the dyadic grid, take the form $\Phi_{m,n}(u) = 2^{-m/2} \Phi(2^{-m} u - n)$ and are related to the smoothing of the signal. These wavelets are derived from the father function $\Phi(u) = \Phi_{0,0}(u)$, which satisfy the property $\int \Phi_{0,0}(u) du = 1$, and are orthogonal to their translated versions, but not to their dilated versions. They generate the approximation coefficients of the signal $S_{m,n} = \int E(u) \Phi_{m,n}(u) du$. A signal can then be recovered from

$$E(u) = \sum_{n=-\infty}^{\infty} S_{k,n} \Phi_{k,n}(u) + \sum_{m=-\infty}^k \sum_{n=-\infty}^{\infty} T_{m,n} \Psi_{m,n}(u) = E_k(u) + \sum_{m=-\infty}^k d_m(u), \quad (6.32)$$

this formula expressing the fact that a signal can be regarded as a series of approximations of itself, with scale index k , and a succession of signal details scaling from k to negative infinity. In particular, if the signal detail at scale m , given by $d_m = \sum_{n=-\infty}^{\infty} T_{m,n} \Psi_{m,n}(u)$, is added to the approximation of the signal at that scale, $E_m(u)$, we obtain the signal at a smaller scale, i.e. with increased resolution: $E_{m-1}(u) = E_m(u) + d_m(u)$. This representation is known as multiresolution representation [14], and is the most important property of the wavelet transform. Both the detail and approximation coefficients at scale index $m + 1$ can be related to the approximation coefficients at the previous scale through

$$S_{m+1,n} = 2^{-1/2} \sum_k c_{k-2n} S_{m,k}, \quad T_{m+1,n} = 2^{-1/2} \sum_k b_{k-2n} S_{m,k}. \quad (6.33)$$

This allows a multiresolution decomposition algorithm of the signal that computes the wavelet coefficients iteratively, starting from previous ones, instead of performing calculations of integrals. In practice, $2^{-1/2} c_k$ is a lowpass filter, that allows the

passage through of low frequencies, and thus of a smoothed version of the signal, while $2^{-1/2}b_k$ is a highpass filter that allows the passage through of high frequencies, and thus of the details in the signal under investigation. These filters define the wavelet. In the reconstruction algorithm the inverse relation is used (see examples in [14]):

$$S_{m-1,n} = 2^{-1/2} \sum_k c_{n-2k} S_{m,k} + 2^{-1/2} \sum_k b_{n-2k} T_{m,k}. \quad (6.34)$$

The wavelet transform is usually implemented by a bank of Vander Lugt matched filters [63]. The wavelet transform analysis of an unknown signal is performed by a bank of filters. It is helpful in this situation to be able to produce the wavelet coefficients for different ξ and u' values. An optical implementation of such a device that includes cylindrical Fourier transform lenses, an acousto-optic cell and a spatial light modulator, and that generates the wavelet coefficient in the $\xi - u'$ plane is presented in [63]. This 2D optical correlator (bank of 1D wavelet filters) can then be used to analyze a 1D signal.

In principle, every application that involves the (fast) Fourier transform can employ wavelets, with the advantage that the best trade-off between resolutions in the u and v domains can be reached with the wavelet transform. Wavelets provide faster signal analysis and better noise thresholding (in fact, near optimal noise reduction properties) when applied to THz image analysis compared to Fourier-transform methods because the (mother) wavelets fit more closely a wide range of unknown signals than the Fourier transform [64]. In particular, the discrete wavelet transform has a complexity order $O(N)$, whereas the fast Fourier transform has complexity order $O(N \log N)$. Medical imaging is an emerging field of THz imaging because THz radiation does not harm the tissue. In this respect, wavelets are deeply involved in modern-day diagnosis [65]. A wavelet-based multiscale Bi-spline algorithm can also be used to recognize and classify chromosome images in an automatic procedure [66]. Related applications of the wavelet transform include efficient signal coding and compression of a wide range of biomedical signals (see [14] and references therein), favored by the fact that the information contained in the signal can be localized within a number of few wavelet coefficients. Wavelet transforms have been found useful in acoustics for speech analysis, but also for detecting defects/irregularities in different materials/equipments during non-destructive automated quality control procedures [67].

Image compression for both still and video imaging is one of the most common applications of wavelets, and is included in the present JPEG and MPEG norms [67]. For example, the JPEG 2000 standard is based on discrete wavelet analysis in Daubechies biorthogonal bases. In general, wavelets are employed whenever a trade-off between image quality and size is an issue. The wavelet-based compression of digitized images involves the extraction of the visible elements only, based on psychovisual features in space and frequency that allow image decomposition at different scales using a set of biorthogonal subclasses of images, followed by encoding of the visible elements using a noise shaping bit allocation procedure which exploits the fact that the high-resolution details are less visible [68].

The wavelet transform can be used to develop a depth-image-based representation (DIBR) codec that lets consumers choose freely the viewpoint [69]. The DIBR allows compact bitstreams and is part of the MPEG-4 standard. This problem arises in free-viewpoint 3D television, in which the viewer can move inside the video with a third stereoscopic dimension and choose the viewing location. Such a problem presents a real challenge since the depth estimation and the image and depth encoding are carried out jointly even if the depth map is unknown.

The wavelet transform is also used to remove noise through different methods, to monitor power quality, or to estimate speed without using sensors (only by analyzing the wavelet transform of the stator current signal). Because in Fourier transform spectrometry the noise power in the sample interferogram is related to the noise power in the wavelet coefficients, low-frequency noise, for example, can become separated from other spectral regions at small scales (small ξ values), when the wavelet coefficients are associated to narrow frequency intervals [70]. On the contrary, the low-frequency noise mixes with data from other spectral regions if the scale increases, case in which the wavelet coefficients are associated with wider frequency intervals.

In another application, the frequency breakdown of an extrinsic Fabry–Perot interferometer has been determined efficiently using wavelet analysis [71], which provided the lowest dominant frequencies of the system and their occurrence times. Noise removal and automatic counting of interference fringes in this system can also be performed with the help of wavelets.

A hybrid frequency-wavelet domain deconvolution can be used to process signals resulting from THz spectroscopy and THz reflection imaging with low signal-to-noise ratio [72]. The hybrid process refers to a combination of wavelet denoising and inverse filtering in the frequency domain. The hybrid frequency-domain wavelet deconvolution increases the bandwidth of the signal besides removing unwanted noise.

Other versions of the wavelet transform are encountered in specific applications. In image applications, at least, the over-complete wavelet transform can be faster and more flexible than the discrete wavelet transform, allowing non-uniform sampling and the possibility of bandwidth adjustment [64]. Chirplet analysis has the advantage over the wavelet transform that the cell shape in which the wavelet dissects the u - v plane is no longer u -invariant. More precisely, chirplets use oblique cells optimized for the local structure of the signal [62].

Note that in some applications the performance of wavelet-based analysis is overruled by a similar analysis in terms of the Gabor coefficients, which can be defined in terms of the short- u Fourier transform as $G_{m,n} = S_F(mu', nv) = \int E(u)G(u - mu') \exp(invu)du$. An example of such an application is subband echo cancellation [17]. However, in most cases due to the fixed width of the window function, the Gabor transform will sample high (low)-frequency signals at high (low) rates, which is not optimal.

6.3.5 The Fractional Fourier Transform and Its Applications in Signal Processing

The FRFT is not, strictly speaking, a phase-space distribution function, since it does not depend on the u and v variables simultaneously. However, it can be seen as a mixed u - v transform because, depending on the degree of fractionality, it is defined in the u domain, in the v domain, or in a mixed u - v space. Actually, the FRFT of order (degree of fractionality) α is defined as [73]

$$F_\alpha(v) = \frac{\exp[i(\pi \operatorname{sgn} \alpha - 2\alpha)]}{4(2\pi |\sin \alpha|)^{d/2}} \exp\left(-\frac{i}{2}v^2 \cot \alpha\right) \int \times \exp\left(i \frac{uv}{\sin \alpha} - \frac{i}{2}u^2 \cot \alpha\right) E(u) du \quad (6.35)$$

for $0 < |\alpha| < \pi$. We have $F_{\pi/2}(v) = \tilde{E}(v)$, $F_0(v) = E(v)$, and $F_{\pm\pi}(v) = E(-v)$. Being linear, FRFT has no cross-terms when superpositions of signals are involved.

The square modulus of $F_{\pi/4}$ in Figs. 6.6a–f correspond to the input signals (a)–(f) in the examples above. As shown in Figs. 6.6b and 6.6c, the FRFT suffers a shift in both u and v domains as the input signal shifts, similar to the phase-space distribution functions discussed above; the FRFT appears to be an intermediate representation between the representations in the u and v domains. In addition, as the degree of fractionality increases from 0 to $\pi/2$, the distance between the Gaussian functions in the superposition in (f) decreases until they overlap and interfere (remember that $|F_0|^2 = I$ and $|F_{\pi/2}|^2 = \tilde{I}$). The intermediate situation, for $\alpha = \pi/4$ is represented in Fig. 6.6f.

It should be emphasized that the FRFT is not only related to the Fourier transform, i.e. to the diffracted electromagnetic wave in the far-field region, but also to the diffracted field in the near-field region, described by the Fresnel approximation of the Kirchhoff's diffraction integral. FRFT with scaled arguments and degree of fractionality $\alpha = \tan^{-1}(kz)$ can describe uniquely the diffraction of a light wave at any transverse plane $z = \text{const.}$, in the near as well as the far-field diffraction regimes [74].

Note that, up to a constant factor, the FRFT is a wavelet transform, in which the mother wavelet is $\Psi(u) = \exp(-iu^2/2)$, i.e. a chirp function, $u' = v \sec \alpha$ and $\xi = \tan^{1/2} \alpha$ [75]. Continuous FRFT are reviewed in [73, 76], while discrete FRFT are detailed in [77].

Analogous to the u - v uncertainty relation in Fourier transform-related domains, a similar uncertainty relation in fractional Fourier domains can be expressed as $\Delta u_\alpha^2 \geq \Delta u_u^2 \cos^2 \alpha + \sin^2 \alpha / (4\Delta u_\alpha^2)$ [78]. Here Δu_α is the standard deviation in the fractional Fourier domain with order α . The u - v uncertainty product is recovered for $\alpha = \pi/2$. In a similar manner, the uncertainty principle between two FRFT orders can be expressed as $\Delta u_\alpha^2 \Delta u_\beta^2 \geq (1/4) \sin^2(\alpha - \beta)$.

The FRFT is also related to the WDF. In fact, the FRFT with order α corresponds to a clockwise rotation of the WDF in the phase space with angle α [79]. A particular

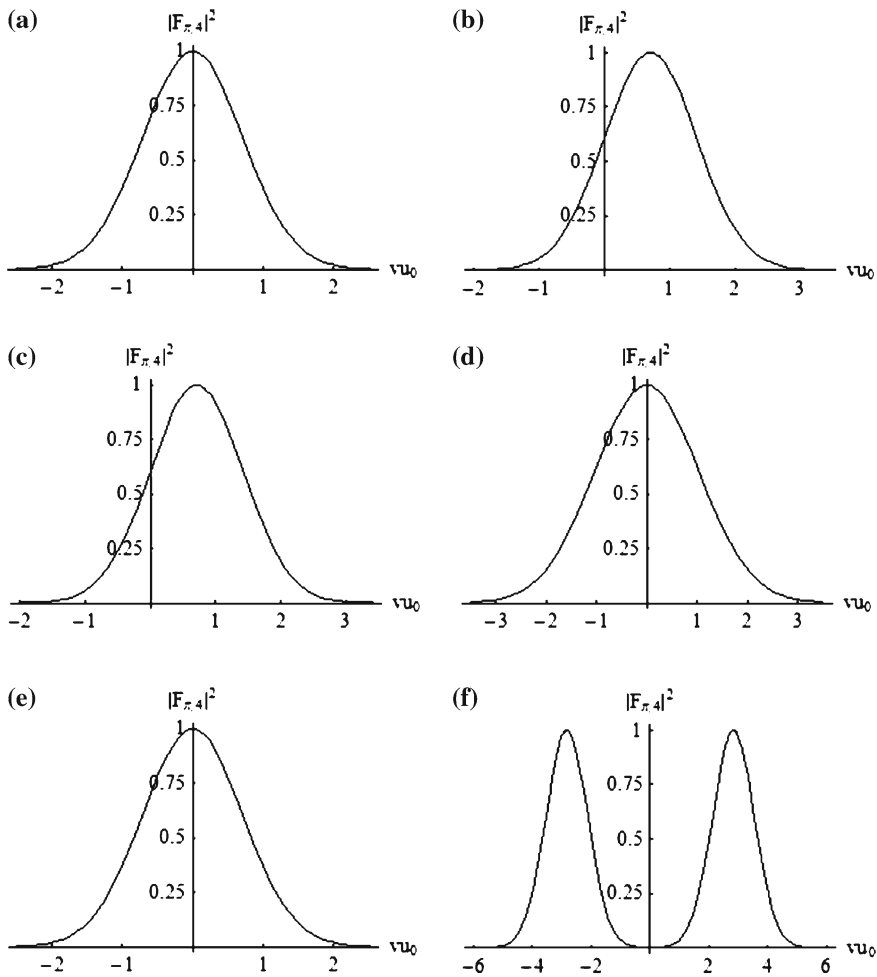


Fig. 6.6 Normalized squared modulus of the FRFT with degree of fractionality $\pi/4$ of the same signals as in Fig. 6.1

form of the rotated WDF that can be measured in tomography is the Radon transform, or fractional power spectrum

$$\tilde{I}_\alpha(v) = \int W(u \cos \alpha + v \sin \alpha, v \cos \alpha - u \sin \alpha) du. \quad (6.36)$$

The fractional power spectrum is the marginal of the WDF rotated with angle α , and is equal to the square modulus of the FRFT of order α [80]. A recursive algorithm that allows phase retrieval from two intensities measured in different fractional domains, α and β , is described in [81].

Since the WDF of a chirp $\exp[i(au^2/2 + bu + c)]$ is a delta function represented by an oblique line in phase space, $\delta(au + b - v)$, which represents the instantaneous frequency of the signal, the degree of fractionality of the FRFT can be tuned to provide an optimal response to a chirped signal. More precisely, the optimum FRFT has an order $\alpha_{\text{opt}} = -\tan^{-1}(1/a)$, and the location of the peak of the FRFT with this degree of fractionality determines the center frequency of the signal: $v_0 = b \sin \alpha_{\text{opt}}$ (for discussions related to the discretized version of FRFT of chirped signals, see [78]). The optimum degree of fractionality corresponds to the most compact fractional domain representation of the chirp, i.e. the smallest Δu_α , while for $\alpha_{\text{opt}} - \pi/2$ we obtain the broadest representation of the signal. The optimum degree of fractionality for the function (e) in the examples considered is $-\pi/4$; $|F_{-\pi/4}|^2 = |F_{\pi/4}|^2$, represented in Fig. 6.6e. FRFT is particularly suitable for the characterization of chirped pulses that propagate through a linear dispersive medium, because the basis functions of the FRFT are linearly chirped functions [82]. Finite signals can be decomposed in a FRFT series expansion in an orthonormal basis of linearly chirped functions with few expansion coefficients [82], such decompositions being useful for signal reconstruction and filtering. Chirps in time domain can be implemented by electro-optical modulators, for example, while in the spatial domain they are produced by lenses. Chirp control is essential for producing ultrashort pulses.

The FRFT in space domain is naturally performed by light propagation in graded-index waveguides with specified lengths, or in set-ups involving free-space propagation and lenses [73]. In fact, the close relation between FRFT and chirp signals can be understood from the fact that quadratic graded-index media are limiting cases of a periodic arrangement of free space and positive lenses that compensate for the spread due to diffraction [75]. Other setups, such as those that implement the anamorphic FRFT (with different orders along perpendicular directions) or a set of FRFT with different degrees of fractionality are mentioned in [73], while a setup that generates a FRFT of an incident pulse with a continuously variable order is described in [83, 84]. The last setup is based on off-axis propagation of a light wave in a hemispherical-rod microlens with a parabolic refractive index, the output being collected on the planar face of the microlens. The discrete implementation of the FRFT has been discussed in [78].

The temporal analog of the setups that implement the FRFT using free-space propagation and lenses are obtained from the setups in the spatial domain using the space-time analogy [85, 86], while the graded-index fiber has been shown to be equivalent in the temporal domain to a dispersive and nonlinear Kerr medium that allows soliton propagation, which modifies temporally the refractive index of the medium [87]. In the last case, if the waveguide has an oblique cut, FRFTs with continuously variable degrees of fractionality are obtained at the output.

FRFT has been applied to spatial filtering. The result is especially promising if the noise can be modeled as linear combination of chirp functions. Then, noise can be filtered out in the fractional domain in which it became separated from the signal. Cascaded filtering in several fractional domains can be applied, if necessary [75]. In addition, multiplexing of signals with oblique WDF can be efficiently achieved in

the FRFT domain if the degree of fractionality is chosen such that the WDF is no longer oblique [75].

Analogously, the separation between two signals can be increased using the scaling property of the FRFT [88]. More precisely, if the signal consisting of two terms is scaled with c , the separation between the terms in the β FRFT domain increases with respect to that in the α FRFT domain with the factor $\sin \beta/c \sin \alpha$. The separation between delayed signals can also be increased by a succession of phase multiplication and addition and subtraction operations [88]. Moreover, fractional correlators implemented with anamorphic FRFT can simultaneously detect different objects or deformations of these objects in different parts of an input image [89]. This application is based on the fact that the order of the FRFT controls the shift-invariant property of an optical correlator.

The analogy between Fresnel diffraction and the FRFT has been used to develop a double-random phase encryption technique for primary images or for their temporal analogs (time-varying signals) into stationary white noise [90]. The α degrees of the FRFTs involved serve in this case as keys. FRFT can be used also in coding schemes which use chirp signals and binary coded sequences. In tissue harmonic imaging, for example, chirp-coded excitation generates other chirp signals with the same phase relationship (unlike binary-coded signals, which do not preserve their phase relationship). Moreover, chirp-coded excitation associated with the FRFT can compress the second harmonic generation signal produced by nonlinear propagation of ultrasounds in water [91].

Another application of the FRFT is direct reconstruction of in-line holograms that visualize small particles, recorded with ultrashort lasers, from which it is possible to extract the 3D location and size of the particles [92]. Compared to other methods, the reconstruction is improved for an optimal degree of fractionalization.

The success of FRFT prompted researchers to consider other fractional transforms, such as the fractional Hilbert [93], Fresnel, Fraunhofer, Mellin, Hartley [94], Zernike, Talbot [73], and Montgomery effects [95], and even the fractional WDF [96]. The space–time duality was applied to implement the setups that generate the fractional Hartley and Mellin transforms in the temporal domain based on the corresponding setups in the spatial domain [86].

There are also transforms closely related to the FRFT. For example, analogous to the short-time Fourier transform for pulses, a short-time FRFT can be defined [78], which has a better time–frequency resolution compared to the short-time Fourier transform. If the window is the same over the signal, the fractional degree α of the short-time FRFT can be chosen by a global optimization procedure, whereas α values for each windowed section can be chosen independently in locally optimized short-time FRFT.

6.4 Conclusions

A short overview of the most commonly used phase-space distribution functions: the WDF, the ambiguity function, the spectrogram, the wavelet transform, and the FRFT, has been presented. Besides their general properties, this review tackled the problems related to the implementation of phase-space distribution functions and mentioned briefly some applications related to THz signal processing. Whenever possible, the space–time duality was emphasized as a useful tool for relating spatial-angular to time–frequency phase spaces and, in particular for relating, setups that implement phase-space distribution functions in these domains. Phase-space distributions do not contain additional information about the signal compared to the information that can be gathered in u - or v -domain analyses, but the information is more efficiently and intuitively presented, and hence easier to interpret, and, more importantly, (some) phase-space distribution functions can be measured with higher resolutions in both u and v domains. The applications of phase-space distribution functions to the characterization and processing of THz signals evolve continuously and, hopefully, together with the growth of the THz research domain.

References

1. D. Dragoman, M. Dragoman, *Prog. Quantum Electron.* **28**, 1 (2004)
2. B.J. Williams, *Nat. Photonics* **1**, 517 (2007)
3. A.M. Weiner, *Rev. Sci. Instrum.* **71**, 1929 (2000)
4. S. Akturk, X. Gu, P. Bownan, R. Trebino, *J. Opt.* **12**, 093001 (2010)
5. A. Monmayrant, S. Weber, B. Chatel, *J. Phys. B* **43**, 103001 (2010)
6. S.P. Jamison, J. Shen, A.M. MacLeod, W.A. Gillespie, D.A. Jaroszynski, *Opt. Lett.* **28**, 1710 (2003)
7. I.A. Walmsley, C. Dorrer, *Adv. Opt. Photonics* **1**, 308 (2009)
8. C. Iaconis, I.A. Walmsley, *Opt. Lett.* **21**, 1783 (1996)
9. T.E. Gureyev, A. Roberts, K.A. Nugent, *J. Opt. Soc. Am. A* **12**, 1942 (1995)
10. C. Dorrer, I.A. Walmsley, *EURASIP J. Appl. Sig. Process.* **10**, 1541 (2005)
11. C. Iaconis, I.A. Walmsley, *Opt. Lett.* **23**, 792 (1998)
12. W. Kornelis, J. Biegert, J.W.G. Tisch, M. Nisoli, G. Sansone, C. Vozzi, S. De Silvestri, U. Keller, *Opt. Lett.* **28**, 281 (2003)
13. P. Bownan, P. Gabolde, R. Trebino, *Opt. Express* **15**, 10219 (2007)
14. P.S. Addison, *Physiol. Meas.* **26**, R155 (2005)
15. B.H. Kolner, *J. Quantum Electron.* **30**, 1951 (1994)
16. L. Cohen, *Proc. IEEE* **77**, 941 (1989)
17. S. Qian, D. Chen, *IEEE Signal Processing Magazine*, 52 (March 1999).
18. E. Sejdić, I. Djurović, J. Jiang, *Digital Sig. Proc.* **19**, 153 (2009)
19. T. Iwai, N. Kawamura, T. Takemori, *Opt. Commun.* **95**, 199 (1993)
20. T.A.C.M. Claassen, W.F.G. Mecklenbräuker, *Philips J. Res.* **35**, 217 (1980)
21. D. Dragoman, *Prog. Opt.* **37**, 1 (1997)
22. D. Dragoman, *EURASIP J. Appl. Sig. Process.* **10**, 1520 (2005)
23. J. Azaña, *EURASIP J. Appl. Sig. Process.* **10**, 1554 (2005)
24. T.A.C.M. Claassen, W.F.G. Mecklenbräuker, *Philips J. Res.* **35**, 276 (1980)
25. F. Peyrin, R. Prost, *IEEE Trans. Acoust. Speech Sig. Proc.* **34**, 858 (1986)

26. A.G. Kostenbauder, IEEE J. Quantum Electron. **26**, 1148 (1990)
27. J. Paye, A. Migus, J. Opt. Soc. Am. B **12**, 1480 (1995)
28. D. Dragoman, M. Dragoman, Appl. Opt. **35**, 7025 (1996)
29. H. Weber, J. Mod. Opt. **39**, 543 (1992)
30. J. Paye, IEEE J. Quantum Electron. **28**, 2262 (1992)
31. M. Beck, M.G. Raymer, I.A. Walmsley, V. Wong, Opt. Lett. **18**, 2041 (1993)
32. A. Gover, E. Dyunin, Y. Lurie, Y. Pinhasi, M.V. Krongauz, Phys. Rev. Special Topics **8**, 030702 (2005)
33. J. Azaña, M.A. Muriel, J. Opt. Soc. Am. A **17**, 2496 (2000)
34. L. Onural, T. Özgen, J. Opt. Soc. Am. **9**, 252 (1992)
35. M.T. Özgen, K. Demirbaş, J. Opt. Soc. Am. A **15**, 2117 (1998)
36. K.B. Wolf, D. Mendlovic, Z. Zalevsky, Appl. Opt. **37**, 4374 (1998)
37. M.C. Beard, G.M. Turner, C.A. Schmuttenmaer, J. Phys. Chem. B **106**, 7146 (2002)
38. A.B. U'Ren, Y. Jeronimo-Moreno, H. Garcia-Gracia, Phys. Rev. A **75**, 023810 (2007)
39. D.S. Monaghan, U. Gopinathan, D.P. Kelly, T.J. Naughton, J.T. Sheridan, Opt. Engn. **48**, 027001 (2009)
40. G.F. Boudreaux-Bartels, in *The Wigner Distribution - Theory and Applications, in Signal Processing*, ed. by W. Mecklenbräuker, F. Hlawatsch (Elsevier, Amsterdam, 1997), pp. 269–317
41. A. Papoulis, J. Opt. Soc. Am. **64**, 779 (1974)
42. T.A.C.M. Claesen, W.F.G. Mecklenbräuker, Philips J. Res. **35**, 372 (1980)
43. D. Dragoman, M. Dragoman, K.-H. Brenner, Opt. Lett. **27**, 1519 (2002)
44. D. Dragoman, M. Dragoman, K.-H. Brenner, Appl. Opt. **39**, 2912 (2000)
45. A.N. Yur'yev, Telecommun. Radio Engn. **49**, 72 (1995)
46. I.G. Cormack, W. Sibbett, D.T. Reid, J. Opt. Soc. Am. B **18**, 1377 (2001)
47. D. Dragoman, M. Dragoman, J. Bähr, K.-H. Brenner, Appl. Opt. **38**, 5019 (1999)
48. W.D. Furlan, G. Saavedra, E. Tajahuerce, Appl. Opt. **34**, 4713 (1995)
49. R. Trebino, K.W. DeLong, D.N. Fittinghoff, J.N. Sweetser, M.A. Krumbügel, B.A. Richman, Rev. Sci. Instrum. **68**, 3277 (1997)
50. D.J. Kane, J. Weston, K.-C.J. Chu, Appl. Opt. **42**, 1140 (2003)
51. J. Paye, M. Ramaswamy, J.G. Fujimoto, E.P. Ippen, Opt. Lett. **18**, 1946 (1993)
52. D.J. Kane, IEEE J. Sel. Top. Quantum Electron. **4**, 278 (1998)
53. A. Baltuška, M.S. Pshenichnikov, D.A. Wiersma, IEEE J. Quantum Electron. **35**, 459 (1999)
54. F. Guty, S. Pitois, P. Grelu, G. Millot, M.D. Thomson, J.M. Dudley, Opt. Lett. **24**, 1389 (1999)
55. S. Akturk, C. D'Amico, A. Mysyrowicz, J. Opt. Soc. Am. B **25**, A63 (2008)
56. S. Akturk, A. Couairon, M. Franco, A. Mysyrowicz, Opt. Express **16**, 17626 (2008)
57. F. Eichhorn, R.K. Olsson, J.C.D. Buron, L. Grüner-Nielsen, J.E. Pedersen, P.U. Jepsen, Opt. Express **18**, 6978 (2010)
58. A. Ellis, U. Österberg, Opt. Lett. **34**, 404 (2009)
59. T. Tsang, M.A. Krumbügel, K.W. DeLong, D.N. Fittinghoff, R. Trebino, Opt. Lett. **21**, 1381 (1996)
60. A. Gaydardzhiev, I. Nikolov, I. Buchvarov, V. Petrov, F. Noack, Opt. Express **16**, 2363 (2008)
61. E.P. Power, A.M. March, F. Catoire, E. Sistrunk, K. Krushelnick, P. Agostini, L.F. DiMauro, Nat. Photonics **4**, 352 (2010)
62. D.T.L. Lee, A. Yamamoto, Hewlett-Packard J., 44 (December 1994).
63. H. Szu, Y. Sheng, J. Chen, Appl. Opt. **31**, 3267 (1992)
64. S. Mickan, D. Abbott, J. Munch, X.-C. Zhang, T. Van Doorn, Microelectron. J. **31**, 503 (2000)
65. M. Unser, A. Aldroubi, A. Laine (eds.), Wavelets in medical imaging, IEEE Trans. Med. Imaging **22** (2003)
66. D. Ming, J. Tian, J. Infrared Milli, Terahz. Waves **31**, 866 (2010)
67. F. Truchetet, O. Laligant, Proc. SPIE **5607**, 1 (2004)
68. M. Antonini, M. Barlaud, P. Mathieu, I. Daubechies, IEEE Trans. Image Process. **1**, 205 (1992)
69. M. Maitre, Y. Shinagawa, M.N. Do, IEEE Trans. Image Process. **17**, 946 (2008)
70. R.K.H. Galvão, S. Hadjiloucas, J.W. Bowen, C.J. Coelho, Opt. Express **11**, 1462 (2003)

71. T.K. Gangopadhyay, S. Chakravorti, K. Bhattacharya, S. Chatterjee, *Meas. Sci. Technol.* **16**, 1075 (2005)
72. Y. Chen, S. Huang, E. Pickwell-MacPherson, *Opt. Express* **18**, 1177 (2010)
73. A.W. Lohmann, D. Mendlovic, Z. Zalevsky, *Prog. Opt.* **38**, 263 (1998)
74. D. Dragoman, M. Dragoman, *Opt. Commun.* **141**, 5 (1997)
75. H.M. Ozaktas, B. Barshan, D. Mendlovic, L. Onural, *J. Opt. Soc. Am. A* **11**, 547 (1994)
76. L.B. Almeida, *IEEE Trans. Sig. Proc.* **42**, 3084 (1994)
77. Ç. Candan, M.A. Kutay, H.M. Ozaktas, *IEEE Trans. Sig. Proc.* **48**, 1329 (2000)
78. C. Capus, K. Brown, *J. Acoust. Soc. Am.* **113**, 3253 (2003)
79. A.W. Lohmann, *J. Opt. Soc. Am. A* **10**, 2181 (1993)
80. A.W. Lohmann, B.H. Soffer, *J. Opt. Soc. Am. A* **11**, 1798 (1994)
81. W.-X. Cong, N.-X. Chen, B.-Y. Gu, *Appl. Opt.* **37**, 6906 (1998)
82. S. Coëtmelec, M. Brunel, D. Lebrun, J.-B. Lecourt, *Opt. Commun.* **249**, 145 (2005)
83. D. Dragoman, K.-H. Brenner, M. Dragoman, J. Bähr, U. Krackhardt, *Opt. Lett.* **23**, 1499 (1998)
84. D. Dragoman, M. Dragoman, K.-H. Brenner, *Appl. Opt.* **38**, 4985 (1999)
85. A.W. Lohmann, D. Mendlovic, *Appl. Opt.* **33**, 7661 (1994)
86. D. Dragoman, M. Dragoman, *Opt. Commun.* **145**, 33 (1998)
87. D. Dragoman, M. Dragoman, K.-H. Brenner, *Opt. Lett.* **24**, 933 (1999)
88. K.K. Sharma, S.D. Joshi, *Opt. Commun.* **265**, 454 (2006)
89. J. García, D. Mendlovic, Z. Zalevsky, A. Lohmann, *Appl. Opt.* **35**, 3945 (1996)
90. C. Cuadrado-Laborde, R. Duchowicz, R. Torroba, E.E. Sucre, *Opt. Commun.* **281**, 4321 (2008)
91. M. Arif, D.M.J. Cowell, S. Freear, *Ultrasound in Med. & Bio.* **36**, 949 (2010)
92. F. Nicolas, S. Coëtmelec, M. Brunel, D. Lebrun, *Opt. Commun.* **268**, 27 (2006)
93. M. Li, J. Yao, *Opt. Lett.* **35**, 223 (2010)
94. D. Dragoman, *Opt. Commun.* **128**, 91 (1996)
95. A.W. Lohmann, H. Knuppertz, J. Jahns, *J. Opt. Soc. Am. A* **22**, 1500 (2005)
96. D. Dragoman, *J. Opt. Soc. Am.* **13**, 474 (1996)

Chapter 7

Computational Methods for the Assignment of Vibrational Modes in Crystalline Materials

Daniele Tomerini and Graeme M. Day

Abstract In this chapter we provide a description of the computational tools used for the calculation of the terahertz absorption spectrum of a crystalline material, with a particular focus on molecular crystals. We explain using examples why it is not correct to use the normal modes of vibration of an isolated molecule to understand the vibrational spectrum of a material in the terahertz range, but that the features in this spectral region are largely related to intermolecular interactions. It is, therefore, necessary to use methods that consider the periodicity of the crystal structure. We describe the two main methods used for the calculation of the vibrational frequencies and their absorption intensities of a crystal: lattice dynamics and molecular dynamics, providing examples showing the benefits and limitations of each method.

7.1 Introduction

The vibrational spectrum of a material is directly related to its internal properties: a vibration is probed when the material absorbs energy from incoming radiation, and the energies at which the material absorbs reflect the interactions between atoms in the material. In classical infrared spectroscopy, it is often possible to directly connect an observed absorption to the distortion (e.g. stretch or bend) of a bond in a molecule, usually without the need of calculation. This is because the vibrational normal modes are often localized in nature and because their associated vibrational frequencies are usually only slightly shifted by their chemical environment.

D. Tomerini · G. M. Day (✉)
Department of Chemistry, University of Cambridge,
Lensfield Road, Cambridge CB2 1EW, UK
e-mail: gmd27@cam.ac.uk

D. Tomerini
e-mail: dt334@cam.ac.uk

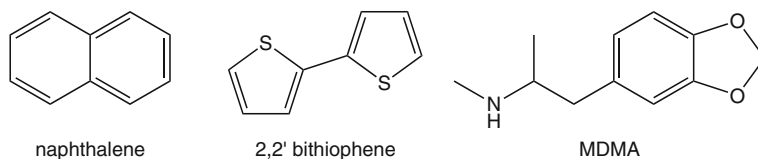


Fig. 7.1 Molecular structures of naphthalene, 2,2'-bithiophene and MDMA

Therefore, certain vibrational frequency ranges are characteristic of known distortions of covalent bonds.

However, the vibrational normal modes become increasingly more complex at lower frequencies; in the terahertz region, it is not generally possible to associate an absorption feature to a simple motion such as the stretching of a bond. Instead, absorption features generally result from collective motions of all the atoms in the material. To correctly assign the nature of molecular motions associated with a particular absorption, it is thus necessary to rely on simulations. If a simulation is theoretically well-founded and can reproduce the positions and intensities of features in an observed spectrum, the results can also be trusted to provide a faithful description of the vibrational motions that give rise to these features. In this chapter, we discuss the methods that are applied to the simulation of lattice modes in crystalline molecular materials and can, therefore, be applied to characterise the features observed in measured terahertz spectra.

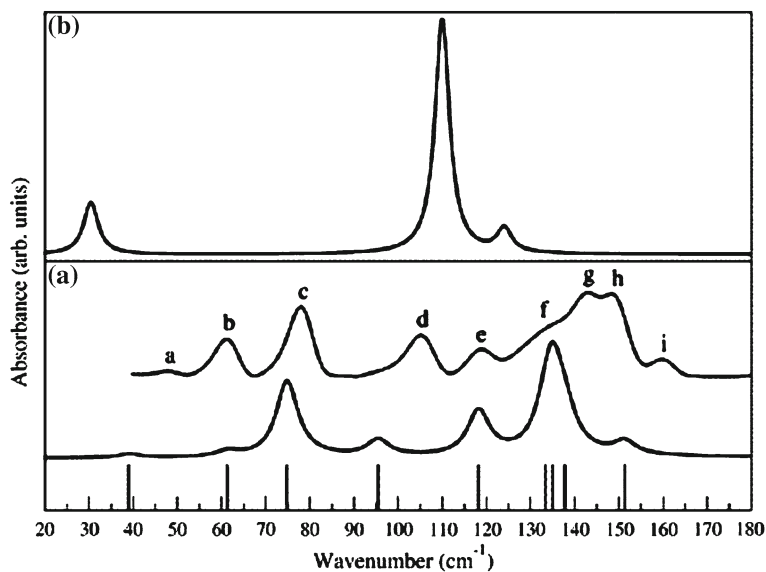
7.1.1 Single Molecule Versus Periodic Crystal Structure Calculations

A tempting approach to calculating the absorption spectrum of a molecular material is to calculate the normal modes of vibration of an isolated molecule, as such single-molecule calculations are generally much cheaper (in computing time and required computing resources) than calculations that include the entire periodic crystal structure. However, the vibrational features observed in the gas phase and in a solid can be radically different: in the gas phase, the interaction between molecules can be neglected, while in solids this is not true, especially when considering low frequency vibrations. Furthermore, pure rotational modes of molecules are allowed in the gas phase (as can be seen in the absorption spectrum of water vapour [1]), while molecular rotations are hindered in the solid phase by molecular close-packing and by the interactions between molecules.

Consider the case of naphthalene (Fig. 7.1), whose lowest frequency infrared active vibrational frequencies are listed in Table 7.1. The terahertz spectrum of the gas phase and the calculation of the isolated molecular vibrational frequencies [2] agree in finding no absorption below 175 cm^{-1} , while the experimental [3] spectrum of crystalline naphthalene shows several features below 100 cm^{-1} . These additional fea-

Table 7.1 Comparison of the three lowest energy infrared/terahertz active absorption frequencies (cm^{-1}) for naphthalene, in crystal and gas phase

Gas phase [2]		Crystal [4, 5]		
Experimental	Calculated	Experimental	Calculated	
166	179	53	45	54
359	376	66	62	74
473	492	98	91	97

**Fig. 7.2** Experimental terahertz spectrum of crystalline 2,2'-bithiophene (a, *upper spectrum*) compared with a solid state calculation (a, *lower spectrum*) and a molecular calculation (b). The strongest experimental features are indicated with *letters*. Reprinted with permission from [6]. Copyright 2005 American Chemical Society

tures only appear for the crystalline sample, so must be related to the intermolecular interactions within the crystal. Indeed, simulations that include the periodic structure of the crystal [4, 5] reproduce the observed frequencies and indicate that the corresponding vibrations relate to whole-molecule motions about the equilibrium crystallographic positions. Another example is the terahertz spectrum of 2,2'-bithiophene, shown in Fig. 7.2. Again, there are clear differences between the vibrational modes of the isolated molecule and those of the crystal: in this case, the isolated molecule does have low-energy vibrational modes near and below 100cm^{-1} . However, this region of the spectrum becomes much more detailed in the crystal and the number and position of these features can only be reproduced in a calculation that includes the entire crystal structure.

Table 7.2 Experimental [7] and calculated [7, 8] frequencies of the terahertz absorption of MDMA (cm^{-1}), from isolated molecule and from lattice dynamics of the crystal, and corresponding assignment to vibrational features

Experimental	Isolated molecule calculation		Crystal calculation	
	Frequency	Assignment	Frequency	Assignment
37.0	36.6	Internal C–C bond torsion	38.0	Rigid molecule rotations
59.3	58.8	Internal C–C bond bending	61.0	Rigid molecule translations
86.6	85.8	Internal CH ₂ group rocking	94.4	Internal C–C bond bending + rigid translations

A trickier example is represented by calculations on the drug molecule 3,4-methylenedioxymethamphetamine (MDMA or ecstasy, Fig. 7.1). In this case, calculations on the isolated molecule [7] seem to provide excellent agreement with the experimental spectrum (Table 7.2), so that features of the terahertz spectrum were assigned to intramolecular vibrations. However, a series of calculations [8, 9] based on the dynamics of the known crystal structure, showed that the *intramolecular* vibrations are shifted out of the terahertz region by coupling to the crystal environment (see Sect. 7.2.2). Moreover, the calculations produce a series of *intermolecular* vibrational modes at the frequencies seen in the experimental spectrum. Here, it seems that the agreement of the frequencies found in the isolated molecule calculation with the experimental spectrum was a result of fortuitous coincidence.

In conclusion, to correctly calculate the terahertz spectrum and the corresponding vibrational modes of a crystalline material it is necessary to employ methods that consider the molecular arrangement in the periodic structure and the associated intermolecular interactions present in a crystal. Two computational approaches are available: lattice dynamics and molecular dynamics (MD).

Lattice dynamics, described in Sect. 7.2, relies on calculating the forces acting on the atoms in the crystal as a periodic system in static equilibrium. A harmonic analysis of the forces leads to the normal modes of the system. MD, on the other hand (Sect. 7.3), is a more general computational approach to investigating the dynamics in chemical systems, where Newton's laws of motion are applied to follow the dynamics of molecules in a crystal *around* its equilibrium structure. The vibrational modes can then be extracted from an analysis of the trajectories of atoms through time.

There are, of course, different types of systems: ionic crystals, covalent crystals, semiconductors, and molecular crystals to name a few. Each of these has its own peculiarity, and methods may need to be carefully tailored to address the differences in their behaviour. In the proceeding sections, we will try to consider these different aspects, but we will focus mainly on molecular organic crystals; for other types of systems, we refer whenever possible to the relevant literature.

7.2 Theory of Crystal Phonons

All the vibrational motions of atoms in a crystal can be described as a superposition of the normal modes of vibration; the quanta of vibrations in a periodic system are called phonons. The normal modes are characterised by the property that each atom of the crystal oscillates with the same frequency ω , and that these oscillations can interact with light of the corresponding frequency, producing absorption signals detectable in vibrational spectroscopy. In the following section, we will introduce how it is possible to calculate these normal mode frequencies for different types of periodic systems.

7.2.1 Phonon in a 1-Dimensional Crystal

We start with the simplest model system: a 1-dimensional (1D) infinite chain of equally spaced atoms, in which first neighbours interact *via* a harmonic interaction. The instantaneous position x_n of the n th atom can be written as

$$x_n = nd_0 + u_n, \quad (7.1)$$

where d_0 is the equilibrium separation between neighbouring atoms, and u_n the displacement from the equilibrium position. Defining the force constant of the harmonic nearest-neighbour interaction as C , and the atomic mass m , leads to the following system of equations:

$$m \frac{d^2 u_n}{dt^2} = C (u_{n+1} - 2u_n + u_{n-1}), \quad (7.2)$$

From the periodicity of the system we expect the solution to be in the form of a travelling wave:

$$u_n(t) = A \exp(ikd_0n - i\omega t), \quad (7.3)$$

where A is the amplitude of motion of an atom, i.e. the maximum displacement from the equilibrium position. Using this form of the solution we have simplified the initial problem to a simpler parametric equation. We can find the so-called dispersion relation between ω and k :

$$\omega = \sqrt{\frac{4C}{m}} \left| \sin \frac{1}{2}kd_0 \right| \quad (7.4)$$

The wavevector k is an important parameter in a crystal and is associated with a crystal momentum $\hbar k$. Quantum transitions within the crystal require that the crystal

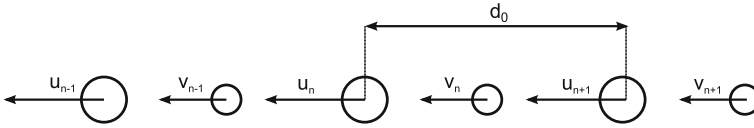


Fig. 7.3 Infinite linear chain of two alternating types of atom separated by a distance $\frac{1}{2}d_0$. The atoms are displayed in their equilibrium position, and the displacement u and v are indicated

momentum is conserved,¹ which has an important consequence in spectroscopy: because of the low momentum of a photon, interaction of a phonon with light is possible only if $k \approx 0$.

Another important rule for allowed transitions in vibrational terahertz and infrared spectroscopy is that the phonon vibration must generate a vibrating electrical dipole to interact with light; we must explore a less simple model to investigate the consequences of this selection rule.

We now consider a linear chain of alternating atoms, of mass m_1 and m_2 , respectively, each of equal distance $\frac{1}{2}d_0$ from each other. If we call u_n and v_n (see Fig. 7.3) the displacement of the atoms from their equilibrium positions, we obtain the system of equations:

$$\begin{aligned} m_1 \frac{d^2 u_n}{dt^2} &= C (v_{n-1} + v_n - 2u_n) \\ m_2 \frac{d^2 v_n}{dt^2} &= C (u_n + u_{n+1} - 2v_n), \end{aligned} \quad (7.5)$$

As with the first monoatomic chain model, the solution we look for will still be in the form of a travelling wave, but now with two amplitudes, A_1 and A_2 , for the two atom types:

$$\begin{aligned} u_n &= A_1 \exp(ikd_0n - i\omega t) \\ v_n &= A_2 \exp(ikd_0n - i\omega t) \end{aligned} \quad (7.6)$$

Substituting into Eq. 7.5 leads to the following matrix relation:

$$\begin{pmatrix} \frac{1}{C}\omega^2 m_1 - 2 & 1 + \exp(-ikd_0) \\ 1 + \exp(ikd_0) & \frac{1}{C}\omega^2 m_2 - 2 \end{pmatrix} \begin{pmatrix} A_1 \\ A_2 \end{pmatrix} = 0 \quad (7.7)$$

Non-trivial solutions exist only if the determinant of the matrix is 0. We can solve the equations to obtain two dispersion relations between ω and k :

$$\omega_{\pm}^2 = C \left(\frac{1}{m_1} + \frac{1}{m_2} \right) \pm C \sqrt{\left(\frac{1}{m_1} + \frac{1}{m_2} \right)^2 - \frac{4 \sin^2(\frac{1}{2}kd_0)}{m_1 m_2}} \quad (7.8)$$

¹ Further detail can be found in most solid state physics texts (for example, see [10]).

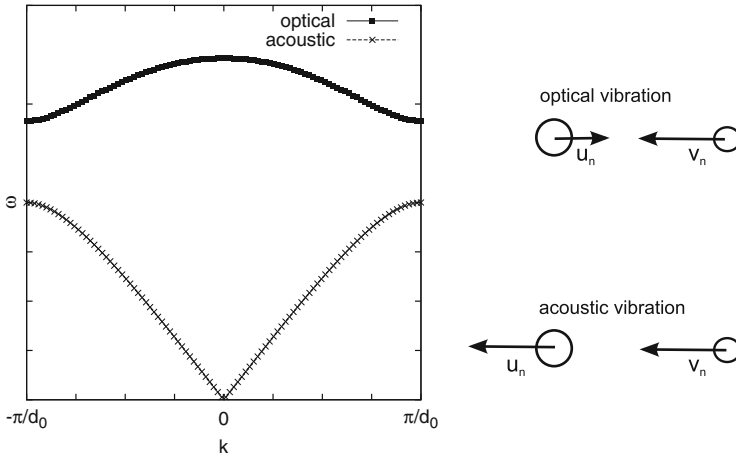


Fig. 7.4 Phonon dispersion (left) for a diatomic linear chain with the mass ratio $m_2/m_1 = 2$ and relative motion (right) of the atoms at $k = 0$

In the spectroscopically interesting region near $k = 0$ we can write the approximate solutions as

$$\begin{aligned} \omega_-^2 &= \frac{C}{2(m_1+m_2)} k^2 d_0^2 \\ \omega_+^2 &= 2C \left(\frac{1}{m_1} + \frac{1}{m_2} \right) \end{aligned} \tag{7.9}$$

The ω_+ solution has a finite frequency at $k = 0$ and, since this vibrational frequency can then be observed by optical spectroscopy, it is therefore known as an optical phonon. The solution ω_- , which tends to $\omega = 0$ at $k = 0$ is called an acoustic phonon.

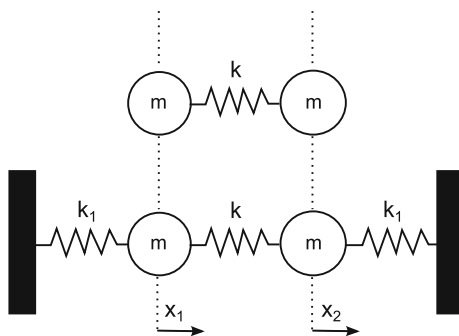
To examine the associated atomic displacements we substitute ω_+ back into Eq. 7.7 to obtain a relation between the amplitudes of the two types of atom:

$$\frac{A_1}{A_2} = -\frac{m_2}{m_1} \tag{7.10}$$

The two neighbouring atoms move with opposing directions (Fig. 7.4), their centre of mass being fixed: if the atoms have opposite charges, the motion creates a vibrating dipole, which can interact with electromagnetic radiation.

Conversely, for the frequency ω_- , we find that $A_1 = A_2$ and all the atoms move coherently together: no dipole variation is possible.

Fig. 7.5 Simple system of a diatomic molecule. In the *upper picture*, two equal masses connected with a spring of elastic constant k . In the *lower* the same molecule interacts through springs of elastic constant k_1 . The displacements x_1 and x_2 are indicated



7.2.2 Normal Modes in Vacuum and in Condensed State

When it comes to molecular solids, it is useful to consider the coupling between the strong bonding within a molecule and the relatively weak intermolecular interactions. As an illustration, consider a model of a homonuclear diatomic molecule: two atoms of mass m connected by a spring of elastic constant k (Fig. 7.5). In a simple model of this molecule in the condensed phase, the atoms also interact with their surroundings (here, a pair of fixed walls) via additional bonds of spring constant k_1 . This second system is equivalent to the isolated molecule when $k_1 = 0$.

The normal modes can be calculated by considering the system of equations

$$\begin{aligned} m \frac{d^2 x_1}{dt^2} &= k_1 x_1 + k(x_2 - x_1) \\ m \frac{d^2 x_2}{dt^2} &= k_1 x_2 + k(x_1 - x_2) \end{aligned} \quad (7.11)$$

and looking for an oscillatory solution for the displacements:

$$\begin{aligned} x_1 &= A_1 \exp(i\omega t) \\ x_2 &= A_2 \exp(i\omega t) \end{aligned} \quad (7.12)$$

Substitution into Eq. 7.11, in matrix representation:

$$\begin{pmatrix} k + k_1 - \omega^2 m & k \\ k & k + k_1 - \omega^2 m \end{pmatrix} \begin{pmatrix} A_1 \\ A_2 \end{pmatrix} = 0, \quad (7.13)$$

which has non-trivial solution only if the matrix is singular. The solutions are:

$$\begin{aligned} \omega_1^2 &= k_1/m \\ \omega_2^2 &= (2k + k_1)/m \end{aligned} \quad (7.14)$$

In the case of a molecule in isolation ($k_1 = 0$) there is only one mode of vibration: stretching of the bond with frequency $\omega_2^2 = 2k/m$. For the constrained molecule interacting with the two walls, there is the same stretching mode, but at increased frequency $\omega_2^2 = (2k + k_1)/m$, and a second vibration at frequency $\omega_1^2 = k_1/m$ corresponding to translation of the whole molecule.

Depending on the strength of the intermolecular interactions, the absorption frequencies of intramolecular vibrations are always shifted to higher frequencies. This is sometimes enough for them to be shifted outside of the terahertz region. The new vibrational modes that are introduced as a consequence of interactions of a molecule with its surroundings correspond to whole-molecule motions. In two- or three-dimensional systems, these can involve molecular rotation as well as the translation seen in this simple 1D example.

7.2.3 Phonons in a 3D Crystal

The procedure to calculate the vibrational spectrum for a 3D crystal is a generalisation of what has been described in the previous sections: one main difference is that atomic displacements are now vectors. Furthermore, for real systems we must usually consider the interactions between all atoms, rather than the simplified nearest neighbour interactions that we used in the model systems.

To derive the equations of motion, we start from the potential energy of the crystal, ϕ .

For small displacements we can expand the potential energy ϕ in a Taylor series up to second order in the displacement u_α^{nl} , the subscript α representing one of the Cartesian coordinates (x, y, z) of atom n within the unit cell l :

$$\phi = \phi_0 + \frac{1}{2} \sum_{\alpha nl} \sum_{\alpha' n' l'} \left(\frac{\partial^2 \phi}{\partial u_\alpha^{nl} \partial u_{\alpha'}^{n' l'}} \right)_0 u_\alpha^{nl} u_{\alpha'}^{n' l'}. \quad (7.15)$$

where the subscript 0 indicates that the potential has been expanded about the equilibrium position. In the equilibrium configuration there are no net forces acting on the atoms, hence there is no linear term; ϕ_0 is the equilibrium potential energy.

From here, we can write the equations of motion:

$$m_n \frac{d^2 u_\alpha^{nl}}{dt^2} = - \sum_{\alpha' n' l'} \left(\frac{\partial^2 \phi}{\partial u_\alpha^{nl} \partial u_{\alpha'}^{n' l'}} \right)_0 u_{\alpha'}^{n' l'} = - \sum_{\alpha' n' l'} \phi_{\alpha\alpha'}^{nn'(l-l')} u_{\alpha'}^{n' l'} \quad (7.16)$$

Due to the translational invariance within a crystal, the force $\phi_{\alpha\alpha'}^{nn'(l-l')}$ depends only on the distance between the unit cells l and l' , so we can drop the l dependence and consider l' as the distance to a reference cell.

As in the previous section, we look for wave-like solutions of the form

$$u_{\alpha}^{n'l'} = \frac{A_{\alpha}^n(\mathbf{k})}{\sqrt{m_n}} \exp(\mathbf{i}\mathbf{k} \cdot \mathbf{r}^{l'} - i\omega(\mathbf{k})t), \quad (7.17)$$

where the frequency depends on \mathbf{k} , which is now a vector (called the wavevector). Substitution into Eq. 7.16 gives

$$\begin{aligned} -\omega^2(\mathbf{k})A_{\alpha}^n(\mathbf{k}) &= \sum_{\alpha'n'l'} \frac{\phi_{\alpha\alpha'}^{nn'l'}}{\sqrt{m_n m_{n'}}} A_{\alpha'}^{n'l'}(\mathbf{k}) \exp(-\mathbf{i}\mathbf{k} \cdot \mathbf{r}^{l'}) \\ &= \sum_{\alpha'n'l'} D_{\alpha\alpha'}^{nn'l'}(\mathbf{k}) A_{\alpha'}^{n'l'}(\mathbf{k}) \end{aligned} \quad (7.18)$$

that are now a set of algebraic equations. $D(\mathbf{k})$ is called the dynamical matrix, and is the mass weighted Fourier transform of the force matrix.

The equations are simplified if we consider only the phonons involved in the absorption of light ($\mathbf{k} = 0$): we can thus drop the exponential dependence in 7.18, leading to:

$$\omega^2(\mathbf{0})A_{\alpha}^n(\mathbf{0}) = \sum_{\alpha'n'l'} D_{\alpha\alpha'}^{nn'l'}(\mathbf{0})A_{\alpha'}^{n'l'}(\mathbf{0}) \quad (7.19)$$

This is an eigenvalue problem, composed of $3n_b$ equations, where n_b is the number of atoms in the unit cell. It is possible to obtain both the eigenvectors $u_{\alpha}^n(\mathbf{k})$ and their associated frequencies $\omega(\mathbf{k})$ by standard linear algebra techniques. Three (acoustic) phonons have a frequency $\omega = 0$ at $\mathbf{k} = 0$: these correspond to bulk translation of all the atoms in the unit cell. The remaining $3n_b - 3$ phonons are optical: they have non-zero frequencies and can interact with an electric field.

From the resulting eigenvectors $A_{\alpha}^n(\mathbf{0})$ it is possible to return to the atomic displacements u_{α}^{nl} using the relation 7.17.

Terahertz intensities I_N are directly correlated with the change in electric dipole moment μ of the system with respect to all of the atomic motions under excitation of a phonon mode Q_N :

$$I_N \propto \left| \frac{\mu}{Q_N} \right|^2 \quad (7.20)$$

The calculation of how the cell dipole varies along each eigenvector depends on the computational method employed. If the electronic part of the system is not treated quantum mechanically (as in force field calculations and classical MD, see Sects. 7.2.4 and 7.3), the dipole variation is most simply evaluated from the rigid displacement of the atomic partial charges or multipoles.

In quantum mechanical methods (Sect. 7.2.5) the dipole has to be related to the perturbation of the electronic distribution by the normal mode displacement; to do so, the contribution of each of the n atoms to the cell dipole variation is expressed using the Born effective charge tensor \mathbf{Z}_n , which is defined as the first derivative of the polarisation \mathbf{P} per unit cell with respect to the atomic displacements \mathbf{u}^{nl} :

$$Z_{n,\alpha\beta} \propto \frac{dP_\alpha}{du_\beta^{nl}} \quad (7.21)$$

where α and β indicate the Cartesian coordinates.

Once the lattice frequencies and associated absorption intensities are known, the spectrum can be simulated by assuming a peak shape for each absorption feature; it is common to express the spectrum as a sum of Lorentzian functions

$$f(x) = \sum_N \frac{I_N}{\pi} \left(\frac{\gamma}{(x - x_N)^2 + \gamma^2} \right), \quad (7.22)$$

centred at the absorption frequencies x_N , whose relative intensity I_N equals the area under the curve. The parameter γ simulates the signal broadening of the experimental spectrum. Examples of this treatment are reported in Figs. 7.7 and 7.10.

7.2.3.1 Simple Parameterisation for Ionic Systems

It should be clear from the previous sections that, in order to perform a phonon calculation, we need a model for the forces acting between atoms within the system of interest. Various computational methods, with different degrees of approximation, have been applied to evaluate the required forces to model the vibrations in crystals.

One of the earliest calculations of the phonon spectrum of an ionic crystal was attempted by Kellermann [11] in 1940 for the simple cubic salt structure NaCl. This is a simple cubic crystal: each atom is located at the corner of a cube, and each Na^+ ion is surrounded by 6 Cl^- neighbours (and vice versa). The system was treated as a field of interacting classical point charges held apart by a repulsive potential, v_0 , between nearest neighbour atoms, which is necessary to keep the atoms at their equilibrium positions. It is not necessary to know the exact form of this potential, but only its behaviour near to the equilibrium position: the first derivative was calculated from the equilibration of forces within the crystal, knowing that the forces on all atoms in the crystal must vanish at the equilibrium structure. The second derivative of the interatomic potential was determined from experimental data on compressibility of the crystal.

From this model for the interatomic forces, a 6D (3D for each atom in the unit cell) dynamical matrix was then constructed and diagonalised. One of the two measurable frequencies of NaCl (two coinciding longitudinal optical phonons, LO) is in remarkable agreement with experimental data (Table 7.3), especially considering the simplicity of the model potential; the other (the transverse optical phonon, TO) is more dependent on the effects of charge displacements (polarisation), which were not included in this first model.

This method is simple enough to be performed on a simple system without the need for a computer (Kellermann produced a phonon spectrum for $\mathbf{k} \neq 0$ as well!),

Table 7.3 Phonon frequencies (THz) of the optical phonons of NaCl for $\mathbf{k} = 0$ by Kellermann compared with experimental values [14] and a calculation that includes charge displacement [15]

Phonon type	Kellermann	Lattice dynamics, with polarisation	Experimental
LO	4.55	4.92	5.17 ± 0.03
TO	9.58	7.84	7.92 ± 0.07

and has been repeated for a number of structurally equivalent alkali halides and oxides [12, 13].

Unfortunately the model for the interactions between atoms here is too simplified to be generalisable to more complex solids. More sophisticated models have been addressed in a number of studies, considering models to account for polarisation of atomic charges [15, 16] and extended interactions beyond nearest neighbours [17]. Many more adjustable parameters must be introduced to the model of interatomic forces to account for these interactions, and the simplicity of the model is lost. Interesting systems usually consist of more than two atoms in the unit cell, so that many different atom–atom interactions must be considered. Furthermore, for crystals of electrically neutral molecules, the interactions between atomic charges are usually not the dominant attractive intermolecular interactions. Instead, a more realistic model of the van der Waals forces is necessary. Overall, it is generally necessary to calculate the phonon spectrum with the aid of a computer, by numerically evaluating the matrix of second derivatives from a detailed description of the forces acting within a crystal.

The quality of a molecular simulation depends on how well the interactions between atoms in the system are represented. Two types of approach have been applied to calculate the necessary forces:

- The atom–atom method: this is a generalisation of the approach used in the NaCl example given above. A functional form is assumed for the important interatomic interactions and these functions are parameterised to provide a description of the energy and forces within the crystal. The combination of functional form and parameters is often referred to as a force field. Electrostatic interactions in the atom–atom method are treated classically, usually by atomic partial charges, and sometimes with higher order atomic or molecular multipole expansions.
- Quantum mechanical electronic structure calculations: from the quantum mechanical point of view, all of the relevant forces ultimately arise from the electrostatic interactions between the electrons and nuclei. The electronic problem can be solved by separating the nuclear and electronic wavefunctions (the Born–Oppenheimer approximation) so that the energy and forces acting within a crystal can be calculated for any configuration of its constituent atoms. The most commonly applied electronic structure method in recent years is density functional theory (DFT) for which several software packages (see Sect. 7.2.5) are available to perform this type of calculation.

Electronic structure calculations on periodic systems are orders of magnitude more computationally expensive than those based on the atom–atom force field approach. The techniques necessary for DFT-based phonon calculations (density functional perturbation theory [18]), along with the necessary computational power, have only been available since the 1990s. While large-scale computing is nowadays common in research facilities, the cost of such calculations still limits their application to the crystal structures of fairly small molecules. For large systems, such as the crystal structures of pharmaceutical molecules with hundreds of atoms within the unit cell, the atom–atom approach is still often the only practical solution. In the next two sections we describe these two approaches in more detail.

7.2.4 The Atom–Atom Potential (Force Field) Method

The quality of a molecular simulation depends on how well the interactions between atoms in the system are represented. The atom–atom potential method has been very successfully applied to modelling a wide range of materials, and some of the early development and applications are described by Pertsin and Kitaigorodskii [19].

In most atom–atom calculations, there are three types of terms in the force field used to describe the interactions between atoms [19]: repulsion–dispersion; electrostatics and intramolecular terms.

- The repulsion–dispersion terms consist of a short-range repulsion, which arises due to unfavourable overlap of electron density as the internuclear separation between non-bonded atoms is decreased, and a longer range attractive term to model London dispersion forces. The two commonly used forms of the repulsion term are an AR^{-n} term (R being the interatomic separation), where n is usually in the range from 9 to 14, or a theoretically better founded exponential, $A \exp(-BR)$. The attractive dispersion interaction between atoms arises from correlated fluctuations in the electron charge distribution around the atoms, the leading term of which corresponds to fluctuating dipole–dipole interactions and has an R^{-6} dependence. R^{-8} and higher terms arise from higher order correlated electron density fluctuations, but are less important and usually omitted. Thus, two common forms of atom–atom repulsion–dispersion terms are:

$$\begin{aligned} U_{ik,\text{repulsion–dispersion}} &= A^{\iota\kappa} R_{ik}^{-n} - C^{\iota\kappa} R_{ik}^{-6} \\ U_{ik,\text{repulsion–dispersion}} &= A^{\iota\kappa} \exp(-B^{\iota\kappa} R_{ik}) - C^{\iota\kappa} R_{ik}^{-6} \end{aligned} \quad (7.23)$$

where R_{ik} is the separation between atoms i and k . These interactions are determined by the parameters A , B and C , whose values depend on the types (i and κ) of atoms involved.

- The electrostatic interactions arise because electronic charge is not spread uniformly within a molecule: its distribution can most simply be modelled by assigning fractional point charges to each atom in the molecule. The electrostatic

interaction between point charges has the usual long range R^{-1} dependence on interatomic separation and does not depend on the mutual orientation of the interacting atoms. However, some features of the electrostatic potential around molecules cannot be adequately modelled using such a simple spherical atom model. For example, localised lone pairs and aromatic π -electron density introduce important anisotropy in the electron charge distribution around atoms. Therefore, some atom-atom models include higher order multipoles (dipole, quadrupole, etc.) on each atom.

- **Intramolecular potentials.** While the repulsion-dispersion and electrostatic terms are used to model the interactions between non-bonded atoms, covalent bonding is treated by a separate set of terms. At its most basic, an intramolecular force field consists of bond stretching functions, usually modelled either as harmonic in the bond length or using a more realistic Morse potential form, 3-atom angle bending terms and 4-atom terms to model the torsional potential within four neighbouring atoms.

Force fields differ in which of the above terms are included, their exact functional form and how the parameters in each term are determined. These parameters depend on the types of atoms that are interacting and are often developed to be transferable between systems with similar chemical functionality, e.g. the parameters describing repulsion-dispersion interactions between carbon atoms might be fitted to model any carbon atoms in organic molecules. More elaborate parameter sets might include separate sets of parameters for carbon atoms in different chemical environments, such as different parameters for aromatic and aliphatic carbon atoms. The advantage of such transferable parameter sets is that there is no need to develop a new force field for each new system that is to be studied.

An example of this approach is the set of repulsion-dispersion parameters developed by Williams for hydrocarbons [20], oxygen [21], nitrogen [22] and fluorine containing [23] hydrocarbons. The parameters in such transferable force fields were fitted to reproduce structural parameters and heats of sublimation of a large set of molecular organic crystal structures and can therefore be used to describe a wide class of organic molecules.

An alternative approach to these transferable parameters is to develop and optimise specific force fields for a single molecule or small family of molecules [5, 24, 25], sometimes without the need to fit to experimental data. While such molecule-specific models involve much more work, the advantage is that the functional form and parameters can be fine-tuned to very accurately describe a particular molecule.

7.2.4.1 All-Atom Versus Rigid-Molecule Calculations

Having chosen a suitable force field, the construction of the dynamical matrix is performed by considering the forces generated by a series of perturbations about the equilibrium structure. In the all-atom approach, this involves evaluating the 2nd

derivatives of the lattice energy with respect to translations of each atom in the unit cell in each of three orthogonal directions: the x , y and z directions in a globally defined axis frame. The resulting dynamical matrix will provide the entire vibrational spectrum of the crystal, including both the intramolecular vibrational modes (bond stretching, angle bending, etc.) and the lattice modes, which are dominated by overall translation and rotation of molecules about their equilibrium positions. It is the latter types of modes that dominate the terahertz region (from 0 to 5 THz). Indeed, despite the number of studies calculating the vibrational spectra of molecular crystals, the interest has often been on the intramolecular frequencies that are more easily accessible by infrared and Raman spectroscopy, with the calculation of the vibrational frequencies in the terahertz range arising as a “by-product” of the calculations.

Developments allowing better experimental access to high quality spectra in the terahertz frequency range has prompted more interest in calculations aimed at characterising the vibrational modes in this region. One commonly employed simplification in these calculations has been the rigid-molecule approach, which takes advantage of the fact that intermolecular and intramolecular interactions often act on very different strength scales; the geometry of small molecules in their crystal structures is often unchanged from their gas phase geometry, indicating that the intermolecular forces in the crystal are much weaker than the intramolecular forces that dictate the molecular geometry. The rigid-molecule approximation assumes that inter- and intramolecular interactions are completely uncoupled, so that all of the intramolecular force field terms can be ignored when calculating the lattice mode region of the vibrational spectrum. Furthermore, the relative positions of atoms within a molecule can be kept fixed, so that the only relevant perturbations from the equilibrium structure are overall molecular translations and rotations.

Thus, in the rigid-molecule approximation, the lattice dynamical equations are reformulated such that the dynamical matrix (Eq. 7.18) refers to molecular centre-of-mass displacements and rotations about molecular moments of inertia rather than atomic displacements. Rigid-molecule lattice dynamics is fully described by Walmsley [26] and Califano [5]. This approach can dramatically reduce the dimensionality of the dynamical matrix and lowers the computational cost of the calculation; for a crystal structure with Z molecules in the unit cell, rigid-molecule lattice dynamics leads to $6Z$ vibrational modes at $\mathbf{k} = 0$, three of which are the acoustic translational modes with $\omega = 0$ at $\mathbf{k} = 0$.

The rigid-molecule approximation is clearly most appropriate when there is a large separation between the lowest energy intramolecular vibrational frequency and the highest energy of these $6Z$ intermolecular vibrational modes, which are typically found in the range from just under 1 THz to about 5 THz (or from approximately 30 to 160 cm^{-1}). If the separation in frequency is large, then coupling of the two types of motion should be small.

7.2.5 Quantum Mechanical Electronic Structure Calculations

The basic requirement to be able to perform a calculation of the electronic structure is the separation of the nuclear coordinates from the electronic coordinates, using the Born–Oppenheimer approximation. Under this assumption the calculation of the electronic wavefunction of a crystal can be viewed as a system of interacting electrons in a field of nuclei. The equilibrium geometry of the crystal is the configuration where there is no net force acting on each nucleus, and can be found by performing a minimisation of the energy of the crystal with respect to the coordinates of the nuclei.

The forces necessary to build the dynamical matrix can be obtained by distortion of the nuclear equilibrium structure: moving an atom away from the equilibrium position generates a restoring force that does not depend only on the equilibrium electronic distribution, but on its variation as well [27], due to the parametric dependence of the electron wavefunction on the nuclear perturbation. The generation of the dynamical matrix thus needs the calculation of the electronic density (a computationally expensive task) for a high number of nuclear configurations, and this contributes to the significant computational cost of such a calculation. The calculation of the electronic charge distribution is usually performed using density functional theory (DFT). Hohenberg and Kohn [28] proved that only the electron density (rather than the wavefunction) is necessary to describe the ground state of a system. Furthermore, for a system of interacting electrons in an external potential V (such as the potential generated by the atomic nuclei in the crystal) there exists a universal functional F of the electron density n , independent of the external potential, such that the energy E is defined as

$$E[n] = F[n] + \int V[\mathbf{r}]n[\mathbf{r}]d\mathbf{r} \quad (7.24)$$

Unfortunately, the theorem proves only the existence of the functional, not its exact form. A practical approach, suggested by Kohn and Sham [29], is to express the functional as a sum of physically recognisable contributions: it is the exchange–correlation potential that is unknown, but possible to approximate. Therefore, many functionals have been suggested and tested for their ability to reproduce the geometries, energies and properties of molecules and crystals. The simplest form, the local density approximation (LDA), relates the energy to the value of the electron density at each point in space. This approach is exact in the limit of a slowly varying electron density, so correctly describes weakly correlated systems such as semiconductors, but fails to describe complex systems where the potential varies more drastically. More elaborate functional forms have been developed through the years, containing dependence on the gradient of the electron density (generalised gradient approximations) and by including the exact exchange energy from Hartree–Fock wavefunction calculations (hybrid functionals, such as the very popular B3LYP functional). The main limitation in current functionals is their unsatisfactory description of the dispersion attraction between molecules, which is often the dominant contribution to the stability of organic molecular solids. DFT-based lattice energy minimisation of

molecular organic crystals usually leads to unrealistic unit cell dimensions because, although the intramolecular bonds are treated correctly, intermolecular interactions are typically underestimated. As an example, the unit cell volume of the explosive material RDX, modelled with the PBE functional [30, 31] gives an energy-converged unit cell with a 20% larger volume than the experimentally determined unit cell. As this structural distortion relates to large changes in intermolecular contact distances, calculated frequencies of vibrational modes in the terahertz region cannot be accurately modelled in such an energy-minimised structure. A common workaround when applying DFT to organic solids where the dispersion attraction is dominant is to avoid the optimisation of the unit cell, constraining the lattice vectors to their experimentally determined values (see column a in Table 7.6). A more satisfactory solution to the dispersion problem in DFT is to supplement the functional by a set of parameterised atom–atom R^{-6} terms of the same form as those included in force fields, leading to methods known as DFT-D [32]. These added terms add very little to the computational cost over pure DFT [31]. However, as with force fields, the parameterisation of these terms is not unique and different parameters are required to correct different functionals.

7.2.5.1 Basis Set and Implementation

In practice, the electronic density in a DFT calculation is expanded as a linear combination of basis functions, with the expansion coefficients to be determined as a part of the calculation. While an infinite number of basis functions might be necessary for mathematical completeness, the number of basis functions that can be included in a calculation is finite. In order to control the resulting finite basis set errors, the choice of basis functions is crucial.

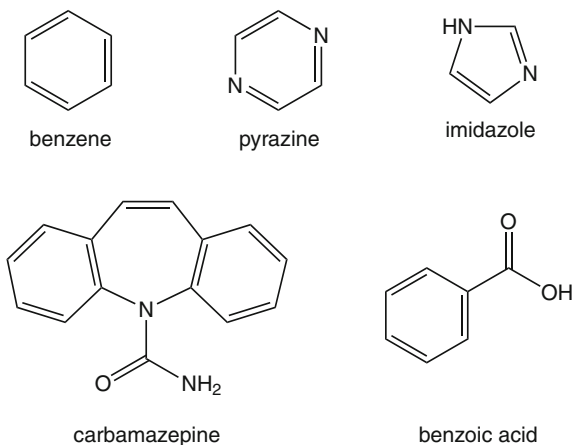
There are two classes of functions commonly employed, each with advantages and drawbacks; we briefly describe them here, along with some of the software packages that employ them²:

- Localised basis set: basis functions are centred at points in space, usually around the nuclei of each atom, and the functions vanish as the distance \mathbf{r} to the nucleus tends to infinity. Thus, the number of basis functions required for a calculation scales linearly with the number of atoms in the unit cell. The two frequently implemented choices of localised basis functions are the atomic-like, Slater-type, orbitals and Gaussian-type orbitals.

Atomic-like orbitals, with a $\exp(-\zeta\mathbf{r})$ radial dependence, represent the best approximation of a real wavefunction in the long range limit: only few functions are necessary to achieve a good description of an atomic orbital. The packages DMol³ [33] and SIESTA [34] use numerically fitted atomic orbitals obtained from solutions of the single atom problem, so that the functions represent the correct radial dependence. The main advantage of this method is its fast convergence with

² This is only a partial list of software: a more complete list can be found at <http://www.psi-k.org/codes.shtml>.

Fig. 7.6 Molecular structures of benzene, pyrazine, imidazole, carbamazepine and benzoic acid



the number of basis functions; on the other hand dealing with this kind of wavefunctions is numerically complex, and there are difficulties in the assessments of how the convergence behaves with larger basis sets [35].

The advantage of Gaussian wavefunctions, used for example in the CRYSTAL package [36], lies in their mathematical properties: the solutions of integrals involving two or more Gaussian functions (one of the main computational tasks to be performed in electronic structure calculations) are easily expressed as combinations of other Gaussian functions centred at a different point. The ease in the manipulation in these functions comes at a cost: the difference in the behaviour of these function from true atomic orbitals both in the short range, with a smooth behaviour at $\mathbf{r} = 0$ instead of a cusp, and in the long range, where they behave as $\exp(-\xi \mathbf{r}^{-2})$ instead of the correct $\exp(-\zeta \mathbf{r})$, means that linear combinations of large numbers of Gaussian basis functions are needed in order to achieve a good representation of the true electron density.

- Plane wave basis sets: each basis function is a plane wave function $\exp(i\mathbf{k} \cdot \mathbf{r})$, whose periodicity makes them natural solutions for periodic systems. Furthermore, the simple mathematical form and the relation between \mathbf{k} and the kinetic energy provides a straightforward approach to systematically improving the basis set completeness, by including higher kinetic energy plane waves until the calculated properties of interest converge to the required level. Among the disadvantages of plane waves are their poor description of localised states (it is necessary to introduce pseudopotentials for the description of tightly bound core electrons) and the dependence of the basis functions on the dimensions of the unit cell. The latter means that large changes in the unit cell volume on energy minimisation will change the kinetic energy cutoff and therefore the consistency of the calculation. The plane wave approach is implemented in codes CASTEP [37] and VASP [38].

7.2.6 Example Calculations

7.2.6.1 Atom–Atom Potential Results

First, we examine the influence of the rigid-molecule approximation, as described in Sect. 7.2.4. Benzene, C_6H_6 (Fig. 7.6), is a prototypical example of a rigid molecule for which the rigid-molecule approach should be appropriate; there is nearly a 300 cm^{-1} gap between the highest frequency lattice modes at around 130 cm^{-1} and the lowest frequency intramolecular vibrations at around 400 cm^{-1} . Taddei et al. [39] examined the influence of the rigid molecule approach on the calculated lattice dynamics of crystalline benzene (Table 7.4). Their study found that coupling of intramolecular modes to the lattice vibrations has a negligible effect on the calculated displacement coordinates associated with the lattice modes, and the effect of allowing coupling of intramolecular vibrations is to lower the frequencies of the lattice modes by $1\text{--}3\text{ cm}^{-1}$. This effect is small compared to differences in calculated frequencies with different parameter sets for the interatomic potentials. Errors resulting from the rigid-molecule approach become more significant with increasing molecular size. Naphthalene, $C_{10}H_8$, has a significantly smaller gap of approximately 50 cm^{-1} between the lowest intramolecular mode and highest lattice mode frequencies. Pawley and Cyvin [40] calculated differences between all-atom and rigid-molecule phonon frequencies for crystalline naphthalene, finding that coupling to intramolecular modes typically lowers the lattice mode frequencies by about 5 cm^{-1} , and by up to 10 cm^{-1} for some lattice modes. These errors are now significant in comparison to errors in the experimental measurements and variations that are found between atom–atom parameter sets. The errors resulting from the rigid-molecule simplification become more severe for molecules with rotatable single bonds, where vibrational frequencies of the free molecule are likely to overlap with the frequency range of the lattice modes. The coupling might not influence all calculated lattice modes equally. For example, Li et al. [41] found that the torsional intramolecular vibration about the exocyclic C–C bond in benzoic acid strongly influences the lattice modes corresponding to molecular rotations about that molecular axis. However, the remaining molecular rotations and translations are satisfactorily modelled in the rigid-molecule approximation.

Next, we examine the sensitivity of the calculated lattice mode frequencies to the form and parameterisation of the intermolecular atom–atom potential. Taddei [39] found that the calculated lattice mode frequencies of benzene are very sensitive to the parameters of the $\exp -6$ atom–atom potential; changing from Williams' [20] parameters, which were fitted to the crystal structures of aromatic hydrocarbons, to Williams' [44] parameters, which were fitted to both aliphatic and aromatic hydrocarbon crystal structures, resulted in a mean absolute change of 8 cm^{-1} in the lattice mode frequencies, with individual frequencies shifting by up to 17 cm^{-1} . Even for such a simple molecule, the choice and validation of the force field parameters is very important. For crystalline benzene, the results shown in Table 7.4 demonstrate that adequate lattice dynamics results can be obtained using a repulsion–dispersion

Table 7.4 Comparison of observed low temperature infrared [42] and Raman [43] with calculated $\mathbf{k} = 0$ lattice mode frequencies of crystalline benzene (cm^{-1})

Symmetry	Observed	Calculated frequencies	
		Rigid molecule	Flexible molecule
<i>Raman absorptions</i>			
A_g	57	55	55
A_g	79	76	75
A_g	92	96	95
B_{1g}	57	61	60
B_{1g}	100	97	96
B_{1g}	128	131	128
B_{2g}	79	84	83
B_{2g}	90	94	93
B_{2g}	Not assigned	102	101
B_{3g}	61	67	66
B_{3g}	92	90	89
B_{3g}	128	129	127
<i>Infrared absorptions</i>			
A_u	Inactive	57	56
A_u	Inactive	66	65
A_u	Inactive	98	95
B_{1u}	Acoustic	0	0
B_{1u}	70	72	72
B_{1u}	85	87	86
B_{2u}	Acoustic	0	0
B_{2u}	53	59	57
B_{2u}	94	102	99
B_{3u}	Acoustic	0	0
B_{3u}	53	53	52
B_{3u}	94	98	98

Calculations were performed using Williams' [44] $\exp -6$ model (see Eq. 7.23) for intermolecular atom-atom interactions, with no explicit model for electrostatic interactions [39]

model with no model of intermolecular electrostatic interactions. However, many molecules of interest contain polar functional groups, leading to a greater importance of electrostatic contributions to intermolecular interactions.

Take imidazole (Fig. 7.6) as an example, where the rigid molecule approach should again be appropriate: imidazole molecules are aligned in the crystal structure so as to form infinite chains of $\text{N-H} \cdots \text{N}$ hydrogen bonds. Neighbouring chains are antiparallel aligned and interact via $\text{C-H} \cdots \text{N}$ contacts, which could also be described as weak hydrogen bonds. Hydrogen bonds are largely electrostatic in nature and, as a result of their prevalence in this crystal structure, the electrostatic contribution to atom-atom interactions contributes approximately 60% of the total lattice energy of the crystal [52]. Calculated rigid-molecule lattice mode frequencies using a range of atom-atom potentials are given in Table 7.5, along with low temperature observed frequencies from Raman and far-infrared spectroscopy. The UNI, FIT and W99 are

Table 7.5 Sensitivity of calculated lattice mode frequencies (in cm^{-1}) of crystalline imidazole to the intermolecular model potential, using the lattice dynamics method

Symm.	Expt.	UNI	FIT- AC	W99- AC	FIT- DMA	W99- DMA	MD(FIT- DMA)	Mode description
A_g	54.5	44.5	41.2	36.1	45.7	40.3	47	Minimal N-H...N hydrogen bond distortion, slipping of hydrogen bonded chains
A_g	79.0	62.6	60.0	60.3	79.3	82.5	79	N-H...N hydrogen bond bending
A_g	86.5	63.4	70.1	66.0	98.8	106.3	99	Minimal N-H...N hydrogen bond distortion, stretching of interchain C-H...O interactions
A_g	100.5	106.4	104.6	98.8	111.7	119.4	109 – 115	N-H...N hydrogen bond bending
A_g	112.0	162.3	119.7	121.5	141.7	137.1	140	Minimal N-H...N hydrogen bond distortion, bending of interchain C-H...O interactions
A_g	158.0	168.4	131.6	123.6	213.4	272.9	211	N-H...N hydrogen bond bending
B_g	62.5	64.3	57.6	53.8	54.8	53.6	56	Minimal N-H...N hydrogen bond distortion, slipping of hydrogen bonded chains
B_g	74.0	72.5	70.4	66.7	86.5	88.4	88	N-H...N hydrogen bond bending
B_g	109.0	110.7	87.8	84.2	108.0	108.0	106	N-H...N hydrogen bond bending
B_g	128.0	133.7	111.2	106.0	157.0	169.6	154	N-H...N hydrogen bond stretching
B_g	163.0	169.8	139.8	132.5	184.1	177.5	181	Twisting about N-H...N hydrogen bond axis
B_g	181.0	183.5	152.0	144.7	206.2	254.0	206	N-H...N hydrogen bond bending
A_u	NA	74.4	64.2	63.8	74.1	74.0	77	N-H...N hydrogen bond bending
A_u	113.0	100.3	83.8	91.7	111.6	104.2	109 – 118	N-H...N hydrogen bond bending/stretching
A_u	NA	129.7	113.3	104.9	141.3	161.2	138	Minimal N-H...N hydrogen bond distortion, bending of interchain C-H...O interactions
A_u	151.0	154.4	126.0	119.0	185.3	172.4	183	N-H...N hydrogen bond stretching
A_u	188.0	183.6	148.3	133.5	198.2	247.9	193	N-H...N hydrogen bond bending
B_u	70.0	57.4	44.8	49.4	61.5	69.2	63	N-H...N hydrogen bond bending

(continued)

Table 7.5 continued

Symm.	Expt.	UNI	FIT- AC	W99- AC	FIT- DMA	W99- DMA	MD(FIT- DMA)	Mode description
B_u	97.0	79.1	76.2	73.2	102.3	114.8	102	Minimal N–H···N hydrogen bond distortion, bending of interchain C–H···O interactions
B_u	128.0	105.0	93.1	89.7	149.9	150.5	147	Twisting about N–H···N hydrogen bond axis
B_u	NA	177.0	142.3	136.0	209.2	269.4	204	N–H···N hydrogen bond bending

Raman active modes (A_g and B_g) [45] and infrared active modes (A_u and B_u) [46] measured at 93 and 100 K, respectively (NA = not available experimentally). All atom–atom model potentials are of the exp -6 form. The UNI potential is Filippini and Gavezzotti's [47] atom–atom model with no explicit electrostatics. The FIT model uses Williams' parameters [21, 22] for all but the N–H hydrogen atom, for which Coombes parameters [48] were used. W99 is Williams' more recent parameter set [49, 50]. AC indicates use of atomic charges and DMA indicates atom centred electrostatic multipoles, determined using a distributed multipole analysis [51] of the molecular wavefunction. Reprinted with permission from [52]. Copyright 2003 American Chemical Society. Phonon mode frequencies from a MD simulation using the FIT–DMA model [53] are included for comparison, in the column headed MD(FIT–DMA)

different parameterisations of the exp -6 functional form for repulsion–dispersion interactions. The UNI model was developed so that electrostatic effects are absorbed into the parameters of the exp -6 terms, so was used without an explicit electrostatic model. FIT and W99 were each paired with atomic partial charge and atomic multipole (DMA) electrostatic models. The UNI model performs remarkably well, given its simplified functional form; the largest errors are a result of underestimating the frequencies of vibrational modes that bend the N–H···N hydrogen bonds, and those that twist the molecules about the hydrogen bond axis. Frequencies of hydrogen bond bending and twisting vibrations are also underestimated using the atomic point charge electrostatic models, but these motions are significantly stiffened when atomic charges are replaced by multipole expansions. Indeed, with the multipole models, vibrational frequencies of the bending modes are largely overestimated. The vibrational modes that lead to minimal distortion of the strong N–H···N hydrogen bonds are relatively insensitive to the potential used in the calculations.

Results reported using the same set of atom–atom potentials for crystalline pyrazine demonstrate that the electrostatic model can have even more dramatic effects on the lattice dynamics of polar molecules that lack strong hydrogen bonds [52]. Pyrazine molecules interact via weak C–H···N hydrogen bonds in the crystal structure and the electrostatic contribution is less dominant than in imidazole (contributing about 35–40 % of the lattice energy). However, the electrostatic model is found to be even more important in determining the lattice dynamics of the crystal: the restoring force for motions that bend the weak C–H···N hydrogen bonds is almost entirely due to dipole–dipole and higher order electrostatic interactions [52, 54]. In fact, with the simplest atomic charge electrostatic model, the crystal structure is unstable to

such molecular motions, resulting in non-physical negative values for the eigenvalues (ω^2) of the dynamical matrix.

Using the most successful atom–atom potentials, the absolute errors in calculated frequencies are not large: for imidazole, most are predicted to within 10–15 cm^{-1} . However, the low symmetry of most molecular crystals leads to many distinct $\mathbf{k} = 0$ lattice modes and the frequency range in which these are found is fairly narrow. Therefore, a one-to-one assignment of calculated and observed frequencies will often not be possible based on the absorption frequencies alone. In attempting to assign spectral features to calculated vibrational modes, it can be helpful to consider the absorption intensities from the dipole transition along each calculated vibrational mode (Eq. 7.20). These intensities can vary greatly between modes, as shown in the terahertz spectra of two of the polymorphs of carbamazepine (Fig. 7.7). In the case of the thermodynamically stable polymorph (form III, a and b in Fig. 7.7), the calculated intensities reproduce the observed relative peak intensities very well, giving confidence in assigning specific calculated normal modes to the observed features. In this case, the features could then be characterised in terms of the type of distortion of the hydrogen bonding in the crystal [55]. In the case of carbamazepine form I (c and d in Fig. 7.7), the crystal is of a particularly low symmetry, leading to a very crowded terahertz spectrum; in this case, even with calculated absorption intensities, it would not be possible to make a confident one-to-one assignment of calculated lattice modes and observed features. Nevertheless, the calculations are still useful for describing the types of molecular vibrations associated with each region of the spectrum.

7.2.6.2 Density Functional Theory Results

Density functional theory calculations have been applied to model the phonon modes of several classes of material such as salts, semiconductors, oxides and molecular organic crystal: general considerations and systems are reported in Baroni's review on density functional theory [58]. For simple systems (such as—see Fig. 7.9), it is possible to routinely achieve nearly perfect agreement between calculated and observed phonon spectra. The same excellent agreement is found for minerals such as forsterite (Mg_2SiO_4), for which the calculated vibrational frequencies differ from measured absorption frequencies by at most 4 cm^{-1} [59]. For more complex materials, when the dispersion forces become relevant, the agreement between calculated and measured frequencies is less reliable. Recent articles directly calculating terahertz spectra of organic molecular crystals have mainly been inspired by applications of terahertz technology for monitoring polymorphism in pharmaceuticals and detection of explosives.

There are a number of studies where it is possible to see the difference in calculated spectra associated with different exchange correlation functionals and basis set types. For example, the explosive material RDX (Fig. 7.8) has been studied using different DFT methods: Allis [60] and Ciezak [61] with atom-centred basis sets using DMol³; Miao [62] studied the same material using plane-wave basis set cal-

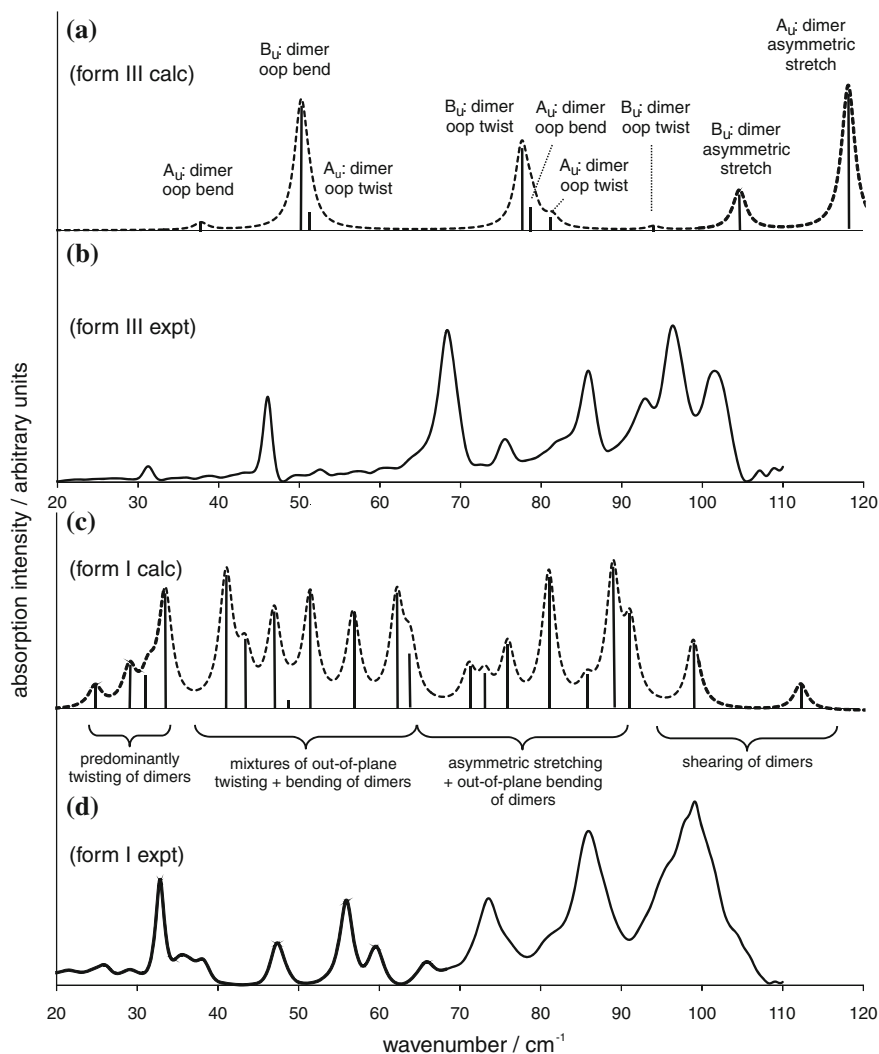


Fig. 7.7 Comparison of calculated (a, c) and observed (b, d) terahertz spectra of two crystal forms of carbamazepine (Fig. 7.6). (a) and (c) show the lattice dynamics calculated spectra of polymorphic forms III and I, respectively, using the FIT-DMA atom-atom potential described in the text. *Vertical lines* indicate the normal mode frequencies, with heights scaled by the calculated absorption intensities. The *dashed lines* represent the simulated spectrum, assuming a Lorentzian line shape with a line width of 2 cm^{-1} . (b) and (d) show the $T = 7\text{ K}$ observed terahertz spectra for forms III and I, respectively. (oop = out-of-plane). Adapted with permission from [55]. Copyright 2006 American Chemical Society

calculations using VASP and Shimojo [31] applied dispersion corrected functionals. Some of these results are summarised in Table 7.6; the lattice dynamics calculations provide good agreement with the observed spectrum, while variations in calculated

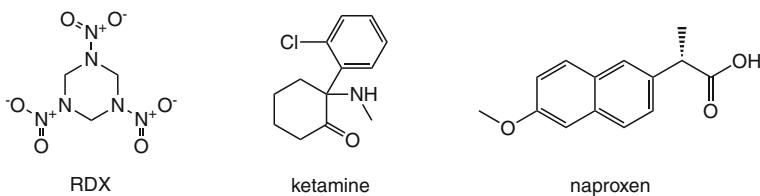
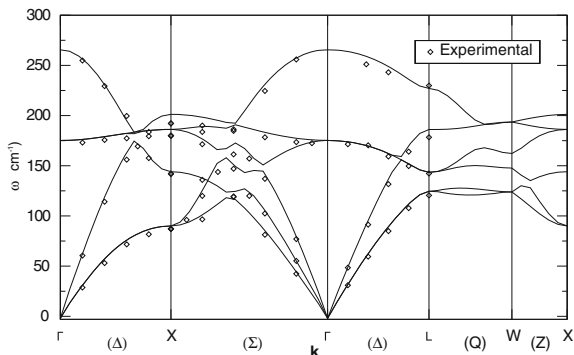


Fig. 7.8 Molecular structures of RDX, ketamine and naproxen

Fig. 7.9 Phonon dispersion relation of MgO calculated with a CASTEP calculation on a $2 \times 2 \times 2$ supercell, compared with neutron diffraction data (open symbols) and infrared reflectivity data (stars). Reproduced from [56] with permission from Elsevier



frequencies associated with different choices of functional, basis set and the inclusion of dispersion-correction terms to the DFT are mostly on the order of about $5\text{--}10\text{cm}^{-1}$. These differences between methods range up to 20cm^{-1} or more for some of the higher frequency vibrations. Overall, these variations are similar in magnitude to the differences between parameter sets and electrostatic models seen with force field based calculations.

Korter et al. have also performed studies to investigate the dependence of lattice dynamics results on the exchange–correlation functionals, considering the drugs MDMA hydrochloride [9] and ketamine [57]. These studies have provided insight into the subtle dependences of calculated spectra on the DFT methods employed. One of the most important observations from their study of MDMA hydrochloride was that the number of normal modes calculated within the $0\text{--}100\text{cm}^{-1}$ range (counting both terahertz active and inactive modes) is not constant, varying from as few as 18 modes in this range using the RPBE functional to as many as 23 using the BLYP functional. Furthermore, it can be seen from a visual inspection of Fig. 7.10 that the calculated intensity of absorptions of similar frequency have high variability with choice of DFT functional, which is a warning sign that the calculated eigenvectors, which describe the atomic displacements associated with each mode, differ significantly from one calculation to another. These two factors lead to significant differences between the predicted spectra from different functionals; in this case, the BP and BOP functionals provided the best agreement with experimental data. This example shows that, even using a potentially very accurate electronic structure method to calculate the lattice

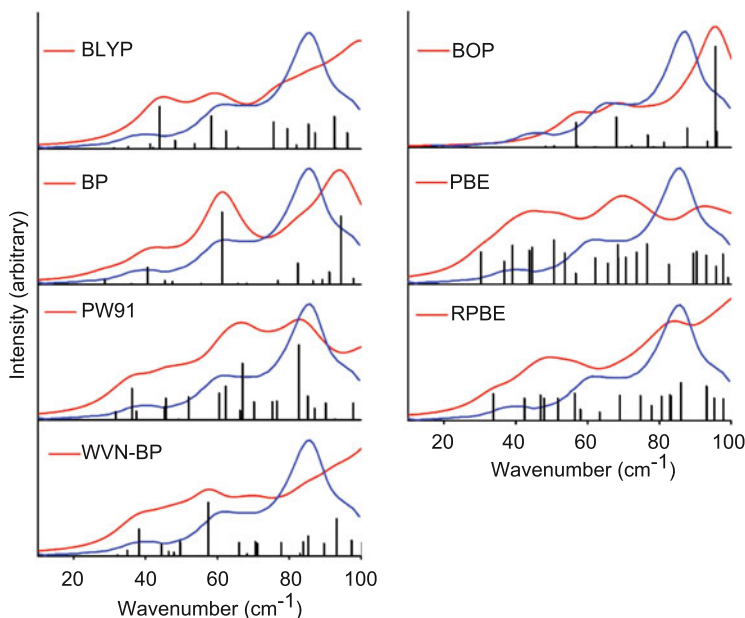


Fig. 7.10 Comparison of DFT lattice dynamics calculated (black lines) terahertz spectra of MDMA-HCl (see Fig. 7.1) using different exchange–correlation functionals with the experimentally observed absorption from a powdered sample of the crystal (blue lines). All calculations were performed within a unit cell fixed at the experimentally determined $T=161\text{K}$ dimensions. The calculated plots are generated by fitting the absorption frequency using a 7 cm^{-1} Lorentzian line shape. Adapted with permission from [57]. Copyright 2010 American Chemical Society

dynamics, a poor choice of DFT functional can have dramatic effects on the quality of the simulated spectrum.

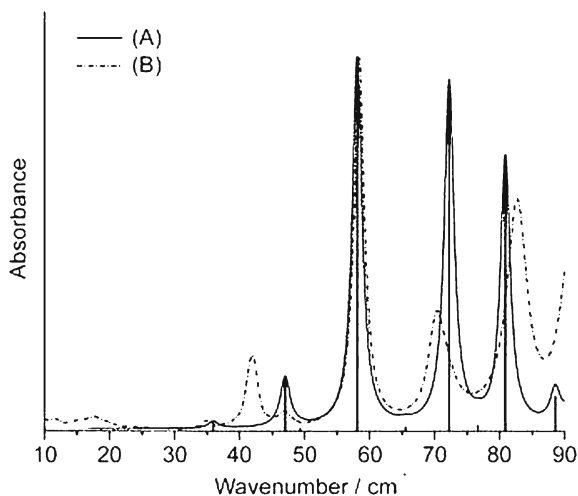
The use of a dispersion correction removes the need to constrain the unit cell to experimentally determined dimensions during the structural minimisation task of a DFT calculation, since effective dispersion correction terms should maintain a realistic unit cell during an unconstrained lattice energy minimisation. For RDX (Fig. 7.8) the effect of the dispersion correction to DFT is to provide agreement of the unit cell volume to within 1 %, without significant increase of the computational cost over pure DFT [31]. The resulting absorption frequencies calculated at the minimised structure are shown in Table 7.6 and show overall excellent agreement with experimentally determined frequencies. It is to be noticed that the choice of the dispersion correction parameters is not unique and can have a dramatic effect on the final results. For example, King [63] performed a series of calculations on naproxen (see Fig. 7.8) showing that, for this system, the dispersion correction implemented in the CRYSTAL09 code [36] generates a 10 % contraction in the unit cell when used with the PBE functional, an error which is almost equal in magnitude to the uncorrected PBE calculation, which results in +12 % volume expansion. It was demonstrated that a fine-tuning of the coefficients is capable of providing agreement within 2.23 % of

Table 7.6 Terahertz calculated absorption frequencies (cm^{-1}) for RDX with various methods

Lattice dynamics—DFT calculations			Molecular dynamics	Experimental
(a) BP	(b) PBE-D	(c) PW91	(d)	(e)
36.3	34.5	28	31	33
42.1	43.1	52	41	41
46.4	54.6	54	49	50
52.0	56.6	56	50	54
60.3	63.4	60	65	59
64.1	67.8	74	66	66
74.2	72.0	73	79	74
84.3	84.5	88	80	83
87.0	85.3	100	88	85
95.5	92.8	98	89	96
101.7	96.0	101	100	100
104.7	106	123	102	103
112.7	121	144	116	109

In column (a) DFT, Gaussian atom-centred basis set, BP functional [60]; column (b) DFT-D using a plane wave basis set [31]; column (c) DFT, plane wave basis set, PW91 functional [62]; column (d) force field-based molecular dynamics [30]; column (e) experimental data [60]

Fig. 7.11 Naproxen simulated spectrum with optimised dispersion parameters (A) compared with low temperature terahertz measurement. From [63]. Reproduced by permission of the PCCP Owner Societies



the experimental low temperature unit cell parameters and excellent agreement with the experimental spectrum (see Fig. 7.11). This result was obtained by rescaling of the dispersion coefficients by a factor 0.52.

More results are shown in the next section, together with MD calculations.

7.3 Molecular Dynamics

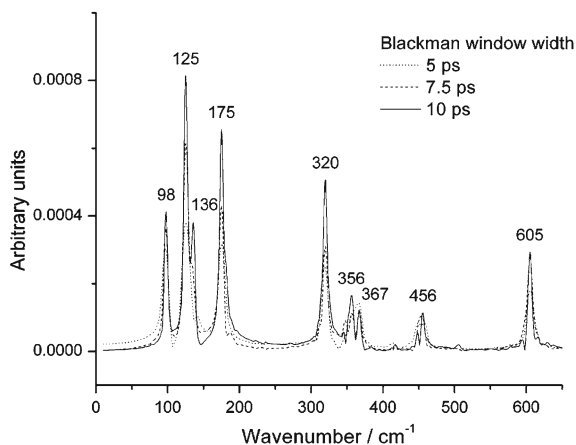
MD is a computational technique that can be used to model the evolution of a system through time. This is performed through the numerical integration of the Newtonian equation of motion arising from the interactions between the particles, starting from an initial configuration: the final result is a collection of snapshots of the atomic configuration, taken at discrete time steps. According to statistical mechanics, physical quantities are obtained through an average over a high number of configurations of the atoms in the system, and the effectiveness of a MD simulation lies in the number (and the completeness) of configurations sampled in the trajectory. The main advantage over lattice dynamics is that anharmonicity and the temperature-dependence of vibrational frequencies is automatically included, while MD suffers from much longer computational times and more complex analysis required to extract vibrational frequencies from the atomic trajectories.

For the calculation of the absorption spectrum of a crystal, it is sufficient to follow its vibrational dynamics around an equilibrium structure. The properties of a crystal can be calculated by assigning random velocities to the atoms near their equilibrium lattice positions, to wait for the equilibration of the system, after which the configuration of the system will evolve, oscillating through time. Initial velocities need not be so high as to break equilibrium conditions, or to introduce interactions that cause instability of the system, and are chosen to provide the final temperature (related to the total kinetic energy) of interest. MD can be performed with controls placed on a number of other macroscopic properties such as pressure, volume and total energy of the system. Apart from thermodynamic controls, the time step chosen to evolve the system is crucially important: the time scale needs to be smaller than the characteristic time associated with vibrations, which is typically in the range of femtoseconds, and the number of steps has to be big enough to sample all of the vibrations on the system.

It is customary to make use of the periodicity of the crystal within MD calculations by use of periodic boundary conditions: the motion of all atoms within a supercell of the unit cell of the crystal structure are treated explicitly. The positions and displacements within this supercell are replicated in all directions, so that each translational copy of an atom has the same velocity as that in the reference cell. Periodic boundary conditions can generate artefacts in the MD calculation if an atom interacts with a copy of itself; for this reason it is generally suggested to consider a supercell large enough that no atom interacts with its image via short range interactions.

As with the lattice dynamics method, a correct description of the dynamics of a system cannot be achieved without a proper handling of the forces acting between atoms. The interactions within a crystal can be computed using electronic structure methods such as DFT, or force fields, as discussed in Sect. 7.2.3.1. However, electronic structure MD methods, developed by Car and Parrinello [64] are so demanding on computational time that, at the moment, they can be used only for crystals with small unit cells (see [65] for an example); furthermore smaller time-steps are needed to account for the dynamics and the rearrangement of the electron density, which is

Fig. 7.12 CASTEP ab initio molecular dynamics simulations of the terahertz absorption of an ammonia crystal at 160 K. The effect of the length of the simulation (Blackman window in the graph) is considered. Reprinted with permission from [65]. Copyright 2008 American Chemical Society



much faster than that of the ions, and requires even smaller time steps, adding to the computation cost.

We refer to Sect. 7.2.4 for details on force fields; we can add here that there are a huge number of force fields that have been applied in MD studies of organic molecules, mostly relating to studies performed in the protein and macromolecule community: as a non-comprehensive list we can mention, among others MM2 [66] and CFF [67] force fields, used for small organic molecules; CHARMM [68] and GROMACS [69], for biomolecules and macromolecules; and UFF [70], with parameters for elements up to the actinoids. Furthermore, as mentioned previously, it is possible to generate and fine-tune a force field specifically designed to apply to a specific system, either where a well-developed force field does not exist or to improve the accuracy of an older force field [71]. Once the trajectory of atoms or molecules in a structure has been generated over a long enough time scale, the information about the vibrational motion of the molecules is contained in the autocorrelation functions: mathematical tools to determine patterns of a function that repeat in time. For a property v , the autocorrelation function, is defined as the time average of the product of that property's value at a particular time with the value at a time origin, t_0 :

$$A(t) = \langle v(t_0)v(t_0 + t) \rangle, \quad (7.25)$$

The brackets indicate an average over all configurations separated by a time interval t .

The autocorrelation function is easy to understand if we consider an example with atoms within a crystal all oscillating with an oscillatory movement of period τ . If the time t is not an integer multiple of τ the average over all configurations will be zero, while when t is a multiple of the vibrational period, τ , the function v will take on the same value at all pairs t and $(t + \tau)$ and the autocorrelation function will be non-zero. For a complex trajectory, the autocorrelation function extracts only the periodic part of the whole movement, with a weight proportional to its contribution. The Fourier

Table 7.7 Calculated NH_3 absorption frequencies (cm^{-1}) from Car Parrinello molecular dynamics and DFT lattice dynamics

Lattice dynamics				Molecular dynamics	Experimental
B3LYP	B3LYP	B3PW91	PW91	PW91	
TZP	6-311G**	6-311G**	TZP	400 eV	
98.1	99.7	93.8	111.2	98	107
121.6	113.4	120.2	142.2	125	138
130.9	132.6	127.5	144.9	136	138
174.8	177.0	174.5	191.5	175	181

The effect of using different exchange correlation functionals (top) and basis sets (bottom) is shown. The molecular dynamics is based on the PW91 DFT functional with a plane wave basis set up to a 400 eV cutoff. Lattice dynamics was performed using atom-centred basis functions and a range of DFT functionals. Reprinted with permission from [65]. Copyright 2008 American Chemical Society

transform of the autocorrelation function gives the frequency spectrum: an example showing calculations on crystalline ammonia is shown in Fig. 7.12. Again, to have a faithful representation of the slowest vibrations, the total simulation time needs to be long enough, while the time steps used in the MD simulation must be short enough to reproduce the fast vibrations. The absorption spectrum is obtained from the electrostatic dipole autocorrelation function.

Information about the eigenvectors can be extracted from the velocity autocorrelation function, noting that (since the simulation tries to sample all microscopic states) the Fourier transform produces the spectrum of all phonon states ($\mathbf{k} \neq 0$ as well). The number of k points sampled in a calculation depends on the size of the supercell used: larger cells provide a denser sampling of k points, as well as a better description of the dynamics of the system. It is possible to separate k points by considering the different phase of velocity for equivalent atoms in different cells: for atoms at positions r_1 and r_2 , separated by a distance \mathbf{R} , the relation between the velocities v is

$$v_2 = v_1 \exp(i\mathbf{k} \cdot \mathbf{R}) \quad (7.26)$$

As a result, by a summation over all equivalent atoms with constraints dictated by the relation in their velocities, it is possible to sort out the $\mathbf{k} = 0$ phonons we are interested in for optical spectroscopy (see [72] or [53] for details of the procedure). Once the frequencies and their dispersion with \mathbf{k} are known, it is possible to extract the associated atomic displacements associated with each vibrational mode from the trajectory.

Where direct comparisons have been made between the results of lattice dynamics calculations and phonon frequencies extracted from MD, the agreement between the two methods is generally very good. Table 7.7 shows DFT-based results for crystalline ammonia. MD frequencies are in fairly good agreement with those from lattice dynamics calculations, although calculations using the same DFT functional (PW91) find that frequencies from lattice dynamics are shifted to higher frequencies by $15\text{--}30\text{cm}^{-1}$ compared to those from MD; this frequency shift could be attributed

to the harmonic approximation applied in the lattice dynamics approach, while also possibly being influenced by differences in the basis sets used in the two calculations.

Rigid-molecule force field based results for imidazole (Table 7.5) also show good agreement between the MD and lattice dynamics approaches: frequencies calculated using the exact same force field (FIT-DMA) agree to within about 5 cm^{-1} and molecular displacements determined from the MD analysis were also reported to be in very good agreement with the eigenvectors calculated from lattice dynamics [53]. Here, the frequency shifts can be directly related to the influence of anharmonicity and we find that the frequencies extracted from MD trajectories are mostly shifted to lower frequency. Interestingly, this shift was found to relate to the influence of the vibration on the hydrogen bonds in the crystal structure: hydrogen bond stretching modes are shifted to lower frequency by anharmonicity, while hydrogen bond bending modes are either unaffected or, surprisingly, shifted to higher frequencies in the MD simulation.

7.4 Conclusions, Summary and Limitations of the Methods

The phonon modes in crystals correspond to collective oscillations of the atoms in the structure. For molecular crystals, the vibrational modes in the terahertz region are largely due to whole molecule motions about their equilibrium positions, including both translational and rotational oscillations of the molecules. Therefore, these modes are very sensitive to the interactions between molecules, making terahertz spectroscopy a powerful probe of the intermolecular forces in crystals. However, the origin of the features observed in experimentally determined spectra are difficult to interpret without the aid of modelling methods. The methods available for simulating the vibrational spectra of crystals are lattice dynamics and MD, either of which can be based on atom–atom (force field) or electronic structure methods, whose main limitations and strengths are summarised below.

7.4.1 Force Fields Versus Electronic Structure (DFT) Calculations

The lattice dynamics approach performed within a force field framework was historically the first to be implemented, thanks to the lesser computational requirements compared with a DFT calculation, allowing the fast calculation of the lattice modes of systems with hundreds of atoms within the unit cell. For example, force fields have been used to calculate the spectrum of a chain of the protein ricin, with a molecular mass in excess of 20,000 Dalton and with more than 300 vibrational modes in the narrow frequency range from 2 to 50 cm^{-1} [73]. Such a system is currently intractable using electronic structure-based methods. The same holds for MD: force field MD has been used to calculate the terahertz spectrum of opsins (proteins responsible for the absorption of light in the eye), weighing around 40,000 Dalton,

where it has even been possible to consider the effect of a hydration shell around the molecule [74].

The most important limitation in force field methods is often in the accuracy of the description of the electronic interactions, which is necessarily approximate and usually limited to fixed atomic partial charges. Furthermore, the effectiveness of a general force field is often related to the similarity of the system under study with the systems to which the force field has been parameterised. Ad hoc, non-empirically derived force fields, while potentially more precise, can take considerable time to be developed and are typically limited to small molecules. On the other hand, DFT results are also sensitive to the choice of functional. DFT calculations are potentially very accurate and should provide a better description of the covalent, intramolecular interactions within a molecule. However, current functionals poorly describe the intermolecular van der Waals interactions between neutral organic molecules. Therefore, such calculations need to be corrected by an atom–atom dispersion correction term.

7.4.2 Lattice Dynamics Versus Molecular Dynamics

Of the two, lattice dynamics is by far the simpler and less computationally demanding method for simulating the lattice modes in crystals. The main advantage of a MD calculation is the flexibility of the method: it is possible to perform calculations at different temperatures, considering the effect on the spectrum explicitly. Furthermore, through the treatment of the vibrations at finite temperature it is possible to include the anharmonicity of the crystal in a natural way. In contrast, lattice dynamics calculations are often limited to a harmonic treatment where the results of the calculation formally relate to zero kelvin.

MD methods may also be applied to non-periodic systems, allowing predictions of the spectra liquids [75] or disordered materials. A related disadvantage of the MD method is that the crystal symmetry cannot be enforced in the simulation, so that it might therefore be difficult to assign the correct symmetry of the normal modes of vibration; in lattice dynamics, symmetry analysis of the lattice modes is straightforward. Lattice dynamics can also be more readily extended to include the effect of long range electrostatic forces, while are known to break the degeneracy (and therefore change the frequency) of some of the normal modes in polar crystals: this effect is known as LO-TO splitting [76].

7.4.3 General Problems to Address

The examples included in this chapter show that the lattice dynamics and MD approaches can give good agreement with the observed frequencies of lattice vibrational modes, and are thus powerful methods for understanding the underlying mole-

cular vibrations that lead to observed features in terahertz spectra. A large focus of work for improving these methods is the development and fine-tuning of the methods used to calculate the interactions in the structures. Apart from further improvements to our force field or electronic structure-based energy models, we also highlight several further effects that should be considered when simulating the spectrum of a crystal using the methods described in the previous sections. These relate to the fact that the computational methods are generally applied to infinite, perfect crystal structures, while real measurements are affected by imperfections and the finite size of the crystals being studied. Among others, we can mention:

- Surface effects, resulting from the finite size of the sample;
- the microcrystalline nature of samples;
- and disorder or impurities in crystal.

7.4.3.1 Surface Effects

It is currently not possible to account accurately for the finite size of the crystal on a measured spectrum: lattice dynamics methods assume an infinite, periodic structure, while MD methods cannot deal with a large enough number of atoms to form a macroscopic crystal. The most significant deviations from the infinite crystal theory occur when the dimension of the crystal are comparable to the wavelength of light.

It is possible to consider finite size effects for very simple crystals. Similarly to what we described in Sect. 7.2.3.1, Ruppin and Engman [77] considered the case of a cubic crystal of finite size and simple structure, introducing the conditions imposed by Maxwell's equations for travelling light into the lattice equations. The results of this treatment are polariton modes: mixed modes with both phonon and photon contributions, that describe the propagation of radiation inside the crystal. These polariton modes may be either non-radiative (where the intensity decays outside the crystal) or radiative (where the intensity does not decay, and can therefore be detected).

The vibrational modes can be further classified according to their behaviour inside the crystal: in bulk modes, the vibration occurs across the entire crystal, while the motions associated with surface modes decrease exponentially away from the surface of the sample into the bulk. The bulk frequencies calculated for finite crystallites are not necessarily coincident with the frequencies arising from the treatment of an infinite crystal, but tend towards the bulk frequencies as the dimension of the crystal is increased. For example, for a finite NaCl crystal there is not one vibrational mode, but a set of modes centred around the transverse and longitudinal frequencies of the infinite crystal, ω_T and ω_L (Fig. 7.13).

The surface modes are intermediate in frequency between ω_T and ω_L , and are characterised by motions that can be sustained at the interface of the crystal (see Fig. 7.14). These modes are therefore strongly dependent on the geometry of the crystallite. Analytic solutions for the modes can be found for simple structures in the case of spherical crystallites, cylinders and rectangular slabs.

Fig. 7.13 Calculated absorption for slab particles of NaCl. In the top figure the particle height is $10\ \mu\text{m}$. In the lower figure, it is $1\ \mu\text{m}$. The absorption frequencies from the infinite crystal, ω_T and ω_L , are indicated. Adapted from [77] with permission from the Institute of Physics

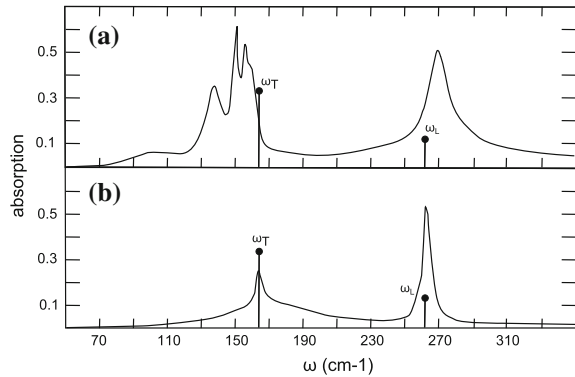
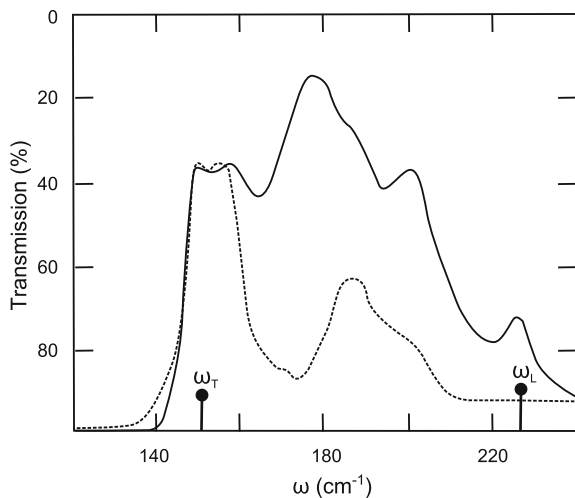


Fig. 7.14 Experimental absorption of small parallelepipeds of KCl of different sizes. The sizes are (in μm) $2 \times 4.5 \times 4.5$ for the full curve, $2.5 \times 9 \times 9$ for the dashed curve (adapted from [77] with permission from the Institute of Physics). The infinite crystal calculated frequencies are indicated as ω_T and ω_L



7.4.3.2 Powder Spectra

Measured absorption spectra often relate to microcrystalline samples, composed of a myriad of randomly oriented microcrystals, often embedded in a binder that displays limited absorption in the terahertz region. Such measurements are affected by the issues exposed in the previous section: the presence of surface modes on crystals of different sizes and with different orientations are also found to depend on the dimension of the sample and on the dielectric constant of the medium in which they are embedded (i.e. the measured frequency would be different for spherical crystallites in air or in a binder).

Balan [78] has calculated the IR powder spectrum of a sedimentary natural clay (kaolinite, $\text{Al}_2\text{Si}_2\text{O}_5(\text{OH})_4$) taking into account the experimental set-up (Fig. 7.15). The geometry of the microcrystals is experimentally known to be thin plates; these are diluted in KBr powder binder, and compressed into a pellet. In a simple treatment, the

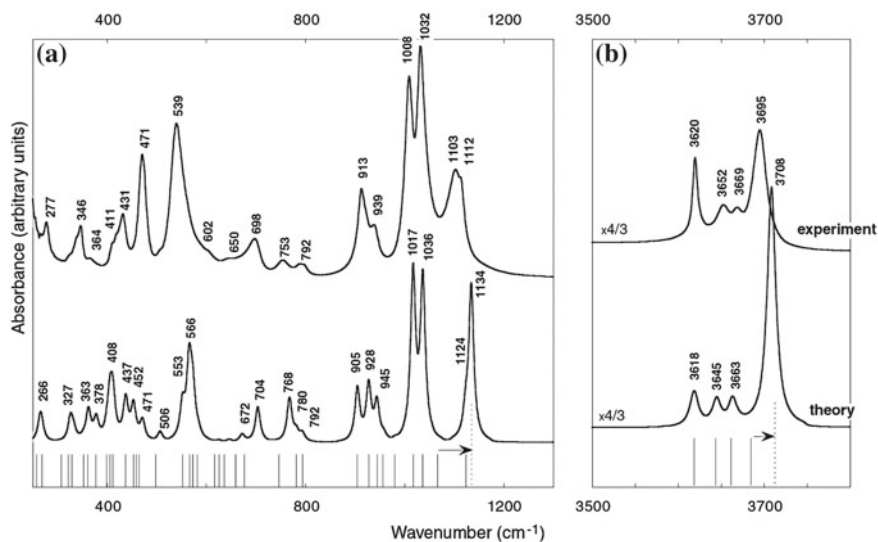
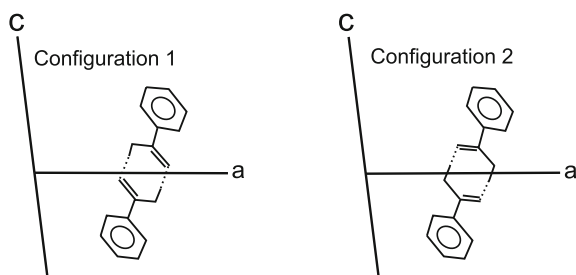


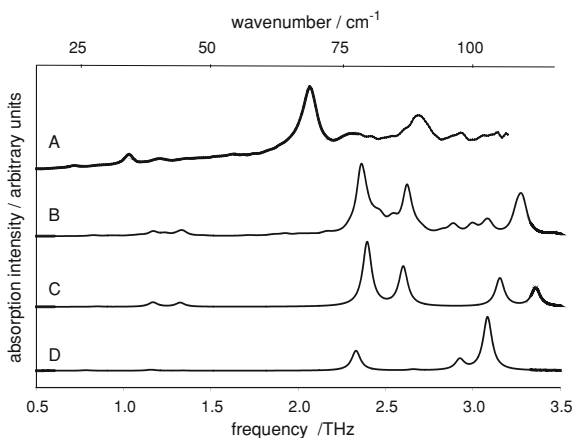
Fig. 7.15 Experimental and calculated infrared spectrum of kaolinite (reproduced from [78] with permission from Elsevier). The frequency eigenvalues are indicated by vertical lines at the bottom of the spectra

Fig. 7.16 Possible configuration of the benzoic acid dimer, and the position inside a crystallographic unit cell (a and c axes shown). The hydrogen bond within the molecule is indicated with a dotted line. Adapted from [79]



binder is theoretically approximated as a uniform dielectric medium, and its influence on the microcrystal consists of a charge polarisation effect on the surface and in the bulk crystal. This effect is averaged over the randomly oriented microcrystals, and the effect was calculated on the normal modes calculated using DFT-based lattice dynamics. The result is that some of the absorption frequencies are shifted with respect to the normal modes of the crystal (see Fig. 7.15) and the absorption of some of the modes is found to be strongly dependent on the dielectric constant of the binder. This calculation resolved some of the issues related to shifted absorption bands that could not be correctly assigned from previous calculations. It is to be noted that this treatment required a detailed knowledge of the microcrystal geometry that might not be possible for many systems, where distributions in size and shape of crystallites are likely to exist.

Fig. 7.17 Experimental and calculated terahertz spectra of crystalline benzoic acid (From [41]. Reproduced by permission of the PCCP Owner Societies). **a** The experimental spectrum, measured at $T = 110\text{ K}$, **b** the calculated spectrum averaged over several supercell models of the disordered structure, **c** the calculated spectrum with all hydrogen bond dimers in the lower energy configuration, **d** the calculated spectrum with all dimers in the higher energy configuration



7.4.3.3 Disorder and Impurities

The periodicity within a crystal can be broken by impurities and defects, whose presence modifies the local environment of molecules inside the crystal and will therefore affect the local intermolecular forces and, consequently, the lattice mode spectrum of a crystal. An example is crystalline benzoic acid, in which molecules are arranged as hydrogen bonded dimers. In this crystal structure, there are two possible configurations for a benzoic acid dimer, differing only in the positions of the protons within the hydrogen bond dimers (see Fig. 7.16). The relative populations of the two types of dimer are temperature-dependent, with 87% of dimers being found in the lower energy configuration at $T = 4\text{ K}$, while the ratio is as high as 1:2 [79] at higher temperatures.

The influence of this disorder on the terahertz spectrum was recently investigated by Li et al. [41], who modelled the disorder by considering several crystalline supercells of the known crystal structure in which the benzoic acid dimers were randomly assigned one of the two configurations in the observed 1:2 ratio. These supercells were then treated using force field-based lattice dynamics calculations and compared to the results of calculations on completely ordered structures. While the frequencies of all vibrational modes are overestimated by the force field method used, it is clear (see Fig. 7.17) that the disorder in the proton positions has a noticeable effect on the simulated spectrum. Furthermore, the effect of the disorder is different from what would be predicted from an average of the spectra from the two ordered models: additional weak features are introduced and the splitting between the stronger features is affected by the disorder.

The treatment of disorder here is only approximate, as a periodic unit cell is still needed for the lattice dynamics approach. However, the results do demonstrate how the spectrum is strongly influenced by the subtle effect of changing the position of a single atom within a molecule. It is easy to imagine that the disorder in other

structures may have an even greater influence on the terahertz spectrum and may be necessary to consider in fully understanding the details in observed spectra. Again, for this kind of treatment it is necessary to have a detailed knowledge of the subtleties of a crystal structure.

Overall, computational methods have an integral role to play in interpreting the terahertz spectra of molecular crystals. While the subtleties of observed spectra may require further development of models to account for the influences of finite crystalline size and imperfections, existing methods can already help understand the molecular motions corresponding to observed features. These methods are thus enabling a chemical interpretation of spectra in terms of the interactions between molecules.

References

1. P.F. Bernath, The spectroscopy of water vapour: Experiment, theory and applications. *Phys. Chem. Chem. Phys.* **4**, 1501–1509 (2002)
2. O. Pirali, N.-T. Van-Oanh, P. Parneix, M. Vervloet, P. Brechignac, Far-infrared spectroscopy of small polycyclic aromatic hydrocarbons. *Phys. Chem. Chem. Phys.* **8**, 3707–3714 (2006)
3. S.C. Capelli, A. Albinati, S.A. Mason, B.T.M. Willis, Molecular motion in crystalline naphthalene: analysis of multi-temperature X-ray and neutron diffraction data. *J. Phys. Chem. A* **110**(41), 11695–11703 (2006)
4. I. Harada, T. Shimanouchi, Normal vibrations and intermolecular forces of crystalline benzene and naphthalene. *J. Chem. Phys.* **44**(5), 2016–2028 (1966)
5. G. Taddei, H. Bonadeo, S. Califano, The calculation of the normal coordinates of molecular crystals using pairwise potential functions. *Chem. Phys. Lett.* **13**(2), 136–139 (1972)
6. P. Hermet, J.-L. Bantignies, A. Rahmani, J.-L. Sauvajol, M.R. Johnson, F. Serein, Far- and mid-Infrared of crystalline 2,2'-Bithiophene: Ab initio analysis and comparison with infrared response. *J. Phys. Chem. A* **109**(8), 1684–1691 (2005)
7. G. Wang, J. Shen, Y. Jia, Vibrational spectra of ketamine hydrochloride and 3,4-methylenedioxymethamphetamine in terahertz range. *J. Appl. Phys.* **102**(1), 013106 (2007)
8. D.G. Allis, P.M. Hakey, T.M. Korter, The solid-state terahertz spectrum of MDMA (Ecstasy)—a unique test for molecular modeling assignments. *Chem. Phys. Lett.* **463**(4–6), 353–356 (2008)
9. P. Hakey, D. Allis, M. Hudson, T. Korter, Density functional dependence in the theoretical analysis of the terahertz spectrum of the illicit drug MDMA (Ecstasy). *IEEE Sens. J.* **10**(3), 478–484 (2010)
10. G. Grosso, G.P. Parravicini, *Solid State Physics*, 1st edn. (Academic Press, New York, 2000)
11. E.W. Kellermann, Theory of the vibrations of the sodium chloride lattice. *Philos. Trans. R. Soc. Lond. Ser. A, Math. Phys. Sci.* **238**(798), 513–548 (1940)
12. G. Raunio, S. Rolandson, Lattice dynamics of NaCl, KCl, RbCl, and RbF. *Phys. Rev. B* **2**(6), 2098–2103 (1970)
13. M.P. Verma, B. Dayal, Lattice dynamics of MgO. *Phys. Status Solidi (B)* **19**(2), 751–756 (1967)
14. G. Raunio, L. Almqvist, R. Stedman, Phonon dispersion relations in NaCl. *Phys. Rev.* **178**(3), 1496–1501 (1969)
15. A.M. Karo, J.R. Hardy, Precise vibrational frequency distributions and the second-order Raman spectrum and specific heat of NaCl. *Phys. Rev.* **141**(2), 696–710 (1966)
16. U. Schröder, A new model for lattice dynamics (“breathing shell model”). *Solid State Commun.* **4**(7), 347–349 (1966)

17. W. Dyck, Lattice dynamics of alkali hydrides and euterides with the NaCl type structure. *J. Phys. C: Solid State Phys.* **14**(29), 4193 (1981)
18. S. Baroni, P. Giannozzi, A. Testa, Green's-function approach to linear response in solids. *Phys. Rev. Lett.* **58**(18), 1861–1864 (1987)
19. A.J. Pertsin, A.I. Kitaigorodskii, in *The Atom-Atom Potential Method: Applications to Organic Molecular Solids*, vol. 43 (Springer Series in Chemical Physics (Springer, Heidelberg, 1987)
20. D.E. Williams, Nonbonded potential parameters derived from crystalline aromatic hydrocarbons. *J. Chem. Phys.* **45**, 3770–3779 (1966)
21. S.R. Cox, L.-Y. Hsu, D.E. Williams, Nonbonded potential function models for crystalline oxohydrocarbons. *Acta Crystallogr. Sect. A* **37**(3), 293–301 (1981)
22. D.E. Williams, S.R. Cox, Nonbonded potentials for azahydrocarbons: the importance of the Coulombic interaction. *Acta Crystallogr. Sect. B* **40**(4), 404–417 (1984)
23. D.E. Williams, D.J. Houpt, Fluorine nonbonded potential parameters derived from crystalline perfluorocarbons. *Acta Crystallogr. Sect. B* **42**(3), 286–295 (1986)
24. G.M. Day, S.L. Price, A nonempirical anisotropic atom-atom model potential for chlorobenzene crystals. *J. Am. Chem. Soc.* **125**(52), 16434–16443 (2003)
25. R. Righini, N. Neto, S. Califano, S. Walmsley, Lattice dynamics of crystalline ammonia and deuterio-ammonia. *Chem. Phys.* **33**(3), 345–353 (1978)
26. S.H. Walmsley, Basic theory of the lattice dynamics of molecular crystals, in *Lattice dynamics and Intermolecular Forces*. Proceedings of the International School of Physics “Enrico Fermi”, vol. 55. (Academic Press, New York, 1975), p. 82
27. P.D. DeCicco, F.A. Johnson, The quantum theory of lattice dynamics. IV. *Proc. R. Soc. Lond. A. Math. Phys. Sci.* **310**(1500), 111–119 (1969)
28. P. Hohenberg, W. Kohn, Inhomogeneous electron gas. *Phys. Rev.* **136**(3B), B864–B871 (1964)
29. W. Kohn, L.J. Sham, Self-consistent equations including exchange and correlation effects. *Phys. Rev.* **140**(4A), A1133–A1138 (1965)
30. S.G. Boyd, K.J. Boyd, A computational analysis of the interaction of lattice and intramolecular vibrational modes in crystalline α -RDX. *J. Chem. Phys.* **129**(13), 134502 (2008)
31. F. Shimojo, Z. Wu, A. Nakano, R.K. Kalia, P. Vashishta, Density functional study of 1,3,5-trinitro-1,3,5-triazine molecular crystal with van der Waals interactions. *J. Chem. Phys.* **132**(9), 094106 (2010)
32. S. Grimme, J. Antony, S. Ehrlich, H. Krieg, A consistent and accurate ab initio parametrization of density functional dispersion correction (dft-d) for the 94 elements H-Pu. *J. Chem. Phys.* **132**, 154104 (2010)
33. B. Delley, An all-electron numerical method for solving the local density functional for polyatomic molecules. *J. Chem. Phys.* **92**, 508–518 (1990)
34. J.M. Soler, E. Artacho, J.D. Gale, A. García, J. Junquera, P. Ordejón, D. Sánchez-Portal, The SIESTA method for ab initio order-N materials simulation. *J. Phys.: Condens. Matter* **14**(11), 2745 (2002).
35. J. Junquera, O. Paz, D. Sánchez-Portal, E. Artacho, Numerical atomic orbitals for linear-scaling calculations. *Phys. Rev. B* **64**(23), 235111 (2001)
36. R. Dovesi, R. Orlando, B. Civalleri, C. Roetti, V.R. Saunders, C.M. Zicovich-Wilson, CRYSTAL: a computational tool for the ab initio study of the electronic properties of crystals. *Zeitschrift für Kristallographie* **220**, 571–573 (2005)
37. S.J. Clark, M.D. Segall, C.J. Pickard, P.J. Hasnip, M.I.J. Probert, K. Refson, M.C. Payne, First principles methods using CASTEP. *Zeitschrift für Kristallographie* **220**, 567–570 (2005)
38. G. Kresse, J. Furthmüller, Efficient iterative schemes for ab initio total-energy calculations using a plane-wave basis set. *Phys. Rev. B* **54**(16), 11169–11186 (1996)
39. G. Taddei, H. Bonadeo, M.P. Marzocchi, S. Califano, Calculation of crystal vibrations of benzene. *J. Chem. Phys.* **58**(3), 966–978 (1973)
40. G.S. Pawley, A model for the lattice dynamics of naphthalene and anthracene. *Phys. Status Solidi (b)* **20**(1), 347–360 (1967)
41. R. Li, J.A. Zeitler, D. Tomerini, E.P.J. Parrott, L.F. Gladden, G.M. Day, A study into the effect of subtle structural details and disorder on the terahertz spectrum of crystalline benzoic acid. *Phys. Chem. Chem. Phys.* **12**, 5329–5340 (2010)

42. I. Harada, T. Shimanouchi, Far-infrared spectra of crystalline benzene at 138K and intermolecular forces. *J. Chem. Phys.* **46**(7), 2708–2714 (1967)
43. H. Bonadeo, M.P. Marzocchi, E. Castellucci, S. Califano, Raman spectrum of a single crystal of benzene. *J. Chem. Phys.* **57**(10), 4299–4303 (1972)
44. D.E. Williams, Nonbonded potential parameters derived from crystalline hydrocarbons. *J. Chem. Phys.* **47**, 4680–4684 (1967)
45. M. Majoube, G. Vergoten, Lattice vibrations of crystalline imidazole and 15N and D substituted analogs. *J. Chem. Phys.* **76**(6), 2838–2847 (1982)
46. C. Perchard, A. Novak, Far-infrared spectra and hydrogen-bond frequencies of imidazole. *J. Chem. Phys.* **48**(7), 3079–3084 (1968)
47. G. Filippini, A. Gavezzotti, Empirical intermolecular potentials for organic crystals: the ‘6-exp’ approximation revisited. *Acta Crystallogr.* **B49**, 868–880 (1993)
48. D.S. Coombes, S.L. Price, D.J. Willock, M. Leslie, Role of electrostatic interactions in determining the crystal structures of polar organic molecules. A distributed multipole study. *J. Phys. Chem.* **100**(18), 7352–7360 (1996)
49. D.E. Williams, Improved intermolecular force field for crystalline oxohydrocarbons including O-H...O hydrogen bonding. *J. Comput. Chem.* **22**(1), 1–20 (2001)
50. D.E. Williams, Improved intermolecular force field for molecules containing H, C, N, and O atoms, with applications to nucleoside and peptide crystals. *J. Comput. Chem.* **22**(11), 1154–1166 (2001)
51. A.J. Stone, M. Alderton, Distributed multipole analysis: methods and applications. *Mol. Phys.* **56**(5), 1047–1064 (1985)
52. G.M. Day, S.L. Price, M. Leslie, Atomistic calculations of phonon frequencies and thermodynamic quantities for crystals of rigid organic molecules. *J. Phys. Chem. B* **107**, 10919–10933 (2003)
53. A.E. Gray, G.M. Day, M. Leslie, S.L. Price, Dynamics in crystals of rigid organic molecules: contrasting the phonon frequencies calculated by molecular dynamics with harmonic lattice dynamics for imidazole and 5-azauracil. *Mol. Phys.* **102**, 1067–1083 (2004)
54. Z. Gamba, H. Bonadeo, Lattice dynamical calculations on azabenzene crystals: the distributed dipole model. *J. Chem. Phys.* **75**(10), 5059–5066 (1981)
55. G.M. Day, J.A. Zeitler, W. Jones, T. Rades, P.F. Taday, Understanding the influence of polymorphism on phonon spectra: lattice dynamics calculations and terahertz spectroscopy of carbamazepine. *J. Phys. Chem. B* **110**, 447–456 (2006)
56. K. Parlinski, J. Lazewski, Y. Kawazoe, Ab initio studies of phonons in MgO by the direct method including LO mode. *J. Phys. Chem. Solids* **61**, 87–90 (2000)
57. P.M. Hakey, D.G. Allis, M.R. Hudson, W. Ouellette, T.M. Korter, Terahertz spectroscopic investigation of S-(+)-ketamine hydrochloride and vibrational assignment by density functional theory. *J. Phys. Chem. A* **114**(12), 4364–4374 (2010)
58. S. Baroni, S. de Gironcoli, A. Dal Corso, P. Giannozzi, Phonons and related crystal properties from density-functional perturbation theory. *Rev. Mod. Phys.* **73**(2), 515–562 (2001)
59. Y. Noel, M. Catti, P. D’Arco, R. Dovesi, The vibrational frequencies of forsterite Mg_2SiO_4 : an all-electron ab initio study with the CRYSTAL code. *Phys. Chem. Miner.* **33**, 383–393 (2006)
60. D.G. Allis, J.A. Zeitler, P.F. Taday, T.M. Korter, Theoretical analysis of the solid-state terahertz spectrum of the high explosive RDX. *Chem. Phys. Lett.* **463**(1–3), 84–89 (2008)
61. J.A. Ciezak, S.F. Trevino, Inelastic neutron scattering spectrum of cyclotrimethylenetrinitramine: a comparison with solid-state electronic structure calculations. *J. Phys. Chem. A* **110**(15), 5149–5155 (2006)
62. M.S. Miao, Z.A. Dreger, J.M. Winey, Y.M. Gupta, Density functional theory calculations of pressure effects on the vibrational structure of α -RDX. *J. Phys. Chem. A* **112**(47), 12228–12234 (2008)
63. M.D. King, W.D. Buchanan, T.M. Korter, Application of London-type dispersion corrections to the solid-state density functional theory simulation of the terahertz spectra of crystalline pharmaceuticals. *Phys. Chem. Chem. Phys.* **13**, 4250–4259 (2011)

64. R. Car, M. Parrinello, Unified approach for molecular dynamics and density-functional theory. *Phys. Rev. Lett.* **55**(22), 2471–2474 (1985)
65. A.M. Reilly, D.S. Middlemiss, M.M. Siddick, D.A. Wann, G.J. Ackland, C.C. Wilson, D.W.H. Rankin, C.A. Morrison, The phonon spectrum of phase-I ammonia: reassignment of lattice mode symmetries from combined molecular and lattice dynamics calculations. *J. Phys. Chem. A* **112**(6), 1322–1329 (2008)
66. N.L. Allinger, Conformational analysis. 130. MM2. A hydrocarbon force field utilizing V1 and V2 torsional terms. *J. Am. Chem. Soc.* **99**(25), 8127–8134 (1977)
67. S.O. Jonsdottir, K. Rasmussen, The consistent force field. Part 6: an optimized set of potential energy functions for primary amines. *N. J. Chem.* **24**, 243–247 (2000)
68. A. MacKerel Jr., C. Brooks III, L. Nilsson, B. Roux, Y. Won, M. Karplus, in *CHARMM: The Energy Function and Its Parameterization with an Overview of the Program*, vol. 1. The Encyclopedia of Computational Chemistry (Wiley, Chichester, 1998), pp. 271–277
69. B. Hess, C. Kutzner, D. van der Spoel, E. Lindahl, Gromacs 4: algorithms for highly efficient, load-balanced, and scalable molecular simulation. *J. Chem. Theory Comput.* **4**(3), 435–447 (2008)
70. A.K. Rappe, C.J. Casewit, K.S. Colwell, W.A. Goddard, W.M. Skiff, UFF, a full periodic table force field for molecular mechanics and molecular dynamics simulations. *J. Am. Chem. Soc.* **114**(25), 10024–10035 (1992)
71. B. Qiu, X. Ruan, Molecular dynamics simulations of lattice thermal conductivity of bismuth telluride using two-body interatomic potentials. *Phys. Rev. B* **80**(16), 165203 (2009)
72. M.M. Siddick, G.J. Ackland, C.A. Morrison, Constrained dynamics and extraction of normal modes from ab initio molecular dynamics: application to ammonia. *J. Chem. Phys.* **125**(6), 064707 (2006)
73. H. Zhang, E. Zukowski, R. Balu, S.K. Gregurick, A dynamics study of the a-chain of ricin by terahertz vibrational calculation and normal modes analysis. *J. Mol. Graph. Model.* **27**(5), 655–663 (2009)
74. S. Thirumuruganandham, H. Urbassek, Low-frequency vibrational modes and infrared absorbance of red, blue and green opsin. *J. Mol. Model.* **15**, 959–969 (2009)
75. A.Y. Zaslavsky, A.S. Lileev, A.K. Lyashchenko, Molecular dynamic simulations of terahertz spectra for water-methanol mixtures. *Mol. Phys.: Int. J. Interface. Chem. Phys.* **108**, 649–656 (2010)
76. H. Schober, D. Strauch, Investigation of the LO-TO splitting in complex binary crystals. *J. Phys.: Condens. Matter* **5**(34), 6165 (1993)
77. R. Ruppin, R. Englman, Optical phonons of small crystals. *Rep. Prog. Phys.* **33**(1), 149–196 (1970)
78. E. Balan, A.M. Saitta, F. Mauri, G. Calas, First-principles modeling of the infrared spectrum of kaolinite. *Am. Mineral.* **86**(11–12), 1321–1330 (2001)
79. C.C. Wilson, N. Shankland, A.J. Florence, Direct determination of the temperature dependence of proton transfer in the benzoic acid dimer by single crystal neutron diffraction. *Chem. Phys. Lett.* **253**(1–2), 103–107 (1996)

Chapter 8

Terahertz Spectroscopy of Crystalline and Non-Crystalline Solids

Edward P. J. Parrott, Bernd M. Fischer, Lynn F. Gladden, J. Axel Zeitler and Peter U. Jepsen

Abstract Terahertz spectroscopy of crystalline and non-crystalline solids is probably one of the most active research fields within the terahertz community. Many potential applications, amongst which spectral recognition is probably one of the most prominent, have significantly stimulated the development of commercial systems and have spurred an increased technical advancement. However, the topic is very complex and multifaceted. Therefore, it is beyond the scope of this chapter to provide a fully comprehensive review of the works performed in this area. We would rather like to demonstrate, based on some selected examples, the potential the technique holds for various different applications. A particular focus will be given to data analysis and, in particular, how we may account for effects resulting from non-ideal sample preparation.

E. P. J. Parrott
Department of Electronic Engineering, The Chinese University of Hong Kong,
Hong Kong, China
e-mail: parrott@ee.cuhk.edu.hk

B. M. Fischer
Institut franco-allemand de recherches de Saint-Louis,
68301 Saint-Louis Cedex, France
e-mail: bernd.fischer@isl.eu

L. F. Gladden and J. A. Zeitler (✉)
Department of Chemical Engineering and Biotechnology,
University of Cambridge,
Cambridge CB2 3RA, UK
e-mail: jaz22@cam.ac.uk

P. U. Jepsen
DTU Fotonik-Department of Photonics Engineering,
Technical University of Denmark,
2800 Kongens Lyngby, Denmark
e-mail: puje@fotonik.dtu.dk

8.1 Introduction

Infrared spectroscopy is one of the most widely used standard techniques for characterisation and investigation of structure and composition of solid, liquid and gaseous samples. There is hardly any chemical research facility not using an infrared spectrometer, and the technique is also commonly used in industrial production sites for material characterisation and quality control. It was proposed four decades ago that the low frequency end of the far-infrared range was very well suited to investigating the material properties of solids [1–3]. However, due to constraints with regard to the available far-infrared spectrometer technology a more comprehensive investigation was delayed and the number of publications reporting the far-infrared spectra of various samples remained low. With the advent of THz-TDS in the 1990s, this changed significantly and the number of reports on spectra of chemical substances, semiconductors, organic materials and bimolecular samples continues to increase to this day.

The characteristic spectroscopic signatures, which are commonly observed in the spectra of many crystalline samples, spurred an increased interest in THz-TDS. Many possible applications based on spectral recognition of these fingerprints were proposed and soon spectral catalogues containing entries of various substances such as explosives, pharmaceuticals, food additives and biomolecules were compiled (<http://thzdb.org>). However, the potential of THz-TDS for the investigation and characterisation of solids goes well beyond spectral recognition alone. Due to the fact that this technology gives experimental access to the full dielectric function, and thus both extinction and phase information, studies of conductivity, internal structure, and impurities are just a few of many applications. Over the past two decades, the spectra of a multitude of different crystalline and non-crystalline samples have been recorded in order to investigate what additional THz-TDS studies can reveal that is not accessible with the more established technologies. In some cases, THz-TDS has indeed found its niche, a trend that is underlined by the still growing number of companies offering commercial systems. In some other cases technical as well as operational restraints still hinder a more widespread application of the technology, while very promising preliminary studies have demonstrated the proof-of-principle for further applications. Inevitably, in a small number of cases it has been shown that terahertz technologies do not appear to give additional insights into those already obtained from well-established techniques.

Given the very large number of reports of spectroscopic data of crystalline and non-crystalline solid samples, the scope of this chapter is not to provide a comprehensive review of all studies that have been performed in this area. Furthermore, our intention is not to provide a spectral data collection. Based on some selected examples, we will outline the potential of terahertz spectroscopy for identification and characterisation of various substances and highlight aspects of the measurements which require careful consideration. In particular, in order to successfully exploit the full potential of THz-TDS measurements, it is essential to understand the contributions to the spectra caused by scattering or multiple reflections. While a careful sample

preparation can minimise these contributions in laboratory-based research or forensic studies, it cannot completely avoid them. Therefore, a detailed knowledge of the phenomena that give rise to the spectral artefacts can help to improve the capabilities of THz-TDS. We will therefore outline, wherever applicable, how sample preparation and data analysis can help to enhance the quality of the recorded data in order to enhance the system performance. In many on-site industrial or security applications, however, where specific sample preparation is not practicable, atmospheric attenuation, superimposed spectroscopic features of mixtures, as well as surface and material scattering, are just some of the restraints that still need to be fully addressed. In this chapter the emphasis is thus on the potential of THz-TDS for analytical studies.

The chapter is structured as follows: in order to facilitate an understanding and interpretation of the data, several measurement considerations need to be addressed. We will briefly discuss the effect of scattering on the terahertz spectra. This is particularly important since, given a lack of well-pronounced spectroscopic features for many samples, scattering artefacts may obscure relevant information. For a more detailed coverage of scattering and scattering effects we refer to the chapter by Zurk and Schecklman. We will then consider aspects of sample preparation and extraction of the optical constants with particular focus on thin films and heterogeneous mixtures. Section 8.3 is dedicated to crystalline solids, with a focus on small organic crystalline materials. The specific signatures which are typically found in the far-infrared spectra of most organic crystalline substances enable not only spectral recognition, but also allow us to extract information about the morphology of the samples; this has led to many studies on polymorphism and phase transitions. While the spectra of non-crystalline solids show typically less pronounced and less distinct features, they can still reveal very important information about structure, conductivity, dynamics and morphology. Section 8.4 describes some latest developments in THz spectroscopy of ordered carbonaceous materials and inorganic glasses.

8.2 Measurement Considerations

8.2.1 Scattering

Scattering is discussed in more detail in Chap. 5; however, the basics are reproduced here in order to discuss their specific effects on spectroscopic measurements at terahertz frequencies.

8.2.1.1 Mie Scattering

Mie theory is derived in general terms from Maxwell's equations by considering the interaction of waves at surfaces between the scattering particle and the surrounding media, the derivation and description are outside the scope of this chapter; however,

excellent treatments are given in the following references: [4–6]. The key parameters are the Mie coefficients a_m and b_m for computing the amplitudes of the scattered field. These are written for the general case as follows:

$$a_m = \frac{n^2 j_m(nx) [x j_m(x)]' - \mu_1 j_m(x) [nx j_m(nx)]'}{n^2 j_m(nx) [x h_m^{(1)}(x)]' - h_m^{(1)}(x) [nx j_m(nx)]'} \quad (8.1)$$

$$b_m = \frac{\mu_1 j_m(nx) [x j_m(x)]' - j_m(x) [nx j_m(nx)]'}{\mu_1 j_m(nx) [x h_m^{(1)}(x)]' - h_m^{(1)}(x) [nx j_m(nx)]'} \quad (8.2)$$

where n is the relative refractive index of the sphere relative to the medium, $x = ka$ is the size parameter, a the radius of the sphere and k is the wavenumber of the electromagnetic (EM) radiation in the medium. μ_1 is the ratio of the magnetic permeability of the sphere to the magnetic permeability of the medium. This will be assumed to be 1 in the subsequent calculations. The functions $j_m(z)$ and $y_m(z)$ are spherical Bessel functions and $h_m^{(1)}(z) = j_m(z) + i y_m(z)$ are the spherical Hankel functions of order $m = (1, 2, \dots)$, with the primed versions identifying the mean derivatives with respect to the argument. As a consequence of these functions, solutions to the scattering efficiencies for a given sphere at a particular wavelength can be found as a series of terms.

Of particular interest to terahertz measurements and imaging is the Mie extinction efficiency, Q_{ext} , which is a measure of the interaction of radiation with a scattering sphere normalised to the particle cross-section, πa^2 . The extinction efficiency can be calculated from a_m and b_m in Eqs. 8.1 and 8.2 as follows [5]:

$$Q_{\text{ext}} = \frac{2}{x^2} \sum_{m=1}^{\infty} (2m+1) \Re(a_m + b_m). \quad (8.3)$$

The key outcome of the Mie theory calculation is the oscillatory behaviour of the extinction efficiency around and above wavelengths comparable to the radius of the scatterer. Figure 8.1a plots the extinction efficiency as a function of frequency (in the terahertz region) for three different scatterers with sizes ranging between 50 and 200 μ . Figure 8.1b shows the absorption coefficient spectrum for a liquid sample containing an air bubble, where a large loss feature is observed at approximately 1 THz. This feature is due to the scattering of the terahertz radiation off a spherical inclusion with approximately the same dimensions as the wavelength of the incident radiation. In this figure the Mie extinction efficiency for a sphere of radius of 150 μm is overlaid for comparison, which can be seen to contain a similar feature centred around the same frequency.

From an experimental point of view it is very important to be aware of Mie scattering when it comes to terahertz spectroscopy of solid samples as the wavelength of terahertz radiation (typically between 3 mm and 75 μm) often overlaps with the length-scale of the particle size of sample material in powder form. Wherever practical

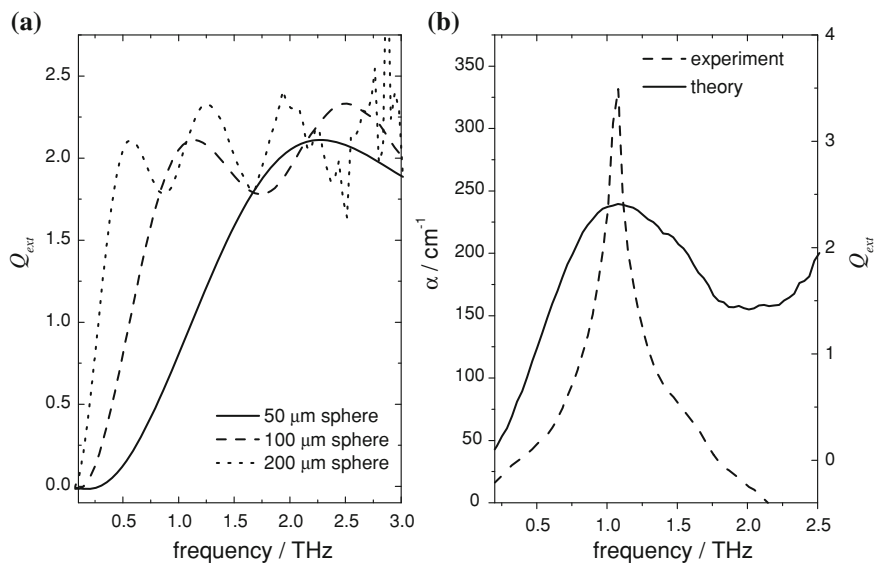


Fig. 8.1 Mie scattering. **a** Simulated Q_{ext} for three different scatterer radii, calculated using Eq. 8.3. **b** Absorption coefficient observed for a liquid sample of ethyl lactate containing a small air bubble (dashed line). The solid line is the corresponding extinction efficiency for a scatterer of a radius of 150 μm

it is advisable to mill the sample to smaller particles sizes and sieve the resulting powder to avoid scattering artefacts.

8.2.1.2 Rayleigh Scattering

Whilst the Mie scattering calculations introduced above will remain valid, it is sometimes useful to consider the analytic solution to the scattering of light due to isotropic, homogeneous and small (in comparison to the wavelength) particles, first formulated by Lord Rayleigh. Because the particle dimensions are small in comparison to the wavelength, it can be assumed that the E-field due to the incident radiation is uniform over the extent of the particle. As a result the field inside the particle (E_{int}) due to the externally varying E-field (E_{ext}) can be represented by the following relation:

$$E_{\text{int}} = \frac{3\epsilon_2}{\epsilon_1 + 2\epsilon_2} E_{\text{ext}} \quad (8.4)$$

where ϵ_1 and ϵ_2 are the permittivities of the sphere and external media respectively. Using Eq. 8.4 it can be shown that the scattering (σ_s) and absorption (σ_a) cross-sections for a spherical particle of radius a can be written as:

$$\sigma_s = \frac{8\pi}{3} k^4 a^6 \left| \frac{\epsilon_1 - \epsilon_2}{\epsilon_1 + 2\epsilon_2} \right|^2 \quad (8.5)$$

$$\sigma_a = k \frac{\Im[\epsilon_1]}{\epsilon_2} \frac{4\pi a^3}{3} \left| \frac{3\epsilon_2}{\epsilon_1 + 2\epsilon_2} \right|^2. \quad (8.6)$$

In particular, it is useful to note the fourth power dependence of the wavenumber on the scattering cross-section (Eq. 8.5). Due to the relatively long wavelengths at terahertz frequencies when compared to the particle sizes of the materials normally measured in pellet form ($<100 \mu\text{m}$), most THz-TDS measurements are undertaken in the Rayleigh scattering regime.

While in most cases, it is favourable to keep the scattering contribution to the extinction spectrum as low as possible in order to obtain a relatively good estimation of the pure absorption properties of a sample, the scattered signal can itself reveal important information about the internal structure of the substance under investigation. Png et al. [7] investigated whether THz-TDS can give an indication on the structural properties of lysozyme samples. They observed that the differences in the extinction spectra, which enabled them to differentiate between fibrillar and globular lysozyme, can be explained by Rayleigh scattering due to the morphological difference of the sample structure.

8.2.1.3 The Christiansen Effect

As we will describe in Sect. 8.2.2, one of the most commonly used sample preparation methods for polycrystalline substances is diluting the sample with a low-absorbing filler material. The mixture can then be pressed into plane-parallel pellets using a hydraulic press. The resulting pellets are mechanically stable and allow for easy handling. The ratio between filler material and sample can be optimised in order to resolve strong absorption features while at the same time avoiding saturation [8]. If the sample under investigation has a coarse grain structure, it is preferable to grind the crystals to a fine powder with grain sizes of the same order of magnitude as the filler material (typically around $100 \mu\text{m}$) to obtain a homogeneous sample and for increased mechanical stability of the pellet. In some cases, however, grinding is not practicable prior to dilution, and the spectroscopic signatures of such coarse samples typically show a characteristic scattering feature: a broadening of the low frequency wing of the absorption bands while the high frequency wing remains very sharp (see Fig. 8.2). This specific line shape (in particular the sharp drop on the high frequency side of the absorption band) cannot easily be described by Mie scattering theory.

Franz et al. have shown that the Christiansen effect, which weights the scattering of the electromagnetic radiation on the crystals by their opacity, can be employed to successfully model such scattering effects [9]. In this approach, the difference in the dielectric function of the filler material and the sample is considered. In THz-TDS, the filler material is typically polyethylene (PE), which exhibits low absorption and a nearly constant refractive index in the THz region. In most cases the refractive index

of the sample material is higher than that of PE and its slope varies significantly in the vicinity of a resonance. When the refractive indices of sample and filler intersect, the mixture appears to be homogeneous. At this frequency, the Christiansen frequency f_{Chr} [10], the scattering contribution is minimised and the sample has a maximum transparency. For other frequencies where the two refractive indices differ, the coarse sample grains have a varying degree of opacity and thus act as scattering centres. Given that the sample typically has a higher refractive index compared to the filler, the intersection usually occurs at the normal mode resonances, where the index rises at the low frequency wing of the resonant feature and drops at the higher frequency end. The opacity, and thus scattering, is therefore enhanced at the low frequency wing of the resonance while it is less pronounced at the high frequency wing.

Based on Raman's work to describe the Christiansen effect for optical light by calculating the attenuation of a wave travelling through a medium which could be divided into thin layers with different but homogeneous refractive indices [11], Franz et al. proposed a formalism to separate the scattering from the material absorption of the sample. If several material parameters such as the refractive index of both the filler and sample material together with the shape, concentration and distribution of the sample grains are known, the following equation can be used to calculate the overall absorption:

$$\alpha' = \alpha + \alpha_{\text{sc}} = \alpha + K^2 \frac{\omega^2}{c^2} (\Delta n^2) S^2, \quad (8.7)$$

where α describes the material absorption, α_{sc} the scattering contribution and Δn is the refractive index difference between sample and filler material. The parameter K describes the sample shape, average size and concentration, whereas S is a parameter describing the typical optical thickness of a thin layer of particles. Note that this formalism already requires a detailed knowledge of the material parameters in order to reproduce the characteristic line shape. Franz et al. have also shown that by assuming a flat baseline for the corrected material absorption and using Eq. 8.7 in a fit to reproduce the experimental data the parameters K and S can be determined phenomenologically.

Figure 8.2 shows the absorption coefficient α of a mixture of finely ground DL-phenylactic acid mixed with PE and pressed with a hydraulic press into a solid pellet (solid black line). The nearly flat baseline indicates that scattering artefacts can almost be neglected. The solid dots show the results for a coarse ground sample. In this case the characteristic asymmetric line shape described previously, where the vibrational modes exhibit broadening on the lower frequency side, is clearly observed. The scattering contribution due to the Christiansen effect can be calculated using the refractive index n of a pure sample or it can be derived from the mixture as described by Franz et al. [9]. The parameters K and S have been chosen such that the sum of the absorption of the finely ground sample (which can be approximated as scattering-free) and the scattering contribution match the spectrum of the coarse ground sample.

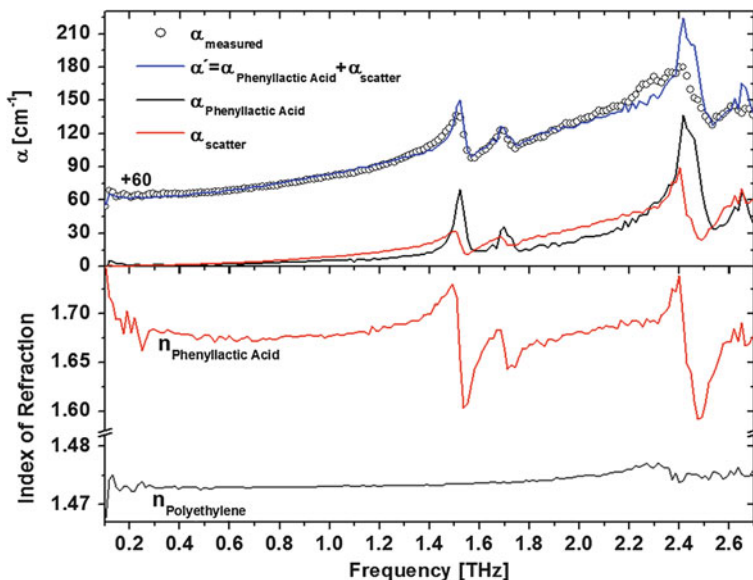


Fig. 8.2 Upper figure Absorption coefficient α of finely ground (*open dots*) and coarse ground (*solid black line*) DL-Phenylactic acid. The contribution of the scattering according to Eq. 8.7 using the refractive index depicted in the lower subfigure is shown as *solid red line*. Lower figure corresponding refractive indices. Figure adapted from [9]

8.2.2 Sample Preparation

The majority of all studies focusing on the characterisation of materials using terahertz spectroscopy is carried out in transmission geometry. This is not to say that there is not a considerable interest in reflection geometry as well, given that this sampling scheme has distinct advantages for the analysis of samples, in particular for routine sample identification in an industrial context or when dealing with strongly absorbing materials. Attenuated total reflection (ATR) in particular shows considerable potential for such applications and a number of studies have started exploring this field.

However, transmission spectroscopy is by far the most commonly used method and a transmission time-domain spectrometer is likely to be the most extensively used instrument for research groups pursuing an interest in spectroscopy. This dominance is due to the fact that it is much easier to understand the light–matter interaction in this geometry and achieve quantitative results given that the path length of the terahertz beam propagating through the sample is well-defined. However, for a fully quantitative measurement there remain a number of important considerations to be taken into account arising from the pulsed nature of the terahertz beam and the resulting complexity of the received signal due to multiple internal reflections that occur when the terahertz pulse propagates through the sample. This topic will be

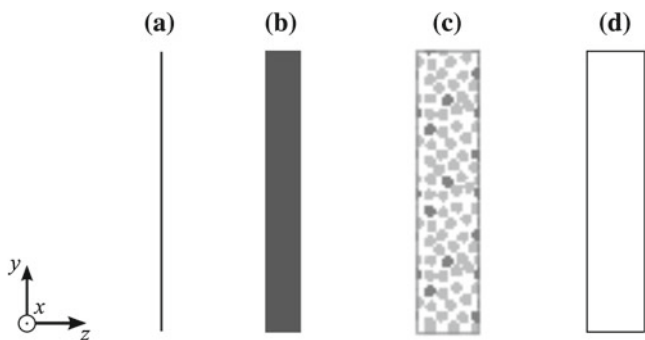


Fig. 8.3 Commonly encountered sample geometries in transmission THz-TDS (beam propagation in z -direction): **a** free standing thin film; **b** homogeneous slab of sample material; **c** porous pellet of sample particles (*dark*) and a transparent binder such as PE (*light*); and **d** thin film of sample on transparent substrate such as z -cut quartz

discussed in Sect. 8.2.3 and the reader is also referred to the chapters by Peiponen and Gornov as well as the chapter by Apostolopoulos and Daniell for a more detailed description.

When it comes to transmission spectroscopy the sample needs to be shaped to form a uniform slab of material with parallel faces in order to allow for the pulse of terahertz radiation to propagate freely through the sample and for any subsequent echo reflections to reach the detector. Sometimes, for example in the case of samples of glasses or single crystals, the sample is already a homogeneous slab of material which can be measured directly in the terahertz spectrometer (Fig. 8.3a, b); however, more frequently the sample is a powder and hence needs to be shaped into a more suitable form for terahertz analysis.

Powdered materials are typically compressed into a disc or pellet with sufficient diameter not to clip the terahertz beam at any point during the propagation through the sample and its sample holder. The beam waist at the focal point is usually in excess of 1 mm and depending on the sample thickness a diameter of 10–20 mm for the sample pellet is commonly encountered. Most materials are too strongly absorbing, show insufficient mechanical stability on direct compaction or there is insufficient material available to form a pellet of the required dimensions. In such cases a pellet is formed by dilution of the sample material with a binder which is transparent at terahertz frequencies (Fig. 8.3c).

The most popular binder for this purpose is PE which is widely available in powder form with a particle size of less than 100 μm . PE has excellent transmission properties at terahertz frequencies. It is easy to mix without sticking to surfaces, chemically inert with most solid materials, not hygroscopic and forms pellets of excellent mechanical stability. Its main disadvantage is its low melting point (which can be as low as 350 K depending on the grade of product) which makes it unsuitable for spectroscopic studies at elevated temperatures. For such experiments poly(tetrafluoroethylene) (PTFE) is a popular alternative. Although sample preparation with PTFE is a little more

difficult, due to its tendency to stick to surfaces, its melting point (around 600 K, again depending on the average molecular weight) is sufficiently high to study most organic molecules.

Alternative sample preparation techniques include casting a free-standing film for polymer materials (Fig. 8.3a) or preparing a thin film of highly absorbing materials on a transparent substrate such as z-cut crystalline quartz or silicon (Fig. 8.3d). The type of sample preparation needs to be considered when extracting the optical constants from the measured time-domain waveform to account for the different losses due to the porosity of the sample as well as the possibility of multiple internal reflections.

8.2.3 Calculation of Optical Constants

As in all other spectroscopic techniques, spectra of materials at terahertz frequencies can be acquired in either a transmission or reflection modality. For transmission mode measurements, the most common calculation directly implements the Beer–Lambert absorption formalism, however, a number of researchers have explored the use of treatments that include multiple internal reflections by involving Fresnel reflection coefficients in order to extract more accurate constants. In reflection mode, optical constants are extracted using the reflection coefficients.

In the case of spectrometers that acquire the spectra using dispersive prisms or gratings at a single frequency at a time, the measured data can be directly transformed into the frequency dependent optical constants. In THz-TDS the time-varying electric field of a terahertz pulse is measured and thus a time-domain waveform is acquired (hence the name). In order to calculate the frequency-dependent optical constants, the time-domain information must be transformed into the frequency domain using a Fourier transform. From this operation, the frequency-dependent optical properties of the sample of interest may be extracted from the broadband frequency representation of the transient. This section summarises the basic theories and equations used to calculate the optical constants from the frequency domain data.

8.2.3.1 Beer–Lambert Law

The Beer–Lambert (BL) formalism is commonly used in the extraction of optical constants from transmission measurements. The frequency-dependent refractive index $n(\nu)$ and absorption coefficient $\alpha(\nu)$ are calculated using the following equations:

$$n(\nu) = 1 + \frac{c}{2\pi\nu(\Delta x)} \{ \angle E_{\text{ref}}(\nu) - \angle E_{\text{sam}}(\nu) \} \quad (8.8)$$

$$\alpha(\nu) = \frac{2}{(\Delta x)} \ln \left\{ \left| \frac{E_{\text{ref}}(\nu)}{E_{\text{sam}}(\nu)} \right| \frac{[n(\nu) + n_{\text{med}}]^2}{4n(\nu)n_{\text{med}}} \right\}, \quad (8.9)$$

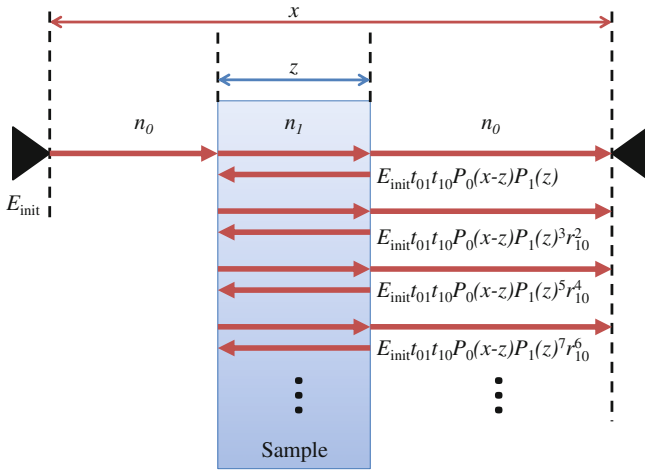


Fig. 8.4 Schematic of a basic model of the propagation of electromagnetic radiation through a sample of thickness z with refractive index n_1 and surrounding media characterised by refractive index n_0 . The terahertz pulse propagates from the source (*left* of the sample) to the detector (*right* of the sample) along x

where Δx is the thickness of the sample, n_{med} is the refractive index of the medium the sample is contained within (for example air) and E_{ref} and E_{sam} are the frequency-dependent E -fields of the terahertz transient measured for a reference and after transmission through the sample, respectively. As discussed in Sect. 8.2.2 commonly, in studies of both crystalline and non-crystalline materials the sample of interest will often be in powdered form. In these cases the sample will often be mixed with a diluent such as PE or PTFE, both of which are almost transparent to terahertz radiation, and pressed into pellets for measurement. The reference E -field, E_{ref} is then measured as the terahertz transient after propagation through a pellet of pure diluent, and containing the same mass of diluent as used in the sample pellet.

8.2.3.2 Treatment of Multiple Reflections

Every interaction of EM radiation with an interface between two materials of differing refractive indices results in the propagation of both a forward, transmitted wave and a backward, reflected wave. The amplitudes of the E -fields of the two waves are governed by the Fresnel reflection and transmission coefficients, which for a normal incident wave at the interface between regions of refractive index n_j and n_k are as follows (Fig. 8.4):

$$r_{jk} = \frac{n_j - n_k}{n_j + n_k} \quad (8.10)$$

$$t_{jk} = \frac{2n_j}{n_j + n_k}. \quad (8.11)$$

The BL formalism outlined previously considers only the first pulse to reach the detector. However, in materials with a significant refractive index mismatch with the surrounding media large subsequent reflections will occur, causing “sawtooth” or so-called “etalon” oscillations in the resultant absorption coefficient and refractive index spectra. These features can be reduced by considering the transmitted E -field as a sum of these reflected pulses [12–15]. This results in the following equation:

$$\begin{aligned} E_{\text{out}}(\nu) &= E_{\text{init}}(\nu) t_{10} t_{01} P_1(z) P_0(x - z) \\ &\quad \left(1 + P_1^2(z) r_{10}^2 + P_1^4(z) r_{10}^4 + P_1^6(z) r_{10}^6 + \dots \right) \\ &= E_{\text{init}}(\nu) t_{01} t_{10} P_1(z) P_0(x - z) \sum_{i=0}^{\delta} \left(P_1^2(z) r_{10}^2 \right)^i \end{aligned} \quad (8.12)$$

where r_{01} , t_{01} and t_{10} are Fresnel reflection and transmission coefficients as defined in Eqs. 8.10 and 8.11, x is the distance from source to detector and P_m (with $m = 0, 1, \dots$) is the material interaction term:

$$P_m(z) = \exp\left(\frac{-i2\pi\nu\tilde{n}_m z}{c_0}\right). \quad (8.13)$$

By comparing the ratio of the measured E -field after propagation through the sample and the initial E -field with the theoretical expression in Eq. 8.12 a value for the optical constants at each frequency may be found by minimising the difference in the theoretical and experimental results. This technique has been used in essentially this form in the study of semiconductors [12, 13], biomolecules [14] and inorganic glasses [16, 17].

A common modification of Eq. 8.12 is to consider an optically thin sample deposited on a much thicker substrate (Fig. 8.3d, of refractive index n_2 and thickness y) as having an infinite number of reflections. Consequently, if E_{ref} represents the E -field measured after propagation through the substrate only, then Eq. 8.12 reduces to the following form:

$$E_{\text{out}}(\nu) = E_{\text{ref}}(\nu) \frac{t_{01} t_{12} P_1(z) P_0(-z)}{t_{02} (1 + r_{01} r_{12} P_1(z)^2)}. \quad (8.14)$$

Equation 8.14 is used in the same way as described previously for the general single material case, and may be employed for both thick and thin materials. However, it is most commonly used in studies involving thin films, for example in the study of ordered carbonaceous materials [18–20, for example].

8.2.3.3 Heterogeneous Mixtures

In many situations powdered materials are embedded, compressed or coated onto a different substrate or matrix, forming a heterogeneous sample. In such situations, whilst the Beer–Lambert calculation introduced in Sect. 8.2.3.1 previously may be used, consideration of the interaction of the terahertz electric field with the heterogeneous sample will give more accurate calculations for the optical properties of the material of interest. This may be achieved by employing an effective medium approximation (EMA). The two EMAs most commonly used in the study of heterogeneous samples with terahertz radiation are attributed to Maxwell–Garnett [21] and Bruggeman [22]. Both take as a starting point the equation for the polarisability of a sphere embedded within a material of a different dielectric permittivity, α_{sp} :

$$\alpha_{\text{sp}} = 4\pi\epsilon_0 a^3 \frac{\epsilon_2 - \epsilon_1}{\epsilon_2 + 2\epsilon_1} \quad (8.15)$$

where a is the radius of the sphere and ϵ_0 , ϵ_1 and ϵ_2 are the permittivities of free space, the host dielectric and the inclusion dielectric, respectively. From Eq. 8.15 both the Maxwell–Garnett (MG) EMA and Bruggeman (BR) EMA may be derived.

Maxwell–Garnett EMA

The MG EMA may be derived from noting that the polarisability of a sphere, defined in Eq. 8.15, is proportional to its volume. Consider the example in Fig. 8.5a. In this case the polarisation of the large sphere of dielectric ϵ_{eff} (the variable to be calculated) embedded within the substrate ϵ_{sub} will just be a sum of the polarisations of the inclusions ϵ_{inc} within the sphere. Therefore:

$$\begin{aligned} \alpha_{\text{eff}} &= \sum \alpha_{\text{inc}} \\ V_{\text{eff}} \frac{\epsilon_{\text{eff}} - \epsilon_{\text{sub}}}{\epsilon_{\text{eff}} + 2\epsilon_{\text{sub}}} &= \sum_{k=1}^N V_{\text{inc},k} \frac{\epsilon_{\text{inc}} - \epsilon_{\text{sub}}}{\epsilon_{\text{inc}} + 2\epsilon_{\text{sub}}} \\ \therefore \frac{\epsilon_{\text{eff}} - \epsilon_{\text{sub}}}{\epsilon_{\text{eff}} + 2\epsilon_{\text{sub}}} &= f \frac{\epsilon_{\text{inc}} - \epsilon_{\text{sub}}}{\epsilon_{\text{inc}} + 2\epsilon_{\text{sub}}} \end{aligned} \quad (8.16)$$

where f is the volume fraction (or filling factor) of the inclusions, defined as:

$$f = \frac{\sum_{k=1}^N V_{\text{inc},k}}{V_{\text{eff}}}. \quad (8.17)$$

Equation 8.16 is the Maxwell–Garnett approximation for a single inclusion embedded within a substrate. As shown in a later paper by Maxwell–Garnett it is simple to extend this to n different types of inclusions within a substrate if one

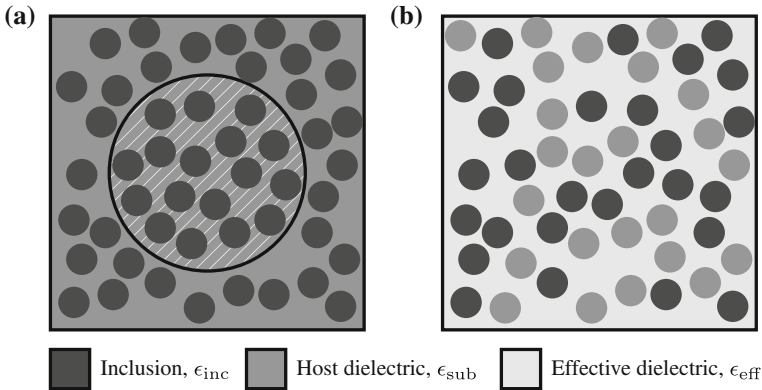


Fig. 8.5 Schematics of the respective effective medium models **a** Maxwell–Garnett (MG) dielectric model and **b** Bruggeman (BR) model

knows the volume fractions of each species of inclusion [23]. There are, however, some limitations of this technique. The most important limitation to be aware of is that this approximation will only truly hold in the limit of a fairly low volume fraction of inclusion. The reason for this is that it is implicitly assumed that there is no interaction between the inclusions as the substrate they are embedded in remains unaffected by their presence. In principle the volume fraction polarisability used above to derive Eq. 8.16 could be reduced to include just a single inclusion and the same result should be possible for any inclusion and similar size sphere. However, if the volume fraction becomes too large then the effective sphere would no longer necessarily be embedded within a homogeneous substrate. In cases where the volume fraction of the inclusion is significantly larger than that of the substrate it may be advantageous to reverse these definitions and instead consider the inclusion as the substrate and vice versa; if this is done it is commonly known as the Cavity Maxwell–Garnett model [24].

Bruggeman EMA

As illustrated in Fig. 8.5b, the set-up for the Bruggeman approximation differs somewhat from that used in the Maxwell–Garnett approximation. Instead of considering the substrate and inclusions separately they are instead both considered as inclusions, this time within a substrate that is in fact the effective dielectric material with permittivity ϵ_{eff} [22]. This elegantly removes the problem encountered by the Maxwell–Garnett model: as the “substrate” is now defined by the inclusions it is implicitly immune to any changes at high volume filling factors. For the permittivity of the substrate within Fig. 8.5b to be accurately represented by ϵ_{eff} , the total polarisability of the spherical particles within must sum to zero. Taking f to signify the volume fraction for the “inclusion” particles and therefore $1 - f$ to signify the

volume fraction for the “substrate” particles and by summing the polarisabilities of these particles the Bruggeman formula is found:

$$f \frac{\epsilon_{\text{inc}} - \epsilon_{\text{eff}}}{\epsilon_{\text{inc}} + 2\epsilon_{\text{eff}}} + (1 - f) \frac{\epsilon_{\text{sub}} - \epsilon_{\text{eff}}}{\epsilon_{\text{sub}} + 2\epsilon_{\text{eff}}} = 0 \quad (8.18)$$

8.2.4 Dynamic Range

In THz-TDS the dynamic range varies greatly with frequency. As discussed in Chap. 1 by Freeman et al. typically the signal-to-noise range in the frequency spectrum that is calculated from the terahertz pulse reaches a maximum just below 1 THz and then drops off exponentially towards higher frequencies until it reaches the noise level (Fig. 8.6). Depending on the characteristics of the emitter/detector devices and the laser used the signal drops to the noise level at the cut-off frequency ν_{max} , which is typically anywhere between 1 and 4 THz, although the spectral bandwidth in some spectrometers can extend up to 7 THz (e.g. by using GaP for detection [25]) or even beyond [26].¹

The dynamic range of a THz-TDS measurement will therefore vary both from instrument to instrument and from sample to sample. Following from Eq. 8.9 Jepsen and Fischer [27] have shown that the maximum absorption that can be measured reliably at a given dynamic range (DR) is

$$\alpha(\nu)_{\text{max}} \Delta x = 2 \ln \left[\text{DR} \frac{4n(\nu)}{(n(\nu) + 1)^2} \right]. \quad (8.19)$$

Here, we assume that n_{med} from Eq. 8.9 is unity, i.e. that the measurement is acquired in a dry nitrogen or vacuum atmosphere. Whenever $\alpha(\nu)_{\text{max}}$ is exceeded the spectrum will not drop to the noise level immediately but rather exhibit an apparent absorption coefficient of α_{max} , which steadily decreases until it reaches zero at ν_{max} .

In the case of a narrow absorption peak exceeding the dynamic range the peak is clipped and its peak shape changes completely. This makes it stand out from the other peaks and it is obvious that the resulting peak is dominated by the artefact. However, the absorption spectra that are acquired from materials which are strongly absorbing over a wide range of frequencies can be much more misleading at first sight. Materials such as polymers or inorganic crystals typically show very broad absorption features or a monotonous increase in absorption up to the frequency where α_{max} is reached. In such cases misinterpretations of the spectra from this frequency to ν_{max} are possible as the resulting spectrum often resembles a broad, albeit somewhat noisy, peak (Fig. 8.6).

In order to measure a good quality terahertz spectrum using THz-TDS it is therefore important to carefully consider the particle size, the amount of sample material,

¹ Useable bandwidths in excess of 20 THz have been reported by using terahertz radiation generated in a plasma. A detailed explanation of how this can be achieved is provided in Chap. 14 by Hoffmann.

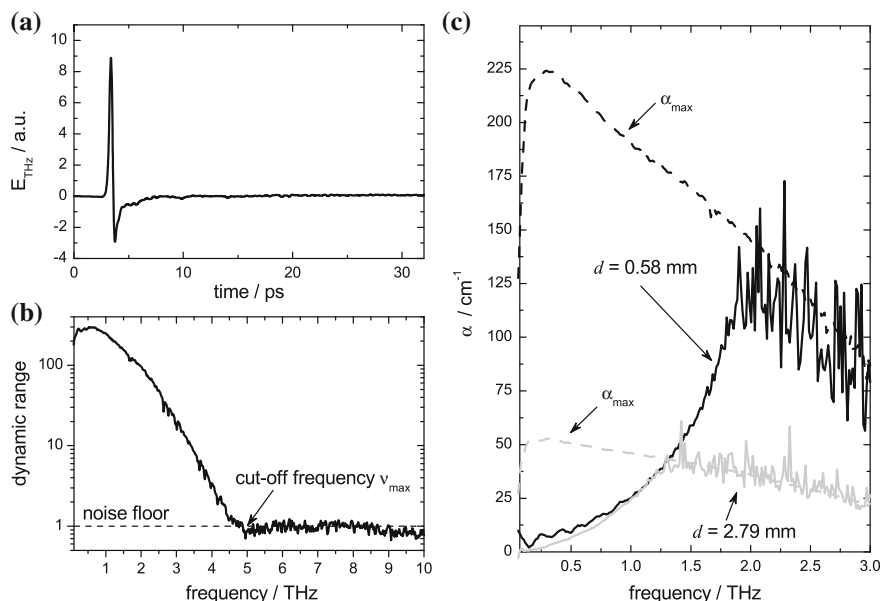


Fig. 8.6 Terahertz pulse **a** and corresponding power spectrum **b**. The cut-off frequency ν_{max} is defined as the frequency at which the signal drops to the noise floor. Absorption spectrum of two samples of poly lactide with different thicknesses **c**. The dashed line marks the maximum dynamic range that can be achieved in this measurement. Figure **c** modified from [27]

the method of sample preparation as well as the most suitable parameter extraction algorithm. In practise there is often a trade-off between spectral resolution, bandwidth and absolute error in the optical constants and it can be necessary to prepare multiple samples of different relative sample concentrations to achieve both a high spectral bandwidth as well as good confidence in the absolute values of α and n .

8.3 Spectroscopy of Crystalline Solids

In this section we will give an overview of how terahertz radiation can be used to study the structure and dynamics of a range of materials. Here, we will focus on crystalline materials while the following section will provide an insight into the type of spectra that can be acquired from non-crystalline materials. A particular focus of this section will be on crystalline samples of small organic molecules.

As outlined in Chap. 7 by Tomerini and Day, terahertz spectroscopy is a very sensitive technique to probe the interaction of crystalline phonons as well as the *intermolecular* hydrogen bonds in small organic molecular crystals. The vibrational modes that can be observed at terahertz frequencies represent the collective motions of the atoms corresponding to translations and librations of the molecules in the unit

cell, and terahertz spectra of this class of materials have been found to be very rich in spectral signatures at terahertz frequencies.

8.3.1 Biomolecules

The first examples using THz-TDS to study biomolecules were reported by Markelz et al. [28] as well as by Walther et al. [29]. Markelz measured the terahertz absorption of lyophilized powders of calf thymus DNA, bovine serum albumin (BSA) and collagen using THz-TDS. The results showed that all three molecules exhibit a broadband terahertz response with no distinct vibrational modes, which was attributed to a large density of low frequency modes. However, it was observed that the broadband response was different between molecules. A conformational change was proposed as a mechanism which may preferentially excite one or some of these low frequency modes, resulting in an observed change in the absorption spectrum. Later research confirmed that terahertz spectroscopy is sensitive to conformational changes, since clear changes in the terahertz spectrum of bacteriorhodopsin were observed upon illumination by light, which is known to cause a change in the conformational state of the biomolecule [30].

Walther and coworkers attempted to differentiate three isomers of retinal: all-*trans*, 13-*cis* and 9-*cis* versions, taking measurements in the solid state at both room (298 K) and low (10 K) temperatures [29]. The low temperature spectra were successfully fitted using a Lorentz oscillator model [31], and by comparing the terahertz spectra of the three isomers the same feature, that was reported at 54 cm^{-1} for all three isomers, was tentatively assigned to an intramolecular vibrational mode of the carbon ring, which is unchanged between the three isomers. This study represented one of the first investigations into the assignment of vibrational features at terahertz frequencies, an area of research that has now matured into a rapidly burgeoning field of its own and is discussed in-depth in the previous chapter by Tomerini and Day. However, whilst crystalline materials, in particular pharmaceutical compounds and explosives, have been at the forefront of the refinement of mode assignment routines, biomolecules have not. This can be explained by the large size and complexity of the biomolecules and as a result, the normal mode distributions, which dominate the terahertz absorbance, are similar for various biomolecules.

Subsequent measurements using THz-TDS have been reported for the various nucleobases and nucleosides (i.e. nucleobases with a deoxyribose sugar molecule attached) of DNA [32]. In two further studies, dry powders of both sulphur-containing biomolecules and sulphur-peptide dimers were investigated using THz-TDS [33] and THz-TDS and Raman spectroscopy [34]. Differences observed in the recorded terahertz spectra for these various biomolecules were attributed in each case to changes in the inter- and intramolecular bonding.

The study of biomolecules in the solid state represented an important step in the evolution of THz-TDS as an analytic technique with applications beyond the specialist laser laboratory. It demonstrated that vibrational spectroscopy at frequen-

cies below what was previously accessible by far-infrared techniques provided exciting new opportunities to characterise relatively similar large molecules by probing their intermolecular and low-frequency intramolecular modes. The results suggested that THz-TDS has a unique sensitivity to intermolecular interactions with many potential applications in chemistry and biology. With more groups becoming active in the field in the following years the focus in terahertz spectroscopy of biomolecules moved away from solid-state spectroscopy towards investigating peptides and proteins in solution (see next chapter by George and Markelz).

More recently, THz-TDS of solids has focussed on investigating much smaller, and hence potentially less complex molecules, in order to better understand the origin of the vibrational modes that are observed at terahertz frequencies. Small organic molecular crystals were found to be a fruitful field of research as the intermolecular interactions between the molecules fall right into the terahertz range. Within this class of materials research into the properties of pharmaceutical drug molecules and explosive materials at terahertz frequencies has been a particular focus of activity.

8.3.2 *Small Organic Molecules*

8.3.2.1 Solid-State Chemistry

The ability to perform non-invasive chemical recognition of materials using THz-TDS has long been proposed as a significant and useful application of the technique. Studies of the terahertz spectra of benzoic acid and its derivatives, and also of glucose, fructose and sucrose demonstrated that chemically similar crystalline materials exhibit very different terahertz signatures due to their different molecular crystal structures [35, 36]. Later studies broadened the range of materials studied to include drugs of abuse such as cocaine and morphine, as well as lactose monohydrate, acetylsalicylic acid, sucrose and tartaric acid (Fig. 8.7a) [37].

Ranitidine hydrochloride was one of the first pharmaceutical drug molecules that was studied using THz-TDS in an investigation by Taday et al. at Teraview, a company involved in the commercialisation of terahertz radiation based in Cambridge, UK [38]. The initial rationale was that pharmaceutical solids had long been known to exist in more than one crystalline form and that such distinct forms, or polymorphs, have the same chemical formula but different crystalline structures that can lead to different physical and chemical properties for the material. Such differences in crystal structure, which are reflected in different lattice energies of the resulting crystals, can impact the pharmaceutical performance of the drug by changes in the rate of drug dissolution and ultimately influence the bioavailability of the drug. Given that terahertz radiation is sensitive to longer range vibrational modes set up within a crystal structure, it seemed likely that THz-TDS was well placed to distinguish between such polymorphs. Indeed, this has been found to be that case.

While it is possible to detect changes in crystal structure between polymorphs by X-ray diffraction experiments, such measurements are typically destructive and

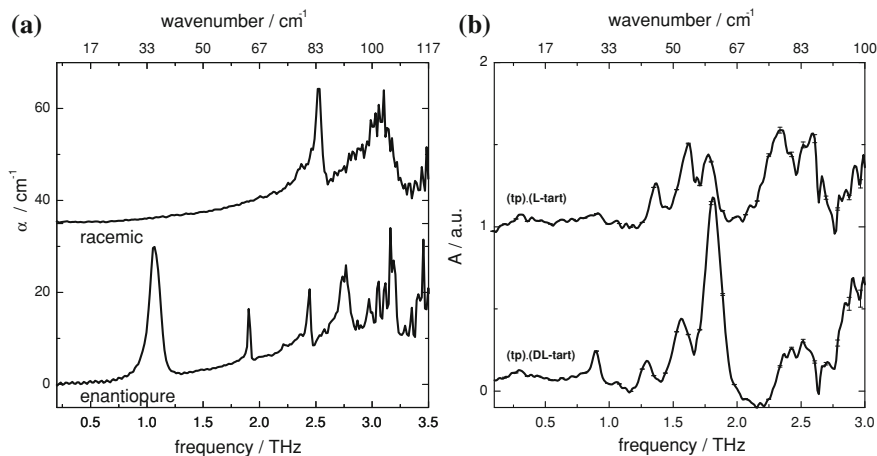


Fig. 8.7 **a** Terahertz spectra of the racemic and enantiopure forms of tartaric acid (Figure modified from [37]); **b** spectra of cocrystals formed between theophylline and both the racemic and enantiopure forms of tartaric acid (Figure modified from [39])

therefore cannot be performed on the final tablet. In 2003, there were effectively no quick and convenient methods for confirming the polymorphic state of the drug while in storage, and so the authors investigated whether THz-TDS could perform this role. Two forms of ranitidine hydrochloride were investigated and they displayed a clear difference in their terahertz absorption across the frequency range, demonstrating that THz-TDS is sensitive to changes in the intermolecular interactions due to alterations to the intermolecular crystalline form.

This finding has generated much interest in the pharmaceutical and analytical chemistry communities as it demonstrated a clear advantage of THz-TDS over any other vibrational spectroscopy techniques. While it is straightforward to differentiate different molecules using infrared or Raman spectroscopy based on the distinct vibrational modes associated with the functional groups present in the molecules, terahertz spectroscopy was found to be more sensitive to the intermolecular interactions between molecules in a crystal and hence it was able to differentiate between different solid-state modifications.

Differences in the terahertz spectra have been reported between polymorphic forms of the pharmaceutical materials carbamazepine (form I and III), enalapril maleate (form I and II), indomethacin (crystalline and amorphous forms) and fenoprofen calcium (crystalline and liquid crystalline forms) [40], furosemide [41] and manitol [42] among others and it is now widely accepted that THz-TDS is an excellent fingerprinting technique to identify different polymorphs of organic molecular crystals.

Two studies that serve as a good example to illustrate the sensitivity of the technique are the investigation of sulfathiazole which has at least five polymorphs all of which were easily identified using THz-TDS but not with Raman or mid-infrared

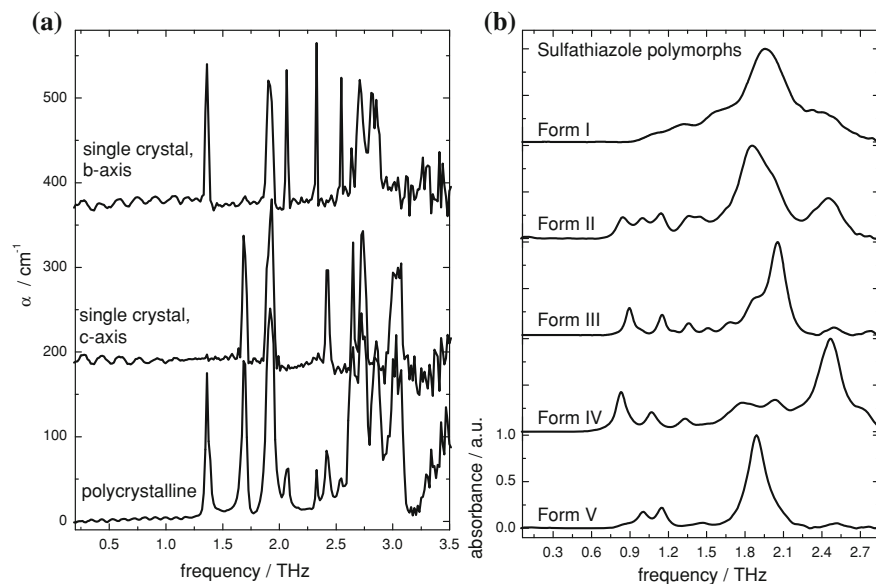


Fig. 8.8 **a** Terahertz spectra of polycrystalline sucrose as well as spectra from a single crystal depending on its orientation to the terahertz beam (unpublished data by Fischer et al.); **b** Terahertz spectra of the five known polymorphs of sulfathiazole. The samples only differ in the crystal packing of the sulfathiazole molecules, the molecules are chemically identical. (Figure modified from [43])

spectroscopy [43] (Fig. 8.8), as well as the straightforward identification of a set of cocrystals [39] that only differs in the stereochemistry of one of the cocrystal formers and appears isostructural in standard X-ray diffraction and Raman spectroscopy analysis.

8.3.2.2 Chemical Imaging

In analogy to near-infrared and Raman imaging it was possible to produce accurate chemical maps by transmission mapping of a set of seemingly identical material pellets that was made using different chemicals by selecting specific vibrational frequencies of the respective terahertz spectra [37].

In addition, chemical mapping has also been demonstrated in reflection mode. This technique is particularly powerful when resolving information at depth from a sample using techniques such as windowed Fourier transforms [44]. Based on this approach Shen et al. were able to demonstrate that it is possible to identify a material buried at depth within a larger pellet based upon the oscillations observed in the terahertz waveform at a second interface, i.e. the buried structure.

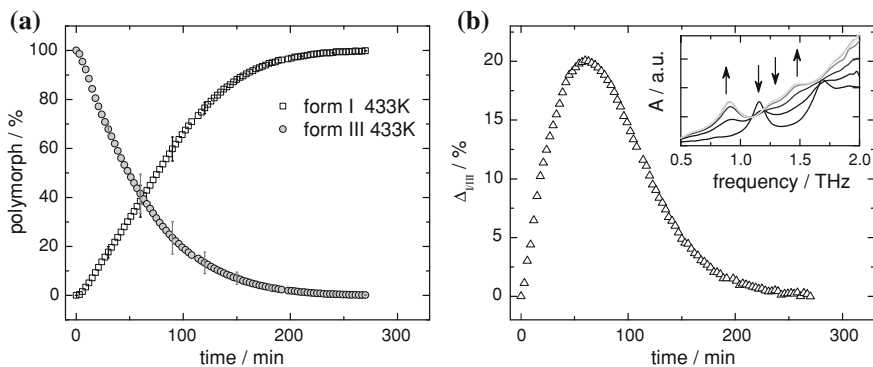


Fig. 8.9 Conversion of carbamazepine form III to I at 433 K. For clarity not all error bars are shown. **a** The decrease in Form III and subsequent formation of Form I follow different kinetics. **b** Amount of carbamazepine in the gas phase during the conversion process. The insert shows the absorption spectra of the sample during the conversion process with *arrows* indicating the associated spectral changes during the phase transition (Figure modified from [46])

8.3.2.3 Phase Transformations

A significant fraction of more recent work on pharmaceutical materials spectroscopy has focused on monitoring in situ phase transformations. For example, the phase transformation of different polymorphic forms of carbamazepine with temperature was monitored using terahertz spectroscopy [45, 46]. It was found that a clear change in the terahertz absorption spectrum could be followed as the temperature was changed. In a later study this process was analysed quantitatively and evidence was found for different rates of formation and loss for the two carbamazepine forms (as shown in Fig. 8.9). The results confirmed that the mechanism of the phase change was mediated via a sublimation step—this agreed with Differential Scanning Calorimetry (DSC) measurements and physical evidence of sublimation during the experiment but had gone previously unnoticed in two earlier studies using Raman spectroscopy and XRPD.

THz-TDS has also been used to successfully follow the temperature-induced phase transformations in sufathiazole [43], DL-cysteine [47], and theophylline [48]; in [48] it was shown that by studying the evolution of the terahertz absorption spectra, the mechanisms of the phase transformations may be elucidated. In addition to crystalline temperature transformations, amorphous to crystalline transitions [49] and dehydration processes [50] have been studied using THz-TDS. In particular, careful analysis of the amorphous to crystalline transition resulted in the identification of seven distinct material phases during the crystallisation of carbamazepine, whereas the evolution of the hydrate terahertz spectra of theophylline monohydrate revealed spectral features that are attributed to evaporating hydrate water as well as an overall evolution from the hydrate to anhydrous terahertz spectrum [50]. Evidence of evaporating hydrate water is not always observed in THz-TDS investigations of hydration

transitions, however, as in a similar study of caffeine hydrate dehydration, only the solid-state phase transformation was observed [51].

THz-TDS has been used to fit kinetic models to time-resolved dehydration reactions [52]. In this case a time resolved dehydration reaction of D-glucose monohydrate has been monitored at various temperatures, in order to investigate the kinetics of the reaction. By monitoring the evolution of a spectral feature, the normalised dehydration fraction was quantified for each spectrum recorded. These data were then fitted to numerous kinetic models and it was found that the two-phase boundary-controlled reaction equation best described the observed kinetics for all reaction temperatures investigated. THz-TDS was therefore able to suggest both a plausible reaction mechanism and to calculate an activation energy for the dehydration reaction (149 kJ mol^{-1}).

THz-TDS has also been used to follow the reaction of benzoquinone and dihydroxybenzene to form quinhydrone, a 1:1 complex stabilised by hydrogen bonds. This reaction has been observed to occur spontaneously, and the reaction mechanism confirmed by monitoring the terahertz spectra and comparing them to spectra of the initial species and quinhydrone formed from solution [53]. Monitoring the formation of products using THz-TDS has also been attempted on the formation of cocrystals via mechano-grinding [54]. The reactants were chosen to be featureless in the terahertz region, whereas the cocrystal product was known to have some strong spectral features, allowing the researchers to follow the growth of this feature during the reaction. The terahertz results appear to suggest the presence of an amorphous phase in the ground cocrystals.

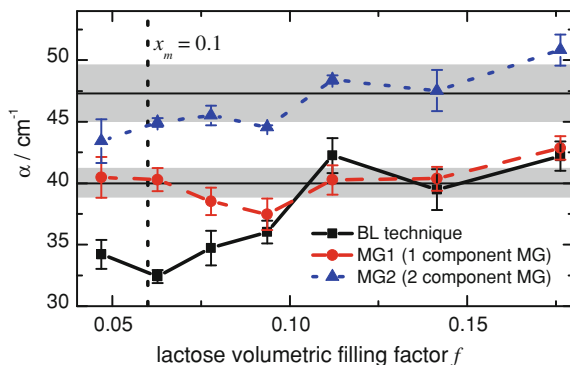
Monitoring phase transitions, and where possible extracting information about the kinetics of these transitions *in situ* represent an exciting use for THz-TDS in the future.

8.3.2.4 Analytical Applications

In order to quantify the amount of a particular pharmaceutical material within a sample, researchers have investigated the potential of chemometrics using multivariate data analysis such as Partial Least Squares (PLS) methods [55]. By using PLS methods it is possible to extract the percentage of a material within these compound samples by considering the absorption spectrum of the tablet recorded using THz-TDS and comparing this to the pure sample spectra. PLS methods have been employed to accurately predict the percentage concentration of two forms polymorphic forms within a pellet [56], and also to chemically map pellets formed of lactose and sucrose [57]. Given sufficiently different spectral features, the accuracy of the THz-TDS PLS techniques have been found to be comparable to or exceeding other commonly used approaches [55, 56].

Mixtures of solid chemical materials have been used to test the analytic capabilities of THz-TDS. Mixtures of isomers of benzoic acid have been measured using THz-TDS and by assuming a simple mixing rule and knowledge of the individual chemical

Fig. 8.10 Comparison of the peak height calculated for the lactose absorption feature in a PE/lactose composite pellet at 0.56 THz using either the BL law (*black squares*), a one-component MG model (*red dots*) or a two-component MG model (*blue triangles*). The corresponding values extracted from pure lactose pellets are shown as the grey bands. Data taken from Ref. [59]



spectra it was possible to accurately predict the concentrations of the various isomers within the mixture, with a total analytical error of about 6% [58].

Effective medium approximations (EMAs) have also been used to further improve the accuracy of extracted optical constants [59]. Using the Maxwell–Garnett [21] approximation outlined in Sect. 8.2.3.3 it is possible to extract consistent optical constants for lactose α -monohydrate embedded in a PE matrix at various filling factors, which agreed with the data for pellets of pure lactose. By contrast, conventional mixing techniques tended to underestimate the optical constants at low filling factors (as shown in Fig. 8.10).

By extending the technique to include a second inclusion (air), the contribution to the dielectric properties of the pellet due to the air could also be included. A drawback to this technique, however, is that the Maxwell–Garnett model assumes spherical inclusions, and often inclusions will not be of a uniform shape. Tuononen advocates the use of Wiener bounds to constrain the value of the dielectric constant of an inclusion given a known filling fraction [60]. This simple treatment yields the maximum and minimum possible values for the dielectric constants and assumes nothing regarding the shape of the inclusions; however, if small changes are to be monitored the changes are likely to be within the upper and lower bounds. Consequently, Scheller and coworkers have advocated an extension to the Maxwell–Garnett model purporting to account for all the limitations of that model [61]. Their formulation can account for ellipsoidal inclusions of varying shapes and sizes and can cope with high filling factors.

8.3.2.5 Beyond the Pellet

The experiments described above have all prepared the samples in a similar fashion—taking powdered samples and pressing them into pellets, commonly after mixing with a diluent such as PE. Melinger and Grischowsky have pioneered an alternative preparation technique based on waveguides [62, 63], and have used waveguide THz-TDS to study pharmaceutical materials, as well as other chemicals and explosives.

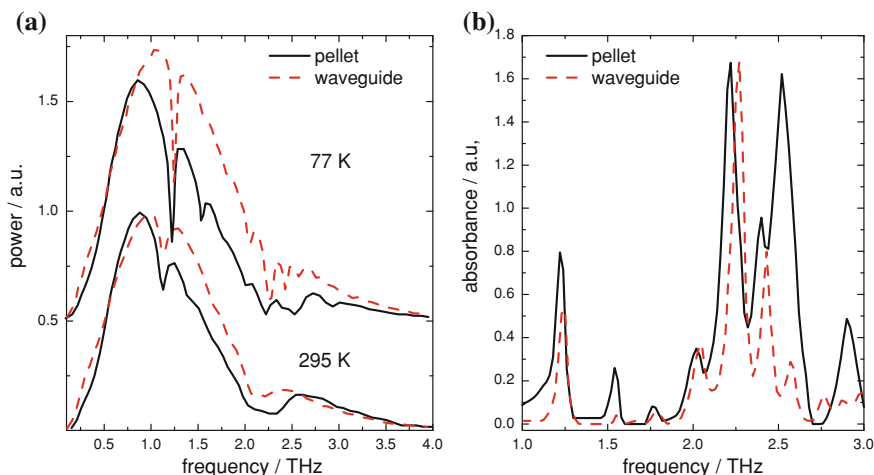


Fig. 8.11 **a** Power spectra for salicylic acid extracted either from a pellet or from a thin film desposited on a waveguide at both 295 K and 77 K; **b** the corresponding absorbances calculated for the pellet and waveguide techniques at 77 K. Data reproduced from Ref. [64]

Laman et al. studied acetylsalicylic acid and its precursors using waveguide THz-TDS and compared these results with conventional THz-TDS using pellets [64]. Figure 8.11 shows a comparison of the power spectra and absorption spectra measured for salicylic acid either through a pellet or using a waveguide film. It is found that whilst similar vibrational frequencies are recorded for the vibrational modes, both the relative intensities and the degree of broadening reported were very different for the two techniques. Broadening can be classified as either homogeneous or inhomogeneous. Homogeneous broadening typically shows a distinct temperature dependence, whereas inhomogeneous broadening is relatively insensitive to temperature. Both the pellet and waveguide THz-TDS spectra display prominent line-narrowing upon cooling, suggesting homogeneous broadening dominates. However, the degree of narrowing at low temperatures is much higher in the waveguide THz-TDS spectra, thereby increasing the ability to distinguish distinct vibrational modes when using this form of sample preparation.

It should be highlighted, however, that waveguide THz-TDS and pellet THz-TDS will not necessarily produce comparable spectra, due to the highly preferred orientation that the thin films grown on the waveguides can exhibit when compared to the pellets. During film deposition the molecules tend to form oriented thin films. As a result, the THz-TDS will couple to vibrational modes within the molecule to a different extent in the film and pressed pellet samples. In addition, there can be some interfacial disorder in pellet samples, which can lead to a shift in the baseline due to the amorphous content, depending on how the sample powder was prepared. This becomes particularly significant when milling the sample material for prolonged periods to achieve a smaller particle size. Clearly, care needs to be taken when

comparing data recorded using the waveguide THz-TDS with traditional pellet THz-TDS.

It is also important to note that the waveguide approach will be limited when looking at different polymorphs or solid-state modifications of a material given that it will be very difficult, if not impossible, to crystallise all different forms selectively on the waveguide surface.

8.3.3 Explosives

Due to the security implications of being able to detect and measure explosive materials, the potential uses of THz-TDS in detecting and understanding explosives has been widely investigated since an initial investigation of the potential security applications of terahertz radiation [65] and the dedicated study of trinitro-s-triazine [66] as well as dinitrotoluene [67]. The research interests have followed two broad themes: identification (with a specific aim of eventual stand-off detection) and interpretation of spectral features using computer simulation.

8.3.3.1 Identification

Trinitrotoluene (TNT), Research Department Explosive (RDX), cyclotetramethylene-tetranitramine (HMX) and pentaerythritol tetranitrate (PETN) have been the explosives of choice for THz-TDS studies. The terahertz spectra of TNT, RDX and PETN mixed with PE and pressed into pellets have been measured up to 6 THz using a thin GaP detector, almost doubling the measured spectral range of these materials [68]. Clearly, increasing bandwidth is advantageous in order to further discriminate between different chemical species. Single crystal samples of HMX, RDX and PETN have also been measured using THz-TDS [69]. Numerous dependencies have been observed in the spectra of these materials based on the orientation of the crystal, suggesting that in the future, if single crystals are available they may help constrain and understand the origin of the vibrational modes. Waveguide THz-TDS has been used to study the spectra of explosives such as TNT and RDX [70]. The extremely low sample amounts required for waveguide THz-TDS (in this case $\approx 150 \mu\text{g}$ is required for the RDX spectrum) is often cited as a significant advantage for this technique, as the amount of explosive material is typically 1 % of the sample mass required for a typical sample pellet. Waveguide THz-TDS produces extremely sharp spectral lines, especially at low temperatures, when compared to similar measurements of pellets, and this, combined with the extremely low sample amounts required, offers a safe and reliable technique for identifying suspect powders.

Clearly, in the security environment, stand-off detection is required (or at the very least preferred) for a technique to be useful. The terahertz spectra of 17 explosives and related compounds measured using THz-TDS have been compiled, including the ability of THz-TDS to reliably identify explosives in transmission mode that were

placed behind 1 mm thick covering materials such as plastic and leather [71]. It has been found that it is still possible to clearly identify the unique fingerprint for the explosives even when concealed within a common cover material; a useful further step would be to investigate the same capability in reflection mode, as this is likely to be the most useful measurement geometry in practice. The terahertz spectrum of RDX has been measured in reflection mode (without any concealing layers) and it was found that it was possible to observe differences between lactose, sucrose and RDX [72].

8.3.3.2 Computer Simulation of Spectral Features

The evolution of the techniques and abilities of computational programming packages to identify and understand crystalline materials is studied in-depth in Chap. 7; however, it is important to note the importance of the study of explosive materials with THz-TDS to this particular field. Explosive compounds represent one of the most widely studied families of crystalline materials with regard to systematic evaluation of the various commercially available density functional theory (DFT) techniques. The DMol³ DFT package has been evaluated in the study of the spectra of PETN, β -HMX and RDX and compared with experimental data [73–75]. PETN has also been studied using different DFT packages, CASTEP and PWscf [76], as has HMX using the plane wave code *ab initio* [77]. These studies focused more upon the computational variables within these calculations, but highlight the scientific importance of the explosive compounds in driving the evolution and development of these computational techniques.

8.3.4 Other Crystalline Materials

The characteristic signatures, which dominate the spectra of organic molecular crystals, have received particular attention due to the potential for specific applications described above. However, they represent only one class of crystalline materials. Indeed, terahertz spectra of semiconductors had been investigated well before the first reports on terahertz spectroscopic studies of organic crystals appeared [78]. Pigments and similar materials have recently been studied by many research groups, as they are potentially relevant to the investigation of paintings and similar works of art. THz imaging has proven to be a very useful tool for revealing previously undiscovered information in the study of layered paintings [79]. Another vast and still growing research field is dedicated to the spectroscopic investigation of ceramics. The list of materials which are currently investigated by THz spectroscopy could certainly be extended, and to give a complete picture is far beyond the scope of this chapter. We therefore would like to refer the interested reader to the detailed description of some of these aspects in Chap. 10 by Johnson and Lloyd-Hughes, and Chap. 21 by Fukunaga and Picollo.

8.4 Spectroscopy of Non-Crystalline Solids

8.4.1 Glasses

An amorphous solid such as a glass is one with a structure which lacks periodicity, extended symmetry and long-range order. As such the characterisation of these materials presents very different challenges to the crystalline materials investigated in Sect. 8.3, as the absence of periodicity removes the sharp spectral features associated with crystalline materials. However, whilst they are isotropic at long length scales, X-ray diffraction measurements have revealed quasi-crystalline arrangements on local (atomic and molecular) scales [80]. Vibrational anomalies in glasses were initially noticed from measurements of the low temperature heat capacities of silica [81], where a clear departure from the vibrational behaviour predicted by Debye theory ($C_p \propto T^3$) was observed. Specifically, a peak in the density of states is observed, with the maximum usually occurring around 1 THz [80]. This peak is commonly called the boson peak. This behaviour appears to be specific to glasses, and is thought to relate to the disorder of the material. Therefore THz-TDS, as a method to probe the frequency range of interest for these features arising from structural disorder, would appear to be a useful tool in understanding the structure and dynamics of glasses, despite the lack of sharp spectral features. Whilst this section focuses on the work that has been performed in order to characterise inorganic glasses, terahertz spectroscopy has also been used to study amorphous organics [36, 40, 49], such as the polymer characterisation discussed in Chap. 13 by Jansen et al.

8.4.1.1 Inorganic Glasses

One of the first spectroscopic measurements using THz-TDS reported in the literature was a study incorporating amorphous materials, such as silica [78]. For this study, a large disc of silica was produced with a diameter of 50 mm and thickness of 6.449 mm in order to maximise the interaction length. This was possible due to the very low terahertz absorption characteristics and allowed a very precise measurement of the low frequency absorption coefficient to be extracted. For comparison studies on materials with larger absorption coefficients such a thick sample would be impractical. Additionally, it is often difficult to produce more exotic samples with such volumes and preserve homogeneity. More recently, studies using THz-TDS of commercially available glasses, which are usually mixtures of different amorphous solids (e.g. SiO_2 , B_2O_3 , Na_2O and Al_2O_3) [82], and SiO_2 and arsenic sulphide (As_2S_3) [83], have been reported.

8.4.1.2 Interpreting the Terahertz Optical Constants

Taraskin et al. [83] proposed a universal frequency dependence for the relationship between the vibrational density of states (VDOS) and the infrared absorption coefficient, for frequencies below that of the boson peak which is of the following form:

$$\alpha(\omega) = C(\omega)g(\omega) \simeq (A + B\omega^2)g(\omega) \quad (8.20)$$

where A and B were material-dependent constants relating to the degree of uncorrelated and correlated charge fluctuations, respectively. In particular, the uncorrelated charge fluctuation coefficient A is related to the variance of the uncorrelated charge distribution σ_1^2 by the following expression:

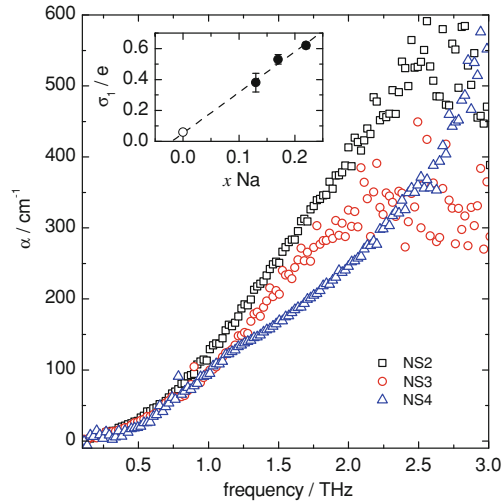
$$\sigma_1^2 = \frac{A\bar{m}c_0\sqrt{\epsilon_\infty}}{2\pi^2n} \quad (8.21)$$

where \bar{m} , ϵ_∞ and n are the average atomic mass, the high frequency limit of the ionic dielectric constant, and the atomic concentration respectively (c_0 is the speed of light in a vacuum). In their work, values for the infrared coupling coefficient for As_2S_3 and SiO_2 were extracted, and the results for SiO_2 agreed with the results obtained using hyper-Raman spectroscopy (HRS) [84], i.e. that the infrared coupling is proportional to the VDOS due to the low value of the B coefficient. Reference [82] found that the inclusion of additional components of the SiO_2 structure, greatly altered the terahertz absorption. Using a Debye-like model for the VDOS, they observed a frequency dependence that was approximately quadratic within the low frequency region (below 1 THz).

8.4.1.3 Further Improvements: Extraction of Accurate Optical Properties

Clearly, the accurate extraction of optical properties of these materials is of importance in order to calculate the coupling coefficient, determine the position of the boson peak and compare the infrared absorption results with other characterisation techniques. All previous studies of the far-infrared absorption in glasses used the information from the first pulse only and neglected information contained in subsequent reflections. In the case of the work by [78], due to the long interaction length the loss of information was relatively low; however, in more highly absorbing materials such as those investigated in the later experiments [82, 83], the use of thin samples limits the time domain due to internal reflections appearing much earlier in time. In materials where the terahertz absorption is high, consideration of the multiple reflections is required to extract a higher resolved measurement of the optical constants, which can be implemented by following the treatment outlined in Sect. 8.2.3.2. Such a multiple reflection extraction algorithm has been recently implemented in the study of amorphous glasses [16, 17]. In particular, it was possible

Fig. 8.12 Absorption coefficients for three sodosilicate glasses, NS_x ($Na_2O \cdot xSiO_2$, $x = 2,3,4$), between 0.1–3 THz. Inset: distribution of uncorrelated charges σ_1 as a function of sodium mole fraction (*closed circles*). σ_1 for pure SiO_2 from Ref. [83] is shown as a *open circle*



to extract accurate low frequency data of highly absorbing sodosilicate glasses, the absorption coefficients of which are plotted in the main figure of Fig. 8.12. Using Eq. 8.21 the distribution of uncorrelated charges for the three sodosilicate glasses was extracted, and an approximately linear correlation with the mole fraction of sodium observed (see the inset in Fig. 8.12), suggesting that the uncorrelated charge fluctuations are dominated by the spatial disorder of the position of the sodium atoms. Such a result was only possible by the acquisition of accurate, low frequency data.

8.4.2 Ordered Carbonaceous Materials

The first use of THz-TDS to study carbon nanotubes (CNTs) was reported by [85] in 2002. In this paper the change in optical properties upon purification of the single-walled CNTs (i.e. removal of the non-nanotube carbonaceous particles and transition metals used in the production) from the pristine (i.e. as produced) CNTs was investigated. The purified samples displayed an increased absorption coefficient and real refractive index across the frequency range investigated (in this case between 0.1 and 0.8 THz). The conductivity can be calculated by the following equation:

$$\epsilon = \epsilon_{\infty} + i \frac{\sigma}{\omega \epsilon_0}. \quad (8.22)$$

An increased absorption coefficient and real refractive index is therefore seen to result in an increased conductivity, which the authors attribute mainly to the increased crystallinity of the purified samples. The group of Jeon, in Korea, remain active in the field of terahertz studies of CNTs with further papers published in 2004 [86],

2005 [18, 87] and 2007 [88, 89]. Reference [86] presented the first use of the Drude–Lorentz (DL) model and Maxwell–Garnett (MG) Effective Medium Approximation (EMA) with THz-TDS measurements. These approaches are used to characterise the structural and electronic properties of these materials; a brief outline of the DL model is now given.

8.4.2.1 The Drude–Lorentz Model

The DL model treats the frequency-dependent dielectric constant ($\epsilon(\omega)$) as a contribution from free and bound oscillators calculated in a classical fashion. This results in the following equation for the frequency-dependent dielectric constant ($\epsilon_{\text{CNT}}(\omega)$):

$$\epsilon_{\text{CNT}} = \epsilon_{\infty} - \frac{\Omega_p^2}{\omega^2 + i\Gamma\omega} + \sum_{j=1}^{\delta} \frac{\Omega_{p,j}^2}{\omega_{0,j}^2 - \omega^2 - i\Gamma_j\omega}, \quad (8.23)$$

where Ω_p and Γ are the Drude plasma frequency and damping rate, and $\Omega_{p,j}$, $\omega_{0,j}$ and Γ_j are the Lorentz oscillator strength, oscillator frequency and damping rate for the j th Lorentz oscillator. The oscillator strength and damping rates may be represented as follows:

$$\Omega_p = \sqrt{\frac{Ne^2}{m\epsilon_0}} \quad (8.24)$$

and

$$\Gamma = \frac{1}{\tau} = Nv\sigma \quad (8.25)$$

where N is the electron density, e is the electric charge, m is the oscillator mass and v is the electron drift velocity. In the case of the Drude oscillator strength and damping rate, these parameters relate to the free, or valence, electrons, whereas for the Lorentz counterparts the parameters refer to the bound electrons.

8.4.2.2 Characterisation of Carbon Materials

The MG EMA (as defined in Sect. 8.2.3.3) needs to be used due to the preparation technique employed to prepare the CNT samples. In Ref. [86], the CNT samples were prepared into a thin film deposited on a silicon window. As a result, the terahertz beam propagates through a matrix formed of both air and CNT, thereby requiring the use of the EMA. Jeon reported that a simple Drude model was not a good fit to their CNT results; a Lorentz mode was required suggesting a combination of metallic and semiconducting nanotubes were present. Later work from Jeon and coworkers focused on the effect of functionalisation of the nanotubes with either hydrogen [87, 88] or fluorine [18], and the observed differences between single-walled and

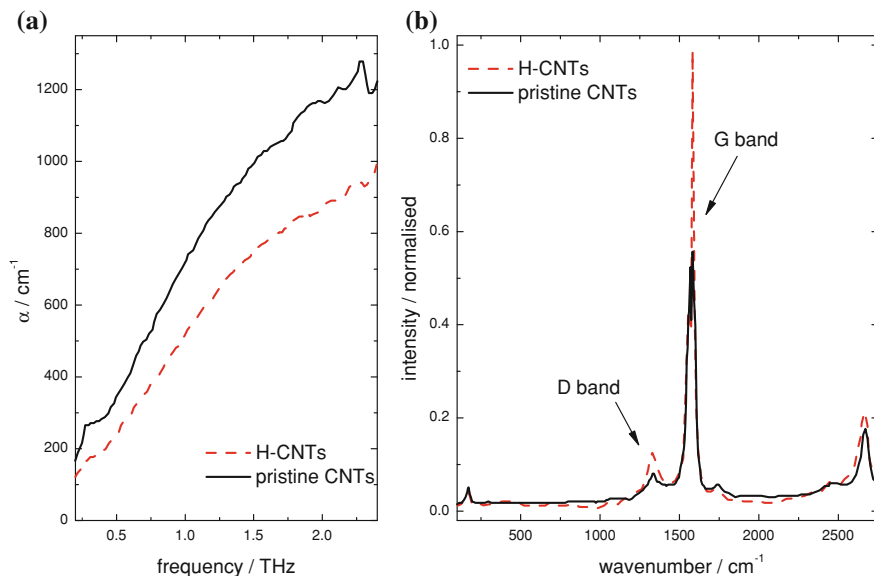


Fig. 8.13 **a** Absorption coefficient between 0 and 2.5 THz for H-CNTs (*dashed line*) and pristine CNTs (*solid line*) **b** Raman spectra for H-CNTs (*dashed line*) and pristine CNTs (*solid line*). The D and G features are highlighted

double-walled CNTs [89]. Kang et al. observed a decrease in the terahertz absorption and real refractive index upon hydrogen functionalisation of CNTs [87]. Using the DL model and the MG EMA they observed a decrease in the free electron carrier density and attributed this to the change in bonding from an sp^2 to an sp^3 bonding regime. This study was continued in Ref. [88] by including Raman spectroscopy, and the terahertz results are displayed along with the Raman spectra in Fig. 8.13. An increase in the I_D/I_G ratio was observed upon hydrogen functionalisation, which is indicative of an increase in sp^3 bonding.

Whilst Jeon and coworkers in Korea have been the most prolific researchers in the characterisation of CNTs, there have been other groups working on this challenge with terahertz spectroscopy. Federici and coworkers in New Jersey, USA performed visible pump-probe terahertz spectroscopy to investigate localised transport in Lorentz-type photoinduced states [90]. As with previous methods, they utilised a (modified) DL model to explain the terahertz transmission properties through the photoexcited layer. Researchers in Japan have also investigated CNTs with THz-TDS. Iwasa and coworkers used THz-TDS to investigate the dielectric properties of aligned CNTs between 0.1 THz and over 300 THz [91]. Large differences between the absorption properties were observed below 30 THz for nanotubes aligned parallel and perpendicular to the E -field orientation. Here, they explain some of the observed differences in terms of how the MG model is formulated to fit the data. Alignment of the CNTs means that the spherical approximation used in the basic

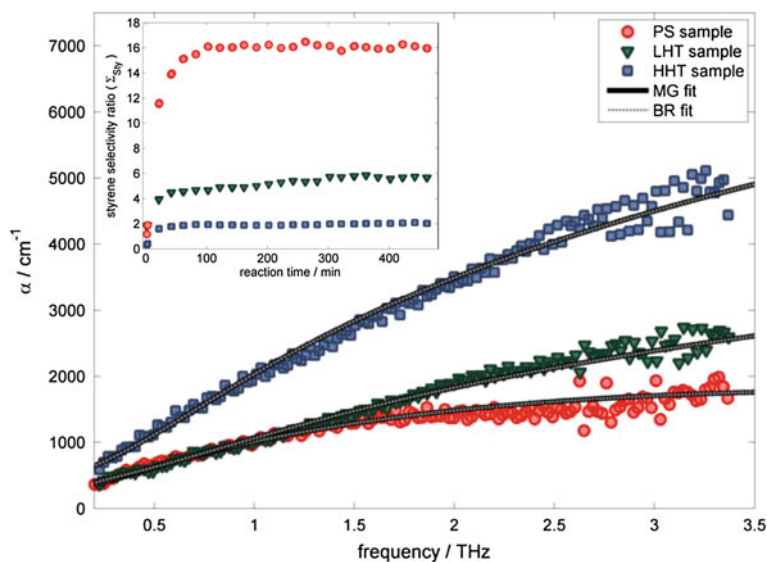


Fig. 8.14 Absorption coefficient for the three types of CNF studied in Ref. [19]. Insert: catalytic activity test results for the three CNF materials

MG model is no longer applicable and so in the limit of zero cross-section in the polarisation direction the MG model then approximates to a simple mixing model. Shimano and coworkers in Tokyo measured the dielectric properties of SWCNTs from 0.1 to 20 THz through optical rectification in a ZnTe crystal [92]. As with previous investigations, they analysed the terahertz absorption spectrum by using a DL model. With some similarities to Ref. [91], Rungsawang et al. investigated the terahertz absorption of rubber containing embedded CNTs and found that by deforming the material (stretching), alignment of the CNT could be induced and measured with THz-TDS [93]. Recently, THz-TDS has been used in order to understand and quantify differences between similar carbon nanofibres (CNFs) and CNTs [19, 20]. The definition of the difference between CNFs and CNTs is somewhat difficult to define, but commonly a CNT is defined as a carbon material exhibiting a cylindrical nanostructure with an inner diameter less than 10 nm and a CNF differs in having an inner diameter ranging between 10 and 100 nm. In the first study [19] the catalytic activity of heat-treated CNF materials was quantified using THz-TDS. Three CNF samples, identical except for their heat-treatment temperature, displayed very different catalytic activity for the dehydrogenation reaction of butane to styrene, as shown in Fig. 8.14. As can be seen in Fig. 8.14, THz-TDS is able to clearly differentiate between the three different CNFs. Using the DL model and EMAs, the observed increase in terahertz absorption with increasing heat-treatment temperature could be replicated, and attributed to an increase in the free electron density.

In a similar fashion, the degree of graphitic order in two commercially available multi-walled CNTs (Baytubes and Nanocyl) was quantified using THz-TDS and

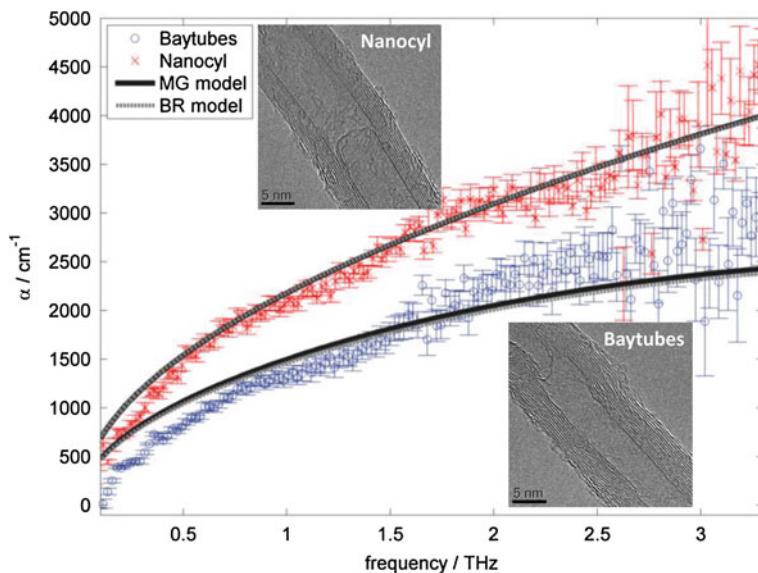


Fig. 8.15 Absorption coefficients for the two nominally similar MWCNTs studied in Ref. [20]. Inserts: Representative HRTEM images of the two MWCNTs highlighting the different graphicity of the two materials

compared to high resolution transmission electron microscopy (HRTEM) images representative of the two samples. The absorption coefficients extracted for the CNTs and the corresponding HRTEM images are shown in Fig. 8.15. The THz-TDS absorption coefficient data showed an increase across the frequency region for the Nanocyl sample when compared to the Baytubes sample, and as before use of the DL model and EMAs suggested that this change could be attributed to an increase in the free electron density in the Nanocyl CNTs. It therefore follows that a larger number of electrons are present in a delocalised bonding regime, which would be consistent with a decrease in the number of defects within the Baytubes CNTs. This correlates with the HRTEM images, where the Baytubes can be seen to display a greater number of terminations and defects in comparison to the Nanocyl sample. The results presented in all of these papers have shown the sensitivity that THz-TDS displays towards the electron density present within CNTs, and therefore by extension other forms of ordered carbon materials, such as graphene and graphite. Whilst previous studies have focused on differences between CNTs such as functionalisation, in the future it would be interesting to develop and probe the extent to which THz-TDS is directly sensitive to defect density by introducing defects into a material in a controllable manner.

In addition, the research papers reported herein used a variety of different preparation and extraction techniques in order to produce the frequency-dependent optical constants for a range of carbonaceous materials. These range from embedding the CNTs in rubber [93], mixing them with a diluent such as KBr [89] to depositing them

in a thin film on a second surface such as silicon [18, 85–88] or quartz [19, 20]. In order to be able to draw conclusions relating to the different materials investigated, it would be important to study the effects of sample preparation on the extracted optical constants and the resulting effect, if any, this would have on the fitting parameters of the DL model used to infer some explanation as to their relative properties.

8.5 Summary

Terahertz spectroscopy of crystalline and non-crystalline solids has developed into one of the largest research fields within the terahertz scientific community. Spectroscopic studies ranging across condensed matter physics, chemical physics, physical chemistry, materials chemistry, pharmaceutical sciences, chemical engineering to the food and paper industries have been reported. In addition to the shear range of activities this field of terahertz technology is also the area which has attracted most attention so far above and beyond the direct interest within the terahertz community. Some of the first materials that were investigated using terahertz spectroscopy methods were semiconductors, but it was in particular the spectra of explosives and drug molecules, which were shown to exhibit pronounced spectroscopic signatures that highlighted the potential for the wider community for this new spectroscopy technique. It was this interest that was the driving force behind the development of the first commercial terahertz systems. However, the initial surge in interest also led to some exaggerated expectations as to how the characteristic spectral features could be used for applications, in particular in the security sector. The field has matured considerably over the past few years and more realistic research-oriented studies once again dominate the community. In this chapter, based on selected examples, we have shown that the applications of terahertz time-domain spectroscopy for investigating the dielectric properties of a given material go far beyond plain spectral recognition. In order to fully exploit these capabilities it is absolutely paramount to combine careful sample preparation with more sophisticated data analysis. Given the complexity of the research topics covered in the community as well as the dynamic nature of the field, the list of data analysis approaches that we present in this chapter must not be considered exhaustive. We would like to refer the interested reader to the other chapters in this book, that cover some of these concepts in more depth.

References

1. G.W. Chantry, *Submillimetre Spectroscopy—A Guide to the Theoretical and Experimental Physics of the Far Infrared Radiation* (Academic Press, New York, 1971)
2. K.D. Möller, W.G. Rothschild, *Far-Infrared Spectroscopy* (Wiley, New York, 1971)
3. E.V. Loewenstein, D.R. Smith, R.L. Morgan, *Appl. Opt.* **12**(2), 398 (1973)
4. M. Kerker, *The scattering of light, and other electromagnetic radiation* (Academic Press, New York, 1969)

5. H.C. van de Hulst, *Light scattering by small particles* (Dover Publications, New York, 1981)
6. C.F. Bohren, D.R. Huffman, *Absorption and scattering of light by small particles* (Wiley, New York, 1983)
7. G.M. Png, R.J. Falconer, B.M. Fischer, H.A. Zakaria, S.P. Mickan, A.P.J. Middelberg, D. Abbott, *Opt. Express* **17**(15), 13102 (2009)
8. W. Withayachumnankul, B.M. Fischer, D. Abbott, *Opt. Express* **16**(10), 7382 (2008)
9. M. Franz, B.M. Fischer, M. Walther, *Appl. Phys. Lett.* **92**(2), 021107 (2008)
10. R. Barnes, L. Bonner, *Phys. Rev.* **49**(10), 732 (1936)
11. C.V. Raman, *Proc. Indian Acad. Sci. A* **29**, 381 (1949)
12. L. Duvillearet, F. Garet, J.L. Coutaz, *Appl. Opt.* **38**(2), 409 (1999)
13. T.D. Dorney, R.G. Baraniuk, D.M. Mittleman, *J. Opt. Soc. Am. A* **18**(7), 1562 (2001)
14. I. Pupeza, R. Wilk, M. Koch, *Opt. Express* **15**(7), 4335 (2007)
15. R. Wilk, I. Pupeza, R. Cernat, M. Koch, *IEEE J. Sel. Top. Quant.* **14**(2), 392 (2008)
16. E.P.J. Parrott, J.A. Zeitler, L.F. Gladden, S.N. Taraskin, S.R. Elliott, *J. Non-Cryst. Solids* **355**(37–42), 1824 (2009)
17. E.P.J. Parrott, J.A. Zeitler, G. Simon, B. Hehlen, L.F. Gladden, S.N. Taraskin, S.R. Elliott, *Phys. Rev. B* **82**(14), 140203 (2010)
18. T.I. Jeon, J.H. Son, K.H. An, Y.H. Lee, Y.S. Lee, *J. Appl. Phys.* **98**(3), 034316 (2005)
19. E.P.J. Parrott, J.A. Zeitler, J. McGregor, S.P. Oei, H.E. Unalan, S.C. Tan, W.I. Milne, J.P. Tessonnier, R. Schlögl, L.F. Gladden, *J. Phys. Chem. C* **113**, 10554 (2009)
20. E.P.J. Parrott, J.A. Zeitler, J. McGregor, S.P. Oei, H.E. Unalan, W.I. Milne, J.P. Tessonnier, D.S. Su, R. Schlögl, L.F. Gladden, *Adv. Mater.* **21**(38–39), 3953 (2009)
21. J.C.M. Garnett, *Philos. T. R. Soc. Lond.* **203**(1), 385 (1904)
22. D.A.G. Bruggeman, *Ann. Phys.* **416**, 636 (1935)
23. J.C.M. Garnett, *Philos. T. R. Soc. Lond.* **205**(1), 237 (1906)
24. J.E. Spanier, I.P. Herman, *Phys. Rev. B* **61**(15), 10437 (2000)
25. W. Fan, A. Burnett, P. Upadhyaya, J. Cunningham, E. Linfield, A. Davies, *Appl. Spectrosc.* **61**(6), 638 (2007)
26. Y.C. Shen, P.C. Upadhyaya, E. Linfield, H. Beere, A. Davies, *Appl. Phys. Lett.* **83**(15), 3117 (2003)
27. P.U. Jepsen, B. Fischer, *Opt. Lett.* **30**(1), 29 (2005)
28. A. Markelz, A. Roitberg, E. Heilweil, *Chem. Phys. Lett.* **320**(1–2), 42 (2000)
29. M. Walther, B. Fischer, M. Schall, H. Helm, P.U. Jepsen, *Chem. Phys. Lett.* **332**(3–4), 389 (2000)
30. A.G. Markelz, S. Whitmire, J.R. Hillebrecht, R. Birge, *Phys. Med. Biol.* **47**, 3797 (2002)
31. H.A. Lorentz, in *Proceedings of the KNAW*, vol. 18, p. 134, 1915
32. B.M. Fischer, M. Walther, P.U. Jepsen, *Phys. Med. Biol.* **47**(21), 3807 (2002)
33. K. Yamamoto, M.H. Kabir, K. Tominaga, *J. Opt. Soc. Am. B* **22**(11), 2417 (2005)
34. N. Brandt, A. Chikishev, A. Kargovsky, M. Nazarov, O. Parashchuk, D. Sapozhnikov, I. Smirnova, A. Shkurinov, N. Sumbatyan, *Vib. Spectrosc.* **47**(1), 53 (2008)
35. M. Walther, P. Plochocka, B. Fischer, H. Helm, P.U. Jepsen, *Biopolymers* **67**(4–5), 310 (2002)
36. M. Walther, B.M. Fischer, P.U. Jepsen, *Chem. Phys.* **288**(2–3), 261 (2003)
37. B. Fischer, M. Hoffmann, H. Helm, G. Modjesch, P.U. Jepsen, *Semicond. Sci. Tech.* **20**(7), S246 (2005)
38. P.F. Taday, I.V. Bradley, D.D. Arnone, M. Pepper, *J. Pharm. Sci.* **92**(4), 831 (2003)
39. E.P.J. Parrott, J.A. Zeitler, T. Friscic, M. Pepper, W. Jones, G.M. Day, L.F. Gladden, *Cryst. Growth Des.* **9**(3), 1452 (2009)
40. C.J. Strachan, T. Rades, D.A. Newnham, K.C. Gordon, M. Pepper, P.F. Taday, *Chem. Phys. Lett.* **390**(1–3), 20 (2004)
41. M. Ge, G. Liu, S. Ma, W. Wang, *Bull. Korean Chem. Soc.* **30**(10), 2265 (2009)
42. R. Chakkittakandy, J.A.W.M. Corver, P.C.M. Planken, *J. Pharm. Sci.* **99**(2), 932 (2010)
43. J.A. Zeitler, D.A. Newnham, P.F. Taday, T.L. Threlfall, R.W. Lancaster, R.W. Berg, C.J. Strachan, M. Pepper, K.C. Gordon, T. Rades, *J. Pharm. Sci.* **95**, 2486 (2006)
44. Y.C. Shen, P.F. Taday, *IEEE J. Sel. Top. Quant.* **14**(2), 407 (2008)

45. J.A. Zeitler, D.A. Newnham, P.F. Taday, C.J. Strachan, M. Pepper, K.C. Gordon, T. Rades, *Thermochim. Acta* **436**(1–2), 71 (2005)
46. J.A. Zeitler, P.F. Taday, K.C. Gordon, M. Pepper, T. Rades, *Chem. Phys. Chem.* **8**, 1924 (2007)
47. M. Franz, B.M. Fischer, M. Walther, *J. Mol. Struct.* **1006**(1–3), 34 (2011)
48. P. Upadhyaya, K. Nguyen, Y. Shen, J. Obradovic, K. Fukushige, R. Griffiths, L. Gladden, A. Davies, E. Linfield, *Spectrosc. Lett.* **39**(3), 215 (2006)
49. J.A. Zeitler, P.F. Taday, M. Pepper, T. Rades, *J. Pharm. Sci.* **96**, 2703 (2007)
50. J.A. Zeitler, K. Kogermann, J. Rantanen, T. Rades, P.F. Taday, M. Pepper, J. Aaltonen, C.J. Strachan, *Int. J. Pharm.* **334**(1–2), 78 (2007)
51. H.b. Liu, Y. Chen, X.C. Zhang, *J. Pharm. Sci.* **96**(4), 927 (2007)
52. H. Liu, X.C. Zhang, *Chem. Phys. Lett.* **429**(1–3), 229 (2006)
53. M. Ge, W. Wang, H. Zhao, Z. Zhang, X. Yu, W. Li, *Chem. Phys. Lett.* **444**(4–6), 355 (2007)
54. K.L. Nguyen, T. Frisci , G.M. Day, L.F. Gladden, W. Jones, *Nat. Mater.* **6**(3), 206 (2007)
55. P.F. Taday, *Philos. T. Roy. Soc. A* **362**(1815), 351 (2004)
56. C.J. Strachan, P.F. Taday, D.A. Newnham, K.C. Gordon, J.A. Zeitler, M. Pepper, T. Rades, *J. Pharm. Sci.* **94**(4), 837 (2005)
57. Y. Shen, P. Taday, D. Newnham, M. Pepper, *Semicond. Sci. Tech.* **20**(7), 254 (2005)
58. Z. Zeng-Yan, J. Te, Y. Xiao-Han, X. Ti-Qiao, X. Hong-Jie, *Chinese Phys. Lett.* **23**(8), 2239 (2006)
59. E.P.J. Parrott, J.A. Zeitler, L.F. Gladden, *Opt. Lett.* **34**(23), 3722 (2009)
60. H. Tuononen, K. Fukunaga, M. Kuosmanen, J. Ketolainen, K.E. Peiponen, *Appl. Spectrosc.* **64**(1), 127 (2010)
61. M. Scheller, S. Wietzke, C. Jansen, M. Koch, *J. Phys. D: Appl. Phys.* **42**(6), 065415 (2009)
62. G. Gallot, S. Jamison, R. McGowan, D. Grischkowsky, *J. Opt. Soc. Am. B* **17**(5), 851 (2000)
63. J.S. Melinger, N. Laman, S.S. Harsha, D. Grischkowsky, *Appl. Phys. Lett.* **89**(25), 251110 (2006)
64. N. Laman, S.S. Harsha, D. Grischkowsky, *Appl. Spectrosc.* **62**(3), 319 (2008)
65. M.C. Kemp, P.F. Taday, B.E. Cole, J.A. Cluff, A.J. Fitzgerald, W.R. Tribe, *Proc. SPIE* **5070**, 44 (2003)
66. F. Huang, B. Schulkin, H. Altan, J.F. Federici, D. Gary, R. Barat, D. Zimdars, M. Chen, D.B. Tanner, *Appl. Phys. Lett.* **85**(23), 5535 (2004)
67. Y. Chen, H. Liu, Y. Deng, D. Schauki, M.J. Fitch, R. Osiander, C. Dodson, J.B. Spicer, M. Shur, X.C. Zhang, *Chem. Phys. Lett.* **400**(4–6), 357 (2004)
68. W.H. Fan, A. Burnett, P.C. Upadhyaya, J. Cunningham, E.H. Linfield, A.G. Davies, *Appl. Spectrosc.* **61**(6), 638 (2007)
69. J. Barber, D.E. Hooks, D.J. Funk, R.D. Averitt, A.J. Taylor, D. Babikov, *J. Phys. Chem. A* **109**(15), 3501 (2005)
70. J.S. Melinger, N. Laman, D. Grischkowsky, *Appl. Phys. Lett.* **93**(1), 011102 (2008)
71. J. Chen, Y. Chen, H. Zhao, G.J. Bastiaans, X.C. Zhang, *Opt. Express* **15**(19), 12060 (2007)
72. Y.C. Shen, T. Lo, P.F. Taday, B.E. Cole, W.R. Tribe, M.C. Kemp, *Appl. Phys. Lett.* **86**(24), 241116 (2005)
73. D.G. Allis, T.M. Korter, *Chem. Phys. Chem.* **7**(11), 2398 (2006)
74. D.G. Allis, D.A. Prokhorova, T.M. Korter, *J. Phys. Chem. A* **110**(5), 1951 (2006)
75. D.G. Allis, J.A. Zeitler, P.F. Taday, T.M. Korter, *Chem. Phys. Lett.* **463**, 84 (2008)
76. A.D. Burnett, J. Kendrick, J.E. Cunningham, M.D. Hargreaves, T. Munshi, H.G.M. Edwards, E.H. Linfield, A.G. Davies, *Chem. Phys. Chem.* **11**(2), 368 (2010)
77. C.T. Konek, B.P. Mason, J.P. Hooper, C.A. Stoltz, J. Wilkinson, *Chem. Phys. Lett.* **489**(1–3), 48 (2010)
78. D. Grischkowsky, S. Keiding, M. van Exter, C. Fattinger, *J. Opt. Soc. Am. B* **7**(10), 20062015 (1990)
79. A.J.L. Adam, P.C.M. Planken, S. Meloni, J. Dik, *Opt. Express* **17**(5), 3407 (2009)
80. E. Courtens, M. Foret, B. Hehlen, R. Vacher, *Solid State Commun.* **117**(3), 187 (2001)
81. R. Zeller, R. Pohl, *Phys. Rev. B* **4**(6), 2029 (1971)
82. M. Naftaly, R. Miles, *J. Non-Cryst. Solids* **351**(40–42), 3341 (2005)

83. S.N. Taraskin, S.I. Simdyankin, S.R. Elliott, J.R. Neilson, T. Lo, *Phys. Rev. Lett.* **97**(5), 1 (2006)
84. B. Hehlen, E. Courtens, R. Vacher, A. Yamanaka, M. Kataoka, K. Inoue, *Phys. Rev. Lett.* **84**(23), 5355 (2000)
85. T.I. Jeon, K.J. Kim, C. Kang, S.J. Oh, J.H. Son, K.H. An, D.J. Bae, Y.H. Lee, *Appl. Phys. Lett.* **80**(18), 3403 (2002)
86. T.I. Jeon, K.J. Kim, C. Kang, I.H. Maeng, J.H. Son, K.H. An, J.Y. Lee, Y.H. Lee, *J. Appl. Phys.* **95**, 5736 (2004)
87. C. Kang, I.H. Maeng, S.J. Oh, J.H. Son, T.I. Jeon, K.H. An, S.C. Lim, Y.H. Lee, *Appl. Phys. Lett.* **87**(4), 041908 (2005)
88. C. Kang, I.H. Maeng, S.J. Oh, S.C. Lim, K.H. An, Y.H. Lee, J.H. Son, *Phys. Rev. B* **75**(8), 1 (2007)
89. I. Maeng, C. Kang, S.J. Oh, J.H. Son, K.H. An, Y.H. Lee, *Appl. Phys. Lett.* **90**(5), 051914 (2007)
90. H. Altan, F. Huang, J.F. Federici, A. Lan, H. Grebel, J. Appl. Phys. **96**(11), 6685 (2004)
91. N. Akima, Y. Iwasa, S. Brown, A.M. Barbour, J. Cao, J. Musfeldt, H. Matsui, N. Toyota, M. Shiraishi, H. Shimoda, O. Zhou, *Adv. Mater.* **18**(9), 1166 (2006)
92. H. Nishimura, N. Minami, R. Shimano, *Appl. Phys. Lett.* **91**(1), 011108 (2007)
93. R. Rungsawang, V.G. Geethamma, E.P.J. Parrott, D.A. Ritchie, E.M. Terentjev, *J. Appl. Phys.* **103**(12), 123503 (2008)

Chapter 9

Terahertz Spectroscopy of Liquids and Biomolecules

D. K. George and A. G. Markelz

Abstract The terahertz regime has particular value for liquid and biomolecular spectroscopy. In the case of liquids, terahertz is sensitive to relaxational and collective motions in liquids [1–13]. Applications include determination of sugar, alcohol, and water content. While there are no narrow band identification features for liquids in the terahertz range, the ability of THz to transmit through packaging materials and high sensitivity of relative water content is considered highly appealing for its use as a method to rapidly verify labeled contents. The determination of the water, sucrose, alcohol, liquid fuel, and petroleum content using terahertz have been demonstrated [1, 10]. The fundamental findings from terahertz measurements of liquids include the hydration number associated with solutes [14, 15], the extent of the perturbation of the liquid structure by the solute [16, 17], and the role of interactions in binary liquids [13, 18]. New collective mode vibrations have been identified for alcohols [19, 20], and the changes in the relaxational dynamics due to mixing, and the role of collective vibrations in ionic liquids [21–24]. In order to achieve these many findings, sensitive measurement techniques and data analysis have been developed. In parallel, great strides in modeling have been made to effectively model the picosecond dielectric response for these highly complex systems.

Biological applications of terahertz have been explored from spectroscopy of biologically relevant molecules as small as sucrose up to organisms such as bacterial spores. Significant progress has been made in fundamental characterization of small biomolecules with accurate modeling of both intramolecular modes, and the intermolecular modes for crystalline material. Initial measurements of small proteins have been explored; however, theoretical understanding is not as well developed. While a variety of groups have demonstrated sensitivity in the THz dielectric response to protein and nucleic acid functional state, the origin of this sensitivity is still some-

D. K. George · A. G. Markelz (✉)

Department of Physics, University at Buffalo, The State University of New York,
New York 14260, USA
e-mail: amarkelz@buffalo.edu

what controversial.

In this chapter, we will discuss measurement methods, modeling of the terahertz response for these systems, and major results. We will conclude with a discussion on future directions for the applications of terahertz for liquid and biomolecular characterization.

9.1 Liquids

9.1.1 Terahertz Response for Liquids

Typically liquid response is characterized for polar and nonpolar liquids. Let us first look at a listing of some common liquids, the dipole moments for constituent molecules, and the THz absorption coefficient at 3 THz in Table 9.1. We see that water has the largest dipole for those listed, whereas benzene's dipole is zero, and the THz absorption coefficient decreases as the dipole moment decreases [9, 18, 19, 25]. This is a reflection of simplest response of the liquid to the applied electric field, which is simply the dipole alignment following the applied field. There is an effective time for this rotation arising from the bonds (usually weak hydrogen bonds) that must be broken for the molecule to rotate. We refer to this effective alignment time as the relaxation time τ . To calculate the dielectric response arising from this relaxation time we quickly review the relationship between the polarization, displacement field, electric field, electric susceptibility χ and permittivity ε :

$$\begin{aligned} P &= \varepsilon_o \chi E \\ D &= \varepsilon_o \varepsilon_r E = E + P \\ \varepsilon_r &= \varepsilon = 1 + \chi \end{aligned} \tag{9.1}$$

We now develop an expression for the permittivity based on the average time for dipole alignment to the applied field, the Debye relaxation time. The molecular response of the liquid to the applied electric field is split into different components, a fast response polarization P_f , where the polarization follows the field instantaneously, and a slow response polarization P_s :

$$\begin{aligned} P &= P_s + P_f \\ P &= \varepsilon_o(\varepsilon - 1)E \\ P_f &= \varepsilon_o(\varepsilon_\infty - 1)E \end{aligned} \tag{9.2}$$

The rate change of P_s is proportional to the difference between the steady-state polarization and polarization at time t :

Table 9.1

Solvent	Dielectric constant	α (3 THz) (cm ⁻¹)	Dipole moment (<i>D</i>)
Cyclohexane ^a	2.02	0.3	0.00
Benzene ^a	2.3	4.8	0.00
Chloroform ^b	4.81	7	1.04
1-Propanol ^c	20	35	1.68
Ethanol ^c	24.55	60	1.69
Methanol ^c	33	110	1.70
Water ^c	80	200	1.85

^aKeiding ^bCheville et al. ^cKindt and Schmuttenmaer

$$\frac{dP_s(t)}{dt} = \frac{P - (P_f + P_s(t))}{\tau} \quad (9.3)$$

At low frequencies the total polarization will go as the slow susceptibility with

$$P_{\nu \rightarrow 0} = \varepsilon_o(\varepsilon_s - 1)E \quad (9.4)$$

For response at harmonic fields, we substitute $E(t) = E_o e^{i\omega t}$ and $P_s(t) = P_s e^{i\omega t}$ into Eq. 9.3

$$\begin{aligned} E(t) = E_o e^{i\omega t} &\Rightarrow P_s(t) = P_s e^{i\omega t} \\ i\omega P_s e^{i\omega t} &= \frac{\varepsilon_o(\varepsilon_s - 1)E_o e^{i\omega t} - \varepsilon_o(\varepsilon_\infty - 1)E_o e^{i\omega t} - P_s e^{i\omega t}}{\tau} \\ i\omega P_s &= \frac{\varepsilon_o(\varepsilon_s - \varepsilon_\infty)E_o - P_s}{\tau} \\ P_s &= \frac{\varepsilon_o(\varepsilon_s - \varepsilon_\infty)E_o}{1 + i\omega\tau} \\ P &= P_f + P_s \\ \varepsilon_o(\varepsilon - 1)E_o &= \varepsilon_o(\varepsilon_\infty - 1)E_o + \frac{\varepsilon_o(\varepsilon_s - \varepsilon_\infty)E_o}{1 + i\omega\tau} \\ \varepsilon &= \varepsilon_\infty + \frac{(\varepsilon_s - \varepsilon_\infty)}{1 + i\omega\tau} \end{aligned} \quad (9.5)$$

The dipole alignment may involve the motion of small clusters as well, so that there are often a number of relaxation times. In general the modeling of the dielectric response for liquids and glasses can be written as:

$$\varepsilon(\omega) = \varepsilon_\infty + \sum_i \frac{\Delta\varepsilon_i}{1 + i\omega\tau_i} \quad (9.6)$$

For some liquids, intermolecular coupling can be sufficiently strong so that vibrations between solvent molecules or within a single solvent molecule will also contribute to the dielectric response. These are typically Lorentzian resonances so that a full dielectric response can be modeled as:

$$\varepsilon(\omega) = \varepsilon_{\infty} + \sum_i \frac{\Delta\varepsilon_i}{1 + i\omega\tau_i} + \sum_j \frac{f(\omega_j)}{(\omega_j^2 - \omega^2) - i\gamma\omega} \quad (9.7)$$

To relate the measured relaxation times and resonant frequencies to the microscopic motions one can calculate the dielectric response using molecular dynamics simulations based on force fields or ab initio calculations. The simulations calculate the trajectories of individual molecules and atoms. One can then calculate the dipole vector for the system for each time step and then determine the dipole–dipole correlation for the system for different times. The dipole–dipole correlation function is related to the product of the absorption coefficient and index by:

$$\alpha(\bar{\nu})n(\bar{\nu}) = \text{Re} \left[\bar{\nu} \left\{ 1 - \exp\left(-\frac{hc(\bar{\nu})}{KT}\right) \right\} \times \int_{-\infty}^{\infty} dt \exp(-i2\pi c\bar{\nu}t \langle \mathbf{M}(t)\mathbf{M}(0) \rangle) \right] \quad (9.8)$$

9.1.1.1 Terahertz Measurement Methods for Liquids

The goal in all of these measurements is to characterize the complex permittivity. The most straightforward method for this determination is a transmission measurement using terahertz time domain spectroscopy (THz TDS). This technique is well discussed in previous chapters and a number of commercial systems are now available. For liquid phase measurements, however, the accurate determination of the permittivity is challenged by: accurate determination of the sample thickness, the high absorption for some liquids, and etalon effects. Several techniques have been developed to address these issues.

9.1.2 Liquid Transmission

The simplest method for characterization of a liquid is a transmission measurement. In the UV/Vis and IR ranges standard cuvettes are available for liquid measurements. However, these standard cuvettes are typically made out of materials which strongly attenuate at THz frequencies. In addition, the typical path lengths for standard cells is 5–10 mm. Demountable solution cells with variable spacers are available commercially, an example is shown in Fig. 9.1a. These cells are very flexible in that the window material can be highly transmissive in the FIR, such as zeonor, polyethylene, water free quartz and Teflon, and the spacer can be chosen for optimal sensitivity for the absorbance of material. In Fig. 9.1b the field transmission for the reference and

sample is shown schematically with:

$$\begin{aligned}
 t &= \frac{E_{\text{sample}}}{E_{\text{reference}}} = \frac{t_{ow}e^{iN_wk_0d_w}t_{wo}e^{ik_0d_s}t_{ow}e^{iN_wk_0d_w}t_{wo}}{t_{ow}e^{iN_wk_0d_w}t_{wo}e^{ik_0d_s}t_{ow}e^{iN_wk_0d_w}t_{wo}} \\
 &= \frac{t_{ws}t_{sw}}{t_{wo}t_{ow}}e^{i(N_s-1)k_0d_s} = \frac{N_S(N_W+1)^2}{(N_W+N_S)^2}e^{i(N_s-1)k_0d_s}
 \end{aligned} \tag{9.9}$$

$$t = |t|e^{i\phi} = \frac{N_S(N_W+1)^2}{(N_W+N_S)^2}e^{-\kappa k_0d_s}e^{i(n_s-1)k_0d_s} \tag{9.10}$$

$$\begin{aligned}
 |t| &= \frac{n_S(n_W+1)^2}{(n_W+n_S)^2}e^{-\kappa k_0d_s} \\
 \phi &= (n_s-1)k_0d_s
 \end{aligned} \tag{9.11}$$

where in Eq. 9.9 t_{ij} is the Fresnel transmission coefficient from material i to material j . The subscripts o , w , and s denote atmosphere, window, and sample. In general the THz spectroscopy system is purged of any gas phase water. $N_{S(W)} = n_{S(W)} + i\kappa_{S(W)}$ is the complex index for the sample (window), which has real and imaginary parts. For κ sufficiently small, there is little phase acquired from the Fresnel terms and these can be written in terms of the real parts of the indices. From this then one can immediately determine n_s by inverting the measured phase and then using this determined n_s to determine κ_s from the magnitude of the transmittance. Equation 9.10 was written without an etalon term. Etalon effects can in many cases be readily removed by simply truncating the transmitted wave before the reflected pulse; however, in some cases samples are too thin to take this approach, as the reflected pulse will overlap the first transmitted pulse. In these cases, the etalon term must be included in the extraction of the optical constants.

$$t = |t|e^{i\phi} = \frac{N_S(N_W+1)^2}{(N_W+N_S)^2} \frac{1-r_{ow}^2e^{i2k_0d}}{1-r_{sw}^2e^{i2N_s k_0d}} e^{-i\kappa k_0d_s} e^{i(n_s-1)k_0d_s} \tag{9.12}$$

The most immediate approach to extract $n_s + i\kappa_s$ when etalon is present is to use the measured sample thickness d , window response $n_w + i\kappa_w$, and the measured $|t|$ and ϕ at each frequency and calculate the roots for the coupled equations for $|t|$ and ϕ based on Eq. 9.12 using a standard 2D complex root determination such as is available from Maple or Matlab. For this type of determination one needs to be aware to sufficiently constrain the sampling so that the roots make sense, such as non-negative indices. Regardless of the computation method, this simple method using the transmission through a fixed path length solution cell suffers from the requirements of precise determination of the sample thickness and window dielectric response.

For sufficiently thick samples, the etalon can be avoided by waveform truncation and one does not need to precisely determine sample thickness and window response by using a variable path length cell [6, 17, 24, 26]. Typically, this is achieved by

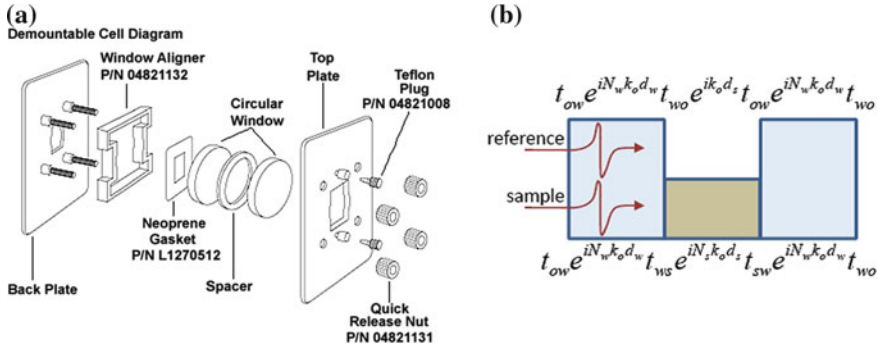
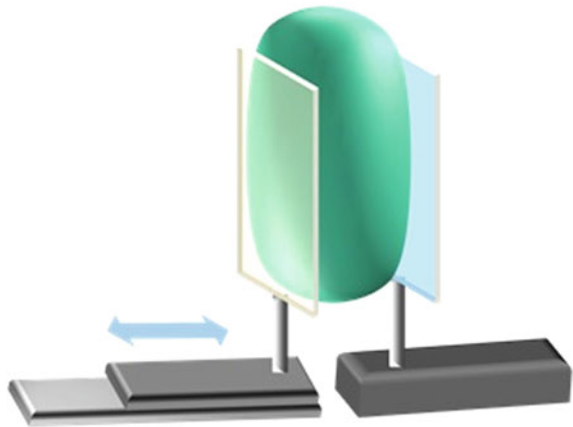


Fig. 9.1 **a** Schematic of commercially available solution cell (Perkin Elmer). **b** Schematic of transmission measurement for a solution cell, with the reference pulses measurement taken for the empty cell and the sample measurement for the liquid filled cell

Fig. 9.2 Schematic of a variable path length cell for THz measurements of liquids



placing the liquid in a flexible container, such as a polyethylene bag, and then compressing the bag between two windows, see Fig. 9.2. While absolute thickness determination can be difficult, changes in thickness with an accurate actuator is straightforward. From Eq. 9.4 one can extract the index from a linear fit to the phase as a function of path length variation. Similarly, the imaginary part of the index, κ , can be determined by a linear fit to the $\ln(|t|)$. This method has been used for THz TDS measurements of a wide variety of solvents. However, it is still not ideal for highly absorbing materials, such as water, due to the limited power and dynamic range of typical THz TDS systems. To have a sufficient signal in these cases the path length must be made very thin, with the resulting contamination of the reflected pulse in the main pulse leads to etalon in the transmittance. When this occurs, a simple linear fit cannot be used.

In the case of highly absorbing liquids a number of approaches have been employed. Tunable high power monochromatic sources have been used to achieve

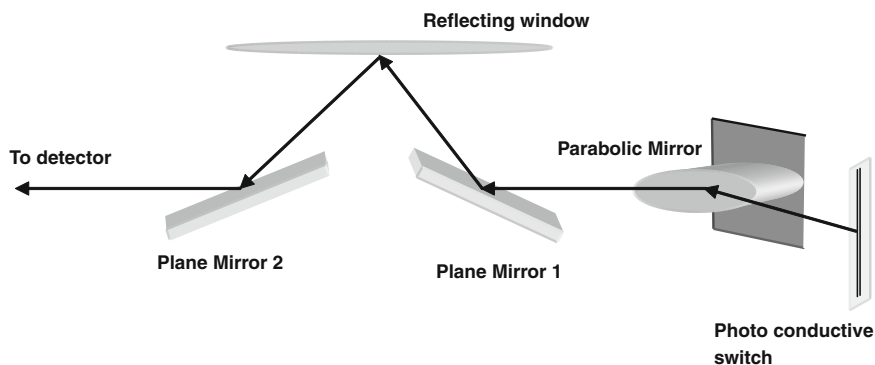


Fig. 9.3 Implementation of reflection THz spectroscopy

high precision permittivity measurements. Xu and coworkers used a free electron laser to characterize the effect of salts on the dielectric response of water, and characterize protein concentration effects for protein-buffer solutions [26, 27]. The output powers for the THz UCSB FELs are 1–15 kW for a 1–6 microsecond pulse width for the MM-FEL and 1–6 kW for 1–20 microsecond pulse width for the FIR-FEL, an approximate factor of 10^7 higher output power than a typical THz TDS system. High power broadband THz TDS systems are becoming more common using tilted phase front or plasma generation. Another highly valuable high power source is the p-Ge laser developed by Bruderman and coworkers [16, 28]. The peak power for the p-Ge laser is 1–10 W; however, similar to the UCSB FEL, these systems are not readily available.

Reflection geometries readily address the dynamic range challenges of highly absorbing materials as the signal is only probing the dielectric interface between a known low loss substrate and the high loss liquid sample [29, 30]. Jepsen group developed the self-referencing geometry for THz TDS, whereas Tanaka group developed ATR geometry more common to IR ATR measurements. In the former method, which is explained in detail below, the liquid lays horizontally on a substrate. The incoming THz light is reflected off the interface between the substrate and liquid. In ATR THz TDS the sample is placed on top of a silicon Dove prism with an apex angle where the is the angle for total internal reflection of THz beam at the sample–prism interface as shown in Fig. 9.4b. The prism is placed at the focus of the THz beam. The beam enters the prism horizontal from one side. Figure 9.3 shows an implementation of reflection THz TDS, while Fig. 9.4a gives a detailed view of the reflection geometry at the sample window, showing the reference and sample beams.

In the self-referencing method, the sample is placed on the upper surface of a horizontal window substrate of appropriate thickness. Based on the refractive index and transmission in the THz region, high purity Si of 1–2 mm thickness is a usual choice. The electric field incident on the bottom surface is partially reflected and partially transmitted. The reflected pulse from the lower surface is used as a reference. The transmitted pulse which passes through the window material again gets partially

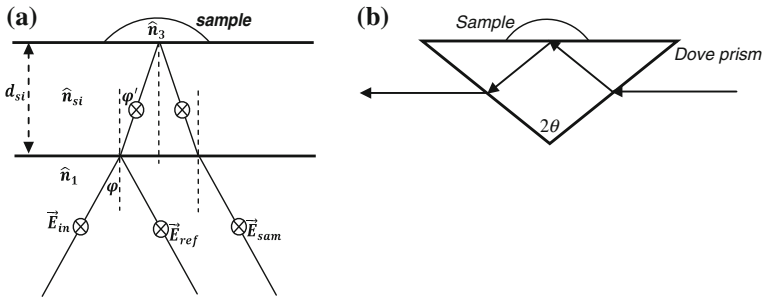


Fig. 9.4 Detailed view of **a** Self-referencing reflection geometry at the silicon window which splits the input THz signal into reference and sample pulses, **b** ATR THz TDS with silicon Dove prism. The sample is placed on top of the window/prism

reflected from the window–sample interface. This pulse which reaches the detector after a time delay carries information about the optical properties of the sample.

In the simplest implementation of transmission THz TDS, which is discussed below, the incident field is purely S-polarized. This can be achieved by the proper orientation of the generating antenna, mirrors, and the window.

The electric field reaching the detector after reflecting off the two interfaces can be represented by the following equations

$$\vec{E}_{\text{ref}} = \hat{r}_{12} \vec{E}_{\text{in}} \tag{9.13}$$

$$\vec{E}_{\text{sam}} = \hat{t}_{12} \hat{r}_{23} \hat{t}_{21} \vec{E}_{\text{in}} \exp(2i\hat{n}_2 w_2 d_{\text{eff}}/c) \times A_{\text{cal}} \exp(i\Delta_{\text{cal}}) \tag{9.14}$$

$\hat{n}_1, \hat{n}_2, \hat{n}_3$ are the complex refractive indices of the material below the lower surface of the window material and of the sample above the window.

\vec{E}_{in} the incident electric field, \vec{E}_{ref} the electric field of the pulse reflected from the lower surface, and \vec{E}_{sam} the electric field reflected from the window–sample interface. $\hat{r}_{12}, \hat{r}_{23}$ are the Fresnel reflection co-efficients at the lower and upper interfaces while $\hat{t}_{12} = \hat{t}_{21}$ is the transmission co-efficient at the lower interface. $A_{\text{cal}} \exp(i\Delta_{\text{cal}})$ represents the calibration factor in amplitude and phase to account for the spatial walk off between reference pulse and the sample pulse. d_{eff} is the effective difference in optical path of the two pulses and is given by

$$d_{\text{eff}} = d_{\text{si}} \left(1 - \frac{\sin^2 \phi}{n_{\text{si}}^2} \right) \tag{9.15}$$

where $\hat{n}_2 = n_{\text{si}}$ is the refractive index of silicon window material and ϕ is the angle of incidence

The ratio of the two electric fields is given by

$$\frac{\hat{E}_{\text{sam}}}{\hat{E}_{\text{ref}}} = \frac{\hat{t}_{12}\hat{r}_{23}\hat{t}_{21}}{\hat{r}_{12}} \exp(2in_2w_2d_{\text{eff}}/c) \times A_{\text{cal}} \exp(i\Delta_{\text{cal}}) \quad (9.16)$$

Calibration factor can be determined by taking a measurement without the sample (air above the window). In this case $\hat{n}_3 = \hat{n}_{\text{air}} = 1$ and

$$A_{\text{cal}} \exp(i\Delta_{\text{cal}}) = \frac{\vec{E}_{\text{sam}}^{\text{air}}}{\vec{E}_{\text{ref}}} \cdot \frac{\hat{t}_{12}}{\hat{t}_{12}'\hat{r}_{23}'\hat{t}_{21}'} \cdot \exp(-2i\hat{n}_2\omega_2) \quad (9.17)$$

Substituting Eq. 9.17 in Eq. 9.16 yields

$$\frac{\vec{E}_{\text{sam}}}{\vec{E}_{\text{ref}}} = \frac{\hat{r}_{23}}{\hat{r}_{23}'} \cdot \frac{\vec{E}_{\text{sam}}^{\text{air}}}{\vec{E}_{\text{sam}}'} \quad (9.18)$$

The general equation for Fresnel reflection coefficient at an interface when the incident electric field is purely ‘s’ polarized is given by

$$\hat{r}_s = \frac{n \cos(\varphi) - n' \cos(\varphi)'}{n \cos(\varphi) + n' \cos(\varphi)'} \quad (9.19)$$

Applying Snell’s law $n \sin(\varphi) = n' \sin(\varphi')$, we get

$$\hat{r}_s = \frac{n \cos(\varphi) - n' \sqrt{1 - \frac{n^2}{n'^2} \sin^2(\varphi)}}{n \cos(\varphi) + n' \sqrt{1 - \frac{n^2}{n'^2} \sin^2(\varphi)}} \quad (9.20)$$

Applying this equation at the window (silicon)—sample interface taking $n_1 = 1$ and using Snell’s equation which gives $n_{\text{si}} \sin(\varphi') = n_1 \sin(\varphi) = \sin(\varphi)$, we get

$$\hat{r}_{23} = \frac{\sqrt{\hat{n}_{\text{si}}^2 - \sin^2 \varphi} - \sqrt{\hat{n}_3^2 - \sin^2 \varphi}}{\sqrt{\hat{n}_{\text{si}}^2 - \sin^2 \varphi} + \sqrt{\hat{n}_3^2 - \sin^2 \varphi}} \quad (9.21)$$

where φ is the angle of incidence at the first interface and the complex index of refraction of the sample Eq. 9.20 can be inverted to obtain $\hat{n}_3 = \hat{n}_{\text{sam}}$;

$$\hat{n}_{\text{sam}} = \frac{\sqrt{(1 - \hat{r}_{23})^2 n_{\text{si}}^2 + 4\hat{r}_{23} \sin^2(\varphi)}}{1 + \hat{r}_{23}} \quad (9.22)$$

where \hat{r}_{23} can be obtained by inverting equation Eq. 9.17.

For the Tanaka method, more closely related to the standard ATR geometry used in the IR, a dove prism is used, with angles cut to ensure that one can insert the prism into a standard THz path, provided that the Rayleigh range is sufficiently long and

the diameter of the beam sufficiently small. However, in this case one is required to remove the sample for referencing, which may not always be convenient. These reflection techniques have achieved the highest precision in the determination of broadband absorption. Another approach to reflection-type measurements to achieve high sensitivity are waveguide methods [31, 32].

9.1.3 Major Findings and Current Directions

Among the immediate applications of terahertz applied to liquids is the rapid determination of water content in beverages and petroleum samples [1, 2]. This provides a rapid means to determine if the labeled contents are accurate. Other material response has also been characterized such as alkanes and seed oils [8, 33].

A major finding is the extent of the hydration shell for various solutes [16, 28, 34–39]. Here the hydration shell refers to the extent that dynamics of the water surrounding the solute are disrupted from bulk dynamics. Havenith and coworkers have been pioneers in this respect. Agreement has been found with their results by a variety of groups using different techniques. Bonn and coworkers have examined how single ions can disrupt the bulk water hydrogen bond network [15].

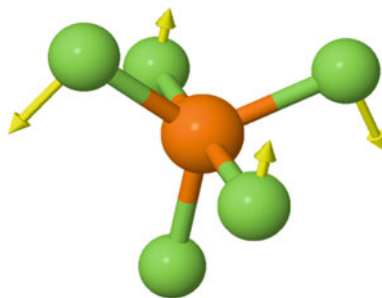
A number of groups have also examined the intermolecular coupling for binary liquids. In these studies the THz response is examined as a function of solvent concentration and it has been established that the concentration dependence does not follow a simple effective medium where the net response is fractional sum of the two constituents and that the remaining response arises from the intermolecular coupling. Of particular interest has been ionic liquids [21–24, 40, 41], where a strong change in relaxation time was found for water mixtures, deviating strongly from pure ionic liquids or pure water [24]. Future directions will likely explore the dependence of the disruption of the hydrogen bond network within a polar solvent as a function of the scale of inhomogeneity of hydrophilic and hydrophobic surfaces. In particular, if a critical scale of variation of hydrophobic/hydrophilic surface results in frustration in the hydrogen bond network and a significant change then in the relaxation time.

9.2 Biomolecules

9.2.1 Terahertz Response from Biomolecule

As mentioned in the introduction, THz has been applied to a variety of biological systems. Here we focus on the response from molecular systems as opposed to tissues and organisms. With respect to biomolecular studies we distinguish small biomolecules from macro biomolecules. Small biomolecules include individual nucleotides, glucose, sucrose, individual amino acids, small pharmaceuticals such as ibuprofen

Fig. 9.5 The vector diagram for the 178.95 cm^{-1} E' mode for phosphorus pentafluoride (from the ChemTube site at the University of Liverpool, www.chemtube3d.com/vibrationsPF5.htm)



and chromophores such as hemes and retinal. These molecules have an average of 10–20 atoms/molecule. Vibrations localized to a single or few bonds are in the infrared and vibrations distributed throughout the molecule are in the $50\text{--}500\text{ cm}^{-1}$ range. In Fig. 9.5 is shown a vector diagram of the 178.95 cm^{-1} vibrational mode for phosphorus pentafluoride to represent the extended vibration across a small molecule. The mode can be calculated using normal mode analysis (NMA) and the eigenvector for the mode is the 3D displacements for each atom for the given mode. When these small molecules are crystallized, the phonon modes of the crystal will have both an intermolecular and intramolecular component. That is, unlike in the case of simple solids such as NaCl or GaAs, molecular crystals have molecules as the crystal basis and the phonon modes may include both long range correlated motion between molecules and internal motion within the molecular basis.

Biological macromolecules include proteins, polypeptides, DNA, and RNA molecules. Here we further distinguish macromolecules with tertiary structure versus disordered macromolecules that may have some secondary structure elements, but not well-defined tertiary structure. Structural hierarchy for proteins is defined in Fig. 9.6. For example, while DNA chains that are at least 4 nucleotides long will have a double helix structure, longer double helix chains will generally not have well-defined structure, but rather a random coil polymer, similar to the structure in Fig. 9.6a. This will also be true for a variety of polypeptides. Poly-lysine greater than 5 peptides long can have an alpha helix structure (see Fig. 9.6b), but in a solution of 30% methanol poly-lysine will be in random coil form. Native state proteins however have well-defined tertiary structure. This structure however is not static. Structural motions are essential for protein–protein and protein–ligand interaction. These motions may be correlated or diffusive. A variety of measurements have attempted to measure these motions. Among the methods applied are neutron scattering and X-ray scattering [42–44]. Unfortunately many of these techniques are limited in their ability to truly distinguish between structurally related motions and local diffusive motions. Modeling plays a key role in interpreting the results. Here terahertz studies only now are beginning to have firmer footing [34]. Here we will focus on the simplest approach to understanding the response. It is very likely that this approach will be entirely outdated very soon, as progress in this area is rapid.

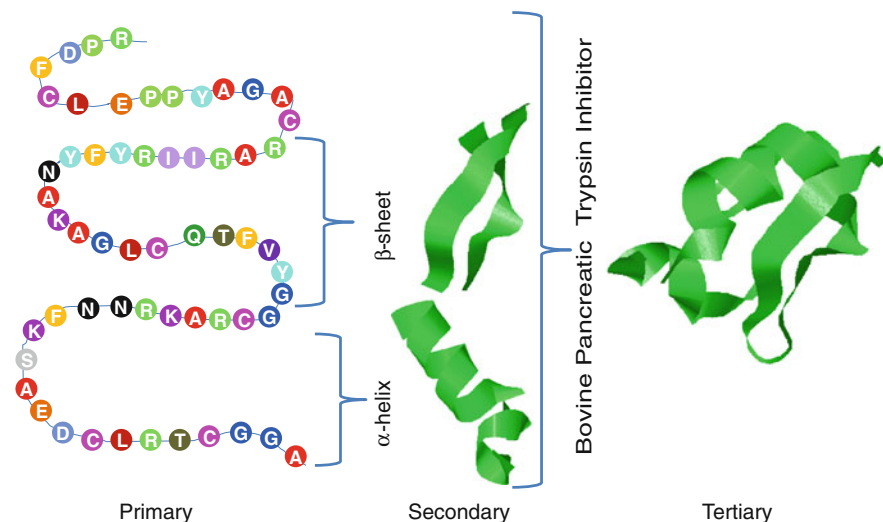


Fig. 9.6 Hierarchy of protein structure shown for bovine pancreatic trypsin inhibitor (BPTI) structure from 1QLQ.pdb. **a** Primary, **b** secondary, **c** tertiary

The simplest approach for protein and RNA response is a full atomic force field calculation. Typically these are done with a variety of molecular mechanics (MM) software. The input to these programs is the protein structure file currently available on the Web from www.pdb.org. The MM software has a database for the molecular force fields and structures associated with amino acids, nucleotides, common salts, solvents, and functional groups (retinal and hemes).

At this writing popular MM programs are CHARMM, AMBER, GROMACS, and NAMD. NAMD and its companion visualization program VMD is available as freeware from the Schulten group (<http://www.ks.uiuc.edu/Research/namd/>). The procedure to calculate the absorbance is either through NMA, quasiharmonic mode analysis or dipole autocorrelation. The most complete description is to use the dipole autocorrelation as discussed in Sect. 9.1.3. Equation 9.8; however, it is difficult to relate the results to specific motions. The most straightforward method is NMA; however, it is also the least realistic. NMA is the determination of the structural vibrations through evaluation of the effective spring constant by calculating the curvature of the 3N dimensional molecular potential at the energy minimum, where N is the number of atoms in the biomolecule, typically > 300 . The process involves first minimizing the potential energy function with respect to the atomic coordinates. The potential energy function is often written in terms for bonding interactions and non-bonding interactions where the potential for the bonding interactions is written as:

$$\begin{aligned}
V(\vec{r}_1, \dots, \vec{r}_N) = & \sum_{\text{bonds}} K_b (r_{np} - r_{np,o})^2 + \sum_{\text{angles}} K_\theta (\theta - \theta_o)^2 \\
& + \sum_{\text{dihedrals}} K_\phi (1 + \cos(n\phi - \delta)) + \sum_{\text{impropers}} K_\varphi (\varphi - \varphi_o)^2 \\
& + \sum_{\text{Urey-Bradley}} K_{\text{UB}} (r_{nl} - r_{nl,o})^2
\end{aligned} \tag{9.23}$$

where r_{np} refers to the vector between atoms n and p , θ refers to the angle made by the bonds of three atoms, n , p , and l , and ϕ refers to the dihedral angle made between the two planes of 4 bonded atoms n , p , l and q . Definitions for the improper angles and more detailed definitions can be found in any of the online manuals for the MM programs listed above. As seen this potential is dependent on coefficients for each of the harmonic terms, K_b , K_θ , K_ϕ , and K_{UB} . These coefficients are the force constants and are part of a database associated with the software. The coefficients are in part determined empirically by comparisons of optical measurements with calculated vibrations for small systems. The potential for the non-bonding interactions is written as:

$$\sum_{\text{nonbonded}} \frac{q_n q_p}{4\pi D r_{np}} + \varepsilon_{np} \left[\left(\frac{R_{\text{min},np}}{r_{np}} \right)^{12} - 2 \left(\frac{R_{\text{min},np}}{r_{np}} \right)^6 \right] \tag{9.24}$$

where the first term is the usual long range Coulomb interaction and the second term is the Lennard–Jones potential. This potential energy function can be evaluated for the atomic coordinates for a given protein as downloaded from structure databases; however, the atomic coordinates substituted into Eq. 9.23 and 9.24 will not in general give the minimized energy. The coordinates for the minimized energy are small deviations from the measured structures. These coordinates are determined through a standard energy minimization process. Once the coordinates of the energy minimized structure are determined one can apply the harmonic approximation to attain effective force constants, eigenfrequencies and eigenvectors for structural vibrations. For small perturbations about the minimum one can then use a harmonic approximation of the potential and thus determine the eigenfrequencies from the curvature of the potential. In one dimension we have:

$$V(x) = V(x_0) + \left. \frac{dV}{dx} \right|_{x=x_0} (x - x_0) + \frac{1}{2} \left. \frac{d^2V}{dx^2} \right|_{x=x_0} (x - x_0)^2 + \dots \tag{9.25}$$

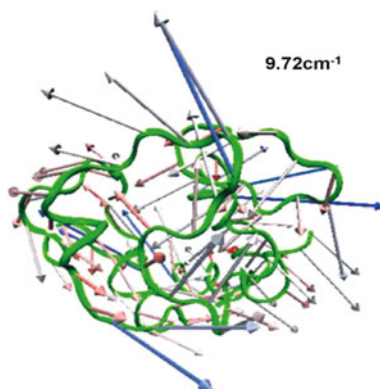
At the potential minimum

$$\left. \frac{dV}{dx} \right|_{x=x_0} = 0$$

$$V(x) \sim V(x_0) + \frac{1}{2} \left. \frac{d^2V}{dx^2} \right|_{x=x_0} (x - x_0)^2 = V(x_0) + \frac{1}{2} k (x - x_0)^2 \tag{9.26}$$

$$\omega = \sqrt{\frac{k}{m}}$$

Fig. 9.7 Vector diagram for the 9.72 cm^{-1} quasi harmonic mode for oxidized cytochrome c (from Yunfen He et. al. Biophys. J. 100, 1058 (2010))



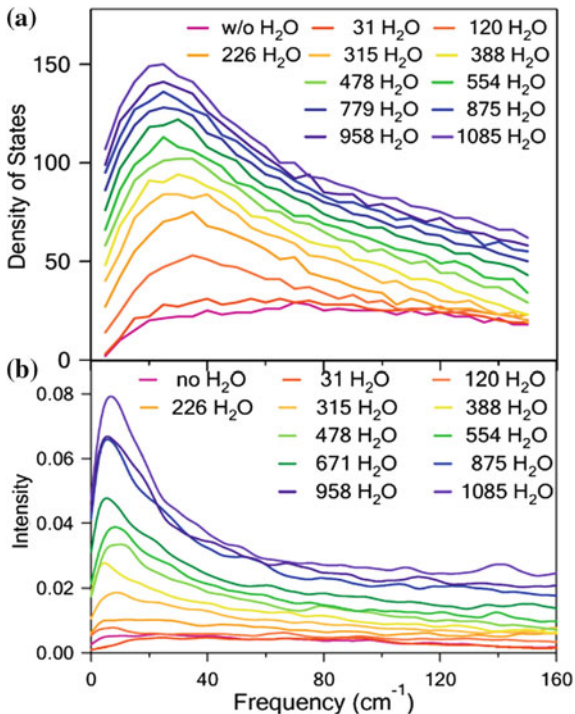
For these very large systems, to determine the eigenfrequencies and eigenvectors the $3N \times 3N$ mass weighted Hessian matrix is diagonalized, where the elements of the matrix are:

$$H_{nij} = \frac{\frac{\partial^2 V}{\partial n_i \partial p_j}}{\sqrt{m_n} \sqrt{m_p}} \quad (9.27)$$

where n, p refer to specific atoms and i, j refer to x, y, z coordinate of that atom. In Fig. 9.7 we show an eigenmode for cytochrome c. The vectors for the mode are drawn somewhat similar to those for the small molecule in Fig. 9.5; where the displacement vector associated with the vibration is shown for each atom however, for the protein with >300 atoms such a representation would be unilluminating. Instead, the atomic displacements are averaged about the alpha carbon of a given peptide and the net displacement for the average is plotted on the alpha carbon. In the terahertz range, the number of modes I is very high and the modes are closely spaced together, with typical mode spacing for frequencies below 100 cm^{-1} (3 THz) of $< 0.5\text{ cm}^{-1}$. Measurement on small molecules have shown that internal vibrational resonances have linewidths typically greater than 5 cm^{-1} at room temperature; thus, it is somewhat justified to evaluate an effective density of states through the histogram of the evaluated eigenfrequencies with bin size $\sim 5\text{ cm}^{-1}$. Figure 9.8a shows the evaluated density of states for NMA using this approach. To determine the light absorption from NMA one uses the “double harmonic” approximation, where the light absorbance is related to the dipole derivative associated with a particular eigenmode.

For mode frequency ν_k , the integrated intensity Γ_k has units of molar absorptivity and is proportional to the absorption coefficient [45]. We draw a distinction of Γ_k with the often calculated absorption intensity, A_k . A_k differs from Γ_k by a factor of ν_k and is not directly related to the derivation of the absorption coefficient from Fermi’s Golden rule. The double harmonic approximation consists of modes calculated from a harmonic expansion of the potential and an approximation of the dipole moment inner product using the quadratic term in the Taylor expansion of the dipole. Γ can be obtained from the dipole derivatives calculated from the quasiharmonic analysis

Fig. 9.8 Normal mode analysis calculations for reduced cytochrome as a function of hydration. **a** Vibrational density of states, **b** absorbance intensity



using [46]:

$$\Gamma_k = \frac{N_0 \pi^2}{3c^2 \epsilon_0 \omega_k} \left(\frac{\partial p}{\partial Q_k} \right)^2 \quad (9.28)$$

where ϵ_0 is the permittivity of vacuum, and N_0 is the Avogadro number and the magnitude of the dipole derivative

The net calculated absorption coefficient is proportional to the sum of Lorentzian oscillators with relaxation rates γ such that we define our quasi harmonic calculated absorption coefficient as

$$\alpha_{\text{QH}}(\omega) = \sum_k \frac{1}{\pi} \frac{\Gamma_k \gamma^2}{(\omega - \omega_k)^2 + \gamma^2} \quad (9.29)$$

Figure 9.8b shows the calculated absorbance using the double harmonic approximation for cytochrome c. While the absorbance calculated in this way does resemble the measured absorbance, unfortunately there are a number of serious flaws to the NMA approach. First the calculation is at zero temperature and second it completely neglects the anharmonicity in the potential. As to the accurate prediction of the terahertz response, it has actually failed a number of tests with respect to correctly

calculating the frequency, hydration, and oxidation dependence. The flaw lies in that while these large-scale vibrations will contribute to the terahertz signal, they do not constitute the entire biomolecular terahertz response. In addition, rotational motions of the surface side chains and solvent will contribute to absorption at these frequencies. Nevertheless, the main prediction of these MM calculations that large-scale correlated motions occur in proteins at terahertz frequencies may be qualitatively correct. Rheinstädter and coworkers have found using inelastic neutron scattering on 2D bacteriorhodopsin protein lattice an optical phonon mode at 3.6 cm^{-1} [42].

9.2.1.1 Terahertz Measurements Methods for Biomolecules: Solid State Measurements

For the microcrystalline small biomolecules, transmission measurements on pressed pellets can be performed. However, Rayleigh scattering will broaden the measured resonances. Nevertheless, measurements on pressed pellets have demonstrated that the THz spectroscopy can distinguish between different isomers. In general the absorption coefficient for these materials is $10\text{--}50\text{ cm}^{-1}$; thus, to remain within the dynamic range of typical THz TDS systems pressed pellets of pure material should be no more than 100 micron thick. It is difficult to form and easily handle such thin pellets. In addition, these thicknesses will introduce etalon effects which will obscure the observation of crystal mode absorbance lines. To overcome this, low absorbance filler material is used, usually polyethylene (PET), although Teflon has also been used frequently. This method of mixing the crystalline powder sample in with filler is sometime referred to as embedding the sample in a matrix. Care should be taken to have uniform mixing of the sample with the filler. A lack of uniform mixing of the sample with the PET can result in apparent resonances due to spatial variation in the frequency content of that the terahertz focus. Often pharmaceutical tablets have THz transparent fillers so measurement of these can be made directly. The filler should have low frequency-independent absorbance over the range of measurement. For small biomolecules, sucrose, lactose, etc., generally form small crystallites and do not require hydration for structural uniformity. Proteins can also be in powder form, also known as lyophilized or freeze dried. A key problem in comparing results from different proteins from different groups is the determination of absolute absorbance. Because pellets often include filler and the pressures used are not uniform, the densities vary and thus the absorption coefficient may not be comparable group to group. In these solid phase measurements we see no distinct features, but rather a glass-like response.

For high precision measurements, extremely sensitive measurement can be performed using a waveguide technique [47]. Here crystalline films are grown on the plates forming the waveguide walls. The samples are necessarily highly uniform. Authors have demonstrated that the results are independent of wall material and a wide variety of materials readily form crystallites on the waveguide walls. However, protein crystallization can be difficult under even highly controlled conditions, so

the waveguide method may not be readily applicable to protein and polynucleotide measurements.

Comparison of these results with calculations is somewhat compromised by the fact that the samples are freeze-dried proteins, which often do not have native state structure. Fully hydrated proteins will have native structure. So it would seem essential that THz measurements be performed with hydrated samples. There are several approaches to achieve these. One is to use films that are hydrated. A second approach is to use liquid phase samples. Films can be formed by dropping solution on substrates and drying. In general, the substrates must be hydrophilic and drying should be controlled to ensure a final uniform thickness. For measurements, the films transmission is normalized to the bare substrate and the sample is held in a hydration controlled cell. Hydration control can be achieved by circulating air over a saturated salt solution or from a dew point generator and pumping this hydrated air through the hydration cell containing the sample. Hydration controlled measurement have found a rapid increase in absorbance for myoglobin and hen egg white lysozyme at 30% by weight water to protein, whereas the change in THz absorbance with hydration suddenly decreases with cytochrome c at this same hydration [48–50]. This change in protein dynamics with hydration is interesting and certainly should be explored further. Hydrate film measurements are limited by the ability to make uniform films and the requirements of controlled humidity. Liquid phase measurements are preferable for sample uniformity.

9.2.1.2 Terahertz Measurements Methods for Biomolecules: Liquid Phase Measurements

The most direct method to ensure uniformity and native state structure for protein and polynucleotides is solution phase measurements. However, given that the powder pellet measurements indicate that the absorption coefficient of most dried proteins at 1 THz is $\sim 10\text{ cm}^{-1}$ and the liquid water absorbance at the same frequency is $\sim 200\text{ cm}^{-1}$, the main effect one sees at room temperature is a decrease in absorbance with increasing protein concentration due to the displacement of the highly absorbing water. However, high precision measurements have shown that the concentration dependence is not a simple linear decrease in absorbance with increasing protein concentration, but rather as the concentration increases, the decrease in absorbance slows and then decreases again more rapidly above a critical concentration. The explanation of this effect has been that the terahertz permittivity of the solvent immediately adjacent to the protein surface is altered by the interaction with the protein and this perturbation extends into the liquid [28, 36, 37]. The extent of the perturbed solvent is referred to the solvation shell. Through precise measurements it has been estimated that the solvation shell extends $\sim 20\text{ \AA}$ from the protein surface and that the terahertz absorbance is higher from the solvation shell water than from bulk water. At high enough concentrations ($>5\text{ mg/ml}$), these hydration shells overlap and no bulk water should be present. The typical protein concentration within a cell is $>200\text{ mg/ml}$, indicating that in the cellular environment all water is

associated with the solvation shells and no bulk water is present; thus, THz measurements of such high concentration solutions are both reasonable biologically and somewhat easier to perform than pellets or hydrated films. In addition, the solvation water appears to have similar temperature dependence as bulk water, with the absorption due to water dropping significantly below 273 K, the freezing point of water. This decrease in absorbance arises from the rotational motions in liquid water slowing down, with the relaxational loss moving to the MHz range. Finally, solution phase measurements also allow one to perform standard assays on the samples used for terahertz studies to confirm native state conformation and functional state such as ligand binding or oxidation. This is essential if one is to be certain that the samples are homogeneous and relevant. For example, fluorescence measurements are often used to confirm binding and UV circular dichroism measurements are used to verify secondary and tertiary structure. Groups have begun to use this method to determine the role of secondary structure in terahertz response, sensitivity to ligand binding, and the structural dependence of the protein dynamical transition [51, 52]. Figure 9.9 shows the measurements done in this way for lysozyme when it is unbound and bound to a small ligand, triacetyl glucosamine (3NAG).

9.2.1.3 Terahertz Measurements Methods for Biomolecules: Crystal Phase Measurements

As protein crystals are generally more than 50% water by weight, they offer a somewhat ideal form for optical measurements. The molecular alignment in crystals offers the possibility of polarization selection of the optically excited modes. Unfortunately these measurements are still somewhat challenging and only one group has successfully performed them at this writing [53]. The main challenge for these measurements is the limitation in the terahertz diffraction limited spot size, which then requires large crystals (~2 mm).

9.2.2 Major Findings and Current Directions

Terahertz measurements of proteins and protein solutions have already made a large impact on outstanding scientific questions. The most profound to date are the determination of the extent of the solvation water and the determination of the origin of the so-called protein dynamical transition. The protein dynamical transition is generally associated with a rapid increase in the average root mean squared atomic displacement for the protein at ~220 K. The imaginary part of the terahertz permittivity has this same rapid increase with temperature. Through THz measurements it has been established that the rapid change is not associated with protein structure, but in fact is seen down to very small peptides. These measurements suggest that the 220 K transition is possibly an indication of thermally activated collective motion of the adjacent solvent, and the size dependence for the occurrence of the transition

indicates the length scale of the collective excitation of the solvent. Overall THz measurement of protein do not indicate narrowband features; there have been a few exceptions to this [54, 55]. The key issue is that the correlated structural motions discussed in the beginning of this section account for only a small part of the dielectric response. Diffuse motion and librational (constrained rotational) motions will constitute the main THz absorbance for these samples. Nevertheless, there are a number of intriguing results from a wide variety of groups that suggest THz is sensitive to protein structure and binding state.

A variety of groups have examined if the THz response changes with protein denaturing. Because of the special sample requirements for terahertz measurements, (low water content or frozen solutions) comparison between different groups needs to be carefully considered. Results for lyophilized samples is the most suspect, as lyophilization itself is a cause of partial denaturing. Further the method used to denature a sample will determine the overall final morphology of the sample. For example, at high protein concentrations, denaturing by pH or thermally will result in disruption of structural bonds and these unprotected groups are free to cross bind between different random coil proteins. This cross-linking can result in the formation of a gel. In general, gels have a lower THz response than the native state samples. The THz absorbance decreases further with increasing aggregation and cross-linking as discussed by Abbott and coworkers in the case of lacto globulin [56]. This decrease in THz response with thermal denaturing was seen also for bovine serum albumin [57]. However, in the case of denaturing by guanidine hydrochloride and urea, the denaturant replaces the structural peptide–peptide bonding, protecting the random coil from interaction with adjacent denatured proteins, preventing gel formation. Terahertz measurements on GdnHCl denatured proteins have found an increase in THz response relative to native state. Measurement of the pure solvent with denaturant have shown that the increase with denaturing does not arise from the absorbance of the denaturant. It is likely that the increased exposure of peptide side changes to the solvent may play a role in the increase of librational contribution to the THz loss [58, 59].

While there have been a number of other interesting studies such as sensitivity to amyloid fibrillation [60], we will discuss only one other common observation to date and that is THz sensitivity to protein ligand binding. A number of groups have considered the binding between biotin and streptavidin [61, 62]. The binding is so strong that it is considered an essential test for any candidate binding assay. Terahertz absorbance increases with binding consistently. Another classic demonstration of THz sensitivity to binding is DNA hybridization [63]. It again has been shown consistently that THz response increases with DNA hybridization. Finally, for small ligand binding to hinge bending proteins, it has been demonstrated that the terahertz response decreases with binding [52]. These consistent results of THz sensitivity to protein binding have not been thoroughly explored. The size of the response, in particular the change in the refractive index with binding, is far in excess the change used for surface plasmon detection. These early results strongly motivate the further exploration of THz response for biological systems.

References

1. P.U. Jepsen, U. Moller, H. Merbold, Investigation of aqueous alcohol and sugar solutions with reflection terahertz time-domain spectroscopy. *Opt. Express* **15**(22), 14717–14737 (2007)
2. U. Moller, D.G. Cooke, K. Tanaka, P.U. Jepsen, Terahertz reflection spectroscopy of Debye relaxation in polar liquids [Invited]. *J. Opt. Soc. Am. B Opt. Phys.* **26**(9), A113–A125 (2009)
3. Y. Yomogida, Y. Sato, R. Nozaki, T. Mishina, J. Nakahara, Comparative dielectric study of monohydric alcohols with terahertz time-domain spectroscopy. *J. Mol. Struct.* **981**(1–3), 173–178 (2010)
4. Y. Yomogida, Y. Sato, R. Nozaki, T. Mishina, J. Nakahara, Comparative study of boson peak in normal and secondary alcohols with terahertz time-domain spectroscopy. *Phys. B Condens. Matter* **405**(9), 2208–2212 (2010)
5. Y. Danten, M. Besnard, J.C. Delagnes, P. Mounaix, Far infrared absorption and terahertz time domain spectroscopy of liquid CS₂: experiments and molecular dynamics simulation. *Appl. Phys. Lett.* **92**(21), 214102 (2008)
6. J.T. Kindt, C.A. Schmuttenmaer, Far-infrared dielectric properties of polar liquids probed by femtosecond terahertz pulse spectroscopy. *J. Phys. Chem.* **100**(24), 10373–10379 (1996)
7. J.P. Laib, D.V. Nickel, D.M. Mittleman, Terahertz vibrational modes induced by heterogeneous nucleation in n-alkanes. *Chem. Phys. Lett.* **493**(4–6), 279–282 (2010)
8. J.S. Li, X.J. Li, Determination principal component content of seed oils by THz-TDS. *Chem. Phys. Lett.* **476**(1–3), 92–96 (2009)
9. S.R. Keiding, Dipole correlation functions in liquid benzenes measured with terahertz time domain spectroscopy. *J. Phys. Chem. A* **101**(29), 5250–5254 (1997)
10. Y.S. Jin, G.J. Kim, C.H. Shon, S.G. Jeon, J.I. Kim, Analysis of petroleum products and their mixtures by using terahertz time domain spectroscopy. *J. Korean Phys. Soc.* **53**(4), 1879–1885 (2008)
11. J.P. Laib, D.M. Mittleman, Temperature-dependent terahertz spectroscopy of liquid n-alkanes. *J. Infrared Millim. Terahertz Waves* **31**(9), 1015–1021 (2010)
12. P. Dutta, K. Tominaga, Dependence of low frequency spectra on solute and solvent in solutions studied by terahertz time-domain spectroscopy. *Mol. Phys.* **107**(18), 1845–1854 (2009)
13. A. Oka, K. Tominaga, Terahertz spectroscopy of polar solute molecules in non-polar solvents. *J. NonCryst. Solids* **352**(42–49), 4606–4609 (2006)
14. T. Arikawa, M. Nagai, K. Tanaka, Characterizing hydration state in solution using terahertz time-domain attenuated total reflection spectroscopy. *Chem. Phys. Lett.* **457**(1–3), 12–17 (2008)
15. K.J. Tielrooij, N. Garcia-Araez, M. Bonn, H.J. Bakker, Cooperativity in ion hydration. *Science* **328**(5981), 1006–1009 (2010)
16. U. Heugen, G. Schwaab, E. Brundermann, M. Heyden, X. Yu, D.M. Leitner, M. Havenith, Solute-induced retardation of water dynamics probed directly by terahertz spectroscopy. *Proc. Natl. Acad. Sci. U. S. A.* **103**, 12301–12306 (2006)
17. J. Xu, K.W. Plaxco, S.J. Allen, J.E. Bjarnason, E.R. Brown, 0.15–3.72 THz absorption of aqueous salts and saline solutions. *Appl. Phys. Lett.* **90**(3), 031908 (2007)
18. B.N. Flanders, R.A. Cheville, D. Grischkowsky, N.F. Scherer, Pulsed terahertz transmission spectroscopy of liquid CHCl₃, CCl₄, and their mixtures. *J. Phys. Chem.* **100**(29), 11824–11835 (1996)
19. Y. Yomogida, Y. Sato, R. Nozaki, T. Mishina, J. Nakahara, Comparative dielectric study of monohydric alcohols with terahertz time-domain spectroscopy. *J. Mol. Struct.* **981**(1–3), 173–178 (2010)
20. Y. Yomogida, Y. Sato, R. Nozaki, T. Mishina, J. Nakahara, Comparative study of boson peak in normal and secondary alcohols with terahertz time-domain spectroscopy. *Phys. B Condens. Matter* **405**(9), 2208–2212 (2010)
21. K. Yamamoto, M. Tani, M. Hangyo, Terahertz time-domain spectroscopy of imidazolium ionic liquids. *J. Phys. Chem. B* **111**(18), 4854–4859 (2007)

22. Y. Shim, H.J. Kim, Dielectric relaxation, ion conductivity, solvent rotation, and solvation dynamics in a room-temperature ionic liquid. *J. Phys. Chem. B* **112**(35), 11028–11038 (2008)
23. J. Sangoro, C. Jacob, A. Serghei, S. Naumov, P. Galvosas, J. Karger, C. Wespe, F. Bordusa, A. Stoppa, J. Hunger, R. Buchner, F. Kremer, Electrical conductivity and translational diffusion in the 1-butyl-3-methylimidazolium tetrafluoroborate ionic liquid. *J. Chem. Phys.* **128**(21), 214509 (2008)
24. M. Koeberg, C.C. Wu, D. Kim, M. Bonn, THz dielectric relaxation of ionic liquid: water mixtures. *Chem. Phys. Lett.* **439**(1–3), 60–64 (2007)
25. J.T. Kindt, C.A. Schmuttenmaer, Far-infrared dielectric properties of polar liquids probed by femtosecond terahertz pulse spectroscopy. *J. Chem. Phys.* **100**(24), 10373 (1996)
26. J. Xu, K.W. Plaxco, S.J. Allen, Probing the collective vibrational dynamics of a protein in liquid water by terahertz absorption spectroscopy. *Protein Sci.* **15**(5), 1175–1181 (2006)
27. J. Xu, K.W. Plaxco, S.J. Allen, Collective dynamics of lysozyme in water: terahertz absorption spectroscopy and comparison with theory. *J. Phys. Chem. B* **110**(47), 24255–24259 (2006)
28. S. Ebbinghaus, S.J. Kim, M. Heyden, X. Yu, U. Heugen, M. Gruebele, D.M. Leitner, M. Havenith, An extended dynamical hydration shell around proteins. *Proc. Natl. Acad. Sci. U. S. A.* **104**(52), 20749–20752 (2007)
29. M. Nagai, H. Yada, T. Arikawa, K. Tanaka, Terahertz time-domain attenuated total reflection spectroscopy in water and biological solution. *Int. J. Infrared Millim. Waves* **27**(4), 505–515 (2006)
30. H. Hirori, K. Yamashita, M. Nagai, K. Tanaka, Attenuated total reflection spectroscopy in time domain using terahertz coherent pulses. *Jpn. J. Appl. Phys. Part 2 Lett. Express Lett.* **43**(10A), L1287–L1289 (2004)
31. B. You, T.A. Liu, J.L. Peng, C.L. Pan, J.Y. Lu, A terahertz plastic wire based evanescent field sensor for high sensitivity liquid detection. *Opt. Express* **17**(23), 20675–20683 (2009)
32. L. Cheng, S. Hayashi, A. Dobroiu, C. Otani, K. Kawase, T. Miyazawa, and Y. Ogawa, Terahertz-wave absorption in liquids measured using the evanescent field of a silicon waveguide. *Appl. Phys. Lett.* **92**(18), 181104 (2008)
33. J.P. Laib, D.V. Nickel, D.M. Mittleman, Terahertz vibrational modes induced by heterogeneous nucleation in n-alkanes. *Chem. Phys. Lett.* **493**(4–6), 279–282 (2010)
34. M. Heyden, J. Sun, S. Funkner, G. Mathias, H. Forbert, M. Havenith, D. Marx, Dissecting the THz spectrum of liquid water from first principles via correlations in time and space. *Proc. Natl. Acad. Sci. U. S. A.* **107**(27), 12068–12073 (2010)
35. D.A. Schmidt, O. Birer, S. Funkner, B.P. Born, R. Gnanasekaran, G.W. Schwaab, D.M. Leitner, M. Havenith, Rattling in the cage: ions as probes of sub-picosecond water network dynamics. *J. Am. Chem. Soc.* **131**(51), 18512–18517 (2009)
36. S.J. Kim, B. Born, M. Havenith, M. Gruebele, Real-time detection of protein-water dynamics upon protein folding by terahertz absorption. *Angewandte Chemie Int. Ed.* **47**(34), 6486–6489 (2008)
37. S. Ebbinghaus, S.J. Kim, M. Heyden, X. Yu, M. Gruebele, D.M. Leitner, M. Havenith, Protein sequence- and pH-dependent hydration probed by terahertz spectroscopy. *J. Am. Chem. Soc.* **130**(8), 2374–2375 (2008)
38. M. Sajadi, Y. Ajaj, I. Ioffe, H. Weingartner, N.P. Ernstring, Terahertz absorption spectroscopy of a liquid using a polarity probe: a case study of trehalose/water mixtures. *Angew. Chem. Int. Ed.* **49**, 454–457 (2010)
39. M.L.T. Asaki, A. Redondo, T.A. Zawodzinski, A.J. Taylor, Dielectric relaxation of electrolyte solutions using terahertz transmission spectroscopy. *J. Chem. Phys.* **116**(19), 8469–8482 (2002)
40. M. Krüger, E. Bründermann, S. Funkner, H. Weingärtner, M. Havenith, Communications: polarity fluctuations of the protic ionic liquid ethylammonium nitrate in the terahertz regime. *J. Chem. Phys.* **132**, 101101 (2010)
41. A. Chakraborty, T. Inagaki, M. Banno, T. Mochida, K. Tominaga, Low-frequency spectra of metallocenium ionic liquids studied by terahertz time-domain spectroscopy. *J. Phys. Chem. A* **115**, 1313–1319 (2011)

42. M.C. Rheinstadter, K. Schmalzl, K. Wood, D. Strauch, Protein–protein interaction in purple membrane. *Phys. Rev. Lett.* **103**(12), 128104 (2009)
43. K. Wood, C. Caronna, P. Fouquet, W. Haussler, F. Natali, J. Ollivier, A. Orecchini, M. Plazanet, G. Zaccari, A benchmark for protein dynamics: Ribonuclease A measured by neutron scattering in a large wavevector-energy transfer range. *Chem. Phys.* **345**, 305–314 (2008)
44. D. Liu, X.-q. Chu, M. Lagi, Y. Zhang, E. Fratini, P. Baglioni, A. Alatas, A. Said, E. Alp, S.-H. Chen, Studies of phononlike low-energy excitations of protein molecules by inelastic X-ray scattering. *Phys. Rev. Lett.* **101**, 135501 (2008)
45. W.B. Person, G. Zerbi, *Vibrational Intensities in Infrared and Raman Spectroscopy*. (Elsevier Scientific Publishing, Amsterdam, 1982)
46. B.S. Galabov, T. Dudev, *Vibrational Intensities* (Elsevier Science, Amsterdam, 1996)
47. J.S. Melinger, N. Laman, S.S. Harsha, S. Cheng, D. Grischkowsky, High-resolution waveguide terahertz spectroscopy of partially oriented organic polycrystalline films. *J. Phys. Chem. A* **111**, 10977–10987 (2007)
48. C.F. Zhang, S.M. Durbin, Hydration-induced far-infrared absorption increase in myoglobin. *J. Phys. Chem. B* **110**(46), 23607–23613 (2006)
49. J. Knab, J.-Y. Chen, A. Markelz, Hydration dependence of conformational dielectric relaxation of lysozyme. *Biophys. J.* **90**, 2576–2581 (2006)
50. Y.F. He, J.Y. Chen, J.R. Knab, W.J. Zheng, A.G. Markelz, Evidence of protein collective motions on the picosecond timescale. *Biophys. J.* **100**(4), 1058–1065 (2011)
51. T. Ding, R.Y. Li, J.A. Zeitler, T.L. Huber, L.F. Gladden, A.P.J. Middelberg, R.J. Falconer, Terahertz and far infrared Spectroscopy of alanine-rich peptides having variable ellipticity. *Opt. Express* **18**(26), 27431–27444 (2010)
52. J.Y. Chen, J.R. Knab, S.J. Ye, Y.F. He, A.G. Markelz, Terahertz dielectric assay of solution phase protein binding. *Appl. Phys. Lett.* **90**(24), 243901 (2007)
53. K.M. Tych, A.D. Burnett, C.D. Wood, J.E. Cunningham, A.R. Pearson, A.G. Davies, E.H. Linfield, Applying broadband terahertz time-domain spectroscopy to the analysis of crystalline proteins: a dehydration study. *J. Appl. Crystallogr.* **44**, 129–133 (2011)
54. E.R. Brown, E.A. Mendoza, D.Y. Xia, S.R.J. Brueck, Narrow THz spectral signatures through an RNA solution in nanofluidic channels. *IEEE Sens. J.* **10**(3), 755–759 (2010)
55. Y.W. Sun, Y.T. Zhang, E. Pickwell-MacPherson, Investigating antibody interactions with a polar liquid using terahertz pulsed spectroscopy. *Biophys. J.* **100**(1), 225–231 (2011)
56. G.M. Png, R.J. Falconer, B.M. Fischer, H.A. Zakaria, S.P. Mickan, A.P.J. Middelberg, D. Abbott, Terahertz spectroscopic differentiation of microstructures in protein gels. *Opt. Express* **17**(15), 13102–13115 (2009)
57. H. Yoneyama, M. Yamashita, S. Kasai, K. Kawase, R. Ueno, H. Ito, T. Ouchi, Terahertz spectroscopy of native-conformation and thermally denatured bovine serum albumin (BSA). *Phys. Med. Biol.* **53**(13), 3543–3549 (2008)
58. H. Chen, L. Wang, Y.G. Qu, T.Y. Kuang, L.B. Li, W.X. Peng, Investigation of guanidine hydrochloride induced chlorophyll protein 43 and 47 denaturation in the terahertz frequency range. *J. Appl. Phys.* **102**(7) 74700 (2007)
59. Y. He, P.I. Ku, J.R. Knab, J.-Y. Chen, A.G. Markelz, Protein dynamical transition does not require protein structure. *Phys. Rev. Lett.* **101**, 178103 (2008)
60. R. Liu, M.X. He, R.X. Su, Y.J. Yu, W. Qi, Z.M. He, Insulin amyloid fibrillation studied by terahertz spectroscopy and other biophysical methods. *Biochem. Biophys. Res. Commun.* **391**(1), 862–867 (2010)
61. Y. Ogawa, S. Hayashi, M. Oikawa, C. Otani, K. Kawase, Interference terahertz label-free imaging for protein detection on a membrane. *Opt. Express* **16**(26), 22083–22089 (2008)
62. A. Menikh, S.P. Mickan, H. Liu, R. MacColl, X.-C. Zhang, Label-free amplified bioaffinity detection using terahertz wave technology. *Biosens. Bioelectron.* **20**(3), 658–662 (2004)
63. M. Brucherseifer, M. Nagel, P.H. Bolivar, H. Kurz, A. Bosserhoff, R. Buttner, Label-free probing of the binding state of DNA by time-domain terahertz sensing. *Appl. Phys. Lett.* **77**(24), 4049–4051 (2000)

Chapter 10

Pump-Probe Spectroscopy at Terahertz Frequencies

Michael B. Johnston and James Lloyd-Hughes

Abstract Optical-pump–terahertz-probe spectroscopy is a technique that can measure directly the conductivity of photoexcited carriers on a picosecond timescale. In this chapter, we introduce the technique and data analysis, and discuss suitable models of the interaction between terahertz radiation and quasiparticles in materials. We then review some recent studies of inorganic and organic semiconductors and nanomaterials.

10.1 Introduction

The development of methods to generate and detect pulses of terahertz (THz) radiation with femtosecond laser pulses has greatly improved spectroscopists' access to the far infrared region of the spectrum. Furthermore the femtosecond to nanosecond dynamics of materials can be studied using THz pulses that are delayed with respect to a photoexcitation beam from the same femtosecond laser. Such studies are often referred to as “pump–probe” spectroscopy, where the “pump” and “probe” may be any combination of THz pulses, visible, or near-infrared pulses or white light continua. In this chapter, we will focus on optical-pump–THz-probe (OPTP) spectroscopy, which is the most commonly cited pump–probe THz spectroscopy configuration at present.

The use of THz radiation in the study of carrier dynamics in semiconductors followed very soon after the development of methods to generate and detect pulsed THz radiation. In 1987, Nuss et al. [1] studied ultrafast charge-carrier dynamics in

M. B. Johnston (✉) · J. Lloyd-Hughes
Department of physics, University of Oxford,
Clarendon Laboratory, Parks Road, Oxford OX1 3PU, UK
e-mail: m.Johnston@physics.ox.ac.uk

J. Lloyd-Hughes
e-mail: j.lloyd-hughes@physics.ox.ac.uk

gallium arsenide using a Cherenkov shock wave in LiTaO_3 to generate a THz transient [2]. *Non-contact* studies of carrier dynamics in group III–V bulk semiconductors [3] and heterostructures [4] became possible following the development of “free space” terahertz time domain spectroscopy in 1989 [5, 6].

By 1997 OPTP measurements had been expanded to systems other than solid-state materials. In particular, Haran et al. [7] and McElroy and Wynne [8] used the technique to observe liquid phase solvation dynamics. In a 2001 study of charge dynamics in GaAs the frequency bandwidth of the technique was extended to include the mid-infrared spectral band, and the time resolution was improved to tens of femtoseconds [9].

In recent years OPTP spectroscopy has become very attractive for studying the electronic properties of a new array of nanoparticles and nanostructures, owing to the contact-free nature of the technique. More powerful THz sources have allowed the development of THz-pump–THz-probe and THz-pump–optical-probe spectroscopy, which is described in Chap. 18.

In this chapter, we introduce the experimental technique and data analysis for optical-pump–terahertz-probe spectroscopy. Subsequently we highlight and review a number of spectroscopic applications in a range of materials systems. The breadth of applicability of the technique means that no one review can cover the numerous materials that have been investigated to date. A number of excellent review articles are available, for example Refs. [10, 11] discuss early work with OPTP spectroscopy, and Refs. [12–15] review more recent work. OPTP studies of correlated electron systems are excluded from this chapter as they are discussed in Chap. 9. Early work on the use of OPTP spectroscopy to examine the dynamic conductivity of high temperature superconductors and colossal magnetoresistance materials was also detailed in Ref. [16].

10.2 Technique

The experimental and theoretical concepts underpinning the technique of OPTP spectroscopy are outlined in this section.

10.2.1 *Experimental Details*

The experimental setup of a typical OPTP system is shown in Fig. 10.1. In this case the THz electric field transmitted through the sample is recorded via electro-optic sampling, as described in previous chapters, using a first lock-in amplifier referenced to the modulation frequency of the terahertz emitter. An additional part of the laser beam is split off before the THz delay stage, and is sent (colinearly with the THz pulse) to the sample in order to photoexcite carriers (beam P2). The photoexcited carriers in the sample alter the material’s conductivity, changing its transmission to

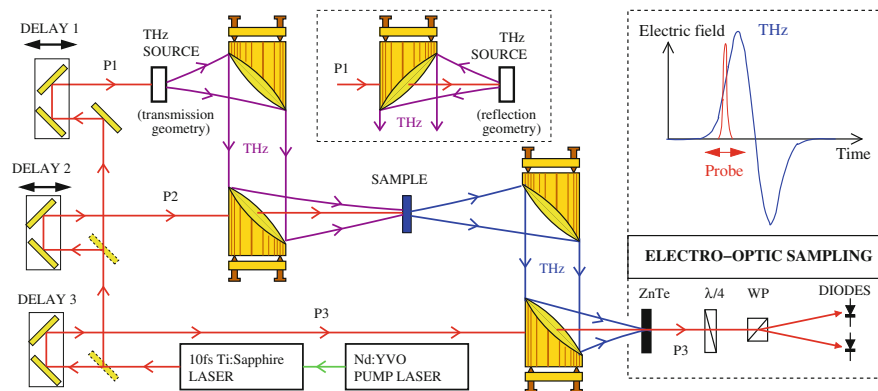


Fig. 10.1 Schematic diagram of a typical Optical Pump Terahertz Probe (OPTP) spectrometer. Mirrors are represented by *solid boxes*, and beam-splitters by *dotted boxes*. Infrared pulses from a femtosecond laser (*red lines*) are incident on a THz source (beam P1). The THz radiation emitted (represented by *purple and blue lines*) is collected and focussed onto a sample by a pair of parabolic mirrors. The transmitted THz beam is focussed onto a THz detector such as an electro-optic crystal (e.g. ZnTe), where gate beam, P3, reads out electric field of the terahertz pulse. Beam P2 is used to photoexcite carriers in the sample, and can optionally originate from an optical-parametric amplifier to provide access to alternative photoexcitation wavelengths

THz radiation. Often this transmission change is small, and therefore the sample pump beam can be modulated mechanically via an optical chopper. The change in the THz electric field occurring at this frequency is then recorded using a second lock-in amplifier (referenced to the chopper). The change in the transmitted electric field ΔE between the pump's 'on' and 'off' states is thus measured, and can be related to the sample's conductivity, as described in Sect. 10.2.2.

There are a couple of issues of note about the sample and the geometry of the spectrometer. The THz beam waist at the sample should be substantially smaller than that of the sample pump beam (P2), so that the probed charge density is uniform. This can be achieved by ensuring that the pump is not focussed at the sample. A carrier distribution that is uniform in depth into the sample is also desirable. This constraint requires that the sample's thickness be less than its absorption depth, typically $1/\alpha \sim 1 \mu\text{m}$ in inorganic semiconductors excited at the bandgap energy. Often in the analysis of OPTP spectra of bulk media the photoexcited region is treated as a thin film with thickness $1/\alpha$. When the photoexcited medium is optically thick or significantly dispersive then an approach such as finite-difference time-domain may be necessary to correctly model the photoinduced change in the terahertz probe pulse [17].

Two classes of experiment can be performed using the setup of Fig. 10.1. At a fixed sample pump delay time (DELAY 2), scanning the THz delay line (DELAY 1) allows the medium's conductivity to be determined over the THz frequency range by recording the transmission change. If this is done at a number of different delay times t before and after the arrival of the sample pump pulse, then the dynamical change in

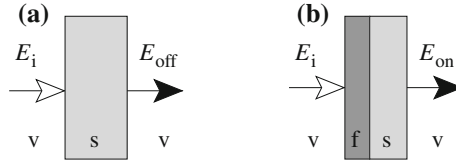


Fig. 10.2 The THz electric field after transmission through **a** unexcited and **b** photoexcited sample are denoted, respectively E_{off} and E_{on} , and can be related to the incident electric field E_i as in Eqs. 10.1 and 10.2. The labels v, s, and f correspond to vacuum, sample, and the photoexcited thin-film

the frequency-dependent conductivity $\Delta\sigma(\omega, t)$ can be measured. The comparison of $\Delta\sigma(\omega)$ with a model of the carrier dynamics in the sample often yields invaluable insights into charge transport. Alternatively, if the THz delay line is set to the peak of the THz electric field, and the sample pump beam delay is altered, then the resulting transmission change is a measure of the conductivity averaged over the range of frequencies in the THz probe pulse.

10.2.2 Parameter Extraction

An expression is now derived for the conductivity $\Delta\sigma(\omega) = \Delta\sigma_1 + i\Delta\sigma_2$ of photoexcited carriers in terms of the change in the transmitted terahertz electric field. The photoexcited region is modeled as a thin film of thickness $\delta = 1/\alpha$ where α is the absorption coefficient of the material at the photoexcitation wavelength.

Denoting the electric field before propagation through the sample as E_i , and the field after transmission through the sample when the pump beam is and is not blocked as E_{off} and E_{on} , respectively (Fig. 10.2), standard boundary condition considerations result in

$$E_{\text{off}} = t_{\text{vs}}t_{\text{sv}}e^{in_s\omega d/c}\text{FP}_{\text{vsv}}E_i, \quad (10.1)$$

$$E_{\text{on}} = t_{\text{vf}}t_{\text{fs}}t_{\text{sv}}e^{in_f\omega\delta/c}e^{in_s\omega(d-\delta)/c}\text{FP}_{\text{vfs}}\text{FP}_{\text{fsv}}E_i, \quad (10.2)$$

where the Fresnel transmission coefficients are $t_{ij} = 2n_i/(n_i + n_j)$, and the subscripts v, s, and f denote, respectively vacuum, the unexcited sample, and the excited thin-film. The Fabry-Perot terms FP_{ijk} account for multiple internal reflections within medium j , and since the reflections produced by the optically-thick substrate can be removed by windowing the time-domain data then $\text{FP}_{\text{vsv}} = \text{FP}_{\text{fsv}} = 1$. In order to evaluate FP_{vfs} we assume that the thin-film limit applies, namely that

$$n_f\delta\omega/c \ll 1 \Rightarrow e^{in_f\delta\omega/c} = 1 + in_f\delta\omega/c. \quad (10.3)$$

This is equivalent to assuming that all internal reflections from the thin-film overlap in the time-domain. This produces

$$\text{FP}_{\text{vfs}} = \sum_{p=0}^{\infty} [r_{\text{fs}} r_{\text{fv}} e^{2in_f \omega \delta / c}]^p = \frac{1}{1 - r_{\text{fs}} r_{\text{fv}} e^{2in_f \omega \delta / c}}. \quad (10.4)$$

Defining the function $T(\omega, t) = E_{\text{on}}(\omega, t)/E_{\text{off}}(\omega, t)$ at a time delay t after the photoexcitation of the sample, and using Eqs. 10.1–10.4 and the relationship between the conductivity σ and dielectric function ϵ_f of the thin film,

$$\epsilon_f = \epsilon_{\infty} + i\sigma/\epsilon_0\omega, \quad (10.5)$$

results in

$$\Delta\sigma(\omega, t) = \frac{1 + n_s}{Z_0\delta} \left(\frac{1}{T} - 1 \right), \quad (10.6)$$

where the further assumption that $n_f \gg n_s$ was made. Experimentally, the amplitude of the change in transmitted electric field between the pump on and off states is measured, i.e. $\Delta E = |E_{\text{on}} - E_{\text{off}}| = E_{\text{off}} - E_{\text{on}}$ (since $E_{\text{on}} < E_{\text{off}}$ due to the additional absorption and reflection of THz radiation when the pump beam is on), and thus $1/T - 1 = \Delta E/E_{\text{on}}$.

It is important to note, however, that the above discussion is valid in the limit where the THz pulse is shorter than the changes in the optical response of the system. More complicated analysis of the experimental data is required when the material is weakly absorbing and the THz and optical pulses propagate at different velocities, or when the conductivity alters on timescales comparable to the THz pulse duration [18–21].

10.2.3 Conductivity Models

Fitting the frequency-dependent transmission using a suitable conductivity model will yield valuable information about the photoexcitations in the sample. For instance, for electrons in bulk III–V semiconductors the electron density and scattering time can be determined. In more complex systems terahertz radiation can couple to other excitations. In the following sections, we therefore briefly mention some of the conductivity models that have been employed to date. In cases where similar conductivity spectra can be produced by physically distinct mechanisms (e.g. excitons and plasmons), varying an experimental parameter such as lattice temperature or photoexcitation fluence can allow the correct mechanism to be established.

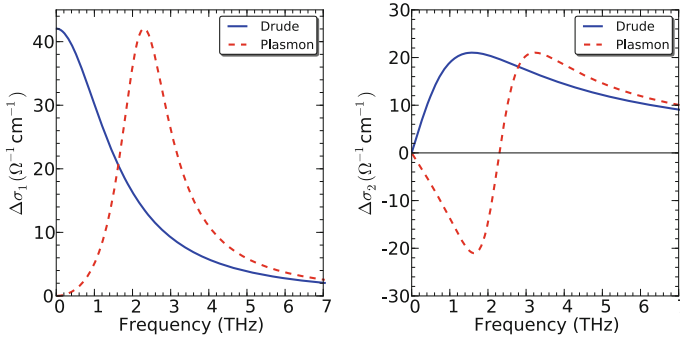


Fig. 10.3 Real (*left*) and imaginary (*right*) parts of the complex conductivity predicted by the Drude model (*solid lines*, Eq. 10.7) and plasmon model (*dashed lines*, Eq. 10.12), for GaAs with $n = 10^{17} \text{ cm}^{-3}$, $\tau = 100 \text{ fs}$ and $\omega_0/2\pi = 2.3 \text{ THz}$

10.2.3.1 Free Electron Plasmas

In this treatment the material of interest is modeled as a plasma, namely a medium in which mobile charges (e.g. electrons) move with respect to a fixed lattice of charges with an opposite sign (e.g. positively charged ions). For photoexcited semiconductors the photoinduced conductivity change $\Delta\sigma(\omega)$ is of the form

$$\Delta\sigma(\omega) = \frac{ne^2}{m^*} \frac{\tau}{1 - i\omega\tau}, \quad (10.7)$$

where n , m^* and τ are respectively the concentration, effective mass and mean scattering time of free carriers.

The frequency-dependent response of a free-electron gas can be understood with reference to the plasma frequency ω_p , defined as

$$\omega_p = \sqrt{\frac{ne^2}{m^*\epsilon_\infty\epsilon_0}}. \quad (10.8)$$

When $\omega < \omega_p$ the plasma can respond to electromagnetic radiation, while above ω_p the plasma can no longer react to the driving force. This interaction produces a frequency-dependent complex refractive index, with a large absorption coefficient below ω_p .

The real part of the photoconductivity $\Delta\sigma_1$ exhibits a maximum at zero frequency, with a value $\Delta\sigma_1(\omega = 0) = ne^2\tau/m^*$, while the imaginary part $\Delta\sigma_2$ peaks at $1/\tau$. In Fig. 10.3 the complex conductivity $\Delta\sigma(\omega) = \sigma_1 + i\sigma_2$ predicted by the Drude model for GaAs is given.

10.2.3.2 Generalized Drude Model

In general, the mean time between electron scattering events τ is a function of energy, rather than independent of energy as is assumed in the model of a free-electron plasma (Eq. 10.7). In order to take account of the energy-dependent relaxation time, the phenomenological approach taken in the Cole-Cole and Cole-Davidson models is to add an exponent to the denominator of Eq. 10.7. The generalized Drude model contains both the Cole–Cole parameter α and the Cole–Davidson parameter β :

$$\Delta\sigma(\omega) = \frac{ne^2}{m^*} \frac{\tau}{(1 - (i\omega\tau)^{1-\alpha})^\beta}, \quad (10.9)$$

where $0 < \alpha < 1$ and $0 < \beta < 1$. The Drude model is recovered in the limits $\alpha \rightarrow 0$, $\beta \rightarrow 1$. The generalized Drude expression can model small deviations from the Drude conductivity well, but does not provide physical insight into the dominant scattering mechanisms. Additionally, it cannot reproduce the negative imaginary conductivities observed in semiconductor nanomaterials.

10.2.3.3 Effective Medium Theories

Nanomaterials offer a particular challenge for spectroscopic studies at THz frequencies. In general the aim is to determine the microscopic electronic properties of nanoparticles by measuring the THz conductivity of an ensemble of nanoparticles. The nanoparticles in a sample are typically surrounded by free space or embedded in a dielectric. Therefore the THz dielectric function of the sample will not just depend upon the optoelectronic properties of the nanoparticles, but also on the geometry of the nanoparticles and the polarizability of the material surrounding them. Since nanoparticles by definition are much smaller than the wavelength of THz radiation, effective medium theory (also discussed in Chap. 3) is valid for modelling the THz response of such samples.

The most commonly used effective medium theories are those developed by Maxwell and Garnett [22] and by Bruggemann [23]. Both theories produce simple analytic expressions relating the dielectric functions of the nanoparticles ϵ_p and surrounding matrix ϵ_m to the dielectric function of the composite ϵ_c . Maxwell Garnett theory is only appropriate for low concentrations of nanoparticles and may be expressed as

$$\frac{\epsilon_c - \epsilon_m}{\epsilon_c + \zeta\epsilon_m} = g \frac{\epsilon_p - \epsilon_m}{\epsilon_p + \zeta\epsilon_m}, \quad (10.10)$$

where ζ is the volume fraction of nanoparticles in the sample and g is a geometrical factor ($g = 2$ for spheres, and $g = 1$ for cylinders with long axis perpendicular to the electric field), which for a particular shape describes how effectively an electric field is screened. In contrast Bruggemann theory is considered less accurate [24], but is valid for all concentrations,

$$g \frac{\epsilon_p - \epsilon_c}{\epsilon_p + \zeta \epsilon_c} = (g - 1) \frac{\epsilon_m - \epsilon_c}{\epsilon_m + \zeta \epsilon_c}. \quad (10.11)$$

Recently an effective medium theory for arbitrary ellipsoidal particle distributions has been presented [25].

In an OPTP experiment the composite sample is perturbed by an optical excitation, therefore ϵ_j ($j = c, p, m$) in Eqs. 10.10 and 10.11 may be replaced with $\epsilon_j + i \Delta\sigma_j / (\omega \epsilon_0)$ according to Eq. 10.5, where $\Delta\sigma$ is the photoinduced change in conductivity [15]. Thus, if one assumes that the matrix is not perturbed, then the measured conductivity change of the sample $\Delta\sigma_c$ can be related directly to the photoinduced change in conductivity of the nanoparticles $\Delta\sigma_p$.

10.2.3.4 Plasmon

An alternative approach is given by the plasmon model. Here, the motion of electrons under an electric field is derived from the equation of motion of a damped, driven simple harmonic oscillator [26]. The conductivity in this model is

$$\Delta\sigma(\omega) = \frac{ne^2}{m^*} \frac{\tau}{1 - i\tau(\omega - \omega_0^2/\omega)}, \quad (10.12)$$

where ω_0 is the angular frequency of the oscillatory response, and is related to the plasma frequency $\omega_p = (ne^2/m^*\epsilon_\infty\epsilon_0)^{1/2}$ of a bulk material by $\omega_0^2 = f\omega_p^2$. For spherical nanoparticles the geometrical factor $f = 1/3$, [26] while for cylindrical nanowires $f = 0$ when the electric field \mathbf{E} is axial and the photon wavevector \mathbf{q} is radial, $f = 1/2$ when \mathbf{E} and \mathbf{q} are radial, and $f = 1/3$ for radial \mathbf{E} and axial \mathbf{q} [27]. The form of Eq. 10.12 is a resonance with a maximum in $\Delta\sigma_1$, and a sign change in $\Delta\sigma_2$, at ω_0 , as can be seen in Fig. 10.3.

Plasmons can be identified in OPTP experiments by varying the optical excitation density. A quadratic increase in the resonant frequency of the THz conductivity spectrum with injected carrier density is good evidence for the presence of plasmons and rules out other possible causes of a Lorentzian spectrum such as phonon resonances or excitons.

10.2.3.5 Exciton

Photoexcited electrons and holes can bind together to form excitons, with binding energies that are enhanced in systems exhibiting quantum confinement. The eigenstates of an exciton can be modeled by comparison to the hydrogen atom, with states 1s, 2s, 2p, 3s, etc. in spectroscopic notation. While the lowest order electric dipole allowed transition (1s–2p) falls in the UV range for hydrogen, the lower effective masses of electrons and holes in semiconductors and high dielectric constant results in a 1s–2p transition in the terahertz frequency range for excitons in e.g. GaAs quantum wells [4, 28]. Such heterostructures can therefore absorb terahertz radiation if excitons reside in their ground state (1s). The frequency dependent complex

conductivity can be determined quantum mechanically from Fermi's golden rule, and is given by

$$\Delta\sigma(\omega) = \frac{n_X e^2}{m^*} \sum_q \frac{f_{1s,q} \omega}{\omega_{1s,q}^2 - \omega^2 - i\omega/\tau_X}, \quad (10.13)$$

where n_X and τ_X are the excitonic density and linewidth, the energy difference between the initial state 1s and final state q is $\hbar\omega_{1s,q}$, and $f_{1s,q}$ is the electric dipole matrix element for the transition [29, 30].

10.2.3.6 Backscattering

Another phenomenological extension to the Drude model is that proposed by Smith [31], in which a carrier retains part of its initial velocity upon scattering. The collisions are assumed to be randomly distributed in time, and the fraction c_n of a carrier's initial velocity after n scattering events allows the Drude model to be generalized to

$$\Delta\sigma(\omega) = \sigma_D(\omega) \left[1 + \sum_{n=1}^{\infty} \frac{c_n}{(1 - i\omega\tau)^n} \right]. \quad (10.14)$$

Here, $\sigma_D(\omega)$ is the Drude conductivity of Eq. 10.7. For elastic collisions the parameter c_n is the expectation value $\langle \cos \theta \rangle$. If the carrier's momentum is randomized then $c_n = 0$, while if it is completely backscattered then $c_n = -1$. Commonly, the infinite series in Eq. 10.14 is truncated at $n = 1$, which corresponds to the assumption that the carrier retains part of its initial momentum during the first scattering event, but in every subsequent scattering events the velocity is randomized. However, with $c_1 = -1$ and $c_{n>1} = 0$ the Drude-Smith model can be seen to be identical to the surface plasmon model upon the substitutions $\omega_0^2 = 1/\tau_{DS}^2$, $1/\tau_{SP} = 2/\tau_{DS}$. Here the subscripts DS and SP distinguish the scattering times used in the Drude-Smith and surface plasmon models.

10.3 Inorganic Semiconductors

10.3.1 Bulk

An early demonstration of the use of OPTP spectroscopy was on the bulk III-V semiconductors GaAs and InP by Saeta et al. [3]. They demonstrated that the photoexcitation of bulk semiconductors well above the Γ -valley minimum can produce a slow rise in the photoconductivity. This was attributed to the higher effective mass of electrons in the L - and X -valleys. As electrons relax energetically from higher lying states in the conduction band (by LO-phonon emission) the

conductivity increased (transmission decreased), taking 3ps to reach a maximum (minimum). Subsequently, Beard et al. [32] investigated the spectrally resolved photoconductivity of bulk GaAs, and extracted directly the frequency-dependent photoconductivity from their data. They found that the modified Drude model (Eq. 10.9) fitted their data. This indicated that the energy dependence of the electron's scattering rate can modify the photoconductive response at terahertz frequencies.

The formation of quasiparticles from an electron-hole plasma was observed for the first time [9], via OPTP spectroscopy with mid-infrared probe pulses. Collective phenomena such as Coulomb screening and scattering from an electron-hole plasma were found to arise after a time delay of the order of the inverse plasma frequency ($\sim 10^{-14}$ s). Before this time has elapsed a regime was observed in which the interaction between two point charges was described by the bare Coulomb potential only, as predicted by some quantum kinetic theories [33]. The ultrafast formation of coupled LO-phonon plasmon modes in InP was investigated subsequently [34].

Subsequent studies on bulk semiconductors have looked at materials with reduced electron decay times, such as low-temperature grown GaAs [35] and radiation-damaged silicon on sapphire [36]. The role of surface defects in GaAs has also been investigated by the chemical passivation of surface states [37, 38]. When carriers are free to diffuse into the bulk a non-exponential photoconductive decay can be witnessed [35, 37].

10.3.2 Excitonic Systems

While interband emission and absorption processes are altered by the presence of excitons, only low momentum states can be accessed optically, and coherent polarization effects can lead to photoluminescence at the excitonic resonances even without a population of excitons [39]. In contrast, the absorption of terahertz radiation promotes transitions between excitons in all momentum states, as has been demonstrated for excitons in GaAs quantum wells [4, 28] and in bulk Cu_2O [40] and silicon [41].

As discussed in Sect. 10.2.3 terahertz radiation can promote excitons from their 1s ground state to higher lying states (e.g. 2p), with a resonant lineshape that can be seen in Fig. 10.4 and as given in Eq. 10.13. Unconfined (3D) excitons have a binding energy of $E_n = R_X/n^2$, where $n = 1, 2, 3 \dots$ and the Rydberg constant is $R_X = 4.2 \text{ meV}$ for GaAs [43]. Quasi-2D excitons can be created within semiconductor quantum wells, with narrow wells and high barriers enhancing the confinement and thus the exciton binding energy. For 2D excitons, the binding energy is $E_m = R_X/(m+1/2)^2$ (where $m = 0, 1, 2 \dots$), i.e. the ground state is more strongly bound than in 3D. The 1s–2p transition apparent in the conductivity spectrum of Fig. 10.4 is at an energy of 5.0 meV (1.2 THz), as the quantum well structure consisted of narrow barriers through which electrons can readily tunnel [42]. Higher 1s–2p transition energies are observed using quantum wells with thicker barriers [28]. Under the application of a magnetic field (Fig. 10.4) the degeneracy of the 2p state is lifted, and dipole allowed transitions between the 1s and $2p^+$ and $2p^-$ states become visible in the terahertz photoconductivity spectrum [42], where + and – denote a magnetic

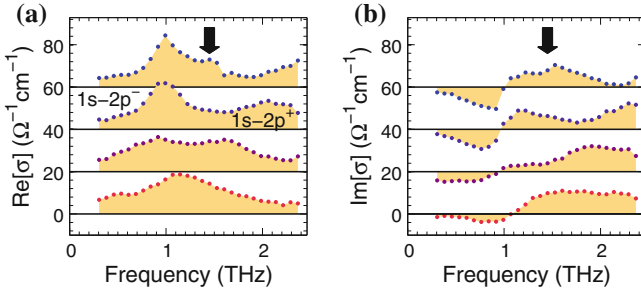


Fig. 10.4 **a** Real and **b** imaginary parts of photoconductivity of a GaAs/AlGaAs quantum well heterostructure with narrow AlGaAs barriers. From bottom to top: applied magnetic field $B = 0, 1.75, 2.75,$ and 3.75 T. At the highest magnetic field (*top curves*) the electron cyclotron resonance is visible, as indicated by the *arrows*. Reproduced with permission from Ref. [42]. ©American Physical Society 2008

quantum number $m = \pm 1$. Figure 10.4 reveals that the peak of the $1s-2p^-$ transition is roughly independent of magnetic field, while the peak of the $1s-2p^+$ transition blueshifts as the magnetic field is increased.

10.3.3 Nanostructures

Optical-pump–THz-probe spectroscopy is particularly useful in determining the conductivity of semiconductor nanostructures, where it can often be challenging to produce reliable electrical contacts. Time-resolved photoconductivity measurements were used to investigate the degree of coupling between semiconductor quantum dots (also called nanoparticles) in disordered arrays [44]. For instance for InP nanoparticles with a 3.2 nm mean diameter the photoconductivity was observed to increase by a factor of six when the interparticle distance decreased from 1.9 to 0.8 nm [44]. Colloidal CdSe quantum dots with diameters from 1 to 10 nm have also been investigated, with the photoinduced change in the THz transmission being assigned to the polarizability of the exciton [45], allowing an investigation of the Auger mechanism of electron-hole energy transfer [46]. Subsequent studies of photoexcited silicon nanocrystals [47, 48] have examined the decay dynamics and spectral dependence of the photoconductivity ($\Delta\sigma(\omega, t)$), revealing that the photoconductivity of amorphous silicon nanocrystals obey a power-law decay rather than an exponential decay. Typically the photoconductivity spectra in these systems exhibits a suppressed $\Delta\sigma_1$ and a small or negative $\Delta\sigma_2$ at low frequency, indicating that bulk transport is inhibited—carrier motion is restricted in one or more dimension. In these cases conductivity models exhibiting a resonance such as the Drude–Smith (Eq. 10.14), plasmon model (Eq. 10.12), or intersubband absorption can be invoked to model the experimental data.

Time-resolved conductivity measurements are invaluable to identify the location of the photoexcited quasiparticles in semiconductor nanostructures within a

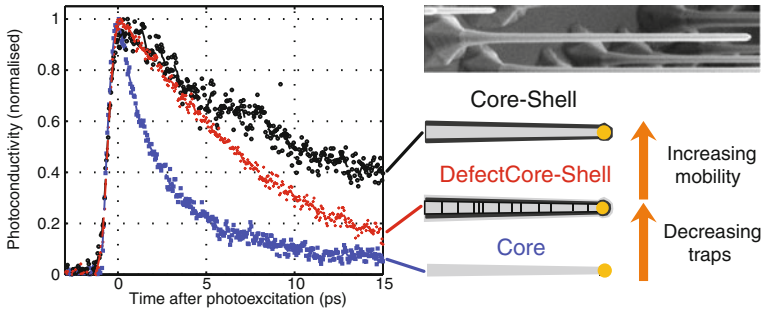


Fig. 10.5 Time-resolved photoconductivity of GaAs nanowire heterostructures (*left*) with and without a protective AlGaAs skin. An electron micrograph of a single nanowire (60 nm diameter) is shown in the *top right*. Reproduced with permission from Ref. [57]. ©American Chemical Society 2009

semiconductor matrix. For instance Cooke et al. investigated the photoconductivity parallel to and perpendicular to chains of InGaAs quantum dots [49]. They found that at cryogenic temperatures the dots efficiently capture electrons, with photoconductivity lifetimes of 3–5 ps, as evidenced by a substantially higher conductivity along the chain than that perpendicular to it. At higher temperatures the photoconductivity anisotropy reduced, owing to thermal excitation of electrons out from the dots. In another study, GaAs superlattices containing ErAs quantum dots (with a lateral dimension of 1–2 nm) were shown to efficiently trap electrons [50] while maintaining the high electron mobility inherent to GaAs. Carrier capture into InAs quantum dots [51, 52], InGaAs quantum wires [53], posts [54] and dots [55] have also been investigated. The amplification of THz radiation within a quantum cascade structure has also been demonstrated using a quantum cascade laser with a laterally-integrated Auston switch [56].

Other recent studies have examined free-standing semiconductor nanowires, which can be produced by metal-organic chemical vapor deposition using gold colloid nanoparticles to catalyze growth [27, 57]. The diameter of the nanowires was set by that of the gold nanoparticles (50 nm), with wire lengths of up to 10 μm . The photoexcitation of GaAs nanowires at 800 nm was demonstrated to produce a transient photoconductivity with a decay time of <2 ps [27]. The frequency dependent conductivity displayed a bulk-like and plasmon-like form, with a plasmon frequency that reduced at later delay times or at lower photoexcitation fluences [27]. Subsequently the growth of an AlGaAs shell, which helps prevent the oxidation of the GaAs core, was shown to increase the decay time to ~ 15 ps [57], as illustrated in Fig. 10.5. When grown at a non-optimal temperature twinning defects were found to lower the electron mobility. The reported electron mobilities are smaller than that of bulk GaAs by a factor of about three. The photoconductivity of oriented germanium nanowires has also been investigated using OPTP spectroscopy [58], with interband recombination times around 100 ps and scattering times of about 100 fs.

10.4 Organic Semiconductors

10.4.1 Graphite and Graphene

Graphite is a naturally occurring allotrope of carbon and has been technologically important for hundreds of years [59]. It is currently used in a wide range of applications from pencils to the moderators of nuclear reactors. Graphite is a semimetal and hence it also finds application in electrodes. However the ultrafast electronic properties of graphite have only recently been investigated.

Graphene is a single layer of graphite and has been shown to have unique electronic properties, owing to low energy electronic excitations acting like massless Dirac Fermions [59]. Isolated graphene has very high mobility [60], and large area graphene sheets have already been produced for touch-screen applications [61].

Near-IR pump–mid-IR probe spectroscopy of free standing graphite (~50 layers of graphene) were initially performed by Kampfrath et al. [62]. After exciting the graphite with 1.6 eV photons from a laser oscillator they observed a fast bi-exponential decay in the photoinduced conductivity with time constants 0.4 and 4 ps. At low frequencies (<3 THz) they claimed that the THz spectra could be fitted very well by a Drude-expression, indicating that photo-carriers behave like a free electron gas. In the 10–25 THz band they observed a photoinduced absorption at low frequencies (<15 THz), and a bleaching at high frequencies. They explained these results in terms of the THz probe interacting with electrons and holes in graphite by two distinct processes: *direct* (interband) and *indirect* (intraband) optical transitions. The domination of the intraband process at low frequency is consistent with Drude behavior.

George et al. [63] performed OPTP measurements on two samples of epitaxial graphite (~12 and ~20 layers of graphene). While Kampfrath et al. used free standing graphite that was exfoliated from a high quality crystal, George et al. used thinner epitaxial graphite, grown on a SiC substrate. They observed a non-exponential decay of the photo-induced THz absorption, that was pump-fluence dependent.

In contrast, Choi et al. [64] observed mono-exponential decays in photoabsorption when performing OPTP spectroscopy on a single graphene layer and on a multi-layer sample (3.3 layers of graphene). These samples were also grown via epitaxy on a SiC substrate. Since the substrate interaction causes the graphene to become *n*-doped, Choi et al. accounted for their results in terms of an optically-induced redistribution of electrons and holes in the graphene bands. The influence of the substrate is clearly less important in the thicker samples of George et al. which probably accounts for the differences in the measurements, in addition the optical excitation fluence used by Choi et al. was significantly higher than that of the other measurements.

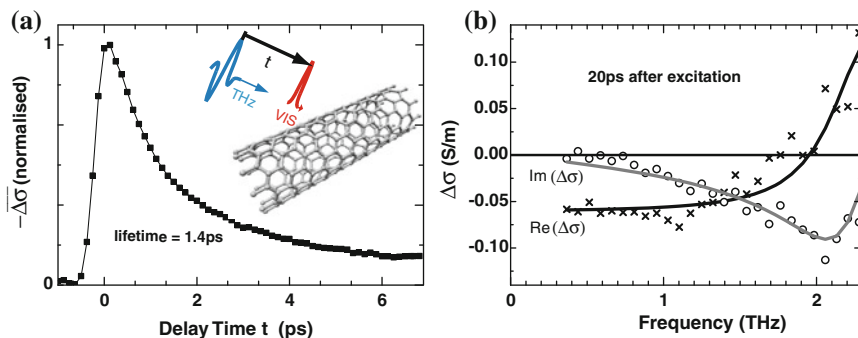


Fig. 10.6 **a** Optically-induced differential THz transmission of single-walled carbon nanotubes (SWNT) in a gelatin matrix as a function of time after excitation with an 800 nm optical pulse at a fluence of $22 \mu\text{J cm}^{-2}$. **b** THz photoconductivity spectrum of SWNTs measured 20 ps after excitation at a fluence of $158 \mu\text{J cm}^{-2}$, which shows a resonance at 11 meV associated with internal exciton transitions. All measurements were performed at room temperature. Reproduced with permission from Ref. [68]. ©American Chemical Society 2009

10.4.2 Carbon Nanotubes

Carbon nanotubes are cylinders of graphene and also have remarkable electronic and mechanical properties. OPTP measurements have revealed that the electronic properties of single-walled carbon nanotubes (SWNTs) depend strongly on interactions between the tubes. Interconnected films of SWNTs with space filling fraction of ~ 0.2 have been studied by Perfetti et al. [65] who observed changes in the THz transmission after optical excitation which they attributed to the bleaching of optical transitions in SWNT with small bandgaps. They extended their work to show that THz absorption of SWNTs is dominated by interband transitions in small gap tubes [66]. In contrast Beard et al. [67] studied denser films of SWNTs (filling fraction ~ 0.8) and observed very efficient free-carrier generation from the dissociation of optically generated excitons.

Individually isolated SWNTs were first measured by Xu et al. [68] who observed terahertz conductivity responses characteristic of excitons. Excitonic conductivity spectra have also been reported by Wang et al. [69] using mid-IR OPTP measurements. Figure 10.6 shows the THz conductivity measurements recorded by Xu et al. on SWNT isolated in a gelatin matrix. After excitation with a 1.55 eV laser pulse a rapid decay in conductivity was observed (Fig. 10.6a), associated with Auger recombination. Figure 10.6b shows the photoconductivity spectrum 20 ps after excitation, when the decay was dominated by single excitons. Their modeled conductivity (solid lines) included a reduction in the Drude conductivity ascribed to phase-space filling and a Lorentzian intra-excitonic transition centered at 2.4 THz (11 meV). OPTP spectroscopy has also been used recently to show that carbon nanotubes embedded in a gelatin film can be used as an ultrafast THz polarizer [70].

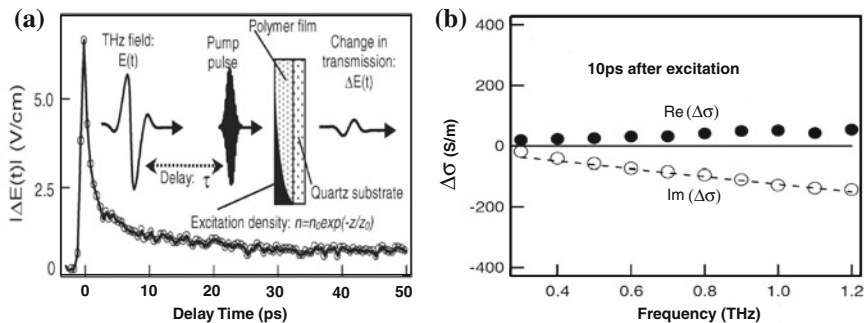


Fig. 10.7 **a** Photo-induced change in THz transmission through a film of poly2-methoxy-5-(2'-ethyl-hexyloxy)-p-phenylene-vinylene (MEH-PPV) at 30 K as a function of time after excitation with a 400 nm optical pulse at a fluence of 6 mJ cm^{-2} . **b** Complex THz conductivity measured 10 ps after initial excitation (circles) and the conductivity expected for bound excitons (lines). Reproduced with permission from Ref. [74]. ©American Physical Society 2004

10.4.3 Semiconducting Polymers

Semiconducting polymers currently show great potential for mass produced light emitting displays [71], integrated circuits [72], and solar cells [73]. There is still much to learn about these relatively young materials, and THz spectroscopy is currently playing a key role in probing their photo-physics. Time resolved photoluminescence and transient absorption spectroscopy have been used extensively to understand energy and charge transfer in a range of material systems, including organic semiconductors. While photoluminescence is excellent at observing energy transfer and transient absorption is ideal for measuring the number density of charged species, it is OPTP spectroscopy that can best measure conductivity. Hendry et al. [74] first used OPTP spectroscopy to distinguish the mechanisms of charge generation in the semiconducting polymer MEH-PPV. Their measurement helped answer a long-running question about the proportion of excitons and free charges generated upon photo-excitation. They found that primarily excitons are generated, while 1% free charges are produced after photo-excitation. Figure 10.7 illustrates the dynamics and spectrally resolved conductivity, where the suppressed $\Delta\sigma_1$ and negative $\Delta\sigma_2$ was modeled as an excitonic resonance above the experimental bandwidth.

Recently there has been particular interest in using semiconducting polymers as cheap, large area solar cells. In particular, the blending of a fullerene derivative (PCBM) with a polymer (P3HT) has shown huge improvements in device efficiencies [73], and offer the possibility of large-scale roll-to-roll solar cell fabrication. Interestingly initial OPTP studies of this system showed that the addition of PCBM did not increase the number of charge carriers generated in the first 2 ps after excitation [75]. In addition, it was found that photo-excitation of P3HT below its energy gap produced similar results to above gap excitation [76]. Parkinson et al. [77] used both laser oscillator and amplifier-based optical-pump-THz-probe spectrometers to

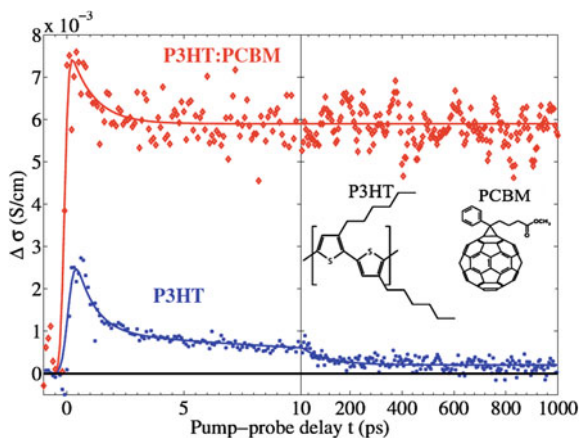


Fig. 10.8 Photo-induced change in conductivity for thin films of P3HT (*circles*) and P3HT:PCBM (*diamonds*) at room temperature as a function of time after excitation with an 800 nm optical pulse at a fluence of 0.4 mJ cm^{-2} . Inset: chemical structures of poly-3-hexylthiophene (P3HT) and [6,6]-phenyl- C_{61} butyric acid methyl ester (PCBM). A three times increase in the initial photoconductivity can be seen when P3HT is blended with PCBM, but when time integrated (not shown) a 20 times increase in photoconductivity is observed. Reproduced with permission from Ref. [77]. ©American Chemical Society 2008

access a large range of fluences (over four orders of magnitude) to photo-excite P3HT-PCBM blends. From the fluence dependence they found that different mechanisms for charge relaxation occurred on different time-scales: at early times ($\sim \text{ps}$) excitons dissociate via interfacial charge transfer and on longer time scales ($> \mu\text{s}$) carrier-carrier recombination dominated the conductivity. They also found that the initial photoconductivity was only three times larger in the blend compared with pure P3HT (Fig. 10.8), but when time-integrated a 20 times increase in the THz conductivity was measured, showing that a more stable charge-separated state exists in the blend, thereby improving solar cell device performance.

10.5 Inorganic–Organic Hybrids

The electronic and optoelectronic properties of hybrid organic–inorganic materials are fundamentally interesting, owing to the quite different ways electronic processes in these materials are modeled. Currently one of the most important applications of these hybrid [78] materials is in dye-sensitized solar cells (also known as Grätzel cells) [79], which are presently better than 10% efficient [78] and are entering commercial production. A schematic diagram of a conventional device is shown in Fig. 10.9a. For typical cells an organic dye absorbs light, a wide-gap inorganic semiconductor (such as TiO_2 , ZnO or SnO_2) acts as an electron conductor and an

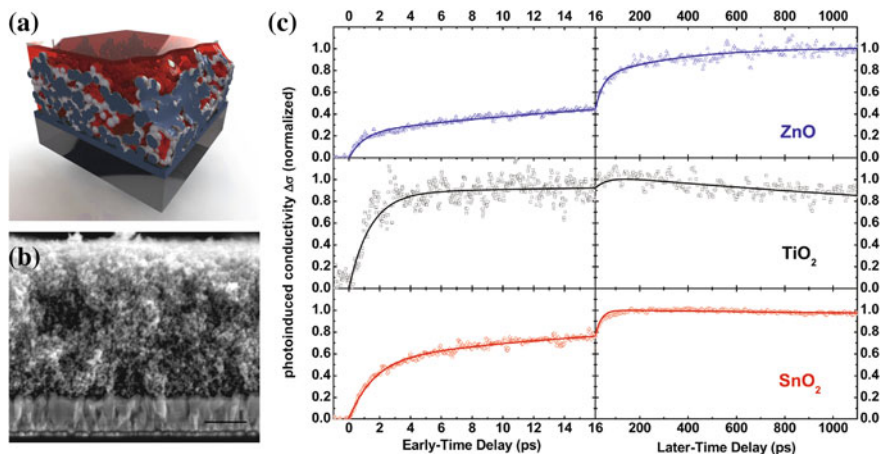


Fig. 10.9 **a** Schematic diagram of a dye-sensitized solar cell showing sintered spheres of metal oxide within an electrolyte. The base represents a glass substrate coated in (semitransparent) fluorine-doped-tin-oxide (FTO). The top contact is absent for clarity. **b** Cross-section TEM of a device before sensitization, showing sintered TiO₂ on top of a semitransparent FTO contact. **c** OPTPS data showing dynamics dye sensitized solar cells constructed using ZnO, TiO₂ and SnO₂ metal oxides. The dye was photoexcited in each case as described in Ref. [81]. ©American Chemical Society 2011

electrolyte acts as a hole transporter. Since Grätzel cells use different materials for light harvesting and charge transport, there is a very wide parameter space to optimize [79]. Optical-pump–terahertz-probe spectroscopy is an excellent method for understanding the fundamental electronic processes in the devices, which should accelerate device optimization.

Turner et al. [80] reported the first study of Grätzel cells using terahertz spectroscopy. They investigated TiO₂ sensitized with Ru535 dye, and observed a non-Drude behavior for the photo-injected charges. They attributed their results to Anderson localization, and used a Drude-Smith backscattering approach to model their data (see Sect. 10.2.3). Importantly they were able to show that electrons in the TiO₂ nanoparticles were quite mobile, despite collectively having a poor bulk mobility. Thus they were able to discount the hypothesis that electronic transport processes are dominated by trapping and detrapping *within* the nanoparticles.

Hendry and co-workers investigated bulk (rutile) TiO₂ [82] and porous TiO₂ [83] using OPTPS and found the THz mobility of these materials to be 1 cm²/(Vs) and 0.01 cm²/(Vs) respectively. Using Maxwell Garnett effective medium theory (Sect. 10.2.3.3) they ascribed this remarkable drop in mobility to charge screening effects in the mesoporous material (TiO₂ has a very high static dielectric constant 100, thus screening is most effective at excluding the THz electric field from the TiO₂ particles). Baxter et al. [84] used Bruggemann effective medium theory and Drude-Smith analysis (Sect. 10.2.3.6) to study the THz conductivity of ZnO nanoparticles. They observed that these nanoparticles also had a lower mobility than thin films of

ZnO. In addition, they found that annealing ZnO increased its THz mobility, but had little effect on the conductivity dynamics. Němec et al. [85] studied dye sensitized ZnO and TiO₂ nanoparticles and analyzed their data by first using Maxwell Garnett effective medium theory to extract the intrinsic conductivity of the nanoparticles before applying a Monte Carlo approach to model localization [86]. Their work highlighted the importance of the electrostatic interactions between photoinjected electrons and the dye cation at the surface of nanoparticles in dye sensitised materials.

The surface treatment of mesoporous TiO₂ in Grätzel cells with TiCl₄ has been shown to greatly improve device performance, however, the mechanisms governing this improvement are not well understood [87]. Tiwana et al. [88] used OPTP spectroscopy combined with device measurements to study charge injection and surface treatment in TiO₂ based cells with Z907 dye as the sensitizer. They observed an initial fast charge injection from the dye to the TiO₂ on a sub-0.5 ps timescale followed by a slower injections on 70–200 ps timescale. In addition they found that while surface TiCl₄ treatment greatly improved the device performance, it did not affect the early charge dynamics, indicating the surface treatment impacts phenomena occurring on longer timescales.

Dye sensitized solar cells fabricated from nominally the same dye and metal oxide show huge variations in performance [89], so it is important to characterize solar cells made from the same materials used to study the photophysics. Recently Tiwana et al. [81] performed a detailed comparative study of charge dynamics in mesoporous ZnO, SnO₂, and TiO₂ dye sensitized solar cells, using OPTPS and device measurement. They found that the reduction in conductivity from the bulk material to nanoparticles could not be explained by electrostatic screening alone. Figure 10.9c show the rise in photoconductivity of sintered ZnO, TiO₂, and SnO₂ after photoexciting the sensitizing dye Z907. The fast rise in conductivity for TiO₂ was attributed to a ultrafast injection of electrons from the dye into the metal oxide. In contrast ZnO and SnO₂ show much slower injection. Tiwana et al. concluded that while TiO₂ based solar cells are well optimized, there is much room for improving devices based on ZnO and SnO₂, such as improving charge injection by developing better matched dyes.

10.6 Outlook

This chapter has outlined the experimental and theoretical background behind the technique of optical-pump–terahertz-probe spectroscopy. Specific examples of the use of time-resolved terahertz spectroscopy were given, with an emphasis on organic and inorganic semiconductors and their nanostructures. The wide applicability of the technique testifies to its growing maturity, and suggests that it will continue to be adopted and improved by researchers worldwide in the years to come.

References

1. M.C. Nuss, D.H. Auston, F. Capasso, *Phys. Rev. Lett.* **58**, 2355 (1987)
2. D.H. Auston, K.P. Cheung, J.A. Valdmanis, D.A. Kleinman, *Phys. Rev. Lett.* **53**, 1555 (1984)
3. P.N. Saeta, J.F. Federici, B.I. Greene, D.R. Dykaar, *Appl. Phys. Lett.* **60**, 1477 (1992)
4. R.H.M. Groeneveld, D. Grischkowsky, *J. Opt. Soc. Am. B-Opt. Phys.* **11**, 2502 (1994)
5. M. van Exter, C. Fattinger, D. Grischkowsky, *Appl. Phys. Lett.* **55**, 337 (1989)
6. M. van Exter, C. Fattinger, D. Grischkowsky, *Opt. Lett.* **14**, 1128 (1989)
7. G. Haran, W.D. Sun, K. Wynne, R.M. Hochstrasser, *Chem. Phys. Lett.* **274**, 365 (1997)
8. R. McElroy, K. Wynne, *Phys. Rev. Lett.* **79**, 3078 (1997)
9. R. Huber, F. Tauser, A. Brodschelm, M. Bichler, G. Abstreiter, A. Leitenstorfer, *Nature* **414**, 286 (2001)
10. M.C. Beard, G.M. Turner, C.A. Schmuttenmaer, *J. Phys. Chem. B* **106**, 7146 (2002)
11. C.A. Schmuttenmaer, *Chem. Rev.* **104**, 1759 (2004)
12. P.U. Jepsen, D.G. Cooke, M. Koch, *Laser Photon. Rev.* **5**, 124 (2011)
13. R. Ulbricht, E. Hendry, J. Shan, T.F. Heinz, M. Bonn, *Rev. Mod. Phys.* **83**, 543 (2011)
14. J.B. Baxter, G.W. Guglietta, *Anal. Chem.* **83**, 4342 (2011)
15. H. Němec, P. Kužel, V. Sundström, *J. Photochem. Photobiol. A-Chem.* **215**, 123 (2010)
16. R.D. Averitt, A.J. Taylor, *J. Phys.-Condes. Matter.* **14**, R1357 (2002)
17. M.C. Beard, C.A. Schmuttenmaer, *J. Chem. Phys.* **114**, 2903 (2001)
18. J.T. Kindt, C.A. Schmuttenmaer, *J. Chem. Phys.* **110**, 8589 (1999)
19. H. Němec, F. Kadlec, P. Kužel, *J. Chem. Phys.* **117**, 8454 (2002)
20. J.M. Schins, *Phys. Rev. B* **83**, 205111 (2011)
21. C. Larsen, D.G. Cooke, P.U. Jepsen, *J. Opt. Soc. Am. B-Opt. Phys.* **28**, 1308 (2011)
22. J.C.M. Garnett, *Philos. Trans. R. Soc. Lond. Ser. A-Math. Phys. Eng. Sci.* **203**, 385 (1904)
23. D.A.G. Bruggeman, *Ann. Phys.-Berlin* **416**, 636 (1935)
24. S. Riikonen, I. Romero, G. de Abajo, *Phys. Rev. B* **71**, 235104 (2005)
25. M. Scheller, S. Wietzke, C. Jansen, M. Koch, *J. Phys. D-Appl. Phys.* **42**, 065415 (2009)
26. H.K. Nienhuys, V. Sundström, *Appl. Phys. Lett.* **87**, 012101 (2005)
27. P. Parkinson, J. Lloyd-Hughes, Q. Gao, H.H. Tan, C. Jagadish, M.B. Johnston, L.M. Herz, *Nano Lett.* **7**, 2162 (2007)
28. R.A. Kaindl, M.A. Carnahan, D. Hägele, R. Lövenich, D.S. Chemla, *Nature* **423**, 734 (2003)
29. R. Huber, R.A. Kaindl, B.A. Schmid, D.S. Chemla, *Phys. Rev. B* **72**, 161314 (2005)
30. R.A. Kaindl, D. Hägele, M.A. Carnahan, D.S. Chemla, *Phys. Rev. B* **79**, 045320 (2009)
31. N.V. Smith, *Phys. Rev. B* **64**, 155106 (2001)
32. M.C. Beard, G.M. Turner, C.A. Schmuttenmaer, *Phys. Rev. B* **62**, 15764 (2000)
33. Q.T. Vu, H. Haug, *Phys. Rev. B* **62**, 7179 (2000)
34. R. Huber, C. Kübler, S. Tubel, A. Leitenstorfer, Q.T. Vu, H. Haug, F. Kohler, M.C. Amann, *Phys. Rev. Lett.* **94**, 027401 (2005)
35. M.C. Beard, G.M. Turner, C.A. Schmuttenmaer, *J. Appl. Phys.* **90**, 5915 (2001)
36. K.P.H. Lui, F.A. Hegmann, *Appl. Phys. Lett.* **78**, 3478 (2001)
37. J. Lloyd-Hughes, S.K.E. Merchant, L. Fu, H.H. Tan, C. Jagadish, E. Castro-Camus, M.B. Johnston, *Appl. Phys. Lett.* **89**, 232102 (2006)
38. C. Headley, L. Fu, P. Parkinson, X.L. Xu, J. Lloyd-Hughes, C. Jagadish, M.B. Johnston, *IEEE J. Sel. Top. Quantum Electron.* **17**, 17 (2011)
39. S.W. Koch, M. Kira, G. Khitrova, H.M. Gibbs, *Nat. Mater.* **5**, 523 (2006)
40. R. Huber, B.A. Schmid, Y.R. Shen, D.S. Chemla, R.A. Kaindl, *Phys. Rev. Lett.* **96**, 017402 (2006)
41. T. Suzuki, R. Shimano, *Phys. Rev. Lett.* **103**, 057401 (2009)
42. J. Lloyd-Hughes, H.E. Beere, D.A. Ritchie, M.B. Johnston, *Phys. Rev. B* **77**, 125322 (2008)
43. D.D. Sell, *Phys. Rev. B* **6**, 3750 (1972)
44. M.C. Beard, G.M. Turner, J.E. Murphy, O.I. Mičić, M.C. Hanna, A.J. Nozik, C.A. Schmuttenmaer, *Nano Lett.* **3**, 1695 (2003)

45. F. Wang, J. Shan, M.A. Islam, I.P. Herman, M. Bonn, T.F. Heinz, *Nat. Mater.* **5**, 861 (2006)
46. E. Hendry, M. Koeberg, F. Wang, H. Zhang, C.D. Donega, D. Vanmaekelbergh, M. Bonn, *Phys. Rev. Lett.* **96**, 057408 (2006)
47. D.G. Cooke, A.N. MacDonald, A. Hryciw, J. Wang, Q. Li, A. Meldrum, F.A. Hegmann, *Phys. Rev. B* **73**, 193311 (2006)
48. L.V. Titova, T.L. Cocker, D.G. Cooke, X.Y. Wang, A. Meldrum, F.A. Hegmann, *Phys. Rev. B* **83**, 085403 (2011)
49. D.G. Cooke, F.A. Hegmann, Y.I. Mazur, W.Q. Ma, X. Wang, Z.M. Wang, G.J. Salamo, M. Xiao, T.D. Mishima, M.B. Johnson, *Appl. Phys. Lett.* **85**, 3839 (2004)
50. R.P. Prasankumar, A. Scopatz, D.J. Hilton, A.J. Taylor, R.D. Averitt, J.M. Zide, A.C. Gossard, *Appl. Phys. Lett.* **86**, 201107 (2005)
51. D.A. Yarotski, R.D. Averitt, N. Negre, S.A. Crooker, A.J. Taylor, G.P. Donati, A. Stintz, L.F. Lester, K.J. Malloy, *J. Opt. Soc. Am. B-Opt. Phys.* **19**, 1480 (2002)
52. T. Müller, W. Parz, K. Unterrainer, S. Sauvage, J. Houel, P. Boucaud, A. Miard, A. Lemaître, *Phys. Rev. B* **77**, 035314 (2008)
53. D.G. Cooke, F.A. Hegmann, Y.I. Mazur, Z.M. Wang, W. Black, H. Wen, G.J. Salamo, T.D. Mishima, G.D. Lian, M.B. Johnson, *J. Appl. Phys.* **103**, 023710 (2008)
54. D. Stehr, C.M. Morris, D. Talbayev, M. Wagner, H.C. Kim, A.J. Taylor, H. Schneider, P.M. Petroff, M.S. Sherwin, *Appl. Phys. Lett.* **95**, 251105 (2009)
55. H.P. Porte, P.U. Jepsen, N. Daghestani, E.U. Rafailov, D. Turchinovich, *Appl. Phys. Lett.* **94**, 262104 (2009)
56. N. Jukam, S.S. Dhillon, D. Oustinov, J. Madeo, C. Manquest, S. Barbieri, C. Sirtori, S.P. Khanna, E.H. Linfield, A.G. Davies, J. Tignon, *Nat. Photon.* **3**, 715 (2009)
57. P. Parkinson, H.J. Joyce, Q. Gao, H.H. Tan, X. Zhang, J. Zou, C. Jagadish, L.M. Herz, M.B. Johnston, *Nano Lett.* **9**, 3349 (2009)
58. J.H. Strait, P.A. George, M. Levendorf, Blood-Forsythe, F. Rana, J. Park, *Nano Lett.* **9**, 2967 (2009)
59. A.H.C. Neto, F. Guinea, N.M.R. Peres, K.S. Novoselov, A.K. Geim, *Rev. Mod. Phys.* **81**, 109 (2009)
60. K.I. Bolotin, K.J. Sikes, Z. Jiang, M. Klima, G. Fudenberg, J. Hone, P. Kim, H.L. Stormer, *Solid State Commun.* **146**, 351 (2008)
61. S. Bae, H. Kim, Y. Lee, X.F. Xu, J.S. Park, Y. Zheng, J. Balakrishnan, T. Lei, H.R. Kim, Y.I. Song, Y.J. Kim, K.S. Kim, B. Ozyilmaz, J.H. Ahn, B.H. Hong, S. Iijima, *Nat. Nanotechnol.* **5**, 574 (2010)
62. T. Kampfrath, L. Perfetti, F. Schapper, C. Frischkorn, M. Wolf, *Phys. Rev. Lett.* **95**, 187403 (2005)
63. P.A. George, J. Strait, J. Dawlaty, S. Shivaraman, M. Chandrashekar, F. Rana, M.G. Spencer, *Nano Lett.* **8**, 4248 (2008)
64. H. Choi, F. Borondics, D.A. Siegel, S.Y. Zhou, M.C. Martin, A. Lanzara, R.A. Kaindl, *Appl. Phys. Lett.* **94**, 172102 (2009)
65. L. Perfetti, T. Kampfrath, F. Schapper, A. Hagen, T. Hertel, C.M. Aguirre, P. Desjardins, R. Martel, C. Frischkorn, M. Wolf, *Phys. Rev. Lett.* **96**, 027401 (2006)
66. T. Kampfrath, K.v. Volkmann, C.M. Aguirre, P. Desjardins, R. Martel, M. Krenz, C. Frischkorn, M. Wolf, L. Perfetti, *Phys. Rev. Lett.* **101**, 267403 (2008)
67. M.C. Beard, J.L. Blackburn, M.J. Heben, *Nano Lett.* **8**, 4238 (2008)
68. X. Xu, K. Chuang, R.J. Nicholas, M.B. Johnston, L.M. Herz, *J. Phys. Chem. C* **113**, 18106 (2009)
69. J.G. Wang, M.W. Graham, Y.Z. Ma, G.R. Fleming, R.A. Kaindl, *Phys. Rev. Lett.* **104**, 177401 (2010)
70. X.L. Xu, P. Parkinson, K.C. Chuang, M.B. Johnston, R.J. Nicholas, L.M. Herz, *Phys. Rev. B* **82**, 085441 (2010)
71. R.H. Friend, R.W. Gymer, A.B. Holmes, J.H. Burroughes, R.N. Marks, C. Taliani, D.D.C. Bradley, J.L. Brédas, M. Logdlund, W.R. Salaneck, *Nature* **397**, 121 (1999)

72. H. Sirringhaus, T. Kawase, R.H. Friend, T. Shimoda, M. Inbasekaran, W. Wu, E.P. Woo, *Science* **290**, 2123 (2000)
73. K. Kim, J. Liu, M.A.G. Namboothiry, D.L. Carroll, *Appl. Phys. Lett.* **90**, 163511 (2007)
74. E. Hendry, J.M. Schins, L.P. Candeias, L.D.A. Siebbeles, M. Bonn, *Phys. Rev. Lett.* **92**, 196601 (2004)
75. X. Ai, M.C. Beard, K.P. Knutsen, S.E. Shaheen, G. Rumbles, R.J. Ellingson, *J. Phys. Chem. B* **110**, 25462 (2006)
76. P.D. Cunningham, L.M. Hayden, *J. Phys. Chem. C* **112**, 7928 (2008)
77. P. Parkinson, J. Lloyd-Hughes, M.B. Johnston, L.M. Herz, *Phys. Rev. B* **78**, 115321 (2008)
78. M.A. Green, K. Emery, Y. Hishikawa, W. Warta, *Prog. Photovolt.* **18**, 346 (2010)
79. M. Grätzel, *Acc. Chem. Res.* **42**, 1788 (2009)
80. G.M. Turner, M.C. Beard, C.A. Schmittenmaer, *J. Phys. Chem. B* **106**, 11716 (2002)
81. P. Tiwana, P. Docampo, M.B. Johnston, H.J. Snaith, L.M. Herz, *ACS Nano* **5**, 5158 (2011)
82. E. Hendry, F. Wang, J. Shan, T.F. Heinz, M. Bonn, *Phys. Rev. B* **69**, 081101 (2004)
83. E. Hendry, M. Koeberg, B. O'Regan, M. Bonn, *Nano Lett.* **6**, 755 (2006)
84. J.B. Baxter, C.A. Schmittenmaer, *J. Phys. Chem. B* **110**, 25229 (2006)
85. H. Němec, J. Rochford, O. Taratula, E. Galoppini, P. Kužel, T. Polívka, A. Yartsev, V. Sundström, *Phys. Rev. Lett.* **104**, 197401 (2010)
86. H. Němec, P. Kužel, V. Sundström, *Phys. Rev. B* **79**, 115309 (2009)
87. C.J. Barbe, F. Arendse, P. Comte, M. Jirousek, F. Lenzenmann, V. Shklover, M. Grätzel, *J. Am. Ceram. Soc.* **80**, 3157 (1997)
88. P. Tiwana, P. Parkinson, M.B. Johnston, H.J. Snaith, L.M. Herz, *J. Phys. Chem. C* **114**, 1365 (2010)
89. H.J. Snaith, L. Schmidt-Mende, *Adv. Mater.* **19**, 3187 (2007)

Chapter 11

Terahertz Spectroscopy: Ellipsometry and Active Polarization Control of Terahertz Waves

Makoto Kuwata-Gonokami

Abstract The principles and experimental methods of terahertz (THz) wave ellipsometry are described. The procedure to determine diagonal and off-diagonal components of the complex dielectric tensor for materials using THz time domain spectroscopy in transmission and oblique reflection geometries are explained. The measured optical activity in artificial chiral grating structures is also described as applications of this technique.

11.1 Introduction

Terahertz (THz) time domain spectroscopy (TDS) provides phase-sensitive information on electromagnetic responses and enables one to determine complex dielectric functions of materials. It is natural to extend this technique to polarization-sensitive measurements, to determine both the diagonal and off-diagonal components of the complex dielectric tensor. It has strong potential for various applications including magneto-optical measurements for non-contact Hall mobility measurements [1, 2], detection of chiral molecules and sensing for biological applications [3, 4]. Recently, with improved sensitivity of polarization rotation [5], quantum hall effects have been clearly confirmed in the THz frequency region [6].

In this section, first, a method for THz time domain ellipsometry in transmission mode is described. Experimental results for the measurement of polarization effects of artificial chiral structures are given. Second, THz-TDS for magneto-optical effects measured in oblique reflection mode are given. Explicit expressions between polarization parameters and dielectric tensors are formulated. As an application, the results of active polarization control of THz waves are also demonstrated.

M. Kuwata-Gonokami (✉)
Department of Physics, University of Tokyo, Tokyo, Japan
e-mail: gonokami@phys.s.u-tokyo.ac.jp

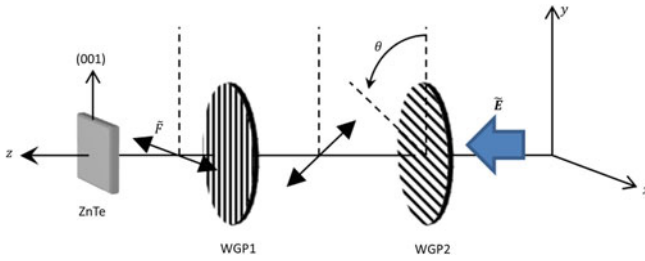


Fig. 11.1 Schematics of experimental setup for polarization state measurements of a THz wave with wire-grid polarizers

11.2 Transmission-Mode Time Domain Ellipsometry

11.2.1 Method of Polarization State Measurement with Wire-Grid Polarizers

In THz-TDS, a nonlinear optical crystal or a detection antenna is used for THz-wave detection. They are sensitive to the direction of polarization of a THz wave. Therefore, a wire-grid polarizer (WGP) is usually placed in front of these devices, in order to determine the polarization direction of a detected THz wave. Placing another WGP in front of the WGP enables one to measure the polarization states of a THz wave. Here, electro-optic (EO) sampling measurement with ZnTe crystal is considered as shown in Fig. 11.1. WGP1 is placed in order to make the polarization direction of detected THz wave oriented parallel to x-axis to maximize the sensitivity of THz-wave detection.

The relation between the electric field vector incident on WGP2, \tilde{E} , and the electric field vector incident on ZnTe crystal, \tilde{F} , is described as

$$\begin{aligned} \tilde{F} &= \begin{bmatrix} 1 & 0 \\ \sin \theta & \cos \theta \end{bmatrix} \begin{bmatrix} \cos \theta & -\sin \theta \\ 0 & 0 \end{bmatrix} \begin{bmatrix} 1 & 0 \\ -\sin \theta & \cos \theta \end{bmatrix} \tilde{E} \\ &= \begin{bmatrix} \cos^2 \theta & \sin \theta \cos \theta \\ \sin \theta \cos \theta & \cos^2 \theta \end{bmatrix} \begin{bmatrix} \tilde{E}_x \\ \tilde{E}_y \end{bmatrix}, \end{aligned} \tag{11.1}$$

where θ is the angle between the y-axis and the direction of polarization for WGP2 as shown in Fig. 11.1. Therefore, each component of \tilde{E} is determined by performing measurements with different values of θ_1 and θ_2 . From the measured amplitude θ from the measurement at θ_1 and θ_2 , \tilde{E} is calculated as

$$\begin{bmatrix} \tilde{E}_x \\ \tilde{E}_y \end{bmatrix} = \begin{bmatrix} \cos^2 \theta_1 & \sin \theta_1 \cos \theta_1 \\ \sin \theta_2 \cos \theta_2 & \cos^2 \theta_2 \end{bmatrix}^{-1} \begin{bmatrix} \tilde{F}_1 \\ \tilde{F}_2 \end{bmatrix}$$

$$= \frac{1}{\cos\theta_1 \cos\theta_2 \sin(\theta_2 - \theta_1)} \begin{bmatrix} \sin\theta_2 \cos\theta_2 & -\sin\theta_1 \cos\theta_1 \\ -\cos^2\theta_2 & \cos^2\theta_1 \cos\theta_1 \end{bmatrix} \begin{bmatrix} \tilde{F}_1 \\ \tilde{F}_2 \end{bmatrix}. \quad (11.2)$$

If we set $\theta_1 = -\pi/4$ and $\theta_2 = \pi/4$,

$$\begin{bmatrix} \tilde{E}_x \\ \tilde{E}_y \end{bmatrix} = \begin{bmatrix} \tilde{F}_1 - \tilde{F}_2 \\ \tilde{F}_1 + 2\tilde{F}_2 \end{bmatrix}. \quad (11.3)$$

However, when \tilde{E}_x is very small, it is difficult to measure \tilde{E}_x with high accuracy from the difference between \tilde{F}_1 and \tilde{F}_2 . In this case, it may be better to set $\theta_1 = 0$ and $\theta_2 = \pi/4$, and the resulting relations are described as :

$$\begin{bmatrix} \tilde{E}_x \\ \tilde{E}_y \end{bmatrix} = \begin{bmatrix} \tilde{F}_1 \\ -\tilde{F}_1 + 2\tilde{F}_2 \end{bmatrix}. \quad (11.4)$$

In this case \tilde{E}_x is simply equal to \tilde{F}_1 , and that value can be obtained with high accuracy.

Polarization azimuth rotation θ and ellipticity angle η are calculated from the following relationships.

$$\theta = \tan^{-1} \left(\frac{\operatorname{Re}\{\tilde{E}_x^* \tilde{E}_y\}}{|\tilde{E}_x|^2 - |\tilde{E}_y|^2} \right) \quad (11.5)$$

$$\eta = -\sin^{-1} \left(\frac{\operatorname{Im}\{\tilde{E}_x^* \tilde{E}_y\}}{|\tilde{E}_x|^2 - |\tilde{E}_y|^2} \right) \quad (11.6)$$

11.2.2 Calculation of Dielectric Tensor

The dielectric tensor of samples from polarization measurements can be obtained. The relationship between the reference wave $\tilde{\mathbf{E}}_{\text{ref}}$, measured without a sample, and that transmitted through a sample $\tilde{\mathbf{E}}_{\text{sample}}$ is described by the square matrix \tilde{T} as,

$$\tilde{\mathbf{E}}_{\text{sample}} = \tilde{T} \tilde{\mathbf{E}}_{\text{ref}}. \quad (11.7)$$

The experimental results with different reference waves $\tilde{\mathbf{E}}_{\text{ref}}^1$ and $\tilde{\mathbf{E}}_{\text{ref}}^2$ can be described as;

$$\begin{bmatrix} \tilde{\mathbf{E}}_{\text{sample}}^1 & \tilde{\mathbf{E}}_{\text{sample}}^2 \end{bmatrix} = \tilde{T} \begin{bmatrix} \tilde{\mathbf{E}}_{\text{ref}}^1 & \tilde{\mathbf{E}}_{\text{ref}}^2 \end{bmatrix} \quad (11.8)$$

Because $\tilde{\mathbf{E}}_{\text{sample}}^1$, $\tilde{\mathbf{E}}_{\text{sample}}^2$, $\tilde{\mathbf{E}}_{\text{ref}}^1$, $\tilde{\mathbf{E}}_{\text{ref}}^2$ can be measured by using the method described in the Sect. 11.2.1, matrix \tilde{T} is determined from the following equation;

$$\tilde{T} = \begin{bmatrix} \tilde{E}_{\text{sample}}^1 & \tilde{E}_{\text{sample}}^2 \end{bmatrix} \begin{bmatrix} \tilde{E}_{\text{ref}}^1 & \tilde{E}_{\text{ref}}^2 \end{bmatrix}^{-1}. \quad (11.9)$$

In the case of a magnetized isotropic medium, the dielectric tensor is presented in the following form:

$$\tilde{\epsilon} = \begin{pmatrix} \tilde{\epsilon}_{xx} & \tilde{\epsilon}_{xy} & 0 \\ -\tilde{\epsilon}_{xy} & \tilde{\epsilon}_{xx} & 0 \\ 0 & 0 & \tilde{\epsilon}_{zz} \end{pmatrix}. \quad (11.10)$$

When light propagates through such media in the z-direction, the eigen modes have circular polarization ($\mathbf{e}_{\pm} = \frac{1}{2}(1, \pm i)^T$) and its eigen values of refractive index have the following relationship to the complex permittivity,

$$\epsilon_0 \tilde{n}_{\pm}^2 = \tilde{\epsilon}_{xx} \pm i \tilde{\epsilon}_{xy}. \quad (11.11)$$

In this case, matrix \tilde{T} is described as follows,

$$\tilde{T} = \begin{bmatrix} \tilde{t}_x & \tilde{t}_{xy} \\ -\tilde{t}_{xy} & \tilde{t}_x \end{bmatrix}, \quad (11.12)$$

and two measurements are not necessary to obtain matrix \tilde{T} . If we set $\tilde{E}_{\text{ref}} = (0, \tilde{E}_{\text{ref}})$, matrix \tilde{T} is simply obtained with the following Eq. (11.7);

$$\begin{bmatrix} \tilde{t}_{xy} \\ \tilde{t}_x \end{bmatrix} = \tilde{E}_{\text{sample}} / \tilde{E}_{\text{ref}}. \quad (11.13)$$

The matrix \tilde{T} can also be diagonalized with circular polarization eigenmodes as follows;

$$\tilde{T} = \begin{bmatrix} \tilde{t}_x & \tilde{t}_{xy} \\ -\tilde{t}_{xy} & \tilde{t}_x \end{bmatrix} = \begin{bmatrix} \mathbf{e}_+ & \mathbf{e}_- \end{bmatrix} \begin{bmatrix} \tilde{t}_+ & 0 \\ 0 & \tilde{t}_- \end{bmatrix} \begin{bmatrix} \mathbf{e}_+ & \mathbf{e}_- \end{bmatrix}^{-1}, \quad (11.14)$$

where \tilde{t}_+ and \tilde{t}_- are transmittances for left and right circularly polarizations, respectively, being related to \tilde{t}_x and \tilde{t}_{xy} ;

$$\tilde{t}_{\pm} = \tilde{t}_x \pm i \tilde{t}_{xy}. \quad (11.15)$$

In the case of a plate sample in air, \tilde{t}_{\pm} is described, taking account of the Fresnel constants on the interfaces and phase change inside the sample, as follows

$$\begin{aligned} \tilde{t}_{\pm} &= \frac{\tilde{E}_{\text{sample}}^{\pm}}{\tilde{E}_{\text{ref}}^{\pm}} = \frac{2}{\tilde{n}_{\pm} + 1} \cdot \frac{2\tilde{n}_{\pm}}{\tilde{n}_{\pm} + 1} \cdot \frac{\tilde{n}_{\pm} - 1}{\tilde{n}_{\pm} + 1} \exp\left(\frac{i\omega L}{c} \tilde{n}_{\pm}\right) / \exp\left(\frac{i\omega L}{c}\right) \\ &= \frac{4\tilde{n}}{(\tilde{n}_{\pm} + 1)^2} \exp\left[\frac{i\omega L}{c} (\tilde{n}_{\pm} - 1)\right]. \end{aligned} \quad (11.16)$$

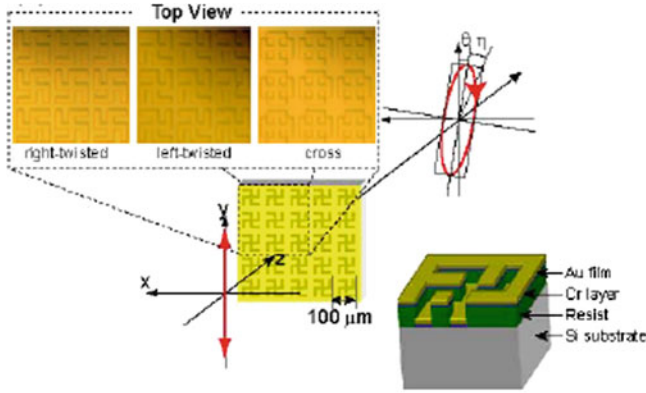


Fig. 11.2 Schematic illustrations of experimental setup and sample

where \tilde{n}_+ and \tilde{n}_- are complex refractive indices of the sample for left and right circularly polarizations, respectively, L is the thickness of the sample and ω is the angular frequency of THz wave \tilde{n}_\pm can be obtained by solving (11.13), (11.15), (11.16) numerically. Each component of the dielectric tensor is obtained with (11.11):

$$\tilde{\epsilon}_{xx} = \frac{\tilde{n}_+^2 + \tilde{n}_-^2}{2\epsilon_0} \tag{11.17}$$

$$\tilde{\epsilon}_{xy} = \frac{\tilde{n}_+^2 - \tilde{n}_-^2}{2i\epsilon_0}. \tag{11.18}$$

11.2.3 Example of Polarization Measurements

In this section, the procedure explained previously is employed to demonstrate the polarization rotation angle and complex dielectric tensor using transmission-mode measurements of an artificial planar periodic structure with chirality. Recent progress on the design and fabrication of artificial subwavelength structures, such as metamaterials, has revealed several novel functions for controlling light [7]. For example, metal chiral structures have been proposed to show optical activity [8], and chirality-dependent polarization-sensitive effects have been reported [9–15]. The development of such artificial structures for THz wave control is important because polarimetry in the THz region is hampered by a lack of good polarization devices in this frequency range.

Figure 11.2 shows schematic illustrations of the experimental setup and sample. Arrays of achiral (cross) and chiral (gammadion patterns) structures were fabricated by depositing a thin gold film on to a resist layer placed upon a high-resistance Si substrate and patterned by electron-beam lithography. The resulting samples, without lift-off treatment, have two metal layers with complementary patterns. The grat-

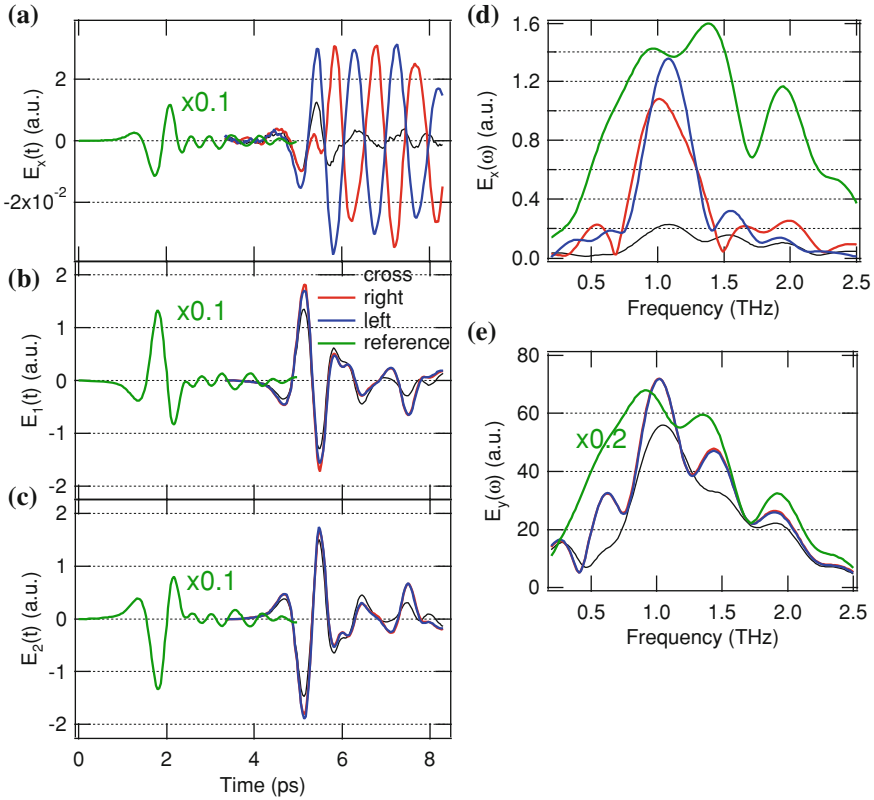


Fig. 11.3 Time domain THz waveforms of transmitted waves obtained in the cross-Nichol arrangement (a), with WGP2 -45° (b) and $+45^\circ$ (c). The *green curves* show reference signals measured without any sample. The *red, blue, and black curves* show the signals for *right- and left- twisted gammadian samples and cross-patterned samples, respectively*. By Fourier transform, the corresponding x- and y-elements of the electric field in the frequency domain are calculated and shown in (d) and (e). In addition, absolute values of electric field are shown in (d). The relative delays between the signals with and without a sample correspond to the propagation delay times of the THz pulses during the propagation through the samples (From [16])

ings are arranged in a two-dimensional square periodic structure with a period of $100\mu\text{m}$. The thicknesses of the gold film and the resist layer are 100 and 180 nm, respectively. Because these structures have fourfold symmetry, around the normal to the substrate, the samples are in-plane isotropic and the dielectric tensor is presented by Eq. (11.10). It was experimentally confirmed that no birefringence was observed at normal incidence. The THz wave, generated by optical rectification with a ZnTe crystal, is focused onto the sample at normal incidence down to a diameter of about 1 mm.

The polarization state of a transmitted wave is determined by using the method explained in the previous sections. The cross-Nicol method (with (11.4)) was used

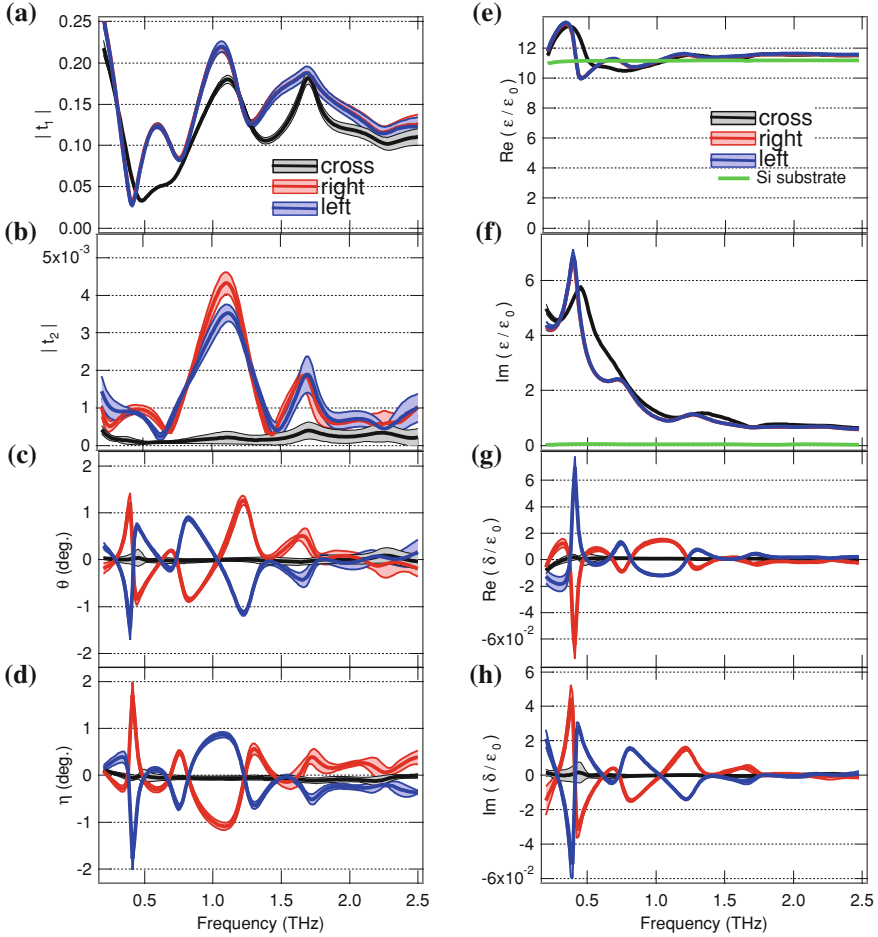


Fig. 11.4 Absolute values of diagonal (a) and off-diagonal (b) elements for the Jones matrix of the sample. Spectra of rotation angle (c) and ellipticity (d). Effective complex dielectric tensor of the sample for *left-* (blue) and *right-*twisted (red) gammadion samples and cross-patterned sample (black). Green curves show the results of the Si substrate (e)–(h) (From [16])

to measure the \tilde{E}_x component with high sensitivity, and 45° polarizer method (with (11.3)) to measure the \tilde{E}_y component. Detailed information about the sample fabrication and experimental setup is described in [16]. Waveforms of the electric fields obtained with the cross-Nicol configuration are shown in Fig. 11.3a and those obtained with the angle of WGP2 at -45° and $+45^\circ$ with x-axis are shown in Figs. 11.3b and c, respectively. The green curves show the signals without sample indicating the waveform of the incident wave, \tilde{E}_{ref} . In Fig. 11.3a, the chiral samples show pronounced orthogonal components of the electric fields and the sign of the electric fields are opposite for right- and left-twisted gammadion samples. This

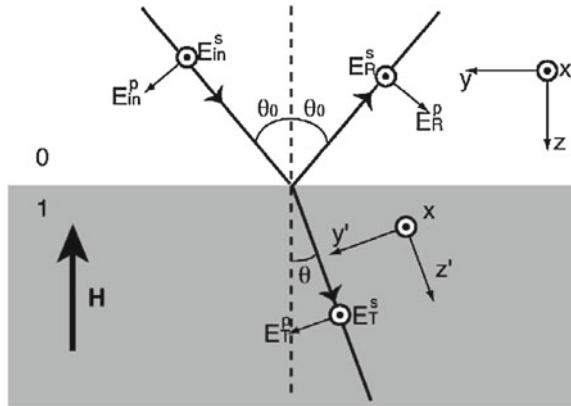
shows that polarization rotation occurs for chiral patterns, and the rotation direction is reverted depending on the chirality of the unit cell pattern. The frequency-domain spectra of the x-component amplitude shown in Fig. 11.3d are almost the same for right- and left- twisted patterns, and much larger than that of the cross pattern. The slight difference observed between the spectra of left- and right-twisted patterns is mainly due to the limitation of reproducibility in the pattern fabrication.

Matrix $\tilde{T}(\omega)$ is obtained by using (11.13). Figure 11.4a and b shows the obtained values of $|\tilde{t}_x|$ and $|\tilde{t}_{xy}|$. The errors indicate the standard deviations for the statistical fluctuation after repeating the measurements eight times. The polarization azimuth rotation and ellipticity angle spectra for the incident linear polarization are calculated using (11.5) and (11.6). Figure 11.4c and d shows the corresponding spectra obtained. Rotations of about 1.5° are observed at 0.4 and 1.2 THz and about 1° at 0.8 THz. From the obtained $\tilde{T}(\omega)$ matrix for the sample, the complex effective dielectric tensor of the sample as a whole can also be determined, including the Si substrate, following the procedure explained above. Figure 11.4e–h shows the spectra of the calculated elements of effective dielectric tensor. The mechanism of polarization rotation of the wave in such a structure will be explained in Sect. 11.3.

11.3 Reflection Mode Time Domain Magneto-Optical Ellipsometry

Reflection mode measurements enable one to investigate the optical properties of materials that are opaque in the frequency region of interest, by analyzing the polarization azimuth rotation ϕ and ellipticity angle η of the reflected light wave. In the case of Magneto-optical Kerr effect (MOKE) measurements, MOKE data are usually analyzed using the small magneto-optical response approximation (SMRA). With SMRA, one assumes that: (i) the off-diagonal component of the dielectric tensor, $\tilde{\epsilon}_{xy}$, is small compared to the diagonal component, $\tilde{\epsilon}_{xx}$ (i.e., $|Q| \ll 1$, where $Q = i\tilde{\epsilon}_{xy}/\tilde{\epsilon}_{xx}$); and (ii) the change of the diagonal component induced by the magnetic field is negligible. Since in this approximation ϕ and η are proportional to $\tilde{\epsilon}_{xy}$, one can obtain the real and imaginary part of $\tilde{\epsilon}_{xy}$ directly from ϕ and η , using the complex refractive index measured with no magnetic field. However, if the medium has a large magneto-optical response, additional measurements are needed to determine the components of the dielectric tensor. This can be done, for example, using a conventional ellipsometry techniques that involve measurements of three polarization-dependent reflection coefficients [17–20]. In the THz frequency region, there are even more opportunities. Specifically, THz measurements are performed in the time domain, so that information on the temporal evolution of the electric field on the THz wave can be obtained. This information allows one to obtain both the amplitude and phase of the THz wave [21, 22], and can be used to obtain the diagonal and off-diagonal components of the dielectric tensor, from experimental data acquired with a conventional MOKE scheme without using SMRA.

Fig. 11.5 Illustration of the reflection problem in the plane of incidence, for the Cartesian coordinate systems $\{xyz\}$ and $\{xy'z'\}$ [23]



In this part, a method is introduced that enables one to determine the real and imaginary parts of $\tilde{\epsilon}_{xx}$ and $\tilde{\epsilon}_{xy}$ from complex reflection coefficients that are obtained in MOKE measurements with oblique incidence [23]. Of course, the method described here can be employed to other materials with off-diagonal components of the dielectric tensor, e.g., chiral media.

11.3.1 MOKE Signal at Oblique Incidence

We assume that the interface coincides with plane $z = 0$ and a permanent magnetic field \mathbf{H} is along the $-z$ direction, while the wave vector of the incident light wave is at angle θ_0 with the interface normal, as shown in Fig. 11.5. For this magneto-optical experiment, this is often referred to as the polar Kerr geometry. For this reason, the measured spectrum will be referred to here as the “magneto-optical Kerr effect spectrum”. It is necessary to note that the Voigt or Cotton-Mouton effect also contributes to the measured signal, since the incidence angle is finite. In the Cartesian coordinate system $\{xyz\}$, the dielectric tensor of the magnetized isotropic medium is presented in the same as (11.10).

In order to obtain the reflection coefficients and the polarization state of the reflected waves, it is convenient to introduce a Cartesian system $\{xy'z'\}$ with the z' axis along the wave vector of the transmitted wave. In this Cartesian coordinate system, the dielectric tensor of the magnetized medium can be presented in the following form:

$$\tilde{\epsilon} = \begin{pmatrix} \tilde{\epsilon}_{xx} & \tilde{\epsilon}_{xy} \cos \theta & -\tilde{\epsilon}_{xy} \sin \tilde{\theta} \\ -\tilde{\epsilon}_{xy} \cos \tilde{\theta} & \tilde{\epsilon}_{xx} + \tilde{\Delta} \sin^2 \tilde{\theta} & \tilde{\Delta} \sin \tilde{\theta} \cos \tilde{\theta} \\ \tilde{\epsilon}_{xy} \sin \tilde{\theta} & \tilde{\Delta} \sin \tilde{\theta} \cos \tilde{\theta} & \tilde{\epsilon}_{zz} + \tilde{\Delta} \cos^2 \tilde{\theta} \end{pmatrix} \quad (11.19)$$

where $\tilde{\Delta} \equiv \tilde{\varepsilon}_{zz} - \tilde{\varepsilon}_{xx}$ and $\tilde{\theta}$ is the refraction angle in medium 1. The evolution equation for the amplitude of the transmitted light wave is described as follows [24]:

$$\left[\tilde{n}^2 (\delta_{ij} - \delta_{iz'}, \delta_{jz'}) - \tilde{\varepsilon}_{ij} \right] = 0, \quad (11.20)$$

where \tilde{n} is the complex refractive index of the sample and the subscripts indicate Cartesian axes x , y' and z' . Equation (11.20) has nontrivial solutions when

$$\begin{aligned} & (\tilde{\varepsilon}_{zz} \cos^2 \tilde{\theta} + \varepsilon_{xx} \sin^2 \tilde{\theta}) \tilde{\eta}^4 - \left[\tilde{\varepsilon}_{xx} \tilde{\varepsilon}_{zz} (1 + \cos^2 \tilde{\theta}) + (\tilde{\varepsilon}_{xx}^2 + \tilde{\varepsilon}_{xy}^2) \sin^2 \tilde{\theta} \right] \tilde{\eta}^2 \\ & + \tilde{\varepsilon}_{zz} (\tilde{\varepsilon}_{xx}^2 + \tilde{\varepsilon}_{xy}^2) = 0. \end{aligned} \quad (11.21)$$

This equation, along with the Snell's law (i.e., $\tilde{\eta} \sin \tilde{\theta} = n_0 \sin \theta_0$ where $\tilde{\theta}$ is the complex refraction angle and n_0 is the refractive index of free space) allows one to arrive at two eigenvalues of the refractive index $\tilde{\eta}$ and the relevant refraction angle $\tilde{\theta}$. Correspondingly, the transmitted light wave can be presented in the following form:

$$\tilde{\mathbf{E}}_T = \tilde{\mathbf{E}}_A e^{-i(\frac{\omega}{c})\tilde{n}A^{z'}} + \tilde{\mathbf{E}}_B e^{-i(\frac{\omega}{c})\tilde{n}B^{z'}} \quad (11.22)$$

Here, subscripts A and B label the modes, i.e., the solutions of (11.21). The magneto-optical response of the medium also results in a nonzero longitudinal component of the transmitted light wave, i.e., $\tilde{\mathbf{E}}_{A,B}$, have nonzero projection on the propagation axis z' . Therefore, the amplitudes of both p and z' components of the transmitted wave are obtained in terms of its s component as $\tilde{E}_{pk} = \tilde{\xi}_k \tilde{E}_{sk}$ and $\tilde{E}_{z'k} = \tilde{\zeta}_k \tilde{E}_{sk}$. Subscript k labels eigenmodes A and B , while coefficients $\tilde{\xi}_k$ and $\tilde{\zeta}_k$ can be obtained from (11.19) and (11.20), respectively as follows:

$$\tilde{\xi}_k = \frac{\tilde{n}^2 - \tilde{\varepsilon}_{xx} - \frac{\tilde{\varepsilon}_{xy}^2 \sin^2 \tilde{\theta}_k}{\tilde{\varepsilon}_{xx} + \tilde{\Delta} \cos^2 \tilde{\theta}_k}}{\tilde{\varepsilon}_{xy} \cos^2 \tilde{\theta}_k + \frac{\tilde{\Delta} \sin^2 \tilde{\theta}_k \cos \tilde{\theta}_k}{\tilde{\varepsilon}_{xx} + \tilde{\Delta} \cos^2 \tilde{\theta}_k}} \quad (11.23)$$

$$\tilde{\zeta}_k = \frac{\tilde{\varepsilon}_{xy}^2 \tilde{\Delta} (\tilde{n}_k^2 - \tilde{\varepsilon}_{xx})}{\tilde{\varepsilon}_{zz} \tilde{\varepsilon}_{xy}} \sin \tilde{\theta}_k \quad (11.24)$$

The polarization effects will be restricted to the p -polarized incident light wave; however, the magneto-optical response ensures the existence of the both s - and p -polarized components in the reflected and transmitted waves (see Fig. 11.5). In the Cartesian system $\{xyz\}$, in which the vacuum-medium interface coincides with the plane $z = 0$, the electric ($\tilde{\mathbf{E}}$) and magnetic ($\tilde{\mathbf{H}}$) fields of the incident (subscript I) and reflected (subscript R) waves can be presented in the following form:

$$\begin{aligned} \tilde{\mathbf{E}}_I &= (0, \tilde{E}_{Ip} \cos \theta_0, \tilde{E}_{Ip} \sin \theta_0) \\ \tilde{\mathbf{H}}_I &= \frac{n_0}{c} (\tilde{E}_{Ip}, 0, 0) \end{aligned} \quad (11.25)$$

$$\begin{aligned}\tilde{\mathbf{E}}_R &= (\tilde{E}_{RS}, -\tilde{E}_{Rp} \cos \theta_0, \tilde{E}_{Rp} \sin \theta_0) \\ \tilde{\mathbf{H}}_R &= \frac{n_0}{c} (-\tilde{E}_{Rp}, -\tilde{E}_{RS} \cos \theta_0, \tilde{E}_{RS} \sin \theta_0)\end{aligned}\quad (11.26)$$

As shown in (11.22), the transmitted wave consists of two eigenmodes; the complex amplitude in the Cartesian system $\{xyz\}$ and relevant electric and magnetic fields are expressed by the following:

$$\begin{aligned}\tilde{\mathbf{E}}_k &= (\tilde{E}_{sk}, \tilde{E}_{pk} \cos \tilde{\theta}_k - \tilde{E}_{zk} \sin \tilde{\theta}_k, \tilde{E}_{pk} \sin \tilde{\theta}_k + \tilde{E}_{zk} \cos \tilde{\theta}_k) \\ \tilde{\mathbf{H}}_k &= \frac{n_k}{c} (-\tilde{E}_{pk}, \tilde{E}_{sk} \cos \tilde{\theta}_k, -\tilde{E}_{sk} \sin \tilde{\theta}_k)\end{aligned}\quad (11.27)$$

where $k = A, B$. The continuity of the tangential components of the electric and magnetic field at $z = 0$ gives

$$\begin{aligned}\tilde{E}_{RS} &= \tilde{E}_{sA} + \tilde{E}_{sB} \\ \tilde{E}_{Ip} \cos \theta_0 - \tilde{E}_{Rp} \cos \theta_0 &= \tilde{\chi}_A \tilde{E}_{sA} + \tilde{\chi}_B \tilde{E}_{sB} \\ -n_0 \tilde{E}_{Ip} - n_0 \tilde{E}_{Rp} &= -\tilde{n}_A \tilde{\xi}_A \tilde{E}_{sA} - \tilde{n}_B \tilde{\xi}_B \tilde{E}_{sB} \\ -n_0 \tilde{E}_{RS} \cos \theta_0 &= \tilde{n}_A \tilde{E}_{sA} \cos \tilde{\theta}_A + \tilde{n}_B \tilde{E}_{sA} \cos \tilde{\theta}_A\end{aligned}\quad (11.28)$$

where

$$\tilde{\chi}_k = \tilde{\xi}_k \cos \tilde{\theta}_k - \tilde{\zeta}_k \sin \tilde{\theta}_k. \quad (11.29)$$

The Solution for (11.28) gives the following expressions for the amplitude reflection coefficients:

$$\tilde{r}_{pp} = \frac{\tilde{E}_{Rp}}{\tilde{E}_{Ip}} = \frac{(\tilde{n}_A \tilde{\xi}_A - \tilde{n}_0 \tilde{\chi}_A / \cos \theta_0) \tau_B - (\tilde{n}_B \tilde{\xi}_B - \tilde{n}_0 \tilde{\chi}_B / \cos \theta_0) \tau_A}{(\tilde{n}_A \tilde{\xi}_A + \tilde{n}_0 \tilde{\chi}_A / \cos \theta_0) \tau_B - (\tilde{n}_B \tilde{\xi}_B + \tilde{n}_0 \tilde{\chi}_B / \cos \theta_0) \tau_A} \quad (11.30)$$

$$\tilde{r}_{sp} = \frac{\tilde{E}_{RS}}{\tilde{E}_{Ip}} = \frac{2n_0(\tilde{n}_B \cos \tilde{\theta}_B - \tilde{n}_A \cos \tilde{\theta}_A)}{(\tilde{n}_A \tilde{\xi}_A + \tilde{n}_0 \tilde{\chi}_A / \cos \theta_0) \tau_B - (\tilde{n}_B \tilde{\xi}_B + \tilde{n}_0 \tilde{\chi}_B / \cos \theta_0) \tau_A} \quad (11.31)$$

where

$$\tau_k = \tilde{n}_k \cos \tilde{\theta}_k + n_0 \cos \theta_0. \quad (11.32)$$

It should be noted here that (11.30) and (11.31) are valid for an oblique angle of incidence and any magnitude of the magneto-optical response. Since \tilde{r}_{pp} and \tilde{r}_{sp} are functions of three complex variables; $\tilde{\varepsilon}_{xx}$, $\tilde{\varepsilon}_{xy}$, $\tilde{\varepsilon}_{zz}$ we can calculate $\tilde{\varepsilon}_{xx}$ and $\tilde{\varepsilon}_{xy}$ from the obtained complex reflection coefficients, as long as $\tilde{\varepsilon}_{zz}$ is known. For example, $\tilde{\varepsilon}_{zz}$ can be obtained with reflection measurement at normal incidence because the reflection coefficients at normal incidence, \tilde{r}_n is described as $\tilde{r}_n = (1 - \sqrt{\tilde{\varepsilon}_{zz}}) / (1 + \sqrt{\tilde{\varepsilon}_{zz}})$.

By using conventional formulas for the polarization azimuthangle ϕ and ellipticity angle η in terms of the Cartesian components of the electric field \mathbf{E} [25];

$$\begin{aligned}\phi &= \frac{1}{2} \tan^{-1} \left(\frac{2\text{Re}\{\tilde{E}_x \tilde{E}_y^*\}}{|\tilde{E}_x|^2 - |\tilde{E}_y|^2} \right), \\ \eta &= \frac{1}{2} \sin^{-1} \left(\frac{2\text{Im}\{\tilde{E}_x \tilde{E}_y^*\}}{|\tilde{E}_x|^2 + |\tilde{E}_y|^2} \right),\end{aligned}\quad (11.33)$$

One can now readily obtain ϕ and η , in terms of \tilde{r}_{pp} and \tilde{r}_{sp} , with (11.30) and (11.31):

$$\begin{aligned}\phi &= -\frac{1}{2} \arg \left(\frac{\tilde{r}_{pp} - i\tilde{r}_{sp}}{\tilde{r}_{pp} + i\tilde{r}_{sp}} \right) \\ \eta &= \tan^{-1} \left(\frac{|\tilde{r}_{pp} - i\tilde{r}_{sp}| - |\tilde{r}_{pp} + i\tilde{r}_{sp}|}{|\tilde{r}_{pp} - i\tilde{r}_{sp}| + |\tilde{r}_{pp} + i\tilde{r}_{sp}|} \right)\end{aligned}\quad (11.34)$$

The procedure based on (11.30), (11.31), and (11.34) will be outlined for the evaluation of $\tilde{\epsilon}_{xx}$ and $\tilde{\epsilon}_{xy}$ from ellipsometric experiments below.

At the end of this section, the obtained Eqs. (11.30) and (11.31) are compared with the result of SMRA. The difference between mode *A* and *B* is reduced to the difference of the sign of magneto-optical response; therefore, + and - subscripts are used instead of *A* and *B*. Substituting the SMRA condition, i.e., $|Q| \equiv |i\tilde{\epsilon}_{xy}|/|\tilde{\epsilon}_{xx}| \ll 1$ and $\tilde{\Delta} \approx 0$ in Eq. (11.21), the following is obtained:

$$\tilde{n}_k = \tilde{n} \left(1 \pm \frac{i\tilde{\alpha}\tilde{Q}}{2} \right), \quad (11.35)$$

$$\sin \tilde{\theta}_k = \frac{n_0 \sin \theta_0}{\tilde{n}} \left(1 \pm \frac{i\tilde{\alpha}\tilde{Q}}{2} \right), \quad (11.36)$$

where $\tilde{\alpha} = \sqrt{n_0^2 \sin^2 \theta_0 / \tilde{\epsilon}_{zz} - 1}$, $\tilde{n} = \sqrt{\tilde{\epsilon}_{zz}}$ is the index of refraction of medium 1 without a magnetic field. With these variables, the quantities $\tilde{\xi}_k$, $\tilde{\zeta}_k$ and $\tilde{\chi}_k$ can be reduced to the following:

$$\tilde{\xi}_k = \frac{\mp \tilde{\alpha} - i\tilde{Q} \sin^2 \tilde{\theta} + i(\tilde{\alpha}^2 \tilde{Q}/2) \tan^2 \tilde{\theta}}{\cos \tilde{\theta}}, \quad (11.37)$$

$$\tilde{\zeta}_k = i\tilde{Q} \sin \tilde{\theta}, \quad (11.38)$$

$$\tilde{\chi}_k = \mp \tilde{\alpha} - 2i\tilde{Q} \sin^2 \tilde{\theta}. \quad (11.39)$$

Substituting these into (11.30) and (11.31), one obtains

$$\tilde{r}_{pp} = \frac{\tilde{n} \cos \theta_0 - \tilde{n} \cos \theta_0}{\tilde{n} \cos \theta_0 + \tilde{n} \cos \theta_0} \quad (11.40)$$

$$\tilde{r}_{sp} = \frac{i \tilde{Q} n_0 \tilde{n} \cos \theta_0}{(\tilde{n} \cos \tilde{\theta} + n_0 \cos \theta_0)(\tilde{n} \cos \theta + n_0 \cos \theta_0) \cos \tilde{\theta}} \quad (11.41)$$

These are the same as (2.31) in [26].

11.3.2 Analysis Based on Intensity Measurements

Before considering in detail the time domain THz ellipsometry, a conventional MOKE technique is revisited for optical frequencies based on light intensity measurements. With MOKE intensity-based measurement techniques, the polarization azimuth angle ϕ and ellipticity angle η of the reflected electromagnetic wave under the magnetic field are obtained [27]. Since ϕ and η depend only on the ratio $\tilde{r}_{sp}/\tilde{r}_{pp}$, see (11.34), both the real and imaginary parts of $\tilde{r}_{sp}/\tilde{r}_{pp}$ can be determined from the MOKE experiment.

When the SMRA conditions are fulfilled (i.e., when the magneto-optical response is small $|Q| \ll 1$, and dependence of $\tilde{\epsilon}_{xx}$ on the magnetic field is negligible), ϕ and η are less than a few degrees. In such a case, (11.30), (11.31) and (11.34) are reduced to the following SMRA equation [26]:

$$\begin{pmatrix} \phi \\ \eta \end{pmatrix} = \begin{pmatrix} \text{Re} \\ \text{Im} \end{pmatrix} \frac{n_0 \tilde{\epsilon}_{xy}}{(\tilde{\epsilon}_{xx} - n_0^2) \sqrt{\tilde{\epsilon}_{xx}}} \frac{\cos \theta_0}{\cos(\theta_0 + \tilde{\theta})} \quad (11.42)$$

In (11.42), $\tilde{\epsilon}_{xx}$ and $\tilde{\epsilon}_{xy}$ are separated; therefore, if $\tilde{\epsilon}_{xx}$ is measured independently (e.g. from the reflectivity at zero magnetic field), the real and imaginary part of $\tilde{\epsilon}_{xy}$ can be determined directly from the measured values of ϕ and η .

When the magneto-optical response is large, SMRA cannot be applicable. In such case, the diagonal component of the dielectric tensor is not negligible and one needs to perform additional measurements to determine $\tilde{\epsilon}_{xx}$ and $\tilde{\epsilon}_{xy}$, even in the case of normal incidence. In particular, this can be done using the conventional ellipsometry technique [17–20]. In this technique, $\tilde{R}_{pp} = \tilde{r}_{pp}/\tilde{r}_{ss}$, $\tilde{R}_{sp} = \tilde{r}_{sp}/\tilde{r}_{ss}$, and $\tilde{R}_{ps} = \tilde{r}_{ps}/\tilde{r}_{ss}$ can be measured by rotating the analyzer with a finite angular frequency [18], while $\tilde{\epsilon}_{xx}$, $\tilde{\epsilon}_{xy}$, and $\tilde{\epsilon}_{zz}$ are obtained by fitting the measured reflection coefficients [19] using exact equations [20].

11.3.3 Analysis Based on the Time Domain THz Ellipsometry

In this section, we explain a method to determine $\tilde{\epsilon}_{xx}$ and $\tilde{\epsilon}_{xy}$ from experimentally obtained \tilde{r}_{pp} and \tilde{r}_{sp} values, when $\tilde{\epsilon}_{zz}$ is obtained from independent measurements. The method is based on time domain THz spectroscopy one; more specifically as “time-domain THz ellipsometry”. The THz spectroscopy technique enables us to

reveal the temporal evolution of the THz electric field [21, 22] and to obtain the phase and amplitude of the reflected THz wave, and the complex reflection coefficient. This technique gives both the real and imaginary parts of $\tilde{r}_{pp}/\tilde{r}_{pp}$ and $\tilde{r}_{sp}/\tilde{r}_p$, where \tilde{r}_p is a reflection coefficient that is determined from a given $\tilde{\epsilon}_{zz}$ [28]. As described below, this procedure allows one to arrive at real and imaginary parts of \tilde{r}_{pp} and \tilde{r}_{sp} , therefore, to obtain ϕ and η , see (11.34).

The case where the incident wave $\tilde{\mathbf{E}}_{in}$ has p-polarization is considered:

$$\tilde{\mathbf{E}}_{in} = \tilde{E}_{in} \mathbf{e}_p \quad (11.43)$$

where $\mathbf{e}_{s,p}$ are eigenvectors for s- and p- polarization. The refracted wave $\tilde{\mathbf{E}}_r^B$ in the case with an external magnetic field, is;

$$\tilde{\mathbf{E}}_r^B = \tilde{E}_{r,p}^B \mathbf{e}_p + \tilde{E}_{r,s}^B \mathbf{e}_s = (\tilde{r}_{pp}^B \mathbf{e}_p + \tilde{r}_{sp}^B \mathbf{e}_s) \tilde{E}_{in}. \quad (11.44)$$

The refracted wave $\tilde{\mathbf{E}}_r^0$, in the case without external magnetic field, is;

$$\tilde{\mathbf{E}}_r^0 = \tilde{E}_{r,p}^0 \mathbf{e}_p = \tilde{r}_p \tilde{E}_{in} \mathbf{e}_p. \quad (11.45)$$

The detected THz electric fields after a polarizer, with angle to p-polarization is φ , are described as follows;

$$\tilde{E}_r^{B,\varphi} = (\tilde{r}_{pp} \cos \varphi + \tilde{r}_{sp} \sin(\varphi)) \tilde{E}_{in} f(\varphi) \quad (11.46)$$

$$\tilde{E}_r^{0,\varphi} = (\tilde{r}_p \cos \varphi) \tilde{E}_{in} f(\varphi) \quad (11.47)$$

where $f(\varphi)$ is detection efficiency that depends on the polarization of THz wave.

The ratio $\tilde{\epsilon}^{B,\varphi} \equiv \tilde{E}_r^{B,\varphi} / \tilde{E}_r^{0,\varphi}$ is measured for two different polarizer angles φ_1 and φ_2 ;

$$\tilde{\epsilon}^{B,\varphi,i} = \frac{\tilde{r}_{pp} \cos \varphi_j + \tilde{r}_{sp} \sin \varphi_j}{\tilde{r}_p \cos \varphi_j} (j = 1, 2). \quad (11.48)$$

Here, \tilde{r}_{pp} and \tilde{r}_{sp} can be calculated from (11.48) as follows;

$$\tilde{r}_{pp} = \frac{\tilde{\epsilon}^{B,\varphi_1} \tan \varphi_2 - \tilde{\epsilon}^{B,\varphi_2} \tan \varphi_1}{\tan \varphi_2 - \tan \varphi_1} \tilde{r}_p \quad (11.49)$$

$$\tilde{r}_{sp} = \frac{\tilde{\epsilon}^{B,\varphi_1} - \tilde{\epsilon}^{B,\varphi_2}}{\tan \varphi_1 - \tan \varphi_2} \tilde{r}_p. \quad (11.50)$$

In summary, \tilde{r}_{pp} and \tilde{r}_{sp} can be obtained by measuring complex THz electric fields at two different polarizer angles with and without external magnetic fields. If we set $\varphi_1 = \pi/4$ and $\varphi_2 = -\pi/4$, (11.49) and (11.50) are simplified as follows;

$$\tilde{r}_{pp} = \frac{\tilde{\epsilon}^{B,\pi/4} + \tilde{\epsilon}^{B,-\pi/4}}{2} \tilde{r}_p \quad (11.51)$$

$$\tilde{r}_{sp} = \frac{\tilde{\epsilon}^{B,\pi/4} - \tilde{\epsilon}^{B,-\pi/4}}{2} \tilde{r}_p \quad (11.52)$$

The next step includes rewriting (11.30) and (11.31) to obtain $\tilde{\epsilon}_{xx}$ and $\tilde{\epsilon}_{xy}$ as functions of \tilde{r}_{pp} and \tilde{r}_{sp} ;

$$\begin{aligned} \tilde{\epsilon}_{xx} &= \tilde{\epsilon}_{xx}(\tilde{r}_{pp}, \tilde{r}_{sp}, \tilde{\epsilon}_{zz}). \\ \tilde{\epsilon}_{xy} &= \tilde{\epsilon}_{xy}(\tilde{r}_{pp}, \tilde{r}_{sp}, \tilde{\epsilon}_{zz}). \end{aligned} \quad (11.53)$$

Following these nonlinear simultaneous equations, $\tilde{\epsilon}_{xx}$ and $\tilde{\epsilon}_{xy}$ are calculated from the measured \tilde{r}_{pp} and \tilde{r}_{sp} and the $\tilde{\epsilon}_{zz}$ given by using numerical calculations, such as the Newton-Raphson method [29].

The procedure to obtain $\tilde{\epsilon}_{xx}$ and $\tilde{\epsilon}_{xy}$ is summarized in Fig. 11.6. The numbers in Fig. 11.6 correspond to the following numbers.

1. Measure the incident THz waves, $E_{in}(t)$, and the reflected THz wave, $E_{out}(t)$, without external magnetic field.
2. Calculate $\tilde{r}_p = \mathcal{F}[E_{out}(t)]/\mathcal{F}[E_{in}(t)]$, where $\mathcal{F}[\dots]$ corresponds to a Fourier transformation.
3. Measure the reflected waves with and without external magnetic field, $E_{out,B}^{\pi/4}(t)$ and $E_{out}^{-\pi/4}(t)$, with the wire-grid polarizer $\varphi = \pi/4$.
4. Measure the reflected THz waves with and without external magnetic field, $E_{out,B}^{-\pi/4}(t)$ and $E_{out}^{\pi/4}(t)$, with the wire-grid polarizer $\varphi = -\pi/4$.
5. Calculate the ratios $\mathcal{F}[E_{out,B}^{\pm\pi/4}(t)]/\mathcal{F}[E_{out}^{\pm\pi/4}(t)]$. These correspond to $\tilde{\epsilon}^{B,\varphi_i}$ in (11.48).
6. Calculate \tilde{r}_{pp} and \tilde{r}_{sp} using (11.51) and (11.52). ϕ and η can be obtained from (11.34).
7. Obtain $\tilde{\epsilon}_{zz}$ from \tilde{r}_p with numerical calculation.
8. Obtain $\tilde{\epsilon}_{xx}$ and $\tilde{\epsilon}_{xy}$ from \tilde{r}_{pp} , \tilde{r}_{sp} ; $\tilde{\epsilon}_{zz}$ with numerical calculations.

11.3.4 Analysis Example

In this section, the procedure explained above can be employed to obtain the complex dielectric tensor using the results of the THz MOKE measurements for n -type InAs.

The first step is to measure the complex reflectivity coefficient \tilde{r}_p in the absence of the magnetic field. A numerical method for the misplacement phase error correction is effective for THz time domain reflection-mode spectroscopy [30, 31]. Since the crystal symmetry does not permit any current parallel to the magnetic field, it is natural to assume that the field along z axis (see Fig. 11.1) does not change the longitudinal component of the dielectric tensor, i.e., $\tilde{\epsilon}_{zz}(\mathbf{H}) = \tilde{\epsilon}_{zz}(\mathbf{H} = 0)$. Within

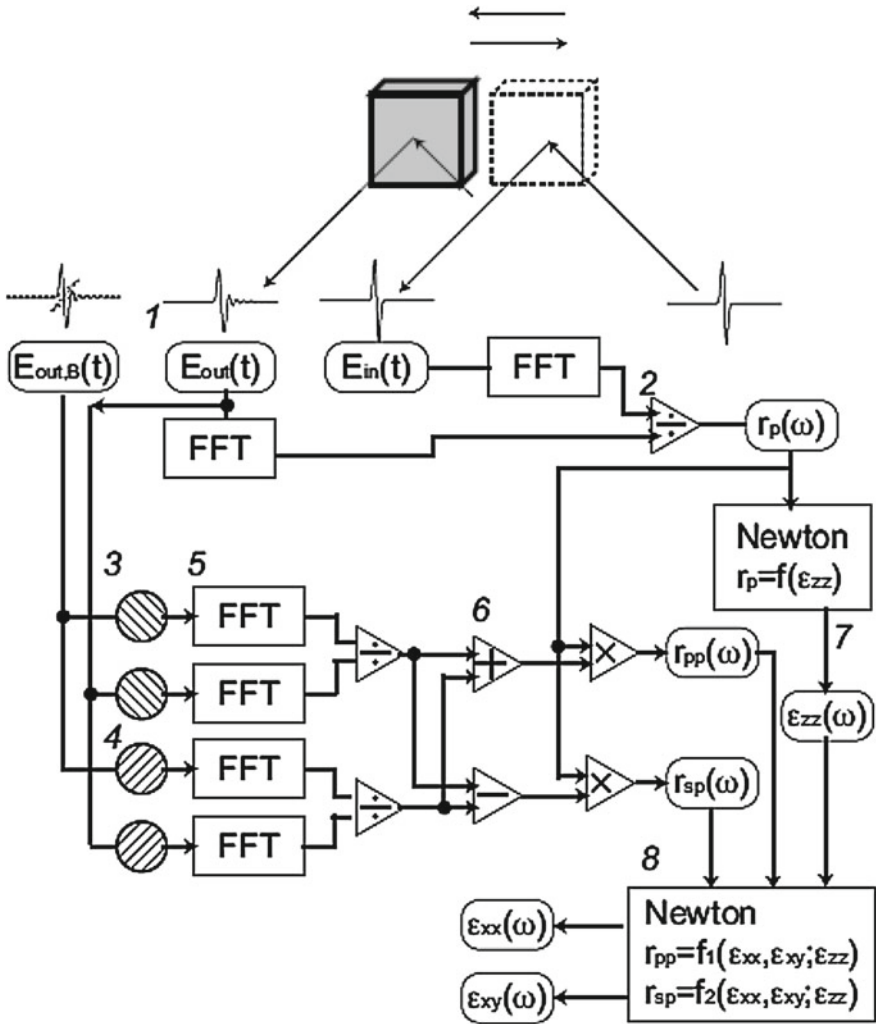


Fig. 11.6 Schematic illustration of the calculation procedure

this approximation, $\tilde{\epsilon}_{zz}$ can be calculated from \tilde{r}_p [21, 22]. The measured THz spectra of \tilde{r}_p and $\tilde{\epsilon}_{zz}$ are shown in Fig. 11.7. Second, by using the experimental procedure described above with a 45° angle of incidence, $\tilde{r}_{pp}/\tilde{r}_p$ and $\tilde{r}_{sp}/\tilde{r}_p$ are measured, which allows us to obtain \tilde{r}_{pp} and \tilde{r}_{sp} , as shown in Fig. 11.4.

From the above complex reflection coefficients \tilde{r}_{pp} and \tilde{r}_{sp} , the polarization plane azimuth angle ϕ and ellipticity angle η of the reflected wave (i.e., MOKE signal) can be obtained, as shown in Fig. 11.9 [28]. In this system, the dielectric response in the THz frequency region originates from the intraband motion of conduction electrons. Therefore, one can use the Drude model to describe the THz response. In the Drude

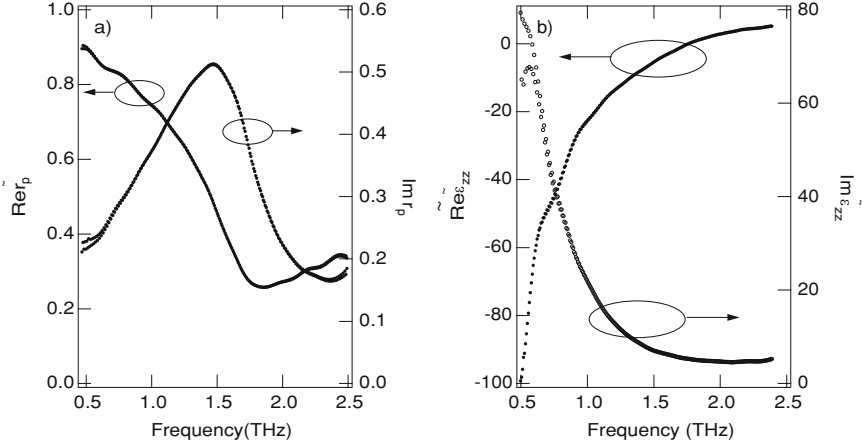


Fig. 11.7 The spectra of **a** \tilde{r}_p and **b** \tilde{z}_{zz} , $\tilde{\varepsilon}_{zz}$ is calculated from measured value of \tilde{r}_p [23]

model framework, the components of the dielectric tensor in the presence of the magnetic field are as follows:

$$\begin{aligned}\tilde{\varepsilon}_{xx} &= \varepsilon_b \left[1 - \frac{\omega_p^2(\omega^2 + i\omega\Gamma)}{(\omega^2 + i\omega\Gamma)^2 - \omega^2\omega_c^2} \right], \\ \tilde{\varepsilon}_{xy} &= \frac{i\omega_p^2\varepsilon_b\omega\omega_c}{(\omega^2 + i\omega\Gamma)^2 - \omega^2\omega_c^2}, \\ \tilde{\varepsilon}_{zz} &= \varepsilon_b \left[1 - \frac{\omega_p^2}{\omega^2 + i\omega\Gamma} \right],\end{aligned}\quad (11.54)$$

where ε_b is the background dielectric constant, $\omega_p = \sqrt{Ne^2/\varepsilon_b m^*}$ is the plasma frequency, N and m^* are the carrier density and effective mass, Γ is the damping constant, and $\omega_c = e|H|/m^*c$ is the cyclotron frequency (Fig. 11.8). Solid lines in Fig. 11.9 represent this Drude model fitting, which are obtained using (11.30), (11.31) and (11.34) at $\omega_p = 1.8$ THz (the corresponding carrier density is $2.1 \times 10^{16} \text{ cm}^{-3}$), $\Gamma = 0.75$ THz, $\omega_c = 0.46$ THz, $\varepsilon_b = 16.3$ and $m^* = 0.026m_e$. One can observe a pronounced resonance feature in the vicinity of the plasma frequency. This effect is often referred to as the magnetoplasma resonance [32].

By using the measured complex reflection coefficients \tilde{r}_{pp} , \tilde{r}_{sp} , and \tilde{z}_{zz} , obtained in the first step, one can reconstruct the diagonal and off-diagonal component of the dielectric tensor by inversely solving (11.30) and (11.31). Here, the Newton-Raphson method for this procedure was employed [29].

Figure 11.10 shows the spectra of the obtained complex dielectric tensor. For comparison, the complex dielectric tensor calculated with the Drude model is also shown; the parameters of which are obtained above. One can observe from Fig. 11.10

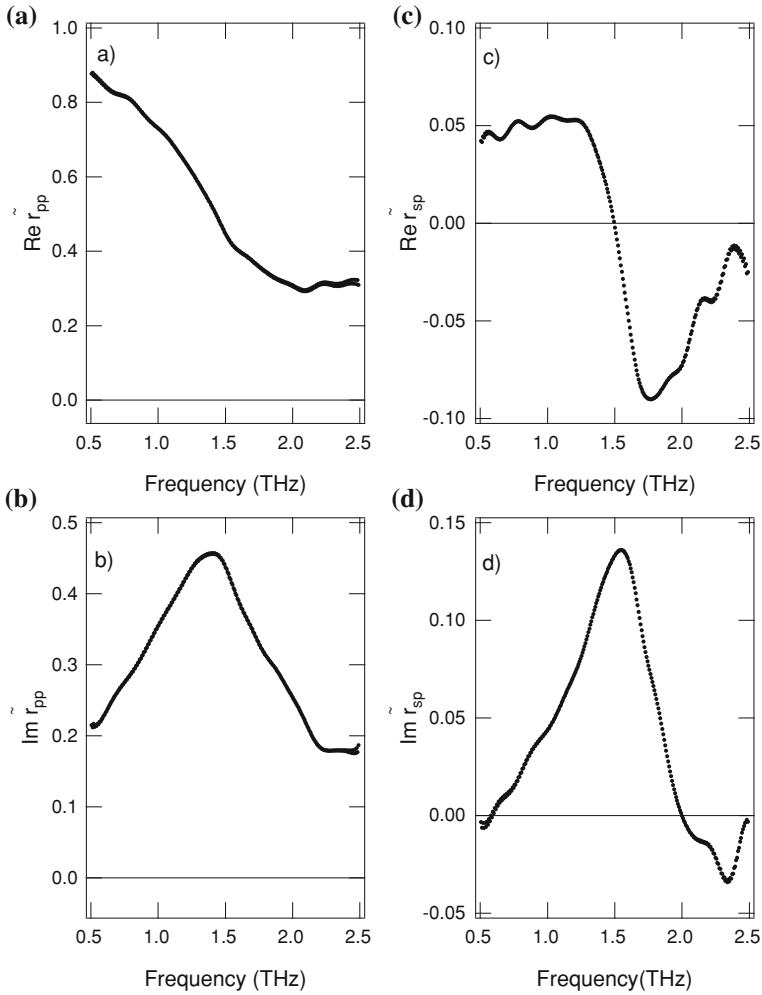
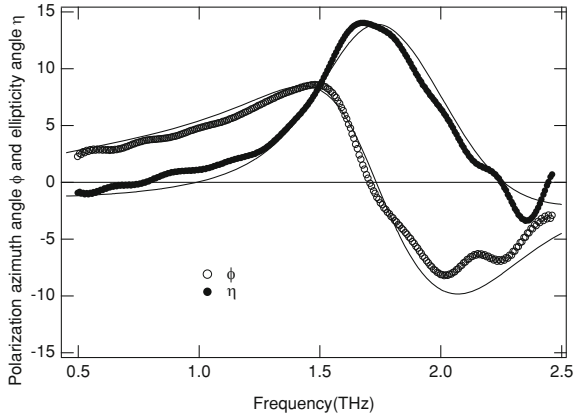


Fig. 11.8 Spectra of (a) $\text{Re}\{\tilde{r}_{pp}\}$, (b) $\text{Im}\{\tilde{r}_{sp}\}$, (c) $\text{Re}\{\tilde{r}_{sp}\}$, and (d) $\text{Im}\{\tilde{r}_{sp}\}$ obtained from measured $\tilde{r}_{pp}/\tilde{r}_p$, $\tilde{r}_{sp}/\tilde{r}_p$, and \tilde{r}_p [23]

that $\tilde{\epsilon}_{xx}$ and $\tilde{\epsilon}_{xy}$, directly calculated from the complex reflection coefficients and do not rely on the particular mechanism of the MOKE, correspond to the ones calculated using the Drude model with parameters obtained from the measured MOKE signal. A slightly bigger (in comparison with other components) discrepancy between the calculated $\text{Im}\{\tilde{\epsilon}_{xy}\}$ and its MOKE fitting is due to the smallness of the magnitude of $\text{Im}\{\tilde{\epsilon}_{xy}\}$.

Finally, the conventional analysis based on SMRA are compared with the results obtained above. Figure 11.11 shows the frequency dependence of the off-diagonal component of the dielectric tensor, $\tilde{\epsilon}_{xy}$, obtained from the measured ϕ and $\tilde{\epsilon}_{zz}$ by

Fig. 11.9 The measured spectra of ϕ (circles) and η (dots) calculated from measured and $\tilde{r}_{pp}/\tilde{r}_p$ and $\tilde{r}_{sp}/\tilde{r}_p$. Solid curves show the results of Drude model fitting [23]



using SMRA (i.e., assuming that $|Q| \ll 1$ and $\tilde{\epsilon}_{xx} \approx \tilde{\epsilon}_{zz}$) and by using the refined method. One can observe from Fig. 11.11 that the obtained off-diagonal component of the dielectric tensor, $\tilde{\epsilon}_{xy}^{ex}$, shows better correspondence with the Drude fitting of measured MOKE signals than $\tilde{\epsilon}_{xy}$, which was calculated in the SMRA framework. Results of the THz experiment presented here are apparently beyond the range of applicability of SMRA ($|Q| \approx 0.5$ and $|\phi + i\eta| \approx 0^{-1}$) and require a more rigorous treatment.

Figure 11.12a and b shows the spectra for the polarization rotation ϕ and ellipticity angle η , respectively, calculated from the measured off-diagonal component of the dielectric tensor $\tilde{\epsilon}_{xy}^{ex}$ using SMRA, calculated from the exact formulae developed above, and measured by the experiment. The correspondence of the measured values and those calculated using the exact expression shows the correctness of the analysis. One can observe from Fig. 11.11 that SMRA results in a nonnegligible deviation in the polarization rotation and ellipticity angle from those measured, particularly in the vicinity of the plasma resonance of 1.8 THz.

In order to describe the difference between the refined method and SMRA, a value is introduced, $\delta = |\tilde{\epsilon}_{xy} - \tilde{\epsilon}_{xy}^{SMRA}|/|\tilde{\epsilon}_{xy}|$; this is a quantitative measure of the SMRA imposed error. Note that here the dielectric tensor is used to calculate the Drude model with parameters obtained from the MOKE signal fits described previously. From this tensor, one can calculate the MOKE signal $\phi + i\eta$, and calculate $\tilde{\epsilon}_{xy}^{SMRA}$ from $\phi + i\eta$ using SMRA. Figure 11.13a shows the frequency dependence of δ and $|Q| = |\tilde{\epsilon}_{xy}/\tilde{\epsilon}_{xx}|$ in the frequency range from 0.5 to 2.5 THz. In Fig. 11.13b, δ is plotted versus $\phi + i\eta$, using frequency as a parameter, where the dotted line and bold line correspond to the frequency regions above and below ω_p .

One can observe that with $\omega > \omega_p$, δ increases monotonically as $|\phi + i\eta|$ increases. With $\omega < \omega_p$, δ does not reduce monotonically as is reduced. From Fig. 11.13a and b it can be noticed that the small MOKE signal does not always correspond to a small $\tilde{\epsilon}_{xy}$ (i.e., $|Q| \ll 1$). In other words, SMRA may fail even when $|\phi + i\eta|$ is relatively small. Note that in metals, for which the magneto-optical response is conventionally

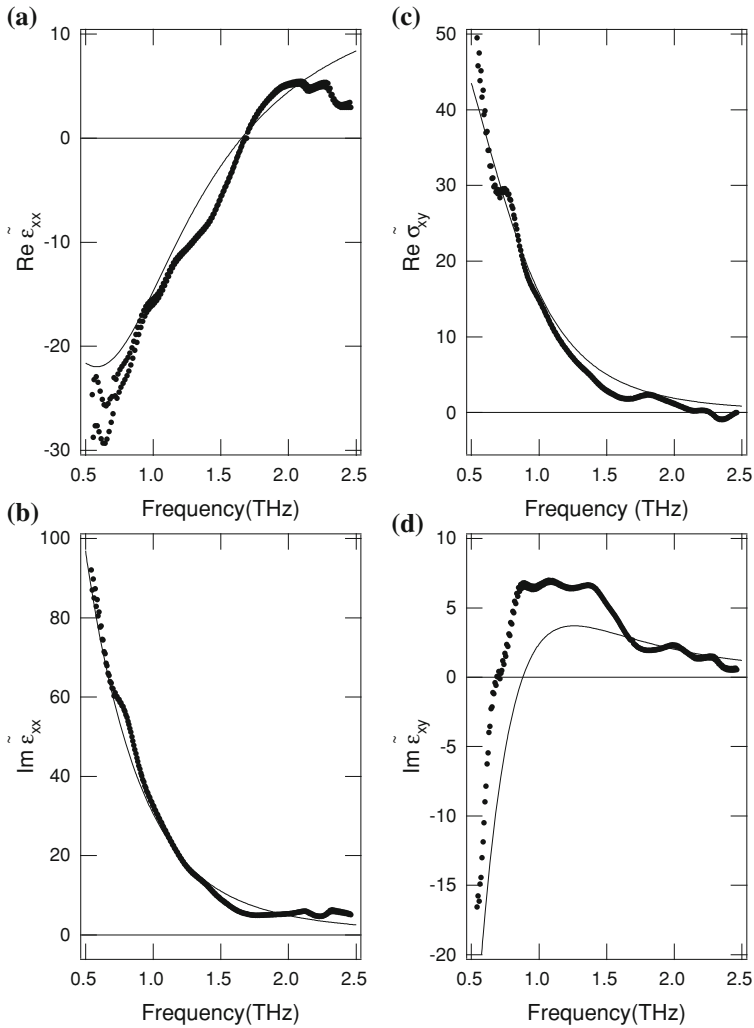


Fig. 11.10 Frequency dependence of (a) $\text{Re}\{\tilde{\epsilon}_{xx}\}$, (b) $\text{Im}\{\tilde{\epsilon}_{xx}\}$, (c) $\text{Re}\{\tilde{\epsilon}_{xy}\}$, and (d) $\text{Im}\{\tilde{\epsilon}_{xy}\}$ obtained from measured spectra of \tilde{r}_{pp} , \tilde{r}_{sp} , and \tilde{r}_p (dots) and calculated spectra from Drude model with parameters obtained by fitting of MOKE signals (lines) [23]

studied by using the MOKE technique, $|Q|$ is of the order of 10^{-2} , and SMRA is usually valid. However, a more careful analysis is necessary when the frequency of the incident wave is resonant to the intrinsic longitudinal electromagnetic modes of the medium, such as plasmons, optical phonons, longitudinal excitons, etc.

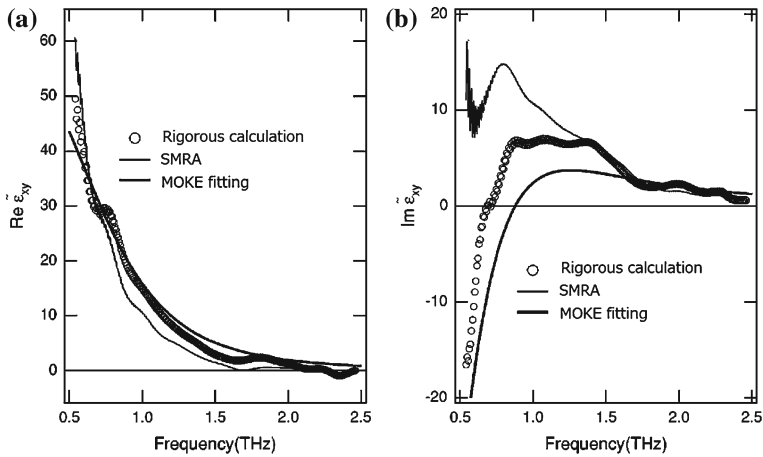


Fig. 11.11 Off-diagonal component of the dielectric tensor obtained from rigorous calculations with our method (*circles*), SMRA (*solid line*), and Drude model fitting (*bold line*) with MOKE [23]

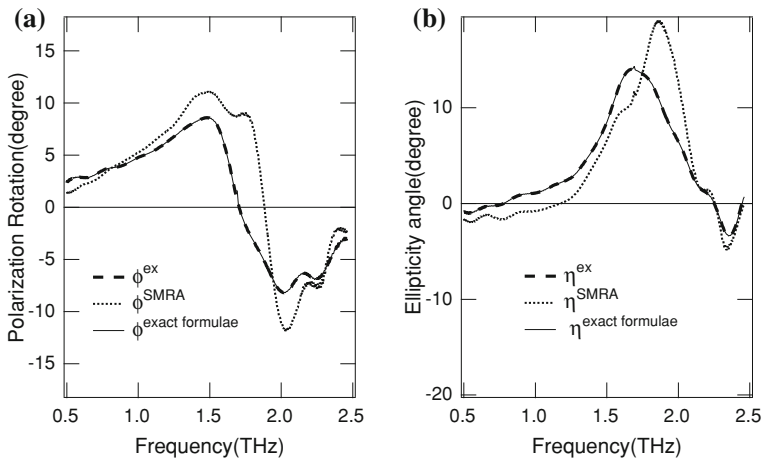


Fig. 11.12 Polarization azimuth (a) and ellipticity angle (b) calculated from the experimentally determined dielectric tensor using SMRA (*dotted lines*), calculated using exact formulae (*thin solid lines*), and measured in the experiment (*bold broken lines*) [23]

11.4 Active Polarization Control of Terahertz Wave

In the optical region, photoelastic modulators are commonly used for highly sensitive polarization measurements [27]. Such polarization modulation devices are required to develop THz polarimetry. If optical activity is induced by an external stimulus, such as photoexcitation in an artificial structure that was introduced in the Sect. 11.2, the polarization state of the THz wave can be modulated. In this section, the optical

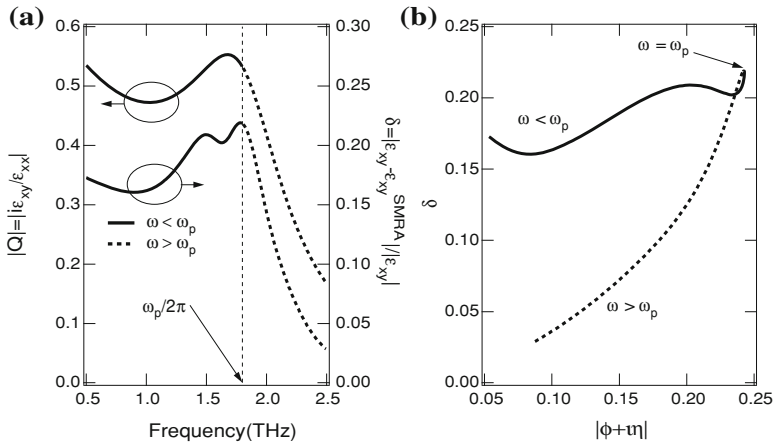


Fig. 11.13 SMRA versus exact analysis [23]. **a** Frequency dependence of the magneto-optical constant Q and the error δ . **b** The relation between δ and the magnitude of MOKE signal

activity in the THz region induced by photoexcitation on silicon is discussed with a subwavelength chiral-patterned metal mask [31]. Two-dimensional arrays of gold chiral masks are fabricated on a silicon substrate, which is an achiral medium. In contrast to the case of visible light waves [9–11, 15], for THz waves gold-patterned films are too thin to induce three-dimensional effects. No significant polarization effect was observed for single-layered metal chiral grating samples, as previously reported [16]. However, significant THz optical activity was observed, illuminating a single-layered chiral grating patterned on silicon samples. The metal chiral gratings and photogenerated carrier distribution form a conducting three-dimensional chiral structure.

Figure 11.14a shows optical microscopic images of the samples. Arrays of achiral (cross) and chiral (gammadion) patterns are fabricated with electron-beam lithography and consist of 100 nm thick gold film on a high resistance Si substrate. A thin Cr film of 5 nm thickness exists between the gold film and the substrate to improve adhesion. The structures are arranged in a two-dimensional square lattice with a period of 100 μm .

Figure 11.14b shows a schematic description of the experimental setup of THz wave polarization measurements. A regenerative amplified Ti:sapphire laser is used as a light source. It is divided into three beams and is used for the generation and detection of THz radiation and photoexcitation of the sample. The optical rectification and free-space electro-optic sampling with ZnTe crystals were employed for THz generation and detection, respectively. To detect the polarization state of THz radiation, the time domain waveforms were measured with wire-grid polarizers, as described in the Sect. 11.2 [33].

Both the pump beam and THz radiation are incoming on the sample surface at normal incidence, and their diameters are approximately 3 and 2 mm, respectively.

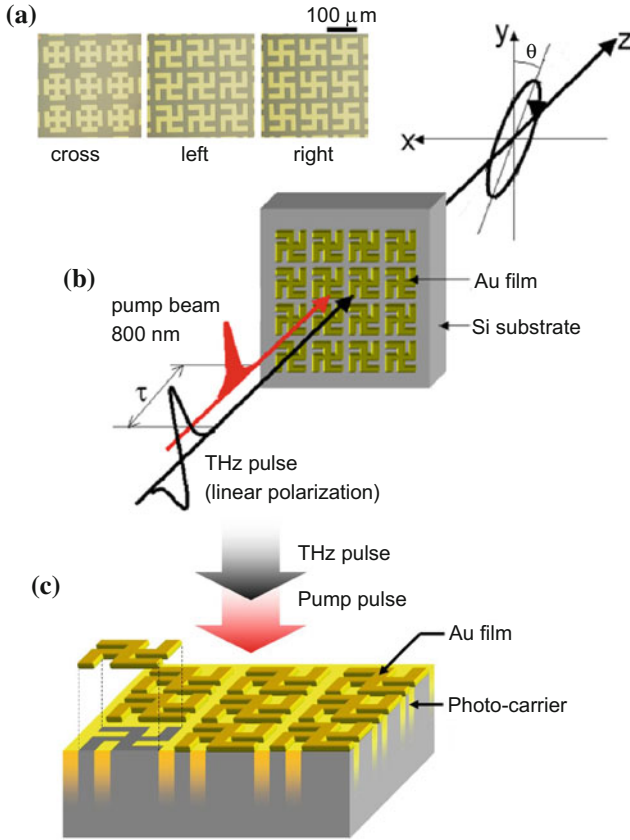


Fig. 11.14 **a** Optical microscopic images of the samples. **b** illustration of excitation. Pump beam and THz wave normally incident on the sample. The polarization azimuth rotation angle θ of the transmitted THz wave is measured. **c** Illustration of complimentary double-layered structure, created by the photoexcitation of carriers in semiconductor substrate (From [33])

The directions of the pump beam and THz pulse are horizontally and vertically polarized, respectively. The THz pulse arrives at the sample at a delay $\tau = 70$ ps after the photoexcitation. Since the lifetime of photocarriers is much longer than the duration of the THz pulse, the response of the carrier can be considered to be in a quasi-steady-state regime.

Figure 11.15 shows the measured transmission spectra and polarization-rotation spectra of chiral and achiral structures. One can observe that an increase in the pump power results in the suppression of the transmittance. The polarization-rotation spectra are shown in Fig 11.15b. The polarization rotation without photoexcitation is negligibly small. However, polarization rotation is observed at around 1 THz, when the chiral gammadion-patterned samples are photoexcited, and the sign of polarization rotation depends on the chirality of the patterns. The magnitude of the polar-

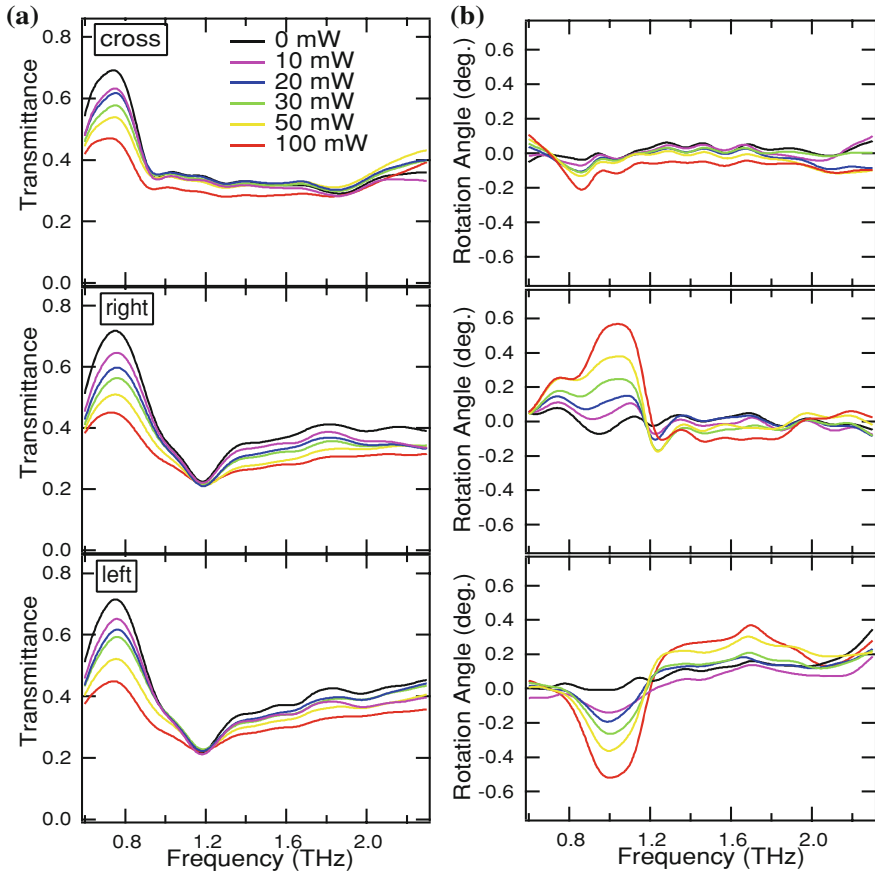


Fig. 11.15 Experimental results of transmission and polarization-rotation spectra. **a** Transmission spectra and **b** polarization-rotation spectra at different photoexcitation powers. *Top, middle and bottom* figures are the results of the samples with cross, right-twisted, and left-twisted metal patterns, respectively (From [23])

ization rotation increases with pump power. One can observe, from Fig. 11.15b, that there is no polarization effect in the achiral cross-patterned sample. This indicates that the observed polarization effect originates from the structure chirality. The polarization rotation effects was not found to depend on the incident polarization direction.

The mechanism of the observed polarization effect can be understood by comparison with the enhancement of optical activity in complementary double-layered chiral structures whose experimental data are shown in Fig. 11.4. In that case, the coincidence of the resonant frequency of the complementary double layers, because of Babinet's principle, and the local enhanced electric fields near the edges of two layers at close lateral positions contributed to realize a large optical activity [16]. In

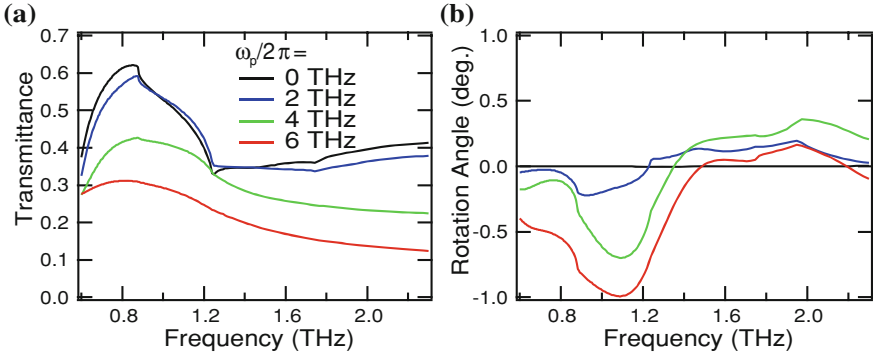


Fig. 11.16 Results of numerical calculation of transmission and polarization-rotation spectra. Numerical calculation results of **a** transmission spectra and **b** polarization-rotation spectra of the left-twisted gammadion structure at different photoexcitation levels, identified by ω_p (From [23])

the case illustrated in Fig. 11.14, the photoexcitation generates a chiral distribution of photocarriers at the surface and inside the semiconductor substrate. The gold metal mask and photocarriers form a double-layered complementary metallic grating, and optical activity results. The present technique of active THz polarization control is based on the formation of a three-dimensional chiral morphology of semiconducting material system.

To examine the validity of the observed phenomena, numerical calculations of transmission spectra and polarization-rotation spectra were performed with the rigorous coupled-wave analysis method. The dielectric response function $\epsilon(z, \omega)$ for the photoexcited region, based on the Drude model, was introduced taking into account the carrier density attenuation along the z direction as follows,

$$\epsilon(z, \omega) = \epsilon_{Si} + \Delta\epsilon(\omega)\exp(-z/d), \quad (11.55)$$

$$\Delta\epsilon(\omega) = \frac{\omega_p^2}{\omega(\omega - i\gamma)} \quad (11.56)$$

where ϵ_{Si} is the dielectric constant of silicon without photoexcitation, the attenuation length $d = 9.8 \mu\text{m}$ is the penetration depth of the pump beam [34]. The damping constant of the Drude model is assumed to be $\gamma/2\pi = 0.5$ THz. The excitation level is expressed by ω_p in (11.56); larger ω_p indicates stronger excitation because ω_p is proportional to the square root of the photoexcited carrier density. The results of the calculation are shown in Fig. 11.16. The suppression of the transmission spectra and the enhancement of optical activity with photoexcitation are well reproduced.

In conventional schemes, carrier lifetime limits the switching time of photocarrier-induced effects. In the present case, however, the photo-induced optical activity decays much faster than the lifetime of photocarriers in silicon ($\sim \mu\text{s}$). Numerical calculations and experiments were performed to clarify the mechanism of such fast decaying, and found that the gammadion-patterned carrier distribution

becomes uniform within about 250 ns, and the optical activity vanishes. By using a semiconductor substrate with a shorter lifetime of carriers or faster carrier diffusion, a faster response of active polarization control can be achieved.

11.5 Conclusion

In this chapter, THz time domain ellipsometry, which makes use of the vectorial nature of THz waves, has been described. Using this method, all the components of the complex dielectric tensor, including off-diagonal parts, can be obtained with high accuracy by extracting both information of amplitude and phase from the x and y components of a THz time domain wave vector. As examples of application, optical activity was observed in artificial chiral grating structures. Such structures can also be used as active polarization modulators. THz ellipsometry can develop new applications for THz-TDS, such as detection of quantum hall [6] and magneto-optical effects. These methods could be employed as powerful spectroscopic tools in the future.

References

1. T. Hofmann, U. Schade, C.M. Herzinger, P. Esquinazi, M. Schubert, *Rev. Sci. Instrum.* **77**, 063902 (2006)
2. B. Parks, S. Spielman, J. Orenstein, *Phys. Rev. B* **56**, 115–117 (1997)
3. K. Yamamoto, K. Tominaga, H. Sasakawa, A. Tamura, H. Murakami, H. Ohtake, and N. Sarukura, Terahertz time-domain spectroscopy of amino acids and polypeptides, *Biophys. J.* **89**, L22–L24 (2005)
4. R.M. Woodward, B.E. Cole, V.P. Wallace, R.J. Pye, D.D. Arnone, E. H Linfield, and M. Pepper, *Phys. Med. Biol.* **47**, 3853–3863 (2002)
5. Y. Ikebe and R. Shimano, *Appl. Phys. Lett.* **92**, 012111 (2008)
6. Y. Ikebe, T. Morimoto, R. Masutomi, T. Okamoto, H. Aoki, R. Shimano, *Phys. Rev. Lett.* **104**, 256802 (2010)
7. V.M. Shalaev, *Nat. Photonics* **1**, 41 (2007)
8. Y. Svirko, N. Zheludev, M. Osipov, *Appl. Phys. Lett.* **78**, 498 (2001)
9. A. Papakostas, A. Potts, D.M. Bagnall, S.L. Prosvirnin, H.J. Coles, N.I. Zheludev, *Phys. Rev. Lett.* **90**, 107404 (2003)
10. T. Valius, K. Jefimovs, J. Turunen, P. Vahimaa, Y. Svirko, *Appl. Phys. Lett.* **83**, 234 (2003)
11. M. Kuwata-Gonokami, N. Saito, Y. Ino, M. Kauranen, K. Jefimovs, T. Vallius, J. Turunen, Y. Svirko, *Phys. Rev. Lett.* **95**, 227041 (2005)
12. A.V. Rogacheva, V.A. Fedotov, A.S. Schwanecke, N.I. Zheludev, *Phys. Rev. Lett.* **97**, 177401 (2006)
13. E. Plum, V.A. Fedotov, A.S. Schwanecke, N.I. Zheludev, Y. Chen, *Appl. Phys. Lett.* **90**, 223113 (2007)
14. M. Decker, M.W. Klein, M. Wegener, S. Linden, *Opt. Lett.* **32**, 856 (2007)
15. K. Konishi, T. Sugimoto, B. Bai, Y. Svirko, M. Kuwata-Gonokami, *Opt. Express* **15**, 9575 (2007)
16. N. Kanda, K. Konishi, M. Kuwata-Gonokami, *Opt. Express* **15**, 11117 (2007)

17. A. Berger, M.R. Pufall, *Appl. Phys. Lett.* **71**, 965 (1997)
18. M. Schubert, B. Rheinländer, J.A. Woollam, B. Johs, C.M. Herzinger, *J. Opt. Soc. Am. A* **13**, 875 (1996)
19. M. Schubert, T.E. Tiwald, J.A. Woollam, *Appl. Opt.* **38**, 177 (1999)
20. M. Schubert, T. Hofmann, *J. Opt. Soc. Am. A* **20**, 347 (2003)
21. M.C. Nuss, J. Orenstein, G. Grüner, in *Terahertz Time-Domain Spectroscopy*. Topics in Applied Physics, Vol. 74 (Springer, Berlin Heidelberg, 1998), Chap. 3, p. 7
22. T.-I. Jeon, D. Grischkowsky, *Appl. Phys. Lett.* **72**, 3032 (1998)
23. Y. Ino, R. Shimano, Y. Svirko, M. Kuwata-Gonokami, *Phys. Rev. B* **70**, 155101 (2004)
24. Y. Svirko, N. Zheludev, *Polarization of Light in Nonlinear Optics* (Wiley, Hoboken, 1998)
25. M. Born and E. Wolf, *Principles of Optics*, 6th edn. (Pergamon, Oxford; Tokyo, 1980), Chap. 1
26. P.M. Oppeneer, *Magneto-optical Kerr Spectra*, Handbook of Magnetic Materials, Vol. 13 (Elsevier Science, Amsterdam, 2001), Chap. 3, p. 229
27. K. Sato, *Jpn. J. Appl. Phys.* **20**, 2403 (1981)
28. R. Shimano, Y. Ino, Y.P. Svirko, M. Kuwata-Gonokami, *Appl. Phys. Lett.* **81**, 199 (2002)
29. W.H. Press, S.A. Teukolsky, W.T. Vetterling, B.P. Flannery, *Numerical Recipes in C*, 2nd edn. (Cambridge University Press, Cambridge, 1992), Chap. 9.7
30. E.M. Vartiainen, Y. Ino, R. Shimano, M. Kuwata-Gonokami, Y.P. Svirko, K.-E. Peiponen, *J. Appl. Phys.* **96**, 4171 (2004)
31. Y. Ino, J.B. Heroux, T. Mukaiyama, M. Kuwata-Gonokami, *Appl. Phys. Lett.* **88**, 041114 (2006)
32. B. Lax, G.B. Wright, *Phys. Rev. Lett.* **4**, 16 (1960)
33. N. Kanda, K. Konishi, M. Kuwata-Gonokami, *Opt. Lett.* **19**, 3000 (2009)
34. D.E. Aspnes, J.B. Theeten, *J. Electrochem. Soc.* **127**, 1359 (1980)

Chapter 12

Liquid Crystals and their Applications in the THz Frequency Range

Nico Vieweg, Christian Jansen and Martin Koch

Abstract We present a survey through the study of liquid crystals with terahertz time domain spectroscopy. The macroscopic dielectric properties such as the refractive index and the absorption coefficient for both ordinary and extraordinary polarization of various liquid crystals are presented and the underlying physical mechanisms are discussed. Furthermore, we deduce the microscopic characteristics such as the order parameter and the polarizabilities from the measured data.

Keywords Liquid Crystals · Birefringence · Order parameter · Molecular polarizabilities

12.1 Liquid Crystals at THz Frequencies

12.1.1 Introduction

Since Friedrich Reinitzer's discovery of the liquid crystals (LC) in 1888, a new age dawned in the understanding of the phases of matter [1]. Before this discovery, people had knowledge of only three phases, the solid, the liquid, and the gaseous state. At first, some scientists had many arguments against Reinitzer's proposal of the new phase. However, in the following years, other groups confirmed Reinitzer's findings. Thus, today the theory of this new state of matter is fully accepted.

The reason for the scientific interest in LCs lies in the unique combination of order, as known from a crystal and fluidity, as observed in a liquid. Moreover, many

M.Koch (✉) · N. Vieweg · C. Jansen
Department of Physics, Philipps-Universität Marburg, 35032Marburg, Germany
e-mail: martin.koch@physik.uni-marburg.de

C. Jansen
e-mail: chr.jansen@gmx.net

LCs exhibit optical anisotropy and a strong response to magnetic or electric fields rendering them ideal candidates for tunable optical components. Today, liquid crystals have found their way into many optical applications, among which the liquid crystal display is certainly the most renowned. Recently, the large potential that LCs hold as base material for switchable terahertz (THz) devices has been discovered. However, to unchain this potential, a profound knowledge of their dielectric properties in the THz frequency regime is mandatory and an understanding of the physical mechanisms forming these properties has to be obtained.

12.1.2 *State of the Art*

Since the early 1970s, researchers have explored the far-infrared (FIR) properties of liquid crystals [2–18]. During these times and with the scientific instruments available, only limited information about the liquid crystal FIR properties were accessible. These methods include measuring the absorption coefficient with a Fourier Transform Infrared (FTIR) spectrometer or a CH₂F₂-based THz laser [18]. However, results on the THz refractive index at single frequencies have been presented only with the latter method [18].

Due to the major breakthrough of THz time domain spectroscopy (THz TDS) in the 1990s, a new interest in the subject of liquid crystals soon followed. With THz TDS, both the THz refractive index n and the absorption coefficient α can be precisely determined from the measured data over a broad frequency range. The first LC THz TDS measurements were made by Turchinovich et al. on PCH5 [19]. This report was followed by several papers published by Prof. Pan's group on 5CB, 6CB, 7CB, 8CB [20–25], PCH5 [20, 22], E7 [26, 27], and a ferroelectric liquid crystal [28]. THz data on 5CB have also been presented by Bonn et al. [29]. Using different spectroscopy techniques, Takanishi et al. and Nishizawa et al. studied P-8-PIMB and MBBA, respectively [30, 31]. Furthermore, our group has also contributed to the field with results on a liquid crystal polymer [32] as well as the macroscopic and microscopic THz properties of LCs such as 5CB, 6CB, 7CB, 8CB [33, 34], 5OCB, PCH5, PCH7 [34], BL037 [35], MLC7029, I52 and 1808 [36], which are also discussed later in this chapter. More recently, Trushkevych et al. reported on the THz properties of the nematic mixture LCMS-107 [37].

THz device concepts based on LCs have been proposed. Among them are magnetically and electrically switchable phase shifters [22, 26, 38–40], filters [22, 41, 42], polarizer [43], and gratings [44] as suggested by Prof. Pan's group. Zhang and coworkers reported recently on a tunable THz photonic crystal [45]. Our group furthermore demonstrated a LC-based dielectric THz-mirror and a sub-THz photonic crystal [46, 47]. Moreover, Khoo et al. suggested a tunable THz device, which combines a metamaterial with liquid crystals [48–50]. This concept has been put into practice by Werner et al. for the near infrared, by Bossard et al. for the THz frequency regime, and by Zhao et al. for the sub-THz range [48, 51–53]. More recently, Yuan et al. proposed an electrically controlled liquid crystal THz switch [54].

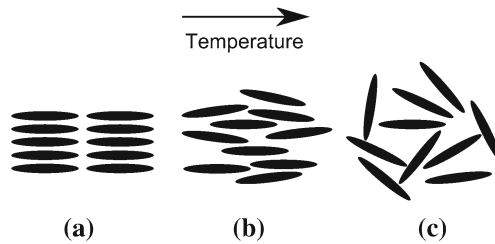


Fig. 12.1 a crystalline, b nematic and c isotropic phase of a liquid crystal

12.1.3 Liquid Crystals Phases

The most commonly employed liquid crystals, also known as calamitics, consist of rod-like molecules. This type can exhibit many different liquid crystal phases [55]. The simplest LC phase is called nematic (greek word for thread). In this phase, the molecules are randomly distributed but tend to align in a preferred direction. In other words, the material shows orientational, but no positional order. The phase transition of a nematic liquid crystal is illustrated in Fig. 12.1. A nematic liquid crystal changes its phase with increasing temperature from a well-ordered crystalline, to a less ordered nematic and finally, to a disordered isotropic liquid phase. From the application point of view, the nematic phase is favored because of the sensitive response of the molecules to electric fields.

12.1.4 Key Properties

Due to the long wavelength, THz devices require thicker LC layers compared to devices operating at optical frequencies, which implies slower switching times and higher losses [56]. For many LC devices the phase shifting capabilities is the major mechanism which is proportional to the product $\Delta n \cdot d$, where Δn is the THz birefringence and d the LC layer thickness. It is obvious that Δn needs to be large, if the layer thickness is supposed to be small. For this reason, the key properties for THz LCs are a high birefringence and a small absorption. Aside from switching times and losses, the stable operation temperature range can also be crucial depending on the application requirements.

12.1.5 Positive versus Negative Dielectric Anisotropy

The first LCs used in switchable optical devices were nematics with positive dielectric anisotropy (PDA). Those are also referred to as the classical LCs [56]. Because of their molecular structure comprising a polar head group, they exhibit a strong electric

dipole moment along the long axis. This property is important for the interactions of LCs with static or low frequency electric fields. PDAs always tend to align parallel to the electric field lines.

In negative dielectric anisotropic (NDA) LCs, the different dielectric anisotropic behavior is, for example, caused by the laterally substituted cyanide (CN) or fluorine (F) groups [57–59]. As a result, a strong permanent dipole moment is formed in the direction perpendicular to the molecular long axis. This dipole moment is of major importance for the interaction of NDAs with electric fields. While the classic PDA LCs prefer a parallel alignment, NDA LCs rather orient perpendicular to the static electric field.

12.1.6 Pure Liquid Crystals versus Mixtures

Depending on the application requirements, LCs need to have certain properties such as a high optical birefringence, a positive or negative dielectric anisotropy, low switching times, chemical stability, etc. However, those requirements are hard to fulfill by a pure substance. Therefore, the LC properties are optimized by mixing up to 20 different single LC components [56, 60–64]. Today, several different nematic mixtures have been developed. Among these mixtures are optimized ones for fast switching, low energy consumption, or high optical contrasts.

12.1.7 Macroscopic Properties – from kHz to UV

To develop a better understanding of the physical interactions of the liquid crystals with electromagnetic waves, we present the frequency-dependent dielectric parameters of 5CB, a member of the cyanobiphenyl (CB) family. The basic dispersion behavior of many nematic LCs is very similar [33], so that 5CB can serve as a representative example.

The frequency dependent refractive index and the absorption coefficient of 5CB are shown in Fig. 12.2a, b, respectively. In addition to the THz data obtained by the authors, data from the lower and higher frequency region, which were previously published by Gestblom et al., Weil et al., as well as Wu and Li are shown for comparison [65–68].

Considering the data presented in Fig. 12.2a, three different regimes can be identified. At kHz frequencies, the permanent dipole moment of the 5CB molecules still follows the electric field. Thus, a high birefringence and large values for the refractive index are observed. In the MHz frequency region the electric field becomes too fast for the permanent dipole to follow and a relaxation behavior sets in. During the relaxation the two curves for the ordinary and the extraordinary refractive index intersect twice. At these points the anisotropy completely vanishes. Starting at GHz frequencies and spanning up to the mid-infrared a steady decrease of both the

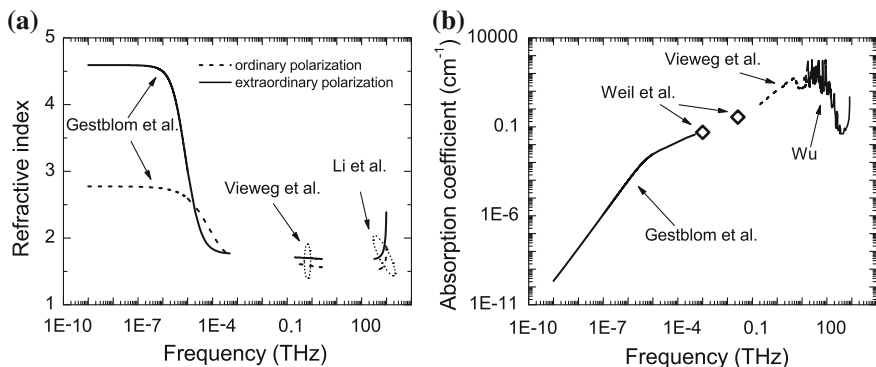


Fig. 12.2 Frequency-dependent refractive index (a) and mean absorption coefficient (b) of 5CB from microwaves to the visible (cf. [65–68])

ordinary and the extraordinary refractive index is found. The absorption spectrum presented in Fig. 12.2b shows an absorption band located at 5 THz [2] that is followed by strong vibrational absorption modes in the mid-infrared region, which lead to a strong resonance dispersion [67, 68]. The modes weaken in the NIR region (between 300 and 430 THz). In addition, the NIR region is not yet influenced by electronic transitions, which take place in the VIS and UV and strongly impact the dispersion characteristics in the high frequency regime.

12.1.8 THz Spectroscopy on Liquid Crystals

A standard THz time domain spectroscopy setup is employed to experimentally investigate the properties of the LCs over a broad frequency and temperature range [69–71]. Femtosecond pulses generated in a titan-sapphire laser, gate photoconductive antennas, which serve as THz emitter and detector [72]. The THz beam is guided by four off-axis parabolic mirrors with the sample positioned in the intermediate focus. The experiments are conducted in a nitrogen atmosphere to avoid water absorption lines in the spectra.

A liquid crystal cuvette consists of two THz transparent windows with 1.3 mm metal wire electrodes on two sides (Fig. 12.3). Materials such as fused silica, Topas, or high density polyethylene are appropriate window materials. While the plastics windows show a lower absorption, fused silica serves well if proper surface conditions or temperature control is required. To align the LCs, an electric 1 kHz AC field of $E_{\text{eff}} = 37 \text{ kV/m}$ is applied to the in-plane electrodes [73]. Measuring the extraordinary material parameters requires the molecular long axis to be aligned parallel to the polarization of the incident THz wave. In contrast, the ordinary parameters are obtained with the LCs long axis oriented perpendicular to the incident THz field

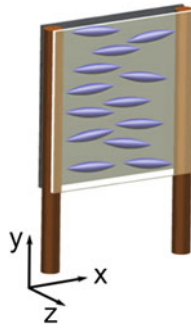


Fig. 12.3 Liquid crystal cuvette

Table 12.1 Liquid crystal material presented in this book chapter

	Pure LCs	Mixtures
PDAs	5CB, 5OCB, PCH5	BL037
NDAs	152, 7CP7BOC	MLC7029, 1808

polarization. Peltier elements connected to a thermoelectric controller enable measurements of the material properties at different temperatures.

Extracting the material parameters from the measured data is a challenging task. The system under investigation has at least three layers. The material parameters change from layer to layer, resulting in reflections from the layer interfaces, which requires a more complex approach to the data analysis. To obtain highly precise material parameters from the measured data we use a novel data extraction algorithm. This algorithm accounts for the cuvette walls and multiple reflections of the THz pulse at the LC cell boundaries [74, 75]. The multilayer data extraction is also discussed in [76].

12.1.9 Macroscopic THz Properties of Liquid Crystals

In the following section, we present experimental results on the macroscopic properties of the LCs, e.g., the refractive index, the birefringence, and the absorption coefficient. Exemplary for the PDA class, we present data on the cyanobiphenyl 5CB, the phenyl-cyclohexane PCH5, the pentyloxy-cyanobiphenyl 5OCB, and the nematic mixture BL037. As representatives for the NDAs, we investigate four substances among which 152 and 7CP7BOC are pure substances, while MLC7029 and 1808 are two nematic mixtures. The LC materials presented within the scope of this chapter are summarized in Table 12.1.

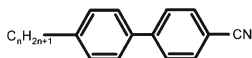


Fig. 12.4 Chemical structure of the cyanobiphenyls. The molecules consist of an alkyl chain (C_nH_{2n+1}), a cyanide head (CN), and a biphenyl core. The index n indicates the number of C atoms in the side chain. The polar cyanide head causes a dipole moment along the molecular long axis

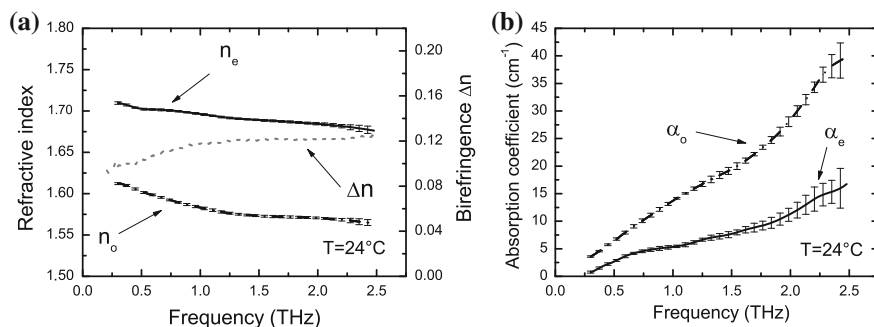


Fig. 12.5 **a** Refractive index and birefringence and **b** absorption coefficient for both ordinary and extraordinary polarization of 5CB at 24 °C

12.1.9.1 Cyanobiphenyl 5CB

Room temperature operation is an important requirement of the LCs used for devices. Cyanobiphenyls, first developed by Gray and coworkers in 1973 [77], offer this property. CBs are ideal candidates for spectroscopic studies, as they are widely available and well characterized.

The chemical structure is depicted in Fig. 12.4. CBs consist of a biphenyl core with a cyanide head (CN) on one and an alkyl chain (C_nH_{2n+1}) on the other side. The index n indicates the number of C atoms in the side chain.

As a representative member of this group we chose 5CB for further investigation. The THz refractive indices n_o and n_e and absorption coefficients α_o and α_e at 24 °C for ordinary and extraordinary polarization are depicted in Fig. 12.5. In comparison, the extraordinary is always larger than the ordinary refractive index ($n_e > n_o$), whereas the absorption coefficient is always larger for ordinary polarization ($\alpha_o > \alpha_e$). For example, the values of the refractive indices at 2 THz are $n_e = 1.69$ and $n_o = 1.57$ and the corresponding absorption coefficients are $\alpha_e = 13 \text{ cm}^{-1}$ and $\alpha_o = 28 \text{ cm}^{-1}$. The birefringence of 5CB at 2 THz is 0.12. The parameter for extraordinary refraction decreases slightly with the frequency, while there is a larger gradient for the ordinary axis. Both the ordinary and extraordinary absorption coefficients rise with the frequency, but there is a stronger increase for the ordinary axis.

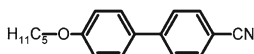


Fig. 12.6 Chemical structure of 5OCB. The molecule contains an alkoxy group ($C_nH_{2n+1}O$), a cyanide head (CN), and biphenyl core

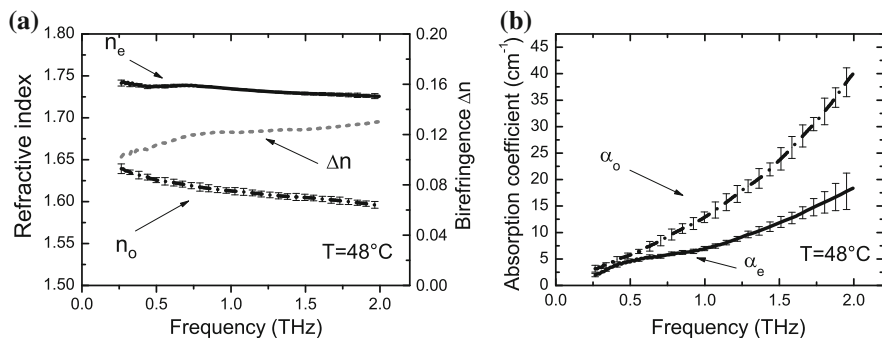


Fig. 12.7 **a** Refractive index and birefringence and **b** absorption coefficient both for ordinary and extraordinary polarization of 5OCB at 48 °C

12.1.9.2 Pentyloxy-Cyanobiphenyl 5OCB

Pentyloxy-cyanobiphenyls (OCBs) share the same basic structure with their CB relatives comprising a biphenyl core, a cyanide head, and an alkyl chain. In contrast to CBs, the alkyl chain in case of the OCBs is linked via an oxygen atom to the core (also called alkoxy chain). The additional oxygen makes the molecule less flexible, which results in a drastic shift of the nematic phase toward higher temperatures. Although 5OCB reaches the nematic phase starting at 48 °C, it exhibits a stability of the nematic phase over a broad temperature range.

The THz material parameters of 5OCB are shown in Fig. 12.7. The additional oxygen atom has only a weak effect on the THz anisotropy. The birefringence is with $\Delta n = 0.13$ at 2 THz only slightly higher than the birefringence of 5CB. The absorption behavior is also quite similar. Compared to 5CB a marginally higher absorption is found.

12.1.9.3 Phenylcyclohexane PCH5

Briefly after the discovery of the CBs, Eidenschink et al. introduced a new liquid crystal family called phenylcyclohexanes (PCHs) [78–80]. In general, PCHs differ from CBs in their core structure, which is shown in Fig. 12.8. While CBs consist of two phenyl rings, the PCHs contain a cyclohexane instead of one of the phenyl rings. PCHs are favored for some applications, as they exhibit a better chemical stability and a broader nematic range than the CBs. They are often employed as a reference material, e.g. for calibration purposes [78–80].

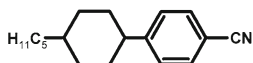


Fig. 12.8 Chemical structure of the phenyl-cyclohexanes. The molecule consist of an alkylchain (C_nH_{2n+1}), a cyanide head (CN), and a combination of phenyl and cyclohexane ring in the core

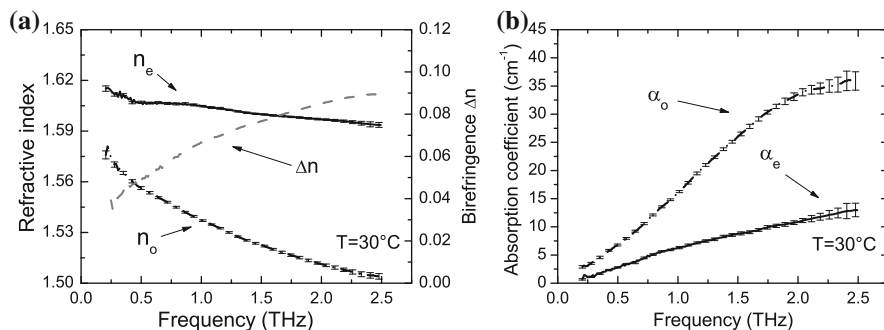


Fig. 12.9 **a** Refractive index and birefringence and **b** absorption coefficient both for ordinary and extraordinary polarization of PCH5 at 30°C

From their optical properties it is known that PCHs exhibit only a small anisotropy because of the short conjugation length. In the THz range, a similar relation can be observed. The THz birefringence of PCH5 with $\Delta n = 0.08$ at 2 THz is smaller than the birefringence of 5CB. The material parameters of PCH5 are presented in Fig. 12.9. The refractive indices are for instance $n_e = 1.59$ and $n_o = 1.51$ at 2 THz and 30°C. In general, the PCHs show a similar dependence on the frequency as the CBs and OCBs.

The presented pure LCs all show a very similar behavior. They exhibit a rather small birefringence and a large absorption at higher THz frequencies. In general, this makes them less attractive for use in THz devices. While the extraordinary absorption coefficient increases only to some extent, we find a strong rise for the ordinary excitation. The absorption in this region is caused by strong torsional motions which lead to a broad absorption band located around 5 THz [2–18]. The absorption band is always larger for the ordinary than for the extraordinary excitation. We attribute this phenomenon to the fact that the rod-like liquid crystals can move easier around their long axis than around the two short axes. Thus, molecular vibrations excited by extraordinary waves are more hindered, which results in a weaker absorption.

12.1.9.4 Nematic Mixture BL037

In order to find a more suitable candidate for THz applications, this section examines the properties of BL037, a mixture that has been optimized with regard to the optical anisotropy. For the optical frequency region the properties are specified to be

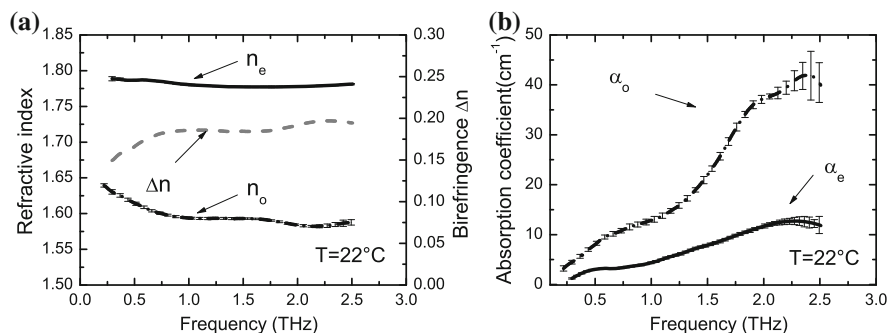


Fig. 12.10 **a** Refractive indices and **b** Absorption coefficients of BL037 at 22°C for ordinary and extraordinary polarization

$\Delta n|_{589\text{ nm}} = 0.282$, $n_e|_{589\text{ nm}} = 1.808$, $n_o|_{589\text{ nm}} = 1.526$. Here, Δn specifies the optical anisotropy and n_e and n_o represent the optical refractive indices. The mixture consists of the known cyanobiphenyls (CBs and OCBs), which are substituted with alkyl or alkoxy groups. In addition, BL037 contains substances with three rings in the core. The core either consists of three directly linked phenyl rings (terphenyl) or it is a combination of a biphenyl and a cyclohexane ring. We will further refer to both substances as TPs and BCs, respectively. TPs are liquid crystals that have a high optical anisotropy due to the good polarizability of this ring system (W. Becker, Merck KGaA). The mixture of these substances combines a high birefringence with a stable nematic phase of about -40°C up to 109°C .

The THz material parameters are shown in Fig. 12.10. The birefringence rises with the frequency from $\Delta n = 0.18$ at 0.5 THz to $\Delta n = 0.2$ at 2 THz and is therefore twice as large as the birefringence of the CBs. While the extraordinary refractive index $n_e = 1.78$ remains relatively constant, the ordinary refractive index decreases slightly from $n_o = 1.6$ at 0.5 THz to $n_o = 1.58$ at 2 THz. The absorption coefficient for the ordinary and the extraordinary polarization are presented in Fig. 12.10b. Within the examined range both coefficients increase with the frequency and as before the ordinary absorption is higher and more dispersive than the extraordinary absorption.

In conclusion, we find that the mixture combines a broad temperature operation range and a high terahertz birefringence. Thus, BL037 is a good candidate for switchable THz devices. However, the absorption coefficient for ordinary excitation rises drastically with the frequency and limits the use of BL037 to the frequency range below 1 THz.

12.1.9.5 I52

As a member of the negative dielectric anisotropy LCs, we investigate 4-ethyl-2-fluoro-4'-[2-(trans-4-n-pentylcyclohexyl)-ethyl]-biphenyl (I52) [80, 81]. The molecule is composed of two phenyl and one cyclohexane ring (Fig. 12.11). While the

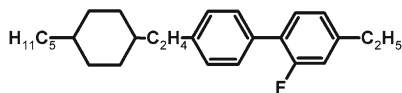


Fig. 12.11 Chemical structure of I52. A fluorine atom is linked laterally to the outer phenyl ring, thus forming a dipole moment perpendicular to the molecular long axis

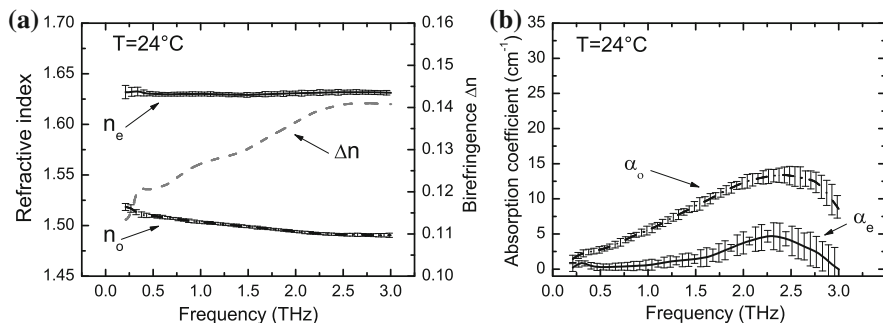


Fig. 12.12 **a** Refractive indices and **b** absorption coefficients for I52 at 24°C for ordinary and extraordinary polarization. The permanent dipole moment is created by a laterally connected fluorine atom

two phenyl rings are linked directly, the cyclohexane ring and the biphenyl system are connected via a C_2H_4 group. At both ends I52 is terminated by two alkyl chains (C_5H_{11} , C_2H_5). The negative dielectric anisotropy is formed by a fluorine atom, which is linked in a lateral position to the outer phenyl ring.

Due to the high stability of the material parameters over a broad temperature range from 24 to 103.4°C, I52 is often employed for instrumental calibration purposes [80]. The most important properties of I52 at a temperature of $T = 20^\circ\text{C}$ are $\Delta n|_{589\text{ nm}} = 0.1459$, $n_e|_{589\text{ nm}} = 1.6495$ and $n_o|_{589\text{ nm}} = 1.5036$, where Δn is the birefringence and n_o and n_e the refractive indices for ordinary and extraordinary polarization.

Figure 12.12 shows the extracted THz material parameters. The extraordinary refractive index remains constant, while the ordinary parameter decreases with increasing frequency. As an example, the refractive indices at 2 THz are 1.49 and 1.63 for ordinary and extraordinary polarization, respectively. Both indices differ only slightly from the values reported for the optical frequency range. The average value of the THz birefringence is $\Delta n = 0.14$ and thus only slightly smaller than the optical value of 0.1459. Thus, I52 shows a larger birefringence than its PDA relatives, e.g., the cyanobiphenyls.

12.1.9.6 7CP7BOC

The second NDA LC is called 2-chloro-4-n'-alkylphenyl esters of 4-n-alkylbicyclo [2,2,2] octane-1-carboxylic acid, to which we will further refer to as 7CP7BOC (Fig. 12.13). It consists of a phenyl ring and a bicyclooctane ring. Both rings are linked

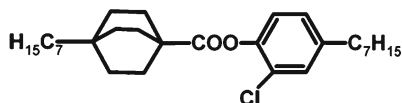


Fig. 12.13 Chemical structure of 7CP7BOC. A cyanide group is connected at a lateral position, resulting in a dipole moment perpendicular to the molecular long axis

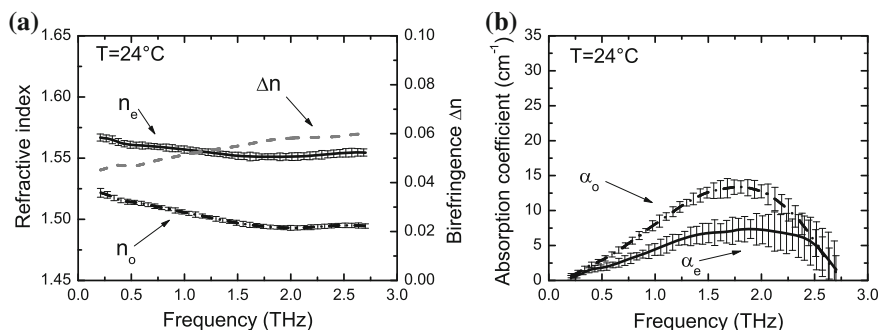


Fig. 12.14 **a** Refractive indices and **b** absorption coefficients for 7CP7BOC at 24 °C for ordinary and extraordinary polarization. The permanent dipole moment is created by a laterally linked cyanide (CN) group

by an ester group (COO) and terminated with a heptyl chain. In contrast to I52, the permanent dipole moment is formed by a chlorine atom linked laterally to the phenyl ring. The optical properties of 7CP7BOC are reported to be $\Delta n|_{589\text{ nm}} = 0.064$, $n_e|_{589\text{ nm}} = 1.5574$ and $n_o|_{589\text{ nm}} = 1.4932$ [82, 83].

The THz material parameters are presented in Fig. 12.14. On average, the THz birefringence of 7CP7BOC $\Delta n = 0.06$ is less than half the value of the birefringence of I52, which is caused by the shorter conjugation length. The refractive indices for both polarization decrease at first slightly but remain nearly constant above 2 THz. As an example, the refractive indices at 2 THz are measured to be 1.49 and 1.55 for ordinary and extraordinary polarization, respectively. From this result we see that the THz-values for the refractive indices are very close to the optical values.

As for I52, a broad absorption band is observed at frequencies around 2 and 2.3 THz for both polarizations of the THz wave. In the investigated frequency range, the ordinary absorption coefficient is always larger than the extraordinary parameter. In this regard, NDAs can be put on a level with PDAs.

Similar to I52, 7CP7BOC is also much more transparent than the above-mentioned classic PDA LCs. Obviously, the dipole direction has a strong impact on the THz properties. A molecule with a lateral permanent dipole seems to favor more damped oscillations around the long axis, which reflects in a lower absorption coefficient.

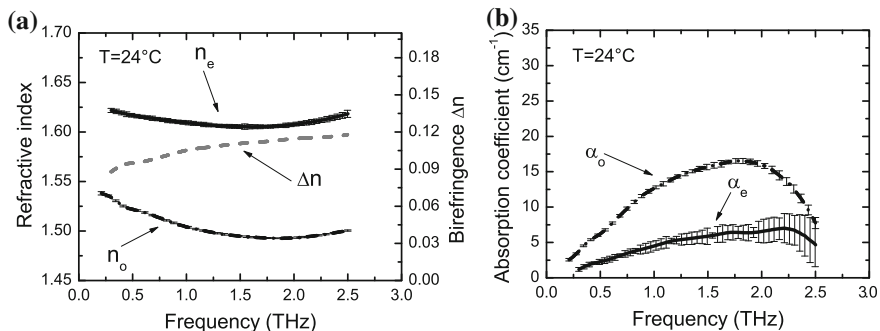


Fig. 12.15 **a** Refractive indices and **b** absorption coefficient of MLC7029 at 24°C for ordinary and extraordinary polarization

12.1.9.7 Nematic Mixture MLC7029

In order to find further evidence of the dipoles impact, we investigated two nematic mixtures with negative dielectric anisotropy.

We first present THz measurements on MLC7029, which is a mixture optimized for fast switching cycles [56, 84]. The optical properties at 20°C of MLC7029 are specified to be $\Delta n|_{593\text{ nm}} = 0.1265$, $n_e|_{593\text{ nm}} = 1.6157$ and $n_o|_{593\text{ nm}} = 1.4892$. In accordance to the optical properties, MLC7029 shows a moderate average birefringence of $\Delta n = 0.11$ at THz frequencies. The refractive indices decrease first with the frequency but increase again above 2 THz. As an example, the indices are determined to be 1.49 and 1.61 at 2 THz for ordinary and extraordinary polarization, respectively. At frequencies around 1.8 THz, MLC7029 shows a broad absorption band, similar to the one of the above presented NDA LCs.

12.1.9.8 Nematic Mixture 1808

The second mixture investigated is 1808. Like its PDA counterpart (BL037), 1808 is designed to have a high optical birefringence. The mixture consists of difluoroalkylterphenyls and alkyl-alkoxytolanes [59, 62, 85] (Roman Dabrowski, Military Technical Academy of Warsaw). Its THz properties are presented in Fig. 12.15. The absorption spectrum of 1808 appears to be more complex. However, the exact recipe is not publically available from the manufacturer and thus it is not possible to finally explain the absorption features here.

The mixture 1808 shows a high birefringence of $\Delta n = 0.2$ at 2 THz. The refractive indices are 1.52 and 1.72 at 2 THz for ordinary and extraordinary refraction, respectively. In comparison, the PDA mixture BL037 has some advantage over 1808 at lower frequencies (0.5–1.2 THz). At higher frequencies a similar birefringence is observed. However, 1808 exhibits a significantly smaller THz absorption.

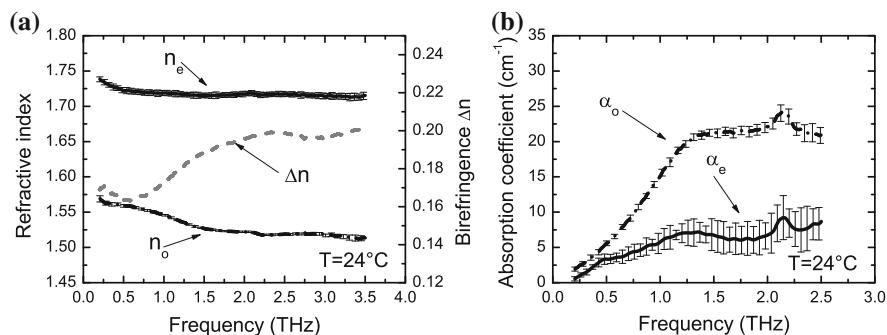


Fig. 12.16 **a** Refractive indices and **b** absorption coefficient of 1808 at 24°C for ordinary and extraordinary polarization

Table 12.2 Birefringence and refractive indices at 2 THz for ordinary and extraordinary polarization of the Liquid Crystal material presented in this chapter

	n_o	n_e	Δn
5CB	1.57	1.69	0.12
5OCB	1.6	1.73	0.13
PCH5	1.51	1.59	0.08
BL037	1.58	1.78	0.2
I52	1.49	1.63	0.14
7CP7BOC	1.49	1.55	0.06
MLC7029	1.49	1.61	0.12
1808	1.52	1.72	0.2

Regarding their birefringence, the pure NDA substances as well as the mixture MLC7029 exhibit a behavior similar to their PDA counterparts. Yet, NDA LCs outperform the PDA LCs with regard to transparency, which we attribute to the different direction of the permanent dipole. The mixture 1808 surpasses the anisotropy of the other LCs by nearly a factor of two. Moreover, 1808 exhibits a lower overall absorption than the PDA mixture BL037 rendering 1808 an excellent choice for THz devices.

To summarize the macroscopic properties of the LCs presented above, the birefringence and the refractive indices for ordinary and extraordinary polarization at 2 THz are given in Table 12.2.

12.1.10 Molecular THz Properties of Cyanobiphenyls

After having considered the macroscopic properties of LCs, this section is dedicated to the investigation of the molecular characteristics of the cyanobiphenyls (CBs) at THz frequencies [73].

Table 12.3 Temperatures for the crystal/nematic (T_{CN}) and the nematic/isotropic phase transition (T_{NI}) as well as the reduced temperature $T_{CN} - T_{NI}$. Ref. [86]

	T_{CN} (°C)	T_{NI} (°C)	$T_{NI} - T_{CN}$ (K)
5CB	24	35.3	11.3
6CB	14.4	30.2	15.8
7CB	30.1	42.9	12.8

First, we will examine the cyanobiphenyls' molecular structure and its implications on the dielectric characteristics of 5CB, 6CB, and 7CB. Finally, an investigation of the anisotropy of the refractive index, the order parameter S as well as the principle and the main polarizabilities will be undertaken along with an interpretation of the underlying physical mechanisms.

12.1.10.1 The Molecular Structure of 5CB, 6CB, and 7CB

In contrast to many other commercially available LCs, the molecular structure of CBs is well known so that experimental observations can directly be linked to features of the molecular structure. The cyanobiphenyls consist of an alkyl chain ($H_{2n+1}C_n$) with a polar cyanide head group (CN), and a rigid core unit formed by a conjugated phenyl ring system. The molecules under investigation consist of the same basic structure and only differ in the length of the alkyl side chain (Fig. 12.4, 12.17).

At increasing temperatures the CBs undergo phase changes from a well-ordered crystalline to a less ordered nematic and finally to a disordered, isotropic phase (Table 12.3). A summary of the corresponding phase transition temperatures T_{CN} and T_{NI} as well as the reduced temperature $T_{CN}-T_{NI}$ can be found in Table 12.3.

Among the cyanobiphenyls under investigation, two fundamental dependencies can be found: First of all, the differing alkyl chain lengths result in alterations regarding certain physical properties such as the polarizability and the density, which reflect in the anisotropy of both the absorption and the refractive index. Furthermore, aside from the total chain length, odd and even numbers of C atoms in the alkyl chain lead to a different macroscopic behavior [87–94].

From a thermodynamic point of view, the LC system tries to reach the lowest energy conformation in order to establish an equilibrium. For an odd number of C atoms, e.g., in 5CB or 7CB, this state of lowest energy is present when the tail is rather aligned in a *trans*-conformation along the principle long axis m (Fig. 12.17). In contrast, CBs with an even number of C atoms, e.g., 6CB reach the lowest energy state when the angle between the last C atom and the axis m becomes large (e.g. $\beta_{6CB} = 66.1^\circ$) [88].

The different conformation behavior of odd- and even numbered CBs is also reflected in differing molecular properties, which is known as the odd and even effect [87–94]. In the following sections, the odd and even effect at THz frequencies

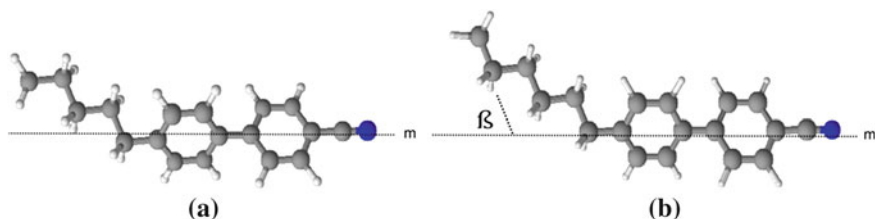


Fig. 12.17 Molecular structure of (a) 5CB and (b) 6CB. A large angle is formed between the last member of the alkyl chain and the long axis for the LCs with an even number of C atoms in the chain (6CB)

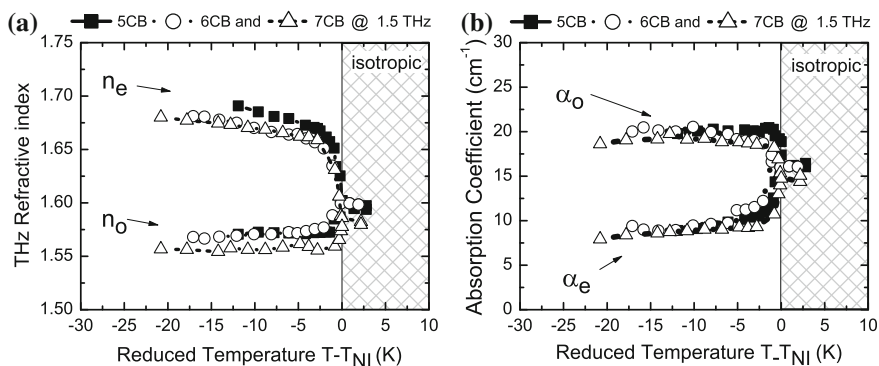


Fig. 12.18 a Refractive index and b absorption coefficient at 1.5 THz versus the reduced temperature for 5CB, 6CB, and 7CB

will be further investigated by studying the anisotropy of the refractive index n , the absorption coefficient α , and the order parameter S .

The frequency dependence of the refractive index and the absorption coefficient of 5CB have been presented further above. For the extraction of microscopic properties the temperature dependence is also required. Thus, we move on to investigating the temperature dependence of these parameters for 5CB, 6CB, and 7CB at a fixed frequency of 1.5 THz. Fig. 12.18 shows the refractive index and the absorption coefficient of the three LCs. For a clear comparison of the three LCs, the x-axis is given in form of the reduced temperature $T-T_{NI}$, where T_{NI} is the temperature at which the transition between the nematic and the isotropic phase occurs (cf. Table 12.3). As expected, the strong polarizability of the LCs in direction of the long molecular axis results in a positive anisotropy (i.e. $n_e > n_o$) of the THz refractive index over the entire nematic phase. The transition between the nematic and the isotropic phase is clearly visible. However, the CBs do not exhibit a change in the material parameters at the transition between the nematic and the crystalline phase.

As the nomenclature suggests, the number of C atoms in the alkyl chain increases from five in case of 5CB to seven in case of 7CB. The density exhibits the inverse behavior with 5CB being the densest material with the highest number of molecules

per unit volume. Thus, 5CB also exhibits the highest refractive index, both in the ordinary and the extraordinary axis, of all the CBs investigated here.

Both 5CB and 7CB possess an odd number of CH₂ groups. Hence, a complete alignment of the tail along the molecular long axis according to the odd and even rule mentioned before can be observed. The two additional CH₂ groups in case of 7CB contribute to the polarizability of the long axis, which leads to an enhanced birefringence. Here, $\Delta n_{5CB} = 0.11$ and $\Delta n_{7CB} = 0.12$ at $T - T_{NI} = -10$ K.

Although the substance 6CB has the second longest tail and is thus the second densest material, its refractive index does not fit with respect to the refractive indices of 5CB and 7CB. Here, the last CH₂ group forms a large angle to the molecular long axis. Therefore, the birefringence is reduced to a value of $\Delta n_{6CB} = 0.10$ as the additional CH₂ group primarily contributes to the polarizability of the molecular axis perpendicular to the long axis. As the birefringence only slightly differs between the CBs, the reader is referred to the following section, where the anisotropy is again discussed with regard to the polarizabilities.

The absorption coefficient shown in Fig. 12.18b exhibits a pronounced linear dichroism. THz waves oriented along the ordinary direction excite a broad torsional vibration mode located around 5 THz [2–18]. Thus, the absorption α_o observed in the ordinary axis is higher than the absorption α_e observed in the extraordinary axis.

12.1.10.2 The Relation between Macroscopic and Molecular Data

Molecular properties, such as the longitudinal and the transverse contributions of the polarizability tensor, are of fundamental interest. However, above absolute zero, the intrinsic thermal energy is the source of a certain degree of disorder in the LC, resulting in the inability of spectroscopic measurements to directly give access to these molecular characteristics. Still, with the order parameter S known, a relation between the spectroscopic data and these molecular properties can be derived as follows [95, 96]:

$$(\zeta_e - \zeta_o) = S(\gamma_{\parallel} - \gamma_{\perp}) \quad (12.1)$$

In this equation, ζ_e and ζ_o stand for the principle polarizabilities, S for the order parameter, and γ_{\parallel} and γ_{\perp} for the longitudinal and transverse polarizability components of the perfectly ordered LC. The main polarizabilities γ_{\parallel} and γ_{\perp} can then be extracted using the equations:

$$\gamma_{\parallel} = \bar{\zeta} + \frac{2}{3S}(\zeta_e - \zeta_o) \quad (12.2)$$

and

$$\gamma_{\perp} = \bar{\zeta} - \frac{1}{3S}(\zeta_e - \zeta_o) \quad (12.3)$$

Here, the mean polarizability is given by

$$\bar{\zeta} = \frac{1}{3}\zeta_e + \frac{2}{3}\zeta_o \quad (12.4)$$

To proceed with our study of the molecular properties of the CBs we will perform the following steps: First, we extract the principle polarizabilities ζ_e and ζ_o by applying Vuks' approximation to the refractometric data [97, 98]. Then, we will determine the order parameter S by using Haller's extension to Vuks' approach. Finally, on the basis of this data we will be able to determine the main polarizabilities γ_{\parallel} and γ_{\perp} .

12.1.10.3 Principle Polarizability

The first step of Vuks approach to deriving the polarizability of anisotropic materials from their refractive index is a generalization of the Lorentz–Lorenz formula [99, 100],

$$\frac{n_{e/o}^2 - 1}{n_{e/o}^2 + 2} = \frac{4\pi}{3} N \zeta_{e/o} \quad (12.5)$$

Here, n denotes the refractive index, N is the number of molecules per unit volume, and $\zeta_{e/o}$ represents the polarizability along the extraordinary and the ordinary polarization, respectively [101]. Vuks assumed that the mean refractive indices of anisotropic molecules in the crystalline state can be treated as isotropic media so that equation (12.5) remains valid. On this basis he derived

$$\frac{n_{e/o}^2 - 1}{\bar{n}^2 + 2} = \frac{4\pi}{3} N \zeta_{e/o}, \quad (12.6)$$

where $\bar{n}^2 = \frac{1}{3}n_e^2 + \frac{2}{3}n_o^2$ is the mean square of the refractive index. In Fig. 12.19a, the principle polarizability of 5CB, 6CB, and 7CB at 1.5 THz as predicted by Vuks' calculations is shown.

The LCs exhibit an anisotropy of the polarizability of $\Delta\zeta_{5CB} = 7.7 \times 10^{-24} \text{ cm}^3$, $\Delta\zeta_{6CB} = 7.2 \times 10^{-24} \text{ cm}^3$, and $\Delta\zeta_{7CB} = 8.8 \times 10^{-24} \text{ cm}^3$ at $T-T_{NI} = -10 \text{ K}$ for 5CB, 6CB, and 7CB, respectively. As previously observed in the birefringence data, the smallest anisotropy is exhibited by 6CB, while $\Delta\zeta$ increases with the chain length in case of 5CB and 7CB. This behavior again can be attributed to the before mentioned odd and even effect.

Figure 12.19b presents the polarizabilities for the ordinary and the extraordinary axis together with their mean value as a function of C atoms in the alkyl chain. As expected, the polarizabilities rise with the number of C atoms in the alkyl chain. While in case of the mean values a linear increase by approximately 5% per CH_2 group is observed, the polarizabilities of the ordinary and the extraordinary axis reveal a strong impact of the odd and even effect: In case of 6CB, the additional CH_2 group mainly contributes to the short molecular axis, whereas the next odd member, i.e., 7CB, mainly strengthens the long axis.

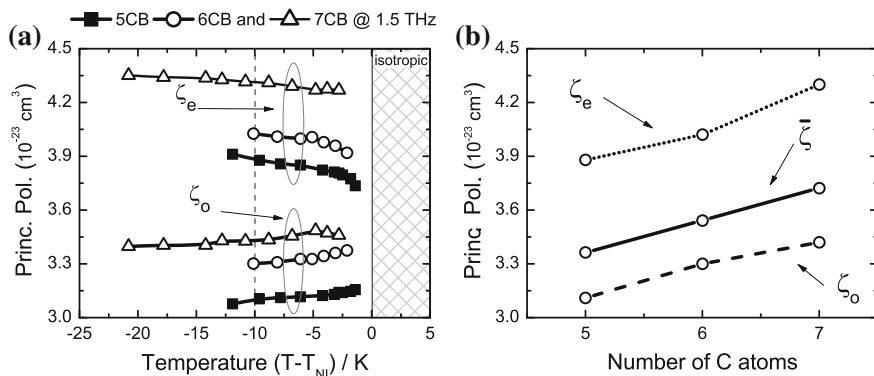


Fig. 12.19 **a** Principle polarizability of 5CB, 6CB, and 7CB at 1.5 THz calculated according to the Vuks's approximation and **b** Principle polarizability of 5CB, 6CB, and 7CB versus the number of C atoms in the alkyl chain. Data are taken from Fig. 12.19a at a reduced temperature of $T - T_{NI} = 10$ K

12.1.10.4 Order Parameter S

The order parameter S is a relevant quantity to characterize the quality of parallel alignment of the LCs in the nematic phase. The S parameter equals unity at absolute zero, where all molecules show a perfect orientation. At temperatures above the phase transition T_{NI} , the S parameter equals zero. Here, the molecules exhibit a random orientation [102–107]. As long as thermal energy is left in the molecular system, i.e., at temperatures above absolute zero, the LC molecules have the ability to move around their center of mass. Hence, even in the nematic phase, despite the presence of an external electric field, only an average preferential orientation results instead of a perfect parallel alignment of all molecules.

To calculate the order parameter from the measured data we employ Haller's extension to Vuks' approximation, which can be written as follows [96, 98]:

$$S = \frac{n_e^2 - n_o^2}{\bar{n}^2 - 1} \frac{\bar{\zeta}}{\Delta\gamma} \quad (12.7)$$

Here, $\bar{\zeta}$ is the mean polarizability and $\Delta\gamma$ is the difference between the longitudinal and transverse polarizability components of the perfectly ordered molecule. In Fig. 12.20a we present the Haller plots ($S \cdot \Delta\gamma / \bar{\zeta}$) over the normalized reduced temperature $T_R = (T - T_{NI}) / T_{NI}$ for 5CB, 6CB, and 7CB, respectively. In the low temperature regime, a linear dependence on a logarithmic scale is observed [98]. The order parameter S equals unity at $T = 0$ K (equivalent to $T_R = -1$) so that a graphical solution for the relative polarizability $\Delta\gamma / \bar{\zeta}$ can be obtained at the intercept of the extrapolated linear fit with the y-axis. For 5CB, 6CB, and 7CB the values of $\Delta\gamma / \bar{\zeta}$ are found to be 0.378, 0.401, and 0.375, respectively.

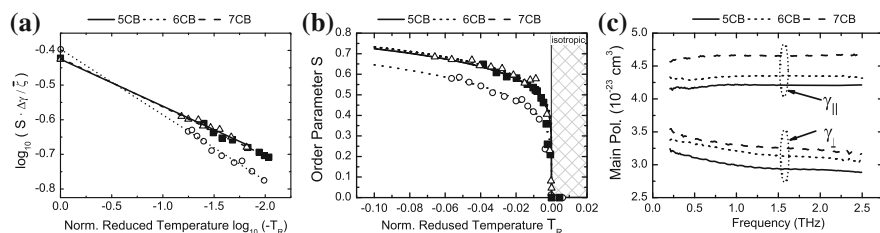


Fig. 12.20 **a** Haller plot of $S \cdot \Delta\gamma/\bar{\zeta}$ on the normalized reduced temperature T_R . **b** Order parameter S of 5CB, 6CB, and 7CB over the normalized reduced temperature τ obtained using Haller's extension to Vuks' approximation and **c** Frequency-dependent main polarizabilities of 5CB, 6CB, and 7CB

With the relative polarizabilities known, the order parameter S can be calculated according to equation (12.7). Figure 12.20b illustrates the dependence of the order parameter S on the normalized reduced temperature T_R for 5CB, 6CB, and 7CB. While the order parameter behaves similar for 5CB and 7CB, it is notably smaller in case of 6CB. This result agrees well with the results obtained by other authors and can be explained by the odd and even effect [108–111]. Molecules containing an odd number of C atoms in the alkyl chain show a higher flexibility than molecules with an even number of CH_2 groups. This behavior leads to a less uniform preferential orientation of the LCs [92].

12.1.10.5 Main Polarizabilities

Now that $\zeta_{e/o}$ and S are known, we will investigate the main polarizabilities of the molecules for the short and the long axis by applying equations (12.2) and (12.3). Figure 12.20c presents the main polarizabilities of 5CB, 6CB, and 7CB in the frequency range from 0.2 to 2.5 THz.

An additional alkyl chain member leads to more polarizability in both, the long and the short molecular axis. In accordance with the results from the study of the molecular structure, we found that odd members create a larger contribution to the polarizability of the molecular long axis, whereas even members contribute mainly to the molecular short axis due to the odd and even effect.

12.1.11 Summary and Outlook

To conclude, this work summarizes recent research performed on liquid crystals at THz frequencies. We presented macroscopic data in form of the refractive indices and the absorption coefficients of a variety of liquid crystals. The investigated substances comprise positive and negative dielectric anisotropy liquid crystals both in their pure form and in mixtures. Furthermore, we derived molecular properties such as the order

parameters S and the main polarizabilities from the macroscopic data using Haller's extension to Vuks' approximation.

One of the future challenges in this field lies in the implementation of liquid crystal-based THz devices, which overcome present drawbacks such as strong losses or slow switching times and which still give sufficient performance despite the low birefringence so far available at these frequencies.

Besides the investigation of new base materials, a paradigm change in the device design seems to become necessary: To avoid losses, instead of transmission-based structures the research should focus on devices operating in reflection mode. Furthermore, designs using only thin liquid crystal layers should be pursued, potentially involving artificial dielectrics such as photonic crystals or metamaterials to cope with the problem of the small interaction length. If innovative approaches are found, liquid crystal devices hold the potential to revolutionize THz technology in a similar, fundamental way as they already did in the optical regime.

References

1. F. Reinitzer, Beiträge zur kenntniss des cholesterins. *Monatsh. Chem.* **9**, 421–441 (1888)
2. M. Evans, M. Davies, I. Larkin, Molecular motion and molecular interaction in the nematic and isotropic phases of a liquid crystal compound. *J. Chem. Soc., Faraday Trans. 2*, **69**, 1011–1022 (1973)
3. B.J. Bulkin, W.B. Lok, Vibrational spectra of liquid crystals. V. far-infrared study of intermolecular modes in 4,4'-azoxydianisole and 4-methoxybenzylidene-4'-n-butylaniline. *J. Phys. Chem.* **77**, 326–330 (1973)
4. E. Sciesinska, J. Sciesinski, J. Twardowski, J.A. Janik, Absorption spectra of p-methoxy benzylidene p-n-butylaniline in the 80–400 cm^{-1} range at temperatures between -200 and 70 °C. *Mol. Cryst. Liq. Cryst.* **27**, 125–140 (1974)
5. M. Evans, R. Moutran, A.H. Price, Dielectric properties, refractive index and far infrared spectrum of cholesteryl oleyl carbonate. *J. Chem. Soc., Faraday Trans. 2*, **71**, 1854–1862 (1975)
6. S. Venugopalan, J.R. Fernandes, G.V. Vani, Far-infrared and raman spectra of the solid phases of CBOOA. *Mol. Cryst. Liq. Cryst.* **31**, 29–46 (1975)
7. G.J. Evans and M. Evans, High and low frequency torsional absorptions in nematic K21. *J. Chem. Soc., Faraday Trans. 2*, **73**, 285–292 (1976)
8. J.R. Fernandes, S. Venugopalan, Infrared spectroscopic study of orientational order and phase transformations in liquid crystalline CBOOA. *Mol. Cryst. Liq. Cryst.* **35**, 113–134 (1976)
9. S. Venugopalan, J.R. Fernandes, V. Surendranath, Far-infrared absorption in the highly ordered smectic phases of TBBA. *Mol. Cryst. Liq. Cryst.* **40**, 149–161 (1977)
10. G.J. Evans, M.W. Evans, Far-infrared spectroscopy of liquid crystals. *Infrared Phys.* **18**, 863–866 (1978)
11. A. Buka, G.P. Owen, A.H. Price, Dielectric relaxation in the nematic and isotropic phases of n-heptyl- and n-heptoxy-cyanobiphenyl. *Mol. Cryst. Liq. Cryst.* **51**, 273–284 (1979)
12. C.J. Reid, M.W. Evans, Assignment of far infrared absorptions in liquid crystalline 4-n-heptyl-4'-cyanobiphenyl. *Mol. Phys.* **40**, 1523–1526 (1980)
13. D. Decoster, J. Depret, Determination du parametre d'ordre de quelques composes nematiques a l'aide d'un laser submillimetrique. *Mol. Cryst. Liq. Cryst.* **56**, 151–156 (Jan. 1980)
14. G.J. Evans, Collective modes in a nematic liquid crystal. *J. Chem. Soc., Faraday Trans. 2*, **79**, 833–845 (1983)

15. J. Shashidhara Prasad, M.M.M. Abdoh, C.I. Venkataramana Shastry, N.C. Shivaprakash, Infrared and far-infrared studies on the nematogenic homologous series trans-4-alkyl-(4-cyanobiphenyl)cyclohexanes. *Mol. Cryst. Liq. Cryst.* **104**, 141–152 (1984)
16. G.J. Evans, K. Moscicki, The polye absorption in liquid crystals. *J. Mol. Liq.* **32**, 149–160 (1986)
17. U.M.S. Murthy, J.K. Vij, Submillimetre wave spectroscopy of 4-n-alkyl-4'-cyano biphenyl liquid crystals. *Liq. Cryst.* **4**, 529–542 (1989)
18. T. Nose, S. Sato, K. Mizuno, J. Bae, T. Nozokido, Refractive index of nematic liquid crystals in the submillimeter wave region. *Appl. Opt.* **36**, 6383–6387 (1997)
19. D. Turchinovich, P. Knobloch, G. Luessem, M. Koch, THz time-domain spectroscopy on 4-(trans-4'-pentylcyclohexyl)-benzonitril, *Proceedings of SPIE*, ed. by I.C. Khoo, vol. 4463, 2001, pp. 65–70
20. R.P. Pan, T.R. Tsai, C.Y. Chen, C.L. Pan, Optical constants of two typical liquid crystals 5CB and PCH5 in the THz frequency range. *J. Biol. Phys.* **29**, 335–338 (2003)
21. R.P. Pan, T.R. Tsai, C.Y. Chen, C.H. Wang, C.L. Pan, The refractive indices of nematic liquid crystal 4'-n-Pentyl-4-cyanobiphenyl in the THz frequency range. *Mol. Cryst. Liq. Cryst.* **409**, 137–144 (2004)
22. C.L. Pan, R.P. Pan, Recent progress in liquid crystal THz optics, *Proceedings of SPIE*, ed. by L.C. Chien, vol. 6135, 2006, p. 61350D
23. R.P. Pan, C.F. Hsieh, C.L. Pan, C.Y. Chen, Temperature-dependent optical constants and birefringence of nematic liquid crystal 5CB in the terahertz frequency range. *J. Appl. Phys.* **103**, 093523 (2008)
24. V.V. Meriakri, C.L. Pan, R.P. Pan, M.P. Parkhomenko, E.E. Chigrai, in Measurement of dielectric properties of liquid crystals in the THz range, *Proceedings of the Conference on Advanced Optoelectronics and Lasers*, Alushta, Ukraine 2008, pp. 109–111
25. V.V. Meriakri, E.E. Chigrai, C.L. Pan, R.P. Pan, M.P. Parkhomenko, in Dielectric properties of liquid crystals in the terahertz frequency range, *Proceedings of the International Conference on Infrared, Millimeter, and Terahertz Waves*, IRMMW/THz, Busan, South Korea, 2009
26. C.Y. Chen, C.F. Hsieh, Y.F. Lin, R.P. Pan, C.L. Pan, Magnetically tunable room-temperature 2 pi liquid crystal terahertz phase shifter. *Opt. Express* **12**, 2630–2635 (2004)
27. C.S. Yang, C.J. Lin, R.P. Pan, C.T. Que, K. Yamamoto, M. Tani, C.L. Pan, The complex refractive indices of the liquid crystal mixture E7 in the terahertz frequency range. *J. Opt. Soc. Am. B* **27**, 1866–1873 (2010)
28. T.T. Tan, R.P. Pan, Y.C. Wang, C.L. Pan, THz time-domain spectroscopic studies of a ferroelectric liquid crystal in the SmA* and SmC* Phases. *Ferroelectrics* **1**, 72–77 (2008)
29. M. Oh-e, H. Yokoyama, M. Koeberg, E. Hendry, M. Bonn, High-frequency dielectric relaxation of liquid crystals: THz time-domain spectroscopy of liquid crystal colloids. *Opt. Express* **14**, 11433–11440 (2006)
30. Y. Takahashi, K. Ishikawa, J. Watanabe, H. Takezoe, M. Yamashita, K. Kawase, Terahertz spectroscopy in smectic phases of a bent-core molecule. *Phys. Rev. E* **71**, 2–4 (2005)
31. J.I. Nishizawa, T. Yamada, T. Sasaki, T. Tanabe, T. Wadayama, T. Tanno, K. Suto, Terahertz dichroism of MBBA liquid crystal on rubbed substrate. *Appl. Surf. Sci.* **252**, 4226–4229 (2006)
32. F. Rutz, T. Hasek, M. Koch, H. Richter, U. Ewert, Terahertz birefringence of liquid crystal polymers. *Appl. Phys. Lett.* **89**, 221911 (2006)
33. R. Wilk, N. Vieweg, O. Kopschinski, T. Hasek, M. Koch, THz spectroscopy of liquid crystals from the CB family. *J. Infrared Milli Terahz Waves* **30**, 1139–1147 (2009)
34. N. Vieweg, M.K. Shakfa, B. Scherger, M. Mikulics, M. Koch, THz properties of nematic liquid crystals. *J. Infrared Milli Terahz Waves* **31**, 1312–1320 (2010)
35. N. Vieweg, M.K. Shakfa, M. Koch, BL037: a nematic mixture with high terahertz birefringence. *Opt. Commun.* (2011)
36. N. Vieweg, M. Koch, Terahertz properties of liquid crystals with negative dielectric anisotropy. *Appl. Opt.* **49**, 5764–5767 (Oct. 2010)

37. O. Trushkevych, H. Xu, T. Lu, J.A. Zeitler, R. Rungsawang, F. Gölden, N. Collings, W.A. Crossland, Broad spectrum measurement of the birefringence of an isothiocyanate based liquid crystal. *Appl. Opt.* **49**, 5212–5216 (2010)
38. C.Y. Chen, T.R. Tsai, C.L. Pan, R.P. Pan, Room temperature terahertz phase shifter based on magnetically controlled birefringence in liquid crystals. *Appl. Phys. Lett.* **83**, 4497–4499 (2003)
39. T.R. Tsai, C.Y. Chen, R.P. Pan, C.L. Pan, X.C. Zhang, Electrically controlled room temperature terahertz phase shifter with liquid crystal. *IEEE Microwave Wirel. Compon. Lett.* **14**, 77–79 (2004)
40. H.Y. Wu, C.F. Hsieh, T.T. Tang, R.P. Pan, C.L. Pan, Electrically tunable room-temperature 2 pi liquid crystal terahertz phase shifter. *IEEE Photonics Technol. Lett.* **18**, 1488–1490 (Jul. 2006)
41. C.L. Pan, C.F. Hsieh, R.P. Pan, M. Tanaka, F. Miyamaru, M. Tani, M. Hangyo, Control of enhanced THz transmission through metallic hole arrays using nematic liquid crystal. *Opt. Express* **13**, 3921–3930 (2005)
42. C.Y. Chen, C.L. Pan, C.F. Hsieh, Y.F. Lin, R.P. Pan, Liquid-crystal-based terahertz tunable lyot filter. *Appl. Phys. Lett.* **88**, 101107 (2006)
43. C.F. Hsieh, Y.C. Lai, R.P. Pan, C.L. Pan, Polarizing terahertz waves with nematic liquid crystals. *Opt. Lett.* **33**, 1174–1176 (2008)
44. C.J. Lin, Y.T. Li, C.F. Hsieh, R.P. Pan, C.L. Pan, Manipulating terahertz wave by a magnetically tunable liquid crystal phase grating. *Opt. Express* **16**, 2995–3001 (2008)
45. H. Zhang, P. Guo, P. Chen, S. Chang, J. Yuan, Liquid-crystal-filled photonic crystal for terahertz switch and filter. *J. Opt. Soc. Am. B* **26**, 101–106 (2009)
46. R. Wilk, N. Vieweg, O. Kopschinski, M. Koch, Liquid crystal based electrically switchable bragg structure for THz waves. *Opt. Express* **17**, 7377–7382 (2009)
47. Z. Ghattan, T. Hasek, R. Wilk, M. Shahabadi, M. Koch, Sub-terahertz on-off switch based on a two-dimensional photonic crystal infiltrated by liquid crystals. *Opt. Comm.* **281**, 4623–4625 (2008)
48. I.C. Khoo, D.H. Werner, X. Liang, A. Diaz, Nanosphere dispersed liquid crystals for tunable negative—Zero—positive index of refraction in the optical and terahertz regimes. *Opt. Lett.* **31**, 2592–2594 (2006)
49. X. Wang, D-H. Kwon, D.H. Werner, I-C. Khoo, A.V. Kildishev, V.M. Shalaev, Tunable optical negative-index metamaterials employing anisotropic liquid crystals. *Appl. Phys. Lett.* **91**, 143122 (2007)
50. S. Xiao, U.K. Chettiar, A.V. Kildishev, V. Drachev, I.C. Khoo, V.M. Shalaev, Tunable magnetic response of metamaterials. *Appl. Phys. Lett.* **95**, 033115 (2009)
51. D.H. Werner, D.H. Kwon, I.C. Khoo, A.V. Kildishev, V.M. Shalaev, Liquid crystal clad near-infrared metamaterials with tunable negativ-zero-positive refractive indices. *Opt. Express* **15**, 3342–3347 (2007)
52. Q. Zhao, L. Kang, B. Du, B. Li, J. Zhou, H. Tang, X. Liang, B. Zhang, Electrically tunable negative permeability metamaterials based on nematic liquid crystals. *Appl. Phys. Lett.* **90**, 011112 (2007)
53. J.A. Bossard, X. Liang, L. Li, S. Yun, D.H. Werner, B. Weiner, T.S. Mayer, P.F. Cristman, A. Diaz, I.C. Khoo, Tunable frequency selective surfaces and negative-zero-positive index metamaterials based on liquid crystals. *IEEE Trans. Antennas Propag.* **56**, 1308–1320 (2008)
54. Y. Yuan, J. He, J. Liu, J. Yao, Proposal of an electrical controlled terahertz switch based on liquid-crystal-filled dual-metallic grating structures. *Appl. Opt.* **49**, 6092–6097 (2010)
55. S. Singh, Phase transitions in liquid crystals. *Phys. Rep.* **324**, 107–269 (2000)
56. D. Pauluth, K. Tarumi, Advanced liquid crystals for television. *J. Mater. Chem.* **14**, 1219–1227 (2004)
57. P. Kirsch, V. Reiffenrath, M. Bremer, Nematic liquid crystals with negative dielectric anisotropy: molecular design and synthesis. *Synlett* **1999**, 389–396 (1999)
58. V. Reiffenrath, J. Krause, H.J. Plach, G. Weber, New liquid-crystalline compounds with negative dielectric anisotropy. *Liq. Cryst.* **5**, 159–170 (1989)

59. P. Kula, A. Spadlo, J. Dziaduszek, M. Filipowicz, R. Dabrowski, J. Czub, S. Urban, Mesomorphic, dielectric, and optical properties of fluorosubstituted biphenyls, terphenyls, and quaterphenyls. *Opto-Electron. Rev.* **16**, 379–385 (2008)
60. S. Gauza, S.T. Wu, A. Spadlo, R. Dabrowski, High performance room temperature nematic liquid crystals based on laterally fluorinated isothiocyanato-tolanes. *J. Disp. Technol.* **2**, 247–253 (2006)
61. Q. Song, S. Gauza, H. Xianyu, S.T. Wu, Y.M. Liao, C.Y. Chang, C.S. Hsu, High birefringence lateral difluoro phenyl tolane liquid crystals. *Liq. Cryst.* **37**, 139–147 (2010)
62. R.D. Dabrowski, J. Dziaduszek, A. Ziolk, L. Szczucinski, Z. Stolarz, G. Sasnouski, V. Bezborodov, W. Lapanik, S. Gauza, S.T. Wu, Low viscosity, high birefringence liquid crystalline compounds and mixtures. *Opto-Electron. Rev.* **15**, 47–51 (2007)
63. S. Gauza, C.H. Wen, B. Tan, S.T. Wu, UV stable high birefringence liquid crystals. *Jpn. J. Appl. Phys.* **43**, 7176–7180 (2004)
64. T.N. Soorya, S. Gupta, A. Kumar, S. Jain, V.P. Arora, B. Bahadur, Temperature dependent optical property studies of nematic mixtures. *Indian J. Pure Appl. Phys.* **44**, 524–531 (2006)
65. B. Gestblom, S. Wrobel, A thin cell dielectric spectroscopy method for liquid crystals. *Liq. Cryst.* **18**, 31–35 (1995)
66. C. Weil, S. Mu, P. Scheele, P. Best, G. Luessem, R. Jakoby, Highly-anisotropic liquid-crystal mixtures for tunable microwave devices. *Electron. Lett.* **39**, 26–28 (2003)
67. S.T. Wu, Absorption measurements of liquid crystals in the ultraviolet, visible, and infrared. *J. Appl. Phys.* **84**, 4462–4465 (1998)
68. J. Li, S.T. Wu, Extended cauchy equations for the refractive indices of liquid crystals. *J. Appl. Phys.* **95**, 896–901 (2004)
69. D. Grischkowsky, S. Keiding, M. Van Exter, C. Fattering, Far-infrared time-domain spectroscopy with terahertz beams of dielectrics and semiconductors. *J. Opt. Soc. Am. B* **7**, 2006–2015 (1990)
70. P.U. Jepsen, R.H. Jacobsen, S.R. Keiding, Generation and detection of terahertz pulses from biased semiconductor antennas. *J. Opt. Soc. Am. B* **13**, 2424–2436 (1996)
71. P.U. Jepsen, D.G. Cooke, M. Koch, Terahertz spectroscopy and imaging—modern techniques and applications. *Laser Photonics Rev.* 1–43, (2010)
72. N. Vieweg, M. Mikulics, M. Scheller, K. Ezdi, R. Wilk, H. Hübers, M. Koch, Impact of the contact metallization on the performance of photoconductive THz antennas. *Opt. Express* **16**, 19695–19705 (2008)
73. N. Vieweg, C. Jansen, M.K. Shakfa, M. Scheller, N. Krumbholz, R. Wilk, M. Mikulics, M. Koch, Molecular properties of liquid crystals in the terahertz frequency range. *Opt. Express* **18**, 6097–107 (2010)
74. R. Wilk, I. Pupeza, R. Cernat, M. Koch, Highly accurate THz time-domain spectroscopy of multy-layer structures. *IEEE J. Sel. Top. Quantum Electron.* **14**, 392–398 (2008)
75. M. Scheller, C. Jansen, M. Koch, Analyzing sub-100- μm samples with transmissionterahertz time domain spectroscopy. *Opt. Comm.* **282**, 1304–1306 (2009)
76. C. Jansen, S. Wietzke, H. Wang, M. Koch, G. Zhao, Terahertz spectroscopy on adhesive bonds. *Polym. Testing* **30**, 150–154 (2011)
77. G.W. Gray, K.J. Harrison, J.A. Nash, New family of nematic liquid crystals for displays. *Electron. Lett.* **9**, 130–131 (1973)
78. R.V. Eidenschink, D. Erdmann, J. Krause, L. Pohl, Substituierte phenylcyclohexane-eine neue klasse flüssigkristalliner verbindungen. *Angew. Chem.* **89**, 103 (1977)
79. L. Pohl, R. Eidenschink, G. Krause, D. Erdmann, Physical properties of nematic phenylcyclohexanes, a new class of low melting liquid crystals with positive dielectric anisotropy. *Phys. Lett.* **60A**, 421–423 (1977)
80. U. Finkenzeller, T. Geelhaar, G. Weber, L. Pohl, Liquid-crystalline reference compounds. *Liq. Cryst.* **5**, 313–321 (1989)
81. D.A. Dunmur, D.A. Hitchen, X.J. Hong, The Physical and Molecular Properties of some Nematic Fluorobiphenylalkanes. *Mol. Cryst. Liq. Cryst.* **140**, 303–318 (Nov. 1986)

82. R. Dabrowski, J. Jadzyn, J. Dziaduszek, Z. Stolarz, G. Czechowski, M. Kasprzyka, The physical and molecular properties of new low melting nematics with negative dielectric anisotropy. *Z. Naturforsch.* **52**, 448–450 (1999)
83. R. Dabrowski, J. Jadzyn, S. Czerkas, J. Dziaduszek, A. Walczak, New low melting nematics 2-chloro-4-alkylphenyl 4-alkylbicyclo-[2,2,2]octane-1-carboxylates with negative dielectric anisotropy. *Mol. Cryst. Liq. Cryst.* **332**, 61–68 (Aug. 1999)
84. Technical Datasheet of MLC7029, Merck KGaA
85. J. Dziaduszek, R. Dabrowski, A. Zióek, S. Gauza, and S.T. Wu, Syntheses and mesomorphic properties of laterally fluorinatedphenyl isothiocyanatolanes and their high birefringent mixtures. *Opto-Electron. Rev.* **17**, 20–24 (2009)
86. V. Vill, *Liquid Crystal Database 4.6* (LCI Publisher, Hamburg, 2005)
87. M.I. Capar, E. Cebe, Odd—even effects in the homologous series of alkyl-cyanobiphenyl liquid crystals: a molecular dynamic study. *J. Comput. Chem.* **28**, 2140–2146 (2007)
88. M.I. Capar, E. Cebe, Molecular dynamic study of the odd-even effect in some 4-n-alkyl-4'-cyanobiphenyls. *Phys. Rev. E.* **73**, 061711 (2006)
89. P. Forstert, B.M. Fung, Chain ordering in cyanobiphenyls and cyanophenylcyclohexanes. *J. Chem. Soc., Faraday Trans. 2.* **84**, 1083–1094 (1988)
90. S. Marcelja, Chain ordering in liquid crystals. I. even-odd effect. *J. Chem. Phys.* **60**, 3599–3604 (1974)
91. J.R. Lalanne, J.C. Rayez, B. Duguay, A. Proutiere, R. Viani, Molecular aspects of the even-odd effect in cyanobiphenyls (nCB): theoretical studies of the molecular geometrical conformation and optical anisotropy. *J. Chem. Phys.* **81**, 344–348 (1984)
92. I. Chirtoc, M. Chirtoc, C. Glorieux, J. Thoen, Determination of the order parameter and its critical exponent for nCB ($n = 5 - 8$) liquid crystals from refractive index data. *Liq. Cryst.* **31**, 229–240 (2004)
93. I. Cacelli, L.D. Gaetani, G. Prampolini, A. Tani, Liquid crystal properties of the n-alkyl-cyanobiphenyl series from atomistic simulations with ab initio derived force fields. *J. Phys. Chem. B* **111**, 2130–2137 (2007)
94. M.I. Capar, E. Cebe, Rotational viscosity in liquid crystals: a molecular dynamics study. *Chem. Phys. Lett.* **407**, 454–459 (2005)
95. N.C. Shashidhara Prasad, M.M.M. Abdoh, Srinivasa, J. Shashidhara Prasad, Refractive indices, densities, polarizabilities and molecular order in cholesteric liquid crystals. *Mol. Cryst. Liq. Cryst.* **80**, 179–193 (1982)
96. R.G. Horn, Refractive indices and order parameters of two liquid crystals. *J. Phys.* **39**, 105–109 (1978)
97. M.F. Vuks, Determination of the optical anisotropy of aromatic molecules from the double refraction of crystals. *Opt. Spektrosk.* **20**, 644–651 (1966)
98. I. Haller, Thermodynamic and static properties of liquid crystals. *Solid-State Chem.* **10**, 103–118 (1975)
99. C.J.F. Böttcher, *Theory of Electric Polarisation* (Elsevier, Amsterdam, 1952)
100. S. Chandrasekhar, N.V. Madhusudana, Orientational order in p-azoxyanisole, p-azoxyphenetole and their mixtures in the nematic phase. *J. Phys. Colloq.* **30**, C4–24 (1969)
101. Group Landolt-Börnstein, *Group VIII Advanced Materials and Technologies Physical Properties of Liquid Crystals* (Springer, Berlin, 2003)
102. W. Maier, A. Saupe, Eine einfache molekulare theorie des nematischen kristallinen zustandes. *Z. Naturforsch. A.* **13** 564 (1958)
103. W. Maier, A. Saupe, Eine einfache molekularstatistische theorie der nematischen kristallin-flüssigen phase teil I. *Z. Naturforsch. A.* **14a**, 882 (1959)
104. M.J. Freiser, Ordered states of a nematic Liquid. *Phys. Rev. Lett.* **24**, 1041–1043 (1970)
105. J.R. McColl, C.S. Shih, Temperature dependence of orientational order in a nematic liquid crystal at constant molar volume. *Phys. Rev. Lett.* **29**, 85–87 (1972)
106. G. Heppke, C. Bahr, *Aufbau der Materie* (W. de Gruyter, Berlin, 1981)
107. P.J. Collings, M. Hird, *Introduction to Liquid Crystals Chemistry and Physics* (Taylor & Francis, London, 2004)

108. S. Urban, A. Würflinger, B. Gestblom, On the derivation of the nematic order parameter from the dielectric relaxation times. *Phys. Chem. Chem. Phys.* **1**, 2787–2791 (1999)
109. A. Buka, W.H. De Jeu, Diamagnetism and orientational order of nematic liquid crystals. *J. Phys. Chem.* **43**, 361–367 (1982)
110. J.A. Ratto, S. Ristori, F. Volino, M. Pineri, M. Thomas, M. Escoubes, R.B. Blumstein, Investigation of a liquid crystal dispersed in an ionic polymeric membrane. *Chem. Mater.* **5**, 1570–1576 (1993)
111. I.H. Ibrahim, W. Haase, On the molecular polarizability of nematic liquid crystals. *Mol. Cryst. Liq. Cryst.* **66**, 189–198 (1981)

Chapter 13

Terahertz Spectroscopy of Polymers

Christian Jansen, Steffen Wietzke and Martin Koch

Abstract Polymers and terahertz (THz) waves form a fruitful symbiosis: on the one hand, non-polar plastics serve as base materials for THz optics as they exhibit low absorption and excellent machinability. On the other hand, THz time-domain spectroscopy (TDS) grants access to unique information about the molecular structure and morphology of polymers, offering an immense portfolio of interesting scientific opportunities. Furthermore, contact-free, non-destructive testing with non-ionizing THz radiation could evolve as a valuable addition to or substitution of ultrasonic and X-ray characterization, especially in quality inspection and process control applications. This chapter aims to give an overview of recent activities in this field, covering both the spectroscopic analysis of polymers with THz waves as well as the non-destructive testing of plastic components with THz systems.

13.1 Introduction

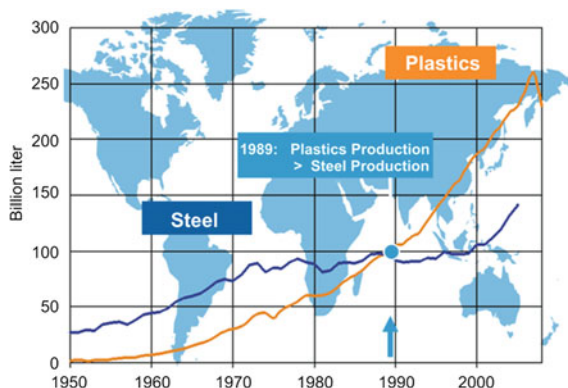
Polymers have become an essential part of our daily life. Apart from forming the basis of many commodities, high-tech plastics start to conquer a variety of structural and functional applications, ranging from aerospace or automotive components to optical devices. The rapid development of this rather young group of materials is depicted in Fig. 13.1. The worldwide production of plastics increased from about 1.5

C. Jansen (✉) · S. Wietzke · M. Koch
Fachbereich Physik, AG Terahertz-Systemtechnik,
Philipps-Universität Marburg,
Hans-Meerwein-Str., MZG C06, 35032 Marburg, Germany
e-mail: chr.jansen@gmx.net

S. Wietzke
e-mail: steffen.wietzke@ingenieur.de

M. Koch
e-mail: martin.koch@physik.uni-marburg.de

Fig. 13.1 The success story of plastics—Benchmarking the worldwide production volume of plastic versus crude steel (Courtesy of *PlasticsEurope*)



billion liters in 1950 to 230 billion liters in 2009 [1] corresponding to the average annual growing rates of about 10 %. In 1989, the polymer production by volume even surpassed that of steel. In the following pages we will investigate the potential of THz spectroscopy as a versatile characterization tool, both for pure polymers and plastic components.

This chapter is divided into two parts. The first part will investigate the macromolecular structure of polymers. Special emphasis is placed on the discussion of spectral features observed at THz frequencies but also on the implications of the polymers' morphology to the interactions with THz waves. In the second part, starting with Sect. 13.3, the focus will shift from fundamental material science to industrial applications of THz time domain spectroscopy (TDS) in the field of plastic component testing, quality inspection, and process control.

13.2 Dielectric Properties of Polymers in the Terahertz Regime

The predominantly used frequency range for the spectroscopic analysis of polymers lies in the near- and mid-infrared (NIR, MIR). In these spectral regions, absorption peaks mainly arise from highly localized intramolecular deformation, such as hindered rotation or stretching oscillation of covalent bonds [2]. However, if collective motions of large molecules, such as inter- and intramolecular vibrations of the polymer chains, are of interest, longer wavelengths have to be considered. The far-infrared (FIR) or terahertz (THz) regime, comprising frequencies from 100 to approximately 6 THz, equivalent to wave numbers from 3 to 200 cm^{-1} , can provide valuable insights into these complex characteristics of polymers. While FIR Fourier transform spectroscopy (FTS) [3] enjoyed much popularity over the past decades, THz time-domain spectroscopy offers some unique advantages, which may expand our understanding of polymer chemistry even further.

The first advantage arises from the data acquisition. The pulsed nature and the coherent detection scheme of THz TDS allows for extracting the dielectric prop-

erties, e.g., in the form of complex permittivity $\underline{\epsilon}$ or complex refractive index \underline{n} , simultaneously with the thickness of the sample [4, 5], as will be briefly discussed in Sect. 13.3.4. This non-destructive, contact-free technique still works when the samples are investigated at cryogenic temperatures so that the thickness ambiguity which normally arises in such measurements from nonlinear thermal expansion can be excluded (cf. Sect. 13.2.3). Other properties that set THz TDS apart are a better signal-to-noise ratio for frequencies below 3 THz and detectors operating at room temperature [6].

The first part of this chapter is organized as follows: after having grouped polymers by their dielectric properties in Sect. 13.2.1, we assign the spectral features to their macromolecular origin, such as skeletal vibrations, orientation polarization, lattice modes, and oscillation of hydrogen bonds, supplementing databases published so far [7–9]. Next, we will study phase transitions of polymers and discuss the potential of THz TDS to investigate the morphology and conformation characteristics [10, 11]. Section 13.2.3 summarizes recent results of temperature-dependent dielectric parameter studies of various polymers. We will show that the glass transition temperature can be reliably determined by the thermal gradient of the refractive index, which is especially valuable in cases where conventional testing methods fail. The majority of technical plastics does not merely consist of pure polymers, but in most cases contains additive materials to enhance their functionality. Thus, the first half of this chapter closes with Sect. 13.2.4, which is dedicated to the study of polymeric compounds with THz TDS, building a bridge between the domains of fundamental material science discussed so far and the industrial applications following in the second half of this work, starting with Sect. 13.3.

13.2.1 Grouping Polymers in the THz Frequency Range

Many polymers are transparent to THz waves, making them attractive base materials for THz system components such as windows [12], Bragg filters [13, 14], lenses [15, 16], or wave guides [17, 18]. Thus, apart from understanding the molecular interactions in these intriguing materials, the spectral properties of polymers are also of interest for the design of THz devices. For instance, polyethylene (PE) offers a low absorption and has already been employed for lenses, but its use is restricted by the extinction bands in the vicinity of 2.2 THz arising from lattice modes that we will discuss later in this chapter. Other low-loss materials are mainly amorphous polymers such as Tsurupica[®] (formerly known as Picarin[®]) or cyclic olefin copolymers (COC) with trademarks such as TOPAS[®] (Ticona) and Zeonex[®]/Zeonor[®] (Zeon Chemicals Co.) [19]. In addition to their low absorption over a much wider frequency range [16], they provide further advantages in terms of easy alignment using visible light and good machinability [20].

As shown in Fig. 13.2, polymers can be divided into a nonpolar and a polar group: the low-refractive ($n < 1.55$), low-loss polymers without overall dipole moments on the left-hand side (shown in Fig. 13.2a, c) and the high-refractive ($n > 1.60$), high-

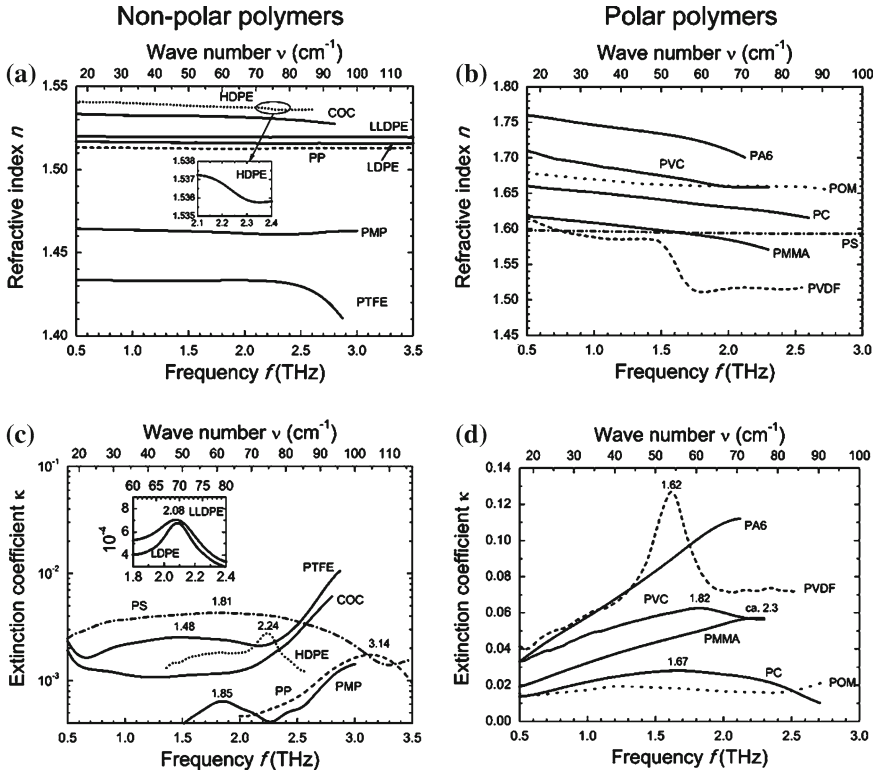


Fig. 13.2 Refractive index n (a), (c) and extinction coefficient κ (b), (d) of nonpolar and polar polymers at THz frequencies. The center frequency of the extinction band is denoted on top of the maximum value. For the abbreviations of the polymers cf. Table 13.1. The group of cyclic olefin copolymers (COC) is represented by a Zeonor[®] (brand name) sample

loss polar polymers on the right-hand side (shown in Fig. 13.2b, d). Polystyrene (PS) can be regarded as a hybrid since only a small dipole moment is present due to a slightly increased electron density at the benzene ring (inductive effects of alkyl groups and hyper conjugation). Extinction bands correspond to a step in the refractive index curve caused by a resonant behavior or orientation polarization (cf. Sect. 13.2.2). The center frequency f_c corresponds to the spectral position of the refractometric inflection point. In the following section, we will attribute these spectral features to their (macro-) molecular origin.

13.2.2 Origin of the Spectral Features

Before further discussing the observed spectral features, we have to take a look at the complex phase structure of polymers [21, 22]. Polymers are never purely crystalline

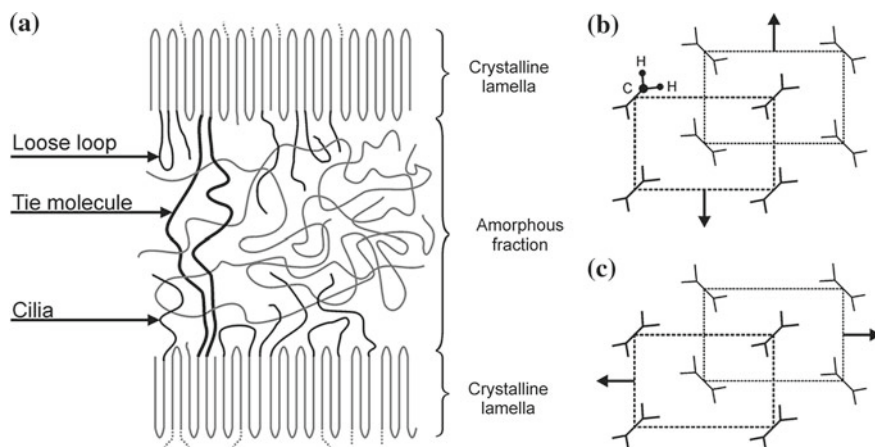


Fig. 13.3 a Semi-crystalline polymers exhibit a complex phase structure: crystalline and amorphous domains are intimately connected by the extremely long macromolecules, giving rise to thermomorphological interactions (cf. Sect. 13.2.3); b–c the origin of lattice modes in PE: cross section through elementary cells perpendicular to the macromolecular axis (simplified bone-like notation of the planar zigzag PE chains, considered as rigidly moving). The relative motion results in the two orthogonal lattice modes B_{1u} (b) and B_{2u} (c) [24, 25]

or purely amorphous but rather exhibit a semi-crystalline morphology (Fig. 13.3). Densely packed crystalline domains consisting of more or less regularly folded chains are surrounded by randomly entangled polymer coils of the amorphous regions. Since the constitutional unit of a macromolecule is repeated thousands of times, each chain can contribute to several domains of the semi-crystalline phase structure. In this way, amorphous and crystalline domains are connected by tie molecules, which link nearby crystalline lamellae, and loose loops or cilia, which originate from the crystalline phase but protrude into the amorphous fraction [23].

Keeping this complex morphology in mind, we can now attribute the previously observed spectral features of polymers in the THz range to four different main types of macromolecular motion: skeletal vibrations, orientation polarization, lattice modes, and oscillation of hydrogen bonds [3]. To summarize the findings for the investigated polymers, Table 13.1 contains a list of the observed spectral fingerprints together with the (macro-) molecular origin which they are attributed to in the literature. A detailed discussion follows in the remainder of this section.

13.2.2.1 Skeletal Vibrations

Skeletal vibrations are (rotatory) oscillations of the backbone chain segments, which comprise correlated deformation, torsion and bending of consecutive backbone chain atoms, i.e., a crank-shaft-like motion [43]. The spectral position and the band intensity depend on the flexibility of the chain and on the strength of the noncovalent

Table 13.1 Center frequency f_c of observed spectral features for various polymers at room temperature

Polymer	f_c/THz		Molecular origin	References
	κ	$\alpha_{\text{Lit.}}$		
HDPE	2.24	2.2	LM(B _{1u})	[3, 24–28]
LLDPE/LDPE	2.08	2.1	LM(B _{2u})	
		2.82		
		6.00		
PP	3.14	3.18	SV	[3]
PMP	1.85	2.1 . . . 2.4	No assignment	[29, 30]
		4.25, 7.04, 7.48, 8.85	No assignment	
PS	1.81	2.40	OP (phenyl group)	[3, 31]
		6.54	Deformation of benzene group	
		7.35	SV	
PTFE	1.48	1.5	LM	[32–34]
		(Splitting for $T < 292\text{K}$)	LM	
		6.09	LM (CF ₂ groups)	
PVDF	1.62	2.1, 1.59, 2.52	LM (modification I, II, III)	[35–37]
		2.55, 3.06, 5.25	SV	[36]
PMMA	(2.3)	2.85	OP (ester group)	[3, 31]
		6.75, 9.60	SV	
PC	1.67	2.25	OP (benzene group)	[3]
		6.6, 7.8	SV	
POM	–	2.70, 3.90, 9.12	SV	[3, 38]
PA6	–	3.00 . . . 3.30	HB	[39–41]
PVC	1.82	1.95	LM	[3, 41, 42]
		2.7	OP (chlorine atom)	
		5.70	SV	

Both the center frequency in terms of the extinction coefficient κ measured by THz TDS and the absorption coefficient from the FIR-FTS literature data $\alpha_{\text{Lit.}}$ are provided, which slightly differ since α is proportional to κ times the frequency f . The assignment to molecular origin is abbreviated as skeletal vibration *SV*, orientation polarization *OP* (functional group involved), lattice mode *LM* (type), and oscillation of hydrogen bonds *HB*. The abbreviations denote the polymers high-, linear low-, and low-density polyethylene (HD-, LLD-, LDPE), polypropylene (PP), polymethylpentene (PMP, brand name: TPX), polystyrene (PS), polytetrafluoroethylene (PTFE), polyvinylidene fluoride (PVDF), polymethylmethacrylate (PMMA), polycarbonate (PC), polyoxymethylene (POM), polyamide 6 (PA6), polyvinyl chloride (PVC)

interaction (dipole–dipole or hydrogen bonds) between neighboring chains [31]. Due to bandwidth limitations of the THz spectrometer, only the skeletal vibrations of PP and POM (rising tail) are visible in Fig. 13.2c, d, respectively.

13.2.2.2 Orientation Polarization

Orientation polarization originates from the rotation of permanent dipoles in an alternating electric field. However, compared to liquids, the oscillation of the polar groups

in the viscous amorphous domains of polymers is much more restricted due to short-range order. On the one hand, the groups are intramolecularly limited in motion by covalent bonds to or in the backbone chain. On the other hand, moving segments experience sterical and electrostatic hindrances by neighboring macromolecules in the coiled amorphous phase. Therefore, Bershtein and Ryzhov refer to this libration, arising from hindered rotation of polar units, as liquid-lattice mode [3]. For instance, the broad extinction band and the corresponding dispersive behavior in the refractive index curve for PMMA ($f_c \approx 2.3$ THz), PC ($f_c = 1.67$ THz) or PS ($f_c = 1.81$ THz) shown in Fig. 13.2c, d originates from libration of the ester group (PMMA) and the phenyl group (PC, PS). PS exhibits hardly any dispersion and a low, very broadband extinction since only a small dipole moment is present at the phenyl side group (cf. Sect. 13.2.1). Since these interactions predominantly originate from the amorphous domains, where the macromolecules are randomly entangled, the orientation polarization also arises as a broad spectral feature.

13.2.2.3 Lattice Modes

Lattice modes result in a pronounced spectral absorption peak in highly crystalline polymers such as high-density polyethylene (HDPE) or polyvinylidene fluoride (PVDF). Intensive studies have been carried out on these two polymers (cf. Table 13.1 for references). Chain segments in the crystalline lamellae are aligned in parallel over a multitude of constitutional repeat units (Fig. 13.3a). Hence, the molecular axes in these ordered regions can be simplified as rigidly moving chains, especially in the case of HDPE [24, 44]. A cross section perpendicular to the parallel molecular axis reveals the elementary cell (Fig. 13.3b). Resonant interactions of lattice vibration (optical branches of the dispersion relation) with electromagnetic waves yield two orthogonal translational lattice modes that are THz active: the B_{1u} and the less pronounced B_{2u} lattice mode, illustrated in Fig. 13.3b, c, respectively.

Figure 13.2 depicts the lattice modes for the three differing branching grades of PE. HDPE, exhibiting highest regularity, i.e. the smallest number of branching points in the backbone chain, is highly crystalline (degree of crystallinity 51.5 %, determined by differential scanning calorimetry). This high density results in the highest refractive index among the PEs due to the Lorentz–Lorenz law [45]. In addition, the extinction band arising from the B_{1u} lattice mode is highly pronounced peaking at $f_c \approx 2.24$ THz. LLDPE (38.9 %), which has a regulated number of short side chains, and the highly branched LDPE (32.2 %) not only show lower refractive indices but also exhibit broadened extinction bands due to lattice disorder arising from chain folding in the lamellae [46] and branching of the backbone chain [26]. Furthermore, the increased lattice distortion due to a higher degree of branching leads to a lower center frequency [26], which we determine to be 2.08 THz. The thermal dependence of this lattice mode, shifting toward lower center frequencies with increasing temperature, will be discussed in Sect. 13.2.3.

In PVDF, the lattice mode arises from the high permanent dipole moment of the C–F-bond (a high difference in electronegativity of 1.6) and the molecular structure

[47]. Depending on the conformation, three lattice types exist: form I (β), II (α), and III (γ) [35, 47, 48]. We show the dielectric parameters for a PVDF lattice mode of form II ($f_c = 1.62$, cf. Fig. 13.2d), arising from a rotation of parallel chains around their longitudinal axes symmetrical to each other (A_u). In comparison with the other polar polymers, PVDF exhibits a strong anomalous dispersion from $n = 1.59$ at 1 THz down to $n = 1.52$ above 2 THz, reflecting the strong dipole moment and a strong intermolecular coupling in PVDF.

PVC exhibits a broad extinction band with a center frequency at 1.82 THz, which has originally been ascribed to a vibration of hydrogen bonds [49]. However, later studies favor the interpretation of this band as a lattice mode [42]. The PTFE spectrum shows a broad extinction band with a center frequency in the vicinity of 1.48 THz and an increasing slope above 2.5 THz. The latter phenomena is attributed to the lower frequency tail of a strong interaction with the twist motion of CF_2 groups at about 6 THz [32]. The former band at room temperature results from interactions with lattice modes and splits at temperatures below 292 K due to a change in the helix conformation [33].

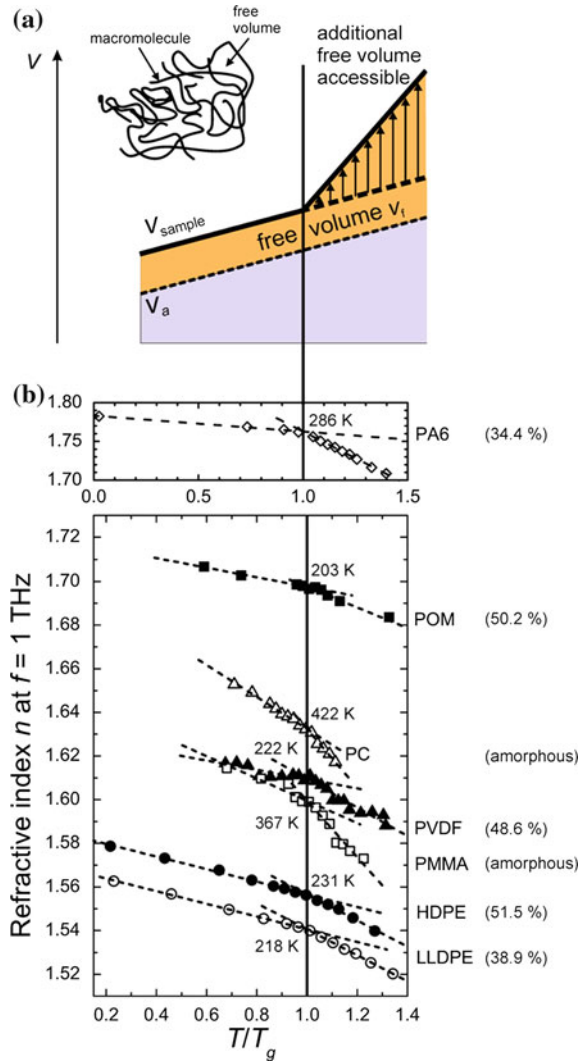
13.2.2.4 Hydrogen Bonding

Hydrogen bonding typically results in a shift of middle-infrared peak frequencies arising from stretching of the involved covalent bonds [50]. However, interactions with hydrogen bonds can also be observed in the THz range. For example, the translation oscillation of the amide group between two hydrogen bonds in the crystalline domains of polyamides can be observed in the vicinity of 3 THz [39]. Due to bandwidth limitation, only the ascending tail of the corresponding extinction band for PA6 can be seen in Fig. 13.2d. Recently, a spectral feature around 2.49 THz in a polyester has been attributed to oscillations of chain segments between hydrogen bonds in the crystalline domains [11].

13.2.3 Monitoring the Glass Transition

From a macroscopic point of view, the glass transition marks the transition between the glassy and the rubbery state of polymers, determining the processing and working temperatures of thermoplastics and elastomers. However, a complete microscopic interpretation is still subject to intense research [23, 51–53]. On the one hand, it cannot be satisfyingly explained by equilibrium thermodynamics as it is no sharp transition and is dominated by relaxation processes [54, 55]. Therefore, the glass transition spans over a certain temperature range and stating the glass transition temperature T_g as discrete value is just a question of definition [56]. On the other hand, the theoretical considerations of kinetics deviate from experimental results when approaching the glass transition, especially in the case of semi-crystalline polymers [55, 57].

Fig. 13.4 Model of the free volume for the glass transition (a) and the two temperature regime behavior of the THz refractive index for different polymers with two linear fits intersecting at glass transition temperature T_g (b). The T_g values are stated separately since the abscissa is normalized for reasons of clarity. The degree of crystallinity is denoted on the right-hand side in brackets



In the following, we consider T_g as the onset of translational backbone chain segment motion inside the amorphous domains and use the model of the free volume as shown in Fig. 13.4a, which allows for an intuitive, even though simplified, understanding of the glass transition [43].

In this model, v_a denotes the volume filled by the atoms while the unoccupied space between the macromolecules is referred to as the free volume v_f . v_a is a linear function of the temperature. In fact, the free volume remains nearly constant at temperatures below T_g [58], where the backbone motion is frozen. At $T > T_g$, there is enough thermal energy so that segmental motion starts and creates additional free volume.

This change yields an increase in the specific volume of the sample, tantamount to a decrease in density, resulting in two regimes of temperature dependence. Thus, due to the Lorentz–Lorenz law [45], the thermal gradient of the refractive index below and above the glass transition should also differ, which we will investigate by temperature-dependent THz TDS measurements [59].

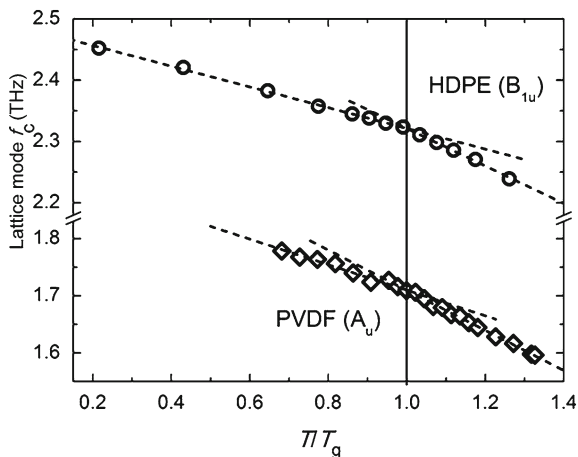
The two temperature regimes of the refractive index are depicted in Fig. 13.4b for a variety of polymers, most of which are semi-crystalline as indicated by the degree of crystallinity. For clarity, we display the refractive index at 1.0 THz over the reduced temperature, normalized to T_g . A linear regression can be applied to each temperature regime. T_g is determined at the intersection. Measurements by differential scanning calorimetry (DSC) have verified the THz TDS results [55]. However, conventional methods for determining T_g such as DSC or dynamic mechanical analysis (DMA) fail for highly crystalline samples. For instance, independent DSC scans of three different chemical laboratories and DMA measurement of two institutes did not yield any conclusive indication of the glass transition in case of HDPE. Yet, THz TDS reliably reveals T_g at the intersection. Further information on this topic can be found in [60] and [61].

While the glass transition is an exclusive feature of the amorphous phase, the domains of a semi-crystalline polymer are intimately connected as can be seen from Fig. 13.3a. Actually, much more has to be known about the thermo-morphological coupling in semi-crystalline polymers in terms of characterization and properties for applications [62]. So far, the literature has only focused on the crystalline domains affecting the amorphous phase [23, 53]. We recently demonstrated by THz TDS measurements that this coupling is a bidirectional effect [61].

Wunderlich subdivides the amorphous domains into the mobile amorphous and the rigid amorphous fraction (MAF and RAF). The RAF forms a constrained nanophase system adjacent to the crystalline lamellae [21]. This coupling yields a broadening of the glass transition region or even results in a separate glass transition at higher temperatures. Considering the temperature dependence of lattice modes at THz frequency in the crystalline domains, we have observed the first experimental evidence for thermo-morphological interactions vice versa [61]. The thermal lattice mode frequency shift depends on both the thermal expansion of the unit-cell dimensions in the crystalline phase and the glass transition taking place in the amorphous domains. Macromolecules of the MAF that have obtained full mobility above T_g affect the crystalline lamellae due to entanglements between the phases and via the RAF (cf. Fig. 13.3). This additional lattice distortion results in a higher thermal gradient of the lattice mode frequency shift for temperatures above T_g as shown for HDPE and PVDF in [61] (Fig. 13.5).

In this context, it is worth noting that the pulsed nature of THz TDS and advanced data extraction algorithms [4, 5] allow for the simultaneous extraction of the thickness and the dielectric material parameters, which is especially useful for measurements at cryogenic temperatures. In contrast to established techniques [27], no correction or extrapolation has to be employed for considering the thermal expansion of the sample, excluding a major source of uncertainty. A comparison with other non-destructive and contact-free techniques is given elsewhere [59].

Fig. 13.5 The frequency shift of the lattice mode in HDPE and PVDF changes at the glass transition due to thermo-morphological coupling between the phases in semi-crystalline polymers



13.2.4 Polymeric Compounds

In the previous sections, we discussed various characteristics of pure polymers and demonstrated the merits of THz TDS as characterization method. Yet, the majority of technical plastics has to be functionalized by compounding the neat polymer as basic material with additives, including fillers for cost reduction or reinforcement, flame retardants, colorants, plasticizers, and many more [63]. This modification step enables custom-tailored solutions for a variety of applications, ranging from commodities to high-tech products. In order to obtain high performance plastics, the additives have to be distributed homogeneously within the polymer matrix, which requires reliable compounding processes [64]. On the one hand, THz spectroscopy is a promising non-destructive technique for the quality control of these compounds and the respective compounding processes [65, 66]. On the other hand, polymeric compounds provide valuable base materials for a variety of THz components, as high refractive indices combined with a good processability can be obtained [67, 68]. That is why we will consider first how additives affect the dielectric properties of the compound.

THz absorption spectroscopy has already been introduced as a potential candidate for analyzing the filler concentration and its spatial variation [69]. Boulay et al. correlate the mica content in polyurethane and the transmission at submillimeter laser lines (443, 526, and 761 GHz). In addition, the lateral concentration variation of mica platelets in PE as host polymer was investigated in a line scan.

In [70] and [71], the authors demonstrated that the dielectric properties of polymeric compounds depend on the additive concentration. Amongst the investigated systems are magnesium hydroxide ($Mg(OH)_2$) in LLDPE, glass fibers in polyamide, as well as calcium carbonate ($CaCO_3$), silicon and silicon dioxide in PP.

Figure 13.6 shows the results of THz TDS transmission measurements on polymeric compounds performed under nitrogen atmosphere. The determination of the

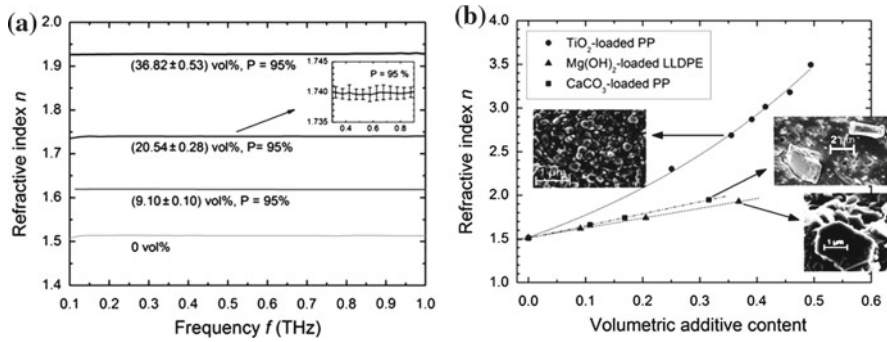


Fig. 13.6 a Refractive index over the frequency for an increasing content of $\text{Mg}(\text{OH})_2$ in LLDPE; b comparison of the refractive indices of polymeric compounds at 800 GHz depending on the additive concentration [71]

sample thickness and the calculation of the dielectric parameters were carried out using the commercially available software Teralyzer Data Extraction Suite [5] that is based on the algorithm discussed in [72]. The accuracy of the measurement is taken into account statistically by considering Student's t -distribution for the employed sample size [73]. The expanded uncertainty formed by the sample standard deviation and the coverage factor k can be regarded as the half-width of a confidence interval that encloses the notional true value of the measurand with a minimum coverage probability P chosen to be 95% [74, 75].

Figure 13.6a displays the refractive index spectra of the material combination LLDPE/ $\text{Mg}(\text{OH})_2$ for different additive concentrations determined by the ignition residue content after combusting the compounds. The extraction algorithm [72] leads to highly accurate refractive index curves, none of which exhibits any significant dispersion. Error bars denoting the confidence interval for $P = 95\%$ cannot be seen in the plot since they are much smaller than the symbols for the sample mean values themselves. Exemplarily, the confidence interval for $P = 95\%$ is presented in the inset of Fig. 13.6a for the compound with 20.54 vol% $\text{Mg}(\text{OH})_2$. Figure 13.6b compares the refractive index n of different compounds at a frequency of 800 GHz. Whereas the refractive indices of LLDPE/ $\text{Mg}(\text{OH})_2$ and PP/ CaCO_3 increase quite linearly with increasing additive content, the titania(TiO_2)-loaded PP reveals a strongly progressive curve.

For the modeling of the dielectric material parameters of heterogeneous mixtures like the presented polymeric compounds, effective medium theories have to be employed [76, 77]. In addition to the permittivity of the mixture components, the shape and the size distribution of the particles embedded in the host medium have to be considered (cf. scanning electron micrographs in Fig. 13.6b).

The frequently used quasi-static models for heterogeneous dielectric mixtures still originate from the first half of the last century. Unfortunately, all of them are limited in their range of applicability by the assumptions in their derivations. One of the first and still widely used approaches to dielectric mixture equations, the

Maxwell–Garnett model from 1904 [78], considers only spherical particles in low concentrations. Bruggeman advanced Maxwell–Garnett’s approach in terms of higher additive contents [79] while still neglecting the influence of particle shape. Another extension to the Maxwell–Garnett model by Polder and van Santen assumes ellipsoidal particle geometries by introducing depolarization factors [80], but is only valid for low particle concentrations. Consequently, existing physical models are either restricted to spherical particles or dilute mixtures.

Recently, the authors proposed an extension to the Bruggeman approach considering ellipsoids instead of spheres. Overcoming the limitations stated above, it provides both shape dependence and full concentration coverage. For further information on this effective medium theory and its application to modeling polymeric compounds in the THz range, the inclined reader is referred to reference [71].

13.3 Applications for THz Systems in the Polymer Processing Industry

So far, the focus of this chapter has been placed on the contributions that THz spectroscopy can make to the fundamental material science of polymers. Now, we will shift the focus from basic research toward industrial applications of THz spectroscopy in the field of polymer processing and plastics component testing.

The growing number of applications relying on plastics leads to a strong demand for quality assurance in this field. Conventional testing is mostly destructive and provides results based on specimen or random examination [81]. As the properties of plastic components are highly sensitive to processing parameters, these measurement results do not necessarily have to be representative for the entire batch. In many cases, a total inspection is crucial since a failing component can potentially cause consequential charges exceeding the production costs by a multiple, especially in the case of high-tech products. Thus, non-destructive testing techniques are required.

Non-destructive and contact-free THz measurements hold a high potential as new sensor technology for both, monitoring of polymer processing, and testing of plastic products. So far, only proof of principles for different application scenarios have been given but a commercialization of THz sensors for the polymer processing industry is still due. However, recent developments, such as the reduction in the price of femtosecond laser sources and improvements in THz emitters and detectors pave the way for a broad scale market introduction. The following sections will provide an overview of potential applications for THz systems, which will comprise the monitoring of polymer compounding processes (13.3.1), measuring moisture content (13.3.2), inspection of plastic weld joints (13.3.3), testing of adhesive bonds (13.3.4) and finally the determination of fiber orientation in reinforced plastic components (13.3.5).

13.3.1 Controlling Compounding Processes with THz Sensors

The quality of a polymeric compound strongly depends on the compound composition and the processing technique. Considering that the field of compounding is dominated by small- and medium-sized enterprises, the companies are under the constraint to offer highly customized products at low prices. Hence, compounding has to rely on flexible, time- and cost-efficient quality management and process control. In-line monitoring would minimize the time required for testing. Consequently, instable process conditions as well as flawed batches could be prevented. Direct feedback from the process not only supports production but also enables a rapid process development for custom-tailored products.

Approved and standardized measurement methods for compound characterization, like mechanical tests, thermal analysis, or light microscopy [81], are mostly offline, i.e., time-consuming and destructive. Recently, there have been several approaches to get closer to the compounding process with on- and in-line measurements. For instance, there are the pressure filter test [82], ultrasonic testing [83], microphotometric measuring [84, 85], and spectroscopic monitoring in the near-infrared [86, 87]. Unfortunately, they all have specific limitations. So far, only temperature and pressure are usually controlled in-line, but this hardly provides enough information about the complex compounding process. Non-destructive testing methods, that provide in situ monitoring, have not been applied yet.

THz TDS might soon establish as a reliable, non-destructive evaluation method for determining the polymer compound composition [65] and also the dispersion quality of additive particles within the polymer matrix [66]. To get THz systems close to the process, Vieweg et al. recently presented a compact fiber-coupled THz time-domain spectrometer for monitoring polymer compounding processes [88] as depicted in Fig. 13.7a. Shock-resistant mounting on a mobile rack enables stable operation of the hermetically encapsulated spectrometer even in a rough industrial environment. The fiber-coupled photoconducting antenna heads with integrated electronics also contribute to the maintenance-free service. The fibers are precisely glued to the optimal excitation position making any further adjustment unnecessary.

The THz pulses are coupled out via lenses made from high-resistivity silicon. Polyethylene lenses are employed for further beam guiding. The vertical setup and a special slit die at the end of the extruder allow for in situ transmission measurements of the melt through two windows made of fused silica at the end of the compounding line (Fig. 13.7b).

In a cooperation with the Southern German Plastics Center (Süddeutsches Kunststoff-Zentrum, SKZ), first in-line measurements were performed. A comparison of the offline results obtained in a THz TDS laboratory setup on injection molded specimen [70] and the in-line measurements on CaCO₃-loaded PP melt is shown in Fig. 13.8a. In both cases, the refractive index (here: averaged from 0.20 to 0.35 THz) allows for the determination of the CaCO₃ volume content. The slight difference in the slopes and the offset arise from the temperature dependence of the refractive index of the PP matrix. The melt temperature lies between 249 and 253 °C under a

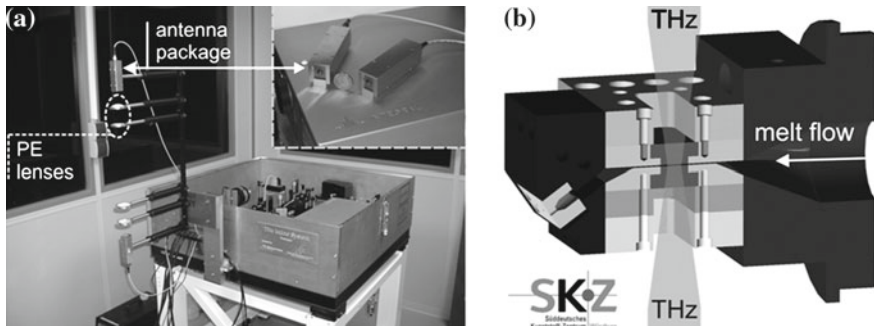


Fig. 13.7 Mobile fiber-coupled THz spectrometer for monitoring polymer compounding processes (a) and the measurement slit die to adapt the THz probe to the extruder (b)

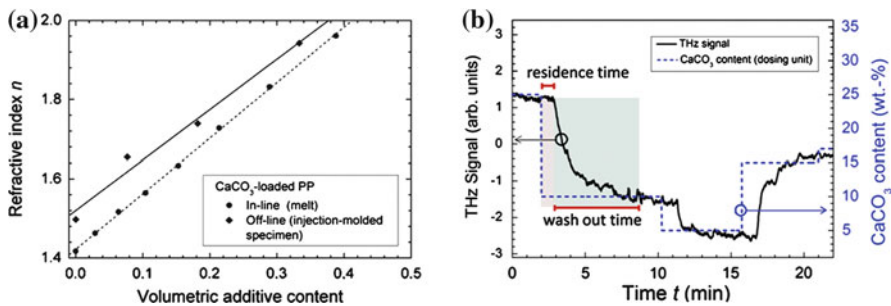


Fig. 13.8 Inline THz measurements on PP melt with a varying content of CaCO_3 performed at the end of an extruder. **a** The refractive index over the volume content of CaCO_3 measured offline on an injection molded specimen and in-line on the compound melt; **b** measurements of the THz amplitude versus time reveal the residence and wash out times of additives in the extruder (Courtesy of Hochrein and Krumbholz)

pressure of 18–23 bar. The offset decreases with increasing additive content since the refractive index of pure CaCO_3 hardly varies with temperature. Additional results of monitoring the compounding process can be found in [89], including a discussion on controlling the dispersion quality.

Another in-line measurement is presented in Fig. 13.8b. Again, polypropylene melt with a varying CaCO_3 is investigated using the measurement slit die depicted in Fig. 13.7b. Yet, to increase the THz TDS measuring speed towards real-time feedback, instead of sampling the full THz wave form, the THz amplitude is determined at a single point of the delay line, only. When the concentration of the additive changes, the THz pulse shifts, which induces a sensitive response in the detected THz amplitude at the fixed time delay. The dashed blue line indicates the to-be weight percentage of CaCO_3 in the melt given by the gravimetric dosing units of the extruder. The solid line corresponds to the THz amplitude data measured at the extruder outlet. The THz data clearly reveals important information about the extruding process such as the residence and wash out time of the additive inside the extruder. Having this informa-

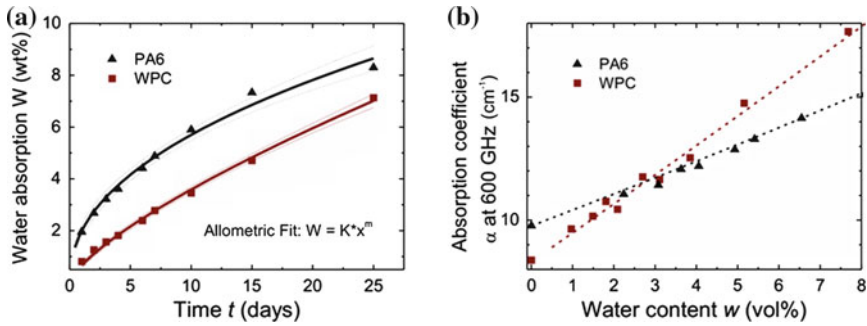


Fig. 13.9 **a** Gravimetrically determined water absorption in polyamide 6 (PA6) and a wood plastic composite (WPC) as a function of time; **b** non-destructive and contact-free THz measurements can reliably determine the water content by monitoring the THz absorption coefficient. The *dashed lines* present theoretical calculations according to an effective medium theory (*Courtesy of Jördens*)

tion allows for a reduction of the extruder's changeover times and thus for savings regarding both, material and energy. For a more detailed discussion, the inclined reader is referred to [65] and [66].

13.3.2 Moisture Monitoring in Plastic Components

Polar liquids like water strongly absorb THz waves [90]. This behavior can be exploited to create highly sensitive THz moisture sensors to monitor the water content in polymeric compounds such as glass-epoxy and glass-polyester [91]. The importance of THz moisture sensing becomes apparent when considering hydrophilic polymers such as polyamide or compounds like wood plastic composite (WPC). WPC components severely suffer from aging due to water absorption as they are often exposed to rough weather conditions.

We will briefly discuss THz moisture sensing by investigating two different material systems: PA6 and a PP-based WPC. Both samples were treated according to DIN 53 495 and placed in distilled water at room temperature for 25 days. Figure 13.9a shows the gravimetrically determined water absorption as a function of time together with an allometric fit according to the diffusion law with a confidence intervals of $P = 95\%$.

In Fig. 13.9b, the absorption coefficient at 600 GHz, measured by transmission THz TDS, is shown as a function of the volumetric water content. A close to linear dependence between the water content and the absorption coefficient is found. This correlation is expected from the theory of heterogeneous mixtures. The dashed lines in Fig. 13.9b present theoretical calculations according to the effective medium theory developed by Landau, Lifshitz and Looyenga [92]. More information on this matter can be found in reference [93].

Another prominent example for THz moisture sensing is the detection of water intrusion in radome panels due to weathering by THz TDS reflection imaging [94]. These results indicate that THz spectroscopy is a promising non-destructive and contact-free sensing method for determining the water content in plastics and polymeric compounds. Especially hydrophilic compounds like WPCs can benefit from this technique.

13.3.3 Inspection of Plastic Weld Joints

Among the available joining techniques for plastics, welding is by far the most popular. The polymer material is softened or melted by heat at the interfaces to be joined so that the macromolecules can mix under pressure and chain entanglements let the parts stick together [95]. This procedure results in a physical, and not a chemical joint.

Welding is normally placed at the end of the value creation chain. However, ensuring the quality of plastic weld joints is not only important due to economical reasons. Inclusions, voids, or delaminations can considerably weaken the strength of a weld, resulting in a loss of structural integrity. Currently, monitoring is limited to the precautionary examination of the welding parameters or destructive testing. For many applications, especially those where a 100% inspection is required, the currently available testing methods cannot provide a sufficient solution.

Recently, THz TDS has been proposed as a promising non-destructive technique to inspect the quality of such welds [96]. Figure 13.10a shows a photograph and a schematic sketch of a representative sample, consisting of two HDPE plates with a thickness of 5.5 mm, each. Only the right half is correctly welded, while the left half contains a typical delamination.

In the upper part of Fig. 13.10b, c, the time-domain waveforms obtained in a transmission experiment are shown for the delaminated and the correctly welded part, respectively. As the measurements were performed under nitrogen atmosphere so that no ringing due to water absorption lines distorts the signal, the reflected pulses are clearly visible. In case of the delamination, both the echo pulses from the internal interface and from the backside can be seen (Fig. 13.10b, top), while in case of the correctly welded sample only the echo from the backside is present (Fig. 13.10c, top).

Recently, the authors developed a more robust detection scheme, which also works if no nitrogen flooding is available and can cope with higher noise levels. In this scheme, the time-domain waveform is Fourier-transformed to the frequency domain. The echo pulses result in Fabry–Pérot oscillations which are superimposed to the THz spectrum. By applying a band pass filter, these oscillations are extracted from the signal. Fourier transforming the filtered data again results in the curves shown in the lower parts of Fig. 13.10b, c for the delamination and the correctly welded sample, respectively. Knowing the refractive index of the bulk material, which in case of the HDPE is $n = 1.54$, allows for the normalization of the abscissa to directly represent

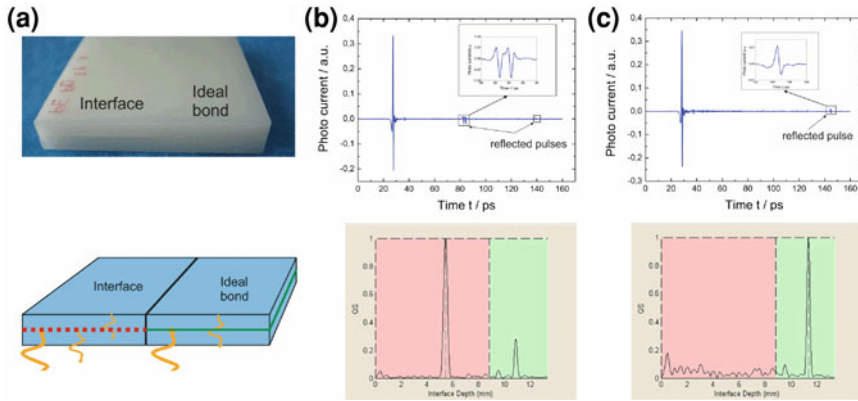


Fig. 13.10 **a** Photograph and sketch of a partly welded sample consisting of two HDPE plates with a thickness of 5.5 mm each. **b–c** show the transmission THz TDS waveforms (*top*) and the quasi space evaluation (*bottom*) for the delamination and the correctly welded sample, respectively

the depth of the interface. In Fig. 13.10b, the first interface is identified at 5.5 mm which corresponds to the thickness of one of the welded plates. The second peak at an interface depth of approximately 11 mm corresponds to the overall thickness of both plates together. In case of the correctly welded sample, only the second peak exists. Thus, an easy differentiation between a good and a bad weld joint is possible. This procedure (patent pending [97]) alternatively works for reflection measurements and can also be applied to other tasks, e.g., to finding inclusions in chocolate or determining the thickness of paper, paints, and coatings.

13.3.4 THz Spectroscopy on Adhesive Bonds

Besides welding, adhesive bonding is one of the most popular joining techniques. Amongst the advantages of adhesive bonding are the compatibility with a variety of different surface conditions and materials combined with flexible adjustment times before curing and low processing costs. Additionally, in contrast to welding, bolted fastening or rivet connection, no heat- or machining-induced alterations occur at the joint area, which can prove advantageous for many applications.

For 100 % quality inspection, required for safety critical components, e.g., in the automotive or aviation industry, destructive mechanical tests are not an option. For such applications, non-destructive testing is mandatory. While ultrasonic or X-ray measurements offer insight into the joint characteristics, the contrast mechanisms for both techniques are relatively weak, especially when a glue layer between polymeric components is of interest. The outstanding contrast mechanisms at THz frequencies render THz TDS testing an ideal approach to the analysis of adhesive bonds.

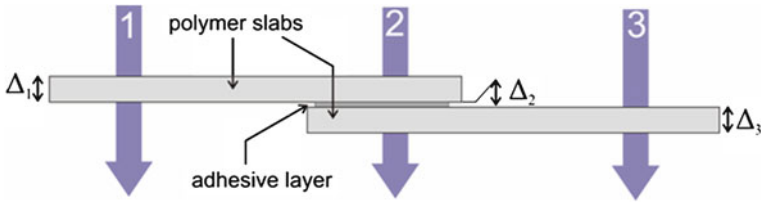


Fig. 13.11 Two adhesively bonded polymer slabs with a thickness of Δ_1 and Δ_3 , respectively. The thickness of the adhesive layer is given by Δ_2 . The arrows mark the points at which THz measurements are performed

Table 13.2 Summary of the employed polymer and adhesive materials

Polymer	Type	Δ_1 (μm)	Δ_3 (μm)	Adhesive base	Brand name
PE	Sabic HDPE	1951	1938	Ethyl cyanoacrylate	Loctite 480
PA	Degussa PA12	1860	1862	Methyl methacrylate	Loctite 3295
PVC	Simona PVC-G	1970	1926	Polyurethane	Teromix 6700

Δ_1 and Δ_3 refer to the thickness of the polymer slabs

To demonstrate the high potential of THz TDS in this field, we investigate three samples consisting of lap-bonded polymeric slabs joint by different adhesives. Both the dielectric parameters and the thickness of the joint layer will be investigated. The principle geometry of the sample is depicted in Fig. 13.11.

In Fig. 13.11, Δ_1 and Δ_3 refer to the thickness of the polymer slabs while Δ_2 specifies the thickness of the adhesive layer. The material systems comprise HDPE, polyamide 12 (PA) and PVC polymer slabs, which are bonded by an ethyl cyanoacrylate-, a methyl methacrylate- and a polyurethane-based adhesive, respectively. In Table 13.2, the thicknesses of the polymer slabs are summarized together with the type specification and the brand name of both the adhesives as well as the polymers.

Three sets of THz TDS measurements are performed to fully characterize the adhesive layer. First, each of the polymer slabs is characterized separately by THz TDS measurements at positions 1 and 3 indicated in Fig. 13.11 to extract both the material parameter as well as the thickness information using commercially available data extraction software [5], which is based on the algorithm proposed in reference [72].

According to this algorithm, a reference and a sample pulse are measured. The measured transfer function $H_{\text{meas}}(\omega)$ is calculated by taking the ratio of the corresponding Fourier spectra. A theoretical transfer function $H_{\text{theory}}(\omega)$ is then formulated. By minimizing the difference between the measured and the theoretical transfer function, $H_{\text{meas}}(\omega) - H_{\text{theory}}(\omega)$, using an implementation of the Nelder–Mead simplex algorithm proposed by Lagarias et al. [98], the thickness- and frequency-dependent complex refractive index of the sample is calculated in a numerical optimization step. The sample thickness is then determined by considering the Fabry–Pérot oscillations superimposed onto the refractive index data. In case of a correctly

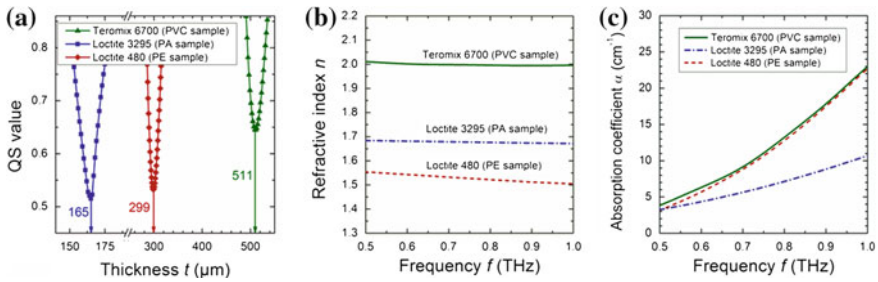


Fig. 13.12 **a** Calculated quasi space peak plotted over the assumed thickness Δ_2 of the adhesive layer. The position of the minimum reveals the correct adhesive layer thickness; **b** the refractive index and **c** the absorption coefficient plotted in the frequency regime between 0.5 and 1 THz for all three samples

chosen thickness, these oscillations disappear. Following the procedure proposed in [72], an additional Fourier transform is applied to the complex refractive index data so that the periodic Fabry–Pérot oscillations result in a distinct peak. Minimizing this peak leads to the correct thickness and the corresponding complex refractive index data of the sample can easily be obtained.

Now that the material parameters and thicknesses of the single polymer layers are known, a measurement at position 2 (see indicated in Fig. 13.11) is performed to analyze the adhesive layer. To extract the material parameter information, an extension of the previously described algorithm proposed in [99] is employed, which is also part of the above-mentioned software package [5]. In this case the theoretic transfer function is calculated by the transfer matrix method [100], using the material parameters and thickness information of the polymer layers as input. Afterwards, the same steps as described for the single layer are performed.

The correct thickness of the adhesive layer is determined by the minimum of the quasi space peak, which refers to the case when the Fabry–Pérot reflections vanish. The quasi space peak value as a function of the assumed thickness is depicted in Fig. 13.12a for all three samples. A thickness of 165, 299, and 511 μm is found for the Loctite 3295, the Loctite 480 and the Teromix 6700 layer, respectively. After having determined the correct thickness, the material parameters can be extracted. The resulting curves for the refractive index and the absorption coefficient are shown in Fig. 13.12b, c, respectively. The polyurethane-based Teromix 6700 exhibits the highest refractive index of approximately 2, followed by the methyl methacrylate-based Loctite 3295 with a refractive index of approximately 1.68 and the ethyl cyanoacrylate with a refractive index between 1.55 and 1.50. Both the Teromix 6700 and the Loctite 480 exhibit a relatively high absorption of 23 cm^{-1} at 1 THz while the Loctite 3295 is less lossy with an absorption coefficient of approximately 11 cm^{-1} at the same frequency.

The experimental data presented above proves that THz TDS can investigate the dielectric material parameters of an adhesive layer inside an assembled component, which paves the way for THz inspection of adhesive bonding. One of the crucial

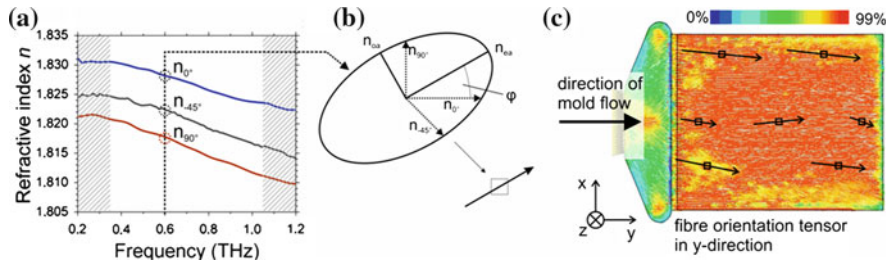


Fig. 13.13 **a** Measured refractive index for three rotation angles of an injection molded, glass-fiber-reinforced polyamide sample; **b** the index ellipsoid model reveals the fiber orientation inside the sample. **c** the measured fiber orientation (*black arrows*) is shown together with a false color image of the simulated fiber tensor calculated by the software Moldflow Plastics Insight

factors for deterioration of the joint strength, especially in polar epoxy-based adhesives [101], is water uptake. As demonstrated in Sect. 13.3.2, the sorption of water, enhanced by capillary diffusion [102], will significantly change the dielectric parameters. Hence, THz TDS could replace destructive mechanical tests and provide direct access to the quality of the adhesive joint affected by water intrusion or aging [101, 102]. Thus, THz TDS opens the door for a wide range of non-destructive, contact-free testing procedures for adhesive bonds. For more detailed information on this subject, please also consider [99].

13.3.5 Determining the Fiber Orientation in Reinforced Plastics

Structural components, e.g., in the automobile and the aviation industry, have to meet high requirements in terms of mechanical strength and stiffness, which cannot be achieved with bulk plastics. However, by enhancing the pure polymers with reinforcing elements, mostly in the form of fibers, these requirements can be met. Since the orientation of the fibers significantly determines the maximum stresses that can be applied to the component and strongly affects the mechanical performance, a reliable orientation control is crucial for a safe operation.

The dielectric properties of such anisotropic compounds depend on the relative orientation of the wave polarization and the incorporated fibers. Thus, this dependence can now be exploited in polarization controlled THz TDS [103], in order to obtain information about the alignment of the fibers, revealing superstructures due to form birefringence.

To obtain the orientation of fibers at a specific point, measurements under three rotation angles (e.g. angles of 0° , 45° and 90° between the THz polarization direction and the sample edge) have to be performed. Three differing refractive index curves result from which the orientation can be derived by considering the values at 600 GHz and applying an index ellipsoid model as shown in Fig. 13.13b. The analyzed sam-

ple is an injection molded polyamide reinforced by 30 wt% short glass fibers. In Fig. 13.13c the results obtained by polarization controlled THz TDS (black arrows) using the procedure described above are compared against simulations of the orientation tensor (false color image) obtained from the numerical Moldflow Plastic Insight software. The length of the arrows corresponds to the fraction of preferentially oriented fibers, determined from the magnitude of the birefringence. While in general the agreement is quite good, deviations from the calculated orientation direction are clearly visible, which can be explained by deflection at the borders of the specimen and the presence of dwell pressure during the injection molding process. Further information about the measurements is given in reference [104].

While glass-fiber-reinforced components can easily be analyzed in a transmission setup, reinforcements by carbon-fibers, which are conducting, only allow for imaging in reflection geometry as demonstrated by Karpowicz et al. in [105] to evaluate fire damage in carbon-fiber composites.

Beside the common carbon- and glass-fiber reinforcements in a standard polymer matrix, fiber-reinforced liquid crystal polymers (LCPs), which for instance are used in helicopter stator blades [106], also present an economically relevant group of high performance composites. Rutz et al. employed THz TDS imaging to determine the fiber orientation in this material system [107].

Polarization-dependent THz TDS can also reveal textures on a smaller scale as (macro-) molecular orientation in polymers results in anisotropic dielectric properties. More information on this topic can be found in the following literature: [108–110].

Acknowledgments The authors would like to express their sincere gratitude to each of the generous individuals who have permitted us to display some version of their data and illustrations for this chapter. This includes Frank Rutz (Fraunhofer Institute for Applied Solid-State Physics, Freiburg); Norman Krumbholz, Christian Jördens (Volkswagen AG, Wolfsburg), Markus Lehnhardt, Saranyu Lüders, Dirk Romeike (Institute for High Frequency Technology, TU Braunschweig), Sangam Chatterjee, Marco Reuter, Tilmann Jung, Maik Scheller and Nico Vieweg (Philipps-Universität Marburg). Further thanks are addressed to Prof. Guozhong Zhao (Capital Normal University of China), Thomas Hochrein, Benjamin Baudrit, Eduard Kraus, Dietmar Kraft, Thomas Zentgraf, Neda Kovacevic, Karsten Kretschmer and Martin Bastian (Southern German Plastics Center (Süd-deutsches Kunststoff-Zentrum)) for providing plastic samples, additional measurements and helpful advice. The authors thank Wibke Dempwolf, Prof. Henning Menzel (Institute of Technical Chemistry, TU Braunschweig), Judith Hehl, Seema Agarwal, Prof. Andreas Greiner (Philipps-Universität Marburg) and Prof. Stefan Sostmann (ContiTech) and Neda Kovacevic, Benjamin Baudrit (SKZ) for DSC and DMA measurements, respectively. The authors also appreciate the fruitful discussions with Rafal Wilk (Menlo Systems); Joachim Pupeza (Max Planck Institute of Quantum Optics); Christian Paulik (Borealis Polyolefine GmbH, Linz, Austria); Tomasz Hasek (Dräger), Kai Baaske (PTB), Ibraheem A. Ibraheem (INRS-EMT); Ole Peters, Michael Schwerdtfeger, Bernd Heinen, Matthias Wichmann, Benedikt Scherger, Matthias Stecher, Kristian Altmann and Thorsten Probst (Philipps-Universität Marburg).

The authors thank the Federal Ministry of Education and Research (BMBF) for funding the projects 13N11052, 13N8572, 13N9406, and 13N9466. Furthermore, we are grateful for the support of the Federal Ministry of Economics and Technology (BMW), grants 182 ZN, 269 ZN, 345 ZN and VP2376001AB9, administered by the German Federation of Industrial Research Associations (AiF). Steffen Wietzke and Christian Jansen like to express their appreciation to the Federal Ministry of Education and Research for funding the preparatory project CHN 10/A11 (fact-finding visit at

the Capital Normal University of China) and to the National Natural Science Foundation of China for Grant No. 50971094, both in the framework of the scientific and technological cooperation between China and Germany.

References

1. PlasticsEurope, Plastics—the Facts 2010: an analysis of European plastics production, demand and recovery for 2009. Technical Report, PlasticsEurope, 2010
2. S. Krimm, Infrared spectra of high polymers. *Fortschr. Hochpolym. Fors.* **2**, 51–172 (1960)
3. V.A. Bershtein, V.A. Ryzhov, Far infrared spectroscopy of polymers. *Adv. Polym. Sci.* **114**, 42–121 (1994)
4. M. Scheller, M. Koch, Terahertz quasi time domain spectroscopy. *Opt. Express* **17**, 17723–17733 (2009)
5. Teralyzer Data Extraction Suite, Lytera UG (haftungsbeschränkt), <http://www.lytera.com>
6. P.Y. Han, M. Tani, M. Usami, S. Kono, R. Kersting, X.-C. Zhang, A direct comparison between terahertz time-domain spectroscopy and far-infrared Fourier transform spectroscopy. *J. Appl. Phys.* **89**, 2357–2359 (2001)
7. R. Piesiewicz, C. Jansen, S. Wietzke, D. Mittleman, M. Koch, T. Kürner, Properties of building and plastic materials in the THz range. *Int. J. Infrared Millim. Waves* **28**, 363–371 (2007)
8. N. Nagai, R. Fukasawa, Abnormal dispersion of polymer films in the THz frequency region. *Chem. Phys. Lett.* **388**, 479–482 (2004)
9. Y.-S. Jin, G.-J. Kim, S.-G. Jeon, Terahertz dielectric properties of polymers. *J. Korean Phys. Soc.* **49**, 513–517 (2006)
10. S. Wietzke, M. Reuter, N. Nestle, E. Klimov, U. Zadok, B. Fischer, M. Koch, Analyzing morphology and thermal history of polybutylene terephthalate by THz time-domain spectroscopy. *J. Infrared Millim. Terah. Waves.* **32**, 952–959 (2011)
11. H. Hoshina, Y. Morisawa, H. Sato, A. Kamiya, I. Noda, Y. Ozaki, C. Otani, Higher order conformation of poly(3-hydroxyalkanoates) studied by terahertz time-domain spectroscopy. *Appl. Phys. Lett.* **96**, 101904 (2010)
12. J. Balakrishnan, B.M. Fischer, D. Abbott, Sensing the hygroscopicity of polymer and copolymer materials using terahertz time-domain spectroscopy. *Appl. Opt.* **48**, 2262–2266 (2009)
13. C. Jansen, S. Wietzke, O. Peters, M. Scheller, N. Vieweg, M. Salhi, N. Krumbholz, C. Jördens, T. Hochrein, M. Koch, Terahertz imaging: applications and perspectives. *Appl. Opt.* **49**, E48–E57 (2010)
14. D. Turchinovich, A. Kammoun, P. Knobloch, T. Dobbertin, M. Koch, Flexible all-plastic mirrors for the THz range. *Appl. Phys. A Mater. Sci. Process.* **74**, 291–293 (2002)
15. Y.H. Lo, R. Leonhardt, Aspheric lenses for terahertz imaging. *Opt. Express* **16**, 15991–15998 (2008)
16. A. Sengupta, A. Bandyopadhyay, B.F. Bowden, J.A. Harrington, J.F. Federici, Characterisation of olefin copolymers using terahertz spectroscopy. *Electron. Lett.* **42**, 1477–1479 (2006)
17. A. Argyros, M.A. van Eijkelenborg, M.C. Large, I.M. Bassett, Hollow-core microstructured polymer optical fiber. *Opt. Lett.* **31**, 172–174 (2006)
18. K. Nielsen, H.K. Rasmussen, A.J. Adam, P.C. Planken, O. Bang, P.U. Jepsen, Bendable, low-loss Topas fibers for the terahertz frequency range. *Opt. Express* **17**, 8592–8601 (2009)
19. B. Fischer, M. Hoffmann, P. U. Jepsen, and M. Walther, Use of the plastic materials topas and zeonex for biotechnological applications in the terahertz range, European Patent Application—EP1505382, 2005
20. J.U.Y. Shin, J.I.Y. Park, C. Liu, J. He, S.C. Kim, Chemical structure and physical properties of cyclic olefin copolymers (IUPAC technical report). *Pure Appl. Chem.* **77**, 801–814 (2005)
21. B. Wunderlich, Thermodynamics and kinetics of crystallization of flexible molecules. *J. Polym. Sci. Part B Polym. Phys.* **46**, 2647–2659 (2008)

22. J. Dobbertin, A. Hensel, C. Schick, Dielectric spectroscopy and calorimetry in the glass transition region of semi-crystalline poly(ethylene terephthalate). *J. Therm. Anal. Calorim.* **47**, 1027–1040 (1996)
23. R.F. Boyer, Transitions and relaxations, in *Encyclopedia of Polymer Science and Technology*, vol. 2, ed. H.F. Mark (Wiley, New York, 1977), pp. 745–839
24. M. Tasumi, S. Krimm, Crystal vibrations of polyethylene. *J. Chem. Phys.* **46**, 755–766 (1967)
25. G.D. Dean, D.H. Martin, Inter-molecular vibrations of crystalline polyethylene and long-chain paraffins. *Chem. Phys. Lett.* **1**, 415–416 (1967)
26. M.I. Bank, S. Krimm, Lattice-frequency studies of crystalline and fold structure in polyethylene. *J. Appl. Phys.* **39**, 4951–4958 (1968)
27. J.R. Birch, K.F. Ping, Temperature dependence of the FIR optical constants of low density polyethylene. *Infrared Phys. Technol.* **36**, 673–677 (1995)
28. J.W. Fleming, G.W. Chantry, P.A. Turner, E.A. Nicol, Temperature effects and the observation of the B2u lattice mode in the far infrared absorption spectrum of polyethylene. *Chem. Phys. Lett.* **17**, 84–85 (1972)
29. J. Birch, E. Nicol, The FIR optical constants of the polymer TPX. *Infrared Phys.* **24**, 573–575 (1984)
30. G.W. Chantry, H.M. Evans, J.W. Fleming, H.A. Gebbie, TPX, a new material for optical components in the far infra-red spectral region. *Infrared Phys.* **9**, 31–33 (1969)
31. V.A. Bershtein, V.A. Ryzhov, Relationship between molecular characteristics of polymers and parameters of far-infrared spectra. *J. Macromol. Sci. Phys. B* **23**, 271–287 (1984)
32. M.J. Hannon, F.J. Boerio, J.L. Koenig, Vibrational analysis of polytetrafluoroethylene. *J. Chem. Phys.* **50**, 2829–2836 (1969)
33. G.W. Chantry, J.W. Fleming, E.A. Nicol, H.A. Willis, M.E.A. Cudby, F.J. Boerio, Far infra-red spectrum of crystalline polytetrafluoroethylene. *Polymer* **15**, 69–73 (1974)
34. G.W. Chantry, E.A. Nicol, R.G. Jones, H.A. Willis, M.E.A. Cudby, On the vibrational assignment problem for polytetrafluoroethylene: 1. The far infra-red spectrum, *Polymer* **18**, 37–41 (1977)
35. M. Kobayashi, K. Tashiro, H. Tadokoro, Molecular vibrations of three crystal forms of poly(vinylidene fluoride). *Macromolecules* **8**, 158–171 (1975)
36. J.F. Rabolt, K.W. Johnson, Low frequency vibrations in polyvinylidene fluoride (form II). *J. Chem. Phys.* **59**, 3710–3712 (1973)
37. M. Latour, R.L. Moreira, Submillimeter infrared absorption and chain conformations of poly(vinylidene fluoride) and copolymers. II. Phase transition analysis. *J. Polym. Sci. Part B Polym. Phys.* **25**, 1717–1723 (1987), cited By (since 1996): 3
38. H. Tadokoro, *Structure of Crystalline Polymers* (Robert E. Krieger Publishing Company, Malabar, Florida, 1990)
39. W.F.X. Frank, H. Fiedler, On the problem of direct observation of H-bridge interactions in polymers by FIR spectroscopy. *Infrared Phys.* **19**, 481–489 (1979), cited By (since 1996): 1
40. C.S. Nie, F. Kremer, A. Poglitsch, G. Bechtold, L. Genzel, Picosecond relaxations in hydrated polyamide-6 observed by millimeter-wave spectroscopy. *J. Polym. Sci. Part A-2 Polym. Phys.* **23**, 1247–1254 (1985)
41. H. Tadokoro, M. Kobayashi, H. Yoshidome, T.A.I. Kazuo, D. Marino, Structural studies of polyesters. II. Far-infrared spectra of aliphatic polyesters: comparison with alpha-polyamides. *J. Chem. Phys.* **49**, 3359–3373 (1968)
42. M. Goldstein, D. Stephenson, W.F. Maddams, Far infra-red spectrum of poly(vinyl chloride). *Polymer* **24**, 823–826 (1983)
43. J.M.G. Cowie, *Polymers: Chemistry and Physics of Modern Materials*, 3rd edn. (Taylor and Francis, Boca Raton, 2008)
44. W. Frank, U. Leute, *Infrared and Millimeter Waves: Electromagnetic Waves in Matter*, vol. 8, Chap. 2 (Academic, New York, 1983)
45. R.B. Beevers, Polymer characterization by refractometry. *J. Polym. Sci. Polym. Phys. Ed.* **12**, 1407–1415 (1974)

46. G. Chantry, *Infrared and Millimeter Waves: Electromagnetic Waves in Matter* (Academic, New York, 1983)
47. K. Tashiro, M. Kobayashi, Structural phase transition in ferroelectric fluorine polymers: X-ray diffraction and infrared/Raman spectroscopic study. *Phase Transition* **18**, 213–246 (1989)
48. R. Hasegawa, M. Kobayashi, H. Tadokoro, Molecular conformation and packing of poly(vinylidene fluoride). Stability of three crystalline forms and the effect of high pressure. *Polym. J.* **3**, 591–599 (1972)
49. A. Warrier, S. Krimm, Intermolecular interactions in crystalline poly(vinyl chloride). *Macromolecules* **3**, 709–710 (1970)
50. R.J. Fredericks, T.H. Doyne, R.S. Sprague, Crystallographic studies of nylon 4. I. Determination of the crystal structure of the alpha polymorph of nylon 4. *J. Polym. Sci. Part A-2 Polym. Phys.* **4**, 899–911 (1966)
51. R.H. Boyd, Relaxation processes in crystalline polymers: molecular interpretation—a review. *Polymer* **26**, 1123–1133 (1985)
52. J.A. Forrest, K. Dalnoki-Veress, J.R. Stevens, J.R. Dutcher, Effect of free surfaces on the glass transition temperature of thin polymer films. *Phys. Rev. Lett.* **77**, 2002–2005 (1996)
53. B. Wunderlich, Reversible crystallization and the rigid-amorphous phase in semicrystalline macromolecules. *Prog. Polym. Sci.* **28**, 383–450 (2003)
54. J.H. Gibbs, E.A. DiMarzio, Nature of the glass transition and the glassy state. *J. Chem. Phys.* **28**, 373–383 (1958), cited By (since 1996): 531
55. J.D. Menczel, R.B. Primeeds, *Thermal Analysis of Polymers: Fundamentals and Applications* (Wiley, Hoboken, 2009)
56. G. Patterson, *Physical Chemistry of Macromolecules*, 2nd edn. (Taylor and Francis, Boca Raton, 2007)
57. K. Nakagawa, Y. Ishida, Dielectric relaxations and molecular motions in poly(vinylidene fluoride) with crystal form II. *J. Polym. Sci. Polym. Phys. Ed.* **11**, 1503–1533 (1973)
58. R. Simha, R.F. Boyer, On a general relation involving the glass temperature and coefficients of expansion of polymers. *J. Chem. Phys.* **37**, 1003–1007 (1962)
59. S. Wietzke, C. Jansen, T. Jung, M. Reuter, B. Baudrit, M. Bastian, S. Chatterjee, M. Koch, Terahertz time-domain spectroscopy as a tool to monitor the glass transition in polymers. *Opt. Express* **17**, 19006–19014 (2009)
60. S. Wietzke, C. Jansen, M. Reuter, T. Jung, D. Kraft, S. Chatterjee, B.M. Fischer, M. Koch, Terahertz spectroscopy on polymers: a review of morphological studies. *J. Mol. Struct.* **1006**(1–3), 41–51 (2011). doi:10.1016/j.molstruc.2011.07.036, <http://www.sciencedirect.com/science/article/pii/S002228601100593X>
61. S. Wietzke, C. Jansen, M. Reuter, T. Jung, J. Hehl, D. Kraft, S. Chatterjee, A. Greiner, M. Koch, Thermomorphological study of the terahertz lattice modes in polyvinylidene fluoride and high-density polyethylene. *Appl. Phys. Lett.* **97**, 022901 (2010)
62. R. Androsch, M.L. Di Lorenzo, C. Schick, B. Wunderlich, Mesophases in polyethylene, polypropylene, and poly(1-butene). *Polymer* **51**, 4639–4662 (2010)
63. J. Murphy, *Additives for Plastics Handbook* (Elsevier, Oxford, 2001)
64. D.B. Todd, *Plastics Compounding: Equipment and Processing* (Hanser, Munich, 1998)
65. N. Krumbholz, T. Hochrein, N. Vieweg, T. Hasek, K. Kretschmer, M. Bastian, M. Mikulics, M. Koch, Monitoring polymeric compounding processes inline with THz time-domain spectroscopy. *Polym. Test.* **28**, 30–35 (2009)
66. N. Krumbholz, T. Hochrein, N. Vieweg, I. Radovanovic, I. Pupeza, M. Schubert, K. Kretschmer, M. Koch, Degree of dispersion of polymeric compounds determined with terahertz time-domain spectroscopy. *Polym. Eng. Sci.* **51**, 109–116 (2011)
67. C. Jansen, S. Wietzke, V. Astley, D.M. Mittleman, M. Koch, Mechanically flexible polymeric compound one-dimensional photonic crystals for terahertz frequencies. *Appl. Phys. Lett.* **96**, 111108 (2010)
68. C. Jansen, C. Jördens, M. Koch, Terahertz-Volumen-Bauelement, German Patent Application, 2008

69. R. Boulay, P. Dube, P.A. Belanger, T. Vu-Khanh, P. Cielo, Analysis of filler concentrations and orientation in reinforced polymers by far-IR techniques. *SPIE* **665**, 352–360 (1986)
70. S. Wietzke, C. Jansen, F. Rutz, D.M. Mittleman, M. Koch, Determination of additive content in polymeric compounds with terahertz time-domain spectroscopy. *Polym. Test.* **26**, 614–618 (2007)
71. M. Scheller, S. Wietzke, C. Jansen, M. Koch, Modelling heterogeneous dielectric mixtures in the terahertz regime: a quasi-static effective medium theory. *J. Phys. D Appl. Phys.* **42**, 065415 (2009)
72. M. Scheller, C. Jansen, M. Koch, Analyzing sub-100- μm samples with transmission terahertz time domain spectroscopy. *Opt. Commun.* **282**, 1304–1306 (2009)
73. G. Blom, *Probability and Statistics: Theory and Applications* (Springer, Berlin, 1989)
74. R. Kacker, A. Jones, On use of Bayesian statistics to make the guide to the expression of uncertainty in measurement consistent. *Metrologia* **40**, 235–248 (2003)
75. B.N. Taylor, C.E. Kuyatt, Guidelines for evaluating and expressing the uncertainty of NIST measurement results. *NIST Technical Note 1297*, 1994 edn. (U.S. Govt. Printing Office, Washington, DC, 1994)
76. L. K. H. van Beek, *Progress in Dielectrics* (Tliffe, London, 1969), Vol. 7, chap. Dielectric behaviour of heterogeneous systems, pp. 69–114.
77. D.K. Hale, The physical properties of composite materials. *J. Mater. Sci.* **11**, 2105–2141 (1976)
78. J.C. Maxwell-Garnett, Colours in metal glasses and in metallic films. *Philos. Trans. R. Soc. London, Ser. A* **203**, 385–420 (1904)
79. D.A.G. Bruggeman, Berechnung verschiedener physikalischer Konstanten von heterogenen Substanzen: I Dielektrizitätskonstanten und Leitfähigkeiten der Mischkörper aus isotropen Substanzen. *Ann. Phys.* **24**, 636–664 (1935)
80. D. Polder, J.H. van Santen, The effective permeability of mixtures of solids. *Physica* **12**, 257–271 (1946)
81. W. Grellmann, S. Seidler, *Polymer Testing* (Hanser, Munich, 2007)
82. M. Bastian, K. Kretschmer, M. Schubert, A new online measurement technique for the evaluation of the degree of dispersion, in *Proceedings of the 21st Annual Meeting of the Polymer Processing Society (PPS21)*, 2005
83. D.R. França, C.-K. Jen, K.T. Nguyen, R. Gendron, Ultrasonic in-line monitoring of polymer extrusion. *Polym. Eng. Sci.* **40**, 82–94 (2000)
84. M. Stephan, S. Große, M. Stintz, U. Blankschein, Real time detection of particulate heterogeneities in polymer extrusion processes using microphotometric measuring method. *Plast. Rubber Compos.* **35**, 432–438 (2006)
85. M. Stephan, S. Große, M. Stintz, U. Blankschein, Microphotometric inline determination of polymer blend morphologies during extrusion processing. *J. Appl. Polym. Sci.* **103**, 258–262 (2007)
86. M. Xanthos, A. Patel, Recent developments in in-line spectroscopy/microscopy for monitoring extrusion processes. *Adv. Polym. Technol.* **14**, 151–157 (1995)
87. D. Fischer, T. Bayer, K.-J. Eichhorn, M. Otto, In-line process monitoring on polymer melts by NIR-spectroscopy. *Fresenius J. Anal. Chem.* **359**, 74–77 (1997)
88. N. Vieweg, N. Krumbholz, T. Hasek, R. Wilk, V. Bartels, C. Keseberg, V. Pethukhov, M. Mikulics, L. Wetenkamp, M. Koch, Fiber-coupled THz spectroscopy for monitoring polymeric compounding processes. *Proc. SPIE* **6616**, 66163M (2007)
89. T. Hochrein, N. Krumbholz, K. Kretschmer, M. Bastian, M. Koch, Terahertz-spectroscopy: a new tool for monitoring compounding processes, in *Proceedings of the 24th Annual Meeting of the Polymer Processing Society (PPS24)*, 2008 (Accepted as invited keynote)
90. J.T. Kindt, C.A. Schmuttenmaer, Far-infrared dielectric properties of polar liquids probed by femtosecond terahertz pulse spectroscopy. *J. Phys. Chem.* **100**, 10373–10379 (1996)
91. R. Boulay, B. Drouin, R. Gagnon, P.A. Belanger, P. Cielo, Far infra-red moisture monitoring in polymeric composites. *Polym. Commun. (Guildford)* **26**, 69–71 (1985)
92. H. Looyenga, Dielectric constants of heterogeneous mixtures. *Physica* **31**, 401–406 (1965)

93. C. Jördens, Einsatz und Optimierung von Terahertz-Systemen in der zerstörungsfreien Messtechnik. Ph.D. Thesis, Technische Universität Carolo-Wilhelmina zu Braunschweig, 2009
94. D. Zimdars, J. White, G. Sucha, G. Fichter, G. Stuk, C. Megdanoff, A. Chernovsky, S.L. Williamson, Terahertz measurement and imaging detection of delamination and water intrusion in ground based radome panels. Proc. SPIE (The International Society for Optical Engineering) **6549**, 654906 (2007)
95. D.A. Grewell, A. Benatar, J.B. Park, *Plastics and composites welding handbook* (Hanser, Munich, 2003)
96. S. Wietzke, C. Jördens, N. Krumbholz, B. Baudrit, M. Bastian, M. Koch, Terahertz imaging: a new non-destructive technique for the quality control of plastic weld joints. J. Eur. Opt. Soc. (Rapid Publications) **2**, 07013 (2007)
97. S. Wietzke, E. Kraus, B. Baudrit, P. Heidemeyer, O. Peters, N. Krumbholz, M. Koch, M. Bastian, Zerstörungsfreie Terahertzprüfung von stoffschlüssigen Kunststoffverbindungen. Technical Report, Süddeutsches Kunststoff-Zentrum, Würzburg, 2010
98. J. Lagarias, J. Reeds, M. Wright, P. Wright, Convergence properties of the Nelder–Mead simplex algorithm in low dimensions. SIAM J. Optim. **9**, 112–147 (1998)
99. C. Jansen, S. Wietzke, H. Wang, M. Koch, G. Zhao, Terahertz spectroscopy on adhesive bonds. Polym. Test. **30**, 150–154 (2010)
100. M. Born, E. Wolf, *Principles of Optics: Electromagnetic Theory of Propagation, Interference and Diffraction of Light*, 7th edn. (Cambridge University Press, Cambridge, 1999)
101. R. Balkova, S. Holcnerova, V. Cech, Testing of adhesives for bonding of polymer composites. Int. J. Adhes. Adhes. **22**, 291–295 (2002)
102. M.P. Zanni-Deffarges, M.E.R. Shanahan, Diffusion of water into an epoxy adhesive: comparison between bulk behaviour and adhesive joints. Int. J. Adhes. Adhes. **15**, 137–142 (1995)
103. N.C.J. Van der Valk, W.A.M. Van der Marel, P.C.M. Planken, Terahertz polarization imaging. Opt. Lett. **30**, 2802–2804 (2005)
104. C. Jördens, M. Scheller, S. Wietzke, D. Romeike, C. Jansen, T. Zentgraf, K. Wiesauer, V. Reisecker, M. Koch, Terahertz spectroscopy to study the orientation of glass fibres in reinforced plastics. Comp. Sci. Technol. **70**, 472–477 (2010)
105. N. Karpowicz, D. Dawes, M.J. Perry, X.-C. Zhang, Fire damage on carbon fiber materials characterized by THz waves. Proc. SPIE **6212**, 62120G (2006)
106. S. Akhtar, A.I. Isayev, Self-reinforced composites of two thermotropic liquid crystalline polymers. Polym. Eng. Sci. **33**, 32–42 (1993)
107. F. Rutz, T. Hasek, M. Koch, H. Richter, U. Ewert, Terahertz birefringence of liquid crystal polymers. Appl. Phys. Lett. **89**, 221911 (2006)
108. M. Latour, R.L. Moreira, Submillimeter infrared absorption and chain conformations of poly(vinylidene fluoride) and copolymers. I. Crystalline and amorphous contributions. J. Polym. Sci. Part B Polym. Phys. **25**, 1913–1921 (1987)
109. D.Y. Shen, S.K. Pollack, S.L. Hsu, Far-infrared study of hydrogen bonding in a semicrystalline polyurethane. Macromolecules **22**, 2564–2569 (1989)
110. A. Boldizar, S. Jacobsson, S. Hard, Far infrared birefringence versus other orientational measurements of high-pressure injection-molded high-density polyethylene. J. Appl. Polym. Sci. **36**, 1567–1581 (1988)

Chapter 14

Nonlinear Terahertz Spectroscopy

Matthias C. Hoffmann

Abstract Until recently, the pulse energies and field strengths of terahertz (THz) pulses have been too low to be used to excite matter or to study nonlinear effects in the THz range. In this chapter we will describe methods of generation and nonlinear spectroscopies with intense single- and few-cycle THz pulses, reporting the current state of the art.

14.1 Introduction

As covered in the previous chapters of this book, terahertz (THz) spectroscopy has been used extensively to study matter in the far-infrared. Particularly with the invention of THz time domain spectroscopy (TDS) using short pulse lasers, this field has developed rapidly in the last three decades [1] and yielded a vast amount of information. THz-TDS has the unique ability to characterize the complete electric field of a THz pulse, yielding full phase and amplitude information, an advantage over typical detectors that measure only intensity. The complex dielectric function of a sample can thus be determined directly [2] without having to rely on Kramers–Kronig relations. This has enabled the observation of new physical phenomena such as collective vibrational excitations, the plasma oscillations of dilute free electron gases in doped semiconductors [3], vortex dynamics in BCS superconductors [4], or Josephson plasma waves in two-dimensional high temperature superconducting cuprates [5]. Further, ultrashort techniques have allowed time resolved pump-probe studies where THz-pulses are used as a probe [6].

However, the use of intense THz radiation to *change* material properties, combined with probes that record these transient effects on short timescales has so far been

M. C. Hoffmann (✉)
Max Planck Department for Structural Dynamics,
University of Hamburg, CFEL, 22607 Hamburg, Germany
e-mail: matthias.c.hoffmann@mpsd.cfel.de

rather limited. This is due to the difficulty in generating sufficiently strong sources in the THz region. Although the excitation of low energy degrees of freedom is possible through impulsive stimulated Raman scattering [7] or related techniques, these are invariably accompanied by unwanted (e.g., above-gap) excitations due to the relatively high photon energies. Additionally, purely infrared-active modes are not accessible via Raman processes. It is therefore highly desirable [8] to be able to manipulate dipole-allowed collective excitations in the meV range *directly*.

Today a large variety of choices of tunable THz radiation sources delivering continuous wave radiation are available on the table-top such as Schottky diode mixers [9], quantum cascade lasers [10, 11], backward wave oscillators [12], and p-germanium lasers [13, 14]. These sources have typical output powers in the milliwatt range, corresponding to intensities of a few hundred mW/cm². Pulsed THz gas lasers have been developed since the 1970s and, when operated with nanosecond pulse duration [15], can reach intensities high enough to allow for nonlinear THz studies. Over the years a considerable amount of nonlinear THz and infrared work on semiconductors has been carried out with gas laser sources. Reference [16] provides a good overview. Gas laser sources are however limited in tunability due to the discrete nature of molecular transition levels in the gain media. Also in the 1970s began the development of THz-free electron lasers based on electron accelerators. The first such source for THz studies was established at USCB in the early 1980s [17] with pulse durations of the order of microseconds [18]. Free electron lasers [19] can offer very high intensities in combination with tunability over a wide frequency range [20]. The free-electron laser FELIX [21] has been in operation for more than a decade and offers pulse energies in the mJ range with pulse durations of a few picoseconds [22, 23]. Using relativistic electron accelerators using bending magnets [24] or coherent transition radiation sources [25], single cycle pulses with energies more than 100 μ J can be reached. Physics using THz radiation from free electron lasers will be discussed in Chap. 23 of this book. In the context of nonlinear spectroscopy, time domain methods allow for the study of nonlinear responses of matter to a strong electric field directly.

In this chapter, we give an overview of the rapidly developing field of ultrafast nonlinear THz spectroscopy. The main focus will be on methods using strong single- or few-cycle pulses on the table top. In Sect. 14.2 we will discuss the current state of the art of THz pulse generation using amplified femtosecond lasers systems. Each of these techniques offers strengths and weaknesses that need to be considered based on the specific application. In Sect. 14.3 we will discuss fundamental techniques how these sources can be used for nonlinear spectroscopy. A general background of nonlinear optics in the THz range and experimental observation of effects such as THz second harmonic generation (SHG) will be introduced in Sect. 14.4. In Sect. 14.5 we will explore nonlinear THz spectroscopy of semiconductors and semiconductor nanostructures. This field is the most mature, and several publications are available on the subject. The focus will be on recent developments using single or few-cycle sources. Section 14.6 will introduce the relatively new field of nonlinear vibrational spectroscopy in the THz range. In Sect. 14.7 we will explore the usage of the magnetic field component of the THz pulses and Sect. 14.7 will highlight current research in

THz control of correlated electron systems. In the last section we will give a summary and brief outlook of the future of the field.

14.2 Generation of High Intensity THz Pulses

An important class of intense table-top THz sources relies on the frequency conversion of femtosecond lasers, delivering coherent few-cycle THz pulses that are intrinsically carrier-envelope-phase stable and thus allow for time domain phase-sensitive detection. While THz generation by nonlinear optical frequency conversion of picosecond pulses has been demonstrated already in the early 1970s [26], rapid developments have taken place more recently, with the widespread availability of femtosecond lasers, most notably the Ti:sapphire solid-state laser. The use of femtosecond lasers enabled higher THz frequencies and conversion efficiencies previously unattainable from optically driven THz sources. Two methods of generating ultrafast electromagnetic pulses with picosecond duration using femtosecond oscillators were established early on and are still the most widely used techniques: photoconductive switches [2, 27] and optical rectification (OR) [28]. Subsequently these techniques were adapted for amplified femtosecond laser systems for the generation of high intensity THz pulses. More recently, generation of THz pulses by ionization processes in plasmas has gained attention. In this section, we will give an overview over recent developments methods of intense short pulse THz generation with an emphasis on OR which can deliver the highest intensity on the table top to date. A more comprehensive review about intense THz generation can be found in Ref. [29] on which this section is based.

14.2.1 THz Pulse Generation by Photoconductive Switches

Using the miniaturized photoconductive switches described in Chap. 1 femtosecond oscillator pulses with energies of about 5 nJ, fJ-energy THz pulses and field strengths in the range of 10 to 100 V/cm can be achieved. The use of amplified femtosecond laser systems allows for energy scaling by enlarging the photoconductive antenna gap to over 1 cm and the bias voltage to several kV. In an early demonstration of this technique, You et al have achieved 0.8 μJ THz pulse energies at 10 Hz repetition rate using semi-insulating GaAs wafers with silver paint electrodes and pulsed bias voltages applied by a spark plug [30].

The maximum THz energies were achieved with an external bias field of 10.7 kV/cm and laser fluencies of 0.05 mJ/cm^2 (Fig. 14.1b). A quadratic dependence of the THz output power on the applied bias field and strong saturation at laser fluencies larger than 50 $\mu\text{J}/\text{cm}^2$ were observed [31] and described by numerically modeling for different materials. In the near field of the emitter, the shape of the THz field is strongly unipolar, making the pulses ideally suited to achieve field

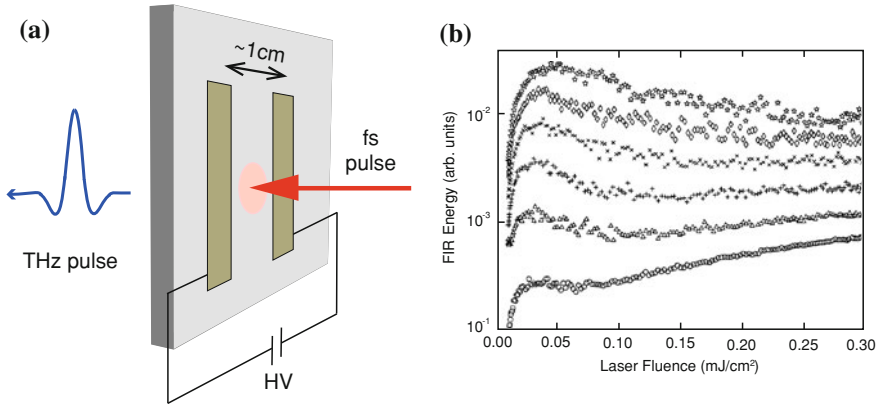


Fig. 14.1 **a** THz generation with a large area photoconductive switch. A GaAs wafer is biased with several kV/cm and excited with a fs laser. **b** Generated FIR energy as a function of pump laser fluence for selected bias fields. 0, 1.5 kV/cm; Δ , 3.0 kV/cm; +, 4.5 kV/cm; \times , 6 kV/cm; \diamond , 7.5 kV/cm; *, 9 kV/cm. Note that for large bias fields, there is a pronounced maximum in the FIR generation at a relatively low laser fluence

ionization of Rydberg atoms [32]. While THz generation with large area emitters has very high conversion efficiency, the rapid degradation of the emitters due to high voltages and the associated thermal load at higher repetition rates and the early onset of saturation have prevented this method from finding more widespread usage. Further, large-aperture THz emitters typically exhibit THz spectra centered at relatively low frequencies. This is usually attributed to a lower acceleration field and the large distance between the electrodes.

To circumvent the problems of large thermal load and saturation, Dreyhaupt et al. have developed large area interdigitated metal-semiconductor-metal (MSM) structures [33, 35]. Here, metal electrodes with 5 μm width and spacing are fabricated on a semi-insulating GaAs substrate with a 1 μm thickness Si_3N_4 insulation layer (Fig. 14.2). A further metallization layer covers every other finger electrode spacing in order to prevent destructive interference of the generated THz field. These structures can be operated with an external bias voltage of less than 50 V and can achieve THz to optical pulse energy ratios of up to 5×10^{-4} using nJ pulses from a femtosecond oscillator. This method can be scaled up further by using amplified laser systems and larger aperture antennas with an active area up to $10 \times 10 \text{mm}^2$. Using pump pulse energies of 4 μJ , THz electric fields up to 36 kV/cm at repetition rates of 250 kHz can be obtained [34]. In these experiments very high THz to optical pulse energy ratios of 2×10^{-3} were achieved at a fluence of 20 $\mu\text{J}/\text{cm}^2$ and bias voltage in the sample of 100 kV/cm.

In summary, photoconductive switches can be used for highly efficient THz generation as the energy of the THz pulse can be supplied by the applied bias field, comparing favorably with OR for small pump pulse energies [36]. Strong saturation effects limit energy scaling at higher laser-pulse energies. For high repetition rate,

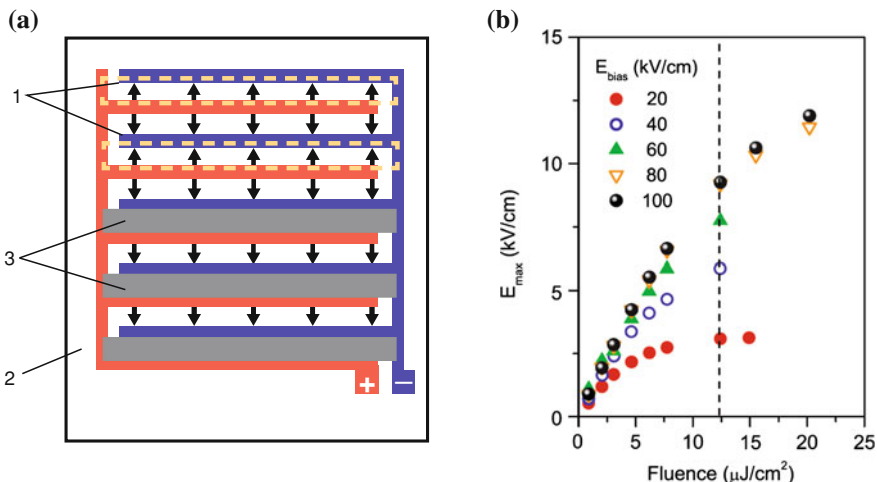


Fig. 14.2 **a** Schematics of the THz emitting MSM structure. 1 Interdigitated finger electrodes, 2 SI GaAs substrate, 3 opaque metallization shadowing one electric field direction. The electric field direction is indicated by arrows [33]. **b** Peak THz electric field as a function of excitation fluence on the photoconductor for different acceleration fields at 250kHz repetition rate [34]

low pulse-power laser systems they provide an effective source for THz single-cycle pulses with frequency bandwidth of less than 5 THz.

14.2.2 Terahertz Generation in Gas Plasmas

A promising technique to obtain extremely broadband single-cycle THz pulses with high field strengths is based on nonlinear processes in gas plasmas ionized by femtosecond lasers. THz generation in plasmas are not limited by damage since the gas target is continuously replenished, and that the available bandwidth of the THz pulses is essentially limited only by the duration of the pump laser pulse, with no material absorption. Furthermore, THz pulses can also be detected in gases using THz-induced SHG or fluorescence. We briefly discuss plasma-based THz generation methods with emphasis on recent developments. More in-depth reviews of these topics can be found in Refs. [37, 38].

14.2.2.1 Two-Color Mixing in Plasmas

When a femtosecond laser pulse is focused in gas, a plasma is generated above a threshold intensity of order TW/cm^2 . This plasma emits a broad continuum of coherent and incoherent radiation. The use of laser plasmas to generate coherent

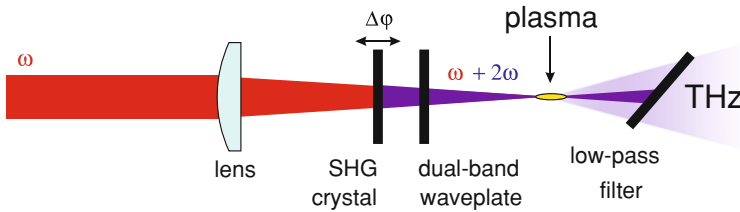


Fig. 14.3 Scheme of the experimental realization of the two-color THz generation in plasma gas targets. $\Delta\phi$ indicates the relative phase between the fundamental and its second harmonic, which can be varied, e.g., by translating the SHG crystal

far-infrared radiation at THz frequencies was first proposed and demonstrated by Hamster et al. [39] in 1993 with TW-level lasers. A significant improvement in efficiency was achieved in 2000 by Cook et al. [40] through mixing of femtosecond pulses with center frequency ω , with their second harmonic at 2ω within the gas plasma, yielding generation efficiency increase by orders of magnitude. In 2007, Kim et al. [41] reported on pump-to-THz conversion efficiencies exceeding 1×10^{-4} and pulse energies up to $5 \mu\text{J}$. The generation of ultrabroadband THz pulses containing frequencies up to 100 THz has been demonstrated very recently by Thomson by using 19 fs laser pulses [42] and carefully optimized BBO crystal angles.

In the most common experimental realization (Fig. 14.3), a 800 nm femtosecond laser pulse generated by an amplified Ti:sapphire laser with a pulse energy of 0.5 mJ or more is focused by a spherical lens into a gas target. Before the focus, an SHG crystal, typically β -BBO, is inserted, to produce 400 nm wavelength light. Both the fundamental and the second harmonic wavelengths are overlapped spatially and temporally at the focus, where the target gas is instantly ionized. The THz generation process is sensitive to the relative phase between the fundamental and the second harmonic fields, which is adjusted either by translating the SHG crystal and exploiting the dispersion of the gas, or by using a phase shifting glass plate. For type I SHG the polarization of the 400 nm light is perpendicular to that of the fundamental. The relative electric field polarization directions can be controlled by a dual-band waveplate inserted between the SHG crystal and the focus to set them, e.g., parallel [43]. The accumulated temporal retardation of the SHG pulse with respect to the fundamental pulse due to material dispersion can be precompensated by a birefringent plate such as α -BBO or calcite.

Typically, ambient air or pure nitrogen is used as the gas target for THz generation. The use of pure nitrogen increases the generation efficiency and avoids absorption of the THz radiation in atmospheric water vapour. By using noble gases with higher tunnel ionization rates (Kr or Xe), the THz generation efficiency can be further improved [41]. The pressure of the target gas also strongly influences the THz generation efficiency. With low pump pulse energies ($850 \mu\text{J}$) after a linear increase in THz emission up to 0.1 bar, a relatively constant signal was measured in the pressure range of 0.1–2 bar [37]. With the pressure increasing even further, the signal drops rapidly due to collision of accelerated electrons with molecules. In contrast

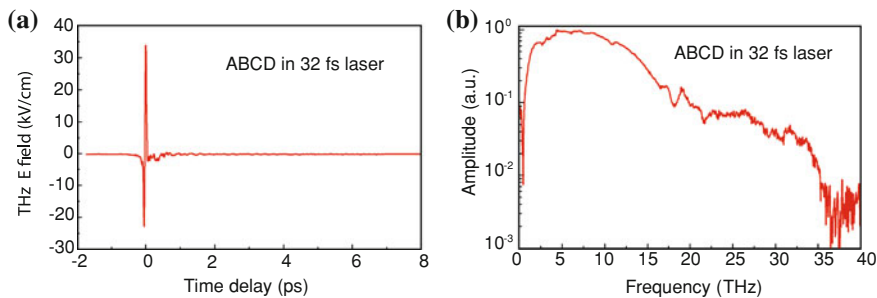


Fig. 14.4 **a** Time domain waveform, **b** a Fourier transform spectrum of a THz pulse generated gas plasma using a 32 fs amplified and detected using air-based coherent detection (ABCD) [47]

to this, at multi-mJ pump energies saturation was observed at higher pump fluences [41]. A systematic study of the THz output energy and spectral content for varied pump energy (up to 6 mJ) and pressure of different gas targets has recently been reported [44]. They observed a significant two-color phasing effect for all gases, and saturation only for the heavier gases (Kr and Xe).

Gas plasmas are also successfully employed in THz *detection*. The nonlinear interaction between a laser field with frequency ω and a THz field in gas can lead to the generation of the second harmonic of the laser field at 2ω frequency which is picked up by a photomultiplier. As shown in Refs. [45, 46] this yields extremely broad detection bandwidth of up to 30 THz (Fig. 14.4) with reasonably good signal-to-noise ratio.

14.2.2.2 Mechanism of THz Generation in Plasmas

To describe THz generation in plasma, a perturbative model based on four-wave frequency mixing was first proposed by Cook et al. [40]. However, the third-order nonlinearity resulting from either bound electrons or free electrons in the plasma is too small to explain the observed THz field strengths [48]. Further, the existence of an intensity threshold for THz generation was observed. In order to account for these effects a semiclassical model based on a transient photocurrent was proposed [44, 49, 50]. In this model, THz radiation results from the unidirectional motion of electrons during tunnel ionization by the symmetry-broken two-color laser field resulting in a current surge. In the strong external electric field of the focused femtosecond laser pulse applied to the atom, the atomic Coulomb potential is distorted and there is a finite probability that the electron will tunnel through the potential barrier. The resulting free electrons and the positively charged ions form a plasma. The free electrons are then further accelerated by the applied field emitting THz radiation.

Recently, a two-step model has been developed [38, 51], which provides an even more detailed insight into the THz generation process. The first step, treated fully quantum mechanically by numerically solving the time-dependent Schrödinger equation, is asymmetric gas ionization by the two-color laser field. The second step, treated analytically, describes the interaction of the ionized electron wavepackets with the surrounding medium. Scattering of the ionized electrons by the atoms of the medium disrupts their original trajectories, which results in a coherent bremsstrahlung echo at THz frequencies. Generally, the full treatment of spatio-temporal propagation in the plasma is quite complex and needs to take into account effects such as plasma-induced phase modulation and defocusing [52]. For a complete description of THz generation in gas plasmas highly sophisticated simulations are required.

In summary, generation and detection of THz pulses in gas plasmas is a rapidly developing technique for ultrafast spectroscopy covering the entire THz range well into the mid-infrared. Because phase mismatch due to phonon absorption present in electro-optic crystals can be circumvented by detection in gases, the undistorted shape of the THz pulse generated in the plasma can be measured, preserving the full bandwidth over an extremely large spectral range.

14.2.3 THz Pulse Generation by Optical Rectification

The generation of ultrashort THz pulses using optical rectification (OR) is one of the most widespread techniques and also historically one of the oldest. OR was first demonstrated in KDP and K*DP crystals in 1962 by Bass et al. [53] using 100 ns pulses from a ruby laser at 694 nm. Far-infrared generation using OR of picosecond pulses in LiNbO₃ has been predicted [26] and demonstrated [54] as early as 1971. Free-space radiation with a bandwidth of 1 THz by rectification of colliding-pulse mode-locked dye laser pulses was generated and detected in the time domain by Hu et al. [55].

14.2.3.1 Theory and Materials

OR is a second-order nonlinear optical process, which is can be viewed as degenerate difference frequency generation between the spectral components of the same femtosecond pump pulse. The nonlinear polarization induced by the pump pulse can be calculated as [56]

$$P_{\text{NL}}(\Omega) = \varepsilon_0 \chi^{(2)} \int_0^{\infty} E(\omega + \Omega) E^*(\omega) d\omega, \quad (14.1)$$

where ε_0 is the permittivity of free space, $\chi^{(2)}$ is the second-order nonlinear susceptibility of the medium, $E(\omega)$ is the one-sided ($\omega > 0$) Fourier-component of the pump pulse, ω and Ω are the optical and THz frequencies, respectively. According to Eq. (14.1), a narrowband pump pulse generates only low THz frequencies, while a broadband optical pulse can generate a broad THz spectrum containing higher THz frequencies.

Besides the nonlinear polarization, the efficient buildup of the THz field over macroscopic distances within medium is also influenced by dispersion. The efficiency of OR is highest when the phase-matching condition [57]

$$\Delta \mathbf{k}(\Omega) = \mathbf{k}(\Omega) + \mathbf{k}(\omega) - \mathbf{k}(\omega + \Omega) = 0 \quad (14.2)$$

is fulfilled. Since $\Omega \ll \omega$, the term $\mathbf{k}(\omega + \Omega) - \mathbf{k}(\omega)$ can be approximated by $\partial k / \partial \omega|_{\omega_0} \times \Omega$, which gives $\Delta k = [n(\Omega) - n_g(\omega_0)]\Omega/c$ in the collinear case. Here ω_0 is the mean pump frequency, c is the speed of light in vacuum, n and n_g are the refractive index and the group index, respectively. Thus, phase matching can also be formulated as matching the $v(\Omega)$ phase velocity of the generated THz radiation to the group velocity $v_g(\omega_0)$ of the optical pump pulse:

$$v(\Omega) = v_g(\omega_0). \quad (14.3)$$

In case of velocity matching and negligible dispersion in the THz range the output is a single THz pulse with its electric field shaped as the time derivative of the optical pump pulse envelope [58]. For Gaussian-shaped envelopes this means that single-cycle THz pulses can be generated.

For phase-matched conditions, the efficiency of a difference frequency process in the absence of pump absorption or depletion, but taking into account THz absorption can be described by [57]

$$\eta_{\text{THz}} = \frac{2\Omega^2 d_{\text{eff}}^2 L^2 I}{\varepsilon_0 n_{\text{NIR}}^2 n_{\text{THz}} c^3} \times \exp[-\alpha_{\text{THz}} L / 2] \times \frac{\sinh^2[\alpha_{\text{THz}} L / 4]}{[\alpha_{\text{THz}} L / 4]^2}, \quad (14.4)$$

where d_{eff} is the effective nonlinear coefficient, L is the material length, I is the pump pulse intensity, α_{THz} is the absorption coefficient in the material at THz frequencies, and n_{NIR} and n_{THz} are the refractive indices at the pump and THz frequencies, respectively. Equation (14.4) can be used to compare the suitability of different nonlinear optical crystals for OR process [59].

14.2.3.2 Collinear Optical Rectification

The most commonly used material for OR is ZnTe. Its main advantage is that velocity matching is approximately fulfilled in collinear geometry for Ti:sapphire pumping and far-infrared radiation below the optical phonon at 5.3 THz. However, ZnTe has

strong two-photon absorption at 800 nm, which leads to the generation of free carriers and, in turn, to increased THz absorption. Hence, the useful pump intensity is limited [60]. The situation is similar with GaP, another semiconductor material frequently used for rectification at 1,035 nm. Here the two-photon threshold is higher but the scaling is limited by the lower nonlinear coefficient and three-photon absorption [61].

GaSe has a moderate nonlinear coefficient of roughly 60 pm/V [62], but in contrast to semiconductors with zinc blende structure it has the advantage that velocity matching is possible based on birefringence. By using short pulse lasers very high THz frequencies [63, 64] up to 40 THz can be achieved. With an amplified laser system at 25 fs multicycle pulses with high field strengths and 12 nJ pulse energy at 30 THz (10 μ m wavelength) have been reported [65].

Recently, stoichiometric LiNbO₃ (sLN) became a widely used material for OR. In lithium niobate (LN), THz electromagnetic waves are strongly coupled to highly polar, “soft” optic phonons associated with ferroelectric phase transition, yielding mixed phonon-polariton modes [66]. The polarizabilities of these modes give rise to many of the favorable nonlinear optical properties of LN. Besides its large effective nonlinearity, LN has a bandgap much larger than that of semiconductors allowing only three-photon absorption to be effective at 800 nm pump wavelength. This allows for high pump intensities, essential for high-energy THz pulse generation. However, the THz refractive index for LN is significantly larger (5.0) than the optical group index (2.3), and therefore collinear velocity matching is not possible. Quasi-phase matching in periodically poled LN can be used to enhance conversion efficiency, resulting in multi-cycle THz pulses [56, 67] with a fixed number of cycles. In bulk LN, generation of single cycle THz pulses with high conversion efficiency can be achieved by the tilted-pulse-front pumping technique with noncollinear velocity matching described in the following section.

14.2.3.3 Noncollinear Optical Rectification with a Tilted Pulse Front

Tilted-pulse-front pumping was proposed and demonstrated by Hebling et al. in 2002 for efficient phase-matched THz pulse generation in LN [68]. In this technique, the THz radiation generated by the tilted pulse front of the pump propagates perpendicular to this front (Fig. 14.5) with the THz phase velocity $v(\Omega)$, according to Huygens’ principle. This leads to a non-collinear propagation geometry, where the angle between the propagation directions of the THz radiation and the pump pulse is equal to the tilt angle γ of the pump pulse front relative to the pump phase fronts (which is perpendicular to the pump propagation direction). The THz wave propagates with a fixed phase relative to the pump pulse front if the following velocity-matching condition is fulfilled:

$$v_g(\omega_0) \cos \gamma = v(\Omega). \quad (14.5)$$

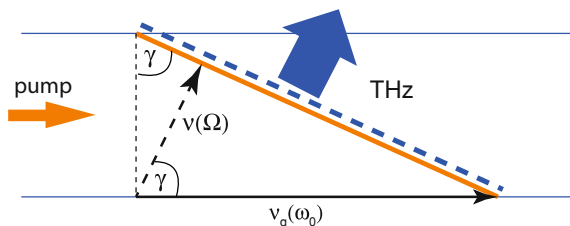


Fig. 14.5 Noncollinear velocity matching using a tilted pulse front. The *thick red/solid line* indicates the pump pulse front, the *thick grey/dashed line* indicates the THz phase front. The *arrows* indicate the propagations direction and velocities of these two surfaces. From [29]

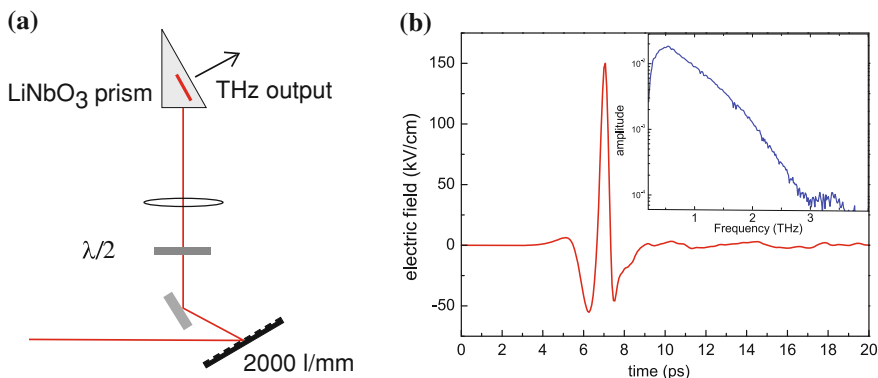


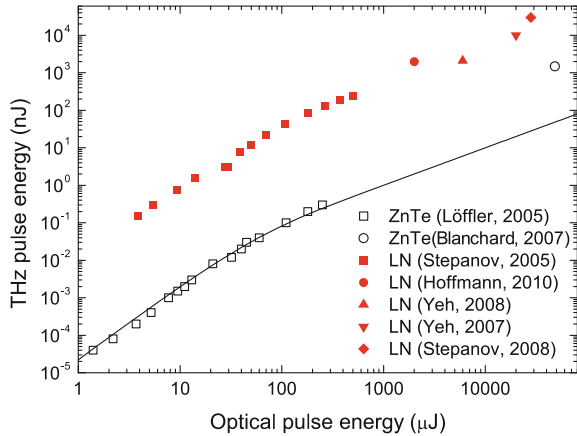
Fig. 14.6 **a** Experimental setup for THz generation by rectification with a tilted pulse front at 800 nm in LN. **b** Typical temporal pulse shape and corresponding spectrum

In the case of LN where $v_g(\omega_0) \geq v(\Omega)$, or equivalently $n_g(\omega_0) \leq n(\Omega)$, Eq. (14.5) can be fulfilled by choosing an appropriate pulse front tilt angle γ .

Due to the large difference between $n(\Omega)$ and $n_g(\omega_0)$, noncollinear rectification in LN requires a pulse front tilt as large as 63° – 65° . In order to provide such large tilt angle, a pulse-front-tilting setup consisting of a grating and a lens is used in experiments (Fig. 14.6). The angular dispersion introduced by the grating is further enlarged by the lens, which also recreates the original short pulse duration inside the medium by imaging the grating surface into the crystal. Additionally, a half wave plate is used to match the polarization of the pulse to the z-axis of the LN crystal. The generated THz polariton wave is coupled out into free space through the surface of the crystal cut at the tilt angle γ .

Figure 14.7 summarizes the scaling behavior of achievable THz output with pump pulse energy. The figure shows results obtained with various sources based on sLN and ZnTe. At low pulse energies, quadratic scaling is observed for both materials, as expected for a second-order process. In ZnTe saturation, linear scaling dominates in when pulse energies of $50 \mu\text{J}$ are exceeded. The scaling behavior can be described using a model from SHG theory where the efficiency η is described as

Fig. 14.7 Scaling of the output THz pulse energy with the pump pulse energy for sources based on sLN and ZnTe. The solid line is a fit using model described in the text. Löffler [69], Blanchard [60], Stepanov [70], Hoffmann [71], Yeh [72], Yeh [73], Stepanov [74]



$\eta \propto \tanh^2(\text{const} \times \sqrt{I_{\text{opt}}})$ [69]. In contrast, the scaling behavior of sLN does not exhibit saturation [70] until very high pump pulse energies are reached. The main limiting factor in THz generation using ZnTe is free-carrier absorption caused by two-photon absorption of the pump light, which limits pump intensity. Although THz energies as high as $1.5 \mu\text{J}$ have been demonstrated by using large pump spots [60] the achieved conversion efficiency of 1.3×10^{-5} was rather low. In contrast, by using LN with a tilted pulse front, THz energies of $10 \mu\text{J}$ [73] and $30 \mu\text{J}$ [74] have been reported with pump-to-THz energy conversion efficiencies of 5×10^{-4} and 1.1×10^{-3} , respectively. These are the most energetic ultrashort THz pulses ever generated from a table-top source.

14.2.4 Intense THz Multicycle Pulses by Difference Frequency Generation in GaSe and ZnTe Crystals

Because of the wide range of phase-matching angles and the low absorption up to long wavelengths, GaSe is an efficient material for the generation of mid-infrared light [62, 75]. Difference frequency generation in GaSe by two near-infrared pulses from the signal and idler of an optical parametric amplifier (OPA) yields tunable pulses covering the entire mid-infrared from 4 to $20 \mu\text{m}$. This process has first been demonstrated [76] in 1994 and is by now a mature and readily available technology. Since the conversion process scales favorably (Eq. 14.4) with smaller difference between input and output wavelengths, high efficiencies can be achieved. By using the signal pulses from two OPAs derived from the same white light seed principle can be modified to generate carrier-envelope phase stable mid-IR pulses [77]. This technique will be discussed in more detail in Chap. 23 of this book. These pulses can be focused tightly and the field can be directly characterized in the time domain by

electro-optical sampling. Focused electric field strengths as high as 100 MV/cm were demonstrated around 50 THz frequency, corresponding to 6 μm wavelength. These intense mid-IR pulses can be further stabilized for long-term drift [78] and used for pump-probe measurements sensitive to the absolute optical phase. By choosing the pump and signal wavelengths in order to take advantage of the broadest possible phase-matching bandwidth, very short mid-infrared pulses can be generated [79]. In this case 30 fs signal pulses at 1.28 μm wavelength were used to achieve few to single-cycle pulses centered at 14 μm with a FWHM spectral bandwidth of about 20 THz.

Intense narrowband THz pulses with lower frequency can be generated by using a type II difference frequency process in ZnTe [80]. In this technique a pair of broadband laser pulses with strong linear chirp and orthogonal polarization are delayed with respect to each other and mixed in a ZnTe. The interferometric beating of the pulses results in multicycle THz pulses with 1 nJ energy and a duration of 3 ps. By changing the time delay between the pump pulses the THz center frequency is tunable in the range of 0.5–2.5 THz with bandwidth of 0.2–0.5 THz. The peak field strength reported at the focus was approximately 5 kV/cm.

14.3 THz Nonlinear Spectroscopy Methods

In this section we will discuss various experimental approaches for carrying out nonlinear spectroscopy with intense THz pulses. Generally, we are interested in deducing the influence of the strong THz pulse onto a sample. This can be achieved by analyzing the transmitted or reflected THz pulse or by probing the sample properties with a second THz or optical pulse at a given time delay. By using a sequence of THz pulses, THz pump/THz probe measurements or two-dimensional THz time domain spectroscopy (2D-THz-TDS) in analogy to 2D-infrared spectroscopy can be carried out.

14.3.1 Intensity Dependent Transmission

The straightforward approach for observing nonlinear processes in a given sample is the use of intensity-dependent transmission experiments. Here, high intensity THz pulses are generated, passed through the sample, and are then detected by electro-optical sampling. The intensity of the THz pulses incident on the sample is then controllably varied. This can be achieved by changing the pulse energy of the pump laser used for the THz generation process; however, due to the nonlinearity of the generation process, this might cause changes in the THz pulse temporal structure which need to be taken into account by carefully referencing the measurement. An alternative is to attenuate the THz beam by a series of silicon wafers or the use of

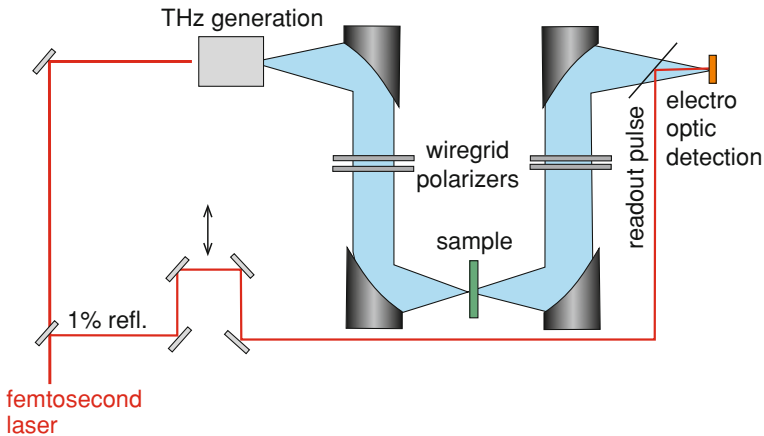


Fig. 14.8 A THz time domain setup for nonlinear transmission experiments. A pair of wiregrid polarizers is used to attenuate the THz field incident on the sample. A second pair can be used to keep the field on the detection crystal constant to prevent nonlinearities in the electro-optical detection

a pair of wiregrid polarizers where the second of these polarizers is kept fixed to maintain polarization while the first one is rotated (Fig. 14.8).

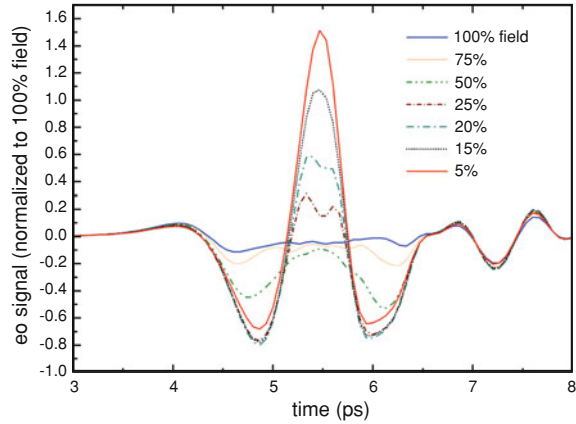
The intensity at the sample can also be varied by scanning the sample through a tight focus. This method is commonly referred to as “z-scan” and commonly employed to measure nonlinear optical constants [57]. While z-scan has been used with intense THz pulses for measurements in semiconductors [81] the technique can be problematic for thick samples with high refractive indices. The reason is that the Gouy phase shift [82, 83] becomes relevant when scanning a material with highly dielectric constant through a THz focus with short Rayleigh range and small alignment errors are picked up due to the inherently phase sensitive nature of the electro optical detection.

14.3.1.1 Linearity of Detection

In transmission geometry-type experiments (Fig. 14.8), the THz pulse is detected by electro-optical sampling in ZnTe or GaP while the THz field is varied. In electro-optic detection the change in ellipticity induced by the THz pulse is analyzed using a quarter wave plate and a Wollaston prism and the two polarization components are recorded using photo diodes or a balanced detector. From the relative difference in signal intensity I between the two photo diodes, the electric field can usually be determined reliably using

$$\frac{\Delta I}{I} = \frac{\omega n^3 E_{\text{THz}} r_{41} L}{2c} (\cos \alpha \sin 2\varphi + 2 \sin \alpha \cos 2\varphi) \quad (14.6)$$

Fig. 14.9 Dependence of the electro-optic signal from a 1 mm thick 110 ZnTe crystal on increasing the THz field strength. The THz pulse was attenuated with a pair of wiregrid polarizers. At fields already on the order of 15 % of the maximum field (300 kV/cm) a strong saturation is visible. The signals are normalized to the field strength calculated from the rotation angle of the wiregrid polarizers



where ω is the laser frequency, L is the length of the crystal, n and r_{41} are the refractive index and the electro-optic coefficient of the ZnTe crystal and α and ϕ are the angles of the THz polarization and probe polarization with respect to the 001 axis of the ZnTe crystal [84]. However in the derivation it is usually assumed that the THz electric field is small and the phase accumulated within the eo-crystal is much smaller than π . For strong THz pulses and thick crystals, this is no longer the case. Figure 14.9 shows an example of the electro-optic signal in the case of a 1 mm ZnTe crystal. The maximum THz field of 300 kV/cm was attenuated in a controlled way by a pair of wiregrid polarizers. The data is normalized to the calculated value of the field using the cosine square of the first polarizer angle. Severe pulse distortions are observed at high field strengths. Already at 15 % of the maximum field a large deviation from the low field regime is visible. This implies that even for thin ZnTe crystals on the order of 100 μm , deviations from linearity in electro-optic detection are to be expected.

In electro-optic crystals such as GaP which have a residual carrier concentration from impurities and hence show a Drude-like absorption at THz frequency so that part of the THz pulse is absorbed and the effective phase matching length L is shorter than in a pure material. This free-carrier absorption can be bleached at high THz field strengths [71] leading to a nonlinearity in the electro-optical detection with seemingly higher field strengths. Jewariya et al. [85] have successfully employed a second pair of wiregrid polarizers after the sample in order to keep the field at the electro-optic detection constant (Fig. 14.8).

14.3.1.2 Analysis in the Time Domain versus Analysis in the Frequency Domain

The detected field transients can be analyzed in the frequency domain to obtain the complex dielectric function or the optical conductivity (see Chap. 2 of this book).

The temporal information within the window used by the Fourier transformation is spread out over the entire spectral range. This restricts the observation of dynamics on a timescale shorter than the THz pulse contained in the transients.

THz transmission data from nonlinear experiments can also be analyzed in the time domain. Here, the “emitted” THz radiation is obtained by subtracting the field E_{in} recorded without the sample in place and the THz field E_{tr} recorded after propagation through the sample and subtracting both in the time domain [86]. The resulting difference field $E_{\text{em}}(t) = E_{\text{tr}}(t) - E_{\text{in}}(t)$ is treated as if it were emitted by the sample. This approach is only valid thin samples however and the phase shift by finite sample thickness needs to be carefully considered.

14.3.2 THz-Pump/THz Probe Experiments

It is also possible to extend the technique discussed above by using a time-delayed second THz pulse to carry out THz-pump/THz probe experiments. This can be achieved by using two different THz sources and overlapping them at the sample or by using the same THz source pumped by two consecutive laser pulses, resulting in a collinear geometry Fig. 14.10. Both THz pulses can be detected by electro-optical detection after traversing the sample. By selectively chopping either the pump or the probe and using lock-in detection the pump and the probe pulses can be separated [87]. By using a chopping scheme with dual frequency modulation, a measurement of changes caused by the pump can be isolated. Differential chopping with double modulation can be used to detect the transmitted waveforms and the changes caused by the pump simultaneously [88]. When the same nonlinear crystal is used for the generation of both the pump and the probe pulses, nonlinear interaction in the crystal is usually observed when both pump femtosecond pulses are temporally and spatially overlapped. This results in severe changes in the THz pulse forms unrelated to any effect in the sample. These effects can be partially compensated by taking a reference measurement without the sample in place at every pump-probe delay step. Two independent THz sources can be used in a noncollinear geometry in order to take advantage of strong pulses generated by a tilted pulse front and a broadband but low intensity ZnTe or plasma-based probe pulse [89].

14.3.3 THz-Pump/Optical-Probe Measurements

The influence of a strong THz field onto the optical properties of a sample can be probed in a THz-Pump-optical probe experiment. Optical probe light in a broad range of wavelengths can be produced by nonlinear optical methods such as an OPA or white light generation (WLG). The changes in optical properties such as reflectivity or transmission at these wavelengths can then easily be accessed. A sensitive method is to monitor THz-induced birefringence by the linear or quadratic electro-optic or

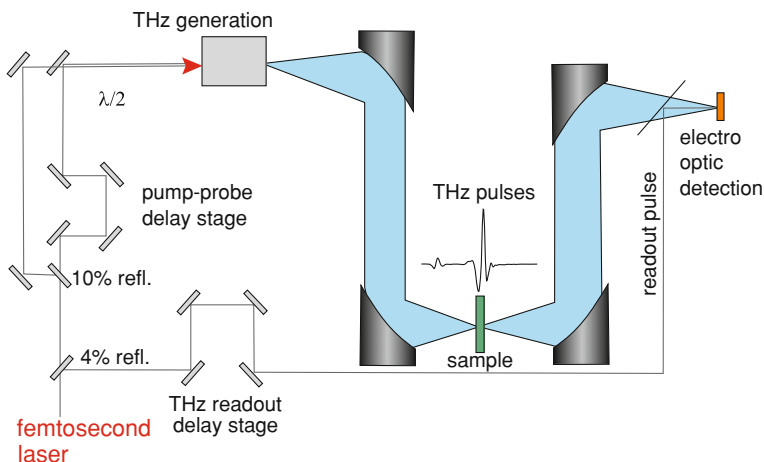


Fig. 14.10 A THz-Pump/THz probe setup with collinear geometry using the same THz generation source pumped by to time delayed pulses. See text for details

magneto-optic effect. The experimental apparatus is very similar to the traditionally used electro-optical sampling setup except that very high field strengths of the THz pulses are used. Small changes in birefringence can be detected. In a spectroscopy system based on a 1 kHz chirped pulse amplified laser system, usually a change in refractive index $\Delta n/n$ of the order of 10^{-5} can still be detected.

Changes in magnetization can be detected by analyzing the polarization state of the probe pulse reflected or transmitted from the sample in the presence of a static magnetic field (time resolved magneto-optic Kerr effect).

14.3.4 Two-Dimensional THz Spectroscopy

Two-dimensional infrared spectroscopy (2D-IR) is a nonlinear spectroscopy technique that has the ability to resolve correlations of vibrational modes in condensed matter [90]. Compared to linear infrared spectra this technique provides additional insight by spreading the vibrational signal information multiple axes. From this frequency correlation spectrum information about the coupling of vibrational modes, anharmonicities, energy transfer rates and molecular dynamics can be obtained. In a typical 2D-IR experiment a sequence of femtosecond mid-infrared pulses which are generated by difference frequency mixing of signal and idler of an OPA is used. The appropriate nonlinear signal is selected via k-vector conservation in a noncollinear four-wave mixing geometry [91] and detected by heterodyning with a local oscillator (Fig. 14.11).

Using phase stable infrared pulses obtained from OR or difference frequency generation in GaSe the infrared field can be detected directly in the time

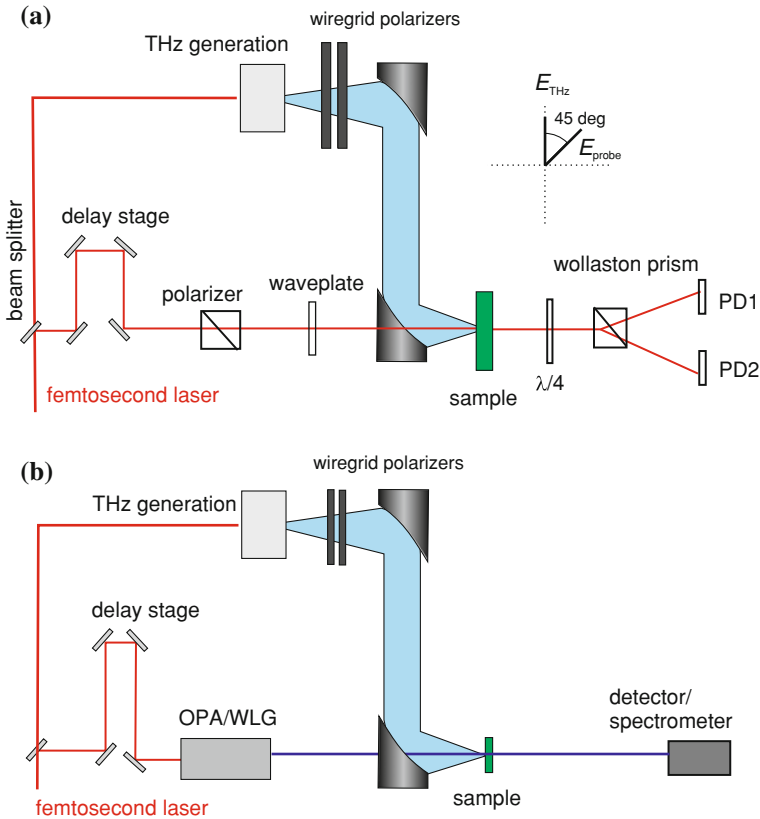


Fig. 14.11 Experimental setups for **a** THz-induced birefringence probe measurements **b** broadband optical probe measurements

domain [78]. This allows for time-domain 2D-IR spectroscopy in a collinear geometry. This principle has been demonstrated by Kuehn et al. [92] using a two-pulse sequence at 25 THz ($12\ \mu\text{m}$) using an n-doped GaAs/AlGaAs quantum well structure as the sample. Figure 14.12 shows the transmitted pulse sequence (a) and the nonlinear signal in the time domain (c) which can be extracted by subtracting the two pulses detected independently (b). Fourier transformation of the nonlinear signal then yields the two-dimensional correlation spectrum with two frequency axes ν_τ and ν_t corresponding to the time delay τ between the pulses and the “real” time t of the electro-optical sampling delay. In the spectral domain, peaks at multiples of the mean excitation frequency ν_0 correspond to different orders of nonlinear processes as represented by Feynman diagram used in conventional nonlinear optical spectroscopy formalism [91]. For example the two possible processes for pump probe signal correspond to $(\nu_t = \nu_0, \nu = -\nu_0)$ and $(\nu_t = \nu_0 \text{ and } \nu_\tau = 0)$, indicated by the two lower (red) circles in Fig. 14.12f. The four-wave mixing signal corresponds

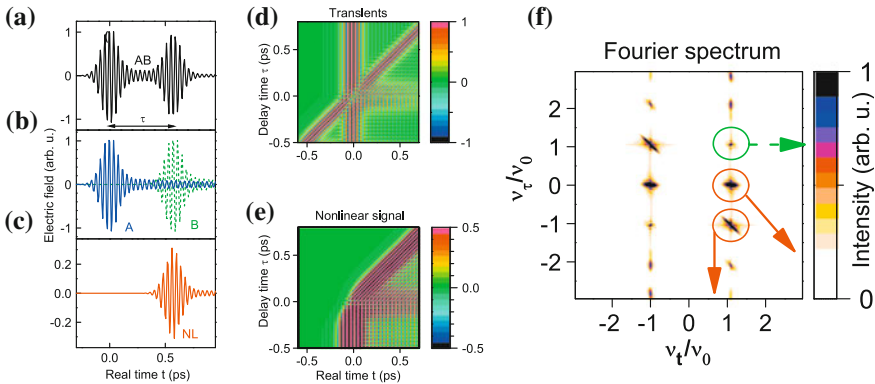


Fig. 14.12 Simulated electric field transients in a collinear 2D-THz experiment [92]. Subtracting the transients of the incoming pulses (b) from the transmitted signal (a) yields the nonlinear signal (c). On the right side the 2D transients (d) and nonlinear signal (e) are shown in the time domain. In the two-dimensional Fourier spectrum (f), dots at integer multiples of the fundamental frequency correspond to different orders of nonlinear processes. Reprinted with permission from Kuehn et al. [92]. Copyright 2009, American Institute of Physics

to ($v_t = \nu_0, v_\tau = +\nu_0$), upper (green) circle. The relevant nonlinear signal can be selected and isolated in the frequency domain and then Fourier transformed back into the time domain. By using this method Kuehn et al. have identified homogenous broadening in the quantum well sample.

Time domain collinear 2D-IR spectroscopy is a novel scheme for coherent spectroscopy that allows the simultaneous measurement of optical nonlinearities of arbitrary order. This method can be easily extended for the entire THz to mid-IR range wherever field coherent electro-optical detection is feasible.

14.4 THz Nonlinear Optics

Classical nonlinear optical effects such as harmonic generation or self-phase modulation in the THz range have remained largely unexplored due to lack of strong sources. Since the pioneering work of Faust and Henry using frequency mixing of an H₂O laser with optical light only few experiments have been performed in which the dispersion of the nonlinear susceptibility in the THz range has been measured directly [23, 93]. Intense few cycle pulses in combination with electro-optic detection should enable the study of these effects directly in the time domain.

The second-order nonlinear susceptibility in non-centrosymmetric crystals has two contributions: the (bound) electrons and the ion cores [94]. This is generally expressed as

$$\chi^2(\omega_1 - \omega, \omega, \omega_1) = \chi_E^2 \left[1 + C_1 \frac{1}{D(\omega)} \right] \tag{14.7}$$

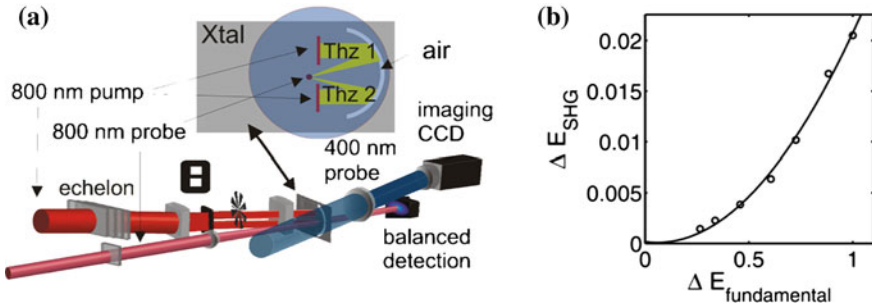


Fig. 14.13 **a** Experimental setup for the observation of THz SHG inside a LiNbO_3 waveguide. Two phonon polaritons are generated by 800 nm femtosecond pulses in a $100\ \mu\text{m}$ thick waveguide by using a tilted pulse front generated by an “echelon” glass structure with discrete steps. The $100\text{-}\mu\text{m}$ thick crystal includes a fs laser-machined “trench” of air in the shape of an arc, which serves as an integrated focusing reflector (see inset.) The two THz waves are incident on this feature, reflected, focused, and crossed at a region of the crystal that has not been irradiated by any excitation light. A variably delayed 800-nm probe pulse is focused to the same spot of the crystal, and the depolarization of probe light is measured. The *top* and *bottom* excitation regions are chopped at two different frequencies, and the nonlinear response is detected at the sum or difference frequency. A separate, variably delayed 400-nm probe beam is used for imaging of the THz fields. **b** The observed power dependence of the observed nonlinear THz signal is quadratic. From [96]

with $D(\omega) = 1 - \frac{\omega}{\omega_{TO}^2} - \frac{i\omega\Gamma}{\omega_{TO}^3}$ where ω_{TO} is the TO phonon frequency and Γ the damping constant and $\chi_E^{(2)}$ is the electronic part of the nonlinear susceptibility. The Faust–Henry coefficient C_1 expresses the ratio between the lattice-induced and the electronic contributions to the nonlinear coefficient. In ferroelectric materials like LiTaO_3 and LiNbO_3 , the contribution of the ionic part to $\chi^{(2)}$ can be an order of magnitude larger than the electronic part [95]. Direct observation of SHG in LiTaO_3 has been reported by Mayer [15] using 40 ns pulse duration gas laser in combination with steep filters in order to suppress the fundamental. A similar experiment in GaAs using a free electron laser at wavelength in the range of 3.5–6 THz has been carried out by Dekorsy et al. [23]. Using table-top time domain methods, SHG in LN has been observed in LiNbO_3 [96]. Here, two phonon polaritons were generated and focused onto the same spot within a LiNbO_3 waveguide, enabling both high fields and tight focusing (Fig. 14.13). At the focus spot components of the electro-optical signal were detected that contained the second harmonic of the two fundamental polaritons.

Strong THz fields can also induce polarization in nonpolar media, leading to transient birefringence, which can then be probed by an optical probe pulse. This is analogous to the optical Kerr effect, and involves a third-order ($\chi^{(3)}$) nonlinear process combining the action of an intense THz field onto the polarization state of a probe pulse at optical frequencies. Figure 14.14a shows the induced birefringence in four different organic solvents as function of time compared with the applied single-cycle THz field [97]. The signal is composed of two contributions, a fast electronic response that follows the square of the THz field directly, and a slower, exponential

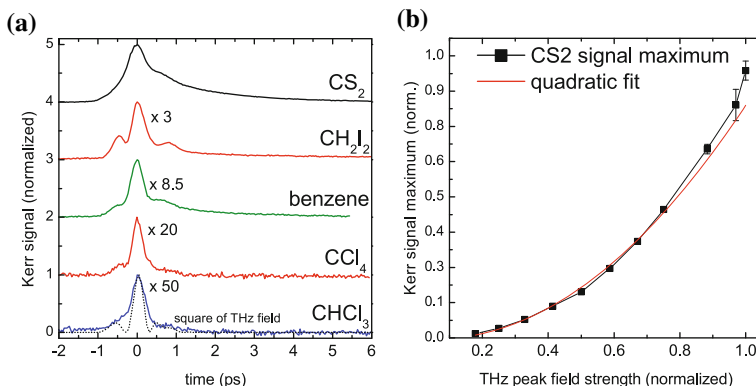


Fig. 14.14 **a** THz-induced birefringence in polarizable liquids. In the time domain, the signal follows the square of the THz pulse. **b** The peak signal scales quadratically with the THz field strength, demonstrating the $\chi^{(3)}$ nature. From [97]

decay resulting from subsequent relaxation of the partially aligned molecules in the liquid which is of the order of a few ps. The overall birefringence of the aligned molecule scales quadratically with the peak THz field (Fig. 14.14b).

14.5 Nonlinear THz Spectroscopy of Semiconductors

THz excitation of semiconductors is the most mature field in nonlinear THz spectroscopy [16]. The interaction of THz radiation with semiconductors has been studied extensively and includes effects such as free-carrier absorption, the photon drag effect, or intersubband transitions. Nonlinear behavior of semiconductors under strong THz excitation has been investigated using gas laser and FEL sources but temporal resolution was limited by long pulse durations [98] or difficulties in synchronizing a femtosecond laser to an FEL source due to timing jitter. OR-based sources on the other hand provide subpicosecond single- or few-cycle pulses with extremely high fields strengths and broad bandwidth. Because of their derivation from a common femtosecond laser sources, the inherent synchronization of the pump and probe pulses allow for time-resolved experiments where the influence of the strong field on a sample can be observed directly with tens of femtosecond resolution. Until recently, however, relatively few studies have been reported on the nonlinear THz characteristics of semiconductors using high fields. In this section we will try to give a brief overview.

14.5.1 The Ponderomotive Force of THz Fields

In the limit of high field strengths, the interaction of an oscillating electric field with matter cannot be simply treated by a perturbative approach. In this case the interaction cannot be described by either neglecting the field aspect or the single-quantum description. A measure for the contribution of the nonperturbative regime is the ponderomotive potential, defined by the time-averaged kinetic energy of an electron driven by the electric field. The nonperturbative regime is reached, when the ponderomotive potential of the electric field exceeds the photon energy $\hbar\omega$ or the ionization potential of the system is exceeded. For an oscillating electric field with frequency ω the ponderomotive potential is given by

$$U_p = \frac{e^2 E^2}{4m_e \omega^2} = \frac{2\pi e^2 I}{mc \omega^2} \quad (14.8)$$

where m is the electron mass and I is the intensity of the light. As can be seen from Eq. (14.8) the ponderomotive potential has a quadratic dependence both on the electric field and on the inverse of the frequency. Therefore, very high values of U_p can be achieved with high field strength, low frequency pulses. In laser ionization of atoms the interaction can be treated as multiphoton ionization when $U_p \ll \hbar\omega$ and as static electric field tunneling ionization when $U_p > I_p > \hbar\omega$. In the latter case, the Keldysh parameter $\gamma = \sqrt{I_p/2U_p} < 1$ where I_p is the ionization potential. The influence of the ponderomotive potential, i.e., effects at the transition between classical and quantum behavior, is expected to be most noticeable when $U_p \sim \hbar\omega$, but less than or comparable to the relevant energy scale in the system like the bandgap in semiconductors.

The first experiment to take advantage of the large ponderomotive potential in a single-cycle THz pulse was the demonstration of ionization of Rydberg atoms by Jones et al. [32]. Here pulses from a photoconductive source with field strengths exceeding 10 kV/cm were used to ionize sodium atoms selectively prepared by a dye laser. The temporal structure of the pulse from the large area photoconductive switch are particularly suitable for this ionization process because of their asymmetric half-cycle nature.

In semiconductors, ponderomotive effects were predicted early on [99], but strong absorption due to the bandgap of the order of typically 1 eV and the resulting high intensity damage have made such observations impossible using laser sources in the optical wavelength range, where E_{photon} is on the order of the bandgap. By using light with significantly longer wavelength than the bandgap, these problems are avoided. In the case of semiconductors, the electron mass in the ponderomotive potential is replaced by the effective mass of the carrier, thereby further increasing the value of U_p . Here the case of $U_p \sim \hbar\omega < E_{\text{gap}}$ can be easily achieved.

An immediate application of the large ponderomotive potential of THz pulses is tunneling ionization of impurities in lightly doped semiconductors such as silicon, germanium, and GaAs at low temperatures. Here the energy levels of deep centers

are tilted by the external electric field of the THz light so that tunneling ionization can occur [100]. This effect occurs already at comparatively low electric fields and has been observed using gas lasers.

Another direct consequence of the ponderomotive potential in semiconductors is the dynamic Franz–Keldysh effect (DFKE). In the static Franz–Keldysh effect a DC electric field causes the deformation of the wavefunctions in a semiconductor so that photon-assisted tunneling from the valence to the conduction band is possible. This leads to an increased absorption at photon energies below the band gap and oscillatory behavior above the gap. At THz frequencies, the DFKE has been demonstrated in quantum wells (QW) using the UCSB free electron laser [101] and on an ultra-fast timescale using mid-infrared pulses at $10\ \mu\text{m}$ wavelength in bulk GaAs [102]. Recently, the excitonic Franz–Keldysh effect has been observed with single-cycle THz pulses in QW [103]. Interaction of intense THz fields with excitons will be discussed in Sect. 14.5.3. High THz fields can also directly distort wavefunctions in low-dimensional nanostructures such as self-assembled quantum dots. This results in a strong modulation of absorption wavelength by the quantum confined Stark effect [104].

14.5.2 THz-Driven Ballistic Transport

The intense THz fields with rise times on the scale of tens to 100 fs can efficiently accelerate carriers in semiconductors into the ballistic transport regime. This effect is most prominent in n-type semiconductors with high mobility such as GaAs or InSb. In these materials mobile free carriers form an electron gas with maximum absorption in the THz frequency range [105] at room temperature. The spectral properties are usually well described by a Drude model using parameters of scattering rate and effective mass which can be assumed to be constant in the small field limit. However, strong THz fields can accelerate carriers very effectively when the effective mass is small. For example, in lightly doped GaAs which as an electron effective mass of $0.063 m_0$, electrons can get accelerated into the ballistic regime and electron energies larger than 1 eV can be achieved this way. The instantaneous electron velocity can far exceed the DC drift velocity at equilibrium. This is generally related to an increase in effective mass of conduction band electrons in a dispersive band structure due to the effect of nonparabolicity of the conduction band valleys at high momentum as well as intervalley transfer.

The most striking consequence of this effect is the strong decrease of THz absorption by the conduction electrons in a lightly doped semiconductor. This effect has been observed in a number of n-type semiconductors such as GaAs [87], InGaAs [106], Ge, Si [107] as well as in photoexcited GaAs [108]. In bulk samples, the increase in THz transmission can be almost one order of magnitude, making these materials suitable for use as saturable THz absorbers at room temperature [71].

The time evolution of carrier heating and subsequent cooling can be observed spectrally using a THz-pump/THz probe scheme [87, 109]. Figure 14.15a shows the

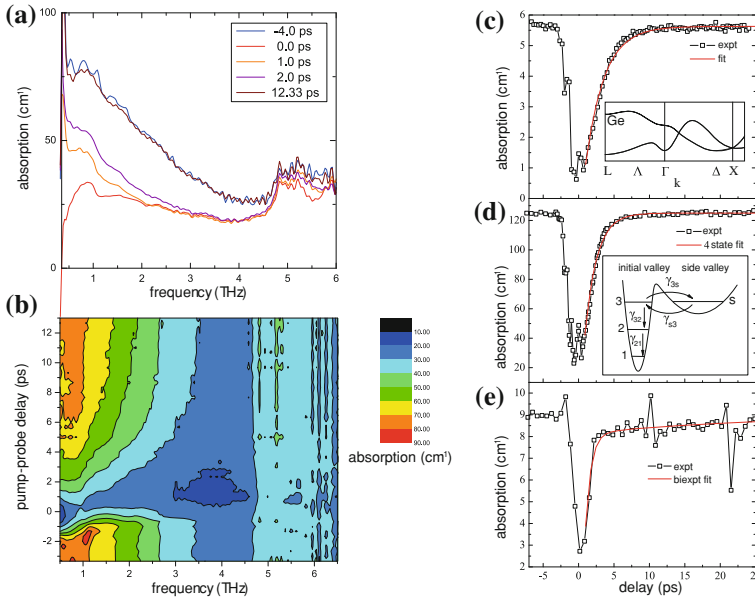


Fig. 14.15 Dynamic behavior of the saturation of free-carrier absorption in the n-type semiconductors. **a** and **b** time and frequency resolved absorption in GaAs probed by a broadband THz pulse, **(c–e)** recovery of the frequency averaged (0.2–2.0 THz) absorption coefficient in Ge, GaAs, and Si. The *solid lines* are fits using a simple rate equation model [107]

absorption coefficient of THz-excited GaAs for selected time delays before and after THz excitation. In Figure 14.15c–e the different dynamics in Ge, GaAs, and Si is compared. In all samples a strong drop in absorption is detected, with a subsequent recovery time of the order of a few picoseconds depending on the material. The decrease and recovery of absorption can be described qualitatively by a simple model of the electron transport [107, 108]. From the spectral analysis of the data it can be seen that the characteristics of the hot electron gas deviates significantly from the Drude behavior and a better theoretical modeling taking into account the hot electron properties is needed.

In the case of a low bandgap semiconductor like InSb, the energy of the electrons accelerated by the THz field can far exceed the bandgap, leading to pair creation of new electron hole pairs [81]. This effect has been observed by Ganichev using photoconductivity measurements of InSb excited by a nanosecond gas lasers [109]. THz pump/THz probe measurements reveal a strong rise in THz absorption continuing for tens of picoseconds after the excitation [110].

Nonlinear transmission studies in combination with modeling of the contribution of several of these nonlinear transport phenomena in GaAs have been reported Kuehn [111]. The interaction of ballistic carriers with the optical phonon was studied in Ref. [112]. Here, high electric field in the THz range were shown to drive the

Fröhlich polaron in a GaAs crystal into a highly nonlinear regime where an electron is impulsively driven from the centre of the surrounding lattice distortion.

14.5.3 Manipulation of Excitons by THz Fields

The application of intense THz fields to semiconductors strongly modifies and controls the optical properties of semiconductors and semiconductor nanostructures by acting on excitons [101, 113, 114].

THz-induced nonlinear optical effects of excitons are of great interest because they provide new insights into the quantum coherence and wave packet dynamics of semiconductors. Further, electrical manipulation of optical absorption with THz frequencies has direct application in optical communications.

In GaAs-based QW excitons have a hydrogen-like spectrum with binding energies is in the range of 10 meV (1 THz corresponds to 4.1 meV). In this context, it is interesting to study excitation of semiconductor QW with an intense single-cycle THz pulse whose Rabi energy approaches the energy of the excitonic $1s-2p$ transition. Such investigations enter the regime of nonlinear optics where the rotating-wave approximation breaks down [115].

In Ref. [116] a experiment-theory investigation of a pump-probe measurement with a strong single-cycle THz pulse and a weak optical probe was carried out to study time-resolved nonlinear effects in the optical spectrum in multiple GaAs/AlGaAs QWs. Excellent agreement with the results of microscopic many-body calculations was obtained, identifying clear ponderomotive contributions and the generation of THz harmonics. This work has been extended by using a tunable narrowband THz pulse generated in ZnTe as shown in Fig. 14.16a–c [117]. Figure 14.16d shows the optical transmission of the sample near the heavy-hole (HH) and light-hole (LH) exciton with and without the THz pulse present at a time delay of 0.6 ps. The clear modulation and increasingly asymmetric HH exciton line shape suggests that the THz radiation and the exciton levels are strongly coupled. A microscopic theory attributes the observed nonlinearities to Rabi sidebands indicating that the $2p$ -dephasing time is three times that of the $1s$ -state.

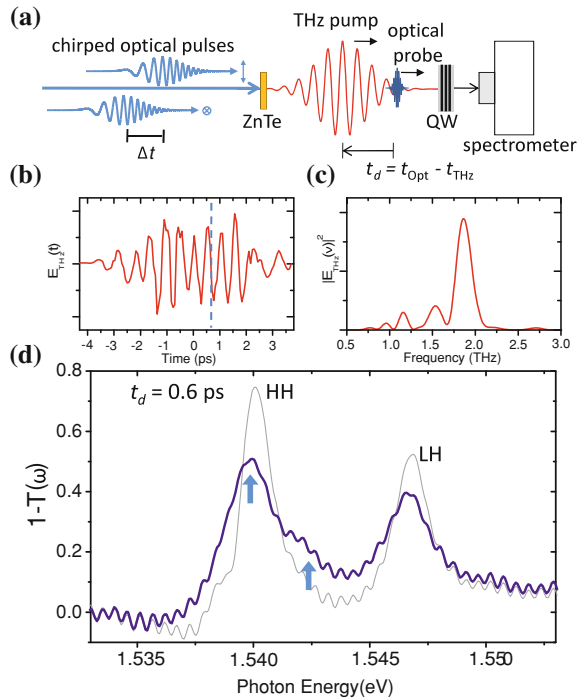
Ogawa et al. have investigated the electro absorption of aligned micelle-wrapped single-walled carbon nanotubes induced by intense THz pump pulses at room temperature [118]. A white light pulse generated in sapphire was used as a probe with 90 fs temporal resolution in an experimental arrangement similar to Fig. 14.11b. The electro absorption signal was found to be enhanced at exciton resonances between 1.1–1.5 eV. Further, changes in spectral shape of the excitonic absorption were observed and the magnitude of the redshift and broadening was found to be quadratically dependent on the THz E-field, and to instantaneously follow the THz oscillation of ~ 1 ps. Such an ultrafast absorption change can be assigned to the THz-field-induced Stark effect in excitons.

In Cu_2O the $1s$ exciton ground state with a binding energy of 150 meV is split by 12 meV into a degenerate ortho and lower energy nondegenerate para state. While

Fig. 14.16 a Schematics of a narrowband THz pump and optical-probe experiment.

b Waveform of the THz radiation at 1.86 THz and **c** its power spectrum. The THz field amplitude is ~ 5 kV/cm.

d Modulated optical transmission spectrum $1-T(\omega)$ (thick solid line) of HH and LH exciton resonances at 5 K when a GaAs/AlGaAs QW system is driven by strong narrowband THz pulses. The arrows indicate the splitting of the HH exciton line. The thin gray line represents the unperturbed spectrum. Reprinted with permission from Jameson et al. [117]. Copyright 2009, American Institute of Physics



interband recombination of ortho excitons is dipole forbidden, para states are optically dark because of their spin of 1. Hence they have extremely long lifetimes on the microsecond timescale. However, spin conservation prohibits direct observation by optical means. THz pulses are able to couple directly to the $1s-2p$ transition of the para excitons with energy of 129 meV irrespective of interband matrix elements. Using intense mid-infrared pulses at $9.6 \mu\text{m}$ wavelength generated by OR of shaped laser pulses Leinß et al. have observed coherent population transfer an internal Rabi flopping caused by monitoring the transmitted field of the pump pulses in the time domain [119].

14.6 Nonlinear Vibrational Spectroscopy

Coherent control over vibrational degrees of freedom using laser pulses has been a long standing goal in ultrafast spectroscopy. Molecular or ionic motions in the THz frequency range are a promising target for coherent control since they are in certain systems directly connected to macroscopic properties such as ferroelectricity, magnetism, or conductivity. Large-amplitude THz motion can be excited by optical ultrashort pulse through the impulsive stimulated Raman scattering process and

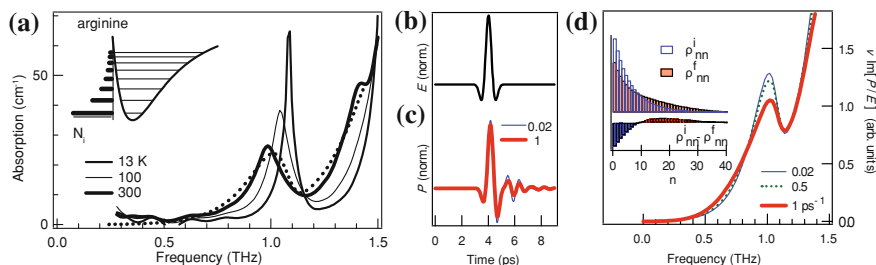


Fig. 14.17 Low-field THz absorption spectra of an L-arginine pellet at 13, 100, and 300 K and simulated spectrum at 300 K as a *dashed line*. The inset shows the anharmonic potential shape for the intermolecular vibration mode. Simulation results: Time profile of the incident electric field **(b)** and **(c)** polarization. **d** Fourier-transformed $\nu P/E$ with different incident electric fields of $\mu E_0 h = 0.02, 0.5,$ and 1 ps^{-1} . The inset shows the initial and final mode populations $\rho_{nn}^{i,f}$ and their change after the maximum field injection. Reprinted with permission from Jewaria et al. [85]. Copyright 2010, American Physical Society

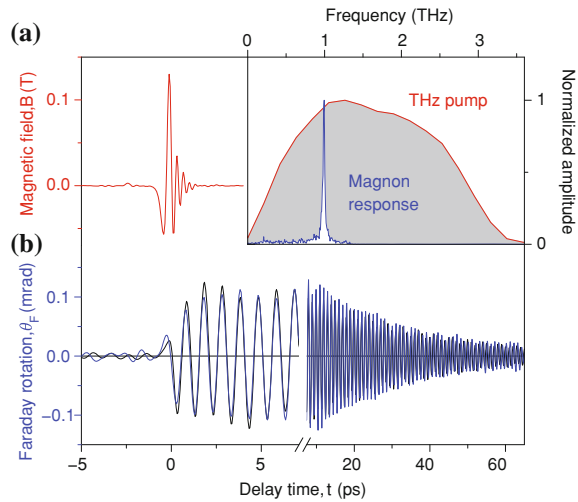
controlled access to the anharmonic regime of the lattice potential along the soft mode has been demonstrated [120]. However, excitation with optical pulses is limited to Raman active modes and the high excitation fluencies necessary in these experiments can lead to damage in opaque samples.

The quantum mechanical analog to the creation of large amplitude motion in an oscillator is *ladder climbing*. This refers to the population of quantum states in a vibrational potential and can be achieved by a strong field applied over a time shorter than the vibrational period of the oscillator. Since most realistic vibrational modes relevant for chemical dynamics are anharmonic, the application of a broadband pulse is more efficient than a strictly monochromatic multi-cycle pulse. Ladder climbing of a phonon mode of the crystalline amino acid excited by a single-cycle THz pulse has been reported recently by Jewariya et al. [121]. In amino acids and other hydrogen-bonded crystalline substances like sugars, the dielectric properties in the THz range are determined by low-lying vibrations which are an admixture of inter- and intramolecular degrees of freedom. These modes can exhibit a large anharmonicity [122] which is visible as a large redshift with increasing temperature in low-field measurements (Fig. 14.17a).

Jewariya et al. have shown through simulations that in THz strong fields a large population change and associated changes in optical densities can be expected already in a simple intensity-dependent transmission experiment.

Nonlinear excitation of vibrational degrees of freedom with impulsive single-cycle pulses may lead to new THz multidimensional spectroscopy methods which have the potential to reveal complex mode coupling in a macromolecular systems. Large THz-induced population changes will be a useful technique to driving collective and functional molecular motion.

Fig. 14.18 **a** Magnetic field of the incident THz pulse as a function of time t . **b** Ultrafast Faraday rotation induced in the NiO sample at room temperature. Harmonic oscillations with a period of 1 ps are due to an antiferromagnetic spin precession. *Blue curve*, experiment; *black line*, simulation Inset: amplitude spectra of the Faraday transient in **b** and the driving THz field in **(a)** From: Reprinted with permission from Kampfrath et al. [123]. Copyright 2011, Nature Publishing Group



14.7 Magnetic Field Effects of THz Pulses

The magnitude of the magnetic field B component associated with an electromagnetic wave in vacuum is related to the electric field E by $|B| = 1/c|E|$. Usually only the electric field is considered, interacting with most materials by electric-dipole coupling while the influence of the magnetic field component is neglected because it is either too weak or too high in frequency to be able to effectively interact with magnetic degrees of freedom of a material. For high field THz pulses this magnetic component becomes considerably large. For example peak electric field strengths of 300 kV/cm are accompanied by a magnetic field component of 0.1 T. This ultrafast magnetic field can be used to impulsively excite magnetic excitations in materials through Zeeman coupling. An example are collective spin precessions, so-called magnons, in antiferromagnets, the most common class of spin ordered materials found in nature. Typically magnons are observed to occur at frequencies in the GHz range up to 1 THz.

THz magnetic field excitation in NiO has recently been demonstrated by Kampfrath et al. [123]. In their experiment a single-cycle THz pulse with a peak magnetic field of 0.13 T was incident on a 45 μm thick NiO thin film. NiO has a magnon at a frequency of 1 THz which is contained fully in the excitation spectrum of the THz pulse (Fig. 14.18a). Since the material has inversion symmetry, the magnon cannot be excited by the magneto-electric dipole interaction. The magnetization change in the material introduced by the THz pulse is probed via the Faraday rotation. Long lived oscillations are observed that correspond to the magnon center frequency of 1 THz. By using a sequence of two THz pulses with variable time delay, the amplitude of the oscillation can be controlled.

A similar experiment demonstrating coherent control of the precession motion of magnetizations in a single crystal YFeO_3 was demonstrated by Yamaguchi et al. [124] using much weaker THz pulses. This material exhibits a quasi-ferromagnetic (0.299 THz) and a quasi-antiferromagnetic (0.527 THz) precession mode which are infrared active and can interact with the electric part of the THz pulse. These magnons were selectively excited by choosing an appropriate interval between two consecutive THz pulses and were observed as free induction decay (FID) signals from the spin system. By observing the circularly polarized FID signals due to ferromagnetic resonance, the energy stored in the spin system, and the conversion back into electromagnetic radiation was also demonstrated.

Both of these experiments show that ultrafast coherent spin control with THz pulses is possible by using the magnetic field component of the THz pulse. There are, however, several technical challenges that must be overcome before further progress can be made. The main problem is the clear separation of the purely magnetic interaction and the effect of the electric field component of the pulses which is orders of magnitude stronger and is able to couple directly to other degrees of freedom of materials such as conduction electrons causing extreme heating. In the work of Kampfrath et al. these problems were avoided by using the insulating antiferromagnetic NiO. On the other hand, the interaction of itinerant electrons in magnetic and superconducting systems with coherent excitations and manipulation via the magnetic field might be even more fascinating to study.

14.8 THz Excitation of Strongly Correlated Materials

Strongly correlated materials are a broad class of materials that show remarkable electronic and magnetic properties, such as metal-insulator transitions, colossal magneto resistance or superconductivity. The common feature that defines these materials is that the electron–electron interaction is sizeable compared to the single particle bandwidth, and each single electron has a complex influence on its neighbors. This is one of the frontiers of modern condensed matter physics research and most phenomena emerging in strongly interacting electron gases are too complex to be described with predictive accuracy.

Transition metal oxides are a prime example of this class which may be subdivided further according to their behavior, e.g., high-temperature superconductors, Mott insulators, spin-Peierls materials, etc. The single most intensively studied effect is probably high-temperature superconductivity in doped cuprates such as $\text{La}_{2-x}\text{Sr}_x\text{CuO}_4$ (LSCO). In all of these materials, the electron correlation and the related phase transitions are strongly related to the atomic structure of the materials. Coupling THz light pulses directly to vibrational degrees of freedom therefore opens an avenue of control over the exotic properties of these materials [8].

In this section, we will discuss briefly a THz-pump/THz-probe experiment where a superconducting phase is induced in erbium-doped LSCO which is not supercon-

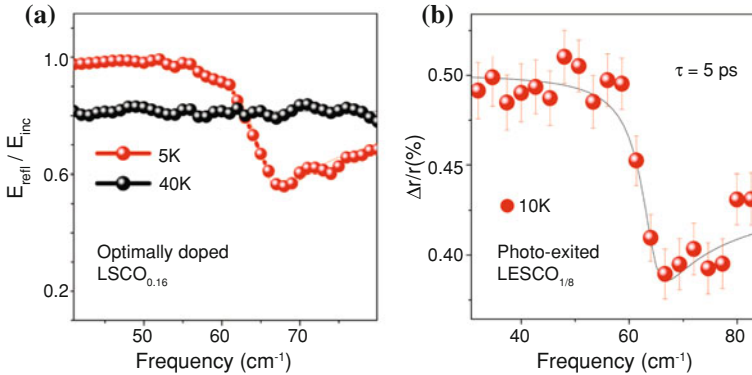


Fig. 14.19 **a** Static *c*-axis electric field reflectance ($r = E_{\text{refl}}/E_{\text{inc}}$) of $\text{LSCO}_{0.16}$, measured at a 45° angle of incidence above (*black dots*) and below (*red dots*) $T_c = 38$ K. Here field reflectances $r = E_{\text{refl}}/E_{\text{inc}}$ are measured as **b** Transient *c*-axis reflectance of $\text{LESCO}_{1/8}$, normalized to the static reflectance. Measurements are taken at 10 K, after excitation with IR pulses at $16 \mu\text{m}$ wavelength. The appearance of a plasma edge at 60cm^{-1} demonstrates that the photo-induced state is superconducting [125]

ducting [125]. For a more detailed discussion of the interaction of strong THz fields with correlated electron systems, the reader is referred to (Chap. 23) of this book.

In some high temperature cuprate superconductors there is a competition between a “stripe-ordered” and a superconducting phase. The stripe-ordered phase is one in which electrons and spins form one-dimensional ordered superlattice, stabilized by a structural distortion of the CuO plane. This form of stripe order is in competition with superconductivity and lowers the transition temperature T_c .

The bulk superconducting phase is identified uniquely in THz spectroscopy by a Josephson plasma resonance (JPR), observed in the *c*-axis THz optical properties and is related to the tunneling between the capacitively coupled superconducting CuO planes [126–128]. This effect is shown in Fig. 14.19a for optimally doped $\text{La}_{1.84}\text{Sr}_{0.16}\text{CuO}_4$. A plasma edge in the reflectance appears near 60cm^{-1} when the temperature is reduced below $T_c = 38$ K.

This feature—characteristic for the superconducting state—is not observed at any temperature in the stripe-ordered compound, non-superconducting $\text{La}_{1.675}\text{Eu}_{0.2}\text{Sr}_{0.125}\text{CuO}_4$, (LESCO), and the *c*-axis conductivity looks similar to the black curve shown in Fig. 14.19a.

If the non-superconducting LESCO is perturbed dynamically by THz light with a frequency of 16 THz—resonant to a phonon frequency coupled to the structural distortion—a change in reflectivity can be detected that resembles the familiar Josephson plasma resonance in optimally doped LSCO (Fig. 14.19b). The measured change in the absolute THz field reflectance is of less than 1 %, the discrepancy being mostly due to the vastly different penetration depth of the pump and probe pulses. The prompt appearance of finite superconducting density, overshooting before relaxing into a plateau at 5 ps time delay, reflects the transition dynamics between striped state

and three-dimensional superconductor. This is a surprisingly short timescale, which supports a picture in which information about the superconducting state is already present in the system before excitation. This experiment clearly illustrates the power of direct manipulation of structural and other low energy degrees of freedom in correlated materials.

The fascinating subject of direct control of the Josephson plasma resonance in a high T_c superconductor by single-cycle THz fields will be discussed in Chap. 23.

14.9 Conclusion and Outlook

Today table-top generation of ultrashort THz pulses with energies up to several micro-Joules and field levels of the order of 1 MV/cm at 1 THz frequency is possible in a routine and reliable manner, paving the way for nonlinear THz spectroscopy. OR and difference frequency generation of femtosecond laser pulses are versatile techniques for single cycle as well as tunable THz pulse generation. Using tilted-pulse-front pumping for rectification of femtosecond pulses in LN, extremely high THz pulse energies (on the 10 μ J scale) and pump-to-THz conversion efficiencies have been demonstrated. Plasma-based sources on the other hand can provide extremely broadband single-cycle pulses that can be used in for probing dynamics in a spectra range covering the entire THz and mid-infrared range.

Single-cycle THz pulses with high field strengths are an ideal tool to directly study the interaction of strong electric fields with matter at ultrafast timescales. The high electric fields can cause dramatic effects in semiconductors and can be used to study highly nonlinear off-equilibrium carrier dynamics. For vibrational spectroscopy nonlinear and two-dimensional THz spectroscopy offers the unique capability to explore the anharmonicity and mutual coupling of low frequency vibrations in solids and large molecules. Using the magnetic field of strong THz pulses to control spin or the tunable THz pulses resonant to vibrations to cause structural transitions demonstrates the powerful possibilities of nonlinear THz methods in the field of correlated electron systems.

The area of nonlinear THz spectroscopy is still at an early stage, but the prospects for spectroscopy of and control over collective degrees of freedom such as motions of dipoles and ions as well as electronic correlations are becoming increasingly clear.

Acknowledgments The author would like to acknowledge helpful discussion with János Hebling, Jozsef Fülöp, Mark D. Thomson and Andrea Cavalleri. Jörg Harms provided technical assistance with preparing the manuscript. Funding was provided by the Max Planck society.

References

1. P.U. Jepsen, D.G. Cooke, M. Koch, *Laser Photonics Rev.* **5**, 124 (2011)
2. C. Fattinger, D. Grischkowsky, *Appl. Phys. Lett.* **54**, 490 (1989)
3. R. Huber et al., *Nature* **414**, 286 (2001)

4. Y. Ikebe et al., Phys. Rev. B **79**, 174525 (2009)
5. V.K. Thorsmølle et al., Phys. Rev. B **66**, 012519 (2002)
6. C.A. Schmuttenmaer, Chem. Rev. **104**, 1759 (2004)
7. L. Dhar, J.A. Rogers, K.A. Nelson, Chem. Rev. **94**, 157 (1997)
8. M. Rini et al., Nature **449**, 72 (2007)
9. R.J. Mattauch et al., T.W. Crowe, Int. J. Infrared Millim. Waves **8**, 1235 (1987)
10. C. Sirtori et al., Phys. Status Solidi A **203**, 3533 (2006)
11. R. Kohler et al., Nature **417**, 156 (2002)
12. G. Kozlov, A. Volkov, in *Millimeter and Submillimeter Wave Spectroscopy of Solids*, ed. by G. Grüner (Springer, Berlin Heidelberg, 1998)
13. E. Bründermann, H.P. Röser, M.F. Kimmitt, Laser und Optoelektronik **25**, 48 (1993)
14. A.A. Andronov, Y.N. Nozdrin, V.N. Shastin, Infrared Phys. **27**, 31 (1987)
15. A. Mayer, F. Keilmann, Phys. Rev. B **22**, 6954 (1986)
16. S. Ganichev, W. Prettl, in *Intense Terahertz Excitation of Semiconductors* (Oxford University Press, Oxford, 2005)
17. L.R. Elias, J. Hu, G. Ramian, Nucl. Instrum. Methods Phys. Res. Sect. A-Accel. Spectrom. Dect. Assoc. Equip. **237**, 203 (1985)
18. L.R. Elias, IEEE J. Quantum Electron. **23**, 1470 (1987)
19. A.F.G. van der Meer, Nucl. Instrum. Methods Phys. Res. Sect. A-Accel. Spectrom. Dect. Assoc. Equip. **528**, 8 (2004)
20. P. Michel et al., in *Proceedings of the 26th International FEL Conference*, ed. by R.E. Bakker et al. (Comitato Conferenze Elettra, Trieste, 2004), p. 8
21. P.W. van Amersfoort et al., Nucl. Instrum. Methods Phys. Res. Sect. A-Accel. Spectrom. Dect. Assoc. Equip. **318**, 42 (1992)
22. G.M.H. Knippels et al., Phys. Rev. Lett. **75**, 1755 (1995)
23. T. Dekorsy, Phys. Rev. Lett. **90**, 055508 (2003)
24. G.L. Carr, Nature **420**, 153 (2002)
25. S. Casalbuoni et al., Phys. Rev. Special Top. Accel. Beams **12**, 030705 (2009)
26. J.R. Morris, Y.R. Shen, Opt. Commun. **3**, 81 (1971)
27. D.H. Auston, P.R. Smith, Appl. Phys. Lett. **43**, 631 (1983)
28. D.H. Auston et al., Phys. Rev. Lett. **53**, 1555 (1984)
29. M.C. Hoffmann, J.A. Fülöp, J. Phys. D **44**, 083001 (2011)
30. D. You et al., Opt. Lett. **18**, 290 (1993)
31. P.K. Benicewicz, J.P. Roberts, A.J. Taylor, J. Opt. Soc. Am. B **11**, 2533 (1994)
32. R.R. Jones, D. You, P.H. Bucksbaum, Phys. Rev. Lett. **70**, 1236 (1993)
33. A. Dreyhaupt et al., Appl. Phys. Lett. **86**, 121114 (2005)
34. M. Beck et al., Opt. Express **18**, 9251 (2010)
35. A. Dreyhaupt et al., Opt. Lett. **31**, 1546 (2006)
36. T. Löffler et al., Opt. Express **13**, 5353 (2005)
37. M.D. Thomson et al., Laser Photon. Rev. **1**, 349 (2007)
38. N. Karpowicz, X. Lu, X.-C. Zhang, J. Mod. Opt. **56**, 1137 (2009)
39. H. Hamster et al., Phys. Rev. Lett. **71**, 2725 (1993)
40. D.J. Cook, R.M. Hochstrasser, Opt. Lett. **25**, 1210 (2000)
41. K.Y. Kim et al., Nat. Photonics **2**, 605 (2008)
42. M.D. Thomson, V. Blank, H.G. Roskos, Opt. Express **18**, 23173 (2010)
43. J.M. Dai, N. Karpowicz, X.C. Zhang, Phys. Rev. Lett. **103**, 023001 (2009)
44. G. Rodriguez, G.L. Dakovski, Opt. Express **18**, 15130 (2010)
45. J. Dai, X. Xie, X.-C. Zhang, Phys. Rev. Lett. **97**, 103903 (2006)
46. N. Karpowicz et al., Appl. Phys. Lett. **92**, 011131 (2008)
47. I.C. Ho, X. Guo, X.C. Zhang, Opt. Express **18**, 2872 (2010)
48. M. Kress et al., Opt. Lett. **29**, 1120 (2004)
49. M. Kress et al., Acta Phys. Pol. A **113**, 769 (2008)
50. K.-Y. Kim et al., Opt. Express **15**, 4577 (2007)
51. N. Karpowicz, X.C. Zhang, Phys. Rev. Lett. **102**, 093001 (2009)

52. I. Babushkin et al., Phys. Rev. Lett. **105**, 053903 (2010)
53. M. Bass et al., Phys. Rev. Lett. **9**, 446 (1962)
54. K.H. Yang, P.L. Richards, Y.R. Shen, Appl. Phys. Lett. **19**, 320 (1971)
55. B.B. Hu, X.-C. Zhang, D.H. Auston, Appl. Phys. Lett. **56**, 506 (1990)
56. K.L. Vodopyanov, Opt. Express **14**, 2263 (2006)
57. R.L. Sutherland, *Handbook of Nonlinear Optics* (Marcel Dekker, Inc., New York, 2003)
58. K. Wynne, J.J. Carey, Opt. Commun. **256**, 400 (2005)
59. J. Hebling et al., J. Opt. Soc. Am. B **25**, B6 (2008)
60. F. Blanchard et al., Opt. Express **15**, 13212 (2007)
61. M.C. Hoffmann et al., Opt. Express **15**, 11706 (2007)
62. G.B. Abdullaev et al., JEPT Lett. **16**, 90 (1972)
63. R. Huber et al., Appl. Phys. Lett. **76**, 3191 (2000)
64. A. Bonvalet et al., Appl. Phys. Lett. **67**, 2907 (1995)
65. K. Reimann et al., Opt. Lett. **28**, 471 (2003)
66. A.S. Barker, R. Loudon, Rev. Mod. Phys. **44**, 18 (1972)
67. Y.-S. Lee et al., Appl. Phys. Lett. **76**, 2505 (2000)
68. J. Hebling et al., Opt. Express **10**, 1161 (2002)
69. T. Löffler et al., Semicond. Sci. Technol. **20**, S134 (2005)
70. A.G. Stepanov et al., Opt. Express **13**, 5762 (2005)
71. M.C. Hoffmann, D. Turchinovich, Appl. Phys. Lett. **96**, 151110 (2010)
72. K.-L. Yeh et al., Opt. Commun. **281**, 3567 (2008)
73. K.L. Yeh et al., Appl. Phys. Lett. **90**, 171121 (2007)
74. A.G. Stepanov et al., Opt. Lett. **33**, 2497 (2008)
75. N.B. Singh et al., Prog. Cryst. Growth Charact. Mater. **37**, 47 (1998)
76. I.M. Bayanov et al., Opt. Commun. **113**, 99 (1994)
77. A. Sell et al., A. Leitenstorfer, R. Huber, Opt. Lett. **33**, 2767 (2008)
78. C. Manzoni et al., Opt. Lett. **35**, 757 (2010)
79. F. Junginger et al., Opt. Lett. **35**, 2645 (2010)
80. J.R. Danielson et al., J. Appl. Phys. **104**, 033111 (2008)
81. H. Wen, M. Wiczor, A.M. Lindenberg, Phys. Rev. B **78**, 125203 (2008)
82. S. Feng, H.G. Winful, R.W. Hellwarth, Opt. Lett. **23**, 385 (1998)
83. P. Kužel et al., Opt. Express **18**, 15338 (2010)
84. P.C.M. Planken et al., J. Opt. Soc. Am. B **18**, 313 (2001)
85. M. Jewariya, M. Nagai, K. Tanaka, Phys. Rev. Lett. **105**, 203003 (2010)
86. P. Gaal et al., Phys. Rev. Lett. **96**, 187402 (2006)
87. M.C. Hoffmann et al., J. Opt. Soc. Am. B-Opt. Phys. **26**, A29 (2009)
88. K. Iwaszczuk et al., Opt. Express **17**, 21969 (2009)
89. A. Dienst et al., TBD (2011)
90. P. Hamm, M. Lim, R.M. Hochstrasser, J. Phys. Chem. B **102**, 6123 (1998)
91. S. Mukamel, *Principles of Nonlinear Optical Spectroscopy* (Oxford University Press, New York, 1995)
92. W. Kuehn et al., J. Chem. Phys. **130**, 164503 (2009)
93. F. Keilmann, Infrared Phys. **31**, 373 (1991)
94. W.L. Faust, C.H. Henry, Phys. Rev. Lett. **17**, 1265 (1966)
95. G.D. Boyd, M.A. Pollack, Phys. Rev. B **7**, 5345 (1973)
96. T. Hornung, K.L. Yeh, K.A. Nelson, in *15th International Conference on Ultrafast Phenomena*, (Optical Society of America, 2006), p. MG8
97. M.C. Hoffmann et al., Appl. Phys. Lett. **95**, 231105 (2009)
98. J.N. Heyman et al., Appl. Phys. Lett. **68**, 3019 (1996)
99. Y. Yacoby, Phys. Rev. **169**, 610 (1968)
100. S.D. Ganichev, I.N. Yassievich, W. Prettl, J. Phys. Condes. Matter **14**, R1263 (2002)
101. K.B. Nordstrom et al., physica status solidi (b) **204**, 52 (1997)
102. A.H. Chin, J.M. Bakker, J. Kono, Phys. Rev. Lett. **85**, 3293 (2000)
103. K. Shinokita et al., Appl. Phys. Lett. **97**, 211902 (2010)

104. M.C. Hoffmann et al., *Appl. Phys. Lett.* **97**, 231108 (2010)
105. M. Dressel, G. Grüner, *Electrodynamics of Solids* (Cambridge University Press, Cambridge, 2002)
106. L. Razzari et al., *Phys. Rev. B* **79**, 193204 (2009)
107. J. Hebling et al., *Phys. Rev. B* **81**, 035201 (2010)
108. F.H. Su et al., *Opt. Express* **17**, 9620 (2009)
109. S.D. Ganichev, J. Diener, W. Prettl, *Appl. Phys. Lett.* **64**, 1977 (1994)
110. M.C. Hoffmann et al., *Phys. Rev. B* **79**, 161201(R) (2009)
111. W. Kuehn et al., *Phys. Rev. Lett.* **104**, 146602 (2010)
112. P. Gaal et al., *Nature* **450**, 1210 (2007)
113. S.G. Carter et al., *Science* **310**, 651 (2005)
114. B.E. Cole et al., *Nature* **410**, 60 (2001)
115. J.T. Steiner, M. Kira, S.W. Koch, *Phys. Rev. B* **77**, 165308 (2008)
116. J.R. Danielson et al., *Phys. Rev. Lett.* **99**, 237401 (2007)
117. A.D. Jameson, *Appl. Phys. Lett.* **95**, 3 (2009)
118. T. Ogawa, S. Watanabe, N. Minami, and R. Shimano, *Appl. Phys. Lett.* **97**, 041111 (2010).
119. S. Leinß et al., *Phys. Rev. Lett.* **101**, 246401 (2008)
120. C.J. Brennan, K.A. Nelson, *J. Chem. Phys.* **107**, 9691 (1997)
121. M. Jewariya, M. Nagai, K. Tanaka, *Phys. Rev. Lett.* (accepted) (2010)
122. M. Walther, B.M. Fischer, P.U. Jepsen, *Chem. Phys.* **288**, 261 (2003)
123. T. Kampfrath et al., *Nat. Photonics* **5**, 31 (2010)
124. K. Yamaguchi, M. Nakajima, T. Suemoto, *Phys. Rev. Lett.* **105**, 237201 (2010)
125. D. Fausti et al., *Science* **331**, 189 (2011)
126. V.Z. Kresin, H. Morawitz, *Phys. Rev. B* **37**, 7854 (1988)
127. H.A. Fertig, S. Dassarma, *Phys. Rev. Lett.* **65**, 1482 (1990)
128. K. Tamasaku, Y. Nakamura, S. Uchida, *Phys. Rev. Lett.* **69**, 1455 (1992)

Chapter 15

Terahertz Near-Field Imaging

Paul C. M. Planken, Aurèle J. L. Adam and DaiSik Kim

Abstract The terahertz (THz) frequency range has proven to be a very interesting frequency range for imaging applications. The smallest spatial features that can theoretically be resolved is limited by diffraction to values of about half of a wavelength, which corresponds to $150\ \mu\text{m}$ for a frequency of 1 THz. To overcome this diffraction limit, THz near-field techniques have been developed. Some of these techniques are unique for the THz frequency range and others are derived from similar techniques used in, for example, the visible region of the electromagnetic spectrum. An interesting feature of many of these near-field techniques is that they measure the electric field rather than the intensity. This makes it also possible to study the near-electromagnetic field itself with a resolving power, as defined as the ratio of the spatial resolution to the wavelength, and bandwidth which are practically unobtainable in the visible region of the electromagnetic spectrum. This chapter describes a number of different techniques to overcome the diffraction limit in the THz frequency range and also the results that have been obtained with them.

P. C. M. Planken (✉) · A. J. L. Adam
Faculty of Applied Sciences, University of Technology Delft,
Lorentzweg 1, 2628 CJ Delft,
The Netherlands
e-mail: P.C.M.Planken@tudelft.nl

A. J. L. Adam
e-mail: A.J.L.Adam@tudelft.nl

D. Kim
Department of Physics and Astronomy,
Center for Subwavelength Optics,
Seoul National University, Seoul, Korea
e-mail: dsk@phya.snu.ac.kr

15.1 Introduction: The Near-Field, the Far-Field, and the Diffraction Limit

15.1.1 The Diffraction Limit and the Far Field

In a conventional, far-field, imaging setup, the spatial resolution Δl is determined by the Rayleigh criterion as

$$\Delta l = 0.61 \frac{\lambda_0}{n \sin(\theta)}, \quad (15.1)$$

with λ_0 the wavelength of the light in vacuum, n the refractive index of the medium, θ half of the opening angle of the focused light beam, and $n \sin(\theta)$ the numerical aperture (NA) of the focusing element. For a typical terahertz (THz) imaging setup, with $f = 0.1$ m, $D = 0.05$ m, $\lambda = 300 \times 10^{-6}$ m, this gives $\Delta l \simeq 730$ μm . Tighter focusing will generally lead to smaller foci and thus an improved spatial resolution, but it is clear that the best obtainable spatial resolution in a THz far-field setup is totally inadequate for microscopy on a scale of 100 μm or less. A more graphic view of this is illustrated in Fig. 15.1. This figure shows calculations of the THz electric field around a perfectly conducting metal cylinder with a diameter significantly smaller than the wavelength and one with a diameter on the order of the wavelength. The field, which is incident from below, has a polarization which is perpendicular to the axis of the cylinder. For the large cylinder, a shadow effect is clearly visible even for distances of more than a wavelength behind and around the cylinder. This contrasts with the calculations for the small cylinder where the wavefront in the immediate vicinity of the cylinder is perturbed, but appears to have repaired itself at a distance from the cylinder larger than the cylinder diameter. Far away from the small cylinder, therefore, its presence, let alone its shape, can no longer easily be inferred from the light field.

15.1.2 The Near Field

Far-field imaging and spectroscopy on objects smaller than about half of a wavelength ($\text{NA} = 1$) are therefore very difficult, especially at THz frequencies where light detection is not trivial. Figure 15.1 does show, however, that even a small object of sub-wavelength dimensions is clearly capable of affecting the light field, but only in a volume around the object comparable in size to that of the object itself. In this near-field then, the object is expected to be visible, provided we have a measurement method that allows us to exclusively measure the field in the immediate vicinity of the object. A good part of this chapter is therefore devoted to discussing the different ways in which this can be achieved in the THz frequency range.

The ability to perform imaging and spectroscopy on a sub-wavelength scale has a number of interesting applications in science and technology. These applications

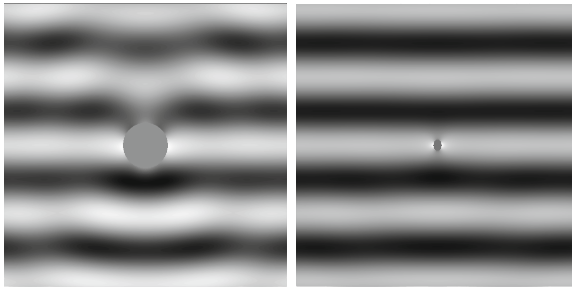


Fig. 15.1 A plane wave with a frequency of 0.2 THz is incident, from *below*, on two perfectly conducting metal cylinders: the *left figure* shows the calculated field distribution around a cylinder with a diameter of a 1,000 μm . The figure on the *right* shows the calculated field distribution around a cylinder with a diameter of 200 μm . *White* indicates positive electric field values, *black* negative. Note that for the small cylinder, the electric near-field immediately around the cylinder is significantly stronger than the incident field. This effect is much less pronounced for the larger cylinder

include the characterization of micro- and nanoscale devices, in particular the spatial distribution of the charge carriers, the characterization of small-volume molecular crystals, and measurements of the phase and magnitude of the electromagnetic field in the immediate neighborhood of subwavelength-sized metal structures such as holes in metal films and metamaterials. Charge carriers can be observed with great contrast because spatially varying carrier densities in real nanoscale transistors, correspond to spatially varying plasma frequencies in the THz range, ensuring a large contrast. Organic and inorganic crystals can be observed because they have unique phonon absorption spectra or phonon-like absorption spectra in the THz frequency range, each THz spectrum constituting a spectral fingerprint of the material. These spectral fingerprints even allow the identification of polymorphs of the same molecule. The electromagnetic field around tiny metal structures, finally, can be studied in extraordinary detail because of the unique property of the technique used for this, THz time-domain spectroscopy, that it measures the *electric field*, rather than the intensity of the light.

15.2 Apertureless Near-Field Microscopy

Apertureless near-field scanning optical microscopy (ANSOM) is based on the idea that the sub-wavelength-sized apex of a tapered metal tip can scatter light and thus act as a tiny source. Bringing the tip close to an object changes the dielectric environment of the tip and thus the amount of light scattered from it, as schematically illustrated in Fig. 15.2a. By measuring the amount of scattered light as the tip is scanned across the object, information on the position-dependent dielectric properties of the object can be obtained with a sub-wavelength spatial resolution. Pioneering experiments

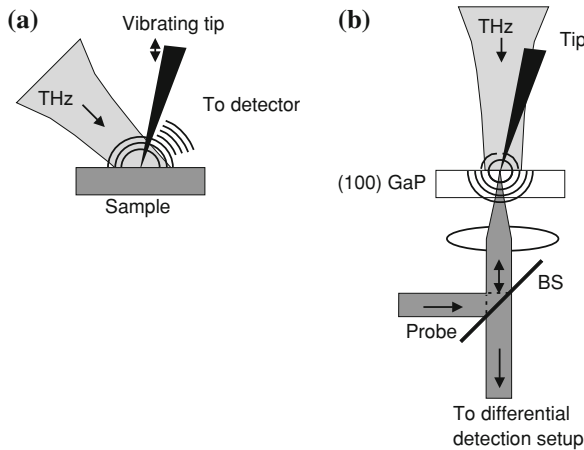
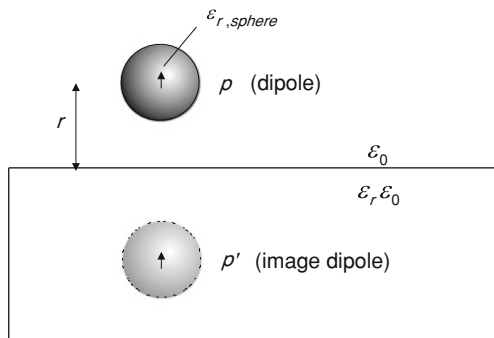


Fig. 15.2 Illustration of THz ANSOM. **a** A THz field incident from above illuminates the tip which is held above a sample/substrate. Light scattered by the tip is collected in the far-field; **b** a metal tip, held above a sample/substrate is illuminated with a THz beam, in this case a single cycle pulse. The tip apex concentrates the electric field to a small sub-wavelength sized region underneath the tip and is detected in the near-field in a GaP electro-optic crystal, using a tightly focused, near-IR probing pulse

using metal tips were performed at visible and infrared wavelengths [1–5]. The first THz ANSOM experiments were performed using THz pulses in a time-domain spectroscopy setup [6, 7]. The near-field of the tip could be measured directly by electro-optic sampling of the field near the tip apex using a focused probe pulse, as illustrated in Fig. 15.2b. An interesting aspect of this approach is the ability to suppress unwanted background signals by a proper choice of the electro-optic crystal orientation. It can be shown that a (100) oriented GaP or ZnTe crystal is capable of measuring the z -component of the electric field, corresponding to the field component perpendicular to the crystal surface, while being blind to the x and y components [6, 8]. A z -component is present only near the tip apex, something which, in the quasi-static approximation, can easily be understood from the boundary conditions of the electric field at a metal surface which only allow the existence of a field component perpendicular to the metal. Note that this is true for a perfect metal only, as for a real metal a small but non-zero tangential component is allowed. This component is very small at THz frequencies and will be ignored for the remainder of this chapter. Near the tip apex therefore, the field lines are distorted and a z -component is created. A spatial resolution of about $5\ \mu\text{m}$ was obtained in this way, limited by the probing beam focal diameter. These experiments differ from visible/infrared ANSOM experiments in that they are capable of measuring the near electric-field rather than the intensity, which, as we will show below, allows one to measure frequency filtering properties of these metal tips. A somewhat different approach, in which a tapered metal tip was used as a probing antenna, predominantly sensitive to the z -component of the near-field, was also shown to be capable of reaching a sub-wavelength spatial resolution [9].

Fig. 15.3 Illustration of a sphere, illuminated with THz light, held above a dielectric half-plane. In the sphere model, the sphere is polarized and subsequently replaced by a point dipole of the corresponding strength. The formation of an image dipole is also taken into account. Note that compared to a perfect metal, the image dipole for a dielectric half-plane is weaker



In another THz ANSOM technique, the field scattered by the tip is measured in the far-field in the specularly reflected direction [10–12]. This means that the signal is superimposed on a large background but, nonetheless, a 150 nm spatial resolution was claimed in these experiments.

In yet another beautiful experiment in which the light source was a THz continuous gas laser, a parabolic mirror was used to measure the backscattered light from a metal tip, and a spatial resolution down to 40 nm was reported [13]. In many ANSOM experiments, the tip is vibrated in a direction perpendicular to the sample surface. When combined with lock-in detection at the vibration frequency, or at a higher harmonic of the vibration frequency, the background signal coming from light scattered off the tip shaft is strongly reduced and the spatial resolution is strongly improved. The reason for this improvement becomes clear when the scattered signal is measured as the tip approaches the sample surface. Such a measured approach curve shows that the near-field signal depends in a highly nonlinear fashion on the tip/sample distance, dramatically increasing just before the tip touches the sample. When we think of the tip as a series of oscillating dipoles, each having an electric near-field that decays with the cube of the distance, it is the dipoles closest to the apex which give the strongest nonlinear variation in the near-electric field versus tip/sample distance [14]. This nonlinear behavior translates into higher harmonics of the modulation signal and by detecting the signal at these harmonics, the signal contribution from regions of the tip other than the apex, are strongly suppressed. Only light scattered near the apex is strongly modulated by the oscillating tip/sample distance and thus more effectively measured than light scattered off the shaft. In ANSOM experiments, the amount of light scattered by the tip increases dramatically when the tip approaches the surface. In a simple, quasi-static, model which treats the tip as a small sphere, Knoll and Keilmann show that this is in part due to the near-field interaction between the tip and the surface [4]. Suppose that we have an incident field ($-$ component) perpendicular to the surface. This field polarizes the sphere, thus creating a dipole moment $p = 4\pi\epsilon_0 R^3 E_0 \frac{\epsilon_{r,sphere} - 1}{\epsilon_{r,sphere} + 2} \equiv \alpha E_0$, with E_0 the amplitude of the incident field, R the radius of the sphere, $\epsilon_{r,sphere}$ the relative permittivity of the sphere material, and α the polarizability of the sphere (Fig. 15.3). This dipole, in

turn, induces an image dipole in the materials underneath. The *total* dipole moment of the system then becomes [4]:

$$p_{\text{tot}} = \frac{\alpha(1 + \beta)}{1 - \frac{\alpha\beta}{16\pi r^3}} E_0 = \alpha_{\text{eff}}^{\perp} E_0, \quad (15.2)$$

with r the distance of the dipole to the surface, $\beta = \frac{\epsilon_r - 1}{\epsilon_r + 1}$, ϵ_r being the relative permittivity of the sample, and $\alpha_{\text{eff}}^{\perp}$ the effective polarizability of the whole sphere/sample system. The scattering cross-section being proportional to $|\alpha_{\text{eff}}^{\perp}|^2$, the equation shows that when the surface is approached and r thus becomes smaller, the amount of scattered light increases rapidly. The model is very simple, but provides excellent physical insight into the scattering process, even though it contains considerably approximations, such as the assumption that the field created by the image dipole at the position of the original dipole is homogenous. However, something that is not explained by the sphere model is the measured characteristic frequency response of the metal tips used in THz ANSOM experiments. It was shown that metal tips can behave rather more like low-pass filters, reducing the bandwidth available in the near-field in THz ANSOM experiments [15–19]. This can be understood from the fact that the metal tip acts more like a wire antenna than like a sphere. The sphere model also tends to underestimate the absolute value of the field strength underneath the metal tip compared to the antenna model as antennas are capable of collecting more light. In the quasi-static approximation, and assuming that the wire is much shorter than the wavelength, the wire antennas can be treated as a series of dipoles having a position-dependent strength (Fig. 15.4a) [14, 20]. This strength follows a triangular distribution as a function of position along the wire, mimicking the triangular current distribution assumed in the wire, as shown in Fig. 15.4b. The antenna has a length d and is held vertically at a distance a above a dielectric half-plane having relative permittivity ϵ_r . It can be shown that the z -component of the electric field at a position (x, y, z) underneath the antenna, inside the dielectric can be written as [14, 20]:

$$E_z \propto \frac{1}{4\pi\epsilon_0(1 + \epsilon_r)} \left(\frac{1}{R_a} + \frac{1}{R_b} - \frac{2}{R} \right), \quad (15.3)$$

with $R^2 = x^2 + y^2 + (z - \frac{a+b}{2})^2$, $R_a^2 = x^2 + y^2 + (z - a)^2$, and $R_b^2 = x^2 + y^2 + (z - b)^2$. Note that R_a , R_b , and R , represent the distance from the point (x, y, z) to the bottom, the top, and the midpoint of the antenna, respectively. Physical insight can be obtained when we look at the field at position $(0, 0, 0)$, underneath the antenna, just inside the dielectric. If we further assume that $a \ll b$, corresponding to a tip/sample distance which is small compared to the tip length, we can approximate the expression by

$$E_z \propto \frac{1}{4\pi\epsilon_0(1 + \epsilon_r)} \frac{1}{a}. \quad (15.4)$$

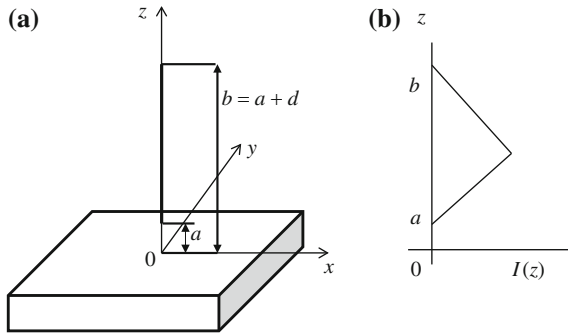


Fig. 15.4 **a**. Principle of THz aperture-less microscopy. A metal tip of length d , held at a distance a from a surface, is illuminated with a THz beam, in this case a single cycle pulse. The tip apex concentrates the electric field to a small sub-wavelength sized region underneath the tip. Light scattered by the tip/sample combination is collected in the far-field. Often, the tip is vibrated to suppress contributions to the signal by light scattered off the tip shaft. **b** Triangular current distribution assumed to be present in the tip

This should be compared to the field of a vertically oriented point dipole, not taking image-dipole effects into account, which falls off as $1/a^3$. The physical/mathematical reason for the $1/a$ decay is not only that in the description of the antenna, we have many dipoles instead of just one but, also, that on the antenna, the strength of these dipoles increases linearly with distance to the apex, as it should for a short linear wire antenna. As the metal is retracted from the surface, therefore, the field of the wire antenna falls off much more slowly than the field of a point dipole, something that has been observed experimentally as shown in Fig. 15.5, where we plot the measured electro-optic signal as a function of tip-substrate distance [14]. Note that the signal plotted in this figure does *not* correspond directly to the actual THz electric field. Rather, it represents the integral of the electric field taken over a distance in the electro-optic crystal of $150\ \mu\text{m}$.

This slow decay is caused by the contribution to the field by the tip shaft, which obviously cannot be ignored. Interestingly, the $1/a$ dependence predicted by the antenna model agrees with the model by van Bladel [21] and Cory et al. [22]. They treat the tip apex as a small cone, and when the cone angle approaches zero, as should be the case for an infinitely thin wire antenna, they obtain the same $1/a$ dependence. The wire antenna model, however, has its shortcomings too. In the above form, it ignores image dipole effects and it assumes that the wire is infinitely thin. It should therefore be considered complementary to the sphere model only. As the tip is vibrated, the source of the field detected synchronously with the vibration, will mostly be located close to the tip apex, since the fields of the dipoles located closest to the apex and thus closest to the surface of the dielectric will be modulated the most. We stress, however, that the frequency contents and the strength of the measured signal are determined by the response of the *entire* antenna to the incident field, not just the apex. One aspect of apertureless near-field microscopy has not been

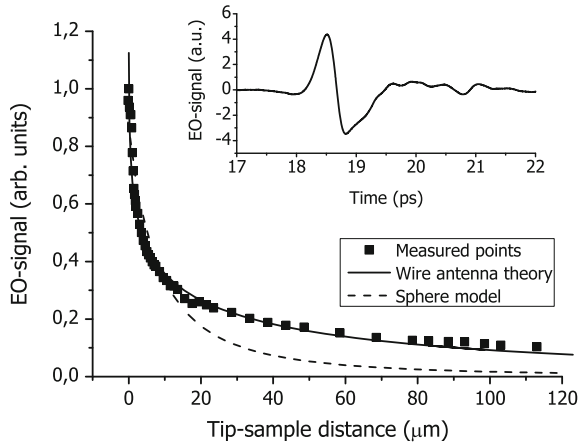


Fig. 15.5 Electro-optic signal measured underneath a tapered copper wire used in a THz ANSOM experiment, as a function of the tip-substrate distance. The substrate is a (100) oriented GaP electro-optic crystal. The *solid curve* represents the electro-optic signal based on the antenna model, the *dashed curve* the electro-optic signal based on the sphere model. Clearly the sphere model fails to reproduce the relatively slow decay observed for larger distances. The *inset* shows the electric near-field measured when the tip-substrate distance is 1 μm . The crystal thickness is 150 μm . Adapted from [14]

mentioned so far. The amplitude of the signal from the tip-sample system is as much determined by the dielectric function of the sample as by the distance between the tip and the sample. This means that care must be taken to avoid confusing variations in tip-sample distance with variations in the dielectric properties of the sample. This can be done, for example, by measuring on topographically flat samples or by measuring the response as a function of THz frequency so that absorption resonances in the sample can clearly be identified.

15.2.1 Variations on the ANSOM Theme

Rather than directly illuminating the tip near the apex, it is also possible to use the guiding properties of the tip to transport the THz radiation to the apex. The radially polarized waves on these wires, also called Sommerfeld waves, can propagate relatively long distances, on the order of several tens of cm's and show a very high potential for applications in THz imaging and micro-spectroscopy. The first clear demonstration of the creation and propagation of these waves at THz frequencies was given by Wang and Mittleman [23]. In subsequent publications various aspects, related to the dispersion, propagation, and confinement near the apex of the wire, were reported [24–27]. A coaxial geometry, made of a wire centered inside a hole in a metal plate surrounded by surface corrugations, was also studied as a way to

excite the Sommerfeld wave [28]. Another method to excite this mode is by exciting the wire with a radially polarized wave created by excitation of a radially symmetric photoconductive emitter [26, 29]. In addition, it was shown how these Sommerfeld waves on tapered wires can be used to do near-field imaging [30, 31]. We note that numerical simulations suggests that propagation of THz light toward the end of a corrugated, tapered metal wire should give rise to strongly localized fields near the apex [32, 33]. This may also give rise to strong THz fields near the tip apex which holds promise for THz nonlinear optics on the micro- and nano-scale, using moderately strong THz sources.

15.3 Aperture Techniques

One way to increase the spatial resolution in THz imaging is to use small, sub-wavelength sized, apertures to reduce either the size of the source, the size of the detector, or both. One of the earliest experiments in this direction at THz frequencies was first performed by Keilmann [34] and later by Hunsche et al. [35] who both used conical tapered, metal waveguides with a small exit aperture to reduce the size of the THz source. A spatial resolution on the order of $\lambda/2$ was obtained by Keilmann and $\lambda/4$ by Hunsche et al. One of the problems of using apertures is that the far-field power transmission of a small aperture scales as a^6 , with a the diameter of the aperture [36–38]. For wavelengths $< \lambda/2$, therefore, the far-field transmission decreases very rapidly indeed. A somewhat different approach was taken by Mitrofanov et al., who decreased the size of THz source by integrating a small aperture in a metallic layer with a photoconductive emitter, to obtain a small source giving a spatial resolution of about $60 \mu\text{m}$ [39]. In subsequent papers Mitrofanov et al. [40] also explored the possibility of integrating small apertures with photoconducting antennas, for the *detection* of THz pulses. With this collection mode detector, of which an example is shown in Fig. 15.6, an impressive spatial resolution of $7 \mu\text{m}$ was eventually obtained [41]. For an electric field measurement, the far-field transmission scales with the aperture size as a^3 . This was confirmed in a THz experiment using apertures as small as $5 \mu\text{m}$, integrated on a photoconducting detector [41]. For apertures this small, the tiny but measurable direct transmission through the 600 nm thick metal layer, in which the aperture is defined, can no longer be neglected. In a separate experiment, the same authors increased the distance between the detector and the hole and found that the field decays inversely proportional to this distance [42, 43].

The property of THz time-domain spectroscopy, namely that it is capable of measuring the electric field rather than the intensity, is clearly an advantage when measuring the transmission properties of small holes in the near-field. It was found, for example, that the near-field measured directly behind an aperture can be viewed as the time-differentiated version of the incident field. This was first observed by Mitrofanov et al. [44, 45] using an aperture in close proximity to a photoconductive antenna, as shown in Fig. 15.7, and later by Adam et al. [46] using near-field electro-optic sampling behind an aperture integrated on an electro-optic detection crystal.

Fig. 15.6 Schematic diagram of the near-field probe used by Mitrofanov et al. [40]. A photoconductive dipole antenna is fabricated on LT GaAs and transferred to a sapphire substrate. The GaAs substrate is thinned and a GaAs cone is formed on top. A 600nm gold film is deposited on the surface, except in the area of the cone, forming the aperture. Adapted from [41]

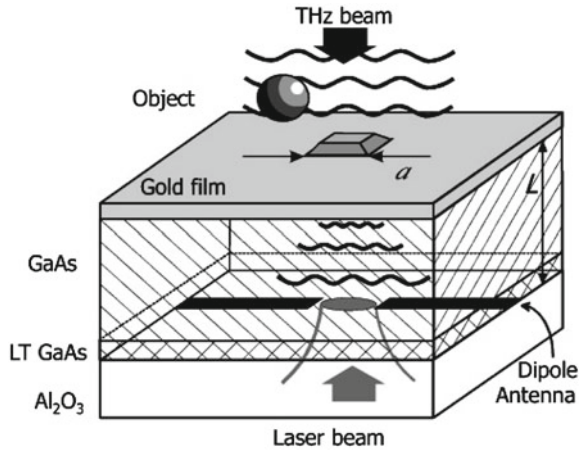
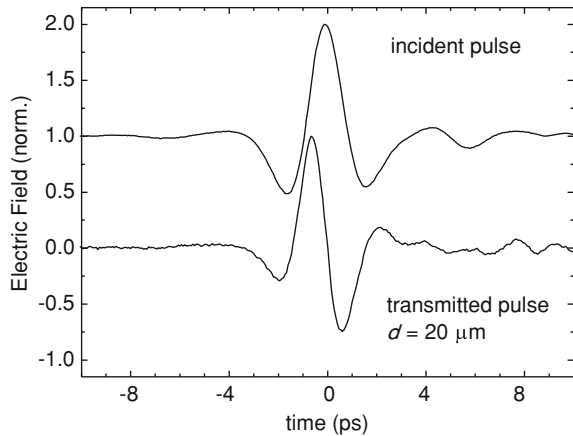


Fig. 15.7 Measured incident THz electric field and THz electric field transmitted by a 20 μm diameter aperture in a gold film, using the device shown in Fig. 15.6. The electric field transmitted by the aperture is clearly the time-derivative of the incident electric field. Adapted from [45]



This differentiation should, perhaps, not come as a surprise as this was also predicted by Bouwkamp, who calculated the near-field behind a circular hole in an infinitely thin, perfectly conducting screen, further assuming that the aperture diameter was much smaller than the wavelength. For example, the expression found by Bouwkamp [37, 38] for the electric near-field component perpendicular to the metal surface, E_z , is:

$$E_z = E_0 \frac{4i}{3} ka \frac{a/\rho}{\sqrt{\rho^2/a^2 - 1}} \cos(\phi), \quad \rho > a \tag{15.5}$$

with a the radius of the hole, ρ the radial coordinate, ϕ the azimuthal angle, E_0 the incident electric field amplitude and k the wavevector of the incident radiation. Note that this equation is valid only in the plane of the metal at $z = 0$, where for $\rho > a$ only E_z is nonzero, as dictated by the boundary condition for the component of the

electric field perpendicular to a perfect metal. Inside the hole at $z = 0$, E_z is zero too. For the in-plane components of the field the reverse is true: at $z = 0$ there can only be a field in the aperture, as the boundary condition for the parallel component dictates that it should be zero at the surface of a perfect metal.

The multiplication of the incident field with the term $ik \propto i\omega$ in the frequency domain, corresponds to differentiation of the THz field in the time-domain [46]. This is reminiscent of the properties of a high-pass filter in electronics and again a reminder that metal structures in general have a frequency-dependent response with associated phase shifts in the transmitted electric field. Other aspects of the model by Bouwkamp have been tested as well, such as the 2D distribution of the field around apertures. Measurements of this will be treated in more detail in the next section. Clearly, the model has its limitations too. For example, Eq. 15.5, predicts infinitely strong electric fields at the edge of the aperture which is physically impossible. However, as we will show in more detail later, the model is capable of explaining many features of THz near-field measurements performed on apertures. For a fixed value of ρ/a for example, Eq. 15.5 shows that the near-field component E_z decreases *linearly* with aperture size a , in sharp contrast with the a^3 dependence for the far-field. For a still small, nonzero, distance to the hole, the dependence of the transmission is neither linear nor cubic. This agrees well with measurements of E_z close to the edge of a circular aperture for three different aperture diameters [46]. To enhance the total transmission through an aperture, the aperture can be surrounded by a bull's eye structure [47–50]. This structure consists of concentric grooves or a grating structure around a small aperture. When the grooves are illuminated, surface waves are created in which funnel additional energy through the aperture, thereby enhancing the total transmission. As the structure is periodic, the enhancement, however, comes at the cost of a narrower bandwidth.

Apertures, of course, do not have to be circular. By using a bow-tie shaped hole in metal film, surrounded by a bull's eye structure, Ishihara et al. managed to obtain a significant, enhanced transmission and a subsequent spatial resolution of $\lambda/17$ [51, 52].

15.3.1 Waveguides, Dynamic Apertures and Quasi Apertures

Parallel plate waveguides [53], may also be used for THz microscopy [54]. By adiabatically tapering the width and the separation of two parallel plates, Zhan et al. [55] were able to confine THz light to an area of $10 \times 18 \mu\text{m}^2$. In the latter example, near the edges of the waveguide the light is not physically confined by the metal as in a regular metal waveguide which is fully closed in all directions perpendicular to the propagation direction, but confinement occurs nonetheless.

It is not always necessary to use a real physical aperture in a metal film to perform aperture microscopy. Chen et al. [56, 57] used an intensity-modulated, focused, optical gating beam on a semiconductor wafer to modulate a very small portion of a THz beam. In a sense, the gating beam induces an inverse aperture, or metallic disc,

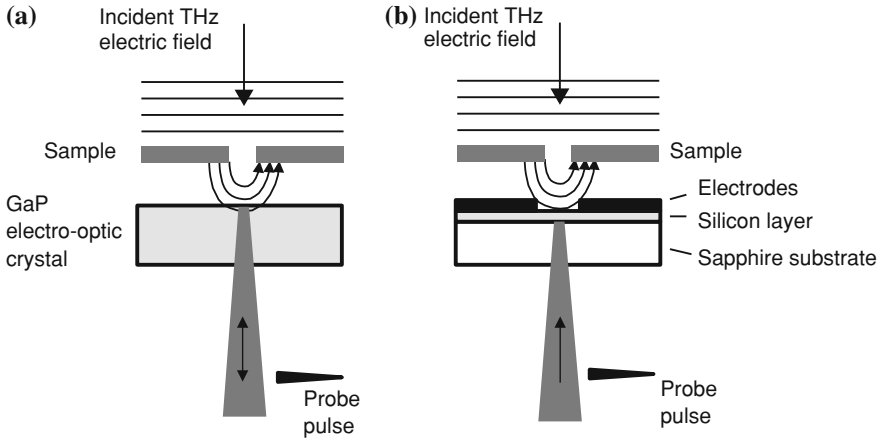


Fig. 15.8 Two different near-field detection methods. **a** A sample, illuminated with a THz pulse, is held close to an electro-optic crystal. The THz electric near-field is sampled with a sub-wavelength spatial resolution using a focused probe pulse; **b** a sample is held in the near-field zone of a small photoconductive antenna detector, gated by a probe pulse. The small dimensions of the antenna structure guarantee a sub-wavelength spatial resolution

to distort a sub-wavelength sized part of the beam. By holding a sample close to the wafer and by detecting only the modulated part of the THz beam, this “dynamic aperture” technique allowed for a $50\ \mu\text{m}$ spatial resolution.

When electro-optic detection is used to measure the THz electric field, a tightly focused probing beam can be used to detect the THz electric near-field in a small volume, as shown in Fig. 15.8a. This method circumvents the THz diffraction limit because the near-IR probing beam has a much smaller wavelength than the THz beam and can thus be focused to much smaller spot sizes [6, 46, 58]. Loosely speaking, the probing beam acts like a detection aperture which limits the sampling area to very small values. It is reminiscent of the electro-optic sampling technique based on the use of specially shaped LiTaO_3 crystal to probe local THz electric fields on striplines and resonators [59, 60].

The advantage of using this technique is that it allows for the separate detection of all three vector components of the electric field by proper choice of the electro-optic crystal orientation. With a (100) crystal orientation, for example, the component of the electric field perpendicular to the (100) surface, E_z can be measured [6, 8]. Using a (111) crystal orientation, the components of the electric field parallel to the (111) crystal, E_x and E_y , can be measured separately as well [61]. In principle, a (110) crystal orientation can be used too to measure the in-plane components, but the advantage of using a (111) crystal is that only a rotation of the probe beam polarization vector over 22.5° is required to shift from measuring E_x to measuring E_y . Thus, a rotation of the detection crystal is not needed, compared to the case in which a (110) crystal is used. This is clearly preferably in experiments in which the detection crystal is very close to, or in contact with, a sample. When the sample is lying on

the surface of the detection crystal, 2D images are obtained when the crystal/sample is raster scanned, while keeping the probe laser and THz beam fixed. When a more powerful THz beam is used, and employing a modified setup in which the THz-induced polarization changes are translated into probe beam intensity changes, an entire 2D image can be obtained in one shot. This was demonstrated by Doi et al. [62] who measured the spatially resolved THz free-induction decay of a small tyrosine crystal in the near-field.

In the same sense that a focused probe beam can be considered a quasi-aperture, a small sub-wavelength sized THz receiving antenna can also be viewed as a small aperture detector (Fig. 15.8b). This is the approach taken by Bitzer et al. [63, 64] in their measurements of the electric near-field of holes and meta-materials. Their antenna is a small photoconducting antenna consisting of H-shaped electrodes with a $10\ \mu\text{m}$ gap, which allows for the measurements of the in-plane electric-field components of the electric near-field. They obtain a spatial resolution of about $20\ \mu\text{m}$ while holding their antenna some $30\ \mu\text{m}$ from their samples, which is more than sufficient to provide spectacular measurements of the time-dependent electric fields near various metal samples, which will be discussed in more detail in the next section. One advantage of their setup is that the detecting chip together with the probe laser can freely be scanned parallel to the sample surface, allowing them to sample the near field over relatively large areas. By tapering the antenna, the spatial resolution can further be improved. This was shown to be an excellent method to further improve the spatial resolution [65–67]. With an electrode spacing of $1.8\ \mu\text{m}$ at the apex of the electrodes, a spatial resolution of better than $5\ \mu\text{m}$ was demonstrated.

Using yet another approach, calculations suggest that using plasmonic dimer antennas, fabricated from doped semiconductors, it may be possible to confine and enhance the THz electric field inside the gap between the two arms of the antenna. By controlling the carrier density, this enhancement and localization can be controlled with possible applications in spectroscopy and imaging [68].

15.4 Near-Field Imaging

As mentioned in the introduction, near-field imaging can be applied to the study of charge carriers, lattice vibrations of organic and inorganic crystals, and also of the THz electromagnetic near-field itself. We will start this section with the results of imaging the near-field of small metal structures, such as slits and holes. The reason for this is that the information gathered on these structures increases our understanding of other techniques that use small metal structures to obtain a sub-wavelength spatial resolution, such as antennas and holes.

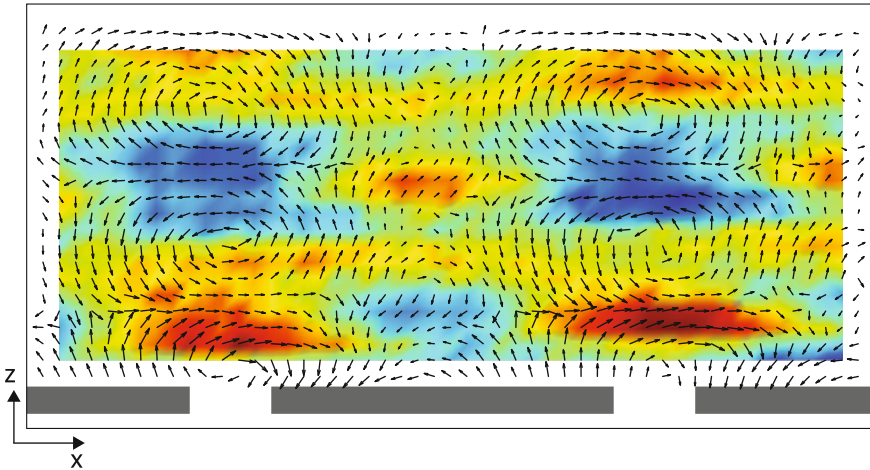


Fig. 15.9 THz electric near-field (vectors) measured behind a metal foil (dark gray) in which multiple, $100\ \mu\text{m}$ wide slits were milled with a period of $500\ \mu\text{m}$. The THz beam is incident from below. The magnetic field component B_y , calculated from the electric field, is shown in color. Red and blue correspond to opposite magnetic field directions. The size of the entire scan is $1,050\ \mu\text{m}$ in the x -direction and $450\ \mu\text{m}$ in the z -direction. Adapted from [72]

15.4.1 Imaging the THz Electric Near-Field

Using the quasi-aperture techniques described in Sect. 15.3, it is possible to measure the electric near-field with a deep sub-wavelength spatial resolution. In near-field electro-optic detection, in principle, all three orthogonal components of the THz electric near-field can be measured, although symmetry often reduces the required number of components to be measured to two. (In fact, something resembling this can also be done in the visible, see for example Lee et al. [69–71]). This was shown in an experiment by Seo et al. [72] and Ahn et al. [73] in which the THz electric near-field was measured behind a sample consisting of $100\ \mu\text{m}$ wide slits cut in a metal foil with a period of $500\ \mu\text{m}$. In this experiment, a broadband single cycle THz pulse with a polarization perpendicular to the slits in the x -direction, is incident from below. A $300\ \mu\text{m}$ thick (100) oriented GaP crystal was used to measure the z -component of the electric near-field, which is the component perpendicular to the metal. A (110) oriented GaP crystal was used to measure the x -component polarized parallel to the metal. Due to the symmetry of the sample, no y -component was present. By combining E_x and E_z , the complete time-dependent THz electric field behind the slits could be obtained. From the measurements, a 2D plot of the electric field vector behind the slits can be constructed at any frequency contained in the bandwidth of the single cycle pulse. An example is shown in Fig. 15.9, in which the electric field vector at a frequency of 1 THz is plotted for a fixed phase, representing a single frame from a movie showing the time evolution of the field during one complete cycle at this frequency. The figure shows vortices and saddle points in the field

behind the slits. The distance in the z -direction between the center of two vortices, is $300\ \mu\text{m}$, corresponding to a frequency of 1 THz. The measurement provides a very nice demonstration of a property of time-dependent electric fields, namely that they must have a nonzero curl according to,

$$\nabla \times \mathbf{E} = -\frac{\partial \mathbf{B}}{\partial t}. \quad (15.6)$$

Using this equation, the electric field measurement shown in Fig. 15.9 can be used to calculate the THz magnetic field component B_y , as shown in the figure in color. With both \mathbf{E} and \mathbf{B} known, other properties of the THz light can also be obtained such as the Poynting vector [72]. Again, this shows the advantage of measuring the THz electric field, rather than the intensity. Incidentally, one interesting aspect of slits is that when the width becomes smaller, the transmission can still be considerable leading to an enormously enhanced field inside the slit [74–76].

Of interest for near-field imaging using apertures, is the electric near-field in the immediate neighborhood of an aperture itself. This can be measured with great accuracy by depositing a metal layer, in which the aperture is defined, directly on top of the electro-optic detection crystal. The aperture is then illuminated with a broadband single cycle THz pulses polarized parallel to the crystal in the x -direction. Figure 15.10a–c shows the components of the electric near field $|E_x|$, $|E_y|$, and $|E_z|$, measured immediately underneath a $150\ \mu\text{m}$ diameter aperture in a 200 nm thick gold layer deposited on the GaP electro-optic detection crystal, at a frequency of 0.2 THz [77]. Again, a (100) crystal was used to detect E_z , whereas a (111) crystal was used to measure E_x and E_y . The figures clearly illustrate that the E_x and E_y components are mostly localized inside the aperture, whereas the z -component of the field is mostly confined to the edges of the aperture. This agrees very well with the predictions made by the model from Bouwkamp [37, 38] and by numerical calculations. The measurements also show that this particular measurement technique measures the field very close to aperture, since for increasing distances to the metal plane, the extent of the field should increase rapidly in the x and y directions. However, E_z is not entirely zero inside the aperture and $E_{x,y}$ are not exactly zero outside the aperture, indicating that the field is not measured exactly in the plane of the aperture but, on average, some $10\ \mu\text{m}$ below it.

As in the case of the slits, the components of the measured field can be combined, in this case E_x and E_y , into a single in-plane electric field vector. This is shown in Fig. 15.10d, where the in-plane field vector at the frequency of 0.2 THz is plotted. In Fig. 15.10e, the field calculated using the model from Bouwkamp is shown, where the length of the calculated field vectors near the edge of the aperture is artificially reduced, since the Bouwkamp model predicts unphysical, infinitely strong fields there. The calculation can thus only be used to compare the *direction* of the field, not the strength. Keeping this in mind, it is clear that the measurements and the calculation are in excellent agreement. Although the incident field is polarized in the x -direction, immediately behind the aperture, all three components of the electric field are present. In fact, the measurements constitute a clear illustration of the boundary conditions

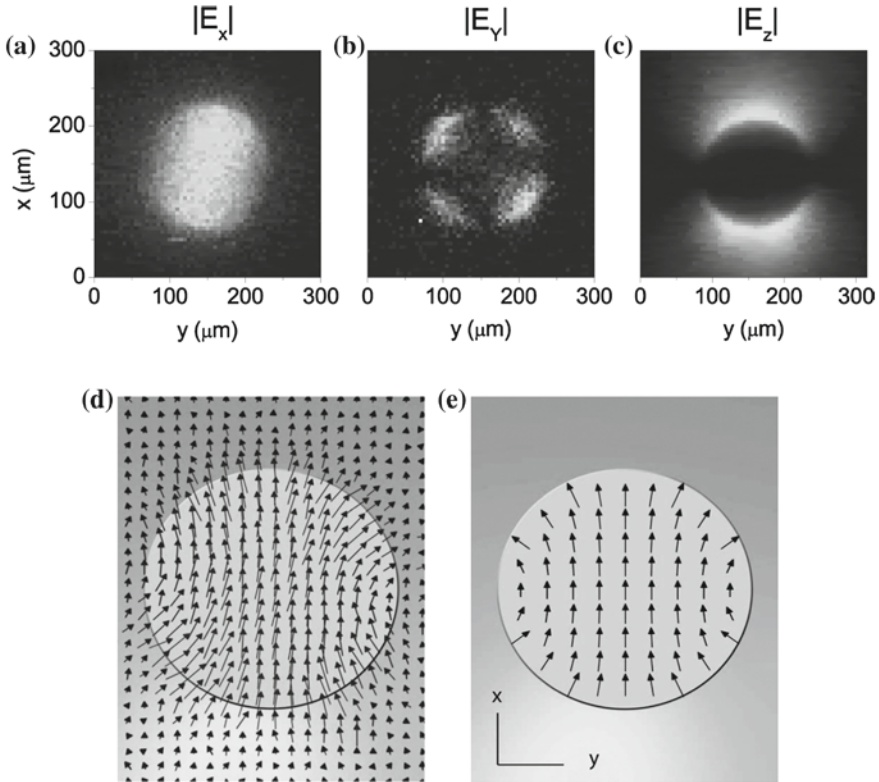
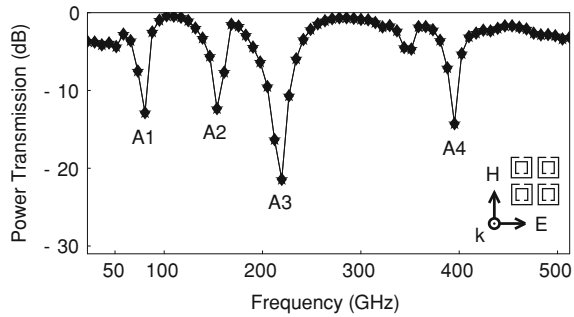


Fig. 15.10 THz electric near-field for a single, isolated, circular aperture ($d = 150 \mu\text{m}$) at 0.2 THz. **a–c** $|E_x|$, $|E_y|$, and $|E_z|$. Scan area = $315 \times 315 \mu\text{m}$; **d** vector field plot illustrating measured transverse components of THz electric near-field; **e** vector field plot based on the model from Bouwkamp. Adapted from [77]

for the electric field at the interface between a perfect metal and a dielectric. These conditions state that at the metal, the component of the field parallel to the metal should be zero. At the metal, only a component perpendicular to the metal can exist. The shape of the aperture forces the creation of a component perpendicular to the metal surface and the metal e.g., thus explaining the creation of both E_y and E_z . The exact shape of the aperture determines the relative size of the three components. For a square aperture, for example, the E_y component is very small and, in fact, quite difficult to measure [77].

A clear advantage of the ability to measure the electric field, rather than the intensity is that it makes it possible to extract more information from the measurements without the need to make further assumptions about the system. For example, the boundary conditions for the component of the electric field perpendicular to the metal surface, E_z , state that this component is discontinuous with an amount proportional to the surface charge density σ . At the metal surface ($z = 0$), we can write for the

Fig. 15.11 Far-field power transmission spectrum of a split-ring resonator array sample. Four dominant resonances (A1–A4) are observed for an incident field polarization direction as indicated in the *inset*. Adapted from [64]



time- and position-dependent surface-charge density,

$$\sigma(x, y, 0, t) = E_z(x, y, 0, t)/\varepsilon, \quad (15.7)$$

where $\varepsilon = \varepsilon_r \varepsilon_0$ is the permittivity of the dielectric, in this case, the GaP crystal. The plot of the z -component of the electric field, therefore, can also be interpreted as a plot of the surface-charge density. In view of the fact that in reality the field is measured a little distance away from the metal, this is approximately true only, explaining why a small but nonzero E_z is also measured inside the aperture. It must be emphasized that the measurements of the near-field of the hole shown here, actually represent measurements of a metallic aperture *on a dielectric substrate*, not an isolated aperture in free space. Some large and some subtle effects occur as a result of the presence of the substrate, such as an increased transmission at low frequencies, and these also depend on the thickness of the metal [78]. One consequence of the use of a thin (thin compared to the wavelength) metal layer, is that there is no real waveguide cut-off apparent in the near-field measurements. The obvious explanation for this is that for a thin metal, one cannot really speak of a waveguide. As discussed earlier in this chapter, below the “cut-off” frequency of a hole in a thin metal layer, the near-field amplitude decreases linearly with frequency. This means that reasonably large near-fields can be measured at frequencies considerably below the cut-off frequency of a conventional waveguide, illustrating the potential of these apertures for near-field imaging [79, 80], and near-field microspectroscopy of very small samples [81].

Electro-optic near-field imaging has, in addition to holes and slits, been applied to the study of spheres [82], hole arrays [77], photonic-crystal fibers [83] and, using a somewhat different geometry, THz surface waves [84].

Bitzer et al. [64] used photoconducting antennas to measure the near-field of THz meta-materials. Meta-materials are materials with optical properties that do not exist in nature. Typically, their properties are determined by performing far-field measurements, but these only provide indirect clues as to the physical processes going on in the immediate neighborhood of these structures. In Fig. 15.11 the far-field power transmission is shown as a function of frequency for a meta-material sample consisting of split-ring resonators (SRR’s), as shown in the inset. The resonators are made of $9\ \mu\text{m}$ thick copper on a $120\ \mu\text{m}$ thick polytetrafluoroethene (PTFE) substrate and

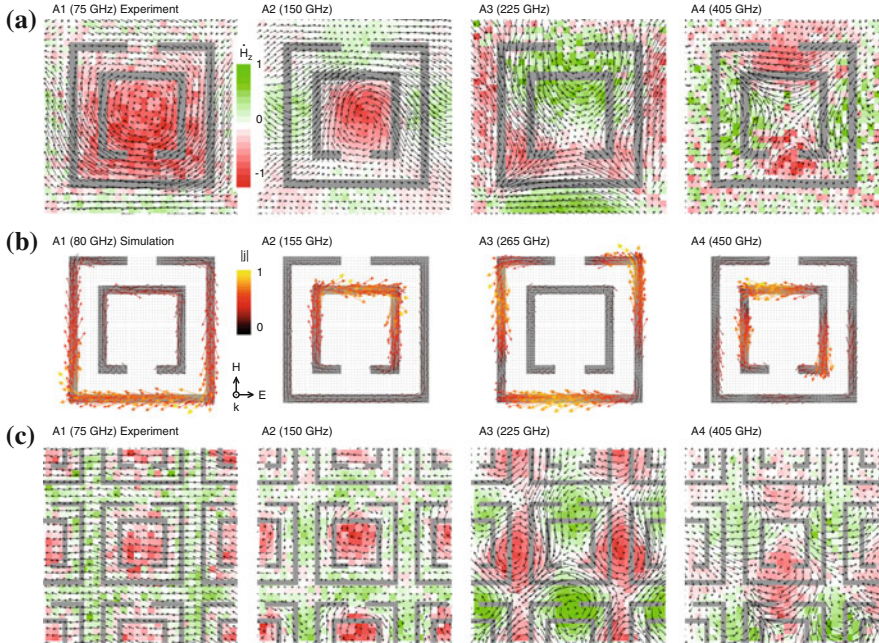


Fig. 15.12 **a** Measured in-plane THz electric near-field (vectors) at a chosen phase at the backside of an isolated split-ring resonator, for the four different resonances A1–A4 shown in Fig. 15.11. The *color code* indicates the time-derivative of the out-of-plane component of the corresponding magnetic field $\partial H_z / \partial t$, derived from the electric field measurements; **b** simulation of the surface current density for a polarization and propagation direction as indicated in the figure; **c** measured in-plane THz electric near-field (vectors) at a chosen phase and $\partial H_z / \partial t$ calculated from the in-plane electric field, at the backside of a split-ring resonator *array*, for the four different resonances A1–A4 shown in Fig. 15.11. Adapted from [64]

their far-field spectrum was measured with a conventional THz time-domain spectroscopy setup. The incident field is polarized in the direction indicated in the figure. Four resonances are clearly observed, corresponding to fundamental excitations of the resonators. Based on these measurements, however, it is not immediately clear what these resonances look like. This can only be observed by performing near-field measurements.

Figure 15.12a shows the 2D spatial distribution of the in-plane, electric near-field vector of a single, isolated, SRR measured with a photoconductive antenna, for four different frequencies corresponding to the four resonances shown in Fig. 15.11 [64]. In the same figure, the magnetic field perpendicular to the plane, calculated from the measured in-plane electric field is also shown. The spatial resolution is on the order of $20 \mu\text{m}$. The figure clearly shows distinct electric and magnetic field patterns corresponding to the different SRR modes, where the electric patterns of the modes at 225 and 405 GHz show evidence of an electric quadrupole pattern. Similar measurements on an array of SRR's are plotted in Fig. 15.12c. They show

destructive (A1 mode) and constructive (A3 mode) interference due to the spatially overlapping fields of individual resonators, whereas the other two modes (A2, A4) remain relatively unperturbed. Figure 15.12b shows simulated surface current densities that correspond to the four resonant modes. The calculations of the currents are fully consistent with the measured magnetic field patterns. These and other [85–89] near-field measurements on metamaterials thus provide essential information on the operation of these important structures.

Wächter et al. [65] have used their tapered photoconductive antenna's to obtain a near-field spatial resolution of about $5\ \mu\text{m}$. Their probe uses a triangular, $1.3\ \mu\text{m}$ thick piece of low-temperature grown GaAs on which the planar tapered wire is fabricated. Near the apex, the gap between the electrodes is $1.8\ \mu\text{m}$. The resolution was tested by imaging a single element of a frequency-selective surface. The outline and dimensions of this element, an asymmetric double-split metallic ring resonator, are shown in Fig. 15.13a. Interestingly, the element is hidden under a layer of black wax, rendering the element invisible. The sample is illuminated by a photoconductive THz emitter located in the near-field of the detector. In Fig. 15.13b, the THz near-field peak image, created by plotting the measured THz peak amplitude spatial distribution, is plotted. The image clearly reveals the hidden ring resonator and the gaps between the metallic lines. Two line scans, one in the x -direction and one in the y direction across the metallic stripes show the excellent spatial resolution of about $5\ \mu\text{m}$ (x -direction) and $7\ \mu\text{m}$ (y -direction) that were obtained in this experiment. In a different experiment, a near-field line scan was made across a metallic thin film deposited on a transparent substrate. In this case, the THz light, generated at the surface of an InAs crystal, was focused onto the sample using parabolic mirrors. In this very different configuration, a spatial resolution of $4.7\ \mu\text{m}$ was reached, confirming the spatial resolution obtained using near-field illumination. Nagel et al. [90] applied the same near-field technique also to the study of THz emission, locally generated and detected, from an exfoliated graphite flake. In this experiment, however, they used a modified version of their near-field probing tip, by coupling the near field to a tapered single wire, connected to a photoconductive antenna. This makes the system sensitive to the axial near-field, allowing the detection of field components polarized perpendicularly to the graphite surface.

The ultimate spatial resolution in THz imaging so far was obtained by Huber et al. [13]. In a THz ANSOM experiment, they studied the THz near-field response of a single semiconductor nanodevice with a spatial resolution of about $40\ \text{nm}$. To obtain this resolution a relatively powerful THz source was used, namely a methanol gas laser with an output power of $5\ \text{mW}$, pumped by a CO_2 laser. In their experiment, a platinum covered atomic force microscope (AFM) tip is illuminated with the THz light at a frequency of $2.54\ \text{THz}$. The THz light backscattered from the tip is measured using a hot-electron bolometer in conjunction with a Michelson interferometer to amplify the signal. The tip is vibrated at a frequency of $35\ \text{kHz}$, and the measured signal is demodulated at the second or third harmonic of that frequency to obtain background-free detection. Figure 15.14a–c shows an AFM image, a THz ANSOM image, and an IR ANSOM image obtained at a wavelength of $11\ \mu\text{m}$, respectively, of a polished cut through a multiple transistor device. The charge carrier concentrations

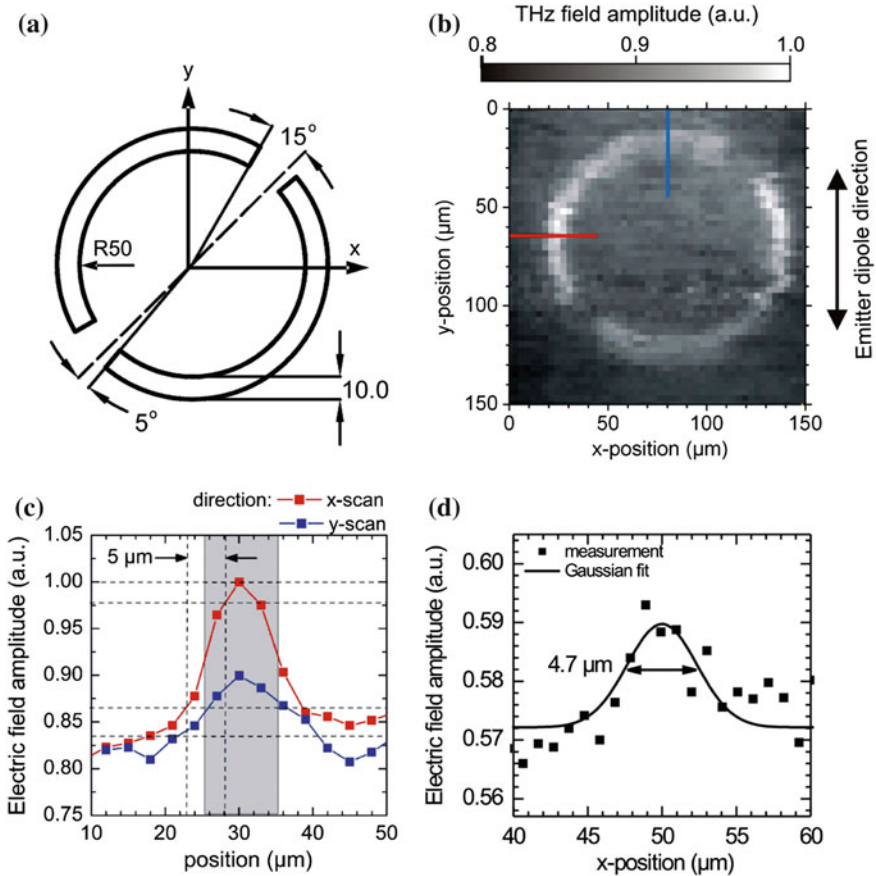
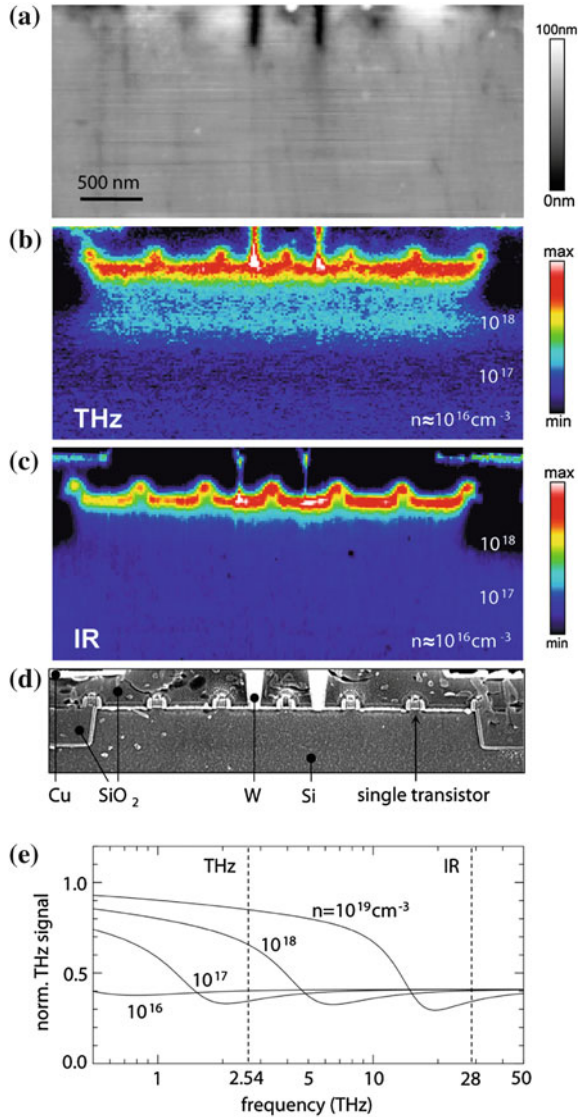


Fig. 15.13 **a** Outline and dimensions of a single element of an asymmetric double-split metallic ring resonator; **b** THz near-field amplitude image of the sample, obtained using a tapered photoconductive antenna. Pixels are $3 \times 3 \mu\text{m}^2$ in size; **c** field amplitude as a function of position along *two lines* across the $10 \mu\text{m}$ wide metallic structure, one in the x -direction the other in the y -direction. Lines are indicated in **b**; **d** measured THz electric field amplitude as a function of position along a line perpendicular to a metallic edge illuminated by THz light incident from the far-field. Adapted from [65]

present in this device at various depths, are also indicated in (b) and (c). This clearly shows that only in the THz image the different carrier concentrations are recognizable. The reason for this is demonstrated in the Fig. 15.14e, which is a calculation of the scattered signal, detected at the second harmonic of the modulation frequency, as a function of THz frequency for carrier concentrations ranging from 10^{16} to 10^{19}cm^{-3} . The graph shows that in the range of carrier concentrations typically present in these devices, THz radiation provides the best possible image contrast because the THz frequency is close to the typical plasma frequencies that correspond to these

Fig. 15.14 **a** AFM image of a polished cut through a multiple transistor device; **b** THz image simultaneously obtained with the AFM image at the second harmonic of the modulation frequency; **c** infrared image ($\lambda = 11 \mu\text{m}$) obtained by measuring the scattered infrared light at the second harmonic of the modulation frequency. The mobile carrier concentrations in **b** and **c** are indicated in the figure, on the *right-hand side*; **d** SEM image of part of the device marked by the *rectangle*; **e** THz signal amplitude detected at the second harmonic of the modulation frequency, as a function of light frequency, for several carrier concentrations. Adapted from [13]



carrier concentrations. In other words, the THz signal varies more strongly with these typical carrier concentrations than the signal at infrared wavelengths, as shown in the figure [91]. In Fig. 15.14d, a SEM image of a small part of the device, outlined by the rectangle in (a) and (b), is shown, providing information on the structure of the device. The results are particularly spectacular when the obtained spatial resolution is expressed as a fraction of the wavelength. A frequency of 2.54 THz corresponds to a wavelength of about $\lambda = 118 \mu\text{m}$. This means that the 40 nm spatial resolution

corresponds to about $\lambda/3,000$, something that is very difficult to achieve in the visible region of the electromagnetic spectrum.

15.5 Conclusions and Outlook

It is clear that THz near-field imaging and spectroscopy constitute an active and promising branch on the “THz tree”. It is only natural to speculate on the directions in which this “branch” will grow. The results by Huber et al. [13] show that the measurement of carriers on the nanoscale forms a very interesting application of THz nanoscopy. In addition, it is clear that THz-TDS is a very powerful technique to probe the time-dependent electric field of light itself on deep subwavelength scales. The information gathered in the THz frequency range will have important implications in the visible region of the electromagnetic spectrum as well since Maxwell’s equations are scale-invariant and only the material properties are somewhat different. In the THz frequency range, however, measurements can be done that are difficult or impossible to do in the visible. For example, it is currently not possible to have a sub-wavelength spatial resolution *and*, simultaneously, a sub-cycle temporal resolution in the visible. Add to that the enormously broad spectrum of many pulsed THz sources and it becomes clear that the capabilities that THz near-field microscopy offers are quite remarkable compared to what is currently possible with visible light. Not all is well, however, since it will be hard to extend the nanoscopy measurements on carriers to, for example, lattice modes of organic molecular crystals, which are fairly weakly absorbing compared to the strong absorbing lattice modes of simpler crystals like GaAs. Still, with current techniques to generate and detect THz light at higher and higher frequencies (see for example Sell et al. [92]) it is probably only a matter of time before these techniques can be applied also to, for example, the molecular fingerprint region of the electromagnetic spectrum. The near-field techniques developed for the THz frequency region are thus seen to have an impact on other regions of the electromagnetic spectrum. Their importance can thus not easily be overestimated. There is a bright future for THz near-field imaging.

References

1. M. Specht, J.D. Pedarnig, W.M. Heckl, T.W. Hänsch, Phys. Rev. Lett. **68**, 476 (1992)
2. F. Zenhausern, Y. Martin, H.K. Wickramasinghe, Science **269**, 1083 (1995)
3. B. Knoll, F. Keilmann, Nature **399**, 134 (1999)
4. B. Knoll, F. Keilmann, Opt. Commun. **182**, 321 (2000)
5. R. Hillenbrand, T. Taubner, F. Keilmann, Nature **418**, 159 (2002)
6. N.C.J. van der Valk, P.C.M. Planken, Appl. Phys. Lett. **81**, 1558 (2002)
7. P.C.M. Planken, C.E.W.M. van Rijmenam, R.N. Schouten, Semicond. Sci. Technol. **20**, s121 (2005)
8. W.A. Kütt, W. Albrecht, H. Kurz, IEEE J. Quantum Electron. **28**, 2434 (1992)

9. R. Adam, L. Chusseau, T. Grosjean, A. Penarier, J.-P. Guillet, D. Charrat, J. Appl. Phys. **106**, 073107 (2009)
10. H.-T. Chen, R. Kersting, G.C. Cho, Appl. Phys. Lett. **83**, 3009 (2003)
11. G.C. Cho, H.-T. Chen, S. Kraatz, N. Karpowicz, R. Kersting, Semicond. Sci. Technol. **20**, S286 (2005)
12. F. Buersegens, R. Kersting, H.-T. Chen, Appl. Phys. Lett. **88**, 112115 (2006)
13. A.J. Huber, F. Keilmann, J. Wittborn, J. Aizpura, R. Hillenbrand, Nano Lett. **8**, 3766 (2008)
14. A.J.L. Adam, N.C.J. van der Valk, P.C.M. Planken, J. Opt. Soc. Am. B **24**, 1080 (2007)
15. K. Wang, D.M. Mittleman, N.C.J. van der Valk, P.C.M. Planken, Appl. Phys. Lett. **85**, 2715 (2004)
16. H.-T. Chen, S. Kraatz, G.C. Cho, R. Kersting, Phys. Rev. Lett. **93**, 267401 (2004)
17. R. Kersting, H.-T. Chen, N. Karpowicz, G.C. Cho, J. Appl. Opt. Pure Appl. Opt. **7**, s184 (2005)
18. Y. Li, S. Popov, A.T. Friberg, S. Sergeev, J. Eur. Opt. Soc. Rap. Public **4**, 09007 (2009)
19. M. Walther, G.S. Chambers, Z. Liu, M.R. Freeman, F.A. Hegmann, J. Opt. Soc. Am. B **22**, 2357 (2005)
20. C.A. Balanis, *Antenna Theory, Analysis and Design*, 2nd edn. (Wiley, New York, 1997)
21. J. van Bladel, Proc. IEEE **71**, 901 (1983)
22. H. Cory, A.C. Boccara, J.C. Rivoal, A. Lahrech, Microwave Opt. Technol. Lett. **18**, 120 (1998)
23. K. Wang, D.M. Mittleman, Nature **432**, 376 (2004)
24. K. Wang, A. Barkan, D.M. Mittleman, Appl. Phys. Lett. **84**, 305 (2004)
25. K. Wang, D.M. Mittleman, Phys. Rev. Lett. **96**, 157401 (2006)
26. V. Astley, R. Mendis, D.M. Mittleman, Appl. Phys. Lett. **95**, 031104 (2009)
27. J.A. Deibel, N. Berndsen, K. Wang, D.M. Mittleman, N.C.J. van der Valk, P.C.M. Planken, Opt. Express **14**, 8772 (2006)
28. A. Agrawal, A. Nahata, Opt. Express **15**, 9022 (2007)
29. J.A. Deibel, K. Wang, M.D. Escarra, D.M. Mittleman, Opt. Express **14**, 279 (2006)
30. M. Awad, M. Nagel, H. Kurz, Appl. Phys. Lett. **94**, 051107 (2009)
31. H. Zhan, V. Astley, M. Hvasta, J.A. Deibel, D.M. Mittleman, Appl. Phys. Lett. **91**, 162110 (2007)
32. S.A. Maier, S.R. Andrews, L. Martín-Moreno, F.J. García-Vidal, Phys. Rev. Lett. **97**, 176805 (2006)
33. H. Liang, S. Ruan, M. Zhang, H. Su, Opt. Commun. **283**, 262 (2010)
34. F. Keilmann, Infrared Phys. Technol. **36**, 217 (1995)
35. S. Hunsche, M. Koch, I. Brener, M.C. Nuss, Opt. Commun. **150**, 22 (1998)
36. H.A. Bethe, Phys. Rev. **66**, 163 (1944)
37. C.J. Bouwkamp, Philips Res. Rep. **5**, 321 (1950)
38. C.J. Bouwkamp, Philips Res. Rep. **5**, 401 (1950)
39. O. Mitrofanov, I. Brener, M.C. Wanke, R.R. Ruel, J.D. Wynn, A.J. Bruce, J. Federici, Appl. Phys. Lett. **77**, 591 (2000)
40. O. Mitrofanov, I. Brener, R. Harel, J.D. Wynn, L.N. Pfeiffer, K.W. West, J. Federici, Appl. Phys. Lett. **77**, 3496 (2000)
41. O. Mitrofanov, M. Lee, J.W.P. Hsu, L.N. Pfeiffer, K.W. West, J.D. Wynn, J.F. Federici, Appl. Phys. Lett. **79**, 907 (2001)
42. O. Mitrofanov, R. Harel, M. Lee, L.N. Pfeiffer, K.W. West, J.D. Wynn, J. Federici, Appl. Phys. Lett. **78**, 252 (2001)
43. O. Mitrofanov, M. Lee, J.W.P. Hsu, R. Harel, J.F. Federici, J.D. Wynn, L.N. Pfeiffer, K.W. West, IEEE J. Sel. Top. Quantum Electron. **7**, 600 (2001)
44. O. Mitrofanov, L.N. Pfeiffer, K.W. West, Appl. Phys. Lett. **81**, 1579 (2002)
45. O. Mitrofanov et al., *Ultrafast Phenomena XIII, Proceedings, Springer series in Chemical Physics*, 2003, p. 286
46. A.J.L. Adam, J.M. Brok, M.A. Seo, K.J. Ahn, D.S. Kim, J.H. Kang, Q.H. Park, M. Nagel, P.C.M. Planken, Opt. Express **16**, 7407 (2008)
47. A. Agrawal, H. Cao, A. Nahata, Opt. Express **13**, 3535 (2005)
48. H. Cao, A. Agrawal, A. Nahata, Opt. Express **13**, 763 (2005)

49. K. Ishihara, G. Hatakoshi, T. Ikari, H. Minamide, H. Ito, K. Ohashi, *Jpn. J. Appl. Phys.* **44**, L1005 (2005)
50. K. Ishihara, T. Ikari, H. Minamide, J. Shikata, K. Ohashi, H. Yokoyama, H. Ito, *Jpn. J. Appl. Phys.* **44**, L929 (2005)
51. K. Ishihara, K. Ohashi, T. Ikari, H. Minamide, H. Yokoyama, J. Shikata, H. Ito, *Appl. Phys. Lett.* **89**, 201120 (2006)
52. Y. Kawano, K. Ishibashi, *Nat. Photonics* **2**, 618 (2008)
53. J. Zhang, D. Grischkowsky, *Appl. Phys. Lett.* **86**, 061109 (2005)
54. M.M. Awad, R.A. Chevillie, *Appl. Phys. Lett.* **86**, 221107 (2005)
55. H. Zhan, R. Mendis, D.M. Mittleman, *Opt. Express* **18**, 9643 (2010)
56. Q. Chen, Z. Jiang, G.X. Xu, X.-C. Zhang, *Opt. Lett.* **25**, 1122 (2000)
57. Q. Chen, X.-C. Zhang, *IEEE J. Sel. Top. Quantum Electron.* **7**, 608 (2001)
58. O. Mitrofanov, *Appl. Phys. Lett.* **88**, 091118 (2006)
59. T. Pfeifer, H.-M. Heiliger, T. Löffler, C. Ohlhoff, C. Meyer, G. Lüpke, H.G. Roskos, H. Kurz, *IEEE J. Sel. Top. Quantum Electron.* **2**, 586 (1996)
60. K. Yang, L.P.B. Katehi, J.F. Whitaker, *Appl. Phys. Lett.* **77**, 486 (2000)
61. N.C.J. van der Valk, W.A.M. van der Marel, P.C.M. Planken, *Opt. Lett.* **30**, 2802 (2005)
62. A. Doi, F. Blanchard, H. Hirori, K. Tanaka, *Opt. Express* **18**, 18419 (2010)
63. A. Bitzer, M. Walther, *Appl. Phys. Lett.* **92**, 231101 (2008)
64. A. Bitzer, H. Merbold, A. Thoman, T. Feurer, H. Helm, M. Walther, *Opt. Express* **17**, 3826 (2009)
65. M. Wächter, M. Nagel, H. Kurz, *Appl. Phys. Lett.* **95**, 041112 (2009)
66. M. Wächter, C. Matheisen, M. Waldow, T. Wahlbrink, J. Bolten, M. Nagel, H. Kurz, *Appl. Phys. Lett.* **97**, 161107 (2010)
67. *35th international conference on infrared, millimeter and terahertz waves*, Rome, 2010
68. V. Giannini, A. Berrier, S. Maier, J.A. Sánchez-Gil, J. Gómez Rivas, *Opt. Express* **18**, 2797 (2010)
69. K.G. Lee, H.W. Kihm, J.E. Kihm, W.J. Choi, H. Kim, C. Ropers, D.J. Park, Y.C. Yoon, S.B. Choi, D.H. Woo, J. Kim, B. Lee, Q.H. Park, C. Lienau, D.S. Kim, *Nat. Photonics* **1**, 53 (2007)
70. J.S. Ahn, H.W. Kihm, J.E. Kihm, D.S. Kim, K.G. Lee, *Opt. Express* **17**, 2280 (2009)
71. K.G. Lee, H.W. Kihm, K.J. Ahn, J.S. Ahn, Y.D. Suh, C. Lienau, D.S. Kim, *Opt. Express* **15**, 14993 (2007)
72. M.A. Seo, A.J.L. Adam, J.H. Kang, J.W. Lee, S.C. Jeoung, Q.H. Park, P.C.M. Planken, D.S. Kim, *Opt. Express* **15**, 11781 (2007)
73. K.J. Ahn, K.G. Lee, H.W. Kihm, M.A. Seo, A.J.L. Adam, P.C.M. Planken, D.S. Kim, *New J. Phys.* **10**, 105003 (2008)
74. M.A. Seo, H.R. Park, S.M. Koo, D.J. Park, J.H. Kang, O.K. Suwal, S.S. Choi, P.C.M. Planken, G.S. Park, N.K. Park, Q.H. Park, D.S. Kim, *Nat. Photonics* **3**, 152 (2009)
75. M.A. Seo, A.J.L. Adam, J.H. Kang, J.W. Lee, K.J. Ahn, Q.H. Park, P.C.M. Planken, D.S. Kim, *Opt. Express* **16**, 20484 (2008)
76. M.A. Seo, H.R. Park, D.J. Park, D.S. Kim, A.J.L. Adam, P.C.M. Planken, *J. Korean Phys. Soc.* **55**, 267 (2009)
77. J.R. Knab, A.J.L. Adam, M. Nagel, E. Shaner, M.A. Seo, D.S. Kim, P.C.M. Planken, *Opt. Express* **17**, 15072 (2009)
78. L. Guestin, A.J.L. Adam, J.R. Knab, M. Nagel, P.C.M. Planken, *Opt. Express* **17**, 17412 (2009)
79. O. Mitrofanov, T. Tan, P.R. Mark, B. Bowden, J.A. Harrington, *Appl. Phys. Lett.* **94**, 171104 (2009)
80. O. Mitrofanov, J.A. Harrington, *Opt. Express* **18**, 1898 (2010)
81. J.R. Knab, A.J.L. Adam, R. Chakkittakandy, P.C.M. Planken, *Appl. Phys. Lett.* **97**, 031115 (2010)
82. A.J.L. Adam, J.M. Brok, P.C.M. Planken, M.A. Seo, D.S. Kim, *C. R. Phys.* **9**, 161 (2008)
83. K. Nielsen, H.K. Rasmussen, A.J.L. Adam, P.C.M. Planken, O. Bang, P.U. Jepsen, *Opt. Express* **17**, 8592 (2009)
84. W. Zhu, A. Nahata, *Opt. Express* **15**, 5616 (2007)

85. A. Bitzer, J. Wallauer, H. Helm, H. Merbold, T. Feurer, M. Walther, *Opt. Express* **17**, 22108 (2009)
86. A. Bitzer, A. Ortner, M. Walther, *Appl. Opt.* **49**, E1 (2010)
87. A. Bitzer, A. Ortner, H. Merbold, T. Feurer, M. Walther, *Opt. Express* **19**, 2537 (2011)
88. M. Walther, B.M. Fischer, A. Ortner, A. Bitzer, A. Thoman, H. Helm, *Anal. Bioanal. Chem.* **397**, 1009 (2010)
89. V.A. Fedotov, N. Papanimakis, E. Plum, A. Bitzer, M. Walther, P. Kuo, D.P. Tsai, N.I. Zheludev, *Phys. Rev. Lett.* **104**, 223901 (2010)
90. M. Nagel, A. Michalski, T. Botzem, H. Kurz, *Opt. Express* **19**, 4667 (2011)
91. F. Keilmann, A.J. Huber, R. Hillenbrand, *J. Infrared Milli, Terahz. Waves* **30**, 1255 (2009)
92. A. Sell, A. Leitenstorfer, R. Huber, *Opt. Lett.* **33**, 2767 (2008)

Chapter 16

Biomedical Imaging

Emma MacPherson

Abstract This chapter builds on the basic principles of THz spectroscopy and explains how they can be applied to biomedical systems as well as the motivation for doing so. Sample preparation techniques and measurement methods for biomedical samples are described in detail. Examples of medical applications investigated hitherto including breast cancer and skin cancer are also presented.

16.1 Why Is Terahertz Radiation Suitable for Investigating Biomedical Systems?

16.1.1 Safety

The energy of a photon at 1 THz, through Plank's law, $\text{Energy} = hf$, where h is Plank's constant, is equal to 6.6×10^{-22} J or 4.1 meV. The energy needed to ionize an atom is of the order 1,000 times higher than this. For example, the ionization energy of sodium is 5.1 eV. Therefore, the energy of THz light is far too low to cause ionization and is safe from this perspective. Additionally, the power levels used in most systems are less than 1 μW which is a million times lower than the THz radiation naturally emitted by the human body (1 W). This means that thermal effects are negligible. Whether there are any non-thermal effects that could potentially cause cell damage at low powers is a current topic of investigation, but hitherto there is no evidence for concern. Research into safe levels of exposure has been carried out through studies on keratinocytes [1] and blood leukocytes [2] with no adverse effects found. Therefore, it is reasonable to conclude that THz light is safe for probing biological samples at

E. MacPherson (✉)
Electronic and Computer Engineering,
The Hong Kong University of Science and Technology,
Clear Water Bay, Hong Kong, China
e-mail: e.pickwell.97@cantab.net

such power levels and many research groups are keen to investigate its potential for medical applications.

16.1.2 Sensitivity toward Intermolecular Interactions

Although safety is always a primary concern, it is also important that we have more reason to investigate other than that it is safe. After all, poking a sample with a stick might well be safe, but it would not tell us anything useful! So, why is it thought that THz light might be a useful technique to investigate biological samples? The answer lies in the fundamental fact that there are intermolecular vibrations with resonances at THz frequencies. These intermolecular interactions have weak, low energy vibrations with broad features that relate to molecular structure. As discussed earlier, there are strong water absorptions at THz frequencies due to hydrogen bonds. Thus, small changes in water content of tissues can be detected using THz light. This is relevant to applications such as cancer diagnosis as the presence of tumor often increases the blood flow, and thus water content within the tissue. Tumor also disrupts the normal tissue matrix on a cellular level. THz imaging is also sensitive to these changes in structure on a macroscopic level and it has been shown that, in addition to water, structural changes contribute significantly to the differences between THz properties of diseased and healthy tissues [4]. Changes in tissue structure are likely to be caused by cross-linking of proteins. Therefore, since THz spectroscopy of proteins is able to show characteristic features, it is likely that THz spectroscopy of biological samples will also provide useful information.

16.2 Sample Preparation

Many THz researchers come from a science or engineering background and have no previous experience in preparing biomedical samples. Collaborations with medical practitioners will help you learn about the samples you are investigating, health and safety, and ethical considerations but they will not necessarily help you to establish a rigorous experimental protocol. The details below highlight aspects that should be considered before embarking on any measurements of biological samples.

16.2.1 Tissue (de)hydration

Since THz light is very sensitive to water content, small changes in the water content of the sample will affect the resulting THz properties of the sample. For instance, if the sample is an excised piece of tissue, once it has been removed, if it is simply left out in the air it will lose water due to evaporation. Therefore, great care must be

taken to preserve the sample such that it does not become dehydrated. If meaningful comparisons between samples are to be drawn, then the samples must have been prepared and handled identically. For instance, they must be stored in the same type of sample holder, kept at the same temperature and humidity and measured at the same time relative to excision.

Sample size and shape is also important—ideally excised samples should be approximately the same size and shape from the beginning so that all samples will be affected in the same way by the environmental factors. This is because the surface area to volume ratio will affect the tissue—clearly tissue from the center of a $1\text{ cm} \times 1\text{ cm} \times 1\text{ cm}$ sample will have become more dehydrated than tissue from the center of a $2\text{ cm} \times 2\text{ cm} \times 2\text{ cm}$ sample. Ideally, it is good to have a large sample excised initially and then take a small slice of the sample from the middle for measurement.

16.2.2 Repeatability

With all tissue samples, it is important to take several measurements. For instance, it is much better to scan a sample such that an area of the sample is measured rather than a single point measurement being made. Additionally, it is necessary to measure several samples harvested from either the same patient or preferably other patients. Since biological samples have natural variation, as much data as possible should be acquired such that average properties can be calculated along with estimations of the errors.

16.2.3 Example Checklist

The key point is to be consistent and, as standard good experimental practice, record all variables. The most tricky part is often determining all the variables as with biological samples there are lots of them! Table 16.1 is an example checklist, it is by no means an exhaustive list, rather, it is designed to help you identify the variables for your case.

16.3 Systems for Samples

The type of sample you are able to obtain and what you want to find out about the sample will determine how you should perform the THz measurement and the type/geometry of THz system you use.

Table 16.1 Checklist for sample and measurement parameters

Variable	Sample 1	Sample 2
Sample details: species, age, gender, healthy...		
Date and time of sample excision		
Humidity and temperature at excision		
Description of sample storage		
Storage humidity and temperature		
Dimensions of excised sample		
Dimensions of sample measured		
Date and time of sample measurement		
Humidity and temperature during measurement		
Filename where data saved		

16.3.1 *Thin Versus Thick*

If the sample is thick (greater than 500 μm) then due to the typically high attenuation of biological tissues it is unlikely that THz light would be able to pass through it and be detected above the noise in a transmission geometry. So, a reflection geometry system should be used. In this case, only information about the surface of the sample will be obtained.

If the sample is thinner than 500 μm then a transmission geometry should be suitable. It is often better to cut samples into thinner slices e.g., 100–300 μm so that the transmitted THz signal is significantly above the noise floor. However, if the sample is too thin, then unwanted etalon effects will be introduced (Fig. 16.1).

16.3.2 *Homogenous Versus Inhomogenous*

If the sample is homogenous then the refractive index and absorption coefficient can be extracted in either reflection or transmission geometry setups. However, if the sample is inhomogenous then this will be more difficult. It may be useful to image an area of the sample and compare the THz data with histology results to identify regions of tissue types, and then group the data such that the THz spectroscopic properties can be obtained.

Occasionally, it is useful to just look at the reflected/transmitted intensity off/through a sample. If this is the case, a continuous wave (CW) THz system might be able to provide sufficient information. However, CW systems have a narrow fre-

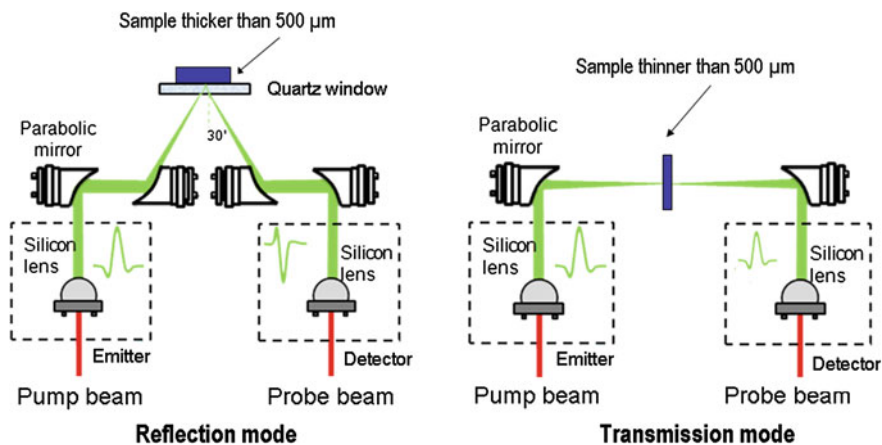


Fig. 16.1 Schematic diagrams to illustrate that biological samples thicker than 500 μm should be measured in reflection geometry and samples thinner than 500 μm should be measured in transmission geometry

quency output and so contrast will only be seen between tissues if their properties at the chosen frequency output are different. Since the area of THz biomedical spectroscopy is relatively new, most studies use a pulsed THz system (which produces broad band THz radiation) so that the frequency dependent properties of the sample can be determined.

16.3.3 Bandwidth and Axial Resolution

As well as determining the frequency range over which the sample can be characterized, the bandwidth of the terahertz system also influences the axial resolution. For a reflection geometry system the axial resolution is given by the coherence length, L_C :

$$L_C = c/2n\Delta f \quad (16.1)$$

where c is the speed of light, n is the refractive index of the sample and Δf is the bandwidth. Therefore, when the bandwidth is increased for a given refractive index, smaller features will be able to be resolved.

The example THz power spectrum in Fig. 16.2 (measured by placing a mirror where the sample should go) starts to fall off at 2 THz resulting in a usable bandwidth of about 1.9 THz.

One problem for biological tissues in particular is that the absorption coefficient of most tissues increases with increasing frequency. For example, the absorption coefficients for water, healthy breast tissue and adipose fat are plotted in Fig. 16.3.

Fig. 16.2 Example THz power spectrum. The maximum usable frequency range for this system is from 0.1 to 2 THz

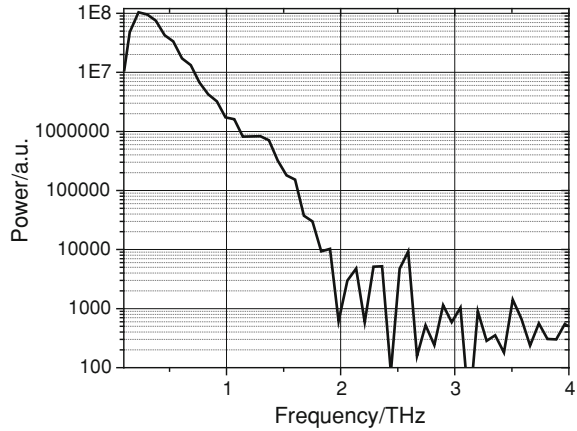
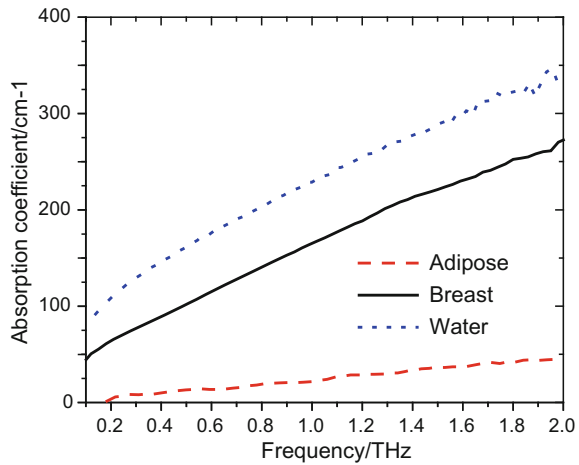


Fig. 16.3 The absorption coefficients for water, healthy breast tissue, and adipose tissue. Data were acquired in transmission geometry



This compounds the signal power roll-off and means that it is even more difficult to achieve high resolution in biological samples.

16.3.4 Signal to Noise Ratio and Penetration Depth

The detectable penetration depth of the terahertz light depends on the attenuation of the sample and also the signal to noise ratio (SNR) of the terahertz signal. For light propagating distance z through a medium with absorption coefficient α , the amplitude A_z is given by:

$$A_z = A_0 e^{-\frac{\alpha}{2}z} \tag{16.2}$$

where A_0 is the initial signal amplitude. Therefore, the furthest distance that THz light can travel in the medium and still be detectable is when:

$$\frac{A_z}{A_0} = \frac{1}{\text{SNR}} \quad (16.3)$$

which means:

$$\ln\left(\frac{A_z}{A_0}\right) = -\ln(\text{SNR}) = -\frac{\alpha}{2}z \quad (16.4)$$

Therefore, the maximum detectable penetration depth is:

$$z = \frac{2}{\alpha} \ln(\text{SNR}) \quad (16.5)$$

If the THz signal is being detected in a reflection geometry then the depth, d into the tissue will be half the distance traveled (assuming normal incidence). Therefore, the maximum penetration depth detectable in a reflection geometry is:

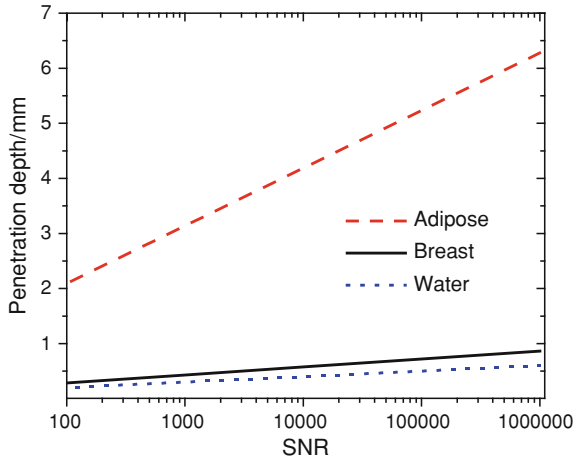
$$d = \frac{1}{\alpha} \ln(\text{SNR}) \quad (16.6)$$

Figure 16.4 illustrates how the penetration depth increases with SNR for water, breast tissue, and adipose tissue at 1 THz for reflection geometry. Since adipose tissue has a much lower attenuation coefficient than water (at 1 THz it is 25 cm^{-1} compared to 225 cm^{-1}), the terahertz light can penetrate much deeper in adipose tissue than in water or breast for a given SNR. This is particularly relevant for the application to breast cancer as the healthy tissue within the breast is largely composed of adipose tissue: if terahertz imaging were performed during surgery, it could potentially be used to look through the adipose tissue for remaining tumour.

16.3.5 Structural Versus Spectroscopic Information

Clearly, the spectroscopic information that can be obtained is dependent on the usable bandwidth of the system. The bandwidth and SNR also affect the time-domain properties of the THz signal as they also influence the axial resolution and penetration depth. The axial resolution and penetration depth determine the capability of the THz system to resolve and identify structural features. For instance, the separation between two reflections in the time-domain response can be used to calculate the thickness of a material.

Fig. 16.4 Penetration depth in adipose tissue (*dashed line*), breast tissue (*solid line*), and water (*dotted line*) as a function of SNR at 1 THz



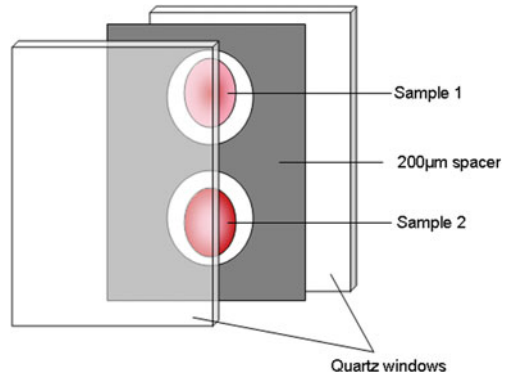
16.3.6 Imaging Versus Spectroscopy

The term THz spectroscopy is used typically when only the frequency dependent properties are of interest. A lot of spectroscopy measurements hitherto have been carried out in transmission geometry as it is easier to extract the properties more accurately. Reflection spectroscopy is becoming increasingly popular as it is often easier for sample preparation although extracting the optical properties is not quite as easy. THz imaging refers to when an image of a sample is taken—this means that data will have been recorded at several points over the sample. This can be done in either transmission or reflection geometry. The time-domain data acquired for the image can also be Fourier transformed to determine the spectroscopic information (as long as suitable acquisition parameters were chosen), though often it is the time-domain properties that are plotted to obtain the image.

16.4 Sample Holders and Effects on Calculations

While measuring biological samples great care needs to be taken to both protect the sample and to keep equipment hygienic. Below are some suggested sample holder geometries, preparation, and measurement tips for transmission and reflection geometry setups.

Fig. 16.5 Schematic diagram showing a sample holder for transmission measurements. The two quartz windows sandwich a 200 μm spacer. The spacer has holes cut so that samples can be placed between the windows to give a uniform sample thickness



16.4.1 Transmission Geometry

Since thin samples are used in transmission geometry, the sample holder should be designed to minimize dehydration. Rather than placing the sample in free space over an aperture, it is better to contain the sample between non-porous windows. This will better preserve the sample and it will also keep the thickness of the sample more uniform. A suggested setup is illustrated in Fig. 16.5.

The windows of the sample holder must be transparent to THz light and it is helpful for them to be transparent at visible frequencies too. Examples of materials that are suitable are *z*-cut quartz, TPX (poly 4 methyl pentene-1), polyethylene, and topas. Quartz is used as an example in Fig. 16.5. The spacer should also be made from a non-porous and incompressible material so that when the windows are pressed against the spacer, the sample will have a uniform thickness. It can be quite tricky cutting biological samples to an appropriate shape and thickness. In this setup, the samples need to be approximately 200 μm thick, but if slightly thicker, they can be shaped to be the thickness of the spacer by gently pressing them between the quartz windows. However, the more rigid the sample is, the more accurate the sample needs to be cut in the first place. If the windows are pressed together with too much force, they may crack (particularly if using quartz) and so it is often more economical to use plastic windows such as TPX.

For the sample measurement, the signal having passed through the windows and the sample is recorded. In order to extract the spectroscopic properties from the sample, a reference measurement is needed. In Fig. 16.6, two alternative geometries are given for the reference measurement. Fig. 16.6a has the same setup as for the sample measurement except with no sample, so there is effectively an air gap (of the same thickness as the sample) between the windows. Fig. 16.6b uses the same windows but places them together without the spacer (and without the sample). This method is preferred over Fig. 16.6a because it reduces etalon effects. The reader is encouraged at this point to think how the calculation of the refractive index and absorption coefficient will be affected by the two geometries (consider the Fresnel

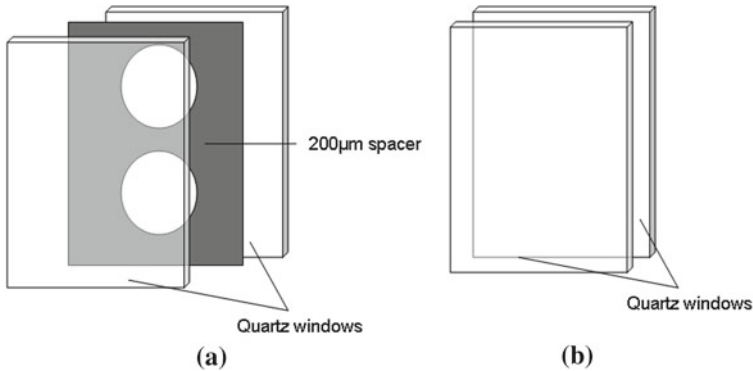


Fig. 16.6 Sample holder set ups for reference measurements. In **a** the quartz windows sandwich the spacer with no sample present. In **b** the two windows are placed together with no spacer present

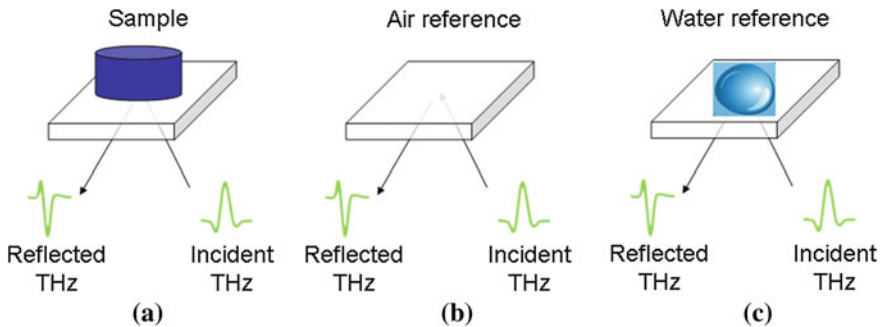


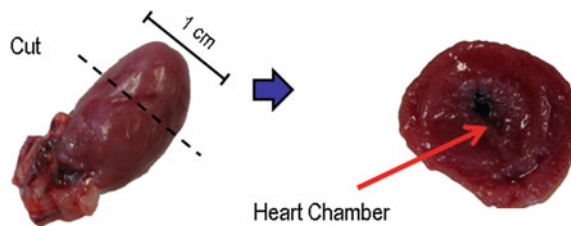
Fig. 16.7 Schematic diagrams to illustrate the sample **(a)** and reference **(b)** and **(c)** measurements used to extract the refractive index and absorption coefficient of the sample in reflection geometry

reflections at each interface). The corresponding equations for this setup can be found in reference [4].

16.4.2 Reflection Geometry

For reflection geometry, the sample preparation is easier as a thick slice of tissue should be placed on the quartz window as illustrated in Fig. 16.7a. One drawback of reflection geometry measurements is that unwanted reflections may result. For instance, reflections from the lower surface of the quartz may have an enduring effect that then interferes with the main sample reflection. One way to overcome this is to also take a measurement of water. Since the THz properties of both air and water are known, the contribution from unwanted reflections can be calculated. The derivation and equations for this are given in reference [5].

Fig. 16.8 Photograph of the heart sample illustrating how it was cut for the measurement



16.5 Interpreting Data in the Time Domain

16.5.1 Deconvolution

The incident THz signal is dependent on the various components of the THz system and particularly the photoconductive devices. Therefore, it is useful to remove the response of the incident THz signal and to determine the sample response function. This can be done by a simple deconvolution. Equation 16.7 below summarizes this process.

$$\text{Sample Response Function} = \text{FFT}^{-1} \left(\frac{\text{FFT}(\text{Sample})}{\text{FFT}(\text{Reference})} \times \text{FFT}(\text{Filter}) \right) \quad (16.7)$$

In this process, the sample is divided by the reference in Fourier space. This can create more noise, and so a filter is applied. Typically, a band pass filter such as a double Gaussian filter is chosen so as to remove both the high and low frequency noise. The resulting sample response function is in the time domain and is often used to construct an image of the sample.

16.5.2 Worked Example

A heart excised from a rat was sliced and then imaged—THz reflection measurements were taken over a 1 cm by 1 cm area by scanning the THz optics. The section of the heart placed on the quartz window contained part of the heart chamber. Figure 16.8 is a photograph of the sample before and after cutting it for the measurement.

Figure 16.9a is a schematic diagram of the sample measurement setup and Fig. 16.9b is the resulting THz image. The image was formed by plotting the maximum electric field in the sample response function at each point. The three sample response functions depicted in Fig. 16.9c are very different—the response function from the area around the sample (A) has a positive peak (it is due to the reflection of the quartz/air interface). The response function from the heart chamber area has a peak and then a trough because the incident signal passes through an air gap before

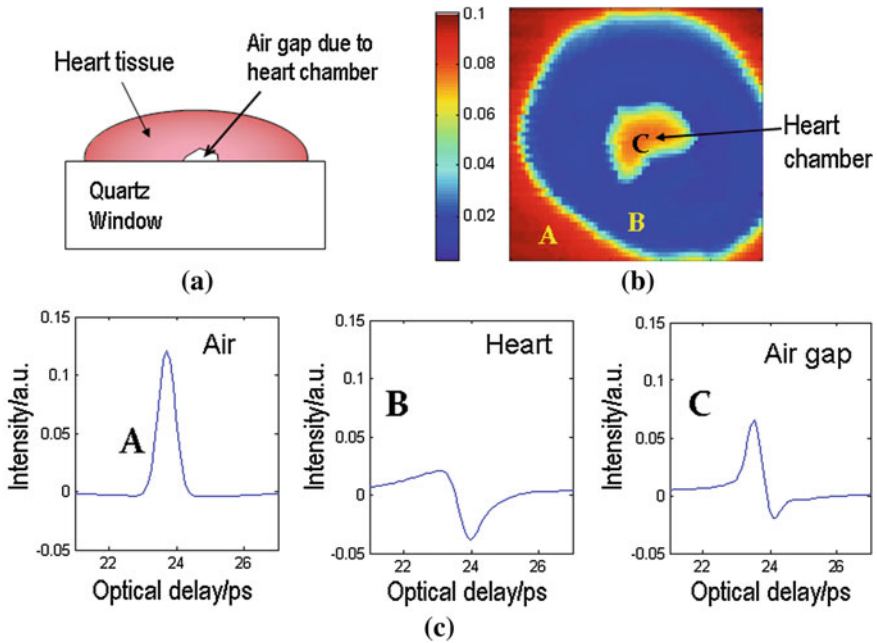


Fig. 16.9 **a** Schematic diagram of sample measurement highlighting the air gap due to the sample chamber; **b** THz image of the heart tissue section, the maximum electric field of the response function is plotted according to the color bar; **c** resulting response functions from the air at the edge of the sample (A), the heart tissue (B) and the heart chamber (C)

then being reflected of the heart chamber wall. The response function that is from the heart tissue (with no air gap) gives a trough as there are no other layers present to cause a peak. Thus, by plotting the maximum electric field from the response functions on a false color scale, the heart chamber can be seen. The refractive index and absorption coefficient of the heart tissue can be calculated through reflection spectroscopy if the sample response functions from the heart tissue (without an air gap, i.e. from area B) are used as detailed in [6].

16.6 Medical Applications Investigated

The previous sections have discussed the motivation and methods for investigating the THz properties of biomedical samples. In this section, applications that have been investigated hitherto will be outlined. More examples and details can be found in previously published review papers [7–9].

16.6.1 Breast Cancer

Ex vivo studies of breast cancer have been able to detect tumor that is of the non-calcified form [10]. This is particularly significant because such tumors are often missed during breast surgery as they are non-palpable and do not show up on X-ray images. Because of this finding, researchers are keen to develop the technique such that THz imaging can be used by clinicians intraoperatively. To determine the feasibility of such a technique, the fundamental THz properties (the absorption coefficient and refractive index) of the constituent tissues within the breast have been measured in transmission spectroscopy [11]. The results are promising—the healthy adipose tissue has a low absorption coefficient such that for an SNR of 1000, tumour buried beneath about 3 mm of adipose tissue could be detected.

16.6.2 Skin Cancer

THz images of skin cancer, namely basal cell carcinoma (BCC) have shown contrast between diseased and healthy tissues [12]. Since THz is able to penetrate the topmost layer of skin, it is possible to see the extent of the tumor beneath the surface—this cannot be seen with the naked eye, nor easily imaged with other existing modalities. The contrast in THz images of skin cancer is due to differences in the fundamental THz properties of the tissues. The refractive index and absorption coefficient of BCC are higher than healthy skin from the same patient [13]. The difference in these properties has been attributed to changes in water content and structural changes caused by increased vascularity and blood flow around the tumor. Simulation work has been conducted to further understand the contrast mechanisms [14, 15]. Recent studies have shown that structural changes contribute more than water content changes for the case of liver cirrhosis [4].

16.6.3 Colon Cancer

THz images of ex vivo colon tissue have been able to distinguish between normal colon, tumor, and even dysplastic tissue [16]. Although this pilot study was conducted ex vivo, with advances in THz wave-guiding and fiber-coupled THz devices, a THz endoscope could be possible in the future.

16.6.4 Dental Caries

The potential of THz imaging to monitor tooth decay was studied by Crawley et al. [17]. They showed that THz light could detect regions of tooth decay (caries) in excised teeth samples. Dentists were interested in the ability of the technique to detect early tooth decay using a non-ionizing imaging modality. Pickwell et al. continued the study to investigate the correlation between mineral content lost and the THz refractive index profile as a function of depth into the enamel [18]. A comparison between THz and transmission microradiography measurements was conducted for samples carefully prepared such that the lesions were in one of four groups:

1. deep with high mineral loss
2. shallow with high mineral loss
3. deep with low mineral loss
4. shallow with low mineral loss

where deep/shallow refers to the depth of decay into the enamel (parameter d in Fig. 16.10b). The extent of mineral loss is represented by parameter R in Fig. 16.10b— R is larger for higher mineral loss. Transmission microradiography is able to measure the mineral content quantitatively as the minerals block the X-rays, however, the sample is cut into $5\ \mu\text{m}$ slices for the measurement and is thus destroyed. The mineral density of the enamel is higher in the inner enamel and decreases approaching the surface. The change in mineral content causes a change in refractive index and this gives rise to two reflections in the response function illustrated in Fig. 16.10a. The distance between the reflections is related to the depth of the enamel decay (d).

The greater the change in THz refractive index between the healthy enamel and the decayed enamel, the greater the parameter R in Fig. 16.10b. This also makes the THz reflections stronger and so shallow lesions (i.e. lesions with a small parameter d in Fig. 16.10b) could still be resolved. However, if both the mineral loss was low and the depth of decay was shallow, it was no longer possible to detect the lesion [19].

16.6.5 Skin

The aforementioned applications were *ex vivo* studies. Very few *in vivo* THz studies have been conducted to date. However, there have been some studies of human skin *in vivo*. Since skin is easily accessible, reflection geometry *in vivo* THz measurements can be made to determine information about the skin such as its moisture content [20] or thickness [21]. As illustrated in Fig. 16.11b the outer layer of the skin is called the stratum corneum and beneath the stratum corneum lies the epidermis. The stratum corneum ranges from about 10 to 200 μm thick depending on the location of the skin. For instance on the wrist it is about 10–20 μm thick, whereas on the palm of the hand it is about 100–200 μm and varies a lot from person to person. TeraView

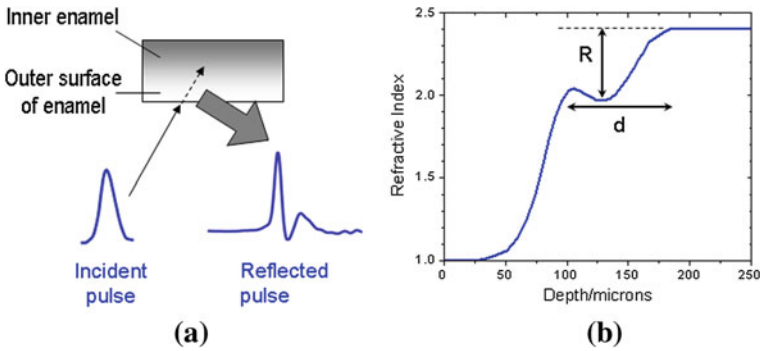


Fig. 16.10 **a** A cross-section of the tooth sample showing the THz reflections arising from enamel. The enamel has lower mineral density in areas of decay, and so there is a gradient of mineral content with the mineral content being lowest on the outer surface of the enamel. **b** The refractive index profile calculated from the reflected pulse. Label *d* marks the depth of the decay into the tooth and label *R* indicates the change in refractive index

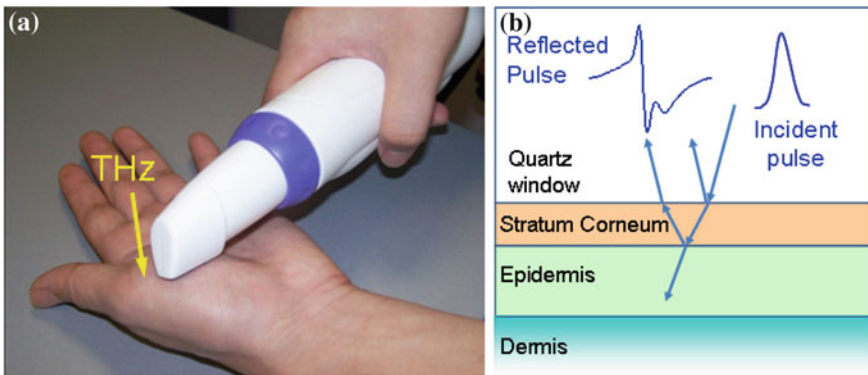


Fig. 16.11 **a** Photograph of the THz probe being used to image the palm; **b** schematic diagram showing the layers of the palm and the resulting reflected THz response function

Ltd Cambridge has designed a handheld THz probe that can be easily used (from a geometry point of view) to measure patients. We have used it to measure human skin *in vivo* to test its capabilities.

We have also shown that THz imaging can potentially be used to look through wound dressings. In our feasibility study, we were still able to determine the optical delay between the stratum corneum and epidermis when the palm was covered with a Tegaderm[®] plaster [22]. Other work along these lines includes THz imaging of porcine skin burns beneath cotton gauze [23].

16.6.6 Protein Spectroscopy

Since THz is sensitive to intermolecular interactions, THz spectroscopy can be used to characterize proteins. This could be useful for diagnosis where the presence of a particular biomarker protein is indicative of disease for example tryptophan [24] and antibodies [25]. THz spectroscopy is sensitive to small changes in molecular structure and concentrations of proteins, and thus has great potential in this area. Spectroscopy of proteins and their interactions with liquids such as water and glycerol is discussed further in (Chap. 3.2).

16.7 Summary

In summary, THz imaging uses non-ionizing radiation at low power levels and is safe to use in biomedical applications. Its great sensitivity to subtle changes in molecular structures gives THz spectroscopy the potential to be a powerful tool for medical diagnosis, be it detecting macroscopic changes in biological tissues or changes in protein concentration in solutions. However, to achieve meaningful results, careful and consistent sample preparation, sample measurement, and data analysis must be performed.

References

1. R.H. Clothier, N. Bourne, Effects of THz exposure on human primary keratinocyte differentiation and viability. *J. Biol. Phys.* **29**, 179–85 (2003)
2. O. Zeni, G.P. Gallerano, A. Perrotta, M. Romano, A. Sannino, M. Sarti et al., Cytogenetic observations in human peripheral blood leukocytes following in vitro exposure to THz radiation: a pilot study. *Health Phys.* **92**, 349–57 (2007)
3. S. Sy, S. Huang, Y.-X.J. Wang, J. Yu, A.T. Ahuja, Y. Zhang, E. Pickwell-MacPherson, Terahertz spectroscopy of liver cirrhosis: investigating the origin of contrast. *Phys. Med. Biol.* **55**, 7587–7596 (2010)
4. P.C. Ashworth, E. Pickwell-Macpherson, E. Provenzano, S.E. Pinder, A.D. Purushotham, M. Pepper, and V.P. Wallace, *Opt. Express* **17**, 12444 (2009).
5. S. Huang, P.C. Ashworth, K.W.C. Kan, C. Yang, V.P. Wallace, Y. Zhang, E. Pickwell-MacPherson, Improved sample characterization in terahertz reflection imaging and spectroscopy. *Opt. Express* **17**(5), 3848–3854 (2009)
6. S.Y. Huang, Y.X. Wang, K.W. Yeung, A.T. Ahuja, Y.-T. Zhang, E. Pickwell-MacPherson, Tissue characterisation using terahertz pulsed imaging in reflection geometry. *Phys. Med. Biol.* **54**, 149–160 (2009)
7. E. Pickwell, V.P. Wallace, Biomedical applications of THz technology. *J. Phys. D Appl. Phys.* **39**, R301–R310 (2006)
8. E. Pickwell-MacPherson, V.P. Wallace, Terahertz pulsed imaging—a potential medical imaging modality? *Photodiagn. Photodyn. Ther.* **62**, 128–134 (2009)
9. E. Pickwell-MacPherson, Practical considerations for in vivo THz imaging. *J. Terahertz Sci. Technol.* **3**(4), 163–171 (2010)

10. A.J. Fitzgerald, V.P. Wallace, M. Jimenez-Linan, L. Bobrow, R.J. Pye, A.D. Purushotham, D.D. Arnone, Terahertz pulsed imaging of human breast tumors. *Radiology* **239**, 533–540 (2006)
11. P.C. Ashworth, E. Pickwell-MacPherson, S.E. Pinder, E. Provenzano, A.D. Purushotham, M. Pepper, V.P. Wallace, Terahertz pulsed spectroscopy of freshly excised human breast cancer. *Opt. Express* **17**(15), 12444–54 (2009)
12. V.P. Wallace, A.J. Fitzgerald, S. Shankar, N. Flanagan, R. Pye, J. Cluff, D.D. Arnone, Terahertz pulsed imaging of basal cell carcinoma ex vivo and in vivo. *Br. J. Dermatol.* **151**, 424–432 (2004)
13. V.P. Wallace, A.J. Fitzgerald, E. Pickwell, R.J. Pye, P.F. Taday, N. Flanagan, T. Ha, Terahertz pulsed spectroscopy of human basal cell carcinoma. *J. Appl. Spectrosc.* **60**(10), 1127–1133 (2006)
14. E. Pickwell, B.E. Cole, A.J. Fitzgerald, V.P. Wallace, M. Pepper, Simulation of terahertz pulse propagation in biological systems. *Appl. Phys. Lett.* **84**(12), 2190–2192 (2004)
15. E. Pickwell, V.P. Wallace, A.J. Fitzgerald, B.E. Cole, R.J. Pye, T. Ha, M. Pepper, Simulating the response of terahertz radiation to human skin using ex vivo spectroscopy measurements. *J. Biomed. Opt.* **10**(6), 064021-1–064021-7 (2005)
16. V.P. Wallace, Terahertz imaging detects cancerous tissue. SPIE Newsroom, 16 Dec 2008. <http://spie.org/x32216.xml?ArticleID=x32216>
17. D.A. Crawley, C. Longbottom, B.E. Cole, C.M. Ciesla, D. Arnone, V.P. Wallace, M. Pepper, Terahertz pulse imaging: a pilot study of potential applications in dentistry. *Caries Res.* **37**, 352–359 (2003)
18. E. Pickwell, V.P. Wallace, B.E. Cole, S. Ali, C. Longbottom, R. Lynch, M. Pepper, A comparison of terahertz pulsed imaging with transmission microradiography for depth measurement of enamel demineralisation in vitro. *Caries Res.* **41**(4955), 2007 (2007)
19. E. Pickwell-MacPherson, S.Y. Huang, Y. Sun, W.C. Kan, Y.T. Zhang, Terahertz image processing methods for biomedical applications. in *Annual International Conference of the IEEE Engineering in Medicine and Biology Society*, Vancouver 2008
20. B.E. Cole, R.M. Woodward, D. Crawley, V.P. Wallace, D.D. Arnone, M. Pepper, Terahertz imaging and spectroscopy of human skin, in vivo. *SPIE Proc.* **2001**(4276), 1–10 (2001)
21. E. Pickwell, B.E. Cole, A.J. Fitzgerald, M. Pepper, V.P. Wallace, In vivo study of human skin using pulsed terahertz radiation. *Phys. Med. Biol.* **49**, 1595–1607 (2004)
22. S.Y. Huang, E. Pickwell-MacPherson, Y.T. Zhang, *A Feasibility Study of Burn Wound Depth Assessment Using Terahertz Pulsed Imaging* (IEEE-EMBS International Summer School and Symposium on Medical Devices and Biosensors, Cambridge, 2007)
23. Z.D. Taylor, R.S. Singh, M.O. Culjat, J.Y. Suen, W.S. Grundfest, H. Lee, E.R. Brown, Reflective terahertz imaging of porcine skin burns. *Opt. Lett.* **33**(11), 1258–60 (2008 Jun 1)
24. C.S. Joseph, A.N. Yaroslavsky, M. Al-Arashi, T.M. Goyette, J.C. Dickinson, A.J. Gatesman, B.W. Soper, C.M. Forgione, T.M. Horgan, E.J. Ehasz, R.H. Giles, W.E. Nixon, Terahertz spectroscopy of intrinsic biomarkers for non-melanoma skin cancer. *Proc. SPIE* **7215**, 72150I (2009)
25. Y. Sun, Y. Zhang, E. Pickwell-MacPherson, Investigating antibody interactions with polar liquids using terahertz pulsed spectroscopy. *Biophys. J.* **100**(1), 225–231 (2011)

Chapter 17

THz Tomography

Takayuki Shibuya and Kodo Kawase

Abstract Terahertz and millimeter waves penetrate various dielectric materials, including plastics, ceramics, crystals, and colorants, allowing terahertz transmission images to be measured [1–5]. Many terahertz images have been recorded and used in various applications. However, these images are almost exclusively 2D, and transmission-mode measurement of such images is limited to thin samples, with the absorption of the sample averaged in the direction of the path of the terahertz beam. Tomographic images can be used to acquire 3D images in the terahertz frequency range, as in the photonic or X-ray regions of the electromagnetic spectrum. In this chapter, we introduce the principle of operation of two types of tomography system: computed tomography (CT) using millimeter to terahertz waves and time-of-flight (TOF) terahertz tomography. The THz-CT technique is similar to X-ray CT, however, it has the advantage that imaging of the internal structure of soft materials is comparatively easy. On the other hand, TOF tomography employs a THz pulse with a width of less than a picosecond, and depth resolution of tens of microns is possible. Additionally, it is possible to measure samples that are opaque in the visible region.

17.1 Computed Tomography Using THz and Millimeter Waves

Two-dimensional THz transmission images were first acquired by Hu and Nuss in 1995 [1]. Those images were of a semiconductor integrated circuit and of a leaf. The image of a freshly cut leaf was compared with that acquired after the leaf had

T. Shibuya

Tokyo Metropolitan Industrial Technology Research Institute, Tokyo, Japan
e-mail: shibuya.takayuki@iri-tokyo.jp

K. Kawase (✉)

Department of Electrical and Electronic Engineering and Information Engineering,
Graduate School of Engineering, Nagoya University, Nagoya464-8603, Japan
e-mail: kawase@nuee.nagoya-u.ac.jp

been allowed to dry for 48 h, which revealed that transmission of THz radiation was much higher in the dry leaf, due to the decreased water content. Since then, various studies have demonstrated developments in THz imaging [2–5]. Two-dimensional transmission imaging measures the average absorption in the direction of the terahertz beam. However, it is often desirable to acquire 3D images. Computed tomography (CT) is a method that allows measurement of the internal structure of samples. CT has been developed primarily in the X-ray region, but it can also be applied to measurements using THz radiation. By using THz radiation, more sensitive measurements of soft materials can be expected compared to using X-rays, because of the reduced transmission at THz frequencies. However, because the THz radiation causes scattering and diffraction, unlike X-rays, there are some additional complications that must be taken into account.

17.1.1 Principle of CT

The filtered back projection (FBP) method [6] is one of the more frequently used CT techniques. First, the coordinate system of the xy plane, shown in Fig. 17.1, is defined, and the distribution of the extinction coefficient of the sample is assumed to be $f(x, y)$. Next, new orthogonalization coordinates of an XY plane, which is rotated by an angle θ around the origin, are defined. Electromagnetic radiation of intensity I_0 enters the sample parallel to the Y axis, and the transmitted intensity $I(X, \theta)$ is as follows:

$$I(X, \theta) = I_0 \exp\left[-\int_{-\infty}^{\infty} f(x, y) dY\right]. \quad (17.1)$$

$I(X, \theta)$ can be measured experimentally, and the absorbance $g(X, \theta)$ can be expressed as:

$$g(X, \theta) = \ln\left[\frac{I_0}{I(X, \theta)}\right] = \int_{-\infty}^{\infty} f(x, y) dY. \quad (17.2)$$

This technique for obtaining the projection data $g(X, \theta)$ associated with $f(x, y)$ is called Radon conversion. The purpose of CT is to calculate $f(x, y)$ from the experimentally measured $g(X, \theta)$. The 2D Fourier transformation of $f(x, y)$ is assumed to be of the form:

$$F(\xi, \eta) = \int_{-\infty}^{\infty} \int_{-\infty}^{\infty} f(x, y) \exp[-i(\xi x + \eta y)] dx dy, \quad (17.3)$$

where the coordinate system (ξ, η) is converted into a polar coordinate system (ω, θ) , according to the following relations:

$$\begin{cases} \xi = \omega \cos \theta \\ \eta = \omega \sin \theta \end{cases} \quad (17.4)$$

Following this transformation, Eq. (17.3) becomes:

$$F(\omega \cos \theta, \omega \sin \theta) = \int_{-\infty}^{\infty} \int_{-\infty}^{\infty} f(x, y) \exp[-i\omega(x \cos \theta + y \sin \theta)] dx dy. \quad (17.5)$$

Using the following relations,

$$\begin{aligned} X &= x \cos \theta + y \sin \theta, \\ dx dy &= dX dY \end{aligned} \quad (17.6)$$

Equation (17.5) can be rewritten as

$$\begin{aligned} F(\omega \cos \theta, \omega \sin \theta) &= \int_{-\infty}^{\infty} \int_{-\infty}^{\infty} f(x, y) \exp(-i\omega X) dX dY \\ &= \int_{-\infty}^{\infty} \int_{-\infty}^{\infty} [f(x, y) dY] \exp(-i\omega X) dX \\ &= \int_{-\infty}^{\infty} g(X, \theta) \exp(-i\omega X) dX \end{aligned} \quad (17.7)$$

$F(\xi, \eta)$ is the two-dimensional Fourier transform of $f(x, y)$, and so $f(x, y)$ can be determined from $g(X, \theta)$, which is obtained in the range $0 \leq \theta < \pi$. Thus, $f(x, y)$ is related to $F(\xi, \eta)$ as follows:

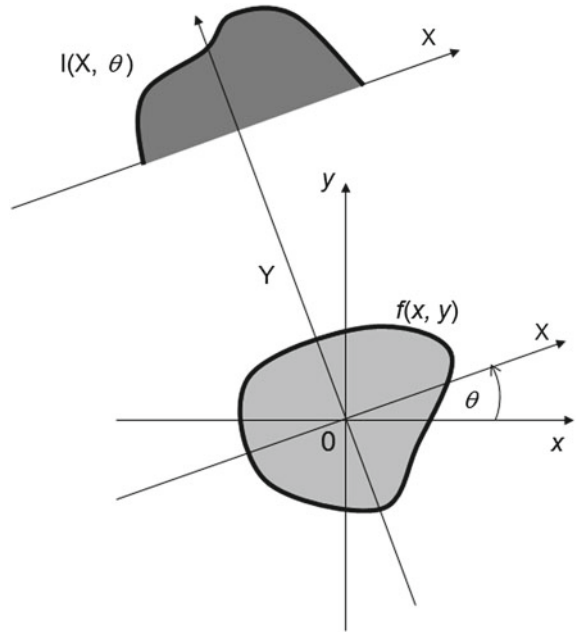
$$f(x, y) = \frac{1}{(2\pi)^2} \int_{-\infty}^{\infty} \int_{-\infty}^{\infty} F(\xi, \eta) \exp[i(\xi x + \eta y)] d\xi d\eta. \quad (17.8)$$

Equation (17.8) can be converted to a polar coordinate system by using Eq. (17.4), resulting in:

$$f(x, y) = \frac{1}{(2\pi)^2} \int_0^{2\pi} \int_0^{\infty} F(\omega \cos \theta, \omega \sin \theta) \exp[i\omega(x \cos \theta + y \sin \theta)] \omega d\omega d\theta. \quad (17.9)$$

To enhance the range of ω in the negative region, the absolute value, $|\omega|$, is taken in Eq. (17.9), so that we have:

Fig. 17.1 Schematic illustration of radon conversion, and the sample coordinate system



$$f(x, y) = \frac{1}{2(2\pi)^2} \int_0^{2\pi} \left[\int_{-\infty}^{\infty} F(\omega \cos \theta, \omega \sin \theta) \exp(i\omega X) |\omega| d\omega \right] d\theta. \quad (17.10)$$

Using the following relationship,

$$\begin{aligned} q(X, \theta) &= \frac{1}{2\pi} \int_{-\infty}^{\infty} F(\omega \cos \theta, \omega \sin \theta) \exp(i\omega X) |\omega| d\omega \\ &= \frac{1}{2\pi} \int_{-\infty}^{\infty} \left[\int_{-\infty}^{\infty} g(X, \theta) \exp(-i\omega X) \right] |\omega| \exp(i\omega X) d\omega, \end{aligned} \quad (17.11)$$

$f(x, y)$ can be expressed as follows:

$$f(x, y) = \frac{1}{4\pi} \int_0^{2\pi} q(X, \theta) d\theta. \quad (17.12)$$

From Eq. (17.11) it follows that $q(X, \theta)$ can be obtained by the inverse Fourier transform of $F(\omega \cos \theta, \omega \sin \theta)$, that is, the Fourier transform of $g(X, \theta)$ after the

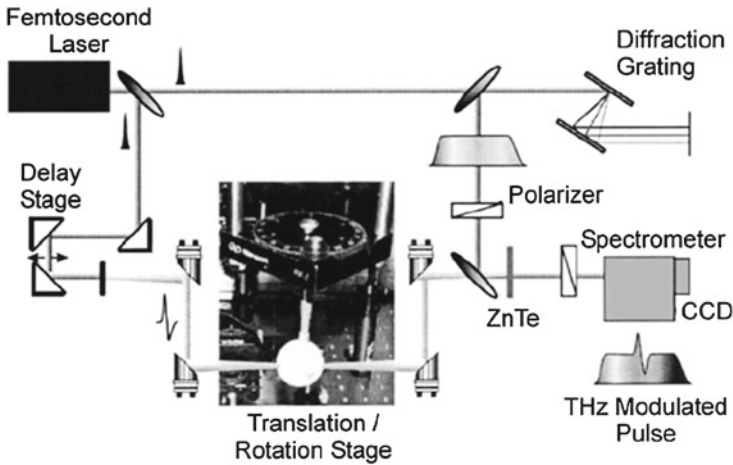
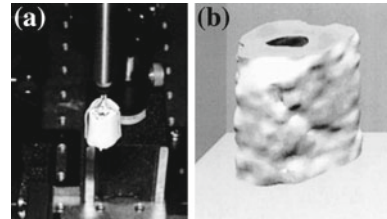


Fig. 17.2 Experimental setup for CT imaging using a THz-TDS system

Fig. 17.3 **a** Optical image of a turkey-bone sample and **b** reconstructed 3D image of the sample measured using THz-TDS CT



filtering process using $|\omega|$. Therefore, $f(x, y)$ can be calculated according to the back-projection process of $q(X, \theta)$, shown in expression (17.12).

17.1.2 Examples of the Application of THz-CT

Ferguson et al. first demonstrated THz-CT [7], using a transmission THz-TDS system. Figure 17.2 shows the experimental setup used for THz-CT. The sample is arranged in the optical path of the THz pulse, and the projection image is acquired by scanning the sample using translation/rotation stages. Figure 17.3a shows an optical image of a section of turkey bone, and Fig. 17.3b shows the THz-CT image of the same sample. Both the central cavity of the bone and the outline can be clearly observed.

In recent years, air pollution due to emissions from internal combustion engines has become a significant problem. In particular, soot particulates from vehicle emissions, of which the principal ingredient is carbon, are harmful to human health. Thus, soot-removal filters installed in the exhaust system can reduce these particulate

Fig. 17.4 Internal view (*left*) and overview (*right*) of a soot-removal filter. The exhaust gas is filtered by passing it through 0.4 mm-thick ceramic walls

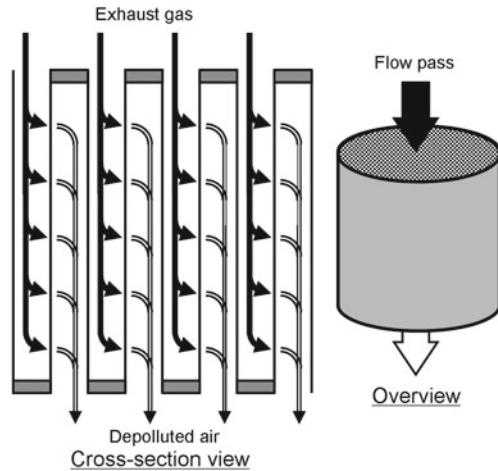
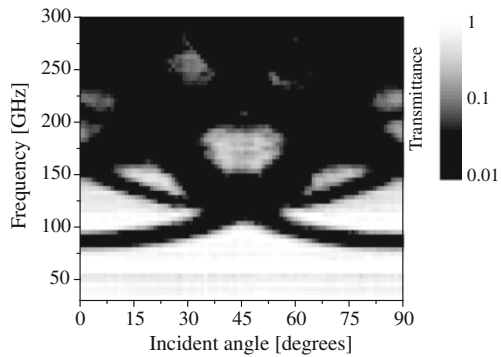


Fig. 17.5 Transmittance mapping as a function of the angle of incidence and frequency; the transmittance is indicated in a pseudo-color plot



emissions. Measurement of the distribution of soot in a soot-removal filter was reported in 2010 as another example of THz/MMW CT [8]. Figure 17.4 shows a schematic diagram of the filter. The exhaust gas is filtered by passing through ceramic walls, and is discharged into the atmosphere. The development of a filter with high soot-trapping efficiency is difficult, because it is hard to characterize the distribution of soot in the filter since that requires dismantling or destroying it. Therefore, a non-destructive technique for measuring the distribution of accumulated soot is desirable.

To construct a tomographic image, it is necessary to measure the transmittance of the filter from all azimuthal angles. Transmittance mapping as a function of the angle of incidence and frequency is shown in Fig. 17.5. The dependence of the transmittance on the angle of incidence is shown in Fig. 17.6 at 65, 80, 150, 175, and 250 GHz. The transmittance is strongly dependent on the angle of incidence at the higher frequencies, resulting in behavior that is similar to that observed in photonic crystals, with pronounced dips. These dips in the transmittance are caused by photonic band

Fig. 17.6 Transmittance as a function of the angle of incidence at several frequencies. Strong dips in the transmittance are seen at higher frequencies

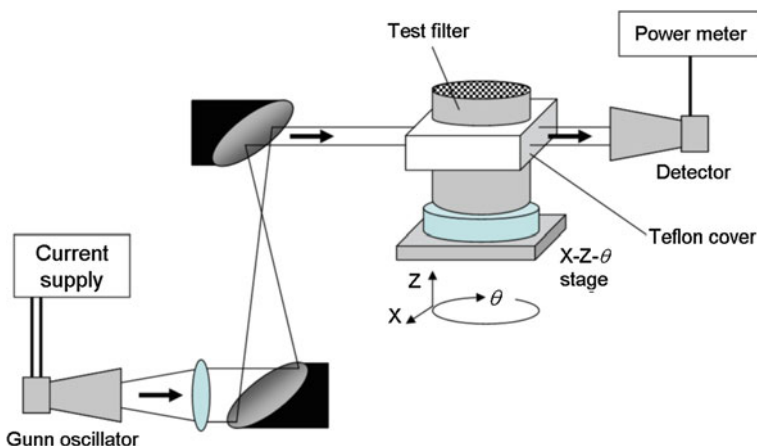
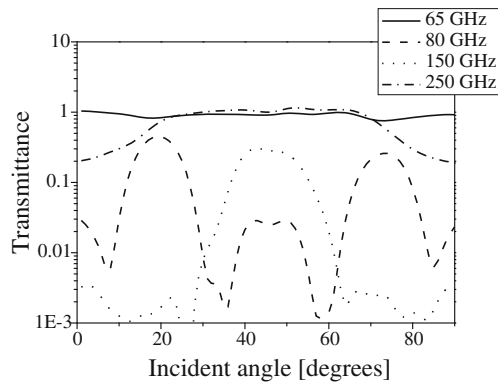


Fig. 17.7 Schematic diagram of the 3D-CT image-acquisition system

gaps in the periodic filter structure, whereas transmittance is almost flat at 65 GHz. Thus, 65 GHz was chosen as the operating frequency of the CT system, so that the position of the soot deposits could be determined without artifacts from the structure of the filter affecting the image.

A schematic diagram of the CT imaging system is shown in Fig. 17.7. A 65 GHz Gunn oscillator was employed as the source, and the output was collimated using a horn antenna and a dielectric lens. The beam diameter was reduced using two parabolic mirrors, to a full-width at half-maximum beam of 9.4 mm, and the sample was placed on an X - Z - θ stage in the path of the collimated beam. Since the sample was cylindrical, it behaved as a rod lens, and so it was enclosed within a Teflon cover to prevent refraction at the sample/air interface. As shown in Fig. 17.8, a test filter with a non-uniform distribution of soot was used. A reconstructed 3D image obtained using a FBP method is shown in Fig. 17.9. The regions of accumulated soot can clearly be seen. Some loss of resolution and distortion of the image occurs

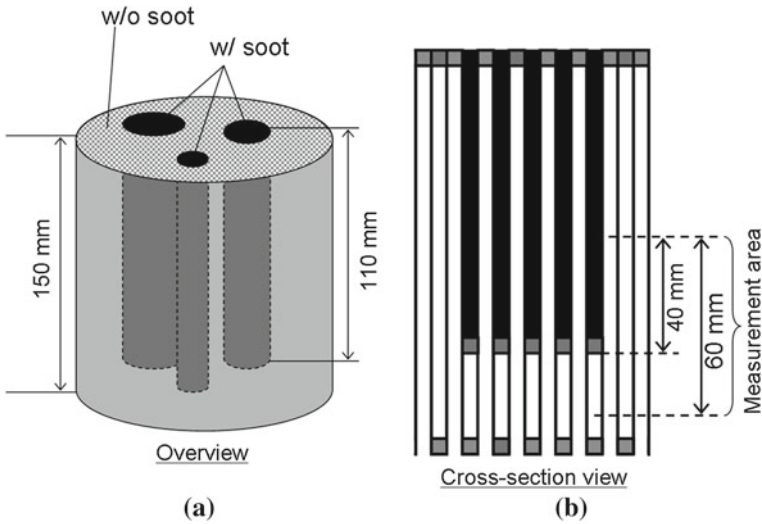


Fig. 17.8 Schematic diagram of the test sample of the soot-removal filter. **a** Soot is located in the three 110 mm-long cylindrical regions shown in black. The density of the soot is 4.7 g/L. The final 40 mm of the filter does not contain any soot. **b** Microstructure of the sample soot-removal filter. The soot is located in the inlet regions of the filter, as shown by the black sections, and the sooty regions terminate part way along the length of the filter. The 60 mm-long measurement region is illustrated

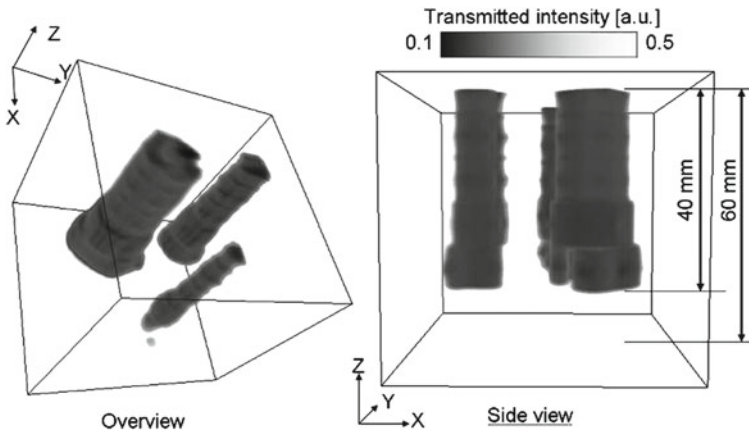


Fig. 17.9 The 3D-CT reconstructed image of the soot-removal filter

because of diffraction due to the mismatch of the refractive indices of the filter and the Teflon cover, and due to artifacts of the Fourier transform.

17.2 Time-of-Flight Terahertz Tomography

Time-of-flight terahertz (TOF-THz) tomography is based on a reflection-type THz-TDS system. Since the electromagnetic field in sub-picosecond terahertz pulses is measured directly using THz-TDS, the multilayered structure of a sample can be imaged by detecting the pulses reflected from the interfaces between layers. This technique is valuable in industry because the unique transmission characteristics of terahertz radiation enable inspection of multilayered paints in industrial products or tablet coatings [9, 10], which cannot be measured using optical coherence tomography (OCT) based on an optical light source [11].

17.2.1 Principle of TOF Tomography

The setup of a TOF-THz tomography system is illustrated in Fig. 17.10. If the sample has a multilayered structure, such as is shown in Fig. 17.10, the pulse is partially reflected because of the discontinuity in the refractive index at each interface, and details of the multilayer structure can be inferred from the reflected pulse train. If we assume that the THz pulse is normally incident on the sample, the delay Δt of the reflected pulse is determined from:

$$\Delta t = \frac{2n_g d}{c}, \quad (17.13)$$

where n_g , d , c are the refractive index, the thickness of each layer, and the speed of light, respectively. If the refractive index of the layers is known, d can be determined as follows by measuring the delay time of each pulse, i.e.,

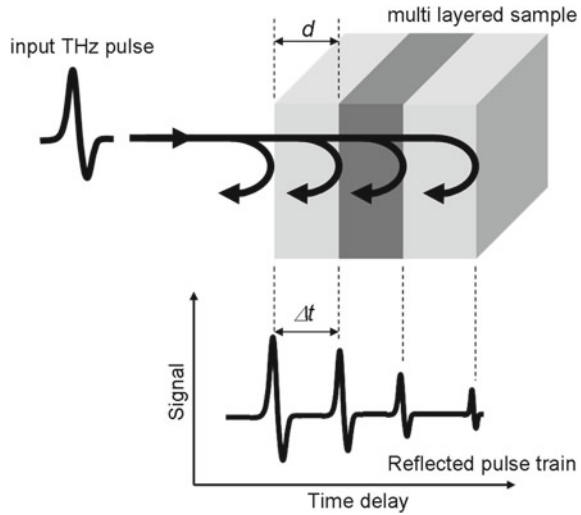
$$d = \frac{c\Delta t}{2n_g}. \quad (17.14)$$

This can readily be extended to samples where the THz pulse is incident on the sample at an angle θ , as follows

$$d = \frac{c\Delta t}{2n_g} \cos \theta. \quad (17.15)$$

The resolution depends on the width of the incident THz pulse, and is improved when the pulse is short. When the THz pulse is not ideal (e.g., a top-hat function), but varies with time in some anomalous manner, distinction of the reflected pulse becomes difficult, and ghost interfaces can appear in the tomographic image. These ghost images can be eliminated using signal processing, for example by employing deconvolution algorithms.

Fig. 17.10 Principle of TOF-THz tomography



Wiener deconvolution is typically used in tomographic sensing. The time variation of the reference, $x(t)$, and sample, $y(t)$, are assumed to be known. Here, $x(t)$ is the waveform of the THz pulse in the THz-TDS system, and $y(t)$ can be found by convolving this with the transfer function $h(t)$, where $h(t)$ is determined by the multilayer film structure of the sample, i.e.,

$$y(t) = \int_{-\infty}^{\infty} h(\tau)x(t - \tau)d\tau = h(t)*x(t). \tag{17.16}$$

This can be rewritten in the frequency domain as:

$$Y(\omega) = H(\omega) \cdot X(\omega). \tag{17.17}$$

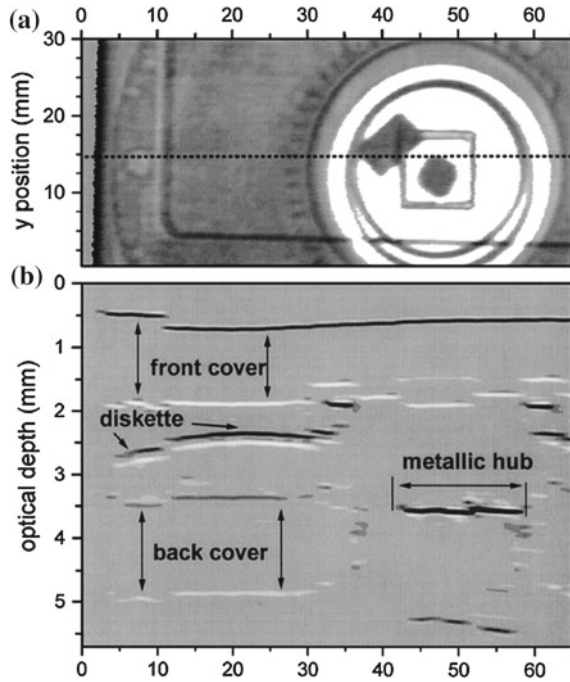
The inverse Fourier transformation of $H(\omega)$ is as follows:

$$h(t) = \mathfrak{F}^{-1} \left\{ Y(\omega) \cdot \frac{1}{X(\omega)} \right\}, \tag{17.18}$$

so that information on the structure of the sample, i.e., $h(t)$, can be obtained. Here, the Wiener filter is used so that the right-hand side of the expression (17.18) may diverge when a value with very small value of $X(\omega)$ is obtained. The Wiener filter, $W(\omega)$, is defined as:

$$W(\omega) = \frac{\overline{X}(\omega)}{|X(\omega)|^2 + 1/a}, \tag{17.19}$$

Fig. 17.11 **a** Conventional reflective THz image of a 3.5 in. floppy disk. **b** Tomographic image of the same floppy disk at a constant vertical position, indicated by the dashed line at $y = 15$ mm in **a**



where the term a is the ratio of the original function to noise. The Wiener filter modifies expression (17.18) so that we have:

$$h(t) = \mathfrak{F}^{-1} \left\{ Y(\omega) \cdot \frac{1}{W(\omega)} \right\}. \tag{17.20}$$

Additional artifacts of the THz pulse can be removed by using windowing, further improving the ability to correctly detect interfaces.

17.2.2 Examples of TOF-THz Tomography

In 1997, Mittleman et al. used TOF tomography to obtain a tomographic image of a floppy disk, and compared it with a conventional THz 2D image [12]. Figure 17.11a shows a conventional THz reflective image, and Fig. 17.11b shows a tomographic image of the same sample. The internal structures are visible in the tomographic image, including the cover, diskette, and metallic hub. The tomographic image in Fig. 17.11a is composed of an array of time-delayed pulses along the line $y = 15$. Figure 17.12b shows the raw reflected-waveform data from a single point in the image. It is not easy to distinguish each interface in the reflected pulse train, because

Fig. 17.12 **a** The THz pulse. **b** The reflected waveform from a single point on the 3.5 in. floppy disk. The curve shown in **c** is the reflected waveform after signal processing. Curve **d** is the refractive index profile of the medium (right-hand axis), derived from curve **c** using Eqs. (17.3) and (17.4)

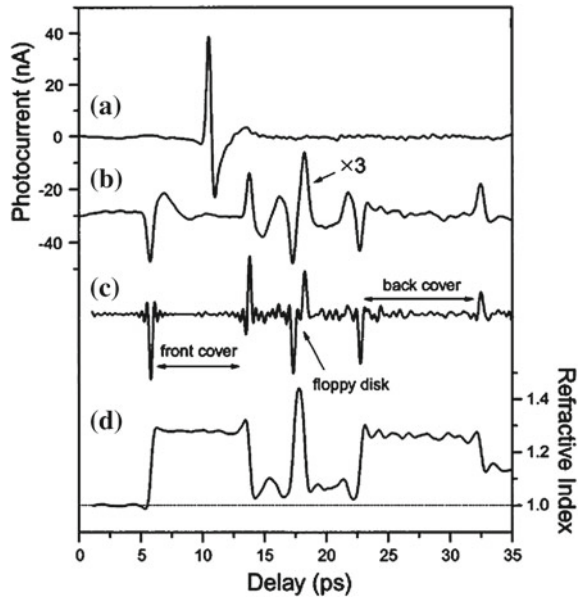
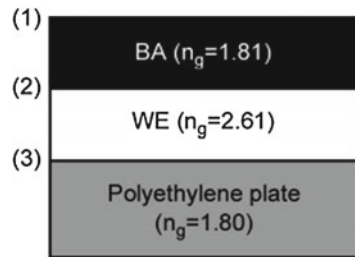


Fig. 17.13 The layer structure of the sample



of the form of the THz pulse. Figure 17.12c shows the reflected pulse train after deconvolution and filtering. The location of the interfaces is much easier to detect in the processed signal. The positive features in the processed waveform correspond to interfaces where the THz beam transitioned from a high-refractive-index medium to a lower refractive index medium, and vice versa for the negative features.

In 2005, Yasui et al. demonstrated tomographic imaging of paint on car body panels using TOF-THz tomography [13]. It is difficult to determine the thickness of each layer using conventional methods. The measured sample is a two-layer paint film, as illustrated in Fig. 17.13. Black acrylic (BA) and white enamel (WE) paints were layered on a polyethylene substrate. The group refractive indexes of BA, WE, and polyethylene are 1.81, 2.61, and 1.80 respectively. Figure 17.15 shows the impulse response signal of the reflected THz pulse train at a single point in the two-layer paint film, where numerical Fourier deconvolution was used to improve the detection of the interfaces. The first two (positive) pulses correspond to the air–BA

Fig. 17.14 The THz signal reflected from a single point on the sample. The numbers correspond to the location of the interfaces in the multilayer structure

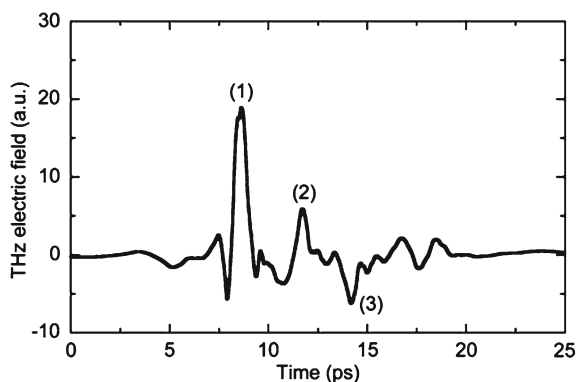
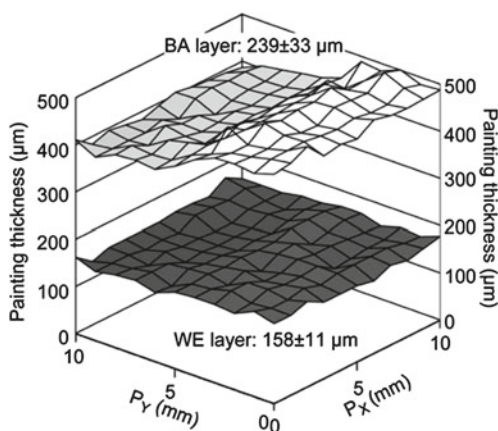


Fig. 17.15 Spatial distribution of the interfaces in a multilayer paint film on a dielectric substrate



and BA–WE boundaries, and the third (negative) pulse corresponds to the WE–substrate boundary. Figure 17.15 shows the spatial variation of the location of the interfaces in the paint film, calculated from the time delay and the group refractive index.

Yasui et al. demonstrated monitoring of the drying process of a single-layer film. As a process to control paint quality, monitoring of paint drying is often required in addition to measurement of the final thickness. The shape of the reflected pulse train will change depending on the dryness of the sample if the refractive index or absorption coefficient of the sample varies depending on whether the paint is wet or dry. Figure 17.16 shows the reflected pulse train from the sample before and after painting. Only one pulse from the air–substrate boundary is observed before painting, while two pulses, from the air–BA and BA–substrate boundaries, appear after painting. The difference in the delay time between the two reflected pulses shortened as the paint dried, and it can be seen that the drying process finished after about 10 min.

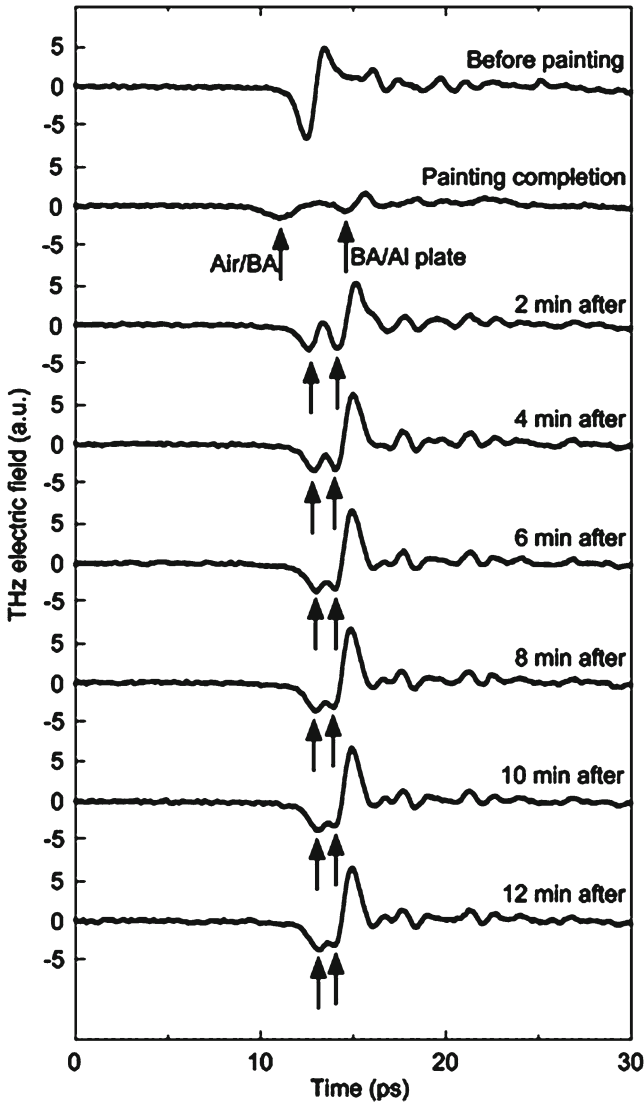


Fig. 17.16 Evolution of a reflected THz pulse train before and after painting. No change in the signal is seen after 10 min, indicating that the paint has dried

Improvement in depth resolution, output power, and robustness, as well as a reduction in the size of the system, are required for industrial applications. Takayanagi et al. developed a TOF tomography system with improved depth resolution using a femtosecond fiber laser system for the pump source [14]. They developed an all-fiber laser system that produced 17 fs optical pulses at a wavelength of 1.56 μm ,

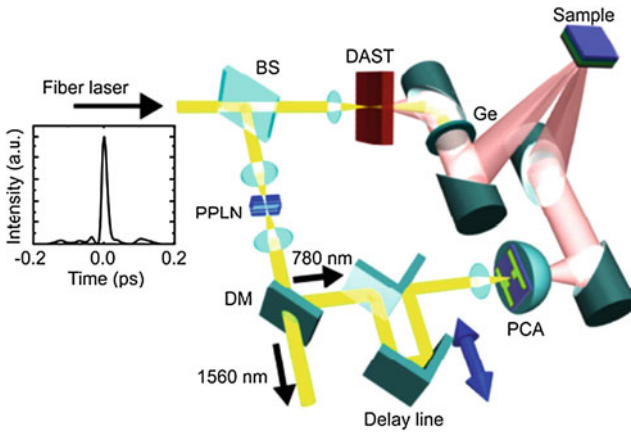
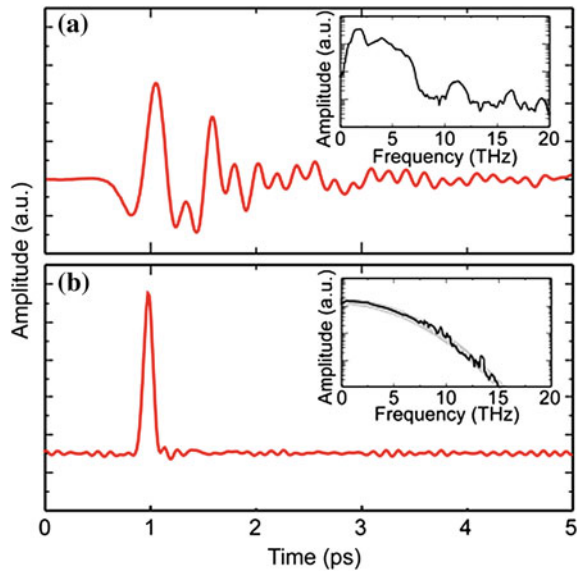


Fig. 17.17 Experimental setup of a high-resolution TOF-THz tomography system using a fiber laser. The inset shows the waveform of the 17 fs fiber laser. *BS* beam splitter; *PPLN* periodically poled lithium niobate; *DM* dichroic mirror; *PCA* photoconductive antenna; *Ge* germanium plate

Fig. 17.18 The reflected THz pulse raw data (a) and after signal processing (b). The insets show the corresponding Fourier transforms. The *gray curve* in the inset of (b) shows the Fourier transform of a Gaussian pulse



and generated and detected broadband terahertz pulses ranging from 0.1 to 27 THz. Their experimental TOF-THz tomography setup is shown in Fig. 17.17; the insert shows the compressed optical pulses. The average power of the pulses was 200 mW, and the repetition rate was 48 MHz.

Figure 17.18a shows the reflected THz signal when an aluminum plate was placed at the sample position. The maximum amplitude is at around 1 ps, with further oscillating components for a few picoseconds afterwards, due to a peculiar

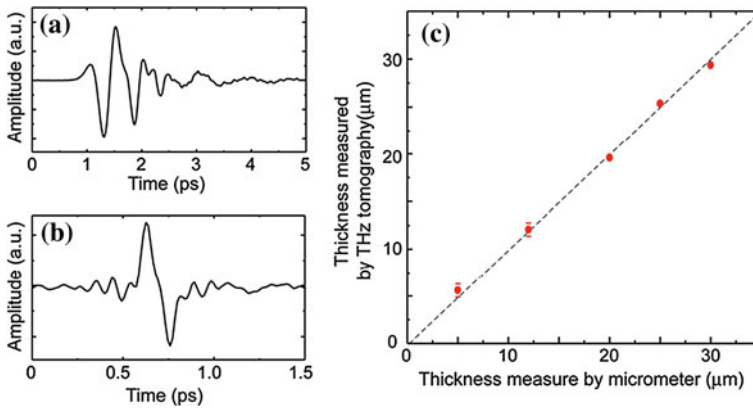


Fig. 17.19 Evaluation of axial resolution using Teflon films. **a** Typical measured reflected pulse, **b** the reflected pulse after signal processing, and **c** the thickness of the Teflon films measured with TOF-THz as a function of thickness measured using a micrometer

absorption characteristic of DAST crystal. This anomalous reflected waveform makes it more difficult to detect interfaces as compared with THz pulse generation using a photoconductive antenna, and signal processing is required to improve the data. Figure 17.18b shows a processed waveform using the data shown in Fig. 17.18a, which has a single peak.

Figure 17.19 shows the TOF-THz data for a Teflon film of varying thickness. Teflon membranes of thickness 5, 12, 20, 25, and 30 microns were used for the measurements. Figure 17.19a and b are reflected THz pulses before and after signal processing from the 12 μm-thick Teflon film. The two interfaces defining the film can be clearly observed in the processed signal. Figure 17.19c shows tomographic measurements of the thickness of the Teflon films. The depth resolution of this system is better than $10/n$ microns, where $n = 1.9$ is the refractive index of the Teflon membrane. It is anticipated that this technology will lead to the development of systems capable of inspecting the thickness of thin films in applications such as inspecting paint, human skin, and the peel of farm fruit and vegetable products.

References

1. B. Hu, M. Nuss, *Opt. Lett.* **20**, 1716 (1995)
2. D. Mittleman, M. Gupta, R. Neelamani, R. Baraniuk, J. Rudd, M. Koch, *Appl. Phys. B Laser Opt.* **68**, 1085 (1999)
3. R. Woodward, B. Cole, V. Wallace, R. Pye, D. Arnone, E. Linfield, M. Pepper, *Phys. Med. Biol.* **47**, 3853 (2002)
4. K. Kawase, Y. Ogawa, Y. Watanabe, H. Inoue, *Opt. Express* **11**, 2549 (2003)
5. A. Dobroiu, M. Yamashita, Y. Ohshima, C. Otani, K. Kawase, *Appl. Opt.* **43**, 5637 (2004)
6. G.T. Herman, *Image Reconstruction from Projections—The Fundamentals of Computerized Tomography* (Academic, New York, 1980)

7. B. Ferguson, S. Wang, D. Gray, D. Abbot, X.C. Zhang, *Opt. Lett.* **27**, 1312 (2002)
8. T. Shibuya, T. Suzuki, K. Suizu, K. Kawase, *J. Infrared Millim. THz waves.* doi:[10.1007/s10762-010-9672-6](https://doi.org/10.1007/s10762-010-9672-6)
9. H. Zhao, X. Guang, J. Huang, *Phys. E* **40**, 3025 (2008)
10. B. Wang, G. Wang, *Appl. Phys. Lett.* **87**, 013107 (2005)
11. W. Lin, G. Wang, *Appl. Phys. Lett.* **91**, 143121 (2007)
12. D. Mittleman, S. Hunsche, L. Boivin, M. Nuss, *Opt. Lett.* **22**, 904 (1997)
13. T. Yasui, T. Yasuda, K. Sawanaka, T. Araki, *Appl. Opt.* **44**, 6849 (2005)
14. J. Takayanagi, H. Jinno, S. Ichino, K. Suizu, M. Yamashita, T. Ouchi, S. Kasai, H. Ohtake, H. Uchida, N. Nishizawa, K. Kawase, *Opt. Express* **17**, 7549 (2009)

Chapter 18

Industrial Applications of Terahertz Imaging

J. Axel Zeitler and Yao-Chun Shen

Abstract This chapter gives a concise overview of potential industrial applications for terahertz imaging that have been reported over the past decade with a discussion of the major advantages and limitations of each approach. In the second half of the chapter we discuss in more detail how terahertz imaging can be used to investigate the microstructure of pharmaceutical dosage forms. A particular focus in this context is the nondestructive measurement of the coating thickness of polymer coated tablets, both by means of high resolution offline imaging in research and development as well as for in-line quality control during production.

18.1 Introduction

The advent of terahertz time-domain technology has brought with it a keen interest in its use in imaging experiments [1–3]. A number of imaging application examples have been reported: metal contacts of a packaged integrated circuit chip, as well as the leaf structure of plants [1]; polymer composites and flames [2]; breakfast cereals and chocolate [4]; tree-ring analysis [5]; medical tissues (see Chap. 16 by MacPherson in this book); analysis of polymer samples [6] and pharmaceutical tablets [7–9], among many other examples. A number of reviews and book chapters have summarised the recent progress in terahertz imaging [4, 6, 10–19]. However, despite the interesting

J. A. Zeitler (✉)
Department of Chemical Engineering and Biotechnology,
University of Cambridge, Cambridge CB2 3RA, UK
e-mail: jaz22@cam.ac.uk

Y.-C. Shen
Department of Electrical Engineering and Electronics,
University of Liverpool, Brownlow Hill, Liverpool L69 3GJ, UK
e-mail: y.c.shen@liverpool.ac.uk

results introduced by all these studies, only a select few applications show industrial promise or have already been successfully demonstrated in an industrial setting.

This chapter briefly highlights some potential areas of industrial application and then focuses specifically on applications in the pharmaceutical industry, a field that shows great promise for industrial terahertz applications.

18.2 Industrial Imaging

18.2.1 General Principles

In order to exploit the unique properties of terahertz radiation for imaging applications in an industrial context commercial imaging technology is required. The instruments need to be rugged and robust enough to operate in an industrial manufacturing environment, while at the same time providing sufficient sensitivity to measure the required process parameters. The cost and reliability of the equipment are further critical factors and, most importantly, there needs to be a compelling case in terms of economic benefits to industry to invest in this relatively young technology rather than the more established measurement sensors.

In one of the first reviews on terahertz imaging more than 15 years ago, Mittleman, Jacobsen and Nuss provided a compelling case for using terahertz technology for the quality control of polymer materials [2]:

“Detection of [air pockets in polymer foam bonds] is a significant quality control issue, and no simple method currently exists. X-ray transmission does not provide a high contrast between the plastic-rubber foam and the air; in addition, health and safety issues preclude the use of X-ray diagnostics here. Ultrasound analysis is effective only with the use of an index-matching fluid, while other probing techniques such as magnetic resonance imaging are too expensive and cumbersome. Probing the parts with microwaves would work quite nicely, except that it would be difficult to detect voids significantly smaller than the wavelength of the radiation used. Since, in this case, it is desirable to detect voids smaller than one centimetre in diameter, this effectively eliminates conventional microwave analysis from consideration.”

In fact, all industrial terahertz imaging applications that have been discussed since are based on this unique combination of high imaging contrast and sufficiently high spatial resolution; as well as inherent safety. Mittleman, Jacobsen and Nuss go on to state that [2]:

“It should be emphasised that one could detect voids of this sort without relying on [small differences in transmittance] by observing the *transit time* of the terahertz pulse through the material, rather than the transmitted *amplitude*. The combination of the amplitude and phase information measured in THz-TDS make for a very powerful tool for quality control measurements.”

The coherent detection scheme together with the resulting time-domain signal of the terahertz pulse lead to the high sensitivity and excellent contrast that can be

achieved in terahertz imaging. This is a major difference to conventional far-infrared technology and it is this property that makes terahertz imaging attractive for industrial applications.

Over the past decade, key developments were initiated by the commercial terahertz equipment manufacturers. During this period the two major drivers in the field were TeraView Ltd. in Cambridge, UK, and Picometrix LLC, Ann Arbor, MI, USA. Both companies have successfully demonstrated new industrial applications, have developed terahertz sensors that can be used in a manufacturing environment and have installed such instruments across a range of industries. At the same time a number of smaller companies have formed and this has greatly accelerated the further development of more robust instrumentation. With the advent of cheaper 800 nm fibre laser technology, an increased interest from more established optics companies and a growing awareness of the potential of terahertz technology by industrial end users, industrial imaging applications have grown considerably.

Most of the studies that have explored the industrial applications of terahertz technology reviewed in this chapter, are proof-of-principle experiments that demonstrate what information terahertz images can reveal. However, there are a few published examples where terahertz sensors were used to measure samples directly under industrial processing conditions. The examples range from the automated imaging of coated pharmaceutical tablets to investigate the thickness and homogeneity of polymer coatings [20]; an in-line sensor that was developed to monitor a polymer compounding process [21]; an in-line thickness gauge to measure the thickness of polymer laminates during production [22]; and an in-line sensor that was demonstrated to measure the thickness of polymer coatings on individual tablets during production [23].

However, in order to establish itself long-term as a complementary imaging technique in nondestructive testing [24–26], terahertz imaging has to further demonstrate how it will add value to currently available technologies. The main competing technologies are X-Ray tomography and imaging; ultrasound testing [27]; infrared thermography; eddy current testing, and optical coherence tomography (OCT) [28].

18.2.2 Contrast Mechanisms

Before we start looking into specific examples of imaging applications we would like to highlight briefly the main physical phenomena that give rise to contrast in terahertz images. The fundamental imaging principles were first described by Mittleman et al. [3] and, for more detail, we would like to refer the reader to the Chap. 17 by Shibuya and Kawase, which provides an excellent introduction to the concept of terahertz pulsed imaging and terahertz tomography. For a good introduction to general terahertz imaging, see Lee [17].

In addition to the standard image signal processing and data analysis techniques, further refinements were developed to improve the extraction of optical constants from transmission measurements of thin single layer samples [29] as well as

multilayered samples [30]. However, other measurement techniques, such as OCT, are more mature and readily suited to measure the thickness of thin samples. For this reason, and due to the limited power that can be generated with the currently available pulsed terahertz sources, most industrial imaging applications are currently performed in reflection mode.

Industrial applications of terahertz imaging will most likely involve the analysis of solid samples that are highly transparent to terahertz radiation and where contrast is achieved either by a change in refractive index, absorption coefficient or scattering.

18.2.2.1 Dielectric Properties and Vibrational Modes

Chapter 8, by Parrott et al., provides an overview of the spectroscopic properties of solids at terahertz frequencies. The main contrast mechanism that is typically exploited in terahertz time-domain reflection, or tomographic, imaging is the difference in refractive index between two materials. In time-domain terahertz imaging the field E of the electromagnetic wave, rather than its intensity, is measured and hence the reflectivity R is

$$R = \frac{|E_{\text{interface}}|^2}{|E_0|^2} = \frac{(n_1 - n_2)^2}{(n_1 + n_2)^2}, \quad (18.1)$$

where $E_{\text{interface}}$ denotes the electric field of the electromagnetic wave of the reflection from the sample interface and E_0 is the reflection from a reference, typically a mirror, and n_1 and n_2 are the refractive indices of the two media that the terahertz pulse is propagating through.

As the terahertz pulse is propagating through the sample a reflection will occur whenever there is a change in refractive index. This change in refractive index can either be due to the propagation of the pulse from one type of material into another or it can be due to a distinct difference in density of the sample matrix which in turn is reflected in a change in optical density.

In most (semi-)transparent materials at terahertz frequencies the refractive index does not change significantly across the frequency components of the terahertz pulse. However, as detailed in Chaps. 7 and 8, in some crystalline materials the intermolecular vibrational modes fall into the terahertz frequency range, and hence pronounced changes in both the absorption coefficient and refractive index can be observed at the distinct frequencies of the vibrational modes.

This change in optical properties can be used to generate contrast in the resulting terahertz images when processing the image data in the frequency domain. It is possible to identify a wide range of small organic molecules [31, 32]; different crystal structures of the same molecule [33–35]; degradation products in polymers [36], and many other types of molecules as outlined in Chap. 8.

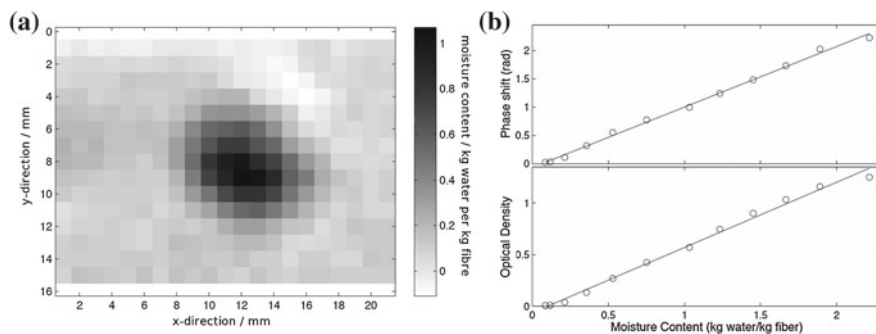


Fig. 18.1 **a** Transmission image through 80 g/m² paper at 0.6 THz showing the distribution of water in terms of absolute moisture content; **b** phase change (*upper panel*) and relative optical-density (*lower panel*) relative to the dry paper sample shown as a function of the water content in the moist sample (modified from [37])

18.2.2.2 Polar Liquids / Moisture

The optical properties are not only influenced by differences in density within the sample matrix or vibrational modes but there is also a strong attenuation of the terahertz pulse due to the presence of polar liquids, as outlined in Chaps. 9 and 16.

This effect can be exploited to quantify the amount of moisture in paper [37, 38] (Fig. 18.1), in food [39] or in non-polar liquids such as crude oil [40]. In such applications terahertz techniques were shown to have advantages in detection sensitivity, acquisition speed and much reduced scattering effects when compared to infrared techniques.

18.2.2.3 Conductivity

As outlined in Chap. 8, Sect. 8.4.2 the conductivity σ of the sample is related to the dielectric constants by $\epsilon = \epsilon_{\infty} + i(\sigma)/(\omega\epsilon_0)$. This means that, with increasing conductivity, both the absorption coefficient and refractive index also increase as $\epsilon = \epsilon' + i\epsilon'' = (n + i\kappa)^2$.

This property can be exploited for the characterisation of the electronic properties of catalysts. Using quantitative physical models it is possible to extract the defect density as well as the graphicity of catalytically active carbon materials such as carbon nanofibres [41]. The same approach can also be used to analyse the electronic properties of hydrocarbons that form on the surface of a catalyst during heterogeneous catalysis. Depending on the reaction conditions, the hydrocarbons can either lead to unwanted deactivation of the catalyst or the carbon structure can play an active role in the catalytic reaction [42–44].

18.2.3 *Nondestructive Testing*

In the field of non-destructive testing a wide range of materials from different industries has been analysed. Typically, the most successful applications have involved materials that are quite transparent at terahertz frequencies. In the food industry the main applications have been the detection of potential contaminations within a food matrix, such as glass splinters in chocolate [4, 45], or to assess the homogeneity of mixtures, such as raisins and cereal, in a boxed product [4]. In contrast a lot more work has been reported for NDT applications in the fields of polymers and ceramics, both again classes of materials that are mostly transparent at terahertz frequencies.

Starting from the early work by Mittleman et al. [2] on composite plastic parts (Fig. 18.2) the basic imaging concept was applied to image the integrity of the space shuttle fuel tank foam insulation [46]. The authors showed that it is possible to locate voids and disbonds that were intentionally incorporated within a test piece of foam insulation using time-domain terahertz imaging. The study by Picometrix showed that it is possible to use a terahertz sensor that was attached to a 30 m long optical fibre in such imaging applications. A similar study investigating the integrity of polyurethane foam was also reported at the same time by Zhong et al. in collaboration with Lockheed Martin [47]. These studies attracted considerable attention both in the terahertz, as well as the wider NDT community. The technology was subsequently evaluated by NASA for its suitability to detect nondestructively the early onset of corrosion on the metal surface under tiles up to 76 mm of thickness used as part of space shuttle insulation [48]. The authors concluded that terahertz imaging was a unique NDT technique for detecting hidden corrosion under the space shuttle tiles, which was previously considered undetectable when there is only access from one side of the structure. Zimdars et al. showed how the entire volume of samples of Kevlar soft shell fan containment systems, silica thermal protection tiles and sprayed on foam thermal insulation can be analysed using terahertz computed tomography [49].

Chapter 13 by Jansen et al., gives a comprehensive overview of how terahertz radiation can be used to analyse polymers together with selected examples of applications. However, as this chapter is primarily concerned with industrial applications of terahertz imaging, it seems appropriate to highlight a few select studies that fall into this remit. Morita et al. published two studies that demonstrated the ability of terahertz NDT to detect leaks as small as 30–40 μm in plastic packaging materials [50] and how this technique could be used for food applications [51]. Again, the main advantages of the technique highlighted by these two studies, compared to competing technologies such as ultrasound, were that no immersion in matching refractive index liquid is required in THz NDT and that it is suitable to investigate opaque materials. Further examples of potential industrial applications of terahertz imaging are the investigation of the fibre alignment in reinforced plastics [52] and the coating integrity of jet engine turbine blades [53, 54]. A good overall summary of the current state of THz NDT applications recently published by Lopato et al. [55] and Hsu et al. provide some interesting insights into recent developments [56].

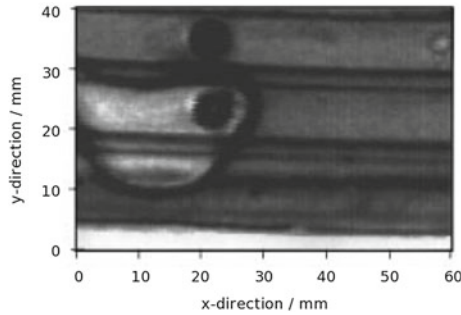


Fig. 18.2 Terahertz image of a moulded composite plastic piece made from two parallel black plastic sheets, with a rubberised foam padding between them. The foam is sprayed between the plastic sheets, holding them together when it dries. The image shows the presence of a defect of roughly 20 mm diameter in the internal foam-filled region on the left of the part (modified from [2])

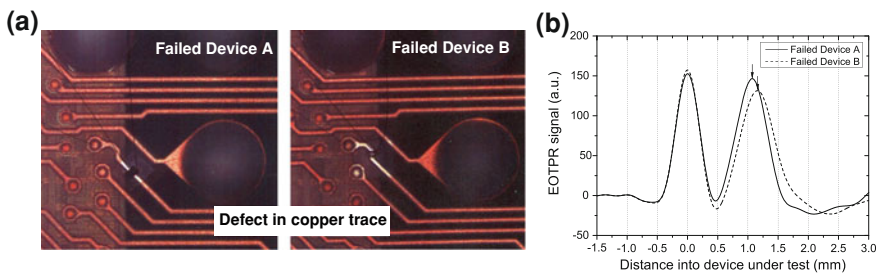


Fig. 18.3 Electro Optical Terahertz Pulse Reflectometry (EOTPR) for semiconductor fault testing. **a** Optical images of the two failed devices showing the cut in the copper traces. **b** Results obtained with EOTPR (source: TeraView Ltd.)

Recently, interest in semiconductor failure testing using pulsed terahertz radiation has rekindled. Very promising results in microelectronic package fault isolation and failure analysis have been reported where the new terahertz instrument shows significant advantages over conventional time-domain reflectometry, both in terms of the resolution that can be achieved as well as the bandwidth and measurement speed [57, 58]. Figure 18.3 shows Electro Optical Terahertz Pulse Reflectometry (EOTPR) results from an accuracy test. Here, the aim was to measure the difference in distance between two cut copper traces in the same circuit of two identical integrated circuit devices. The difference in position of the leading edge of the cut is $89 \mu\text{m}$. During operation pulses are launched into the device under test via a high frequency circuit probe. Portions of the pulse are reflected back as it encounters changes in impedance within the integrated circuit such as open or short circuit defects. Reflections are recorded as a function of time and result in the EOTPR waveform. The arrows on plot b) of Fig. 18.3 indicate the reflections due to the cut in the copper traces. The positive reflection indicates that the cut has resulted in an open circuit. The peak posi-

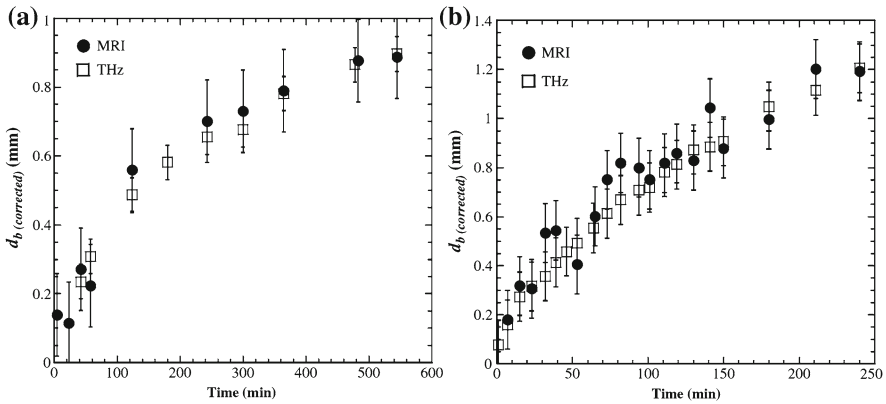


Fig. 18.4 Nondestructive measurement of the penetration front of a solvent (in this case acetone) into different polymers at room temperature: **a** polycarbonate; and **b** polyvinylchloride. The terahertz data was acquired in reflection through the polymer sample. The results were compared to MRI analysis of similar samples and excellent agreement was found (modified from [59])

tion gives the location of the fault and from the location we can obtain the separation between the faults in devices A and B. This example illustrates how EOTPR can be used to identify a fault and determine its location. As this development is driven by the semiconductor industry together with terahertz instrument manufacturers, this field of industrial applications is likely to grow considerably in the coming years.

Another very interesting application of terahertz imaging is the measurement of liquid ingress into polymers as described by Obradovic et al. [59]. Using terahertz reflection imaging it was possible to quantify the ingress of acetone into two samples of polymer (Fig. 18.4). The results of this study suggested that terahertz imaging has the potential to characterise liquid mobility and subsequent conformational changes in the polymer matrix.

Two studies that should be mentioned in the field of polymer analysis in an industrial context are the development of an online polymer compounding sensor that can be used to monitor the compounding process during manufacture [21], and an in-line terahertz measurement gauge that was developed to control the lamination process of a two-layer roofing plastic insulation membrane [22]. The latter study demonstrated that the layer thickness of the laminate can be measured reliably and, at the same time, that delaminations can be detected in real time during process conditions (Fig. 18.5). The work is of particular significance as, rather than as part of a proof-of-principle study, this measurement sensor was installed on the production line of a company. To our knowledge, this is the first time that a terahertz sensor has been endorsed by an industrial end user in this way and put to routine use in a manufacturing environment.

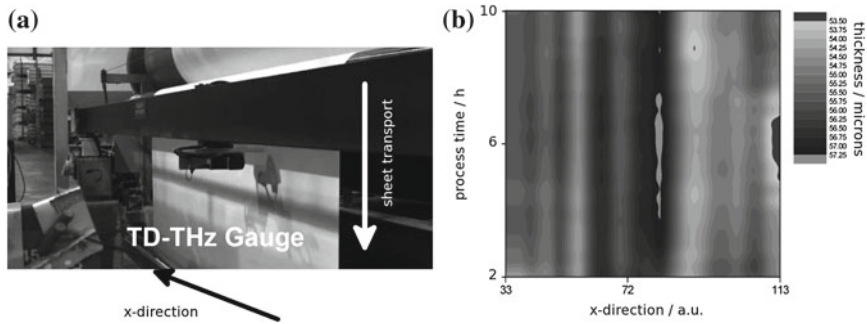


Fig. 18.5 Terahertz gauge mounted on a gantry in the production line of the plastic sheet lamination process. **a** Photograph of the setup; **b** Measurement results over process time. The total thickness of the sheet is represented by different grey values (modified from [22])

18.2.4 Real-Time Imaging

As the previous section shows, there are a number of exciting applications for terahertz imaging in an industrial context. However, from the technology point of view, one considerable limitation is that all imaging experiments have to be performed by raster scanning over the object of interest. The image is mapped out pixel by pixel, which can take anything between a couple of minutes to a couple of hours depending on the size of the object and the spatial resolution required for the particular application. This lack of real-time imaging capability is a genuine limitation of terahertz imaging as it limits the current industrial imaging applications to 1D measurements in process control (e.g. terahertz depth gauge, with process time providing the second dimension) or to offline 2D and 3D measurements with limited throughput in terms of number of samples or size of object that can be analysed.

The first successful demonstration of how to achieve real-time 2D imaging using terahertz radiation was made by Wu et al. [60–62]. For this purpose the same measurement concept that is commonly used in the detection of terahertz pulses in THz-TDS, as outlined in detail in Chap. 1, was used in a 2D configuration rather than in 1D. Using frequency upconversion by means of an electro-optic crystal such as ZnTe it was possible to image the terahertz beam using a CCD focal-plane camera. In this configuration imaging is performed in transmission and the image quality is limited by the low brightness of the commonly used pulsed sources as well as the purity of the ZnTe crystal which limits its applications. However, the advantage of this technology is that the terahertz pulses are inherently broadband, and hence spectral information of the samples can be analysed easily. This imaging concept has been used to discern different chemicals [63, 64], monitoring the drying process of paint [65] and revealing hidden objects in plastic pipes and polymer matrices [66].

Using a gas laser operating at 2.52 THz, Lee and Hu took this 2D imaging concept forward to achieve faster acquisition speeds by utilising a focal plane array detector and exploiting the much higher brightness of the gas laser (10 mW output power

compared to μW power in the time-domain systems), thereby achieving a much better signal-to-noise ratio at frame rates of up to 60 frames per second [67]. They later demonstrated the same imaging principle by using more compact Quantum Cascade Lasers [68] instead of the gas laser [69]. This development potentially opens up new opportunities by utilising QCLs that can be switched between different output frequencies [70] as well as by extending the imaging work to tomography applications [71].

18.3 Pharmaceutical Industry

18.3.1 *Specific Imaging Requirements*

In the pharmaceutical industry the most commonly used, and most commercially valuable, dosage form for administering a drug to a patient is the tablet. A tablet is a compacted powder designed to be swallowed. Once it reaches the desired site in the gastrointestinal tract—either the stomach, the small intestines or the colon—it will disintegrate. The drug molecules will subsequently dissolve and, once in solution absorption (typically through the intestinal mucosa) occurs before the drug is distributed throughout the body by blood circulation.

The microstructure, distribution, particle size and morphology of all materials that are part of the tablet formulation, such as the drug molecules and the excipient components, have a strong impact on physical attributes that are important during manufacture. These include tablet hardness, robustness and adhesion to the tablet punch, as well as more chemical characteristics such as the stability of the drug molecules which, in turn, influences the tablet shelf-life and ultimately its bioavailability, i.e. how much of the drug molecules actually reaches the bloodstream.

In recent years solid dosage forms with sophisticated polymer coatings, or insoluble porous matrix structures, have been developed. Such advanced drug delivery techniques have gained more and more importance in order to meet increasing expectations for efficient and controlled drug delivery. This in turn has resulted in more complex processes for the production of such structures, which require exact control to ensure the quality of the resulting product. Consequently, there is a strong demand in the pharmaceutical industry for non-destructive imaging technology to assess the microstructure of the tablet throughout product development and manufacturing in order to ensure its quality while optimising the productivity and, ultimately, profitability.

Various imaging methods have been proposed to assess product performance and quality through evaluating the physical and chemical uniformity within a tablet [8, 72, 73]. Infrared and/or FTIR-Raman imaging are able to reveal the uniformity of drug molecules of a sample (near the surface). However, using this technique, a full 3D chemical map would require slicing through the tablet many times: an approach which is destructive, time-consuming and which may introduce artefacts to the tablet

under investigation. On the other hand, X-ray computed microtomography provides a full high resolution 3D map of the microstructure of a tablet; yet its contrast is limited by the small differences in electron density within a typical formulation (except for inorganic pigments that are used in some coatings). It has thus little or no chemical specificity to differentiate: for example, drug molecules from excipients within a tablet. In addition, the data acquisition and reconstruction is relatively time-consuming and there can be safety concerns when using ionising radiation depending on the environment the instrument is operated within.

As discussed above, the ‘ideal’ imaging technique should be capable of mapping and analysing the internal structures within complex pharmaceutical products non-destructively. It should be able to reveal structural defects such as coating delamination, capping and cracking inside a tablet, as well as having the ability to map chemical non-uniformities such as a segregation of drug and excipient particles. The technique needs to be non-destructive and non-invasive (leaving the sample intact and in its original state during analysis), accurate and efficient, easy and safe to use.

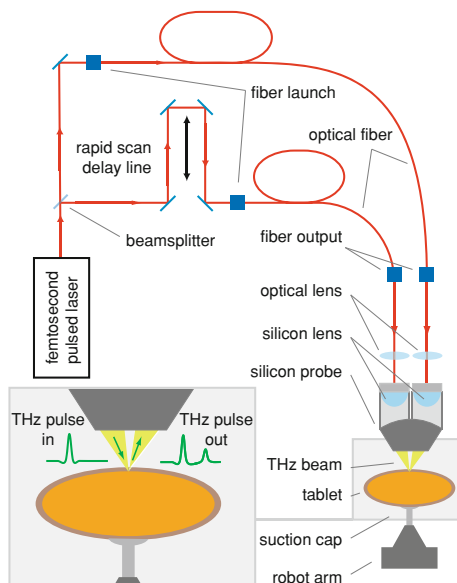
Imaging of pharmaceutical dosage forms using terahertz radiation is a very attractive option due to the fact that most materials that are used as excipients for tablets are amorphous and hence do not exhibit any distinct spectral features while at the same time they are (semi-)transparent. This makes it possible to carry out non-destructive imaging at depth due to the high penetration depth that can be achieved. On the other hand, most drug molecules are small organic molecular crystals and have distinct vibrational modes at terahertz frequencies (see Chap. 8 by Parrott et al. for further details). This means that not only can drug particles be identified within the tablet matrix but different drug molecules can be distinguished quantitatively.

In subsequent sections we will discuss first the practical aspects of terahertz imaging instrument/measurement in the context of pharmaceutical applications, followed by an overview of some recent application highlights of terahertz imaging in pharmaceuticals and solid dosage forms. A number of more detailed technical reviews on pharmaceutical applications of terahertz time-domain spectroscopy and imaging were published recently and the reader is referred to these reviews for any further details that are beyond the scope of this chapter [7, 9, 74, 75].

18.3.2 Instrumentation

To date, the most commonly used terahertz imaging technique for the quantitative characterisation of pharmaceutical solids is terahertz time-domain spectroscopy in reflection, also referred to as terahertz pulsed imaging (TPI) [20, 76]. Figure 18.6 shows the schematic diagram of a typical TPI system (in this case the TPI imager 2000, TeraView Ltd., Cambridge, UK), which was specifically designed for applications in the pharmaceutical industry. The core technology of the TPI system is based on terahertz generation and detection using an ultrafast laser as described in Chap. 1 of this book by Freeman et al. In brief, a beam splitter separates the near-infrared laser light into an excitation beam and a probe beam. Terahertz pulses are generated by

Fig. 18.6 Schematic diagram of a typical terahertz imaging setup used to image pharmaceutical tablets. The tablet samples are manipulated using a six-axis robotic arm. The system is capable of automatically point mapping over the entire surface of an arbitrarily shaped tablet. This configuration is utilised in the TPI imaga 2000 instrument by TeraView Ltd. (modified from [20])



optical excitation of a biased photoconductive antenna [77]. In this system terahertz pulses emitted from the photoconductive antenna are collimated and focused onto the sample using a silicon lens system. The reflected and backscattered terahertz pulses are then collected and focused, using the same silicon lens system, onto an unbiased photoconductive antenna for the laser-gated terahertz detection [78].

In TPI measurements, the transient electric field of the terahertz pulses is recorded as a function of the time delay between the terahertz pulse and the optical probe pulse. By sweeping the optical delay using a rapid variable delay stage, the entire terahertz waveform can be measured in less than 10 ms. As most pharmaceutical tablet excipients are transparent or semi-transparent to terahertz radiation, terahertz pulses incident on a tablet surface will penetrate through different coating layers. At each coating interface or abrupt change in refractive index (between drug particles and excipient matrix), a portion of the terahertz pulse is reflected back to the detector. This provides the contrast mechanism to map the drug and interfaces from different coating layers or subsurface structures within the tablet (Fig. 18.7).

To acquire a TPI map of a tablet terahertz waveforms are measured at $200\ \mu\text{m}$ steps over the whole surface of a sample. Most pharmaceutical tablets have curved surfaces and, hence, a precise model of the surface shape and curvature of the tablet under investigation is the prerequisite for a reliable and quantitative TPI measurement. This surface model is obtained before the terahertz mapping step by using a laser gauge that uses a visible laser beam with a wavelength of $670\ \text{nm}$ [20]. The model is generated automatically by moving the tablet in front of the laser gauge using the six-axis robot system. Once the topology model is acquired it can be used to present the tablet sample to the terahertz optics. During the entire TPI mapping step the tablet

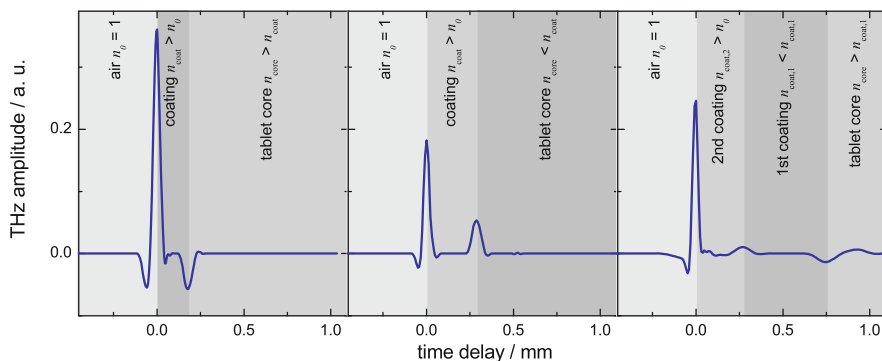


Fig. 18.7 Terahertz time-domain waveforms after signal processing of two samples of coated pharmaceutical tablets. The first two samples are coated with a single polymer layer. The *first reflection* is due to the interface between free space (air $n_0 = 1$) and the polymer coating. The *second reflection* originates from the interface between the polymer coating and the tablet core. In the sample on the *left* the refractive index on the coating material, n_{coat} , is higher than the refractive index of the tablet core, n_{core} , and hence a negative peak is observed. The opposite is the case for the sample in the *centre*. Here, $n_{\text{coat}} > n_{\text{core}}$, resulting in a second positive peak. In the third sample (*right*) there are two coating layers on top of one another with $n_{\text{coat},2} > n_{\text{coat},1} < n_{\text{core}}$

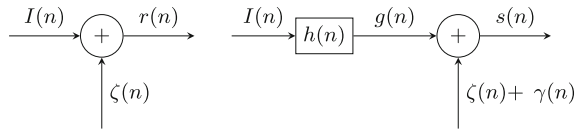
is kept precisely at the focal position with sample surface always perpendicular to the terahertz probe [79]. Consequently, no sample preparation is required and most pharmaceutical solid dosage forms with common shapes and surface curvatures can be directly imaged using this instrument [20].

In most imaging systems, in order to reduce the effects of water vapour absorption, the whole terahertz system and the sample under investigation have to be either purged with dry nitrogen gas or be evacuated throughout the measurement. However, this may not always be possible for some pharmaceutical solid dosage forms and is certainly not convenient for industry applications. By integrating both the THz emitter and detector into a specially designed silicon lens system (Fig. 18.6), the terahertz generation and detection are completely confined within the silicon lens system without any exposure of the terahertz pulse to the atmosphere before leaving the silicon optics. As the distance between the silicon lens and the sample is less than 8 mm, the effects of water vapour absorption on the terahertz waveform are minimal and no nitrogen purging is required, which greatly simplifies the measurements.

18.3.3 Signal Processing

The measured raw waveform is the convolution of the sample response and the system response of the instrument used as well as other effects such as systematic signal distortions, random noise and sample-structural effects.

Fig. 18.8 Block diagram in problem definition without sample (*left*) and with sample (*right*). Adapted from [84]



Of these effects the systematic distortions are the most significant contributors to TPI measurement errors as they cause time delays, dispersion, phase change and after-runners in the THz pulse [80]. Causes of these distortions include reflections and subsidiary oscillations in the emitter; water molecule resonance absorption as THz radiation propagates through the system, and dispersive effects of the waveguides. Random noise includes emitter noise resulting from intensity fluctuations in the ultrafast laser, Johnson- Nyquist noise generated by charge carriers in the substrate in the absence of THz electrical field, thermal background radiation and more [81, 82]. Without proper modelling, structural effects of the sample cannot be quantified, adding to the complexity of signal analysis. These structural effects include back reflection and scattering effects. Back reflections are also known as parasitic reflections. Usually the intensity of this is insignificant compared to the fundamental reflections but it can become significant when there is a lamination problem in which an air gap is present between different layers of the sample [79]. Compared to imaging techniques utilising infrared or visible radiation TPI suffers from relatively less scattering effects as terahertz radiation wavelengths are significantly larger than most of the scattering structures of a sample [83]. However, scattering effects can become significant when there are a significant number of edges on the sample, such as embossing and breaking on pharmaceutical tablets or when the surface is very rough.

18.3.3.1 Definition of the Problem

The definition of the signal processing problem is modified from Refs. [84] and [85] under the assumption that the TPI measurement system is a linear time-invariant (LTI) system. Figure 18.8 shows the block diagram of a TPI system without and with the sample respectively. We refer to a sample as a particular point on the pharmaceutical tablet under examination, which will later contribute to a pixel of the terahertz image.

$r(n)$ is the TPI measurement in free space. Since the TPI measurement is based on reflection, $r(n)$ is obtained from a perfect terahertz reflection on a mirror. It is commonly known as the reference signal.

$$r(n) = I(n) + \zeta(n) \quad (18.2)$$

$I(n)$ is the input signal generated by the THz emitter. $\zeta(n)$ captures the background effects and corresponds to the detector reading before the emitter generates THz pulse. It is commonly known as the baseline signal. $\zeta(n)$ can be considered as additive

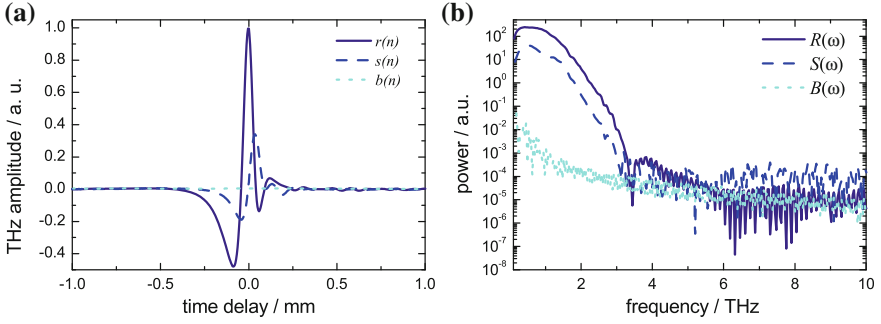


Fig. 18.9 Baseline, reference and raw sample signals in the: **a** time and **b** frequency domain

white Gaussian noise (AWGN), which is independently and identically distributed [86], and which is commonly referred to as the background signal.

A terahertz waveform comprises many time-discrete samples. Therefore, for theoretical clarity, the signal indices in the time domain are denoted by n instead of t in order to emphasise the discrete nature of TPI waveforms. The total number of data points, N , is large (usually $N = 512$), and hence the signals can be considered continuous in any mathematical operation.

When a sample is present in the TPI system, the resulting signal, also known as the sample signal $s(n)$ is:

$$s(n) = g(n) + \zeta(n) + \gamma(n) \quad (18.3)$$

$\zeta(n) + \gamma(n)$ is the system overall AWGN. $g(n)$ is the product of circular convolution (denoted by \otimes) of the input signal $I(n)$ and the original impulse response of the sample $h(n)$. Therefore, $s(n)$ can also be defined as:

$$s(n) = I(n) \otimes h(n) + \zeta(n) + \gamma(n) \quad (18.4)$$

Substituting Eq. 18.2 into 18.4 leads to

$$s(n) - \zeta(n) = (r(n) - \zeta(n)) \otimes h(n) + \gamma(n) \quad (18.5)$$

The objective of signal processing is to obtain $\bar{h}(n)$ (the estimate of $h(n)$), given the baseline $\zeta(n)$, reference $r(n)$ and sample signals $s(n)$. This operation is generally known as deconvolution, as it is an attempt to extract $h(n)$ from the convolution \otimes . Figure 18.9 shows the baseline, reference and sample signals acquired from a pharmaceutical tablet.

Since $\zeta(n)$ is AWGN and not convoluted, it can be removed by simple subtraction. Eq. 18.5 now becomes:

$$s'(n) = r'(n) \otimes h(n) + \gamma(n) \quad (18.6)$$

where $s'(n)$ and $r'(n)$ are baseline-subtracted $s(n)$ and $r(n)$. Baseline subtraction is always the first and necessary step of signal processing. For notation simplicity, $s(n)$ and $r(n)$ should now be understood as $s'(n)$ and $r'(n)$. The overall AWGN of the system is always higher in the presence of the sample as compared to the baseline; this difference is represented by $\gamma(n)$ in Eq. 18.6 (Fig. 18.10).

18.3.3.2 Inverse Filtering

Conventionally, the estimated sample signal $\bar{h}(n)$ is obtained by dividing the raw signal $s(n)$ with the reference signal $r(n)$ in frequency domain:

$$\bar{h}(n) = \text{FFT}^{-1} \left\{ \frac{\text{FFT}[s(n)]}{\text{FFT}[r(n)]} \right\} \quad (18.7)$$

Equation 18.6 written in the frequency domain becomes

$$S(\omega) \approx R(\omega)H(\omega) + \Gamma(\omega) \quad (18.8)$$

The division between $S(\omega)$ and $R(\omega)$ is then

$$\bar{H}(\omega) \approx \frac{S(\omega)}{R(\omega)} = H(\omega) + \frac{\Gamma(\omega)}{R(\omega)} \quad (18.9)$$

Equation 18.9 shows that the division in the frequency domain amplifies any high frequency noise in the signal particularly when $|R(\omega)| \approx 0$ [85]. Coupling the frequency domain division with an appropriate band-pass filter, $f(n)$, can suppress these anomalies. The deconvolution now becomes [87]:

$$\bar{h}(n) = \text{FFT}^{-1} \left\{ \frac{\text{FFT}[s(n)]}{\text{FFT}[r(n)]} \text{FFT}[f(n)] \right\} \quad (18.10)$$

This operation is generally known as inverse filtering. The band-pass filters that have been used in practice for terahertz signal deconvolution are the Double Gaussian (DG) and the Customised Skewed Gaussian (CSG) filters.

Double Gaussian filter

This is the most conventional filter used in TPI signal processing. Woodward et al. [88] and Pickwell et al. [89] used it to analyse TPI data for in vivo studies of human skin. As the name implies, it uses two Gaussian filters to act as high-pass and low-pass filters. The high-pass filter passes higher frequency components but attenuates lower frequency components. The opposite is true for low-pass filter. The time-domain DG filter is defined as:

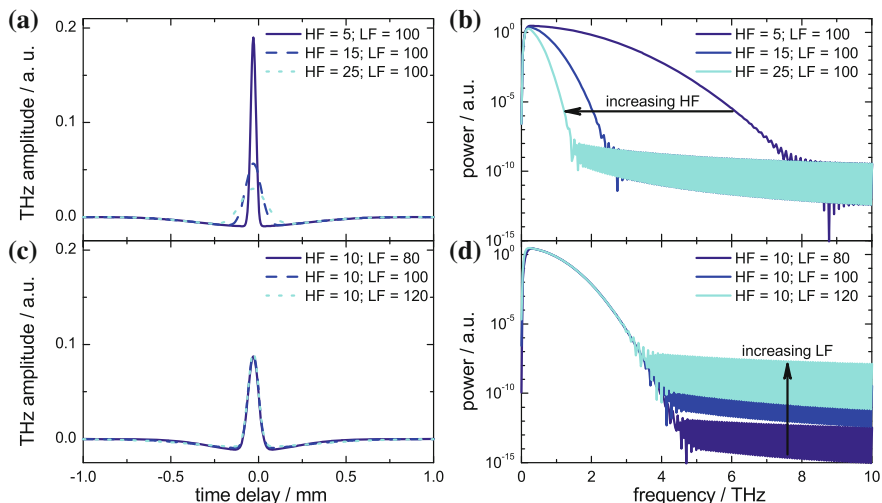


Fig. 18.10 The DG filter. Time-domain representations at different values of **a** HF and **c** LF; corresponding frequency-domain representations **b** HF and **d** LF

$$f_{\text{DG}}(t) = \exp\left(-\frac{t^2}{\text{HF}^2}\right) - \exp\left(-\frac{t^2}{\text{LF}^2}\right) \quad (18.11)$$

where HF and LF define the pulse width of the high-pass and low-pass filters respectively.

At low LF, the shape of the deconvolved signals is distorted: it is difficult to differentiate between the interface peak and the deconvolution artefact, which emerges as two ‘shoulders’ at both ends of the surface peak (Fig. 18.11). Another type of artefact is the shifted signal ‘tail’ at high value of both HF and LF. At appropriate values of LF and HF, the deconvolution is satisfactory, resulting in deconvolved signals with distinguishable peaks and flat base.¹ In this acceptable parameter range, a lower value of HF and a higher value of LF improve the signal preservation due to an overall broader filter bandwidth, thus it is the best combination for the deconvolution.

Customised Skewed Gaussian Filter

In the context of TPI application in tablet coating analysis, the CSG is the most popular approach, as it is implemented in the commercial software package supplied by TeraView Ltd. The filter used in this method is a skewed DG filter customised to suit the application in tablet coating analysis. CSG is defined in time domain as:

¹ The signal base is the part of the signal that corresponds to terahertz wave propagation through the coating layer (between peaks) or deeper into the tablet matrix (after the last peak). Ideally, it should be flat so that peaks can be identified easily.

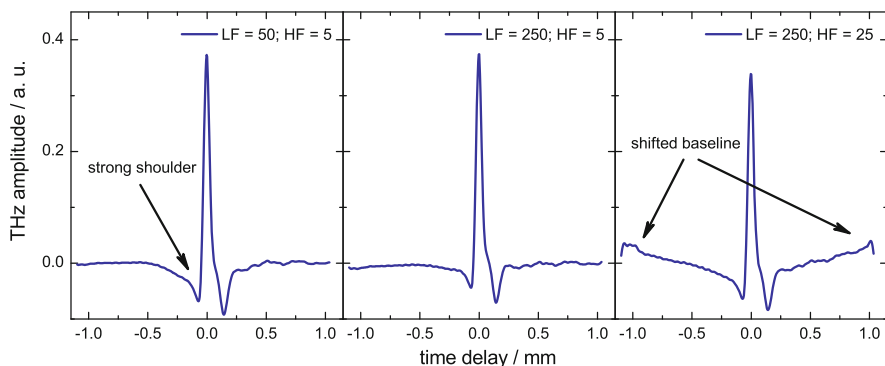


Fig. 18.11 DG inverse filter deconvolved signals at different values of HF and LF

$$f_{\text{CSG}}(t) = \frac{1}{\sqrt{2\pi}} \exp \left[- \left(\frac{500t}{\text{PW}} \right)^2 \right] \quad (18.12)$$

where the PW corresponds to the pulse width of the Gaussian filter (Fig. 18.12).

Another important parameter of this method is the cut-off frequency (CF), which does not appear in the filter function but is incorporated in the deconvolution algorithm. As shown in Fig. 18.12b, it sets the frequency above which the high frequency components are removed from the frequency domain division (to prevent noise amplification as shown in Eq. 18.9). Figure 18.13 shows the effects of the different filter settings on a typical time-domain waveform.

18.3.4 Imaging of Pharmaceutical Tablets

18.3.4.1 General Principle

Figure 18.14a shows a typical terahertz time-domain waveform of a single pixel on a tablet which was coated with one polymer layer. The maximum at 0.00 mm is due to the reflection of terahertz pulse at the surface of the tablet, the interface between air and the coating.² The second peak at 0.38 mm is caused by the reflection of the terahertz pulse at the interface between coating and tablet core.

By plotting the mapped image points along one axis a B-scan (Fig. 18.14b) of the tablet can be obtained. This is a representation commonly used in ultrasonography or OCT. In this representation the curvature of the object is removed by projecting the image into a plane with all surface reflections lined up at $t = 0$ mm. This representation is useful to detect variations in coating thickness as well as density

² In all figures in this chapter the time delay is quoted in mm optical delay with $n_{\text{air}} = 1$.

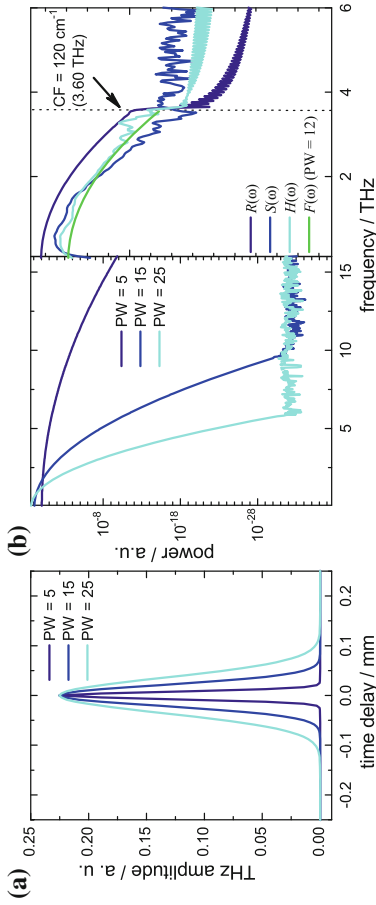


Fig. 18.12 The CSG filter. **a** Time-domain representations at different values of PW. **b** Corresponding frequency domain representations (*left*) and example for the implementation of the cut-off frequency, CF, during the signal processing in the frequency domain (*right*)

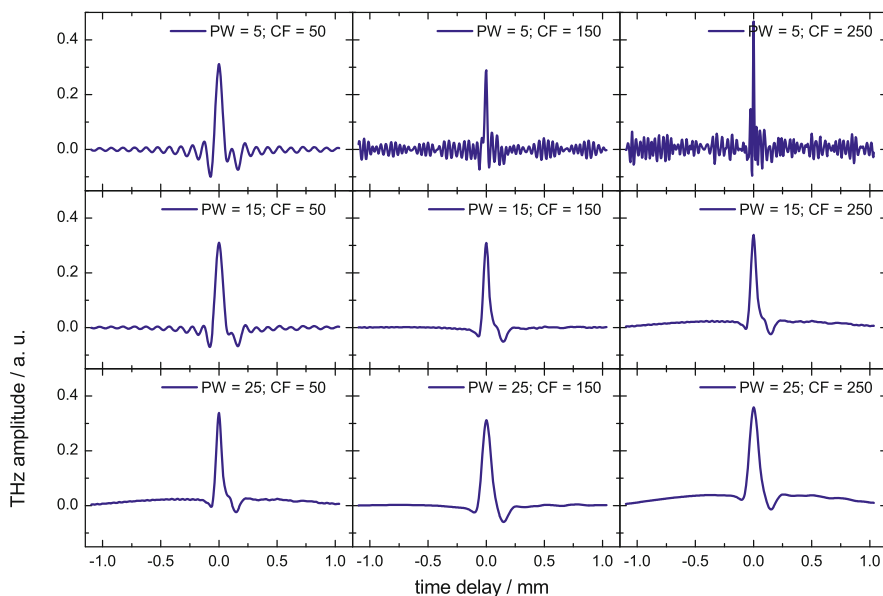


Fig. 18.13 CSG inverse filter deconvolved signals at different values of PW and CF. In this example the setting of PW = 15 and CF = 150 results in a good deconvolution

variations deeper in the tablet matrix. Alternatively, all pixels can be mapped out in a conventional 2D map (Fig. 18.14c).

Note that TPI is a 3D imaging technique and each TPI measurement provides a true 3D data cube: the x - and y -axes describe vertical and horizontal dimensions and the z -axis represents the time-delay dimension (depth-direction) of the sample. The lateral resolution is limited by the wavelength of the terahertz radiation and the depth resolution is limited by the pulse duration. For most pharmaceutical tablets, the achieved spatial resolution is typically in the range of 150–250 μm in lateral and 30–40 μm in axial direction [20, 79].

The surface topography model that was measured in the first step of the TPI measurement prior to acquiring the terahertz pulses as outlined in Sect. 18.3.2 is stored separately during the TPI measurement (Fig. 18.14d). This information can be combined with the 2D map to generate a 3D representation (Fig. 18.14e) and to extract tomographic slices from the data set (Fig. 18.14f).

18.3.4.2 Parameters

The most widely used application of TPI analysis of coated tablets is the non-destructive measurement of the coating thickness and its spatial distribution over the surface of the tablet. The coating thickness d can be directly extracted from the time-domain waveform:

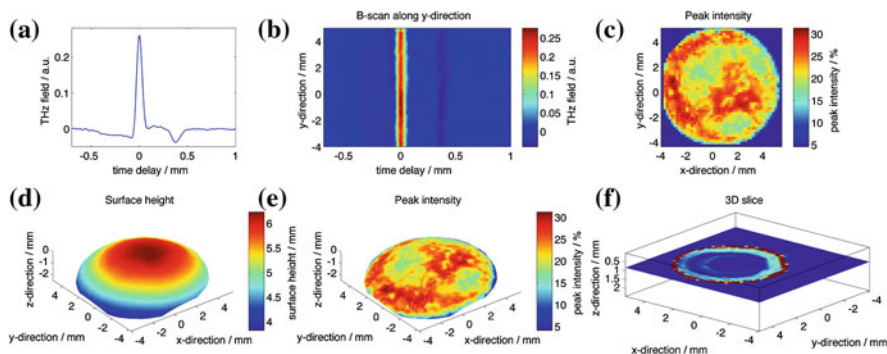


Fig. 18.14 Terahertz image of a single-layer coated tablet: **a** typical time-domain waveform of a single pixel; **b** B-scan map measured along the y-direction of the map at $x = 0$ mm. The *red line* at $t = 0$ mm represents the surface of the tablet while the subsequent *dark line* around $t = 0.40$ mm corresponds to the interface between the coating and the tablet core. **c** 2D map of all pixels acquired for one surface of the tablet. In this map the peak intensity (relative amplitude of the surface reflection compared to the amplitude of $r(n)$) is plotted. **d** Map of the surface height measured using the optical laser gauge; **e** 3D representation of the peak intensity map; and **f** 3D slice through the tablet

$$d = \frac{\Delta t c}{2n}, \tag{18.13}$$

where Δt is the time delay between the surface reflection and the reflection from the coating/core interface, c is the speed of light and n is the refractive index of the coating layer.

The refractive index of the coating layer can be measured by THz-TDS either using a free standing film of coating material which was cast out and dried or, if the tablet is sufficiently transparent, by directly using a coated tablet as a sample and an uncoated tablet core as a reference in a transmission measurement. Estimating the refractive index of the coating based on the volume fractions and the individual refractive indices of the different materials that make up the coating formulation is not recommended. As shown in Fig. 18.15 the TPI coating thickness measurements have been validated using X-ray microtomography as an independent technique on samples of the same tablets [90].

It is important to keep in mind that, while an accurate value for the refractive index is essential to obtain absolute coating thicknesses in most applications, it is the relative difference in coating thickness (for example the distribution of the film on the surface of a tablet or the relative differences in thickness between tablets of the same coating batch) that is of more interest.

Figure 18.16 shows images and histograms of the coating thickness distribution for a single-layer coated tablet. The big advantage of terahertz imaging is that the technique is capable of measuring not only an average coating thickness but also to resolve the homogeneity of the coating thickness across the entire surface of the tablet. Both the mean and the standard deviation of the coating thickness can be

Fig. 18.15 Validation of the coating thickness measured by TPI using X-ray microtomography. For both measurements the same tablet was used. Very good agreement is found between the two techniques (modified from [90])

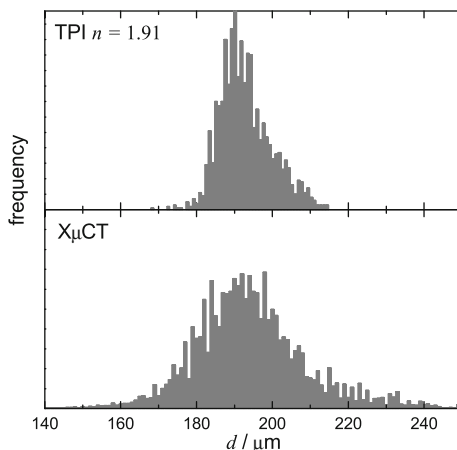
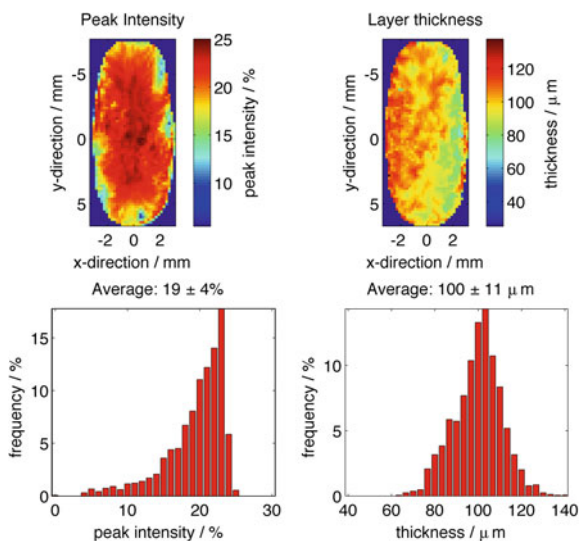


Fig. 18.16 False colour images and histograms of the peak intensity map (*left*), and the coating thickness distribution (*right*) for a single-layer coated tablet



measured non-destructively. In our example the histogram clearly indicates that the coating thickness over the entire surface of the tablet follows a normal distribution (Fig. 18.16); yet it is clear from the image that there is a distinctly thicker coating in the top left when compared to the bottom right. Such local variations in coating thickness are of no concern in a cosmetic coating, which is applied to give the tablet a uniform colour, gloss and visual appeal. However, if the coating is designed to control the drug release rate by means of a diffusion barrier, such local variation in coating thickness are critical as they will determine the overall diffusion rate of the tablet.

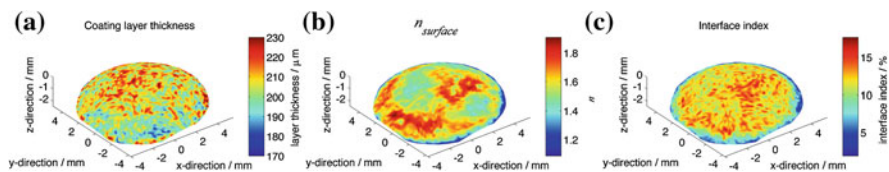


Fig. 18.17 Terahertz maps of **a** coating thickness, **b** surface refractive index, and **c** interface index. All maps show the same tablet in exactly the same orientation

In addition to the coating thickness (Fig. 18.17a) of a single layer, the waveform contains additional useful information: the amplitude of the first peak provides information on the refractive index at the tablet surface (Fig. 18.17b), which can be used to map out the tablet or coating hardness and/or density [91, 92]. Furthermore, it is possible to measure the coating thickness not only for the top layer but also for any subsequent layers which might be coated onto the tablet [20, 76].

A further property that can be extracted from the terahertz waveforms is the interface index, Π , which is defined as

$$\Pi = \frac{|R_n|}{|R_0|}, \quad (18.14)$$

where R_n is the amplitude of the reflection at the n th interface and R_0 is the amplitude of the reflection from the surface of the sample. Figure 18.17c shows a map of the interface index.

18.3.5 Applications

18.3.5.1 Analysis of Tablet Coatings

As outlined in Sect. 18.3.1, coating of tablets with one or more polymer layers is a very common process step in pharmaceutical manufacturing. Traditionally, coatings were used merely for cosmetic purposes, to mask the taste of bitter drugs or to facilitate swallowing of the tablet. However, during the past decades functional coatings have become increasingly common. Functional coatings can be used to control the drug release site in the body as well as the release kinetics. A wide range of different types of coatings are used for this purpose. For example, enteric coatings, using polymers that are poorly soluble at low pH, are used to protect the drug molecules in the tablet against degradation in the acidic environment of the stomach; while sustained release coatings, where the polymer layer forms a porous diffusion barrier, are used to obtain a slow but sustained release profile. Typically, poorly soluble polymers across a broad range of pH are used for this purpose and the drug release kinetics is controlled by

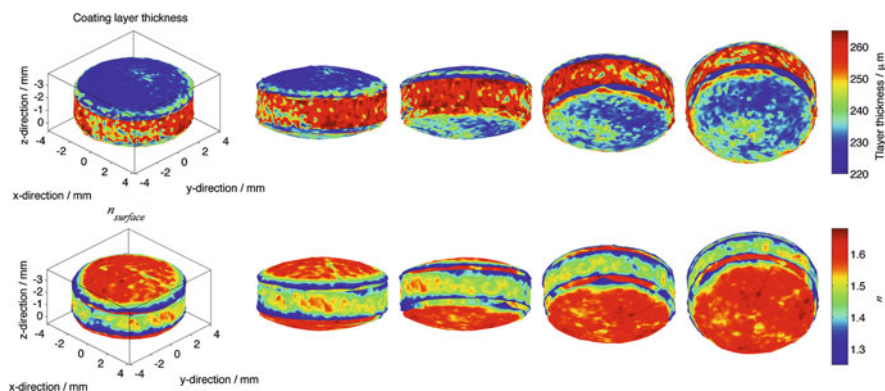


Fig. 18.18 3D maps of coating layer thickness (*top*) and surface refractive index (*bottom*) for a biconvex tablet

the polymer film thickness and its porosity. The quality of tablet coating will thus have direct implications on product performance [93].

In a proof-of-principle work, Fitzgerald et al. studied coated pharmaceutical tablets using a table-top flat-bed terahertz imaging system [76]. It was found that the coating thickness of sugar-coated tablets could be determined quantitatively and non-destructively. However, the coating thickness map obtained in this experiment only covered part of the tablet surface, as the samples had curved surfaces but acquisition was limited to a single xy plane. The success of this work led to the further development of commercial TPI instruments which were specifically designed for fully automated acquisition of terahertz images of arbitrarily shaped tablets as outlined in Sect. 18.3.2 [20, 79]. Using this instrument the coating thickness and uniformity could be readily obtained for a wide range of pharmaceutical dosage forms such as film-coated tablets, multi-layered controlled release tablets and soft gelatine capsules [20]. In other studies, TPI has been successfully applied for the analysis of coating thickness and uniformity of sustained release tablets [94], and for detecting weak spots in the coating that are not visible to the naked eye [95]. Malaterre et al. successfully applied TPI to investigate the coating characteristics of push-pull osmotic systems, a further controlled release tablet technology that is based on multiple coatings [96].

Because the TPI measurement covers the whole tablet surface, aspects of coating defects along with their site, depth and size can be identified using virtual terahertz cross-sections. Figure 18.18 shows a typical result for the intra-tablet variation in coating layer thickness for biconvex tablets, where the top and bottom surfaces of the tablet exhibit different coating characteristics to the centre band. In this example the coating thickness around the centre band of the tablet ($d = 255 \mu\text{m}$) is thicker compared to the thickness of the the top and bottom surfaces and there is only a small difference in mean thickness between the top ($d = 227 \mu\text{m}$) and bottom surfaces ($d = 236 \mu\text{m}$).

Both cases, where the thickness of the centre band is thicker compared to the top and bottom surfaces as well as the opposite case, have been observed. Here, the density of the centre band was found to be lower compared to the top and bottom surfaces [97]. This difference in density is reflected in the lower refractive index of the surface of the polymer coating (Fig. 18.18). The results of the studies so far suggest that such variation in the microstructure of the coating is dependent on the process conditions during the coating operation. Factors such as tablet geometry, relative exposure to the spray zone and in particular the process scale, batch size and resulting pressure in the coating bed have been suggested to contribute to these findings. In general the effect seems more pronounced the smaller the process scale and batch size [94, 95]. The TPI results were confirmed by scanning electron microscopy (SEM) as well as by light microscopy on the same batch of tablets.

The standard quality control test for film coating is to determine the weight gain during coating by comparing the average mass of an uncoated tablet with that of a coated tablet. For this test it is assumed that the coating layer is uniformly distributed over the whole surface of the individual tablet and between all tablets of the same batch. However, the TPI results clearly demonstrated that this assumption is not always valid [94, 95].

One application of TPI coating measurements for which the measurement of the absolute layer thickness is critical is so-called active coating of tablets. In active coating a drug molecule (active pharmaceutical ingredient) is mixed into the soluble coating polymer. This layer typically contains a drug which is meant to be released quickly upon administration to the patient. In contrast, the tablet core might be a matrix formulation that will release further drug molecules slowly by diffusion once the active coating has disintegrated. Using such advanced drug delivery systems the drug release can be controlled very precisely and in turn the number of tablets the patient has to take per day can be reduced. For tablets with an active coating a uniform layer thickness throughout the production batch is extremely important as any deviation from the target thickness will either lead to too little drug in the tablet, which might not achieve the desired therapeutic effect, or more critically too high drug doses, which are toxic for the patient. Brock et al. have recently demonstrated a very good correlation between the coating thickness as measured by TPI and the drug content of the coated tablet as measured by high performance liquid chromatography after dissolving the same tablets (Fig. 18.19). TPI is unique in its quantitative ability to reliably measure the drug content even for very thick coating layers [98].

Another potential imaging method for coating analysis is OCT using near-infrared radiation [99, 100]. Zhong et al. reported experimental results of using OCT and TPI for quantitatively characterising pharmaceutical tablet coatings in the thickness range of 10–140 μm (Fig. 18.20) [101]. It was found that the OCT set-up for this application has an axial resolution of 0.9 μm , and is capable of quantifying thin coatings in the range of 10–60 μm . The maximum thickness of 60 μm that can be measured by OCT is limited by strong scattering of near-infrared light within the tablet coating and core due to its relatively short wavelength in the range of 0.5–1.0 μm . Terahertz radiation has a wavelength in the range of hundreds of microns, and thus TPI is much less affected by scattering limitations in this application. Using TPI it was

Fig. 18.19 Correlation between coating layer thickness as measured by TPI and the drug content in an active coating as measured subsequent by destructive chromatography (modified from [98])

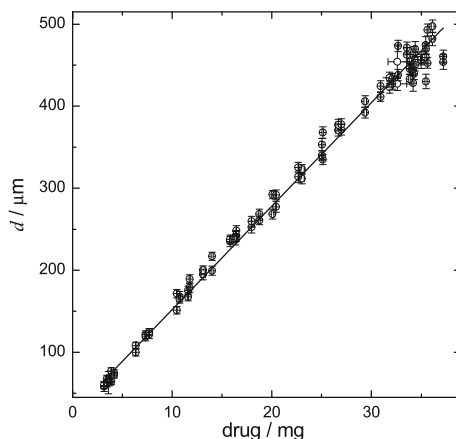
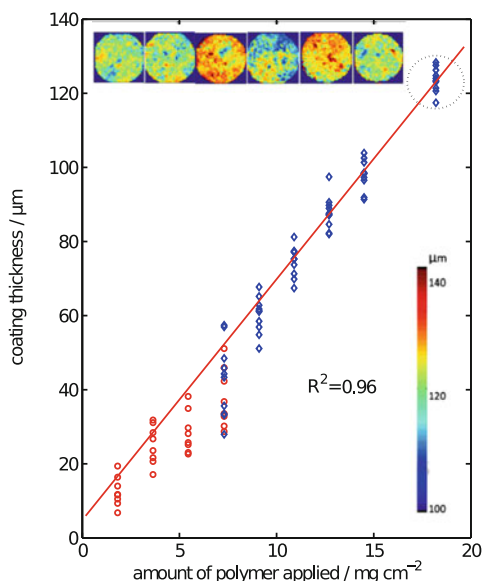


Fig. 18.20 The averaged coating thickness of individual tablets against the amount of polymer applied. The *diamonds* represent TPI results whilst the *circles* represent the OCT results; The *inset* shows TPI coating thickness maps (2D maps in xy directions) obtained for the tablets referring to the *circled data points* with a weight gain of 18.2 mg/cm^2 . A large tablet-to-tablet variation of coating thickness is visible (modified from [101])



possible to measure thicker coatings in the range of $40\text{--}140 \mu\text{m}$ and beyond. The authors concluded that OCT and TPI are complementary analytical techniques for the non-destructive and quantitative characterisation of pharmaceutical tablet coatings [101]. OCT was better suited to resolve thin coatings which were below the resolution limit of TPI while TPI had clear advantages in analysing coating layers that were thicker than $60 \mu\text{m}$.

18.3.5.2 Analysis and Monitoring of the Coating Process

TPI was used to monitor the progress of the coating process by offline analysis of samples that were removed at regular intervals from the tablet bed during film coating [102]. As expected, a linear correlation in coating thickness with the amount of applied polymer was found. In this study a sustained release coating was used and the authors found a linear correlation between the drug release and the coating thickness as measured by TPI. Scale-up of the process from the laboratory scale to the pilot scale resulted in a significant change in coating characteristics. The larger the process scale, the more dense the polymer film was found to be.

In two separate studies the results from TPI were compared with near-infrared (NIR) spectroscopy and imaging [103, 104]. Both TPI and NIR methods were able to measure the build-up of the coating layer as well as to detect small defects in the coating non-destructively. NIR imaging was found to be better at resolving thinner coating layers in the early stages of the coating process. It also has a higher spatial resolution compared with TPI. However, TPI has the advantage that its thickness measurements do not require further calibration even for very thick coating layers. This is in contrast to the NIR methods which always rely on thickness calibration by means of chemometric models that need to be specifically designed for each coating process.

This quality makes TPI interesting as a calibration tool for NIR and Raman measurements. Both techniques estimate the thickness of the coating based on the relative change in strength of spectral features. These spectral features are from chemicals that are either only found in the tablet core, in which case their attenuation indicates increasing coating thickness, or which are specific to the coating and hence stronger peaks relate to thicker coatings. The TPI measurements can thus be used to calibrate the NIR and Raman spectra for absolute coating thickness. In the example of an in-line Raman sensor Müller et al. demonstrated how a TPI calibration can be used to determine the endpoint of a coating process [105].

In a recent study, May et al. demonstrated for the first time how terahertz pulsed technology can be used to quantitatively measure the coating thickness of randomly moving tablets in a production scale pan coater using an in-line terahertz sensor (Fig. 18.21) [23]. The acquisition time to produce a coating thickness map of an entire tablet can be as much as 60 min using the TPI method outlined previously. In contrast the in-line sensor is able to assess the thickness of a single tablet in less than 9 ms during directly in the coater without interfering with the coating process. Direct thickness measurements of film coatings are achieved with sub-micron resolution without the need for any prior chemometric calibration models. Figure 18.22 shows a typical plot of coating thickness measured by the in-line process sensor as a function of process time. The ability to measure the coating thickness distribution in the coating pan in situ (Fig. 18.22b) cannot be achieved using any of the currently available near-infrared or Raman sensor technology, as each measurement point acquired with these techniques inherently represents the temporal and spatial average over a large number of tablets. The coating thickness distributions that are measured during the process clearly highlight the need for a better process understanding: while

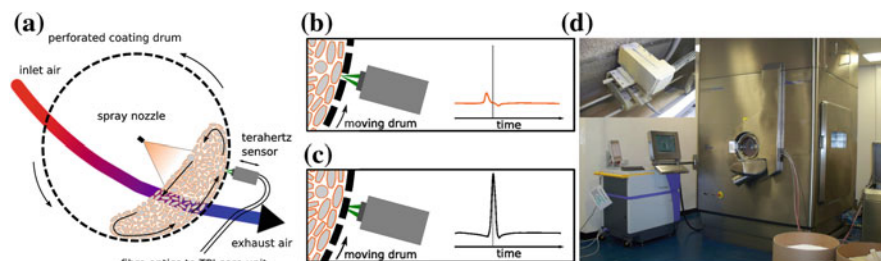


Fig. 18.21 Terahertz in-line sensor for coating thickness measurements. **a, c** Schematic of the sensor configuration; and **d** photograph of the sensor fitted into a production scale coater; the terahertz spectrometer on the *left* of the photograph is connected to the terahertz gauge using an optical fibre. The *inset* shows the terahertz sensor fitted behind the coating drum as outlined in (a) and (b) (modified from [23])

the measurement of the average coating thickness agrees well between the in-line and offline reference method, the in-line sensor reveals that there is a considerable population of tablets with much higher coating thickness in the coater that is not represented by the sample taken for offline analysis. In principle the in-line sensor allows terahertz technology to make their way from the development laboratory to the manufacturing floor. This exciting new sensor technology could have considerable impact in process understanding, process analytical technology (PAT) and quality-by-design (QbD) developments of film coating processes, although more research is required to assess its full potential.

18.3.5.3 Uncoated Tablets—Tablet Inspection and Solvent Diffusion

The ability of using TPI for the analysis of the “hardness” of pharmaceutical tablets was investigated by May et al. [92]. As shown in Fig. 18.23, radially symmetric spatial distributions in tablet density due to the shape of the punch used in the tablet manufacture were observed.

A strong correlation between the TPI results and those from diametric compression tests, the traditional destructive hardness test, was found and the TPI results were explained by means of finite element analysis (FEA) simulations. It was concluded that the TPI method is advantageous in that it is non-destructive in nature and at the same time provides additional information on the spatial distribution of the tensile strength of the tablet under study. This information can then be used to detect stresses originating from the compaction process that are buried under the surface of a tablet. Palermo et al. investigated the ability of TPI to quantitatively measure density maps of a tablet [91]. By using a multivariate calibration model, it was possible to predict the density of compacted mixtures of four excipients. Other studies [106, 107] indicate that TPI might also be useful for characterising tablet surface roughness and tablet bulk properties such as porosity non-destructively. More recently, Tuononen et

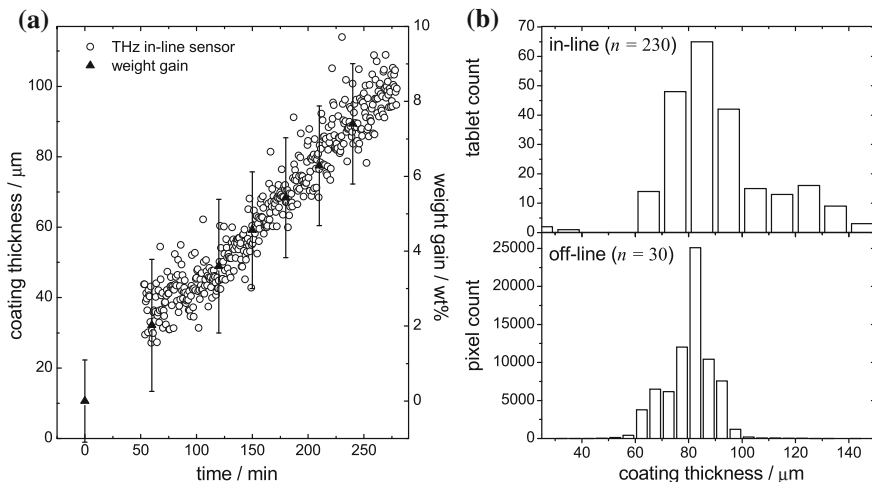


Fig. 18.22 Coating thickness measured by the in-line sensor: **a** coating thickness from 30 s averages as measured by the terahertz in-line sensor (*open circles*) and corresponding weight gain measurement (*filled triangles*); **b** variation in coating thickness of tablets sampled during 10 min process time using the in-line sensor (*top*) and from tablets removed at the same time using the offline TPI measurement. For the TPI measurement the histogram is plotted using all pixels from the images from all faces of the tablet (modified from [23])

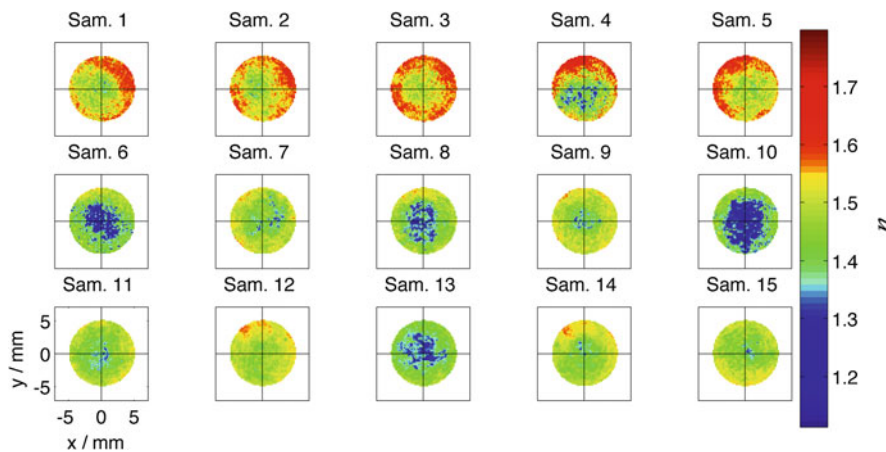
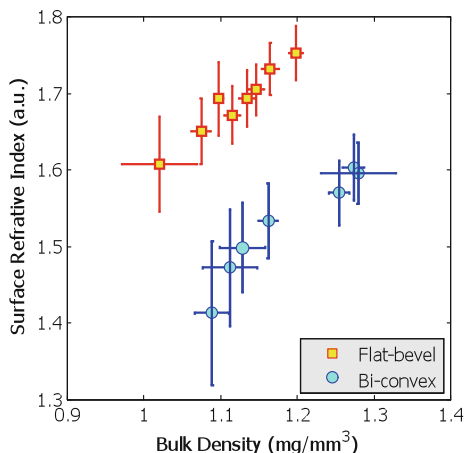


Fig. 18.23 Surface refractive index maps of 14 mm diameter, bi-convex tablets compressed at a compaction force of 8.87 kN (modified from [92])

al. showed that it was possible to estimate the real and imaginary part of the permittivity of the pure component of a starch acetate tablet [108]. All these results suggest that TPI is also suitable for the non-destructive analysis of uncoated pharmaceutical tablets. Other techniques such as X-ray computed tomography can also be used to

Fig. 18.24 Correlation between the surface refractive index and the bulk density of tablets of different geometry (modified from [92])



map the tablet density variation [109]. TPI has the additional advantage that terahertz radiation is non-ionising and hence inherently safe, which can be beneficial when it comes to industrial applications (Fig. 18.24).

Another area of interest for terahertz imaging is the study of solvent ingress into solid polymers. The topic is of great practical importance in the industry both with respect to the processing as well as the applications for polymers [110]. For certain applications (e.g. controlled drug delivery) solvent transport is desirable; however, in others, it causes degradation and contamination of the polymer (e.g. packaging) [111]. Accurate and time-resolved measurements of the liquid ingress process are very valuable for the validation of theoretical models of this process. The general measurement principle that terahertz technology can be used to study solvent diffusion processes into a polymer matrix was first demonstrated by Obradovic et al., as outlined in Sect. 18.2.3 [59]. In a related study, Portieri et al. investigated the hydration process of matrix tablets made from hydroxypropyl methylcellulose (HPMC) [112]. HPMC is a soluble polymer that is commonly used in the production of sustained release tablets. Once in contact with the dissolution medium the polymer swells and a layer of hydrogel is formed as a result of polymer hydration and chain relaxation. This layer then acts as a diffusion barrier for the subsequent release of drug molecules that are embedded in the polymer matrix. HPMC matrix tablets have become the model system to study this type of drug delivery system with a large range of experimental data as well as theoretical models published on this system [113, 114]. As shown in Fig. 18.25, initial experiments show that the shape and integrity of the gel layer formed after adding a 10 μl water drop onto an HPMC tablet can be mapped out using TPI. This information complements the results from other techniques such as magnetic resonance imaging [115] or infrared imaging [114].

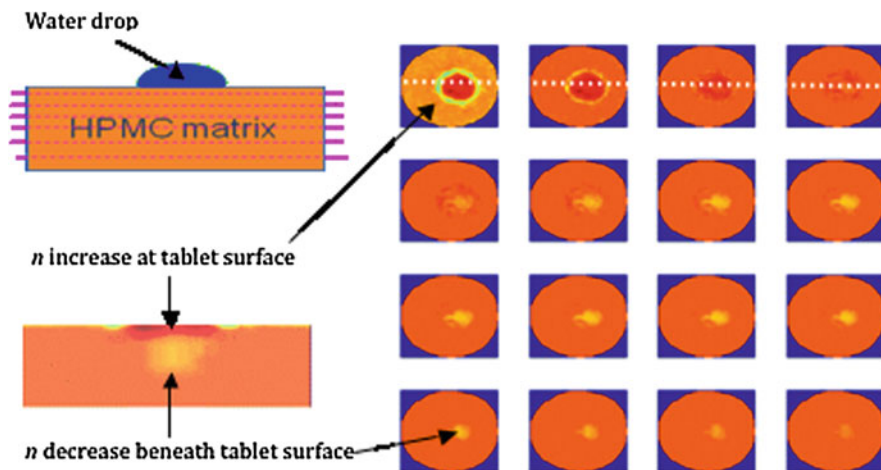


Fig. 18.25 Cross-sectional refractive index maps at various depths of $30\ \mu\text{m}$ interval (*right*) and at $x = 0\ \text{mm}$ (*bottom-left*). Two distinct regions are clearly visible: a high-density shell (gel layer) at sample surface; and a low-density porous region (water channels) below the surface. The *white dotted line* in the figure (*right*) is where $x = 0\ \text{mm}$, and the *red dotted lines* in the figure *inset* (*top-left*) represent various depths where cross-section maps were sliced

18.3.5.4 Dissolution Performance Prediction

The current regulatory framework in the pharmaceutical industry requires that a dissolution test of a small number of tablets ($n < 20$) is required by law to determine whether or not the quality of the entire batch ($n \gg 10^5$) is achieved and hence whether the product can be released to the market. A dissolution test works by exposing a tablet to a known quantity of dissolution medium (in the most simple case this is water) and by measuring how much drug is released from the tablet over time. This is done by taking samples of the liquid at regular intervals and subsequent analysis either by UV spectroscopy or liquid chromatography. This process, which can take up to 2 days for sustained release tablets, is very labour intensive and costly and has little statistical significance on the quality of the batch given the small sample size of tablets that are tested.

In a feasibility study, Spencer et al. demonstrated that the mean dissolution time (MDT) obtained using the standard dissolution test correlates with the coating thickness as measured by TPI [116]. In this study enteric coated tablets were investigated. This type of coating protects the drug molecules within the tablet from the acidic environment in the stomach, which is important for drug molecules that are unstable in such conditions or that would otherwise cause local irritations of the stomach. The coating is designed to remain intact at low pH and to dissolve quickly upon increasing the pH. It is not surprising that the correlation that was found by Spencer et al. was not very strong given that the coating thickness has no direct influence on the release rate as long as it remains intact at low pH. However, what is much more

important is that TPI was found to be a very powerful tool to ensure that no holes were present in the coating and that no drug is released at low pH, which is the main quality control concern in enteric coatings.

Following up from this study, Ho et al. investigated the potential of using terahertz data to predict the dissolution performance of coated sustained-release tablets where the thickness of the coating is expected to directly affect the drug release [97]. The correlation between coating thickness and MDT was very clear and much stronger than in the study by Spencer et al. In addition, the authors highlighted that changes in coating density, for instance as a result from scale-up, are also a good indicator for the dissolution performance of the coated tablet. In a further study by Ho et al., the whole terahertz waveforms, rather than the coating thickness and coating density alone, were used to predict the tablet dissolution performance [117]. Using a two-component PLS model, it was possible to predict the MDT for each tablet non-destructively. Such a multivariate method is particularly useful to predict the dissolution performance of tablets with very thin coatings, as currently the coating thickness below 30–40 μm cannot be determined by TPI.

Ho et al. also evaluated the applicability of TPI for the understanding of the process scale-up [102]. For this study a total of 190 sustained-release tablets that were sampled during the scale-up operation of a film coating process from the lab to the pilot scale were analysed by TPI and dissolution testing. Although the same mass of polymer was applied to all tablets the drug release from the tablets manufactured at pilot scale was significantly slower compared to the lab scale. The TPI results clearly revealed differences in coating thickness and density that explained these differences.

In a related study, the film coating thickness, drug layer uniformity and the effect of curing on the drug release from sustained-release coated pellets were investigated [118]. Pellets are spherical particles that are much smaller than tablets. They are typically used to fill capsules. Significant differences in film coating thickness, surface roughness and drug layer uniformity were found. No correlation between coating thickness and drug release was found. This was due to the fact that the solubility of the drug in the pellet core was very low and hence the release rate was limited by the drug solubility rather than the diffusion rate through the coating. The pellets used in this study (5 mm) were much larger in diameter compared to the dimensions of the pellets typically used in the industry (<1 mm). The large diameter was chosen to allow measurements using the TPI system. Future experiments will have to show whether smaller particles can be reliably measured using terahertz imaging and whether such measurements are practical and quantitative.

All the studies show that TPI has an excellent sensitivity with which to assess the coating quality of pharmaceutical tablets. A clear correlation of the TPI results to dissolution performance was found. The speed and ease of TPI mapping may make it an attractive non-destructive alternative for dissolution testing both in product development and with the potential to play a significant role to improve the product safety by increasing the number of tablets that are tested to a statistically meaningful level in the quality control of the end product. However, it was highlighted that TPI can only predict the dissolution behaviour if the coating is the rate determining

factor of the drug delivery system and that other parameters need also to be taken into account.

18.3.5.5 Chemical Mapping

Given the sensitivity of terahertz radiation to the intermolecular interactions in typical drug molecules as outlined in Chap. 8, chemical mapping is an exciting extension of the structural imaging outlined before for the characterisation of complex heterogeneous samples. The basis of chemical mapping is the acquisition of a 3D data set where two axes describe vertical and horizontal spatial dimensions and the third axis represents the spectral frequency dimension. As previously discussed, the electric field of terahertz radiation is recorded as a function of time in a TPI measurement. The spectral information of this signal can be obtained by Fourier transformation. The absorption coefficient, $\alpha(\nu)$, and the refractive index, $n(\nu)$, are then calculated for each pixel as [79]:

$$n(\nu) + j \frac{\alpha(\nu)c}{4\pi\nu} = \frac{1 - S(\nu)/R(\nu)}{1 + S(\nu)/R(\nu)} \quad (18.15)$$

where $S(\nu)$ and $R(\nu)$ are the Fourier transforms of the measured terahertz waveforms reflected from a sample and a reference mirror. The absorption spectra $\alpha(\nu)$ provide means for chemical mapping of pharmaceutical solid dosage forms [34, 119]. Note that a transmission configuration, rather than the reflection geometry as discussed in this section, can also be used for chemical sensing and imaging [19, 120].

In the near-infrared and mid-infrared range, FTIR and Raman spectroscopy have been successfully developed for chemical mapping [121–123]. However, many pharmaceutical tablet coatings are opaque to infrared radiation, owing to either strong absorption or scattering. Therefore, conventional infrared techniques are most suitable for mapping out the surface distributions of chemicals as a 2D chemical mapping technique. In addition, near-infrared and mid-infrared imaging technology sometimes struggles to discriminate between pharmaceutical polymorphs as such polymorphs often only differ by subtle shifts in their respective vibrational spectra. Terahertz radiation, on the other hand, can penetrate much deeper into a tablet. At the same time it is very sensitive to subtle changes in crystal structure [124–126]. Therefore, in principle, TPI provides the necessary penetration depth and spectral specificity for non-destructive chemical mapping in a 3D matrix.

Using a model tablet sample that contained well-confined domains of lactose and tartaric acid, Shen et al. demonstrated how the spectral signature of the materials could indeed be extracted non-destructively at depth [35]. A time-partitioned Fourier transform of the reflected terahertz waveform with a fixed window width was employed to produce depth-resolved spectral components of the pulse [35, 79]. There are many potential applications for this technique in the context of pharmaceutical dosage forms such as investigating the spatial distribution of different polymorphic forms in a dosage form. Changes in the crystal structure of the drug can be induced

during manufacture of the dosage form by compaction or coating or by moisture uptake during storage of a tablet [8]. However, it is important to mention that the model tablet used [35, 79] was made of polyethylene, which is almost transparent to terahertz radiation. For a realistic pharmaceutical tablet, the spectral resolution at depth will be influenced strongly by scattering and refraction caused by the tablet matrix. Further work will be necessary to develop a robust method to routinely perform 3D chemical mapping experiments. In addition, most commercial TPI systems provide a lateral resolution of around 200 μm and better resolution is necessary in order to resolve small polymorph/hydrate particles within pharmaceutical dosage forms.

18.3.5.6 Summary of Pharmaceutical Applications

Over the past five years, terahertz technology was developed into a new tool for the physical characterisation of solid dosage forms in the pharmaceutical industry. Located in the far-infrared region of the electromagnetic spectrum, terahertz spectra directly probe intermolecular vibrations such as phonon lattice modes of crystalline solids. This gives terahertz spectroscopy a high sensitivity for the rapid discrimination and quantification of polymorphs, hydrates, cocrystals and other solid-state modifications of drug molecules as well as for the analysis of solid form transformation dynamics [33, 124, 127–130]. On the other hand, terahertz radiation can penetrate deep into pharmaceutical tablets as most common pharmaceutical excipients are amorphous and semi-transparent to terahertz radiation. As summarised in this section, this can be exploited in TPI as a powerful tool for the non-destructive and quantitative characterisation of coatings on tablets.

18.4 Outlook

A number of properties make terahertz radiation very attractive for industrial applications: it can penetrate deep into a wide range of technical materials such as polymers, ceramics and semiconductors. The low photon energy gives terahertz radiation an inherent safety advantage compared to X-ray techniques, and, compared to other well-established NDT such as ultrasonics, terahertz radiation has higher resolution to offer while completely avoiding coupling problems from free space given the low refractive index mismatch. At the same time the measurements reveal a wealth of information on the microstructure of the materials probed, including the internal structure, defects, density gradients, moisture content and intermolecular interaction.

However, to live up to this enormous potential, there are a number of challenges that terahertz sensors have to master. First and foremost the technology has to become faster, more stable and more affordable, which requires new approaches to many details of the terahertz system architecture. The current laser stability, the overall instrument reliability, together with the requirement of regular service visits in order

to maintain the instrument performance, are huge obstacles that need to be addressed. In addition, it would be desirable to extend the spectral range of the current instruments from 100 cm^{-1} to, for example 300 cm^{-1} . This would allow the terahertz spectrum to cover both the intermolecular and some of the intramolecular vibration modes, thus providing better spectral specificity for a larger range of materials. The broader spectral range would also help to characterise thinner layer structures with higher spatial resolution. On the signal processing side there are still a number of open questions, such as how to best account for scattering losses from sharp edges in terahertz images as well as how best to reconstruct volumetric tomographic data sets while taking refraction into account quantitatively. Moreover, advances in both software and hardware have to be made to make this technology accessible in non-specialist communities.

In this chapter we have highlighted a range of what we believe to be very promising applications, ranging from industrial sensors for in-line control of a production line in polymer composite processing to fault detection in semiconductors and tablet inspection in the pharmaceutical industry amongst others. Terahertz technology has the potential to play a significant role in all these areas.

Acknowledgments The authors would like to thank Ms. Bee Yin Yeo for her help in putting together Sect. 18.3.3 of this chapter.

References

1. B. Hu, M. Nuss, *Opt. Lett.* **20**(16), 1716 (1995)
2. D. Mittleman, R. Jacobsen, M.C. Nuss, *IEEE J. Sel. Top. Quantum Electron.* **2**(3), 679 (1996)
3. D. Mittleman, S. Hunsche, L. Boivin, M. Nuss, *Opt. Lett.* **22**(12), 904 (1997)
4. D. Mittleman, M. Gupta, R. Neelamani, R. Baraniuk, J. Rudd, M. Koch, *Appl. Phys. B Lasers Opt.* **68**(6), 1085 (1999)
5. J.B. Jackson, M. Mourou, J. Labaune, J.F. Whitaker, I.N.I. Duling, S.L. Williamson, C. Lavier, M. Menu, G.A. Mourou, *Meas. Sci. Technol.* **20**(7), 075502–075511 (2009)
6. C. Jansen, S. Wietzke, O. Peters, M. Scheller, N. Vieweg, M. Salhi, N. Krumbholz, C. Jördens, T. Hochrein, M. Koch, *Appl. Opt.* **49**(19), E48 (2010)
7. J.A. Zeitler, P.F. Taday, D.A. Newnham, M. Pepper, K.C. Gordon, T. Rades, *J. Pharm. Pharmacol.* **59**(2), 209 (2007)
8. J.A. Zeitler, L.F. Gladden, *Eur. J. Pharm. Biopharm.* **71**(1), 2 (2009)
9. Y.C. Shen, *Int. J. Pharm.* **417**, 48 (2011)
10. B. Ferguson, X. Zhang, *Nat. Mater.* **1**(1), 26 (2002)
11. D. Mittleman (ed.), *Sensing with Terahertz Radiation*. Springer Series in Optical Sciences Series, (Springer, Berlin, 2003)
12. K. Kawase, *Opt. Photonics News* **15**(10), 34 (2004)
13. W. Chan, J. Deibel, D. Mittleman, *Rep. Prog. Phys.* **70**(8), 1325 (2007)
14. M. Tonouchi, *Nat. Photonics* **1**(2), 97 (2007)
15. S. Dexheimer (ed.), *Terahertz Spectroscopy: Principles and Applications*. Optical Science and Engineering, (CRC Press, Boca Raton, 2007)
16. I. Duling, D. Zimdars, *Nat. Photonics* **3**, 630 (2009)
17. Y.S. Lee, *Principles of Terahertz Science and Technology* (Springer, New York, 2009)
18. P.U. Jepsen, D.G. Cooke, M. Koch, *Laser Photonics Rev.* **5**(1), 124 (2010)

19. M. Walther, B.M. Fischer, A. Ortner, A. Bitzer, A. Thoman, H. Helm, *Anal. Bioanal. Chem.* **397**(3), 1009 (2010)
20. J.A. Zeitler, Y. Shen, C. Baker, P.F. Taday, M. Pepper, T. Rades, *J. Pharm. Sci.* **96**(2), 330 (2007)
21. N. Krumbholz, T. Hochrein, N. Vieweg, T. Hasek, K. Kretschmer, M. Bastian, M. Mikulics, M. Koch, *Polym. Testing* **28**(1), 30 (2009)
22. D. Zimdars, I. Duling, G. Fichter, J. White, *AIP Conf. Proc.* **1211**(1), 564 (2010)
23. R.K. May, M.J. Evans, S. Zhong, I. Warr, L.F. Gladden, Y. Shen, J.A. Zeitler, *J. Pharm. Sci.* **100**(4), 1535 (2011)
24. L. Cartz, *Nondestructive testing* (ASM International Materials Park, Ohio, 1995)
25. C. Hellier, *Handbook of nondestructive evaluation* (McGraw-Hill, New York, 2001)
26. M. Soleimani, R. Bayford, *Philos. Trans. R. Soc. A Math. Phys. Eng. Sci.* **367**(1900), 3017 (2009)
27. D. Ensminger, L. Bond, *Ultrasonics: fundamentals, technologies and applications*, 3rd edn. Mechanical Engineering, (Taylor and Francis, Boca Raton, 2009)
28. D. Stifter, *Appl. Phys. B Lasers Opt.* **88**(3), 337 (2007)
29. I. Pupeza, R. Wilk, M. Koch, *Opt. Express* **15**(7), 4335 (2007)
30. R. Wilk, I. Pupeza, R. Cernat, M. Koch, I. Pupeza, R. Cernat, *IEEE J. Sel. Top. Quant. Electron.* **14**(2), 392 (2008)
31. M. Walther, B. Fischer, P.U. Jepsen, *Chem. Phys.* **288**(2–3), 261 (2003)
32. B. Fischer, M. Hoffmann, H. Helm, R. Wilk, F. Rutz, T. Kleine-Ostmann, M. Koch, P. Jepsen, *Opt. Express* **13**(14), 5205 (2005)
33. C.J. Strachan, T. Rades, D.A. Newnham, K.C. Gordon, M. Pepper, P.F. Taday, *Chem. Phys. Lett.* **390**(1–3), 20 (2004)
34. Y. Shen, P.F. Taday, D.A. Newnham, M. Pepper, *Semicond. Sci. Tech.* **20**(7), S254 (2005)
35. Y. Shen, P.F. Taday, D.A. Newnham, M. Kemp, M. Pepper, R. Hwu, K. Linden, *Terahertz and Gigahertz Electronics and Photonics IV* (SPIE Press, California, 2005), pp. 24–31
36. K. Yamamoto, M. Yamaguchi, M. Tani, M. Hangyo, S. Teramura, T. Isu, N. Tomita, *Appl. Phys. Lett.* **85**(22), 5194 (2004)
37. D. Banerjee, W. von Spiegel, M. Thomson, S. Schabel, H. Roskos, *Opt. Express* **16**(12), 9060 (2008)
38. H. Zhang, K. Mitobe, N. Yoshimura, in *International Symposium on Electrical Insulating Materials (ISEIM)*, (IEEE, 2008), pp. 87–90
39. P. Parasoglou, E.P.J. Parrott, J.A. Zeitler, J. Rasburn, H. Powell, L.F. Gladden, M.L. Johns, *Terahertz Sci. Technol.* **3**, 172 (2010)
40. R. Cunnell, T. Luce, J. Collins, R. Rungsawang, J. Freeman, H. Beere, D.A. Ritchie, L.F. Gladden, M.L. Johns, J.A. Zeitler, in *34th International Conference on Infrared, Millimeter, and Terahertz Waves, IRMMW-THz 2009* (IEEE, 2009), pp. 1–2
41. E.P.J. Parrott, J.A. Zeitler, J. McGregor, S. Oei, H. Unalan, S. Tan, W. Milne, J. Tessonier, R. Schlogl, L.F. Gladden, *J. Phys. Chem. C* **113**(24), 10554 (2009)
42. J. McGregor, Z. Huang, E.P.J. Parrott, J.A. Zeitler, K. Nguyen, J. Rawson, A. Carley, T. Hansen, J.P. Tessonier, D. Su, D. Teschner, E. Vass, A. Knop-Gericke, R. Schlögl, L.F. Gladden, *J. Catal.* **269**(2), 329 (2010)
43. M. de Silva, C. McElroy, J. McGregor, A. York, J.A. Zeitler, L.F. Gladden, in *35th International Conference on Infrared Millimeter and Terahertz Waves (IRMMW-THz)*, (2010), pp. 1–2
44. R. Arrigo, M. Havecker, S. Wrabetz, R. Blume, M. Lerch, J. McGregor, E.P.J. Parrott, J.A. Zeitler, L.F. Gladden, A. Knop-Gericke, R. Schlögl, D. Su, *J. Am. Chem. Soc.* (2010)
45. C. Jördens, M. Koch, *Opt. Eng.* **47**(3), 037003 (2008)
46. D. Zimdars, J. Valdmanis, J. White, G. Stuk, S. Williamson, W. Winfree, E. Madaras, in *AIP Conference Proceedings*, (2005), pp. 570–577
47. H. Zhong, J. Xu, X. Xie, T. Yuan, R. Reightler, E. Madaras, X. Zhang, *IEEE Sens. J.* **5**(2), 203 (2005)
48. R.F. Anastasi, E.I. Madaras, J.P. Seebo, S.W. Smith, J.K. Lomness, P.E. Hintze, C.C. Kammerer, W.P. Winfree, R.W. Russell, in *Proceedings of the SPIE*, (2007), pp. 1–6

49. D. Zimdars, G. Fichter, A. Chernovsky, in *33rd International Conference on Infrared, Millimeter and Terahertz Waves (IRMMW-THz 2008)* (IEEE, 2008), pp. 1–3
50. Y. Morita, A. Dobroiu, K. Kawase, C. Otani, *Opt. Eng.* **44**(1), (2005)
51. Y. Morita, A. Dobroiu, C. Otani, K. Kawase, *J. Food Prot.* **68**(4), 833 (2005)
52. C. Jördens, M. Scheller, S. Wietzke, D. Romeike, C. Jansen, T. Zentgraf, K. Wiesauer, V. Reisecker, M. Koch, *Compos. Sci. Technol* **70**(3), 472 (2010)
53. D. Zimdars, J. White, G. Fichter, A. Chernovsky, S.L. Williamson, *Proc. SPIE* **6949**(1), 69490B (2008)
54. C. Chen, D. Lee, T. Pollock, J. Whitaker, *Opt. Express* **18**(4), 3477 (2010)
55. P. Lopato, T. Chady, R. Sikora, *Int. J. Comput. Math. Electr. Electron. Eng. (COMPTEL)* **30**(4), 1260 (2011)
56. D.K. Hsu, K.H. Im, C.P. Chiou, D.J. Barnard, *AIP Conf. Proc.* **1335**(1), 533 (2011)
57. Y. Cai, Z. Wang, R. Dias, D. Goyal, in *Proceedings of the 60th Electronic Components and Technology Conference (ECTC)* (2010), pp. 1309–1315
58. J.M. Chin, V. Narang, X. Zhao, M.Y. Tay, A. Phoa, V. Ravikumar, L.H. Ei, S.H. Lim, C.W. Teo, S. Zulkifli, M.C. Ong, M.C. Tan, *Microelectron. Reliab.* **51**(9–11), 1440 (2011)
59. J. Obradovic, J. Collins, O. Hirsch, M.D. Mantle, M.L. Johns, L.F. Gladden, *Polymer* **48**(12), 3494 (2007)
60. Q. Wu, T. Hewitt, X. Zhang, *Appl. Phys. Lett.* **69**(8), 1026 (1996)
61. Z. Jiang, X. Zhang, *Opt. Lett.* **23**(14), 1114 (1998)
62. M. Usami, T. Iwamoto, R. Fukasawa, M. Tani, M. Watanabe, K. Sakai, *Phys. Med. Biol.* **47**(21), 3749 (2002)
63. M. Yamashita, M. Usami, K. Fukushima, R. Fukasawa, C. Otani, K. Kawase, *Appl. Opt.* **44**(25), 5198 (2005)
64. M. Usami, M. Yamashita, K. Fukushima, C. Otani, K. Kawase, *Appl. Phys. Lett.* **86**(14), 3 (2005)
65. T. Yasuda, T. Yasui, T. Araki, E. Abraham, *Opt. Commun.* **267**(1), 128 (2006)
66. T. Yasuda, Y. Kawada, H. Toyoda, H. Takahashi, *Opt. Express* **15**(23), 15583 (2007)
67. A. Lee, Q. Hu, *Opt. Lett.* **30**(19), 2563 (2005)
68. R. Kohler, A. Tredicucci, F. Beltram, H. Beere, E.H. Linfield, A. Davies, D.A. Ritchie, R. Iotti, F. Rossi, *Nature* **417**(6885), 156 (2002)
69. A.W.M. Lee, B.S. Wil, S. Kumar, Q. Hu, J.L. Reno, *IEEE Photon. Technol. Lett.* **18**(13), 1415 (2006)
70. P. Dean, N.K. Saat, S.P. Khanna, M. Salih, A. Burnett, J. Cunningham, E.H. Linfield, A.G. Davies, *Opt. Express* **17**(23), 20631 (2009)
71. K. Nguyen, M.L. Johns, L.F. Gladden, C. Worrall, P. Alexander, H. Beere, M. Pepper, D.A. Ritchie, J. Alton, S. Barbieri, E.H. Linfield, *Opt. Express* **14**(6), 2123 (2006)
72. F. Clarke, *Vib. Spectrosc.* **34**(1), 25 (2004)
73. V. Busignies, B. Leclerc, P. Porion, P. Evesque, G. Couarraze, P. Tchoreloff, *Eur. J. Pharm. Biopharm.* **64**(1), 38 (2006)
74. J. Aaltonen, K.C. Gordon, C.J. Strachan, T. Rades, *Int. J. Pharm.* **364**(2), 159 (2008)
75. C. McGoverin, T. Rades, K.C. Gordon, *J. Pharm. Sci.* **97**(11), 4598 (2008)
76. A.J. Fitzgerald, B.E. Cole, P.F. Taday, *J. Pharm. Sci.* **94**(1), 177 (2005)
77. D. Auston, *Appl. Phys. Lett.* **26**(3), 101 (1975)
78. D. Auston, K. Cheung, P. Smith, *Appl. Phys. Lett.* **45**(3), 284 (1984)
79. Y. Shen, P.F. Taday, *IEEE J. Sel. Top. Quantum Electron.* **14**(2), 407 (2008)
80. J.R. Fletcher, G.P. Swift, D. Dai, J.M. Chamberlain, P.C. Upadhy, *J. Appl. Phys.* **102**(11), 113105 (2007)
81. W. Withayachumnankul, H. Lin, S. Mickan, B. Fischer, D. Abbott, in *Photonic Materials, Devices, and Applications II* (Maspalomas, Gran Canaria, 2007)
82. W. Withayachumnankul, B. Fischer, H. Lin, D. Abbott, *J. Opt. Soc. Am. B* **25**(6), 1059 (2008)
83. V. Wallace, P.F. Taday, A.J. Fitzgerald, R. Woodward, J. Cluff, R. Pye, D.A. Arnone, *Faraday Discuss.* **126**, 255 (2004)
84. B. Ferguson, D. Abbott, *Microelectr. J.* **32**(12), 943 (2001)

85. R. Neelamani, H. Choi, R. Baraniuk, *IEEE Trans. Signal Process.* **52**(2), 418 (2004)
86. D.L. Donoho, *IEEE Trans. Inf. Theory* **41**(3), 613 (1995)
87. Y. Chen, S. Huang, E. Pickwell-Macpherson, *Opt. Express* **18**(2), 1177 (2010)
88. R. Woodward, B. Cole, V. Wallace, R. Pye, D.A. Arnone, E.H. Linfield, M. Pepper, *Phys. Med. Biol.* **47**(21), 3853 (2002)
89. E. Pickwell, B.E. Cole, A.J. Fitzgerald, M. Pepper, V.P. Wallace, *Phys. Med. Biol.* **49**(9), 1595 (2004)
90. I. Russe, D. Brock, K. Knop, P. Kleinbudde, J.A. Zeitler, in *8th World Meeting on Pharmaceutics, Biopharmaceutics and Pharmaceutical Technology* (Istanbul, 2012), p. 2
91. R. Palermo, R. Cogdill, S. Short, J. Drennen Iii, P. Taday, *J. Pharma. Biomed.* **46**(1), 36 (2008)
92. R. May, L. Han, J. Alton, S. Zhong, J. Elliott, C. Byers, L. Gladden, M. Evans, Y. Shen, J. Zeitler, in *34th International Conference on Infrared, Millimeter, and Terahertz Waves, IRMMW-THz 2009* (IEEE, 2009), pp. 1–2
93. G.M. Jantzen, J.R. Robinson, in *Modern pharmaceutics*, ed. by C.T. Rhodes, G.S. Banker (CRC Press, New York, 2002), pp. 501–528
94. L. Ho, R. Mueller, M. Romer, K.C. Gordon, J. Heinamaki, P. Kleinebudde, M. Pepper, T. Rades, Y.C. Shen, C.J. Strachan, P.F. Taday, J.A. Zeitler, *J. Controlled Release* **119**(3), 253 (2007)
95. L. Ho, R. Mueller, C. Krueger, K.C. Gordon, P. Kleinebudde, M. Pepper, T. Rades, Y. Shen, P.F. Taday, J.A. Zeitler, *J. Pharm. Sci.* **99**(1), 392 (2010)
96. V. Malaterre, M. Pedersen, J. Ogorka, R. Gurny, N. Loggia, P. Taday, *Eur. J. Pharm. Biopharm.* **74**(1), 21 (2009)
97. L. Ho, R. Mueller, K.C. Gordon, P. Kleinebudde, M. Pepper, T. Rades, Y. Shen, P.F. Taday, J.A. Zeitler, *J. Controlled Release* **127**(1), 79 (2008)
98. D. Brock, J.A. Zeitler, A. Funke, K. Knop, P. Kleinebudde, submitted to *Int. J. Pharm.* (2012)
99. S. Zhong, H. Shen, Y.C. Shen, J.A. Zeitler, L. Ho, M. Evans, P. Taday, M. Pepper, T. Rades, K.C. Gordon, R. Muller, P. Kleinebudde, in *34th International Conference on Infrared, Millimeter, and Terahertz Waves, IRMMW-THz 2009* (IEEE, 2009), pp. 1–2
100. J.M.A. Mauritz, R.S. Morrisby, R.S. Hutton, C.H. Legge, C.F. Kaminski, *J. Pharm. Sci.* **99**(1), 385 (2010)
101. S. Zhong, Y.C. Shen, L. Ho, R.K. May, J.A. Zeitler, M. Evans, P.F. Taday, M. Pepper, T. Rades, K.C. Gordon, R. Mueller, P. Kleinebudde, *Opt. Laser Eng.* **49**(3), 361 (2011)
102. L. Ho, R. Mueller, K.C. Gordon, P. Kleinebudde, M. Pepper, T. Rades, Y. Shen, P.F. Taday, J.A. Zeitler, *Eur. J. Pharm. Biopharm.* **71**(1), 117 (2009)
103. R. Cogdill, R. Forcht, Y. Shen, P. Taday, *J. Pharm. Innov.* (2), 29 (2007)
104. L. Maurer, H. Leuenberger, *Int. J. Pharm.* **370**(1–2), 8 (2009)
105. J. Müller, D. Brock, K. Knop, J.A. Zeitler, P. Kleinebudde, *Eur. J. Pharm. Biopharm.* **80**, 690–697 (2012)
106. M. Juuti, H. Tuononen, T. Prykäri, V. Kontturi, M. Kuosmanen, E. Alarousu, J. Ketolainen, R. Myllylä, K.-E. Peiponen, *Meas. Sci. Technol.* (1), 015301 (2009)
107. H. Tuononen, E. Gornov, J.A. Zeitler, J. Aaltonen, K.-E. Peiponen, *Opt. Lett.* **35**(5), 631 (2010)
108. H. Tuononen, K. Fukunaga, M. Kuosmanen, J. Ketolainen, K.-E. Peiponen, *Appl. Spectrosc.* **64**(1), 127 (2010)
109. I. Sinka, S. Burch, J. Tweed, J. Cunningham, *Int. J. Pharm.* **271**(1–2), 215 (2004)
110. T. Hyde, L. Gladden, *Polymer* **39**(4), 811 (1998)
111. S.G. Harding, M.L. Johns, S.R. Pugh, P.J. Fryer, L.F. Gladden, *Food Addit. Contam.* **14**(6–7), 583 (2012)
112. A. Portieri, P.F. Taday, Y.C. Shen, in *58th Pittsburgh Conference on Analytical and Applied Spectroscopy*, (PITTCON 2007) (Chicago, USA, 2007)
113. J. Siepmann, *Adv. Drug Deliv. Rev.* **48**(2–3), 139 (2001)
114. S. Kazarian, K. Chan, *Macromolecules* **36**(26), 9866 (2003)
115. Y.Y. Chen, Hughes, L. P., L.F. Gladden, M.D. Mantle, *J. Pharm. Sci.* **99**(8), 3462 (2010)

116. J. Spencer, Z. Gao, T. Moore, L. Buhse, P.F. Taday, D.A. Newnham, Y. Shen, A. Portieri, A. Husain, *J. Pharm. Sci.* **97**(4), 1543 (2008)
117. L. Ho, R. Mueller, K.C. Gordon, P. Kleinebudde, M. Pepper, T. Rades, Y. Shen, P.F. Taday, J.A. Zeitler, *J. Pharm. Sci.* **98**(12), 4866 (2009)
118. L. Ho, Y. Cuppok, S. Muschert, K. Gordon, M. Pepper, Y. Shen, F. Siepmann, J. Siepmann, P. Taday, T. Rades, *Int. J. Pharm.* **382**(1–2), 151 (2009)
119. R. Cogdill, S. Short, R. Forcht, Z. Shi, Y. Shen, P. Taday, C. Anderson, J. Drennen, *J. Pharm. Innov.* **1**(1), 63 (2006)
120. B. Fischer, M. Hoffmann, H. Helm, G. Modjesch, P.U. Jepsen, *Semicond. Sci. Tech.* **20**(7), S246 (2005)
121. E.N. Lewis, P.J. Treado, R.C. Reeder, G.M. Story, A.E. Dowrey, C. Marcott, I.W. Levin, *Anal. Chem.* **67**(19), 3377 (2012)
122. J.L. Koenig, S.Q. Wang, R. Bhargava, *Anal. Chem.* **73**(13), 360A (2001)
123. F.C. Clarke, M.J. Jamieson, D.A. Clark, S.V. Hammond, R.D. Jee, A.C. Moffat, *Anal. Chem.* **73**(10), 2213 (2001)
124. J.A. Zeitler, D.A. Newnham, P.F. Taday, T.L. Threlfall, R.W. Lancaster, R.W. Berg, C.J. Strachan, M. Pepper, K.C. Gordon, T. Rades, *J. Pharm. Sci.* **95**(11), 2486 (2006)
125. E.P.J. Parrott, J.A. Zeitler, T. Friscic, M. Pepper, W. Jones, G.M. Day, L.F. Gladden, *Cryst. Growth Des.* **9**(3), 1452 (2009)
126. R. Li, J.A. Zeitler, D. Tomerini, E.P.J. Parrott, L.F. Gladden, G.M. Day, *Phys. Chem. Chem. Phys.* **12**(20), 5329 (2010)
127. P.F. Taday, I. Bradley, D.A. Arnone, M. Pepper, *J. Pharm. Sci.* **92**(4), 831 (2003)
128. C.J. Strachan, P.F. Taday, D.A. Newnham, K.C. Gordon, J.A. Zeitler, M. Pepper, T. Rades, *J. Pharm. Sci.* **94**(4), 837 (2005)
129. J.A. Zeitler, D.A. Newnham, P.F. Taday, C.J. Strachan, M. Pepper, K.C. Gordon, T. Rades, *Thermochim. Acta* **436**(1–2), 71 (2005)
130. J.A. Zeitler, K. Kogermann, J. Rantanen, T. Rades, P.F. Taday, M. Pepper, J. Aaltonen, C.J. Strachan, *Int. J. Pharm.* **334**(1–2), 78 (2007)

Chapter 19

Millimeter-Wave and Terahertz Imaging in Security Applications

Arttu Luukanen, Roger Appleby, Mike Kemp and Neil Salmon

Abstract The relatively short wavelength of mm-wave and THz radiation coupled with good transmission through many dielectric materials allows images to be formed of concealed objects. This chapter gives an overview of the detectors, their associated circuitry, and system developments over the past 10 years, focussing on personnel security screening. We will discuss the phenomenology of imaging at these wavelengths, introduce the reader to the basic architectures being used and developed for image forming instruments, show examples of systems, and also discuss the feasibility of spectroscopic THz imaging for security screening applications.

19.1 Introduction

Electromagnetic radiation in the millimeter to terahertz band (30 GHz to 10 THz) is nonionizing and therefore its use is free from public health concerns associated with the use of frequent exposure to nuclear radiation and X-rays. One of the first imaging systems was developed by the Royal Radar Establishment in the 1950s [1], a rather remarkable feat considering that the system was based on thermionic valve

A. Luukanen (✉) · R. Appleby
MilliLab co VTT Technical Research Centre of Finland, Finland, Europe
e-mail: arttu.luukanen@vtt.fi

R. Appleby
Queen's University Belfast, Cambridge, UK
e-mail: r.appleby@qub.ac.uk

M. Kemp
Iconal Technology Limited, Cambridge, UK
e-mail: mike.kemp@iconal.com

N. Salmon
MMW Sensors Ltd, Manchester, UK
e-mail: Neil.Salmon@MMW-Sensors.com

technology. Later in the 1970s, passive millimeter-wave (MMW) imaging in the band 100–300 GHz was investigated using semiconductor technology, as a means to detect nuclear radiation shielding materials and concealed explosives [2, 3]. During the 1980s and the early 1990s a better understanding of the phenomenology of passive MMW imaging was developed, due to the increasing number of proof of concept imaging systems that had been designed and operated in the atmospheric transmission windows and absorption bands in this region. The motivation for much of this work was to demonstrate the ability of systems in this waveband to detect and recognize metal and non-metallic threats concealed under clothing. In the mid to late 1990s a number of video rate imaging systems was developed at 35 GHz and 90 GHz and from 2000 until 2011 demonstration systems were developed to 1 THz and beyond, spurred on by the September 11th event in 2001. Some of the prototypes have been commercialized and are currently in use or under evaluation.

This chapter provides an overview of the imaging technologies that are being developed and deployed for security screening applications.

19.2 Phenomenology of Security Screening

Imaging for security applications can either be achieved passively where the natural radiation emitted and reflected by the object of interest is used or actively where a transmitter provides illumination and the image is formed from this reflected light.

In this section both passive and active imaging are described, followed by the properties of the atmosphere and relevant materials.

19.2.1 System Performance Metrics in Passive MMW Imaging

Security screening aims to detect, recognise and identify threats carried on people with a high probability and a low false alarm rate, ideally at video rates on moving subjects. The detection is based on the measurement of minute spatial variations in the natural thermal (black body) radiation emitted by the target. Systems required to do this must have good receiver operating characteristics [4] and to achieve this it is important to understand the basic performance metrics of an imager, how contrast in an image arises, and the phenomenology of imaging in various scenarios.

The noise equivalent power (NEP) of a detector relates to post-detection signal-to-noise ratio as $\text{SNR} = P_{\text{in}} (\text{NEP}_{\text{sys}} \sqrt{\Delta f_{\text{ENBW}}})^{-1}$, where Δf_{ENBW} is the post-detection effective noise bandwidth for data collection in a single pixel in the image.

The noise equivalent temperature difference (NETD), of a passive MMW imaging system is given by the radiometer equation Eq. 19.1, where T_A is the antenna temperature (the radiation temperature of the pixel being viewed), T_R is the receiver noise temperature, and $\Delta \nu_{\text{RF}}$ is the radiometric bandwidth [5]. Often mechanical scanning

of N_i image pixels with N_{rec} receivers is utilized which reduces the per-pixel dwell time and increases $\Delta f_{\text{ENBW}} \propto N_i/N_{\text{rec}}$. This leads to tradeoffs in systems designs between the number of receiver channels in the focal plane array, the field of view (FOV), the noise, and the image update frame rate.

$$\text{NETD}_{\text{sys}} = (T_A + T_R) \sqrt{\frac{\Delta f_{\text{ENBW}}}{\Delta \nu_{\text{RF}}}} = \frac{\text{NEP}_{\text{sys}} \sqrt{\Delta f_{\text{ENBW}}}}{k_B \Delta \nu_{\text{RF}}}. \quad (19.1)$$

The angular resolution $\Delta\theta$, in a passive MMW image is set by the diffraction limit associated with the size of the primary optics aperture D , this being given by $\Delta\theta \sim \lambda/D$ where λ is the radiation wavelength.

19.2.2 Contrast in Passive MMW Imagers

The radiometric contrast between an object and its background is governed by their different radiation temperatures. The radiation temperature T_{RAD} of any part of the subject is described to a first approximation by Eq. 19.2, where T_{ILL} is the illuminating radiation temperature, and T_{SUB} and Γ_{SUB} are the subject thermodynamic temperature and reflectance, respectively. The illuminating temperatures will be dependent on the environment, while the reflectances are dependent on material properties. Metal has a reflectance of 100% and human skin a reflectance of between 5% and 40%, depending on frequency, incidence angle, and body region. For normal incidence the reflectance in going from one medium into a second is given by Eq. 19.3, where n is the complex refractive index of the media. For air, the refractive index, n_1 , is unity.

$$T_{\text{RAD}} = T_{\text{ILL}} \Gamma_{\text{SUB}} + T_{\text{SUB}} (1 - \Gamma_{\text{SUB}}), \quad (19.2)$$

$$\Gamma = \left(\frac{n_1 - n_2}{n_1 + n_2} \right)^2. \quad (19.3)$$

More complex models exist for the reflection from multiple layers of clothing and non-metallic threats against the body [6]. Signatures then become dependent upon the reflectance, Γ , emissivity e , and transmittance, γ of the constituent materials, which sum to unity as indicated in Eq. 19.4. The absorption coefficient α of radiation in these materials is determined by the imaginary part of the refractive index n'' and is given by Eq. 19.5. Furthermore, in moving up into the submillimeter-wave (SMMW) band, scattering plays an increasing role in the blurring of the edge of objects. In scenarios where thin layers of energetic materials are placed close to the body internal reflections may need to be accounted for. Details of the properties of clothing, skin, and energetic materials are provided in Sect. 19.2.7 below.

$$\Gamma + e + \gamma = 1, \quad (19.4)$$

$$\alpha = \frac{4\pi}{\lambda} n''. \quad (19.5)$$

For stand-off security screening, particularly at the higher frequencies, absorption and emission from the atmosphere will appreciably reduce the contrast in images. This, together with the absorption and scattering in the overlying layers of clothing, limits the maximum usable upper frequency. The radiation temperature T_R of the subject measured at the imager location is given by Eq. 19.6, where T_0 is the atmospheric temperature and τ is the optical depth of the atmosphere between the subject and the imager, this being the line integral of the atmospheric absorption, α , along the line of sight, as given in Eq. 19.7. Atmospheric attenuation in the MMW and SMMW band is discussed below.

$$T_R = T_{\text{RAD}} e^{-\tau} + T_0 (1 - e^{-\tau}), \quad (19.6)$$

$$\tau = \int_{\text{IMAGER}}^{\text{SUBJECT}} \alpha \, ds. \quad (19.7)$$

The diffraction limit, $\Delta\theta \sim \lambda/D$, limits the use of lower cost and more mature technology at the lower MMW frequencies to short-range ($\lesssim 5$ m) or portal applications only. For the same reason, operation well into the SMMW band is necessary for stand-off security screening in order to achieve the necessary spatial resolution. The upper frequency limit for stand-off systems is governed by the reduction in contrast of threats, which is determined by the extinction (absorption and scattering) in overlying clothing and the atmosphere.

19.2.3 Passive MMW Imaging Phenomenology

Illumination of subjects is an important factor that determines the phenomenology in passive MMW imaging. The natural illumination in the millimeter wave band arises from a multitude of spatially incoherent modes of thermal (Planck) radiation, much like in the visible part of the spectrum. For this reason passive MMW images have a very natural appearance and are easy to interpret, which is a great asset in security screening. A convention of dark shades for high radiation temperatures gives the ground a darker appearance and the sky a lighter appearance, resulting in images similar in appearance to those of visible monochromes. This is the black-is-“hot” convention. However, the reverse, white-is-“hot” convention, is also used.

Indoor images taken in the millimeter and sub-millimeter wave band show phenomenology associated with uniform illumination. This is because the radiation temperature of emission inside a building is almost isotropic and held at a level determined by the indoor building temperature. In these scenarios the contrast in

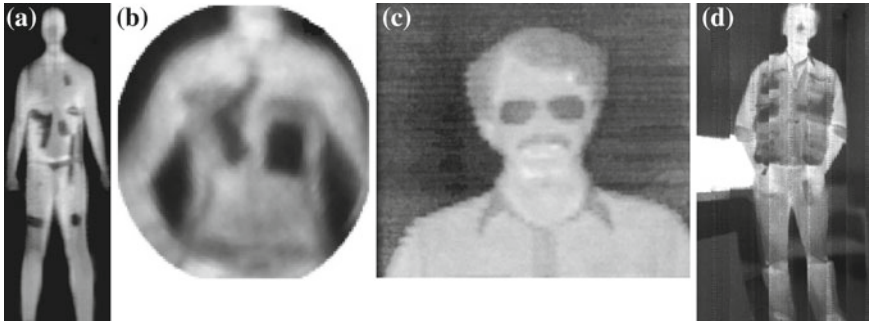


Fig. 19.1 Passive indoor imaging at (a) 94 GHz [7], (b) 350 GHz [8], (c) 600 GHz (wearing glasses) [9] and (d) broadband (0.2 – 1 THz) [10]. The increase in the visibility of clothing is apparent when moving from the lower to the higher frequencies, by the change in contrast of shirt collars and seams (White-is-“hot”)

the image arises from the difference between the illumination from the building and that from the human body, which may be typically ~ 20 °C. An example of such imagery is shown in Fig. 19.1, where the body appears at a fairly uniform radiation temperature and concealed objects appear at lower radiation temperatures. This phenomenology is also characteristic of outdoor imagery at the higher frequencies (>300 GHz) and in the atmospheric absorption bands, as the illuminating radiation temperature is almost isotropic, a consequence of the high atmospheric attenuation. In these regimes contrast over the subject is largely a result of differences in emissivity and physical temperature, rather than reflectivity.

Outdoor images taken in the atmospheric transmission windows at 35 GHz and 94 GHz have the characteristic features associated with relatively “cold” illuminating radiation from the sky and “warm” radiation from the ground. The sky radiation temperature will typically be in the region 20–180 K and dependent on frequency, zenith angle and weather conditions. Illuminating radiation from below is generally much “warmer,” typically in the region 250–300 K and dependent on the ground material. This gives rise to characteristic features associated with “cold” radiation being reflected from upward facing body surfaces, such as the shoulders and chest regions and “warm” radiation being reflected from downward facing surfaces, as illustrated in Fig. 19.2a. This illumination can also enhance the contrast of highly reflective items such as those made of metal.

Phenomenology associated with the frequency variation in the attenuation of clothing and hair is also recognized. As frequency increases, the attenuation of hair and clothing rises, due to increased absorption and scattering, as the wavelength approaches that of clothing weave size and hair strand diameter (~ 100 μm). This is illustrated in Fig. 19.2b, which shows a 94 GHz image of a person with a full head of hair. None of the hair is visible in the image. This is to be compared with the passive images of a persons at ~ 600 GHz Fig. 19.1, where hair is very apparent.

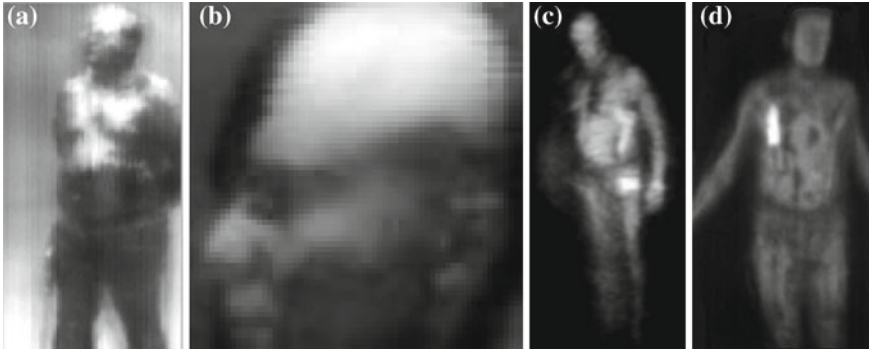


Fig. 19.2 **a** and **b**: Passive outdoor images at 94 GHz. “Cold” radiation from the sky is reflected by upward facing body surfaces, generating contrast. No hair is discernable in these images, even though the person has a full head of hair [12]. (Black-is-“hot”). Portal images **c** using spatially incoherent illumination at 35 GHz from a noise source inside a mode scrambling cavity [13] and **d** at 94 GHz from thermally warm panels illustrating concealed threats as white [14]. (White-is-“hot”)



Fig. 19.3 (Left) Still frames from 10 fps passive mm-wave video imagery (MMW and visible with privacy overlay algorithm) from the Millivision Portal 350 system. (Right) The user interface of the Millivision Walk-by 350 system. [64]

Polarization has not been shown to be a powerful discriminator in passive MMW imaging, as the degree of linear polarization is generally below 20% and that of circular polarization below 1% [11]. For this reason systems tend to operate with just a single polarization.

Artificial illumination schemes arose out of attempts to increase the image contrast in indoor screening scenarios. Spatially and temporally incoherent illumination was generated using electronic noise sources and mode stirrers, or heated absorbers acting as radiators, emulating outdoor illumination, but in a more controlled fashion. As the illumination is spatially incoherent, the phenomenology of this type of imaging

has more in common with passive MMW imaging than radar imaging, (discussed below) and is therefore described here. Images from security screening portals that use this technique at 35 GHz and 94 GHz are shown in Fig. 19.2c and d as well as in Fig. 19.3.

19.2.4 Active (Coherent) Millimeter Wave Imaging

Active sensing in the millimeter wave band was a natural progression of radar techniques used at the lower frequencies. The benefit of using an active technique is that a controlled stimulus can be used to probe a region, which may be an area that has little measurable passive signature, and that range gating can be used. The use of coherent detection methods allows for greatly enhanced signal-to-noise ratio. The central governing equation here is the radar equation, $P_R = P_T G_T A_R \sigma / [(4\pi)^2 R_R^2 R_T^2]$, which gives the level of power returned from a subject (less than or equal to the beam width of the antenna), P_R , for a given transmit power, P_T , where G_T is the gain of the transmit antenna, A_R is the area of the receiver antenna, R_T is the transmitter to subject range, R_R is the receiver to subject range, and σ is the radar scattering cross-sectional area of the subject [15]. This R^4 dependence can reduce to R^2 when the radar transmits and receives using a single antenna [19].

As the total noise in a receiver system is proportional to the radio frequency bandwidth, the highest signal-to-noise ratios are achieved when the active source transmits in the narrowest possible spectral bandwidth and the receiver bandwidth is then tuned to this. This is almost the reverse of imaging radiometry, where wider radiation bandwidths generate higher signal-to-noise ratios.

In further contrast to passive MMW imaging, the illumination needs to be coherent over the signal integration time. This requires the source to be both spatially and temporally coherent. However, narrow bandwidths introduce clutter in the form of speckle, etalon, and multi-path effects, making threats difficult to discriminate. The use of radar techniques, for example range gating, can reduce the scatter from overlying layers of clothing to reveal concealed threats beneath. The unambiguous range resolution, ΔR , in radars is inversely related to the bandwidth of the modulation, $\Delta\nu_{RF}$, and is given by $\Delta R = c / (2\Delta\nu_{RF})$, where c is the speed of light. However, increasing the bandwidth requires greater powers to be transmitted, particularly if centimeter- scale range resolution is required for threat discrimination.

For attenuation of the illuminating radiation in the atmosphere and in clothing, similar arguments apply to those of passive systems. However, an active system is less vulnerable to the extinction by clothing and the atmosphere thanks to their larger dynamic range. This means they can generally operate out to greater ranges and at higher frequencies than the passive counterparts.

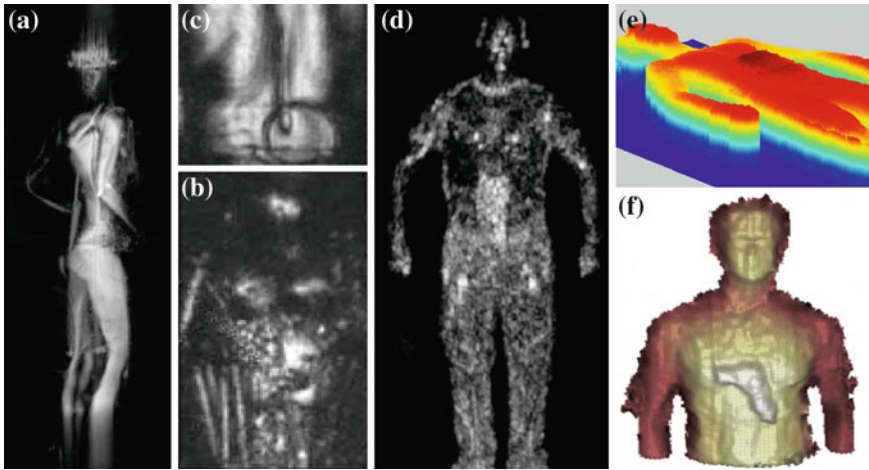


Fig. 19.4 **a** Portal active imaging at 24–34 GHz of a mannequin [16] and **b** at 24 GHz of a person carrying concealed weapons, using active coherent illumination [17]. **c** A disk of simulant energetic material is revealed by scattering from edges, while the bulk material is transparent. *Stand-off* active imaging at 350 GHz **d**, **e** [18] and at **f** 600 GHz using coherent illumination [19]. A concealed package on the stomach area is recognized by the contrast in the 2D image **d** and by its 3D form using range gating **e**. Similar range gating discriminates characteristic form at 600 GHz **f**.

19.2.5 Active Millimeter Wave Imaging Phenomenology

In active imaging contrast over a subject is very much dependent on the reflectivity and scattering from materials and the body. Furthermore, as the technique is not dependent on illumination from external sources, there is little difference between indoor and outdoor imaging phenomenology.

Portal imaging systems operating at the lower frequencies (24–35 GHz) are capable of generating detailed full three-dimensional images of a subject, as illustrated in Fig. 19.4. At the low frequencies the difference in reflectivity between energetic materials on skin and the skin by itself can be small; however, the presence of these threats may be detected by the scattering from their edges.

Stand-off imaging systems operating at the higher frequencies are capable of generating images at range with good spatial resolution as illustrated by systems operating at 350 GHz and 600 GHz in Fig. 19.4d–f. Concealed objects are apparent in the two-dimensional images, but further discrimination in three dimensions may be provided by range gating. This is illustrated in the figure, where a depth profile of reflection over the front area of the body may be created to reveal concealed threats. At higher frequencies it becomes increasingly difficult to discriminate concealed threats in a purely two dimensional image, due to the increased scattering and the reduction of signal level by the overlying clothing.

Scattering as a phenomenon is very apparent in active imaging in the submillimeter wave band, as illustrated by the image of a person’s face and hair in Fig. 19.5.

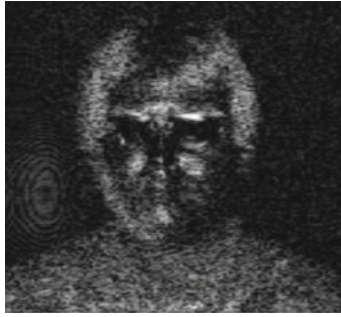


Fig. 19.5 Stand-off active imaging using illumination at 640 GHz (D. Petkie, Wright State University, 2011). The left-side of the face has a couple of days' growth of stubble compared to the right-hand side, which is clean shaven. This is apparent in the image and may be expected, as hair strand diameter is $\sim 100 \mu\text{m}$ and growth rate is $\sim 300 \mu\text{m}$ per day, which are appreciable fractions of the $\sim 470 \mu\text{m}$ wavelength

Although the person appears to have a full head of hair in the visible band, there is little millimeter wave signal return from the top of the head, but a significant amount of scattering from a relatively short growth of stubble.

Polarization offers powerful capabilities in active systems as it can be used to discriminate between plane reflectors and edges. Plane reflectors change the handedness of circular polarization, i.e., right-hand circular polarization is reflected to left-hand circular polarization. Detecting right-handed returns therefore rejects the plane surface reflections, emphasizing the scatter from edges, as they have a predominantly linear polarization component. In addition, multi-path effects can also be discriminated by exploiting circularly polarized radiation and these effects are discussed more fully in [20]. Generally, full polarimetric systems, operating in transmit and receive, have the potential to reveal a multitude of detail about concealed threats.

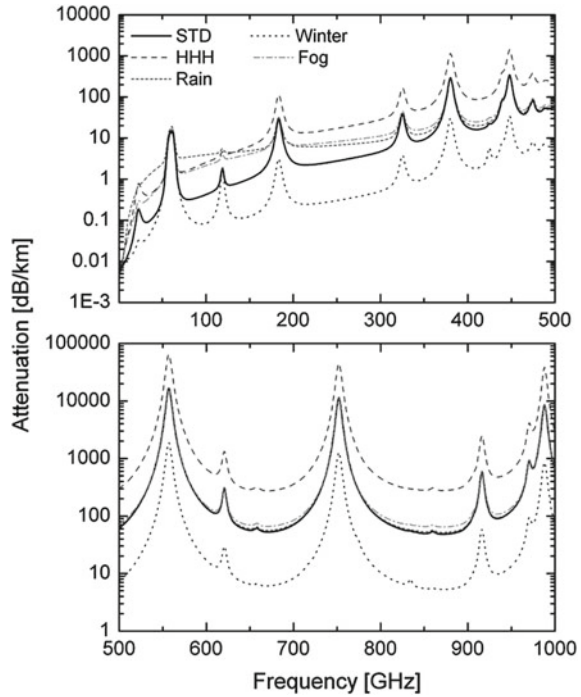
19.2.6 Atmospheric Transmission

The atmospheric attenuation up to 1 THz is shown for a variety of weather conditions in Fig. 19.6. The attenuation rises with frequency and there are regions of high attenuation due to the rotational absorption lines of molecular oxygen and water vapor.

19.2.7 Material Properties

In an imaging system designed for security screening, the observed image is dependent on the optical properties of clothing, metal, and skin, and can be described

Fig. 19.6 Atmospheric attenuation in the band up to 1 THz for various weather conditions [21]: STD—Standard US atmosphere; HHH—Hot and humid; Winter— -10°C , Fog—100 m visibility, Rain—4 mm/hr



in terms of their transmittance γ , emissivity e , and reflectance Γ , as shown in Table 19.1. More detailed information can be found on the transmission of clothing in Reference [22] and on the millimeter wave properties of energetic materials in References [23–26]. A spectrum of the absorption coefficient and reflectance of these materials are presented in Fig. 19.19. From the table it is clear that metal has a reflectivity of unity, which is frequency independent. Zirconia, from which ceramic knives are made, is also a strong reflector. The emissivity of skin increases with frequency and the transmission of clothing decreases with frequency. Many explosives have a high transmission at 100 GHz, which decreases as the frequency is increased.

As can be seen in the table, a 5-mm thick sample will have a small contrast against the body, the transmittance being zero in this case, as no radiation is passed through the body. However, some energetic mixtures generally have higher emissivities, giving them a larger signature. Many objects, including clothing and formulated explosives, often have fiber, which scatters the incident radiation. This will cause radiation which would normally be transmitted or reflected to be scattered over a wider angle, changing the level of signal return and modifying the local illumination of objects. The effect is a smearing out of the spatial details of the objects.

Moisture in the form of human body perspiration and its effect on clothing transmission needs to be considered when comparing signatures from real subjects with simulations. The large dipole moment on the water molecule means that even small

Table 19.1 Optical properties of 5 mm thick energetic materials, skin, metal, denim, *t*-shirt [27] and leather [22]

Frequency (GHz)	Emissivity (ϵ)			Reflectance (Γ)			Transmittance (γ)		
	100	500	1,000	100	500	1,000	100	500	1,000
Nitro based energetic compounds on skin	0.76	0.95	0.94	0.24	0.05	0.06	0	0	0
Metal	0	0	0	1	1	1	0	0	0
Ceramic (Zirconia)	0	0	0	0.9	0.9	0.9	0	0	0
Skin	0.65	0.91	0.93	0.35	0.09	0.07	0	0	0
Denim	0.09	0.49	0.85	0.01	0.01	0.05	0.9	0.5	0.1
Tee-shirt	0.04	0.2	0.3	0	0	0.05	0.96	0.8	0.65
Leather							0.8	0.42	0.09

amounts of water can significantly increase the attenuation in clothing, which is apparent in imagery. However, simulations may be based on optimistically high levels of transmission, arising from laboratory measurements of relatively dry clothing samples.

19.3 Imaging System Design Overview

The engineers designing passive image forming systems for mm-wave to THz frequencies typically face several challenges:

- (a) “Detector-starvation”—High cost of detectors, an economic limit set by the small number of uses in this band.
- (b) Wide field-of-view coverage, a requirement set by the end-user.
- (c) Diffraction-limited optical systems are compulsory, as end-users require systems to be compact requiring the aperture to be minimized.
- (d) Passive systems are also prone to “Signal-starvation”—Low signal levels at detectors, a fundamental limit set by the Planck emission formula.

For passive systems the Planck black body emission formula indicates the signal power at 94 GHz corresponding to a 1 K level of sensitivity at an ambient temperature of 300 K is ~ 260 fW (in single mode,¹ 20% relative bandwidth). Compare this with the single-mode power available in the LWIR (8–12 μm) of ~ 30 pW, i.e. some two orders of magnitude more signal power is present in the thermal infrared. Active systems, on the other hand, may suffer less from low signal levels, as it may be possible to use higher transmit powers.

The high costs of detectors can to some extent be off-set by using mechanical scanning to scan the subject with a single or small number of detectors. However, due to the long wavelength of the radiation, the optics are often large (~ 1 m diameter)

¹ One polarization, one spatial mode.

and making reliable, vibration-free scanning systems for near real-time frame refresh rates (≤ 30 Hz) a significant engineering challenge.

A specialized methodology, used in the design of MMW to THz systems, is referred to as or *quasi-optics* or *Gaussian optics*, a branch of optics where diffraction within an instrument is considerable and the optical beam, by design, has a Gaussian intensity distribution [28, 29]. The simultaneous requirements for large FOV and diffraction limited performance across the FOV poses a challenge to the design of the optics, as optical aberrations increase rapidly when moving away from the paraxial region to the off-axis beams.

As an alternative to focal plane image formation, pupil-plane image formation can also be employed [30–32]. In a focal plane imaging system the detectors are located after the image forming optics, while in a pupil-plane system image formation takes place in either electronics or optics (after upconversion). Prototypes are still at the design stage but could potentially be used to build an imager of planar geometry which could be fixed to a wall.

An interesting combination of electronic and optical image formation is the use of adaptive holograms: Utilizing well-established methods of holography, one can design a reflective (or transmissive) surfaces with a phase or amplitude pattern that corresponds to the interference pattern of the illuminating input beam (of a transceiver) and the transferred (output) beam, focussed to a given location in the target space. Phase holography is preferable from the standpoint of efficiency, as an amplitude hologram necessarily loses a substantial fraction of the input power. One approach that has been recently developed [17] employs a large array of patch antennas, each of which is connected to a p-i-n phase shifter. The phase shifter can be a p-i-n diode, liquid crystal polymer (LCP), or RFMEMS phase shifter [33, 34]. Even the use of optical excitation in a photoconductor has been investigated [35]. The benefits of this so-called “reflectarray” beam steering approach are numerous, including low loss (since no lengthy feeding networks are required), scalability, adaptability, and the strong leveraging effect through the utilization of digital pattern generation techniques.

19.4 Detector Technologies

In this section we give a brief overview of coherent and incoherent detection methods for MMW and THz imaging. For more a comprehensive treatment we refer the reader to excellent reviews [36–38].

A detector is a device that rectifies the electric fields of an incoming wave, converting its power into an rms voltage (or current), with an integration time commensurate with application requirements. In the process of rectification the phase of the wave is lost and as such they are only suitable for incoherent detection systems. A mixer on the other hand multiplies the electric field of the incoming wave with a locally generated field, shifting the wave either up or down in frequency. In the process of mixing both the phase and amplitude of the original incoming wave are retained and

can be further processed, either by optical imaging technology or by analog to digital conversion and digital signal processors.

19.4.1 Coherent up or Downconversion

Phase (or time) coherent detection in the context of MMW to THz receivers is carried out by mixing the incoming field (signal) $V_s e^{i\omega_s t}$ with a high-purity reference signal (local oscillator, LO) $V_r e^{i\omega_r t}$ within a nonlinear circuit element, such as a diode. In most common situations, $V_s \ll V_r$.

Heterodyning produces an intermediate frequency (IF) signal at a frequency $\omega_{IF} = \omega_s - \omega_r \ll \omega_s, \omega_r$ with an amplitude that is multiplied by the (ideally noiseless) LO: $V_{IF} = V_r V_s$. A typical heterodyne radiometer architecture is shown in Fig. 19.7. The incoming THz field is coupled via an antenna to a waveguide incorporating the mixer. The mixer may be preceded by a low-noise amplifier (LNA), especially if the frequency is below ~ 100 GHz where integrated amplifiers are readily available. To compensate for $1/f$ noise and drifts, a so-called Dicke-switch [39] is typically placed before the mixer. The LO signal is coupled via a matching network to the mixer. Typically, the output of the mixer is filtered by a bandpass filter, which removes the upper sideband signals ($2\omega_s, 2\omega_r, \omega_s + \omega_r$). This is followed by an IF LNA, which amplifies the IF signal. Finally, the output of the IF LNA is coupled via a video filter to a detector, which converts the IF signal to baseband, i.e., the video signal and in this process the phase information is lost. The output of the video detector is now proportional to the incoming THz power. The first reported solid-state heterodyne downconversion receiver systems designed for passive MMW security imaging appeared in the early 1990s [40, 41]

Large image forming arrays of SMMW heterodyne radiometers tend to suffer from “LO starvation”: Schottky mixers typically require ~ 1 mW of LO power. Given that most available source technologies can barely produce such power levels at a few hundred GHz, a source per receiver is required. This in turn requires either a fully integrated LO source, or alternatively an efficient method of LO power distribution across the array. A solution to the former may be monolithically integrated heterodyne receiver arrays [42, 43]. The latter could be solved by the use of optically generated LO using LT-GaAs THz photomixers as per-pixel LO sources [44–46].

Coherent optical upconversion is an approach that has been investigated actively over the recent years [32, 47]. The method is an optical analog to coherent downconversion in the electrical domain. In this method, the incoming THz field is coupled via an antenna to an electro-optic modulator where it is mixed with an optical LO signal. The modulator is a device whose optical index of refraction is a function of the (THz) electric field. The THz power generates sidebands around the optical carrier frequency. The carrier is suppressed with a bandpass filter, and the sideband signals are consequently detected by a photodiode. The attractive feature of this approach lies in its ability to harness the vast array of optical telecommunications hardware readily available today and the use of fiber-optical techniques to distribute the sig-

Fig. 19.7 A typical heterodyne receiver architecture. Components that are often omitted are represented by dashed lines

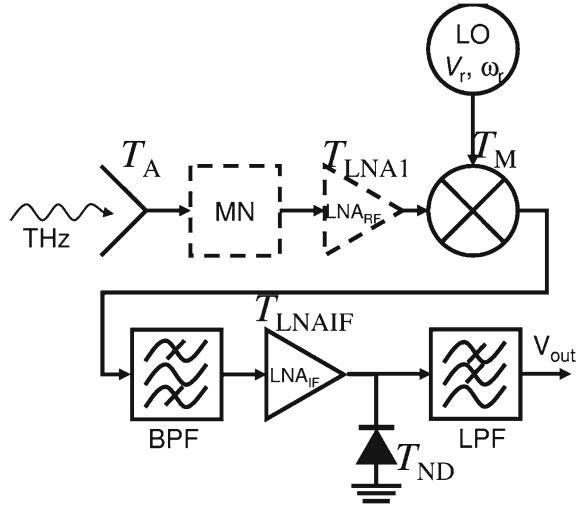
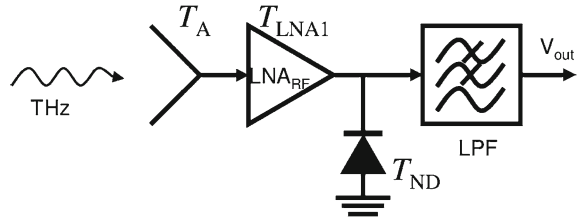


Fig. 19.8 The architecture of a preamplified direct detection receiver



nals from different channels across large distances much more easily than mm-wave signals.

19.4.2 Preamplified Direct Detection

Preamplified direct detection relies upon an LNA stage with large bandwidth which is used to “boost” the incoming electromagnetic signal above the noise of the detector that follows the LNA.

A simple schematic of the preamplified direct detection architecture is shown in Fig. 19.8. An important benefit of preamplified direct detection is that it does not require an LO source. This considerably simplifies the realization of receiver arrays. The inherent drawback is that the frequency coverage of the receiver is limited by the availability of LNA technologies to frequencies below ~ 200 GHz, a fact that at present restricts the application of this technology to short range imaging applications only due to the diffraction limit. This could well change in the future, as substantial R&D efforts are under way to develop LNAs up to 1 THz [48–50].

Until recently, the detector of choice following the LNA has been the Schottky diode. Contrarily, their excellent mixing performance in heterodyne instruments, the conventional Schottky barrier diode is a relatively poor detector: A DC bias is required to bias the diode to an impedance that can be impedance matched to the output of the LNA, and in order to gain sufficient responsivity. The DC bias gives rise to a substantial amount of $1/f$ noise, which needs to be circumvented with a Dicke switch.

Recent developments in low-barrier Schottky and zero-bias diodes [51–54] that have much lower $1/f$ noise significantly reduces the gain required from the preceding LNA stage(s): The lower the noise of the diode detector, the less amplification is required to reach a situation where the LNA noise dominates the system noise. This is highly desirable from the standpoint of system complexity and consequently, system cost [55].

All but one of the presently commercially available passive mm-wave cameras are based on preamplified direct detection arrays. Small production numbers, highly specialized fabrication processes associated with the manufacturing of MMW LNAs, and the need for accurate mounting to associated packaging (incorporating waveguides, coupling horns etc.) lead to high component costs. Thus, the design of passive systems is often a compromise between the radiometric performance (NETD scaling as $N_{\text{ch}}^{-1/2}$ due to increase in per-pixel integration time) and the cost of the camera frontend.

Efforts to reduce the per-channel cost are under way, especially focussing in the development of highly integrated receiver systems based on low cost materials such as Si and SiGe [43, 56]. The integrated receivers can potentially replace the compound semiconductor receiver technology if larger receiver counts at a competitive FPA cost can be achieved. The larger number of receivers may partly compensate for the inferior noise performance compared to higher performance InP or GaAs MMICs.

19.4.3 Incoherent (Unamplified) Direct Detection

With sensitive enough detectors, the LNA can be omitted altogether. At present, the most sensitive room temperature MMW detectors are zero-bias diodes and low-barrier Schottky diodes with NEPs around $1 \text{ pW}/\sqrt{\text{Hz}}$, improving with operating temperature and is directly proportional to T [57]. Operation in the SMMW region is possible, but the impedance matching of diodes to antennas becomes challenging. Bolometers with a NEP of $\sim 25 \text{ pW}/\sqrt{\text{Hz}}$ at room temperature [58] are readily adapted for SMMW operation. However, at the quoted NEPs, unamplified direct detectors are only applicable to active imaging, with holographic imaging as one example [59, 60]. If cooling is allowed, cryogenic bolometers ($\text{NEP} \propto T^{3/2}$ to $T^{5/2}$) and superconductor-insulator-superconductor diodes provide an alternative for passive detection. The added system backend complexity caused by the need for refrigeration is compensated by their high performance, low manufacturing cost, scalability to staring focal plane arrays, and frequency agility.

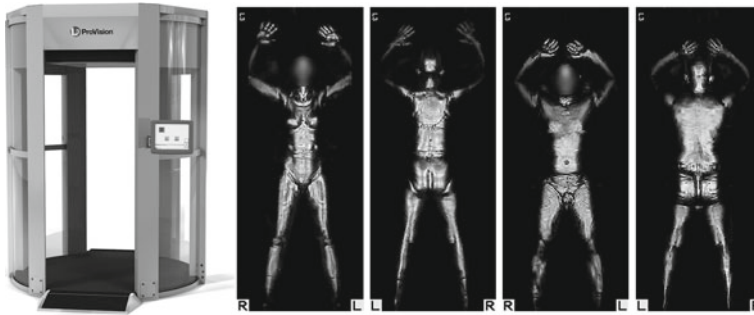


Fig. 19.9 (Left) The L-3 ProVision active mm-wave portal. (Right) 2-D projections of the volumetric data sets on two individuals (first two: *female*; last two: *male*). The faces are blurred for privacy. [61]

19.5 Millimeter-Wave Portals

In this section we give examples of some of the commercially available MMW portals, or short-range systems (typically providing still imagery).

19.5.1 L-3 ProVision

The L-3² ProVision³ system is an active holographic MMW portal, whose origins date back to the early 1990s. The technology employed in the portal was developed by Battelle Pacific Northwest Labs [62, 63], and later licensed to L-3. The system consists of a linear array of 35 GHz radar transceivers, mounted on a platform that carries out a cylindrical scan of the subject person, located on the rotation axis of the linear array. The image is formed through computational methods (FFTs). Given the ranging capability, the system provides volumetric (3D) still images of the subject. Image scan time is about 2 s, with several seconds required to compute and display the image. At present, the L-3 ProVision is globally the most widely deployed portal system (Fig. 19.9).

19.5.2 Millivision

Millivision's⁴ technology builds on arrays of preamplified direct detectors operating at 94 GHz. The Millivision Portal system 350⁵ and the Walk-by system 350 utilize

² L3 Communications <http://www.sds.l-3com.com/index.htm>.

³ ProVision@<http://www.sds.l-3com.com/advancedimaging/provision.htm>.

⁴ <http://www.millivision.com/>

⁵ <http://www.millivision.com/portal-350.html>.

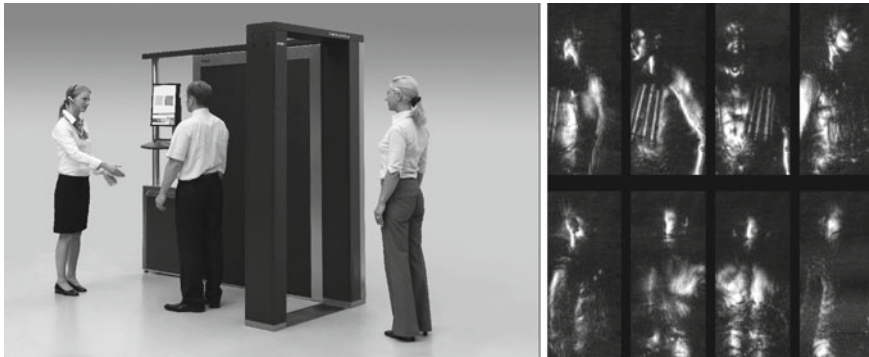


Fig. 19.10 (Left) The Smiths eqo portal. (Right) MMW imagery (frames from a movie) from the Agilent technologies prototype, an early precursor of the eqo [17]

artificial enhancement of contrast by heated or cooled panels whose temperature is substantially different from that of the ambient surroundings or the human body. The systems are also near-real time, providing about a frame rate of 10Hz. In the portal system, subject rotation by 360° yields full-body all-aspect imagery, while the walk-by system deploys two imagers (front/back) to cover both sides of the subject.

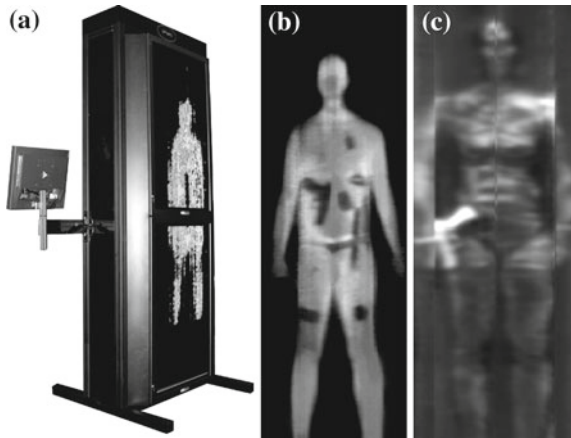
19.5.2.1 Smiths eqo

The Smiths⁶ eqo⁷ system is an active MMW portal (shown on the left in Fig. 19.10). The system is unique in the sense that it does not involve moving parts. An initial demonstrator was constructed by Agilent Technologies, and published in 2006 [17]. In the Agilent Technologies approach, image formation is carried out by reflecting a transceiver beam at 24 GHz off a digitally programmable reflector which focuses the transmitted mm-wave beam to a desired location on the target. Different “voxels” correspond to a specific digital phase pattern which is programmed onto the reflector. Thanks to the electronic scanning, only a small number of mm-wave electronic components are required, and due to the digital nature of the system it benefits from the rapid advance of digital microelectronics for the phase pattern generation subsystems. The system provides real-time video, and its highly adaptive nature does not suffer from depth-of-field issues that typically hamper the performance from imaging systems using physical lenses or mirrors.

⁶ Smiths Detection http://www.smithsdetection.com/?no_cache=1&L=4&e=1

⁷ <http://www.smithsdetection.com/eqo.php>

Fig. 19.11 **a** The Sago Systems Inc. iPat portal. **b** indoors and **c** outdoors imagery acquired with the system. (Images courtesy of C. Martin, Sago Systems, Inc.)



19.5.2.2 Sago Systems, Inc.

Sago's⁸ imaging systems utilize a linear array of preamplified direct detection receivers operating at 94 GHz. The image is formed using a clever combination of mechanical and electrical scanning [65, 66]. The benefit of Sago's approach is the small number of high frequency amplifiers required, which allows the use of state-of-the-art LNAs without compromising system cost. Near real time imaging is possible, but with degraded NETD since the system scans in both directions leaving little per-pixel integration time. Sago has built several versions of the frequency-scanned radiometers, an example of which is shown in Fig. 19.11.

19.6 Stand-off Imaging

Stand-off imaging of concealed explosives and weapons has been the focus of intensive research for several years. The technical challenges are substantial, not only due to the longer imaging distance, but also due to the fact that stand-off imaging scenarios often require video rate imaging systems in order to be able to screen moving people. This section only includes systems and prototypes that produce near-real-time imagery.

19.6.1 Passive Stand-Off Imaging Systems

The challenges associated with passive stand-off systems are mostly associated with the development of SMMW receiver arrays with sufficient sensitivity for passive detection. As described in Sect. 19.2, since passive systems rely on ambient black-

⁸ Sago Systems Inc. <http://www.trexenterprises.com/Subsidiaries/sago.html>

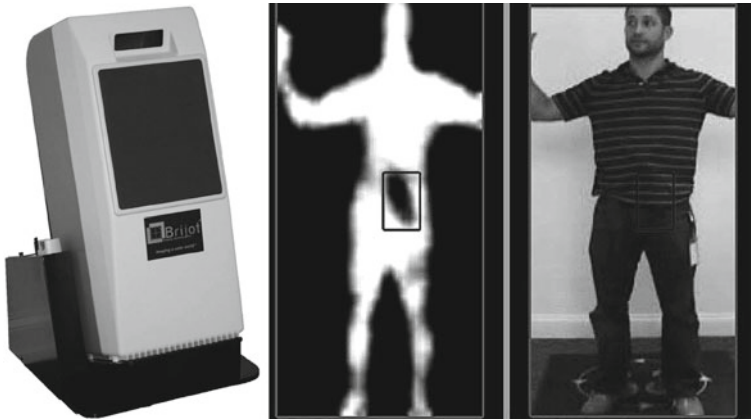


Fig. 19.12 The Brijot GEN2 passive MMW camera, and corresponding imagery. Images courtesy of Brijot Imaging Systems Inc.

body illumination they suffer from atmospheric and clothing attenuation more than their active counterparts [67].

19.6.1.1 Brijot Imaging Systems

Brijot⁹ Imaging Systems sell several product variations based on a preamplified direct detection receiver array imager operating at a center frequency of 94 GHz. The Brijot GEN2¹⁰ system (see Fig. 19.12) which incorporates mechanically scanned optics is capable of full-body imaging at 4–12 Hz frame rate with an image resolution of about 6 cm × 6 cm at a distance of 3–5 m. The company also sells solutions which include two units for simultaneous front- and backside imaging (Fig. 19.13).

19.6.1.2 Thruvision Systems

The stand-off systems from Thruvision¹¹ utilize an 8-channel heterodyne down-conversion receiver operating at 250 GHz, coupled with reflective telescopic optics intended for imaging from 3 m up to ~25 m. The T5000¹² is essentially a ruggedized version of the T4000¹³ system, intended for outdoors use. The T4000 angular

⁹ Brijot® is now MicroSemi <http://www.brijot.com/>

¹⁰ GEN2 ® <http://www.brijot.com/products/gen2>

¹¹ Thruvision has been acquired by Digital Barriers <http://www.thruvision.com/>

¹² Has become TS4 http://www.thruvision.com/Products/TS4_Sub_Pages/TS4_Product_Page.htm

¹³ TS5 http://www.thruvision.com/Products/TS5_Sub_Pages/TS5_Product_Page.htm

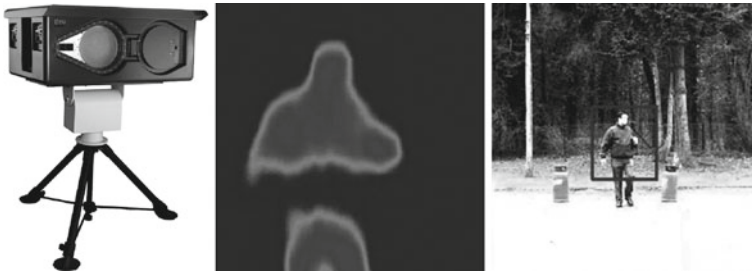


Fig. 19.13 The Thruvision T5000 ruggedized camera, and corresponding imagery

resolution (defined as the full width at half maximum of the Gaussian point spread function) and angular FOV are $\sim 1.26^\circ$ and $18.9^\circ(\text{H}) \times 24.8^\circ(\text{V})$, respectively. For the T5000, the numbers are $\sim 1.0^\circ$ and $17.3^\circ(\text{H}) \times 15.5^\circ(\text{V})$. Thruvision also offers a portal system, the T8000. Image acquisition time is variable from 3 to 30 s, with a spatial resolution of $20 \text{ mm} \times 20 \text{ mm}$.

19.6.1.3 VTT/NIST Passive THz Camera

The use of cryogenically cooled bolometer arrays as sensitive SMMW detectors may offer a solution for stand-off imaging. While the need for cooling brings about several other issues, such as the need for a cryocooler, the necessary cool down time for operations and larger weight and power consumption, this approach nevertheless has shown some promise in providing a route in the near term future for stand-off imaging.

A research prototype system developed jointly by Aalto University, NIST, and VTT is a broadband incoherent system that utilizes superconducting antenna-coupled microbolometers [68] configured in a linear array [69, 70]. The electrical NEP of these sensors is $\sim 8 \times 10^{-15} \text{ W}/\sqrt{\text{Hz}}$. The detector array is mounted onto the second stage of a commercial pulse tube cryocooler, and is operated at temperatures between 4 K and 7 K. The benefit of a pulse tube cooler is its high reliability and long maintenance period ($\sim 20\,000 \text{ h}$).

The nominal design bandwidth of the detectors is from 200 GHz to 1 THz, and the effective center frequency of 640 GHz has been inferred from detector beam pattern measurements. The image is formed using a folded, all-reflective variant of the Schmidt telescope that provides a large FOV. A periscopic conical scanner allows for the formation of a 2D image at frame rates up to about 10 Hz. At 7 Hz, the system NETD has been measured to be $\sim 0.5 \text{ K}$ with a spatial resolution of $(4 \text{ cm})^2$ at a focus distance of 5 m. The spatial resolution is limited by the sampling of the image, a tradeoff between the number of detectors in the linear array and the relatively large angular FOV of $\pm 15^\circ(\text{H})$ by $\pm 7.5^\circ(\text{V})$.

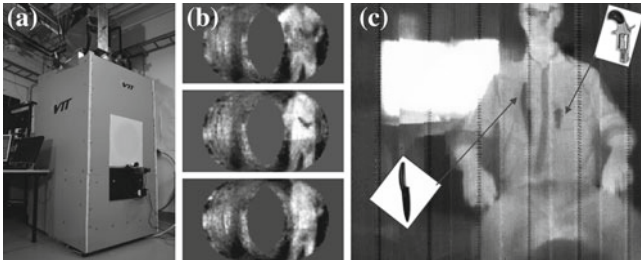


Fig. 19.14 **a** An image of the passive video-rate THz camera. **b** Three frames from a passive THz video acquired at frame rate of 7 Hz at 5 m focus distance, with the top frame showing a person concealing a gun under fleece jacket, center frame with the jacket opened, and bottom frame showing a wallet in the back left pocket of trousers. The hole in the center of the field is only due to partly filled linear detector array; **c** Raster-scanned still image taken with a similar detector array, acquired at 2.5 m focus distance. Image acquisition time was 2 min

An image of the system, SMMW frames from a movie and still images taken with a similar system are shown in Fig. 19.14. A smaller version of the system with improved sampling (and a smaller FOV), along with a multi-spectral version are under development.

19.6.1.4 Jena/IPHT Safe-Visitor

The SAFE-VISITOR passive camera prototype also utilizes cryogenic microbolometers [8, 71]. The sensors are configured in a circular array of 20 detectors and are operated within a commercial dry $^4\text{He}/^3\text{He}$ sorption cooler at a bath temperature of 0.3 K. As bolometers improve quickly with temperature, the electrical NEP of the bolometers is $\sim 1 \times 10^{-16} \text{ W}/\sqrt{\text{Hz}}$. In comparison with the system described in 19.6.1.3, the benefit of the excellent NEP is twofold: (i) it requires a smaller number of detectors to sample an image at a given required NETD and frame rate and (ii) it allows for smaller THz bandwidth, simplifying optics design and reducing the effect of clothing attenuation. These benefits are however counterbalanced by the lower bath temperature requirement, necessitating the use of a more expensive sorption cooler that requires an automated regeneration cycle of 2 h every 24 h (Fig. 19.15).

The image is formed using a Cassegrain telescope with an aspherical primary mirror, and a spiral-scanning secondary. The optical configuration is quite compact, a common merit of the Cassegrain telescope, but it has a somewhat limited radial FOV of 5° , corresponding to 1.6–10 m. The system design bandwidth is from 335 to 375 GHz, defined by a set of bandpass filters, and it can be run at frame rates up to 10 Hz.

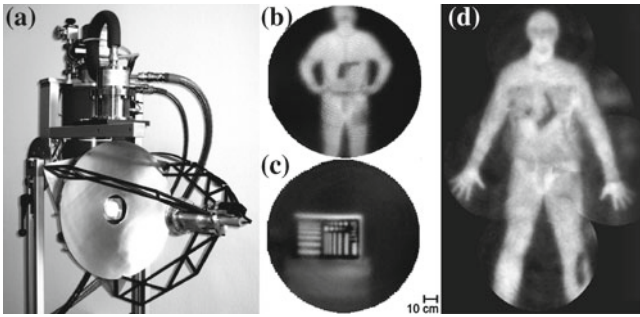


Fig. 19.15 **a** An image of the SAFE-VISITOR system **b** a passive image of a person with a mock-up gun at 8 m stand-off **c** a passive image of a resolution target at 8 m **d** a full-body montage from several smaller FOV images at 5 m (taken with a laboratory pre-cursor system) [8, 71]

19.6.2 Active Stand-Off Imaging Systems

Active stand-off imaging systems employ an artificial source of radiation that is used to illuminate the target, located at a distance from the source and the detector. The primary benefits of active imaging are those described in Sect. 19.2.

19.6.2.1 Imaging SMMW Radar Systems

Among promising candidates for active stand-off imaging are the 350 GHz and 675 GHz frequency-modulated continuous-wave (FMCW) radar imagers developed by PNNL and JPL, respectively [18, 19]. The ranging capability is of great importance, as it avoids the strong first-surface (clothing) reflections to reveal the much weaker signatures beneath the clothes [72]. The JPL system consists of a conventional (albeit very high frequency) monostatic low-power ($250 \mu\text{W}$) radar frontend that is frequency-swept across 662–688 GHz, yielding a theoretical range resolution of ~ 6 mm. Because of the high center frequency, the 26 GHz bandwidth corresponds to only $\sim 4\%$ relative bandwidth, allowing for straightforward implementation of the RF and scanning optics components. The system has been demonstrated in the imaging of concealed objects at a record stand-off range of 25 m at a frame rate of 0.2 Hz (see Fig. 19.16). At present, the system can only cover a relatively small FOV of $50\text{ cm} \times 50\text{ cm}$, limited by the optomechanical scanning and the chirp generator.

The PNNL system transmits approximately 4 mW, chirped from 340 GHz to 360 GHz, corresponding to a range resolution of 8 mm. The radar is coupled to conical scanning optics designed for stand-off ranges of 2 m, 5 m, and 10 m with a full-body FOV and an image acquisition time of ~ 10 s. Sample images are shown in 19.4d and e. In the case of both systems, full-body coverage at video rates requires substantial development efforts, especially if multi-channel transceiver systems are

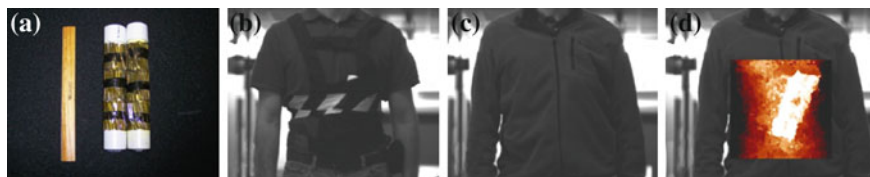


Fig. 19.16 Target scenario and SMMW image overlay for through-jacket detection of a mock pipe bomb. The image was acquired in 5 s at a range of 25 m. **a** Mock pipe bomb **b** the bomb strapped to torso **c** jacket covering the threat **d** SMMW image overlay. Image adapted from [19]

required for real-time imaging. Steps toward such architectures have already been undertaken [73].

19.7 Multispectral and Spectroscopic Imaging

As discussed in Sect. 19.2, properties of materials are frequency dependent. The transmission/absorptivity, emissivity, reflectivity, and scattering of objects of interest, background, and barriers all change with frequency. This leads to the possibility of combining images at several frequencies in order to improve image contrast, in just the same way as a color photograph often reveals more information than black and white images.

In the THz region (above 600 GHz or so), it was found in the early 2000s that many common explosives exhibit characteristic absorption lines in their THz spectra. This offers the intriguing possibility that THz spectroscopy could be used as a safe method of detecting and identifying explosives concealed on the body.

19.7.1 Multispectral Imaging

Kemp et al. [74, 75] have shown how multi-spectral imaging can greatly improve the interpretation of B-scan images – see Fig. 19.17. Here, the broadband image shows a B-scan depth slice through a number of test objects covered with cloth. The multispectral image separates the image into three frequency bands (0.5–0.7; 0.7–1.0; and, 1.0–3.0 THz) which are colored red, green, and blue, respectively, and then recombined into a false-color image. This reveals differences between the test objects due to the way they absorb high frequencies and texture in the cloth which is largely due to scattering.

Overall, there has been relatively little work carried out in this area. This is probably due to the cost and complexity of developing imaging systems which operate at two or more frequencies.

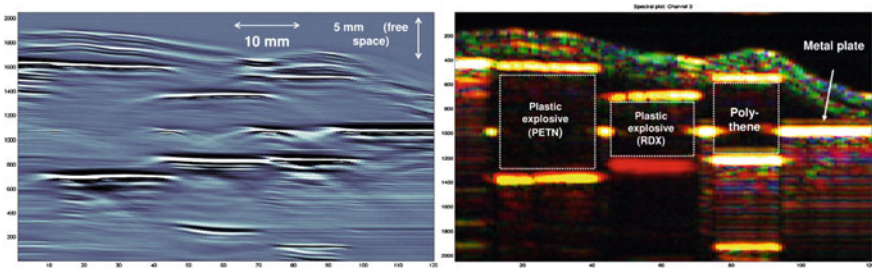


Fig. 19.17 Broadband and multispectral THz *B*-scan images of a number of objects hidden beneath two layers of cloth

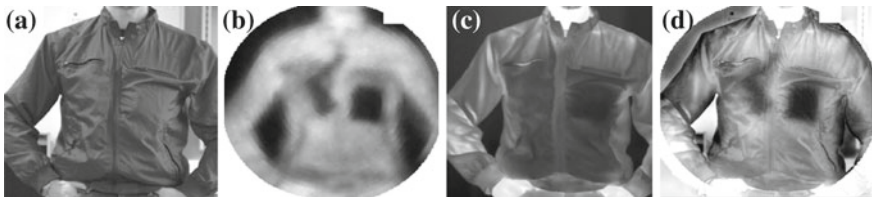


Fig. 19.18 Image fusion example from the Safe VISITOR project: **a** visible image **b** THz image **c** infrared image **d** fused image [8, 71]

Grossman et al. at NIST [76] developed a rotating frequency-selective filter wheel which could be used in front of a broadband microbolometer imager for multispectral imaging. The bolometric cameras detailed in Sect. 19.6 could be readily adapted for multi-frequency detection given the frequency-agility of bolometers.

Of course, multispectral imaging need not be restricted to MMW-THz frequencies alone: infrared thermal imaging can be used to infer the presence of hidden objects through the way they block heat conduction to the surface; infrared and visible wavelength imaging can help distinguish the outline of the body from the background and provide surface detail to facilitate interpretation. The fusion of visible, infrared, and MMW images has been explored since the earliest days of MMW imaging for security [77] and is used in a number of commercial products. Fig. 19.18 shows an example.

19.7.2 THz Spectroscopic Imaging

The THz spectra of common energetic compounds (RDX, PETN, HMX, TNT) and commercial explosives based on these compounds (PE4, Semtex-H) were first reported in 2003 [78]. These results are shown in Fig. 19.19 and have subsequently been validated and extended by a number of groups [79–83] using time domain THz spectroscopy and FTIR. The strong absorption features, particularly of RDX-based explosives around 800 GHz, appear to open up the possibility of material-specific

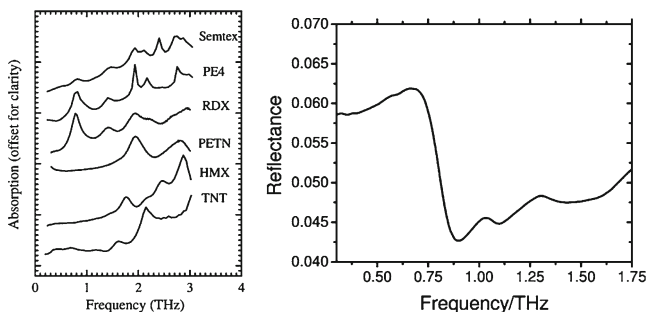


Fig. 19.19 (Left) THz transmission spectra of the raw explosive materials TNT, HMX, PETN, and RDX together with the spectra of the compound explosives PE4 and Semtex H. (Right) Reflection spectrum of the explosive Semtex H [85]

detection of these materials. These features are relatively distinct from harmless, potential confusion, and barrier materials. Kawase [84] has also identified strong signatures in a number of drugs of abuse and cutting agents.

Practical detection systems will need to operate in reflection rather than transmission mode due to the high absorption coefficients of the explosives themselves and, for people screening applications, due to absorption by the body. Fig. 19.19 shows the reflection spectrum of Semtex H, a mixture of RDX and PETN; the spectral features due to the resonances are still visible, but are much weaker when measured in reflection geometry measurements. The spectral features are also present in scattered radiation, but here the overall signal strength is several orders of magnitude lower, again making detection more challenging. Laboratory experiments have demonstrated real-time detection of RDX-based explosives at modest stand-off distances around 1 m [85] using smooth, flat samples, and specular reflection. Spectroscopic imaging has also been demonstrated in the laboratory [86]. It continues to prove extremely challenging, however, to progress beyond this toward a system which could be deployed on the wide variety of configurations that would be met in any practical deployment. Scattering from explosives and clothing causes significant measurement artifacts [87, 88] and the strong absorption from clothing at frequencies of 2 THz and above, which are needed to see many of the spectral features, means that the signal becomes lost in the noise. Doubts have been raised over whether practical systems will ever be achieved [89].

19.8 Future Directions

MMW portals have matured to the point where the next steps will be associated with backend processing, such as automated target recognition (ATR) algorithms that would substantially reduce the manpower cost of operating these systems. Also the privacy issues that have been associated with active MMW portals will be remediated by ATR. Systems such as the L-3 ProVision have already started deploying systems

with ATR features. For the short-range stand-off passive MMW imagers the major driver will be to reduce system costs. Significant cost reductions will be enabled through, lower cost receiver technology, new packaging solutions, and semiconductor process developments that may include the development of integrated receiver front ends incorporating either new materials, e.g., SiGe, InSb, or InP LNAs with Si backend circuitry.

In addition to cost reductions, major improvements in system performance are still required, especially for medium to long-range stand-off imaging. Component technology for room-temperature SMMW systems either does not exist or is far too expensive for passive imaging. Future innovations in, e.g., THz LNA, oscillator, and integrated heterodyne receiver development are likely, albeit the cost of the technology may remain high for several years. Cryogenic imagers are possibly at the highest technology readiness level with respect to passive SMMW imaging, but this approach has to be proven in the field in order to show that the benefits outweigh the costs of cooling.

The most promising route for long-range stand-off imaging is through active SMMW radar imaging. The primary challenge is to increase the frame rate of these systems to near-real-time and full-body coverage. Given the cost of the SMMW front end components, brute force scale-up to multi-channel receivers will be expensive. Alternatives are provided through the development of rapid, electronic beam steering technology combined with higher power sources.

Interestingly, the field is also seeing product differentiation as systems vendors are beginning to provide systems tailored for various operational scenarios, creating a range of products. Furthermore, a major trend in security technology is the progress toward systems of systems, i.e., multi-sensory solutions in which the MMW or SMMW imaging systems complement other orthogonal sensors. This is likely to produce highly effective, comprehensive security screening solutions, neither MMW nor SMMW imaging provides a “silver bullet” to counter threats.

Spectroscopic imaging, or multi-color THz imaging remains an intriguing possibility that could enable better discrimination of hazardous items, but will certainly not provide a high degree of specificity due to the atmospheric and clothing extinction, as well as the fact that the THz resonances of solid and liquid materials at ambient conditions are broad, making them difficult to discriminate from the background.

Finally, it is worth noting that while much of the systems development in the past few years has been very much security applications driven, the by-product has been a completely new set of tools for observing the world within the least well-known range of the electro-magnetic spectrum for many other applications.

References

1. R.M. Granham, N.T.W. Graham, Flight trials with the green minnow equipment. RRE memorandum 1461, Royal Radar Establishment, 1958
2. D.T. Hodges, E.E. Reber, F.B. Foote, Safeguards applications of far infrared radiometric techniques for the detection of contraband. *J. Nucl. Mater. Manag.* **9**(4), 83 (1980)

3. E.E. Reber, F.B. Foote, R.L. Schellenbaum, R.G. Bradley, Evaluation of active and passive near millimeter-wave radiometric imaging techniques for detection of concealed objects. Department of Commerce National Technical Information Service DE81 031 938, Sandia National Laboratories, July 1981
4. http://en.wikipedia.org/wiki/Receiver_operating_characteristic
5. F.T. Ulaby, R.K. Moor, A.K. Fung, *Microwave Remote Sensing - Active and Passive*, vol. 1 (Microwave Remote Sensing Fundamentals and Radiometry, Artech House, 1981)
6. N.A. Salmon, Polarimetric scene simulation in millimeter-wave radiometric imaging. *SPIE* **5410**, 260–269 (2004)
7. C.A. Martin, J.A. Lovberg, W.H. Dean, E. Ibrahim, High-resolution passive millimeter-wave security screening using few amplifiers. *SPIE* **6548**, 654806 (2007)
8. T. May, G. Zieger, S. Anders, V. Zakosarenko, H.-G. Meyer, M. Schubert, M. Starkloff, M. Rößler, G. Thorwirth, U. Krause, Safe visitor: visible, infrared, and terahertz object recognition for security screening application. *SPIE* **7309**, 73090E (2009)
9. D.T. Petkie, C. Casto, F.C. De Lucia, S.R. Murrill, B. Redman, R.L. Espinola, C.C. Franck, E.L. Jacobs, S.T. Griffin, C.E. Halford, J. Reynolds, S. O'Brien, D. Tofsted, Active and passive imaging in the THz spectral region: phenomenology, dynamic range, modes, and illumination. *J. Opt. Soc. Am. B* **25**(9), 1523–1531 (2008)
10. A. Luukanen, L. Grönberg, T. Haarnoja, P. Helistö, K. Kataja, M. Leivo, A. Rautiainen, J. Penttilä, J.E. Bjarnason, C.R. Dietlein, M.D. Ramirez, E.N. Grossman, Passive THz imaging system for stand-off identification of concealed objects: results from a turn-key 16 pixel imager. *SPIE* **6948**, 69480O (2008)
11. N.A. Salmon, R. Appleby, P.R. Coward, Polarimetric millimeter-wave imaging. *SPIE* **4373**, 82–85 (2001)
12. G.N. Sinclair, R.N. Anderton, R. Appleby, Passive millimeter-wave concealed weapon detection. *SPIE* **4232**, 142–151 (2001)
13. P.R. Coward, R. Appleby, Development of an illumination chamber for indoor millimeter-wave, imaging. *SPIE* **5077**(1), 54–61 (2003)
14. R. Doyle, B. Lyons, A. Lettington, T. McEnroe, J. Walshe, J. McNaboe, P. Curtin, Illumination strategies to achieve effective indoor millimeter wave imaging for personnel screening applications. *SPIE* **5789**(1), 101–108 (2005)
15. F.T. Ulaby, R.K. Moor, A.K. Fung, *Microwave Remote Sensing - Active and Passive, Vol. II, Radar Remote Sensing and Surface Scattering and Emission Theory*, Artech House, 1982
16. D.M. Sheen, D.L. McMakin, T.E. Hall, Cylindrical millimeter-wave imaging technique and applications. *SPIE* **6211**, 62110A (2006)
17. P. Corredoura, Z. Baharav, B. Taber, G. Lee, Millimeter-wave imaging system for personnel screening: scanning 10^7 points a second and using no moving parts. *SPIE* **6211**, 62110B (2006)
18. D.M. Sheen, T.E. Hall, R.H. Severtsen, D.L. McMakin, B.K. Hatchell, P.L.J. Valdez, Standoff concealed weapon detection using a 350-GHz radar imaging system. *SPIE* **7670**, 767008 (2010)
19. K.B. Cooper, R.J. Dengler, N. Llombart, A. Talukder, A.V. Panangadan, C.S. Peay, I. Mehdi, P.H. Siegel, Fast high-resolution terahertz radar imaging at 25 meters. *SPIE* **7671**, 76710Y (2010)
20. D.M. Sheen, D.L. McMakin, W.M. Lechelt, J.W. Griffin, Circularly polarized millimeter-wave imaging for personnel screening. *SPIE* **5789**, 117–126 (2005)
21. M.J. Rosker, H.B. Wallace, Imaging through the atmosphere at terahertz frequencies. in *Proceedings of IEEE/MTT-S International Microwave, Symposium*, pp. 773–776 2007
22. J.E. Bjarnason, T.L.J. Chan, A.W.M. Lee, M.A. Celis, E.R. Brown, Millimeter-wave, terahertz, and mid-infrared transmission through common clothing. *Appl. Phys. Lett.* **85**(4), 519–521 (2004)
23. N.E. Alexander, C.C. Andrés, R. Gonzalo, Multispectral mm-wave imaging: materials and images. *SPIE* **6948**, 694803 (2008)
24. M.R. Leahy-Hoppa, M.J. Fitch, X. Zheng, L.M. Hayden, R. Osiander, Wideband terahertz spectroscopy of explosives. *Chem. Phys. Lett.* **434**(4–6), 227–230 (2007)

25. M.J. Fitch, M.R. Leahy-Hoppa, E.W. Ott, R. Osiander, Molecular absorption cross-section and absolute absorptivity in the THz frequency range for the explosives TNT, RDX, HMX, and PETN. *Chem. Phys. Lett.* **443**, 284–288 (2007)
26. A.D. Burnett, W.H. Fan, P.C. Upadhyay, J.E. Cunningham, H.G.M. Edwards, J. Kendrick, T. Munshi, M. Hargreaves, E.H. Linfield, A.G. Davies, Broadband terahertz time-domain and raman spectroscopy of explosives. *SPIE* **6549**, 654905 (2007)
27. R. Appleby, H.B. Wallace, Standoff detection of weapons and contraband in the 100 GHz to 1 THz, region. **55**(11), 2944–2956 (2007)
28. P. Goldsmith, *Quasi-optical Systems : Gaussian Beam Quasi-optical Propagation and Applications*. IEEE, 1998
29. P.F. Goldsmith, Quasi-optical techniques. *Proc. IEEE* **80**(11), 1729–1747 (1992)
30. N.A. Salmon, J. Beale, J. Parkinson, S. Hayward, P. Hall, R. Macpherson, R. Lewis, A. Harvey, Digital beam-forming for passive millimetre wave security imaging. in *Proceedings of Second European Conference Antennas and Propagation EuCAP 2007*, pp. 1–11, 2007
31. J. Christensen, A. Carlström, A. Emrich, P. de Maagt, Spaceborne submm-wave interferometry. in *Proceedings of IEEE Antennas and Propagation Society International Symposium 2006*, pp. 2387–2390, 2006
32. C.A. Schuetz, J. Murakowski, G.J. Schneider, D.W. Prather, Radiometric millimeter-wave detection via optical upconversion and carrier suppression. *IEEE Trans. Microwave Theor. Techniques* **53**(5), 1732–1738 (2005)
33. H. Kamoda, T. Iwasaki, J. Tsumochi, T. Kuki, 60-GHz electrically reconfigurable reflectarray using p-i-n diode. in *Proceedings of IEEE MTT-S International Microwave Symposium Digest MTT '09*, pp. 1177–1180, 2009
34. A. Moessinger, S. Dieter, W. Menzel, S. Mueller, R. Jakoby, Realization and characterization of a 77 GHz reconfigurable liquid crystal reflectarray. in *Proceedings of 13th International Symposium Antenna Technology and Applied Electromagnetics and the Canadian Radio Science Meeting ANTEM/URSI 2009*, pp. 1–4, 2009
35. M.R. Chaharmir, J. Shaker, M. Cuhaci, A.-R. Sebak, Novel photonically-controlled reflectarray antenna. *IEEE T Antenn. Propag.* **54**(4), 1134–1141 (2006)
36. P.H. Siegel, Terahertz technology. *IEEE Trans. Microwave Theor. Tech.* **50**(3), 910–928 (2002)
37. E.R. Brown, Fundamentals of terrestrial millimeter-wave and THz remote sensing. *Int. J. High Speed Electron. Syst.* **13**, 995–1097 (2003)
38. P. Siegel, R. Dengler, Terahertz heterodyne imaging part ii: Instruments. *Int. J. Infrared Millimeter Waves* **27**, 631–655 (2006). 10.1007/s10762-006-9109-4
39. R.H. Dicke, The measurement of thermal radiation at microwave frequencies. *Rev. Sci. Instrum.* **17**(7), 268–275 (1946)
40. P.F. Goldsmith, C.-T. Hsieh, G.R. Huguenin, J. Kapitzky, E.L. Moore, Focal plane imaging systems for millimeter wavelengths. *IEEE Trans. Microwave Theor. Tech.* **41**(10), 1664–1675 (1993)
41. G.R. Huguenin, Millimeter wave focal plane array imager. *SPIE* **2211**, 300–301 (1994)
42. C. Jung, C. Lee, B. T., G. Chattopadhyay, A. Peralta, R. Lin, J. Gill, I. Mehdi, Silicon micro-machining technology for THz applications. in *35th International Conference on Infrared Millimeter and Terahertz Waves (IRMMW-THz)*, pp. 1–3, 2010
43. U.R. Pfeiffer, E. öjefors, Terahertz imaging with cmos/bicmos process technologies. in *Proceedings of ESSCIRC*, pp. 52–60, 2010
44. E.K. Duerr, K.A. McIntosh, S.M. Duffy, S.D. Calawa, S. Verghese, C.-Y.E. Tong, R. Kimberk, R. Blundell, Demonstration of a 630-GHz photomixer used as a local oscillator. in *Proceedings of IEEE MTT-S International Microwave Symposium Digest*, vol 1, 127–130, 1999
45. P.G. Huggard, L. Azcona, B.N. Ellison, P. Shen, N.J. Gomes, P.A. Davies, Application of 1.55 & μm photomixers as local oscillators & noise sources at millimetre wavelengths. in *Proceedings of Conference Infrared and Millimeter Waves and 12th International Conference Terahertz Electronics Digest of the 2004 Joint 29th International Conference*, pp. 771–772, 2004
46. T. Noguchi, A. Ueda, Y. Sekimoto, S. Asayama, M. Ishiguro, Photonic local oscillator for sis mixers. in *Proceedings of 18th Annual Meeting of the IEEE Lasers and Electro-Optics Society LEOS 2005*, pp. 171–172, 2005

47. A.R. Harvey, P.M. Blanchard, G.M. Smith, K. Webster, A.H. Greenaway, Optical up-conversion for passive millimeter-wave imaging. *SPIE* **3064**, 98–109 (1997)
48. D. Pukala, L. Samoska, T. Gaier, A. Fung, X.B. Mei, W. Yoshida, J. Lee, J. Uyeda, P.H. Liu, W.R. Deal, V. Radisic, R. Lai, Submillimeter-wave InP mmic amplifiers from 300–345 GHz. *IEEE Microw Wirel Co.* **18**(1), 61–63 (2008)
49. I. Kallfass, A. Tessmann, A. Leuther, H. Massler, M. Schlechtweg, O. Ambacher, Millimeter-wave monolithic integrated circuits for imaging and remote sensing at 140, 200, and 300 GHz. *SPIE* **7485**, 74850L (2009)
50. W.R. Deal, X.B. Mei, V. Radisic, K. Leong, S. Sarkozy, B. Gorospe, J. Lee, P.H. Liu, W. Yoshida, J. Zhou, M. Lange, J. Uyeda, R. Lai, Demonstration of a 0.48 THz amplifier module using InP HEMT transistors. *IEEE Microwave Wirel. Compon. Lett.* **20**(5), 289–291 (2010)
51. J.N. Schulman, T.Y. Hsu, H.P. Moyer, J.J. Lynch, $1/f$ noise of sb-heterostructure diodes for pre-amplified detection. *IEEE Microwave Wirel. Compon. Lett.* **17**(5), 355–357 (2007)
52. E.R. Brown, A.C. Young, J. Zimmerman, H. Kazemi, A.C. Gossard, Advances in schottky rectifier performance. *IEEE Microwave Mag.* **8**(3), 54–59 (2007)
53. J.L. Hesler, T.W. Crowe, Nep and responsivity of thz zero-bias schottky diode detectors. in *Proceedings of and the 2007 15th Int Infrared and Millimeter Waves Conference Terahertz Electronics. IRMMW-THz. Joint 32nd International Conference*, pp. 844–845, 2007
54. D. Schoenherr, C. Bleasdale, T. Goebel, C. Sydlo, H.L. Hartnagel, R. Lewis, P. Meissner, Extremely broadband characterization of a schottky diode based THz detector. in *35th International Conference on Infrared Millimeter and Terahertz Waves (IRMMW-THz)*, pp. 1–2, 2010
55. J.J. Lynch, P.A. Macdonald, H.P. Moyer, R.G. Nagele, Passive millimeter wave imaging sensors for commercial markets. *Appl. Opt.* **49**(19), E7–E12 (2010)
56. J.W. May, G.M. Rebeiz, Design and characterization of w-band SiGe RFICs for passive millimeter-wave imaging. *IEEE Trans. Microwave Theor. Techniques* **58**(5), 1420–1430 (2010)
57. J.N. Schulman, K.S. Holabird, D.H. Chow, H.L. Dunlap, S.T., E.T. Croke, Temperature dependence of sb-heterostructure millimetre-wave diodes. *Electron. Lett.* **38**(2), 94–95 (2002)
58. A.J. Miller, A. Luukanen, E.N. Grossman, Micromachined antenna-coupled uncooled microbolometers for terahertz imaging arrays. *SPIE* **5411**, 18–24 (2004)
59. N.H. Farhat, W.R. Guard, Holographic imaging at 70 GHz. *Proc. IEEE* **58**(12), 1955–1956 (1970)
60. A. Tamminen, J. Ala-Laurinaho, A.V. Raisanen, Indirect holographic imaging at 310 GHz. *Proc. Eur. Radar Conf. EuRAD* **2008**, 168–171 (2008)
61. L-3 SafeView. <http://www.safe-view.com/ch/advancedimaging/L-3last> accessed 8th Feb 2010
62. D.L. McMakin, D.M. Sheen, H.D. Collins, T.E. Hall, R.R. Smith, Millimeter-wave high-resolution holographic surveillance system. *SPIE* **2092**, 525–535 (1994)
63. D.L. McMakin, D.M. Sheen, A. Schur, W.M. Harris, G.F. Piepel, Initial test and evaluation of the millimeter-wave holographic surveillance system. *SPIE* **2932**, 103–114 (1997)
64. <http://www.millivision.com/>, last accessed 10th February, 2011
65. J.A. Lovberg, C. Martin, V. Kolinko, Video-rate passive millimeter-wave imaging using phased arrays. in *Proceedings of IEEE/MTT-S International Microwave, Symposium*, pp. 1689–1692, 2007
66. C.A. Martin, C.E. García González, V.G. Kolinko, J.A. Lovberg, Rapid passive mmw security screening portal. *SPIE* **6948**, 69480J (2008)
67. H.B. Wallace, Analysis of rf imaging applications at frequencies over 100GHz. *Appl. Opt.* **49**(19), E38–E47 (2010)
68. A. Luukanen, J.P. Pekola, A superconducting antenna-coupled hot-spot microbolometer. *Appl. Phys. Lett.* **82**, 3970–3972 (2003)
69. A. Luukanen, L. Grönberg, M. Grönholm, P. Lappalainen, M.M. Leivo, A. Rautiainen, A. Tamminen, J. Ala-Laurinaho, C.R. Dietlein, E.N. Grossman, Real-time passive terahertz imaging system for standoff concealed weapons imaging. *SPIE* **7670**, 767004 (2010)
70. E. Grossman, C.R. Dietlein, J. Ala-Laurinaho, M.M. Leivo, L. Grönberg, M. Grönholm, P. Lappalainen, A. Rautiainen, A. Tamminen, A. Luukanen, Passive terahertz camera for standoff security screening. *Appl. Opt.* **49**(19), E106–E120 (2010)

71. E. Heinz, D. Born, G. Zieger, T. May, T. Krause, A. Krüger, M. Schulz, S. Anders, V. Zakosarenko, H.-G. Meyer, M. Starkloff, M. Rößler, G. Thorwirth, U. Krause, Progress report on Safe VISITOR approaching a practical instrument for terahertz security screening. *SPIE* **7670**, 767005 (2010)
72. K.B. Cooper, R.J. Dengler, N. Llombart, T. Bryllert, G. Chattopadhyay, E. Schlecht, J. Gill, C. Lee, A. Skalare, I. Mehdi, P.H. Siegel, Concealed object contrast enhancement using radar methods in a submillimeter-wave active imager. in *Proceedings of 33rd International Conference Infrared, Millimeter and Terahertz Waves IRMMW-THz 2008*, pp. 1–2, 2008
73. C. am Weg, W. von Spiegel, R. Henneberger, R. Zimmermann, T. Loeffler, H. Roskos, Fast active THz cameras with ranging capabilities. *J. Infrared Millimeter Terahertz Waves* **30**, 1281–1296 (2009). 10.1007/s10762-009-9565-8
74. M.C. Kemp, A. Glauser, C. Baker, Recent developments in people screening using terahertz technology: seeing the world through terahertz eyes. *SPIE* **6212**, 62120T (2006)
75. M.C. Kemp, A. Glauser, C. Baker, Multi-spectral terahertz imaging using reflected and scattered radiation. *Int. J. High Speed Electron. Syst.* **17**, 403–414 (2007)
76. E.N. Grossman, C.R. Dietlein, J. Chisum, A. Luukanen, J.E. Bjarnason, E.R. Brown, Spectral decomposition of ultra-wide-band terahertz imagery. *SPIE* **6548**, 654807 (2007)
77. N.C. Currie, F.J. Demma Jr, D.D. Ferris, R.W. McMillan, M.C. Wicks, K. Zyga, Imaging sensor fusion for concealed weapon detection. *SPIE* **2942**, 71–81 (1997)
78. M.C. Kemp, P.F. Taday, B.E. Cole, J.A. Cluff, A.J. Fitzgerald, W.R. Tribe, Security applications of terahertz technology. *SPIE* **5070**, 44–52 (2003)
79. K. Yamamoto, M. Yamaguchi, F. Miyamaru, M. Tani, M. Hangyo, T. Ikeda, A. Matsushita, K. Koide, M. Tatsuno, Y. Minami, Noninvasive Inspection of C-4 Explosive in Mails by Terahertz Time-Domain Spectroscopy. *Japanese J. Appl. Phys.* **43**, L414–L417 (2004)
80. D.J. Cook, B.K. Decker, G. Maislin, M.G. Allen, Through container THz sensing: applications for explosives screening. *SPIE* **5354**, 55–62 (2004)
81. Y. Shen, P.F. Taday, M.C. Kemp, Terahertz spectroscopy of explosive materials. *SPIE* **5619**, 82–89 (2004)
82. F. Huang, B. Schulkin, H. Altan, J.F. Federici, D. Gary, R. Barat, D. Zimdars, M. Chen, D.B. Tanner, Terahertz study of 1,3,5-trinitro-s-triazine by time-domain and fourier transform infrared spectroscopy. *Appl. Phys. Lett.* **85**(23), 5535–5537 (2004)
83. W.R. Tribe, D.A. Newnham, P.F. Taday, M.C. Kemp, Hidden object detection: security applications of terahertz technology. *SPIE* **5354**, 168–176 (2004)
84. K. Kawase, Y. Ogawa, Y. Watanabe, H. Inoue, Non-destructive terahertz imaging of illicit drugs using spectral fingerprints. *Opt. Express* **11**(20), 2549–2554 (2003)
85. C. Baker, W.R. Tribe, T. Lo, B.E. Cole, S. Chandler, M.C. Kemp, People screening using terahertz technology (invited paper). *SPIE* **5790**, 1–10 (2005)
86. Y.C. Shen, T. Lo, P.F. Taday, B.E. Cole, W.R. Tribe, M.C. Kemp, Detection and identification of explosives using terahertz pulsed spectroscopic imaging. *Appl. Phys. Lett.* **86**(24), 241116 (2005)
87. D.M. Sheen, D.L. McMakin, T.E. Hall, Speckle in active millimeter-wave and terahertz imaging and spectroscopy. *SPIE* **6548**, 654809 (2007)
88. M. Theuer, G. Torosyan, J. Jonuscheit, R. Beigang, Terahertz reflection spectroscopy for stand-off detection of explosives. in *Terahertz Wave Technology for Standoff Detection of Explosives and other Military and Security Applications*, volume SET-129. NATO Research and Technology Organisation, 2008
89. M.C. Kemp, Explosives detection using terahertz spectroscopy—a bridge too far? *IEEE TRANS. TERAHERTZ SCI. TECH.* **1**(1), 282–292 (2011)

Chapter 20

Characterisation of Works of Art

Kaori Fukunaga and Marcello Picollo

Abstract Terahertz (THz) imaging is an emerging technique for the non-invasive analysis of artworks. Since THz waves can penetrate opaque materials, various imaging systems that make use of THz waves have been developed in order to detect certain chemicals and defects in materials. More recently, THz imaging has been applied to the examination of works of art. The first experiments in the use of THz imaging in the field of art have provided very encouraging results.

20.1 Introduction

The frequency band in the terahertz (THz) region typically refers to the 0.1–30 THz range (from 3 to 300 cm^{-1}). This region of the electromagnetic spectrum lies in the gap between microwaves and the infrared, and has historically been defined as the “terahertz gap”, due to its relative lack of convenient and inexpensive sources, detectors and systems for THz waves [1]. In recent decades, this spectroscopic region has been explored mainly by scientists who directly developed the THz systems on their own premises for their own specific research applications. These in-house

K. Fukunaga
National Institute of Information and Communications Technology (NICT),
Koganei, Tokyo 184-8795, Japan
e-mail: kaori@nict.go.jp

M. Picollo (✉)
“Nello Carrara” Institute for Applied Physics,
of the Italian National Research Council (IFAC-CNR),
Via Madonna del Piano 10, 50019 Sesto Fiorentino, Italy
e-mail: m.picollo@ifac.cnr.it

M. Picollo
Department of Physics and Mathematics,
University of Eastern Finland
111F-80101 Joensuu Finland,

THz systems, which are custom-made, were usually non-friendly devices that were difficult for non-specialised operators to use in general applications. Thanks to the progress of laser technology, various types of stable THz sources have been developed in recent years, with peak power values ranging in scale from microwatts to milliwatts. Stable femto-second fibre lasers that operate at room temperature have encouraged the development of THz spectroscopy and imaging systems for general purposes. Indeed, THz waves can penetrate opaque materials, such as radio waves, and make it possible to obtain spectral features of various materials, such as those for vibrational spectroscopy [2–6]. Since the energy of THz waves emitted from existing systems is extremely low, i.e. of a magnitude similar to that of room temperature, this electromagnetic region is considered to be completely non-invasive for operators, living organisms and objects. Hence, it can be applied to the study of living matters, including human beings. These advantages are effectively used in developing new non-destructive test equipment, especially for security issues. Some international airports have installed THz security cameras to detect concealed weapons of the type which cannot be recognised by metal detectors, and a non-invasive mail inspection system has been developed to detect illegal drugs or poisonous substances inside envelopes and/or packages [7, 8]. The information available from the measurement of THz absorption/reflection is not limited to the level of the absorption or refractive index, which can also be obtained in microwave and millimetre wave regions. Almost all materials show their own particular spectral features in the THz range, thanks to their phonon interactions, molecular rotations, hydrogen bond behaviour and various low-energy excitation modes. Crystal polymorphs, for example, can be recognised easily in THz spectra, rather than in those collected in the mid-infrared region, and the data obtained make it possible to distinguish original/generic medicines [9].

The first THz images were acquired by Hu and Nuss in 1995 by using a terahertz time-domain spectroscopy (THz-TDS) system [10]. In this system, femto-second optical pulses were used to generate broadband THz radiation, also via a second-order nonlinear optical process in which a short optical pulse is used to generate and also detect THz radiation via nonlinear optical interactions between the optical pulse and a medium: typically, a semiconductor [11–16]. The recent history of the field has been one of rapid expansion, with the development of both new imaging techniques and also new technologies for THz sensing [17].

THz imaging can be performed by the transmission or the reflection of THz waves. In particular, THz-TDS reflection imaging uses THz pulses that propagate in specimens: in this technique, pulses reflected from the surface and from the internal boundaries in the reflective index of the specimen are detected. In general, the internal structure of the analysed object is observed in cross-sectional images obtained by using micro-specimens taken from the work that is being analysed. On the other hand, in THz-TDS imaging, a map of the layer of interest can easily be obtained without the need to collect any samples.

Due to the increasing possibilities involved in the commercial use of THz imaging systems at affordable but yet expensive costs, THz imaging is an emerging technique for the non-invasive analysis of artworks. Indeed, the first experiments in the use of THz imaging in the field of art have provided very encouraging results.

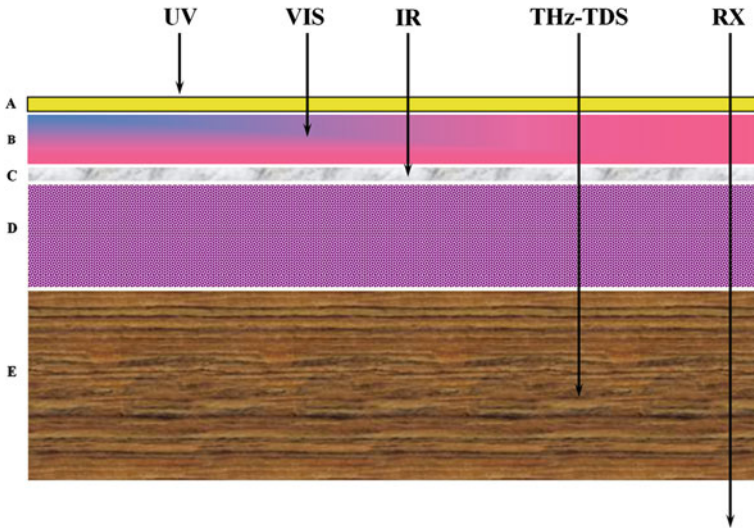


Fig. 20.1 Diagram showing the depth of penetration of the imaging diagnostic techniques, reported in the text, for a panel painting (simplified stratigraphic scheme): (A) varnish layer; (B) paint layers; (C) *imprimitura* layer with drawing; (D) preparation layers; (E) wood support

In studying works of art, and paintings in particular, the most frequently used imaging techniques are trans-illumination, trans-irradiance and X-ray radiography (XRR) techniques, which work in transmittance, while photographic documentation of the object in diffuse and raking visible light, ultraviolet (UV) fluorescence, infrared (IR) imaging, IR false colour and IR reflectography are usually performed in the reflectance mode (Fig. 20.1). Each of these enables conservators, curators and scientists to obtain specific information on the structure of the painting, the technique and materials used by the artist, as well as about the conservation condition of the object. As far as the first application of a THz imaging system on works of art is concerned, this was performed in 2006 in transmission mode on a nineteenth century canvas painting [18].

In practical terms, the THz power applied is usually not strong enough to perform THz transmission imaging of panel paintings, whereas this can be done by means of XRR. However, THz imaging can be used to obtain the internal structure of materials in a non-invasive way by using, for example, THz-TDS tomography, even when it is performed in reflectance. The results obtained with THz-TDS tomography can be compared with those achieved invasively with the study of cross-sections on micro-samples. Traditional cross-section images enable the investigation of the layer composition and depth only on two dimensions, but do not provide analysts with information on the third dimension of the sample (or investigated area). On the other hand, in THz-TDS tomography each pixel of the image contains its own cross-section information (stratigraphic information), so that the area information on the layer of interest is also obtained by extracting the corresponding peaks in signals in

a time domain. A three-dimensional internal structure can be obtained by gathering images.

One drawback of this technique, however, is related to the presence of substances that totally reflect THz radiation. An example of such substances is represented by thick and homogeneous gold leaves that can mask the structure underneath, because they reflect the THz waves.

20.2 State of the Art of Imaging Techniques Applied to the Characterisation of Artworks

Preliminary non-invasive investigations are needed before starting any conservation procedure on valuable artworks, in order to assist conservators in their decision-making process. When one is dealing with artefacts, such as paintings, drawings or other graphics art works that can be considered as flat objects, imaging techniques offer an ideal approach for performing non-invasive, yet in-depth, examinations. Generally speaking, imaging techniques are based on the acquisition of a virtual picture of the surface that can be super-imposed on the visible image. This picture usually provides a 2D map in which features that are not detectable through visual examination can be pointed out. The use of imaging techniques in the art conservation field ranges from well-established methodologies, such as high-resolution digital photography, visible raking light, UV fluorescence, XRR, IR reflectography, etc., to cutting-edge applications, such as multi- and hyper-spectral imaging techniques [19, 20] or THz imaging [21]. In principle, all the above techniques could be used in order to reach the desired level of knowledge on the object under analysis. Nevertheless, in many practical cases, various factors, such as time, costs and the availability of pieces of equipment, may limit one's resorting to a wide set of scientific methodologies, and the investigations needed should be limited to simple and affordable methods [22]. Depending on the needs and importance of the object under analysis, as well as on the resources available, different imaging techniques can be used in order to obtain the information desired. That is, a basic protocol for preliminary diagnostics on paintings can typically include one or more of the following imaging techniques, to which multi-, hyper-spectral and THz imaging methodologies can also be added:

- *High definition digital photography in the visible range (380–750 nm)* for documenting the conditions and characteristics of polychrome surfaces, with the possibility of magnifying details and selected areas.
- *Visible raking light* for highlighting deformations and changes in the flatness of the support due to constraints connected with both the manufacture and use of the support itself, as well as external effects such as climatic variations, earlier conservation treatments, etc.
- *IR imaging (photography or reflectography)* for the examination of underlying drawings, hidden particulars, *pentimenti*, etc., and for obtaining indications for understanding artists' techniques. Obviously, the informative content of IR images

greatly depends on the extension of the spectral interval investigated, and, hence, on the detector used for their acquisition. Devices used for IR imaging are silicon-based CCD cameras (400–1,100 nm), as well as cameras based on solid-state sensors, such as Indium Gallium Arsenite (InGaAs), Platinum Silicide (PtSi), Indium antimonide (InSb) and Mercury Cadmium Telluride (MCT) in the near IR region (approximately 800–2,500 nm) or vidicon-tubes (400–2,200 nm).

- *XRR* for the examination of the nature and structure of the original support due to the high penetration of the X-ray. It enables an in-depth inspection of the artwork, and is especially useful for obtaining information on under layers and the inner structure of the object, the conservation over time of the support and so forth. Although routinely used, this technique requires specific instrumentation, equipped laboratories and trained staff. Thus, its use is limited to selected cases.
- *UV fluorescence imaging* for identifying selected pictorial materials, retouches, non original interventions, etc., on the basis of the fluorescence emitted in the visible and near IR regions by certain materials when illuminated by using UV (e.g. Wood lamps) or blue radiations.
- *Trans-illumination (visible) and trans-irradiation (Near-Infrared)* for inspection of the conservation of supports that are partially transparent to visible light: for example, in the case of unlined canvas [23]. In these Transmitted Imaging techniques, the object is placed between the light source and the camera, with the painted surface generally facing the camera. The radiation transmitted through the investigated surface is then recorded. However, the painting could also be placed in the opposite direction, in order to obtain different and complementary information on the artists' techniques and the conservation conditions of the artwork.

20.3 THz Imaging and Art Conservation: Chronicle

As far as the authors know, to date only a limited number of scientific published papers deal with the application of THz techniques to the analysis of artists' materials, art mock-ups, or laboratory art panel tests, and only a few touch upon actual artworks.

As regards imaging methodologies, the first application of a THz imaging system in the art conservation field was performed in transmission mode to a $10 \times 10 \text{ cm}^2$ portion of a nineteenth century canvas painting (a female portrait found at a flea market), and the data obtained were then compared with those acquired using the X-ray fluorescence (XRF) technique [18]. Laboratory tests on different areas (measuring about 3 mm in diameter) of the painting, using a THz-TDS spectroscopic device in transmission, showed that the output signal depended on the materials investigated. However, even if XRF data were registered on the same areas of the painting where the THz-TDS spectroscopic information was acquired, identification of the actual composition of the paint layers was not made by the authors. Hence, the comparison between the THz-TDS transmission spectra and the chemical composition of the paint layer was incomplete. The authors acquired their THz images by means of a photoconductive antenna detection system, with 0.1–1 THz width frequency

windows, which was extensively reported in the article by Rutz and co-authors in the same book of proceedings [24]. In it, THz-images were taken by moving the painting in a 2D grid pattern with a resolution of 0.5 mm/pixel through the focus of the THz-beam, and the corresponding waveform was measured at each step-position. Each waveform was transformed with the FFT algorithm in order to obtain its frequency content, which held information on several parameters suitable for plotting THz-images: for instance, differences in the refractive indexes or in the thickness of the paint layers could be seen by plotting an image with the temporal position of the main peak. In the case of thicker layers or materials with more highly refractive indexes, the delay in the pulse was greater. In addition, it was possible to report the information obtained about the absorption features of the paint materials in other images by considering the peak-to-peak values. By playing with THz-TDS images, each pixel could combine information regarding absorption, scattering, and reflection losses of the investigated material. Consequently, a THz-imaging measurement made it possible to produce multiple false colour pictures, which provided different information on the properties of the paint layers.

At the same time, experiments were performed at the National Institute of Information and Communications Technology (NICT) in Tokyo on painting mock-ups that were focused on acquiring THz spectra of various artists' materials, such as pigments and binders (www.thzdb.org), as well as the application of THz imaging to the analysis of artworks [25, 26]. This study was the first actual application of false-colour THz imaging methodology, obtained by developing THz false colour algorithms, to the investigation and discrimination of artists' materials in paintings and stained glass (Fig. 20.2). Although several types of THz systems have become commercially available in recent years, a very promising development in THz devices has been seen, by the authors, namely in a THz camera system based on micro bolometer array technology. With this system, real-time THz false colour maps of paintings and stained glass have been created by dividing the 0.5–15 THz frequency range into three bands, which were represented in RGB colours, respectively. The THz false colour of each spectrum was obtained by replacing the average transmittance rate in each band with a 0–255 gray-scale level (Fig. 20.3). As far as the authors are concerned, the camera control software could be upgraded by means of this procedure, or using similar algorithms, in order to directly show on the camera display. In addition, the authors noted that NICT and the Riken (Rikagaku Kenkyūsho, a natural sciences research institute in Japan) have been the first institutions to make a spectral database on artists' materials, which included more than 200 spectra of products related with art materials, available online. With the use of these spectral data, THz spectroscopy can be utilised to determine materials found in artworks, such as pigments with similar composition and the same colour, e.g. natural and artificial blue ultramarine.

Subsequently, a fresco-painting model was studied by researchers of the University of Michigan, of the École Nationale Supérieure de Techniques Avancées in Paris, and of the Louvre Museum, who found that THz reflection imaging makes it possible to distinguish pigments [27, 28]. In their research, the time delays and intensity signatures of THz pulses reflected from multilayer systems of plaster, painted sur-

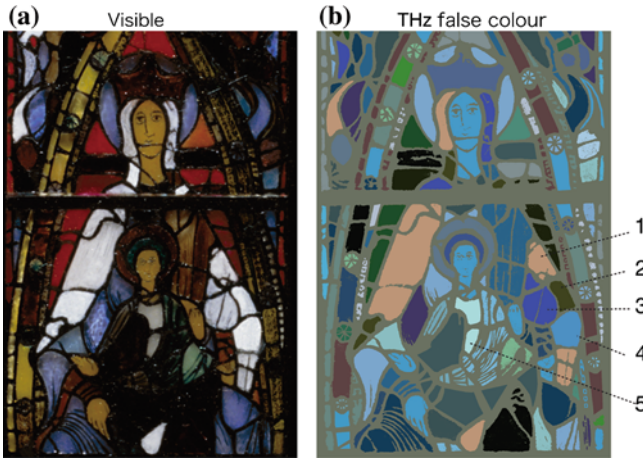


Fig. 20.2 **a** Detail of the Virgin of Vendome, twelfth century stained glass from the Holy Trinity Abbey in Vendome (France), and **b** its THz false colour image. In the THz false colour image **b** five different white materials, used to produce white glass, are differentiated by their diverse THz spectra: (1) lead white; (2) lithopone; (3) zinc white; (4) titanium white; (5) lime white. Figure modified from Fukunaga et al. [25]

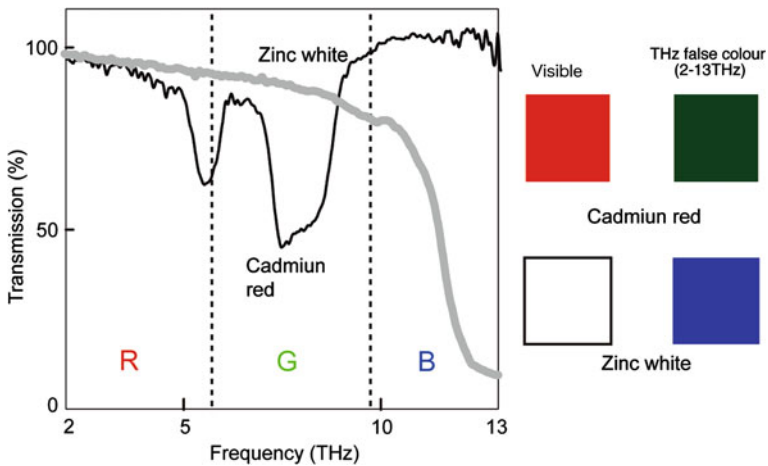


Fig. 20.3 THz transmittance spectra of cadmium red and zinc white pigments with three different false RGB zones. The THz false colour obtained for the two pigments are shown in the right

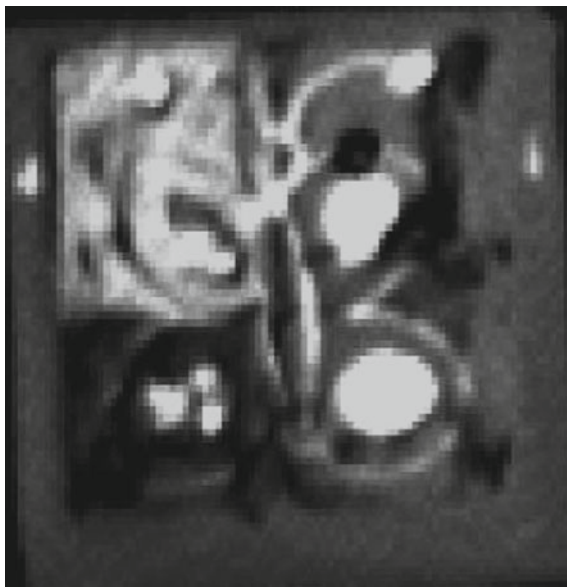
faces and graphite sketches were investigated in order to demonstrate the feasibility of using THz techniques for inspecting and resolving fresco artworks embedded in subsurface layers within a wall or ceiling. The authors acquired THz data on two different fresco samples, using two different THz-TDS devices. The first sample was a $60 \times 35 \times 4.35$ mm thick plaster-of-Paris (calcium carbonate/calcium sulphate

semihydrate/silica) slab. It was prepared following the *buon fresco* traditional painting technique using dielectric pigments, such as titanium dioxide (white), limonite iron oxide-based clay (burnt Sienna) and mixed carbon-iron oxide (black). The back surface of the plaster sample was painted with a conductive paint layer consisting of two separate strips prepared with silver epoxy, which contained 50–70% silver flake and 30–50% of phenol novolac epoxy resin (a reaction product of epichlorohydrin and phenol–formaldehyde novolac), and titanium dioxide bound with water, respectively. The second sample consisted of a 2D graphite sketch of a butterfly covered by 4 mm of plaster-of-Paris that terminated with an opaque paint layer (pigment with water as a binder) split into four colour quadrants: black, white, yellow ochre (limonite iron oxide-hydroxide clay) and burnt Sienna. The first THz-TDS system, which was intended to establish the feasibility of time-domain ranging for layered media in the first sample, employed a free-space THz-TD reflectometer consisting of an interdigitated metal finger, semi-insulating-photoconductive-GaAs THz emitter, and a low temperature-grown-GaAs (LT-GaAs) Hertzian-dipole receiver. In the second experiment, the integrated optical-fibre coupled transceiver head of a Picometrix T-Ray™ terahertz-imaging system was scanned over the second fresco sample, providing a normal THz-beam incident angle, a spatial resolution down to 2 mm, a selectable focal plane and rapid data acquisition (<5 min for a 7 × 7 cm plaster sample with 0.5 mm step size).

From the data reported by the authors, the high contrast in reflectivity in the THz region of the white, the burnt Sienna and the black painted layers on the front surface made it possible to easily distinguish these materials one from the other. As expected, the silver paint stripe on the back surface generated a greater reflection than the white paint stripe did. The second test showed that the pulsed-THz beams were able to penetrate the 4-mm depth of the plaster substrate, and made it possible to image the graphite lines of the depicted butterfly from the far side of the plaster when the THz-transceiver focal plane was adjusted to the back of the plaster substrate. The experimentation conducted on this laboratory sample, together with THz spectroscopic measurements on the pure pigment powders, which provided the complex refractive index values for those materials, revealed that in the 0.14–0.48 THz range it was possible to have the optimum contrast between the different pigments based on their reflectivities (Fig. 20.4). In particular, the titanium dioxide white pigment showed the greatest reflectivity, whereas the yellow ochre paint appeared to be the darkest. The other two pigments presented similar reflectivity to the THz radiation applied. Furthermore, in the region above 0.6 THz, both white and yellow ochre pigments became opaque, while the butterfly drawing was still visible through the burnt Sienna and the carbon-iron oxide black pigments.

A recent work confirmed that THz imaging can successfully be applied to investigations of oil paintings on canvas [29]. In this paper, the authors showed that it was possible to image the substructure of paintings on canvas by monitoring the time delay between reflections off different layers (THz-TDS). THz-TDS enabled them to measure the optical thickness of the different layers which constituted the structure of the painting, thus providing information on the depth of the painting structure. As a case study, THz-TDS images acquired on a linseed-oil laboratory test

Fig. 20.4 THz-TDS image in reflection mode of a 2D graphite sketch of a butterfly covered by 4 mm of plaster-of-Paris with an opaque paint layer on top. The graphite figure of a butterfly is clearly recognisable in the THz-TDS image formed integrating the spectral information in the 0.14–0.48 THz range. Figure modified from Jackson et al. [27]



panel on canvas, which consisted of several rectangular patches of raw umber, an iron and manganese oxide-based brown earth pigment, with different thicknesses covered with lead white, were examined. Here, the reflection measurements were performed on the verso of the painting, from the canvas side. This is because it is relatively flat compared with the recto; therefore, the reflection/refraction problems caused by the curvature of the front surface of the painting were partially overcome. The THz-TDS results were also compared with those obtained by using the infrared reflectography and XRR techniques on the same object. By means of the data reported, the authors showed that it was possible to use the THz-TDS imaging technique for analysing the substructure of a painting, since it provides information on the thickness of the paint layers.

The experimental set-up was provided with a photoconductive switch to generate broadband THz pulses, which were focussed onto the back of the test panel. The THz beam was directed perpendicular to the canvas.

The most important part of this work was related to the authors' prediction of the smallest absolute thickness measurable using their THz-TDS methodology. Indeed, by assuming a refractive index of 1.9 for the raw umber and the ground of the canvas, they estimated that two peaks separated by about 0.65 ps could still be identified as two separable signals, which meant that paints with a thickness of 50 μm could still be measured using their experimental set-up. In addition, they estimated that, for materials with a refractive index of 1.9, it was still possible to measure thicknesses of about 12 μm by means of the changes in the time separation of 0.15 ps. However, in order to reach these values, the deconvolution of the contributions of the closely spaced layers would require a more elaborate signal processing.

In the paper by Abraham and co-authors [30], a broadband THz-TDS was used to reveal hidden sketches and underdrawings on laboratory canvas panels. The authors also demonstrated that it was possible to obtain information from their THz data about the different thicknesses of the paint layers. They acquired THz images in both transmission and reflection geometry, while they simultaneously provided the 0.1–1.5 THz range transmittance spectra of the pigments used in their study. The authors concluded from these spectroscopic data that, in their case study, it was not possible to distinguish specific fingerprint absorption of the THz radiation of the selected pigments. Indeed, only a global attenuation of THz amplitude after the transmission through the specimens was observed, although the different intensities in the transmission of some of the investigated pigments could be used for their identification. In general, however, a spectroscopic distinction of these materials in the 0.1–1.5 THz range was not very obvious.

The broadband THz spectrometer used in this work was based on a standard transmission THz-TDS setup: a 50 fs Ti–Sapphire laser with a 76 MHz repetition rate. THz imaging was obtained by raster scanning the sample with a *XY* linear motor stage. The lateral resolution of the system was previously measured and evaluated at 220 μm at 2 THz, which corresponds to the Rayleigh diffraction limit. However, in order to reduce the acquisition time, a 0.5-mm scan step in both *X* and *Y* directions was generally applied.

The authors computed the THz images acquired by using the temporal and/or spectral amplitude of the signal, as well as directly using the arrival time of the THz pulse, such as the temporal phase shift. In this way, the 3D maps obtained made it possible to extract information on the refractive indexes and about the thickness of the investigated samples. The accuracy of the measurement of the thickness was related to the registration of the arrival time of the THz pulse and the acquisition step of the delay line.

The smallest variation in thickness measured in transmittance by the authors was determined by the ability to precisely determine the temporal position of the THz main peak. In their paper, a minimum variation of 30 μm in the paint thickness was calculated for the blue ultramarine pigment, with an estimated refractive index of 1.93. As expected, when working in reflection, the evaluation of the system was different, because a more complex THz waveform was obtained. Nevertheless, the results obtained were compatible with those obtained in transmission geometry, and the slight discrepancies were tentatively explained by the authors as being due to the reflection geometry, which did not require any previous reference measurement (canvas without painting), unlike what was done for the transmission measurements. The possibility of evaluating the thickness of a layer, once the refractive index of its compounds is known, was also an advantage offered by the reflection geometry, which provided a direct measurement of the painting thickness by taking into account the time of flight of the THz pulse, over the transmission geometry. In their paper the authors also estimated the smallest variation in thickness that can be measured with their system. They found that, with a rough precision of 100 fs for the time delay between the two peaks, the corresponding smallest change in the paint thickness (using a refractive index of 1.93) was about 8 μm . This result was also in agreement

with the work by Adam et al. [29]. However, as reported in Abraham et al. [30], the images acquired in reflectance mode usually had a lower signal-to-noise ratio than the ones registered in transmittance mode, due to the complexity of the THz signal after being reflected by the investigated object.

One of the most important applications of THz imaging in the art conservation field has been the case study performed at the end of 2008 on the panel painting *Polittico di Badia* (circa 1300) by Giotto di Bondone, on display at the Uffizi Gallery in Florence, Italy [21]. This work could be considered to represent the first applications of the pulsed THz-TDS reflection imaging technique on an actual tempera panel painting belonging to one of the most important museums in the world. It was investigated using a portable TDS-THz imaging system T-Ray™ 4000 by Picometrix, which worked approximately in the 0.5–1.2 THz range that required a scanning time of about 10 min in order to investigate an area of 150 mm², with the detection unit placed in front of the painting at a distance of approximately 20 mm. The THz imaging methodology involved focused mainly on: (a) an understanding of the conservation and appearance of the gold leaves of both the background and the decorations; (b) the possibility of identifying pigments and the conservation over time of the paint layers; (c) an analysis of the internal physical structure of the painting (stratigraphy of the different layers).

The results of this analysis revealed that the artist, in following a medieval procedure for making panel paintings, had spread a gesso layer directly over the wooden support in order to flatten the carved wood base. A canvas was then placed on the gesso layer, and, subsequently, another gesso layer was used as a preparatory layer for the painting itself. In the paint layer, gold foils covered by paint could be clearly observed, and the consumption or ageing of the gold could be estimated by noting the amount of reflection. This application stressed the fact that THz-TDS imaging using THz pulse had made it possible to fill in the information gap about panel paintings that had hitherto existed between two other diagnostic imaging techniques, namely IR reflectography and XRR, because it provided useful data on the internal physical structural information on non-metal objects, similar to the THz tomography technique (Fig. 20.5). THz tomography technique made it possible to acquire non-invasive cross-section images of works of art, thus obtaining results that could be compared with those obtained by taking micro-samples from the investigated object.

In addition to the above-mentioned studies, a THz reflective imaging system with a free electron laser has been developed by the *Ente per le Nuove Tecnologie, l'Energia e l'Ambiente* (ENEA, Frascati, Italy) [31]. This system has been used to perform non-invasive diagnostics in various fields of research, including the cultural heritage. Although the proposed system is not transportable, high-power source systems can be profitably applied in order to observe artworks that are masked by a thick layer of plaster or hidden items in archaeological and historic objects (Fig. 20.6). The same research group at ENEA, in collaboration with the colleagues of the NICT, have initiated a mutual project in the area of Technologies as applied to the Cultural Heritage within the framework of the Agreement between the Governments of Italy and Japan for cooperation in Science and Technology, entitled THz-ARTE “Terahertz

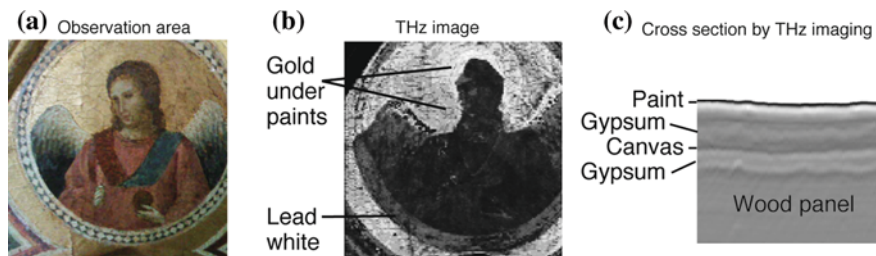
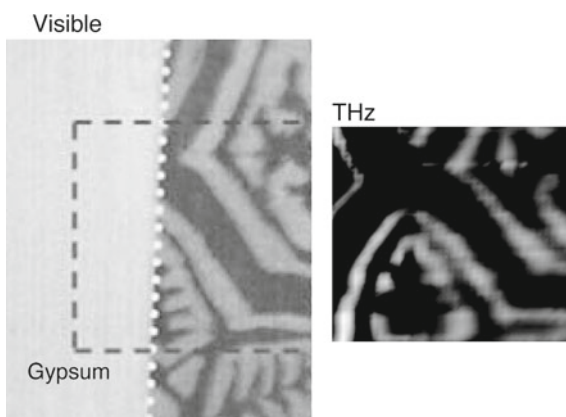


Fig. 20.5 RGB image (a) and THz-TDS reflectance image (b) of a detail of the Polittico di Badia polyptych by Giotto. The pulsed THz-TDS image revealed high reflection values of the gold leaf. In addition, the presence of gold leaves beneath the paint layers can clearly be observed around the outline of the head and wings of the Angel. The non-invasive cross-section image, whose structure can be observed in all the examined parts in the work, is shown in image (c). Here, the layered structure of the painting is clearly noticeable based on the reflection waveform in the time domain. Figure modified from Fukunaga and Picollo [21]

Fig. 20.6 Image in the visible range of the painting mock-up, partially cover with a thick layer of gesso (left). The other image, in the THz region (right), is a detail (rectangular frame) where the pattern of the painting covered by gesso is clearly evident. The THz image was acquired with the free electron laser THz system developed by ENEA



Advanced Research Techniques for non-invasive analysis in art conservation” [32].

Other considerations relative to the use of the THz imaging technique in the art conservation field have dealt with the feasibility of extending this technique to the investigation of ancient papyruses, mummies and archaeological bones, as well as to the study of art and/or archaeological wood found in the cultural heritage, where it has been used for dendrochronological purposes [33–36].

The latter application, in particular, compared THz and X-ray tree-ring imaging techniques by adapting tree-ring analysis methods that are used in dendrochronology (the science of dating wooden objects by comparing the tree-ring patterns). As reported by the authors [35, 36], some of the tree-ring measurement techniques are invasive and time-consuming. Hence, art-conservators usually prefer to use a few mechanically non-destructive techniques, which can provide satisfactory measurement of tree rings in wooden objects. A few years ago, excellent results were obtained

by resolving tree rings as narrow as 0.15 mm, using soft XRR [37]. Moreover, the same authors were able to resolve rings in three-dimensional painted-wood folk art by using micro-focus X-ray computed tomography (XRCT). Despite the fact that THz imaging is performed in either transmission or reflection mode, the authors explored and implemented two methods of reflection-mode, time-domain THz pulse imaging for resolving tree-ring information, in order to facilitate the tree-ring dating of artefacts. In this work, tree-rings in the tangential (parallel to ring growth) and cross-sectional (parallel to grain fibres or to the end-grain surface) planes, THz ranging, and *en face* tomographic methodologies, respectively, were sampled and investigated. The data acquired were compared with those obtained with routine photographic techniques, to determine the statistical accuracy of the THz images. In addition, the THz-TDS imaging methodology focused on analysing primed and paint wood, so as to check the applicability of this technique in extracting information from the wood surface hint by opaque materials, such as paint layers in the case of panel paintings. Indeed, it would be very profitable to be able to determine the ring patterns that exist under the paint layers within these framed substrates without removing the frame or otherwise disturbing the integrity of the painting. Furthermore, for validation purposes the results reported by the authors were compared with similar measurements of wood that had been made using X-ray imaging methodologies.

For their research, the reflection measurements were carried out using a Picometrix QA-1,000 terahertz time-domain imaging system, consisting of a femtosecond laser fibre coupled to an XYZ-translatable, photoconductive and co-linear THz transceiver.

As stressed by the authors in their conclusions, the THz-TDR measurements of wood reported were very preliminary. THz ranging tangential measurements were found to be not very penetrative; however, the tree-rings measured showed a good correlation to their photographic references. The tree rings imaged along the longitudinal and end-grain surfaces were spatially resolvable using *en face* tomography, and the statistical accuracy of the ring series for the wood samples was good as compared to their reference chronologies. However, the ring series for the varnished specimen were unsatisfactorily matched. As regards the THz measurements on the primed and painted wood specimens, their tree-rings were not uniformly resolved, but enough information was obtained from these measurements for their ring series to be satisfactorily compared to the reference chronology (Fig. 20.7). In the authors' opinion, however, the THz imaging technique could have further applications in this field, apart from dating application, that deal with the study of stress and fatigue in wood by monitoring the water content, or with the conservation of artworks over time.

The study by Öhrström and co-authors, instead, focused on the feasibility and the morphodiagnostic impact of THz imaging of historic remains, such as Egyptian mummified tissues and macerated bone [33]. These delicate materials need to be analysed using minimal-impact methodologies at a macroscopic and/or microscopic scale for studying tissues and/or cell structures/DNA, respectively. In their paper, these authors examined artificially embalmed ancient Egyptian mummy tissues, a fish, a human hand and a macerated human lumbar vertebra, using THz-pulse imaging system.

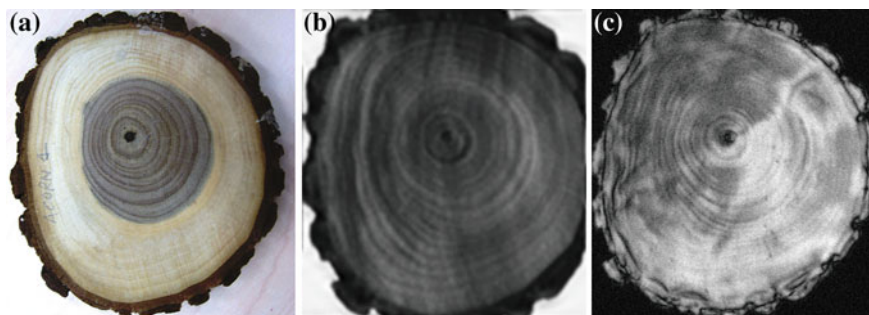


Fig. 20.7 RGB image (a) and THz-TDS reflectance image of the uncoated walnut sample (b) as well as THz-TDS image of the walnut specimen beneath the primer (c). Figure modified from Jackson et al. [35]

The THz images in transmission mode were recorded by spatially raster-scanning the samples through the focus of a standard THz time-domain spectroscopic system [10, 38]. From the data reported, it was evident that the spatial resolution information provided by THz imaging system used was not as good as the information provided by conventional X-ray imaging techniques. Broadband THz time-domain imaging on mummified tissues provided the authors with frequency-dependent information on the THz transmission and optical density distribution in the sample. However, in the case of thick and optically dense materials being used in order to obtain better quality images, the authors suggested utilising a different instrumental approach, with the use of a stronger continuous wave as reported by Karpowicz et al. and Appleby and Wallace [39, 40]. In any case, the THz imaging technique can be applied to the non-invasive investigation and detection of concealed items in archaeological and historic objects, such as funerary amulets or metallic objects/tools hidden in shrouded mummies. In addition, it is probable that the THz spectroscopic technique can also be used successfully to identify organic materials, e.g. balsamic essences used for embalming processes. Finally, as the authors suggested, THz techniques could be more extensively experimented in the field of paleopathology.

One of the most recent applications of THz-TDS spectroscopic imaging methodology focuses on the measurements of papyrus texts, including images of hidden papyri [34]. This technique, which is already used in the non-invasive imaging of several materials, such as postal envelopes [41] and, for the artistic field, in multi-layer mural paintings [27], parchment manuscripts [42] and pigment identification [25], was proposed here by the authors as a non-ionising and non-invasive technique for building layer-by-layer images of archaeological and ancient texts, e.g. papyri. Using a T-Ray 4000 commercial system by Picometrix, Inc., which covers the 0.1–1.5 THz frequency range, samples of new papyrus were investigated. These specimens were prepared, following traditional preparation techniques for materials and ancient papyri, using contemporary papyrus sheets (approximately 120- μm thick) and inks prepared from carbon black and red ochre pigments bound with Arabic gum. In order to perform reflection and transmission measurements at

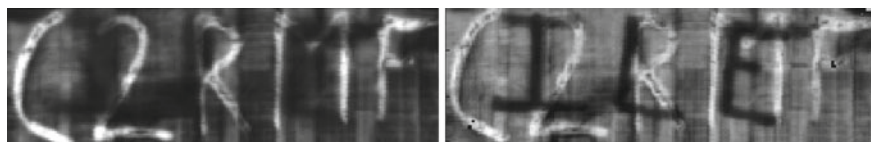


Fig. 20.8 THz images of multiple layers of papyrus samples layers from which exposed and hidden papyrus texts are readable in the THz domain. *Left* THz image of second layer of papyrus with a distance of 13 mm between the two layers. *Right* THz image of second layer of papyrus with a distance of 5 mm, in white the ink and in dark the shadow of the top layer. Figure modified from Labaune et al. [34]

normal incidence on the papyri, with minimal set-up reconfiguration of the system, the

T-Ray 4000 instrumentation utilised an INCONEL®-coated pellicle beam splitter, with 30% reflection, 30% transmission and 40% absorption. The reflection measurement scheme presented a major advantage compared to the transmittance mode, which deals with the possibility of obtaining information on the internal structure directly from the reflections produced by dielectrically heterogeneous interfaces inside the sample.

The authors demonstrated that the THz transmission and reflection analysis of different inks make it possible to differentiate between the inks that were used to produce papyrus texts. Furthermore, scans of multiple layers of samples demonstrated that it is possible to read exposed and hidden papyrus texts in the THz domain (Fig. 20.8). For the moment, the instrumental set-up described by the authors was capable of correctly viewing the texts on different papyrus sheets when the distance between two papyri was of a few millimetres. However, in their opinion, it should be possible to increase the resolution to <1 mm.

The above-mentioned experiments/applications were carried out by using mainly THz-TDS systems. In addition, as already mentioned above, a THz camera with micro-bolometer arrays sensor that has been developed at NICT and NEC can be used as a portable THz imaging system [43].

In addition, there are various types of THz imaging systems under development in research institutes around the world; for example, computed tomography (CT) THz with a continuous wave [44]. This means that, in a few more years' time, different THz systems will be ready for use in several different fields, including art conservation.

20.4 Conclusions

In practical terms, the THz power applied is usually strong enough to perform THz transmission imaging of paper or canvas paintings; however, unlike XRR, it is not penetrating enough for panel paintings. All the same, THz imaging can be used to establish the internal structure of materials in a non-invasive way by using, for

example, THz-TDS tomography, even when it is performed in reflectance. The results obtained with THz-TDS imaging can be compared with those achieved invasively with the study of cross-sections on micro-samples. Traditional cross-section images make it possible to investigate the layer composition and depth only in two dimensions, but do not provide analysts with information on the third dimension of the sample (or investigated area). On the other hand, in THz-TDS imaging each pixel of the image contains its own cross-section of information (stratigraphic information). Thus, area information on the layer of interest is also obtained by extracting the corresponding peaks in signals in the time domain. A 3D internal structure can be established by gathering images. However, one drawback of this technique involves the presence of substances that totally reflect the THz radiation. Thick and homogeneous gold leaves that can mask the structure underneath because they reflect the THz waves are an example of these substances.

THz-TDS imaging can be used to acquire spectra of the compounds constituting the paint layers (pigments, dyes, binders), even when these are covered by layers of varnish, because most of the natural and synthetic resins used as varnish show little and weak spectral features. However, since the available frequency range of existing THz imaging systems is still limited to less than 3 THz, the spectral information in the frequency domain would not be enough to unequivocally determine unknown materials. Certain artists' materials, such as lead white and cinnabar, for instance, show high reflection, compared to other white and red pigments. The area painted only by these pigments can be easily seen; but in order to better determine the analysed materials, other analytical methodologies, such as NIR or XRF, are usually required.

As far as THz imaging techniques applied to the investigation of ancient papyrus, mummies and archaeological bones, as well as to the study of art and/or archaeological wood found in cultural heritage for dendrochronological purposes, are concerned, the very promising first results reported in a few papers need to be extended to a more extensive set of case studies, in order to better refine the experimental methodologies.

The experiments with THz imaging systems introduced above have suggested that this technique could have a useful application in the cultural heritage field. The THz imaging technique, however, is a new technique and consequently, as already mentioned, THz data on artists' materials and on actual artworks will need to be collected extensively, thoroughly studied, and verified by means of careful comparisons of the results with those obtained by using other well-established diagnostic and analytical methodologies.

Acknowledgments The authors would like to thank Cristina Acidini (Soprintendente per il Polo Museale Fiorentino), Antonio Natali and Angelo Tartuferi, Director and Curator of the Uffizi Gallery, respectively, who kindly gave permission for the analysis of the Giotto painting, and Stefano Scarpelli, Susanna Bracci and Irl N. Duling III for their collaboration in the examination and analysis of the painting. In addition, the authors are most grateful to Bianca Jackson and Julien Labaune of the Institut de la Lumière Extrême, Ecole Polytechnique, Palaiseau (France) for their valuable support and suggestions. Moreover, the authors are grateful to Yuichi Ogawa of Kyoto University, Iwao Hosako of NICT, and Mauro Bacci of IFAC-CNR for their comments.

References

1. W.L. Chan, J. Deibel, D.M. Mittleman, *Rep. Prog. Phys.* **70**, 1325 (2007)
2. D.M. Mittleman, M. Gupta, R. Neelamani, R.G. Baraniuk, J.V. Rudd, M. Koch, *Appl. Phys. B* **68**, 1085 (1999)
3. D.M. Mittleman, *Sensing with terahertz radiation* (Springer, Berlin, 2003)
4. M. Tonouchi, *Nature Photonics* **1**, 97 (2007)
5. T. Yasui, T. Yasuda, K. Sawanaka, T. Araki, *Applied Optics* **44**, 6849 (2005)
6. D. Zimdars, J.S. White, G. Stuk, A. Chernovsky, G. Fichter, S. Williamson, in *Proceedings of the Lasers and Electro-Optics and 2006 Quantum Electronics and Laser Science Conference, paper CLMM1* (Long Beach, CA (USA), 2006)
7. Institute of Physics, T-rays, *VISIONS*, 22, available from <http://visions.iop.org>, (2008)
8. H. Hoshina, Y. Sasaki, A. Hayashi, C. Otani, K. Kawase, *SPIE Newsroom*, (2009). doi: [10.1117/2.1200902.1505](https://doi.org/10.1117/2.1200902.1505), (2009)
9. C.J. Strachan, P.F. Taday, D.A. Newnham, K.C. Gordon, J.A. Zeitler, M. Pepper, T. Rades, *Journal of Pharmaceutical Sciences* **94**, 837 (2005)
10. B.B. Hu, M.C. Nuss, *Opt. Lett.* **20**, 1716 (1995)
11. D.H. Auston, K.P. Cheung, *J. Opt. Soc. Am. B* **2**, 606 (1985)
12. A.P. DeFonzo, M. Jarwala, C. Lutz, *Appl. Phys. Lett.* **50**, 1155 (1987)
13. P.R. Smith, D.H. Auston, M.C. Nuss, *IEEE J. Quantum Electron.* **24**, 255 (1988)
14. C. Fattinger, D. Grischkowsky, *Appl. Phys. Lett.* **53**, 1480 (1988)
15. C. Fattinger, D. Grischkowsky, *Appl. Phys. Lett.* **54**, 490 (1989)
16. D.M. Mittleman, R.H. Jacobsen, M.C. Nuss, *IEEE Sel. Top. Quantum Electron.* **2**, 679 (1996)
17. P.H. Siegel, *IEEE Trans. Microw. Theory Tech.* **50**, 910 (2002)
18. W. Köhler, M. Panzer, U. Klotzsch, S. Winner, M. Helm, F. Rutz, C. Jördens, M. Koch, H. Leitner, in *Proceedings of the European Conference of Non-Destructive Testing*, P181, Berlin, 2006.
19. D. Saunders, R. Billinge, J. Cupitt, N. Atkinson, H. Liang, *Studies in Conservation* **51**, 277 (2006)
20. M. Kubik, in: *Physical Techniques, in the Study of Art, Archaeology and cultural Heritage, vol. 2*, ed. by D. Creagh, D. Bradley (Elsevier, Amsterdam, 2007), pp. 199–255
21. K. Fukunaga, M. Picollo, *Appl. Phys. A* **100**, 591 (2010)
22. S. Keck, *Appl. Opt.* **8**(1), 41 (1969)
23. C. Cucci, M. Picollo, M. Vervat, *J. Cult. Heritage* **13**, 83 (2012)
24. F. Rutz, S. Wietzke, M. Koch, H. Richter, S. Hickmann, V. Trappe, U. Ewert, in *Proceedings of the European Conference of Non-Destructive Testing, We.2.8.2*, Berlin, 2006
25. K. Fukunaga, Y. Ogawa, S. Hayashi, I. Hosako, *IEICE Electron. Express* **4**(8), 258 (2007)
26. I. Hosako, N. Sekine, M. Patrashin, S. Saito, K. Fukunaga, Y. Kasai, P. Baron, T. Seto, J. Mendrok, S. Ochiai, H. Yasuda, *Proc. IEEE* **95**, 1611 (2007)
27. J.B. Jackson, M. Mourou, J.F. Whitaker, I.N. Duling III, S.L. Williamson, M. Menu, G.A. Mourou, *Opt. Commun.* **281**, 527 (2008)
28. J.B. Jackson, M.R. Mourou, J.F. Whitaker, I.N. Duling, M. Menu, J. Labaune, G.A. Mourou, in *Proceedings of EOS Annual Meeting 2008*, Paris, (2008)
29. A.J.L. Adam, P.C.M. Planken, S. Meloni, J. Dik, *Opt. Express* **17**, 3407 (2009)
30. E. Abraham, A. Younus, J.C. Delagnes, P. Mounaix, *Appl. Phys. A* **100**, 585 (2010)
31. A. Doria, G.P. Gallerano, M. Germini, E. Giovenale, A. Lai, G. Messina, I. Spassovsky, F. Valente, L. d'Aquino, in *Proceedings of the Joint 30th International Conference on Infrared and Millimeter Waves and 13th International Conference on Terahertz Electronics IRMMW-THz2005*, Williamsburg, Virginia (USA), (2005)
32. G.P. Gallerano, A. Doria, E. Giovenale, G. Messina, A. Petralia, I. Spassovsky, K. Fukunaga, I. Hosako, in *Proceedings of the Joint 34th International Conference on Infrared and Millimeter Waves and Terahertz Electronics IRMMW-THz2009*, Busan (South Korea), (2009)
33. L. Öhrström, A. Bitzer, M. Walther, F.J. Rühli, *Am. J. Phys. Anthropol.* **142**, 497 (2010)

34. J. Labaune, J.B. Jackson, S. Pagès-Camagna, I.N. Duling, M. Menu, G.A. Mourou, *Appl. Phys. A* **100**, 607 (2010)
35. J.B. Jackson, M. Mourou, J. Labaune, J.F. Whitaker, I.N. Duling III, S.L. Williamson, C. Lavier, M. Menu, G.A. Mourou, *Meas. Sci. Technol.* **20**, 075502 (2009)
36. J.B. Jackson, J. Labaune, G. Mourou, I. Duling, C. Lavier, M. Menu, in *Proceedings of SPIE 7391, O3A Optics for Arts, Architecture, and Archaeology II*, ed. by L. Pezzati, R. Salimbeni (Munich, 2009)
37. T. Okochi, Y. Hoshino, H. Fujii, T. Misutani, *Dendrochronologia* **24**, 155 (2007)
38. D. Grischkowsky, S. Keiding, M. van Exter, C. Fattinger, *J. Opt. Soc. Am. B* **7**, 2006 (1990)
39. R. Appleby, H.B. Wallace, *IEEE Trans. Antennas Propag.* **55**, 2944 (2007)
40. N. Karpowicz, H. Zhong, J.Z. Xu, K.I. Lin, J.S. Hwang, X.C. Zhang, *Semicon. Sci. Technol.* **20**, S293 (2005)
41. Y. Sasaki, H. Hoshina, M. Yamashita, G. Okazaki, C. Otani, K. Kawase, in *Proceedings of the Conference Infrared, Millimeter, and Terahertz Waves*, vols. 1–2, Cardiff, (2007)
42. K. Fukunaga, Y. Ogawa, S. Hayashi, I. Hosako, in *Proceedings of the 33rd International Conference Infrared, Millimeter, and Terahertz Waves*, vols. 1–2, Pasadena, CA (USA), (2008)
43. N. Oda, H. Yoneyama, T. Sasaki, M. Sano, S. Kurashina, I. Hosako, N. Sekine, T. Sudoh, T. Irie, in *Proceedings of SPIE 6940*, ed. by B.F. Andresen, G.F. Fulop, P.R. Norton, (Orlando, FL, USA, 2008)
44. N. Sunaguchi, Y. Sasaki, M. Kawai, T. Yuasa and C. Otani, in *Proceedings of the 33rd International Conference Infrared, Millimeter, and Terahertz Waves*, vols. 1–2, Pasadena, CA (USA), (2008)

Chapter 21

Terahertz Plasmonic Structures

Adam J. Baragwanath, Andrew J. Gallant and J. Martyn Chamberlain

Abstract Here, we review the background physics of surface plasmons and plasmonic devices. In doing so, we describe how terahertz radiation can be used to excite plasmonic effects. These effects are shown to be beneficial for applications such as terahertz waveguiding, sensing, imaging and wavefront engineering.

21.1 Introduction

This chapter deals with terahertz (THz) frequency electromagnetic excitations at the interface between two materials: one is an electrical conductor and the other is a dielectric. The interfaces may be smooth or patterned with pits, corrugations or holes. Key questions, helping us to understand the nature of the excitation or excitations (and their potential application) will include: is a wave or a (quasi) particle perspective preferable; does the excitation propagate, or is it confined to the surface; and how may such a confinement (if it is present) be engineered through the choice of materials or through geometry choice?

This topic has generated considerable interest in the last decade. Applications at THz frequencies are now emerging in the development of: sensors (including biological sensors); techniques for guiding, concentrating and manipulating THz

A. J. Baragwanath

Department of Physics, Durham University, South Road, DurhamDH1 3LE, UK
e-mail: a.j.baragwanath@durham.ac.uk

A. J. Gallant (✉)

School of Engineering and Computing Sciences, Durham University, South Road,
DurhamDH1 3LE, UK
e-mail: a.j.gallant@durham.ac.uk

J. M. Chamberlain

Department of Physics, Durham University, South Road, DurhamDH1 3LE, UK
e-mail: martyn.chamberlain@durham.ac.uk

radiation; and new methods for THz imaging and microscopy. Devices can be constructed using the standard techniques of semiconductor processing technology, as the characteristic length scales are commensurate with the THz wavelength (i.e. a fraction of a millimetre); and so this task can be easily accomplished. The field is often described as plasmonics, by analogy with electronics, to describe the study of the underlying physics and the applications of surface electromagnetic excitations at interfaces. Here, the quasi-particle nature of the excitation is emphasised although it should not be thought that all phenomena are most easily discussed in this way.

A plasmon may be very broadly defined as “a quantum quasi-particle representing the elementary excitations, or modes, of the charge density oscillations in a plasma” [1]. Historically, the topic became of interest to THz specialists in the late 1950s, with observations of the THz frequency emission from ionic plasma in attempted nuclear fusion experiments [2]. Developments in semiconductor material quality and in THz instrumentation led to the first exploration of the properties of the volume (or: bulk, 3D) solid-state plasmon, of which there is an extensive literature [3, 4]. Although this chapter focuses on effects that occur, by definition, at the interface of two materials, it is helpful first to remind the reader of the Drude model of a 3D metal, as it predicts important properties of the material permittivity (or dielectric function), $\epsilon(\omega)$. This model considers a gas of electrons uniformly distributed through a periodic structure of fixed ions and leads to the expression for $\epsilon(\omega)$ at an angular frequency, ω :

$$\epsilon(\omega) = \epsilon_{\infty} \left[1 - \frac{\omega_p^2}{\omega^2 + j\Gamma\omega} \right]. \quad (21.1)$$

In this expression, Γ represents a collision rate for electrons and is set at zero for the perfect electronic conductor, or PEC. The (3D) plasma frequency takes on the form: $\omega_p = \sqrt{ne^2/m\epsilon_{\infty}\epsilon}$, where the (3D) density of electrons is n and all other symbols have their usual meanings. This is the frequency at which the (3D) electron gas oscillates: it lies in the ultraviolet region for metals and in the THz region for semiconductors. The 3D plasmon is the virtual particle of this excitation. From [1], $\epsilon(\omega)$ is complex and so:

$$\Re[\epsilon(\omega)] = \epsilon_{\infty} \left[1 - \frac{\omega_p^2}{\omega^2 + \Gamma^2} \right]. \quad (21.2)$$

This means that, for a metal, $\Re[\epsilon(\omega)] < 0$ at $\omega < \omega_p$. When ω exceeds ω_p , $\Re[\epsilon(\omega)]$ becomes positive and the material then exhibits dielectric behaviour. In simple physical terms, the electron gas cannot keep pace with the rapidly changing applied electric field. This variation of ϵ with ω should be borne in mind when considering the effects at the interface of a metal and a dielectric.

The plasmonic phenomena discussed here may be described by an electromagnetic wave formalism [1]; or, alternatively, a quasi-particle approach can be adopted using the analogy that “the plasmon is to the plasma charge density what the photon is to the electromagnetic field” [5]. In the first approach, all that is needed

is knowledge of how ϵ varies with frequency and geometry. However, no specific knowledge is required of the actual microscopic processes responsible for the variation of ϵ for systems such as metal/dielectric interfaces or metal sheets periodically punctured with holes. The quasi-particle view requires an understanding of such processes, including charge movements, scattering and tunnelling, leading to such graphic phrases as “the plasmon rolling like a ball over the landscape” [6]. The reader is warned that a plethora of terms exists in the literature, including: surface plasmon, surface plasmon polariton (SPP), surface electromagnetic excitation (or wave), Zenneck wave, Zenneck–Sommerfeld wave, localised surface plasmons, Brewster modes, local modes, shape modes. . . etc. Furthermore (and to complicate even further), some of these terms may be preceded by adjectives such as: resonant, non-resonant, radiative or non-radiative!

It will be seen in Sect. 21.2 that a very important tool for clarifying and categorising plasmonic phenomena is the dispersion relation, which is a graphical method of relating the wave vector of the entity under discussion to the frequency; or, alternatively, it is the link between its spatial and temporal characteristics. There are many excellent reviews of the general field (including THz applications); and the reader is referred to the classic texts by [1, 7, 8] for a closer discussion. Most of the literature adopts an optical, rather than an electrical engineering, approach to surface plasmons: the concepts of equivalent circuits, characteristic impedances etc. are rarely deployed, although one author [9] has argued that the circuit paradigm provides a clearer basis for discussion.

Plasmonics has advanced significantly (in terms of theory and potential application) due to the discovery of two main phenomena. These are: (a) the so-called Spoof Plasmon effect [6], occurring at THz frequencies at the interface between suitably structured metallic surfaces and a dielectric; and (b) extraordinary optical transmission (EOT) [10], first noted at THz frequencies by Gómez Rivas [11]. The concept of the Spoof Plasmon is discussed later (Sect. 21.2.1), where it is shown that the plasma frequency of a metal can be lowered through the use of surface “decoration.” EOT involves a greater-than-expected transmission through an aperture in a metallic substrate. The mechanism of EOT is subject to considerable debate; the reader is referred to reviews by Garcia-Vidal [12] and de Abajo [13] that deal more specifically with the question of radiation passing through periodic arrays of small holes.

The theory of optical transmission through subwavelength holes [14] is considered elsewhere in this Volume. For a subwavelength aperture in an infinitely thin, perfectly conducting substrate, Bethe showed that the transmission efficiency was proportional to $(r/\lambda)^4$, where r is the radius of the aperture and λ the incident wavelength. A more comprehensive analysis for real materials, and for substrates of finite thickness, involves tunnelling effects through the aperture and coupling to surface plasmons. This area of investigation has encompassed: single apertures; the 1D case of subwavelength slits; 2D arrays of subwavelength holes of various shapes; together with single apertures flanked by periodic corrugations (bullseye structures). The transmission properties of such systems are governed, *inter alia*, by: hole dimensions, hole shape, array periodicity, ratio of basis-to-lattice, material of array, material

of supporting substrate, angle of incident radiation, frequency of incident radiation and array thickness. Unsurprisingly, there is a vast literature on the topic, including THz observations, theory and applications.

In this context, the observations of R. W. Wood (“Woods anomalies”) relating to the dark bands in the reflection spectrum of a metallic grating are of interest. In 1973, the first connection between the presence of Wood’s anomalies and the excitation of surface plasmons was introduced. Hutley and Bird [15] drew upon the similarities between experiments conducted by Teng and Stern [16], who used 10keV electron beams to excite surface plasmons on metal gratings, and Wood’s experiments.

This chapter is organised as follows: Sect. 21.2 deals with the background physics of a number of basic plasmonic phenomena; and Sect. 21.3 describes a number of applications of these basic ideas. Finally, there is a short Conclusion. It should be noted that this chapter relates closely to Chap. 15 (Near-field terahertz imaging) and Chap. 22 (Metamaterials). With regard to metamaterials, we adopt the definition that they may be described by a set of effective homogeneous parameters; and that these parameters are determined by the collective response of small conducting resonators [17]. As such, the resonator scale is firmly set in the subwavelength limit. At the microscopic level, however, many of the important aspects of metamaterial performance can be ascribed to plasmonic effects. For further discussion on this matter, the interested reader is referred to articles by: Hibbins [18, 19]; Acuna [20]; and Navarro-Cia [21].

21.2 The Physics of THz Plasmonic Phenomena

21.2.1 *Introductory Theory and Classification of Plasmonic Phenomena*

We first present background theory that is relevant to an understanding of plasmonic phenomena at THz frequencies. We review the case of a 2D arrangement, where two semi-infinite half-spaces of different materials (a dielectric and a metal) are juxtaposed. This will enable us to classify plasmonic phenomena and will form the basis of the subsequent analysis of more complicated geometries. It is shown in Sect. 21.2.2 that—by suitable choice of materials—THz frequency surface excitations may propagate at such a simple interface along distances of up to several metres; similarly, the associated electric fields in the dielectric may extend to several millimetres. In Sect. 21.2.3, we consider how this situation is altered if the surface is “decorated” with simple corrugations. This theme is continued in Sect. 21.2.4: we shall see how significant confinement effects can be engineered through choice of surface geometry. The remainder of the section deals with THz frequency properties of arrays of holes and gratings formed on metallic surfaces.

A rigorous analysis of the electromagnetic modes supported in a materials arrangement, depicted in Fig. 21.1, is given from a systems perspective in [1]. As noted pre-

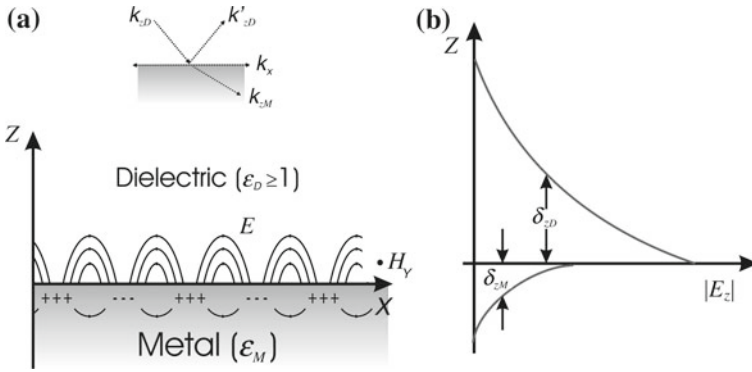


Fig. 21.1 **a** Representation of an SPP at the boundary between a metal and a dielectric. Subscripts (*M, D*) represent metal and dielectric, respectively; the superscript (') indicates a reflected wavevector. **b** The relative decay of the electric field into the dielectric and the metal (*top and bottom* respectively)

viously, in this approach all that is necessary is to know the geometry and the value of $\epsilon(\omega)$. More physical insight may be gained from simple treatments [7, 8, 22] which consider a wave incident on the interface through the dielectric at some angle θ_i to the normal; and with electric vector in the plane of the paper. The case of most interest is when $\theta_c = \sin^{-1} [\sqrt{\epsilon_M}/\sqrt{\epsilon_D}]$. Above this critical angle, radiation does not propagate in the metal: the oscillating electric field is then totally reflected, but interface bound charges will oscillate, giving rise to strongly decaying (evanescent) fields at the interface between the two materials. A more detailed analysis [1] leads to the conclusion that, when $\omega < \omega_p$, the surface wave is trapped with exponential decays of the amplitude of the electric field amplitude into both media provided that $\epsilon_D(\omega)$ is positive and $\epsilon_M(\omega)$ is negative. Further discussion of the extent of this trapping, or confinement, is given later.

By solving Maxwell's equations with the appropriate boundary conditions, the excitation dispersion relation can be determined for the propagation direction (x) and for the direction normal to the boundary (z), into the dielectric and metal, respectively [7]:

$$k_x = \frac{\omega}{c} \sqrt{\frac{\epsilon_D \epsilon_M}{\epsilon_D + \epsilon_M}} \tag{21.3}$$

and

$$k_{z,D} = \frac{\omega}{c} \sqrt{\frac{\epsilon_D^2}{\epsilon_D + \epsilon_M}}, \tag{21.4a}$$

$$k_{z,M} = \frac{\omega}{c} \sqrt{\frac{\epsilon_M^2}{\epsilon_D + \epsilon_M}}. \tag{21.4b}$$

Table 21.1 The types of EM modes existing at a planar dielectric/metal interface, assuming $\epsilon_D > 1$. After [1]

Mode	$\Re(\epsilon_M)$	$\Im(\epsilon_M)$	Nature of k_x	Nature of k'_{zD}		Nature of k_{zM}	
				\Re	\Im	\Re	\Im
Brewster modes	>0	$=0$	Real	>0	$=0$	>0	$=0$
	>0	>0	Complex	>0	<0	>0	>0
Localised SPPs	$0 > \Re(\epsilon_M) > -\epsilon_D$	$=0$	Pure imaginary	<0	$=0$	>0	$=0$
	$0 > \Re(\epsilon_M) > -\epsilon_D$	>0	Complex	>0	<0	<0 or >0	>0
Propagating SPPs	$\epsilon_D > \Re(\epsilon_M)$	$=0$	Real	$=0$	<0	$=0$	>0
	$\epsilon_D > \Re(\epsilon_M)$	>0	Complex	>0	<0	<0 or >0	>0

Note that, the excitation is generally described as a SPP, using the quasi-particle nomenclature, and recognising the implicit coupling between photon and plasmon. In the above equations, the subscripts refer to the SPP k -vector components (see Fig. 21.1a for clarify) these are allowed to be complex for real ω . For an excitation propagating along the interface, the wave vector k_x remains real. To ensure that the surface excitation remains bound, the normal components of the wave vector k_z must be imaginary so that the field decays evanescently away from the interface. Whether or not these conditions will be met depends critically on the values of the real and imaginary parts of ϵ_D and ϵ_M , which leads to a helpful way to categorize the modes that can be sustained at the interface.

Table 21.1 summarises all the modes; an analogous diagrammatic treatment is given by [1]. The region in Table 1 corresponding to the *Brewster modes*, exists when $\Re(\epsilon_M) > 0$. For a real metal, i.e. when $\Im(\epsilon_M) > 0$, these modes can be regarded as true surface modes. These surface polaritons comprise a mixture of surface charge waves and propagating photons. Strictly speaking, these entities are not conventionally described as surface *plasmon* polaritons; this classification is reserved for the case when $\Im(\epsilon_M) > 0$. In practice, Brewster modes are not encountered at THz frequencies for metal/dielectric or semiconductor/dielectric interfaces.

The modes corresponding to those labelled *localised* SPPs possess a non-propagating surface wave, highlighted by the pure imaginary value of k_x . For a perfectly electrically conducting (PEC) material, i.e. when $\Im(\epsilon_M) = 0$, these modes can be considered radiative as the evanescent energy of the surface wave is dissipated away from the surface via the real, propagating k_z modes. Such modes become non-radiative for the case of a real metal as the k_z modes become evanescent i.e. they can no longer radiate the evanescent surface wave. The role of localised SPPs at THz frequencies will be discussed later, in the context of a patterned conducting surface.

Finally, we consider propagating SPPs, for which $\epsilon_D > \Re(\epsilon_M)$. The pure imaginary nature of both k_{zD} and k_{zM} display the evanescent decay of the field perpendicular to the surface, whilst the real value of k_x highlights the propagating nature of the established surface wave. These non-radiative modes are known formally as propagating SPPs; they are fully trapped at the conductor–dielectric boundary. For a real metal, the imaginary nature of k_x results in these modes becoming pseudo-

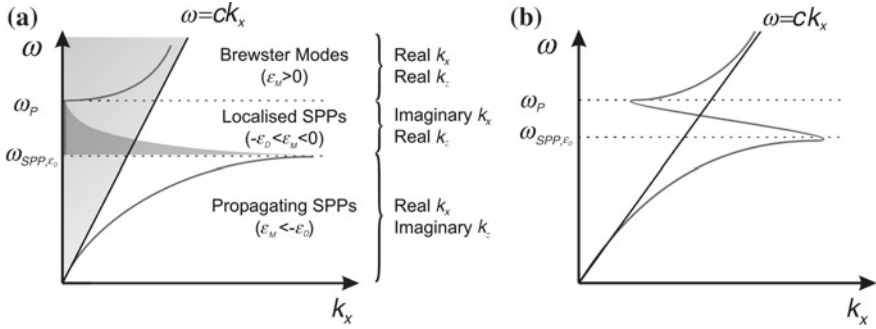


Fig. 21.2 **a** Dispersion relation for a lossless Drude metal. Free-space photons lie in the shaded light grey region, to the left of the *light line*. The broadening of the localised SPPs (indicated by the shaded *dark grey* region) arises due to the strong evanescent nature of these modes. **b** Dispersion relation when losses are included. After [1]

propagating i.e. there is only a certain distance the SPPs can travel before damping-induced losses imposed by the metal become overwhelming.

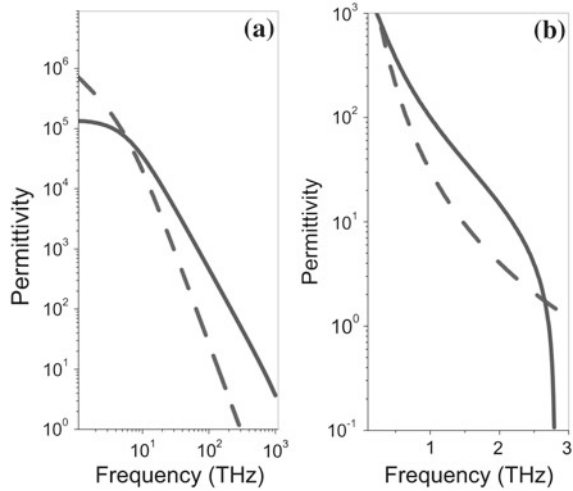
Figure 21.2 shows two versions the dispersion relation (ω, k_x) . Other reviews [1, 7, 8] discuss: the derivation of this relation; the importance of the regions of the dispersion relation diagram; and effects of absorption and loss in the metal. We now consider a few salient points, however, for future reference. The first is that the *light line*, which separates allowable free-space photons from the compound excitations. Second, between the Brewster modes and the propagating SPPs reside the localised SPP modes. In this region, a significant broadening of the mode is often observed due to the metallic losses. The propagating SPP branch can be seen to approach the limiting frequency ω_{SPP} as k_x increases.

For a perfect Drude metal, this frequency can be shown to be [7]:

$$\omega_{SPP} = \frac{\omega_p}{\sqrt{(1 + \epsilon_D)}}. \tag{21.5}$$

Sometimes this is referred to as a pure surface plasmon (dropping “polariton”) to emphasise the surface-wave-like nature of the excitation. At lower frequencies the propagating SPP mode approaches the light line, where these modes take on a more “photon-like” appearance [1], behaving more as a photon travelling at grazing incidence. Alternatively, the wave-like nature of the entity is highlighted by describing it as a Zenneck Wave [23, 24].

Fig. 21.3 Variation of $\Re(\epsilon)$ (solid lines) and $\Im(\epsilon)$ (dashed lines) with frequency for **a** gold and **b** InSb. After [26], ©2009 IEEE



21.2.2 THz Frequency Plasmons at the Planar Metal/Dielectric Interface

The extent of localization of the SPP, as measured by the propagation distance along the interface and by the electric field attenuation perpendicular to the interface, are of great importance. The main results are: (a) the SPP wavelength is given by $\lambda_{\text{SPP}} = 2\pi/\Re(k_x)$; and (b) the imaginary component of the SPP wave vector component in the x direction provides a measure of the propagation length along the surface $L_{\text{SPP}} = 1/2\Im(k_x)$. The decay length of the mode from the interface into either the metal or the dielectric is $L_{z,l} = 1/2\Re(k_{z,l})$, where: $k_{z,l}$ is the complex perpendicular wave vector component; l is an index ($1 = \text{dielectric}, 2 = \text{metal}$) and $k_{z,l} = \sqrt{k_x^2 - \epsilon_l(\omega) \left[\frac{\omega}{c}\right]^2}$.

It is instructive to determine these values at a frequency of 1 THz for interfaces between gold and air and between the high mobility semiconductor indium antimonide (InSb) and air. Using the materials data [25] for these two materials, Fig. 21.3 [26] shows the variation of $\Re(\epsilon)$ and $\Im(\epsilon)$ for these two materials. Note that, the frequency scales differ markedly. Using this information, together with the previous equations, values for λ_{SPP} , L_{z1} and L_{SPP} may be calculated [26]. Table 21.2 shows these values at 1 THz. Clearly, for gold, the much higher electron density ($5.9 \times 10^{28} \text{ m}^{-3}$) gives rise to a larger value for ω_p than for InSb (electron density $2 \times 10^{22} \text{ m}^{-3}$), leading to larger values of the permittivity, ϵ , and hence greater impedance mismatch at the air interface and greater penetration into the air. Furthermore, the excitation propagates several metres along the gold surface as a direct result of the weak wave/surface interaction. Also apparent are: the stronger confinement for InSb; and that, as the frequency approaches ω_p , a less than one-wavelength confinement is possible, breaking the Rayleigh limit.

Table 21.2 Parameters at 1 THz for interfaces between air and two conducting materials, Gold and InSb. After [26], ©2009 IEEE

Material	$n(\text{cm}^{-3})$	$\omega_p/2\pi$ (THz)	$\Re(\epsilon_M)$	$\Im(\epsilon_M)$	λ_{SPP} (m)	L_{SPP} (m)	L_{z1} (m)	L_{z2} (m)
Gold	59×10^{27}	2.2×10^3	-86×10^3	0.62×10^6	0.3×10^{-3}	30	25×10^{-3}	40×10^{-9}
InSb	20×10^{21}	2.8	-99	30	0.29×10^{-3}	15×10^{-3}	0.24×10^{-3}	2.3×10^{-6}

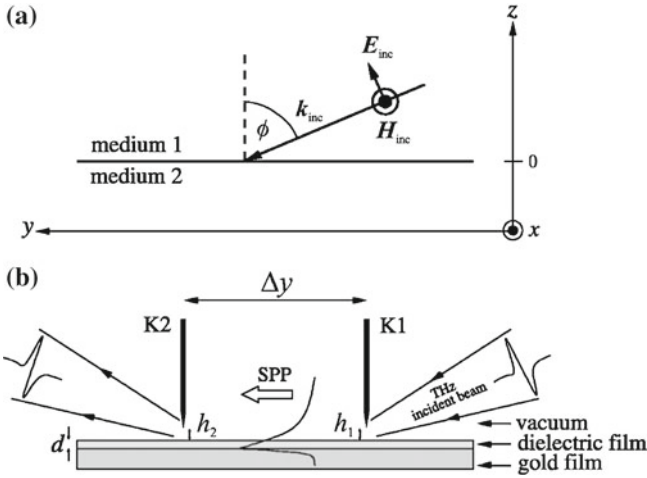


Fig. 21.4 Aperture excitation geometry. Reprinted figure with permission from [34]. ©2004 by the American Physical Society

From Fig. 21.2, in order to satisfy quasi-momentum conservation, it is necessary to provide an additional wave vector component to the SPP. At visible and near-infrared frequencies prism coupling is normally used [27]. This approach has been described for THz SPP studies using Teflon [28] and silicon [29] prisms to measure, respectively: the THz frequency permittivity of the semiconductor InAs and of distilled water; and the propagation of SPPs along thin plastic films. However, the most-favoured approach at THz frequencies is to use a broadband aperture excitation technique [30] originally developed for second harmonic generation, as shown in Fig. 21.4. The method has been used to investigate the propagation of SPPs along silicon [31] and InSb surfaces [32], in both cases demonstrating that confinement of SPPs takes place on semiconductors at THz frequencies in a similar fashion to metals at shorter wavelengths. Whilst the propagation of SPPs along simple interfaces between air and a metal (or semiconductor) is of some interest, there are important applications of the measurement method in sensing the properties of thin films of biological or plastic materials placed on such interfaces. The problem was first discussed by Kaminow [33] who argued that greater confinement is obtained with shorter wavelengths. Maier [8] analysed a three component system e.g. a metal/plastic film/air layering. Saxler [34], using the aperture excitation technique, investigated SPP phenomena in cyclotene films laid on gold. Saxler probed the spatial and spectroscopic field distribution of the SPPs and concluded that stronger confinement to the surface occurs in the presence of the dielectric film. Related experiments are described by Isaac [35] who claims that the properties of deposited films that are as thin as 50 nm may be probed using this method.

Jeon [36] gives a thorough overview of the THz Zenneck wave, discussing in some detail if this is truly a Zenneck wave (i.e. propagating significant distances in

a loss-less fashion). A waveguide arrangement is deployed to launch the wave over the metal surface and Jeon concludes that deficiencies in the launching system will prevent true Zenneck wave behaviour. This is a very pertinent point, often disregarded by other authors, that all elements in the “circuit” need to be designed together. Gong [37] considers the large evanescent field associated with the very weak guiding of the Zenneck wave over the smooth metal. Gong shows, experimentally, that a very thin dielectric layer will reduce the extent of the field 100-fold, demonstrating the potential of the arrangement for sensing applications.

21.2.3 Corrugated Structures with Characteristic Dimensions Commensurate with the THz Wavelength

As a preliminary to the discussion of a spoof plasmon in Sect. 21.2.4, we consider a metal surface decorated with corrugations of dimensions that are commensurate with the THz wavelength. In these arrangements, a hole is frequently used to sample the THz radiation; this section therefore also serves as an introduction to Sect. 21.2.5, where the phenomenon of EOT is considered in more detail. The geometry in which a hole is flanked by annular corrugations is termed a bullseye. However, to begin this discussion we consider first the experiments of Zhu [38] who measures the vector components [39] of the THz electric field at the centre of a bullseye which is not pierced with a central hole (see Fig. 21.5). The bullseye consists of 25 concentric annular grooves each of rectangular cross-section, with a width of 500 μm and a depth of 100 μm ; the centre-to-centre spacing is 1 mm. The bullseye is illuminated vertically by a broadband THz beam from a standard time-domain spectroscopy (TDS) system with frequency range approximately 100 GHz to 1.5 THz. The electric field at the centre of the bullseye is measured with an electro-optic detector; and the use of a TDS system enables the temporal build-up of the signal to be monitored. Note that coupling of the THz beam with the structure takes place with normal incidence geometry, in contrast to coupling discussed previously. Caglayan [40] argues that the coupling is effective because the periodic grating structure of the bullseye provides additional pseudo-momentum; however, coupling can also be obtained for normal incidence even when there is only one annular ring present [41]. A pragmatic explanation is to simply state that scattering and diffraction will occur as the THz beam hits the metallic corrugation, coupling to surface plasmons; these will then propagate as SPPs to the next corrugation, where the same process takes place again. The resonant corrugation structure thus encourages the build-up of a signal at a wavelength corresponding to the grating period. This may be easily seen in the time-domain trace (Fig. 21.5) as the detector receives signals carried by successive pulses of SPPs.

Propagation also occurs in the direction from the centre towards the edge of the array; but these SPPs are not captured by the detector. The vector field of the THz wave can be measured and this shows an expected exponential fall-off away from the metal surface. Note that, the SPPs involved here (where the surface features are

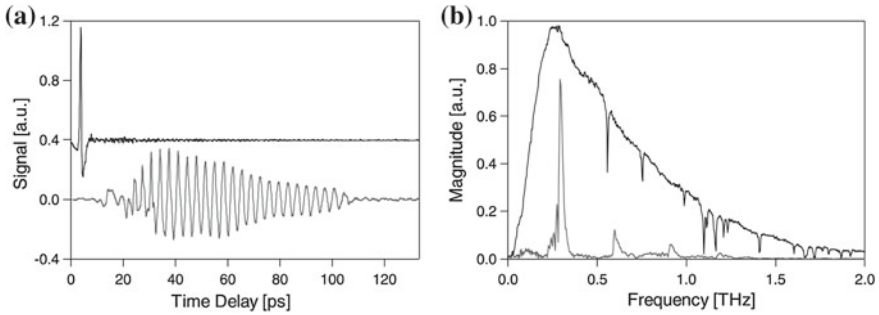


Fig. 21.5 Measured time-domain waveforms for the incident THz pulse (*upper waveform*) and the E_z component of the THz surface plasmon measured at the centre of the bullseye structure. The waveforms, offset vertically for clarity, were measured under different experimental configurations. Reprinted with permission from [38]

not obviously subwavelength) are the same as those discussed previously; and that the major role of the corrugations is to assist the coupling process, and not to provide confinement *per se*.

Before proceeding to discuss bullseyes with a central hole, it is first helpful to comment on the process of transmission of light through a very small hole that has no intentional surface decoration. This is discussed in detail elsewhere in this Volume for THz frequency radiation: the process involves an evanescent coupling between the plasmons on the input surface, through the orifice, to the output surface where re-radiation occurs. Following transmission measurements through subwavelength (300 nm diameter) holes at optical frequencies ($\lambda \approx 600$ nm), it was found that: unexpected enhancements occurred in the transmission of the hole and the directionality of the emerging beam; and that the hole shape was important in controlling these. Using electron-beam-induced plasmon emission, it was deduced that: localised surface plasmons are excited on the incident face; and that these subsequently tunnel through the hole, before re-radiation at the exit surface. This basic approach is used to account for the THz transmission studies of Agrawal [41, 42] who investigated the transmission properties of bullseye structures with central holes using TDS measurements. The geometry of these structures is very similar to that used by Zhu [38]; bullseyes with one, two, four and six grooves are considered with separation of the order of the incident wavelength. As may be seen [38], the TDS method enables the contributions of the coupling of the incident THz wave to each successive annular groove to be followed directly. Studies of the effect of groove depth and width are reported [41] leading to the possibility of control of the transmitted pulse shape. It is noted, empirically, that a depth of roughly one-tenth of the wavelength provides best coupling. The effects of changing the phase of the annular grooves with respect to the central aperture have also been studied [43]; the transmitted intensity can be manipulated, from enhancement to suppression, as the phase is changed. The inclusion of a defect onto the surface pattern structure (i.e. the absence of a groove) also shows up on the TDS trace as a suppressed oscillation at a specific temporal location [42].

The explanation of all of these phenomena is in terms of coupling of the THz radiation to surface plasmons to form SPPs with a resonant frequency, caused by the array periodicity, followed by tunnelling through the aperture and subsequent re-radiation. There may, in addition, be a non-resonant direct transmission through the aperture.

Finally, note that patterning the exit face of the metal with a similar annular groove pattern [44] adds an additional component to the overall process: the initial coupling of radiation to the input face is followed by the propagation of resonant SPPs towards the aperture and subsequent tunnelling through it. The exit process itself has two components: the first is direct radiation into the far-field of the aperture; the second is from SPPs that propagate along the exit face but, because of the corrugations on that face, will radiate into the forward (exit) direction. If the exit face were plane, then the SPPs would be bound to the interface and subsequently attenuated, so that the integrated intensity of the transmitted radiation would be less i.e. the presence of any exit face corrugations can be said to enhance the output power.

The plasmons considered above are “genuine” plasmons, with properties such as confinement and propagation length primarily determined by the nature of the interface conductor. The corrugations, separated by a distance of the order of the wavelength, mainly act as centres for plasmon/photon scattering and coupling. We now consider the case of distinctly subwavelength features, where the geometry dictates confinement to a much greater extent.

21.2.4 *The Spoof SPP*

Techniques to improve surface wave confinement have been researched for several decades. For transmission lines, Goubau [45] reported that surface wave confinement could be enhanced by structuring the metal surface of a wire. A series of corrugations at the air/metal interface act to increase the electric field penetration into the interface and therefore reduce the impedance mismatch. In 2004, Pendry [6] addressed specifically the case for confining SPPs at the surface of PECs. This is particularly pertinent to the THz region where, on first inspection, metals appear not to be well suited for SPP confinement. The Drude model shows that the permittivity of a metal tends to that of a perfect electrical conductor (i.e. minus infinity) at frequencies much lower than ω_p . In the THz region, for metals, both the real and imaginary parts of the permittivity are many orders of magnitude greater than those at visible frequencies. This leads to a high impedance mismatch at the metal/dielectric interface, and hence poor confinement of the SPP to the surface.

As discussed in the previous section, for metals at THz frequencies, an SPP is really travelling as a weakly confined, lossy, wave. In order to move from this regime to that of a bound SPP, the metal/dielectric interface must be modified to reduce the impedance mismatch. Pendry considered the problem from an “effective medium” perspective where both the permittivity and permeability of the metal are tailored by machining arrays of sub wavelength indentations or holes. Unlike our discussions in previous sections, the surface decorations for the Pendry case must be subwavelength both with regards to their feature size and their spacing. Hence, the features are not

“seen” individually by the incident radiation; instead, they collectively create an artificial material which has an effective permittivity and permeability.

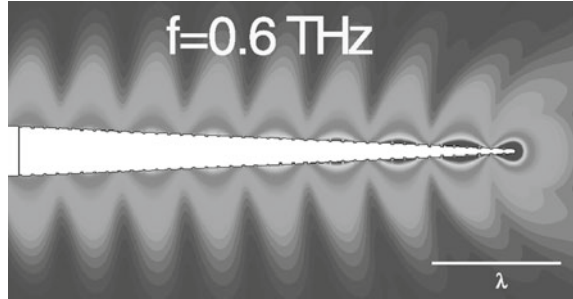
Importantly, Pendry showed that a structured metal can have an effective plasma frequency which is lower than that of a bulk metal. In simple terms, the holes dilute the plasma frequency of a metal. For the square hole array case, where the hole is filled with a material of permittivity ϵ_h and permeability μ_h , the effective plasma frequency, $\omega'_p = \pi c_0 / a \sqrt{\epsilon_h \mu_h}$ [6, 13]. This corresponds to the cut-off frequency of the hole for TE₀₁ when the hole is considered as a waveguide. Hence, the plasma frequency of metal can be lowered through surface decoration into the THz region. This enables a structured metal/dielectric interface excited with THz (and microwave) frequencies to show surface wave confinement comparable to that found at semiconductor/dielectric interfaces (e.g. InSb/air). The conditions are thus met for bound SPPs. Pendry referred to the SPPs generated through the use of structured surfaces as “spoof” SPPs, i.e. imitations of “genuine” plasmons. From a device implementation perspective, the bound spoof SPP concept is very significant. Confined SPP effects can be achieved, in the THz region, at metal/air rather than just semiconductor/air interfaces. A plethora of surface micromachining techniques, usually adapted from the integrated circuit industry, are available for the fabrication of these spoof metal surfaces.

Williams [46] experimentally confirmed the existence of spoof SPPs on a metal in the THz region. They used THz TDS to measure SPP propagation along copper surfaces patterned with arrays of micromachined square pits and showed wavelength scale confinement over an octave of THz frequency. Williams used diffraction at a knife edge to launch the spoof SPPs. It should be appreciated that the quasi-momentum conservation arguments outlined previously as requirements for the coupling of incident radiation to “genuine” SPPs also hold for spoof surfaces. For example, Hibbins [47], reported the use of a wax prism to launch a spoof SPP on a metal at microwave frequencies.

So far, we have considered planar surfaces for the propagation of SPPs. However, similar effects can be observed with cylindrical conductors (i.e. wires). This geometry was first considered by Sommerfeld in 1899 [48]. However, more recently it has proved attractive for the guided propagation of THz pulses. Bare metal wires provide low signal attenuation and dispersion compared to conventional parallel plate waveguides, coax or fibres [49]. Furthermore, several groups have shown that by tapering the end of a wire [50–52], the electric field can be confined into a sub-wavelength spot. However, along the length of the wire, the radial electric field confinement of the SPPs typically spans several wavelengths. This poor confinement can be exploited as a mechanism to couple between wires (e.g. for a beam splitter) [49]. However, a key disadvantage is that a poorly confined SPP suffers from bending losses [53]. This fundamentally limits the ability to use this type of guided propagation in compact, integrated, THz systems.

As with planar surfaces, spoof SPPs also provide a mechanism for well-confined transmission of terahertz radiation along wires [54]. Figure 21.6 shows a tapered wire configuration decorated with sub wavelength periodic grooves. Simulations with this geometry suggest subwavelength confinement of the electric field along the length of the wire and deep subwavelength confinement at the tip. As will be discussed further

Fig. 21.6 Superfocusing on a corrugated cone of length 2 mm with constant groove depth of 5 μm and a lattice constant 50 μm . The radius, R , is reduced from 100 to 10 μm , demonstrating how the E field can be focussed and concentrated at the tip of conical structures. The plot shows the magnitude of the E field on a logarithmic scale spanning 2 orders of magnitude. Reprinted figure with permission from [54]. ©2006 by the American Physical Society



in Sect. 21.3, this has applications in the sensing and imaging of small quantities of material.

Finally, an alternative approach, employed by Chau [55] to lower the plasma frequency of a metal, is to use ensembles of subwavelength sized metallic particles. As with the micromachined devices presented previously, the subwavelength particles collectively have an effective permittivity (and permeability) which differs from that of their bulk. Chau observed THz pulse transmission through metallic particles which were randomly distributed in a sample cell. This transmission was through collective thicknesses (≈ 1.2 mm), much greater than the skin depth of the metal, and demonstrated a positive permittivity. In this configuration, the SPPs are formed at the surface of the metallic particles; coupling (and, hence, SPP propagation) occurs between the closely spaced particles [55].

21.2.5 Gratings and Arrays of Apertures

21.2.5.1 Introduction

There is as yet no unequivocal explanation for the phenomenon of EOT through 2D subwavelength hole arrays [10]. Although it is generally acknowledged that SPPs play a vital role in this observed “anomaly,” the precise nature of transmission through the array is hotly debated [56–65]; with some authors [66, 67] even claiming no role for SPPs. We present, first, an outline of how the presence of a 2D array affects the dispersion relation of SPPs. An overview will then (Sect. 21.2.5.2) be given of the mechanisms thought to be involved in transmission; and how these are affected by the hole shape and size, the lattice arrangements, material geometry, material properties and thickness.

When light is incident upon a 2D metal hole array with subwavelength holes and periodicity, each hole edge serves as a diffraction point at which p -polarised light can couple to SPPs. The 2D lattice provides in-plane momentum with integer multiples of $2\pi/L$ in both the x and y directions, where L is the period of the array. This increased in-plane momentum allows the freely propagating light to couple to SPP modes, which are subsequently initiated along the metal–dielectric boundary. The wave vector of the SPP can thus be expressed as:

$$k_{\text{SPP}} = \frac{2\pi}{\lambda} \sin \theta \pm mG_x \pm nG_y \quad (21.6)$$

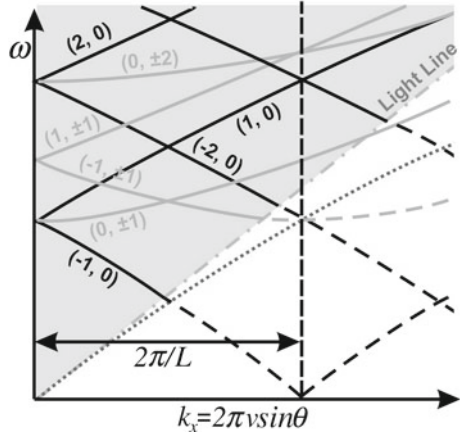
Here, λ is the wavelength of the incident radiation, θ is the angle of incidence of light on the array, m and n are integers whilst G_x and G_y are the reciprocal lattice vectors in the x and y directions, respectively. For the case of a square array, $G_x = G_y = 2\pi/L$. After propagating along the metal, the established SPPs are subsequently re-emitted into free-space light upon arrival at another diffraction point. The spatial periodicity of the array results in a periodicity existing for the wave vector of the SPP modes, which allows for Bloch wave and Brillouin zone analogies to be drawn. The folding of the Bloch wave vector at the Brillouin zone boundary results in resonant frequencies at the Γ point that are a function of the lattice constant. Ultimately, for normal incidence, the transmission peak resonances are approximated by the following relationship, confirming the strong dependence on the lattice constant [60]:

$$\lambda_{\text{peak}} = \frac{L}{\sqrt{(m^2 + n^2)}} \sqrt{\epsilon_D}. \quad (21.7)$$

Dispersion curves for SPPs on a 2D hole array display transmitted resonant frequencies as a function of incident angle. The (m, n) nomenclature corresponds to integer steps taken along the reciprocal lattice, and serve as a label for the resonances. Taking such steps in reciprocal space ultimately maps out diffraction spots, allowing an equivalence to be drawn for the observed resonances: the wavelengths responsible for a particular transmission resonance correspond to missing diffraction spots, due to the wave being “trapped” along the surface [68]. The 2D nature of the periodicity results in momentum gained from the y component being projected onto the x diagram. A typical dispersion curve for a 2D metal hole array for the $\Gamma - x$ orientation can be seen in Fig. 21.7.

The black curves in Fig. 21.7 are similar to those for a periodic array of sub-wavelength slits and display p -polarised characteristics only. The light grey curves correspond to the momentum gained from y periodicity, which is projected onto the orientation. These curves display a mixture of p and s polarisation characteristics, highlighted by their flatter appearance and lack of splitting with increasing angle. At 0° incidence angle, multiple resonance peaks are observed highlighting how transmission can be enhanced over a wide frequency range, even for perpendicular illumination. All the higher order modes lie to the left of the light line; such

Fig. 21.7 Typical dispersion curve for a 2D metal hole array for orientation. *Black curves* correspond to momentum contributions from x periodicity, whilst *light grey curves* display y projected momentum. The *dark grey dotted line* corresponds to the standard surface plasmon dispersion curve. After [69]



modes can be excited without the need for prism coupling, i.e. they can be excited using free-space light.

Two-dimensional gratings are an extremely elegant tool for both the study and exploitation of SPPs; not only does the physical structure of the array generate SPPs without need for a further coupling mechanism, but the “dilution” of the metal with dielectric filled holes acts to increase the confinement of the SPPs to the metal surface. The following section will review experiments undertaken on 2D hole arrays at THz frequencies, summarising the current proposed theories for EOT and the other associated anomalies.

21.2.5.2 Phenomenology and Theory

The first demonstration of enhanced THz transmission through a 2D subwavelength hole array was undertaken by Gómez Rivas [11]. Using a doped silicon substrate (doped so that the plasma frequency was in the THz region), hole arrays were created using perpendicular cuts of a wafer saw on both sides of the silicon wafer. Strong resonant peaks were observed not only at the cut-off frequency for the holes, but more unexpectedly, also at much lower frequencies. The position of the resonant peaks was correlated to the period of the array, whilst thinner substrates were shown to improve dramatically overall transmission.

The work of Qu et al. was the first to display THz EOT through a metallic subwavelength hole array at THz frequencies [70], a regime in which metals should classically be unable to support SPP modes due to their PEC properties. Lithographically patterned aluminium hole arrays on high resistivity silicon substrates displayed SPP resonances for both the metal–silicon and metal–air interfaces, with rectangular holes showing increased transmission and phase shift over circular counterparts. Much sharper resonances were observed for the case of free-standing metal

foil hole arrays [71], owing to the increased coupling between SPPs on the front and back of the array, as previously observed in the optical regime [61]. Resonances continued to 100 ps (in the time domain), displaying a long SPP lifetime and ultimately a long propagation distance. This work was also the first to test different metals for the same array and hole dimensions by sputtering optically thick silver on the original aluminium foil. Resonances were found to appear at the same frequencies for each metal; but a change in the magnitude of the transmitted resonance was observed. This has been confirmed in further work, where even poor conductors such as lead were found to support SPPs, with the transmitted intensity dominated by the ratio of the real to imaginary parts of the metal dielectric constant [72]. Interestingly, SPP resonances have also been found to exist on metals whose thickness is less than the skin depth, with the strength of the resonance increasing with increasing thickness [73]. THz transmission through superconducting plasmonic hole arrays has also been reported [74].

Much work has been undertaken to optimise conditions for SPPs in 2D hole arrays at THz frequencies. Janke et al. were the first to analyse the effect of varying hole shape, where square holes of varying sizes were made in a doped silicon array [75]. Increased transmission was observed for holes of increasing size; however the resonances became broader, indicating a decreased surface lifetime for the SPPs with increasing hole width. The resonances observed in this experiment differed from the predictions calculated using Eq. 21.7 due to the presence of channelled grooves on the substrate (as a consequence of the fabrication process). The presence of these grooves will dramatically alter the coupling and decoupling of SPPs and subsequent transmission through the holes. The importance of hole orientation has also been demonstrated [76] using elliptical hole arrays in ultra-thin, doped silicon wafers. When the long axis of the ellipses were aligned perpendicular to the polarisation of the E -field, vast transmission was observed for frequencies well below that of the cut-off. Rotating the sample through 90° shifted the position of the resonance to higher frequencies, and drastically reducing the transmission. The strong transmission for the initial orientation was attributed to the greater preservation of beam polarisation over the second direction, as confirmed in [70].

Further detailed studies investigating how the hole shape affects the transmission have been carried out using free-standing metal foils [71]. Greater transmission was found to occur for non-symmetric holes compared with the symmetric case. This work also displayed that as the aspect ratio of a rectangular hole (aligned with the long axis perpendicular to the polarisation of the E -field) was increased, the relative transmission decreased. Furthermore, results found in the optical regime, where a decreasing aperture width redshifts the resonant frequency [77, 78], were not replicated here; the frequency remaining almost constant. Importantly, this work was the first to recognise the onset of the SPP resonance occurring after that of the direct (non-resonant) transmission. Such an analysis is only possible using TDS techniques, where a single bipolar pulse irradiates the sample. The time-domain analysis of this resonance also serves as a measure of the lifetime (and ultimately propagation distance) of the SPPs on the surface of the metal via either an exponential

fit to the decaying oscillation in the time domain, or the width of the resonance in the frequency domain.

Further work has analysed the effect of hole diameter on the lifetime of the SPP [79, 80]. Miyamaru [81] was the first to provide fits to the lifetimes of SPPs showing a decrease in lifetime as the diameter of the hole was increased. Neglecting ohmic losses, this decrease in lifetime was attributed to the increased scattering cross-section with increasing hole diameter, i.e. SPPs were scattered more frequently, as there was less distance between the holes. It is interesting to point out that similar effects observed in the optical regime (where the time domain cannot be directly accessed) are explained in terms of localised surface plasmons or shape effects [58, 78, 82].

A further complication regarding the variation of hole size is the magnitude of the coupling which is believed to exist between the SPPs and the non-resonant transmission. A detailed study by Han [83] measured the transmittance of rectangular apertures with varying hole widths. This study confirmed the results of previous work [71] in that the normalised peak transmission decreases with increasing hole width; however the results were found also to differ in that a redshift in peak frequency was observed with decreasing hole width, in line with results observed in the optical regime [43, 77, 78]. Further analysis revealed that the peak transmission initially increases, and then subsequently decreases, with increasing hole width. This suggests the existence of an optimal width; these results were interpreted using a Fano analysis. Typically, a Fano analysis provides a method to describe the coupling between a resonant and a non-resonant process, as is perceived to be the case for 2D hole arrays. Han argues that with increasing hole width, the degree of coupling to SPPs increases, whilst both the cut-off frequency and metal-filling fraction decreases; the latter two cases enabling a greater degree of non-resonant (direct) transmission. Furthermore, Han calculates that the coupling constant between the two regimes is found to increase with increasing hole width. Han concludes the analysis by stating that, as the hole width is increased, the combination of the increased direct transmission, the increased excitation of SPPs and the increased coupling between these two states leads to damping of the SPPs, broadening their resonance and shifting their peak to higher frequencies. This onset of the negative impact of the direct transmission through increasingly broader holes offers an explanation to the “optimum” hole width.

There exists only one experiment in which the length of the hole is varied, whilst the hole width and 2D period remain constant [84]. With the long axis of the hole aligned perpendicularly to the polarisation of the E -field, as the length of the hole is increased a redshift of the resonant frequency is observed. The authors attribute this shift to changing resonance regimes; for short hole lengths standard SPP modes are thought to dominate, whilst localised SPPs govern the transmission for longer hole lengths. This classification was supported by analysing the same arrays with two differing beam diameters. The arrays with the longest holes, where localised SPPs are thought to dominate, displayed very little change in transmission between the two beam diameters. A much greater dependence was observed for the shorter holes, where a vast difference in transmission was observed due to the effective collecting area of the array being reduced with the smaller beam diameter.

Further confirmation of this theory was presented by observing the change in peak transmission frequency when paper was placed next to the array. The theoretical work of Bravo-Abad [85] suggests holes of larger dimensions have a greater proportion of the E -field within the holes, whilst smaller holes have a greater proportion residing on the metal surface. This suggests larger holes should be less sensitive to a change in the neighbouring dielectric for two reasons: first, any established SPP is less dependent on the surface of the metal as a smaller proportion resides there; whilst, second, if the observed resonance is truly a localised SPP and only depends on the specific geometry of a single hole, it should be almost independent of the metal surface. This was observed to be the case as the paper was introduced: the smaller holes demonstrated a clear redshift in frequency, whilst the larger holes exhibited no shift.

Miyamaru [86] investigated the finite size effect for the transmission of hole arrays finding that, with more than 20 holes, a good quality band pass filter is achieved; and that ten holes were enough to observe EOT. The work of Matsui [87] investigated the transmission properties of random and aperiodic arrays. Random arrays found only to produce broad resonances which redshifted to lower frequencies when hole diameters were increased, suggesting waveguide cut-off was the dominant transmission factor. This ruled out the existence of so called “shape resonances” thought to exist for individual apertures. Aperiodic arrays (with 5, 12, and 18° rotational symmetry) were found to produce strong, sharp resonant features with a characteristic “Fano” asymmetrical appearance. Finally, note Qu [88] who observed so-called “fractal” surface plasmons. An abundance of resonances in the frequency domain was attributed to the interference between SPPs propagating in all directions of the metal hole array. This work not only highlights the long propagation distances involved with SPPs at THz frequencies, but also the unrestricted propagation directions of these excitations.

In conclusion: even with the considerable research activity, summarised above, into the THz transmission properties of metal hole arrays, no single theory has been found allowing resonances to be either explained or predicted. THz-TDS provides an elegant method to study the lifetime and properties of SPPs, including how they are strongly affected by hole and lattice geometries. The Fano interaction goes some way to matching the asymmetry of the resonances yet offers no real explanation as to the mechanisms involved or of the nature of the coupling interaction. Any theory seeking to explain the EOT anomaly must be able to explain, amongst other factors: the observed blueshift and broadening of a resonance with increasing hole width parallel to the polarisation; the redshift and broadening observed as hole length perpendicular to the polarisation is increased; the change in frequency associated with a change in period; and the reason that random arrays of holes produce no resonance.

21.3 Applications

21.3.1 Guiding THz Waves with Plasmons

TDS systems, detailed elsewhere in this Volume, have been the “workhorse” for THz spectroscopy and imaging instrumentation for over a decade. Fibre-fed emitters and receivers have enabled the TDS systems to become more compact and flexible [89]. However, there still exists a requirement to eliminate the need for bulky parabolic mirror arrangements which are used to focus free space THz radiation onto a sample. Waveguides for SPPs provide a potential route to eliminate free-space THz optics in these systems. They enable THz radiation to be used to interrogate subwavelength samples for microscopy applications. In Sect. 21.2.4, we introduced the single wire waveguide; this has attracted much attention because of its design simplicity [90]. In its favour, the wire offers broadband guidance with low dispersion over long propagation distances [49]. However, it should be noted that, in practice, THz radiation is usually generated from dipole-based photoconductive emitters which produce a linearly polarised beam. The Sommerfeld wave on a wire is radially polarised; hence coupling from typical THz sources is inefficient [91]. Radially symmetric photoconductive antennas [51] have been developed which can overcome this problem. Alternatively, a diffraction/scattering type launch has been demonstrated on a patterned wire [92]. Grooves (500 μm wide, 100 μm deep with 1 mm period) circumferentially milled into a 1 mm stainless steel wire were shown to launch SPPs from an incident THz pulse. This approach enhances coupling from free-space THz radiation to the wire-guided SPPs; but leads to narrowing of the broadband pulse due to the inherent periodicity of the grooves.

Structuring of the wire itself is not essential, however, to achieve this result. Agrawal [93] showed that a bullseye arrangement could be used to couple SPPs onto a bare wire. Here, the wire was inserted into the centre of the aperture, so as to form a coaxial waveguide. The authors suggest that a TEM mode can be excited in this configuration, even with a linearly polarised source.

It should be noted that single wire-guided propagation has proved far less attractive in the microwave region, where a 10 mm diameter wire carries 75% of its transmitted power at 10 GHz in a circular area of 400 mm radius around the wire [94]. However, at 1 THz, with a 100 μm wire, this radius is less than 1 mm [95]. Dielectric coatings can be used to confine the field but lead to dispersion [96]. As discussed previously, spoof SPPs provide an alternative route to further confine this radius [54]. To date, this has not been experimentally demonstrated at THz frequencies.

The deep subwavelength electric field confinement achievable by tapering the end of a wire has been exploited by Awad [97] for near-field imaging. Awad achieved a feature size resolution of $\lambda/50$ at a 0.3 THz centre frequency when imaging metal tracks on a GaAs substrate. Walther [98] developed a THz-TDS system without far-infrared parabolic optics. In this work, a 110 mm long, 254 μm diameter platinum/iridium wire with a sharp tip was placed in contact with a photoconductive emitter. Lactose powder, dispersed along 55 mm of the wire, showed characteristic

absorption at 0.53 THz. Interestingly, the wire-guided approach was found to be less susceptible to water vapour in the atmosphere than is the case for free-space THz TDS, thus avoiding the need for nitrogen purging during scanning. This is an important practical step towards field-deployable systems, where nitrogen purging is undesirable.

An alternative to wire-guiding is to use planar plasmonic devices. It is interesting in this regard to note that Ulrich and Tacke [99] first suggested that periodic metal structures, based on simple wire meshes, may be valuable as THz waveguides. Devices commonly available at microwave frequencies such as straight waveguides, *Y*-splitters and 3dB-couplers have been fabricated for THz applications from arrays of periodically perforated metal films [100]. These operate in the spoof SPP regime and show tight confinement and low propagation loss.

21.3.2 Manipulation: Modulators and Switches

THz modulators and switches are essential components of THz circuits, for use in such diverse areas as on-chip sensing, broad-band communication [101] and imaging. For example, if fast THz modulators could be further developed, they could replace mechanical scanners and speed up imaging, as has been demonstrated recently [102] with a single-pixel THz imaging system that includes a spatial modulator as a crucial component. Another significant application will be the development of phased-array radar that incorporate phase modulators that can be used to direct THz beams. Plasmonic technologies have great promise in delivering modulators and switches that are fast, have good depth of modulation, require low power levels for implementation and can be satisfactorily operated at room temperature. Furthermore, plasmon-based modulators, which are realised using micromachining technology, can be produced on the same semiconductor chip as plasmon-interconnect (see previous section), which offers considerable design flexibility.

Manipulation devices of this type rely on external perturbations to change their THz optical transmission or reflection. Such perturbations might include: magnetic and electric fields, optical probes or temperature changes. In practice, electrically addressable modulators are likely to be of most practical use in the future development of THz systems. Recently, metamaterial devices, that incorporate repeated numbers of elements such as split-ring resonators on a subwavelength scale, have been reported [103–106]. Since metamaterial devices are beyond the scope of this chapter, their performance will not be reviewed here, although it should be noted that SPP effects are essential to their operation.

Pan [107] demonstrated the use of a magnetically controlled nematic liquid crystal (NMC) to vary the transmission properties of a 2D metallic hole array. The NMC occupies the holes in the array and, as the refractive index is changed, so does the effective permeability of the device leading, in turn, to a shift in the SPP absorption frequency and transmission. Although this is far too slow to be utilised practically, it is noteworthy that the idea of changing the refractive index of a material placed in

the orifices of the array has been deployed to create an optically addressable device operating on the ps timescale [108]. As an alternative to modifying the refractive index of the liquid “filler” through its photophysical properties, Gómez Rivas [109] reported the use of an optical perturbation of the SPP characteristics through changes in the carrier density of a semiconductor (indium antimonide) slab interfaced to air. The authors claim modulation of the in-plane THz transmission is possible with ultra-low optical (532 nm) fluences and with a picosecond response time. In a more direct arrangement, Hendry [110] describes how the THz frequency transmission properties of a single slit through a silicon slab, decorated with surface corrugations on both faces, may be controlled optically so as to produce an enhancement of transmission with a very short response time.

Thermal perturbations of the electrical properties of a semiconductor, along the surface of which THz frequency SPPs are propagating, are likely to be far too slow to be of practical relevance. Nevertheless, it may be noted that an experimental investigation of this effect, for indium antimonide surfaces, is reported by Gómez Rivas [111] and a theoretical analysis is provided by Sanchez-Gil [112].

Nishimura [113] argued that metamaterials-based modulator devices may not have the necessary required performance characteristics as a result of conduction and radiation losses in conventional materials. These authors have proposed to harness 2D plasmon effects associated with the channel of a high electron mobility transistor (HEMT). This follows the work of Dyakonov and Shur [114], who noted that 2D plasmons could travel at a greater rate along the HEMT channel than is permitted for individual carriers. Nishimura et al. have modelled a gated HEMT structure operating as a THz transmission modulator and found that a 60% extinction ratio and very fast operation at frequencies of up to 10 THz is possible.

21.3.3 Engineering the THz Wavefront with Plasmonic Devices

Lezec [115] first pointed out the possibility that the directionality of light emerging from a small aperture might be controlled through the use of a bullseye structure surrounding the aperture. These authors argued that: as the light falling upon a small aperture surrounded by corrugations was coupled to SPPs at specific angles for a given wavelength; so the reverse process might occur for corrugations on the exit surface. Agrawal [42] demonstrated this effect for the first time at THz frequencies. Chen [116] designed tunable plasmonic lenses, based on indium antimonide microslits, but has not reported experimental validation. The emergence of the THz Quantum Cascade Laser (QCL) as a practical, compact THz frequency source, that might potentially operate at room temperature [117], has led to further significant activity in the development of plasmonic devices formed on the output facet of a QCL. Yu [118] argued that suitably designed plasmonic structures on QCL facets could achieve enhanced performance or new functionality in the near- and far-fields, an area that was termed “wavefront engineering.” Examples include lasers with: high collimation, polarisation control, super-focussing in the near- and far-fields, beam steering

from a single device and the formation of beams with specific angular momentum. Akalin [119] reviewed these claims for plasmonic beam shapers, comparing them with the performance of external silicon lenses and horn antennas which reduce the impedance mismatch at the laser facet. Recently, Yu [120] reported the first real implementation of the concept of wavefront engineering. With a simple 1D grating design, the beam divergence reduced from approximately 180° to 10° which resulted in significant increases in power collection efficiency in comparison with unpatterned devices. The structure was incorporated onto the substrate below the laser aperture, without compromising the high temperature performance of the device. In the case of this particular structure, Yu argues that THz radiation from the aperture is coupled into spoof SPPs, instead of being directly radiated into the far-field.

21.3.4 Sensing

Almost all of the THz plasmonic sensing applications reported to date harness the dependence of the SPP resonant frequency on the properties of the interfacing dielectric. Two-dimensional hole arrays provide an easy method to exploit such properties, where SPPs are readily excited and confined to distances within the order of a wavelength. The first example of this in the THz regime was reported in 2005 by Tanaka [121]. Here, thin polypropylene films of varying thickness were attached to a 2D aluminium hole array. As the thickness of the dielectric film was increased, the resonant frequency of the SPPs was found to redshift, whilst the power transmittance was found to rapidly decrease. If a dielectric film were placed on both sides of the array, power transmittance was found to decrease less severely due to efficient coupling of SPPs on either side of the array. Such effects were even observed for film thicknesses much thinner than the wavelength of radiation used.

The sensitivity of SPPs to very thin (extreme subwavelength) layers of dielectric was demonstrated by Miyamaru [80], where a clear shift in resonant frequency was observed between printed paper and clear paper. This work also reported the effects of increasing the amount of glycerine absorbed on a nylon membrane attached to the hole array. Redshifts could be observed for quantities as small as 800 pL, with an accuracy of ± 0.2 THz quoted for the peak frequency. Miyamaru argues that the long “lifetime” of the SPPs enhances the absorption process of the THz radiation in the sample under investigation. Yoshida [122] was the first to demonstrate biological sensing, detecting femtomol quantities of horseradish peroxidase on a 2D hole array. This work highlights that the observed shift in resonance frequency is of paramount importance in detecting small amounts of proteins; it also demonstrates the increased sensitivity of the plasmonic method over conventional THz-TDS techniques.

Further work has been undertaken to investigate the effects of a dielectric layer of an asymmetric metal–dielectric interface. In this study, increasing thicknesses of photoresist were spin-coated onto a lithographically defined aluminium hole array on silicon [123]. Miyamaru [124] investigated the reflection properties of hole arrays when changing the neighbouring dielectric. Dramatic redshifts and transmission

enhancements were observed and ascribed to the increased field confinement around the apertures as a result of the presence of the dielectric layer. Yoshida [125] using free-standing arrays exploited the existence of a sharp dip observed in the standard resonance peak of the array. This feature made it easier to detect slight shifts in frequency, thus improving the sensitivity of the sensor. Finally, Tian [126] embedded 2D stainless steel hole arrays into a quartz sample cell. Different isotopes of liquid methanol were then introduced into the cell, where shifts in the SPP resonant frequency were observed as the sample was changed. The shifts in frequency allowed the isotopes to be distinguished more accurately than by standard THz-TDS. This work also highlighted how liquids can be used as the neighbouring dielectric, instead of the solid films used previously. Further theoretical work proposes SPP-like fibre based sensors for the detection of gaseous samples [127], where sensor resolutions of the order of 10^{-4} Refractive Index Units (RIU) are predicted.

The use of SPPs in the infrared region of the spectrum has been exploited for decades to monitor binding interactions. THz radiation is extremely sensitive to low frequency intermolecular environments; so it might be argued that THz-SPPs could offer an even more sensitive technique for the analysis of biological binding interactions than currently possible using infrared methods.

21.3.5 Imaging

THz imaging often suffers from poor resolution owing to the long wavelengths of the radiation involved. It has been suggested that extreme confinement of radiation on corrugated wires using SPPs may improve spatial resolution in THz images [54, 90]. There are, however, many practical problems (e.g. coupling efficiencies) that may preclude realisation of this concept. Nevertheless, there are considerable opportunities to exploit plasmonic phenomena in near-field imaging using apertures, which is a well-established method for THz near-field microscopy [128]. The applicability of the technique is limited by the low transmission through a subwavelength aperture. However, by surrounding an aperture with periodic corrugations whose period matches the frequency of operation of THz source, a dramatic enhancement of the signal through the aperture can be achieved leading to greater transmission and improved spatial resolution. This has been demonstrated by Ishihara et al., where 100 μm apertures were surrounded by periodic corrugations, and illuminated with a THz-wave parametric oscillator [129]. Large transmission enhancements were observed at wavelengths commensurate with the period of the corrugations. Resolution tests of the apertures showed that 50 μm (i.e. $\lambda/4$) resolution was achieved. Transmission artefacts were observed when periodic corrugations were situated at either side of the apertures and attributed to the decoupling of SPPs on the far side of the hole. Planarized arrays were found to yield no such artefacts; however, they did display a field enhancement when the resolution test-piece was brought close to the aperture. Further work by Ishihara et al. used the same periodic structures but replaced the circular aperture with a bow-tie shape [130]. The greater field confinement associated with this shape led to an increased resolution of $\lambda/17$. Besides these

two examples, plasmonic apertures have not yet been exploited for near-field THz imaging elsewhere. The ability to greatly enhance transmission and control output beam shape [120] whilst still beating the diffraction limit, may provide a strong impetus to THz near-field imaging.

A further demonstration of plasmon-assisted THz imaging has been reported using 2D hole arrays [131]. By fabricating hole arrays of different periodicities, imaging could be achieved at a range of frequencies by placing the arrays, in-turn, in contact with the desired object. Raster scanning of a focussed THz beam over the array allowed a plasmon-assisted image to be acquired. It was found the presence of the hole array allowed for the detection of a soluble ink pattern on paper, which could not be detected without the array. Such increased sensitivity was further displayed by imaging a fingerprint on a polypropylene film. The final example of plasmon-assisted THz imaging takes a completely different approach and requires no actual device to be fabricated. Maraghechi [132] shows that, by embedding a dielectric object inside a random array of subwavelength metallic particles, the successful coupling, re-radiation and near-field propagation of plasmons allow the object to be spatially resolved. The subwavelength size of the metallic particles results in the “metal” possessing a positive real permittivity, effectively becoming a dielectric at THz frequencies. The embedded object thus behaves as one dielectric embedded within an outer dielectric. This means that the whole experiment resembles traditional non-destructive THz imaging of dielectric objects. Reconstruction algorithms allow the raw data to be enhanced, providing a ninefold increase in spatial resolution. This approach could be valuable for biological imaging and sensing at THz frequencies: if subwavelength gold particles could be dispersed on, or in, a biological sample (thereby providing an SPP resonance of a known frequency) superior sensitivity would be achieved.

The few examples which do exist in the literature of plasmon assisted imaging at THz frequencies demonstrate the distinct advantages over standard imaging techniques. These include: increased field confinement at the tip of a wire; enhanced transmission through very small aperture sizes; and superior volume sensitivity via the use of a 2D hole array.

21.4 Conclusion

In this chapter, we have reviewed the essential physics and some of the early applications of surface plasmons and plasmonic devices. Almost certainly other applications will soon emerge in such new fields as quantum entanglement [133] and slow light [134] in addition to further developments in all of the areas considered above. The realisation of such essential active components as cheaper broadband THz systems [135] and THz QCLs that operate at, or close to, room temperature will encourage the design and development of plasmonic structures with new functionality, leading to significant advances in THz communications, microscopy, communications, sensing and imaging. The fact that plasmonic devices can easily be made using standard clean room techniques will provide an additional impetus to this field.

References

1. E.C.L. Ru, P.G. Etchehoin, *Principles of Surface Enhanced Raman Spectroscopy and Related Plasmonic Effects* (Elsevier, Amsterdam, 2008)
2. M.F. Kimmitt, *Far Infrared Techniques* (Pion Ltd., London, 1970)
3. T. Dumelow, D.R. Tilley, *J. Opt. Soc. Am. A* **10**(4), 633–645 (1993)
4. E.D. Palik, J.K. Furdyna Rep, *Prog. Phys.* **33**(12), 1193 (1970)
5. D. Pines, *Elementary Excitations in Solids: Lectures on Protons, Electrons and Plasmons* (Perseus Press, Reading, MA, 1999)
6. J.B. Pendry, L. Martin-Moreno, F.J. Garcia-Vidal, *Science* **305**(5685), 847–848 (2004)
7. H. Raether, *Surface Plasmons on Smooth and Rough Surfaces and on Gratings* (Springer, Berlin, 1988)
8. S.A. Maier, *Plasmonics: Fundamentals and Applications* (Springer, New York, 2007)
9. F. Medina, F. Mesa, R. Marques, *IEEE T. Microw. Theory* **56**(12), 3108–3120 (2008)
10. T.W. Ebbesen, H.J. Lezec, H.F. Ghaemi, T. Thio, P.A. Wolff, *Nature* **391**(6668), 667–669 (1998)
11. J.G. Rivas, C. Schotsch, P. H. Bolivar, H. Kurz *Phys. Rev. B* **68**(20), 201306 (2003)
12. F.J. Garcia-Vidal, L. Martin-Moreno, T.W. Ebbesen, L. Kuipers *Rev. Mod. Phys.* **82**(1), 729–787 (2010)
13. F.J.G. de Abajo *Rev. Mod. Phys.* **79**(4), 1267–1290 (2007)
14. H.A. Bethe *Phys. Rev.* **182**(7–8), 163–182 (1944)
15. M.C. Hutley, V.M. Bird *Opt. Acta* **20**(10), 771–782 (1973)
16. Y.Y. Teng, E.A. Stern *Phys. Rev. Lett.* **19**(9), 511 (1967)
17. W. Withayachumnankul, D. Abbott, *IEEE Photon. J.* **1**(2), 99–118 (2009)
18. A.P. Hibbins, B.R. Evans, J. R. Sambles *Science* **308**(5722), 670–672 (2005)
19. A.P. Hibbins, M.J. Lockyear, J.R. Sambles, *Phys. Rev. B* **76**, 16 (2007)
20. G. Acuna, S.F. Heucke, F. Kuchler, H.T. Chen, A.J. Taylor, R. Kersting *Opt. Express* **16**(23), 18745–18751 (2008)
21. M. Navarro-Cia, M. Beruete, S. Agrafiotis, F. Falcone, M. Sorolla, S.A. Maier *Opt. Express* **17**(20), 18184–18195 (2009)
22. J.R. Sambles, G.W. Bradbery, F.Z. Yang *Contemp. Phys.* **32**(3), 173–183 (1991)
23. A. Sihvola, J.R. Qi, I. V. Lindell *IEEE Antennas Propag.* **52**(1), 124–136 (2010)
24. J. Zenneck *Ann. Phys.* **23**(10), 846–866 (1907)
25. M.A. Ordal, L.L. Long, R.J. Bell, S.E. Bell, R.R. Bell, R.W. Alexander, C.A. Ward *Appl. Opt.* **22**(7), 1099–1119 (1983)
26. J.G. Rivas, A. Berrier, *Asia Pac. Microwave Conf.* **1–5**, 1293–1296 (2009)
27. J. Homola *Anal. Bioanal. Chem.* **377**(3), 528–539 (2003)
28. H. Hirori, K. Yamashita, M. Nagai, K. Tanaka *Jpn. J. Appl. Phys.* **2**(43), L1287–L1289 (2004)
29. J.F. O’Hara, R.D. Averitt, A.J. Taylor *Opt. Express* **13**, 6117–6126 (2005)
30. E.V. Alieva, Y.E. Petrov, V.A. Yakovlev, E.R. Eliel, E.W.M. van der Ham, Q.H.F. Vreken, A.F.G. van der Meer, V. A. Sychugov. *JETP Lett.* **66**(9), 609–613 (1997)
31. J.G. Rivas, M. Kuttge, P.H. Bolivar, H. Kurz, J.A. Sanchez-Gil *Phys. Rev. Lett.* **93**(25), 256804 (2004)
32. T.H. Isaac, J.G. Rivas, J.R. Sambles, W.L. Barnes, E. Hendry *Phys. Rev. B* **77**(11), 113411 (2008)
33. I.P. Kaminow, W.L. Mammel, H.P. Weber *Appl. Opt.* **13**(2), 396–405 (1974)
34. J. Saxler, J.G. Rivas, C. Janke, H.P.M. Pellemans, P.H. Bolivar, H. Kurz *Phys. Rev. B* **69**(15), 155427 (2004)
35. T.H. Isaac, W.L. Barnes, E. Hendry *Appl. Phys. Lett.* **93**(24), 241115 (2008)
36. T.I. Jeon, D. Grischkowsky *Appl. Phys. Lett.* **85**(25), 6092–6094 (2004)
37. M.F. Gong, T.I. Jeon, D. Grischkowsky *Opt. Express* **17**(19), 17088–17101 (2009)
38. W.Q. Zhu, A. Nahata *Opt. Express* **15**(9), 5616–5624 (2007)

39. K.G. Lee, H.W. Kihm, J.E. Kihm, W.J. Choi, H. Kim, C. Ropers, D.J. Park, Y.C. Yoon, S.B. Choi, H. Woo, J. Kim, B. Lee, Q.H. Park, C. Lienau, D. S. Kim *Nature Photon.* **1**, 53–56 (2007)
40. H. Caglayan, I. Bulu, E. Ozbay *Opt. Express* **13**(5), 1666–1671 (2005)
41. A. Agrawal, H. Cao, A. Nahata. *New J. Phys.* **7**, 249 (2005)
42. A. Agrawal, H. Cao, A. Nahata *Opt. Express* **13**, 3535–3542 (2005)
43. H. Cao, A. Agrawal, A. Nahata *Opt. Express* **13**, 763–769 (2005)
44. A. Agrawal, A. Nahata, *Opt. Express* **14**, 1973–1981 (2006)
45. G. Goubau, *J. Appl. Phys.* **21**(11), 1119–1128 (1950)
46. C.R. Williams, S.R. Andrews, S.A. Maier, A.I. Fernandez-Dominguez, L. Martin-Moreno, F. J. Garcia-Vidal *Nature Photon.* **2**(3), 175–179 (2008)
47. A.P. Hibbins, E. Hendry, M.J. Lockyear, J.R. Sambles *Opt. Express* **16**(25), 20441–20447 (2008)
48. E. Sommerfeld, *Ann. Phys. Chem* **67**, 233–290 (1899)
49. K. L. Wang, D.M. Mittleman, *Nature* **432**(7015), 376–379 (2004)
50. Y.B. Ji, E.S. Lee, J.S. Jang, T.I. Jeon *Opt. Express* **16**(1), 271–278 (2008)
51. T.I. Jeon, J.Q. Zhang, D. Grischkowsky *Appl. Phys. Lett.* **86**(16), 031104 (2005)
52. V. Astley, H. Zhan, R. Mendis, D.M. Mittleman, in *Conference on Lasers and Electro-Optics and Quantum Electronics and Laser Science* (New York, USA, 2009), pp. 1720–1721
53. V. Astley, J. Scheiman, R. Mendis, D.M. Mittleman *Opt. Lett.* **35**(4), 553–555 (2010)
54. S.A. Maier, S.R. Andrews, L. Martin-Moreno, F.J. Garcia-Vidal *Phys. Rev. Lett.* **97**(17), 176805 (2006)
55. K.J. Chau, A.Y. Elezzabi *Phys. Rev. B* **72**(7), 075110 (2005)
56. W.L. Barnes, W.A. Murray, J. Dintinger, E. Devaux, T.W. Ebbesen *Phys. Rev. Lett.* **92**(10), 107401 (2004)
57. S.A. Darmany, A.V. Zayats, *Phys. Rev. B* **67**(3), 035424 (2003)
58. A. Degiron, T.W. Ebbesen, *J. Opt. A. - Pure Appl. Op.* **7**, S90–S96 (2005)
59. Z.Y. Fan, L. Zhan, X. Hu, Y.X. Xia *Opt. Commun.* **281**(21), 5467–5471 (2008)
60. H.F. Ghaemi, T. Thio, D.E. Grupp, T.W. Ebbesen, H.J. Lezec *Phys. Rev. B* **58**(11), 6779–6782 (1998)
61. A. Krishnan, T. Thio, T.J. Kima, H.J. Lezec, T.W. Ebbesen, P.A. Wolff, J. Pendry, L. Martin-Moreno, F.J. Garcia-Vidal *Opt. Commun.* **200**(1–6), 1–7 (2001)
62. L. Martin-Moreno, F.J. Garcia-Vidal, H.J. Lezec, K.M. Pellerin, T. Thio, J.B. Pendry, T.W. Ebbesen *Phys. Rev. Lett.* **86**(6), 1114–1117 (2001)
63. A. Mary, S.G. Rodrigo, L. Martin-Moreno, F.J. Garcia-Vidal *Phys. Rev. B* **76**(19), 159414 (2007)
64. Z.C. Ruan, M. Qiu *Phys. Rev. Lett.* **96**(23), 233901 (2006)
65. U. Schroter, D. Heitmann *Phys. Rev. B* **58**(23), 15419–15421 (1998)
66. M.M.J. Treacy *Phys. Rev. B* **66**(19), 195105 (2002)
67. J.M. Vigoureux *Opt. Commun.* **198**(4–6), 257–263 (2001)
68. S.M. Williams, J.V., *Coe Plasmonics* **1**, 87–93 (2006)
69. J.V. Coe, J.M. Heer, S. Teeters-Kennedy, H. Tian, K.R. Rodriguez *Annu. Rev. Phys. Chem.* **59**, 179–202 (2008)
70. D.X. Qu, D. Grischkowsky, W.L. Zhang *Opt. Lett.* **29**(8), 896–898 (2004)
71. H. Cao, A. Nahata *Opt. Express* **12**(16), 3664–3672 (2004)
72. A.K. Azad, Y.G. Zhao, W.L. Zhang, M.X. He *Opt. Lett.* **31**(17), 2637–2639 (2006)
73. A.K. Azad, W.L. Zhang *Opt. Lett.* **30**(21), 2945–2947 (2005)
74. Z. Tian, R. Singh, J.G. Han, J.Q. Gu, Q.R. Xing, J. Wu, W.L. Zhang *Opt. Lett.* **35**(21), 3586–3588 (2010)
75. C. Janke, J.G. Rivas, C. Schotsch, L. Beckmann, P.H. Bolivar, H. Kurz *Phys. Rev. B* **69**(20), 205314 (2004)
76. A.K. Azad, Y. Zhao, W. Zhang *Appl. Phys. Lett.* **86**(14), 141102 (2005)
77. A. Degiron, H.J. Lezec, N. Yamamoto, T.W. Ebbesen *Opt. Commun.* **239**(1–3), 61–66 (2004)

78. K.J.K. Koerkamp, S. Enoch, F.B. Segerink, N.F. van Hulst, L. Kuipers *Phys. Rev. Lett.* **92**(18), 183901 (2004)
79. T.H. Isaac, W.L. Barnes, E. Hendry *Phys. Rev. B* **80**(11), 115423 (2009)
80. F. Miyamaru, M. Tanaka, M. Hangyo *Phys. Rev. B* **74**(15), 153416 (2006)
81. F. Miyamaru, S. Hayashi, C. Otani, K. Kawase, Y. Ogawa, H. Yoshida, E. Kato *Opt. Lett.* **31**(8), 1118–1120 (2006)
82. K.L. van der Molen, K.J.K. Koerkamp, S. Enoch, F.B. Segerink, N.F. van Hulst, L. Kuipers *Phys. Rev. B* **72**(4), 045421 (2005)
83. J.G. Han, A.K. Azad, M.F. Gong, X.C. Lu, W.L. Zhang *Appl. Phys. Lett.* **91**(7), 071122 (2007)
84. F. Miyamaru, M.W. Takeda *Phys. Rev. B* **79**(15), 153405 (2009)
85. J. Bravo-Abad, L. Martin-Moreno, F.J. Garcia-Vidal, E. Hendry, J.G. Rivas, *Phys. Rev. B* **76**(24), 241102(R) (2007)
86. F. Miyamaru, M. Hangyo *Appl. Phys. Lett.* **84**(15), 2742–2744 (2004)
87. T. Matsui, A. Agrawal, A. Nahata, Z. V. Vardeny. *Nature* **446**(7135), 517–521 (2007)
88. D.X. Qu, D. Grischkowsky *Phys. Rev. Lett.* **93**(19), 196804 (2004)
89. <http://www.Teraview.Com/terahertz/id/74>, Teraview, Accessed 22 December 2010
90. V. Astley, R. Mendis, D.M. Mittleman *Appl. Phys. Lett.* **95**(3), 031104 (2009)
91. J.A. Deibel, K. Wang, M. Escarra, N. Berndsen, D.M. Mittleman, *C.R. Acad., Sci. II B* **9**(2), 215–231 (2008)
92. H. Cao, A. Nahata *Opt. Express* **13**(18), 7028–7034 (2005)
93. A. Agrawal, A. Nahata *Opt. Express* **15**(14), 9022–9028 (2007)
94. M. J. King, J. C. Wiltse, *IEEE T. Antenn. Propag.* **10**(3), 246–254 (1962)
95. M. Wachter, M. Nagel, H. Kurz *Opt. Express* **13**, 10815–10822 (2005)
96. N.C.J. van der Valk, P.C.M. Planken *Appl. Phys. Lett.* **87**(7), 071106 (2005)
97. M. Awad, M. Nagel, H. Kurz *Appl. Phys. Lett.* **94**(5), 051107 (2009)
98. M. Walther, M.R. Freeman, F.A. Hegmann *Appl. Phys. Lett.* **87**(26), 261107 (2005)
99. R. Ulrich, M. Tacke *Appl. Phys. Lett.* **22**(5), 251–253 (1973)
100. W.Q. Zhu, A. Agrawal, A. Nahata *Opt. Express* **16**(9), 6216–6226 (2008)
101. T. Kleine-Ostmann, K. Pierz, G. Hein, P. Dawson, M. Koch *Elec. Lett.* **40**(2), 124–126 (2004)
102. W.L. Chan, K. Charan, D. Takhar, K.F. Kelly, R.G. Baraniuk, D.M. Mittleman *Appl. Phys. Lett.* **93**(12), 121105 (2008)
103. W.L. Chan, H.T. Chen, A.J. Taylor, I. Brener, M.J. Cich, D.M. Mittleman *Appl. Phys. Lett.* **94**(21), 213511 (2009)
104. H.T. Chen, S. Palit, T. Tyler, C.M. Bingham, J.M.O. Zide, J.F. O’Hara, D.R. Smith, A.C. Gossard, R.D. Averitt, W.J. Padilla, N.M. Jokerst, A.J. Taylor *Appl. Phys. Lett.* **93**(9), 091117 (2008)
105. M. Jarrahi, *IEEE Phot. Soc. Winter Topicals Meeting Series* **57**, 56–57 (2010)
106. S. Zarei, M. Jarrahi, *IEEE Phot. Soc. Winter Topicals Meeting Series* 30–31 (2010)
107. C.L. Pan, C.F. Hsieh, R.P. Pan, M. Tanaka, F. Miyamaru, M. Tani, M. Hangyo *Opt. Express* **13**(11), 3921–3930 (2005)
108. J. Dintinger, I. Robel, P.V. Kamat, C. Genet, T.W. Ebbesen *Adv. Mater.* **18**(13), 1645–1648 (2006)
109. J.G. Rivas, J.A. Sanchez-Gil, M. Kuttge, P.H. Bolivar, H. Kurz *Phys. Rev. B* **74**, 245324 (2006)
110. E. Hendry, F.J. Garcia-Vidal, L. Martin-Moreno, J.G. Rivas, M. Bonn, A.P. Hibbins, M.J. Lockyear *Phys. Rev. Lett.* **100**(12), 123901 (2008)
111. J.G. Rivas, M. Kuttge, H. Kurz, P.H. Bolivar, J.A. Sanchez-Gil *Appl. Phys. Lett.* **88**(8), 082106 (2006)
112. J.A. Sanchez-Gil, J.G. Rivas *Phys. Rev. B* **73**, 205410 (2006)
113. T. Nishimura, N. Magome, T. Otsuji *Jpn. J. Appl. Phys.* **49**(5), 054301 (2010)
114. M. Dyakonov, M. Shur *Phys. Rev. Lett.* **71**(15), 2465–2468 (1993)
115. H.J. Lezec, A. Degiron, E. Devaux, R.A. Linke, L. Martin-Moreno, F.J. Garcia-Vidal, T. W. Ebbesen. *Science* **297**(5582), 820–822 (2002)

116. M.K. Chen, Y.C. Chang, C.E. Yang, Y.H. Guo, J. Mazurowski, S. Yin, P. Ruffin, C. Brantley, E. Edwards, C. Luo *Opt. Techn. Lett.* **52**(4), 979–981 (2010)
117. G. Scalari, C. Walther, M. Fischer, R. Terazzi, H. Beere, D. Ritchie, J. Faist *Laser & Photon. Rev.* **3**(1–2), 45–66 (2009)
118. N.F. Yu, R. Blanchard, J.A. Fan, Q.J. Wang, M. Kats, F. Capasso, INEC: 2010 3rd Int. Nanoelectronics Conf. **1–2**, 70–71 (2010)
119. T. Akalin, W. Mauneult, P. Gellie, E. Peytavit, A. Andronico, P. Filloux, G. Leo, J.F. Lampin, C. Sirtori, H.E. Beere, D.A. Ritchie, S. Barbieri, APMC: 2009 Asia Pac. Microwave Conf. **1–5**, 183–185 (2009)
120. N.F. Yu, Q.J. Wang, M.A. Kats, J.A. Fan, S.P. Khanna, L.H. Li, A.G. Davies, E.H. Linfield, F. Capasso *Nature Mater.* **9**(9), 730–735 (2010)
121. M. Tanaka, F. Miyamaru, M. Hangyo, T. Tanaka, M. Akazawa, E. Sano *Opt. Lett.* **30**(10), 1210–1212 (2005)
122. H. Yoshida, Y. Ogawa, Y. Kawai, S. Hayashi, A. Hayashi, C. Otani, E. Kato, F. Miyamaru, K. Kawase *Appl. Phys. Lett.* **91**(25), 253901 (2007)
123. J.G. Han, X.C. Lu, W.L. Zhang, *J. Appl. Phys.* **103**(3), 033108 (2008)
124. F. Miyamaru, Y. Sasagawa, M.W. Takeda *Appl. Phys. Lett.* **96**(2), 021106 (2010)
125. S. Yoshida, K. Suizu, E. Kato, Y. Nakagomi, Y. Ogawa, K. Kawase, *J. Mol. Spectrosc.* **256**(1), 146–151 (2009)
126. Z. Tian, J.G. Han, X.C. Lu, J.Q. Gu, Q.R. Xing, W.L. Zhang *Chem. Phys. Lett.* **475**(1–3), 132–134 (2009)
127. A. Hassani, M. Skorobogatiy *Opt. Express* **16**(25), 20206–20214 (2008)
128. R. Degl’Innocenti, M. Montinaro, J. Xu, V. Piazza, P. Pingue, A. Tredicucci, F. Beltram, H.E. Beere, D.A. Ritchie *Opt. Express* **17**(26), 23785–23792 (2009)
129. K. Ishihara, T. Ikari, H. Minamide, J. Shikata, K. Ohashi, H. Yokoyama, H. Ito *Jpn. J. Appl. Phys.* **2**(44), L929–L931 (2005)
130. K. Ishihara, K. Ohashi, T. Ikari, H. Minamide, H. Yokoyama, J. Shikata, H. Ito *Appl. Phys. Lett.* **89**(20), 201120 (2006)
131. F. Miyamaru, M.W. Takeda, T. Suzuki, C. Otani *Opt. Express* **15**, 14804–14809 (2007)
132. P. Maraghechi, C. Straatsma, Z. Liu, V. Zhao, A.Y. Elezzabi *Opt. Express* **17**(19), 16456–16464 (2009)
133. E. Altewischer, M.P. van Exter, J. P. Woerdman *Nature* **418**(6895), 304–306 (2002)
134. Q. Gan, Z. Fu, Y.J. Ding, F.J. Bartoli *Phys. Rev. Lett.* **100**(25), 256803 (2008)
135. C.C. Renaud, M. Pantouvaki, S. Gregoire, I. Lealman, P. Cannard, S. Cole, R. Moore, R. Gwilliam, A.J. Seeds, *IEEE J. Quantum Elect.* **43**(11–12), 998–1005 (2007)

Chapter 22

Metamaterials

Petr Kužel and Hynek Němec

Abstract We provide an overview of the THz research in metallic and dielectric metamaterials. We introduce the appropriate length scales and averaging procedures to define effective metamaterial properties. A broader discussion of elaboration technologies and experimental determination of metamaterial properties is provided. Finally, we focus on applications aiming to achieve negative refractive index and active control of THz light.

22.1 Introduction and a Few Historical Remarks

Electromagnetic metamaterials are man-made structures which can exhibit specific on-demand electric and/or magnetic response not found in natural materials. These structures are usually periodic with the period and the motive much smaller than the wavelengths of the targeted spectral range, typically $< \lambda/10$. This condition being fulfilled, the response of metamaterials is essentially due to individual resonances of structured patterns within the unit cell which can be described by effective (averaged) material parameters: usually by the effective dielectric permittivity ε and magnetic permeability μ .

Historically, the first targeted applications concerned the phenomena related to the negative refractive index which requires simultaneously negative ε and μ . Some of these phenomena had been first predicted by Veselago [1]. Nevertheless, the general interest of the scientific community in metamaterials, which has arisen much later, is mainly due to the pioneering work of Pendry who introduced the metamaterial concept by showing the way to decrease the plasma frequency of metals down to microwave and terahertz range [2, 3] and how to achieve the negative effective permeability at microwaves [4]. He also proposed and theoretically demonstrated

P. Kužel (✉) · H. Němec

Institute of Physics, Academy of Sciences of the Czech Republic, Prague, Czech Republic
e-mail: kuzelp@fzu.cz

the principle of a superlens, a slab with negative refraction allowing one to achieve a subwavelength spatial resolution [5]. The word “metamaterial” first appeared in the paper by Smith et al. in 2000 [6], where the first structured material with simultaneously negative permeability and permittivity was demonstrated at microwave frequencies. The first real breakthrough in the terahertz metamaterial science came about 4 years later: in 2004, Yen et al. [7] demonstrated a planar structure exhibiting a range of negative effective magnetic permeability. Later, an equally important paper on THz metamaterials was published by Chen et al. [8]. Here, the authors show that, besides the negative refraction, there are other perspectives for metamaterial applications in the THz technology; namely, external control of the metamaterial resonances (their spectral tuning or switching on/off) promises great potential for the manipulation of the terahertz light.

During the past several years a number of books have been published focusing on the properties and design of metamaterials [9–11] that the interested reader may consult. In this chapter, after an introduction discussing different regimes of the electromagnetic response of structured matter, we provide merely the main advances in metamaterial science developed in the THz spectral region during the past few years. We also attract the reader’s attention to a recently published review on the manipulation of terahertz radiation using metamaterials [12].

22.2 Length Scales: Averaging of Electric and Magnetic Quantities

22.2.1 Atomic Scale

Microscopically, the classical electromagnetic theory describes the electromagnetic field and its interaction with matter which consists of an ensemble of charged particles. The field which enters into play is local and may vary by many orders of magnitude on a nanoscopic scale (namely in the vicinity of charges). The coupling between charges and the field is described by Maxwell–Lorentz equations for the local electric field \mathbf{e} and magnetic induction \mathbf{b} :

$$\begin{aligned}\nabla \cdot \mathbf{e} &= \frac{\rho}{\varepsilon_0} \\ \nabla \cdot \mathbf{b} &= 0 \\ \nabla \times \mathbf{e} + \frac{\partial \mathbf{b}}{\partial t} &= 0 \\ \frac{1}{\mu_0} \nabla \times \mathbf{b} - \varepsilon_0 \frac{\partial \mathbf{e}}{\partial t} &= \mathbf{j}\end{aligned}\tag{22.1}$$

where \mathbf{j} and ρ denote the local current and density of charge, respectively. Employing classical mechanics picture of point charges, these quantities have a discrete nature expressed by Dirac δ -functions:

$$\begin{aligned}\rho(\mathbf{r}, t) &= \sum_{\alpha} q_{\alpha} \delta(\mathbf{r} - \mathbf{r}_{\alpha}(t)) \\ \mathbf{j}(\mathbf{r}, t) &= \sum_{\alpha} q_{\alpha} \mathbf{v}_{\alpha} \delta(\mathbf{r} - \mathbf{r}_{\alpha}(t)).\end{aligned}\quad (22.2)$$

The solution of the electromagnetic problem, i.e., of Eqs. (22.1) and (22.2) supplemented by the Lorentz force $\mathbf{f} = \rho\mathbf{e} + \mathbf{j} \times \mathbf{b}$, on a macroscopic scale would imply finding the positions (and their time evolution) of a huge number of charges. This is not feasible and also such detailed information is not needed for practical applications. It is then convenient to proceed to a space averaging of the local quantities on the atomic scale [13, 14]. The appropriate scale for this averaging is ~ 10 nm, which means that this concept is valid up to the frequencies of radiation in the vacuum UV spectral range ($\lambda \gg 10$ nm). The local response of the charges (current of free charges and dipolar polarization of the bound charges) can then be accounted for by complex and frequency-dependent material parameters ε (dielectric permittivity) and μ (magnetic permeability) which describe the macroscopic polarization \mathbf{P} and magnetization \mathbf{M} of the medium and connect the spatially averaged vector fields $\mathbf{E} = \langle \mathbf{e} \rangle$ and $\mathbf{B} = \langle \mathbf{b} \rangle$ to newly introduced vectors \mathbf{D} and \mathbf{H} :

$$\begin{aligned}\mathbf{D}(\omega) &= \varepsilon(\omega) \mathbf{E}(\omega) = \varepsilon_0 \mathbf{E} + \mathbf{P} \\ \mathbf{B}(\omega) &= \mu(\omega) \mathbf{H}(\omega) = \mu_0 (\mathbf{H} + \mathbf{M})\end{aligned}\quad (22.3)$$

which should satisfy the Maxwell equations for macroscopic fields:

$$\begin{aligned}\nabla \cdot \mathbf{D} &= 0 \\ \nabla \cdot \mathbf{B} &= 0 \\ \nabla \times \mathbf{E} + \frac{\partial \mathbf{B}}{\partial t} &= 0 \\ \nabla \times \mathbf{H} - \frac{\partial \mathbf{D}}{\partial t} &= 0\end{aligned}\quad (22.4)$$

The quantities \mathbf{e} and \mathbf{b} contain the near-field information, i.e., the behavior of local fields on the atomic scale, while the vectors \mathbf{E} , \mathbf{D} , \mathbf{H} , \mathbf{B} describe correctly the far field but we cannot use them to retrieve the near field.

Note that in this chapter we use the convention where the harmonic wave in the complex notation is described by the phase factor $\exp(+i\omega t)$ and the complex material response is then given by $\varepsilon = \varepsilon' - i\varepsilon''$, $\mu = \mu' - i\mu''$.

The dielectric polarization of media is connected to a dynamical separation of bound charges which define the electric dipole moments; the magnetic polarization in materials then arises from the orbital currents or from unpaired electron spins. The characteristic distances and sizes of the current loops are then on sub-nm scale which may impose some limits to the strength of the resonant interaction with the field. Namely, the resonant phenomena in magnetic systems tend to occur in the

microwave range which results in an absence (or at least weakness) of the natural magnetic material response at THz frequencies.

Patterning the materials brings another length scale into play. The macroscopic fields on the atomic scale may now regain a local character with respect to the length scale of the newly introduced inhomogeneity (artificial structure). Patterns within the unit cell of the metamaterial structure can be considered as artificial metamaterial atoms characterized by electric and magnetic dipolar moments which are now defined not only by the material used but also by the geometry, i.e., by the extent of the possible charge separation and by the area of the surface delimited by the current loops. The size of the unit cell is chosen to be substantially smaller than the targeted wavelength and, at the same time, much larger than the interatomic distances. On the one hand, at the length scale of the wavelength the meta-atoms constitute elementary electric and magnetic dipole moments which can be macroscopically described by effective permeability and permittivity obtained by an averaging procedure (analogous to that used at the atomic scale); on the other hand, the magnitudes of the dipoles may significantly exceed those observed on the atomic scale and the positions of the resonant frequencies can be tailored by the geometry and the length scale of the structure.


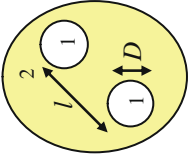
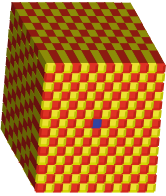
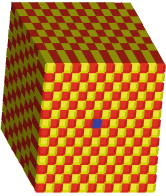
The important parameters are the dimensions of the unit cell and of the individual meta-atoms (denoted by l and D respectively, in the schemes in Table 22.1) or, more precisely, their ratios to the wavelength. We may distinguish three different regimes which are described below and summarized in Table 22.1; two of them are of concern for the physics discussed in this chapter.

22.2.2 Composites

By composites we mean here the structures which can be described within a static approximation which involves the standard effective medium theory (column 2 in Table 22.1). For example, if we consider a purely dielectric composite, then the electromagnetic field can be considered as almost homogeneous inside the dielectric inclusions. This is expressed by the conditions for the applicable radiation wavelengths $\lambda \gg \sqrt{\varepsilon_2}l$ and $\lambda \gg \sqrt{\varepsilon_1}D$ in Table 22.1. We do not expect any additional geometry-related resonances in this spectral range and the medium can be described by effective medium approximation (EMA). Within this approximation the effective permittivity of the composite is evaluated in terms of the dielectric functions of the components, of their shape, and of their volume fractions. No anomaly of the magnetic permeability is expected here ($\mu_{\text{eff}} \approx 1$) if we deal with intrinsically non-magnetic components. The two most widely used effective medium models are the Maxwell–Garnett model [15]:

$$\frac{\varepsilon_{\text{eff}} - \varepsilon_2}{\varepsilon_{\text{eff}} + \eta\varepsilon_2} = f \frac{\varepsilon_1 - \varepsilon_2}{\varepsilon_1 + \eta\varepsilon_2} \quad (22.5)$$

Table 22.1 Inhomogeneities on various length scales compared to the wavelength and their description. (EMA = effective medium approximation)

Category	Atomic scale ~ 10 nm	Composites	Metamaterials	Photonic crystals
Scheme				
Microscopic description	e, b	Dielectric or metallic inclusions: l, D, ϵ_i (or σ_i)	Extension of EMA (Mie scattering theory) other homogenization procedures	Periodic ϵ
Macroscopic description	Averaging: E, B, D, H	EMA (Maxwell–Garnett, Bruggeman...)	$\lambda \gg \sqrt{\epsilon_2}l, \sqrt{\epsilon_2}D$ $\lambda \gg \sqrt{\epsilon_1}D$	Band structure
Validity of macroscopic description	$\lambda \gg 10$ nm	$\epsilon_{\text{eff}}, \mu_{\text{eff}}$	$\epsilon_{\text{eff}}, \mu_{\text{eff}}$	$\lambda \approx \sqrt{\epsilon}l$
Effective parameters	ϵ, μ	Dielectrics: no geometrical resonance metals; plasmonic resonance	Each element is individually resonant no coupling between elements	—
Origin of resonant behavior	Polarization of bound charges orbital currents, spins			Resonances due to interferences coupling between periodically distributed elements
Reciprocal space (reciprocal parameter G)	—	$0 \approx \omega/c \ll G$	Below the first bandgap $\omega/c < G$	Band structure with bandgaps spatial dispersion of the photonic crystal

and the Bruggeman model [16]:

$$f \frac{\varepsilon_1 - \varepsilon_{\text{eff}}}{\varepsilon_1 + \eta \varepsilon_{\text{eff}}} + (1 - f) \frac{\varepsilon_2 - \varepsilon_{\text{eff}}}{\varepsilon_2 + \eta \varepsilon_{\text{eff}}} = 0 \quad (22.6)$$

where f is the volume filling fraction of the ε_1 material in the composite, η is the shape factor ($\eta = 2$ for spherical inclusions and $\eta = 1$ for cylinders with the axis perpendicular to the probing electric field). The Maxwell–Garnett theory does not consider the inclusion (ε_1) and the matrix (ε_2) in a symmetrical manner and, in fact, this model provides a reasonable estimation of the effective dielectric properties if the inclusions are not percolated and the filling factor f is smaller than about 0.3. The Bruggeman’s model takes into account the possible percolation of both components and therefore it is especially convenient for the description of the phenomena close to the percolation threshold.

As an example, bulk artificial composites for the THz range have been proposed made by deep reactive plasma etching of silicon [17, 18]; these structures can serve as more or less complex antireflective coatings [17, 19, 20] or as thick layers with on-demand refractive index (depending on the filling factor) or with high artificial birefringence [18]. An example of such a structure is shown in Fig. 22.1. Within the static approximation, it is possible to replace the structure by an equivalent electric circuit, which is shown in Fig. 22.1b. The capacitances C_x and C_y directly provide access to the effective permittivities ε_x and ε_y of the composite for the two possible polarizations of the probing electric field:

$$\begin{aligned} \varepsilon_x &= 1 + f_y \frac{f_x (\varepsilon - 1)}{\varepsilon (1 - f_x) + f_x} = n_x^2 \\ \varepsilon_y &= 1 + f_x \frac{f_y (\varepsilon - 1)}{\varepsilon (1 - f_y) + f_y} = n_y^2 \end{aligned} \quad (22.7)$$

where $\varepsilon = 11.68$ is the permittivity of silicon. The effective refractive index of the structure can be tuned between 1 and 3.4. In the case of etched silicon walls along the x -direction ($f_x = 1$) we get a highly anisotropic composite:

$$\begin{aligned} \varepsilon_x &= (1 - f_y) + f_y \varepsilon \\ \varepsilon_y &= \frac{1}{(1 - f_y) + \frac{f_y}{\varepsilon}} \end{aligned} \quad (22.8)$$

which corresponds to parallel capacitors for p -polarization (ε_x , E parallel to the walls) and to capacitors in series for s -polarization (ε_y , E perpendicular to the walls). The maximum birefringence is obtained for $f_x = 1$ and $f_y = 0.67$ and amounts as $n_x - n_y = 1.25$.

The effective medium approach can be also used for metal-dielectric composites with very small metallic particles where the conductivity (connected to the imaginary part of the permittivity) of inclusions dominates. The condition $\lambda \gg |\sqrt{\varepsilon_1}| D$ in a metal leads then essentially to the requirement that the metallic particle size is much

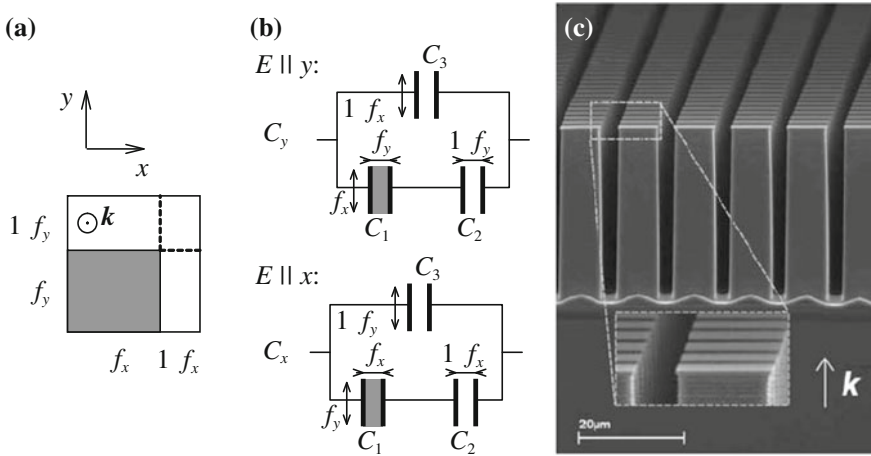


Fig. 22.1 **a** Schemes of a unit cell of an etched material with permittivity ϵ placed in air; the polarization of the electric field is indicated; **b** equivalent circuits for evaluating the effective response. **c** Example of etched structure: scanning electron microscope picture. After [18]

smaller than the electromagnetic skin depth. Then the details of the metal structure are too small to lead to shape-dependent resonances in the targeted spectral range (condition $\lambda \gg c\sqrt{L_{\text{int}}C_{\text{int}}}$ is satisfied, where L_{int} and C_{int} are internal inductance and capacitance of a meta-atom which are related to its shape and topology).

The response of subwavelength metallic particles is very specific and different from that of dielectric particles. This is related to the fact that the metallic conductivity inherently involves the plasmonic resonance which has a longitudinal character in a homogeneous medium (the frequency of the corresponding transverse resonance of charge carrier motion vanishes due to the lack of the restoring force). Inhomogeneities introduced in the medium then lead to the occurrence of a restoring force owing to the charge separation. In other words, the subwavelength metallic particles exhibit a high dipolar polarizability which depends on their size. The applied THz electric field then can induce charges at their edges which lead to a high effective dipole moment of the particles and a transverse plasmonic resonance may appear in the THz range in ϵ_{eff} [21]. Similar phenomena were also observed due to conduction-band charge carriers in photoexcited nano- or micron-sized semiconductor particles [22–24]. The plasmonic resonance is not critically dependent on the shape of meta-atoms and its existence is essentially due to the nature of metallic conductivity; for this reason it can be described by a standard EMA in analogy with the dielectrics. To illustrate the effective response of such a medium we use the Maxwell–Garnett model (22.5) considering the conductive particles, i.e.

$$\epsilon_1 = \epsilon_p - i \frac{\sigma_p}{\omega \epsilon_0}, \tag{22.9}$$

where ω is the angular frequency of the radiation, ε_p is a background permittivity of the particles, and σ_p is their conductivity due to free carriers; the σ_p term is dominant in metals and its magnitude can be tuned by the excitation fluence in the photoexcited semiconductors. We assume the Drude-like behavior of the conductivity:

$$\sigma_p = \frac{\sigma_0}{1 + i\omega\tau_c}, \quad \sigma_0 = \frac{N_c e^2}{m} \tau_c, \quad (22.10)$$

where τ_c is the momentum scattering time of the carriers, m is their mass, and N_c is their concentration. Introducing (22.9) into (22.5) we find:

$$\varepsilon_{\text{eff}} = \varepsilon - i \frac{\sigma}{\omega \varepsilon_0} = \varepsilon + \varepsilon_\sigma,$$

where ε is the background permittivity of the composite which does not depend on σ_p and σ is the effective conductivity due to the metallic contribution. We find [23]:

$$\sigma = \sigma_p \frac{\varepsilon_2 (1 + f \eta) - \varepsilon (1 - f)}{\varepsilon_2 (f + \eta) + \varepsilon_p (1 - f) - \frac{i\sigma_p}{\omega \varepsilon_0} (1 - f)} \equiv \frac{A}{B - \frac{i\sigma_p}{\omega \varepsilon_0} (1 - f)}. \quad (22.11)$$

Taking into account the Drude formula (22.10) we obtain a dielectric resonant response of the effective medium (damped harmonic oscillator formula):

$$\varepsilon_\sigma = \frac{\omega_p^2 A}{B} \frac{1}{\omega_p^2 (1 - f)/B - \omega^2 + i\omega/\tau_c}, \quad (22.12)$$

where the plasma frequency of the carriers in the metal is equal to $\omega_p = \sqrt{N_c e^2 / m \varepsilon_0}$. The dissipation is connected with the scattering of carriers (τ_c). The restoring force appears here due to the depolarization fields and the related separation of charges accumulated at the edges of particles; its value is related to the plasma frequency. The transverse resonant frequency:

$$\omega_0 = \frac{\omega_p}{\sqrt{\varepsilon_2 \frac{\eta+f}{1-f} + \varepsilon_p}} \quad (22.13)$$

can be tuned from 0 for $f = 1$ (homogeneous metal) up to the spectral range of ω_p for $f \rightarrow 0$.

The response of larger metallic particles may contain a magnetic contribution induced by eddy currents inside inclusions: in this case one observes a magnetic field outside the particle and the shape of the field corresponds to the magnetic dipole. It means that the effective magnetization of the composite medium can be nonzero even if the constituents are nonmagnetic. At low frequencies (the lowest order term of the power expansion in $\sqrt{\varepsilon_1} D/\lambda$) the permeability of the spherical metallic inclusion due to eddy currents will be [25]

$$\mu_1 \approx 1 + \frac{\varepsilon_1 \omega^2 D^2}{40 c^2}. \quad (22.14)$$

We can define an effective permeability of the medium in a manner analogous to Eqs.(22.5) or (22.6) for the permittivity within Maxwell–Garnet or Bruggeman approximation, respectively (with $\mu_2 = 1$). Nevertheless, even in this case the dominant effect in the THz spectral range comes from the effective permittivity and a large number of metallic inhomogeneous systems can be described without introducing the effective magnetic properties [26]. For example, for gold spherical inclusions ($\sigma_{\text{gold}} \approx 2.1 \times 10^5 \Omega^{-1} \text{cm}^{-1}$ [27]) with a diameter of 100 nm and a filling factor $f = 0.1$ we obtain $\mu_{\text{eff}} \approx 1 - 0.004i$ at 1 THz.

22.2.3 Metamaterials

In metamaterials the electromagnetic field is inhomogeneously distributed within the fine details of the unit cell structure. The incident radiation scatters on the pattern and gives rise to the resonances which are closely connected to this inhomogeneous distribution of the local field. In principle, each scattering element is individually resonant and no interaction (interference) between the neighboring unit cells needs to be considered in order to obtain the effective resonant behavior (in practice, weak coupling between neighboring elements always exists). We deal with dielectric or metallic inclusions (scatterers) forming a motive of the structure characterized by a high permittivity or conductivity, i.e., $|\varepsilon_1| \gg |\varepsilon_2|$. The size of the individual scatterers is much smaller than the wavelength of the probing radiation in vacuum (or in the surrounding medium ε_2). This enables a procedure of homogenization of the sample, i.e., attribution of effective permeability and permittivity to the metamaterial. These effective parameters must then be able to describe the electromagnetic properties of the metamaterial from the macroscopic point of view (transmission, reflection).

A direct theoretical extension of the previous paragraph on composites is the Mie theory for fields inside and outside the spherical particles (first developed by Mie [28]). The solution of the electromagnetic field distribution inside and outside inclusions upon plane wave incidence is obtained as a multipole expansion in terms of Mie scattering coefficients which can be expressed by using spherical Bessel functions [25] for spherical inclusions or by using cylindrical Bessel functions [29] for cylindrical inclusions. In the low-frequency part of the spectra the lowest order Mie coefficients are dominating and one can develop a quasi-static extension of the Maxwell–Garnett formula for this spectral range. One obtains for spherical inclusions [30]:

$$\begin{aligned} \varepsilon_{\text{eff}} &= \varepsilon_2 \frac{1 + 3iT_1^E/u_2^3}{1 - 3iT_1^E/(2u_2^3)} \\ \mu_{\text{eff}} &= \mu_2 \frac{1 + 3iT_1^H/u_2^3}{1 - 3iT_1^H/(2u_2^3)}, \end{aligned} \quad (22.15)$$

where (T_1^E) and (T_1^H) are electric and magnetic dipole components of the scattering T -matrix of a single sphere:

$$\begin{aligned} T_1^E(\omega) &= \frac{j(u_1)[u_2 j(u_2)]' \varepsilon_1 - j(u_2)[u_1 j(u_1)]' \varepsilon_2}{h(u_2)[u_1 j(u_1)]' \varepsilon_2 - j(u_1)[u_2 h(u_2)]' \varepsilon_1}, \\ T_1^H(\omega) &= \frac{j(u_1)[u_2 j(u_2)]' - j(u_2)[u_1 j(u_1)]'}{h(u_2)[u_1 j(u_1)]' - j(u_1)[u_2 h(u_2)]'}, \end{aligned} \quad (22.16)$$

for intrinsically non-magnetic materials. Here, j and h are the spherical Bessel and Hankel functions, respectively, with the index $l = 1$, and $[xj(x)]'$ is a derivative of the expression in the square brackets with respect to the argument x . The parameters u_1 and u_2 can be understood as reduced frequencies or reduced size-parameters:

$$\begin{aligned} u_1 &= \sqrt{\varepsilon_1} \omega D / (2c) \\ u_2 &= \sqrt{\varepsilon_2} \omega D / (2c) \end{aligned} \quad (22.17)$$

It follows that the effective medium parameters in the quasistatic limit defined by (22.15) become dispersive even for a metamaterial composed of non-dispersive components. Comparing to the conditions of validity for the Metamaterial category shown in Table 22.1 we find that $u_1/\pi \approx 1$, $u_2/\pi \ll 1$. This can be achieved for high permittivity inclusions [29, 31]. It means that even if the inclusion is much smaller than the wavelength ($u_2/\pi \ll 1$), the electromagnetic field can be resonant at some frequency with a natural mode of oscillation inside the inclusion ($u_1/\pi \approx 1$). Such a condition corresponds to a pole in the scattering T -matrix; it is called the lowest order Mie resonance and it can have a magnetic or electric origin. In an analogous manner, higher multipole terms of the scattering matrix, which are not provided explicitly in this work, are at the origin of higher order Mie resonances. The resonant behavior of such structures can lead to negative ε_{eff} , μ_{eff} [31, 32] or even to the negative refractive index n [30, 33].

The spatial distribution of the near-field can be used, as originally proposed by Pendry et al. [4], for evaluation of the effective properties of the medium. The tensors of effective permittivity and permeability of the metamaterial are defined as the ratios of suitably averaged electric and magnetic displacements and fields:

$$\begin{aligned} \varepsilon_{\text{eff}}^{ij} &= \frac{\langle D_i \rangle}{\langle E_j \rangle}, \\ \mu_{\text{eff}}^{ij} &= \frac{\langle B_i \rangle}{\langle H_j \rangle}. \end{aligned} \quad (22.18)$$

where the averaging procedures were inspired by the integral form of the Maxwell equations:

$$\begin{aligned} \oint_C \mathbf{E} \cdot d\mathbf{l} &= -\frac{\partial}{\partial t} \int_S \mathbf{B} \cdot d\mathbf{S} \\ \oint_C \mathbf{H} \cdot d\mathbf{l} &= \frac{\partial}{\partial t} \int_S \mathbf{D} \cdot d\mathbf{S} \end{aligned} \quad (22.19)$$

Here, the fields are integrated over closed loops while the displacements are integrated over surfaces delimited by these contours. Thus, the macroscopic electric and magnetic fields $\langle \mathbf{E} \rangle$ and $\langle \mathbf{H} \rangle$ need to be calculated as average values along a curve. Pendry et al. [4] have proposed to average local field values along Cartesian axes of the unit cell with dimensions $a \times b \times c$ (which is chosen such that the contour does not intersect the enclosed metamaterial pattern), e.g.

$$\langle H \rangle_x = \frac{1}{a} \int_{(0,0,0)}^{(a,0,0)} \mathbf{H} \cdot d\mathbf{r}. \quad (22.20)$$

In contrast, the components of the electric and magnetic displacements \mathbf{D} and \mathbf{B} are averaged over the faces of the unit cell:

$$\langle B \rangle_x = \frac{1}{b \times c} \int_{S_{yz}} \mathbf{B} \cdot d\mathbf{S}. \quad (22.21)$$

The inhomogeneous distribution of the electromagnetic field inside the unit cell practically does not influence the average value of the fields while it strongly affects the average value of the displacement vectors. In this sense, highly inhomogeneous distribution of the near-field, reflecting a strong interaction of the radiation with the metamaterial pattern (a weak interaction would not significantly change a quasi-homogeneous character of the incident plane wave within the unit cell) may lead to high values of ϵ_{eff} and/or μ_{eff} which, in turn, describe the resonant electromagnetic behavior of the structure. This averaging procedure has been originally developed for metallic scatterers like split rings [4], but it has been successfully used also in the case of dielectric resonators [31].

With metals it is possible to deposit on a substrate planar (or even layered) structures such that their geometrical shape maximizes the electric and/or magnetic response, i.e., the charge separation (electric dipole) and the current loop (magnetic dipole). The details of the shape of such metallic inclusions then define the resonance frequency and the resonant strength. The magnetic dipole moment is related to the currents flowing along metallic rings and it can be induced if the magnetic field of the incident radiation points through the ring. The negative effective permeability was first demonstrated with split-ring resonators (SRRs) [6] and most of the experimental works in the THz spectral range published till date deal with this metamaterial structure.

22.2.4 Comparison with Photonic Crystals

As already pointed out, with metamaterials the periodicity of the structural pattern is not a requirement; each scattering element is individually resonant and the interaction between the neighboring unit cells is weak. On the other hand, if the radiation wave-

length λ becomes comparable to (or even smaller than) the characteristic distances in the structure, interferences between scattered (partially reflected and diffracted) waves become an important issue: the category of photonic crystals shown in the last column of Table 22.1 has only sense if we consider periodic structures. The condition $\lambda \approx \sqrt{\varepsilon}l$ then ensures that constructive and destructive interference phenomena may occur in the relevant frequency range for some propagation and scattering directions. This leads to the formation of the photonic band structure. From the point of view of the dispersion curves in the reciprocal space, the spectral domain where the periodic photonic structure can be described as a metamaterial remains on the lowest dispersion branch below the first band gap; the condition $\lambda \gg l$ is equivalent to $\omega/c \ll G$ (where G is the reciprocal lattice parameter of the periodic photonic structure), i.e., we deal with the wave vectors well below the Brillouin zone boundary. As the characteristic dimensions of the structure increase above $\lambda/10$ (we get closer to the Brillouin zone boundary), the homogenization of the medium may progressively become possible only if we admit the spatial dispersion (dependence of ε_{eff} and μ_{eff} on the wave vector), which is a consequence of the non-locality of the response of the structure and which is in agreement with the band structure. In a periodic medium the field distribution can be described by a Bloch wave which is a linear combination of plane waves, e.g., for the electric field:

$$\mathbf{E}(\mathbf{r}, t) = \exp(i\omega_m t) \sum_{\mathbf{G}} \mathbf{e}_{\mathbf{K}, \mathbf{G}} \exp[-i(\mathbf{K} + \mathbf{G}) \cdot \mathbf{r}], \quad (22.22)$$

where \mathbf{K} is the wave vector, m is the index of the photonic band, and the sum runs over all reciprocal lattice vectors. In the metamaterial regime a single propagative mode exists with $\mathbf{G} = 0$ within the linear combination of the above expression; the other modes are evanescent and form the near-field distribution within the metamaterial pattern. In the photonic crystal regime several propagative modes may exist which correspond to diffraction orders.

The transition between the metamaterial and photonic crystal regime was studied in the THz range by several groups [34, 35]. The authors investigated the response of single split rings in the near-field [34] and the position of the resonant frequencies as a function of the metamaterial lattice period [34] and their mutual orientation [35]. The lowest order modes are only marginally influenced by these parameters, i.e., radiative coupling between them is weak and they can be described within the metamaterial regime. On the other hand, higher order modes experience a significant spectral shift and reshaping upon a change of the parameters proving the electromagnetic coupling between the meta-atoms: this regime approaches the photonic crystal regime. The coupling between the laterally adjacent metamaterial atoms in a planar structure then depends on their density, orientation, and unit cell design [36].

22.3 Numerical Calculations and Software

Optical properties of THz metamaterials are mostly calculated using commercially available electromagnetic field simulators, which permit straightforward numerical simulations of almost arbitrary complex structures with quite versatile boundary conditions. These programs typically employ some of the well-known methods [37] for a numerical solution of Maxwell's equations (22.4). For example, the Ansoft HFSS utilizes a finite-element method and optionally, the method of moments is also implemented [38]. The CST Microwave Studio solvers use either a finite-difference time-domain algorithm, or a finite integration technique [39]. Unfortunately, we did not find in the literature any comparison in terms of accuracy or calculation speed of these approaches applied to simulations of THz metamaterials. Other numerical methods are used only seldom and in rather specific cases. Among them, transfer matrix method is suitable for simulations of periodic metamaterials [31, 40–43]. Rigorous coupled-wave analysis can be employed for the investigation of planar gratings [44, 45].

22.4 Experimental Characterization

In the THz spectral range two experimental methods are mainly employed for a broadband characterization of metamaterials: Fourier-transform infrared spectroscopy (FTIR), and time-domain THz spectroscopy (TDTS). Both methods provide access to transmittance and reflectance spectra. FTIR is typically used for the measurement of the power (intensity) spectra, whereas TDTS enables simultaneous characterization of the amplitude and phase in the THz spectral range.

We will discuss various approaches reported in the literature, each of them providing a different amount of information about the electromagnetic response of metamaterials. The measured power or amplitude spectra can reveal the existence of resonances and their spectral positions and strengths, but they provide only little insight into their nature. An agreement between the measured and calculated power spectra of the investigated structure is frequently considered as a proof of the targeted metamaterials properties [46–48]. A somewhat extended view can be obtained by measuring spectra at different sample orientations, polarizations of the incident light, and angles of incidence; in this way it is possible to distinguish between electric and magnetic resonances [49, 50]. A detailed picture can be gained by a retrieval of effective optical properties from the measured spectra. The results are able to bring direct proofs of negative effective refractive index or, e.g., negative effective magnetic permeability [31, 50–52]. This advantage is paid by a high level of sophistication of the experimental methods required for unambiguous characterization of metamaterials exhibiting both effective dielectric and effective magnetic response in the same spectral range. Finally, an ultimate amount of information comparable to that available from numerical simulations can be obtained from the measurement

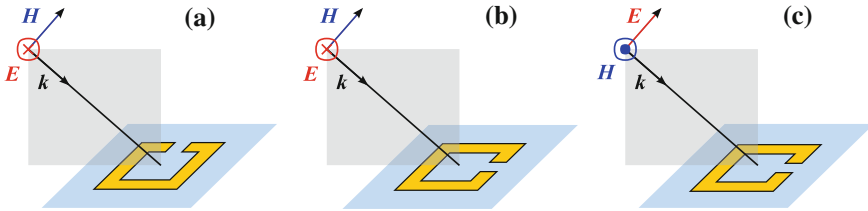


Fig. 22.2 Geometries employed for investigation of split-ring-based metamaterials; the gray surface indicates the incidence plane. **a** s -polarized incident beam with in-plane electric field of the mirror symmetry of the metamaterial excites the magnetic resonance solely by the magnetic field. **b** s -polarized light with out-of-plane electric field of the mirror symmetry of the metamaterial enables a coupling of the magnetic resonance to the incident electric field. **c** p -polarized light does not allow exciting the magnetic resonance

of distribution of electromagnetic fields within the metamaterial structure by using near-field THz imaging techniques [34, 53].

22.4.1 Electric and Magnetic Resonances

Most THz metamaterials targeted to exhibit a magnetic resonance are based on SRRs. Their magnetic response originates from circular currents induced in the split rings. The magnetic resonance can be excited magnetically, when the incident magnetic field has a component perpendicular to the plane of the SRR [4], Fig. 22.2a,b. In structures composed of just limited number of layers of split rings, this requires an oblique incidence of the probing radiation. Alternatively, the magnetic resonance can be excited electrically, when the structure does not show the mirror symmetry with respect to the incident electric field [49].

These simple arguments made it possible to assess the nature of the response for the first THz metamaterials based on SRRs. Yen et al investigated a THz metamaterial composed of double SRRs by FTIR spectroscopy [7]. The light irradiated the sample at 60° from the normal. In this configuration, only the s -polarized light may excite the magnetic resonance at ~ 1 THz whereas no magnetic response is expected for the p -polarized light. This behavior was confirmed by the measurement of the reflectance ratio $|r_s/r_p|^2$ (r_s and r_p are complex reflectances for the s - and p -polarized light, respectively) which shows a broad peak at the spectral position of the magnetic resonance of the metamaterial [7]. Driscoll et al. studied a structure composed of symmetrized pairs of SRRs where the coupling of the electric field to the magnetic resonance is suppressed [50], see inset of Fig. 22.3a. The increase of the angle of incidence of an s -polarized light from the normal to 45° then leads to a clear appearance of a resonance which can be reliably associated with a magnetic response (Fig. 22.3a).

The difference between electric and magnetic excitation of the magnetic resonance was experimentally studied by Gundogdu et al. in an array of single SRRs with a magnetic resonance predicted at ~ 6 THz [49]. The metamaterial was irradiated with an s -polarized light, the angle of incidence was varied, and two different orientations of the metamaterial were used. When the split rings possess the mirror symmetry with respect to the electric field vector, the electric field cannot couple to the magnetic resonance. The component of the magnetic field which couples to the magnetic resonance then increases with increasing angle of incidence; this results in the observed increase of the resonance strength (Fig. 22.3b). When the metamaterial is rotated by 90° , the electric field can couple to the magnetic dipole and a strong resonance almost independent of the angle of incidence appears in the optical spectra (Fig. 22.3c).

Most of the studied metamaterials possess a mirror-plane symmetry containing the direction of propagation. Their eigenstates are linearly polarized waves [54]. However, there have been also several efforts to manipulate the polarization state of the light by using chiral metamaterials. Characterization of such metamaterials then involves determination of the ellipticity and the azimuth of transmission or reflection eigenstates [55].

22.4.2 Retrieval of Effective Properties

A detailed insight into the properties of metamaterials can be gained through the determination of their effective optical properties such as effective refractive index and wave impedance or effective magnetic permeability and dielectric permittivity. These properties can be in principle obtained when both complex transmittance (t) and complex reflectance (r) spectra are measured. For normal incidence the transmittance and reflectance spectra read as [43, 56]:

$$\begin{aligned} t &= \frac{1}{\cos(\omega Nd/c) + \frac{i}{2}(Z + Z^{-1}) \sin(\omega Nd/c)} \\ r &= \frac{i}{2}(Z - Z^{-1}) \sin(\omega Nd/c) t \end{aligned} \quad (22.23)$$

where d is the sample thickness, ω is the angular frequency, c is the speed of light in vacuum, N is the complex (effective) refractive index, and Z is the complex relative (effective) wave impedance of the metamaterial. The complex permittivity and permeability are then related to N and Z :

$$\begin{aligned} \mu &= NZ \\ \varepsilon &= N/Z \end{aligned} \quad (22.24)$$

Note that the expressions in (22.23) are complex conjugates to the original ones reported in [43]; this is owing to our convention of the complex formalism.

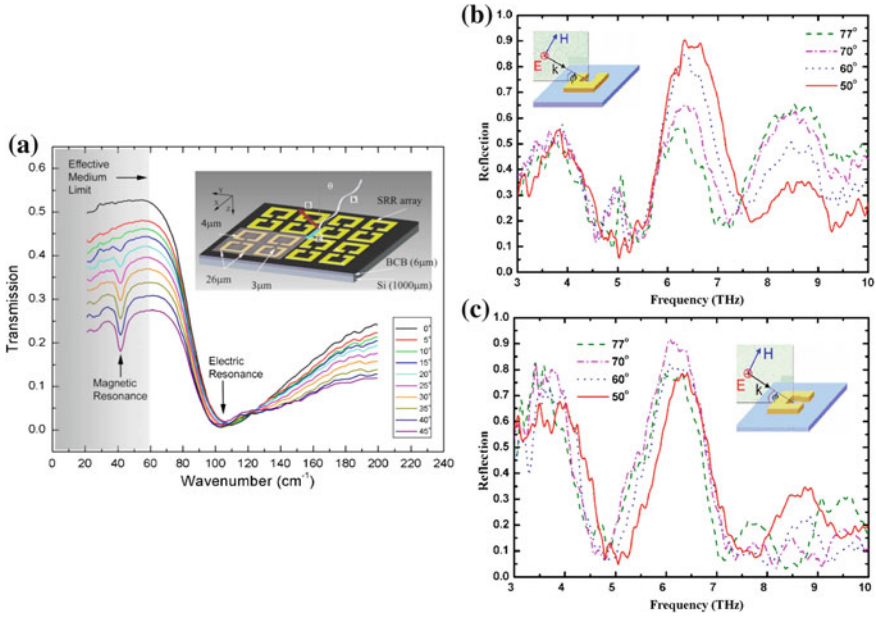


Fig. 22.3 **a** Transmittance spectra of a symmetrized array of single SRRs measured by an *s*-polarized light for various angles of incidence. A narrow magnetic resonance appears for nonzero angle of incidence when a magnetic field component perpendicular to the split-ring surface induces circular currents in the split rings. There is also a much stronger electric resonance almost independent of the angle of incidence. After [50]. **b, c.** Reflectance spectra measured by *s*-polarized light in an array of single SRRs. The spectra exhibit a magnetically **b** and electrically **c** excited magnetic resonance around 6 THz. After [49]

These equations can be straightforwardly inverted, yielding

$$\begin{aligned}
 Z &= \sqrt{\frac{(1+r)^2 - t^2}{(1-r)^2 - t^2}} \\
 N &= \frac{c}{\omega d} \arccos \left[\frac{1 - r^2 + t^2}{2t} \right].
 \end{aligned}
 \tag{22.25}$$

The transmission function t relates the output electric field to the input one: $t = E_{\text{out}}/E_{\text{in}}$. In spectroscopy, a reference measurement is frequently performed without the sample in the beam path; the transmission function in this case is equal to the phase change due to the propagation in vacuum: $t_0 = \exp(-i\omega d/c)$. The spectroscopic transmittance is then usually defined as a relative one with respect to the reference $t' = t/t_0$. In a similar manner the spectroscopic reflectance is defined with respect to some reference reflection measurement r_0 : $r' = r/r_0$ (for a perfect metal mirror $r_0 = -1$).

There are several theoretical and experimental challenges. First of all, as already discussed, the homogenization limit for the metamaterials is typically set as $D < \lambda/10$. However, a considerable activity in the research of electromagnetic metamaterials has been devoted to structures above this limit ($> \lambda/10$). This implies a non-negligible spatial dispersion of the effective optical parameters observed when the light propagation direction is varied. At the same time the discontinuous nature of the metamaterial leads to ambiguities in the retrieved parameters. This is essentially related to the reflectance phase. The exact position of the input and output faces of the metamaterial is not defined and the uncertainty is comparable to the period l of the pattern in the direction perpendicular to the surface ($> \lambda/10$). From the practical point of view, it is not clear where to position a mirror for the reference measurement: the phase of the reflectance is ambiguous within $\sim i\omega l/c$. If the metamaterial does not contain a mirror plane perpendicular to the propagation direction, the metamaterial reflectance and, in turn, also the retrieved effective optical properties in principle depend on from which side of the metamaterial the reflectance is measured. At least for metamaterials periodic in the propagation direction, it is possible to evaluate the phase shift introduced by a single period, which enables rigorous definition of the refractive index [56].

Metamaterial test samples for the THz range and for higher frequencies often consist of a single patterned plane (single-layer metamaterials) with the physical thickness much smaller than the probing wavelength. The problem here is 2-fold. We can ask an analogous question on the atomic level: is it reasonable at all to define ε and μ for the description of the electromagnetic response of a single atomic layer and will these functions still correctly describe the response if a bulk sample is grown? In the metamaterial science, we have an additional degree of freedom: the possibility to choose the period of the pattern. In order to assign a meaningful effective bulk permittivity and permeability to a thin film metamaterial from the spectroscopic results a convenient effective thickness d_{eff} should be chosen. For example, this thickness may be understood as a decay length of the local fields out of the metamaterial plane [57]. This brings a large ambiguity to the effective parameter retrieval procedure both from the point of view of the reflectance phase (as pointed out above) and from the point of view of the choice of d_{eff} . At the same time this approach of the estimation of bulk effective parameters from a thin film can be only valid if the targeted bulk metamaterial has an out-of-plane period close to d_{eff} . One intuitively feels that, for example, for a period of the layer stacking smaller than d_{eff} , the interaction between the metamaterial planes will significantly influence the near-field pattern and modify the effective response of the bulk sample.

Finally, there are technical complications associated with the multivalency of the square root and arccos functions. The condition of the passivity of the metamaterial leads to a certain disambiguation of (22.25), since it implies $\text{Re } Z > 0$ and $\text{Im } N > 0$. However, the solution for the refractive index contains several branches originating from the arccos function. In some cases it may be difficult to select the right one; this is particularly true for thick samples, for which the branches are closely spaced.

From the experimental point of view, it is difficult to obtain the phase information at high frequencies. Nevertheless, in the THz range the phase can be still measured by

means of TDTS. The transmittance phase can be generally measured very accurately and its precision is limited only by the accuracy of delay stages. Measurement of the reflectance phase is complicated since when the sample is replaced by a reference mirror, a longitudinal offset resulting in a substantial phase shift may be introduced. It is necessary to take extreme precautions to eliminate this shift, since even micrometer offsets may cause a significant error in optical parameters retrieved from optical spectra [58].

Minowa et al. [51] measured complex reflectance and complex transmittance spectra of phosphor bronze wire grid by TDTS. Due to a tens-of-microns displacement of the sample with respect to the reference mirror in the reflectance measurements, the reflectance phase had to be optimized numerically during the retrieval of the effective optical properties. The results then confirmed that the effective permittivity of the wire grid shows a plasmonic resonance in the THz region for electric field parallel to the wires [2] and that the effective permittivity is positive for electric field perpendicular to the wires. Awad et al. [52] investigated a metamaterial made of H-shaped wire-pair resonant structures which were designed to exhibit a range with negative refractive index. The negative refractive index was confirmed experimentally, but no details about its retrieval from the experimental data were provided [52].

An approach avoiding the difficulties connected with the measurements of the reflectance spectra consists in a measurement of amplitude transmittance at several incidence angles. This approach was used by Driscoll et al. for the characterization of an array of SRRs by FTIR spectroscopy [50, 57]. However, a full inversion of the equations connecting the transmitted power to N and Z was not performed; instead, the magnetic response was modeled by a modified Lorentzian function and only its parameters were retrieved by fitting the experimental data [50].

22.4.3 Retrieval of N and Z from Time-Windowed Signal

TDTS consists in measuring the temporal profile of the electric field of a broadband THz pulse transmitted or reflected by a sample. The multiple internal reflections of the THz pulse in an optically thick sample are measured as a series of mutually delayed echoes in the time domain (Fig. 22.4b).

$$\begin{aligned} t' &= \sum_{i=0}^{\infty} t'_i \\ r' &= \sum_{i=0}^{\infty} r'_i \end{aligned} \tag{22.26}$$

The temporal windowing can be then applied to such data in order to separate the signals belonging to these echoes [59] and calculate the transmission or reflection functions t'_i, r'_i for these partial waves. In order to obtain two complex spectroscopic quantities allowing one to determine N and Z (or ε and μ) it is then sufficient to consider two of such measured transmittance or reflectance signals. The methods of extraction of N and Z from these quantities without any ad hoc assumption about the behavior of ε and μ were described in [60], where the lowest order transmittance

and reflectance functions t'_0 , t'_1 , and r'_0 were considered. For normal incidence one obtains:

$$\begin{aligned} t'_0 &= \frac{4Z}{(Z+1)^2} \exp[-i\omega(N-1)d/c] \\ t'_1 &= t_0 \left(\frac{Z-1}{Z+1} \right)^2 \exp(-2i\omega Nd/c) \\ r'_0 &= \frac{Z-1}{Z+1} \end{aligned} \quad (22.27)$$

A thorough analysis of the sensitivity of these retrieval methods and of their experimental errors was also presented in [60]. These methods allow a quite accurate determination of N while the error in the determination of Z is usually significantly higher: successful evaluation of the dielectric and magnetic dispersion then crucially depends on the accuracy of the wave impedance measurements.

As pointed out above the metamaterial samples are frequently very thin and in this case the separation of echoes in the time domain is impossible. For this reason it was proposed to attach the metamaterial in an optical contact to a thick transparent substrate and analyze the echoes coming from the reflection on a backside of the substrate (see Fig. 22.4). A metamaterial consisting of a grid of high-permittivity rods made of paraelectric SrTiO₃ (Fig. 22.5a) has been characterized by using this approach by Němec et al. [31]. For an incident wave with electric field perpendicular to the dielectric rods, the metamaterial should exhibit a magnetic response and a negative effective magnetic permeability associated with the lowest order Mie resonance [29, 31]. The metamaterial was attached to a 2 mm thick silicon wafer, which made it possible to temporally resolve the internal reflections in the substrate. The substrate without the metamaterial sample attached then served for the reference measurement. The metamaterial reflectance and transmittance read as

$$\begin{aligned} t' &= \frac{E_{\text{sam}}^{(0)}}{E_{\text{ref}}^{(0)}} \\ r' &= \frac{E_{\text{sam}}^{(1)}}{E_{\text{ref}}^{(1)}} \cdot \frac{r_s}{t'} \end{aligned} \quad (22.28)$$

where $r_s = (N_s - 1)/(N_s + 1)$ is the reflectance on the substrate–air interface and N_s is the (possibly complex) refractive index of the substrate (see Fig. 22.4). Note that the large phase shifts induced by the substrate exactly cancel out, as identical substrates are used in both measurements. The reflectance phase is thus free of systematic errors due to possible mispositioning of the reference (a good contact between the metamaterial and the substrate is required). The retrieved effective permeability shows a strong resonance at 0.264 THz and a region with negative effective permeability above this resonance (Fig. 22.5c). Two weaker magnetic resonances originating from higher order Mie-modes are observed at ~ 0.53 THz and 0.61 THz. The response is not purely magnetic as weak resonances are clearly observed also in the permittivity.

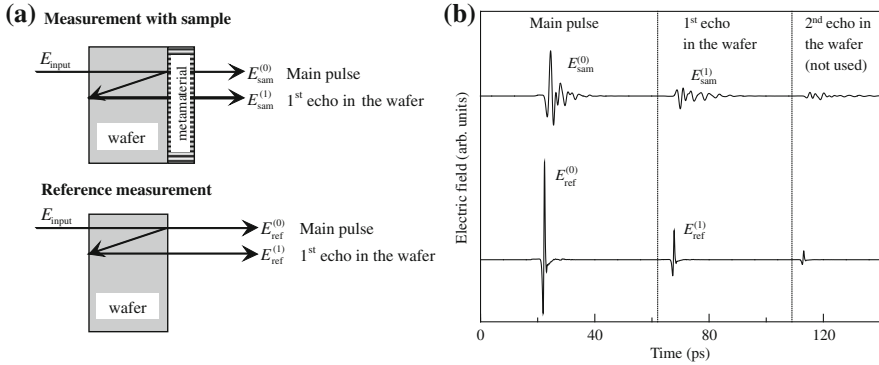


Fig. 22.4 **a** Scheme of the arrangement for transmittance and reflectance measurement in TDTS, along with a sketch of the required reference signals. The THz beam is shifted upon reflections only for graphical clarity. **b** Illustration of a typical waveform obtained in TDTS

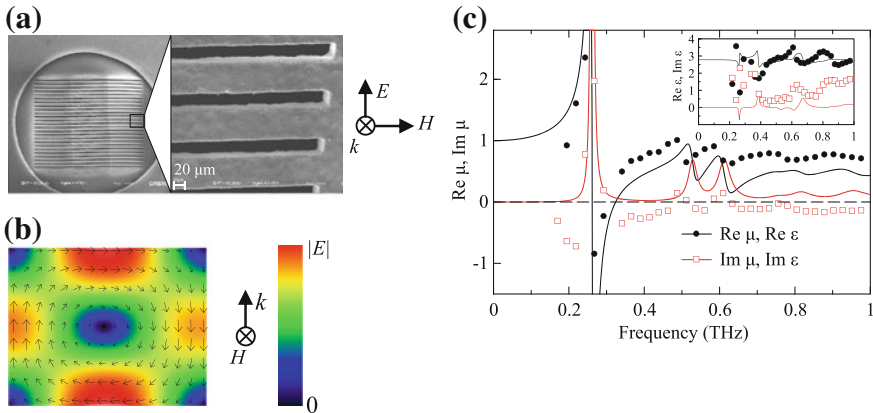


Fig. 22.5 **a** Scanning electron microscopy image of an array of SrTiO₃ rods. **b** Distribution of the electric field in a rod at the lowest order magnetic resonance frequency. The circular current is responsible for the magnetic response. **c** Effective magnetic permeability and dielectric permittivity spectra. Symbols: measurement, lines: calculations by multidimensional transfer matrix method

The spectral resolution of this method is imposed by the time-windowing and it is then essentially determined by the substrate thickness. In [31] a 2 mm thick Si wafer was used which limited the frequency resolution to ~ 22 GHz and led to a broadening of the observed resonance in μ_{eff} .

It should be noted that the measurements can be greatly simplified for composites or for metamaterials with a symmetry which does not allow the magnetic response. The magnetic permeability is then equal to 1 and the resonant permittivity can be retrieved simply from complex transmittance measurements by well-established standard methods of TDTS [18, 61, 62].

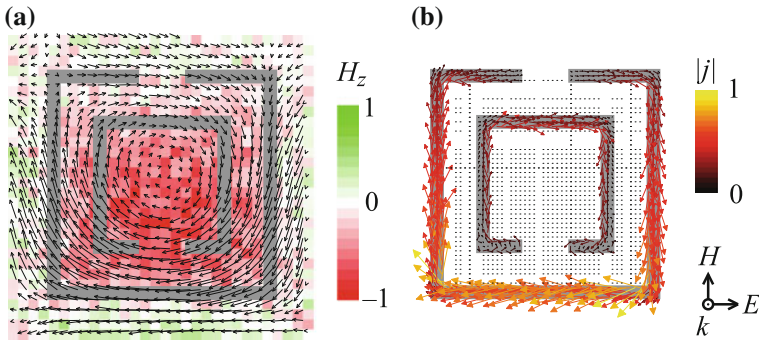


Fig. 22.6 **a** Measured electromagnetic near-field distribution close to a double SRR at a resonance frequency denoted as A1 in Ref. [53]. The vector plots show the in-plane electric field vectors in the x - y -plane at the backside of the sample. The color code indicates the time derivative of the out-of-plane component of the corresponding magnetic field, $\partial H_z/\partial t$, derived from the electric field vectors. **b** Simulated surface current density. After [53]

22.4.4 Near-Field Methods

An ultimate experimental technique which can facilitate understanding of the metamaterial physics and provide an amount of information comparable to that obtained from numerical simulations is the near-field THz imaging. Bitzer et al. [34] developed a TDTS equipped with a THz detector based on an antenna with a $10\ \mu\text{m}$ wide gap between H-shaped electrodes on an ion-implanted silicon-on-sapphire substrate. By scanning the position of the detector chip across the metamaterial, they obtained a two-dimensional (2D) map of the electric field components in the metamaterial plane with a subwavelength spatial resolution. From Maxwell's equations, it is then possible to reconstruct even the spatial profile of the magnetic field perpendicular to the metamaterial plane [53]. The near-field imaging technique was used to investigate the field distribution at a resonant frequency in an array of double SRRs [53]. The result of such a measurement along with the calculated current density distribution in the split ring is illustrated in Fig. 22.6 for the case of the lowest magnetic resonance. The plots show the eddy currents leading to the magnetic response, and the induced magnetic field inside the split rings.

Finally, let us mention the work by Seo et al. who employed near-field imaging for investigation of a slit array in a metal foil [63]. In this work, two electro-optic crystals sensitive to different components of the electric field were alternatively used as detectors. This allows a full characterization of the electric field vector, which in turn enables evaluation of all derived quantities such as Poynting vector or all components of the magnetic field vector.

22.5 Fabrication of THz Metamaterials

Many THz metamaterials are prepared in the form of patterned layered structures which makes the fabrication easier compared to 3D metamaterials. Planar metamaterials can be straightforwardly machined by lithography or by direct laser writing. Both these techniques can be combined with further micromachining steps to prepare more sophisticated structures.

22.5.1 Lithography

Typical dimensions of metallic resonators in THz metamaterials are of the order of tens of micrometers and the smallest details of the metallic patterns then reach units of microns. This predestinates the optical or UV lithography followed by a lift-off process as a routine technique for the fabrication of planar THz metamaterials. Indeed, many THz metamaterials have been fabricated by this method, e.g., [7, 8, 47, 49, 50, 64, 65] to cite just a few early papers dealing with THz metamaterials. The technology was further enhanced to fabricate more complex structures. Yen et al. employed a self-aligned technique called a photo-proliferation process to produce thick metallic patterning of a double-SRR array with a period $\sim 30\text{--}50\ \mu\text{m}$ which exhibits a magnetic resonance near 1 THz [7], Fig. 22.7a. The first layer of the pattern was prepared by optical lithography in a standard way. In the second step the exposure was performed from the back side of the sample and the primary metallic pattern served as the mask. This approach allows depositing thick metallic structures while avoiding alignment problems. In the work by Katsarakis et al. [47], the authors repeated the UV lithography process several times in a layer-by-layer fashion to build a negative-permeability metamaterial consisting of five aligned metallic layers of SRRs (mutually isolated by polyimide layers) with the alignment accuracy of $0.5\ \mu\text{m}$ ensured by a commercially available aligner. These resonators were arranged in a square lattice with a period of $7\ \mu\text{m}$, and the operating frequency was around 6 THz.

Chen et al. performed two lithographical steps to deposit an ohmic electrode and interconnected resonators [8, 66, 67], (Fig. 22.9). The final metamaterial array and the doped semiconductor substrate form together a Schottky diode. Wu et al. employed a UV stereo-microlithography for the fabrication of an array of vertical rods ($30\ \mu\text{m}$ diameter, 1 mm height) [68]. Their stereo-microlithographical system contained a beam-shaping element delivering a mask pattern to the projection lens, which focused the UV light onto the surface of the resin. Under the exposure, a thin layer of solid polymer structure was formed by the computer generated mask pattern according to the sliced cross-section of the digital 3D model. By stacking the layers sequentially in the course of lowering the elevator, a solid polymer copy was fabricated of the liquid resin according to the digital 3D model. After coating of the

rods array by a metal, the structure served as a plasmonic high pass filter with cutoff frequency of 0.7 THz.

Optical lithography was also used to fabricate planar arrays of 50- μm SRRs on bimaterial cantilevers designed to bend out-of-plane in response to a thermal stimulus [69], Fig. 22.7b. This resulted in a controlled response of the electric and magnetic resonance (~ 0.5 THz) as the SRRs reorient within their unit cells.

From the point of view of potential applications, it is important that optical lithography can manufacture even flexible THz metamaterials [70–74].

The spatial resolution in optical lithography is limited by the wavelength of the employed light source. One advantage of shorter wavelength sources is the possibility to deliver nearly vertical sidewalls. This opportunity was utilized by Moser et al who used X-ray lithography to form a free-standing THz metamaterial with a negative refractive index at Fig. 22.7c. Deep X-ray lithography was used for the production of stacked split ring structures resonant around 5 THz to obtain a larger height of the pattern (dimension perpendicular to the lithography plane) in order to reduce the anisotropy [76]. A good spatial resolution is particularly important for metamaterials targeted for higher frequencies, since they involve smaller motives. Electron beam lithography was thus successfully used for the preparation of SRRs with magnetic resonance in the mid-infrared spectral region [77]. Chen et al. combined the electron beam lithography for the deposition of metallic patterns with the optical lithography followed by a reactive ion etching of a thin silicon layer: the resulting structure contained 50- μm -sized metallic resonators connected to small silicon capacitor-like structures [78]; the silicon pads were excited optically during the THz experiments in order to switch the metamaterial resonant frequency (see Fig. 22.12 and the corresponding text).

Lithographical techniques can be efficiently combined with deep etching procedures, typically to produce vertical semiconducting rods. Kadlec et al. [18] prepared a metallic mask using an optical lithography, and subsequently employed an anisotropic deep inductive plasma etching to produce silicon pillars or walls with characteristic lateral dimensions below 10 μm and with a height up to 80 μm , Fig. 22.1c. Such layers can exhibit an on-demand refractive index determined by the geometrical parameters of the structure. Similarly, Bruckner et al. [17] prepared a mask by an electron-beam lithography and performed a deep etching to produce an array of 500 μm high silicon pillars with a lateral dimension of ~ 40 μm ; these played the role of a broadband antireflection coating. Finally, Saha et al. [79] imprinted a similarly fabricated rigid-wall structure on both sides of a high-density polyethylene. Such a structure with 60- μm period then acted as a quarter-wave plate operating between 2.6 and 3.8 THz, depending on the depth of the imprint.

22.5.2 Laser Writing

Direct laser writing is quite a versatile process. In the early times, a double-split-ring structure combined with cut wires was fabricated by direct laser writing comple-

mented by electroplating [80]. The fabricated 100- μm resonators exhibited a pass-band around 2 THz, which was attributed to the negative refractive index. Direct laser writing was also used for the elaboration of various planar metallic microresonators with electric resonant response on a flexible polyimide substrate [71]. With a characteristic period of about 50 μm , they exhibited a resonance in the THz range. Direct laser writing can be used to obtain even tinier patterns with resonances reaching the mid-infrared region. Moreover, the fabrication of 3D structures is also possible. These capabilities were combined by Rill et al. [81] to develop a negative-index metamaterial with a resonance at around 100 THz corresponding to the pattern period of 1 μm .

Direct writing by proton beam is suitable for cutting strictly vertical structures as the large mass of the protons allows them to maintain straight tracks through many microns of the resist. By using an additional electroplating step, Chiam et al. produced high narrow metallic structures, Fig. 22.7i. The resulting array of split rings enclosed by 40- μm closed square rings exhibited similarities with electromagnetically induced transparency, such as a large group index and low losses for frequencies around 1.25 THz.

22.5.3 Other Techniques

Laser cutting is a promising technique with the potential to micromachine a wide variety of materials. In Ref. [31, 83], an array of 30- μm grooves was drilled by a femtosecond laser into 20–50 μm thick SrTiO_3 wafers. The resulting array of high-permittivity rods exhibited a strong Mie resonance accompanied by a negative effective magnetic permeability (Fig. 22.5). Micromachining was also used for cutting an array of 100- μm -sized SRRs [84].

Various efforts have been made to reduce the costs and to achieve a greater versatility of the fabrication process of THz metamaterials. Early attempts demonstrated the possibility to prepare simple structures like THz wire-grid polarizers by ink-jet printing [85, 86]. Walther et al. [87] employed an ink containing a suspension of silver nanoparticles and printed an array of SRRs on a flexible kapton foil, Fig. 22.7e. Due to their large dimensions (0.5 mm), they were targeted rather for sub-THz frequencies. Ink-jet printed cut wires were prepared by Takano et al. to study an insulator-to-metal transition [88]. Another direction is devoted to the possibility to fabricate THz metamaterials by self-organization. Pawlak et al. [89] investigated a directional solidification of eutectics which leads to a realization of self-organized particles with an SRR-like cross section, Fig. 22.7f.

The above list of techniques is far from exhaustive – below we provide a few examples which go beyond the above classification. Hollow staple nanostructures resembling 3D Ω -shaped metallic nanostripes were designed and produced by Zhang et al. [90] exhibiting a negative effective permeability at tens-THz frequencies, Fig. 22.7d. Tuniz et al. [91] presented a metamaterial acting both as a polarizer and as a high-pass filter: it was based on a fiber drawing where a macroscopically sized

(\varnothing 1 cm) preformed metal-dielectric fiber was heated and reduced in size (below 1 mm diameter) which produced the desired size of the patterns. The output fiber then contained $\sim 100 \mu\text{m}$ spaced metallic fibers with a diameter of $8 \mu\text{m}$. Miyamaru et al. employed laser processing to deposit a large number of metamaterial layers and assembled them together to obtain a bulk magnetically active metamaterial [92, 93] – the resonant frequency of 0.35 THz was achieved with 100- μm SRRs. Wen et al. [94] employed plasma etching to prepare a metamaterial composed of cut VO_2 wires. VO_2 exhibits a metal-to-insulator transition which predestines the use of such a metamaterial for thermally controlled switches. Crystallographic wet etching was employed by Chen et al. [95] to develop a broadband antireflection coating made of tens-microns-sized pyramids formed in a silicon wafer by crystallographic wet etching, Fig. 22.7g. Notable is also a negative-refractive-index chiral metamaterial by Zhang et al. which contains planar metallic wires (= capacitors) connected by 3D metallic bridges (= inductances) [96], Fig. 22.7h. Wire-cut electrical discharge machining was employed to develop a metamaterial with high effective refractive index based on a metallic grating [97].

22.6 Applications

Several principal research directions in the THz metamaterials can be traced from the published literature. (i) The first one is the search for structures with negative refractive index, which was historically the first motivation for the metamaterial development. As it is in principle much easier to find or to design a sample with a negative permittivity, the authors deal mainly with the problem of how to obtain the negative permeability. (ii) Another class of papers is devoted to the application where the authors look for the way to tune or modulate the metamaterial resonance. In a number of works the accent is put on structures where the magnetic response is forbidden by the symmetry and the metamaterials exhibit an artificial dielectric resonance controlled by an external parameter like electric field or fotoexcitation. In this sense, here we deal with the search for the tunability by means of metamaterial structures. (iii) The plasmonics is a modern topic of research aiming at applications in the development of chemical and biochemical sensors and which can help to miniaturize various optical components. A number of papers on research in the field of THz plasmonics with metamaterials have been published [98–101]—we will not discuss the THz plasmonics here as a separate chapter of this book is devoted to the advances in this topic. (iv) The strong interaction of light with metamaterial structures allows one to conceive metamaterial-based absorbers, (v) artificial birefringence of anisotropic metamaterials allows one to achieve the metamaterial-based polarimetry and finally, (vi) some specific effects like cloaking, waveguiding, or achieving “slow-light” effects with metamaterials have also been reported.

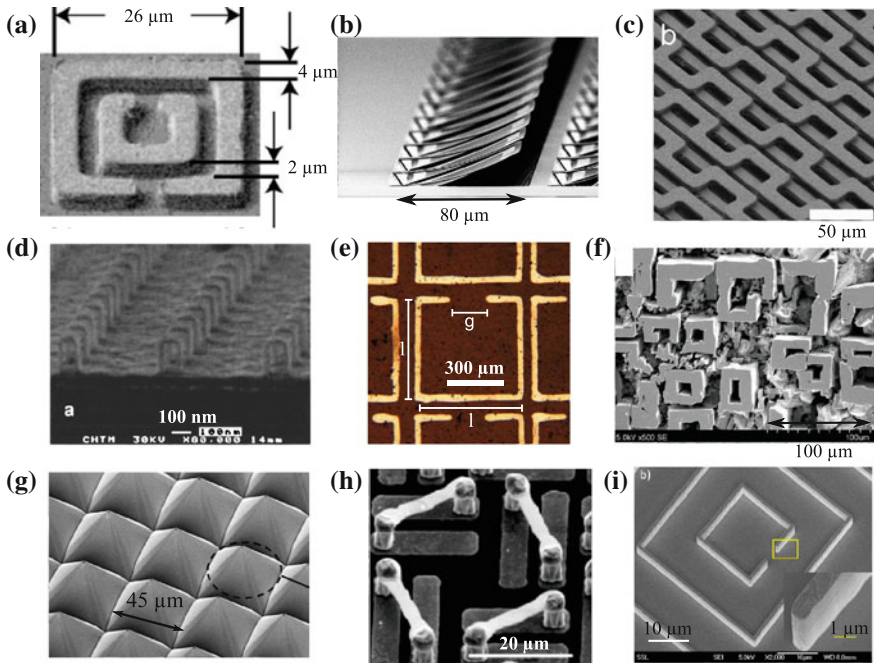


Fig. 22.7 A few examples of THz metamaterial structures. **a** A secondary ion image of a double-split ring taken by focus ion-beam microscopy, after [7]. **b** SEM picture of SRRs on bimaterial cantilevers, after [69]. **c** SEM image of double-S metamaterial, after [75]. **d** Omega-like metallic nano-strips, after [90]. **e** Ink-jet printed split rings, after [87]. **f** SEM image of a split-ring-like structure grown from SrTiO₃-TiO₂ eutectics and covered by metal, after [89]. **g** SEM image of silicon micropyramids, after [95]. **h** SEM image of a chiral material, after [96]. **i** SEM image of a metallic resonator fabricated by proton writing. The height of the resonator is 4 μm. After [82]

22.6.1 Negative Permeability

The majority of structures aiming at the negative μ are based on the split-ring resonators (SRRs). These can have various shapes, e.g., circular or square double-SRRs as shown papers [6, 7] (see Fig. 22.7a) or single SRRs or single SRRs [47, 50, 87], (see Fig. 22.7e). The magnetic dipole moment is related to the currents flowing along metallic rings and the disadvantage of these structures is that the effective magnetic response can be induced only for an oblique incidence of the radiation when the magnetic field points through the ring as shown in Fig. 22.2a, b. Various approaches have been proposed and explored to overcome this problem.

Recently, Miyamaru et al. stacked together 100 layers of 2D dielectric sheets patterned with SRRs and obtained a bulk piece of metamaterial with a thickness of 10 mm [102]. This allowed performing experiments with the incident wave vector lying in the split-ring plane; in this geometry either the magnetic or the electric field is perpendicular to the plane of the SRRs. In agreement with theoretical predictions

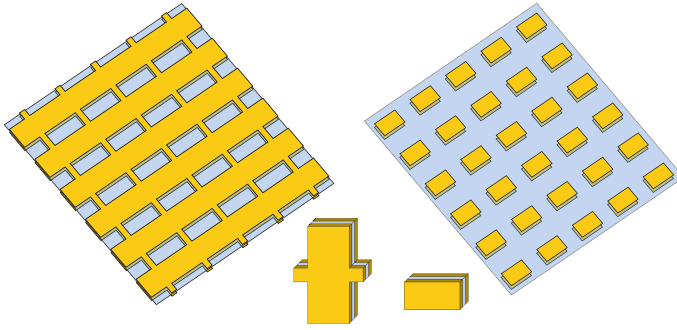


Fig. 22.8 Fishnet (*left panel*) and cut-wire pair (*right panel*) structures consisting of metallic double layer (*yellow*) separated by a thin dielectric material (*blue*). The negative permittivity and permeability can be achieved here for a normal incidence of the radiation [105]

[4, 6] the electric field perpendicular to the plane of the SRRs does not lead to any resonant response, whereas for magnetic field perpendicular to the plane of the SRRs, a strong narrow magnetic mode and a broader weaker electric mode (resulting from the half-wavelength electric dipole resonance of one side of the SRR) are observed.

Another solution has been proposed by Fan et al. who developed a layer of 3D stand-up metamaterials prepared by multilayer-electroplating technique consisting of out-of-plane SRRs standing upon the substrate [103, 104]. For the normal incidence the magnetic-field vector perpendicular to the SRR plane induces circular currents in the rings and a strong magnetic response appears. A similar idea on a more elaborated basis has been demonstrated by the same group with so-called reconfigurable THz metamaterials [69], see Fig. 22.7b.

Other possibilities to create magnetically active metamaterials take advantage of the displacement currents in dielectrics which can form parts of the current loops. Various kinds of structures composed of finite length (cut) wire pairs or with the fishnet double-layer topology were developed [105, 106]. The currents flow here through the metallic parts but the displacement currents between the two adjacent layers with deposited cut wires or fishnets (which are separated by a thin dielectric) allow one to obtain closed current loops and to achieve a resonant magnetic response even for the normal incidence, see Fig. 22.8.

The Mie resonances of dielectric inclusions provide another interesting mechanism for the creation of magnetic resonances based entirely on displacement currents, and even offer a versatile route for the fabrication of isotropic metamaterials operating at THz frequencies. In these structures, ferroelectric or polaritonic compounds with high permittivity can be typically used and also their tunable behavior presents an advantage in designing commandable structures [107–109].

The discussed phenomena were first demonstrated in a ferroelectric $(\text{Ba,Sr})\text{TiO}_3$ ceramics in the GHz frequency range [32]. In the THz range thermally tunable magnetic Mie resonances were obtained in an array of SrTiO_3 rods for the *s*-polarized THz beam, i.e., E perpendicular to the rods (Fig. 22.5a). The resonant behavior is

closely connected to the high value of the permittivity in SrTiO₃ (~ 300 at room temperature and ~ 1200 at 100 K in the sub-THz range [110]). The resonant behavior can be understood with simple physical arguments: the wave front of an incident plane electromagnetic wave undergoes a strong distortion close to the metamaterial in order to satisfy simultaneously the continuity and discontinuity conditions of tangential and normal electric-field components at the SrTiO₃–air interfaces, respectively. The electric field, which develops inside an SrTiO₃ bar, is then predominantly tangential close to the surface of the bar. This leads to the creation of displacive eddy currents within the bar cross-section (Fig. 22.5b) which enhance the magnetic field in SrTiO₃ polarized along the bar. A resonant behavior is then expected at specific frequencies determined by the geometry and dielectric constants of the rods (Fig. 22.5c). The effective properties of the metamaterials were thermally tuned over a broad spectral range owing to the dielectric tunability of the SrTiO₃ crystal [31].

22.6.2 Tunable Metamaterials

In the metamaterial science the THz technology serves, on the one hand, as a platform for extension of GHz-scaled structures up to the optical range. On the other hand, properly designed structures utilizing specific THz material properties allow one to create metamaterial devices targeted for THz applications. It is expected that many of these applications will require manipulation of the flow of THz radiation either passively (waveguides, splitters) or actively by a variation of an external parameter (modulators, switches, tunable filters). At the same time, properties of metamaterials rely on strong electromagnetic resonances and, consequently, experimental demonstrations of their functionality and their subsequent applications are restricted to narrow spectral intervals determined by the overlap of the desired electric and magnetic response. Active spectral tuning of the metamaterial resonance then appears as a highly desirable property of functional structures.

In a majority of the reported works the tuning or switching of metamaterial properties is generally achieved by a modification of the capacitance of a suitable meta-atom. This can be achieved by a change in the conductivity of the material (semiconductor) which forms the capacitor pads or which fills the space between the capacitor pads [8]. Another possibility is a change of the permittivity of the material forming the capacitor. The external control parameter (electric field, illumination, temperature, or magnetic field) then modifies either the amplitude (strength) of the resonance or its spectral position [31]. In all-dielectric metamaterials the control of the metamaterial response can then be obtained by a tuning of the dielectric permittivity of one (e.g. ferroelectric, high permittivity) component. Recently, a notion of reconfigurable anisotropic metamaterial was introduced where the modulation of the resonance is due to meta-atoms reoriented with respect to the incoming radiation in response to an external control parameter [69].

The first step in the active control of the metamaterial resonant response direction was made by Chen et al. [8] who demonstrated an active planar metamaterial device with a real-time control of a purely electrical resonant response by a low applied volt-

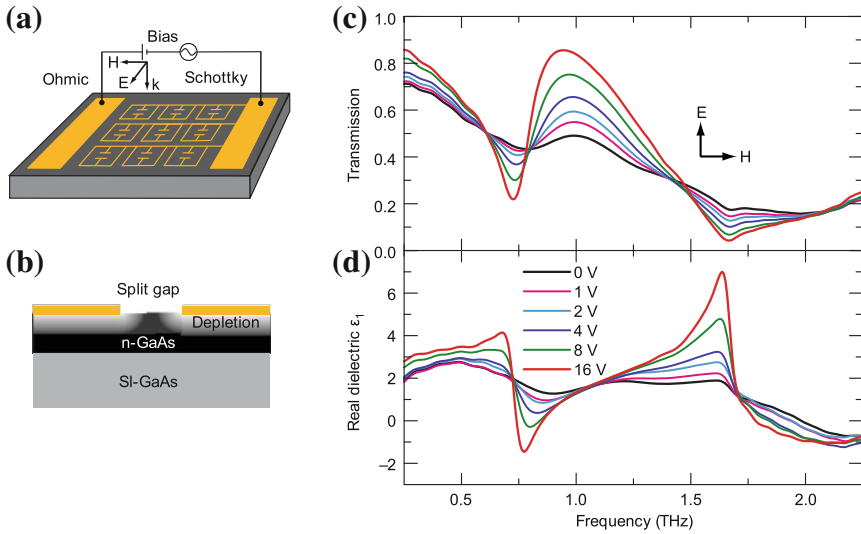
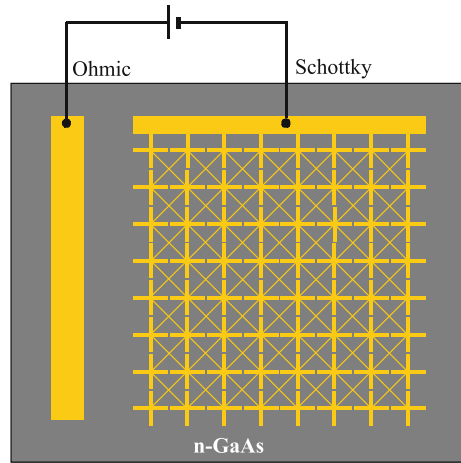


Fig. 22.9 Planar electrically resonant metamaterial for THz light modulation. **a** Scheme of the structure: the metamaterial elements are patterned with a period of $50\ \mu\text{m}$ to form a planar array of $5 \times 5\ \text{mm}^2$. A voltage bias applied between the Schottky and ohmic contacts controls the substrate charge carrier density near the split gaps, tuning the strength of the resonance. **b** Diagram of the substrate and the depletion region near the split gap, where the grayscale indicates the free charge carrier density. **c** Frequency-dependent transmitted intensity of THz radiation and **d** the corresponding permittivity for various reverse gate biases. After [8]

age. The device consisted of an array of gold resonator elements with a symmetry not allowing the magnetic response. The metallic structures were deposited on a $1\ \mu\text{m}$ thick moderately n -doped GaAs layer. The metal and n -GaAs form a Schottky junction and the conductively connected metamaterial resonators serve as a metallic gate (Fig. 22.9). Without an applied voltage the split-gap capacitors are short circuited by the conductive substrate; upon application of a voltage, a resonant behavior appears resulting from a restored capacitance of the split-gap: due to an electrostatic force the carriers in the substrate below and near the metallic pads are displaced and a depleted layer is created, i.e., the conductive connection mediated by the carriers is broken (see Fig. 22.9). The transmission function of such a planar device strongly depends on the presence of the resonance near 1 THz which is controlled by an applied bias 0–16 V and a power modulation of up to 50% has been observed at $\sim\text{kHz}$ modulation frequencies [8]. A multipixel spatial modulator for THz beams was proposed later based on the above described split-ring arrays assembled into a 4×4 pixel matrix where each pixel of $1 \times 1\ \text{mm}^2$ was controlled independently by an external voltage [111].

Electromagnetic properties like resonant surface current density and local electric field distribution of the nonmagnetic split-ring-based planar metamaterials with various symmetries have been studied by the same group in subsequent papers in view

Fig. 22.10 Schematic layout of the cross structure with externally tunable bias supply for modulation of the THz light, after [115]



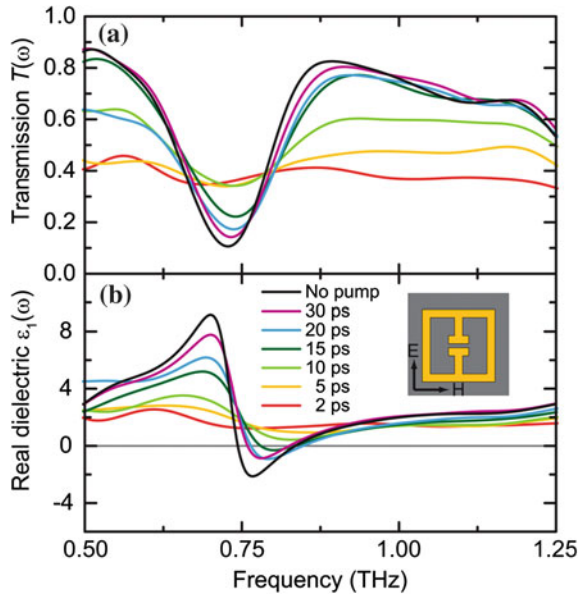
of tailoring their response [65, 112, 113]. The phase modulation of the THz radiation has been recently demonstrated by using similar principle and similar metamaterial structures [114].

A modified design of the metamaterial pattern has been proposed by Paul et al. [115] in order to obtain a polarization-independent response. This device operates on the same principle of Schottky contact and depletion layer as described above. The active layer consists of gold crosses deposited on *n*-doped GaAs layer (see Fig. 22.10). An amplitude modulation of up to 30 % has been achieved by means of control bias voltage with modulation frequencies not exceeding 100 kHz.

The same principle of carrier depletion in a Schottky diode structure was used to achieve an electronic control of extraordinary transmission of THz radiation through subwavelength metal hole arrays [67]. The metal hole arrays were deposited by photolithography on a 2 μm thick moderately *n*-doped GaAs layer. Without external bias the transmission through the holes is significantly decreased (as compared to that of a structure deposited directly on semi-insulating GaAs without the doped layer) due to the conductivity of free carriers in the *n*-doped layer. Upon applying a reverse voltage the transparency of the structure for the THz radiation increases at resonant frequencies; this demonstrates the restoring of extraordinary transmission effect with increasing depletion area in the holes.

Optical switching of a THz metamaterial has been first demonstrated by Padilla et al. [116] and subsequently, on a picosecond timescale, by Chen et al. [117]. Here, a nonmagnetic metallic metamaterial pattern (similar to that shown in Fig. 22.9) is deposited on an undoped semiconductor. Without illumination (in the ground state) the meta-atom shows a resonance in the sub-THz range (0.75 THz in [117]) owing to the capacitance of the split-gap which leads to a low transmittance of the structure close to the resonant frequency. The optically controlled switching has an advantage of a possible ultrafast response of the structure demonstrated in [117]. In order to achieve this, ErAs/GaAs superlattices have been grown by molecular beam

Fig. 22.11 Transmittance and real part of the dielectric function of a metamaterial with a motive shown in the inset deposited on ErAs/GaAs superlattice. Free carriers are injected into the semiconductor by photoexcitation; evolution of the spectra on the picosecond timescale after photoexcitation is shown. After [117]



epitaxy on top of a semi-insulating GaAs substrate below the metamaterial structure. The conductivity of the semiconductor structure is switched on by photoinjection of electrons into the conduction band of GaAs by using a femtosecond optical pulse at 800 nm. A carrier concentration of about $4 \times 10^{16} \text{ cm}^{-3}$ is sufficient to shunt the capacitive regions of the metamaterial pattern destroying the metamaterial resonance; consequently, the THz transmittance of the structure is increased under illumination by about 50% [117]. The free carrier lifetime is ultrashort (in the picosecond and subpicosecond range) and it can be tuned by changing the period of the superlattice [118]; the parameters of the superlattice in Ref. [117] were chosen such that the low THz transmittance of the metamaterial is recovered within 20 ps (see Fig. 22.11). Similar experiments were also made with double-ring resonator structures deposited on a high-resistivity silicon substrate [119] and experiments without the time resolution of the modulation were carried out with classical double SRRs deposited on high-resistivity GaAs [120].

An optically induced tuning of the metamaterial resonant frequency has been demonstrated in [78]. Here, the gold split-rings, with the same geometrical form as those in [8] and [117], were deposited on sapphire. The capacitor plates of the split ring were partly made of a high-resistivity silicon film; this allowed the authors to control their conductivity by optical excitation of charge carriers in silicon. In this manner the split-ring capacitance dependent on the size of conducting capacitor pads could be dynamically controlled by illumination with amplified laser pulses. An optical switching of the metamaterial resonance between 0.85 and 1.05 THz has been observed.

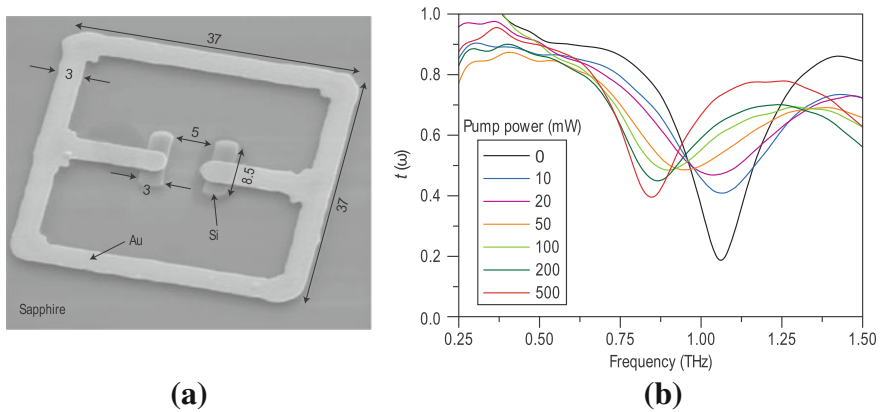


Fig. 22.12 **a** Scanning electron microscopy image of the unit cell of optically frequency-tunable planar metamaterial. Dimensions are in micrometers. **b** Terahertz electric-field transmission amplitude of the metamaterial measured by TDTS. After [78]

A metamaterial electrically resonant (non-magnetic) split-ring structure deposited on a dielectric substrate has been recently proposed consisting of three capacitor gaps, two of them being filled with a suitable semiconductor layer [121]. The calculations were made for silicon. If an optical pulse excites the silicon film the two capacitors are shunted. This significantly changes the effective LC term of the meta-atom and the resonant frequency is displaced from 0.7 to 1 THz in the presented simulations [121]. The idea of dual electrically resonant meta-atoms with two different split-gaps has been experimentally demonstrated in the THz range previously [122].

The capacitance of the SRRs has been also tuned by changing the permittivity in the split-gap of the capacitor: the authors of [123] used drops of silicon nanospheres diluted in ethanol to influence reversibly the resonance frequency of SRR-based metamaterial by up to 10 %.

The temperature tuning of metamaterial resonances has been also demonstrated. In a dielectric metamaterial composed of an array of high-permittivity SrTiO₃ rods (see Fig. 22.5a) a tunable negative effective permeability was achieved due to the temperature-dependent permittivity of SrTiO₃ which defines the resonant confinement of the THz radiation inside the rods [31]. The range, where the negative permeability was achieved, was tuned between 0.2 and 0.4 THz. The permittivity of SrTiO₃ is in principle tunable by electric field in the THz spectral range [124, 125]; however, the electric-field tuning of the effective magnetic permeability in this metamaterial structure has not been experimentally demonstrated, yet. A tunable dielectric (or ferroelectric) can be also used as a substrate for metallic metamaterial resonant elements. In this case the tuning of the resonant frequency is achieved through a modification of the dielectric permittivity of the substrate between the capacitor pads of the metamaterial resonator; a thermal tuning of such a planar metamaterial deposited on an SrTiO₃ single crystal substrate has been recently achieved [126]. The dramatic

change of the inductance and resistance of a material close to the superconducting phase transition was used to tune thermally a metamaterial based on niobium nitride (NbN) superconductor [127]. Electric-SRRs were fabricated from a thin NbN layer (deposited on MgO substrate by RF magnetron sputtering) using a photolithography and reactive ion etching. The electric resonances of the planar metamaterial then exhibited an appreciable frequency change and sharpening upon thermal switching between the normal and superconducting state [127].

The thermal tunability of VO₂ cut-wires has been also demonstrated in the THz spectral range [94]. Thermal triggering of the insulator–metal transition (temperature change between 300 and 340 K) leads to an increase in the conductivity of VO₂ wires and, consequently, to a 65 % change of the THz transmittance of the metamaterial layer.

Although a magnetic metamaterial tunability has not been reported in the THz range, a magnetically tunable negative refractive index was observed in the microwave range by He et al. [128] by taking advantage of magnetic properties of a ferrite. Recently, an electrically resonant THz metamaterial controlled by an external magnetic field has been demonstrated [129]. Here, the split-gap capacitor of an electric-SRR similar to that shown in the inset of Fig. 22.11b was replaced by a parallel plate capacitor; one capacitor plate was sustained by a flexible cantilever beam coated with a magnetic thin-film. This allowed the authors to tune the metamaterial resonance by bending the cantilever in an externally applied magnetic field [130].

Finally, reconfigurable anisotropic metamaterials based on SRRs have been proposed and demonstrated recently [69]. Planar arrays of SRRs are fabricated on bimaterial cantilevers designed to bend out-of-plane in response to a thermal stimulus, Fig. 22.7b. The magnetic response of the split-ring is component of the magnetic field vector perpendicular to the split-ring plane. The control of the orientation of the split rings with respect to the magnetic field of the incoming THz radiation then provides a mean for the modulation of the effective magnetic response of the structure.

22.6.3 Other Applications

The interaction of radiation with metamaterials is very strong close to the resonances, therefore it is interesting to study the possibility to conceive metamaterial-based absorbers. This concept is expected to be especially fruitful at THz frequencies where it is difficult to find strong natural absorbing elements. An ideal absorber is obtained if both reflectance and transmittance of a designed absorptive sheet are equal to 0. It follows from Eq. (22.23) that the reflectivity vanishes if $Z = 1$ (no impedance mismatch with the surrounding air). The transmission then exponentially decreases with kd , where k is the effective absorptive index of the sheet and d is the sheet thickness. It means that, in contrast to other targeted applications of metamaterials, for this particular field of research it is desirable to maximize the effective loss k of the metamaterial. This is a direction of the metamaterial research that has received attention only in few works up to now [130–133]. The structure consists in general

of two planes with metallic patterns separated by a thin dielectric sheet. The shape of the patterns then essentially defines the effective dielectric permittivity and the combination of the two patterns results in an effective magnetic response due to circulating currents between the two layers. The magnetic response then can be quasi-independently tuned by the distance between the two layers. Electrically resonant meta-atoms were chosen for the first layer, while cut-wires [130] or a continuous metallic sheet [131] or metallic crosses [132] were selected for the second one. The best performance was achieved in the geometry with the continuous metallic sheet for which an absorptivity exceeding 95% was experimentally obtained at the resonant frequency.

Antireflective coatings were proposed based on fabrication of metamaterial-based slabs with on-demand refractive indices and negligible absorption. These structures were made either by deep reactive plasma etching of silicon [17, 19, 20] or by stacking of metal meshes embedded in dielectric substrate [134].

Metamaterials frequently display a high artificial birefringence which can then be utilized in the manipulation of polarization of the THz radiation. A birefringence of up to 1.25 can be achieved in silicon walls over a thickness of $\sim 80 \mu\text{m}$ obtained by reactive plasma etching [18]. Peralta et al. [135] have designed and experimentally studied electrically resonant elliptical SRRs which show high in-plane anisotropy (frequency shift in the resonance position). Such components can be used in THz polarimetric devices and for example as birefringent wave plates. Quarter-wave plates based on electrically resonant metamaterials were demonstrated in [136] between 0.6 and 0.7 THz. Half- and quarter-wave plates based on negative refractive index were demonstrated by Weis et al. [137]; these devices are based on cut-wire-pair metamaterials and exhibit refractive indices of opposite signs for orthogonal polarizations. In contrast, for many applications, metamaterials are sought with a high-Q resonant behavior which is not affected by the angle of incidence and the polarization of the incoming wave. Such structures for the THz range have been recently proposed with a unit cell consisting of two concentric resonators with interdigitated fingers placed between the rings [138].

Slowing down the light can simplify optical data processing and storage. In conventional approaches, the light is slowed down by means of coherent excitation of electronic states. Such a scheme imposes severe constraints, including narrow bandwidth, limited working wavelengths, and a strong temperature dependence [99, 139]. An alternative approach has been recently proposed and consists in the development of optical meta-structures [140]. The authors theoretically proposed a left-handed heterostructure for the THz range, where a negative-refractive-index core with gradually decreasing thickness is surrounded by positive-refractive-index cladding. The beam in the negative-refractive-index layer propagates in a zigzag fashion and experiences negative Goos-Hänchen lateral displacements on the core-cladding interface [141]. For a suitable core thickness, the beam propagation will be compensated by the Goos-Hänchen shift and the light will finally stop. The critical thickness depends on the frequency of radiation which means that the gradually decreasing thickness of the core permits a broadband operation. An analogous proposition by Gan et al. is based on slowing surface plasmon polaritons in a graded metallic

grating [99]. Their group velocity vanishes at cutoff frequency which is determined by the groove height. The grading then again allows a broadband operation as different frequency components are stopped at different places in the structure. A strong reduction in the group velocity was achieved experimentally in a metamaterial structure made of concentric split- and closed rings [82]. The structure was designed in such a way that both rings exhibit the same resonant frequencies, but with significantly different quality factors. This leads to a narrow window of transparency in a broad absorption band which is associated with a strong reduction in the group velocity.

22.7 Concluding Remarks

The terahertz spectroscopy and the metamaterial science are both very new disciplines; this enabled them to meet each other during the phase of a very fast development before their maturity. On the one hand, the THz domain bridges the microwave and optical spectral regions and the THz spectroscopy provides some interesting experimental possibilities (phase sensitivity, near-field spectroscopy): in this sense it significantly contributes to the boost of the metamaterial research development. On the other hand, metamaterial structures with specific response and behavior are now demanded in order to allow more convenient spatial and temporal control of THz waves with devices aiming at industrial applications. It is hoped that the topics and examples discussed in this chapter do evince an intense interaction between these two fields of research and provide an impression of what can still be discovered.

The length scales are such that the technologies of elaboration of appropriately sized structures become mature. The latest technological trends involve efforts in developing 3D metamaterials and in introducing cheap technologies of metamaterial production. Patterned metals, semiconductors, and high-permittivity dielectrics (ferroelectrics) are currently used for the development of various structures which allow control of the strength of the interaction between the THz light and the metamaterial device. Namely, the optical and electric control of the conduction band carriers in semiconductor micro- and nanostructures and the temperature and electric-field control of the permittivity in ferroelectric inclusions provide the basis for the modulation of the resonant interactions. As it follows from the above text, significant progress has been achieved in understanding these interactions and in designing new operating devices. Nevertheless, the field for the optimization of these structures and for further research still remains vast and especially the transfer of the ideas and technologies from the laboratory to the industry for real-world applications has barely started.

References

1. V.G. Veselago, Electrodynamics of substances with simultaneously negative values of ϵ and μ . *Sov. Phys. Usp.* **10**, 509–514 (1968)
2. J.B. Pendry, A.J. Holden, W.J. Stewart, Extremely low frequency plasmons in metallic mesostructures. *Phys. Rev. Lett.* **76**, 4773–4776 (1996)
3. J.B. Pendry, A.J. Holden, D.J. Robbins, W.J. Stewart, Low frequency plasmons in thin-wire structures. *J. Phys. Condens. Matter* **10**, 4785 (1998)
4. J.B. Pendry, A.J. Holden, D.J. Robins, W.J. Stewart, Magnetism from conductors and enhanced nonlinear phenomena. *IEEE Trans. Microw. Theory Tech.* **47**, 2075–2084 (1999)
5. J.B. Pendry, Negative refraction makes a perfect lens. *Phys. Rev. Lett.* **85**, 3966–3969 (2000)
6. D.R. Smith, W.J. Padilla, D.C. Vier, S.C. Nemat-Nasser, S. Schultz, Composite medium with simultaneously negative permeability and permittivity. *Phys. Rev. Lett.* **84**, 4184 (2000)
7. T.J. Yen, W.J. Padilla, N. Fang, D.C. Vier, D.R. Smith, J.B. Pendry, D.N. Basov, X. Zhang, Terahertz magnetic response from artificial materials. *Science* **303**, 1494 (2004)
8. H.-T. Chen, W.J. Padilla, J.M.O. Zide, A.C. Gossard, A.J. Taylor, R.D. Averitt, Active terahertz metamaterial devices. *Nature* **444**, 597–600 (2006)
9. R. Marqués, F. Martín, M. Sorolla, *Metamaterials with Negative Parameters* (Wiley, New York, 2008)
10. S.A. Ramakrishna, T.M. Grzegorzczuk, *Physics and applications of negative refractive index materials*, (CRC Press, Boca Raton, 2009)
11. W. Cai, V. Shalaev, *Optical metamaterials*, (Springer, New York, 2010)
12. H.-T. Chen, J.F. O’Hara, A.K. Azad, A.J. Taylor, Manipulation of terahertz radiation using metamaterials. *Laser Photonics Rev.* **5**, 513–533 (2011)
13. L.D. Landau, E.M. Lifshitz, L.P. Pitaevskii, *Electrodynamics of Continuous Media*, (Butterworth-Heinemann, Oxford, 1984)
14. J.D. Jackson, *Classical electrodynamics* (Wiley, Hoboken, 1998)
15. J.C. Maxwell Garnett, Colours in metal glasses and in metallic films. *Phil. Trans. R. Soc.* **203**, 385–420 (1904)
16. D.A.G. Bruggeman, Calculation of various physics constants in heterogenous substances. *Annalen Der Physik* **24**, 636–664 (1935)
17. C. Brückner, T. Käsebier, B. Pradarutti, S. Riehemann, G. Notni, E.-B. Kley, A. Tünnermann, Broadband antireflective structures applied to high resistive float zone silicon in the THz spectral range. *Opt. Express* **17**, 3063–3077 (2009)
18. C. Kadlec, F. Kadlec, P. Kuzel, K. Blary, P. Mounaix, Materials with on-demand refractive indices in the terahertz range. *Opt. Lett.* **33**, 2275–2277 (2008)
19. S. Biber, D. Schneiderbanger, L.-P. Schmidt, Design of a controllable attenuator with high dynamic range for THz-frequencies based on optically stimulated free carriers in high-resistivity silicon. *Frequenz* **59**, 141–144 (2005)
20. Y.W. Chen, P.Y. Han, X.-C. Zhang, Three-dimensional inverted photonic grating with engineerable refractive indices for broadband antireflection of terahertz waves. *Opt. Lett.* **35**, 3159–3161 (2010)
21. Y. Zheng, A. Johnson, E. Pyde, K.J. Chau, Particle-size effects on the terahertz transmittance of metallic particle ensembles: comparison with effective medium theory. *Appl. Phys. Lett.* **96**, 211111 (2010)
22. H.-K. Nienhuys, V. Sundström, Influence of plasmons on terahertz conductivity measurements. *Appl. Phys. Lett.* **87**, 012101 (2005)
23. H. Nemeč, P. Kuzel, V. Sundström, Charge transport in nanostructured materials for solar energy conversion studied by time-resolved terahertz spectroscopy. *J. Photochem. Photobiol. A* **215**, 123–139 (2010)
24. E. Hendry, M. Koeberg, B. O’Regan, M. Bonn, Local field effects on electron transport in nanostructures TiO₂ revealed by terahertz spectroscopy. *Nano Lett.* **6**, 755–759 (2006)
25. K.J. Button, *Infrared and Millimeter Waves, Millimeter components and techniques*, Chap. 6, vol. 13 (Academic, New York, 1985), pp. 175–185

26. Y. Zheng, A. Johnson, E. Pyde, K.J. Chau, Particle-size effects on the terahertz transmittance of metallic particle ensembles: Comparison with effective medium theory. *Appl. Phys. Lett.* **96**, 211111 (2010)
27. M. Walther, D.G. Cooke, C. Sherstan, M. Hajar, M.R. Freeman, F.A. Hegmann, Terahertz conductivity of thin gold films at the metal-insulator percolation transition. *Phys. Rev. B* **76**, 125408 (2007)
28. G. Mie, Beiträge zur Optik trüber Medien, speziell kolloidaler Metallösungen. *Ann. Phys.* **25**, 376–445 (1908)
29. S. O'Brien, J.B. Pendry, Photonic band-gap effects and magnetic activity in dielectric composites. *J. Phys. Condens. Matter* **14**, 4035–4044 (2002)
30. V. Yannopoulos, A. Moroz, Negative refractive index metamaterials from inherently non-magnetic materials for deep infrared to terahertz frequency ranges. *J. Phys. Condens. Matter* **17**, 3717–3734 (2005)
31. H. Nemeč, P. Kuzel, F. Kadlec, C. Kadlec, R. Yahiaoui, and P. Mounaix, Tunable terahertz metamaterials with negative permeability. *Phys. Rev. B* **79**, 241108(R) (2009)
32. Q. Zhao, L. Kang, B. Du, H. Zhao, Q. Xie, X. Huang, B. Li, J. Zhou, L. Li, Experimental demonstration of isotropic negative permeability in a three-dimensional dielectric composite. *Phys. Rev. Lett.* **101**, 027402 (2008)
33. K. Vynck, D. Felbacq, E. Centeno, A.I. Cabuz, D. Cassagne, B. Guizal, All-dielectric rod-type metamaterials at optical frequencies. *Phys. Rev. Lett.* **102**, 133901 (2009)
34. A. Bitzer, J. Wallauer, H. Helm, H. Merbold, T. Feurer, M. Walther, Lattice modes mediate radiative coupling in metamaterial arrays. *Opt. Express* **17**, 22108–22113 (2009)
35. R. Singh, C. Rockstuhl, F. Lederer, W. Zhang, The impact of nearest neighbor interaction on the resonances in terahertz metamaterials. *Appl. Phys. Lett.* **94**, 021116 (2009)
36. D.R. Chowdhury, R. Singh, M. Reiten, J. Zhou, A.J. Taylor, J.F. O'Hara, Tailored resonator coupling for modifying the terahertz metamaterial response. *Opt. Express* **19**, 10679–10685 (2011)
37. M.N.O. Sadiku, *Numerical Techniques in Electromagnetics*, 2nd ed. (CRC Press LLC, Boca Raton, 2001)
38. <http://www.ansoft.com/>
39. <http://www.cst.com/>
40. J.B. Pendry, A. MacKinnon, Calculation of photon dispersion relations. *Phys. Rev. Lett.* **69**, 2772–2775 (1992)
41. J.B. Pendry, Photonic band structures. *J. Mod. Opt.* **41**, 209–229 (1994)
42. P. Markoš, C.M. Soukoulis, Numerical studies of left-handed materials and arrays of split ring resonators. *Phys. Rev. E* **65**, 036622 (2002)
43. D.R. Smith, S. Schultz, P. Markoš, C.M. Soukoulis, Determination of effective permittivity and permeability of metamaterials from reflection and transmission coefficients. *Phys. Rev. B* **65**, 195104 (2002)
44. S. Zhang, W. Fan, K.J. Malloy, S.R. Brueck, N.C. Panoiu, R.M. Osgood, Near-infrared double negative metamaterials. *Opt. Express* **13**, 4922–4930 (2005)
45. M.G. Maharam, T.K. Gaylord, Rigorous coupled-wave analysis of planar-grating diffraction. *J. Opt. Soc. Am.* **71**, 811–818 (1981)
46. T.F. Gundogdu, N. Katsarakis, M. Kafesaki, R.S. Penciu, G. Konstantinidis, A. Kostopoulos, E.N. Economou, C.M. Soukoulis, Negative index short-slab pair and continuous wires metamaterials in the far infrared regime. *Opt. Express* **16**, 9173–9180 (2008)
47. N. Katsarakis, G. Konstantinidis, A. Kostopoulos, R.S. Penciu, T.F. Gundogdu, M. Kafesaki, E.N. Economou, Th Koschny, C.M. Soukoulis, Magnetic response of split-ring resonators in the far-infrared frequency regime. *Opt. Lett.* **30**, 1348–1350 (2005)
48. W.J. Padilla, D.R. Smith, D.N. Basov, Spectroscopy of metamaterials from infrared to optical frequencies. *J. Opt. Soc. Am. B* **23**, 404–414 (2006)
49. T.F. Gundogdu, I. Tsiapa, A. Kostopoulos, G. Konstantinidis, N. Katsarakis, R.S. Penciu, M. Kafesaki, E.N. Economou, Th Koschny, C.M. Soukoulis, Experimental demonstration of negative magnetic permeability in the far-infrared frequency regime. *Appl. Phys. Lett.* **89**, 084103 (2006)

50. T. Driscoll, G.O. Andreev, D.N. Basov, S. Palit, T. Ren, J. Mock, S.-Y. Cho, N.M. Jokerst, D.R. Smith, Quantitative investigation of a terahertz artificial magnetic resonance using oblique angle spectroscopy. *Appl. Phys. Lett.* **90**, 092508 (2007)
51. Y. Minowa, T. Fujii, M. Nagai, T. Ochiai, K. Sakoda, K. Hirao, K. Tanaka, Evaluation of effective electric permittivity and magnetic permeability in metamaterial slabs by terahertz time-domain spectroscopy. *Opt. Express* **16**, 4785–4796 (2008)
52. M. Awad, M. Nagel, H. Kurz, Negative-index metamaterial with polymer-embedded wire-pair structures at terahertz frequencies. *Opt. Lett.* **33**, 2683–2685 (2008)
53. A. Bitzer, H. Merbold, A. Thoman, T. Feurer, H. Helm, M. Walther, Terahertz near-field imaging of electric and magnetic resonances of a planar metamaterial. *Opt. Express* **17**, 3826–3834 (2009)
54. Ch. Menzel, C. Rockstuhl, F. Lederer, Advanced Jones calculus for the classification of periodic metamaterials. *Phys. Rev. A* **82**, 053811 (2010)
55. R. Singh, E. Plum, C. Menzel, C. Rockstuhl, A.K. Azad, R.A. Cheville, F. Lederer, W. Zhang, N.I. Zheludev, Terahertz metamaterial with asymmetric transmission. *Phys. Rev. B* **80**, 153104 (2009)
56. D.R. Smith, D.C. Vier, Th Koschny, C.M. Soukoulis, Electromagnetic parameter retrieval from inhomogeneous metamaterials. *Phys. Rev. E* **71**, 036617 (2005)
57. T. Driscoll, D.N. Basov, W.J. Padilla, J.J. Mock, D.R. Smith, Electromagnetic characterization of planar metamaterials by oblique spectroscopic measurements. *Phys. Rev. B* **75**, 115114 (2007)
58. A. Pashkin, M. Kempa, H. Nemeč, F. Kadlec, P. Kužel, Phase-sensitive time-domain terahertz reflection spectroscopy. *Rev. Sci. Instrum.* **74**, 4711–4717 (2003)
59. L. Duvillaret, F. Garet, J.-L. Coutaz, A Reliable Method for Extraction of Material Parameters in Terahertz Time-Domain Spectroscopy. *IEEE J. Sel. Top. Quantum Electron.* **2**, 739–746 (1996)
60. H. Nemeč, F. Kadlec, P. Kužel, L. Duvillaret, J.-L. Coutaz, Independent determination of the complex refractive index and wave impedance by time-domain terahertz spectroscopy. *Opt. Commun.* **260**, 175–183 (2006)
61. P. Uhd Jepsen, D.G. Cooke, M. Koch, Terahertz spectroscopy and imaging - Modern techniques and applications. *Laser Photon. Rev.* **5**, 124–166 (2011)
62. W.J. Padilla, M.T. Aronsson, C. Highstrete, M. Lee, A.J. Taylor, R.D. Averitt, Electrically resonant terahertz metamaterials: Theoretical and experimental investigations. *Phys. Rev. B* **75**, 041102 (2007)
63. M.A. Seo, A.J.L. Adam, J.H. Kang, J.W. Lee, S.C. Jeoung, Q.H. Park, P.C.M. Planken, D.S. Kim, Fourier-transform terahertz near-field imaging of one-dimensional slit arrays: mapping of electric-field-, magnetic-field-, and Poynting vectors. *Opt. Express* **15**, 11781–11789 (2007)
64. A.K. Azad, J. Dai, W. Zhang, Transmission properties of terahertz pulses through subwavelength double split-ring resonators. *Opt. Lett.* **31**, 634–636 (2006)
65. W.J. Padilla, M.T. Aronsson, C. Highstrete, M. Lee, A.J. Taylor, R.D. Averitt, Electrically resonant terahertz metamaterials: theoretical and experimental investigations. *Phys. Rev. B* **75**, 041102(R) (2007)
66. H.-T. Chen, S. Palit, T. Tyler, C.M. Bingham, J.M.O. Zide, J.F. O'Hara, D.R. Smith, A.C. Gossard, R.D. Averitt, W.J. Padilla, N.M. Jokerst, A.J. Taylor, Hybrid metamaterials enable fast electrical modulation of freely propagating terahertz waves. *Appl. Phys. Lett.* **93**, 091117 (2008)
67. H.-T. Chen, H. Lu, A.K. Azad, R.D. Averitt, A.C. Gossard, S.A. Trugman, J. F. O'Hara, and A. J. Taylor, Electronic control of extraordinary terahertz transmission through subwavelength metal hole arrays. *Opt. Express* **16**, 7641–7648 (2008)
68. D. Wu, N. Fang, C. Sun, X. Zhang, Terahertz plasmonic high pass filter. *Appl. Phys. Lett.* **83**, 201–203 (2003)
69. H. Tao, A.C. Strikwerda, K. Fan, W.J. Padilla, X. Zhang, R.D. Averitt, Reconfigurable terahertz metamaterials. *Phys. Rev. Lett.* **103**, 147401 (2009)

70. M. Aznabet, M. Navarro-Cía, S.A. Kuznetsov, A.V. Gelfand, N.I. Fedorinina, YuG Goncharov, M. Beruete, O. El Mrabet, M. Sorolla, Polypropylene-substrate-based SRR- and CSRR- meta-surfaces for submillimeter waves. *Opt. Express* **16**, 18312–18319 (2008)
71. H. Tao, A.C. Strikwerda, K. Fan, C.M. Bingham, W.J. Padilla, X. Zhang, R.D. Averitt, Terahertz metamaterials on free-standing highly-flexible polyimide substrates. *J. Phys. D: Appl. Phys.* **41**, 232004 (2008)
72. X. Liu, S. MacNaughton, D.B. Shrekenhamer, H. Tao, S. Selvarasah, A. Totachawattana, R.D. Averitt, M.R. Dokmeci, S. Sonkusale, W.J. Padilla, Metamaterials on parylene thin film substrates: Design, fabrication, and characterization at terahertz frequency. *Appl. Phys. Lett.* **96**, 011906 (2010)
73. H. Tao, J.J. Amsden, A.C. Strikwerda, K. Fan, D.L. Kaplan, X. Zhang, R.D. Averitt, F.G. Omenetto, Metamaterial silk composites at terahertz frequencies. *Adv. Mater.* **22**, 3527–3531 (2010)
74. N.R. Han, Z.C. Chen, C.S. Lim, B. Ng, M.H. Hong, Broadband multi-layer terahertz metamaterials fabrication and characterization on flexible substrates. *Opt. Express* **19**, 6990–6998 (2011)
75. H.O. Moser, J.A. Kong, L.K. Jian, H.S. Chen, G. Liu, M. Bahou, S.M.P. Kalaiselvi, S.M. Maniam, X.X. Cheng, B.I. Wu, P.D. Gu, A. Chen, S.P. Heussler, S. bin Mahnood, and L. Wen, Free-standing THz electromagnetic metamaterials. *Opt. Express* **16**, 13773–13780 (2008)
76. B.D.F. Casse, H.O. Moser, J.W. Lee, M. Bahou, S. Inglis, L.K. Jian, Towards three-dimensional and multilayer rod-split-ring metamaterial structures by means of deep x-ray lithography. *Appl. Phys. Lett.* **90**, 254106 (2007)
77. S. Linden, C. Enkrich, M. Wegener, J. Zhou, T. Koschny, C.M. Soukoulis, Magnetic response of metamaterials at 100 terahertz. *Science* **306**, 1351–1353 (2004)
78. H.-T. Chen, J.F. O'Hara, A.K. Azad, A.J. Taylor, R.D. Averitt, D.B. Shrekenhamer, W.J. Padilla, Experimental demonstration of frequency-agile terahertz metamaterials. *Nature Photon.* **2**, 295–298 (2008)
79. S.C. Saha, Y. Ma, J.P. Grant, A. Khalid, D.R.S. Cumming, Imprinted terahertz artificial dielectric quarter wave plates. *Opt. Express* **18**, 12168–12175 (2010)
80. H.O. Moser, B.D.F. Casse, O. Wilhelmi, B.T. Saw, Terahertz response of a microfabricated rod-split-ring-resonator electromagnetic metamaterial. *Phys. Rev. Lett.* **94**, 063901 (2005)
81. M.S. Rill, C. Plet, M. Thiel, I. Staude, G. von Freymann, S. Linden, M. Wegener, Photonic metamaterials by direct laser writing and silver chemical vapour deposition. *Nature Mat.* **7**, 543–546 (2008)
82. S.Y. Chiam, R. Singh, C. Rockstuhl, F. Lederer, W. Zhang, A.A. Bettiol, Analogue of electromagnetically induced transparency in a terahertz metamaterial. *Phys. Rev. B* **80**, 153103 (2009)
83. R. Yahiaoui, H. Nemeč, P. Kuzel, F. Kadlec, C. Kadlec, P. Mounaix, Broadband dielectric terahertz metamaterials with negative permeability. *Opt. Lett.* **34**, 3541 (2009)
84. C. Kang, C.-S. Kee, I.-B. Sohn, J. Lee, Characterization of terahertz wave transmission through complementary metamaterials with split ring resonator arrays, in *Abstracts from 34th International conference on Infrared, Millimeter, and Terahertz Waves* (Busan, South Korea, 2009), pp. 767–768
85. T. Kondo, T. Nagashima, M. Hangyo, Fabrication of wire-grid-type polarizers for THz region using a general-purpose color printer. *Jpn. J. Appl. Phys. Part 2* (42), L373–L375 (2003)
86. K. Takano, T. Kawabata, C.-F. Hsieh, K. Akiyama, F. Miyamaru, Y. Abe, Y. Tokuda, R.-P. Pan, C.-L. Pan, M. Hangyo, Fabrication of terahertz planar metamaterials using a super-fine ink-jet printer. *Appl. Phys. Express* **3**, 016701 (2010)
87. M. Walthers, A. Ortner, H. Meier, U. Löffelmann, P.J. Smith, J.G. Korvink, Terahertz metamaterials fabricated by inkjet printing. *Appl. Phys. Lett.* **95**, 251107 (2009)
88. K. Takano, K. Shibuya, K. Akiyama, T. Nagashima, F. Miyamaru, M. Hangyo, A metal-to-insulator transition in cut-wire-grid metamaterials in the terahertz region. *J. Appl. Phys.* **107**, 024907 (2010)

89. D.A. Pawlak, S. Turczynski, M. Gajc, K. Kolodziejak, R. Diduszko, K. Rozniatowski, J. Smalc, I. Vendik, How far are we from making metamaterials by self-organization? The microstructure of highly anisotropic particles with an SRR-like geometry. *Adv. Funct. Mater.* **20**, 1116–1124 (2010)
90. S. Zhang, W. Fan, B.K. Minhas, A. Frauenglass, K.J. Malloy, S.R.J. Brueck, Fabrication of 1D and 2D vertical nanomagnetic resonators. *J. Vac. Sci. Tech. B* **22**, 3327–3330 (2004)
91. A. Tuniz, B.T. Kuhlmeier, R. Lwin, A. Wang, J. Anthony, R. Leonhardt, S.C. Fleming, Drawn metamaterials with plasmonic response at terahertz frequencies. *Appl. Phys. Lett.* **96**, 191101 (2010)
92. F. Miyamaru, M. Wada Takeda, K. Taima, Characterization of terahertz metamaterials fabricated on flexible plastic films: toward fabrication of bulk metamaterials in terahertz region. *Appl. Phys. Express* **2**, 042001 (2009)
93. F. Miyamaru, S. Kuboda, K. Taima, K. Takano, M. Hangyo, M. Wada Takeda, Three-dimensional bulk metamaterials operating in the terahertz range. *Appl. Phys. Lett.* **93**, 081105 (2010)
94. Q.-Y. Wen, H.-W. Zhang, Q.-H. Yang, Y.-S. Xie, K. Chen, Y.-L. Liu, Terahertz metamaterials with VO₂ cut-wires for thermal tunability. *Appl. Phys. Lett.* **97**, 021111 (2010)
95. Y.W. Chen, P.Y. Han, X.-C. Zhang, Tunable broadband antireflection structures for silicon at terahertz frequency. *Appl. Phys. Lett.* **94**, 041106 (2009)
96. S. Zhang, Y.-S. Park, J. Li, X. Lu, W. Zhang, X. Zhang, Negative refractive index in chiral metamaterials. *Phys. Rev. Lett.* **102**, 023901 (2009)
97. A. Pimenov, A. Loidl, Experimental demonstration of artificial dielectrics with a high index of refraction. *Phys. Rev. B* **74**, 193102 (2006)
98. C.R. Williams, S.R. Andrews, S.A. Maier, A.I. Fernández-Domínguez, L. Martín-Moreno, F.J. García-Vidal, Highly confined guiding of terahertz surface plasmon polaritons on structured metal surfaces. *Nature Photon.* **2**, 175–179 (2008)
99. Q. Gan, Z. Fu, Y.J. Ding, F.J. Bartoli, Ultrawide-bandwidth slow-light system based on THz plasmonic graded metallic grating structures. *Phys. Rev. Lett.* **100**, 256803 (2008)
100. A. Ishikawa, S. Zhang, D.A. Genov, G. Bartal, X. Zhang, Deep subwavelength terahertz waveguides using gap magnetic plasmon. *Phys. Rev. Lett.* **102**, 043904 (2009)
101. J. Lee, K. Lee, H. Park, G. Kang, D.-H. Yu, K. Kim, Tunable subwavelength focusing with dispersion-engineered metamaterials in the terahertz regime. *Opt. Lett.* **35**, 2254–2256 (2010)
102. F. Miyamaru, S. Kuboda, K. Taima, K. Takano, M. Hangyo, M.W. Takeda, Three-dimensional bulk metamaterials operating in the terahertz range. *Appl. Phys. Lett.* **96**, 081105 (2010)
103. K. Fan, A.C. Strikwerda, H. Tao, X. Zhang, R.D. Averitt, 3D Stand-up Metamaterials with a Purely Magnetic Resonance at Terahertz Frequencies, in *Proceeding of the 30th Conference on Lasers and Electro-Optics / International Quantum Electronics and Laser Science Conference (CLEO/QELS '10)*, San Jose, CA, USA, CTuF1, 18–20 May 2010
104. K. Fan, A.C. Strikwerda, H. Tao, X. Zhang, R.D. Averitt, Stand-up magnetic metamaterials at terahertz frequencies. *Opt. Express* **19**, 12619–12627 (2011)
105. C.M. Soukoulis, J. Zhou, T. Koschny, M. Kafesaki, E.N. Economou, The science of negative index materials. *J. Phys. Condens. Matter* **20**, 304217 (2008)
106. J. Carbonell, C. Croënne, F. Garet, E. Lheurette, J.L. Coutaz, D. Lippens, Lumped elements circuit of terahertz fishnet-like arrays with composite dispersion. *J. Appl. Phys.* **108**, 014907 (2010)
107. Q. Zhao, J. Zhou, F. Zhang, D. Lippens, Mie resonance-based dielectric metamaterials. *Mat. Today* **12**, 60–69 (2009)
108. P. Kuzel, H. Nemeč, F. Kadlec, Highly tunable structures for the THz range based on strontium titanate heterostructures and metamaterials, in *Proceedings of 2nd International Congress on Advanced Electromagnetic Materials in Microwaves and Optics* (Pamplona, Spain, September, 2008), pp. 21–26
109. K. Shibuya, K. Takano, N. Matsumoto, K. Izumi, H. Miyazaki, Y. Jimba, M. Hangyo, Terahertz metamaterials composed of TiO₂ cube arrays, in *Proceedings of 2nd International Congress on Advanced Electromagnetic Materials in Microwaves and Optics* (Pamplona, Spain, September, 2008), pp. 21–26

110. P. Kuzel, F. Kadlec, Tunable structures and modulators for THz light. *Comptes Rendus Physique* **9**, 197–214 (2008)
111. W.L. Chan, H.-T. Chen, A.J. Taylor, I. Brener, M.J. Cich, A spatial light modulator for terahertz beams. *Appl. Phys. Lett.* **94**, 213511 (2009)
112. H.-T. Chen, J.F. O'Hara, A.J. Taylor, R.D. Averitt, C. Highstrete, M. Lee, W.J. Padilla, Complementary planar terahertz metamaterials. *Opt. Express* **15**, 1084–1095 (2007)
113. A.K. Azad, A.J. Taylor, E. Smirnova, J.F. O'Hara, Characterization and analysis of terahertz metamaterials based on rectangular split-ring resonators. *Appl. Phys. Lett.* **92**, 011119 (2008)
114. H.-T. Chen, W.J. Padilla, M.J. Cich, A.K. Azad, R.D. Averitt, A.J. Taylor, A metamaterial solid-state terahertz phase modulator. *Nature Photon.* **3**, 148–151 (2009)
115. O. Paul, C. Imhof, B. Lagel, S. Wolff, J. Heinrich, S. Hofling, A. Forchel, R. Zengerle, R. Beigang, M. Rahm, Polarization-independent active metamaterial for high-frequency terahertz modulation. *Opt. Express* **17**, 819–827 (2009)
116. W.J. Padilla, A.J. Taylor, C. Highstrete, M. Lee, R.D. Averitt, Dynamical electric and magnetic metamaterial response at terahertz frequencies. *Phys. Rev. Lett.* **96**, 107401 (2006)
117. H.-T. Chen, W.J. Padilla, J.M.O. Zide, S.R. Bank, A.C. Gossard, A.J. Taylor, R.D. Averitt, Ultrafast optical switching of terahertz metamaterials fabricated on ErAs/GaAs nanoislands superlattices. *Opt. Lett.* **32**, 1620–1622 (2007)
118. C. Kadow, S.B. Fleischer, J.P. Ibbetson, J.E. Bowers, A.C. Gossard, J.W. Dong, C.J. Palmstrom, Self-assembled ErAs islands in GaAs: Growth and subpicosecond carrier dynamics. *Appl. Phys. Lett.* **75**, 3548 (1999)
119. Y. Shi, Q. Zhou, W. Liu, J. Liu, C. Zhang, Anomalous transmission of terahertz waves in arrays of double-ring resonators induced by a 400 nm pump pulse. *Appl. Phys. Lett.* **98**, 191112 (2011)
120. J.-M. Manceau, N.-H. Shen, M. Kafesaki, C.M. Soukoulis, S. Tzortzakis, Dynamics response of metamaterials in the terahertz regime: blueshift tunability and broadband phase modulation. *Appl. Phys. Lett.* **96**, 021111 (2010)
121. N.-H. Shen, M. Kafesaki, T. Koschny, L. Zhang, E.N. Economou, C.M. Soukoulis, Broadband blueshift tunable metamaterials and dual-band switches. *Phys. Rev. B* **79**, 161102(R) (2009)
122. Y. Yuan, C. Bingham, T. Tyler, S. Palit, T.H. Hand, W.J. Padilla, N.M. Jokerst, S.A. Cummer, A dual-resonant terahertz metamaterial based on single-particle electric-field-coupled resonators. *Appl. Phys. Lett.* **93**, 191110 (2008)
123. T. Driscoll, G.O. Andreev, D.N. Basov, S. Palit, S.Y. Cho, N.M. Jokerst, D.R. Smith, Tuned permeability in terahertz split-ring resonators for devices and sensors. *Appl. Phys. Lett.* **91**, 062511 (2007)
124. P. Kuzel, F. Kadlec, H. Nemecek, R. Ott, E. Hollmann, N. Klein, Dielectric tunability of SrTiO₃ thin films in the terahertz range. *Appl. Phys. Lett.* **88**, 102901 (2006)
125. C. Kadlec, V. Skoromets, F. Kadlec, H. Nemecek, J. Hlinka, J. Schubert, G. Panaitov, P. Kuzel, Temperature and electric field tuning of the ferroelectric soft mode in a strained SrTiO₃/DyScO₃ heterostructure. *Phys. Rev. B* **80**, 174116 (2009)
126. R. Singh, A.K. Azad, Q.X. Jia, A.J. Taylor, H.-T. Chen, Thermal tunability in terahertz metamaterials fabricated on strontium titanate single-crystal substrates. *Opt. Lett.* **36**, 1230–1232 (2011)
127. J. Wu, B. Jin, Y. Xue, C. Zhang, H. Dai, L. Zhang, C. Cao, L. Kang, W. Xu, J. Chen, P. Wu, Tuning of superconducting niobium nitride terahertz metamaterials. *Opt. Express* **19**, 12021–12026 (2011)
128. G. He, R.-X. Wu, Y. Poo, P. Chen, Magnetically tunable double-negative material composed of ferrite-dielectric and metallic mesh. *J. Appl. Phys.* **107**, 093522 (2010)
129. B. Ozbey, O. Aktas, Continuously tunable terahertz metamaterial employing magnetically actuated cantilevers. *Opt. Express* **19**, 5741–5752 (2011)
130. H. Tao, N.I. Landy, C.M. Bingham, X. Zhang, R.D. Averitt, W.J. Padilla, A metamaterial absorber for the terahertz regime: design, fabrication and characterization. *Opt. Express* **16**, 7181–7188 (2008)

131. H. Tao, C.M. Bingham, A. C. Strikwerda, D. Pilon, D. Shrekenhamer, N.I. Landy, K. Fan, X. Zhang, W. J. Padilla, R. D. Averitt, Highly flexible wide angle of incidence terahertz metamaterial absorber: design, fabrication and characterization. *Phys. Rev. B* **78**, 541103(R) (2008)
132. N.I. Landy, C.M. Bingham, T. Tyler, N. Jokerts, D.R. Smith, W.J. Padilla, Design, theory, and measurement of a polarization-insensitive absorber for terahertz imaging. *Phys. Rev. B* **79**, 125104 (2009)
133. J. Grant, Y. Ma, S. Saha, L.B. Lok, A. Khalid, D.R.S. Cumming, Polarization insensitive terahertz metamaterial absorber. *Opt. Lett.* **36**, 1524–1526 (2011)
134. J. Zhang, P.A.R. Ade, P. Mauskopf, L. Moncelsi, G. Savini, N. Whitehouse, New artificial dielectric metamaterial and its application as a terahertz antireflection coating. *Appl. Opt.* **48**, 6635–6642 (2009)
135. X.G. Peralta, E.I. Smirnova, A.K. Azad, H.-T. Chen, A.J. Taylor, I. Brener, J.F. O’Hara, Metamaterials for THz polarimetric devices. *Opt. Express* **17**, 774–783 (2009)
136. A.C. Strikwerda, K. Fan, H. Tao, D.V. Pilon, X. Zhang, R.D. Averitt, Comparison of birefringent electric split-ring resonator and meanderline structures as quarter-wave plates at terahertz frequencies. *Opt. Express* **17**, 136–149 (2009)
137. P. Weis, O. Paul, C. Imhof, R. Beigang, M. Rahm, Strongly birefringent metamaterials as negative index terahertz wave plates. *Appl. Phys. Lett.* **95**, 171104 (2009)
138. I.A.I. Al-Naib, C. Jansen, N. Born, M. Koch, Polarization and angle independent terahertz metamaterials with high Q-factors. *Appl. Phys. Lett.* **98**, 091107 (2011)
139. L.V. Hau, S.E. Harris, Z. Dutton, C.H. Behroozi, Light speed reduction to 17 metres per second in an ultracold atomic gas. *Nature* **397**, 594 (1999)
140. K.L. Tsakmakidis, A.D. Boardman, O. Hess, Trapped rainbow storage of light in metamaterials. *Nature* **450**, 397–401 (2007)
141. P.R. Berman, Goos-Hänchen shift in negatively refractive media. *Phys. Rev. E* **66**, 067603 (2002)

Chapter 23

THz Control in Correlated Electron Solids: Sources and Applications

M. Först, M. C. Hoffmann, A. Dienst, S. Kaiser, M. Rini, R.I. Tobey,
M. Gensch, C. Manzoni and A. Cavalleri

Abstract Materials with strongly correlated electrons often show rich phase diagrams with dramatic differences in physical properties as doping, applied pressure, or magnetic fields are changed. Even subtle perturbations can cause colossal rearrangements in the electronic spectrum, and irradiation with light can be used to drive spectacular rearrangements in the structural, electronic, and magnetic properties. Here, we discuss the use of THz radiation to selectively excite one single degree of freedom at a time to drive a phase change. This is in contrast to what is done in most studies, which achieve photo-induced phase transitions by non-specific excitation in the visible spectral range. This chapter will combine a summary of developments in instrumentation for strong THz fields with some selected scientific applications of THz control of correlated electron systems.

M. Först · M. C. Hoffmann · S. Kaiser · A. Cavalleri (✉)
Max Planck Department for Structural Dynamics,
University of Hamburg - CFEL,
Hamburg, Germany
e-mail: andrea.cavalleri@mpsd.cfel.de

A. Dienst · A. Cavalleri
Department of Physics, Clarendon Laboratory,
University of Oxford, Oxford, UK

M. Rini
Joint Research Centre, European Commission, Karlsruhe, Germany

R.I. Tobey
Optical Condensed Matter Physics, Zernike Institute for Advanced Materials,
University of Groningen, Groningen, The Netherlands

M. Gensch
Helmholtz-Zentrum Dresden-Rossendorf, Dresden, Germany

C. Manzoni
Istituto di Fotonica e Nanotecnologie (IFN) - CNR,
Dipartimento di Fisica, Politecnico di Milano, Milan, Italy

23.1 Introduction

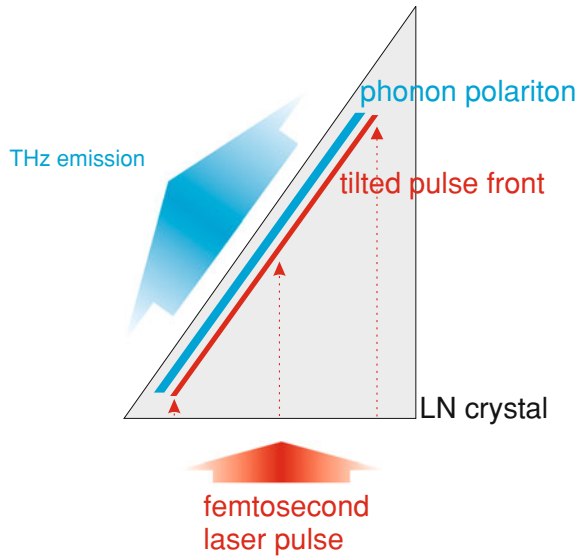
Photo-induced phase transitions are a frontier field in the study of light–matter interaction. In a solid, stimulation with high photon density light can perturb a stable ground state and induce transient metastable phases, often not found near equilibrium. The concept of a photo-induced phase transition is not rigorously defined, but here we refer to any light-simulated non-equilibrium process in which at least one *order parameter* changes. Order may be connected to atomic structural or magnetic symmetries, superconducting or charge-density-wave order or any other type of order that is well-defined near equilibrium. Typically, the states of matter reached through photo-stimulations are also metastable, as they are protected by free energy barriers that make return to the ground state slow, not limited by heat dissipation alone but by cooperative kinetics such as nucleation and growth. Photo-induced phase transitions, as broadly defined above, cover laser-induced melting in semiconductors [1–4], metals [5], semimetals [6, 7], and carbon-based compounds [8–10] and photo-induced dynamics in strongly correlated electron systems.

Solids with strongly correlated electrons are those in which electron–electron interactions, are not any more a perturbation on their kinetic energy, but are comparable or higher and dictate the choice of ground state [11]. Even subtle perturbations in charge occupancy, by chemical doping [12] or excitation with light [13], then cause colossal rearrangements in the electronic spectrum, coupled to the atomic arrangements through electron–phonon coupling. We mention studies of photo-induced phase transitions in magnetoresistive manganites [14–22], non-magnetic oxides like VO₂ [23–32], organic salts [33, 34], charge-density wave dichalcogenites [35–38] or cuprate superconductors [39–43].

In this chapter we focus on one significant new development [44–46], the use of intense mid-infrared or THz pulses to drive phase transitions. As opposed to using eV energy scale excitations, THz radiation can be used to selectively excite one single degree of freedom on low energy scales and to drive a phase change. We will combine a summary of developments in instrumentation with some selected scientific applications. Most of the applications discussed here have been driven by the authors of this work.

The chapter is organized as follows. In Sect. 23.2, we discuss characteristics and generating methods for high-intensity pulses near 1 THz. One application of such pulses is discussed in Sect. 23.2.2, in which the properties of high temperature (high T_c) superconductors are gated at ultrahigh speeds. In Sect. 23.3 we report on the use of mid-infrared radiation to drive bonds in magnetoresistive manganites selectively. A new technique by which high-intensity mid-infrared pulses are generated with a stable carrier envelope phase (CEP) is used to clarify the microscopic mechanism of such nonlinear vibrational control. Finally, we discuss the developments in new sources based on radiation from relativistic electrons.

Fig. 23.1 Schematic for high intensity single cycle THz generation using the tilted-pulse-front technique. Phase matching is achieved by tilting the phase front of the near-infrared pulse, ensuring overlap of the intensity front with the THz field over long distances



23.2 Quantum Phase Control with High-Field THz Pulses

23.2.1 High-Field Single-Cycle Terahertz Pulses: Generation

While broadband single-cycle THz pulses in free space have been available for more than 20 years [47], their pulse energies have typically been far too small to observe nonlinear responses. In this section we will provide an overview of generation methods of intense single-cycle pulses. More detailed discussion can be found in Chap. 14 of this book and in the literature [48].

Optical rectification of mJ-energy femtosecond laser pulses via the tilted-pulse front technique [49] can be used to generate intense THz single-cycle pulses with energies of tens of microJoules and peak field strengths of several hundred kV/cm [50]. This technique is based on the high nonlinear coefficient on stoichiometric LiNbO_3 .

Compared to other nonlinear materials like ZnTe and GaSe this material takes the advantage of having a very large band gap and a high damage threshold. However, due to the large mismatch between optical group index and THz refractive index, efficient phase matching for optical rectification is not possible in this material. To achieve efficient THz output, it is necessary to introduce a noncollinear phase matching scheme by tilting the normal of the intensity front of the femtosecond laser relative to the propagation direction (see Fig. 23.1). For LiNbO_3 the required tilt angle is approximately 63° and can be obtained by using a combination of a reflection grating with an imaging system such as a telescope or lens. The tilted pulse front propagates inside the lithium niobate, and builds up a phonon-polariton

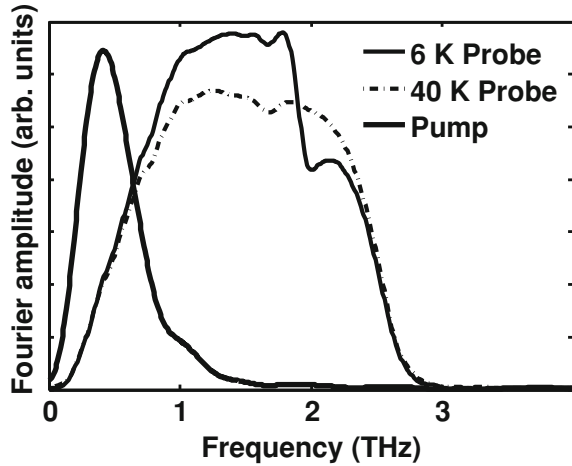
wave [51, 52], which is coherently amplified while being driven by the femtosecond laser. Photorefractive damage in the material can be minimized by using magnesium-oxide doping. The spectrum of the resulting THz pulses extends to about 3 THz and is limited by the intrinsic material absorption of LiNbO_3 close to the lowest optical phonon frequency. The spectral peak is determined by the laser pulse duration and is usually between 0.4 and 1.0 THz. The overall THz generation efficiency can reach values of 10^{-3} . When focused to a diameter of about 1 mm, field peak field strengths of several 100 kV/cm can be achieved.

Another promising technique to obtain single-cycle THz pulses with high field strengths using femtosecond lasers is the generation by nonlinear processes in gas plasmas. THz generation in plasmas has the advantages that there is no damage threshold for the emitter, since the gas target is continuously replenishable, and that the available bandwidth of the THz pulses is essentially limited only by the duration of the pump laser pulse, since no material absorption like optical phonons need to be considered. A large increase in efficiency for THz generation in plasmas was achieved in 2000 by Cook and coworkers [53] through mixing of femtosecond pulses with center frequency ω with their second harmonic at 2ω within the gas plasma. In 2007, Kim et al. reported on pump-to-THz conversion efficiencies exceeding 1×10^{-4} and pulse energies up to $5 \mu\text{J}$ [54]. Ultrabroadband THz pulses containing frequencies up to 100 THz has been demonstrated recently by Thomson by using 19 fs laser pulses [55].

23.2.2 Nonlinear Interlayer Coupling in High T_c Superconductors

Cuprates near optimal doping consist of superconducting planes separated by dielectric layers, forming stacks of intrinsic Josephson junctions and underpinning three-dimensional superconducting transport. The combination of tunneling, which has an equivalent inductive impedance, and capacitive coupling between the planes, leads to collective plasma oscillations of superconducting electrons at terahertz (THz) frequencies, which are typically referred to as Josephson plasma waves [56]. These long-lived, weakly damped oscillations occur because the resistive impedance from non-condensed quasi-particles is, near equilibrium, shorted by the inductor, resulting in LC interlayer electrostatics. Because incident electromagnetic fields couple to the Josephson plasmon, THz spectroscopy provides a useful tool for time- and frequency-domain studies [57, 58]. The plasma wave frequency ω_p near equilibrium is determined by the inductance L and capacitance C , determined by the tunneling and the stacked layers, respectively. The tunneling strength can be modulated by the application of an external magnetic field or voltage [59, 60], possible because tunneling across a weak link depends on the order-parameter phase difference φ between the two superconductors, which is affected by application of external fields [61, 62]. To achieve this effect on the ultrafast timescale, interlayer voltage drops of few to tens of mV are needed, corresponding to THz-frequency transients with peak electric fields of tens of kV/cm.

Fig. 23.2 Fourier amplitude of THz traces reflected from the sample above and below the transition temperature (*thin dashed-dotted and solid curves*). The pump spectrum is shown in comparison as a *thick solid line*



THz pump–THz probe experiments were conducted on $\text{La}_{1.84}\text{Sr}_{0.16}\text{CuO}_4$, an optimally doped compound with $T_C = 36$ K. The sample was excited with high-intensity THz pulses tuned to 400 GHz, well below the 2-THz Josephson plasma resonance.

The peak field reached 100 kV/cm. The pump or gate field, polarized along the c -axis, modulates the quantum mechanical phase difference between adjacent layers, strongly perturbing interlayer coupling between the planes. Probing was achieved with low-fluence pulses generated by optical rectification and detected by electrooptic sampling in Zinc Telluride (ZnTe). Figure 23.2 shows the Fourier amplitude of THz probe traces reflected from equilibrium $\text{La}_{1.84}\text{Sr}_{0.16}\text{CuO}_4$ above and below the transition temperature, representing the development of a frequency-domain plasma edge below T_C for light polarized parallel to the c -axis. The incoming field was also recorded after reflection from a gold-coated portion of the sample.

From the static reflectivity of $\text{La}_{1.84}\text{Sr}_{0.16}\text{CuO}_4$ the complex frequency-dependent c -axis dielectric function $\varepsilon(\omega)$ was extracted by fitting with the two-fluid model [63].

Single-cycle pump pulses centered at 400 GHz were generated by tilted-pulse-front excitation in Lithium Niobate (LiNbO_3), as discussed in Sect. 23.2.1. Pump-probe experiments were performed at 6 K with the pump polarization parallel to the c -axis and field strengths of approximately 100 kV/cm. To extract the transient frequency-dependent dielectric function $\varepsilon(\omega)$ for different pump-probe time delays τ , the amplitude- and phase-resolved probe traces were investigated with a model that considered surface layer of unknown conductivity, over an unperturbed semi-infinite superconductor with the equilibrium optical properties.

The physics of Josephson plasma waves is encapsulated in the loss function, defined as $-\text{Im}(1/\varepsilon(\omega))$. This quantity has a Lorentzian shape and is centered at the Josephson plasma frequency, with a width that is related to damping. The contour plot in Fig. 23.3 depicts the frequency-dependent loss function measured in our experiments as a function of pump-probe time delay.

Fig. 23.3 Contour plot of normalized frequency-dependent loss function as a function of pump-probe time delay τ

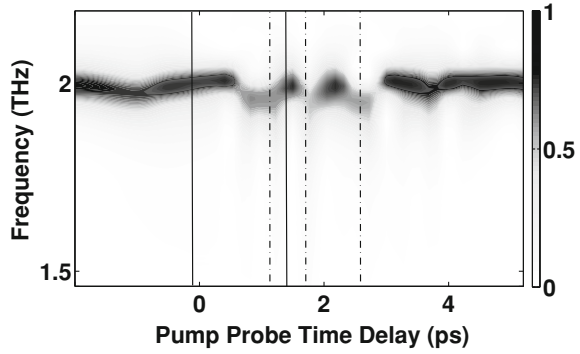
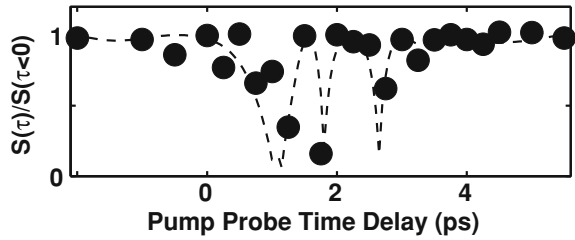


Fig. 23.4 Superconductive transport strength evaluated from experimental data with a fit based on the measured pump field (*dashed line*)



At positive time delays the peak is strongly reduced and shifts toward lower frequencies, indicating a weakening in the plasmonic response. In Fig. 23.4 we display the time-dependent strength of c -axis superconducting transport (dots), evaluated as $S(t) = \lim_{\omega \rightarrow 0} \omega \text{Im}(\sigma(\omega, \tau))$, with σ being the optical conductivity. At equilibrium, this quantity is proportional to the superfluid density ρ_S [64], reflecting interlayer coupling strength in the present case.

To model our experimental observations, we consider the Josephson inductance $L = h/(2eI_C \cos(\varphi_0))$, which depends on the pump-induced phase difference φ_0 and leads to a modulated resonance frequency $\omega_p^* = (LC)^{-1/2} = \omega_p \cos(\varphi_0)^{1/2}$. The normalized superfluid density (dashed-dotted line) deduced in this manner reflects the observed modulation of the loss function and agrees well with the experimentally determined reduction in interlayer coupling $S(t)$. In our picture, the pump field modulates the interlayer coupling by repeatedly driving φ_0 through values of $\pm\pi/2$, at which the inductance diverges as $L \rightarrow \infty$. This is equivalent to a complete decoupling of the layers, at which point transport becomes resistive. At intermediary times, φ_0 is repeatedly driven close to π , leading to a temporary recovery of c -axis transport through inductive coupling.

23.3 Quantum Phase Control Through Vibrational Excitation

23.3.1 Control of the Semicovalent Bond

Manganites are oxides of transition metals typically synthesized in quasi-cubic perovskite structures with formula $RE_{1-x}AE_xMnO_3$, where RE is a trivalent rare earth ion, such as La, Pr, and Nd, and AE is a divalent alkaline earth ion such as Sr and Ca. The RE and AE ions act as charge reservoirs for the manganese ions and control the average Mn charge from 3+ to 4+. The magnetic nature of the Mn-O-Mn bond, in which the sign of the exchange interaction is connected to the size of the electron transfer integral and charge distribution, is responsible for the complexity in these compounds. Typically, “straight” bonds result in ferromagnetic coupling and metallic bonding, while for Mn-O-Mn bonding angles below 180° , insulating phases and anti-ferromagnetic order ensue [65]. Thus, metal-insulator and magnetic transitions can be achieved by changes in doping, application of magnetic fields or pressure.

Among all manganites $Pr_{1-x}Ca_xMnO_3$ is an interesting example, due to its strongly distorted structure. Indeed, the relative radii of Pr and Ca ions differ by a significant amount, leading to large Mn-O-Mn bond angle and small electronic hopping amplitude, which occurs between Mn ions through the bridging oxygen. As a result, this compound shows insulating behavior at all doping levels. For $x = 0.3$ the system is particularly unstable toward a competing metallic phase, which can be induced by the application of magnetic fields [66, 67], electric fields [68], X-ray irradiation [69], laser irradiation, and pressure, resulting in ‘colossal’ changes in the resistivity by up to nine orders of magnitude.

A key parameter is the geometrical “tolerance factor”, Γ defined as:

$$\Gamma = \frac{(A - O)}{\sqrt{2}(Mn - O)},$$

which depends on the average A-O (A=Pr,Ca,La,Sr...) and Mn-O distances. Γ quantifies the degree of orthorhombic distortion from an ideal cubic perovskite symmetry and is related to the Mn-O-Mn bond angle (θ), and hence to orbital overlap and to the transfer integral t between Mn^{3+} and Mn^{4+} sites. The hopping matrix element is maximum for $\Gamma = 1$ (cubic structure, $\theta = 180^\circ$), where metallic behavior is expected, and decreases for smaller angles ($\Gamma < 1$, $\theta < 180^\circ$), as is the case for symmetry-lowering orthorhombic distortions.

Resonant vibrational excitation can be applied to modulate such tolerance factor. Excitation of IR-active phonon modes can be used to perturb the lattice, changing bond angles and distances selectively. This modifies the overlap of neighboring electronic wavefunctions and the associated electron hopping probability. This concept can be demonstrated by direct excitation of a phonon mode at mid-infrared wavelengths.

Fig. 23.5 Optical conductivity spectrum of $\text{Pr}_{0.7}\text{Ca}_{0.3}\text{MnO}_3$ at low temperature (10 K). The highest frequency mode at $17 \mu\text{m}$ is assigned to the Mn-O stretching vibration

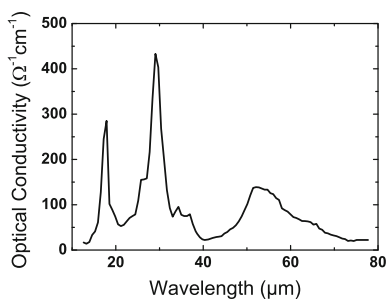
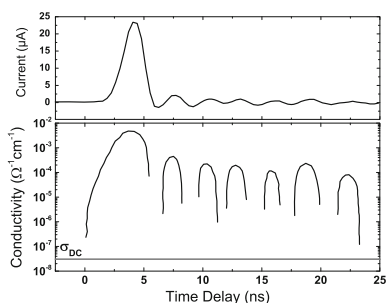


Fig. 23.6 Time-dependent transport measurements, showing that vibrational excitation results in a $\sim 10^3$ increase in the sample current (*upper panel*) and a $\sim 10^5$ increase in the sample conductivity (*lower panel*)



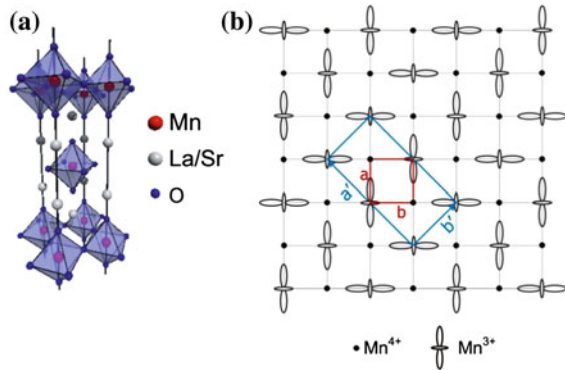
The optical conductivity spectrum of $\text{Pr}_{0.7}\text{Ca}_{0.3}\text{MnO}_3$ shown in Fig. 23.5 exhibits a three-peak structure that is characteristic of most perovskites. The highest frequency IR active mode at $17 \mu\text{m}$ corresponds to the Mn-O stretching vibration, which modulates the tolerance factor Γ and is thus expected to be strongly coupled to the electron system.

High-intensity pulses at this wavelength were generated with an optical parametric amplifier (OPA), pumped by mJ pulses at 1 kHz repetition rate from a titanium sapphire laser. Figure 23.6 displays a prompt, five-order-of-magnitude drop in resistivity following vibrational excitation with femtosecond mid-infrared pulses, generated by difference frequency generation (DFG) between signal and idler. The sample current was monitored with a 4 ns temporal resolution. Experiments were carried out at 30 K, with the sample in the charge-ordered, anti-ferromagnetic insulating phase.

From this, a five-order-of-magnitude change of sample conductivity, from $\sim 3 \cdot 10^{-8} \Omega^{-1} \cdot \text{cm}^{-1}$ to at least $\sim 5 \cdot 10^{-3} \Omega^{-1} \cdot \text{cm}^{-1}$, is estimated. We stress that at the photon energy and laser fluence used in these measurements, both interband carrier excitations and laser heating effects could be ruled out as the origin of this resistivity drop. These measurements thus provide evidence that a metallic state is formed promptly by direct vibrational excitation, and that this state persists for hundreds of picoseconds.

To highlight the ultrafast microscopic mechanism underpinning of such dramatic changes in more detail, we investigated the response of $\text{La}_{1/2}\text{Sr}_{3/2}\text{MnO}_4$,

Fig. 23.7 Structure of $\text{La}_{1/2}\text{Sr}_{3/2}\text{MnO}_4$. **a** Three dimensional structure of single layer $\text{La}_{1/2}\text{Sr}_{3/2}\text{MnO}_4$. **b** Below $T_{\text{oo}} = 220$ K, lattice-commensurate ordering of $\text{Mn}3d$ e_g -like orbitals breaks the symmetry of the tetragonal lattice and results in optical birefringence



a half-doped, single-layer manganite in which electronic and orbital structures can be directly connected to the macroscopic optical properties.

Figure 23.7a shows the 3D lattice structure of single-layer $\text{La}_{1/2}\text{Sr}_{3/2}\text{MnO}_4$. The manganese cations occupy the center of oxygen octahedra, and form planes separated by lanthanum and strontium dopants. Within the planes, lattice-commensurate ordering of the high-lying $\text{Mn}3d$ e_g -like orbitals develops below $T_{\text{oo}} = 220$ K, yielding a long-range orbital pattern as shown in Fig. 23.7b. The electronic properties are dominated by the crystal-field-split $\text{Mn}3d$ orbitals, which are strongly hybridized with $2p$ orbitals from neighboring oxygen atoms, and are thus very sensitive to distortions in the Mn-O bond. This low temperature orbital configuration breaks the tetragonal lattice symmetry and results in an optical birefringence—a rotation of the probe polarization when not aligned to either principle axis.

Large amplitude, coherent distortions of the Mn-O bonds were driven with femtosecond pulses at $16\ \mu\text{m}$ ($625\ \text{cm}^{-1}$, $77\ \text{meV}$) wavelength, resonant with a similar IR-active stretching vibration as the one studied in the cubic $\text{Pr}_{0.7}\text{Ca}_{0.3}\text{MnO}_3$. A second OPA was used to generate broadband probe pulses, which in our experiments were tuned between $10\ \mu\text{m}$ ($0.12\ \text{eV}$ photon energy) and $600\ \text{nm}$ ($2.2\ \text{eV}$).

The top panel of Fig. 23.8 shows the IR driven time-dependent reflectivity of $\text{La}_{1/2}\text{Sr}_{3/2}\text{MnO}_4$ at $650\ \text{nm}$, measured at a temperature of $90\ \text{K}$, below the orbital ordering temperature. We find a prompt transition to a long-lived phase that survives for hundreds of picoseconds after excitation. The same process probed at other wavelengths in the infrared yielded qualitatively similar temporal profiles. The transient changes in reflectivity, measured at $100\ \text{ps}$ time delay, are shown in the middle panel of Fig. 23.2 for photon energies between $120\ \text{meV}$, and $2.2\ \text{eV}$. We observe an increase in reflectivity at all measured photon energies below $1\ \text{eV}$.

The bottom panel of Fig. 23.8 shows the static reflectivity of $\text{La}_{1/2}\text{Sr}_{3/2}\text{MnO}_4$, measured at the 90 – $110\ \text{K}$ and at room temperature. Below $T_{\text{oo}} = 220\ \text{K}$, the static reflectivity exhibits a resonance near $1.3\ \text{eV}$, corresponding to intersite excitations between adjacent manganese atoms, reflecting the cooperative, long-range Jahn–Teller distortion. Above T_{oo} , this feature is lost and spectral weight shifts to lower energies. A comparison between reflectivity changes obtained by vibrational

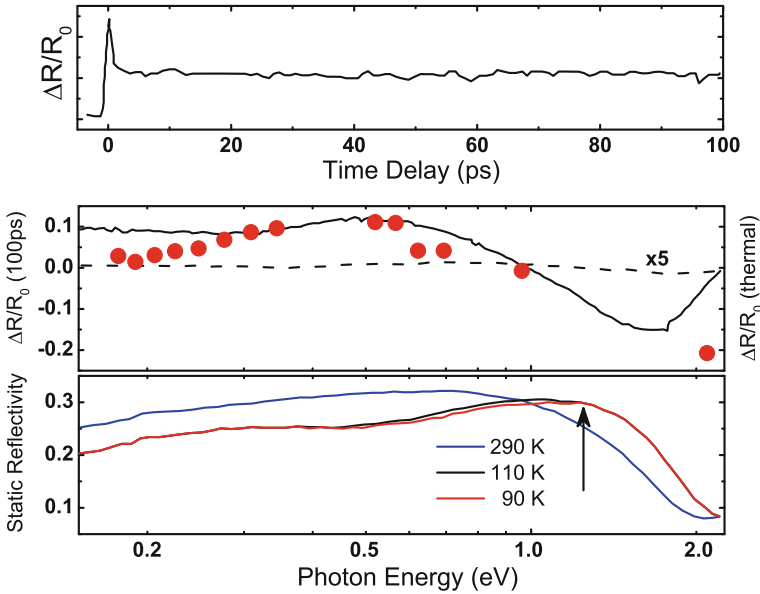
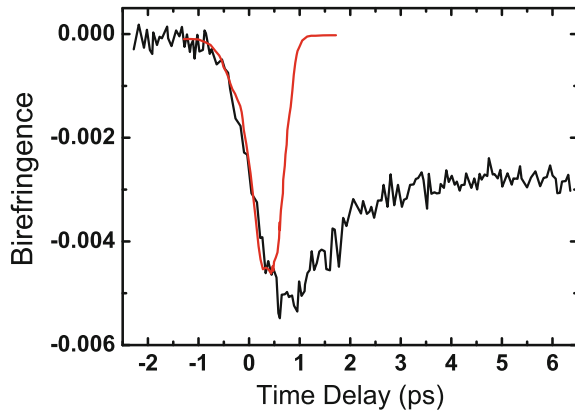


Fig. 23.8 Static and transient reflectivity spectra. (Top) Vibrationally induced changes in reflectivity at 90 K, probed at 650 nm. (Middle) The spectral response at 100 ps time delay (data points) compared to changes in reflectivity when the sample is heated above T_{∞} (solid line) and to sample temperature increased by 20 K (dashed line). (Bottom) The spectral feature at 1.3 eV (arrow) is associated with orbital ordering

Fig. 23.9 Ultrafast loss of birefringence. Excitation of the vibrational resonance at 80 meV results in the prompt destruction of orbital ordering and a loss of birefringence at 650 nm (black). A cross-correlation (red) of the mid-IR pump and 650 nm indicates that melting occurs within the pump pulse



excitation and by static temperature tuning is also shown in the middle panel of Fig. 23.8. We note that the spectral response of the transient phase is the same as the change in static reflectivity when $\text{La}_{1/2}\text{Sr}_{3/2}\text{MnO}_4$ is heated between 90 K and room temperature, suggesting a similarity between the photo-induced phase and the thermally melted orbitally ordered state.

Ultrafast loss of orbital ordering can be directly confirmed by measuring time-dependent birefringence [70], which at 650 nm is proportional to the orbital-order parameter, as measured with resonant X-ray diffraction [71]. Figure 23.9 shows time-dependent birefringence detected at 650-nm after the same vibrational excitation. A prompt drop is observed, directly indicating melting of orbital order. This state persists for hundreds of picoseconds. In Fig. 23.9, we also include a cross-correlation of mid-IR pump and 650-nm probe pulses, as measured by the electro-optic effect in ZnTe. The data show that birefringence is lost on a timescale identical to the rise time of the excitation pulse, indicative of the ultrafast nature of this process. This is an indication that the electronic phase transition is non-thermal, in that it occurs on a timescale that is significantly shorter than the known thermalization time for hot optical phonons in solids [72]. However, the lack of carrier-envelope phase stability results in excitation of lattice vibrations with different absolute phases for subsequent pump pulses, and the signature of the electric field is lost by averaging over many pump-probe cycles.

23.3.2 Mid-Infrared Pulses with Stable Absolute Phase

A very important parameter for the control of a pulse electric field is the CEP, which defines the temporal offset of the peak of the intensity envelope from the carrier wave. For pulses with few-optical-cycle duration, a CEP variation produces a strong change in the waveform. Nonlinear optical processes can be used to measure and manipulate CEP drifts [73], and can be exploited to stabilize it; in particular, difference frequency (DF) mixing between pulses at distinct frequencies, and with carrier-envelope phases φ_1 and φ_2 , give rise to a pulse with absolute phase $\varphi_{DF} = \varphi_1 - \varphi_2 - \pi/2$. When the two waves are derived from the same laser source or are different components of a broadband pulse, they are mutually phase-locked and $\varphi_1 = \varphi_2 + \Delta\varphi$, where $\Delta\varphi$ is their constant phase difference. The difference frequency process then generates a CE phase stable wave with phase $\Delta\varphi - \pi/2$.

Phase-stable near- and mid-IR pulses have been generated by mixing two spectral portions of a single broadband pulse [74, 75], which are automatically phase-locked THz generation by optical rectification, which produces long wavelength radiation with a stable CEP from an unstable near infrared pulse, as discussed in Par. 2.1, can be understood in these terms [76]. Other schemes for the generation of THz and MIR pulses are based on DFG between two synchronized pulses of different carrier frequencies [77]; in this case, the two pulses follow different optical paths, and fluctuations of their path lengths may influence the CEP of the beam at the DF. The ability to detect and instantaneously correct spurious CEP drifts becomes therefore crucial in phase-sensitive experiments. In the visible and the near IR, f -to- $2f$ interferometry [78] is employed to detect real-time CEP jitter [79, 80].

Here, we discuss a scheme for long-term phase stabilization of MIR pulses, achieved by detecting and compensating its drift [81]. The detection technique is based on the DF mixing between the MIR field (with phase φ_{MIR}) and a gate

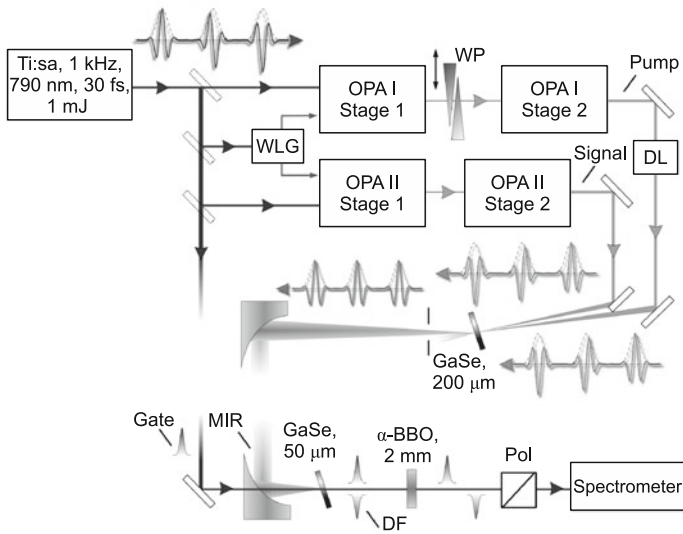


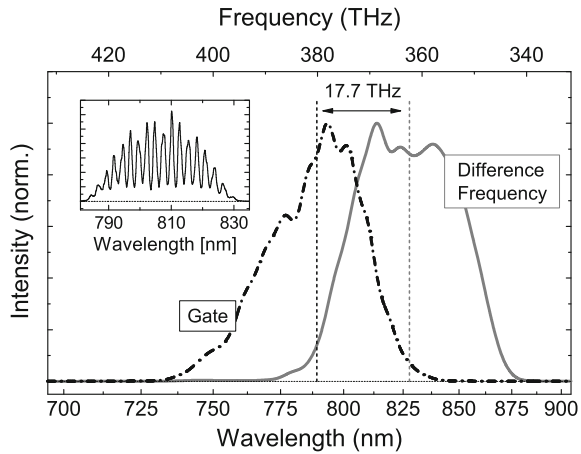
Fig. 23.10 Setup for the production of tunable light pulses at mid-infrared wavelengths (*upper part*) and for the characterization of their absolute phase (*lower part*). WLG is the white-light generation stage; DL is the delay line for Pump-Signal synchronization; WP are fused silica wedge plates; DF is the side-band pulse at the difference frequency

pulse (with phase φ_{Gate}), and on spectral interferometry between the gate and the DF field. Due to the difference frequency process, the DF pulses have absolute phase of $\varphi_{\text{Gate}} - \varphi_{\text{MIR}} - \pi/2$: spectral interference between the gate and the DF pulse thus gives rise to a fringe pattern which in the frequency domain has phase $\varphi_{\text{Gate}} - (\varphi_{\text{Gate}} - \varphi_{\text{MIR}} - \pi/2) + \text{const} = \varphi_{\text{MIR}} + \text{const}$. The interference therefore allows single-shot retrieval [82] of the absolute-phase jitter of the MIR pulse, and is independent from the carrier-envelope phase of the gate pulse.

The stable mid-infrared source is displayed in Fig. 23.10, based on two non-collinear two-stage infrared OPAs. The two OPAs are seeded by two portions of the same white light, obtained by self-phase modulation in a 2-mm-thick sapphire plate; this ensures that the OPAs are seeded by phase-locking. The beams from the two OPAs are combined in a 200 μm thick *z*-cut GaSe, oriented for type II DFG; the process provides 2.5- μJ MIR pulses at a wavelength of about 17 μm (≈ 17.6 THz frequency); the DFG process not only shifts the two OPAs to the MIR spectral range, but thanks to the phase-locking of the common seed it provides the key mechanism to produce phase-stable fields. The phase difference $\Delta\varphi$ between pump and the signal pulses can be finely tuned by adjusting their relative path lengths by a fused-silica wedge pair placed before the saturated second stage of OPA I; tuning of $\Delta\varphi$ allows direct control of the CEP of the MIR pulse.

The phase-drift detection is depicted in the lower panel of Fig. 23.10: the MIR pulses are combined with a fraction of the laser source pulses, acting as gate, in a 50- μm thick *z*-cut GaSe crystal for DFG. Their polarizations and the orientation

Fig. 23.11 Spectra of the gate (dash-dotted line), together with the sideband (solid line) arising from difference frequency mixing with the MIR pulses in the GaSe crystal. The weighted center of each spectrum and the corresponding shift is also given. *Inset:* fringe pattern from balanced spectral interference between gate and DF pulses



of the crystal is adjusted for type II $[e(\text{MIR}) + o(\text{DF}) \rightarrow e(\text{Gate})]$ interaction. The co-propagating, cross-polarized gate and DF pulses are then delayed to about 1 ps by a 2-mm thick α -BBO plate, projected to the same polarization by an achromatic polarizer and directed to a spectrometer. The DFG process in the thin GaSe crystal is also feasible for EO sampling [83, 84] of the MIR electric field, which allows in situ evaluation of the pulse electric field. In Fig. 23.11 we report the spectra of gate (dash-dotted line) and DF pulses (solid line), together with the fringes arising from their balanced interaction (inset). From the phase of the fringe pattern, the CEP drift of the MIR pulse can be deduced. Figure 23.12 gives an example of short- and long-term characterization of CEP fluctuations of our MIR source. The system exhibits a phase jitter with a root mean square of 80 mrad over 15 s [panel (a)], confirming that DF between two phase-locked beams leads to passive phase-stabilization. However, significant drift can be observed when monitoring the MIR pulses for hours of free-running operation [panel (b)].

This slow drift can be actively compensated by moving the wedge. The data in Fig. 23.12b show that, after the activation of the control system, the MIR absolute phase fluctuations could be compensated, with a residual rms jitter of only 110 mrad.

23.3.3 Vibrational Control as Nonlinear Phononics

The device discussed in Sect. 23.3.2 can be used to further clarify the physics of selective vibrational control in manganites. We first note that linear coupling between the electromagnetic radiation and an infrared-active vibrational mode of the crystal lattice leads to oscillatory atomic motions. However, one expects the lattice to be brought back to rest at the end of the pulse without net work performed. The phase

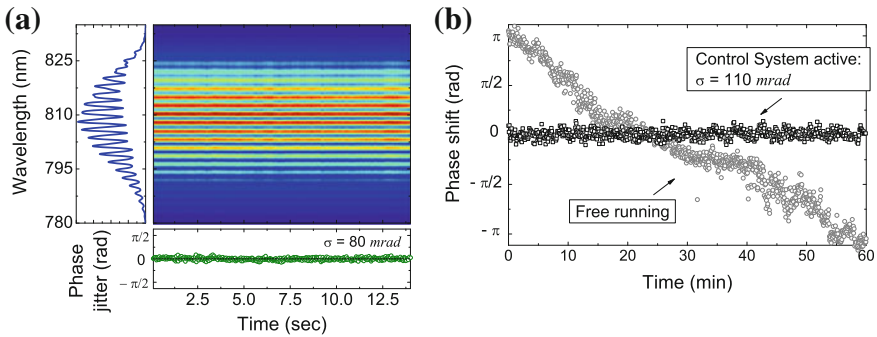


Fig. 23.12 **a** Interferogram recorded for 15 s; the retrieved phase has a jitter of 80 mrad. **b** The same analysis conducted for 1 h: Both free-running and closed-loop measurements are displayed

transition must then be driven by higher order coupling terms, and the physics is difficult to identify without being able to follow the driving field directly.

Similar to the experiments in orbitally ordered $\text{La}_{0.5}\text{Sr}_{1.5}\text{MnO}_4$, single crystals of ferromagnetic-metallic $\text{La}_{0.7}\text{Sr}_{0.3}\text{MnO}_3$ (LSMO) [85–88] were held at 14 K base temperature and excited with mid-infrared radiation at fluences up to 2 mJ/cm^2 . Figure 23.13 shows the time-resolved reflectivity changes for vibrational excitation at $14.3 \mu\text{m}$, resonant with the 75-meV (605 cm^{-1}) stretching mode of MnO_6 octahedra. Similar to what was observed for excitation in the near-infrared, the sample reflectivity decreased during the pump pulse relaxing into a long-lived state, connected to demagnetization of ferromagnetic LSMO [89, 90]. These dynamics are accompanied by coherent phonon oscillations, with frequencies that depend on the excitation wavelength. The Fourier transforms for mid- and near-IR excitation peak at frequencies of the Raman-active rotational E_g mode at 1.2 THz (40 cm^{-1}) and of the rotational A_{1g} mode at 5.8 THz (193 cm^{-1}), respectively [91].

In Figure 23.13b and c, we plot the coherent phonon oscillations and their amplitudes. The amplitude clearly follows the absorption profile of the 75-meV MnO_6 stretching mode, evidencing that the photo-induced dynamics can only be driven when the lattice is distorted.

Nearly 40 years ago, proposals were made of a nonlinear interaction mechanism between a resonantly driven vibration and the crystal lattice, referred to as ionic Raman scattering (IRS) [92, 93]. It was predicted that excitation of an IR-active phonon serves as the intermediate state for a Raman scattering process. In that picture, comparable to optical rectification in nonlinear optics, a rectified phonon field exerts a directional force onto a crystal lattice, inducing an abrupt displacement of the atoms from the equilibrium positions. In the IRS mechanism, the equation of motion of the lattice after infrared excitation can be written as

$$\ddot{Q}_{\text{RS}} + \Omega_{\text{RS}}^2 Q_{\text{RS}} = A Q_{\text{IR}}^2 \quad (23.1)$$

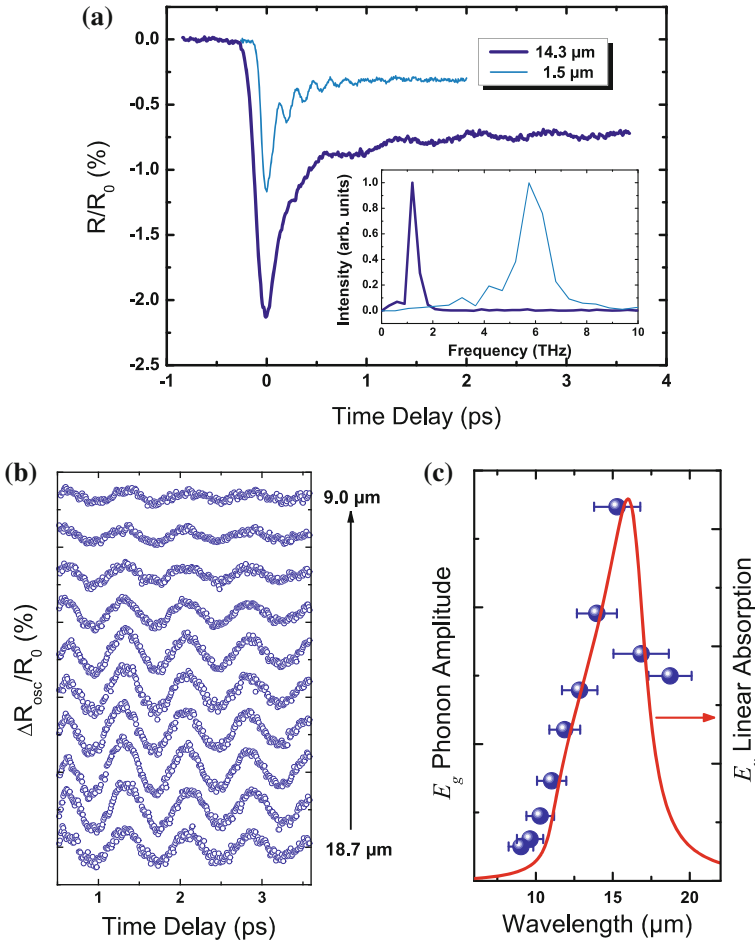
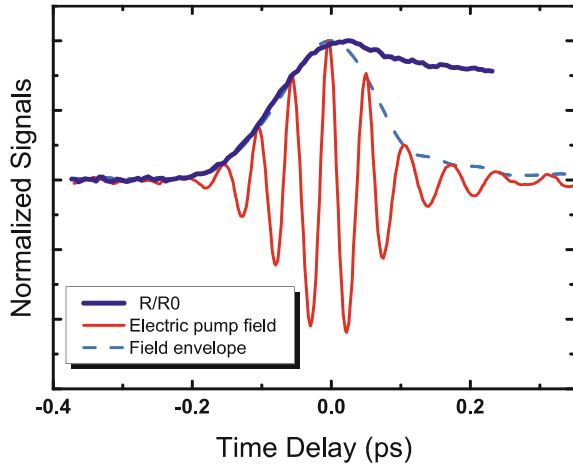


Fig. 23.13 **a** Time-resolved, 800nm-wavelength reflectivity changes of $\text{La}_{0.7}\text{Sr}_{0.3}\text{MnO}_3$ for mid-IR excitation at $14.3\ \mu\text{m}$ and for near-IR excitation at $1.5\ \mu\text{m}$. The inset shows the Fourier transforms of the oscillatory signal for different pump wavelengths. **b** Coherent phonon oscillations of the E_g mode as a function of the mid-IR pump wavelength. **c** Phonon amplitude derived from these data, together with the linear absorption profile of the IR-active E_u mode

Here, Q_{RS} and Q_{IR} are the coordinates of the low-frequency Raman mode and the resonantly excited high-frequency IR-active mode respectively. The driving force on the right-hand side is second order in the mid-infrared phonon coordinate, and induces a displacive lattice response. Furthermore, only those modes with symmetries belonging to the product group of the infrared vibration are observed, supporting the IRS mechanism. With $E_g \subset E_u \otimes E_u$ for the D_{3d}^6 point group of the distorted perovskite LSMO, and the resonantly excited IR-active mode being of E_u symmetry, this requirement is fulfilled.

Fig. 23.14 Relative change of the sample reflectivity, induced by carrier-envelope phase stable mid-IR excitation in resonance with the MnO_6 stretching vibration (*dark blue solid line*), along with the electric field of the pump pulse measured via electro-optic sampling (*red*)



A second experimental observation substantiates our assignment. Rectification is expected to be independent of the absolute electric field phase of the mid-infrared pump pulses. We excited the system by mid-IR pulses in which the carrier-envelope phase offset was stabilized (see Sect. 23.3.2). Figure 23.14 shows the time-resolved reflectivity rise at the earliest time delays, displayed alongside the carrier-envelope phase-stable pump field, which was measured by electro-optic sampling in a $50 \mu\text{m}$ thick GaSe crystal.

To increase the temporal resolution, we further used as probe an OPA which delivered broadband IR pulses ($1.2\text{--}2.2 \mu\text{m}$) compressed to 14 fs. The probe light was spectrally filtered around $1.6 \mu\text{m}$ in front of the detector. The response of the solid does not show any signature of the phase of the electric field. Instead, the sample reflectivity follows the electric field envelope in agreement with our contention that the driving force results from rectification of the phonon field.

In summary, mid-infrared excitations can stimulate condensed matter through IRS. The key insight is that a rectified phonon field—in analogy to optical rectification in nonlinear optics—can exert a directional force onto the crystal, inducing an abrupt displacement of the atoms from the equilibrium positions. This rectification mechanism could be extended to, e.g., difference-frequency generation between pairs of non-degenerate excitations, opening up avenues for the control of condensed matter with light.

23.4 Undulator-Based Sources for Nonlinear THz Physics

In the previous section, we have shown two examples of the new physics that can be explored with nonlinear THz excitation. We note that tabletop sources are limited in the pulse characteristics in many ways. On the one hand, well-controlled

pulses are generated from the visible to approximately 20- μm wavelength, with pulse energies that decrease at longer wavelengths. The bandwidths are relatively broad, typically exceeding 10%. At longer wavelengths, the availability of strong THz fields is restricted to the few-THz range, below 3 THz for the tilted-pulse-front technique.

Alternative strategies should be developed for high-energy, narrowband THz transients that can be applied to a wide range of nonlinear THz experiments. It is desirable to generate narrow bandwidth and tuneable THz sources in the frequency range between 0.3 and 15 THz, with pulse strengths beyond the 100 μJ range. Electron accelerator sources offer an interesting alternative.

According to the Larmor formula, an accelerated electron radiates [94] with a power $P = 2e^2a^2\gamma^4/(3c)^3$, where e is the elementary charge, a the acceleration, c the speed of light and γ the ratio of the relativistic electron mass to the electron rest mass $\gamma = E/m_0c^2$. Thus, at relativistic energies, the integral radiated power is then increased by a factor γ^4 . If relativistic electrons are passed through an undulator, a periodic magnetic structure that induces a sinusoidal trajectory onto the electrons, tuneable narrow bandwidth radiation can be generated. The spectral bandwidth is determined by the number of undulator periods $\Delta\nu/\nu \sim 1/N_u$ and so is the opening angle of the radiation $\theta_u \sim \sqrt{(1/N_u)}$. The central frequency ν_u of the radiation is tuned by changing the magnetic field strength B [95]. The radiated energy scales linearly with the number of electrons N_e in the bunch and femtoJ—picoJ pulse energies are typically achieved [96].

THz free electron lasers (FELs), operational since the late 1970s, make use of an *optical resonator* to amplify the generated THz power in an undulator [96, 97]. Relativistic electrons serve as both *active laser medium* and *energy pump*. Upon every passage energy is transferred from the electrons to the photons. A few percent of the energy stored in the optical mode is coupled out and few 10 μJ pulse energies can be reached. Most FELs are nowadays driven by radio frequency (RF) accelerators which dictate the upper limit of their repetition rate. The minimum rate is defined by the length of the optical resonator and typically in the MHz regime. Laser-activated switching schemes can be used to reduce the repetition frequency if required [98]. Normal conducting RF accelerators have the drawback that they do not allow to work in continuous wave (cw) operation and only micropulse trains of up to few μs duration are generated with a repetition rate in the few Hz regime [96]. Two of the most recently finalized facilities, the Jefferson Lab FEL [99] and FELBE [100], are based on superconducting RF technology and additionally offer true cw operation at MHz repetition.

A second approach makes use of recent progress of accelerator technology to generate highly charged, ultrashort electron bunches. For frequencies smaller than the inverse electron bunch duration, electrons in a bunch radiate coherently, emitting pulse energies that scale quadratically with the number of electrons N_e . High pulse energies in the few 10 to few 100 μJ regime in the THz frequency range can now be reached already from a single pass through an undulator, since the number of accelerated electrons N_e in a short electron bunch can be of the order of $\sim 10^8$ – 10^{10} and amplification can reach corresponding magnitudes [101]. One such device is

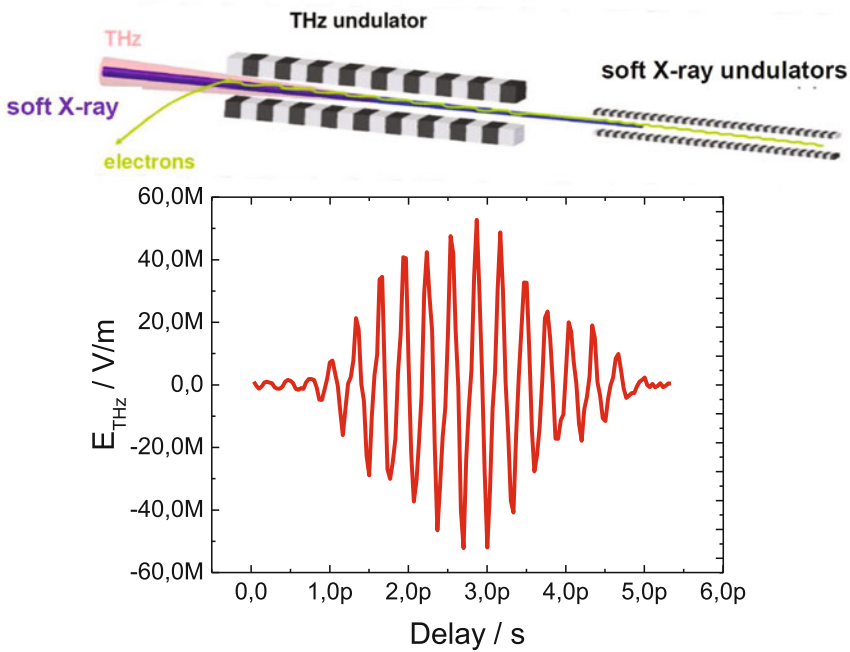


Fig. 23.15 (top) Cascaded design of a soft X-ray undulator followed by a THz undulator at the FLASH facility in Hamburg. The CEP stable THz pulse is fully synchronized to the femtosecond soft X-ray pulse emitted by the same electron bunch as can be seen from the sequential THz/X-ray cross-correlation (for details on the methodology see [103]) of a 3 THz pulse (bottom)

currently in operation, working in parasitic mode at the soft X-ray FEL FLASH in Hamburg [102]. The FLASH THz undulator allows to generate THz pulses with a spectral bandwidth of 10% around the center frequency and additionally provides for intrinsically synchronized THz pump X-ray probe experiments on the few femtosecond timescale (see Fig. 23.15) [103–105].

Similar facilities are currently being developed at the ELBE accelerator in Dresden [106] and at Jefferson laboratory [107]. The facility under construction at ELBE will provide variable repetition rates between 1 and 200 KHz, pulse energies on the 100 μ J level and a tuning range between 0.3 and 3 THz, making this an almost ideal source for THz control experiments.

23.5 Conclusion

The use of high field THz to drive low-lying excitations in complex condensed matter is a field with great potential. The combination of tabletop techniques with accelerator-based sources is proving to bring a healthy balance and new opportuni-

ties. Especially, while on tabletops one has significantly more control on the pulse characteristics, which is exemplified in the exquisite control of the CEP discussed in paragraph 3.2; short pulses and thus few optical cycles are needed to drive the nonlinear optical properties used to manipulate them. As a result, excitation is limited to broad bandwidths and cannot be easily reconnected to narrow-bandwidth, long-timescale couplings that are often of interest in condensed matter research. Second, efficient generation in most nonlinear crystals is limited to frequencies below 3 THz and above 15 THz, due to optical phonon absorption and dispersion. To this end, generation in plasmas can help cover the near-10-THz fraction of the spectrum, although with relatively low fields.

On the other hand, FELs and superradiant accelerator sources allow for long pulses and narrow bandwidths, making it possible to study spectrally selective dynamics on longer timescales. Importantly, accelerator-based sources are generated in non-dispersive vacuum, and thus, all spectral ranges from 1 THz to the near IR are accessible. Yet, control of the pulse characteristics and precise stabilization with external lasers are still challenging.

We mention the pulse energy as an important methodological frontier. At the moment, pulse energies of few μJ are typically available, and a wealth of new studies would become possible if one was able to achieve pulses in the 100 μJ to multi-mJ, exploring the areas of research in which matter is driven further away from equilibrium.

The materials research explored to date covers only a small subset of what is possible. In the future, one will be able to compare the response of selected excitations over a broad section of the electromagnetic spectrum, for example measuring the response of a system to two different vibrations and quantifying the effect that a specific lattice distortion has on the macroscopic properties of a system. Second, spectral and temporal shaping, including the shape of the polarization, will make it possible to dynamically control the lattice parameters via nonlinear phononics as described in Sect. 23.3.3. These techniques will improve our understanding of complex materials and open a new era of controlling the structure of matter.

References

1. C.V. Shank et al., *Phys. Rev. Lett.* **51**, 900 (1983)
2. P. Saeta et al., *Phys. Rev. Lett.* **67**, 1023 (1991)
3. K. Sokolowski-Tinten et al., *Phys. Rev. B* **58**, 11805 (1998)
4. C.W. Siders et al., *Science* **286**, 1140 (1999)
5. B. Siwick et al., *Science* **302**, 5649 (2003)
6. K. Sokolowski-Tinten et al., *Nature* **422**, 287 (2003)
7. D. Sciaini et al., *Nature* **458**, 56 (2009)
8. D.H. Reitze et al., *Phys. Rev. B* **45**, 2677 (1992)
9. A. Cavalleri et al., *Europhys. Lett.* **57**, 281 (2002)
10. S.L. Johnson et al., *Phys. Rev. Lett.* **94**, 057407 (2005)
11. M. Imada, A. Fujimori, Y. Tokura, *Rev. Mod. Phys.* **70**, 1034 (1998)
12. Tokura et al., *Rev. Mod. Phys.* (1999)

13. S. Koshihara et al., *Phys. Rev. Lett.* **68**, 1148 (1992)
14. Myano et al., *Phys. Rev. Lett.* **78**, 4257 (1997)
15. M. Fiebig et al., *Science* **280**, 1925 (1998)
16. T. Ogasawara et al., *Phys. Rev. B* **63**, 113105 (2000)
17. R.A. Averitt et al., *Phys. Rev. Lett.* **87**, 017401 (2001)
18. D. Polli, M. Rini, S. Wall et al., *Nature Materials* **6**, 643 (2007)
19. S. Wall et al., *Phys. Rev. Lett.* **103**, 097402 (2009)
20. M. Rini et al., *Phys. Rev. B* **80**, 155113 (2009)
21. P. Beaud et al., *Phys. Rev. Lett.* **103**, 155702 (2009)
22. H. Ichikawa et al., *Nature Materials* **10**, 105 (2011)
23. A. Cavalleri et al., *Phys. Rev. Lett.* **87**, 237401 (2001)
24. A. Cavalleri et al., *Phys. Rev. B* **70**, 161102(R) (2004)
25. A. Cavalleri, H. Chong, S. Formaux, T.E. Glover, P.A. Heimann, B.S. Mun, H. Padmore, J.C. Kieffer, R.W. Schoenlein, *Phys. Rev. B* (Brief report) **69**, 153106 (2004)
26. A. Cavalleri, M. Rini, H. Chong, T.E. Glover, P.A. Heimann, J.C. Kieffer, R.W. Schoenlein, *Phys. Rev. Lett.* **95**, 67405 (2005)
27. M. Rini, et al., *Opt. Lett.* **30**, 558 (2005)
28. M. Rini et al., *Appl. Phys. Lett.* **92**, 181904 (2008)
29. D.J. Hilton et al., *Phys. Rev. Lett.* **99**, 226401 (2007)
30. A. Cavalleri et al., *J. Phys. Soc. Japan* **75**, 01004 (2007)
31. C. Kubler et al., *Phys. Rev. Lett.* **99**, 116401 (2007)
32. M. Rini et al., *Appl. Phys. Lett.* **92**, 181904 (2008)
33. H. Okamoto et al., *Phys. Rev. Lett.* **98**, 037401 (2006)
34. S. Wall et al., *Nature Phys.* **7**, 114 (2011)
35. J. Demsar, L. Forro, H. Berger, D. Mihailovic, *Phys. Rev. B* **66**, 041101 (2002)
36. L. Perfetti et al., *Phys. Rev. Lett.* **97**, 067402 (2006)
37. N. Dean et al., *Phys. Rev. Lett.* **106**, 016401 (2011)
38. S. Hellmann et al., *Phys. Rev. Lett.* **105**, 187401 (2010)
39. R.D. Averitt et al., *Phys. Rev. B* **63**, 140502 (2001)
40. J. Demsar et al., *Phys. Rev. Lett.* **82**, 4918 (1999)
41. R.A. Kaindl et al., *Science* **287**, 470 (2000)
42. N. Gedik et al., *Science* **300**, 1410 (2007)
43. A. Pashkin, M. Porer, M. Beyer et al., *Phys. Rev. Lett.* **105**, 067001 (2010)
44. M. Rini et al., *Nature* **449**, 72 (2007)
45. R.I. Tobey, D. Prabhakaran, A.T. Boothroyd, A. Cavalleri, *Phys. Rev. Lett.* **101**, 197404 (2008)
46. D. Fausti, R.I. Tobey et al., *Science* **331**, 189 (2011)
47. C. Fattinger, D. Grischkowsky, *Terahertz Beams, Appl. Phys. Lett.* **54**, 490 (1989)
48. M.C. Hoffmann, J.A. Fülöp, *J. Phys. D* **44**, 083001 (2011)
49. J. Hebling, G. Almasi, I. Kozma, J. Kuhl, *Opt. Express* **10**, 1161 (2002)
50. K.L. Yeh, M.C. Hoffmann, J. Hebling, K.A. Nelson, *Appl. Phys. Lett.* **90**, 171121 (2007)
51. R.M. Koehl, S. Adachi, K.A. Nelson, *J. Chem. Phys.* **110**, 1317 (1999)
52. T. Feurer, N.S. Stoyanov, D.W. Ward, J.C. Vaughan, E.R. Statz, K.A. Nelson, *Annu. Rev. Mater. Res.* **37**, 317 (2007)
53. D.J. Cook, R.M. Hochstrasser, *Opt. Lett.* **25**, 1210 (2000)
54. K.Y. Kim, A.J. Taylor, J.H. Glowina, G. Rodriguez, *Nature Photon.* **2**, 605 (2008)
55. M.D. Thomson, V. Blank, H.G. Roskos, *Opt. Express* **18**, 23173 (2010)
56. J. Orenstein, A.J. Millis, *Science* **288**, 468 (2000)
57. K. Tamasaku, Y. Nakamura, S. Uchida, *Phys. Rev. Lett.* **69**, 1455 (1992)
58. V.K. Thorsmølle et al., *Opt. Lett.* **26**, 1292 (2001)
59. A.A. Schafgans et al., *Phys. Rev. Lett.* **104**, 157002 (2010)
60. R. Kleiner, P. Müller, *Phys. Rev. B* **49**, 1327 (1994)
61. B.D. Josephson, *Rev. Mod. Phys.* **36**, 216 (1964)
62. B.D. Josephson, *Phys. Lett.* **1**, 251 (1962)
63. S.V. Dordevic et al., *Phys. Rev. Lett.* **91**, 167401 (2003)

64. D.N. Basov et al., *Science* **1**, 49 (1999)
65. J.B. Goodenough, *Phys. Rev.* **100**, 564 (1955)
66. M.V. Zimmermann, J.P. Hill, Doon Gibbs, et al. *Phys. Rev. Lett.* **83**, 4872 (1999)
67. Y. Tomioka, A. Asamitsu, H. Kuwahara, Y. Moritomo, Y. Tokura, *Phys. Rev. B* **53**, R1689 (1996)
68. A. Asamitsu, Y. Tomioka, H. Kuwahara, Y. Tokura, *Nature* **388**, 50 (1997)
69. V. Kiryukhin, D. Casa, J.P. Hill, B. Keimer, A. Vigliante, Y. Tomioka, Y. Tokura, *Nature* **386**, 813 (1997)
70. T. Ogasawara et al., *Phys. Rev B* **63**, 113105 (2001)
71. T. Ishikawa, K. Ookura, Y. Tokura, *Phys. Rev. B* **59**, 8367 (1999)
72. D.V.D. Linde, J. Kuhl, H. Klingenberg, *Phys. Rev. Lett.* **44**, 1505 (1980)
73. A. Baltuška, T. Fuji, T. Kobayashi, *Phys. Rev. Lett.* **88**, 133901 (2002)
74. C. Vozzi, C. Manzoni, F. Calegari, E. Benedetti, G. Sansone, G. Cerullo, M. Nisoli, S. De Silvestri, S. Stagira, *J. Opt. Soc. Am. B* **25**, B112 (2008)
75. R. Huber, A. Brodschelm, F. Tauser, A. Leitenstorfer, *Appl. Phys. Lett.* **76**, 3191 (2000)
76. J. Hebling, K.-L. Yeh, M.C. Hoffmann, B. Bartal, K.A. Nelson, *J. Opt. Soc. Am. B* **25**, B6 (2008)
77. A. Sell, A. Leitenstorfer, R. Huber, *Opt. Lett.* **33**, 2767 (2008)
78. M. Kakehata, H. Takada, Y. Kobayashi, K. Torizuka, Y. Fujihira, T. Homma, H. Takahashi, *Opt. Lett.* **26**, 1436 (2001)
79. R. Zinkstok, S. Witte, W. Hogervorst, K. Eikema, *Opt. Lett.* **30**, 78 (2005)
80. G. Cirmi, C. Manzoni, D. Brida, S. De Silvestri, G. Cerullo, *J. Opt. Soc. Am. B* **25**, B62 (2008)
81. C. Manzoni, M. Först, H. Ehrke, A. Cavalleri, *Opt. Lett.* **35**, 757 (2010)
82. L. Lepetit, G. Chériaux, M. Joffre, *J. Opt. Soc. Am. B* **12**, 2467 (1995)
83. K. Liu, J. Xu, X.C. Zhang, *Appl. Phys. Lett.* **85**, 863 (2004)
84. C. Kübler, R. Huber, S. Tübel, A. Leitenstorfer, *Appl. Phys. Lett.* **85**, 3360 (2004)
85. C. Zener, *Phys. Rev.* **84**, 403 (1951)
86. P.W. Anderson, H. Hasegawa, *Phys. Rev.* **100**, 675 (1955)
87. Y. Okimoto, T. Katsufuji, T. Ishikawa, T. Arima, Y. Tokura, *Phys. Rev B* **55**, 4206 (1997)
88. P.G. Gennes, *Phys. Rev.* **118**, 141 (1960)
89. T. Ogasawara, M. Matsubara, Y. Tomioka, M. Kuwata-Gonokami, H. Okamoto, Y. Tokura, *Phys. Rev. B* **68**, 180407 (2003)
90. R.D. Averitt, A.I. Lobad, C. Kwon, S.A. Trugman, V.K. Thorsmølle, A.J. Taylor, *Phys. Rev. Lett.* **87**, 017401 (2001)
91. E. Granado et al., *Phys. Rev. B* **58**, 11435 (1998)
92. A.A. Maradudin, R.F. Wallis, *Phys. Rev. B* **2**, 4294 (1970)
93. T.P. Martin, L. Genzel, *Phys. Stat. Sol. (b)* **61**, 493 (1974)
94. G.L. Carr et al., *Nature* **420**, 153 (2002)
95. J.A. Clark, *The Science and Technology of Undulators and Wigglers*, (Oxford University Press, New York, 2004)
96. D.A. Jaroszynski et al., *Phys. Rev. Lett.* **71**, 3798 (1993)
97. C.A. Brau, *Science* **239**, 1115 (1988)
98. M.F. Doty et al., *Rev. Sci. Instr.* **75**, 2921 (2004)
99. S. Benson et al., *Nucl. Instr. Meth. A* **582**, 14 (2007)
100. S.A. Zyagin et al., *Rev. Sci. Instr.* **80**, 073102 (2009)
101. B. Faatz et al., *Nucl. Instr. And Meth. A* **475**, 363 (2001)
102. M. Gensch et al., *Infrared Phys. Technol.* **51**, 423 (2008)
103. U. Frähling et al., *Nature Photon.* **3**, 523 (2009)
104. M. Gensch, *AIP Conf. Proc.* **1214**, 19 (2010)
105. F. Tavella et al., *Nature Photon.* **5**, 162 (2011)
106. U. Lehnert et al., *Proceedings of the 32nd International Free Electron Laser Conference*, (Malmö, August, 2010), pp. 23–27
107. S.V. Benson et al., *Nucl. Instr. And Meth. A* (2010). doi:[10.1016/j.nima.2010.12.093](https://doi.org/10.1016/j.nima.2010.12.093)

Index

(2D-THz-TDS), 367

A

ABCD ray transfer matrix, 34, 54
ABCD transfer matrix, 34
ABCD matrix, 34, 35, 54, 51, 53
ABCD transformation matrix, 38
ABCD matrices, 34, 35, 46, 54
Aberration, 36, 37, 39, 46, 53, 54
Aberration effects, 46
Absorption, 303, 312, 313
Absorbers, 593, 601
Absorption coefficient. *See* optical constants
Active control of the metamaterial, 596
Additive concentration, 339
Adhesive bonds, 345
Adhesive layer, 347
Alkoxy, 308
Alkyl chain, 315
A-monohydrate, 71
Amorphous, 332
Amorphous and crystalline domains, 332
Anchor point, 68
Angular distribution, 90, 91
Angular spectra, 91
Angular weighting function, 87
Anharmonicity, 381
Anisotropic, 318
Anisotropic media, 65
Anisotropy, 303, 310, 313, 318
Anode, 19
Antireflective coatings, 574, 602

Artificial birefringence, 574, 593, 602
Atmospheric attenuation, 499
Atmospheric water vapour, 360
Attenuated total reflection, 198
Axicons, 41
Auger mechanism, 261
Autocorrelation function, 179

B

(Ba,Sr)TiO₃, 595
Ballistic transport, 377
Basis set
 localised, 167
 plane waves, 168
Beam profile, 87
Beam radius, 31, 45
Beam waist, 32, 37, 43, 50, 54
Beam waist radius, 31
Beat frequency, 16
Beer–Lambert, 61
Behaviour, 576
Benzene, 169
Biological, 416
Biomedical, 415
Biomolecules, 207
Birefringence, 303, 304, 308–314, 321
Bolometer, 23, 510
Boson peak, 217
Breast cancer, 415
Bremsstrahlung, 14, 362
Brillouin zone boundary, 580
Bruggeman, 65, 58, 340
Bruggeman approach, 340

B (*cont.*)

Bruggeman model, 574
 B-scan, 468
 Bulk, 593

C

CaCo₃, 339
 Calculated intensity, 175
 Cancer, 416
 Carbon nanofibres, 222
 Carbon nanotubes, 219
 Carrier envelope phase, 621
 Cauchy, 67
 Causality, 60, 70
 CdSe
 quantum dot, 261
 Center frequency, 331
 Chemical imaging, 210
 Chiral metamaterials, 583
 Christiansen effect. *See* scattering
 Circular polarization, 276
 Coating thickness, 470
 Coherence length, 11
 Coherent control, 380
 Corrugated horn antenna, 41
 Cole-Cole model, 257
 Cole-Davidson model, 257
 Colon cancer, 427
 Comb slow-wave structure, 19
 Complex permeability, 61
 Complex permittivity, 58–60
 Complex point source, 34
 Complex refractive index, 57, 60
 Complex susceptibility, 60
 Components, 330
 Compound characterization, 341
 Compounding process, 341
 Computed tomography, 434
 Conductivity
 models, 255
 of a thin film, 266
 Contact-free testing, 348
 Converging beam, 82, 86, 90
 Cross-polarisation, 36, 51
 Cross-polarisation effects, 29
 Cross-sections, 523
 Crystalline, 332
 Crystallinity, 337
 Cu₂O, 260
 Cuprate superconductors, 312
 Curved mirror, 32

Cuvette, 305
 Cyanobiphenyl, 304
 Cyclohexane, 306, 308
 Cyclotron frequency, 289

D

Data extraction software, 346
 Decomposition into higher order modes, 41
 Deconvolution algorithms, 441
 Defocusing, 43
 Defocusing as well as tilt and offset mis-matched beams, 43
 Defocussed system, 43
 Degree of crystallinity, 334, 337
 Delay line, 3
 Delay time, 64
 Density functional theory, 166
 Dental caries, 428
 Detection bandwidth, 12
 DFT-D, 166
 DFT. *See* density functional theory
 Diatomic chain model, 157
 Dichalcogenites, 612
 Dielectric composite, 572
 Dielectric permittivity, 571, 583
 Dielectric tensor, 273, 275
 Difference frequency, 17, 24
 Difference frequency generation, 366, 621
 Differential scanning calorimetry, 211
 Diffuse visible light, 523, 525
 Dipole, 86
 Dipole moment, 312, 331
 Dirac Fermion, 263
 Disorder effects, 186
 Dispersion quality, 341
 Distortion, 36, 37, 46, 51, 52
D-matrix, 8
 Drude, 257, 259, 369
 Drude model, 256
 Drude–Lorentz model, 5, 220, 256
 Drude–Smith model, 259
 Dynamic range, 205
 Dynamical matrix, 160

E

Echelon, 374
 Eddy currents, 589, 596
 Effective, 585
 Effective magnetic permeability, 583
 Effective medium, 65, 66

- Effective medium approximation (EMA)
 - Bruggeman, 204
 - Maxwell–Garnett, 203
 - spectral quantification, 215
 - Effective medium theory
 - Maxwell Garnett, 257, 267, 268
 - Bruggemann, 257
 - Effective optical properties, 581
 - Effective permeability, 577, 578
 - Effective permittivity, 552, 553, 578
 - Effective refractive index, 583
 - Electron-hole plasma, 260
 - Electron beam lithography, 591
 - Electron-phonon coupling, 612
 - Ellipsoidal mirror, 37
 - Ellipticity, 368
 - Ellipticity angle, 275
 - EMA, 575
 - Emitter THz, 3
 - Enamel, 428
 - Energetic materials optical properties of, 500
 - Enantiomers. *See* pharmaceuticals, 210
 - Enhanced optical transmission, 555, 558
 - ErAs/GaAs superlattices, 598
 - Etalon, 81, 82, 90, 202
 - Etalon effect, 202
 - Ethyl cyanoacrylate, 346
 - Excitons, 255, 258, 260, 265, 379
 - Experiments, 305
 - Exchange-correlation functional
 - definition of, 175
 - effect of, 175
 - Explosives THz spectra of, 514
 - Exposure, 415
 - Extinction bands, 331
 - Extinction coefficient, 60
 - Extraction algorithm, 82, 84, 92
- F**
- Fabry-Perot, 254
 - Far-field, 5
 - Faust–Henry coefficient, 374
 - Felbe, 627
 - Ferroelectric, 595, 596, 600
 - Fiber orientation, 348
 - Fill fraction, 65, 66
 - Filler concentration, 338
 - Filtered back projection, 434
 - Flash, 628
 - Focussing mirrors, 35
 - Force fields, 164
- Form birefringence, 348
 - Fourier, 64
 - Fourier transform, 3, 200
 - Fourier-transform infrared spectroscopy (FTIR), 23, 581, 582, 586
 - Four-wave mixing, 371
 - Franz–keldysh effect, 377
 - Free electron lasers, 356
 - Free electron gas, 256
 - Free volume, 336
 - Free carrier absorption, 256
 - Fresnel, 62, 63
 - Fresnel coefficients, 200
 - Fullerene, 265
- G**
- GaAs
 - nanowire, 262
 - passivation, 260
 - quantum well, 258
 - Gas laser, 459
 - Gas target, 359
 - GaSe, 364, 622
 - Gaussian beam mode analysis, 30, 32, 48, 51, 54
 - Gaussian beam mode, 30, 32, 49
 - Gaussian beam telescope, 33, 35
 - Gaussian beam, 31, 32, 33, 39, 41, 43
 - Gaussian–Hermite modes, 45, 46
 - Gaussian–Laguerre modes, 47
 - Gaussicity, 42, 47, 51, 52
 - Geometrical optics, 29, 32, 33, 49, 51
 - Geometrical theory of diffraction (GTD), 49
 - Glass transition temperature, 336
 - Glass transition, 335
 - Glasses, 217
 - Glass-fiber-reinforced components, 349
 - Golay detector, 24
 - Graphite, 263
 - Graphene, 263, 264
 - Gunn diode, 18
- H**
- Harmonic oscillator, 576
 - Half-wave plate, 40
 - HDPE, 337
 - Heated cathode, 19
 - Hertz vector, 86
 - Heterodyne radiometer, 503
 - Heterogeneous dielectric mixtures, 340

H (*cont.*)

- High- and low-pass filters, 40
- High Tc superconductors, 614
- High-, linear low-, and low-density polyethylene (HD-, LLD-, LDPE), polypropylene (PP), polymethylpentene (PMP, brand name: TPX), polystyrene (PS), polytetrafluorethylene (PTFE), polyvinylidene fluoride (PVDF), polymethylmethacrylate (PMMA), polycarbonate (PC), polyoxymethylene (POM), polyamide 6 (PA6), polyvinyl chloride (PVC), 333
- High-density polyethylene (HDPE), 334
- Higher order Gaussian beam modes, 42, 45, 47
- Higher order mode decomposition, 46
- High-temperature superconductivity, 383
- Hole array, 553–558, 560–562, 564
- Homogenous, 418
- Homogenization, 577, 580, 585
- Horn antenna, 39, 41, 50
- Horn beams, 42
- Hot electron bolometre, 24
- Hydrogen bonding, 172, 335
- Hydrophilic polymers, 343

I

- Idler beam, 17
- Image fusion, 514
- Imaging radar, 512
- Imaging
 - coating thickness, 470
 - nondestructive testing. *See* nondestructive testing
 - pharmaceutical, 460
 - pharmaceutical tablets, 478
 - signal processing. *See* signal processing
 - tablets coatings, 468
- Impatt diode, 18
- Index ellipsoid model, 348
- Identification of
 - biomolecules, 207
 - cocrystals, 210
 - drugs, 208
 - explosives, 215
 - hydrates, 211
 - pigments, 216
 - polymorphs, 208
 - semiconductors, 216
 - small organic molecular crystals, 208
- Inductive plasma etching, 591

- Infrared false colour, 523
- Infrared imaging, 523, 524
- Infrared reflectography, 524, 524
- InGaAs
 - quantum post, 262
 - quantum dot, 262
- Inhomogenous, 418
- Injector, 22
- Ink-jet printing, 592
- In-line measurements, 341
- InP
 - nanoparticle, 261
 - phonon–plasmon modes, 260
- Inspection of plastic weld joints, 344
- Intensity, 61
- Interactions
 - intramolecular, 162
 - electrostatic, 162
 - London forces, 163
 - repulsion–dispersion, 163
- Inter- and intramolecular vibrations, 329
- Interface index, 473
- Inverse filtering. *See* signal processing inverse filtering, 466
- Invivo, 428
- Ionic raman scattering, 624
- Isolated molecule calculation, 152

J

- Jahn-teller distortion, 619
- Josephson plasma waves (j. Orensteina and j. Millis), 614

K

- Kaolinite, 184
- Kramers-Kronig, 67

L

- La_{1/2}/Sr_{3/2}/MnO₄, 618
- Ladder climbing, 381
- Landau level, 21
- Larmor formula, 627
- Laser cutting, 592
- Laser writing, 590, 591
- Lattice modes, 334
- Lens, 37, 35, 51
- Lens parameters, 50
- Length scale, 572
- Light line, 545, 554

LiNbCo₃, 11, 364, 613
Line shape, 196, 197
Linearity of detection, 368
Liquid crystal polymers (LCPS), 349
Lithium niobate, 11
Lithography, 590
LLDPE/Mg(OH)₂, 339
Local density approximation, 166
Localisation, 268
Local field, 577
Local oscillator, 24
Log-spiral antenna, 16
Lorentz force, 571
Lorentzian functions, 161
LO-TO splitting, 182
Low-loss polymers, 331
LT-GaAs, 5

M

Macroscopic, 306
Magnetic permeability, 571
Magneto-optical Kerr effect, 280, 371
Magnon, 382
Magneto-optical effects, 273
Magnetoplasma resonance, 289
Manganites, 617
Maximum entropy method, 74
Maxwell Garnett, 58, 65
Maxwell–Garnett model, 340, 572, 575
Maxwell–Lorentz equations, 570
Mechanical misalignment, 43
MEH-PPV, 265
Meta-atoms, 572
Metal chiral structures, 277
Metal-dielectric composite, 574
Metal-insulator transitions, 383
Metamaterial, 61, 542, 560, 561, 570, 593, 595, 596, 598, 601
Metamaterial resonance, 596, 599
Mg(OH)₂, 339
Mg(OH)₂ in LLDPE, 339
Methyl methacrylate adhesive, 346
Michelson polarising interferometer, 39
Michelson, 43
Micro-bolometer THz camera, 535
Microcrystalline samples, 184
Micromachining, 590
Mid infrared spectroscopy, 210
Mie, 58, 66
Mie resonance, 578, 587, 592, 595
Mie scattering. *See* scattering

Mie theory, 577
Mismatched and defocussed system, 43, 47
Millimetre-wave portal, 506
Mirror, 47
Misplacement error, 71
Mixture, 304, 309, 310, 313
Mode-locked laser, 2
Moisture, 455
Moisture monitoring, 343
Molecular, 314
Molecular dynamics, 178
Molecular gas laser, 18
Molecular origin, 332
Monitoring the compounding process, 342
Monoatomic chain model, 156
Morphology, 332
Mott insulators, 383
Multilayered structure, 441
Multi-spectral imaging, 513

N

NaCl, 161
Nanoparticle
 CdSe, 261
 InP, 261
Nanostructure, 261
Nanowire
 core–shell, 262
 GaAs, 262
 Ge, 262
Near infrared imaging, 210
Near-field THz imaging, 210
Negative permeability, 593
Negative permittivity, 593
Negative real refractive index, 61
Negative refractive index, 569
Nematic, 303, 308
Newton-raphson, 84, 90
Niobium nitride (NBN), 601
Noise equivalent power (NEP), 492
Noise equivalent temperature difference (NETD), 492
Noncollinear optical rectification, 364
Non-collinear propagation, 364
Nondestructive testing, 453
 liquid ingress, 458
 roofing membrane, 458
 turbine blades, 456
Non-destructive, contact-free testing, 348
Nonlinear optical frequency conversion, 357
Nonlinear phononics, 623

- N** (*cont.*)
 Nonlinear THz spectroscopy, 356
 Non-polar, 331
 Norm, 71
 Normal modes
 in molecular crystals, 165
- O**
 Odd- and even, 315
 Odd number, 317
 Off-axis mirrors, 51
 Optical activity, 293
 Optical conductivity, 369
 Optical constants, 200, 202, 206
 absorption coefficient, 200
 heterogenous mixtures, 203
 multiple Reflections, 201
 refractive index, 200
 Optical kerr effect, 374
 Optical lithography, 590, 591
 Optical parametric amplifier, 618
 Optical phonon, 614
 Optical pump terahertz probe spectrometer, 253
 Optical rectification, 362, 613
 Optical switching of, 598, 599
 Optical upconversion in imaging systems, 503
 Order parameter, 317, 319, 321, 612
 Orientation, 319
 Orientation polarization, 334
 Over moded horn antennas, 50
- P**
 Parabolic mirror, 36-38, 52, 53
 Paraboloid, 37
 Paraboloidal mirrors, 54
 Paraxial wave equation, 30, 45
 Partial reflections and standing waves, 52
 Partial reflections, 35, 36, 47, 48, 54
 Passivation
 GaAs, 260
 PC, 334
 Permeability, 60
 Permittivity, 540, 546, 551, 552, 564, 577
 Permittivity and permeability, 585
 Pharmaceuticals, 192
 enantiomers, 209
 hydrates, 211
 phase transformations, 211
 polymorphism, 208
 Phase, 64, 65
 Phase curvature, 34, 46
 Phase gratings, 41
 Phase matching, 11, 17
 Phase radius of curvature, 32, 45, 46
 Phase slippage, 39, 43, 45, 46, 49
 Phase structure, 332
 Phase transformations, 211
 Phase unwrapping, 85, 86, 90
 Phase velocity, 363
 Phase-retrieval techniques, 41
 Phonon polaritons, 374, 613
 Phonons
 acoustic, 157
 optical, 157
 PO, 49
 Photo current, 5
 Photo-conductive antenna, 4
 Photoconductive switches, 357
 Photoconductivity, 254
 Photo-dember effect, 14
 Photo-induced phase transitions, 612
 Photonic crystals, 580
 Physical optics, 30, 49
 Plane wave, 82, 86, 90-92
 Plasma frequency, 256
 Plasma-based THz generation, 359
 Planar lens antennas, 53
 Plasmon, 255, 258, 259, 262, 359, 544
 Plasmonic resonance, 575, 586
 Plasmonics, 593
 Plastics, 329
 Plastic weld joints, 344
 PMMA, 334
 Pockels effect, 11
 Polar, 331
 Polarimetric devices, 602
 Polarising grid, 39
 Polarising Michelson interferometers, 39
 Polarisation, 32, 39, 40, 48, 51, 54
 Polarisation effects, 43, 48
 Polarisation behaviour, 48
 Polarisation-rotating interferometer, 40
 Polaritonic compounds, 595
 Polarization, 7, 17, 349
 Polarization azimuth rotation, 275
 Polarizability, 315, 317, 318, 320
 Polarization controlled THz TDS, 348
 Polarization rotation, 39
 Polarization state, 62
 Polarization-dependent THz TDS, 348
 Polder and van Santen, 340
 Polyamide (PA), 344, 335
 Polycarbonate (PC), 333, 458
 Polyethylene (PE), 303
 Polymer compound composition, 341

Polymeric compounds, 338
 Polymers
 foam insulation, 456
 methacrylate (PMMA), 334
 Polymorphism. *See* pharmaceuticals
 Polynomial, 70, 71
 Polystyrene (PS), 331
 Polyurethane, 346
 Ponderomotive potential, 376
 PP/CaCo₃, 339
 Preamplified direct detection, 504
 Pr_{1-x}Ca_xMnO₃, 617
 PS, 334
 PTFE, 335
 Pump-probe experiment, 252
 Pupil-plane image formation, 502
 PVC, 335
 PVDF, 337
 Pyroelectric detector, 23

Q

Quantitative analysis, 211
 Quantum cascade laser, 22, 262, 460, 561
 Quantum dot
 ErAs, 262
 Quantum dot
 CdSe, 261
 InGaAs, 262
 Quantum post
 InGaAs, 262
 Quantum wells, 379
 Quantum wire
 InGaAs, 262
 Quarter-wave plate, 40
 Quartz, 90
 Quasi space, 347
 Quasi-optical circuits, 39

R

Rabi flopping, 380
 Radiometric contrast, 493
 Radon conversion, 434
 Raking visible light, 523
 Raman imaging, 210
 Raman scattering, 356, 380
 Raman spectroscopy, 207, 209, 211, 221
 Rayleigh scattering. *See* scattering Rayleigh
 Reactive ion etching, 591
 Reactive plasma etching, 574
 Real time imaging, 459
 Recapture time, 7
 Receiver THz, 3

Reconfigurable, 595, 596
 Reconfigurable anisotropic metamaterials, 601
 Reflectance, 584
 Reflectarray, 502
 Reflection, 70
 Re-focussing mirrors, 36
 Refractive index, 81, 331, 493, 530
 Refractive index oscillations, 92
 Refractive index. *See* optical constants
 Reinforced plastics, 348
 Relaxation, 304
 Resolution, 419
 Roof mirror, 39, 40
 Rigid molecule approximation, 165
 Rydberg atoms, 358

S

Sample holder
 pellet, 199
 poly tetrafluoroethylene (PTFE), 199
 polyethylene (PE), 196
 Sample preparation, 416
 Scattering, 46, 47, 498
 Christiansen effect, 196
 Mie, 196
 Rayleigh, 196
 Scattering matrix, 47, 48
 Sample preparation
 Polyethylene (PE), 199
 pellet, 199
 Poly(tetrafluoroethylene) (PTFE), 199
 Scattering, in active imaging, 498
 Schottky contact, 598
 Schottky diodes, 24
 Schottky junction, 597
 Self phase modulation, 373
 Semiconductors
 inorganic, 259
 inorganic-organic hybrids, 266
 nanostructure, 261
 organic, 263
 polymers, 265
 Semiconductor failure testing, 457
 Semi-crystalline, 332
 Semi-crystalline morphology, 332
 Si, 260
 Signal beam, 17
 Signal processing, 464
 customised skewed gaussian filter, 467
 deconvolution, 465
 double Gaussian filter, 466
 inverse filtering, 466
 Simulations

S (*cont.*)

- atom–atom, 162
- quantum mechanical, 162
- molecular dynamics, 179
- Skeletal vibrations, 333
- Skin, 428
- Skin cancer, 415
- Small magneto-optical response approximation, 280
- Snell, 61
- Soft X-ray, 628
- Spectroscopy, 329
- Split-ring resonators (SRRs), 560, 582
- Spoof plasmon, 541, 549
- Solar cell
 - dye sensitized, 266, 268
 - polymer, 265
- Solar cell, 265
- Soot, 438
- SRRs, 586, 589–591, 593, 594, 600–602
- SrTiO₃, 587, 595, 600
- Stand-off imaging, 508
- Structure, 307
- Strongly correlated electrons, 611
- Subwavelength holes, 541, 550
- Superconductivity, 383
- Superfluid density, 616
- Superlens, 569
- Surface modes, 183
- Surface plasmon polariton, 541
- Surface-plasmon-resonance, 65
- Synchrotron radiation, 14

T

- Teflon films, 448
- Temperature, 214
- Temperature tuning, 600
- Temporal windowing, 586
- Terahertz false colour, 526, 527
- Terahertz gap, 521
- Terahertz pulsed imaging (TPI), 461
- Terahertz spectral database, 526
- Terahertz time domain spectroscopy, 302, 355
- Terahertz time-domain spectroscopy reflection imaging, 522
- Terahertz time-domain spectroscopy tomography, 523, 536
- Thermo-morphological coupling, 337
- Thick lens, 32, 35, 38, 51
- Thickness, 84
- Thin lens, 32, 35, 51
- Thin-film limit, 254
- THz device, 302

- THz field strengths, 361
- THz moisture sensors, 343
- THz nonlinear optics, 373
- THz spectroscopy, 415
- THz time domain ellipsometry, 273
- THz-pump/THz probe experiments, 370
- Ti: sapphire, 2, 313
- Tilt angle, 364
- Tilted-pulse front, 613
- Time domain spectroscopy, 550
- Time of flight terahertz tomography, 441
- Time-bandwidth product, 2
- Time-domain, 58, 63
- Time-domain THz spectroscopy (TDTS), 581, 586
- Titania(TiO₂)-loaded PP, 339
- TO phonon, 374
- Tolerance factor, 617
- Tolerancing effects, 43
- Torsional vibration, 317
- Transfer function, 83
- Transient absorption, 265
- Trans-illumination, 523, 525
- Trans-irradiance, 523, 525
- Transmittance, 584
- Transmittance and reflectance spectra, 583
- Truncated, 84
- Truncation, 39, 46, 47, 51, 52, 54
- Tunability, 593
- Tuning of, 596
- Two-fluid model, 615
- Two-phase composite, 65, 66
- Two-photon absorption, 364

U

- Ultraviolet fluorescence, 523, 524
- Unambiguous range resolution, 497
- Undulator, 626, 627
- Unit cell, 572

V

- Vandermonde, 77
- Vibrations, 309
- Vibrational density of states, 218
- VO₂, 593, 601
- Volume filling fraction, 574

W

- Walk-off length, 10, 12
- Water absorption, 344
- Water content, 344

Wave equation, [60](#)
Waveguide spectroscopy, [214](#)
Wave impedance, [583](#)
Wave plates, [602](#)
Wavevector, [155](#)
White light continuum, [251](#)
Wiener, [66](#)
Wiener deconvolution, [442](#)
Wiggler, [20](#)
Wire-grid polarizer, [274](#)
Wood plastic composite (WPC), [344](#)
Wood water content, [533](#)
Woods anomalies, [542](#)

X

X-ray diffraction, [208](#), [210](#), [217](#)

X-ray fluorescence, [525](#)
X-ray lithography, [591](#)
X-ray radiography, [523](#), [525](#)

Y

Yule-walker, [76](#)

Z

Zenneck wave, [541](#), [545](#), [548](#)
Zero-bias diode, [505](#)
ZnO, [266–268](#)
Zinc telluride, [9](#)
ZnTe, [363](#)
Z-scan, [368](#)